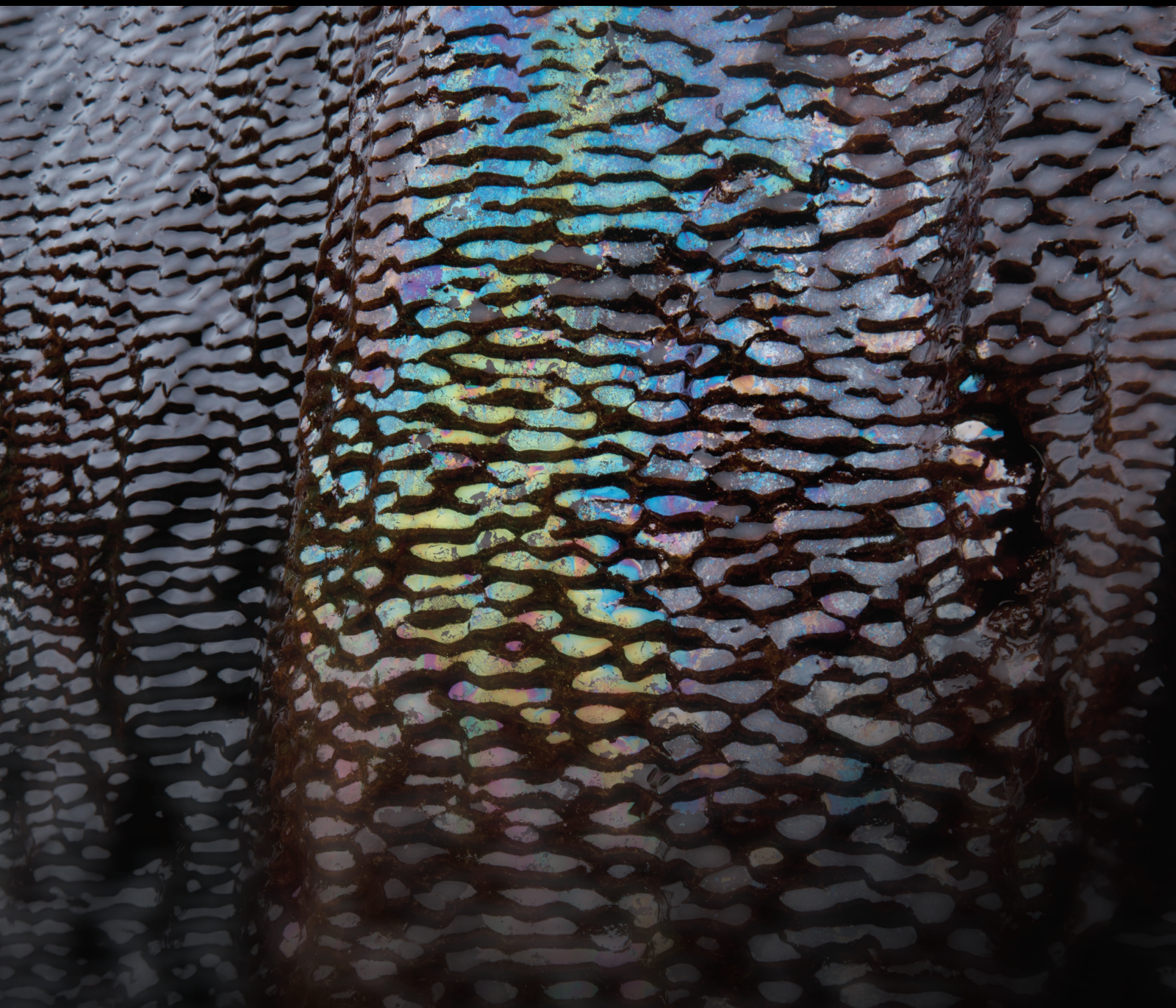


Mechanisms of Shale Oil and Gas Accumulation

Lead Guest Editor: Kun Zhang

Guest Editors: Haikuan Nie, Shu Jiang, Zhiye Gao, and Dongdong Liu



Mechanisms of Shale Oil and Gas Accumulation

Geofluids

Mechanisms of Shale Oil and Gas Accumulation

Lead Guest Editor: Kun Zhang

Guest Editors: Haikuan Nie, Shu Jiang, Zhiye Gao,
and Dongdong Liu







Copyright © 2022 Hindawi Limited. All rights reserved.

This is a special issue published in "Geofluids." All articles are open access articles distributed under the Creative Commons Attribution License, which permits unrestricted use, distribution, and reproduction in any medium, provided the original work is properly cited.



























Chief Editor

































Umberta Tinivella, Italy

Associate Editors

Paolo Fulignati , Italy
Huazhou Li , Canada
Stefano Lo Russo , Italy
Julie K. Pearce , Australia

Academic Editors

Basim Abu-Jdayil , United Arab Emirates
Hasan Alsaedi , USA
Carmine Apollaro , Italy
Baojun Bai, USA
Marino Domenico Barberio , Italy
Andrea Brogi , Italy
Shengnan Nancy Chen , Canada
Tao Chen , Germany
Jianwei Cheng , China
Paola Cianfarra , Italy
Daniele Cinti , Italy
Timothy S. Collett , USA
Nicoló Colombani , Italy
Mercè Corbella , Spain
David Cruset, Spain
Jun Dong , China
Henrik Drake , Sweden
Farhad Ehya , Iran
Lionel Esteban , Australia
Zhiqiang Fan , China
Francesco Frondini, Italy
Ilaria Fuoco, Italy
Paola Gattinoni , Italy
Amin Gholami , Iran
Michela Giustiniani, Italy
Naser Golsanami, China
Fausto Grassa , Italy
Jianyong Han , China
Chris Harris , South Africa
Liang He , China
Sampath Hewage , Sri Lanka
Jian Hou, China
Guozhong Hu , China
Lanxiao Hu , China
Francesco Italiano , Italy
Azizollah Khormali , Iran
Hailing Kong, China

Karsten Kroeger, New Zealand
Cornelius Langenbruch, USA
Peter Leary , USA
Guangquan Li , China
Qingchao Li , China
Qibin Lin , China
Marcello Liotta , Italy
Shuyang Liu , China
Yong Liu, China
Yueliang Liu , China
Constantinos Loupasakis , Greece
Shouqing Lu, China
Tian-Shou Ma, China
Judit Mádl-Szonyi, Hungary
Paolo Madonia , Italy
Fabien Magri , Germany
Micòl Mastrocicco , Italy
Agnes Mazot , New Zealand
Yuan Mei , Australia
Evgeniy M. Myshakin , USA
Muhammad Tayyab Naseer, Pakistan
Michele Paternoster , Italy
Mandadige S. A. Perera, Australia
Marco Petitta , Italy
Chao-Zhong Qin, China
Qingdong Qu, Australia
Reza Rezaee , Australia
Eliahu Rosenthal , Israel
Gernot Rother, USA
Edgar Santoyo , Mexico
Mohammad Sarmadivaleh, Australia
Venkatramanan Senapathi , India
Amin Shokrollahi, Australia
Rosa Sinisi , Italy
Zhao-Jie Song , China
Ondra Sracek , Czech Republic
Andri Stefansson , Iceland
Bailu Teng , China
Tivadar M. Tóth , Hungary
Orlando Vaselli , Italy
Benfeng Wang , China
Hetang Wang , China
Wensong Wang , China
Zhiyuan Wang , China
Ruud Weijermars , Saudi Arabia

Bisheng Wu , China
Da-yang Xuan , China
Yi Xue , China
HE YONGLIANG, China
Fan Yang , China
Zhenyuan Yin , China
Sohrab Zendeboudi, Canada
Zhixiong Zeng , Hong Kong
Yuanyuan Zha , China
Keni Zhang, China
Mingjie Zhang , China
Rongqing Zhang, China
Xianwei Zhang , China
Ye Zhang , USA
Zetian Zhang , China
Ling-Li Zhou , Ireland
Yingfang Zhou , United Kingdom
Daoyi Zhu , China
Quanle Zou, China
Martina Zucchi, Italy



Contents

Retracted: Enrichment Factors and Resource Potential Evaluation of Qingshankou Formation Lacustrine Shale Oil in the Southern Songliao Basin, NE China

Geofluids



Retraction (1 page), Article ID 9798084, Volume 2022 (2022)

Analysis of Sedimentary Environment Conditions for Lacustrine Fine-Grained Sedimentary Rocks and Its Control of Lithofacies Development: A Case Study of the Lower Submember of Member 3 of Shahejie Formation in FY-1 Well, Dongying Sag, Bohai Bay Basin, China

Jun Peng , Ledan Yu , Tianyu Xu, Yubin Wang, and Haodong Han


Research Article (16 pages), Article ID 6640706, Volume 2021 (2021)

Sedimentary Facies of the Longmaxi Formation Shale Gas Reservoir in the Weiyuan Area Based on Elemental Characteristics

Yijia Wu , Hongming Tang , Ying Wang , Jing Li , Yanxiang Zeng , Songlian Jiang , and Yongcheng Mu 


Research Article (17 pages), Article ID 5021298, Volume 2021 (2021)

Effect of Shale Sample Particle Size on Pore Structure Obtained from High Pressure Mercury Intrusion Porosimetry

Zhiye Gao , Longfei Duan, Qinrong Hu , Shuling Xiong, and Tongwei Zhang


Research Article (15 pages), Article ID 5581541, Volume 2021 (2021)

Mineral Heterogeneity Characterization of the Lacustrine Yanchang Shales, Ordos Basin Using Micro-Fourier Transform Infrared Spectroscopy (Micro-FTIR) Technique

Bing Luo, Zhiguo Shu, Yalin Chen, Zhuo Li , Yufei Hou, Liwei Wang, Youdong Yang, and Zhikai Liang

Research Article (10 pages), Article ID 5585701, Volume 2021 (2021)

Jurassic Terrestrial Shale Gas Potential of the Northern Kashi Sag in the Tarim Basin, Northwestern China

Wei Wu, Zhiwei Liao , Honghan Chen, Shaohu Li, Ao Su, Irshad Hussain, and Niubin Zhao


Research Article (16 pages), Article ID 5542447, Volume 2021 (2021)

Genetic Types and Main Control Factors of Microfractures in Tight Oil Reservoirs of Jimsar Sag

Xiangye Kong , Jianhui Zeng , Xianfeng Tan , Haowei Yuan, Dan Liu, Qun Luo, Qianyou Wang, and Rusi Zuo


Research Article (19 pages), Article ID 5558551, Volume 2021 (2021)

Characteristics of Organic Macerals and Their Influence on Hydrocarbon Generation and Storage: A Case Study of Continental Shale of the Yanchang Formation from the Ordos Basin, China

Lei Xiao, Zhuo Li , Yufei Hou, Liang Xu, Liwei Wang, and Youdong Yang



Research Article (17 pages), Article ID 5537154, Volume 2021 (2021)

Slope Belts of Paleouplifts Control the Pore Structure of Organic Matter of Marine Shale: A Comparative Study of Lower Cambrian Rocks in the Sichuan Basin

Pengfei Wang, Chen Zhang, Aoran Liu , Pengfei Zhang, Yibo Qiu, Xin Li, Shanshan Yu, Shuqing Yao, Sanyi Liu, and Zhenxue Jiang

Research Article (18 pages), Article ID 5517655, Volume 2021 (2021)

A Study on Astronomical Cycle Identification and Environmental Response Characteristics of Lacustrine Deep-Water Fine-Grained Sedimentary Rocks: A Case Study of the Lower Submember of Member 3 of Shahejie Formation in Well Fanye-1 of Dongying Sag, Bohai Bay Basin, China

Ledan Yu , Jun Peng , Tianyu Xu, Yubin Wang, and Haodong Han



Research Article (15 pages), Article ID 5595829, Volume 2021 (2021)

Geochemical Characteristics of the Middle Devonian Dacaozi-Tanshanping Shale Strata in the Yanyuan Basin, Southwest China: Implications for Organic Matter Accumulation and Preservation

Ziya Zhang , Wei Yang , Xingyu Li , Yan Song, Zhenxue Jiang, and Qun Luo





Research Article (24 pages), Article ID 5586065, Volume 2021 (2021)

Evaluation of Favorable Shale Gas Intervals in Dawuba Formation of Ziyun Area, South Qian Depression

Kun Yuan , Wenhui Huang, Xinxin Fang , Ting Wang, Tuo Lin, and Rong Chen




Research Article (19 pages), Article ID 6688141, Volume 2021 (2021)

Research on the Oil-Bearing Difference of Bedding Fractures: A Case Study of Lucaogou Formation in Jimsar Sag

Jia Lu , Chen Zhang , Jianhui Zeng , and Haowei Yuan 






Research Article (21 pages), Article ID 5567491, Volume 2021 (2021)

Petrographic Characterization and Maceral Controls on Porosity in Overmature Marine Shales: Examples from Ordovician-Silurian Shales in China and the U.S.

Lin Wei , Shasha Sun , Dazhong Dong, Zhensheng Shi, Jia Yin, Shudi Zhang, Maria Mastalerz , and Xiong Cheng


Research Article (31 pages), Article ID 5582262, Volume 2021 (2021)

Early Paleozoic Extension-Compression Transition and Formation of a Paleo-Oil Reservoir System in the NW Sichuan Basin: Implications for Deeply Buried Hydrocarbon Accumulation

Xiao Liang , Shu-gen Liu , Liang-liang Wu , Bin Deng , Jing Li , Meng-lin Zhang , and Xu-hang Tan 

Research Article (25 pages), Article ID 5538174, Volume 2021 (2021)




Three-Dimensional Morphology and Connectivity of Organic Pores in Shale from the Wufeng and Longmaxi Formations at the Southeast Sichuan Basin in China

Tao Jiang , Zhijun Jin, Zongquan Hu, Wei Du, Zhongbao Liu, and Jianhua Zhao



Research Article (14 pages), Article ID 5579169, Volume 2021 (2021)

Contents



Quantitative Characterization and Determination of the Main Factors That Control Fracture Development in the Lower Paleozoic Shale in Southeastern Chongqing, China

Zhiping Zhang, Xiangye Kong , Qing Chen , Ye Zhang, Zhi Deng, Chuan Yu, Zhian Lei, Haijie Zhang, Xiaofeng Wang, Guanghua Yao, Licheng Yang, and Xianfeng Tan 
Research Article (11 pages), Article ID 5591681, Volume 2021 (2021)

Characteristics and Origin of Methane Adsorption Capacity of Marine, Transitional, and Lacustrine Shales in Sichuan Basin, China

Xianglu Tang , Wei Wu, Guanghai Zhong, Zhenxue Jiang , Shijie He, Xiaoxue Liu, Deyu Zhu, Zixin Xue, Yuru Zhou, and Jiaping Yang
Research Article (12 pages), Article ID 6674815, Volume 2021 (2021)

Characteristics of Hydration Damage and Its Influence on Permeability of Lamellar Shale Oil Reservoirs in Ordos Basin

Pengfei Zhao , Xiangyu Fan, Qiangui Zhang , Bowei Yao, Mingming Zhang, Liang He, Yu Qiang, and Jinhua Liu
Research Article (15 pages), Article ID 6646311, Volume 2021 (2021)

A Comparative Study of the Micropore Structure between the Transitional and Marine Shales in China

Pengfei Jiao , Genshun Yao, Shangwen Zhou , Zhe Yu, and Shiluo Wang
Research Article (14 pages), Article ID 5562532, Volume 2021 (2021)









Organic-Inorganic Geochemical Characteristics of the Upper Permian Pusige Formation in a High-Saline Lake Basin, Tarim Basin: Implications for Provenance, Paleoenvironments, and Organic Matter Enrichment

Jingbin Wang , Zhiliang He , Dongya Zhu , Zhiqian Gao, Xiaowei Huang, and Quanyou Liu
Research Article (26 pages), Article ID 6651747, Volume 2021 (2021)


Pore Space Reconstruction of Shale Using Improved Variational Autoencoders

Yi Du, Hongyan Tu, and Ting Zhang 
Research Article (11 pages), Article ID 5545411, Volume 2021 (2021)



Pore Properties of the Lacustrine Shale in the Upper Part of the Sha-4 Member of the Paleogene Shahejie Formation in the Dongying Depression in East China

Ziyi Wang , Liuping Zhang , Yuan Gao , Wenxiu Yang , Yongshi Wang , Huimin Liu , Zhaoyang Li , and Shanshan Zhou 
Research Article (20 pages), Article ID 6616843, Volume 2021 (2021)

Experimental Studies on Shale Cracks and Permeability Evolution Based on Acoustic Emission Monitoring



Hao Chen , Hongkui Ge , Xiaoqiong Wang , Jianbo Wang , and Shan Wu 
Research Article (16 pages), Article ID 6620538, Volume 2021 (2021)

Genesis of Dolomite in Middle Permian Maokou Formation in Eastern Sichuan: Constraints from *In Situ* Geochemistry, Sr-Mg Isotopes, and Fluid Inclusions

Yanxia Jiang, Xianfeng Tan , Chengjiang Zhang, Wei Jiang, Jia Wang, Long Luo , Dongping Tan, Wei Wang, and Zhifu Xiong








Research Article (22 pages), Article ID 6611140, Volume 2021 (2021)

[Retracted] Enrichment Factors and Resource Potential Evaluation of Qingshankou Formation Lacustrine Shale Oil in the Southern Songliao Basin, NE China

Long Luo , Dongping Tan, Xiaojun Zha, Xianfeng Tan , Jing Bai, Cong Zhang, Jia Wang, Lei Zhang, and Xuanbo Gao



Research Article (1 page), Article ID 6645467, Volume 2021 (2021)

Impact of Geological Factors on Marine Shale Gas Enrichment and Reserve Estimation: A Case Study of Jiaoshiba Area in Fuling Gas Field

Siyu Yu , Xixin Wang , Shaohua Li, Yuming Liu , Liming Xiao , Xin Liu , Wen Zhao , and Jiaen Zhang 

Research Article (9 pages), Article ID 6637360, Volume 2021 (2021)

Coevolutionary Dynamics of Organic-Inorganic Interactions, Hydrocarbon Generation, and Shale Gas Reservoir Preservation: A Case Study from the Upper Ordovician Wufeng and Lower Silurian Longmaxi Formations, Fuling Shale Gas Field, Eastern Sichuan Basin

Zhijun Jin , Haikuan Nie, Quanyou Liu, Jianhua Zhao, Ruyue Wang , Chuanxiang Sun, and Guanping Wang

Research Article (21 pages), Article ID 6672386, Volume 2020 (2020)

Retraction

Retracted: Enrichment Factors and Resource Potential Evaluation of Qingshankou Formation Lacustrine Shale Oil in the Southern Songliao Basin, NE China

Geofluids

Received 2 June 2022; Accepted 2 June 2022; Published 12 December 2022

Copyright © 2022 Geofluids. This is an open access article distributed under the Creative Commons Attribution License, which permits unrestricted use, distribution, and reproduction in any medium, provided the original work is properly cited.

Geofluids and the authors have retracted the article. “Enrichment Factors and Resource Potential Evaluation of Qingshankou Formation Lacustrine Shale Oil in the Southern Songliao Basin, NE China” [1]. The data presented is the result of a collaboration by Jilin Oilfield, China Geological Survey and Northeast Petroleum University. The authors did not obtain permission from all data owners before publication, and therefore the article has been retracted and removed. The retraction and removal has been approved by the Chief Editor of the journal. The authors agree to the retraction and the notice.

References

- [1] L. Luo, D. Tan, X. Zha et al., “Enrichment Factors and Resource Potential Evaluation of Qingshankou Formation Lacustrine Shale Oil in the Southern Songliao Basin, NE China,” *Geofluids*, vol. 2021, Article ID 6645467, 20 pages, 2021.

Research Article

Analysis of Sedimentary Environment Conditions for Lacustrine Fine-Grained Sedimentary Rocks and Its Control of Lithofacies Development: A Case Study of the Lower Submember of Member 3 of Shahejie Formation in FY-1 Well, Dongying Sag, Bohai Bay Basin, China

Jun Peng ¹, Ledan Yu ¹, Tianyu Xu,¹ Yubin Wang,¹ and Haodong Han²

¹School of Geoscience and Technology, Southwest Petroleum University, Chengdu, Sichuan, 610500, China

²Chengdu Geological Survey Center, China Geological Survey, Chengdu, Sichuan, 610081, China

Correspondence should be addressed to Ledan Yu; yldxsyhxs@126.com

Received 30 November 2020; Accepted 17 August 2021; Published 13 September 2021

Academic Editor: Julie Pearce

Copyright © 2021 Jun Peng et al. This is an open access article distributed under the Creative Commons Attribution License, which permits unrestricted use, distribution, and reproduction in any medium, provided the original work is properly cited.

In recent years, the studies on fine-grained sedimentation mainly focus on the rock type, sedimentary environment, sedimentation, and sequence stratigraphy, while those on the relationship between sedimentary environment and lithofacies development are rare. However, a clear understanding on the relationship is of great significance to the muddy shale oil and gas exploration. This paper studied the muddy shale of semideep and deep lacustrine facies in the lower submember of Member 3 of Shahejie Formation in FY-1 Well, Dongying Sag, Bohai Bay Basin, East China. Based on geochemical data, the sedimentary environment media conditions and vertical changes of this submember were analyzed by means of core description, thin section authentication, X-ray diffraction (XRD), and other technologies, and the relationship between sedimentary environment and lithofacies development was discussed. The results show that this environment underwent three stages and is featured by cyclicity. From the bottom up, it experienced the semideep, deep, and deep/semideep waters under the relatively dry-cold/relatively warm-wet, warm-wet, and warm-wet/relatively warm-wet paleoclimates, respectively. Correspondingly, the paleoredox transited three stages from reducibility to high reducibility to high reducibility/reducibility; the paleosalinity changed from saline water to brackish water to brackish/saline water. Paleoproductivity was low/relatively high at the beginning, then became high, and finally relatively high. In this submember, the lithofacies primarily includes organic-rich mudstone, organic-rich lime mudstone, organic-rich lime-bearing mudstone, and organic-contained argillaceous limestone/lime mudstone. The sedimentary environment controls the mineral composition and content in the lithofacies and thus determines the lithofacies types. Meanwhile, the cyclicity of environmental change not only leads to that of the lithofacies development but also affects the positions of the lithofacies and its assemblages in sequence stratigraphic framework.

1. Introduction

Fine-grained sediments refer to the clayey and silty ones with the diameter less than $62\ \mu\text{m}$, mainly containing pyrites, organic matters, and clay, felsic, and carbonate minerals [1, 2]. The fine-grained sedimentary rock (also known as the muddy shale) is composed of fine-grained sediments, and it covers about two-thirds of the sedimentary rocks [3]. The organic-rich fine-grained rock in deep water is a crucial

source rock and has become a key object in unconventional oil and gas exploration [3–7]. Many scholars' studies on fine-grained sedimentation have focused on mineral composition, rock type, sedimentary environment, and the properties of source-reservoir-cap assemblages of oil and gas [8–12]. Their achievements in the field have promoted the development of fine-grained sedimentology. However, it is still a worldwide scientific challenge to classify and describe the fine-grained sedimentary environment precisely due to

the complex formation mechanism and various lithofacies types of these sediments. Besides, the relationship between this environment and the lithofacies is rarely studied. Thus, the environment cannot be analyzed rapidly and accurately according to lithofacies types. In view of this, it is essential to probe into its sedimentary environment media conditions and figure out its control effect on lithofacies development so as to lay a solid geological theory foundation for the unconventional muddy shale oil and gas exploration.

The sedimentological and geochemical indicators preserved in sedimentary strata can reflect the change of the sedimentary environment. Armstrong et al. and Yuri et al. studied the redox property and salinity by mineral composition and geochemical and palaeontological methods [13, 14]. Romero and Slatt and Rodriguez found that for fine-grained rocks in deep water, the hydrocarbon generation potential $((S_1 + S_2)/TOC)$ also reflected the water depth and redox property, and its content was positively correlated with the two factors [10, 15]. Guo et al. indicated that the climate changed with alternating wet and dry conditions in Member 3 of Hetaoyuan Formation in BY-1 Well of the Biyang Sag. The research region was divided into 7 high-frequency cycles according to four substitutive indicators, i.e., paleoclimate, paleosalinity, paleoproductivity, and paleoredox [16]. Pang et al. classified the lithofacies in the upper submember of Member 4 and the lower submember of Member 3 of Shahejie Formation in FY-1 Well into 11 types and divided the paleoenvironmental evolution of 6 stages [17]. Wang et al. studied the fine-grained sedimentary system of lacustrine shale through core description, thin section observation, and geochemical tests. It is considered that the mud shale from the upper submember of Member 4 and lower submember of Member 3 of Shahejie Formation in Jiyang depression is a product of the combined action of mechanical and biochemical mixed sedimentation under the relatively stable water environment [18]. Shi et al. combined sedimentological and geophysical methods such as field section measurements, core analyses, well logs, and seismic section interpretation to study the sedimentary evolution from the middle Permian to the early Triassic. In addition, provenance analysis was performed for the sediments from both flanks of the Bogda Mountain [19]. Shi et al. used the outcrops in the north rim of the Bogda Mountain, cores, seismic, drilling, and logging data of the Fukang and Jimusar sag to illuminate the middle Permian-lower Triassic stratigraphic distribution, characteristics of sedimentary facies, and climate change in the Bogda region. Based on the above research, a tectono-climate-sedimentary evolution of the middle Permian to early Triassic can be rebuilt [20]. Previous research has been centered on the mineral composition, rock type, and sedimentary environment [8–12], of which the third one is studied mostly based on geochemical indicators rather than sedimentological ones. Besides, there are rare studies on the relationship between this environment and the lithofacies. Therefore, the sedimentological and geochemical indicators, which are sensitive to the sedimentary environment, were used in this paper comprehensively to clarify the characteristics of this environment and its control of lithofacies development, which will be helpful to further

understand the sedimentary rule of fine-grained sedimentary rocks.

There is a large set of such rocks in the Paleogene Shahejie Formation, Dongying Sag, Bohai Bay Basin, where the oil and gas resources are abundant, showing a high exploitation level [17, 21–23]. Meanwhile, the rock cores from cored wells and the test materials (thin sections, XRD, elements, and organic geochemistry) are complete, making it the best region to study the sedimentary environment and its relationship with lithofacies development. In recent years, scholars have made great progress in this set of fine-grained sedimentary rocks, which promotes shale oil and gas exploration. However, rare studies are conducted on the environment of fine-grained lacustrine rocks whose lithology changes frequently and its control of the lithofacies. Based on previous studies, the lower submember of Member 3 of Shahejie Formation in FY-1 Well of the Dongying Sag was taken for an example in this paper to analyze the sedimentary environment media conditions and vertical changes, discuss the relationship between sedimentary environment and lithofacies development, and clarify the control mechanism of this environment on different lithofacies types. Technical methods including core observation, thin section authentication, and XRD were utilized in combination with information such as sedimentological indicators and geochemical analysis. The research achievements are conducive to the unconventional muddy shale oil and gas exploration, showing a theoretical significance to the fine-grained sedimentology.

2. Geological Setting

2.1. Structural-Sedimentary Evolution Characteristics. Bohai Bay Basin is located in East China. It is a Mesozoic-Cenozoic fault basin that developed in North China Plate after Paleozoic Sedimentation and Movements during Indosinian and Yanshan periods (Figures 1(a) and 1(b)) [24–26]. Jiyang depression locates in the southeast of this basin and developed four secondary sags, i.e., Chezhen Sag, Zhanhua Sag, Huimin Sag, and Dongying Sag (Figure 1(c)) [24]. Its structural evolution characteristics have been inherited by the Dongying Sag. Through multistage structural movements, the bottom of this sag develops the pre-Mesozoic basement, the middle is the layer forming in the rift stage, and the top is the one forming in the depression stage. The fault-depression stage of the structural evolution of this sag occurred in Paleogene. It is the primary extensional faulting stage when many extensional faults are developed with intense movements. Thus, a typical asymmetric dustpan-shaped sagged is formed into many salients developing around it. It is “faulted and steep in the north, and overlapped and gentle in the south.” A series of synsedimentary normal faults of the sag further divide it into four petroleum generating subsags (Boxing, Lijin, Niuzhuang, and Minfeng) and the northern steep slope zone, central anticlinal zone, southern gentle slope zone, and various fault structure zones and other secondary structural units (Figure 1(d)) [26–29].

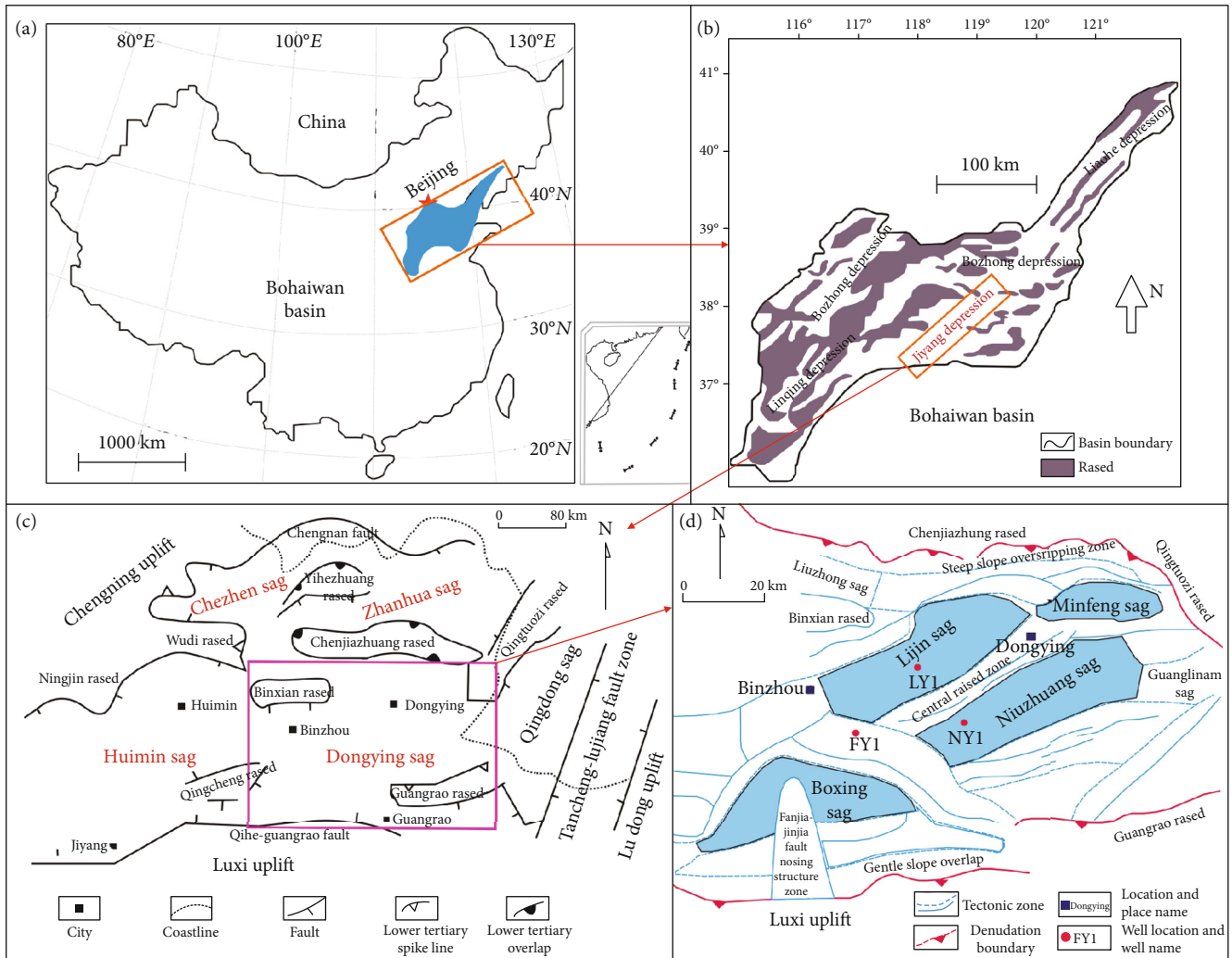


FIGURE 1: (a) Location of Bohai Bay Basin in northern China (revised by [24–26]); (b) schematic diagram of tectonic zone of Bohai Bay Basin (revised by [24, 26]); (c) regional location and schematic diagram of tectonic zone of Jiyang depression (revised by [24]); (d) well position chart and schematic diagram of tectonic zone of Dongying Sag (revised by [26–29]).

2.2. Stratum Development Characteristics. The Dongying Sag has developed Paleozoic (Pz), Mesozoic (Mz), Eocene (E), Neogene (N), and Quaternary (Q) strata from bottom to top. Thereinto, the Eocene stratum is widely distributed, with a thick sedimentary layer. The thickest part is over 7 kilometers, but it is gradually thinned and sharpened from the center of the edge. From the bottom to the top, this stratum is divided into Kongdian Formation, Shahejie Formation, and Dongying Formation, of which the Shahejie Formation includes 4 members, as shown in Figure 2 [24, 30–32]. Member 3 is characterized by the lacustrine sedimentation of dark gray and gray muddy shales, with the thickness of 700-1,000 m. The middle part is as thick as 1,200 m or above. This member is further divided into the lower, middle, and upper submembers from bottom to top. The lower one develops the deep lacustrine sedimentation of dark gray mudstone, oil shale, and grayish-brown oil shale that are interbedded in unequal thick, with a small amount of thin sand, gray limestone, and dolomite (Figure 2). The stratum of this member records how the lake

environment and climate change, so it is an ideal region to study the sedimentary environment.

3. Data and Experimental Methods

Rock core analysis by X-ray fluorescence (XRF): the rock core located in the depth of 3,052-3,251 m in the lower sub-member of Member 3 of Shahejie Formation in FY-1 Well was elaborated, and its element content was tested by the NITON XL3t-950 Handheld Mineral Element Analyzer (an instrument based on the XRF spectral analysis technology) developed by Thermo Scientific [33]. In order to ensure the data validity, the test points were spaced 2.5 cm apart according to the Nyquist sampling theorem, with each one taking 20 s [34]. In this test, mineral and soil models were adopted to measure different element contents. The former was used for major elements, while the latter was used for trace ones with the content less than 1%. This study tested Ti, Si, S, K, Ca, Fe, V, Ba, Zr, Mn, Zn, etc., to analyze the

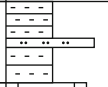
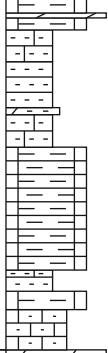
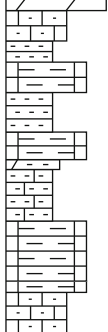
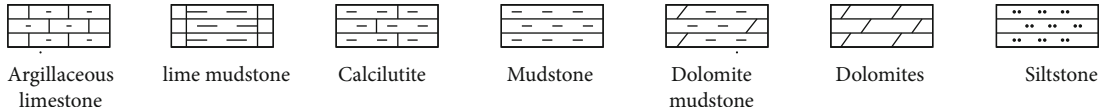
System	Stratum				Thickness (m)	Lithology	Lithology description
	Series	Group	Formation	Member			
Paleogene system	Eocene	Es (shahejie formation)	Es ₃	M	200~600		Mainly thick gray mudstone and oil mudstone with thin sand layer.
				L	100~450		Dark gray mudstone, oil mudstone and gray-brown oil shale vary in thickness, with a small amount of thin sand layer, gray limestone and dolomite.
			Es ₄	U	270~350		Dark gray, gray-brown mudstone, oil shale and thin limestone, argillaceous limestone interlayer, inclusion limestone and dolomite.
							

FIGURE 2: Characteristics of stratum development in Dongying Sag, Jiyang depression (revised by [24, 30–32]).

paleoenvironment and classified the element indicators representing the paleoclimate, paleowater depth, paleosalinity, paleoredox, and paleoproductivity in the test data [16].

Whole-rock analysis by X-ray diffraction (XRD): this is a common method to determine the mineral composition of rocks. Firstly, the rock samples were ground into grains in the size of about 5 μm or less than 200 mesh. Secondly, they were pressed and moulded and then tested to obtain the mass percentage of minerals. The TTR X-ray diffractometer manufactured by Rigaku Corporation, Japan, was adopted for the XRD test according to the industrial standard of SY/T 5163-2010 [34–36].

Total organic carbon (TOC) analysis: the dry samples were ground into grains with a diameter of 0.2 mm, and the diluted hydrochloric acid (pure hydrochloric acid: water = 1 : 7) was used to remove the inorganic carbon components. Then, these samples were burned in the high-temperature oxygen fluid (oxygen purity: 99.9%) to convert the TOC into carbon dioxide. Finally, based on the corresponding relation of carbon content between TOC and carbon dioxide, the content of the latter was detected by an infrared/thermal conductivity detector, and that of the former was calculated accordingly. The LECOCS-230 Carbon

Sulfur Analyzer was used in this test, and the test conditions refer to the national standard of GB/T 19145-2003 [34–36].

4. Results and Discussion

4.1. Paleoenvironmental Analysis. Elements, which are prevalent in various sediments, are extremely sensitive to environmental change. Their migration and enrichment rules are affected by the geological environment [37]. However, petrological and other sedimentological indicators can also reflect sensitively the condition when the sediments are formed in the lake basin [38–40]. Therefore, based on the sedimentological and geochemical indicators that reflect the lacustrine sedimentation, this paper analyzed the paleoenvironment from paleoclimate, paleowater depth, paleoredox, paleosalinity, and paleoproductivity and discussed the control effect of sedimentary environment on lithofacies development.

4.1.1. Paleoclimate. Sedimentological indicators, such as color, lithology, mineral composition, and sedimentary structure [40, 41], and geochemical ones, for example, the Na/Al [17, 27, 41–43] and dry-wet index C ($C = \frac{\sum(\text{Fe} + \text{Mn} + \text{Cr} + \text{V} + \text{Co} + \text{Ni})}{\sum(\text{Ca} + \text{Mg} + \text{Sr} + \text{Ba} + \text{K} + \text{Na})}$)

[40, 44, 45], are sensitive to the paleoclimate and thus used for the analysis.

The change of substitutive indicators for the paleoclimate in the lower submember of Member 3 of Shahejie Formation in FY-1 Well is featured with periodicity and cyclicity. Firstly, in the stage of 3,169.15-3,251 m (Stage 1, the same in the following), the light gray-gray organic-contained argillaceous limestone is developed at the bottom, with the rock core becoming gray-dark gray upward. Besides, there is a higher proportion of dark gray lime mudstone that reflects the deepening of water body. The wave structure of the calcite is occasionally seen, interbedded with a large number of arenites composed of micritic calcite [37, 46, 47]. The sedimentary structure is dominated by the flat lamina. The Na/Al value is high, showing a decreasing trend from bottom to top, while the dry-wet index (C) is low (with a mean value of 0.4), showing an increasing trend along the same direction. Besides, the calcite content is high (1%-77%), with an average value of 42.92%, but it tends to decline in this direction. The contents of clay mineral (3%-52%) and quartz (5%-36%) are low. Their mean values are 18.85% and 21.79%, respectively, showing an increasing trend. Based on the above changes, it is speculated that the environment is relatively dry and cold in this stage due to the arid climate in the upper submember of Member 4 of Shahejie Formation, but it became relatively warm and wet from the bottom up (Figures 3 and 4). Secondly, in the stage of 3,086.55-3,169.15 m (Stage 2, the same in the following), the rock core is dark gray, and the lithological characters mainly include lime mudstone, lime-bearing mudstone, and mudstone, with the massive and stratified structures developed. There are more organic matters in this stage. Meanwhile, the Na/Al value keeps decreasing, while the C value increases to 0.6. As for the mineral composition, the calcite content, ranging from 2% to 74%, shows the same trend as in Stage 1, but its mean value decreases to 36.1%. The contents of clay mineral (3%-59%) and quartz (10%-45%) increase, with their mean values rising to 25.47% and 23.95%, respectively. As shown by the change of these indicators, the climate is warm and wet in this stage (Figures 3 and 4). Finally, in the stage of 3,051-3,086.55 m (Stage 3, the same below), the rock core remains dark gray, and the lime-bearing mudstone and lime mudstone are formed. The sedimentation develops from massive structure to laminated one. In this stage, the organic matter content is still high. There is a little increase in the Na/Al, while the C value decreases to 0.5. The average content of calcite increases slightly to 36.64%, and those of clay mineral and quartz decrease to 24.91% and 19.87%, respectively. It is found from these changes that the climate remains warm and wet in Stage 3 and will become relatively warm and wet gradually (Figures 3 and 4).

According to the variation trend of sedimentological and geochemical indicators in this submember, the paleoenvironment undergoes the relatively dry-cold/relatively warm-wet climate in Stage 1, the warm-wet climate in Stage 2, and the warm-wet/relatively warm-wet climate in Stage 3.

4.1.2. Paleowater Depth. The water depth is studied based on geochemical indicators, including Th/U, Fe/Mn, $(Fe + Al)/(Ca + Mg)$, and TOC, and sedimentological ones, such

as color, lithology, and mineral composition (pyrite, carbonate mineral, and quartz) [15, 17, 27, 40, 41, 43, 44, 48–51].

In the lower submember of Member 3 of Shahejie Formation, the change of substitutive indicators for the paleowater depth is characterized by phasing and cyclicity. In the first stage, the relatively dry and cold climate becomes relatively warm and wet, and the light gray-gray rock core turns dark. The lithology is mainly the lime mudstone, and the sedimentary structure is characterized by the flat lamina. The contents of pyrite and TOC are low, and the mean value of the former is merely 2.37%. However, there is an increasing trend for them from bottom to top. The ratios of element associations, such as Fe/Mn and $(Fe + Al)/(Ca + Mg)$, are high and tend to decline when going upward. Therefore, the water is shallow in this stage, but it becomes deeper slightly in the upward direction (Figures 3 and 4). Secondly, the climate is warm and wet in Stage 2, and the rock core is mainly dark gray. Besides, the massive and stratified structures are developed, with a higher shaliness. The pyrite content continues to increase steadily, with its mean value rising from 2.37% in Stage 1 to 3.4% in this stage. The TOC content is stable, and the ratios of element associations reduce to a lower level. It can be seen from the change of all indicators that the water is deep in this stage (Figures 3 and 4). Finally, the climate becomes relatively warm and wet in the third stage. However, it is warm and wet on the whole. The rock core is mainly dark gray-gray. The sedimentation develops from a massive structure to a laminated one, with the shaliness increasing. The average pyrite content is 3.11%, and the TOC content is comparatively high. The association ratios of Fe/Mn and $(Fe + Al)/(Ca + Mg)$ increase slightly. These changes indicate that the water remains deep in this stage after the deepening in the previous one (Figures 3 and 4).

As shown by the changes of all the above indicators, the water depth evolves through 3 stages in the lake basin of the lower submember. In the first stage, there are little freshwater flows from rivers into the basin and a relatively dry/relatively warm-wet climate caused the low precipitation. Meanwhile, the water evaporates significantly, resulting in the decrease in the inflow, and the increases in drainage. Thus, the water is shallow, but it will become deep upward. The climate is warm and wet in the second stage when the water depth increases rapidly to its maximum. In the third stage, the water is still deep when the climate becomes relatively warm and wet.

4.1.3. Paleoredox. The paleoredox condition is a crucial factor affecting the preservation of organic matters, and indicators for its study include geochemistry and sedimentological indicators such as color and mineral composition [13, 14]. In this paper, geochemical indicators, V/Cr, Ni/Co, V/(V + Ni), and TOC, and sedimentological indicators, color and pyrite, were adopted for its study [15, 17, 27, 40–43, 45, 49, 52–63].

The change of all indicators for the paleoredox in the lower submember of Member 3 of Shahejie Formation is periodic and cyclic. In the first stage, the relatively dry and cold climate becomes relatively warm and wet, and the water

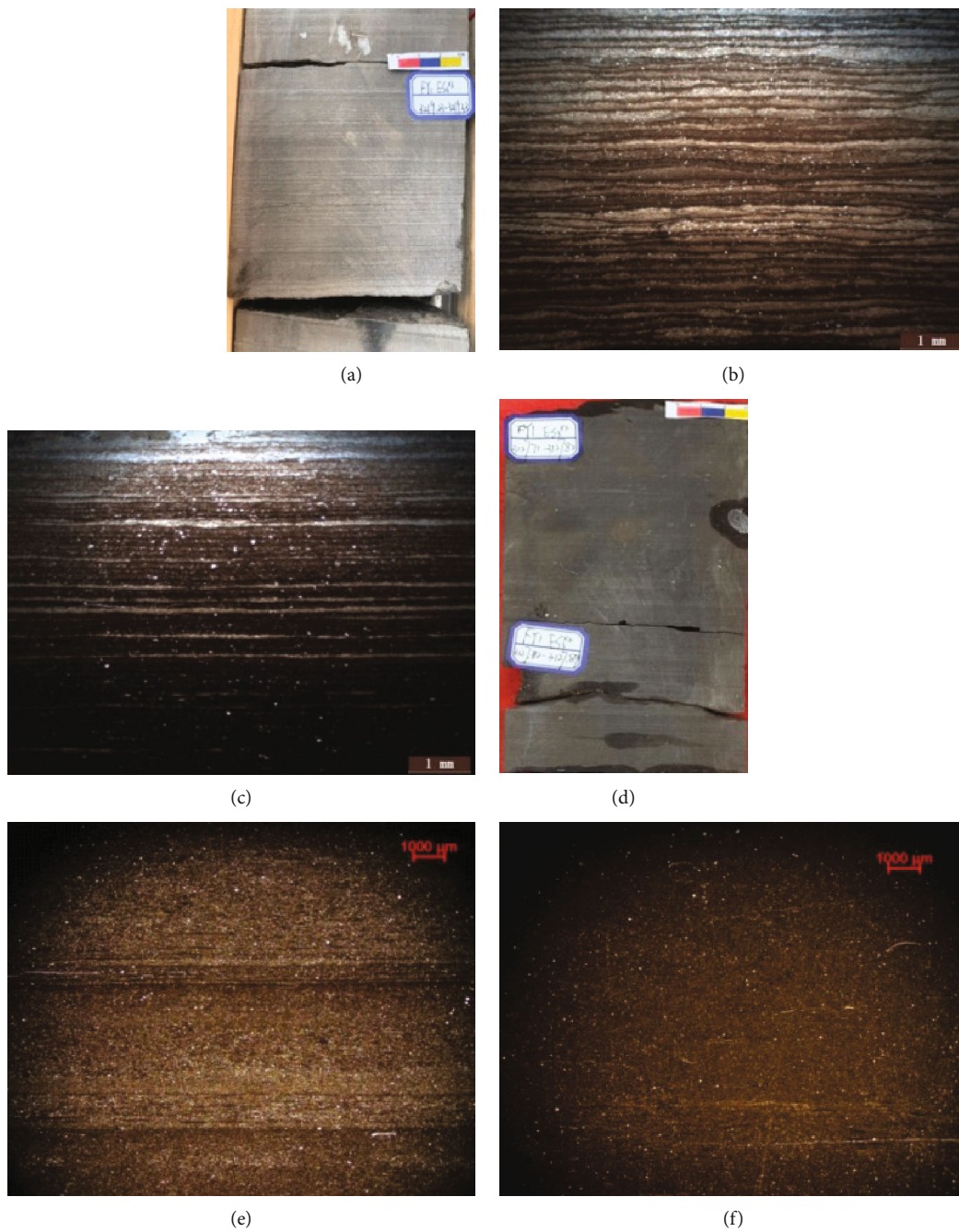


FIGURE 3: Continued.

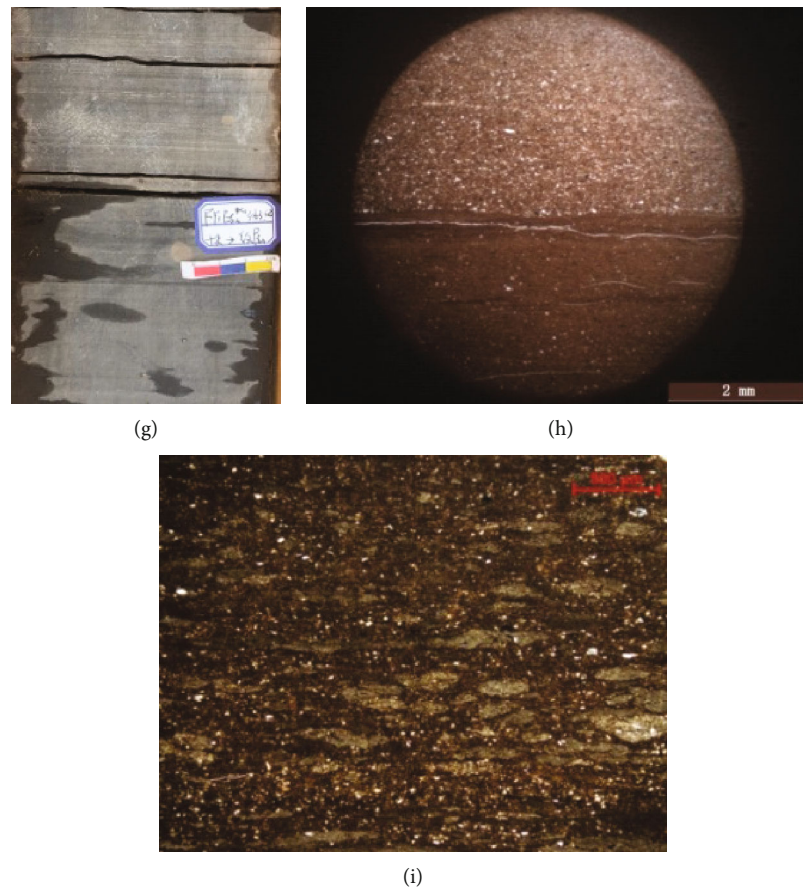


FIGURE 3: Development characteristics of fine-grained sedimentary rocks in the lower submember of Member 3 of Shahejie Formation in FY-1 Well of the Dongying Sag: (a) organic-contained lime mudstone, flat lamina, clear boundary between lime and argillaceous laminae, FY-1 Well, 3,219.23~3,219.33 m; (b) organic-contained argillaceous limestone, flat lamina, the lime lamina is thicker than argillaceous one, FY-1 Well, 3,248.44 m; (c) organic-rich lime mudstone, flat lamina, the argillaceous lamina is thicker than lime one, FY-1 Well, 3,181.17 m; (d) organic-rich lime-bearing mudstone, massive structure, FY-1 Well, 3,127.71~3,128.03 m; (e) organic-rich lime-bearing mudstone, stratified structure, FY-1 Well, 3,176.13 m; (f) organic-rich mudstone, massive structure, testa fragments, FY-1 Well, 3,123.24 m; (g) organic-contained lime mudstone, from massive structure to laminated one, FY-1 Well, 3,063.68 m; (h) from organic-rich mudstone to silty claystone, massive structure, bedded testa fragments, FY-1 Well, 3,086.12 m; (i) organic-rich lime-sand mudstone, massive structure, a large amount of arenites composed of micritic calcite, FY-1 Well, 3,080.25 m.

is shallow. The rock core is mainly light gray-gray, with a low TOC content. In this stage, the pyrite content decreases, with a mean value of 2.37%. However, it tends to rise from the bottom up. The association ratios of V/Cr, Ni/Co, and $V/(V + Ni)$ are low, with their average values being 3.43, 5.02, and 0.48, respectively. These indicators show that this stage is characterized by a weak reducing/reducing environment. Secondly, the climate is warm and wet, and the water is comparatively deep in Stage 2. In addition to a high TOC value, the pyrite content continues to increase steadily, and its mean value rises from 2.37% in Stage 1 to 3.4% in Stage 2. The above association ratios keep increasing to 4.52, 7.27, and 0.69, respectively. It can be seen from this that the water is deeper in this stage, showing a strong reducing environment. Finally, in the third stage, the climate is unchanged, and the water remains deep. The content of TOC is still high, and that of the pyrite is 3.11% averagely. The ratios of V/Cr, Ni/Co, and $V/(V + Ni)$ reduce to 4.17, 5.63, and 0.50,

respectively. According to these changes, this stage is in a strong reducing/reducing environment (Figures 3 and 5).

The variation of these indicators shows how the water body in the lake basin changes with the redox property in the lower submember of Member 3 of Shahejie Formation. Firstly, there is little river water flowing into the basin due to the low precipitation under an arid climate. In addition, evaporation is significant. Consequently, the water inflow is lower than the drainage. Thus, the water becomes shallow, showing a low reducibility. After this arid climate, the precipitation and water inflow increase slightly. The pyrite content is also a little higher, indicating a gradual increase in water depth and reducibility. Then, the climate becomes warm and wet, resulting in the deepest water and the highest reducibility. However, after entering a relatively warm-wet climate in the third stage, both the depth and the reducibility decline. In conclusion, the redox property goes through 3 stages that are characterized by weak reducing/reducing

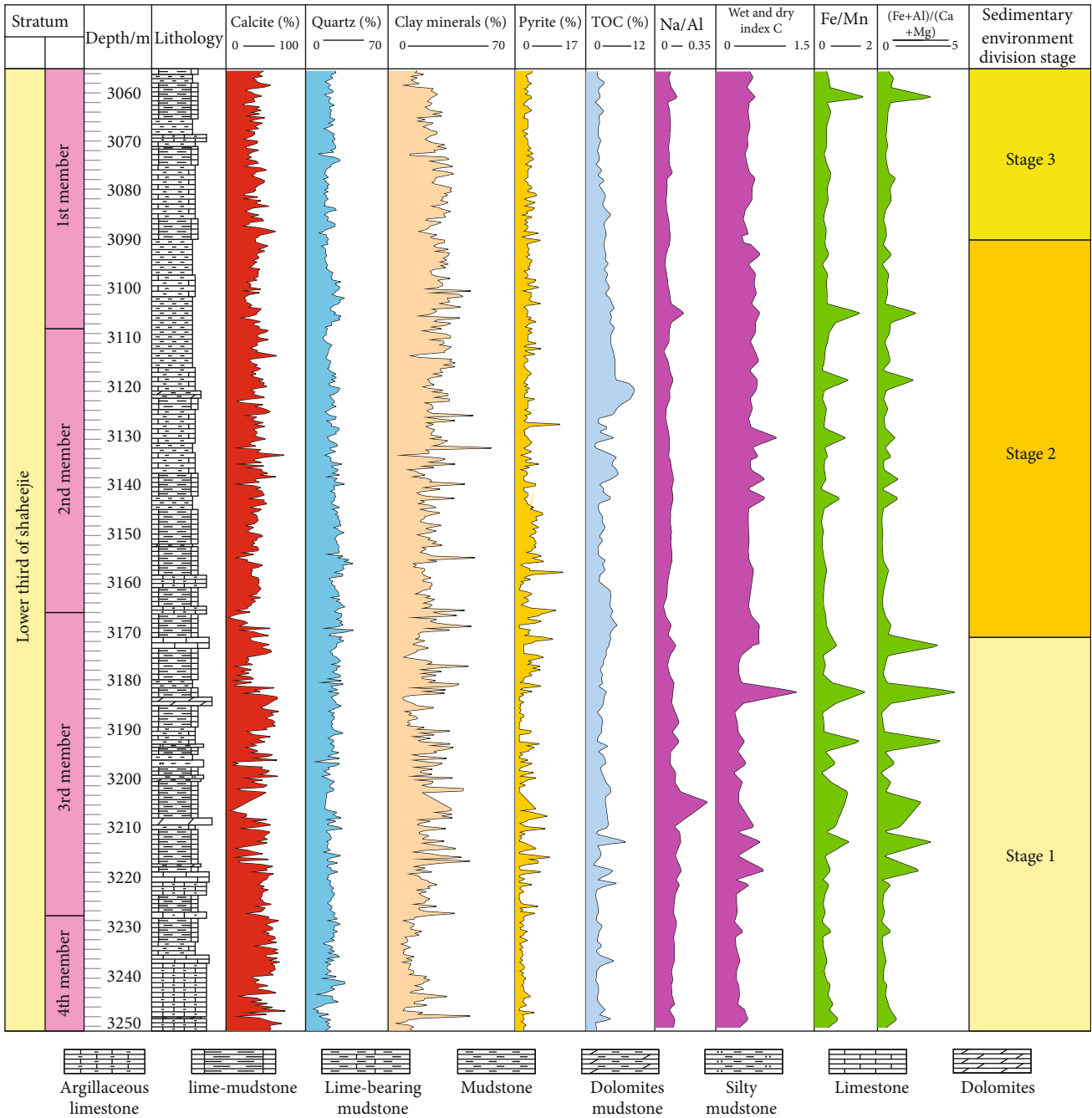


FIGURE 4: Analysis results of the paleoclimate and paleowater depth in the lower submember of Member 3 of Shahejie Formation in FY-1 Well.

water, strong reducing water, and strong reducing/reducing water, respectively.

4.1.4. *Paleosalinity.* The paleosalinity in this paper is analyzed by geochemical indicators of Sr/Ba and Ca/(Ca + Fe), and dolomite content [17, 40–45, 50, 61, 64–69].

The change of all indicators for the paleosalinity in the lower submember of Member 3 of Shahejie Formation presents the periodicity. The first stage shows a high water salinity under a relatively dry/relatively warm-wet climate. The Sr/Ba is high, its maximum value is 7.28, and its average

value is 2.61. It tends to increase from the bottom up. As for Ca/(Ca + Fe), its maximum and mean values are 0.93 and 0.79, respectively. The dolomite content is high, ranging between 1% and 46%, and its average value is 8.05%. It can be known from these indicators that this stage is in a saline water environment with a high salinity. Secondly, the climate is warm and wet, and the water is deepest in Stage 2. The Sr/Ba reduces to the lowest level, with an average value of 1.00. The Ca/(Ca + Fe) decreases to 0.73 on average. Meanwhile, the dolomite content that is low in this stage ranges from 1% to 25%, and its mean value reduces to

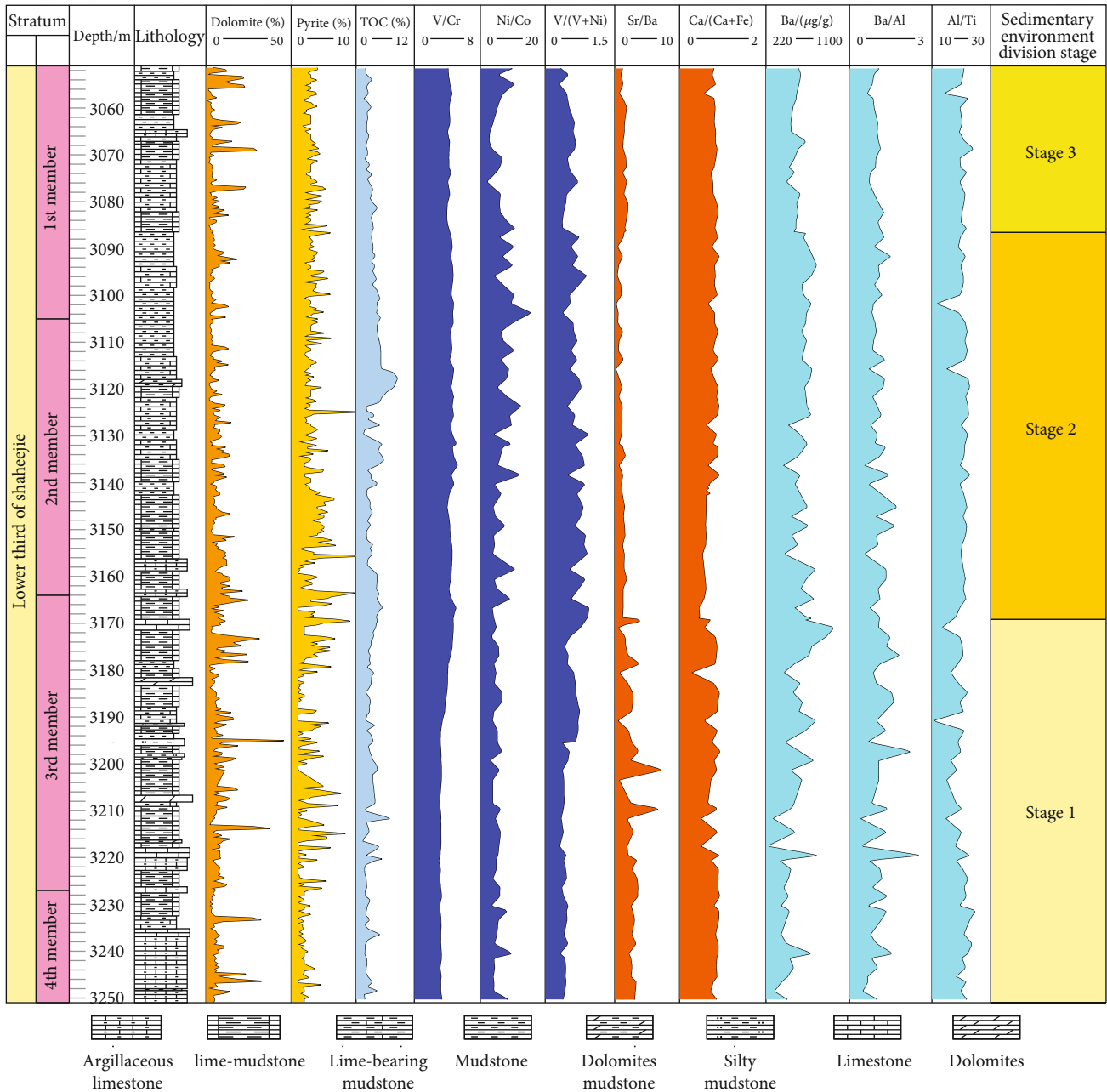


FIGURE 5: Analysis results of the paleoredox, paleosalinity, and paleoproductivity in the lower submember of Member 3 of Shahejie Formation in FY-1 Well.

6.48%. These changes indicate that it is a brackish water environment with a low salinity. Finally, in the third stage, the climate is still warm and wet. The average values of Sr/Ba and Ca/(Ca + Fe) increase slightly to 1.48 and 0.8, respectively. The dolomite content is higher than that in Stage 2, ranging between 1% and 36%, and its mean value rises to 6.58%. The change of all the above indicators shows that the salinity increases slightly in this stage, but the general variation is not obvious. Thus, it is a saline/brackish water environment (Figure 5).

As shown by these indicators, there are 3 stages for the salinity variation in the lower submember. In Stage 1 when

the climate is relatively dry and cold, the salt is separated out due to the evaporation, resulting in a high salinity. Later, the climate becomes relatively warm and wet, and the salinity reduces slightly. In Stage 2 under a warm-wet climate, the water is deepest, and the salinity keeps reducing. At last, the climate becomes relatively warm and wet in Stage 3. Despite the slight increase in salinity, its overall level is still low.

4.1.5. Paleoproductivity. Paleoproductivity refers to the rate at which organisms fix the energy during the energy cycle in geologic history. It indicates the initial mass of organic matters in marine or lake bottom sediments. In this paper,

TABLE 1: The sedimentary environment media conditions and lithofacies assemblages in the lower submember of Member 3 of Shahejie Formation in FY-1 Well of the Dongying Sag.

Stage	Paleoclimate	Paleowater depth	Paleosalinity	Paleoredox	Paleoproductivity	Lithofacies assemblages
Stage 1	Relatively dry and cold-relatively warm and wet	Semideep water	Saline water	Low reducibility/reducibility	Low/relatively high	Organic-contained argillaceous limestone/lime mudstone, organic-rich lime mudstone
Stage 2	Warm and wet	Deepwater	Brackish water	High reducibility	High	Organic-rich mudstone, organic-rich lime-bearing mudstone, organic-rich lime mudstone
Stage 3	Warm and wet-relatively warm and wet	Deep/semideep water	Saline/brackish water	High reducibility/reducibility	Relatively high	Organic-rich lime-bearing mudstone, organic-rich lime mudstone

it is analyzed based on geochemical indicators, such as Ba, Ba/Al, Al/Ti, and TOC [16, 50], and sedimentological indicators, including color, lithology, and sedimentary structure.

In the lower submember of Member 3 of Shahejie Formation, the indicators for the paleoproductivity change periodically. In Stage 1, the rock core is mainly light gray-gray, with a low TOC content. The organic-contained argillaceous limestone is formed at the bottom, and the dark gray lime mudstone that reflects the deepening of the water body is developed upward. The sedimentary structure is mainly the flat lamina. In the meantime, the Ba is 226.24-933.81 $\mu\text{g/g}$, with the average value being 517.94 $\mu\text{g/g}$. It is lower at the bottom, but it increases upward. The ratio of Ba/Al varies in the same way. As for Al/Ti, the ratio reduces slightly first and then increases, ranging between 10 and 24.71. Its mean value is 19.29. This means that the paleoproductivity increases gradually in this stage. In Stage 2, the rock core is dark gray, and the lime-bearing mudstone and mudstone are formed. The sedimentation mainly develops massive and stratified structures, with an increasing number of organic matters. Besides, the Ba value tends to be stable between 390 $\mu\text{g/g}$ and 749.7 $\mu\text{g/g}$, and its mean value is 611 $\mu\text{g/g}$. The ratio of Ba/Al shows the same trend, while that of Al/Ti remains high and stable, with an average value of 20.45. In this stage, the productivity is high. Finally, the rock core is still dark gray, and the lime-bearing mudstone and lime mudstone are developed in Stage 3. The massive structure changes into laminated one. There are still a large number of organic matters. The mean value of Ba reduces to 528.66 $\mu\text{g/g}$, and that of Al/Ti is 20.21. The paleoproductivity remains high in this stage (Figures 3 and 5).

According to the change of all indicators for the paleoproductivity in the lower submember of Member 3 of Shahejie Formation, the values only change slightly, except those that are low at the bottom. Meanwhile, the paleoproductivity is highest in Stage 2. Therefore, its evolution is divided into Stage 1 when the paleoproductivity is low/relatively high, Stage 2 when it is high, and Stage 3 when it is relatively high.

4.1.6. Analysis Results of Paleoenvironment. The paleoenvironment in the lower submember of Member 3 of Shahejie Formation in FY-1 Well of the Dongying Sag is analyzed from paleoclimate, paleowater depth, paleoredox, paleosalinity, and paleoproductivity based on geochemical and sedi-

mentological indicators. Thereinto, the former includes Na/Al, dry-wet index (C), TOC, Fe/Mn, $(\text{Fe} + \text{Al})/(\text{Ca} + \text{Mg})$, V/Cr, Ni/Co and $V/(V + \text{Ni})$, Sr/Ba, $\text{Ca}/(\text{Ca} + \text{Fe})$, Ba, and Ba/Al. The latter includes color, lithology, sedimentary structure, and mineral composition (clay mineral, calcite, dolomite, pyrite, and quartz). The results show that the sedimentary environment media conditions undergo 3 stages in FY-1 Well (Figures 4 and 5).

4.2. The Control Effect of Sedimentary Environment on the Lithofacies. The sedimentary environment media conditions affect the rock color, lithology, sedimentary structure, mineral composition, and geochemical components and thus determine the different development positions of the lithofacies and its assemblages in strata [66–77]. According to the vertical changes of sedimentological and geochemical indicators, this environment evolves through 3 stages in the lower submember of Member 3 of Shahejie Formation in FY-1 Well. Its control effect on the lithofacies is summarized based on the paleoenvironmental analysis in each stage (Table 1 and Figure 6).

Stage 1 (3,169.15-3,251 m): there is low precipitation under an arid climate, so the water flowing into the lake basin is limited. The evaporation is greater than the inflow, resulting in shallow water. Thus, the relatively closed lake basin is formed. When the terrigenous input is low and the water salinity is high, a large number of saline minerals will be separated out, which is conducive to the development of the limestone. However, high-salinity water is harmful to organisms. For example, there will be fewer algae, and they can hardly be preserved, causing low lake productivity. Moreover, in the shallow lake, the reducibility is low, and the oxygen is sufficient at the bottom, which adverstes to the generation and preservation of organic matters. Accordingly, the contents of them and the pyrite are low. Therefore, the light gray-gray organic-contained argillaceous limestone and lime mudstone are formed in this stage, and the sedimentary structure is characterized by the flat lamina. When the climate becomes warm and wet, the precipitation and water inflow increase. In the meantime, the water depth and terrigenous input also increase gradually. The lake basin becomes open. At this time, there are more clay minerals, and organic matters can be generated and preserved in a better way in the deep water. Hence, this stage has an increasing

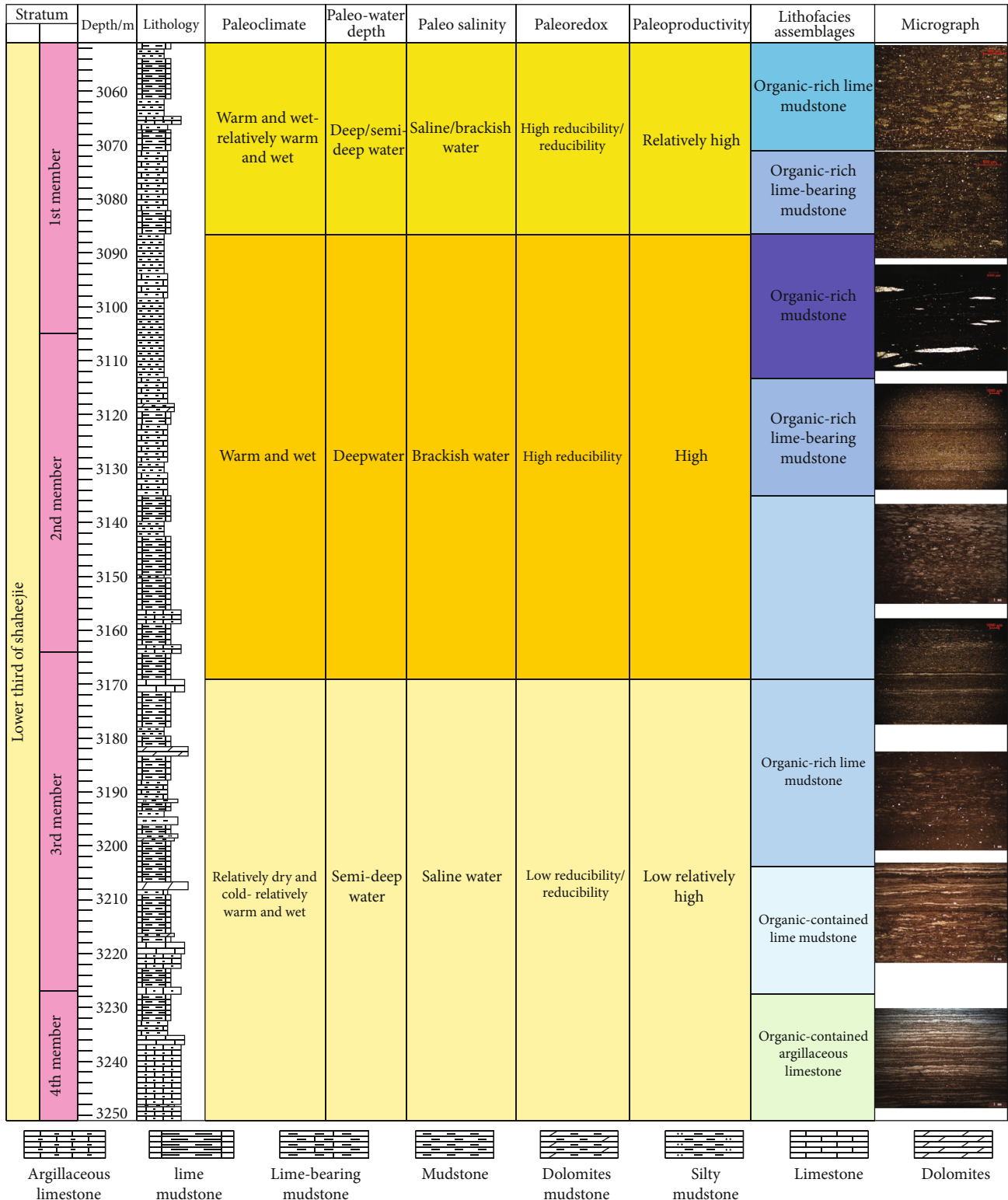


FIGURE 6: Sedimentary environment media conditions and lithofacies assemblages in the lower submember of Member 3 of Shahejie Formation in FY-1 Well of the Dongying Sag.

amount of dark gray rocks that reflect the gradual deepening of the water body. The sedimentation changes towards the massive structure, and the organic-rich lime mudstone is formed at the same time.

Stage 2 (3,086.55-3,169.15 m): after the climate becomes warm and wet, the water is deepest due to the increasing amount of precipitation and terrigenous clasts. Meanwhile, the paleosalinity reduces, showing a high reducibility. In

addition to the low salinity, terrigenous nutrients are also helpful to the growth of aquatic organisms. Thus, the algae and other organisms can thrive, causing a high biological productivity. When the oxygen in the water is consumed, the reducibility will be further enhanced. In the meantime, the lake stratification occurs in this stage. That is, the upper part contains sufficient oxygen, while the lower one is under oxidizing or oxygen-deficient condition. The lake bottom is in a strong reducing environment, in which the pyrite is developed most and the organic matters are preserved best. Besides, the water environment is generally calm. In this stage, the dark gray lime mudstone, lime-bearing mudstone, and mudstone are formed, but the carbonate minerals are developed poorly. As the sedimentation can hardly be affected by climate seasonally, there are many massive structures and some stratified ones. Therefore, this stage mostly develops the organic-rich lime-bearing mudstone and mudstone, with a small amount of organic-rich lime mudstone formed at the same time.

Stage 3 (3,051–3,086.55 m): when the warm and wet climate becomes relatively warm and wet, the water is deep on the whole, and its high reducibility begins to reduce. The salinity increases slightly, and there are still a large number of organic matters. Due to the enhancement of evaporation, the lime sedimentation increases gradually, and the lithology primarily includes the dark gray lime-bearing mudstone and lime mudstone. The structural lenticle that is formed when the lime lamina composed of the calcite is broken by the windstorm can be discovered occasionally. There is also a weak bottom current during the sedimentary period. Therefore, the organic-rich lime-bearing mudstone and lime mudstone are mainly developed in this stage.

In conclusion, the lower submember of Member 3 of Shahejie Formation in FY-1 Well mainly develops the organic-rich mudstone, lime-bearing mudstone and lime mudstone, and organic-contained argillaceous limestone/lime mudstone. The sedimentary environment undergoes the semideep, deep, and deep/semideep waters under the relatively dry-cold/relatively warm-wet, warm-wet, and warm-wet/relatively warm-wet paleoclimates, respectively. The paleoredox transits from reducibility to high reducibility to high reducibility/reducibility, and the salinity changes in the sequence of saline water, brackish water, and brackish/saline water. Correspondingly, the paleoproductivity is low/relatively high, high, and relatively high in the three stages. According to the change of environmental factors and corresponding lithofacies assemblages, the organic-rich mudstone, lime-bearing mudstone, and lime mudstone are formed in the brackish and deep water under a warm-wet/relatively warm-wet climate, while the organic-contained argillaceous limestone/lime mudstone and organic-rich lime mudstone are developed in the saline and semideep water under a relatively dry-cold/relatively warm-wet climate (Table 1 and Figure 6). This study shows that the abundance of organic matters is mainly controlled by the salinity, and the climate affects the lithology and sedimentary environment media conditions. When the environment experiences the relatively dry-cold/relatively warm-wet, warm-wet, and relatively warm-wet climates in the three stages, respectively, the water environment, organic matter content, and lithology will change accordingly.

5. Conclusions

By taking the lower submember of Member 3 in FY-1 Well, Dongying Sag, Bohai Bay Basin as the study object, this paper analyzes the vertical changes of sedimentary environment media conditions in this submember and elaborates how the environment of fine-grained sedimentary rocks controls the lithofacies development. The conclusions are as follows:

- (1) The sedimentary environment media conditions underwent three phases. In Phase I when the climate was relatively dry and cold/relatively warm and wet, the water in the lake basin was shallow. When the climate was warm and wet in Phase II, the water deepened rapidly. When the climate was warm and wet/relatively warm and wet in Phase III, the water became deeper. Besides, the redox property transited three stages accordingly from reducibility to high reducibility to high reducibility/reducibility. The salinity that was high in Phase I decreased in Phase II and became low in Phase III. Paleoproductivity was low/relatively high at the beginning, then became high, and finally relatively high.
- (2) The change of sedimentary environment media conditions controls the lithofacies. Under an arid climate, the organic-contained argillaceous limestone and lime mudstone are developed better. When the climate becomes warm and wet, the organic-rich lime mudstone is formed. Under a warm-wet climate, the organic-rich lime-bearing mudstone and mudstone are developed best. When entering a relatively warm-wet climate, the organic-rich lime-bearing mudstone and lime mudstone are developed better.
- (3) The abundance of organic matters is affected by the salinity, and the lithology and sedimentary environment media conditions are controlled by the climate. Meanwhile, climate is also a main reason for the change of lithology and sedimentary conditions. As the climate changes from the relatively dry-cold/relatively warm-wet to warm-wet, and ultimately warm-wet, the sedimentary water environment, organic matter content, and lithology change accordingly.

Data Availability

All data in the article is presented in the form of tables and graphs. All the data in this article is accessible to readers.

Additional Points

Highlights. (1) Sedimentological and geochemical indicators are combined to analyze the sedimentary environment evolution in the lower submember of Member 3 of Shahejie Formation in FY-1 Well of the Dongying Sag, which provides a reference for the study on the environmental evolution of lacustrine fine-grained sedimentary rocks. (2) The control effect of sedimentary environment on the lithofacies is discussed, which compensates for the paucity of research

on their relationship, and plays a vital role in the muddy shale oil and gas exploration and the identification of favorable lithofacies. (3) The abundance of organic matters is controlled by the salinity, and climate is the primary cause of the sedimentary environment media condition change. Climate change can result in changes in sedimentary water environment, organic matter content, and lithology.

Conflicts of Interest

There are no conflicts of interest with respect to the results of this paper.

Authors' Contributions

The authors contributed equally to this work. All authors have read and agreed to the published version of the manuscript.

Acknowledgments

This study was supported by the Study on Astronomical Stratigraphic Period of Lacustrine Shale and High Resolution Sedimentary Cycle in Logging (41872166) of the National Natural Science Foundation of China and the Exploration and Development Research Institute, Shengli Oilfield Company, SINOPEC.

References

- [1] A. C. Aplin and J. H. Macquaker, "Mudstone diversity: origin and implications for source, seal, and reservoir properties in petroleum systems," *AAPG Bulletin*, vol. 95, no. 12, pp. 2031–2059, 2011.
- [2] Z. Jiang, C. Liang, J. Wu et al., "Several issues in sedimentological studies on hydrocarbon-bearing fine grained sedimentary rocks," *Acta Petrolei Sinica*, vol. 34, no. 6, p. 1032, 2013.
- [3] J. Schieber, W. Zimmerle, and P. V. Sethi, *Shales and Mudstones Volume 1: Basin Studies, Sedimentology and Paleontology*, Schweizerbart'sche Verlagsbuchhandlung, Stuttgart, 1998.
- [4] D. G. Hill, T. E. Lombardi, and J. P. Martin, "Fractured shale gas potential in New York," *Northeastern Geology and Environmental Sciences*, vol. 26, no. 1/2, pp. 57–78, 2004.
- [5] S. L. Montgomery, D. M. Jarvie, K. A. Bowker, and R. M. Polastro, "Mississippian Barnett Shale, Fort Worth basin, north-central Texas: gas-shale play with multi-trillion cubic foot potential," *AAPG Bulletin*, vol. 89, no. 2, pp. 155–175, 2005.
- [6] K. Zhang, C. Jia, Y. Song et al., "Analysis of Lower Cambrian shale gas composition, source and accumulation pattern in different tectonic backgrounds: a case study of Weiyuan block in the upper Yangtze region and Xiuwu Basin in the lower Yangtze region," *Fuel*, vol. 263, no. 2019, article 115978, 2020.
- [7] O. R. Lazar, K. M. Bohacs, J. H. Macquaker, J. Schieber, and T. M. Demko, "Capturing key attributes of fine-grained sedimentary rocks in outcrops, cores, and thin sections: nomenclature and description guidelines," *Journal of Sedimentary Research*, vol. 85, no. 3, pp. 230–246, 2015.
- [8] J. H. Macquaker and A. E. Adams, "Maximizing information from fine-grained sedimentary rocks: an inclusive nomenclature for mudstones," *Journal of Sedimentary Research*, vol. 73, no. 5, pp. 735–744, 2003.
- [9] R. G. Loucks and S. C. Ruppel, "Mississippian Barnett Shale: lithofacies and depositional setting of a deep-water shale-gas succession in the Fort Worth Basin, Texas," *AAPG Bulletin*, vol. 91, no. 4, pp. 579–601, 2007.
- [10] R. M. Slatt and N. D. Rodriguez, "Comparative sequence stratigraphy and organic geochemistry of gas shales: commonality or coincidence?," *Journal of Natural Gas Science and Engineering*, vol. 8, no. 8, pp. 68–84, 2012.
- [11] M. Pommer and K. L. Milliken, "Pore types and pore-size distributions across thermal maturity, Eagle Ford Formation, southern Texas," *AAPG Bulletin*, vol. 99, no. 9, pp. 1713–1744, 2015.
- [12] D. Yan, H. Wang, Q. L. Fu, Z. Chen, J. He, and Z. Gao, "Geochemical characteristics in the Longmaxi formation (early Silurian) of South China: implications for organic matter accumulation," *Marine and Petroleum Geology*, vol. 65, pp. 290–301, 2015.
- [13] H. A. Armstrong, B. R. Turner, I. M. Makhlof et al., "Origin, sequence stratigraphy and depositional environment of an upper Ordovician (Hirnantian) deglacial black shale, Jordan," *Palaeogeography, Palaeoclimatology, Palaeoecology*, vol. 230, no. 3, pp. 352–355, 2006.
- [14] Z. N. Yuri, V. G. Eder, and A. G. Zamirailova, "Composition and formation environments of the Upper Jurassic-Lower Cretaceous black shale Bazhenov formation (the central part of the West Siberian Basin)," *Marine and Petroleum Geology*, vol. 25, no. 3, pp. 289–306, 2008.
- [15] A. M. Romero, *Geochemical Characterization of the Woodford Shale, Central and Southeastern Oklahoma*, The University of Oklahoma, Oklahoma, 2010.
- [16] L. Guo, Z. Li, X. Xie et al., "High-frequency variation of geochemical elements and its geological implication on lacustrine organic-rich mudstone and shale formation: an example from the core-taking segment of well BY1 in the Biyang depression," *Geoscience*, vol. 29, no. 6, pp. 1360–1368, 2015, (in Chinese with English abstract).
- [17] S. Pang, Y. Cao, and C. Liang, "Lithofacies characteristics and sedimentary environment of Es^{4U} and Es^{3L}: a case study of well FY1 in Dongying sag, Bohai Bay Basin," *Oil & Gas Geology*, vol. 40, no. 4, pp. 799–806, 2019, (in Chinese with English abstract).
- [18] Y. Wang, H. Liu, G. Song et al., "Lacustrine shale fine-grained sedimentary system in Jiyang depression," *Acta Petrolei Sinica*, vol. 40, no. 4, pp. 395–410, 2019, (in Chinese with English abstract).
- [19] Y. Shi, H. Ji, J. Yu, P. Xiang, Z. Yang, and D. Liu, "Provenance and sedimentary evolution from the Middle Permian to Early Triassic around the Bogda Mountain, nw China: a tectonic inversion responding to the consolidation of Pangea," *Marine and Petroleum Geology*, vol. 114, article 104169, 2020.
- [20] Y. Shi, J. Wang, G. Zhang et al., "Tectono-climatic-sedimentary evolution and coupling mechanism during the middle Permian-early Triassic in Bogda area, Xinjiang," *Journal of Palaeogeography (Chinese Edition)*, vol. 23, no. 2, pp. 389–404, 2021, (in Chinese with English abstract).
- [21] S. Sun, H. Liu, Y. Cao, S. Zhang, Y. Wang, and W. Yang, "Milankovitch cycle of lacustrine deepwater fine grained sedimentary rocks and its significance to shale oil: a case study of the upper Es⁴ member of well NY1 in Dongying sag," *Journal of China of Mining & Technology*, vol. 46, no. 4, pp. 846–855, 2017, (in Chinese with English abstract).
- [22] C. Liang, J. Zaixing, C. Yingchang, W. Jing, and H. Fang, "Sedimentary characteristics and origin of lacustrine organic-rich shales in the salinized Eocene Dongying depression,"

- Geological Society of America Bulletin*, vol. 130, no. 1, pp. 154–174, 2017.
- [23] C. Liang, Y. Cao, Z. Jiang, J. Wu, S. Guoqi, and Y. Wang, “Shale oil potential of lacustrine black shale in the Eocene Dongying depression: implications for geochemistry and reservoir characteristics,” *AAPG Bulletin*, vol. 101, no. 11, pp. 1835–1858, 2017.
- [24] Y. Ma, *Lacustrine Shale Stratigraphy and Eocene Climate Recorded in the Jiyang Depression in East China*, China University of Geosciences, 2017, (in Chinese with English abstract).
- [25] Z. Chen, W. Jiang, L. Zhang, and M. Zha, “Organic matter, mineral composition, pore size, and gas sorption capacity of lacustrine mudstones: implications for the shale oil and gas exploration in the Dongying depression, eastern China,” *AAPG Bulletin*, vol. 102, no. 8, pp. 1565–1600, 2018.
- [26] B. Ma, K. A. Eriksson, Y. Cao, Y. Jia, Y. Wang, and B. C. Gill, “Fluid flow and related diagenetic processes in a rift basin: evidence from the fourth member of the Eocene Shahejie formation interval, Dongying depression, Bohai Bay Basin, China,” *AAPG Bulletin*, vol. 100, no. 11, pp. 1633–1662, 2016.
- [27] J. Wu, Z. Jiang, and X. Wang, “Sequence stratigraphy characteristics of lacustrine fine-grained sedimentary rocks: a case study of the upper fourth member of Paleogene Shahejie formation, Dongying sag, Bohai Bay Basin,” *Natural Gas Geoscience*, vol. 29, no. 2, pp. 199–210, 2018, (in Chinese with English abstract).
- [28] L. Gao, B. Sun, and Y. Wang, “Sedimentary characteristics and controlling factors of beach-bar sandstones of the upper section of the fourth member of Shahejie formation on the southern slope of Dongying sag, Bohai Bay Basin,” *Petroleum Geology & Experiment*, vol. 40, no. 5, pp. 669–675, 2018, (in Chinese with English abstract).
- [29] M. Wang, J. Lu, Z. Zuo, H. Li, and B. Wang, “Characteristics and dominating factors of lamellar fine-grained sedimentary rocks: a case study of the upper Es₄ member-lower Es₃ member, Dongying sag, Bohai Bay Basin,” *Petroleum Geology & Experiment*, vol. 40, no. 4, pp. 470–478, 2018, (in Chinese with English abstract).
- [30] C. Lampe, G. Song, L. Cong, and X. Mu, “Fault control on hydrocarbon migration and accumulation in the Tertiary Dongying depression, Bohai Basin, China,” *AAPG Bulletin*, vol. 96, no. 6, pp. 983–1000, 2012.
- [31] C. Liang, Z. Jiang, Y. Cao, M. Wu, L. Guo, and C. Zhang, “Deep-water depositional mechanisms and significance for unconventional hydrocarbon exploration: a case study from the lower Silurian Longmaxi shale in the southeastern Sichuan Basin,” *AAPG Bulletin*, vol. 100, no. 5, pp. 773–794, 2016.
- [32] Z. Li, W. Yang, Y. Wang et al., “Anatomy of a lacustrine stratigraphic sequence within the fourth member of the Eocene Shahejie formation along the steep margin of the Dongying depression, eastern China,” *AAPG Bulletin*, vol. 103, no. 2, pp. 469–504, 2019.
- [33] Analytical Methods Committee and Royal Society of Chemistry, “Evaluation of analytical instrumentation. Part XXIII. Instrumentation for portable X-ray fluorescence spectrometry,” *Accreditation and Quality Assurance*, vol. 13, no. 8, pp. 453–464, 2008.
- [34] S. Li, R. Zhu, J. Cui, Z. Luo, H. Jiao, and H. Liu, “Sedimentary characteristics of fine-grained sedimentary rock and paleoenvironment of Chang 7 member in the Ordos Basin: a case study from well Yaoye 1 in Tongchuan,” *Acta Sedimentologica Sinica*, vol. 38, no. 3, pp. 1–13, 2019, (in Chinese with English abstract).
- [35] J. Wang, F. Tan, and X. Fu, “Sedimentary rock work method,” *Beijing: Geological Publishing House*, vol. 18, p. 28, 2015, (in Chinese with English abstract).
- [36] K. Zhao, *Characteristics and Genesis Analysis of Carbonate lamina in the Upper Fourth Member and the Lower Third Member of Shahejie Formation in Dongying Depression*, China University of Geosciences, Wuhan, Bohai Bay Basin, 2019, (in Chinese with English abstract).
- [37] Y. Wang, G. Song, H. Liu et al., “Formation environment and sedimentary structures of fine grained sedimentary rock in Jiyang depression,” *Journal of Northeast Petroleum University*, vol. 39, no. 3, pp. 7–14, 2015, (in Chinese with English abstract).
- [38] J. P. Smol and B. F. Cumming, “Tracking long-term changes in climate using algal indicators in lake sediments,” *Journal of Phycology*, vol. 36, no. 6, pp. 986–1011, 2000.
- [39] A. M. Bloom, K. A. Moser, D. F. Porinchu, and G. M. Macdonald, “Diatom-inference models for surface-water temperature and salinity developed from a 57-lake calibration set from the Sierra Nevada, California, USA,” *Journal of Paleolimnology*, vol. 29, no. 2, pp. 235–255, 2003.
- [40] L. Peng, Y. Lu, P. Peng et al., “Heterogeneity and evolution model of the lower Shahejie member 3 mud-shale in the Bonan subsag, Bohai Bay Basin: an example from well Luo 69,” *Oil & Gas Geology*, vol. 38, no. 2, pp. 219–227, 2017, (in Chinese with English abstract).
- [41] J. Wu, Z. Jiang, J. Tong, L. Yang, J. Li, and H. Nie, “Sedimentary environment and control factors of fine grained sedimentary rocks in the upper fourth member of Paleogene Shahejie formation, Dongying sag,” *Acta Petrolei Sinica*, vol. 37, no. 4, pp. 464–473, 2016, (in Chinese with English abstract).
- [42] J. Wu, Z. Jiang, and C. Liang, “Lithofacies characteristics of fine grained sedimentary rocks in the upper submember of member 4 of Shahejie formation, Dongying sag and their relationship with sedimentary environment,” *Acta Petrolei Sinica*, vol. 38, no. 10, pp. 1110–1120, 2017, (in Chinese with English abstract).
- [43] S. Liu, Y. Cao, and C. Liang, “Lithologic characteristics and sedimentary environment of fine-grained sedimentary rocks of the Paleogene in Dongying sag, Bohai Bay Basin,” *Journal of Palaeogeography*, vol. 21, no. 3, pp. 479–488, 2019, (in Chinese with English abstract).
- [44] W. Yang, X. Wang, Y. Jiang et al., “Quantitative reconstruction of paleoclimate and its effects on fine-grained lacustrine sediments: a case study of the upper Es₄ and lower Es₃ in Dongying sag,” *Petroleum Geology and Recovery Efficiency*, vol. 25, no. 2, pp. 29–35, 2018, (in Chinese with English abstract).
- [45] W. Yang, Y. Jiang, and Y. Wang, “Study on shale facies sedimentary environment of lower Es₃-upper Es₄ in Dongying sag,” *Journal of China University of Petroleum*, vol. 39, no. 4, pp. 19–25, 2015, (in Chinese with English abstract).
- [46] W. A. Yong, W. A. Xuejun, S. O. Guoqi et al., “Genetic connection between mud shale lithofacies and shale oil enrichment in Jiyang depression, Bohai Bay Basin,” *Petroleum Exploration and Development*, vol. 43, no. 5, pp. 696–704, 2016, (in Chinese with English abstract).
- [47] Y. Wang, H. M. Liu, G. Q. Song et al., “Carbonate genesis and geological significance of shale hydrocarbon in lacustrine facies mud shale: a case study of source rocks in the upper sub-member of member 4 and lower submember of member 3 of

- Shahejie formation, Dongying sag,” *Acta Petrolei Sinica*, vol. 38, no. 12, pp. 1390–1399, 2017, (in Chinese with English abstract).
- [48] S. J. Davies and T. Elliott, “Spectral gamma ray characterization of high resolution sequence stratigraphy: examples from Upper Carboniferous fluvio-deltaic systems, County Clare, Ireland,” *Geological Society, London, Special Publications*, vol. 104, no. 1, pp. 25–35, 1996.
- [49] R. M. Slatt, P. R. Philp, Y. Abousleiman et al., “Pore-to-regional-scale integrated characterization workflow for unconventional gas shales,” in *Shale Reservoirs: Giant Resources for the 21st Century*, AAPG Memoir 97, J. A. Breyer, Ed., American Association of Petroleum Geologists, Tulsa, OK, 2012.
- [50] X. Du, H. Liu, H. Liu et al., “Methods of sequence stratigraphy in the fine-grained sediments: a case from the upper fourth sub-member and the lower third sub-member of the Shahejie formation in well Fanye 1 of Dongying depression,” *Geological Science and Technology Information*, vol. 35, no. 4, pp. 1–10, 2016, (in Chinese with English abstract).
- [51] Q. Liu, X. Zeng, X. Wang, and J. Cai, “Lithofacies of mudstone and shale deposits of the Es³-Es⁴ formation in Dongying sag and their depositional environment,” *Marine Geology & Quaternary Geology*, vol. 37, no. 3, pp. 147–156, 2017, (in Chinese with English abstract).
- [52] Y. Zheng, R. F. Anderson, A. van Geen, and J. S. Kuwabara, “Authigenic molybdenum formation in marine sediments: a link to pore water sulfide in the Santa Barbara Basin,” *Geochimica et Cosmochimica Acta*, vol. 64, no. 24, pp. 4165–4178, 2000.
- [53] T. J. Nameroff, S. E. Calvert, and J. W. Murray, “Glacial-interglacial variability in the eastern tropical North Pacific oxygen minimum zone recorded by redox-sensitive trace metals,” *Paleoceanography*, vol. 19, no. 1, pp. 1–19, 2004.
- [54] T. J. Algeo and J. B. Maynard, “Trace-element behavior and redox facies in core shales of upper Pennsylvanian Kansas-type cyclothems,” *Chemical Geology*, vol. 206, no. 3–4, pp. 289–318, 2004.
- [55] D. Z. Piper and R. B. Perkins, “A modern vs. Permian black shale—the hydrography, primary productivity, and water-column chemistry of deposition,” *Chemical Geology*, vol. 206, no. 3–4, pp. 177–197, 2004.
- [56] J. N. Pattan, N. J. Pearce, and P. G. Mislankar, “Constraints in using cerium-anomaly of bulk sediments as an indicator of paleo bottom water redox environment: a case study from the Central Indian Ocean Basin,” *Chemical Geology*, vol. 221, no. 3–4, pp. 260–278, 2005.
- [57] G. Xiong, X. Jiang, X. Cai, and H. Wu, “The characteristics of trace element and REE geochemistry of the cretaceous mudrocks and shales from southern Tibet and its analysis of redox condition,” *Advances in Earth Science*, vol. 25, no. 7, pp. 730–745, 2010, (in Chinese with English abstract).
- [58] Z. Yong, X. Zhang, and H. Deng, “Differences about organic matter enrichment in the shale section of Ediacaran Doushan-tuo formation in West Hubei of China,” *Journal of Chengdu University of Technology (Science & Technology Edition)*, vol. 39, no. 6, pp. 567–574, 2012, (in Chinese with English abstract).
- [59] S. Wang, D. Dong, Y. Wang, J. Huang, and B. Pu, “Geochemistry evaluation index of redox-sensitive elements for depositional environments of Silurian Longmaxi organic-rich shale in the south of Sichuan Basin,” *Marine Origin Petroleum Geology*, vol. 73, no. 3, pp. 27–34, 2014, (in Chinese with English abstract).
- [60] Q. Du, S. Guo, X. Shen, Z. Cao, X. Zhang, and Y. Li, “Palaeo-water characteristics of the member 1 of Paleogene Shahejie formation in southern Nanpu sag, Bohai Bay Basin,” *Journal of Palaeogeography*, vol. 18, no. 2, pp. 173–183, 2016, (in Chinese with English abstract).
- [61] F. Wang, X. Liu, X. Deng et al., “Geochemical characteristics and environmental implications of trace elements of Zhifang formation in Ordos Basin,” *Acta Sedimentologica Sinica*, vol. 35, no. 6, pp. 1265–1273, 2017, (in Chinese with English abstract).
- [62] K. Zhang, Z. Li, S. Jiang et al., “Comparative analysis of the siliceous source and organic matter enrichment mechanism of the Upper Ordovician–Lower Silurian shale in the upper-lower Yangtze area,” *Minerals*, vol. 8, no. 7, p. 283, 2018.
- [63] K. Zhang, Y. Song, S. Jiang et al., “Mechanism analysis of organic matter enrichment in different sedimentary backgrounds: a case study of the Lower Cambrian and the Upper Ordovician–Lower Silurian, in Yangtze region,” *Marine and Petroleum Geology*, vol. 99, pp. 488–497, 2019.
- [64] E. Custodio, “Aquifer overexploitation: what does it mean?,” *Hydrogeology Journal*, vol. 10, no. 2, pp. 254–277, 2002.
- [65] J. Xu, R. Pu, L. Yang, and A. Li, “The palaeosalinity analysis of carboniferous mudstone, Tarim Basin,” *Acta Sedimentologica Sinica*, vol. 28, no. 3, pp. 509–517, 2010, (in Chinese with English abstract).
- [66] X. Peng, L. Wang, and L. Jiang, “Geochemical characteristics of the Lucaogou formation oil shale in the southeastern margin of the Junggar Basin and its environmental implications,” *Bulletin of Mineralogy, Petrology and Geochemistry*, vol. 31, no. 2, pp. 121–127, 2012, (in Chinese with English abstract).
- [67] X. Tan, J. Tian, J. Huang, X. Lin, and J. Ma, “Material responses and accumulation patterns in cyclic sediment records of continental clastic rocks: taking the Paleogene Kongdian formation of Wangjiagang area in Jiyang depression as an example,” *Oil & Gas Geology*, vol. 34, no. 3, pp. 332–341, 2013, (in Chinese with English abstract).
- [68] S. Zhang, S. Chen, S. Cui et al., “Characteristics and types of fine-grained sedimentary rocks lithofacies insemi-deep and deep lacustrine, Dongying sag,” *Journal of China University of Petroleum (Edition of Natural Science)*, vol. 38, no. 5, pp. 9–17, 2014, (in Chinese with English abstract).
- [69] Y. Fu, L. Shao, L. Zhang et al., “Geochemical characteristics of mudstones in the Permo-Carboniferous strata of the Jiaozuo coalfield and their paleoenvironmental significance,” *Acta Sedimentologica Sinica*, vol. 36, no. 2, pp. 415–426, 2018, (in Chinese with English abstract).
- [70] J. Schieber, “Facies and origin of shales from the mid-Proterozoic Newland Formation, Belt Basin, Montana, USA,” *Sedimentology*, vol. 36, no. 2, pp. 203–219, 1989.
- [71] S. Zhang, H. Liu, S. Chen et al., “Classification scheme for lithofacies of fine grained sedimentary rocks in faulted basins of eastern China: insights from the fine grained sedimentary rocks in Paleogene, southern Bohai Bay Basin,” *Acta Geologica Sinica*, vol. 91, no. 5, pp. 1108–1119, 2017, (in Chinese with English abstract).
- [72] S. Angulo and L. Buatois, “Integrating depositional models, ichnology, and sequence stratigraphy in reservoir characterization: the middle member of the Devonian-Carboniferous Bakken formation of subsurface southeastern Saskatchewan revisited,” *AAPG Bulletin*, vol. 96, no. 6, pp. 1017–1043, 2012.

- [73] D. Bonar and M. D. Sacchi, “Denoising seismic data using the nonlocal means algorithm,” *Geophysics*, vol. 77, no. 1, pp. A5–A8, 2012.
- [74] J. Ochoa, J. M. Wolak, and M. H. Gardner, “Recognition criteria for distinguishing between hemipelagic and pelagic mudrocks in the characterization of deep-water reservoir heterogeneity,” *AAPG Bulletin*, vol. 97, no. 10, pp. 1785–1803, 2013.
- [75] S. F. Konitzer, S. J. Davies, M. H. Stephenson, and M. J. Leng, “Depositional controls on mudstone lithofacies in a basinal setting: implications for the delivery of sedimentary organic matter,” *Journal of Sedimentary Research*, vol. 84, no. 3, pp. 198–214, 2014.
- [76] J. Zhang, Z. Jiang, X. Jiang, S. Wang, C. Liang, and M. Wu, “Oil generation induces sparry calcite formation in lacustrine mudrock, Eocene of east China,” *Marine and Petroleum Geology*, vol. 71, pp. 344–359, 2016.
- [77] J. Peng, T. Xu, and L. Yu, “Sedimentary characteristics and controlling factors of lacustrine fine-grained rocks of the fourth member of Shahejie formation in Dongying depression,” *Lithologic Reservoirs*, vol. 32, no. 5, pp. 1–11, 2020.

Research Article

Sedimentary Facies of the Longmaxi Formation Shale Gas Reservoir in the Weiyuan Area Based on Elemental Characteristics

Yijia Wu ^{1,2}, Hongming Tang ¹, Ying Wang ², Jing Li ², Yanxiang Zeng ²,
Songlian Jiang ² and Yongcheng Mu ²

¹Southwest Petroleum University, Chengdu 610599, China

²Institute of Geological Exploration and Development of CNPC Chuanqing Drilling Engineering, Chengdu 610056, China

Correspondence should be addressed to Yijia Wu; wuyj_dyy@cnpc.com.cn

Received 15 July 2021; Accepted 27 July 2021; Published 11 September 2021

Academic Editor: Kun Zhang

Copyright © 2021 Yijia Wu et al. This is an open access article distributed under the Creative Commons Attribution License, which permits unrestricted use, distribution, and reproduction in any medium, provided the original work is properly cited.

The Lower Silurian Longmaxi Formation in the southern Sichuan Basin is composed of a series of dark carbonaceous shales deposited in a hydrostatic shelf reduction environment. In this study, the ratio of uranium to thorium (U/Th), the total organic carbon (TOC), and the biological silicon content (Si_{Bio}) were selected as the characteristic parameters to precisely analyze the sedimentary environment and its impact on reservoir quality. The results show that the Weiyuan area in the Early Silurian Longmaxi period experienced two transgression-regression cycles, forming two third-class sequences, SSQ1 and SSQ2, which can be divided into six sedimentary microfacies: organic-rich siliceous argillaceous shelf, organic-rich silicon-containing argillaceous shelf, organic-rich silty argillaceous shelf, deep-water silty argillaceous shelf, shallow-water silty argillaceous shelf, and shallow-water argillaceous silty shelf microfacies. The organic-rich siliceous argillaceous shelf and organic-rich silicon-containing argillaceous shelf microfacies developed in the deepest transgressive system tract (TST1), with high U/Th, high TOC, and high Si_{Bio} , which are identified as the main control facies for reservoir development. These two microfacies are located in the middle of the study area, while a transition occurs in the east affected by the Neijiang Uplift. According to the classification criteria proposed in this article, the favourable shale gas reservoirs in Weiyuan area are characterized with high U/Th (>1.25), high TOC (>3%), and high Si_{Bio} (>15%). This paper proposed an evaluation method for shale sedimentary facies based on elemental and electrical logging characteristics, avoiding the limitations of core samples, which makes the quantitative division of shale sediments and the efficient recognition of high-quality reservoirs available. It is of great significance for delineating the potential production areas in the study area and beneficial for the scaled development of shale gas reservoirs.

1. Introduction

Shale gas refers to the accumulation of free or absorbed natural gas in reservoir rocks dominated by organic-rich mudstone and shale [1–3]. The organic-rich shale is mainly developed in a low-energy reduction sedimentary environment with abundant sources of organic matter, fast deposition rate, and relatively deep and stable water bodies [4–6]. Previously, different reports confirmed the presence of diverse hydrodynamic conditions under altered sedimentary environments [7]. Shale gas reservoirs that grow in different

sedimentary microenvironments have inimitable total organic carbon (TOC) characteristics, gas contents, porosities, sedimentary structural characteristics, reservoir thicknesses, and mineral compositions [8, 9]. Variances in physical characteristics can enhance the quality of shale gas reservoirs and evolve the control effect of sedimentary microfacies on the changes and distributions of reservoir properties [8, 10–13]. In recent years, research on shale sedimentary facies has been directly used to determine favourable zones and well drilling locations [14–16]. The basis of previous research on shale sedimentary facies is mostly

emphasized on data from core descriptions, thin section observations, laboratory analyses, etc. [17]. Based on core observations, whole-rock mineral X-ray diffraction analysis, thin section analysis, TOC measurements, and helium porosity measurements, Liu et al. [17, 18] classified shale sedimentary facies and studied the characteristics of lithofacies at different scales and their significance for shale gas exploration. Radwa et al. [19] analyzed the sedimentary facies of the upper Bahariya sandstone reservoir in the East Bahariya area of the Northwest Desert of Egypt based on the analysis of core photos, microresistivity imaging logging, mud logging, and conventional wireline logging data. Sun et al. [20] reconstructed the sedimentary evolution and analyzed the variation in sedimentary characteristics by means of visual categorization and analyzing grain size frequency distribution of sediments from boreholes for Quaternary in northern Jiangnan Basin. By analyzing the characteristics of lithofacies, trace-element ratios, and size of pyrite framboids, Han et al. [21] found that the dominant factors controlling organic matter enrichment in the Ordovician-Silurian Wufeng-Longmaxi Formation in the southeastern part of the Upper Yangtze region were regional tectonic activity. Wu et al. [22] described the associations of organic matter and mineral (OMMA) and demonstrated the impact of OMMA on the quality of shale gas reservoirs for shales in Wufeng and Longmaxi Fm. in Sichuan Basin. Chen et al. [23] compared the upper Permian Longtan Formation in the Qinglong area of western Guizhou based on rock type, mudstone colour, biological distribution, etc., based on the analysis of sedimentary facies from typical wells and typical sections. They analyzed the sedimentary environment of the organic-rich shale. Quaid et al. [24] characterized four different lithofacies in the Roseneath and Murteree shales in Cooper Basin, Australia, through a combination of wireline logging analysis, thin section petrology, X-ray diffraction, and pyrolysis analysis and established a deposition model for the Roseneath and Murteree shales. Mohammed et al. [25] discussed the geochemical and petrological characteristics of shale samples from two wells in the Late Jurassic Arwa member in the Al-Jawf Basin, Yemen; analyzed the abundance of organic matter, kerogen type, thermal maturity, and biogenicity; and evaluated the organic matter source and environmental conditions during shale deposition using biomarkers and stable isotope analysis results. Although these analytical methods are accurate and useful, they are limited by the number of core samples and core sampling costs. It is impossible to efficiently characterize the distribution of sedimentary facies based on microscopic reservoir research.

The current study institutes and demonstrates a classification standard for the sedimentary microfacies of the Longmaxi shale based on elemental and electrical characteristics by innovatively introducing geochemical elemental changes and electrical characteristics into the sedimentary microfacies division, which can be used in the quantitative evaluation of shale sedimentary microfacies without core data. As shale gas and oil are both generated and stored in shale, sedimentary facies control the development of shale reservoirs. The efficient division of sedimentary facies can quickly

locate high-quality shale reservoirs and is of countless importance for selecting shale gas areas and well-drilling locations.

In this study, a comprehensive division of sedimentary microfacies is carried out based on elemental characteristics, electrical properties, and core analysis and laboratory data from 12 shale evaluation wells in the Lower Silurian Longmaxi Formation in the Weiyuan area of the southern Sichuan Basin, China. In-depth analysis of the relationship between microfacies and locations of high-yield wells is directed, the classification standard of the sedimentary microfacies in the Weiyuan area is recognised, the main control facies and belts for high shale gas production are elucidated, and the empathetic of the distribution rules of high-quality reservoirs is excavated, providing a theoretical basis for the selection of favourable shale gas zones and well-drilling locations in this area.

2. Geological Setting

2.1. Sedimentary and Stratum Characteristics. During the deposition of the Wufeng Fm., the region west of Longmen Mountain, located to the west of the Sichuan Basin, was rifted during the continuous subduction of the Paleotethys Ocean. With the northward subduction of the South Qinling Ocean to the north of the Sichuan Basin, the Yangtze Block approached the North China Block, while the Cathaysian Block to the east of the Sichuan Basin was further strapped to the northwest. Consequently, the Qianzhong Uplift was exposed to the water surface, resulting in further narrowing of the Upper Yangtze Craton Basin. By the time of deposition of the Longmaxi Fm., the Qianzhong Uplift further expanded and connected with the Kangdian Ancient Land in the western Sichuan Basin. To the east of the Sichuan Basin, the Xuefeng Underwater Uplift started to form. The initial development of the Xuefeng Underwater Uplift to the east of the basin and the further uplift in the Chuanzhong area made the sedimentary environment of the Sichuan Basin and its surrounding areas a comparatively quiet shelf environment surrounded by a paleouplift belt with a semienclosed water body. The Early Silurian sedimentary evolution in the Weiyuan area has shown that during the Rhuddanian Stage, from 440 Ma to 438 Ma, the sedimentary basement in the Weiyuan area was high on both sides and low in the middle due to the compression of the Qianzhong Uplift and Chuanzhong ancient uplift [26]. The Longmaxi Formation deposited a set of deep-water organic-rich siliceous shales in a deep-water anoxic outer shelf sedimentary environment. After entering the Aeronian Stage, the Weiyuan area was still in a deep-water marine environment. The deposition rate of the organic-rich shale was low, and comparatively thin black shales were deposited. During the late Longmaxi Terechian stage, tectonic compression was more intense, and the strata continued to be uplifted; consequently, shallow-water inland shelf subfacies were successively deposited in the Weiyuan area [27].

The target layer of the current project is the Longmaxi Fm., a set of stable dark marine shales that can be divided into the Longmaxi-1 Member and Longmaxi-2 Member by

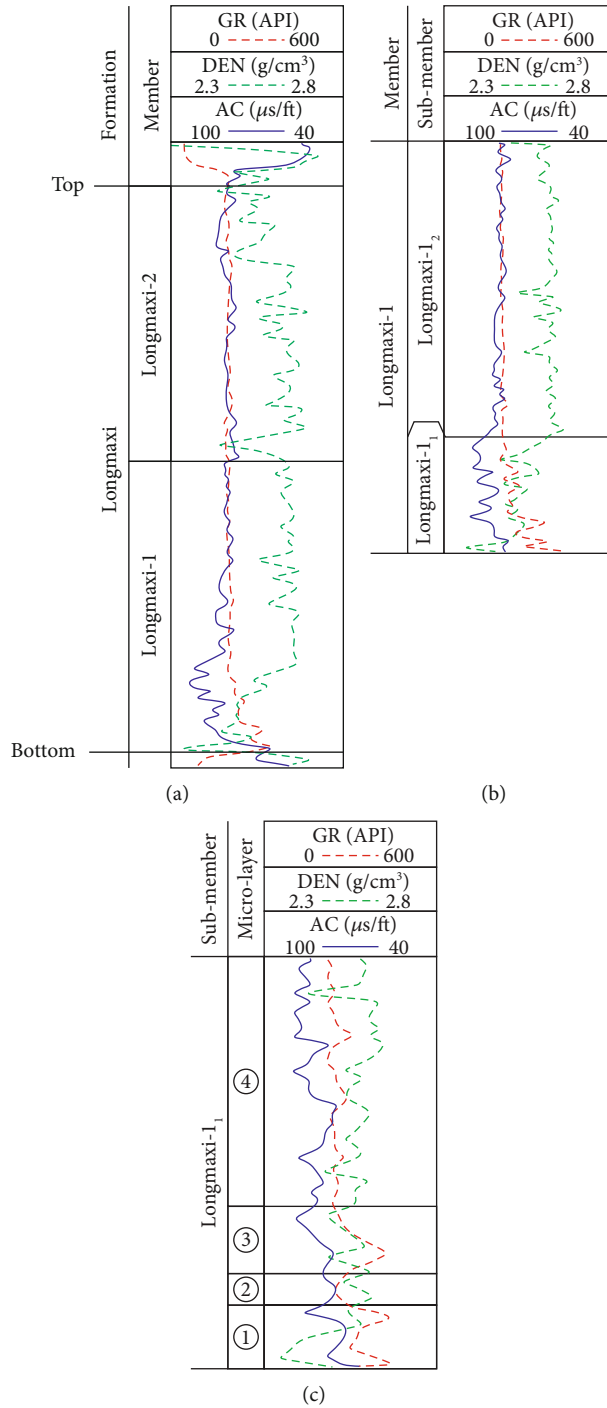


FIGURE 1: Electrical stratification characteristics of the Longmaxi Fm. in the Weiyuan area.

logging characteristics. The natural gamma curve presents a sharp upward peak at the Wufeng Fm. and Longmaxi Fm. boundary, showing a maximum at the bottom of the Longmaxi Fm. According to the halfway point between the rising gamma and declining density logs, the Longmaxi Fm. can be divided into the Longmaxi-1 Member and the Longmaxi-2 Member from bottom to top (Figure 1(a)). The Longmaxi-1 Member features a set of black carbonaceous shales deposited after rapid sea level rise during the Early Silurian. This member is rich in paleontological fossils such as graptolite,

with silty bands at its top. The Longmaxi-2 Member is composed of grey and grey-green shale, with many silty bands and a few graptolites [28, 29].

The Longmaxi-1 Member is divided into the underlying Longmaxi-1₁ Submember and the overlying Longmaxi-1₂ Submember by lithological characteristics. The Longmaxi-1₂ Submember is dark grey shale at its bottom, while the underlying Longmaxi-1₁ Submember is grey-black shale at its top. The natural gamma curve in the Longmaxi-1₁ Submember is generally higher than that in the Longmaxi-1₂

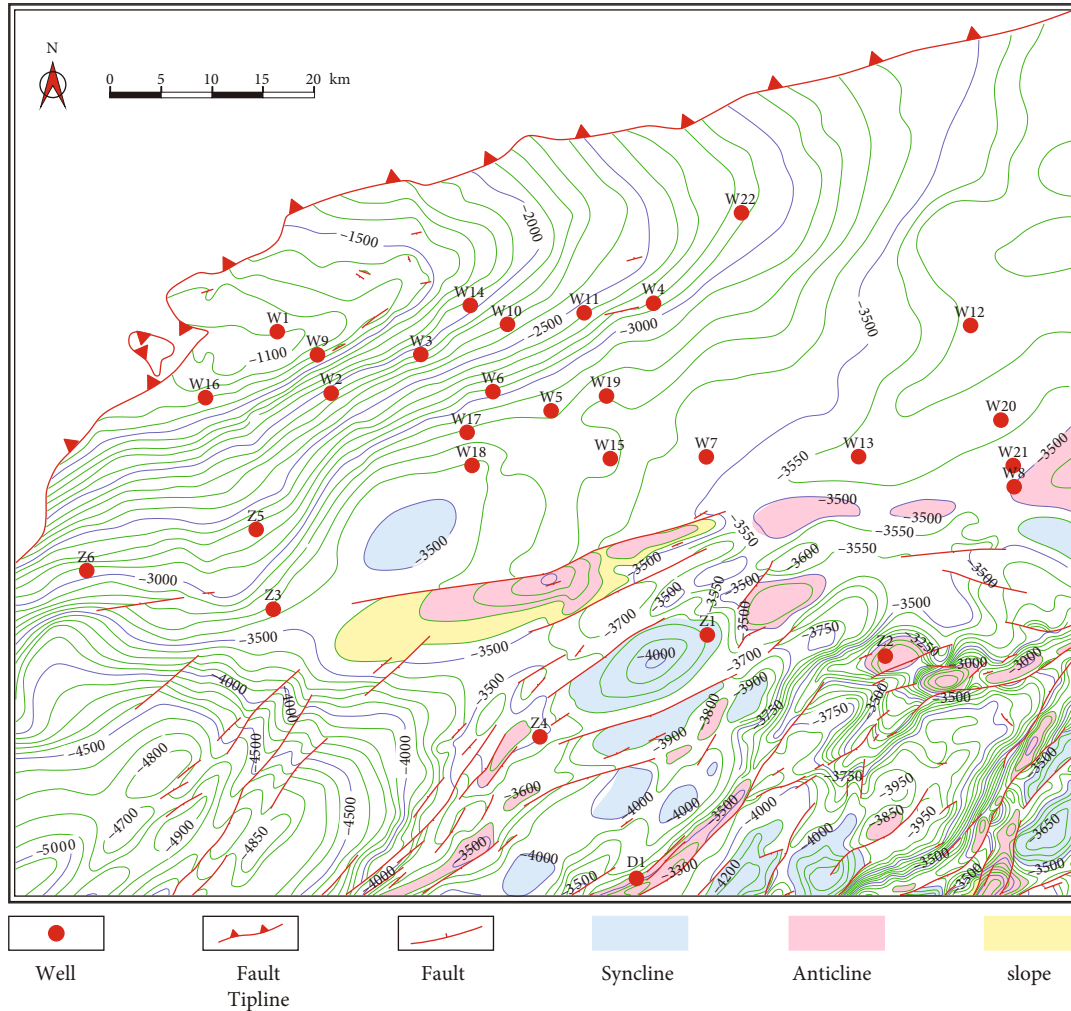


FIGURE 2: Structural contour map of the Weiyuan area.

Submember, and the increasing trend is enhanced at the bottom of the Longmaxi- 1_2 Submember. After entering the Longmaxi- 1_1 Submember, a decrease in acoustic time difference occurs and institutes a box-shaped curve. In contrast to the acoustic time difference, the waveform density first increases in the form of a funnel and decreases in a box shape after entering the Longmaxi- 1_2 Submember (Figure 1(b)).

In the Longmaxi- 1_1 Submember, four microlayers, namely, Microlayer ①, Microlayer ②, Microlayer ③, and Microlayer ④, are divided according to their electrical characteristics (Figure 1(c)). Microlayer ④ has higher gamma than the bottom of its overlying Longmaxi- 1_2 Submember. Compared with the underlying Microlayer ③, Microlayer ④ has a box-shaped low natural gamma curve, lower acoustic time difference, and higher density. Microlayer ③ has a high gyro-shaped natural gamma curve, showing a high acoustic time difference and low density. Microlayer ② has a low flat box-shaped natural gamma curve, similar to the natural gamma curve of Microlayer ④. The maximum natural gamma value in the Longmaxi Fm. is observed at the bot-

tom of Microlayer ①, and the boundary of Microlayer ① is at the halfway point of the decreasing natural gamma curve.

2.2. Tectonic Characteristics. The study area is located in the southeastern slope belt of the Weiyuan Anticline (Figure 2). The Lower Silurian Longmaxi Fm. has been garled totally in the northwestern Weiyuan area and amplifying gradually to the southeast. The strata dip gently, and the burial depth increases gradually from northwest to southeast. The faults in the study area are normally less developed, and only a few northeast-southwest faults are present in the southeast region.

3. Samples and Data Sources

The data employed in this study come from 12 assessment wells in the study area, which are distributed in different structural positions throughout the Weiyuan block. In Well 8, 21 core samples were collected from the bottom of the Longmaxi Fm. and analyzed by a Rock-Eval 6 pyrolysis instrument to obtain the TOC content, rock pyrolysis, and

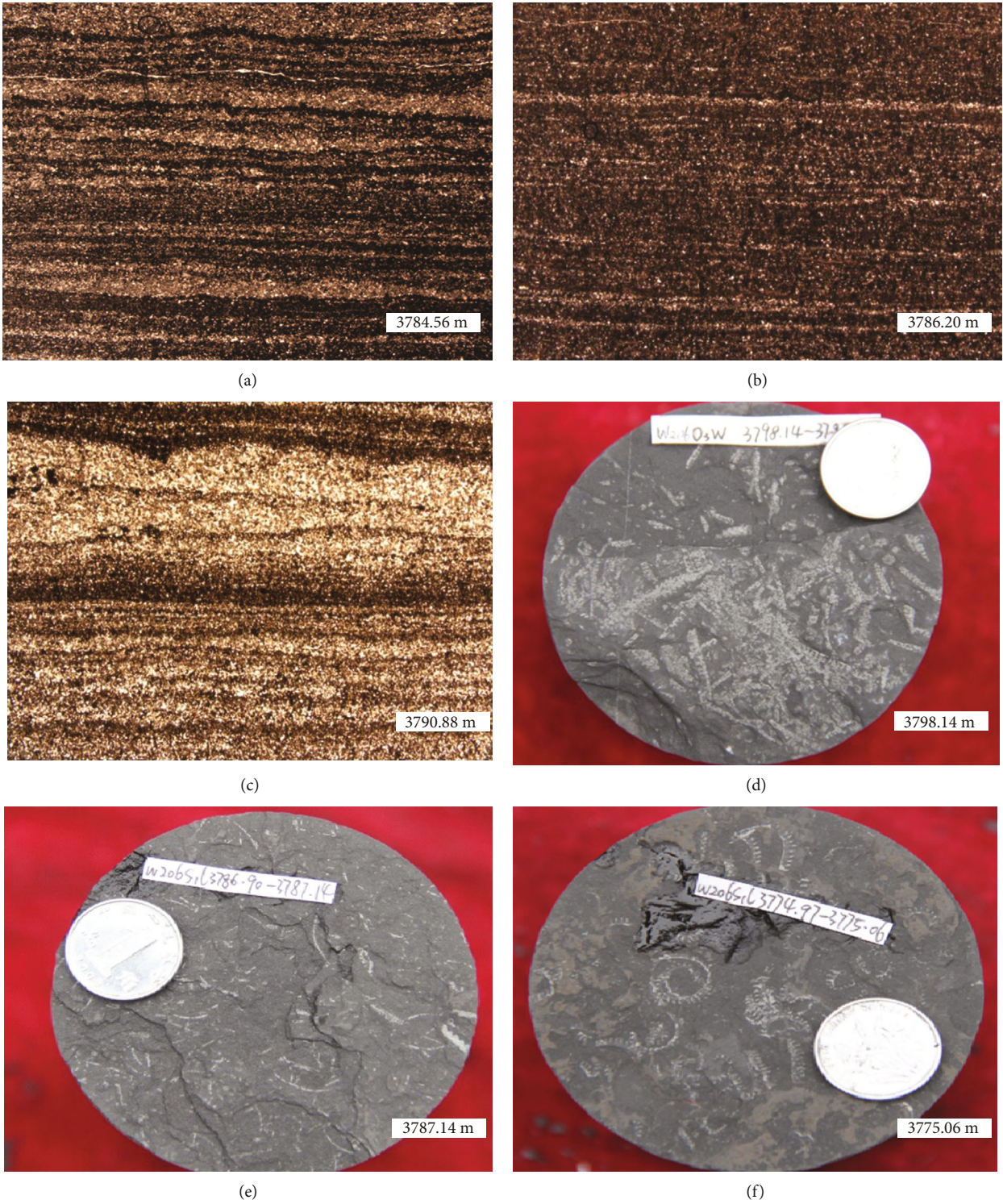


FIGURE 3: Continued.

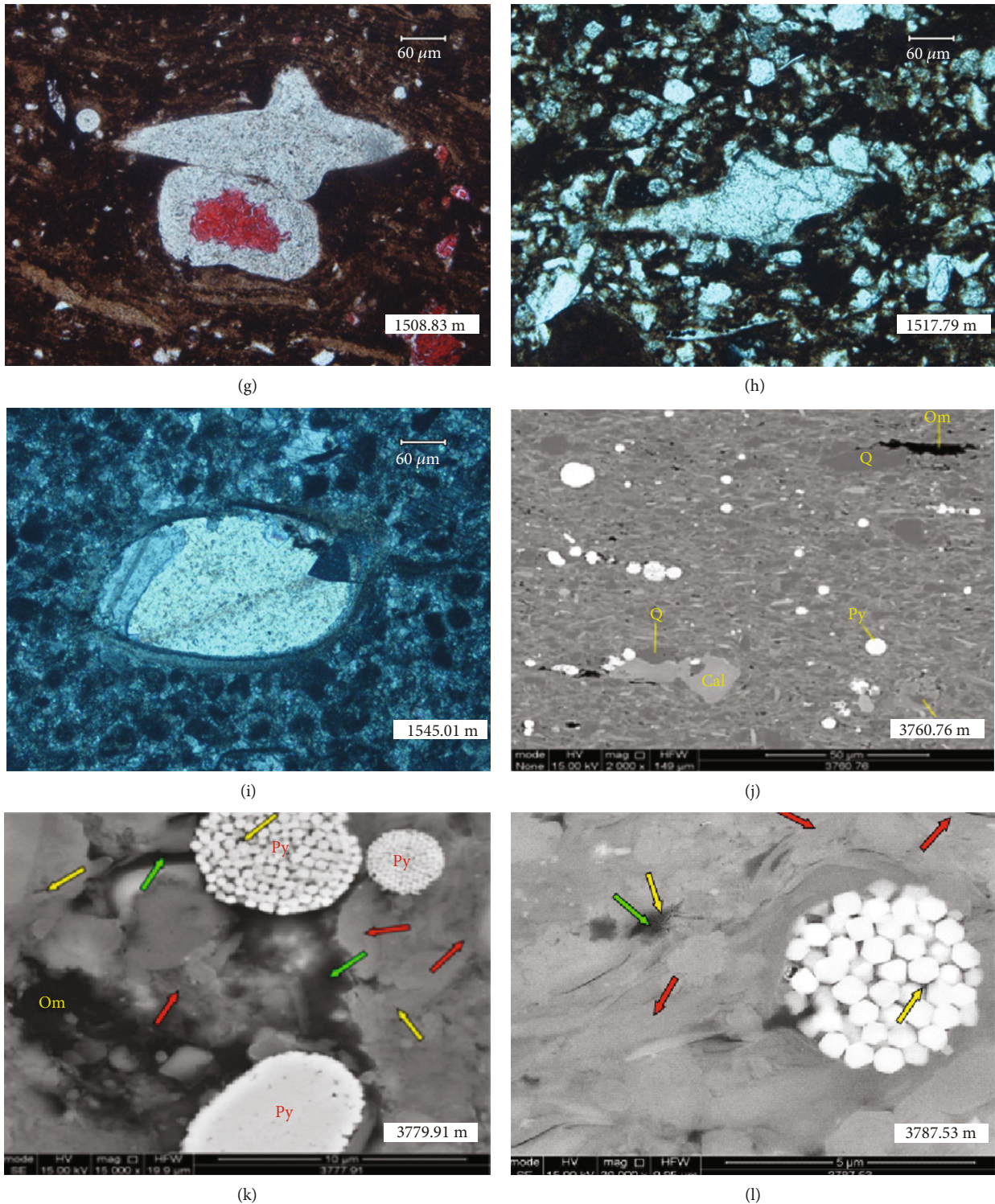


FIGURE 3: Sedimentary facies indicators of Well 8 and Well 1 in the Weiyuan area: (a) horizontal grain, silty carbonaceous shale; (b) horizontal grain, silty shale; (c) black carbonaceous shale; (d) graptolite in Microlayer ①; (e) graptolite in Microlayer ②; (f) graptolite in Microlayer ③; (g) siliceous spicule of Longmaxi Fm.; (h) siliceous spicule; (i) ostracod; (j) pyrite framboids in Microlayer ④; (k) pyrite framboids in Microlayer ③; (l) pyrite framboids in Microlayer ②.

thermal maturity. Ten core samples were selected for thin section fluorescence analysis, 10 core samples were selected for Ar-ion milling scanning electron microscopy analysis (AIM-SEM), and 23 core samples were selected for X-ray

diffraction analysis. Eighteen core samples from Well 12, 30 core samples from Well 20, 23 core samples from Well 8, and 38 core samples from Well 23 were tested by a Rock-Eval 6 pyrolysis instrument to obtain the TOC

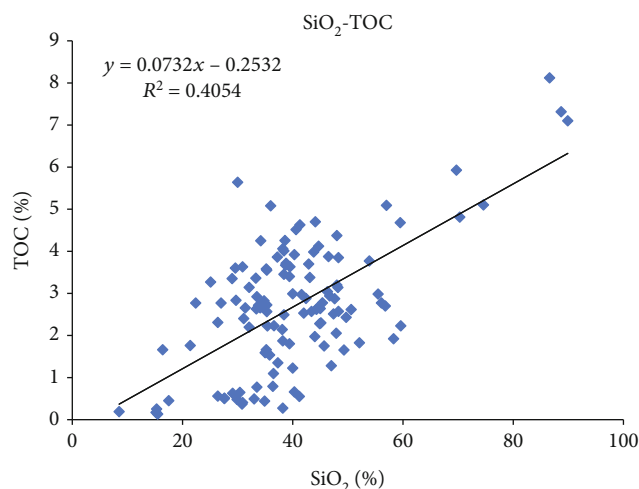


FIGURE 4: Relationship between TOC and U/Th from 4 evaluation well cores in the Weiyuan area.

contents and examined by an Axios-MAX X-ray fluorescence spectrometer to obtain the U and Th contents. A total of 142 cutting samples in the target layer were collected from Well 7. Element contents, including Si, Al, Ti, V and Cr, were analyzed by a CIT-3000SY X-ray fluorescence spectrometer. In addition, 40 core samples of the Lower Silurian Longmaxi Fm. were taken from Well 3, Well 2, Well 14, Well 10, Well 1, Well 11, Well 4, Well 7, and Well 8 to test the TOC contents by a CS230 carbon-sulfur analyzer, and the quartz content was evaluated by X-ray diffraction analysis. Logging data, including GR, AC, CNL, DEN, TOC, U, and Th curves, provided by China Petroleum Logging Co., Ltd. Southwest Branch were collected from 10 wells, together with the testing production data of 13 horizontal wells in the study area.

4. Sedimentary Facies Characteristics

Previous studies on the sedimentary facies of the Lower Silurian Longmaxi Fm. in the Sichuan Basin have shown that this formation consists of shallow sea shelf facies deposited in an inner shelf environment corresponding to the upper Longmaxi Fm. and an outer shelf depositional environment corresponding to the lower Longmaxi Fm [30–33]. The outer shelf is below the storm wave base with a water depth of 40 m~200 m, which represents a quiet, oxygen-poor, and deep-water-reducing marine environment. The lithology is mainly black, grey-black carbonaceous argillaceous shale, grey-black shale, and silt-containing shale. The inner shelf is in a relatively shallow-water area between the normal wave base and storm wave base with a water depth of 20 m~40 m and is a standing water low-energy environment that is merely affected by severe storm waves. The sediments are mainly dark terrigenous argillaceous siltstone and silty mudstone. The main research goal in this study is targeting the bottom of the Longmaxi Fm., which belongs to the outer shelf sedimentary facies.

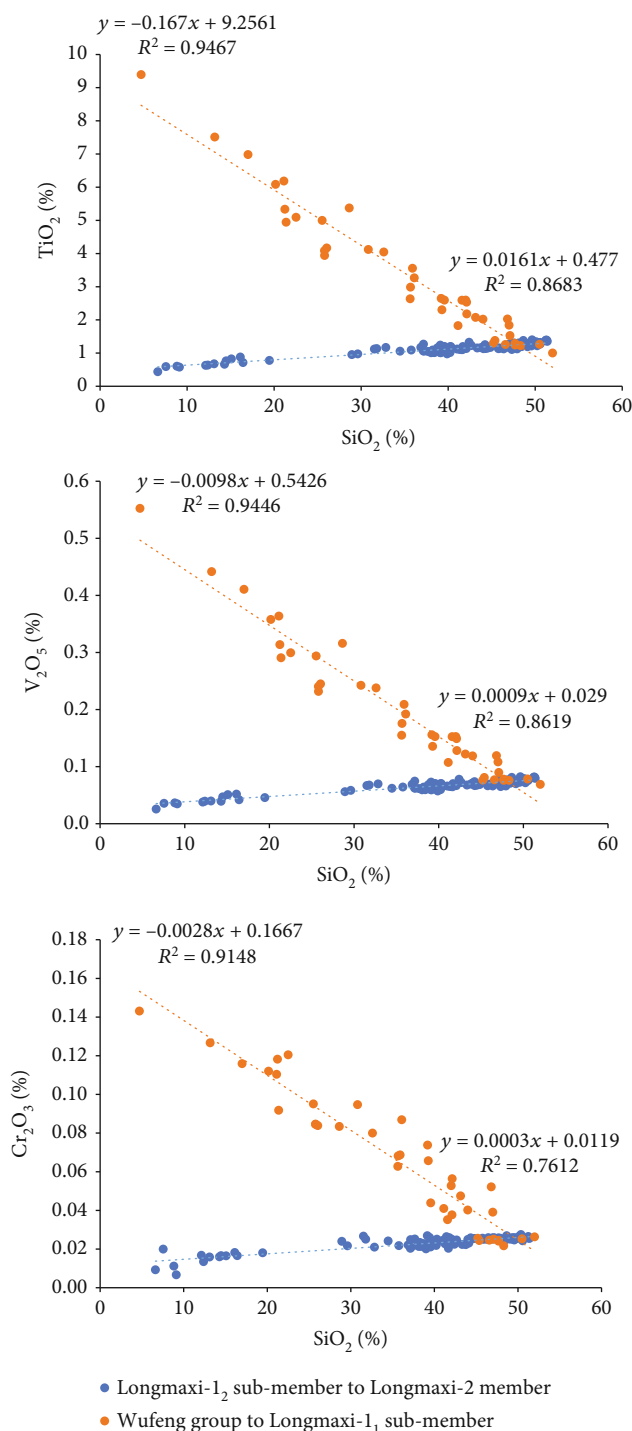


FIGURE 5: Relationships between SiO_2 and TiO_2 , V_2O_5 , and Cr_2O_3 of the Longmaxi Fm. in the study area.

4.1. *Markers of Sedimentary Facies.* Markers of sedimentary facies form the basis of facies analysis and palaeogeographical studies [34, 35]. The current project has been inclusively focused on the development of classification and sedimentary microfacies characteristics based on previous studies and sedimentary facies markers such as sedimentary structures, paleontological markers, sequence characteristics,

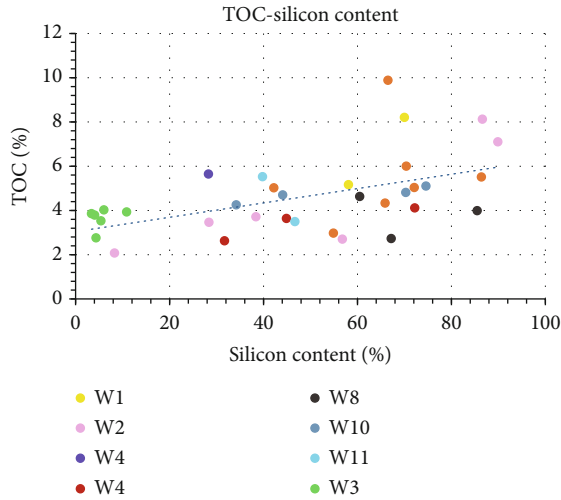


FIGURE 6: Relation between TOC and silicon content in seven evaluation wells in the study area.

geochemical elements, and logging facies characteristics in the Longmaxi Fm. in the study area.

4.1.1. Sedimentary Structures. Sedimentary structures are moulded under physical, chemical, and biological impacts during or after sediment deposition, showing heterogeneous sediment compositions, structures, and colours [36]. Principal observations from Well 8 showed that multiple bedding structures are urbanised in the Longmaxi-1₁ Submember, chiefly horizontal bedding, rhythmic bedding, and massive bedding, indicating weak hydrodynamic forces during deposition. Bright-dark horizontal beddings are composed of thin layers of silt and black peat. Moreover, small amounts of dolomite and needle-shaped mica are found in the silt (Figures 3(a)–3(c)).

4.1.2. Palaeobiological Markers. Palaeobiological markers are the imperative indicators for unifying marine and nonmarine facies in sedimentary environments. The environment strictly controls the distribution of biotic groups and ecological geographies [37]. There is adaptive and differentiated specific biota in different sedimentary environments [38, 39]. The core and thin section identification data of Well 8 show that the Longmaxi Fm. consists of diverse graptolite fossils. As relatively large and well-preserved fossils, monograptids and rastrites are most commonly observed in the core (Figures 3(d)–3(f)). These organisms have been recognised to live in a deep-water environment (usually below 60 m) characterized by a quiet and reducing environment. In general, graptolites were first observed in Micro-layer ④. In addition, abundant siliceous skeletons of organic fossils, such as sponges, radiolarians, and spicules, can also be found (Figures 3(g)–3(i)), representing a deeper deep-water shelf sedimentary environment.

4.1.3. Characteristics of Syngenic Minerals. The syngenic mineral assemblage is a central indicator to assess the oxidizing or reducing conditions of a sedimentary environ-

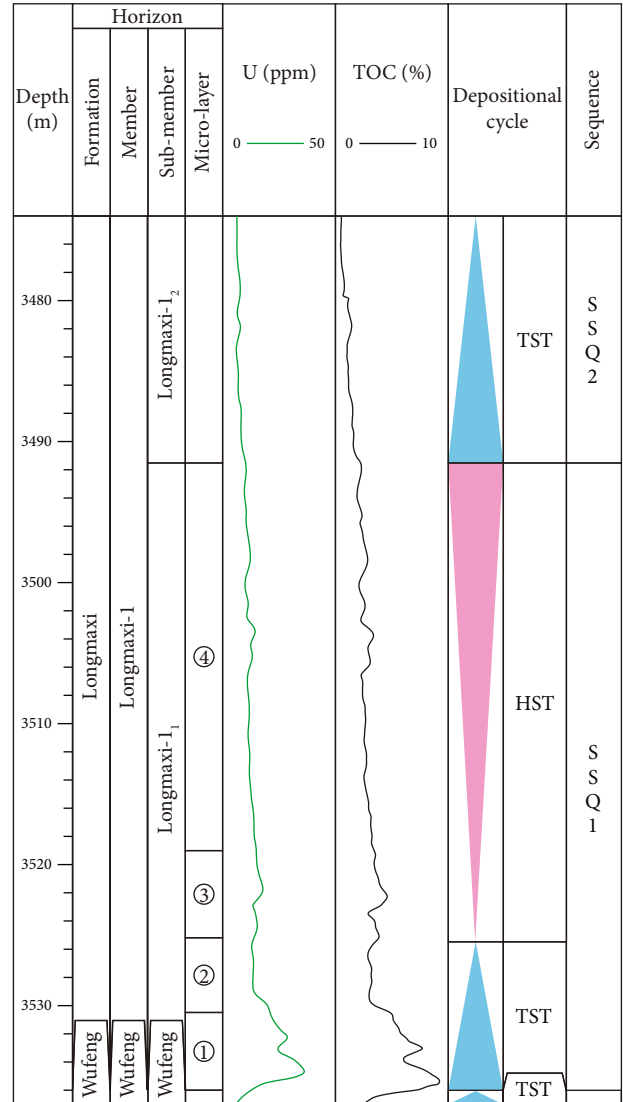


FIGURE 7: Sequence characteristics of Well 5 in the Weiyuan area.

ment [31]. Since Fe is sensitive to the Eh value of the medium, in the reducing environment of marine basins, with a decrease in the Eh value, the valence of Fe also changes accordingly, and it is more likely to form ferrous pyrite. Pyrite patches, pyrite bands, and pyrite clumps are frequently seen in the black shale of the Longmaxi Fm. in the study area, especially in the bottom strata. Additionally, the appearance of framboidal pyrite indicates that the basin was in a strongly reducing environment during the early deposition of the Longmaxi Fm. (Figures 3(j)–3(l)).

4.1.4. Geochemical Element Features. Early studies have demonstrated that various macro- and microelements are indicators of the sedimentary environment [40–44]. In the study of the shale sedimentary environment, aluminium (Al), uranium (U), and the U/Th ratio are usually used to indicate the water depth of the sedimentary environment [45]. Based on elemental mud logging data of 12 evaluation wells in the study area, U/Th and biogenic silicon Si_{Bio} are

TABLE 1: Classification of the sedimentary microfacies of the Longmaxi Fm.

Sedimentary facies	Subfacies	Microfacies	U/Th	TOC (%)	Si _{Bio} (%)
Shelf	Inner shelf	Shallow-water argillaceous silty shelf	<0.15	<1.5	<2.0
		Shallow-water silty argillaceous shelf	0.15~0.5	1.5~2.0	<2.0
	Outer shelf	Deep-water silty argillaceous shelf	0.5~1.25	2.0~3.0	10.0~15.0
		Organic-rich silty argillaceous shelf	0.5~1.25	3.0~5.0	10.0~15.0
		Organic-rich silicon-containing argillaceous shelf	1.25~2.0	3.0~5.0	15.0~20.0
		Organic-rich siliceous argillaceous shelf	>2.0	>5.0	>20.0

selected as characteristic parameters to build the classification criteria of sedimentary microfacies in this area.

(1) *U/Th*. The microelements U and Th, as imperative indicators of the paleo-ocean oxidation-reduction environment, are frequently used as the criteria to judge oxidizing or reducing environments according to the ratio of U/Th [46]. In the large-scale transgression period, the sedimentary environment in the Weiyuan area was anoxic and strongly reducing, conducive to the enrichment and preservation of organic matter. Therefore, the organic-rich shale was mostly formed in an anoxic environment. Correspondingly, the content of U increased sharply, ranging from 10 ppm to 40 ppm, and the U/Th value increased to more than 2.0. In contrast, the sedimentary environment formed during regression was shallow water with relatively oxidizing solid conditions. There was a less organic matter in this environment, but siltstone, silty mudstone, and calcareous silty mudstone were easier to form, reflecting that the transitional marine environment was affected by the supply of terrestrial sediments. Correspondingly, the content of U decreased sharply, ranging from 5 ppm to 15 ppm, and the U/Th value decreased to 0.5~1.25 [47].

The elemental content analysis in the target shale from four evaluation wells shows that the U/Th value of the Longmaxi-1₁ Submember is significantly higher than that of the upper Longmaxi Fm., and the peak value appears in Micro-layer ①. There is a relatively good positive correlation between TOC content and the U/Th ratio, indicating that the anoxic sedimentary environment was more conducive to preserving organic matter (Figure 4).

(2) *Biogenic Silicon Content Index*. Shale reservoirs have low porosity and permeability, and industrial productivity requires large-scale sand-up fracturing [48, 49]. Siliceous minerals such as quartz, feldspar, and mica, both terrigenous and biogenic, are the main brittle minerals conducive to volume fracturing. However, Ti, V, and Cr are all derived from terrigenous debris. Therefore, the content of terrigenous SiO₂ in mineral components is significantly positively correlated with TiO₂, V₂O₅, and Cr₂O₃, while the content of biogenic SiO₂ is significantly negatively correlated [50]. The intersection diagram of SiO₂ content and TiO₂, V₂O₅, and Cr₂O₃ content shows that SiO₂ in the Longmaxi-1₁ Submember is mainly biogenic and negatively correlated with the TiO₂, V₂O₅, and Cr₂O₃ contents. SiO₂ in the Long-

maxi-1₂ Submember to Longmaxi-2 Member is mainly terrigenous and positively correlated with the TiO₂, V₂O₅, and Cr₂O₃ contents (Figure 5).

Biogenic siliceous shale components, usually derived from biological skeletons, can amplify the fracturing by increasing rock brittleness and also direct organic matter accumulation. An intersection analysis of the silicon content and TOC in the cores of seven evaluation wells in the study area was conducted, and the silicon content showed a positive correlation with TOC (Figure 6). Micro-layer ①, the most favourable development target layer, was deposited in a period of rapidly rising basin water level with considerable organic matter accumulation. Therefore, the silicon content in the lower Longmaxi Fm. is mostly biogenic silicon.

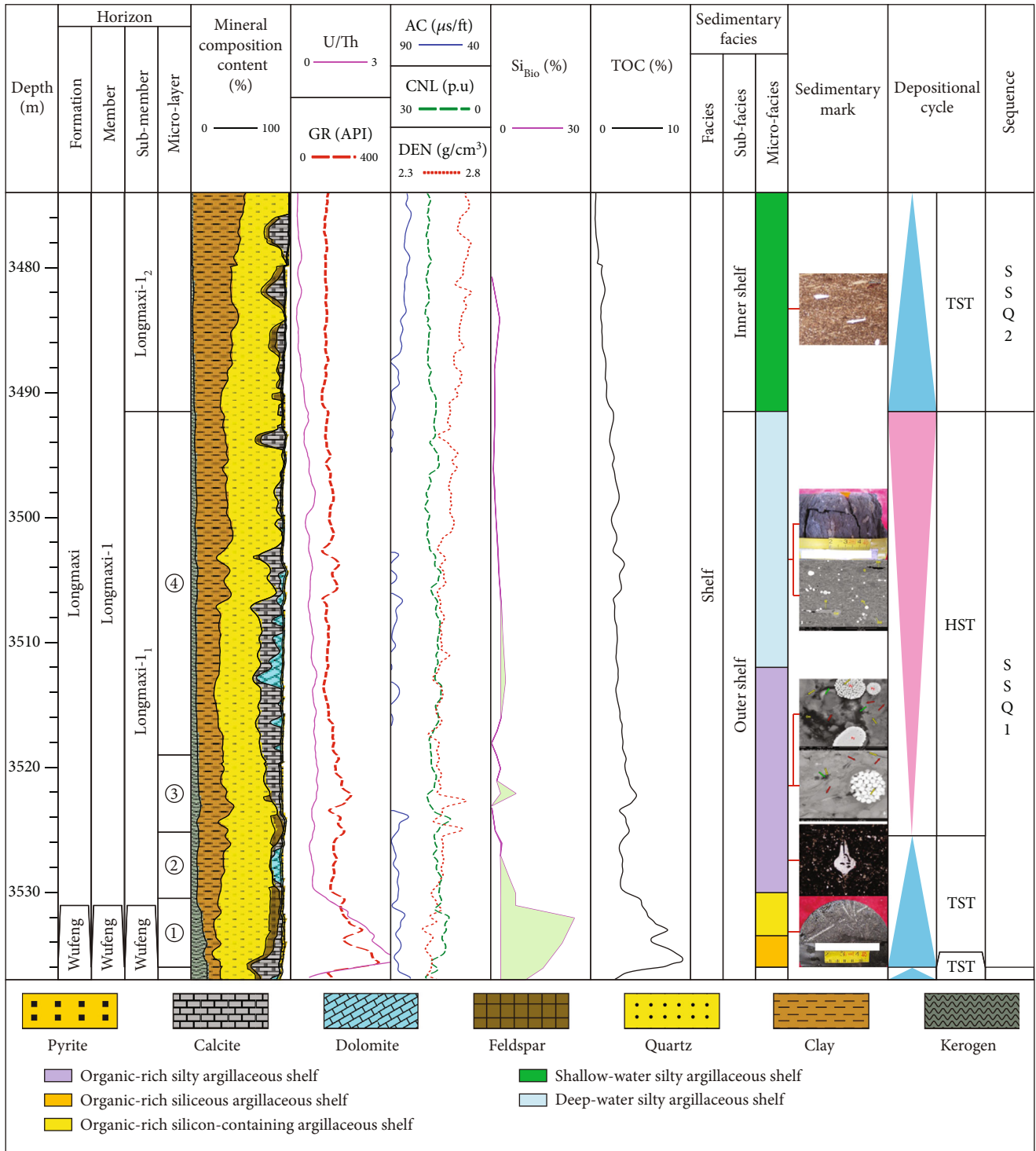
The current project has been cited the calculation method of excess silicon proposed by Holdaway and Clayton [51]. In contrast to the elemental mud logging data, the content of biogenic silicon Si_{Bio} in the Longmaxi-1₁ Submember is calculated for seven evaluation wells in the study area as the identification basis of sedimentary microfacies:

$$Si_{Bio} = Si_{elementary} - \left[\left(\frac{Si}{Al} \right)_{bg} \times Al_{elementary} \right], \quad (1)$$

where Si_{Bio} is the biogenic silicon content, %; Si_{elementary} is the silicon content from elemental mud logging, %; and (Si/Al)_{bg} is the weighted average Si/Al elemental content ratio in the nonreservoir section of the Longmaxi Fm., which varies within 2.6~3.6, and the average value is 3.11.

4.1.5. Sequence Characteristics. This paper draws on the experience of Barnett shale in identifying multiple third-class sequences based on the U curve, GR, and TOC [52, 53]. Based on the curve form of the U log and the organic carbon mass fraction $w(\text{TOC})$, two complete third-class sequences were identified in the Longmaxi Fm. in the study area (Figure 7).

Third-class sequence SSQ1: the top boundary of SSQ1 lies at the bottom of the Longmaxi-1₂ Submember, and the bottom boundary of SSQ1 lies at the bottom of the Longmaxi-1₁ Submember. The thick black carbonaceous shale at the bottom of the Longmaxi-1₁ Submember formed in the transgressive system tract (TST), representing sea level rise. The U element curve is bell-shaped and increases promptly from bottom to top. The sediment is characterized



(a)

FIGURE 8: Continued.

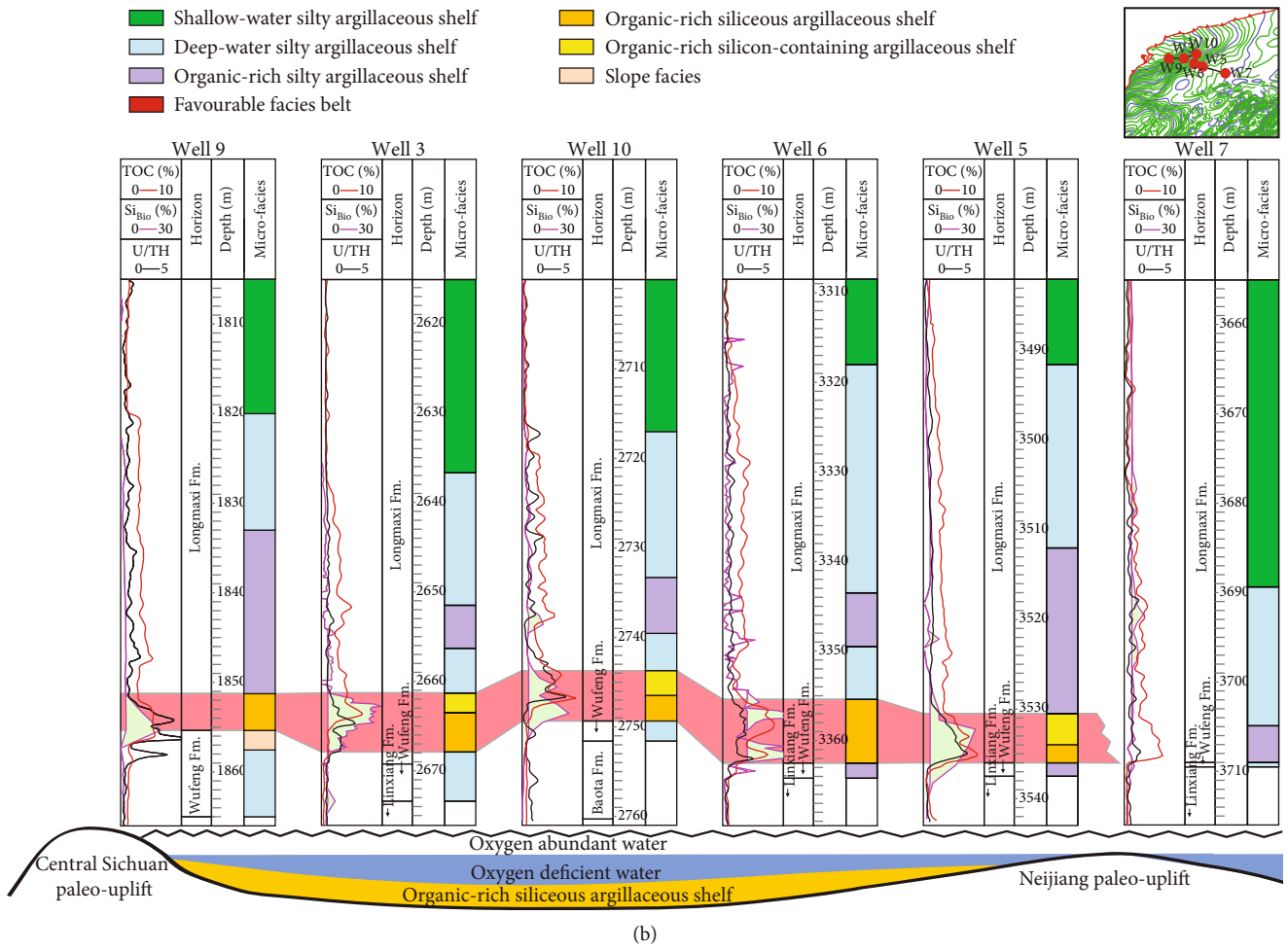
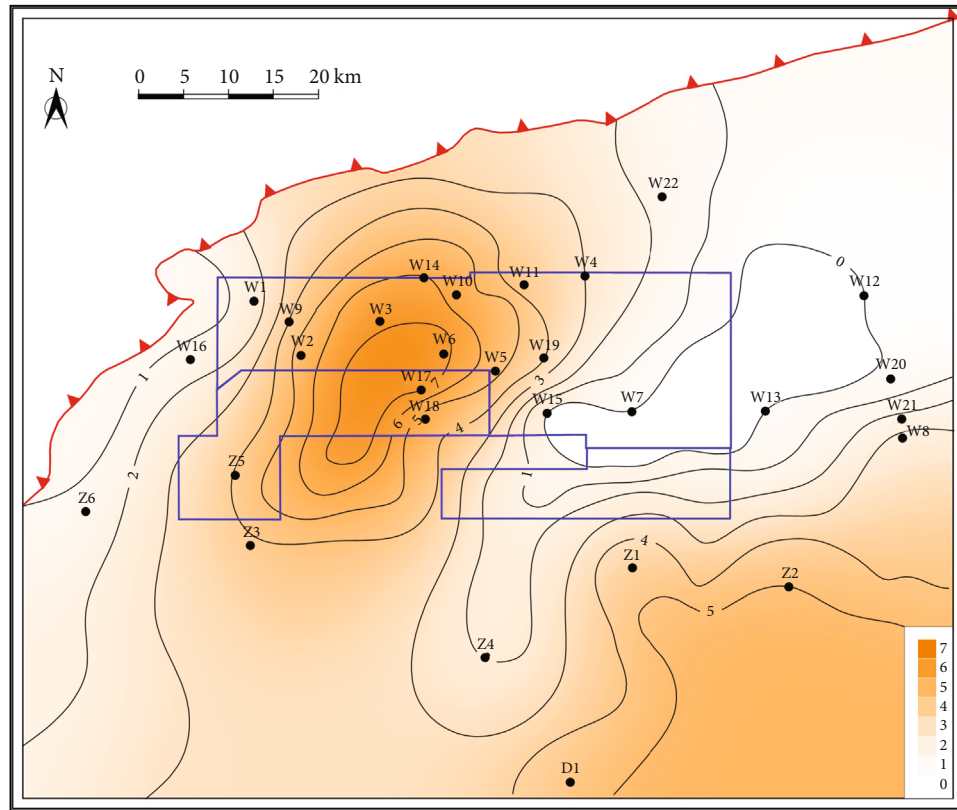


FIGURE 8: Continued.



(c)

FIGURE 8: Sedimentary environment in the Weiyuan area. (a) Sequence characteristics of Well 5 in Weiyuan area. (b) Sedimentary facies column and paleouplift. (c) Thickness distribution of favourable sedimentary microfacies.

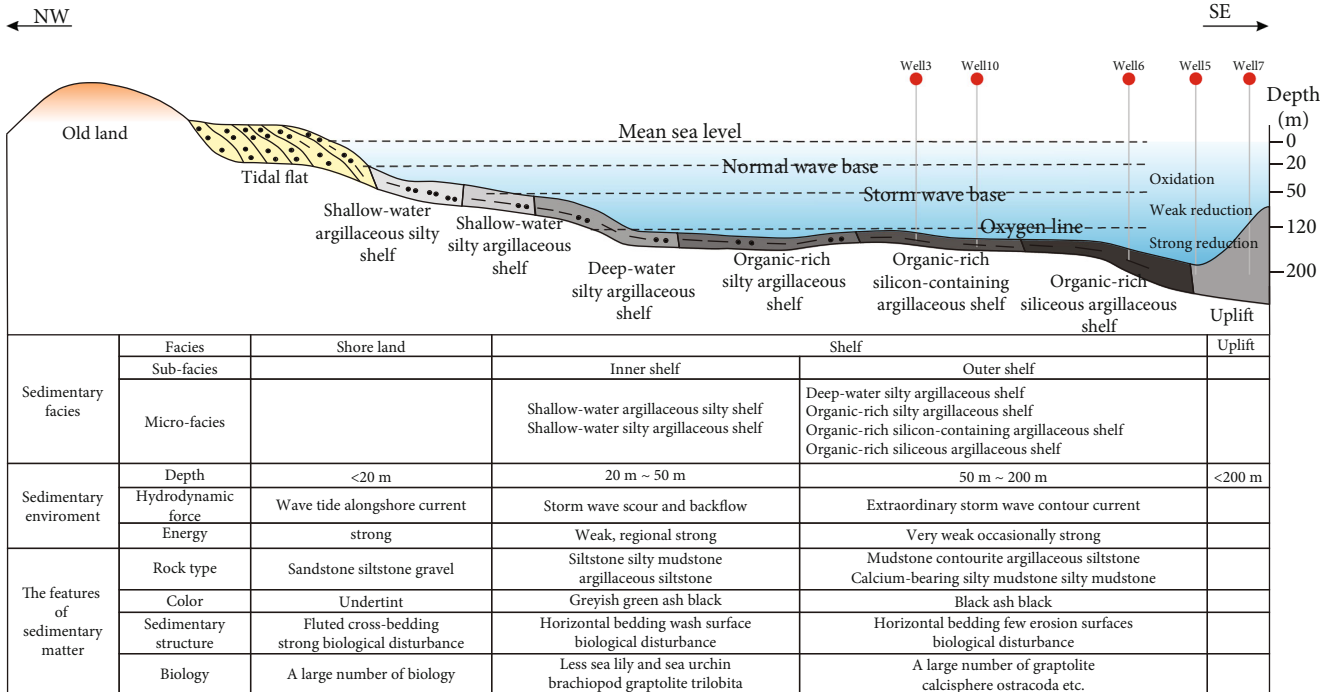


FIGURE 9: Sedimentary model of Longmaxi Fm. in the Weiyuan area.

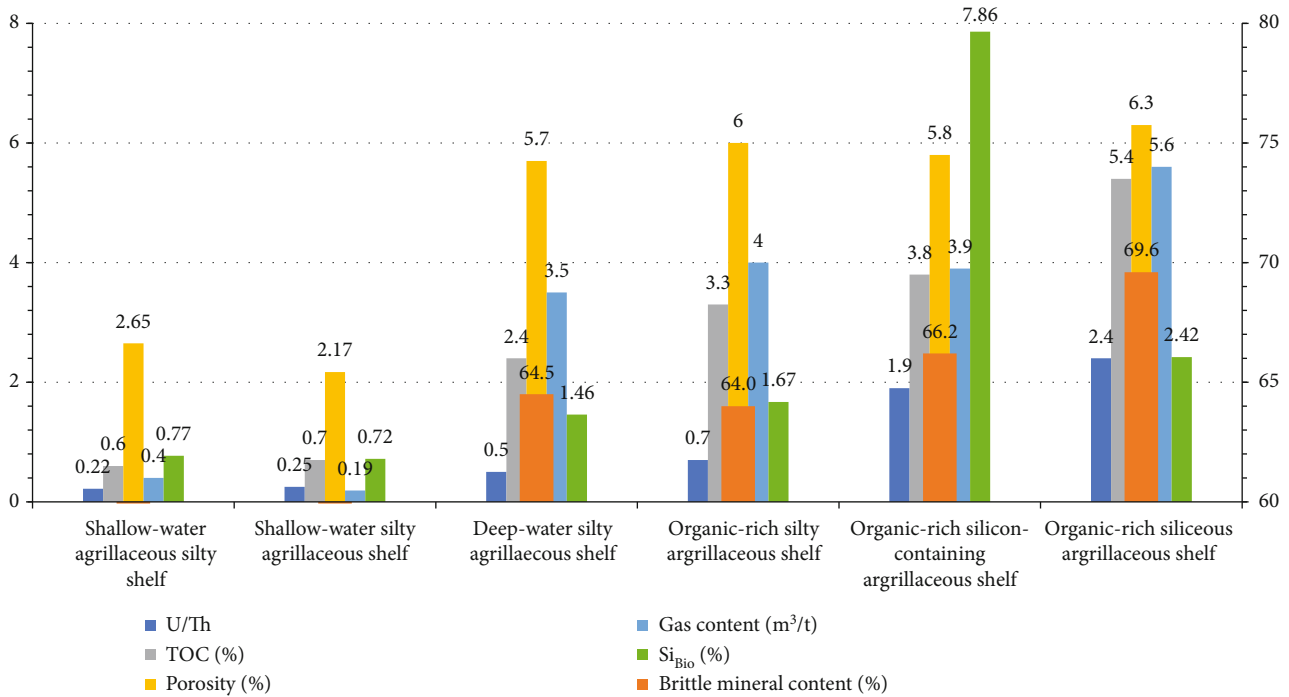


FIGURE 10: Reservoir properties of the six types of sedimentary microfacies in the Longmaxi Formation in the study area.

by rich biological content, a large number of graptolite fossils, and siliceous and calcareous bioclastic. The TOC calculated is high, $w(\text{TOC}) \geq 5\%$, representing a high-quality reservoir section with high hydrocarbon generation potential. The organic-rich silty mudstone and deep-water silty mudstone in the upper Longmaxi-1₁ Submember are formed in the highstand system tract (HST), and $w(\text{TOC})$ decreases to 2%~5%, which is a retrograding sequence that becomes shallow upward and is the secondary source rock formed during the HST.

The top boundary of SSQ2 lies at the top of the Longmaxi Fm. The bottom boundary of SSQ2 lies at the bottom of the Longmaxi-1₂ Submember. The TST, developed in the microfacies of the shallow-water silty argillaceous shelf face in the Longmaxi-1₂ Submember, is a transition from regional regression to transgression, which is correlated with the rapid rise of sea level and the rapid intrusion of water bodies. The shallow-water silty argillaceous shelf face of the Longmaxi-2 Member formed in the lowstand system tract (LST), representing a receding sea level, shallow water bodies, and relatively coarse sediments. The U element curve is funnel-shaped with a gradual decrease in amplitude, and $w(\text{TOC})$ is low ($\leq 2\%$).

4.2. Classification of Microsedimentary Facies. In this paper, based on previous studies, three parameters, namely, the U/Th ratio, the biogenic silicon content (Si_{Bio}), and the organic carbon mass fraction $w(\text{TOC})$, are optimized, and a quantitative classification standard of sedimentary microfacies for the Longmaxi Fm. in the study area is established. Six sedimentary microfacies are identified in the target layer (Table 1). Among them, shallow-water argillaceous silty shelf and shallow-water silty argillaceous shelf microfacies

are developed in the inner shelf with a U/Th ratio less than 0.5, TOC content less than 2.0%, and biogenic silicon content index less than 2.0%, representing an oxidizing to weakly oxidizing sedimentary environment corresponding to a lowstand-transgressive systems tract. Organic-rich siliceous argillaceous shelf, organic-rich silicon-containing argillaceous shelf, organic-rich silty argillaceous shelf, and deep-water silty argillaceous shelf microfacies are developed in the outer shelf. Their U/Th ratio is generally between 0.5 and 3.0. The TOC content is approximated between 2.0% and 7.0%. The biogenic silicon content index is between 2.0% and approximately 30.0%, which belongs to a reducing sedimentary environment corresponding to a transgressive-highstand system tract.

Figure 8(a) shows the sedimentary characteristics of the typical wells in the Weyuan area. When the sea level rises, the basin is in a low-energy environment and develops a TST system tract. The MFS appears in the SSQ1, suggesting a standing-water reducing environment with the lowest energy. The organic-rich siliceous argillaceous shelf and organic-rich silicon-containing argillaceous shelf develop in such environment and produce more organic contents and biogenic silica that contribute to the development of shale gas reservoir. From bottom to top, the microfacies can be divided into an organic-rich siliceous argillaceous shelf, organic-rich silicon-containing argillaceous shelf, organic-rich silty argillaceous shelf, deep-water silty argillaceous shelf, shallow-water silty argillaceous shelf, and shallow-water argillaceous silty shelf microfacies.

4.2.1. Organic-Rich Siliceous Argillaceous Shelf and Organic-Rich Silicon-Containing Argillaceous Shelf Microfacies. The organic-rich siliceous argillaceous shelf and organic-rich

silicon-containing argillaceous shelf microfacies are located in outer shelf waters with the lowest energy. These waters are a strongly reducing environment with weak hydrodynamic conditions and are unaffected by ocean currents and stormy currents. Such microfacies are steadily developed in the Weiyuan shale gas field. Their representative lithologies are mainly grey-black and black carbonaceous shales and locally dark block-like silty argillaceous shales. They have the typical characteristics, namely, high U/Th ($U/Th \geq 1.25$), high organic carbon mass fraction ($w(\text{TOC}) \geq 3.0\%$), and high biogenic silicon content ($Si_{\text{Bio}} \geq 15\%$). The sedimentary structure is dominated by horizontal bedding and massive bedding. Nodular, banded, and spotted pyrites are relatively developed. Many framboidal pyrites can be observed under a scanning electron microscope. The sedimentary structure is rich in graptolite fossils and a few macrobenthos fossils, mostly silicified to varying degrees. The above characteristics reflect the sedimentary environment's weak hydrodynamic conditions, indicating deep-water depositional characteristics, that is, low energy, reducing conditions, low speed, and undercompensation, suitable for accumulating and preserving abundant organic matter and the conversion to oil and gas under suitable conditions.

4.2.2. Organic-Rich Silty Argillaceous Shelf and Deep-Water Silty Argillaceous Shelf Microfacies. Organic-rich silty argillaceous shelf microfacies are deposited in low-energy water environments. These waters belong to a weakly reducing sedimentary environment with weak hydrodynamic conditions and are unaffected by ocean currents and stormy currents. The representative lithologies are dark organic-rich silty shales with U/Th ranging from 0.5 to 1.25, $w(\text{TOC})$ generally ranging from 3% to 5%, and a high biogenic silicon content (Si_{Bio} ranging from 10% to 15%). The sedimentary structure is dominated by horizontal bedding and rhythmic bedding. Nodular, banded, and spotted pyrites are relatively developed. A large number of graptolite fossils are observed in the core section. A few macrobenthos fossils and a small number of biological debris, such as siliceous spicules and ostracods, indicate deep-water depositional characteristics, that is, low energy, weakly reducing conditions, low speed, and undercompensation.

4.2.3. Shallow-Water Silty Argillaceous Shelf and Shallow-Water Argillaceous Silty Shelf Microfacies. Shallow-water silty argillaceous shelf microfacies are remarkably well established in the Weiyuan shale gas field and are generally located at the bottom of the inner shelf. Its sedimentary water body is relatively shallow and has high mud content. The representative lithologies are mainly grey-green and yellow-green silty mudstones with locally thin layers of siltstones. Shallow-water argillaceous silty shelf microfacies are situated in the shallow-water oxidizing area close to the shore. Reflected by the frequent rise and fall of sea level, the colour of sedimentary products is relatively light. The representative lithologies are mainly dark grey block-like argillaceous siltstone, silty mudstone with thin layers of grey calcium-containing argillaceous siltstone and grey-white micritic limestone, and tempestite occasionally. These two

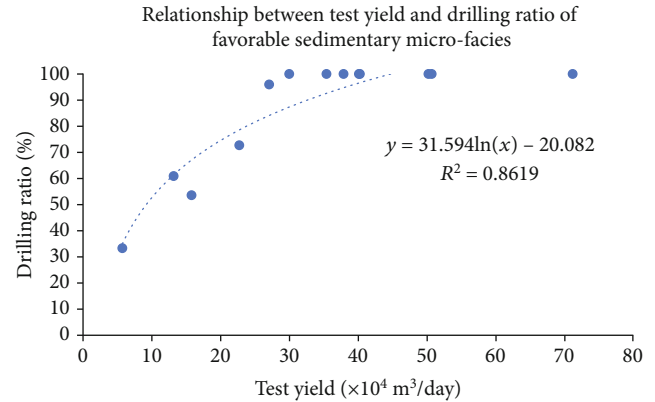


FIGURE 11: Relation between the test yield of horizontal wells and the drilling penetration rate of favourable sedimentary microfacies in the Weiyuan area.

types of sedimentary microfacies develop from the Longmaxi-1₂ Submember to the Longmaxi-2 Member. Their U/Th ratio is usually less than 0.5. They are in an oxidizing environment with a low organic matter content, where $w(\text{TOC})$ is generally less than 2.0%, and the biogenic silicon content is extremely low ($Si_{\text{Bio}} \leq 2.0\%$). Sometimes, biological disturbance structures are found. A small number of animal combinations, such as sponge spicules, trilobites, and ostracods, are found, indicating that the hydrodynamic conditions during deposition were relatively weak and the water depth was relatively shallow, showing an oxidizing environment.

Figure 8(b) presents an east-west contrast chart of the sedimentary facies of six evaluation wells in the study area. In Figure 8(b), the organic-rich siliceous argillaceous shelf microfacies and organic-rich siliceous argillaceous shelf microfacies with a high organic matter content are mainly distributed in Microlayer ① vertically and gradually thicken from west to east in the plane. In the middle of the study area, affected by the Neijiang ancient uplift, the water body becomes shallow, and the sedimentary facies change.

Figure 8(c) shows the planar thickness distribution of the organic-rich siliceous argillaceous shelf and organic-rich silicon-containing argillaceous shelf microfacies. The thickness of the favourable microfacies varies between 0 and 7 m, and the depocentre is located in the middle of the study area near Well 5 and Well 17.

4.3. Sedimentary Model. The comprehensive analysis of sedimentary physiognomies and sedimentary microfacies in the study area shows that the deposition period of the Longmaxi Fm. in this area experienced two complete three-stage sea level transgression cycles. SSQ1 starts with the Longmaxi Formation deposition, with seawater invading from the eastern Sichuan Basin. The water body increases rapidly and afterwards decreases slowly. A set of deep-water carbonaceous siliceous shales with thicknesses of approximately 50 m is deposited, which successively experiences the vertical evolution sequence of an organic-rich siliceous argillaceous shelf, organic-rich silicon-containing argillaceous shelf, organic-rich argillaceous mud shelf, and deep-water silty

argillaceous shelf microfacies. SSQ2 begins with the sedimentation of the Longmaxi-1₂ Submember and ends at the top of the Longmaxi Fm. The water depth experiences a short rise and continues to decline, and the sediments are relatively coarse-grained. The sedimentary environment transitions to shallow shelf microfacies, gradually transforming into a shallow silty argillaceous shelf and shallow argillaceous silty shelf microfacies. Affected by the Neijiang Uplift, organic-rich siliceous argillaceous shelf and organic-rich silicon-containing argillaceous shelf microfacies are not developed in the study area (Figure 9).

5. Relation between Sedimentary Facies and Shale Gas Reservoir Quality

The microfacies of the organic-rich siliceous argillaceous shelf and the organic-rich silicon-containing argillaceous shelf developed in the Longmaxi period of the Early Silurian in the study area have a U/Th ratio generally higher than 1.25 and belong to a deep-water highly reducing sedimentary environment. The sedimentary products are mainly grey-black and black carbonaceous mudstones, with thicknesses ranging from 0 m to 7.1 m, showing a trend of gradual thickening and then thinning from west to east and finally pinching out in the eastern part of the study area due to a phase change. Core tests show that the organic-rich siliceous argillaceous shelf microfacies and the organic-rich silicon-containing argillaceous shelf microfacies have a high organic carbon content (TOC > 2.0%) and a high biosilicon content ($Si_{Bio} \geq 15\%$), indicating a strong hydrocarbon generation capacity. Porosity is mostly over 3.5%, which provides storage space for hydrocarbons. The total gas content is generally more than 2.5 m³/t, which means that the microfacies have commercial exploitation value. The brittle mineral content is more than 65%, which is beneficial for volume modification (Figure 10). Considering the characteristics above, the deep-water strongly reducing marine environment suitable for organic-rich siliceous argillaceous shelf microfacies and organic-rich silicon-containing argillaceous shelf microfacies is the main controlling factor for the development of high-quality shale reservoirs.

The information gained during exploration shows that the test yield of horizontal wells in the study area is positively correlated with the drilling ratio of organic-rich silica mud shelf microfacies and organic-rich siliceous mud shelf microfacies (Figure 11). For horizontal wells with a test yield greater than 30×10^4 m³, all fracturing sections are located in the organic-rich siliceous argillaceous shelf microfacies and organic-rich silicon-containing argillaceous microfacies.

6. Conclusions

The current study is of great significance for the readers to delineate the potential production areas and amplify the scaled development of shale gas reservoirs, by providing a more efficient and quantitative categorization method for sedimentary microfacies in shale.

The Longmaxi Fm. in the Weiyuan area comprises a set of dark carbonaceous shales formed in a hydrostatic reduc-

ing environment. Two complete third-class sequences, SSQ1 and SSQ2, composed of TST and HST can be identified in the strata. SSQ1 developed in a relatively deeper still-water environment with high TOC and high biogenic silicon content. Hot shale reservoirs are mainly formed in the TST of SSQ1.

The shale of the Longmaxi Fm. deposited in the Weiyuan area is a shelf face, which can be divided into two subfacies: the inner shelf and outer shelf. The outer shelf subfacies developed in SSQ1, while the inner shelf subfacies developed in SSQ2. According to U/Th, TOC, and Si_{Bio} , a categorization of sedimentary microfacies is established and applied in the current project. In the outer shelf subfacies, six microfacies can be identified, including organic-rich siliceous argillaceous shelf microfacies, organic-rich silicon-containing argillaceous shelf microfacies, organic-rich silty argillaceous shelf microfacies, deep-water silty argillaceous shelf microfacies, shallow-water silty argillaceous shelf microfacies, and shallow-water argillaceous silty shelf microfacies.

Organic-rich siliceous argillaceous shelf microfacies and organic-rich silicon-containing argillaceous shelf microfacies are the most favourable microfacies for developing hot shale gas reservoirs. The depocentre is located in the central study area near Well 17 and Well 18. The sedimentary facies control the distribution of dark organic-rich siliceous shale, with thicknesses ranging from 0 to 7.1 m and thickening to the southeast. In the eastern part of the study area, the hot shale reservoirs are distributed in the organic-rich siliceous argillaceous shelf and organic-rich silicon-containing argillaceous shelf microfacies thin and pinch out towards the Neijiang Uplift.

Data Availability

The data are available in this article.

Conflicts of Interest

The authors declare that there are no conflicts of interest regarding the publication of this paper.

Acknowledgments

This research was financially supported by the Science and Technology Cooperation Project of the CNPC-SWPU Innovation Alliance (No. 2020CX020100) and the Study on Well Layout for Three-Dimensional Development in the Sichuan-Chongqing Main Shale Gas Producing Area (No. CQ2020B-3-1-1).

References

- [1] C. JB, "Fractured shale-gas systems," *AAPG Bulletin*, vol. 86, no. 11, pp. 1921–1938, 2002.
- [2] Z. Jinchuan, J. Zhijun, and Y. Mingsheng, "Reservoiring mechanism of shale gas and its distribution," *Natural Gas Industry*, vol. 24, no. 7, pp. 15–18, 2004.
- [3] D. M. Jarvie, R. J. Hill, T. E. Ruble, and R. M. Pollastro, "Unconventional shale-gas systems: the Mississippian Barnett

- Shale of north-central Texas as one model for thermogenic shale-gas assessment,” *AAPG Bulletin*, vol. 91, no. 4, pp. 475–499, 2007.
- [4] H. K. Nie, Z. L. He, G. X. Liu et al., “Status and direction of shale gas exploration and development in China,” *Journal of China University of Mining & Technology*, vol. 49, no. 1, pp. 13–15, 2020.
- [5] L. Zeng, Z. Shu, W. Lyu et al., “Lamellation fractures in the Paleogene continental shale oil reservoirs in the Qianjiang Depression, Jiangnan Basin, China,” *Geofluids*, vol. 2021, Article ID 6653299, 10 pages, 2021.
- [6] J. Yin, C. Gao, M. Zhu et al., “Oil Accumulation Model and Its Main Controlling Factors in Lower Yanchang Formation, Wuqi-Dingbianarea, Ordos Basin, China,” *Geofluids*, vol. 2021, Article ID 5511563, 10 pages, 2021.
- [7] K. Zhang, Y. Song, S. Jiang et al., “Shale gas accumulation mechanism in a syncline setting based on multiple geological factors: an example of southern Sichuan and the Xiuwu Basin in the Yangtze Region,” *Fuel*, vol. 241, no. 2019, pp. 468–476, 2019.
- [8] K. Zhang, Y. Song, S. Jiang et al., “Mechanism analysis of organic matter enrichment in different sedimentary backgrounds: a case study of the Lower Cambrian and the Upper Ordovician-Lower Silurian, in Yangtze region,” *Marine and Petroleum Geology*, vol. 99, no. 2019, pp. 488–497, 2019.
- [9] K. Zhang, Y. Song, C. Jia et al., “Vertical sealing mechanism of shale and its roof and floor and effect on shale gas accumulation, a case study of marine shale in Sichuan basin, the Upper Yangtze area,” *Journal of Petroleum Science and Engineering*, vol. 175, no. 2019, pp. 743–754, 2019.
- [10] Z. Tong, L. Shengxiang, W. Feng, and P. Yongmin, “Sedimentary models and lithofacies types of lacustrine mud shale in the Sichuan Basin,” *Natural Gas Industry*, vol. 36, no. 8, pp. 22–28, 2016.
- [11] R. G. Loucks and S. C. Ruppel, “Mississippian Barnett Shale: lithofacies and depositional setting of a deep-water shale-gas succession in the Fort Worth Basin, Texas,” *AAPG Bulletin*, vol. 91, no. 4, pp. 579–601, 2007.
- [12] S. Cheng, B. Li, K. Zhang et al., “Study on the mechanism of organic matter enrichment in early Cambrian marine shales in the lower Yangtze area, South China: an example using well jxy1,” *Geofluids*, vol. 2020, Article ID 2460302, 11 pages, 2020.
- [13] Y. A. N. Detian, C. H. E. N. Daizhao, W. A. N. G. Zhuozhuo, L. jing, Y. Xiangrong, and Z. Bao, “Climatic and oceanic controlled deposition of Late Ordovician-Early Silurian black shales on the North Yangtze platform, South China,” *South China. Marine and Petroleum Geology*, vol. 110, pp. 112–121, 2019.
- [14] Y. Xiang-Rong, Y. de-Tian, W. Xiao-Song et al., “Different formation mechanism of quartz in siliceous and argillaceous shales: a case study of Longmaxi Formation in South China,” *Marine and Petroleum Geology*, vol. 94, pp. 80–94, 2018.
- [15] K. Zhang, Z. Li, S. Jiang et al., “Comparative analysis of the siliceous source and organic matter enrichment mechanism of the Upper Ordovician-Lower Silurian shale in the Upper-Lower Yangtze Area,” *Minerals*, vol. 8, no. 7, p. 283, 2018.
- [16] K. Zhang, Z. Jiang, L. Yin et al., “Controlling functions of hydrothermal activity to shale gas content-taking lower Cambrian in Xiuwu Basin as an example,” *Marine and Petroleum Geology*, vol. 85, no. 2017, pp. 177–193, 2017.
- [17] Z. LIU, B. GAO, Y. ZHANG, W. DU, D. FENG, and H. NIE, “Types and distribution of the shale sedimentary facies of the Lower Cambrian in Upper Yangtze area, South China,” *Petroleum Exploration and Development*, vol. 44, no. 1, pp. 20–31, 2017.
- [18] Z. Liu, G. Liu, Z. Hu et al., “Lithofacies types and assemblage features of continental shale strata and their implications for shale gas exploration: a case study of the Middle and Lower Jurassic strata in the Sichuan Basin,” *Natural Gas Industry B*, vol. 7, no. 4, pp. 358–369, 2020.
- [19] R. O. Almoqaddam, M. Darwish, A. N. el-Barkooky, and C. Clerk, “Sedimentary facies analysis of the Upper Bahariya sandstone reservoir in East Bahariya C area, North Western Desert, Egypt,” *Egyptian Journal of Petroleum*, vol. 27, no. 4, pp. 1103–1112, 2018.
- [20] L. Q. Sun, X. Liang, B. Ma et al., “Characteristics of sedimentary environment since Quaternary in northern Jiangnan Basin, China: reconstruction of paleoenvironments,” *Quaternary International*, vol. 589, pp. 12–24, 2021.
- [21] Y. Han, B. Ran, S. Liu et al., “Main controlling factors of organic-matter enrichment in the Ordovician-Silurian marine organic-rich mudrock in the Yangtze Block, South China,” *Marine and Petroleum Geology*, vol. 127, article 104959, 2021.
- [22] J. Wu, C. Liang, R. Yang, and J. Xie, “The significance of organic matter-mineral associations in different lithofacies in the Wufeng and longmaxi shale-gas reservoirs in the Sichuan Basin,” *Marine and Petroleum Geology*, vol. 126, article 104866, 2021.
- [23] R. Chen, K. Yuan, Z. Y. Zhang, and Q. F. Xu, “Sedimentary environment of organic-rich shale in the Upper Permian Longtan Formation in Qinglong area, western Guizhou, China,” *China Geology*, vol. 2, no. 1, pp. 108–109, 2019.
- [24] Q. K. Jadoon, E. M. Roberts, B. Henderson, T. G. Blenkinsop, R. A. J. Wüst, and C. Mtelela, “Lithological and facies analysis of the Roseneath and Murteree shales, Cooper Basin, Australia,” *Journal of Natural Gas Science and Engineering*, vol. 37, pp. 138–168, 2017.
- [25] M. H. Hakimi, A. S. Alaug, A. F. Ahmed, and M. M. A. Yahya, “Sedimentary environmental conditions and petroleum source rock potential of the Late Jurassic Arwa Member shales in Al-Jawf sub-basin, Yemen,” *Journal of African Earth Sciences*, vol. 149, pp. 474–486, 2019.
- [26] Y. H. Guo, Z. F. Li, D. H. Li et al., “Lithofacies palaeogeography of the Early Silurian in Sichuan area,” *Journal of Palaeogeography*, vol. 6, no. 1, pp. 20–29, 2004.
- [27] B. Pu, Z. Dong, and F. Wang, “Re-division and evolution of sedimentary subfacies of Longmaxi shale in southern Sichuan Basin,” *Journal of China University of Petroleum*, vol. 44, no. 3, pp. 15–24, 2020.
- [28] Y. Li, M. Li, J. Zhang et al., “Influence of the Emeishan basalt eruption on shale gas enrichment: a case study of shale from Wufeng-Longmaxi formations in northern Yunnan and Guizhou provinces,” *Fuel*, vol. 282, article 118835, 2020.
- [29] Z. Jin, H. Nie, Q. Liu, J. Zhao, and T. Jiang, “Source and seal coupling mechanism for shale gas enrichment in upper Ordovician Wufeng Formation - Lower Silurian Longmaxi Formation in Sichuan Basin and its periphery,” *Marine and Petroleum Geology*, vol. 97, pp. 78–93, 2018.
- [30] C. Mou, X. Wang, Q. Wang et al., “Relationship between sedimentary facies and shale gas geological conditions of the Lower Silurian Longmaxi Formation in southern Sichuan

- Basin and its adjacent areas,” *Journal of Palaeogeography*, vol. 18, no. 3, pp. 457–472, 2016.
- [31] K. Zhang, C. Jia, Y. Song et al., “Analysis of Lower Cambrian shale gas composition, source and accumulation pattern in different tectonic backgrounds: a case study of Weiyuan Block in the Upper Yangtze region and Xiuwu Basin in the Lower Yangtze region,” *Fuel*, vol. 263, no. 2020, article 115978, 2020.
- [32] H. Zheng, B. Gao, Y. Peng, H. Nie, and F. Yang, “Sedimentary evolution and shale gas exploration direction of the Lower Silurian in Middle-Upper Yangtze area,” *Journal of Palaeogeography*, vol. 15, no. 5, pp. 645–656, 2013.
- [33] G. Xusheng, “Rules of two-factor enrichment for marine shale gas in southern China: understanding from the Longmaxi Formation shale gas in Sichuan Basin and its surrounding area,” *Acta Geologica Sinica*, vol. 88, no. 7, pp. 1210–1218, 2014.
- [34] J. Hu, S. Zhang, and B. Zhang, “Sedimentary facies and sedimentary environment of shale of Bakken Formation in Williston Basin,” in *14th National Academic Conference on Organic Geochemistry*, pp. 565–566, Zhuhai, 2013.
- [35] Q. Xie, Z. Wang, Y. Ouyang et al., “Sequence stratigraphy and sedimentary facies of Feixianguan Formation in the Kaijiang-Liangping Area of Sichuan Basin, China,” *Open Journal of Geology*, vol. 10, no. 6, pp. 641–660, 2020.
- [36] Z. Wangzhong and T. Fuwen, “Paleogeographic features of late Triassic lithofacies and source rocks in Qiangtang Basin,” *Journal of sedimentary*, vol. 38, no. 4, pp. 876–885, 2020.
- [37] W. Ji, F. Hao, H. Schulz, Y. Song, and J. Tian, “The architecture of organic matter and its pores in highly mature gas shales of the Lower Silurian Longmaxi Formation in the Upper Yangtze Platform, South China,” *AAPG Bulletin*, vol. 103, no. 12, pp. 2909–2942, 2019.
- [38] D. Hu, H. Zhang, and K. Ni, “Main controlling factors for in southeastern gas preservation conditions of marine shales margins of the Sichuan Basin,” *Natural Gas Industry*, vol. 34, no. 6, pp. 17–23, 2014.
- [39] C. Fan, H. Li, Q. Qin, S. He, and C. Zhong, “Geological conditions and exploration potential of shale gas reservoir in Wufeng and Longmaxi Formation of southeastern Sichuan Basin, China,” *Journal of Petroleum Science and Engineering*, vol. 191, article 107138, 2020.
- [40] J. F. Yan, Y. P. Men, Y. Y. Sun et al., “Geochemical and geological characteristics of the Lower Cambrian shales in the middle-upper Yangtze area of South China and their implication for the shale gas exploration,” *Marine and Petroleum Geology*, vol. 70, pp. 1–13, 2016.
- [41] R. S. Taylor, D. J. DeMaster, and D. J. Burdige, “Assessing the distribution of labile organic carbon from diverse depositional environments on the West Antarctic Peninsula shelf,” *Deep Sea Research Part I: Oceanographic Research Papers*, vol. 156, article 103166, 2020.
- [42] W. KH, “Environmental influences on the chemical composition of shales and clays,” *Physics & Chemistry of the Earth*, vol. 8, pp. 307–333, 1971.
- [43] X. Wang, Y. Zhu, G. G. Lash, and Y. Wang, “Multi-proxy analysis of organic matter accumulation in the Upper Ordovician-Lower Silurian black shale on the Upper Yangtze Platform, south China,” *Marine and Petroleum Geology*, vol. 103, pp. 473–484, 2019.
- [44] K. Zhang, J. Peng, W. Liu et al., “The role of deep geofluids in the enrichment of sedimentary organic matter: a case study of the Late Ordovician-Early Silurian in the upper Yangtze region and early Cambrian in the lower Yangtze region, South China,” *Geofluids*, vol. 2020, Article ID 8868638, 12 pages, 2020.
- [45] K. Zhang, J. Peng, X. Wang et al., “Effect of organic maturity on shale gas genesis and pores development: a case study on marine shale in the upper Yangtze region, South China,” *Open Geosciences*, vol. 12, no. 1, pp. 1617–1629, 2020.
- [46] S. MR, “Geochemical paleoredox indicators in Devonian-Mississippian black shales, Central Appalachian Basin (USA),” *Chemical Geology*, vol. 206, no. 3-4, pp. 373–391, 2004.
- [47] L. Wan, X. Chuantao, and S. Wenrui, “Sedimentary facies in of the Longmaxi Formation Wufeng Formations the Jiaoshiba shale gas field,” *Acta Geologica Sichuan*, vol. 35, no. 4, pp. 517–521, 2015.
- [48] T. Wang, K. Zhang, L. Xiong et al., “Paleogeomorphology restoration of Wufeng Formation-Lower Member of Longmaxi Formation in Zigong area of Sichuan Province and its oil and gas significance,” *Petroleum Geology & Experiment*, vol. 40, no. 6, pp. 764–770, 2018.
- [49] B. Figueiredo, C. F. Tsang, J. Rutqvist, and A. Niemi, “Study of hydraulic fracturing processes in shale formations with complex geological settings,” *Journal of Petroleum Science and Engineering*, vol. 152, pp. 361–374, 2017.
- [50] Y. U. Sang, S. L. Yang, H. A. N. Chen, F. Zhou, K. Qian, and W. Shi, “The exploration and recognition of stimulated reservoir volume for shale gas in Sichuan Basin - Taking well W201 as an example,” *Advanced Materials Research*, vol. 734-737, pp. 1303–1307, 2013.
- [51] H. K. Holdaway and C. J. Clayton, “Preservation of shell microstructure in silicified brachiopods from the Upper Cretaceous Wilmington Sands of Devon,” *Geological Magazine*, vol. 119, no. 4, pp. 371–382, 1982.
- [52] R. M. Slatt and N. D. Rodriguez, “Comparative sequence stratigraphy and organic geochemistry of gas shales: commonality or coincidence?,” *Journal of Natural Gas Science and Engineering*, vol. 8, pp. 68–84, 2012.
- [53] M. O. Abouelresh and R. M. Slatt, “Lithofacies and sequence stratigraphy of the Barnett Shale in east-central Fort Worth Basin, Texas,” *AAPG Bulletin*, vol. 96, no. 1, pp. 1–22, 2012.

Research Article

Effect of Shale Sample Particle Size on Pore Structure Obtained from High Pressure Mercury Intrusion Porosimetry

Zhiye Gao ^{1,2}, Longfei Duan,^{1,2} Qinhong Hu ³, Shuling Xiong,^{1,2} and Tongwei Zhang⁴

¹State Key Laboratory of Petroleum Resources and Prospecting, China University of Petroleum, Beijing 102249, China

²Unconventional Petroleum Research Institute, China University of Petroleum, Beijing 102249, China

³Department of Earth and Environmental Sciences, University of Texas at Arlington, Arlington, Texas 76019, USA

⁴Bureau of Economic Geology, University of Texas at Austin, Austin, Texas 78712, USA

Correspondence should be addressed to Zhiye Gao; gaozhiye@163.com

Received 28 January 2021; Accepted 10 August 2021; Published 3 September 2021

Academic Editor: Jinze Xu

Copyright © 2021 Zhiye Gao et al. This is an open access article distributed under the Creative Commons Attribution License, which permits unrestricted use, distribution, and reproduction in any medium, provided the original work is properly cited.

With the rapid development of unconventional oil and gas, the pore structure characterization of shale reservoirs has attracted an increasing attention. High pressure mercury intrusion porosimetry (HPMIP) has been widely used to quantitatively characterize the pore structure of tight shales. However, the pore structure obtained from HPMIP could be significantly affected by the sample particle size used for the analyses. This study mainly investigates the influence of shale sample particle size on the pore structure obtained from HPMIP, using Mississippian-aged Barnett Shale samples. The results show that the porosity of Barnett Shale samples with different particle sizes obtained from HPMIP has an exponentially increasing relation with the particle size, which is mainly caused by the new pores or fractures created during shale crushing process as well as the increasing exposure of blind or closed pores. The amount and proportion of mercury retention during mercury extrusion process increase with the decrease of shale particle size, which is closely related to the increased ink-bottle effect in shale sample with smaller particle size. In addition, the fractal dimension of Barnett Shale is positively related to the particle size, which indicates that the heterogeneity of pore structure is stronger in shale sample with larger particle size. Furthermore, the skeletal density of shale sample increases with the decrease of particle size, which is possibly caused by the differentiation of mineral composition during shale crushing process.

1. Introduction

In recent years, more and more attention has been paid to the production of oil and gas from unconventional reservoirs, which will make a great contribution to the world's energy supply in the future [1]. The total shale gas production in the world was 670.3 billion m³ in 2018, with the top three producing countries being the USA, Canada, and China, producing 607.2 billion m³, 48.0 billion m³, and 10.8 billion m³, respectively [2].

Different from conventional hydrocarbon reservoirs, shale reservoirs with low porosity and extralow permeability contain abundant nanopores [3–6], which significantly control the storage and seepage capacity of shale reservoirs [7]. Therefore, it is quite meaningful to characterize shale pore structure, such as pore shape, pore size, and pore connectiv-

ity [8]. Many advanced technologies have been applied in shale pore structure characterization [9–11], such as imaging method (scanning electron microscopy, micro-nano CT, atomic force microscopy, etc.), nuclear magnetic resonance, gas physisorption, and high pressure mercury intrusion porosimetry (HPMIP) [7, 12–20].

HPMIP has been widely used in pore structure characterization of different porous media, such as concrete, food, metallurgy, catalyst, material science, medicine and pharmacy, and chemical and petroleum engineering [21–24]. Recently, HPMIP becomes a very useful tool to quantitatively characterize shale pore structure, and many important pore structure parameters (such as skeletal and apparent density, porosity, pore connectivity, permeability, fractal dimension, and tortuosity) could be derived from HPMIP data [25–29]. The advantages of HPMIP include simple

TABLE 1: Six particle sizes of shale sample B7191.

Mesh	Bulk	Large than 20 mesh	20-50 mesh	50-100 mesh	100-270 mesh	Less than 270 mesh
Particle size range/ μm	5000	>830	270-830	150-270	53-150	<53
Representative particle size/ μm	5000	2915	550	210	102	27

principle [30], wide pore-throat size coverage (3 nm~300 μm) [28, 31], and short experimental time (~2 hours) [32, 33]. However, HPMIP has some shortcomings. For example, mercury is toxic, and its leakage may cause a damage to human health. In addition, samples tested by HPMIP are contaminated by mercury and cannot be reused for other pore structure analyses.

One of the basic assumptions for HPMIP analysis is the cylindrical pore shape. However, the actual pore morphology of shale samples is very complex, which could cause a deviation between HPMIP results and the real pore structure [34, 35]. The contact angle used in HPMIP is usually a constant value. However, the actual contact angle could change in different compositions of shale samples due to their strong heterogeneity, which could also make the HPMIP results deviate from the actual situation [36, 37].

Furthermore, the particle size of shale sample also has a great influence on the results of pore structure measured by HPMIP, which is known as the particle size effect. HPMIP can be used to determine the pore structure of intact shale samples or crushed shale samples (such as cuttings). However, there is no standard particle size of shale sample recommended for HPMIP, and different particle sizes were used in different studies. For example, Rourke [38] used a horizontal 1 inch core plug, and Gao et al. [39] used irregular shale samples at ~1 cm in linear dimensions. This could lead to differences in pore structure information even if the same shale sample was used due to the particle size effect. During HPMIP analysis, mercury could enter larger pores through narrower pore throat, and these larger pores are counted as smaller pores. Consequently, the intact shale sample is not the ideal target used for revealing the real pore structure information by HPMIP, and smaller particle size was used in HPMIP analysis in order to obtain more reliable pore-throat size distribution [40]. However, few previous studies were conducted on the influence of sample particle size on pore structure derived from HPMIP and its causing mechanisms [41].

By comparing the pore structure parameters of Barnett Shale samples with different particle sizes obtained from HPMIP, this study investigates the influence of particle size on the HPMIP results and the influencing mechanism. The outcomes of this study will promote the application of HPMIP in the pore structure characterization of shale reservoirs. In addition, hydraulic fracturing is an important technology to extract shale petroleum [42–45]. Previous studies have shown that the pore structure of fractured shale varies with the concentration of proppant in fracturing fluid. For example, after water fracturing, the change of pores with large pore throat is very small, and the proportion of pore throat is increased. The use of clean water plus 1% ceramsite proppant resulted in high proportion of large pore throats

and large pore sizes in fractured shales, with the highest shale permeability [46–49]. The fracturing process of shale reservoir is also one type of sample crushing process, which reduces the size of shale matrix and changes the original pore system. Shale gas production behavior is very complicated, and large amounts of fracturing fluids are commonly retained within shale reservoirs after shale gas production, both of which are significantly affected by the fractured shale pore system. Therefore, the outcomes of this study also have a great significance for the improved understanding of shale gas production mechanism and the retention mechanism of fracturing fluids.

2. Samples and Experimental Methods

2.1. The Experimental Samples. The Mississippian Barnett Shale sample B7191 at the depth of 2191.82 m (7191 ft) from Blakely #1 core in Wise County of Texas was used in this study. Barnett Shale was a marine shelf deposit, and its thickness is from 61 to 305 m across the Fort Worth Basin. Barnett Shale can be divided into three sublayers: upper Barnett Shale, Forestburg limestone, and lower Barnett Shale [50]. The upper and lower Barnett Shale is mainly composed of siliceous mudstone while interbedded lime mudstone is less developed. The Forestburg limestone is composed of argillaceous lime mudstone [51]. The mineral composition of Barnett Shale is as follows: quartz and plagioclase (45 wt%-55 wt%), carbonates (mainly calcite, some dolomite and siderite) (15 wt%-25 wt%), clay minerals (20 wt%-35 wt%), and pyrite (2 wt%-6 wt%) [51, 52]. The total organic carbon (TOC) content of Barnett Shale is about 3.5 wt%~4.5 wt%, and the kerogen is mainly type II.

The mineral composition of sample B7191 is mainly quartz, feldspar, clay minerals, and pyrite. The TOC of B7191 is about 3.8%, and its porosity is about 4.8% based on ~1.5 cm-sided cube [50, 52]. The sample B7191 was pulverized manually by hammer and then sieved through sieves with different mesh sizes. As shown in Table 1, the particle size of sample B7191 is divided into six grades to be used in this work. The representative particle size uses the average of two bounding sizes for result plotting.

2.2. The Theory of HPMIP. Micromeritics AutoPore IV 9510 was used to perform HPMIP tests in this study. This instrument could generate the highest pressure of 60,000 psia (413 MPa) and detect the pore-throat diameter down to 3 nm. All the samples were dried in a 60°C oven for more than 48 hours before the HPMIP experiment in order to remove the moisture within pore spaces.

2.2.1. The Principle of HPMIP. Mercury is a nonwetting fluid to most rocks including shale and external pressure should

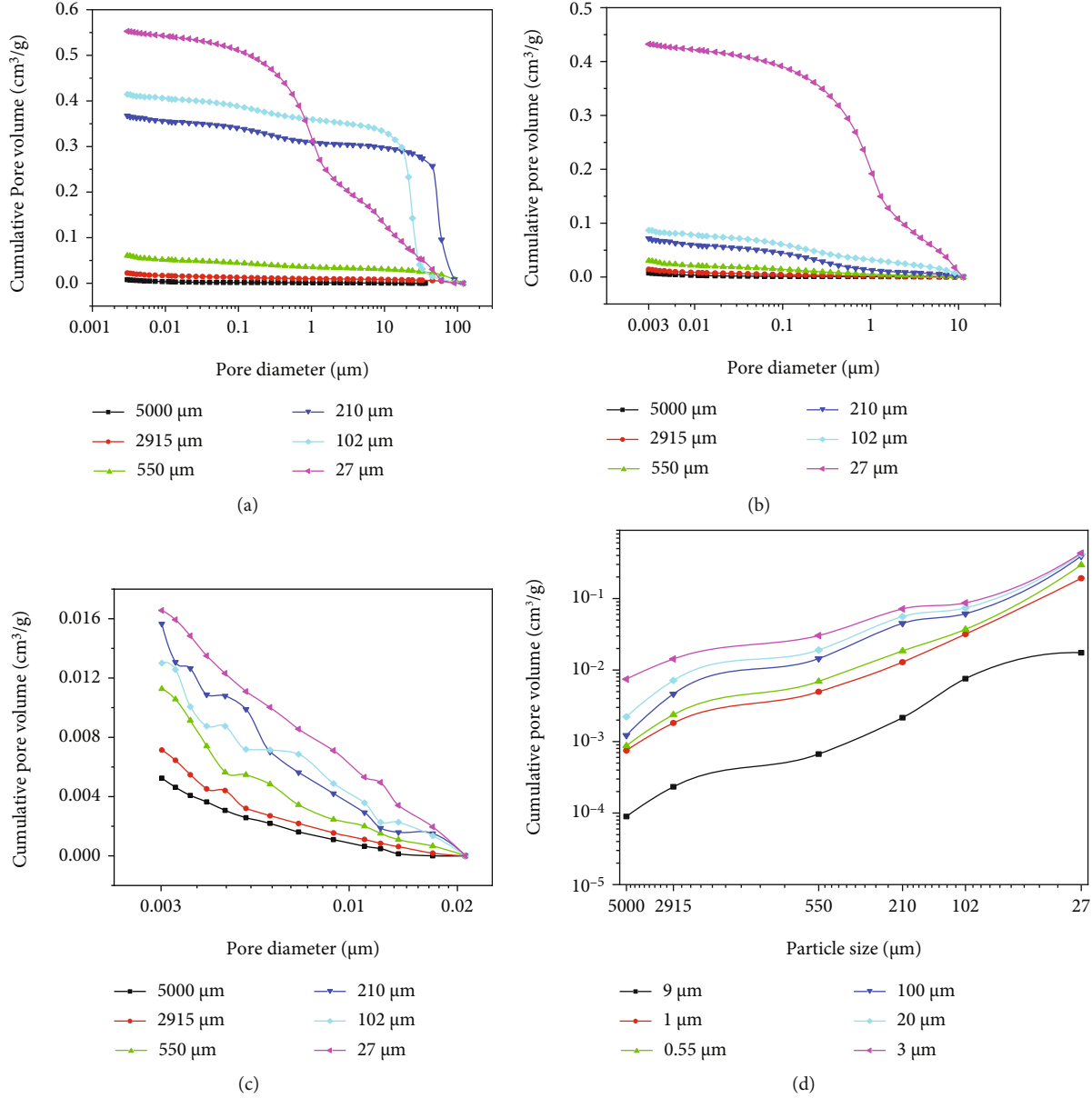


FIGURE 1: Cumulative mercury intrusion volume of shale samples with different particle sizes: (a) complete mercury intrusion curves; (b) removal of mercury intrusion volume in pores larger than $10\ \mu\text{m}$; (c) removal of mercury intrusion volume in pores larger than $20\ \text{nm}$; (d) cumulative mercury intrusion volume of shale with different particle sizes for different pore sizes.

be applied on mercury to push it into pore spaces. The diameter of pores that mercury could enter is inversely proportional to the applied pressure, and this relationship was presented by Washburn’s equation [53] on the basis of assuming that all the pores were cylindrical [54, 55], which is shown in Equation (1):

$$D = -4\gamma \cos \frac{\theta}{P}, \quad (1)$$

where D is the pore diameter, γ is the surface tension of mercury ($485\ \text{dye/cm}$) [28], θ is the contact angle between mercury and pore surface (130°) [28], and P is pressure.

2.2.2. *Fractal Dimension Derived from HPMIP.* Fractal theory is a mathematical method to describe the irregularity and complexity of materials as well as other nonlinear problems [26, 40, 56–58]. The fractal dimension of pore structure should be between 2 and 3 [36, 55, 59], which can reflect the complexity of pore structure [36, 60]. Recently, fractal dimension has been used to quantify the heterogeneity of shale pore structure [40, 61, 62]. The larger the fractal dimension is, the stronger is the heterogeneity [61, 63, 64].

For HPMIP tests, Mandlbrot’s method [4, 26, 65] was used to obtain the fractal dimension of shale pore structure, which is shown in Equation (2):

$$\ln S_{\text{Hg}} = (D - 2) \ln P_c + \ln \alpha, \quad (2)$$

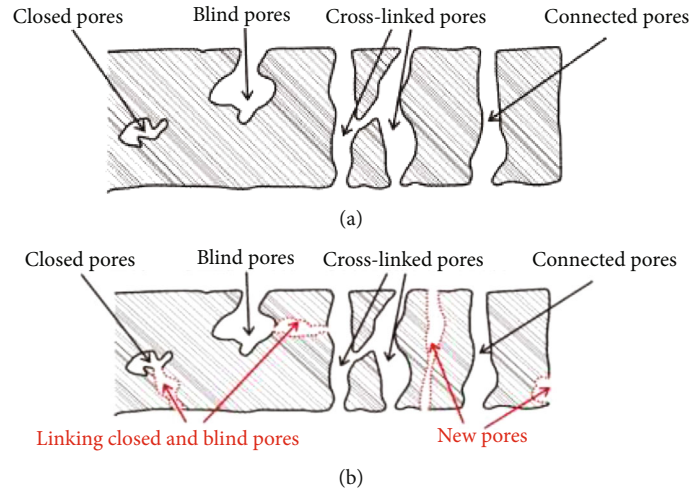


FIGURE 2: Pore structure models modified from Giesche (2006): (a) before breakage; (b) after breakage.

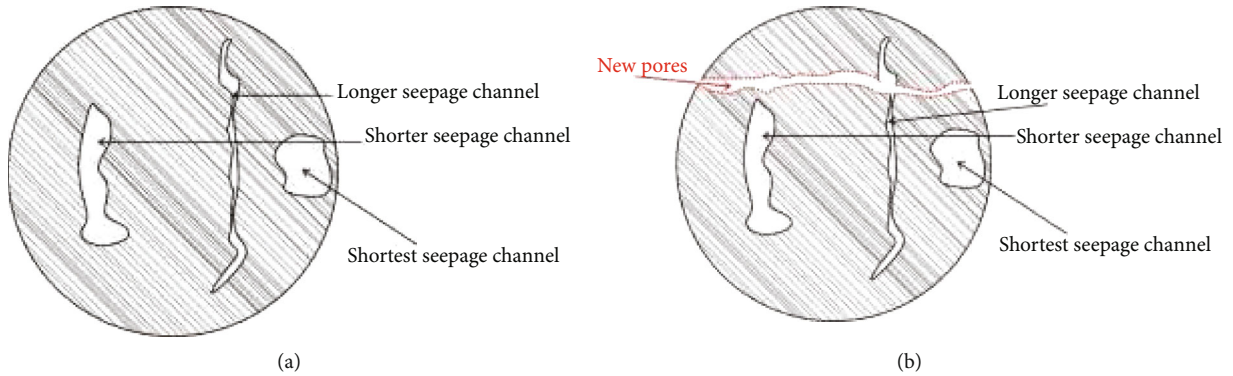


FIGURE 3: Pores with different seepage channels in the rock: (a) before breakage; (b) after breakage.

where D is the fractal dimension, S_{Hg} is the mercury saturation, P_c is the capillary pressure, and α is a constant.

3. Results and Discussion

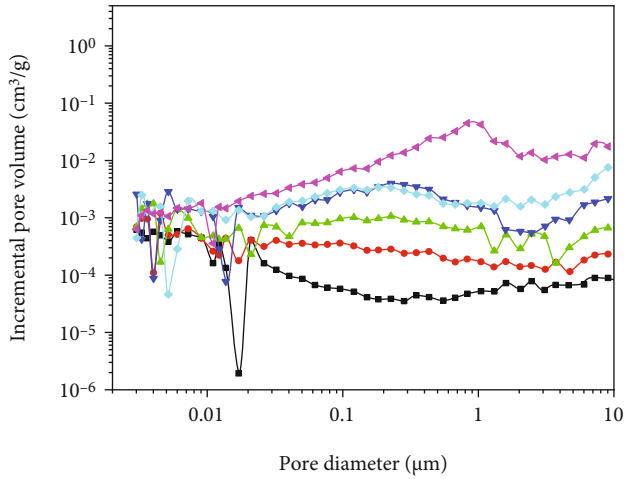
3.1. Effect of Sample Particle Size on the Cumulative Intrusion Volume. During the early mercury intrusion stage with low intrusion pressures, mercury entered large pores. A large proportion of these large pores were interparticle pores generated artificially due to the loose packing of powdered shale particles, which was also treated as conformance effect [50]. As a result, the mercury intrusion volume during this early stage could not reflect the actual pore volume. As shown in Figure 1(a), the relationship between mercury intrusion volume and sample particle size was weak when the pores larger than $10\ \mu\text{m}$ were taken into account. In order to eliminate the influence of artificial pores or conformance effect, the mercury intrusion volume of pores larger than $10\ \mu\text{m}$ was subtracted from the cumulative mercury intrusion volume, which was shown in Figure 1(b). In order to define the lower pore size limit that sample particle size can affect the cumulative mercury intrusion volume, mercury intrusion volume of pores larger than $20\ \text{nm}$ was also removed in Figure 1(c). As shown in Figures 1(b)–1(d), the cumulative mercury intrusion volume increased with the

decrease of sample particle size for pores less than $20\ \text{nm}$ and pores between $20\ \text{nm}$ and $10\ \mu\text{m}$, which indicated that the sample particle size could affect the mercury intrusion volume of both mesopores ($2\text{--}50\ \text{nm}$ in diameter) and macropores ($>50\ \text{nm}$).

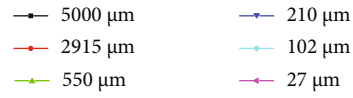
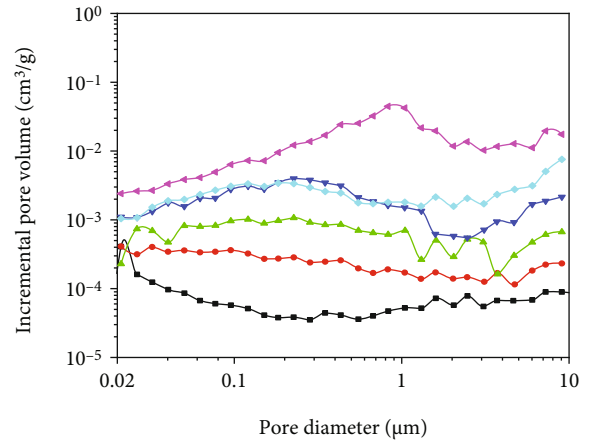
For HPMIP tests, the effect of sample particle size on cumulative mercury intrusion volume is related to the pore structure of shale. According to the pore accessibility, pores in shale could be divided into connected pores, cross-linked pores, blind pores, and closed pores as shown in Figure 2(a) [66]. The connected pores and cross-linked pores have good connectivity and seepage capacity, and the mercury is easy to flow into and occupy these pores. For blind pores with poor connectivity and isolated/closed pores, it is difficult for mercury to enter these pores, and HPMIP can hardly recognize the information of such pores.

The original shale pore structure could be changed during the sample crushing process. For example, the closed pores and blind pores could be exposed to external space during crushing process, thus improving the pore connectivity of these pores (as shown in Figure 2(b)).

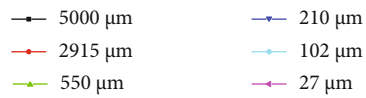
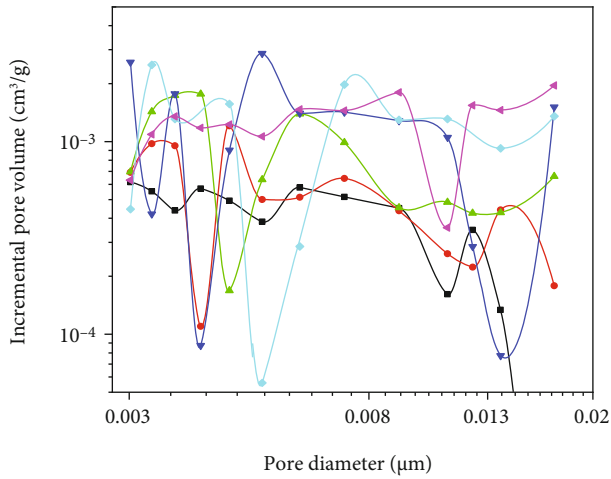
In addition, the crushing process is accompanied by strong external forces, which could create new pores or cause the merging and collapse of pores [67], especially on the surface and inside of brittle minerals.



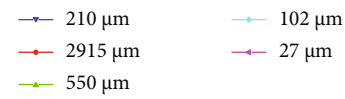
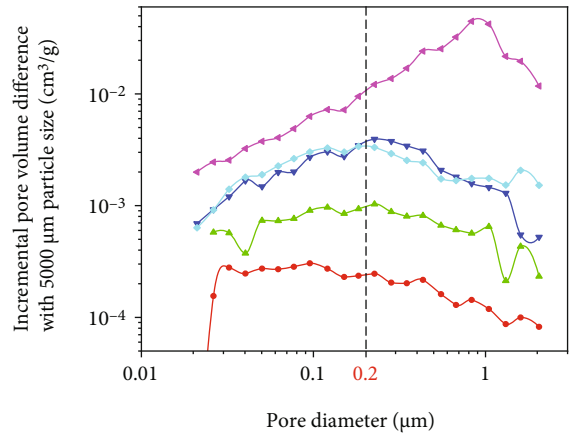
(a)



(b)



(c)



(d)

FIGURE 4: Continued.

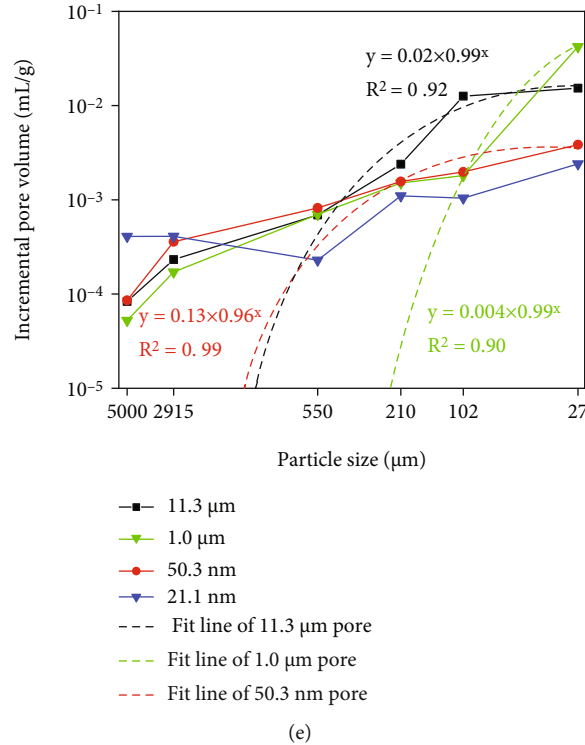


FIGURE 4: The incremental mercury intrusion volume of shale samples with different particle sizes: (a) complete curve; (b) pore size range of 20 nm-10 μm ; (c) pore size range of 3-20 nm; (d) the relationship between the incremental pore volume difference with 5000 μm particle size and pore diameter; (e) the relationship between incremental pore volume and shale particle size.

As shown in Figures 1(b) and 1(c), the increment of cumulative mercury intrusion volume with a decrease of particle size in the pore size range of 20 nm-10 μm was much higher than that under 20 nm.

Previous studies showed that the micropores (<2 nm in diameter) and some mesopores were mainly organic matter-hosted pores and intergranular pores of clay minerals, which had relatively long seepage channels [24]. The longer the seepage channel is, the more likely it is to be connected with the external space by crushing as shown in Figure 3. According to Figure 1(b), the pore volume of larger pores increased more obviously with the decrease of particle size, compared with micropores and small mesopores. It is speculated that the total volume of smaller mesopores is much lower than that of macropores, and the seepage channel of larger pores is possibly longer than smaller pores. Consequently, the crushing of the sample is more likely to increase the connectivity of macropores.

As a result, the pore volume of sample B7191 increased with the decrease of particle size, which was due to the increased pore accessibility caused by the newly generated pores and the exposure of both blind and closed pores resulting from sample crushing.

Some studies pointed out that sample crushing could result in the differentiation of mineral composition. For example, clay minerals have good elasticity and are distributed among mineral particles in shale, which are easy to break away from shale during crushing process [51]. However, brittle minerals such as quartz and feldspar, which have

larger particle size and stronger hardness, are likely to remain in shale during crushing process. The affinity of mercury to different minerals is different, and different external pressures were required for mercury to enter the pores with the same pore size associated with different minerals. Consequently, the measured pore structure information by HPMIP could also be affected by mineral differentiation caused by sample crushing process.

3.2. Effect of Sample Particle Size on the Incremental Pore Volume. As shown in Figure 4(a), the incremental pore volume of pores between 20 nm and 10 μm has a good relationship with the sample particle size of B7191 while this relationship disappeared for pores less than 20 nm.

As shown in Figure 4(b), the pore volume of a certain pore size in the range of 20 nm-10 μm generally increased with the decrease of the sample particle size. More specifically, there was an exponential relationship between pore volume and sample particle size (Figure 4(e)). Furthermore, the incremental pore volume difference between B7191 sample with 5000 μm particle size and other smaller particle sizes became more obvious with the increase of pore size in the range of 20-200 nm as shown in Figure 4(d). However, an opposite phenomenon was observed for pores larger than 200 nm.

It is speculated that in the pore-throat size range of 20-200 nm, the length of seepage channel increased with the increase of pore size, which made larger pores more easily to be connected with external surface during the sample

crushing process while the length of seepage channel became shorter as the pore size increased in the range of >200 nm.

For pores between 3 nm and 20 nm, no obvious relationship existed between the incremental pore volume and sample particle size (Figure 4(c)), which indicated the sample crushing process had a random effect on the pore volume and connectivity of pores below 20 nm.

3.3. Effect of Sample Particle Size on the Mercury Retraction Efficiency. The hysteresis phenomenon between mercury intrusion curve and extrusion curve was observed for all sample sizes in Figure 5. Several theories, such as contact angle hysteresis, the effect of ink-bottle pores, and penetration-connectivity model [25], have been proposed to interpret the hysteresis phenomenon, and the effect of ink-bottle pores was used in this study. Ink-bottle pores are the pores connected with external surface through much smaller pore throats (Figure 6). During mercury extrusion process, the flow of mercury would easily break in the narrower pore throats, which could make the mercury stuck within the shale sample and then lead to the hysteresis phenomenon.

As shown in Figure 7(a), the mercury retention volume for pores between 20 nm and $10\ \mu\text{m}$ and pores between 3 nm and $10\ \mu\text{m}$ showed a consistent trend, with increasing volume with the decrease of sample particle size. More specifically, the mercury retention volume significantly increased when the sample particle size became less than $102\ \mu\text{m}$. Consequently, many pore throats larger than 20 nm appeared when blind pores were connected with external surface and new pores were produced during sample crushing process, which could enhance the ink-bottle effect and lead to more mercury retention volume. However, the mercury retention volume did not increase significantly with the decrease of sample particle size for pores between 3 nm and 20 nm.

The mercury retention rate is defined as the ratio of the mercury retention volume to the mercury intrusion volume. For all the shale samples with different particle sizes, the mercury retention rate of pores between 3 nm and 20 nm was significantly higher than that of pores between 20 nm and $10\ \mu\text{m}$ (Figure 7(b)), which indicated that the effect of ink-bottle pores was more obvious in smaller pores. As shown in Figure 7(c), the smaller the pore-throat diameter is, the greater is the mercury retention rate.

3.4. Effect of Sample Particle Size on Fractal Dimension. The fractal curves of the six B7191 samples with different particle sizes were presented in Figure 8, which showed two or three trend lines with different slopes. The fractal dimensions (D_1, D_2, D_3) of six B7191 samples with different particle sizes and their corresponding pore size ranges are presented in Figures 9(a)–9(c).

D_1 corresponded to larger pores, and D_3 corresponded to smaller pores while D_2 fell between D_1 and D_2 . As shown in Figures 8(d) and 8(e), D_2 and D_3 had the same value for sample B7191 with particle sizes of $210\ \mu\text{m}$ and $102\ \mu\text{m}$. For most of the shale samples used in this study, the fractal dimensions showed the order of $D_1 > D_3 > D_2$ (Figure 9(a)).

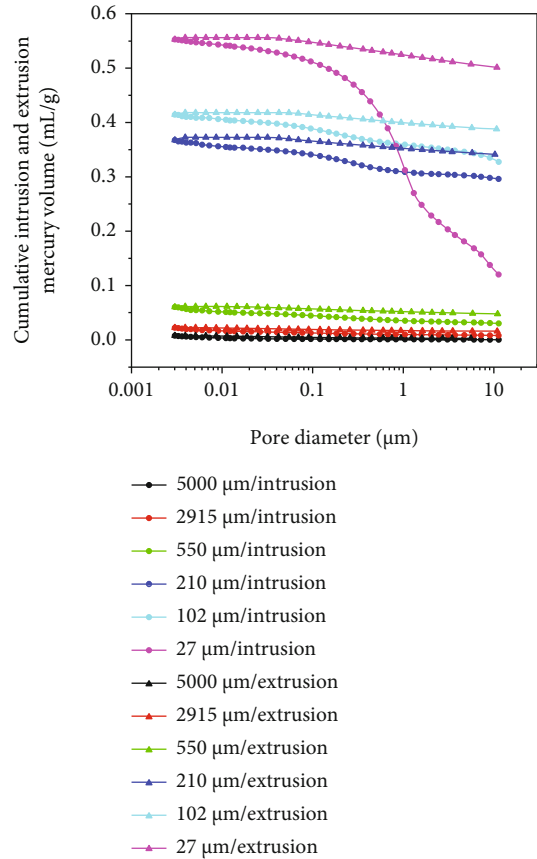


FIGURE 5: Mercury intrusion and extrusion curves of shale samples with different particle sizes.

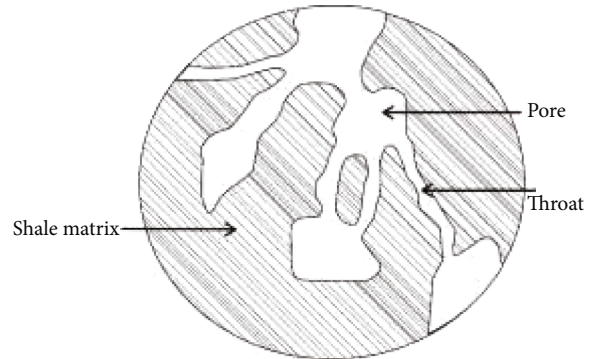


FIGURE 6: Schematics of ink-bottle pores.

The pore structure of larger pores was most heterogeneous, followed by the smaller pores, and the pore structure of middle range pores was less heterogeneous.

In addition, D_1 presented an S-shaped curve with the decrease of sample particle size as shown in Figure 9(a), and the effect of sample particle size on these larger pores was relatively random due to the influence of loose packing or conformance.

It can be seen that D_2 and D_3 basically showed a decreasing trend with the decrease of sample particle size, indicating

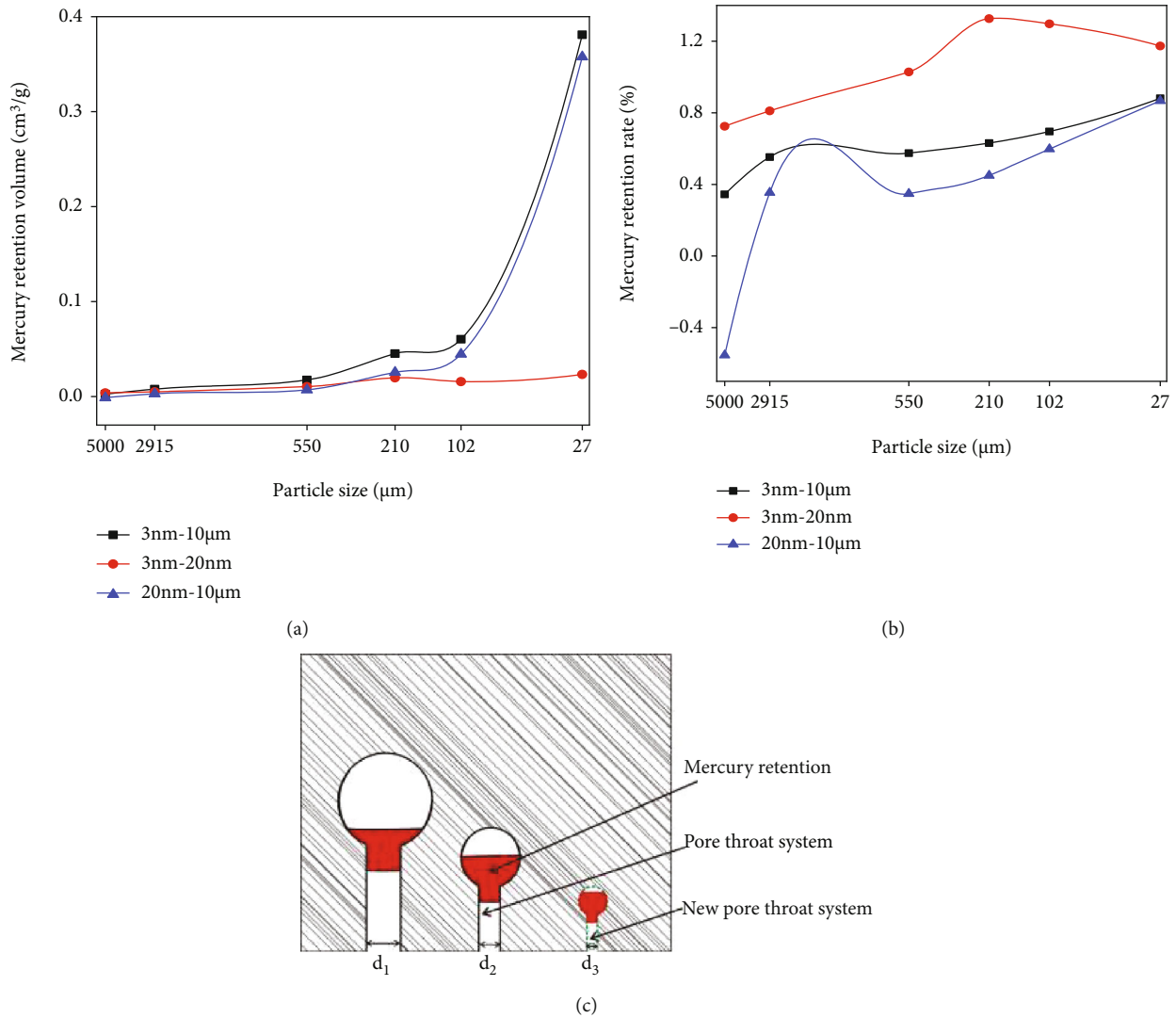


FIGURE 7: Effect of particle size and pore size on mercury retention. (a) The relationship between mercury retention volume and shale particle size. (b) The relationship between mercury retention rate and shale particle size. (c) Schematic diagram of mercury retention within different pore-throat systems.

that sample crushing process reduced the pore structure complexity of smaller pores.

Figure 9(c) showed that the corresponding pore size range of D_2 first increased with the decrease of the sample particle size, reached the maximum value for the sample with particle size of 210 μm, and then decreased continuously. The D_2 of the sample with particle size of 210 μm had the lowest value, and the corresponding pore size range of D_2 was the largest. This indicated that a certain degree of crushing greatly increased the amount and pore size range of pores with less heterogeneity, but excessive crushing could lose this effect.

One possible reason for this phenomenon is that the new pores were produced instantaneously by crushing without experiencing complicated diagenetic processes and had very smooth surfaces. However, if the particle size was too small, the newly generated pores during crushing process tended to have complex surfaces (Figure 10(b)).

3.5. Effect of Sample Particle Size on Other Pore Structure Parameters. The bulk density of shale sample B7191 decreased gradually with the decrease of sample particle size (Figure 11(a)), which was due to the new pore spaces generated during the sample crushing process. However, the skeletal density increased with the decrease of sample particle size (Figure 11(a)), which was probably caused by the differentiation of mineral compositions during the sample crushing process. The densities of clay minerals are generally lower than those of brittle minerals [68–71]. Therefore, the sample crushing process could make more clay minerals to break away from the shale sample, leading to the larger skeletal density of samples with smaller particle sizes.

As shown in Figures 11(b)–11(d), porosity, average pore size, and total mercury intrusion volume showed a roughly increasing trend with the decrease of sample particle size. The exponential relationship between porosity and sample

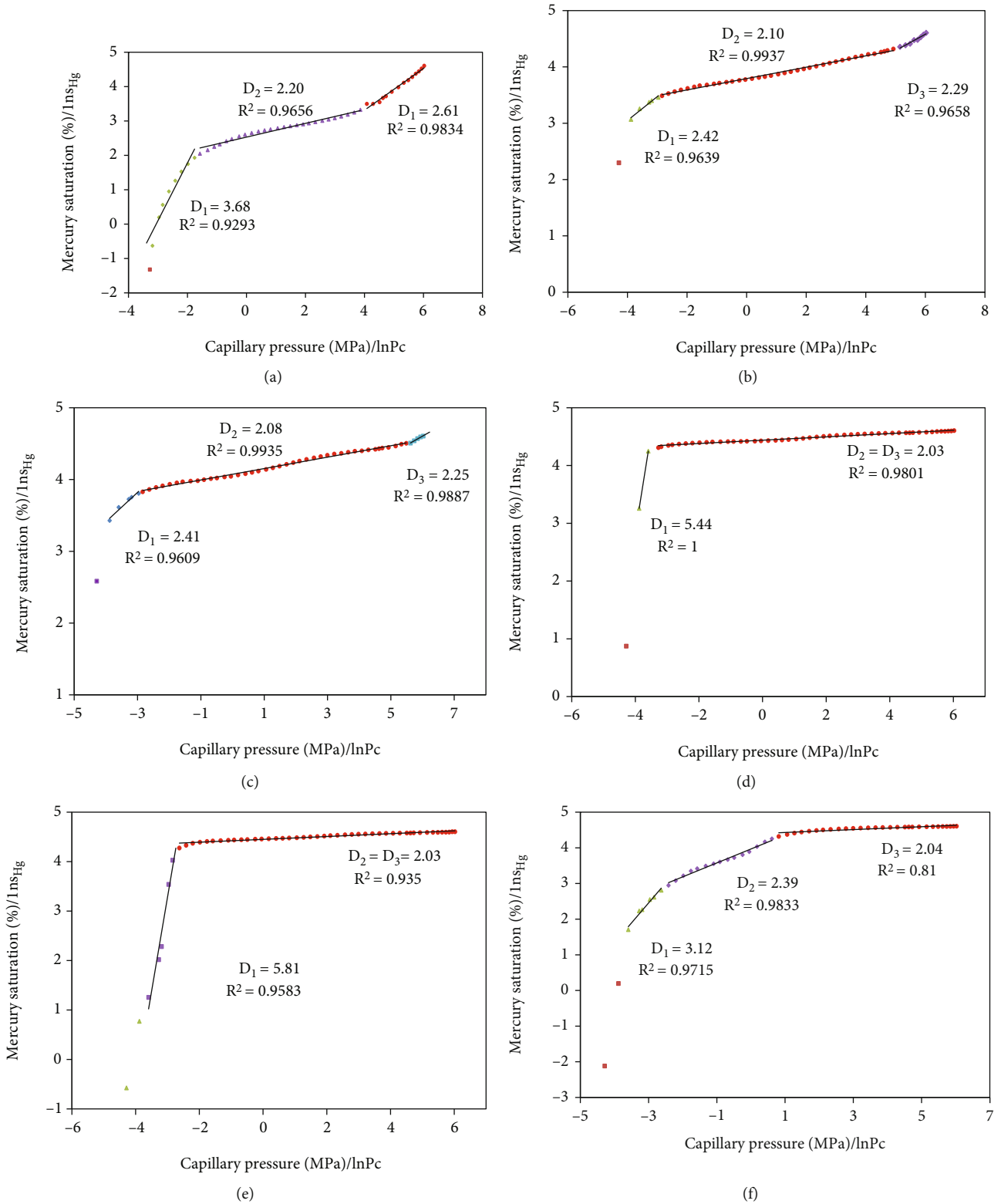


FIGURE 8: Fractal dimensions of shale samples with different particle sizes: (a) 5000 μm ; (b) 2915 μm ; (c) 550 μm ; (d) 210 μm ; (e) 102 μm ; (f) 27 μm .

particle size was presented by Equation (3).

$$\varnothing = 66.18e^{-0.00223L}, \quad (3)$$

where φ is the porosity (%) and L is the sample particle size (μm).

However, permeability, the median pore diameter (volume), and total pore area showed a peak value when the

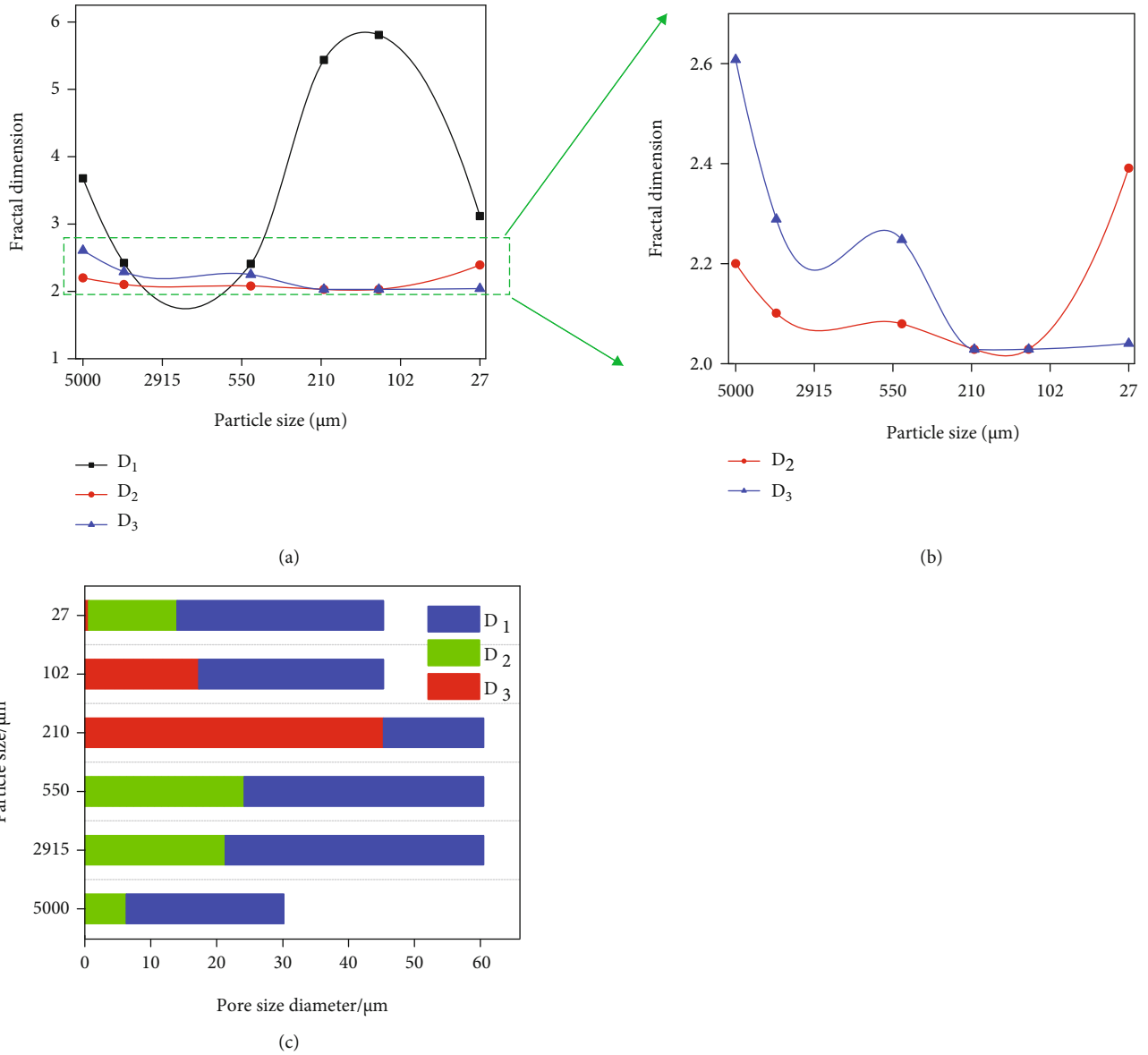


FIGURE 9: Effect of particle size on fractal dimensions of shale pore structure. (a) Fractal dimensions d_1 , d_2 , and d_3 of shale samples with different particle sizes. (b) Fractal dimensions d_2 and d_3 of shale samples with different particle sizes (excluding D_1). (c) The pore size ranges of fractal dimensions d_1 , d_2 , and d_3 of shale samples with different particle sizes.

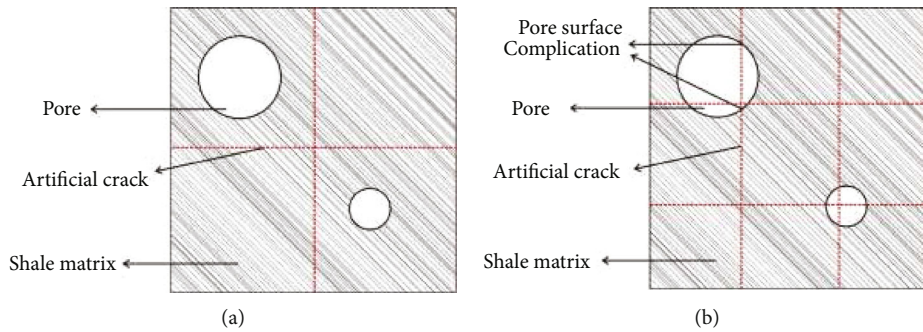


FIGURE 10: Effect of particle size on shale pore structure: (a) larger shale particle size; (b) smaller shale particle size.

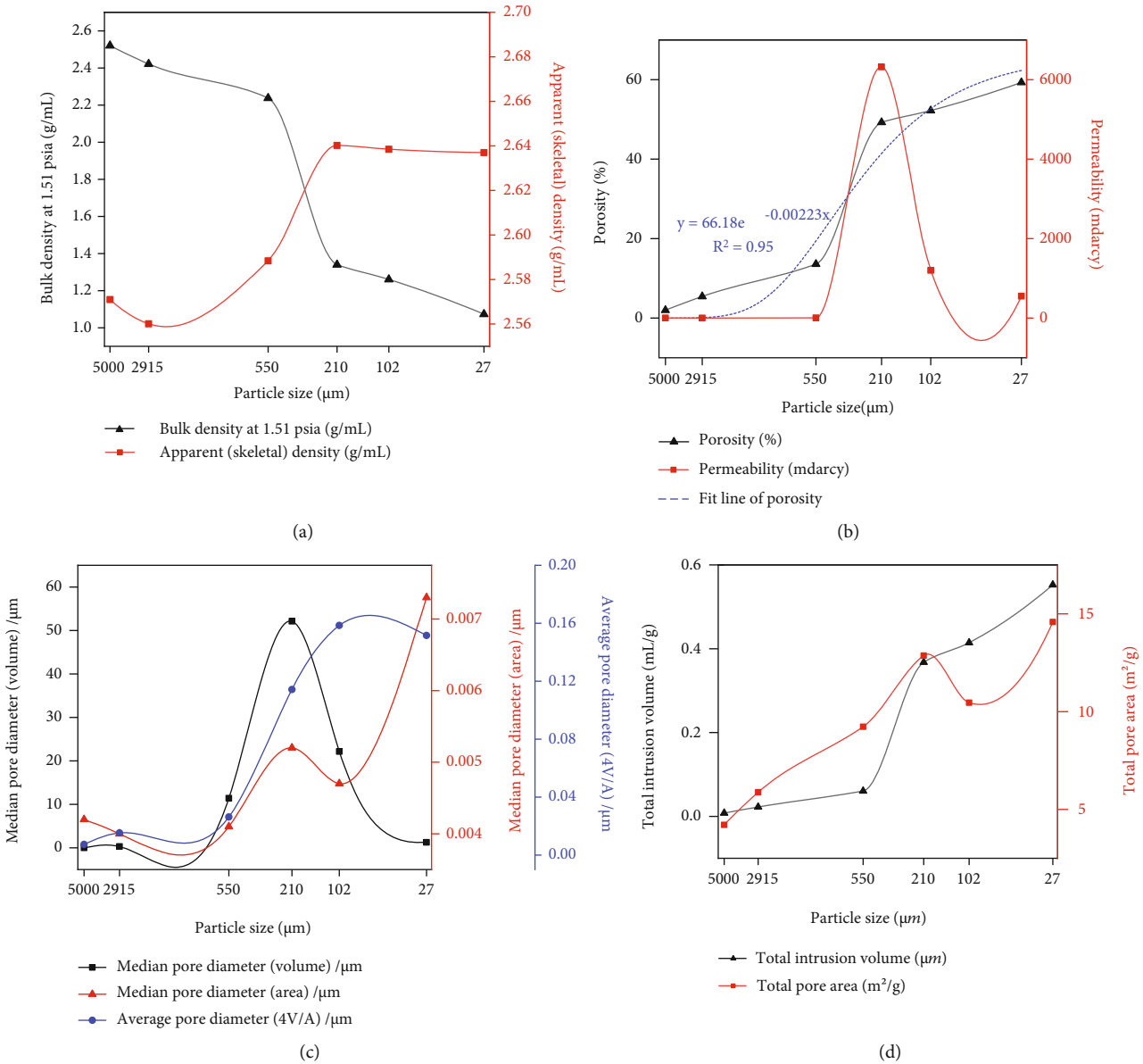


FIGURE 11: The relationship between pore structure parameters and particle size: (a) skeletal density and bulk density; (b) porosity and permeability calculated according to Katz and Thompson (1986); (c) median pore diameter and average pore diameter; (d) total mercury intrusion volume and total pore area.

sample particle size is 210 μm . The pore size range of smooth pores (D_3) in the sample with particle size of 210 μm was also the largest (Figure 9(c)), which indicated the smooth pores tended to have higher permeability.

3.6. The Models for Shale Samples with Different Particle Sizes. Based on the abovementioned viewpoints, two mercury intrusion and extrusion models were established for shale samples with coarse and fine particle sizes (Figure 12). There are two parts in the shale with identical pore structure before sample crushing process, which contains ink-bottle pores, ordinary pores (throat $d_1 > d_2$) and closed pores with different seepage lengths (Figure 12(a)).

The mercury intrusion and extrusion processes of shale with coarse (before sample crushing process; Figure 12(b))

and fine particle (after sample crushing process; Figure 12(c)) are divided into 5 stages: low pressure intrusion, high pressure intrusion, higher pressure intrusion, high pressure extrusion, and low pressure extrusion.

During low pressure intrusion, mercury firstly enters pores with larger pore throat of d_1 . During high pressure mercury intrusion, mercury enters pores with smaller pore throat of d_2 . As the shale particle size decreases, closed pores with long seepage channels are connected with external surface, and some new pores with narrower pore throat of d_3 are generated. Therefore, mercury begins to fill the pores with pore throat of d_3 under higher intrusion pressure (Figure 12(c)).

During the extrusion process, mercury firstly comes out of pores with smaller pore throats under higher pressure and

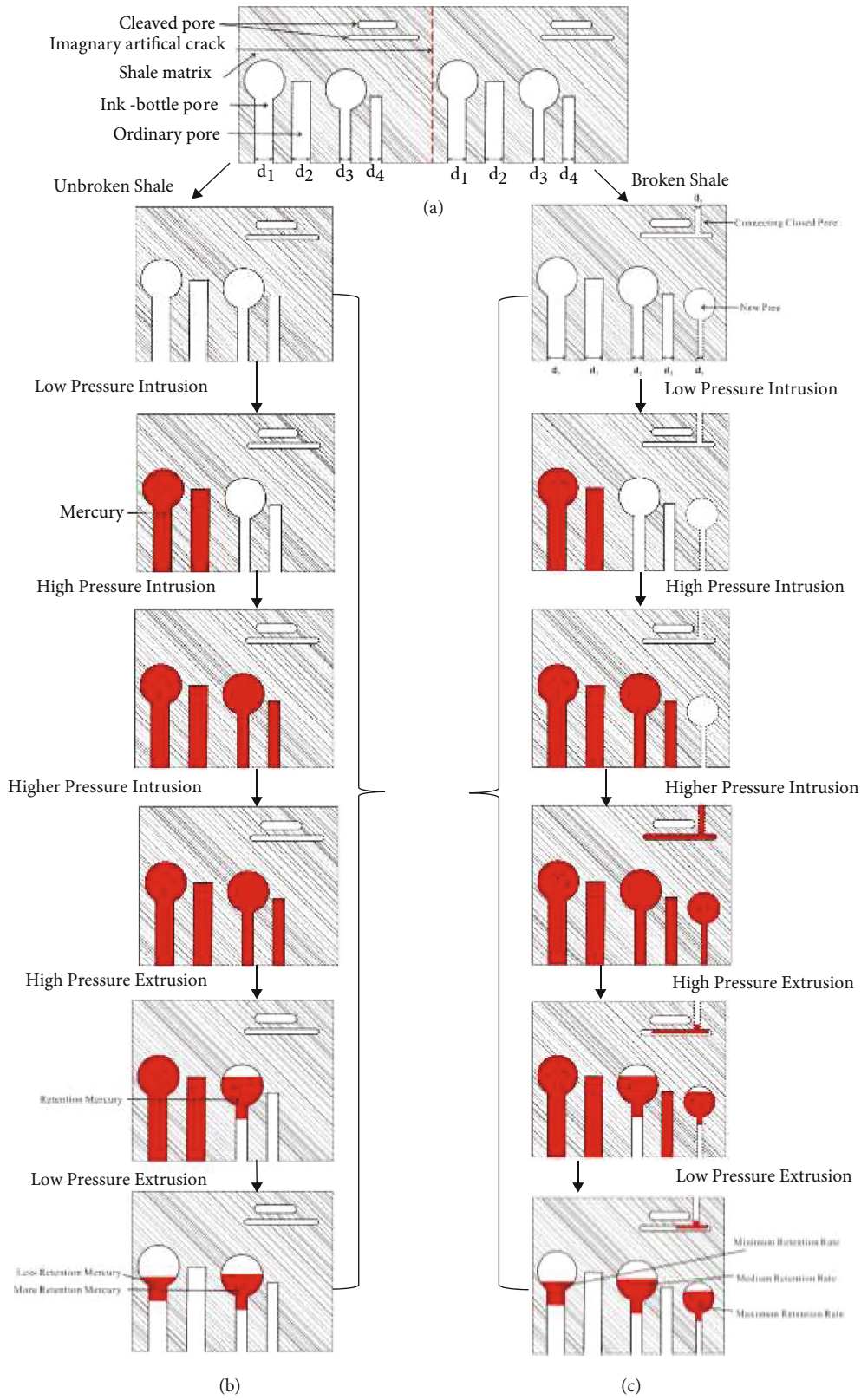


FIGURE 12: Schematic of mercury intrusion and extrusion in shale with different particle sizes: (a) shale sample with two identical parts; (b) shale sample with relatively large particle size before sample crushing process; (c) shale sample with relatively small particle size after sample crushing process.

then pores with larger pore throats under low pressure. Ordinary pores with cylindrical shape show a complete mercury extrusion while some part of intruded mercury is retained within ink-bottle pores and ink-bottle pores with smaller pore throats have higher mercury retention efficiency.

4. Conclusions

- (1) New pore spaces were generated, and the pore accessibility of blind-closed pores was increased during sample crushing process, both of which increased the measured porosity and pore volume
- (2) The effect of sample particle size on pore volume measured by HPMIP varied for pores with different pore sizes. For pores less than 20 nm, the effect of sample particle size on pore volume was limited while the decrease of sample particle size significantly increased the pore volume for pores between 20 nm and 10 μm
- (3) With the decrease of shale sample particle size, the effect of ink-bottle pores was enhanced, leading to the increase of mercury retention during mercury extrusion process. Moreover, the smaller the pore throat is, the greater will be the mercury retention rate
- (4) The fractal dimensions showed the order of $D_1 > D_3 > D_2$, which indicated that the pore structure of larger pores in shale was more complex. D_2 and D_3 were positively related with the sample particle size, indicating that sample crushing process reduced the pore structure complexity. In addition, B7191 sample with particle size of 210 μm had the largest amount and pore size range of smooth pores, increasing its permeability
- (5) Sample crushing process could lead to the differentiation of mineral compositions. Clay minerals are easy to be lost while brittle minerals tend to retain during sample crushing process. Therefore, the skeletal density increased with the decrease of sample particle size

Data Availability

The data in this manuscript will be available up on the readers' request.

Conflicts of Interest

The authors declare that they have no conflicts of interest.

Acknowledgments

This research was supported by the National Natural Science Foundation of China (Nos. 41972145 and 41830431) and the Strategic Cooperation Technology Projects of CNPC and CUPB (ZLZX2020-01-05), as well as

the Foundation (No. PRP/indep-3-1707 and No. PRP/indep-3-1615) of State Key Laboratory of Petroleum Resources and Prospecting from China University of Petroleum at Beijing.

References


- [1] J. Zhao, S. Zheng, and L. Wang, "Analysis of reservoir pore distribution based on casting slice and high pressure mercury," *Yunnan Chemical Technology*, vol. 47, no. 4, pp. 107-108, 2020.
- [2] H. Zhang, Y. Jiang, K. Zhou et al., "Connectivity of pores in shale reservoirs and its implications for the development of shale gas: a case study of the Lower Silurian Longmaxi Formation in the southern Sichuan Basin," *Natural Gas Industry B*, vol. 7, no. 4, pp. 348-357, 2020.
- [3] C. Zou, R. Zhu, K. Liu et al., "Tight gas sandstone reservoirs in China: characteristics and recognition criteria," *Journal of Petroleum Science Engineering*, vol. 88-89, pp. 82-91, 2012.
- [4] Y. Wu, T. Fan, J. Zhang et al., "Characterization of the upper ordovician and lower Silurian Marine Shale in Northwestern Guizhou Province of the upper Yangtze Block, South China: implication for shale gas potential," *Energy Fuels*, vol. 28, no. 6, pp. 3679-3687, 2015.
- [5] S. Luo, J. Lutkenhaus, and H. Nasrabadi, "A novel and practical framework for incorporating nanopores in existing compositional simulators to model the unusually high GOR observed in shale reservoirs," *Journal of Petroleum Science Engineering*, vol. 195, article 107887, 2020.
- [6] B. Liu, H. Wang, X. Fu et al., "Lithofacies and depositional setting of a highly prospective lacustrine shale oil succession from the Upper Cretaceous Qingshankou Formation in the Gulong sag, northern Songliao Basin, northeast China," *AAPG Bulletin*, vol. 103, no. 2, pp. 405-432, 2019.
- [7] N. Jia, W. Lv, T. Chang et al., "A new method for precisely measuring core porosity with high efficiency and no destruction," *Acta Petrolei Sinica*, vol. 39, no. 7, pp. 824-828, 2018.
- [8] Q. Gao, S. Han, Y. Cheng, Y. Li, C. Yan, and Z. Han, "Apparent permeability model for gas transport through micropores and microfractures in shale reservoirs," *Fuel*, vol. 285, article 119086, 2021.
- [9] F. S. Anselmetti, S. Luthi, and G. P. Eberli, "Quantitative characterization of carbonate pore systems by digital image analysis," *AAPG Bulletin*, vol. 82, no. 10, pp. 1815-1836, 1998.
- [10] P. Iassonov, T. Gebrenegus, and M. Tuller, "Segmentation of X-ray computed tomography images of porous materials: a crucial step for characterization and quantitative analysis of pore structures," *Water Resources Research*, vol. 45, no. 9, pp. 706-715, 2009.
- [11] M. Schmitt, C. P. Fernandes, J. A. B. da Cunha Neto, F. G. Wolf, and V. S. S. Dos Santos, "Characterization of pore systems in seal rocks using nitrogen gas adsorption combined with mercury injection capillary pressure techniques," *Marine and Petroleum Geology*, vol. 39, no. 1, pp. 138-149, 2013.
- [12] G. R. Chalmers, R. M. Bustin, and I. M. Power, "Characterization of gas shale pore systems by porosimetry, pycnometry, surface area, and field emission scanning electron microscopy/transmission electron microscopy image analyses: examples from the Barnett, Woodford, Haynesville, Marcellus, and Doig units Characterization of Gas Shale Pore Systems," *AAPG Bulletin*, vol. 96, no. 6, pp. 1099-1119, 2012.

- [13] F. Yang, Z. Ning, C. Hu, B. Wang, and H. Liu, "Characterization of microscopic pore structures in shale reservoirs," *Acta Petrolei Sinica*, vol. 30, no. 2, pp. 301–311, 2013.
- [14] G. Sang, S. Liu, R. Zhang, D. Elsworth, and L. He, "Nanopore characterization of mine roof shales by SANS, nitrogen adsorption, and mercury intrusion: impact on water adsorption/retention behavior," *International Journal of Coal Geology*, vol. 200, pp. 173–185, 2018.
- [15] W. Jian, Z. Lu, L. Jin, X. Zhang, F. Zhang, and B. Zhang, "Acid-base alternation diagenesis and its influence on shale reservoirs in the Permian Lucaogou Formation, Jimusar Sag, Junggar Basin, NW China," *Petroleum Exploration Development*, vol. 47, no. 5, pp. 962–976, 2020.
- [16] D. Zhu, Z. Jiang, S. Jiang et al., "Water-bearing characteristics and their influences on the reservoir capacity in terrestrial shale reservoirs: a case study of the lower Jurassic Ziliujing Formation in the Northeast Sichuan Basin, China," *Marine Petroleum Geology*, vol. 123, article 104738, 2020.
- [17] K. Zhang, C. Jia, Y. Song et al., "Analysis of Lower Cambrian shale gas composition, source and accumulation pattern in different tectonic backgrounds: a case study of Weiyuan Block in the Upper Yangtze region and Xiuwu Basin in the Lower Yangtze region," *Fuel*, vol. 263, article 115978, 2020.
- [18] K. Li, S. Kong, P. Xia, and X. Wang, "Microstructural characterisation of organic matter pores in coal-measure shale," *Advances in Geo-Energy Research*, vol. 4, no. 4, pp. 372–391, 2020.
- [19] M. Sun, L. Zhang, Q. Hu et al., "Multiscale connectivity characterization of marine shales in southern China by fluid intrusion, small-angle neutron scattering (SANS), and FIB-SEM," *Marine Petroleum Geology*, vol. 112, article 104101, 2020.
- [20] W. Ji, F. Hao, H.-M. Schulz, Y. Song, and J. Tian, "The architecture of organic matter and its pores in highly mature gas shales of the lower Silurian Longmaxi Formation in the upper Yangtze platform, south China," *AAPG Bulletin*, vol. 103, no. 12, pp. 2909–2942, 2019.
- [21] X. Hou and J. T. Carstensen, "Application of mercury porosimetry in the study of solid dosage form," *Journal of Beijing Medical College*, vol. 17, no. 2, pp. 131–134, 1985.
- [22] S. P. Rigby and S. Daut, "A statistical model for the heterogeneous structure of porous catalyst pellets," *Advances in Colloid and Interface Science*, vol. 98, no. 2, pp. 87–119, 2002.
- [23] E. Rojas, M. . . L. Perez-Rea, G. Gallegos, and J. Leal, "A porous model for the interpretation of mercury porosimetry tests," *Journal of Porous Media*, vol. 15, no. 6, pp. 517–530, 2012.
- [24] B. Li, F. Chen, D. Xiao, S. Lu, and C. Gong, "Effect of particle size on the experiment of low temperature nitrogen adsorption: a case study of marine gas shale in Wufeng-Longmaxi formation," *Zhongguo Kuangye Daxue Xuebao/Journal of China University of Mining Technology*, vol. 48, no. 2, pp. 395–404, 2019.
- [25] H. Giesche, "Mercury porosimetry: a general (practical) overview," *Particle Particle Systems Characterization*, vol. 23, no. 1, pp. 9–19, 2006.
- [26] K. Li, "Analytical derivation of Brooks-Corey type capillary pressure models using fractal geometry and evaluation of rock heterogeneity," *Journal of Petroleum Science Engineering*, vol. 73, no. 1-2, pp. 20–26, 2010.
- [27] Y. Yao and D. Liu, "Comparison of low-field NMR and mercury intrusion porosimetry in characterizing pore size distributions of coals," *Fuel*, vol. 95, no. 1, pp. 152–158, 2012.
- [28] Z. Gao and Q. Hu, "Estimating permeability using median pore-throat radius obtained from mercury intrusion porosimetry," *Journal of Geophysics and Engineering*, vol. 10, no. 2, article 025014, 2013.
- [29] L. M. Formosa, D. Damidot, and J. Camilleri, "Mercury intrusion porosimetry and assessment of cement-dentin interface of anti-washout-type mineral trioxide aggregate," *Journal of Endodontics*, vol. 40, no. 7, pp. 958–963, 2014.
- [30] Y. Chen, Y. Qin, and H. Tian, "Particle size effect of pore structure of anthracite by mercury porosimetry," *Natural Gas Geoscience*, vol. 26, no. 9, pp. 1629–1639, 2015.
- [31] R. Rezaee, A. Saeedi, and B. Clennell, "Tight gas sands permeability estimation from mercury injection capillary pressure and nuclear magnetic resonance data," *Journal of Petroleum Science Engineering*, vol. 88-89, pp. 92–99, 2012.
- [32] R. G. Larson and N. R. Morrow, "Effects of sample size on capillary pressures in porous media," *Powder Technology*, vol. 30, no. 2, pp. 123–138, 1981.
- [33] J. T. Comisky, M. Santiago, B. McCollom, A. Buddhala, and K. E. Newsham, "Sample size effects on the application of mercury injection capillary pressure for determining the storage capacity of tight gas and oil shales," in *Canadian unconventional resources conference*, Calgary, Alberta, Canada, November 2011.
- [34] R. G. Loucks, R. M. Reed, S. C. Ruppel, and D. M. Jarvie, "Morphology, genesis, and distribution of nanometer-scale pores in siliceous mudstones of the Mississippian Barnett Shale," *Journal of Sedimentary Research*, vol. 79, no. 12, pp. 848–861, 2009.
- [35] C. R. Clarkson, J. L. Jensen, P. K. Pedersen, and M. Freeman, "Innovative methods for flow-unit and pore-structure analyses in a tight siltstone and shale gas reservoir," *AAPG Bulletin*, vol. 96, no. 2, pp. 355–374, 2012.
- [36] D. Avnir and M. Jaroniec, "An isotherm equation for adsorption on fractal surfaces of heterogeneous porous materials," *Langmuir*, vol. 5, no. 6, pp. 1431–1433, 1989.
- [37] S. Lowell, J. E. Shields, M. A. Thomas, and M. Thommes, *Characterization of Porous Solids and Powders: Surface Area, Pore Size and Density*, Springer Science & Business Media, 2012.
- [38] R. Rourke, "Laminates structure of an expanded core panel and a flat sheet of material which does not easily bond and a process for making the same," 1982, U.S. Patent 4,315,050.
- [39] Z. Gao, Q. Hu, and H. Liang, "Gas diffusivity in porous media: determination by mercury intrusion porosimetry and correlation to porosity and permeability," *Journal of Porous Media*, vol. 16, no. 7, pp. 607–617, 2013.
- [40] R. Haul, "Adsorption, surface area and porosity," *Zeitschrift Für Physikalische Chemie*, vol. 63, no. 1_4, pp. 220–221, 1969.
- [41] Y. Shu, Y. Xu, S. Jiang et al., "Effect of particle size on pore characteristics of organic-rich shales: investigations from small-angle neutron scattering (SANS) and fluid intrusion techniques," *Energies*, vol. 13, no. 22, p. 6049, 2020.
- [42] T. Guo and H. Zhang, "Formation and enrichment mode of Jiaoshiha shale gas field, Sichuan Basin," *Exploration Development*, vol. 41, no. 1, pp. 28–36, 2014.
- [43] S. Wang, C. Zou, D. Dong, Y. Wang, J. Huang, and Z. Guo, "Biogenic silica of organic-rich shale in Sichuan Basin and its significance for shale gas," *Acta Scientiarum Naturalium Universitatis Pekinensis*, vol. 50, no. 3, pp. 476–486, 2014.
- [44] R. Yang, S. He, J. Yi, and Q. Hu, "Nano-scale pore structure and fractal dimension of organic-rich Wufeng- Longmaxi

- shale from Jiaoshiba area, Sichuan Basin: investigations using FE-SEM, gas adsorption and helium pycnometry,” *Marine and Petroleum Geology*, vol. 70, pp. 27–45, 2016.
- [45] M. Sun, B. Yu, Q. Hu, R. Yang, Y. Zhang, and B. Li, “Pore connectivity and tracer migration of typical shales in south China,” *Fuel*, vol. 203, pp. 32–46, 2017.
- [46] M. Meng, H. Ge, Y. Shen et al., “The effect of clay-swelling induced cracks on imbibition behavior of marine shale reservoirs,” *Journal of Natural Gas Science Engineering*, vol. 83, article 103525, 2020.
- [47] M. Meng, H. Ge, Y. Shen, L. Li, T. Tian, and J. Chao, “The effect of clay-swelling induced cracks on shale permeability during liquid imbibition and diffusion,” *Journal of Natural Gas Science Engineering*, vol. 83, article 103514, 2020.
- [48] L. Chen, X. Li, J. Bi, P. Zhang, Z. Wei, and Y. Hua, “Influence of proppant on pore structure of shale in northern Guizhou during hydraulic fracturing,” *Mining Technology*, vol. 19, no. 4, 2019.
- [49] Z. Sun, Y. Wang, Z. Wei, Y. Ni, and Y. Li, “Pore structure alteration characteristics of different mineralogical composition shale during shale-fracturing fluid physical-chemical interactions,” *Geofluids*, vol. 2019, Article ID 103514, 13 pages, 2019.
- [50] Z. Gao and Q. Hu, “Wettability of Mississippian Barnett Shale samples at different depths: investigations from directional spontaneous imbibition,” *AAPG Bulletin*, vol. 100, no. 1, pp. 101–114, 2016.
- [51] R. G. Loucks and S. C. Ruppel, “Mississippian Barnett Shale: lithofacies and depositional setting of a deep-water shale-gas succession in the Fort Worth Basin, Texas,” *AAPG Bulletin*, vol. 91, no. 4, pp. 579–601, 2007.
- [52] H. D. Rowe, R. G. Loucks, S. C. Ruppel, and S. M. Rimmer, “Mississippian Barnett Formation, Fort Worth Basin, Texas: bulk geochemical inferences and Mo-TOC constraints on the severity of hydrographic restriction,” *Chemical Geology*, vol. 257, no. 1-2, pp. 16–25, 2008.
- [53] E. W. Washburn, “Note on a method of determining the distribution of pore sizes in a porous material,” *Proceedings of the National Academy of Sciences of the United States of America*, vol. 7, no. 4, pp. 115–116, 1921.
- [54] W. R. Purcell, “Capillary pressures—their measurement using mercury and the calculation of permeability therefrom,” *Journal of Petroleum Technology*, vol. 186, no. 2, pp. 39–48, 1949.
- [55] R. P. Mayer and R. A. Stowe, “Mercury porosimetry: filling of toroidal void volume following breakthrough between packed spheres,” *Journal of Physical Chemistry*, vol. 70, no. 12, pp. 3867–3873, 1966.
- [56] A. P. Radlinski, M. A. Ioannidis, A. L. Hinde et al., “Angstrom-to-millimeter characterization of sedimentary rock microstructure,” *Journal of Colloid and Interface Science*, vol. 274, no. 2, pp. 607–612, 2004.
- [57] J. Cai, B. Yu, M. Zou, and L. Luo, “Fractal characterization of spontaneous co-current imbibition in porous media,” *Energy & Fuels*, vol. 24, no. 3, pp. 1860–1867, 2010.
- [58] J. Lai and G. Wang, “Fractal analysis of tight gas sandstones using high-pressure mercury intrusion techniques,” *Journal of Natural Gas Science Engineering*, vol. 24, pp. 185–196, 2015.
- [59] F. Yang, Z. Ning, and H. Liu, “Fractal characteristics of shales from a shale gas reservoir in the Sichuan Basin, China,” *Fuel*, vol. 115, pp. 378–384, 2014.
- [60] Y. Yao, D. Liu, D. Tang, S. Tang, and W. Huang, “Fractal characterization of adsorption-pores of coals from North China: an investigation on CH₄ adsorption capacity of coals,” *International Journal of Coal Geology*, vol. 73, no. 1, pp. 27–42, 2008.
- [61] R. F. Angulo, V. Alvarado, and H. Gonzalez, “Fractal Dimensions from Mercury Intrusion Capillary Tests,” in *SPE Latin America Petroleum Engineering Conference*, Caracas, Venezuela, 1992.
- [62] E. M. Schlueter, R. W. Zimmerman, P. A. Witherspoon, and N. G. W. Cook, “The fractal dimension of pores in sedimentary rocks and its influence on permeability,” *Engineering Geology*, vol. 48, no. 3-4, pp. 199–215, 1997.
- [63] A. Dathe, S. Eins, J. Niemeyer, and G. Gerold, “The surface fractal dimension of the soil-pore interface as measured by image analysis,” *Geoderma*, vol. 103, no. 1-2, pp. 203–229, 2001.
- [64] X. Ma, S. Zhang, and Z. Lang, “Calculation of fractal dimension of pore structure by using subsection regression method,” *Journal of the University of Petroleum, China*, vol. 28, no. 6, pp. 54–56, 2004.
- [65] B. B. Mandelbrot, “The fractal geometry of nature,” *American Journal of Physics*, vol. 51, no. 3, 1998.
- [66] Q. Hu, “Quantifying effective porosity of oil and gas reservoirs,” in *2018 AAPG International Conference and Exhibition*, Cape Town, South Africa, 2018.
- [67] R. He, *Characteristics of Nanometer Scale Pores Associated with Solid Bitumen and Its Influences on Pore Development of Shales*, [Ph.D. thesis], University of Chinese Academy of Sciences, 2018.
- [68] A. L. Day, R. Sosman, and J. C. Hostetter, “The determination of mineral and rock densities at high temperatures,” *American Journal of Science*, vol. supplement 4-37, no. 217, pp. 1–39, 1914.
- [69] S. Kim and J.-H. Ree, “Quantification of the spatial distribution of mineral phases and grains in rock using a 2-D multiple-area density map technique,” *Tectonophysics*, vol. 522-523, pp. 176–186, 2012.
- [70] M. Abzalov, “Measuring and modelling of dry bulk rock density for mineral resource estimation,” *Applied Earth Science*, vol. 122, no. 1, pp. 16–29, 2013.
- [71] I. Maruyama and S. Muto, “Change in relative density of natural rock minerals due to electron irradiation,” *Journal of Advanced Concrete Technology*, vol. 14, no. 11, pp. 706–716, 2016.

Research Article

Mineral Heterogeneity Characterization of the Lacustrine Yanchang Shales, Ordos Basin Using Micro-Fourier Transform Infrared Spectroscopy (Micro-FTIR) Technique

Bing Luo,^{1,2} Zhiguo Shu,^{1,2} Yalin Chen,^{1,2} Zhuo Li^{1,2,3}, Yufei Hou,³ Liwei Wang,³ Youdong Yang,³ and Zhikai Liang³

¹SINOPEC Jiangnan Oilfield Company, Qianjiang, Hubei 433123, China

²Research Institute of Petroleum Exploration and Development, SINOPEC Jiangnan Oilfield Company, Wuhan, Hubei 430223, China

³State Key Laboratory of Petroleum Resources and Prospecting, China University of Petroleum, Beijing 102249, China

Correspondence should be addressed to Zhuo Li; lizhuopaper@163.com

Received 29 January 2021; Accepted 1 August 2021; Published 29 August 2021

Academic Editor: Huazhou Li

Copyright © 2021 Bing Luo et al. This is an open access article distributed under the Creative Commons Attribution License, which permits unrestricted use, distribution, and reproduction in any medium, provided the original work is properly cited.

Shale is a typical fine-grained sedimentary rock with small grain sizes of matrix components, significant lithofacies variation of rock texture and structure, and strong heterogeneity of organic matter and mineral compositions. Characterization of mineral compositions and their heterogeneity in micro- to nanoscale are the key parameters to gas shale pore structure and rock physical properties. In order to study the microscale mineralogy heterogeneity of the lacustrine shales in the Triassic Yanchang Formation in the Ordos Basin, the micro-Fourier transform infrared spectroscopy (micro-FTIR) technique was conducted. Based on the specific micro-FTIR spectra peaks, the abundance of mineral compositions can be quantitatively determined in the selected microscale areas. The results show that within the range of 80 μm micro-FTIR test interval, both massive argillaceous shale and silty interlayered shale show obvious heterogeneity; in particular, the relatively homogeneous shale observed by the naked eyes also has strong mineral heterogeneity. The results of micro-FTIR spectra are basically consistent with the bulk X-ray diffraction (XRD) data. The advantage of this micro-FTIR technique includes higher resolution (less than 100 μm) and in situ mineral characterization of shale samples at micro- and nanoscale.

1. Introduction

Shales have received worldwide attention due to their emergence as effective unconventional hydrocarbon reservoirs [1–5]. Shale gas is an unconventional gas resource which is generated and accumulated in organic-rich shales [6]. Shale gas is primarily found in free gas and adsorbed gas occurrences [7, 8]. Shales are typical fine-grained sedimentary rock with complex matrix components, multiscale heterogeneity of mineral and organic matter (OM) compositions, and significant lithofacies variation in rock texture and structure, which have important impacts on shale gas exploration and development [9–14]. Accurate determination and fine characterization of mineral composition and distribution in the micro- and nano-

scale is of great significance for pore structure characterization and petrophysical evaluation of gas shales [15–19]. At present, the evaluation of the mineral composition of gas shale mainly depends on bulk rock mineral analysis based on microscope observation on thin sections and X-ray detection. However, the existing techniques have limitations in higher resolution and in situ fine characterization, and it is difficult to evaluate the heterogeneous distribution characteristics of mineral compositions at high resolution using these methods [20–23]. Under actual geological conditions, the microscale heterogeneity of mineral compositions, distribution, and rock texture in shale is still significant [24–27]. Therefore, the characterization of shale heterogeneity needs improvement in the spatial resolution and in situ mineral composition measurement.

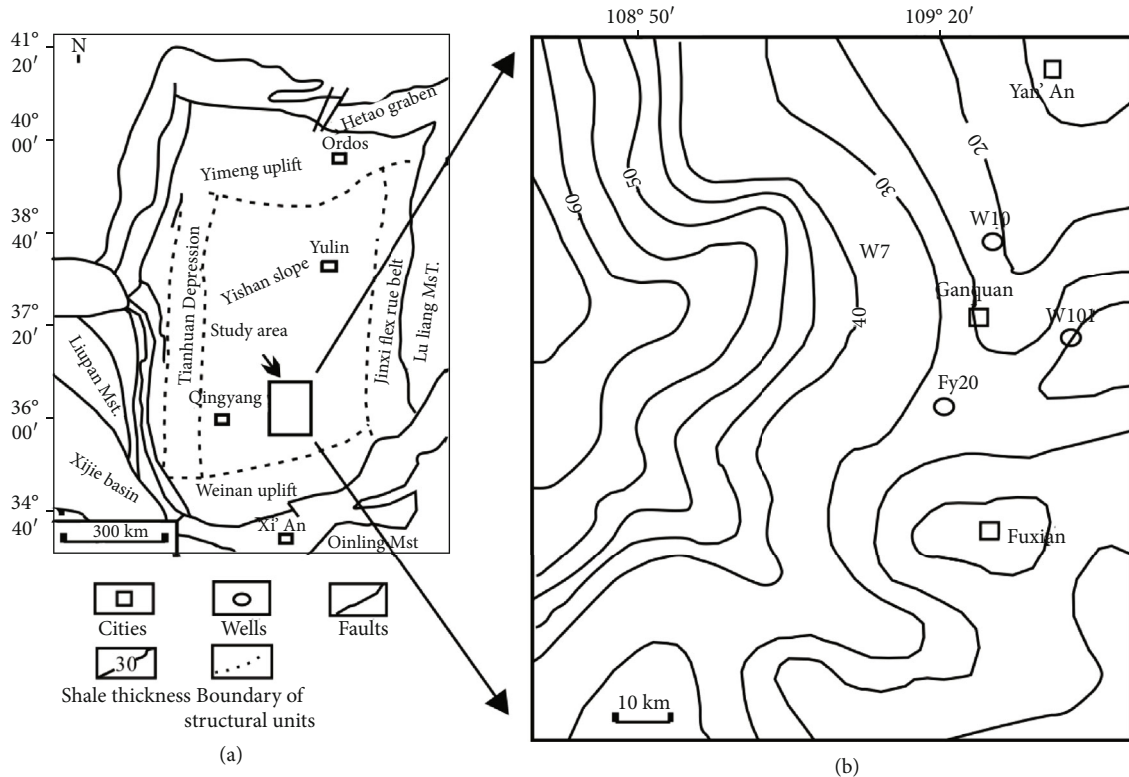


FIGURE 1: Regional tectonic profile and the location of the sampling well in the Ordos Basin, China.

Transmission Fourier transform infrared (FTIR) spectroscopy has been widely used for many years to effectively assess mineral compositions [28–30]. However, traditional FTIR experiments are time consuming and prone to problems. Diffuse reflectance FTIR spectroscopy (DRIFTS) requires the use of a diluent, such as potassium bromide (KBr), for high-quality reflectance results [31]. DRIFTS has the advantage of no physical contact with the analyte, and the technique can be automatically performed and compared with previous results. Attenuated total reflectance- (ATR-) FTIR has been used in a wide range of fields in the field of geology [32, 33]. Unlike transmission and DRIFTS, ATR-FTIR can be used to treat very few samples without dilution. However, ATR-FTIR still requires crushing and homogenization of the powder samples, resulting in loss of spatial and heterogeneity information. This approach requires that surfaces be highly polished, and even then, the quality of the DRIFTS spectra tends to be much lower than the spectra acquired using ATR. The novel micro-FTIR experiment provides a direct measurement technology of mineral distribution in micro- to nanoscales [22]. FTIR microscopy does not require the samples to be pulverized. The principle of micro-FTIR is based on the specific absorption characteristics of infrared rays by chemical bonds in macerals and minerals [34, 35]. Previous research has used spatially resolved FTIR to create three component mineralogy maps [28]. This allows for localized measurements to characterize composition heterogeneous in very small scales. Therefore, multiple micro-FTIR measurements across a sample can be performed rapidly and precisely.

Therefore, micro-FTIR experiment is suitable for higher-resolution characterization of mineral distribution heterogeneity of shale. Another advantage of micro-FTIR spectrum is that in situ measurements can be carried out at submicron scale, which is particularly effective for analyzing mineral heterogeneity in fine-grained gas shales [22].

In this study, two different lacustrine shale samples from the Triassic Yanchang Formation in Ordos Basin were analyzed by micro-FTIR, which provided more detailed data of heterogeneous mineral composition and rock texture and structure. The objectives of this paper are as follows: (1) to study the micromineral heterogeneity of shale by micro-FTIR experiments, (2) to quantitatively characterize the in situ mineral composition of shale by micro-FTIR spectra, and (3) to compare the micro-FTIR results with the traditional bulk shale XRD method.

2. Samples and Methods

Two lacustrine shale samples with different rock texture features from the Triassic Yanchang Formation, Ordos Basin, were selected after carefully examining more than 20 shale samples. These samples were collected in Well FY-2 (Figure 1). The study area is located on the southeast Yishan slope of the Ordos Basin (Figure 1(b)). The target reservoir is the 7th member of the Yanchang Formation (Chang-7 member) of the Upper Triassic strata (Figure 2).

The Ordos Basin, located on the northwestern North China plate, can be divided into six structural units: the

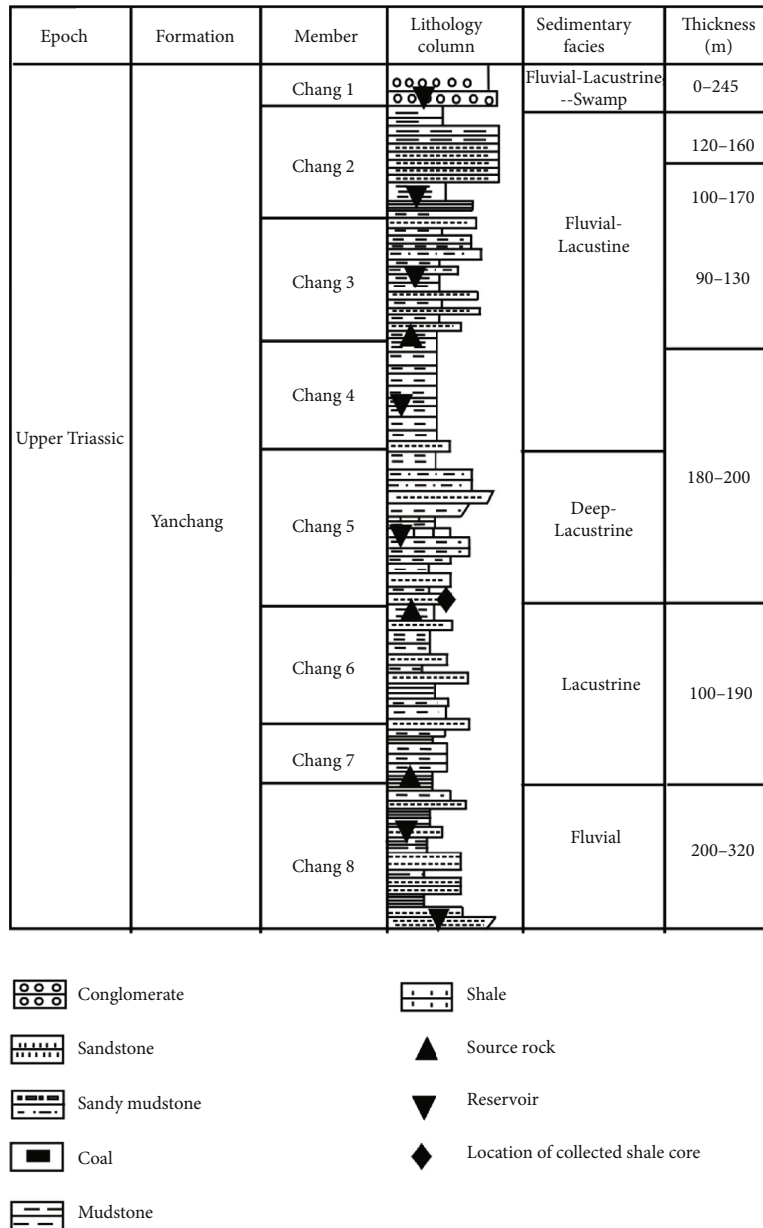


FIGURE 2: Stratigraphic column and depositional environment of the upper Triassic Yanchang Formation in the Ordos Basin, NW China.

Yimeng uplift zone in the north, the Weibei uplift zone in the south, the Jinxi flexural fold zone in the east, the Yishan slope, the Xiyuan obduction zone, and the Tianhuan depression in the west (Figure 1(a)). Late Triassic strata formed in a large-scale inland freshwater lacustrine environment in the internal part of the Ordos Basin. The Chang-7 member deposits consist of deep and semideep facies that are mostly black or blackish gray organic-rich shales, which are primary source rocks in the study area [36, 37].

Each sample was separated into several parts for bulk mineral composition, thin section petrological observation, and micro-FTIR spectra measurements. Thin sections of the lacustrine shale samples were prepared with a thickness of about 80 μm. Petrological observation on the thin sections

was performed on an OLYMPUS microscope with crossed polarized light and plane polarized light. Additional samples were prepared as blocks, then were polished for an ultrasmooth surface. A micro-FTIR spectra experiment was performed using a Bruker Lumos FTIR microscope (Bruker Optics, Billerica, MA). A total of 200 spectra (100 spectra for each sample) were collected. There was a micro-FTIR measurement spacing interval of 80 μm across each sample (for a total of 8 mm in length) to get the in situ heterogeneous characteristics in shale samples (red blocks in Figure 3).

Each spectrum ranges from 400 to 4000 cm⁻¹, with a resolution of 4 cm⁻¹. A nonnegative least squares (NNLS) curve-fitting method was used to quantify the matrix components in samples [21]. Standards for composition calibration

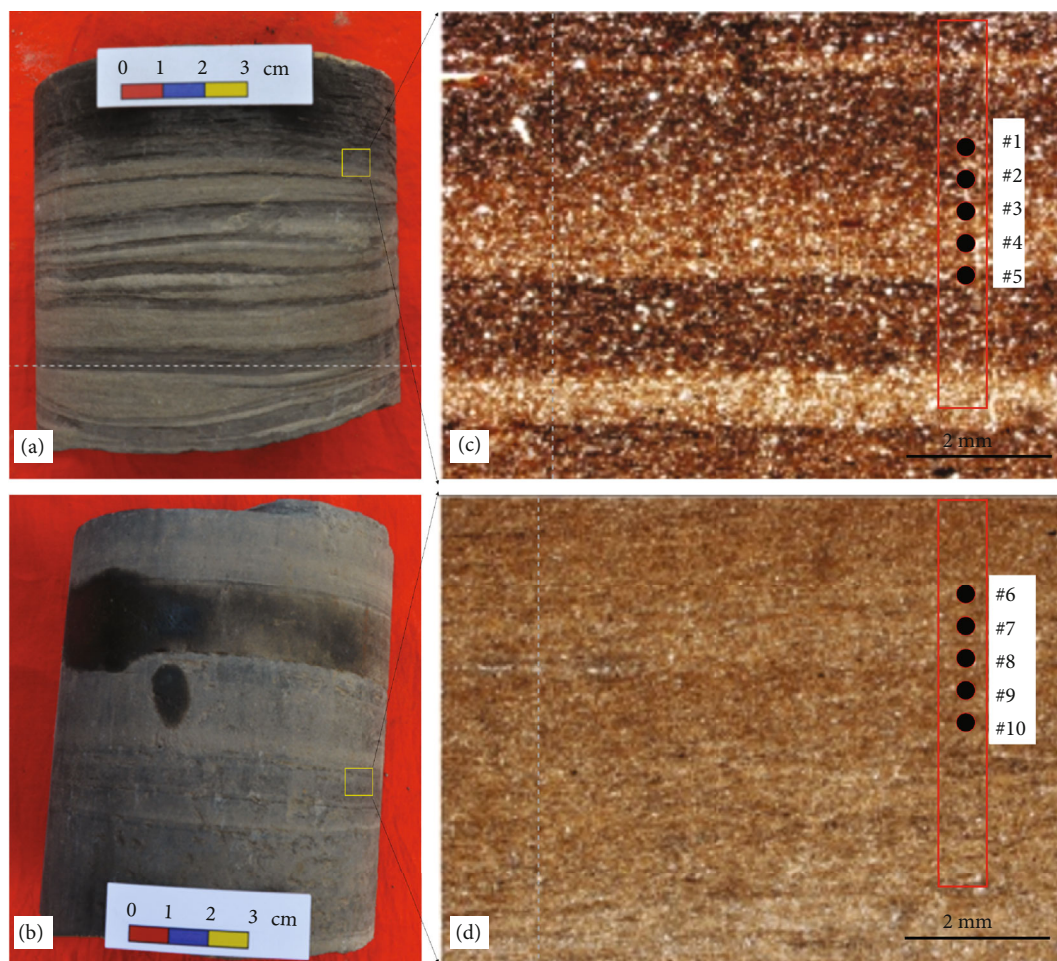


FIGURE 3: Photos of cores and thin sections of shale samples L-1 and L-2. (a) Silty laminated shale (sample ID L-1, 1400 m). (b) Massive argillaceous shale (sample ID L-2, 1625 m). (c) Thin section images of sample L-1, showing silty laminae in silty laminated shale that can be seen by naked eyes. (d) Thin section images of sample L-2, showing argillaceous shale without silty laminae.

TABLE 1: Mineral composition and geochemical characteristics of the Yanchang shale samples.

Sample ID	Lithology	Depth (m)	TOC (%)	Ro (%)	Mineral content (%)					
					Quartz	Feldspar	Calcite	Dolomite	Pyrite	Clay
L-1	Silty laminated shale	1400	1.7	0.93	35.2	11.1	7.1	2.2	3.1	41.1
L-2	Massive argillaceous shale	1625	3.5	1.02	25.3	15.8	5.2	0	4.2	48.8

followed published databases [21–23, 34–38]. Averaged spectra were used for the prediction of bulk mineral compositions and compared with bulk XRD results.

3. Results

3.1. Bulk Mineral Compositions and TOC Contents. Mineral compositions and TOC contents of the lacustrine Yanchang shale samples are listed in Table 1. The TOC of the massive argillaceous shale is 3.5%, relatively richer in OM than the silty laminated shale with a TOC value of 1.7%. The equivalent Ro values of the two samples are both in the oil generation window (0.9–1.1%). XRD results show that the mineral compositions in the Yanchang shale are dominated by quartz

and clay minerals. The silty laminated shale has higher quartz contents, while the massive argillaceous shale has higher feldspar and clay contents. Both samples have relatively high clay contents (41.1% and 48.8%). For the silty laminated shale, the quartz, feldspar, carbonate, and pyrite contents are 35.2%, 17.1%, 2.2%, and 3.1%. For the massive argillaceous shale, the quartz, feldspar, carbonate, and pyrite contents are 25.3%, 15.8%, 5.2%, and 4.2%.

3.2. Mineral Information Derived from Micro-FTIR. Laminae of the sample L-1 can be clearly seen (Figure 3(a)). Silty laminae are commonly grayish-white and are different from adjacent clayey laminae in grain size and mineral composition. Most grains in silty laminae range from 40 μm to 160 μm in size, while grains in clayey laminae are mostly less

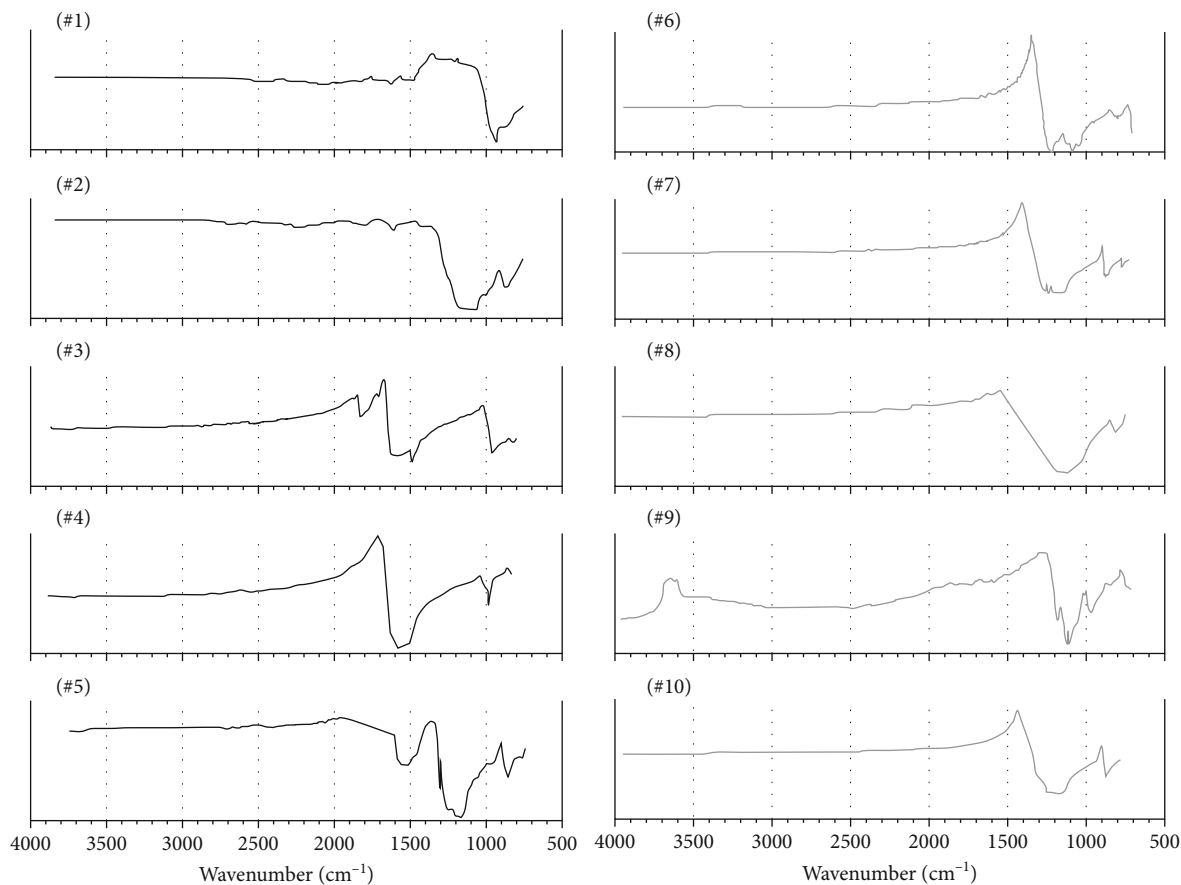


FIGURE 4: Micro-FTIR spectra of selected measurement spots, see location in Figures 1(c) and 1(d).

than $6\ \mu\text{m}$ in size (Figure 3(c)). The detrital grains and the mud matrix or organic matter are mixed and poorly sorted in the massive argillaceous shale, and the grain sizes are mostly less than $10\ \mu\text{m}$ (Figure 3(d)).

The micro-FTIR spectra measured for ten selected spots on the polished surface of the shale samples L-1 and L-2 are shown in Figure 4.

The spectra are highly diverse even when the measured spots are closely located. Micro-FTIR is a surface technique involving specular reflectance, which can produce derivative-shaped peaks or apparent absorbance dips [39]. A previous study has reported the characteristic peaks in micro-FTIR spectra; for example, carbonates have characteristic peaks at $1630\ \text{cm}^{-1}$, $900\ \text{cm}^{-1}$, and $720\ \text{cm}^{-1}$; phyllosilicates display characteristic peaks at $1280\text{--}1150\ \text{cm}^{-1}$ and $1060\text{--}1020\ \text{cm}^{-1}$; and quartz expresses a unique peak at $1360\ \text{cm}^{-1}$ [21] (Table 2).

Mineral composition data of the selected measured spots obtained by NNLS processing are listed in Table 3. The sum of the mineral phases should ideally reach 100 vol.%, but actually accounted for 80%–90%. This indicates that some minor minerals like phosphates are ignored during the model prediction process. The selected spots in the silty laminated shale sample (L-1) have relatively high quartz (28.26–42.39 wt%), feldspar (11.95–14.24 wt%), and clay mineral (36.39–44.09 wt%) contents. A higher clay mineral content (44.01–49.64 wt%) was determined in the massive argilla-

ceous shale sample (L-2) than in the silty laminated shale sample (L-1). In addition, there are large variations in mineral content within a microscale region in both L-1 and L-2.

4. Discussion

4.1. Quantification of Mineralogy through Micro-FTIR Spectra. The KBr FTIR spectra of standard minerals and kerogen have been published [21]. Previous studies presented that the characteristic infrared absorption band range of carbonate minerals is between 1500 and $1400\ \text{cm}^{-1}$, mainly due to the vibration of the internal Co bond [21–23]. The infrared absorption characteristics of silicate minerals are between $1200\text{--}800\ \text{cm}^{-1}$ and $600\text{--}400\ \text{cm}^{-1}$. The peak at $798\text{--}780\ \text{cm}^{-1}$ corresponds to the tetrahedral bridging bond in quartz. Phyllosilicates can be separated from quartz according to the occurrence of minerals. The results of tensile vibration of the hydrogen oxygen bond are $3750\text{--}3400\ \text{cm}^{-1}$. The characteristic infrared absorption band of kerogen is in the wavelength range of $1800\text{--}1000\ \text{cm}^{-1}$ (hydrocarbon bond stretching of aliphatic hydrocarbon) [21].

In order to constrain the quantitative analysis of mineral components in rocks, the FTIR spectra of shales and pure minerals have been carefully compared by previous studies, such as the relative contents of clay, quartz, carbonate, and organic matter in shales [20–23]. The overlapping of infrared bands of some analytes and the resulting errors are inevitable.

TABLE 2: Micro-FTIR spectra peaks of specific minerals.

Minerals	Carbonates	Phyllosilicates	Hydrogen oxygen	Kerogen	Quartz	Silicate
Micro-FTIR spectra peaks (cm ⁻¹)	1600, 900, and 720	1280–1150 and 1060–1020	3750-3400	1800-1000	1360	1200-800 and 600-400

TABLE 3: Mineral composition calculated from micro-FTIR spectra of the Yanchang shale samples.

Sample ID	Spot ID	Mineral composition (wt%)								
		Quartz	Feldspar	Calcite	Dolomite	Pyrite	Clay	Illite/smectite	Kaolinite	Chlorite
L-1	#1	32.07	14.24	—	1.3	—	42.54	32.66	—	8.36
	#2	28.26	11.95	—	—	3.2	39.75	24.71	6.54	7.27
	#3	42.39	12.68	—	2.2	—	36.39	24.80	—	10.80
	#4	38.60	13.80	4.95	—	2.05	44.09	31.57	—	11.79
	#5	37.94	13.64	4.1	—	3.11	43.06	26.18	—	15.77
L-2	#6	34.77	15.65	—	—	0.21	47.47	25.06	—	16.36
	#7	26.09	15.29	5.33	—	0.44	44.01	33.06	—	10.64
	#8	36.56	13.11	—	1.6	—	49.64	21.41	—	12.53
	#9	30.24	10.12	—	11.04	—	42.97	27.18	—	—
	#10	31.47	12.51	4.01	—	1.8	45.67	22.71	8.22	—

Some studies have shown that in the middle range of the infrared wavelength, the mineral concentration of an artificial mixture can be quantitatively obtained from the spectrum of mineral standards [34, 35]. The complexity of the matrix components of gas-bearing shale brings challenges to the quantitative study of FTIR minerals. The deviation between the standard spectral characteristics of a single mineral and the actual shale samples easily leads to systematic error, resulting in the total mass fraction of mineral components in shale less than 100 wt.% [21]. In addition, the omission of some trace minerals (such as anatase, phosphate, and pyrite) will also lead to the underestimation of FTIR [21–23]. Despite these potential problems, FTIR quantitative and independent parallel analysis by XRD and elemental chemistry yielded comparable data for quartz and carbonate content, which XRD showed was higher than FTIR and elemental analysis. The results of FTIR and XRD are also comparable in clay content. The chemical spectroscopy method for quantitative analysis of shale components is limited by its basic assumptions. The compounds are converted to mineral concentrations using equations based on the ratio of possible pure mineral elements.

4.2. In Situ Heterogeneity Characteristics. In the present study, the heterogeneous distribution of mineral compositions in the lacustrine shale samples (red blocks in Figure 3) were derived from the totally obtained 200 micro-FTIR spectra and shown in Figure 5.

The spacing of 80 μm for each micro-FTIR measurement spots were selected to get in situ heterogeneous characteristics in shale samples. Therefore, micro-FTIR spectra measurements are able to capture the specific information expressed by the heterogeneity at high spatial resolution [21].

In general, silty laminae with higher quartz content (40–60 wt %) had lower concentrations of clay minerals. It was observed that, despite general agreement between the averaged FTIR results and the XRD data (Table 1), there are large standard deviations for most minerals. The mean value determined from micro-FTIR predicted values are compared with the XRD-measured bulk sample values (Figure 6). Overall, the mineral compositions calculated from the micro-FTIR compared well to the bulk XRD results.

Recent studies have shown that shale has strong heterogeneity in mineral composition, structure, and pore structure [40–48]. The lighter layers contain more quartz and less clay minerals than the darker ones. Changes in mineralogical composition from microscopic FTIR spectra along the length of the sample are clearly shown (Figure 5). Color changes in the measurement area are noted in the mineral composition derived from microscopic FTIR, which is reflected in mineralogical changes along the measurement area. The quartz and clay mineral compositions most clearly show the layered structure of the L-1 sample (Figure 5). The distribution of quartz and clay shows the layered structure of the L-1 sample most clearly, showing alternating distribution of high concentration and low concentration along the y -axis perpendicular to the bedding plane. Laminae is attributed to seasonal cycles [49–50], which may explain fluctuations in organic and mineral content.

At the micron scale, the regular changes of mineral composition and distribution obtained by microscopic FTIR spectra (Figure 5) can be used to precisely understand the heterogeneity and high-quality reservoir characterization of shales. In addition, minerals are the result of sensitive changes in physical and chemical conditions due to depositional environment evolution. In the shale gas production process, large

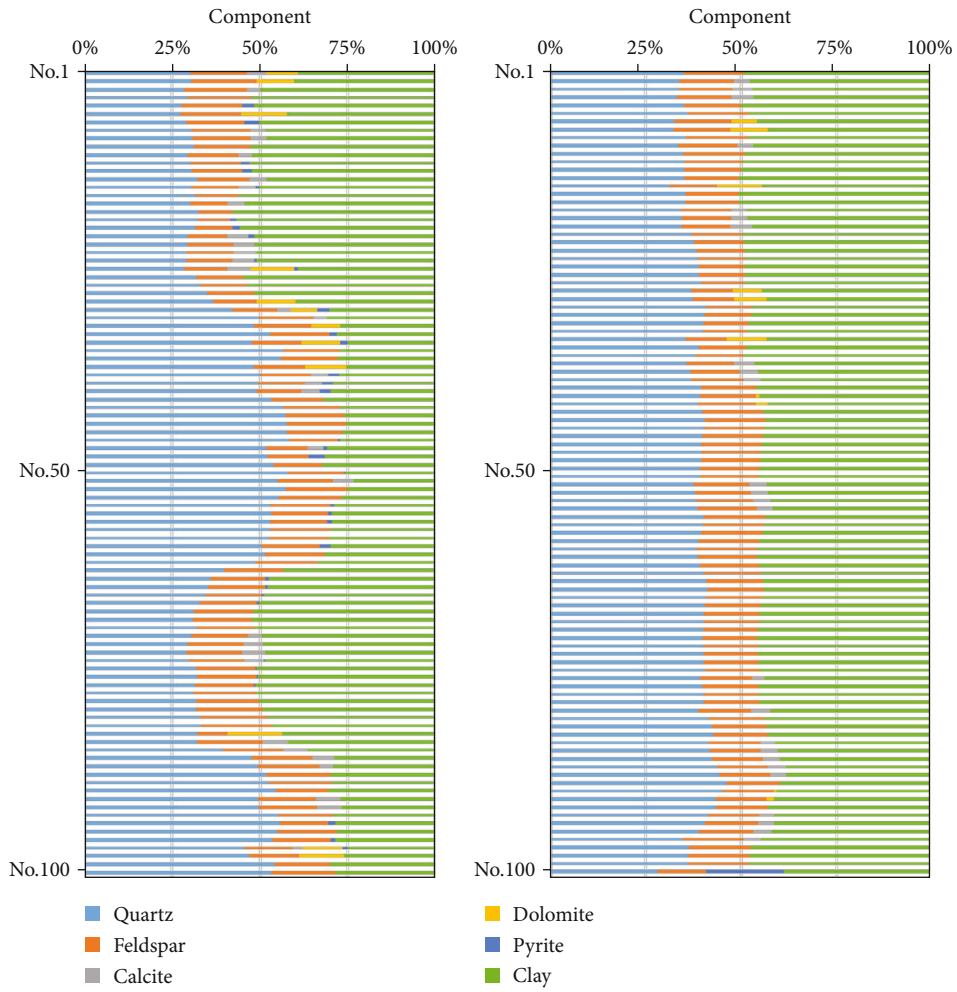


FIGURE 5: Distribution of mineralogy composition along the measured region (red blocks in Figure 1) of the (a) silty laminated sample and (b) the massive argillaceous shale.

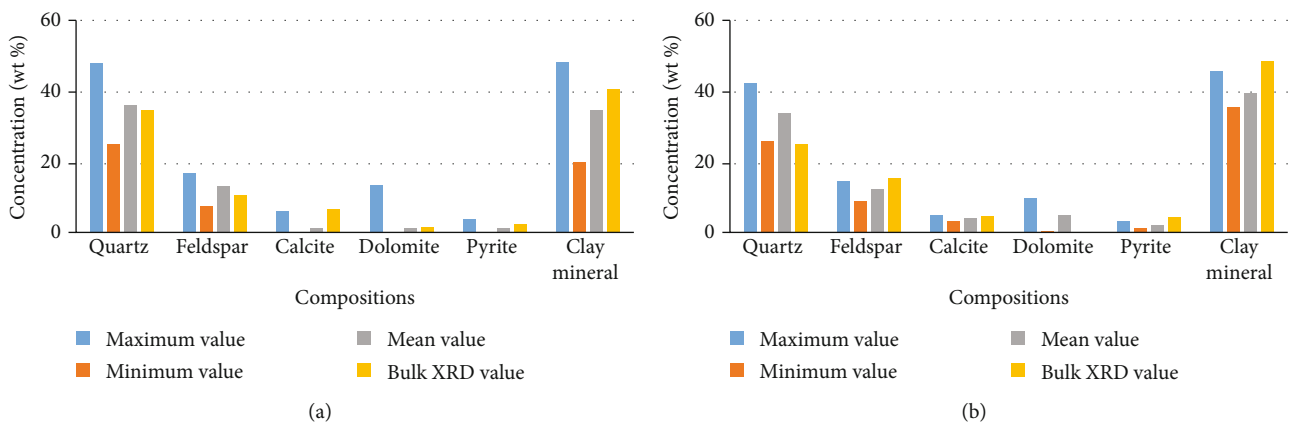


FIGURE 6: Histograms showing the maximum, minimum, and mean values of (a) silty laminated sample L-1 and (b) massive argillaceous shale L-2. The mean value determined from micro-FTIR-predicted values are compared with the XRD-measured bulk sample values.

changes may occur, which may lead to more changes in cross well productivity [2–4]. Therefore, a better understanding of the changes in development and production can provide important guidance for the efficient development of lacustrine shale gas. Considering the small mismatch value and good fit-

ting, we believe that the micro-FTIR technique provides an effective method for quantitative evaluation of the shale matrix at a micron scale. Two main advantages of the micro-FTIR are proposed. Firstly, this is an in situ technique to avoid destructive and potentially contaminated grinding of the sample. It

can be used to analyze in situ shale samples with constant kerogen mineral assemblage and spatial information. Secondly, the micro-FTIR spectra measurements can capture the abundant information expressed by heterogeneity at high spatial resolution.

5. Conclusions

Based on the above study, the following conclusions can be drawn:

- (1) Mineral compositions in the Yanchang shale are dominated by quartz and clay minerals. The massive argillaceous shale is OM richer than the silty laminated shale. The silty laminated shale has higher quartz contents, while the massive argillaceous shale has higher feldspar and clay contents
- (2) The micro-FTIR results are basically consistent with the bulk shale XRD results. The analyzed massive argillaceous shale and silty laminated shales in the study area show obvious heterogeneity within the measurement interval of 80 μm . The mineral composition of homogeneous samples observed by naked eyes is also strongly heterogeneous when measured by the micro-FTIR technique
- (3) The micro-FTIR technique provides a fast and non-destructive method to determine the heterogeneity of mineral components in shale samples. The mineral composition information of sample heterogeneity can be obtained by multiple measurements
- (4) The micro-FTIR techniques can precisely characterize the in situ compositional heterogeneity of shale samples and capture abundant information expressed by shale heterogeneity while providing resolution for shale mineralogy research

Data Availability

The mineral composition, geochemical characteristics, and micro-FTIR spectra experiment result data used to support the findings of this study are included within the article.

Conflicts of Interest

The authors declare that they have no conflicts of interest.

Acknowledgments

This study was supported by the National Natural Science Foundation of China (No. 41502123) and the National Major Project of China (No. 2016ZX05034-001).

References

- [1] J. B. Curtis, "Fractured shale-gas systems," *AAPG Bulletin*, vol. 86, pp. 1921–1938, 2002.
- [2] S. L. Montgomery, D. M. Jarvie, K. A. Bowker, and R. M. Pollastro, "Mississippian Barnett Shale, Fort Worth Basin, north-central Texas: gas-shale play with multi-trillion cubic foot potential," *AAPG Bulletin*, vol. 89, no. 2, pp. 155–175, 2005.
- [3] D. M. Jarvie, R. J. Hill, T. E. Ruble, and R. M. Pollastro, "Unconventional shale-gas systems: the Mississippian Barnett shale of north-central Texas as one model for thermogenic shale-gas assessment," *AAPG Bulletin*, vol. 91, pp. 475–499, 2007.
- [4] R. M. Pollastro, D. M. Jarvie, R. J. Hill, and C. W. Adams, "Geologic framework of the Mississippian Barnett Shale, Barnett-Paleozoic total petroleum system, Bend Arch-Fort Worth Basin, Texas," *AAPG Bulletin*, vol. 91, no. 4, pp. 405–436, 2007.
- [5] R. G. Loucks, R. M. Reed, S. C. Ruppel, and U. Hammes, "Spectrum of pore types and networks in mudrocks and a descriptive classification for matrix-related mudrock pores," *AAPG Bulletin*, vol. 96, no. 6, pp. 1071–1098, 2012.
- [6] K. Zhang, Z. Jiang, L. Yin et al., "Controlling functions of hydrothermal activity to shale gas content-taking lower Cambrian in Xiuwu Basin as an example," *Marine and Petroleum Geology*, vol. 85, pp. 177–193, 2017.
- [7] K. Zhang, Y. Song, S. Jiang et al., "Shale gas accumulation mechanism in a syncline setting based on multiple geological factors: an example of southern Sichuan and the Xiuwu Basin in the Yangtze Region," *Fuel*, vol. 241, pp. 468–476, 2019.
- [8] K. Zhang, Y. Song, C. Jia et al., "Vertical sealing mechanism of shale and its roof and floor and effect on shale gas accumulation, a case study of marine shale in Sichuan basin, the Upper Yangtze area," *Journal of Petroleum Science and Engineering*, vol. 175, pp. 743–754, 2019.
- [9] R. G. Loucks and S. C. Ruppel, "Mississippian Barnett Shale: lithofacies and depositional setting of a deep-water shale-gas succession in the Fort Worth Basin, Texas," *AAPG Bulletin*, vol. 91, no. 4, pp. 579–601, 2007.
- [10] M. Mastalerz, L. L. He, Y. B. Melnichenko, and J. A. Rupp, "Porosity of coal and shale: insights from gas adsorption and SANS/USANS techniques," *Energy & Fuels*, vol. 26, no. 8, pp. 5109–5120, 2012.
- [11] Z. Li, Z. Jiang, H. Yu, and Z. Liang, "Organic matter pore characterization of the Wufeng-Longmaxi shales from the Fuling gas field, Sichuan Basin: evidence from organic matter isolation and low-pressure CO₂ and N₂ adsorption," *Energies*, vol. 12, no. 7, p. 1207, 2019.
- [12] W. Ji, F. Hao, H. Schulz, Y. Song, and J. Tian, "The architecture of organic matter and its pores in highly mature gas shales of the Lower Silurian Longmaxi Formation in the Upper Yangtze Platform, south China," *AAPG Bulletin*, vol. 102, no. 12, pp. 2909–2942, 2019.
- [13] K. Zhang, Y. Song, S. Jiang et al., "Mechanism analysis of organic matter enrichment in different sedimentary backgrounds: a case study of the Lower Cambrian and the Upper Ordovician-Lower Silurian, in Yangtze region," *Marine and Petroleum Geology*, vol. 99, pp. 488–497, 2019.
- [14] B. Liu, J. Sun, Y. Zhang et al., "Reservoir space and enrichment model of shale oil in the first member of Cretaceous Qingshankou Formation in the Changling sag, southern Songliao Basin, NE China," *Petroleum Exploration and Development*, vol. 48, no. 3, pp. 608–624, 2021.
- [15] K. Zhang, J. Peng, X. Wang et al., "Effect of organic maturity on shale gas genesis and pores development: a case study on marine shale in the upper Yangtze region, South China," *Open Geosciences*, vol. 12, no. 1, pp. 1617–1629, 2020.

- [16] K. Zhang, P. Jun, L. Weiwei et al., "The role of deep geofluids in the enrichment of sedimentary organic matter: a case study of the Late Ordovician-Early Silurian in the upper Yangtze region and early Cambrian in the lower Yangtze region, south China," *Geofluids*, vol. 2020, Article ID 8868638, 12 pages, 2020.
- [17] Z. Li, Z. Liang, Z. Jiang et al., "The impacts of matrix compositions on nanopore structure and fractal characteristics of lacustrine shales from the Changling Fault Depression, Songliao Basin, China," *Minerals*, vol. 9, no. 2, p. 127, 2019.
- [18] Z. Li, Z. Liang, Z. Jiang, H. Yu, Y. Yang, and L. Xiao, "Pore connectivity characterization of lacustrine shales in Changling Fault Depression, Songliao Basin, China: insights into the effects of mineral compositions on connected pores," *Minerals*, vol. 9, no. 3, p. 198, 2019.
- [19] B. Liu, A. Bechtel, R. F. Sachsenhofer, D. Gross, R. Gratzner, and X. Chen, "Depositional environment of oil shale within the second member of Permian Lucaogou Formation in the Santanghu Basin, Northwest China," *International Journal of Coal Geology*, vol. 175, pp. 10–25, 2017.
- [20] S. Bernard, B. Horsfield, H. M. Schulz, R. Wirth, A. Schreiber, and N. Sherwood, "Geochemical evolution of organic-rich shales with increasing maturity: a STXM and TEM study of the Posidonia Shale (Lower Toarcian, northern Germany)," *Marine and Petroleum Geology*, vol. 31, no. 1, pp. 70–89, 2012.
- [21] Y. Chen, A. Furmann, M. Mastalerz, and A. Schimmelmann, "Quantitative analysis of shales by KBr-FTIR and micro-FTIR," *Fuel*, vol. 116, pp. 538–549, 2014.
- [22] Y. Chen, M. Mastalerz, and A. Schimmelmann, "Characterization of chemical functional groups in macerals across different coal ranks via micro-FTIR spectroscopy," *International Journal of Coal Geology*, vol. 104, pp. 22–33, 2012.
- [23] K. E. Washburn, J. E. Birdwell, M. Foster, and F. Gutierrez, "Detailed description of oil shale organic and mineralogical heterogeneity via Fourier transform infrared microscopy," *Energy & Fuels*, vol. 29, no. 7, pp. 4264–4271, 2015.
- [24] Z. Li, Z. Jiang, Z. Liang, H. Yu, and Y. Yang, *Pore-Structure Characterisation of Tectonically Deformed Shales: Wufeng-Longmaxi Formation in Western Hunan Province, Southern Impact of Laminae on Pore Structures of Lacustrine Shales in the Southern Songliao Basin, NE China*, Australian Journal of Earth Sciences, 2019.
- [25] K. Zhang, J. Chengzao, S. Yan et al., "Analysis of Lower Cambrian shale gas composition, source and accumulation pattern in different tectonic backgrounds: a case study of Weiyuan Block in the Upper Yangtze region and Xiuwu Basin in the Lower Yangtze region," *Fuel*, vol. 263, article 115978, 2020.
- [26] B. Liu, Y. Gao, K. Liu et al., "Pore structure and adsorption hysteresis of the middle Jurassic Xishanyao shale formation in the Southern Junggar Basin, northwest China," *Energy Exploration & Exploitation*, vol. 39, no. 3, pp. 761–778, 2021.
- [27] D. Liu, Z. Li, Z. Jiang et al., "Impact of laminae on pore structures of lacustrine shales in the southern Songliao Basin, NE China," *Journal of Asian earth sciences*, vol. 182, article 103935, 2019.
- [28] B. H. Ruessink and D. G. Harville, "Quantitative analysis of bulk mineralogy: The applicability and performance of XRD and FTIR," in *Proceedings of the Society of Petroleum Engineers Formation Damage Control Symposium*, Lafayette, LA, 1992.
- [29] M. M. Herron, A. Matteson, and G. Gustavson, "Dual-range FT-IR mineralogy and the analysis of sedimentary formations," in *Proceedings of the Society of Core Analysts Annual Technical Conference*, Calgary, Alberta, Canada, 1997.
- [30] B. D. Ballard, "Quantitative mineralogy of reservoir rocks using Fourier transform infrared spectroscopy," in *Proceedings of the Society of Petroleum Engineers Annual Technical Conference and Exhibition*, Anaheim, CA, 2007.
- [31] P. R. Griffiths and J. A. Haseeth, *Fourier Transform Infrared Spectroscopy*, Wiley-Interscience, Hoboken, NJ, 2nd edition, 2007.
- [32] C. M. Müller, B. Pejčić, L. Esteban, C. D. Piane, M. Raven, and B. Mizaikoff, "Infrared attenuated total reflectance spectroscopy: an innovative strategy for analyzing mineral components in energy relevant systems," *Scientific Reports*, vol. 4, article 6764, 2014.
- [33] M. Klinkenberg, R. Dohrmann, S. Kaufhold, and H. Stanjek, "A new method for identifying Wyoming bentonite by ATR-FTIR," *Applied Clay Science*, vol. 33, no. 3-4, pp. 195–206, 2006.
- [34] D. C. Cronauer, R. W. Snyder, and P. C. Painter, "Characterization of oil shale by FTIR spectroscopy," *Abstracts of Papers of the American Chemical Society*, pp. 122–130, 1982.
- [35] M. Mastalerz and R. Marc Bustin, "Electron microprobe and micro-FTIR analyses applied to maceral chemistry," *International Journal of Coal Geology*, vol. 24, no. 1-4, pp. 333–345, 1993.
- [36] H. Li, H. Guo, Z. Yang, and X. Wang, "Tight oil occurrence space of Triassic Chang 7 member in Northern Shaanxi Area, Ordos Basin, NW China," *Petroleum Exploration and Development*, vol. 42, no. 3, pp. 434–438, 2015.
- [37] L. Sun, J. Tuo, M. Zhang, C. Wu, Z. Wang, and Y. Zheng, "Formation and development of the pore structure in Chang 7 member oil-shale from Ordos Basin during organic matter evolution induced by hydrous pyrolysis," *Fuel*, vol. 158, pp. 549–557, 2015.
- [38] M. Mastalerz and R. M. Bustin, "Application of reflectance micro-Fourier transform infrared analysis to the study of coal macerals: an example from the late Jurassic to early Cretaceous coals of the Mist Mountain Formation, British Columbia, Canada," *International Journal of Coal Geology*, vol. 32, no. 1-4, pp. 55–67, 1996.
- [39] P. R. Griffiths and J. A. D. Haseeth, *Fourier Transform Infrared Spectrometry*, John Wiley & Sons, INC., Publication, 2nd edition, 2006.
- [40] X. Tang, J. Zhang, X. Wang et al., "Shale characteristics in the southeastern Ordos Basin, China: implications for hydrocarbon accumulation conditions and the potential of continental shales," *International Journal of Coal Geology*, vol. 128-129, pp. 32–46, 2014.
- [41] X. Wang, S. Gao, and C. Gao, "Geological features of Mesozoic lacustrine shale gas in south of Ordos Basin, NW China," *Petroleum Exploration and Development*, vol. 41, no. 3, pp. 326–337, 2014.
- [42] D. J. K. Ross and R. M. Bustin, "Characterizing the shale gas resource potential of Devonian-Mississippian strata in the Western Canada sedimentary basin: application of an integrated formation evaluation," *AAPG Bulletin*, vol. 92, no. 1, pp. 87–125, 2008.
- [43] D. J. K. Ross and R. Marc Bustin, "The importance of shale composition and pore structure upon gas storage potential of shale gas reservoirs," *Marine and Petroleum Geology*, vol. 26, no. 6, pp. 916–927, 2009.

- [44] P. C. Hackley, "Geological and geochemical characterization of the Lower Cretaceous Pearsall Formation, Maverick Basin, south Texas: A future shale gas resource?," *AAPG Bulletin*, vol. 96, no. 8, pp. 1449–1482, 2012.
- [45] D. M. Jarvie, R. J. Hill, T. E. Ruble, and R. M. Pollastro, "Unconventional shale-gas systems: the Mississippian Barnett Shale of northcentral Texas as one model for thermogenic shale-gas assessment," *AAPG Bulletin*, vol. 91, no. 4, pp. 475–499, 2007.
- [46] T. J. Kinley, L. W. Cook, J. A. Breyer, D. M. Jarvie, and A. B. Busbey, "Hydrocarbon potential of the Barnett Shale (Mississippian), Delaware Basin, west Texas and southeastern New Mexico," *AAPG Bulletin*, vol. 92, no. 8, pp. 967–991, 2008.
- [47] R. G. Loucks, R. M. Reed, S. C. Ruppel, and D. M. Jarvie, "Morphology, genesis, and distribution of nanometer-scale pores in siliceous mudstones of the Mississippian Barnett shale," *Journal of Sedimentary Research*, vol. 79, no. 12, pp. 848–861, 2009.
- [48] R. J. Hill, D. M. Jarvie, J. Zumberge, M. Henry, and R. M. Pollastro, "Oil and gas geochemistry and petroleum systems of the Fort Worth Basin," *AAPG Bulletin*, vol. 91, no. 4, pp. 445–473, 2007.
- [49] X. M. Xiao, B. Q. Zhao, Z. L. Thu, Z. G. Song, and R. W. T. Wilkins, "Upper Paleozoic petroleum system, Ordos Basin, China," *Marine and Petroleum Geology*, vol. 22, no. 8, pp. 945–963, 2005.
- [50] C. Jiang, X. Wang, L. Zhang et al., "Geological characteristics of shale and exploration potential of continental gas shale in Chang 7 member of Yanchang Formation, southeast Ordos Basin," *Geology in China*, vol. 40, no. 6, pp. 1880–1888, 2013.

Research Article

Jurassic Terrestrial Shale Gas Potential of the Northern Kashi Sag in the Tarim Basin, Northwestern China

Wei Wu,¹ Zhiwei Liao ,² Honghan Chen,¹ Shaohu Li,¹ Ao Su,³ Irshad Hussain,¹ and Niubin Zhao¹

¹Department of Petroleum Geology, School of Earth Resources, China University of Geosciences (Wuhan), Wuhan 430074, China

²State Key Laboratory of Coal Mine Disaster Dynamics and Control, School of Resources and Safety Engineering, Chongqing University, Chongqing 400044, China

³Department of Petroleum, School of Geosciences, Yangtze University, Wuhan 430100, China

Correspondence should be addressed to Zhiwei Liao; zwliao16@cqu.edu.cn

Received 29 January 2021; Revised 1 April 2021; Accepted 7 June 2021; Published 3 August 2021

Academic Editor: Kun Zhang

Copyright © 2021 Wei Wu et al. This is an open access article distributed under the Creative Commons Attribution License, which permits unrestricted use, distribution, and reproduction in any medium, provided the original work is properly cited.

Evaluation of terrestrial shale gas resource potential is a hot issue in unconventional oil and gas exploration. Organic-rich shales are widely developed in the Jurassic strata of Tarim Basin, but their shale gas potential has not been described well. In this study, the Lower-Middle Jurassic fine-grained sedimentary rocks (Kangsu and Yangye Formations) in northern Kashi Sag, northwestern Tarim Basin, were taken as the study object. The comprehensive studies include petrology, mineralogy, organic geochemistry, and physical properties, which were used to characterize the organic matter and reservoir characteristics. Results show that the Jurassic terrestrial shale in the northern Kashi Sag was mainly deposited in lakes, rivers, and deltas. The thickness of black lacustrine shale developed in the Early-Middle Jurassic in the study area is generally over 100 m. The total organic carbon (TOC) content is rich, averaging 2.77%. The vitrinite reflectance (R_o) values indicate that the Lower Jurassic shale organic matter is in the early mature–mature stage, while the Middle Jurassic is in the mature stage. Besides, organic matter is primarily II and III in kerogen types. The whole shale contains a large number of clay minerals, especially illite. The average brittle minerals such as quartz and feldspar are 28.67%, and the average brittleness index is 38.63%. Nanoscale pores containing intergranular pores, dissolution pores, and organic pores, coupled with microcracks, are well developed in Jurassic shale. The sample's average pore volume is 0.017 cm³/g, and the specific surface area is 9.36 m²/g. Mesoporous contribute the most to pore volume, while the number of microporous is the largest. Both of them provide most of the surface area for the shale. Combined with regional geologic settings, we propose that the Jurassic terrestrial shale has good-excellent shale gas exploration potential and development prospects.

1. Introduction

The remarkable success of shale gas in North America led to the vigorous development of shale gas exploration and increased the investigation of global shale gas potential, thus changing the world energy pattern [1–5]. In recent years, China has also made rapid development in shale gas, and commercial shale gas fields such as Fuling, Changning-Weiyuan, and Zhaotong have been discovered in South China [6, 7]. With the deepening of exploration and development, the pressure to increase shale gas reserves and production in the future is still tremendous. There is an urgent need

to expand new fields and strata. The continental basins in China are widely distributed, and the continental shale is developed in many strata such as Mesozoic-Cenozoic [8–11], which is one of the required replacement fields for shale gas exploration. Industrial discoveries of continental shale gas are found in several Triassic stratigraphic wells in Ordos Basin and Jurassic strata in Sichuan Basin [12, 13]. However, compared with marine shale, the output of continental shale gas is lower. Due to the limitation of low exploration degree and complex reservoir conditions [8, 14–16], the large-scale exploration and development of continental shale gas still need further research.

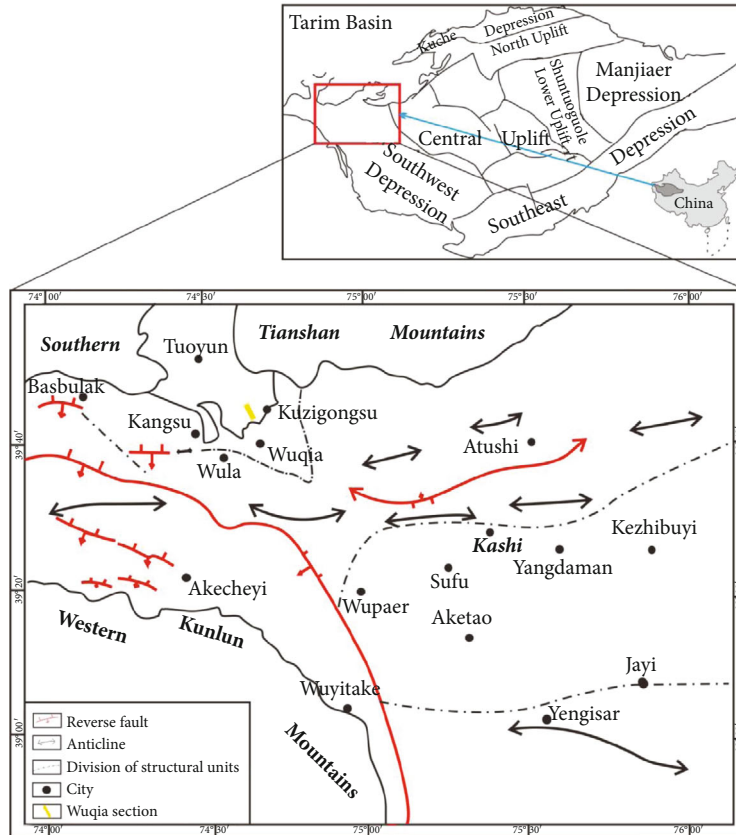


FIGURE 1: Location of the study area and the structure outline map of the Kashi Sag in Tarim Basin, northwestern China (after [34]).

There is a good prospect for oil and gas exploration in Kashi Sag of Tarim Basin [17–19]. Thick Jurassic organic-rich continental shale was deposited in this area, but no major hydrocarbon exploration breakthrough has been made so far. Previous studies show that source rocks are developed in Kashi Sag from Paleozoic to Cenozoic [20–22], such as Cambrian-Ordovician, Carboniferous-Permian, Jurassic, and Upper Cretaceous-Paleogene. Among them, Jurassic source rocks and Carboniferous-Permian source rocks are considered the two primary source rocks in the study area [23–25]. Concretely, the former is mainly composed of continental fine-grained sedimentary rocks, with a wide area, large thickness, high organic matter content, and good hydrocarbon generation potential [26, 27]. It is considered the most favourable shale gas development area in Tarim Basin [28, 29].

However, there are few detailed studies on Jurassic continental shale gas in this area, and it is urgent to carry out more related researches. On this basis, this study takes the Middle and Lower Jurassic Kangsu Formation and Yangye Formation in Kashi Sag, Tarim Basin, as research objects and comprehensively uses petrology, mineralogy, and organic geochemistry to analyze the organic matter and reservoir characteristics of continental shale, which provides a reference for exploration and preliminary evaluation of shale gas resources in Kashi Sag.

2. Geological Background

Kashi Sag is located in the north of Southwest Depression in Tarim Basin. Since Sinian (Ediacaran), its paleogeography and structural pattern have been controlled by Tarim Plate, South Tianshan Mountains, and West Kunlun Mountains [30, 31]. This sedimentary depression is adjacent to the piedfort thrust belt of West Kunlun Mountains in the west and the Maigaiti slope in the east. Tianshan Mountains and West Kunlun Mountains converge in the west of the study area, which covers about 2.44×10^4 km² [32, 33]. In the south and north Kashi Sag, there are fold-thrust belts in the northern margin of West Kunlun Mountains and the southern margin of South Tianshan Mountains, respectively, which overlap and influence each other in the west of Wuqia County (Figure 1). The northern fold-thrust belt is characterized by east-west segmentation and north-south discontinuity, while the southern fold-thrust belt shows a typical strike thrust nappe structure. According to the study of Zhou et al. [34], Kashi Sag can be divided into four structural units: Kashi deep Sag, South Tianshan piedmont fold-thrust belt, Kuzigongsu Late Triassic-Middle Jurassic fault depression, and West Kunlun piedmont fold-thrust belt.

Kashi Sag, together with the whole Tarim Basin, is a relatively stable platform during the Paleozoic period, consisting of shallow sea carbonate rocks and terrigenous clastic rocks [31, 35]. In the Early Permian, the Eurasian, South

Tianshan, and West Kunlun orogenic belts were gradually formed under the influence of the late Hercynian tectonic movement, resulting in the absence of Late Permian and Triassic strata in Kashi. After the Early Jurassic, the southwestern Tarim Basin has entered the continental sedimentary period [36–38]. The Lower Jurassic Shalitashi Formation (J_{1s}) and Kangsu Formation (J_{1k}) are mainly variegated conglomerates and coal seam, containing plant fossils, indicating the sedimentary environment of near-source alluvial fan, braided river delta, and shallow lake. The Middle Jurassic Yangye Formation (J_{2y}) and Taerga Formation (J_{2t}) are mainly composed of gray mudstone intercalated with a conglomerate in lithology, which belongs to fan delta, braided river, and shore-shallow lacustrine deposits [39–41]. Generally speaking, the Early and Middle Jurassic is mainly continental coal-bearing clastic rock deposits and coastal shallow lake deposits. All kinds of sediments are distributed in strips along the front of the Kunlun Mountains, which is related to the types of sedimentary basins. Kashi Sag’s sediments are distributed in a ring shape, with shallow lake facies at the center and rivers and alluvial fan facies at the periphery [42]. During the Late Jurassic, Tarim Craton Basin’s sedimentary pattern did not change significantly; i.e., the Upper Jurassic Kuzigongsu Formation (J_{3ku}) is mainly conglomerate interbedded with mudstone conglomerate and sandstone in lithology, indicating an alluvial fan environment. Based on previous studies, the main development horizons of Jurassic terrigenous shale in Kashi Sag are the Lower Jurassic Kangsu Formation and Middle Jurassic Yangye Formation (Figure 2).

3. Samples and Methods

Six outcrop samples were collected in the north of Wuqia County, Kizilsu Kirgiz Autonomous Prefecture, Xinjiang, China. These samples are numbered from WQ-01 to WQ-06, of which four (WQ-01–WQ-04) are from the Kangsu Formation, and two are from the Yangye Formation (WQ-05–WQ-06) (Figure 3). Analyses of total organic carbon (TOC), vitrinite reflectance (R_o), mineral composition, and absorption-desorption capability were conducted to characterize their organic matter features and reservoir properties. To minimize the potential effects of surface weathering and contamination, all of the collected samples used for analyses were freshly cut after removing the weathered surface.

TOC and X-ray diffraction (XRD) analyses of the samples were carried out at the Xinjiang Mineral Experiment Research Institute (XMERI), China. First, each specimen was split and pulverized into more delicate powders in an agate mortar than the size of the 200 mesh. We weighed approximately 200 mg of powder and processed it at 60°C to dissolve carbonate with 10 percent hydrochloric acid (HCl). We cleaned the samples with deionized water after that and dried them for 12 hours. Finally, the samples were analyzed by a carbon-sulfur analyzer XKSY-SB-646 to determine total organic carbon content. The analytical error was reported to be better than 1% based on replicate analyses of the Chinese national standard GB/T 19144-2010. A D/max-2600 X-ray diffractometer was used to test the mineral com-

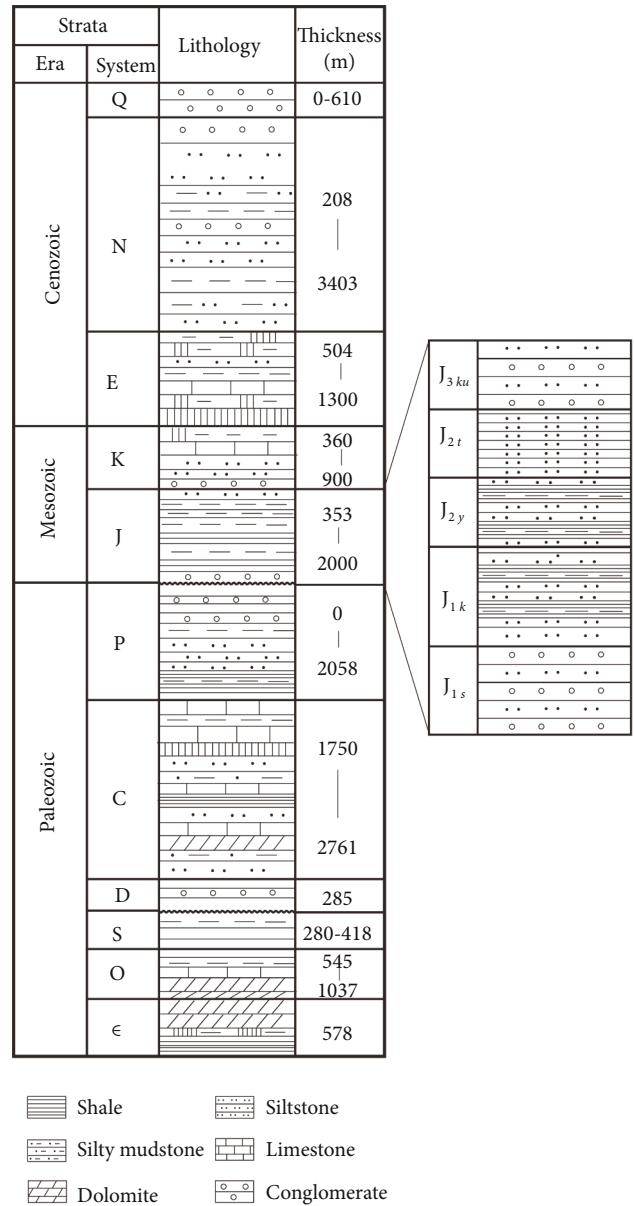


FIGURE 2: Comprehensive stratigraphic column of Kashi Sag in Tarim Basin (after [34]).

position of samples in the study. In the copper holders, powdered samples were placed and screened for full-rock design from 5 to 90° and clay-fractional composition from 3 to 30°. We used Cu K- α radiation and a 2° min⁻¹ graphite monochromator with 0.02° stage diameter and higher analytical accuracy than 0.02°.

The R_o , scanning electron microscopy (SEM), energy-dispersive spectroscopy (EDS), and isothermal adsorption experiments were conducted in the Key Laboratory of Tectonics and Petroleum Resources of the Ministry of Education, China. For R_o measurements, the polished sections were measured using Leica DM4500P polarimetric microscope and CRAIC 308 PV microphotometer.

Six thin sections were highly polished using a Gatan Model 697, Ilion II Broad Beam Argon Milling System. The

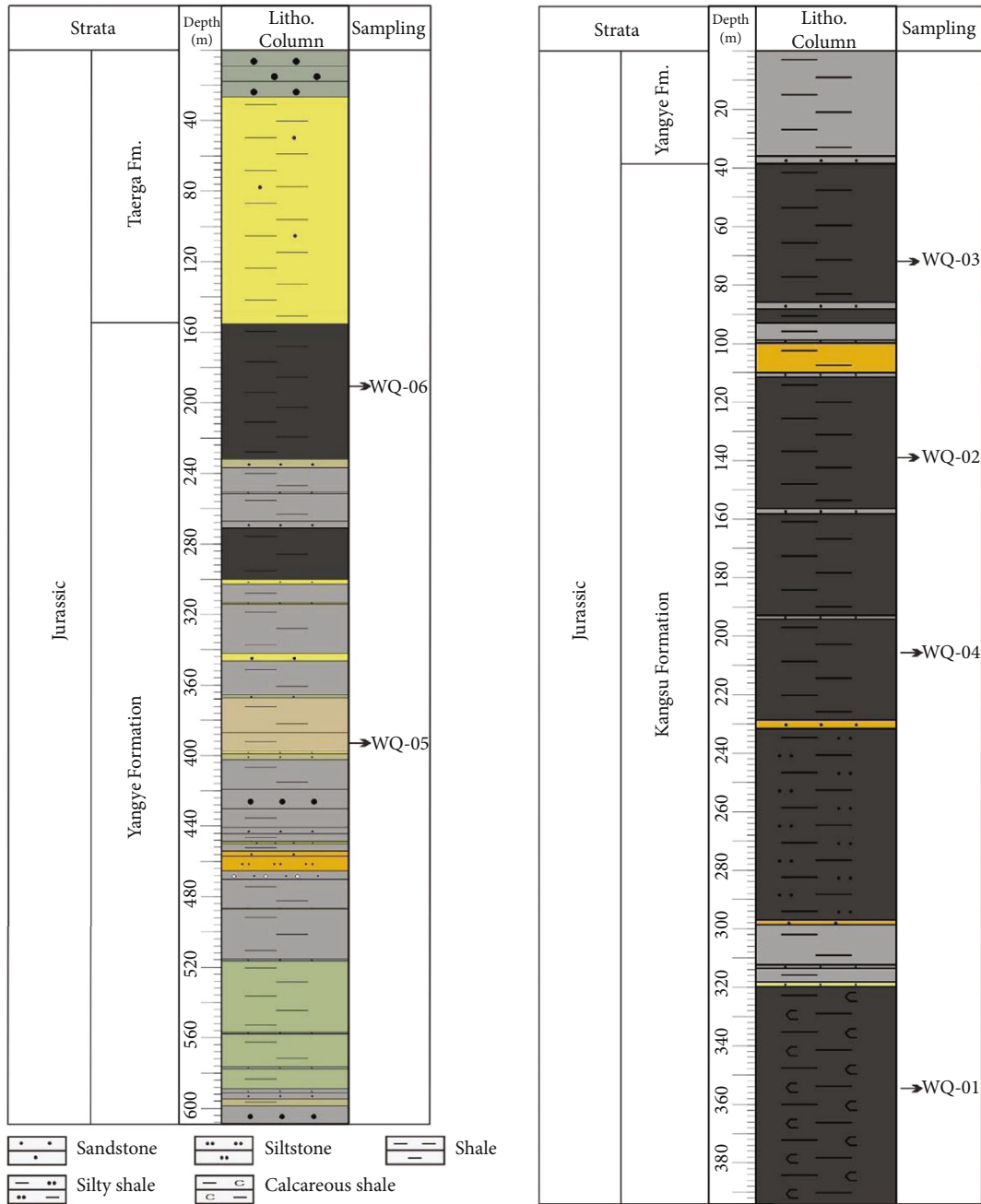


FIGURE 3: Stratigraphic column of Wuqia County north section in Tarim Basin.

EVO LS 15 scanning electron microscope and AZTEC X-MAX 20 spectrometer were used to identify and analyze the morphological characteristics of minerals and pores. Isothermal adsorption experiments of liquid nitrogen were carried out in this study. 5-10 g of screened powder samples with particle size between 0.28 and 0.45 mm was selected and then baked at 105°C for 8 hours. Finally, the samples were measured by a fully automatic surface and porosity analyzer ASAP2020.

4. Results

In this study, the detailed outcrop section in the Wuqia area was investigated in the field. The northern section of Wuqia

County is located about 6 km northwest of Wuqia County, near Kangsu Coal Mine (Figure 1). The measured section length is approximately 1.3 km, and the actual thickness of the stratum is about 1000 m. The exposed strata are mainly the Jurassic Kangsu Formation and Yangye Formation in ascending order. Due to terrains, this section is divided into two sections for field observation (Figure 3).

4.1. Petrologic Feature. The lithology of the Kangsu Formation is dominated by black-gray mudstone, black carbonaceous mudstone, and dark siltstone, interbedded with conglomerate rock (Figures 4(a) and 4(b)). The thickness of shale is the highest lithology in the Kangsu Formation, with

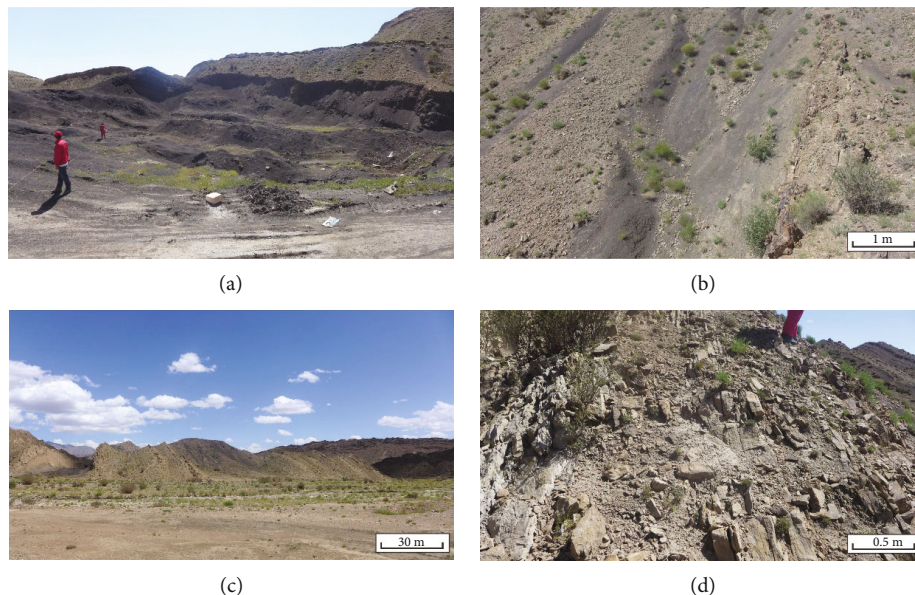


FIGURE 4: Lithological characteristics of the Kangsu Formation and Yangye Formation of Wuqia section. (a) Full view of the Kangsu Formation. (b) Black carbonaceous mudstone in the Kangsu Formation. (c) Complete view of the Yangye Formation. (d) Gray siltstone in the Yangye Formation.

a total of 245 m. The rocks are mainly gray and dark in colors, and mudstone often contains lenticular siderite, reflecting the weak oxidation-weak reduction environment. Gravels are poorly sorted, and particle sizes are generally distributed in 2–6 cm, and some larger ones can reach 10 cm. Their roundness is good, which is generally subround–round. From the point of view of sedimentary sequence, the grain size of whole section gradually becomes finer upward, which is reflected as a transgressive process. This situation may be related to the extensional tectonics in Kashi Sag during the Early Jurassic period [40, 41]. When the crust continuously extended and thinned horizontally, which caused regional subsidence, this results the lake basin expansion and water level rise. The above petrological traits display that the sedimentary environment of the study area in this period is mainly rivers, shallow lakes, and deltas around the lake basin.

The boundaries of the Yangye Formation and Kangsu Formation are conformable contacts, and the Yangye Formation is often unconformably contacted with Paleozoic strata in general. In the Wuqia section, the Yangye Formation is primarily composed of dark gray mudstone and black carbonaceous mudstone, interbedded with greyish-green medium-fine sandstone and minor conglomerate rock in the bottom (Figures 4(c) and 4(d)). The thickness of single-layer sandstone is relatively small, generally 1–8 m, with good sorting and roundness. Besides, it is rich in plant fossils and iron-bearing nodules, reflecting lacustrine sediment characteristics. The Taerga Formation is mainly gray-green, black-gray mudstone and gray-green siltstone and conformably contacted with the underlying Yangye Formation.

4.2. Mineral Composition and Organic Matter Features. The mineral composition of the six samples from Jurassic terrestrial shales in northern Kashi Sag is shown in Table 1. The results displayed that the clay mineral content is between

60 and 72%, with an average of 66%. The quartz content is between 25 and 35%, with an average of 29%. In general, the mineral composition of terrestrial shale is relatively stable, with clay minerals (chlorite + illite + kaolinite) as the main minerals, followed by brittle minerals (quartz + feldspar) (Table 1). Also, sample WQ-05 in the study contains a small amount of gypsum, suggesting that the climate was relatively dry at that time. The TOC of the Jurassic Kangsu Formation shale in Kashi Sag ranges from 1.42% to 3.36%, with an average value of 2.02%, which belongs to high-quality source rocks. The TOC of the Yangye Formation (4.27%) is higher than that of the Kangsu Formation in general. The R_o from the Kangsu and Yangye Formations were 0.849% and 0.788%, respectively, and both of them were in the mature stage (Table 1).

4.3. Reservoir Features. The results of isothermal adsorption tests are shown in Table 2 and Table 3. The total pore volume of the samples measured in this study ranges from 0.011 to 0.024 cm³/g, with an average of 0.017 cm³/g. According to the BJH (Barrett–Joyner–Halenda) model, the average pore size of terrestrial shale in the Wuqia area is between 9.10 and 12.83 nm, with an average of 11.10 nm (Table 2).

Compared with various calculation methods of specific surface area, the BET (Brunauer–Emmett–Teller) specific surface area can reflect it more accurately. Multipoint BET specific surface area = $t - \text{plot}$ external area + $t - \text{plot}$ total internal surface area of microporous. The specific surface area of the six samples BET specific surface area ranges from 5.46 to 14.31 m²/g, with an average of 9.36 m²/g. BJH unique circumference is more suitable for the analysis of pore size distribution. The six samples' BJH specific surface area ranges from 4.70 to 11.27 m²/g, with an average of 7.27 m²/g (Table 3).

TABLE 1: Minerals and geochemical characteristics of Jurassic shale in Kashi Sag.

Samples	Strata	TOC (%)	R_o (%)	Relative mineral content (%)					
				Chlorite	Illite	Kaolinite	Quartz	Feldspar	Gypsum
WQ-01	J_{1k}	1.42	$\frac{0.764 - 1.009}{0.897(16)}$	N.A.	N.A.	N.A.	N.A.	N.A.	N.A.
WQ-02	J_{1k}	1.61	$\frac{0.674 - 0.900}{0.785(13)}$	N.A.	N.A.	N.A.	N.A.	N.A.	N.A.
WQ-03	J_{1k}	1.67	$\frac{0.687 - 0.790}{0.728(4)}$	N.A.	N.A.	N.A.	N.A.	N.A.	N.A.
WQ-04	J_{1k}	3.36	$\frac{0.603 - 0.858}{0.742(11)}$	26	28	6	35	5	N.D.
WQ-05	J_{2y}	4.80	$\frac{0.678 - 0.851}{0.792(7)}$	25	34	6	26	4	5
WQ-06	J_{2y}	3.74	$\frac{0.882 - 0.928}{0.905(2)}$	24	38	10	25	3	N.D.

N.A.: not available; N.D.: not detectable.

TABLE 2: BJH pore volume of Jurassic shale in northern Kashi Sag.

Samples	Total volume (cm ³ /g)	Microporous (cm ³ /g)	Mesoporous (cm ³ /g)	Macroporous (cm ³ /g)	Average pore size (nm)
WQ-01	0.011	0.00120	0.006	0.0046	9.67
WQ-02	0.024	0.00025	0.016	0.0072	11.52
WQ-03	0.015	0.00015	0.009	0.0054	12.83
WQ-04	0.017	0.00014	0.012	0.0047	12.19
WQ-05	0.015	0.00010	0.012	0.0035	11.31
WQ-06	0.023	0.00026	0.017	0.0055	9.10

TABLE 3: Specific surface area of Jurassic shale in Kashi Sag (m²/g).

Samples	BET specific surface area	t -plot specific surface area		Total specific surface area	BJH specific surface area		
		Microporous surface area	Surface area except microporous		Microporous	Mesoporous	Macroporous
WQ-01	5.46	4.59	0.87	4.70	3.47	1.05	0.18
WQ-02	13.91	4.32	9.58	10.69	2.34	8.06	0.28
WQ-03	7.94	2.37	5.57	5.39	1.16	4.02	0.21
WQ-04	8.17	2.20	5.97	6.14	0.99	4.97	0.18
WQ-05	6.34	0.95	5.39	5.43	0.77	4.55	0.12
WQ-06	14.32	3.38	10.94	11.27	1.78	9.28	0.20

5. Discussion

5.1. Characteristics of Jurassic Shale. Based on the lithologic character from two sections in this study, it was suggested that the strata of Jurassic in Kashi Sag were mainly continental sediments, and the organic-rich shale primarily developed in the Lower Jurassic Kangsu Formation and Middle Jurassic Yangye Formation, which is considered one of the three sets of the potential source rocks in Kashi Sag [27]. Comprehensive research shows that organic-rich shale in the Middle and Lower Jurassic continental facies is closely related to the paleo-sedimentary environment. Zhong et al. [40] considered the evolution of paleoclimate from dry (J_{1s}) to wet

(J_{1k} - J_{2y}), and then to dry (J_{3kz}) in the Jurassic of the study area according to the color, lithology, sedimentary structure, paleontology, and geochemistry of rocks. The Early Jurassic Shalitashi Formation was attributed to the alluvial fan deposition under dry and oxidative conditions, which is not conducive to the deposition of organic-rich shale. During the Kangsu Formation deposition, it evolved into fluvial sediments, recording a humid climate and depositing dark shale with high organic matter content. Later, the basin showed difference between the north and the south in the Middle Jurassic. The northern basin was dominated by a freshwater environment, while a brackish-saline water environment dominated the southern basin. The paleoclimate evolved into

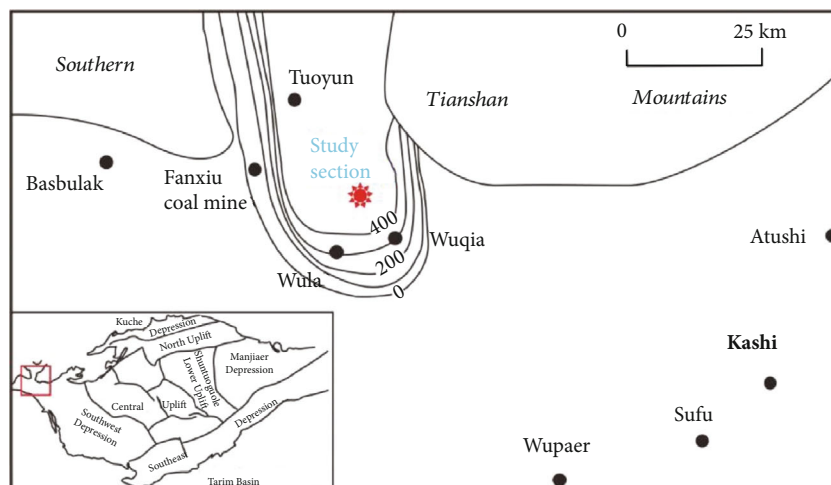


FIGURE 5: Thickness distribution of Middle and Lower Jurassic carbonaceous shale in northern Kashi Sag.

semihumid–semidry conditions, and the sedimentary facies changed from delta front to deep–semideep lacustrine and then to shore–shallow lake lacustrine. Therefore, the sedimentary shale of the Yangye Formation was characterized by the immense thickness and high content of organic matter. In the Late Jurassic, the basin evolved into fluvial and alluvial fan deposits in a dry and semidry environment, without shale sediments rich in organic matter. The whole sequence of Jurassic reflected a complete sedimentary cycle of shallow lacustrine–deep lacustrine–shallow lacustrine facies. The sedimentological observation in this study also confirms the above conclusion.

The water depth of the Yangye Formation in the Wuqia section is more significant than that of the Kangsu Formation, and the TOC content of the former is higher than that of the latter. Combined with previous research results, this study holds that the organic-rich strata are generally distributed in NW–SE direction, with multiple sedimentary centers (e.g., Yangye–Kuzigongsu and Yigeziya and Kekeya area). The high-quality source rocks have an excellent corresponding relationship with the semideep lacustrine and deep lacustrine environment, which are mainly developed in the piedmont fault basin system [29], along with the Talas–Fergana strike-slip fault system [31, 32]. The lacustrine carbonaceous shale is exposed in the Kuzigongsu graben zone, Keziletao graben zone, and the piedmont of the South Tianshan Mountains in the western part of Kangsu Town. The thickness of carbonaceous shale reached a maximum of more than 400 m in Wuqia Coal Mine of the northern Wuqia County, i.e., Kuzigongsu Graben. It decreases radially around and gradually pinches out at the Graben basin (Figure 5). Generally speaking, the northern part of Wuqia County is a favorable exploration area for shale gas because of its wide distribution and ideal shale thickness.

5.2. Features of the Organic Matter. TOC is one of the main indices for evaluating shale [43–45]. The content of TOC in Jurassic shale in the study area is high, which provides abundant substances for shale gas generation. According to Li and Zhang [4], the TOC of Lower Jurassic shale in Kashi Sag is

generally more than 1.0%, the highest is greater than 5.0%, the chloroform asphalt “A” is between 0.001% and 0.1%, and the maximum hydrocarbon generation potential can reach 2.5 mg/g. The TOC of Middle Jurassic shale is mostly between 1.0% and 2.0%, and the hydrocarbon generation potential is above 0.5 mg/g. However, TOC in Kuzigongsu section is between 1.5% and 3.5%, with an average of 2.5%. Besides, according to the study of Xiao et al. [29], the average total organic carbon content of Jurassic shale in the Southwest Tarim Depression is 2.1%. These results are consistent with our conclusions. According to the criteria of Dong et al. [15], the lower limit of TOC content in shale gas production is 0.5%, and the better TOC content of gas-producing shale should be more than 2.0%. Therefore, according to the organic matter abundance standard, Jurassic shale in Kashi Sag belongs to high TOC shale. TOC content and organic-rich shale thickness control the self-sealing of shale [46]. The high TOC content and the great thickness also lead to the enhancement of the self-sealing ability of Jurassic shale. It is worth noting that the TOC of Jurassic shale in northern Kashi Depression is generally medium-good, but judging from the hydrocarbon generation potential ($S_1 + S_2$), extracted soluble organic matter (chloroform asphalt “A”), and total hydrocarbon (HC), the evaluation level of shale is lower than TOC, which may be affected by maturity. Generally speaking, for the early mature source rocks, the TOC evaluation results are not much different from those based on $S_1 + S_2$, chloroform asphalt “A,” and HC. However, for mature–overmature samples, the evaluation result based on the latter will be lower than those found on the former, and the difference is more significant in the stage of high maturity or overmaturity [47, 48].

For the thermogenic shale gas system, organic matter’s maturity is an important indicator to evaluate shale gas potential. A higher degree of thermal evolution is necessary for shale gas generation and organic pore formation [19]. Recent studies have investigated the types of Jurassic kerogen and thermal maturity of organic matter in northern Kashi Sag. The $\delta^{13}C_{org}$ of kerogen from the Kangsu Formation ranges from -20.7% to -25.5% , with a mean of -23.3% ,

indicating that the organic matter in the Kangsu Formation may be kerogen type III. The Yangye Formation ranges from -25.5% to -28.1% , with a mean of -25.8% , indicating that the organic matter in the Yangye Formation is mainly kerogen type II_2 [22]. According to the microscopic observation of kerogen from Jurassic source rocks, Chen [49] claimed that the Lower Jurassic is mainly composed of vitrinite and inertinite, relatively low content of sapropelic and crustaceous materials, and is characterized by type III organic matter. The Middle Jurassic is mainly composed of vitrinite, and the content of inertinite is relatively low, showing the characteristics of type II-III organic matter. This phenomenon indicates that the source of organic matter has changed obviously with the deepening of lake water depth. Besides, the previous work suggested that the vitrinite reflectance values of the Kangsu Formation from the Kuzhigongsu section range from 1.3% to 1.8%, while the Yangye Formation ranges from 0.9% to 1.8% [4]. According to the samples collected by Da et al. [27], the average R_o of Jurassic in the Kuzigongsu section is 0.94%. These results are consistent with our test results (Table 1), indicating that the black shales in the sections are mature to highly mature (0.6%–1.0%, $n = 6$). Moreover, the mudstone in the sedimentary center has a high maturity, even reaching the stage of high maturity–overmaturity [50]. Thus, the thickness, kerogen type, TOC, and maturity of the black shales of the Kangsu and Yangye Formations in northern Kashi Sag indicate that these rocks are potential targets for exploration of shale gas.

5.3. Reservoir Brittleness. The intergranular pores of clay minerals in shale are well developed, but the cementation is complex, and the sorting is poor. Moreover, the clay minerals have a small particle size, strong plasticity, and water sensitivity, making the reservoir permeability decrease [51, 52]. In the late diagenetic stage, if there is no strong deformation, it is difficult for a single intergranular pore of clay minerals to have a good hydrocarbon migration ability. The specific surface area of clay minerals is larger than that of quartz minerals, and the more developed the intergranular pores, the stronger the gas adsorption capacity. The higher content of clay minerals is beneficial to developing the original microporous and microfractures in shale reservoirs (Figures 6(a) and 6(b)), which provide storage space for shale gas [43, 53, 54]. However, such a problem negatively impacts shale gas exploitation because it is not conducive to hydraulic fracturing, which is contrary to the implications of brittle minerals. Brittle minerals such as quartz and carbonate are prone to fracture under stress (Figure 6(c)).

On the one hand, the higher content of brittle minerals is beneficial to the development of microfractures and the improvement of reservoir performance; on the other hand, it is also helpful to the later exploitation of shale gas and achieves better fracture-making effect in the process of artificial fracturing [55, 56]. Compared with North American marine Barnett shale, the content of brittle minerals from Jurassic shale samples in the north of Kashi Depression is relatively low, which may be due to the deposition in a deep lake-semideep lake environment, far away from terrigenous denudation area. This situation reduces the input of many

clastic materials, resulting in relatively high clay mineral content in the study's terrigenous shale.

The following formula in this study is selected to evaluate the brittleness index of the shale reservoir: Brittleness index = $(\text{quartz} + \text{feldspar} + \text{calcite} + \text{dolomite}) / (\text{quartz} + \text{feldspar} + \text{calcite} + \text{dolomite} + \text{clay minerals}) \times 100\%$ [54, 57–60]. Through calculation, the shale's brittleness index of samples in the northern Kashi Sag ranges from 28.0% to 44.9%, with an average of 38.6% (Table 4). On the whole, it shows poor brittleness, which is not conducive to fracturing theoretically. Generally speaking, the evaluation of marine shale gas reservoir requires that the brittleness index in shale should be no less than 40% [57, 61, 62]. However, the evaluation method of marine shale gas cannot be simply copied in evaluating continental shale gas reservoirs. For example, Song et al. [63] found that the clay mineral content of continental shale is higher in general. Still, the brittle mineral content is lower, making the fracturing ability of shale worse than that of marine shale [53]. Therefore, the evaluation criteria of continental shale gas need to be further studied.

5.4. Characteristics of the Reservoir

5.4.1. Scanning Electron Microscope Observation. Through SEM observation of six samples of Jurassic shale in Tarim Basin, four types of reservoir space have been identified, i.e., organic pores, intergranular pores, intragranular pores, and microfractures. Organic pores are widely developed in organic-rich shale and are essential parts of shale reservoir space [64]. As shale gas can be adsorbed on the surfaces of mineral particle and organic matter, the porosity of organic matter directly controls adsorbed natural gas content [51, 65, 66].

In the study, the organic matter pores in the northern Kashi Sag are mostly nanoscale and round to oval. There are other irregular shapes, such as crescent shapes and slit shapes (Figures 7(a) and 7(b)). However, not all organic compounds have nanopores related to the maturity of organic compounds. For example, organic matter with low maturity usually contains fewer pores. Organic matter is mainly distributed on microbedding planes or microsedimentary discontinuity, and it is easy to form an interconnected pore network with strong permeability. The lipophilicity of organic matter makes organic matter's nanopore become the virtual storage space for natural gas [67, 68]. As the most important mineral component in Jurassic shale in this study, its highest content can reach 70.1%, and illite is the highest. Illite is usually flaky or fibrous, and slit or wedge-shaped pores are formed between the chips. In transforming montmorillonite into illite, the volume of minerals decreases, which leads to the formation of gaps between mineral particles (Figure 7(c)).

Intergranular pores are very abundant in young or shallow sediments, and they are usually well connected [69]. The irregular shape of intergranular pores and the large pore diameter of shale samples are beneficial to shale gas enrichment. In the process of diagenesis, the primary mineral crystals are subjected to physical and chemical actions such as mechanical collision, extrusion, and dissolution in acid or

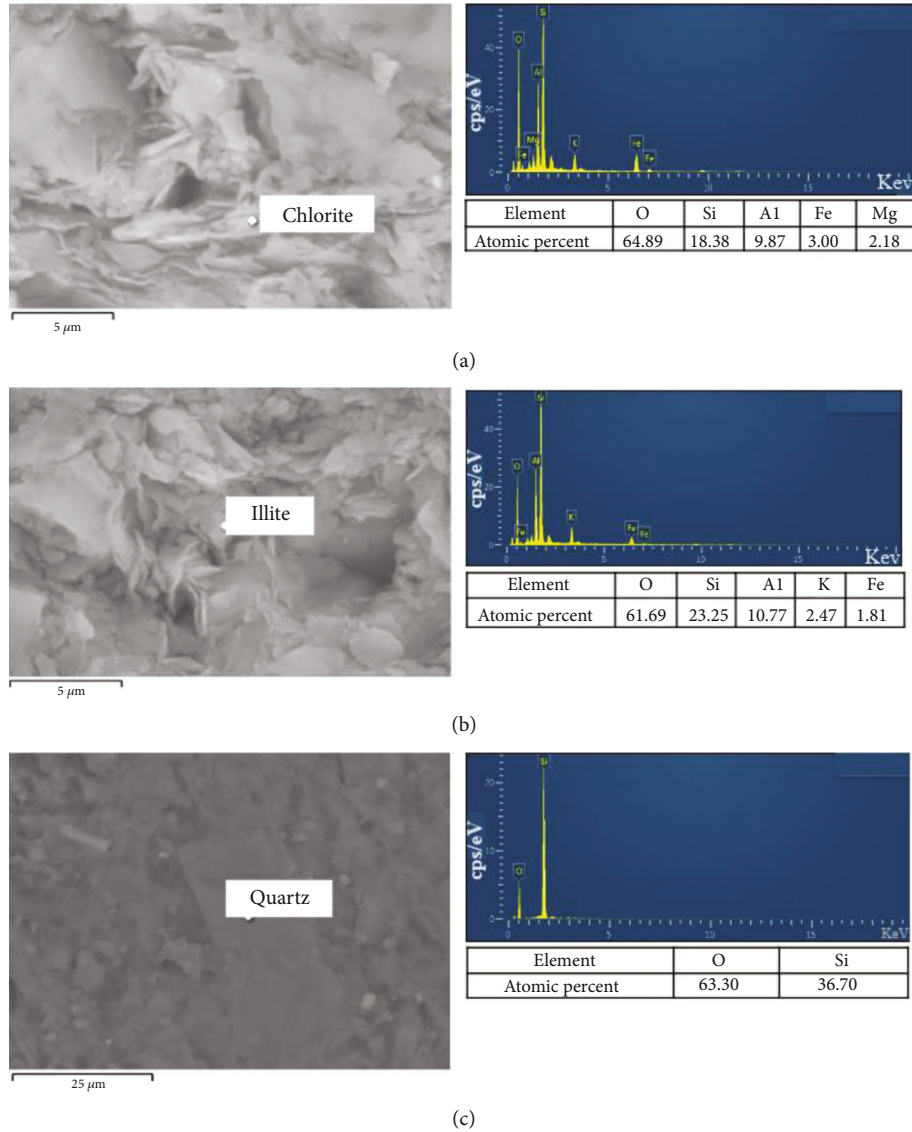


FIGURE 6: SEM images showing the mineralogical composition of the Jurassic shales in Wuqia section. (a) Bladed-shaped chlorite in the Kangsu Formation. (b) Filamentous illite in the Yangye Formation. (c) Quartz in the Kangsu Formation.

TABLE 4: Brittleness index of Jurassic shale in northern Kashi Sag (%) (S samples were collected by [29]).

Number	Clay mineral	Mineral		Brittleness index
		Quartz	Feldspar	
WQ-03	60	35	5	40.0
WQ-04	65	26	4	31.6
WQ-05	72	25	3	28.0
S-2 (J_{2y})	57.7	41.9	0.4	42.3
S-3 (J_{2y})	62.4	34.4	3.2	37.6
S-12 (J_{1k})	51.9	32.4	9.9	44.9
S-14 (J_{1k})	55.1	42.0	2.9	44.9
Mean	60.6	30.8	2.6	38.6

alkaline solution. And the crystals are broken or dissolved, forming a large number of intergranular pores. Intragranular pores mainly appear in irregular shapes and sizes of particles, mineral aggregates, and crystals (Figure 7(d)) [70]. The genetic types can be classified into primary and secondary. However, immediately after diagenesis, the number of pores in the particles was mostly destroyed and decreased, while the number of pores in the secondary particles increased. Because clay minerals are mainly distributed in cluster aggregates, many pores are distributed among internal clay crystal plates or plates. The morphology of these pores is primarily controlled by the crystal alignment [71].

In addition, fractures in shale samples are well developed and divided into structural fractures and diagenetic fractures. The former is mainly a wide range of macrocracks (Figure 7(e)). The latter is a fracture caused by the shrinkage of minerals. In the diagenetic process, the cause of formation is mainly caused by dry shrinkage, phase change, or

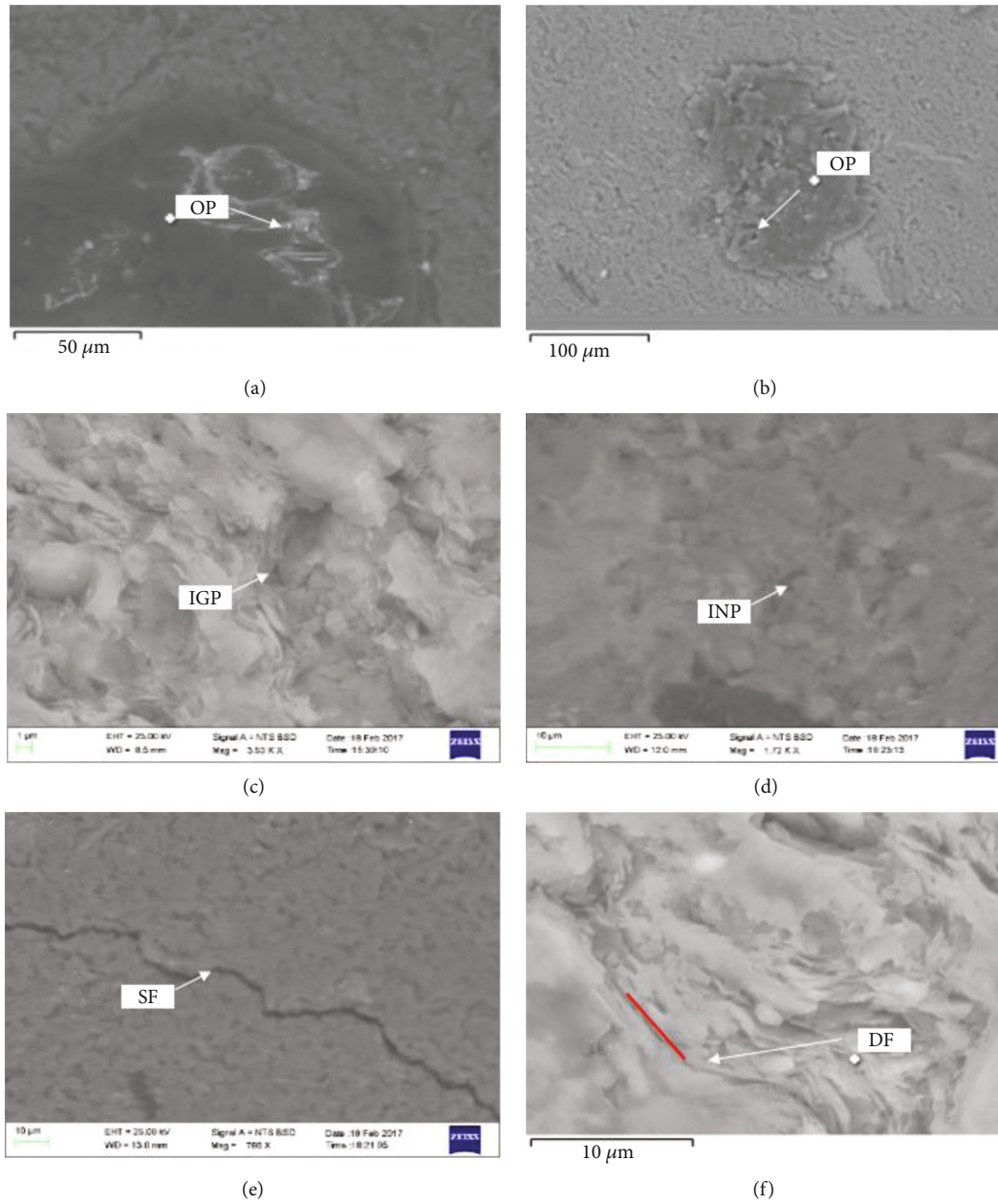


FIGURE 7: SEM images showing the pore types of Jurassic shales in Wuqia section. (a) Pore of organic matter (J_2y). (b) Pore of organic matter (J_1k). (c) Intergranular pore of illite-smectite mixed-layer mineral (I/S) (J_1k). (d) Intragranular pores of chlorite grain (J_1k). (e) Structural fracture (J_2y). (f) Diagenetic fracture (J_1k).

dehydrated minerals' thermal shrinkage (Figure 7(f)). The dehydration of clay minerals makes the volume smaller, which leads to more shrinkage microcracks with a width from 0.5 to 2 μm. Therefore, fracture plays a vital role in oil and gas production in shale reservoirs [72].

5.4.2. Pore Structure

(1) *Adsorption Isotherm.* According to the isothermal nitrogen adsorption-desorption curves of six samples (Figure 8), the pore type of samples can be analyzed [73–75]. All adsorption curves show inverted S-type, although they are slightly

different in morphology. Based on a classification scheme [76], adsorption isotherm is divided into five types. In this study, the adsorption curve of shale samples in northern Kashi Sag is close to type II. In the low-pressure stage ($P/P_0 < 0.1$), the adsorption curve presents an upward convex shape, and nitrogen molecules are adsorbed by a monolayer. At this time, the adsorption amount is small. When the relative pressure $P/P_0 = 0.10 - 0.45$, nitrogen molecules begin to undergo multilayer adsorption, and the adsorption increment is small. When P/P_0 is in the range of 0.45–0.80, the adsorption curve is slightly concave and rises slowly. Multilayer adsorption of nitrogen

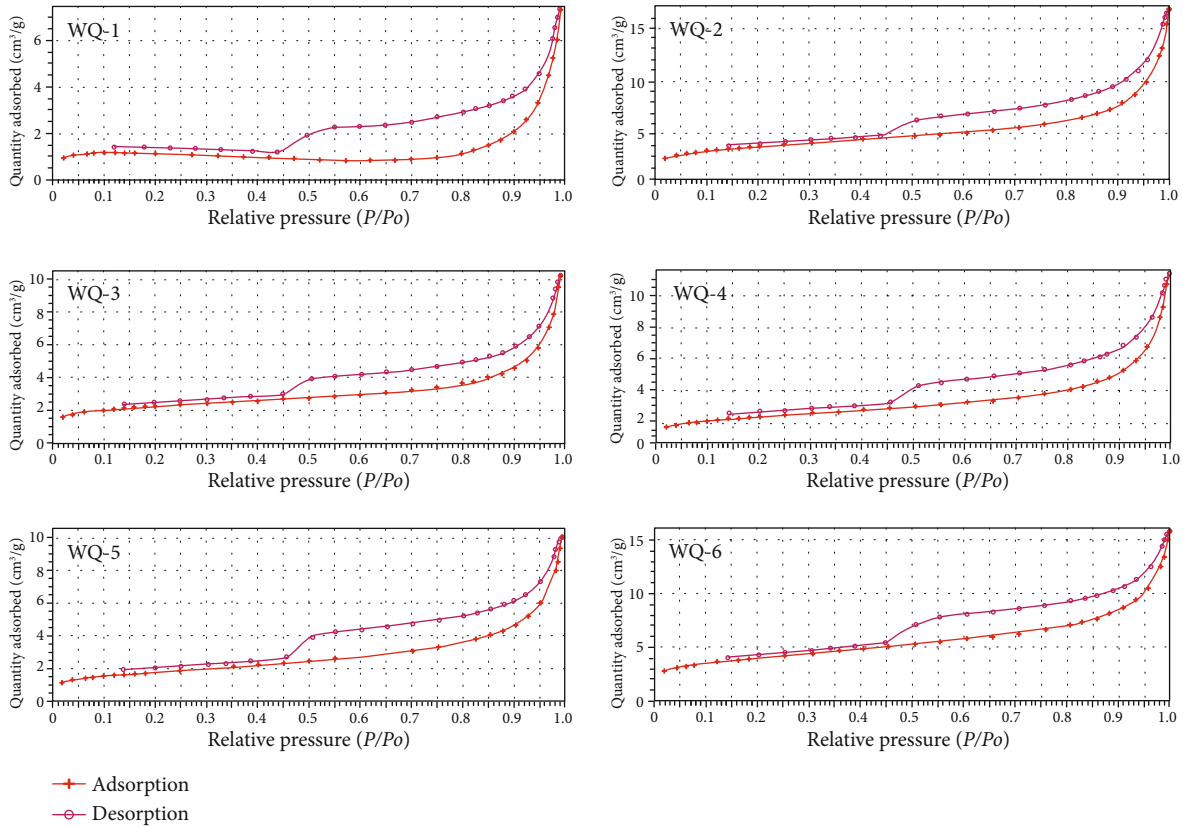


FIGURE 8: Nitrogen isothermal adsorption-desorption curves of Jurassic shale in Wuqia section.

molecules occurs, and the adsorption increment increases. When P/P_0 is in the range of 0.8–1.0, the adsorption curve rises rapidly, and the angle is concave. The nitrogen molecules are capillary condensed, and the adsorption capacity increases quickly. When P/P_0 reaches 0.9, the slope of the curve increases, and the adsorption capacity increases linearly [77]. The samples' adsorption curve and desorption curve do not coincide in high pressure, forming an adsorption loop (Figure 8).

The sorption isotherms have been classified by the International Union of Pure and Applied Chemistry (IUPAC) into six types, and the desorption isotherms into four categories designated H1 to H4 [78]. Different adsorption loop shape types reflect specific pore structure characteristics and type styles. The H1-type loop is often obtained from pore structures with regular size and arrangement. The H2-type loop is generally considered to be caused by porous adsorbate or homogeneous particle piled pores. Compared with H4-type, H3-type has a larger adsorption capacity at the high pressure, which is considered slit pores formed by stacking flaky particles. H4-type is also slit pores, which differ from the particle piled pore and are similar to those generated by layered structures. However, it is nearly impossible to describe the exact pore characteristics by a specific adsorption loop because of the complex pore morphology. In general, the adsorption curves of the six samples are very steep near the saturated vapor pressure, and the desorption curves

are very steep at the medium pressure, which is close to the H3-type loop recommended by IUPAC and also has the characteristics of H4-type loop (between H3 and H4). Therefore, this form may be related to the superposition of the multiple standards loop, which is the comprehensive reflection of pore morphology. The above research shows that the pores of Jurassic shale gas reservoirs in Kashi Sag are mainly composed of nanopores characterized by irregular (amorphous) pores in structure; besides, the particle interior also has the characteristics of slit-like pores with parallel walls and contains other pores with various forms. Thus, this study suggested that this slit pore may be related to high clay mineral content in shale. Generally speaking, closed pores, including cylindrical pores with one end closed, parallel plate pores, and conical pores, cannot generate adsorption loops. However, all the six samples in this study displayed adsorption loops, which indicates that Jurassic continental shale gas reservoir's pore morphology was in an open state [79]. Those pores were mainly cylindrical pores with two ends empty and parallel plate pores with four sides hollow (i.e., cone, cylinder, plate, and ink bottle). Overall, this situation is conducive to improving the desorption efficiency of shale gas and the permeability of reservoirs, thus increasing production.

(2) *Specific Surface Area and Pore Volume.* The computing methods of the specific surface area mainly include multi-point BET, t -plot external surface area, the t -plot total

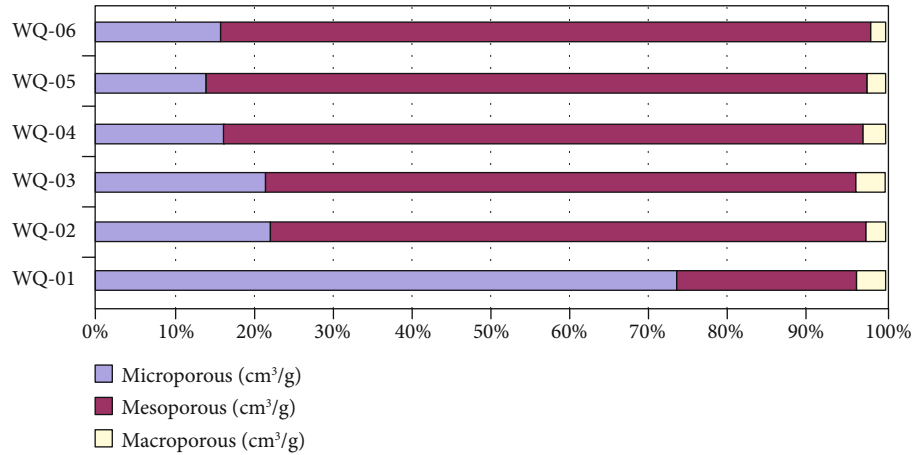


FIGURE 9: Specific surface area percentage of BJH pore in northern Kashi Sag.

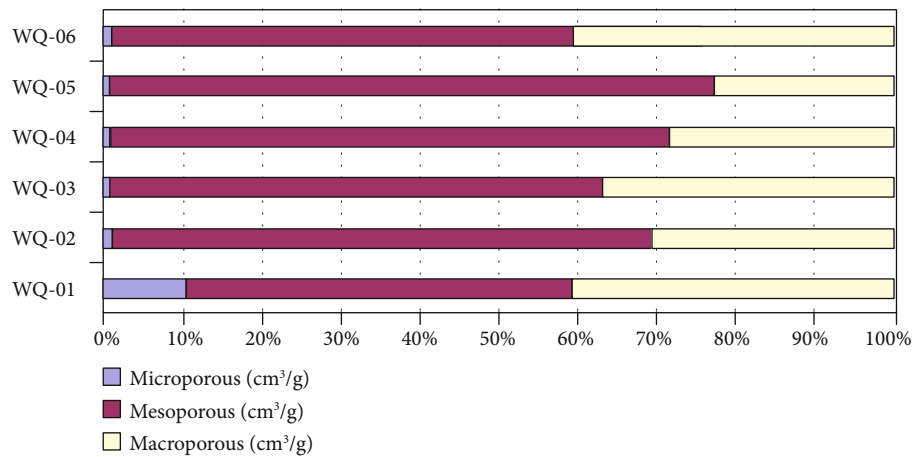


FIGURE 10: Volume percentage of BJH pore in northern Kashi Sag.

internal surface area of microporous, and BJH adsorption model. The multipoint BET method is the macroscopic total specific surface area, and BJH specific surface area is the total specific surface area of pores in a particular range. Generally, the BET method calculates the total specific surface area, and BET specific surface area = $t - \text{plot external area} + t - \text{plot total internal surface area of microporous}$. In contrast, the pore volume and pore size distribution are calculated by the BJH method. Therefore, compared with various calculation methods of specific surface area, BET specific surface area can reflect it more accurately and honestly [80–82]. According to the standards of the IUPAC, this study divides pores into microporous (<2.0 nm), mesoporous (2.0–50.0 nm), and macroporous (>50.0 nm) [78, 83]. After classifying the experimental data of Table 3, the pore-specific surface area percentages of macroporous, mesoporous, and microporous of each sample were calculated, respectively (Figure 9). As is shown in Table 3, the BET specific surface area of shale samples ranges from 5.46 to 14.31 m²/g, with an average of 9.36 m²/g. The adsorption capacity of shale is positively correlated with its specific surface area [84]. Therefore, the relatively high specific surface area of shale samples in Kashi Sag

can improve the adsorption capacity of shale for methane. Meanwhile, according to the statistics of the specific surface area distribution of BJH, it can be seen that the mesopore's specific surface area occupies the majority. However, the specific surface area of microporous from the WQ-01 representative has a large percentage. After all, the minimum interval measured is 1.0 nm. In comparison, the minimum aperture of other samples measured is 1.7 nm. Therefore, the smaller pore-specific surface area of different samples was not measured. This also reflects that the actual proportion of microporous specific surface area is considerable. On the whole, microporous and mesoporous provide the central pore-specific surface area in this study.

The pore volume ratio of each pore size range is calculated separately, as shown in Figure 10. It can be seen that the mesoporous and macroporous provide the main pore volume in the Wuqia area. Concretely, the pore volume of microporous is relatively small, accounting for about 1%–10%. Thus, this study suggests that there may be two reasons to explain the small proportion of microporous. One is that the minimum pore size measured by the BJH method is

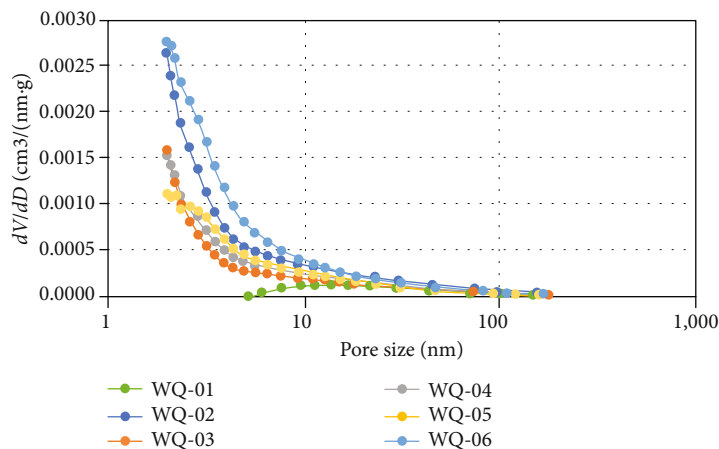


FIGURE 11: Frequency curve of BJH pore size distribution of shale samples in northern Kashi Sag.

1.7 nm (WQ-01 is 1.0 nm), and smaller pores are difficult to measure; on the other hand, according to the SEM observation, the distribution range of microporous is so tiny that its existence is rarely observed.

(3) *Pore Size Distribution*. The percentage of pore-specific surface area and volume in each pore size range cannot reflect all pore distribution frequencies. Therefore, the pore size distribution needs further analysis. The ordinate “ dV/dD ” in Figure 11 means the relative number of pores without considering the pore volume. On the whole, with the increase of pore diameter, the relative number of pores gradually decreases, indicating that the number of pores is mainly provided by the range of small pore diameter (2–8 nm). Therefore, the pore volume and specific surface area of mesoporous are primarily provided by small pore size. In contrast, the larger pore (8–50 nm) contributes less to the pore volume and specific surface area. When the pore diameter is close to 2 nm, the change rate of the pore volume of samples WQ-2–5 reaches the peak. This is because the minimum pore diameter of those samples is 1.98 nm. It can be speculated that when the pore diameter is less than 2 nm, the peak value will become larger; that is, the number of pores less than 2 nm is considerable. It is worth noting that since the minimum pore diameter of the WQ-01 sample is 6.61 nm, there may be deviation in the value of the WQ-01 sample.

6. Conclusions

In the northern Kashi Sag, the Middle and Lower Jurassic shale is a typical continental shale, mainly deposited in lake, river, and delta environments. The organic-rich shale primarily develops in the top of the Lower Jurassic and the lower part of the Middle Jurassic. This shale is generally more than 100 m and up to 400 m in thickness. The average total organic matter content is greater than 2%, R_o ranges from 0.6% to 1.8%, and organic matter is primarily II and III in kerogen types. Thus, the Middle and Lower Jurassic shale in the study has a good material basis for hydrocarbon generation. Meanwhile, the continental shale has a relatively high concentra-

tion of clay minerals, and the pores and fractures are well developed, which is conducive to the adsorption of shale gas. Microporous and mesoporous provide most of the specific surface area of shale, while mesoporous and macroporous provide most of the pore volume. The results referring to brittleness index, average pore volume, and specific surface area indicate that the reservoir’s physical properties are relatively good. Overall, we propose that the Jurassic terrestrial shale in northern Kashi Sag has good-excellent shale gas exploration potential and development prospects.

Data Availability

All data, models, and code generated or used during the study appear in the submitted article.

Conflicts of Interest

The authors declare that they have no conflicts of interest.

Acknowledgments

This study was jointly supported by the Fundamental Research Funds for the Central Universities (No. 2021CDJQY-028) and the project “Research on the Investigation and Evaluation of Xinjiang Unconventional Energy Mineral Resources.” We would like to thank the Xinjiang Bureau of Geo-exploration and Mineral Development for their help on the field.

References

- [1] Z. J. Jin, Z. R. Bai, B. Gao, and M. W. Li, “Has China ushered in the shale oil and gas revolution?,” *Oil & Gas Geology*, vol. 40, no. 3, pp. 451–458, 2019.
- [2] C. N. Zou, R. K. Zhu, Z. Q. Chen et al., “Organic-matter-rich shales of China,” *Earth-Science Reviews*, vol. 189, pp. 51–78, 2019, (in Chinese with English abstract).
- [3] W. Z. Zhao, A. L. Jia, Y. S. Wei, J. L. Wang, and H. Q. Zhu, “Progress in shale gas exploration in China and prospects for future development,” *China Petroleum Exploration*, vol. 25, no. 1, pp. 31–43, 2020.

- [4] H. X. Li and Y. W. Zhang, "Global shale gas exploration and development today and China's shale gas development strategy," *Sino-Global Energy*, vol. 5, pp. 22–29, 2015.
- [5] C. Z. Yan, Y. Z. Huang, C. M. Ge, D. Z. Dong, and K. M. Cheng, "Shale gas: enormous potential of unconventional natural gas resources," *Natural Gas Industry*, vol. 29, no. 5, pp. 1–7, 2009.
- [6] H. K. Nie, Z. L. He, G. X. Liu et al., "Status and direction of shale gas exploration and development in China," *Journal of China University of Mining & Technology*, vol. 49, no. 1, pp. 14–35, 2019.
- [7] X. Wu, Z. Y. Ren, and Y. Wang, "Situation of world shale gas exploration and development," *Resource & Industries*, vol. 15, no. 5, pp. 61–67, 2013.
- [8] L. Zhang, J. Li, Z. Li, J. Zhang, R. Zhu, and Y. Bao, "Advances in shale oil/gas research in North America and considerations on exploration for continental shale oil/gas in China," *Advance in Earth Science*, vol. 6, pp. 700–711, 2014.
- [9] X. X. An, W. H. Huang, S. Y. Liu, and H. Y. Jiang, "The distribution, development and expectation of shale gas resources," *Resources & Industries*, vol. 12, no. 2, pp. 103–109, 2010.
- [10] D. X. Zhang and T. Y. Yang, "An overview of shale-gas production," *Acta Petrolei Sinica*, vol. 34, no. 4, pp. 792–801, 2013.
- [11] Y. Song, Z. Li, Z. X. Jiang, Q. Luo, D. D. Liu, and Z. Y. Gao, "Progress and development trend of unconventional oil and gas geological research," *Petroleum Exploration and Development*, vol. 44, no. 4, pp. 638–648, 2017.
- [12] Z. F. Wei, Y. L. Wang, G. Wang et al., "Enrichment mechanism of the Upper Carboniferous-Lower Permian transitional shale in the east margin of the Ordos Basin, China: evidence from geochemical proxies," *Geofluids*, vol. 2020, article 8867140, 14 pages, 2020.
- [13] D. Z. Dong, C. N. Zou, Y. Yang et al., "Progress and prospects of shale gas exploration and development in China," *Acta Petrolei Sinica*, vol. S1, pp. 107–114, 2012.
- [14] D. Zhao, Y. Guo, Y. Zhu, G. Wang, X. Chong, and X. Hu, "Analysis of micro-scale heterogeneity characteristics in marine shale gas reservoir: pore heterogeneity and its quantitative characterization," *Journal of China University of Mining & Technology*, vol. 47, no. 2, pp. 296–307, 2018.
- [15] D. Dong, Y. Wang, X. Huang et al., "Discussion about geological characteristics, resource evaluation methods and its key parameters of shale gas in China," *Natural Gas Geoscience*, vol. 9, pp. 1583–1601, 2016.
- [16] W. X. Hu, S. P. Yao, X. C. Lu, H. G. Wu, F. N. Sun, and J. Jin, "Effects of organic matter evolution on oil reservoir property during diagenesis of typical continental shale sequences," *Oil & Gas Geology*, vol. 40, no. 5, pp. 947–956, 2019.
- [17] Q. Zhang, F. Wang, Z. Xiao, Y. Lu, and Y. Wu, "The discussion of natural gas source in Well Ake 1," *Natural Gas Geoscience*, vol. 6, pp. 484–487, 2003.
- [18] J. F. Zhang, D. L. Wang, Z. M. Wang, X. Li, and X. F. Su, "Natural gas deposit formation geochemistry of Akmomu gas field Kashi Sag in Tarim Basin," *Natural Gas Geoscience*, vol. 4, pp. 507–513, 2005.
- [19] W. Liu, F. Yang, J. C. Wu, and H. Z. Xiao, "The discussion on natural gas source in Akmomu gasfield, northern margin of Kashi Sag," *Natural Gas Geoscience*, vol. 3, pp. 486–494, 2015.
- [20] L. Qian, Y. H. Lu, L. C. Huang et al., "Source and gathering features of Kelatuo natural gas in the Kashi Sag, Tarim Basin," *Chinese Journal of Geology*, vol. 42, no. 2, pp. 253–266, 2007.
- [21] J. H. Luo, Z. C. Che, and L. Liu, "The origin of Kashi Depression and the guide for exploration," *Northwest University (Natural Science Edition)*, vol. 5, pp. 69–72, 1998.
- [22] M. M. Meng, Z. H. Kang, Y. H. Xu, C. Yu, and Q. Liu, "Geochemical characteristics of source rocks and oil-source correlation in the Kashi Sag, Tarim Basin," *Petroleum Geology and Experiment*, vol. 38, no. 2, pp. 266–273, 2016.
- [23] M. H. Sun, *The Study on Sequence Stratigraphy and Sedimentary System of Mid-Lower Jurassic in Southwestern Tarim*, Xinjiang University, 2013.
- [24] J. M. Zhan, X. Q. Li, and Q. Zhou, "The study on hydrocarbon generation history of Jurassic coal measures source rocks in Kashi Sag," *Journal of Anhui University of Science and Technology (Natural Science)*, vol. 2, pp. 1–4, 2005.
- [25] C. Wu, S. M. Zhai, B. Qiu, Y. Hong, W. Xiao-yun, and L. Song, "Hydrocarbon evaluation of Kashi Sag in Tarim Basin," *Xinjiang Petroleum Geology*, vol. 24, no. 3, pp. 221–223, 2003.
- [26] T. J. Li and X. R. Luo, "The Jurassic petroleum system in the Kashi Depression of the Tarim Basin," *Petroleum Geology and Experiment*, vol. 1, pp. 39–43, 2005.
- [27] J. Da, Y. Song, M. J. Zhao, G. Y. Fu, and Z. L. Yang, "Evolution and potential discussion of hydrocarbon source rock in north margin of Kashi Sag, Tarim Basin," *Xinjiang Petroleum Geology*, vol. 1, pp. 77–80, 2007.
- [28] X. Y. Gao, L. F. Liu, X. Q. Shang, Y. Wang, T. X. Su, and Q. W. Dai, "Characterization of Jurassic shale reservoirs and the geological background of shale gas accumulations in Tarim Basin," *Acta Petrolei Sinica*, vol. 4, pp. 647–659, 2013.
- [29] W. Y. Xiao, X. X. Lv, Z. K. Bai, Y. F. Wang, and J. Tu, "Characteristics of Jurassic shales and potential of shale gas in Southwest Depression of Tarim Basin," *Journal of China Coal Society*, vol. 41, no. z2, pp. 491–501, 2016.
- [30] X. Y. Zhou, J. H. Luo, and G. R. Mai, "Tectonic characteristics and petroleum geology of Kashi Sag and its surrounding areas in Tarim basin. Version 1," Petroleum Industry Press, Beijing, 2005.
- [31] J. H. Luo, X. Y. Zhou, B. Qiu, Z. L. Yang, H. Yin, and X. L. Shang, "Structural features of fold-thrust zone in Kashi Depression, western Tarim Basin," *Oil & Gas Geology*, vol. 2, pp. 199–203, 2004.
- [32] X. B. Li, "Petroleum geology characteristics of Kashi Depression," *Xinjiang Petroleum Geology*, vol. 4, pp. 285–289, 1995.
- [33] X. A. Chen, X. L. Zhang, and Q. P. Qu, "Characteristics of Piedmont structure and hydrocarbon prospect in the southwest of the Tarim Basin," *Xinjiang Petroleum Geology*, vol. 20, no. 6, pp. 468–472, 1999.
- [34] X. Y. Zhou, Y. Z. Hu, S. Liu et al., *Petroleum geology in the northern outcrop area of Kashi Sag, Tarim Basin. Version 1*, Petroleum Industry Press, Beijing, 2003.
- [35] D. W. Lv, Y. Song, L. Q. Shi, Z. Wang, P. Cong, and A. J. T. van Loon, "The complex transgression and regression history of the northern margin of the Palaeogene Tarim Sea (NW China), and implications for potential hydrocarbon occurrences," *Marine and Petroleum Geology*, vol. 112, p. 104041, 2020.
- [36] Y. Ding, J. P. Gong, and H. Wang, "Synthetic evaluation of source rocks in Southwest Depression of the Tarim Basin," *Petroleum Geology and Experiment*, vol. 4, pp. 336–339, 1999.
- [37] D. Z. Dong and A. C. Xiao, *Petroleum Geology and Petroleum Resources in the Southwest Depression of Tarim Basin*, Petroleum Industry Press, Beijing, 1st edition, 1998.

- [38] W. Z. Zhao and G. Y. Zhang, *Passive Continental Margin Evolution and Petroleum Geology: A Case Study of Southwestern Tarim Basin*, Petroleum Industry Press, Beijing, 1st Ed edition, 2007.
- [39] T. S. Yong, "Carboniferous lithofacies palaeogeography and its oil-bearing properties of Tarim platform," *Xinjiang Petroleum Geology*, vol. 3, pp. 13–24, 1983.
- [40] D. K. Zhong, X. M. Zhu, G. W. Wang, and Q. B. Xie, "Paleoenvironments of Jurassic of Kashi Sag in Tarim Basin," *Journal of Palaeogeography*, vol. 4, pp. 47–54, 2002.
- [41] D. K. Zhong, X. M. Zhu, Z. G. Shen, J. S. Chen, and L. Zhou, "Sedimentation and evolution of the Jurassic in the Kashi Depression, Tarim Basin," *Chinese Journal of Geology (Scientia Geologica Sinica)*, vol. 3, pp. 385–391, 2003.
- [42] B. S. Sun, Z. R. Liu, and Z. M. Wang, "New knowledge on geology of Kashi Depression in southwest Tarim," *Xinjiang Geology*, vol. 1, pp. 78–84, 2003.
- [43] P. C. Hackley, "Geological and geochemical characterization of the Lower Cretaceous Pearsall Formation, Maverick Basin, South Texas: a future shale gas resource," *AAPG Bulletin*, vol. 19, no. 5, pp. 1428–1449, 2012.
- [44] D. Strapoc, M. Mastalerz, and A. Schimmelmann, "Geochemical constraints on the origin and volume of gas in the New Albany Shale (Devonian–Mississippian), eastern Illinois Basin," *AAPG Bulletin*, vol. 94, no. 11, pp. 1713–1740, 2010.
- [45] D. W. Lv, Z. X. Li, D. D. Wang et al., "Sedimentary model of coal and shale in the Paleogene Lijiaya Formation of the Huangxian Basin: insight from petrological and geochemical characteristics of coal and shale," *Energy & Fuels*, vol. 33, no. 11, pp. 10442–10456, 2019.
- [46] K. Zhang, C. Jia, Y. Song et al., "Analysis of Lower Cambrian shale gas composition, source and accumulation pattern in different tectonic backgrounds: a case study of Weiyuan Block in the Upper Yangtze region and Xiuyu Basin in the Lower Yangtze region," *Fuel*, vol. 263, article 115978, 2020.
- [47] W. Z. Zhao, C. N. Zou, and Y. Song, *Advances in Theories and Methods of Petroleum Geology*, Petroleum Industry Press, Beijing, 1996.
- [48] D. M. Jarvie, "Shale resource systems for oil and gas: part 1—shale-gas resource systems," *AAPG Memoir*, vol. 97, pp. 69–87, 2012.
- [49] C. Chen, *Comprehensive Evaluation and Regionalization of Shale Gas Resources in Tarim Basin (Engineering Master Thesis)*, China University of Petroleum (EastChina), 2013.
- [50] M. J. Zhao, Z. M. Wang, Y. Song et al., "Source and accumulation of oil and gas in Kashi Sag, Tarim Basin, NW China," *Petroleum Exploration and Development*, vol. 2, pp. 50–54, 2005.
- [51] S. Chen, Y. Zhu, H. Wang, H. Liu, W. Wei, and J. Fang, "Shale gas reservoir characterisation: a typical case in the southern Sichuan Basin of China," *Energy*, vol. 36, no. 11, pp. 6609–6616, 2011.
- [52] W. D. Zhang, M. Guo, and Z. X. Jiang, "Parameters and method for shale gas reservoir evaluation," *Natural Gas Geoscience*, vol. 22, no. 6, pp. 1093–1099, 2011.
- [53] X. M. Xiao, Z. G. Song, Y. M. Zhu, and H. W. Yin, "Summary of shale gas research in North American and revelations to shale gas exploration of Lower Paleozoic strata in China south area," *Journal of China Coal Society*, vol. 5, pp. 721–727, 2013.
- [54] S. Q. Wang, S. Y. Wang, and L. Man, "Appraisal method and key parameters for screening shale gas play," *Journal of Chengdu University of Technology (Science & Technology Edition)*, vol. 40, no. 6, pp. 609–620, 2013.
- [55] S. L. Montgometry, D. M. Jarvie, K. A. Bowker, and R. M. Polastro, "Mississippian Barnett Shale, Fort Worth Basin—North Central Texas: gas-shale play with multi-trillion cubic foot potential," *AAPG Bulletin*, vol. 2, no. 89, pp. 155–175, 2005.
- [56] E. A. Letham and R. M. Bustin, "Klinkenberg gas slippage measurements as a means for shale pore structure characterization," *Geofluids*, vol. 16, no. 2, pp. 264–278, 2016.
- [57] Y. Tu, H. Y. Zou, H. P. Meng, Z. Xia, and N. Li, "Evaluation criteria and classification of shale gas reservoirs," *Oil & Gas Geology*, vol. 1, pp. 153–158, 2014.
- [58] R. Lewis, D. Ingraham, M. Pearcy, J. Williamson, W. Sawyer, and J. Frantz, "New evaluation techniques for gas shale reservoirs," in *Reservoir Symposium*, pp. 1–11, Schlumberger Houston, 2004.
- [59] Y. X. Li, J. C. Zhang, S. L. Jiang, and S. B. Han, "Geologic evaluation and targets optimization of shale gas," *Earth Science Frontiers*, vol. 19, no. 5, pp. 332–338, 2012.
- [60] M. D. Bunaman, W. Xia, and J. Shelton, "Shale gas play screening and evaluation criteria," *China Petroleum Exploration*, vol. 14, no. 3, pp. 51–64, 2009.
- [61] D. J. Hou, S. J. Bao, X. P. Mao et al., "Discussion on the key issues of resource potential evaluation for shale gas," *Journal of Earth Sciences and Environment*, vol. 3, pp. 7–16, 2012.
- [62] S. F. Lu, W. B. Huang, F. W. Chen et al., "Classification and evaluation criteria of shale oil and gas resources: discussion and application," *Petroleum Exploration and Development*, vol. 39, no. 2, pp. 249–256, 2012.
- [63] Y. Song, F. L. Gao, X. L. Tang, L. Chen, and X. M. Wang, "Influencing factors of pore structure differences between marine and terrestrial shale reservoirs," *Acta Petrolei Sinica*, vol. 41, no. 2, pp. 1501–1512, 2020.
- [64] R. Gareth, R. Chalmers, M. Bustin, and I. M. Power, "Characterization of gas shale pore systems by porosimetry, pycnometry, surface area, and field emission scanning electron microscopy/transmission electron microscopy image analyses: examples from the Barnett, Woodford, Haynesville, Marcellus, and Doig units," *AAPG Bulletin*, vol. 96, no. 6, pp. 1099–1119, 2012.
- [65] H. K. Nie, Z. J. Jin, and J. C. Zhang, "Characteristics of three organic matter pore types in the Wufeng-Longmaxi shale of the Sichuan Basin, southwest China," *Scientific Reports*, vol. 8, no. 1, article 7014, 2018.
- [66] X. P. Luo, P. Wu, J. H. Zhao, and N. Yang, "Study advances on organic pores in organic matter-rich mud shale," *Journal of Chengdu University of Technology (Science & Technology Edition)*, vol. 42, no. 1, pp. 50–59, 2015.
- [67] H. Kumar, D. Elsworth, J. P. Mathews, and C. Marone, "Permeability evolution in sorbing media: analogies between organic-rich shale and coal," *Geofluids*, vol. 16, pp. 43–55, 2015.
- [68] Y. J. Han, B. Horsfield, R. Wirth, N. Mahlstedt, and S. Bernard, "Oil retention and porosity evolution in organic-rich shales," *AAPG Bulletin*, vol. 101, no. 6, pp. 807–827, 2017.
- [69] C. Luo, S. G. Liu, and Z. L. Luo, "Pore structure characteristics of black shale in the Lower Cambrian Niutitang Formation of Nangao section in Danzhai, Guizhou Province," *Geological Science and Technology Information*, vol. 33, no. 3, pp. 93–105, 2014.

- [70] P. Luo and L. M. Ji, "Reservoir characteristics and potential evaluation of continental shale gas," *Natural Gas Geoscience*, vol. 24, no. 5, pp. 1060–1068, 2013.
- [71] R. G. Loucks, R. M. Reed, S. C. Ruppel, and D. M. Jarvie, "Morphology, genesis, and distribution of nanometer-scale pores in siliceous mudstones of the Mississippian Barnett Shale," *Journal of Sedimentary Research*, vol. 79, no. 12, pp. 848–861, 2009.
- [72] J. B. Curtis, "Fractured shale-gas systems," *AAPG Bulletin*, vol. 86, no. 11, pp. 1921–1938, 2002.
- [73] D. Brown, "Research getting unconventional boost," *American Association of Petroleum Geologists Explorer*, vol. 31, p. 810, 2010.
- [74] H. K. Nie, J. C. Zhang, X. B. Ma, and R. K. Bian, "A preliminary study of negative adsorption phenomena of shale adsorption gas content by isothermal adsorption," *Earth Science Frontiers*, vol. 6, pp. 282–288, 2013, (in Chinese with English abstract).
- [75] Q. L. Zhang, "The analysis of abnormal phenomena in shale isothermal adsorption volumetry test," *Coal Geology & Exploration*, vol. 43, no. 5, p. 3133, 2015.
- [76] D. H. Brunauer, "The four seasons of Marina Forrester," *Journal of Evolutionary Psychology*, vol. 15, no. 1-2, pp. 54–59, 1994.
- [77] L. Cao and Y. H. Guo, "Study on pore structure characteristics of mud shale in Wuxiang Block of eastern Qinshui Basin," *Coal Science and Technology*, vol. 48, no. 4, pp. 230–236, 2020.
- [78] J. Rouquerol, D. Avnir, C. W. Fairbridge et al., "Physical chemistry division commission on colloid and surface chemistry, subcommittee on characterization of porous solids: recommendations for the characterization of porous solids," *International Union of Pure and Applied Chemistry*, vol. 68, pp. 1739–1758, 1994.
- [79] S. B. Chen, Y. M. Zhu, H. Y. Wang, H. L. Liu, W. Wei, and J. H. Fang, "Structure characteristics and accumulation significance of nanopores in Longmaxi shale gas reservoir in the southern Sichuan Basin," *Journal of China Coal Society*, vol. 37, no. 3, pp. 438–444, 2012.
- [80] J. H. De Boer, D. H. Everett, and F. S. Stone, *The Structure and Properties of Porous Materials*, DH Everett, FS Stone, 1958.
- [81] E. P. Barrett, L. G. Joyner, and P. P. Halenda, "The determination of pore volume and area distributions in porous substances: I. Computations from nitrogen isotherms," *Journal of the American Chemical Society*, vol. 73, pp. 373–380, 1951.
- [82] W. J. Thomas and B. Crittenden, *Adsorption Technology and Design*, Elsevier Science & Technology, 1998.
- [83] S. Lu, J. Li, P. Zhang et al., "Classification of microscopic pore-throats and the grading evaluation on shale oil reservoirs," *Petroleum Exploration and Development*, vol. 45, no. 3, pp. 436–444, 2018.
- [84] Y. L. Kang, Y. B. Chen, X. C. Li, L. J. You, and M. J. Chen, "Effect of particle size on methane sorption capacity of shales," *Natural Gas Geoscience*, vol. 28, no. 2, pp. 272–279, 2017.

Research Article

Genetic Types and Main Control Factors of Microfractures in Tight Oil Reservoirs of Jimsar Sag

Xiangye Kong ^{1,2}, Jianhui Zeng ^{1,2}, Xianfeng Tan ³, Haowei Yuan,^{1,2} Dan Liu,⁴ Qun Luo,⁵ Qianyou Wang,⁶ and Rusi Zuo⁷

¹College of Geosciences, China University of Petroleum, Beijing 102249, China

²State Key Laboratory of Petroleum Resources and Prospecting, China University of Petroleum, Beijing 102249, China

³College of Petroleum and Gas Engineering, Chongqing University of Science and Technology, Chongqing 401331, China

⁴Institute of Exploration Techniques, CAGS, Langfang Hebei 065000, China

⁵Unconventional Natural Gas Institute, China University of Petroleum, Beijing 102249, China

⁶Department of Earth, Ocean and Ecological Sciences, University of Liverpool, Liverpool L69 3GP, UK

⁷State Key Laboratory of Marine Geology, Tongji University, Shanghai 200092, China

Correspondence should be addressed to Jianhui Zeng; zengjh@cup.edu.cn and Xianfeng Tan; xianfengtan8299@163.com

Received 28 January 2021; Accepted 1 July 2021; Published 24 July 2021

Academic Editor: Paolo Madonia

Copyright © 2021 Xiangye Kong et al. This is an open access article distributed under the Creative Commons Attribution License, which permits unrestricted use, distribution, and reproduction in any medium, provided the original work is properly cited.

Microfractures are key for migrating and aggregating hydrocarbon source rocks and fracturing oil-gas exploitation in tight reservoirs. In this study, rock samples from the Lucaogou Formation tight reservoirs in Xinjiang, China, were studied using multidisciplinary techniques to investigate the genetic types and main control factors of microfractures. Results indicated that the Lucaogou Formation mainly developed diagenetic microfractures followed by tectonic microfractures, with slight formations of granular microfractures. These observations were used to clarify the relationship between the development of microfractures and the pore fluid content, lithology, mineral composition, and stratum thickness. A higher pore fluid content corresponded to a lower compressive strength of the rocks and a larger ring count, resulting in a higher probability of failure and microfracture formation. Tight reservoirs containing more quartz and carbonate minerals were found to develop more microfractures. Quartz grains showed fractures at the margins under stress, which increased the pore permeability of rocks. Carbonate minerals tended to form microfractures owing to corrosion. Microfracture formation mechanisms differed depending on lithology, and microfractures were found to develop most in dolomite and dolomitic siltstones and least in mudstone. Muddy rocks developed fewer tectonic fractures because they can easily absorb stress and undergo plastic deformation. Within a certain stratum thickness range, the average single-well fracture space and stratum thickness showed positive correlations. Moreover, the fracture space increased and the fracture density decreased as the stratum thickness increased. When the stratum thickness was less than 2.5 m, the fracture space increased linearly with the stratum thickness, and when the stratum thickness was greater than 2.5 m, the fracture space remained constant. This study will provide an essential scientific basis for enhancing tight oil recovery.

1. Introduction

Natural fractures are widespread in tight reservoirs [1–4]. Microfractures affect not only the migration and accumulation of oil and gas but also the outcome of oil-gas development. However, existing research on microfractures is not comprehensive [5]. The formation, development, and connection of microfractures provide channels for the migration and

aggregation of oil and gas in tight reservoirs [6–9]. Microfractures are important spaces in tight reservoirs that gradually form large-scale and complex fracture networks [10–13]. Microfractures are defined as fractures with an opening of $<100\ \mu\text{m}$ and are unrecognisable on imaging logs or core samples but can be observed using microscopy (e.g., casting thin sections or scanning electron microscopy (SEM)); they are predominantly diagenetic or corroded fractures [14, 15].

Fractures with an opening between 100 nm and 1 mm are defined as microfractures, and fractures with a width of $<1 \mu\text{m}$ are called supermicrofractures [16, 17]. The formation of microfractures is affected by tectonic movements, sedimentary environment, burying conditions, fluid properties, and other factors [18]. The genetic types of microfractures are defined by tectogenesis, which is related to diagenesis. When tectonic loading is applied externally, a rock can fracture and eventually fail along faults. Conversely, internal stresses may be related to increased fluid pressure inside the rock due to the dehydration of clays. The joints of microfractures can be analysed via the stress analysis of a rose diagram [19]. During diagenesis, sediments are affected by compacted shrinkage, mineral cementation, metasomatism, and recrystallisation. These occurrences induce the contraction and expansion of strata and the recombination and conversion of minerals. Such changes are accompanied by the development of microfractures to different degrees [20]. Microfracture formation is largely affected by early-stage compaction and late-stage corrosion. Corroded carbonate minerals can easily form corroded fractures, which normally develop along cleavages. Compacted rocks often develop compressed fractures [21–23]. The reservoirs in the Upper Palaeozoic Shihezi Formation were derived from diverse sources and contained various sediments, resulting in severe longitudinal lithological heterogeneity [21]. Diagenesis induces changes in lithological composition and significantly affects the physical properties of reservoirs. Diagenesis also differs considerably among strata, which can develop diverse and structurally complex pores. Microfractures are believed to be the main channels of reservoir seepage, and the distributive laws and developmental characteristics of microfractures are controlled by diagenesis and lithology [24].

Microfractures are detected and evaluated mainly using mercury intrusions, image analysis, imaging logs, and magnetic logs of core data. Considering that microfracture control mechanisms depend on the reservoir lithology, diagenesis, and pore type, a specific lithology can be recognised for any horizon. Thereafter, valid porosity and permeability evaluation models can be established based on lithology and horizon constraints. Wang and Rahman developed a microfracture evaluation model and an identification method to analyse more than 70 wells [25]. The relative error of permeability using logging evaluations was less than 10%, and many new active gas layers were observed [26]. Overall, among wells with a gas production rate exceeding the lower economic limit ($3 \times 10^4 \text{ m}^3/\text{d}$), more than 90% developed microfractures [27]. The wells with high single-well gas production rates developed high-permeability microfractures, thus validating the results of the model [24, 25].

The Lucaogou Formation in the Jimsar Sag of Junggar Basin in Xinjiang, China, is typical continental tight oil strata showing developed tight oil reservoirs with high-quality hydrocarbon source rocks, featuring active oil-gas exploitation, large oil-gas reserves, and significant exploration potential [7, 28, 29]. The Lucaogou Formation is one of China's most important tight oil strata. Since 2010, commercial oil production has been realised in several wells in the Jimsar Sag (including wells J23, J25, and

J30), representing a breakthrough in tight oil production in the southeast Junggar Basin [30, 31]. The Lucaogou Formation strata mainly comprise carbonate rocks, mudstone, and powder-fine sandstone [29]. Previous works in this region were mainly focused on the macroscale, such as the geological structure and sedimentary environment; however, little research has been conducted at the microscale. The role of fractures in reservoirs of Jimsar Sag has also been noted [31].

Hence, this study focused on qualitatively and quantitatively identifying microfractures in the Lucaogou Formation to clarify the causes and basic parameters of microfracture development. The developmental characteristics and control factors of the microfractures were elucidated, and the influence of microfracture development on reservoir properties was determined.

2. Geological Settings

The Junggar Basin is the second-largest basin in China. It is rich in tight oil reservoirs and shows high potential for exploration and development. It belongs to the Ural-Mongolia Orogenic Belt, which is surrounded by multiple orogenic belts, such as the Altai and Bogda Mountains. Its north is bounded by the Shaqi Uplift and Jimsar Sag, and its south is bounded by the Houbaozi Fault. Its west is bounded by the Xidi Fault and Beisantai Uplift, and its east transitions from a slope to the Guxi Uplift (Figures 1 and 2). The Junggar Basin is surrounded by several other basins such as Tuha, Erie, and Santanghu Basins [32–35]. The Junggar Basin initially formed during the Hercynian activity period. In the late Early Permian, the Bogda Trough at the south margin of the basin was closing for orogenesis. In the late Middle Permian, the Lucaogou Formation started experiencing lacustrine facies sedimentation, forming the main hydrocarbon source rocks in this region. In the Late Triassic, the Indo-China Movement occurred, leading to severe uplifting of the Guxi Uplift and the Permian differential corrosion. During the Yanshan Movement, frequent and severe tectonic movements occurred inside the Junggar Basin, inducing gentle uplift in the southeast. The Himalayan Movement formed from the Neogene to Quaternary, leading to the rest of the basin evolution [32, 34, 36, 37].

The internal tectogenesis of Jimsar Sag is relatively stable, and the inner strata of the basin are complete, with maximum sedimentation thickness of 5000 m. The stratigraphic framework of Jimsar was formed after the Himalayan orogeny. The strata are mostly in conformable contact, and the deficient part comprises the Huangshanjie Formation, Jurassic Kelazha Formation, and Triassic Haojiagou Formation. The Lucaogou Formation (P2l) originates from the Permian and is beneath the Wutonggou Formation (P3wt) and above the Jiangjunmiao Formation (P2j). Full-well cores were collected from well J174 in the basin. Based on its lithology, magnetic logs, electric data, and systematic analysis, the Lucaogou Formation can be divided into two segments (P2l2 and P2l1) and four layers (P2l21, P2l22, P2l11, and P2l12) [38].

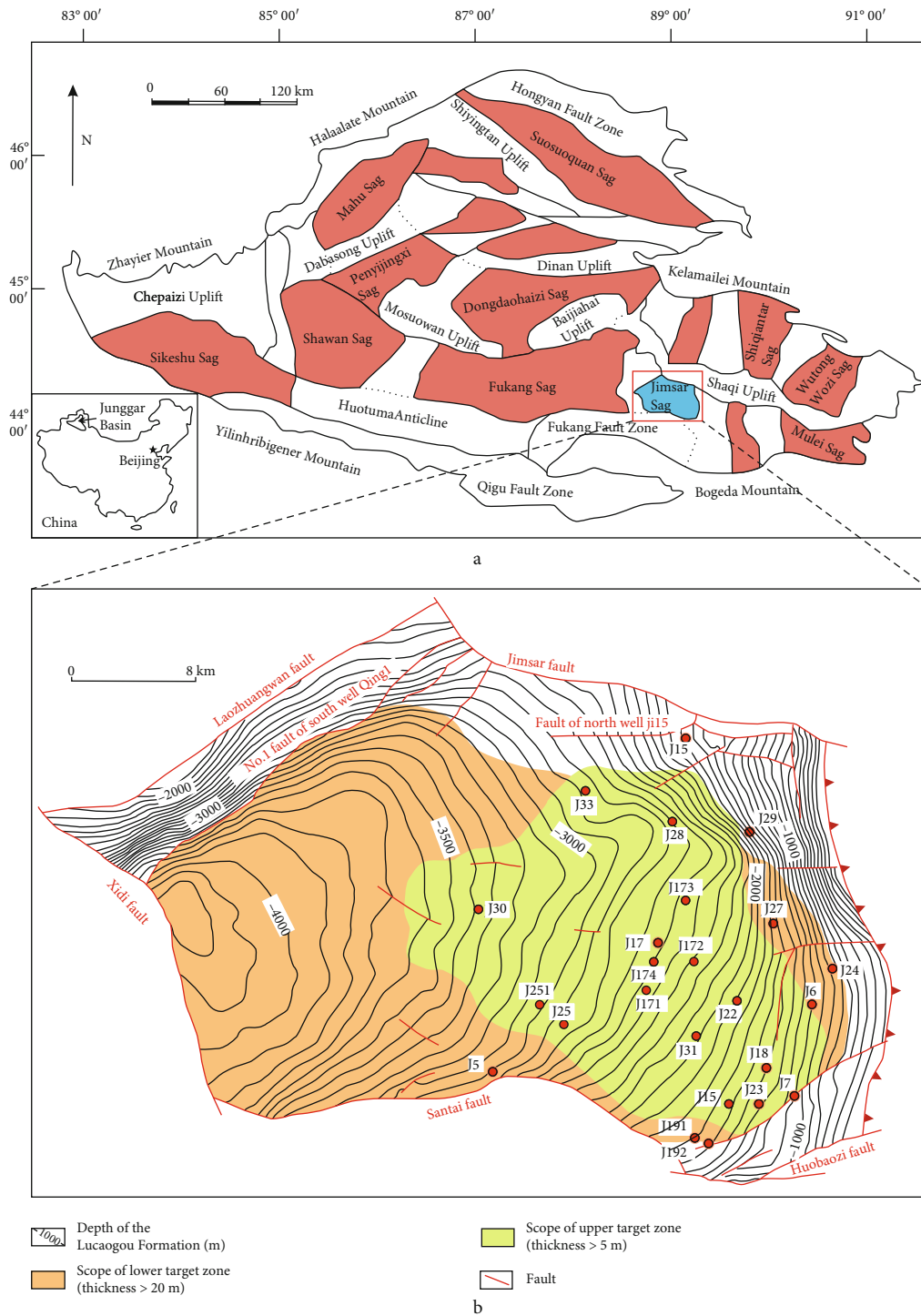


FIGURE 1: Structural division of the Junggar Basin.

The Lucaogou Formation was affected by mechanical sedimentation, thus comprising hybrid sedimentary rocks deposited in salty lakes. During the Penecontemporary period, rocks in this area experienced severe dolomitisation; hence, dolomites normally developed with micrite and microcrystalline structures, with small grain-sized detritus enriched with carbonate rocks, mudstone, and powder-fine sandstones that were mostly interlayered. The rock types

mainly include mudstone, fine siltstone, and carbonate rocks. The fine siltstone mainly includes dololite fine siltstone, lithic feldspar fine siltstone, and dolomitic fine siltstone. The carbonate rocks mainly include muddy microlite dolomite, fine sandy dolomite, and sand detritus dolomite. The carbonate rocks are dominated by dolomitic rocks and limestone, which comprise up to 74.15% in some areas. Thus, the Lucaogou Formation is generally rich in carbonate minerals

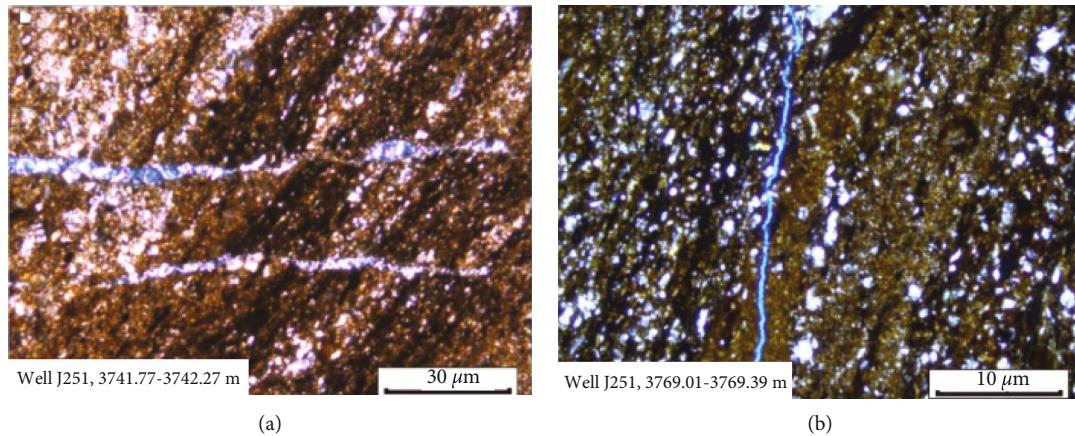


FIGURE 2: Typical microfractures with a high opening in casting thin section of the Lucaogou Formation in the Jimsar Sag: (a) well J251, 3741.77-3742.27 m; (b) well J251, 3769.01-3769.39 m.

and is highly brittle, making it suitable for large-scale exploitation [39]. The Lucaogou Formation is well developed with microfractures. The tight sandstone in the study area is rich in clay but has fewer authigenic minerals than the crystals of common sandstone reservoirs. In addition to autogenetic causes (including the cause of alteration), terrigenous detritus sedimentation is observed.

3. Methodology

72 rock samples were collected from 22 exploration wells in the Middle Permian of the Lucaogou Formation. These samples included grey dolerite, feldspathic, dolomitic lithic sandstone, and dolomitic mudstone. Before the tests, the core samples were washed with a mixture of trichloromethane and alcohol to eliminate residual oil and then dried at 115°C for 26 h under vacuum. Each core sample was drilled to a size with a diameter and length of 2.54 and 5.00 cm, respectively. The following methods were adopted for investigations: casting thin sections, SEM, acoustic emission (AE), and nuclear magnetic resonance (NMR). Casting thin sections and SEM can clearly visualise the morphology, occurrence, filling, and peripheral mineral contact of microfracture development. AE and NMR can clarify the structural characteristics of rocks.

3.1. Microscopy. The casting thin section and scanning electron microscopy experiments were completed in the State Key Laboratory of Petroleum Resources and Exploration, China University of Petroleum (Beijing). The samples were detected by ZEISS Merlin and GeminiSEM instruments. Casting thin sections were used to study the quantity, type, and distribution of pores. A staining resin or liquid glue was perfused into the rock pores under vacuum. The resin or glue solidified at a certain temperature and pressure, and the rock was then ground into sections, which were used to observe pore structures under polarisation [40]. Figure 2(a) shows a cast thin section with two microfractures with an opening of 2–5 μm . The microfractures exhibit an oblique crossing strike with bedding; hence, they appear to be tectonic fractures that mainly formed because of external forces.

Figure 2(b) shows a cast thin section with only one microfracture with an opening of 1–3 μm that developed along the layers. Thus, it appears to be a bedding fracture. SEM is a comprehensive analyser that affords high-resolution images and can be used to observe microfractures up to several nanometres [41, 42]. More than 200 SEM images and cast thin sections were acquired from 10 wells in the study area, including J174, J251, J36, and J172. Secondary microfractures were mainly observed, with only a few original intergranular pores, and they mostly developed along the layers. Figure 3 shows that the fractures developed inside minerals or along mineral margins with complex arrangements.

3.2. Acoustic Emissions. The rock triaxial acoustic emission experiment was completed in the Laboratory of Rock Mechanics, China University of Petroleum (Beijing). The test loading was carried out by the MTS 815 rock mechanics test system of MTS Company, and the acoustic emission acquisition was carried out by the PCI-II acoustic emission monitoring system of PAC Company. The AE technique visualises the changes in internal materials in rocks using AE events. AE events record the AE induced in the rocks owing to changes resulting from external forces. An AE experiment was performed, and the variations in the energy count and AE count were used to analyse the fracture process. The fracture process occurs in three stages. In the crack concentration stage, the initial microfractures gradually grow under external forces; thus, the AE curve manifests as a smooth rising line. In the fracture expansion stage, the expansion is intermittent; hence, numerous fractures are formed, showing a zigzag curve. In the broken damage stage, the rocks suddenly experience instantaneous failure [43, 44]. Research on the Yanchang Formation in the Ordos Basin showed that microfractures are formed when the external force imposed on a rock reaches the fracturing intensity. Hence, AE events can be measured using an AE curve to indicate the exact location of microfractures [45–47]. The experiments verified that after passing Caesar's phenomenon, the first small-scale microrupture period is the microfracture formation period. As shown in Figure 4, the cumulative number of AE events

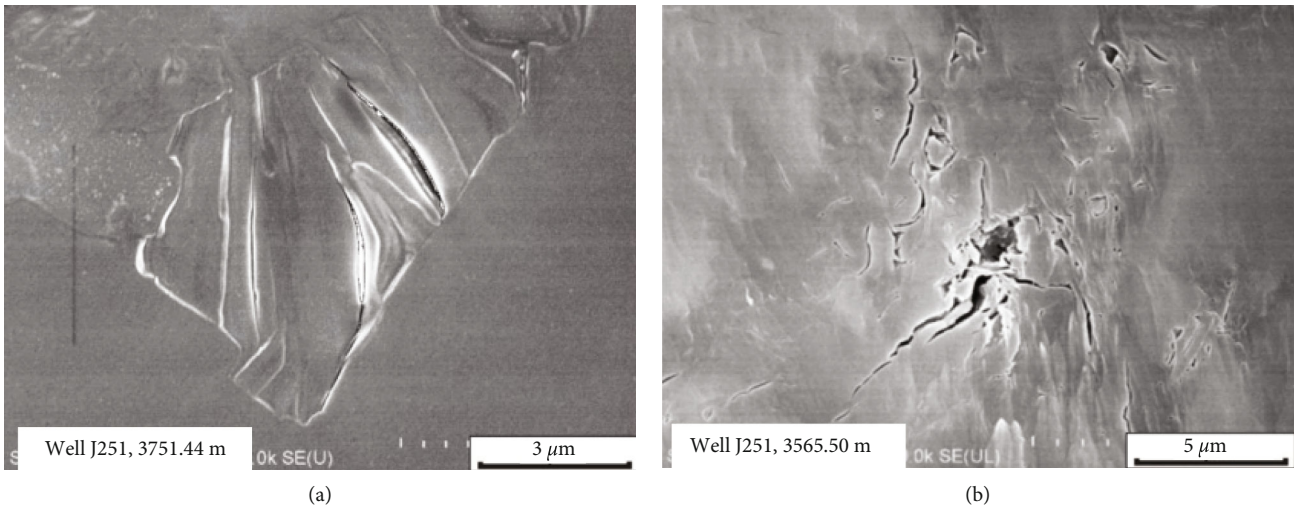


FIGURE 3: Typical microfractures are developed inside minerals or along mineral margins in microscopic scale of the Lucaogou Formation in the Jimsar Sag: (a) well J251, 3751.44 m; (b) well J251, 3565.5 m.

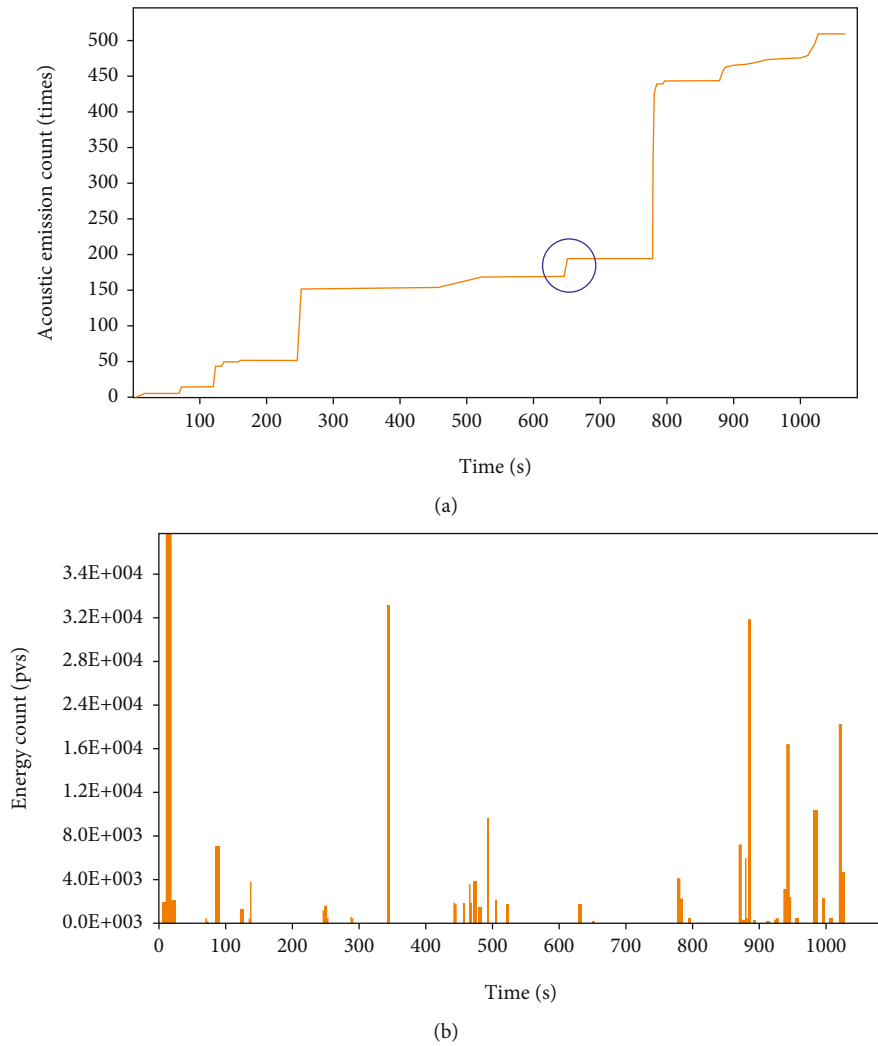


FIGURE 4: The acoustic emission curve of the three-axis compression process: (a) curve of acoustic emission count with time; (b) curve of energy count with time.

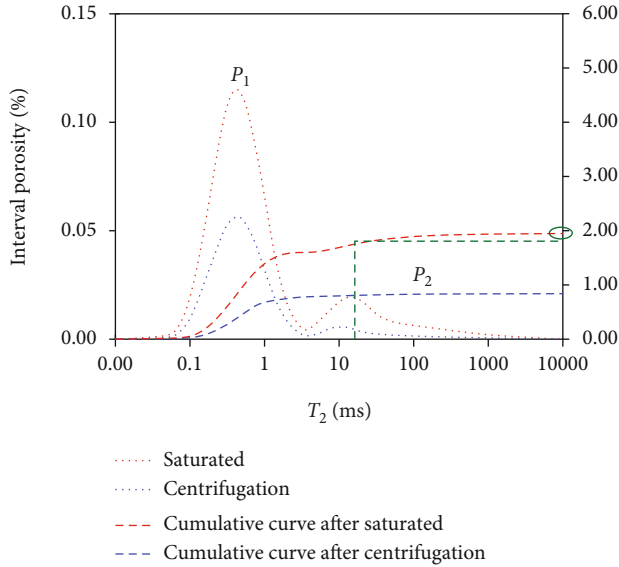


FIGURE 5: NMR T_2 features (saturated curve, centrifugation, cumulative curve after saturation, and cumulative curve after centrifugation) of samples from well 174.

on the AE curve was used to determine the number of microfractures [48].

3.3. Nuclear Magnetic Resonance. The NMR T_2 distributions were measured at 20°C using a 2 MHz Suzhou Niumag Analytical Instrument at State Key Laboratory of Petroleum Resources and Prospecting. The rock samples were subjected to NMR tests. The area of the NMR T_2 spectrum indicates the variation in the pore structure and is proportional to the pore fluid concentration in rocks. Herein, the relaxation time was used to observe the pore size distributions of rock samples. When the relaxation time is long, the corresponding T_2 spectrum indicates the pore volume of relatively large-sized pores. The microfractures of tight sandstone can be studied via the qualitative and quantitative analyses of NMR data [49]. Figure 5 shows that a new peak appeared in the T_2 spectra under the saturated status, and the original peak moved leftwards to form a double peak. These results indicate the formation of numerous microfractures that contributed to the porosity of the rock samples. When the NMR T_2 spectra were observed in the irreducible water state, the right-side peak disappeared. Considering that fractures easily broke in the centrifugal status, the right-side peak can be considered to indicate microfracture formation. The fracture/microfracture percentage ratio can be defined as the sum of T_2 spectral amplitudes with a relaxation time T_2 of >10 ms divided by the total number of T_2 spectral amplitudes [50, 51]. Because microfractures can easily break during centrifugation and NMR analysis, the fracture/microfracture percentage ratio was used to represent the developing degree of microfractures in each sample.

3.4. Experimental Procedure. First, porosity experiments based on helium were performed to select samples with consistent lithology and relatively large porosity. The sam-

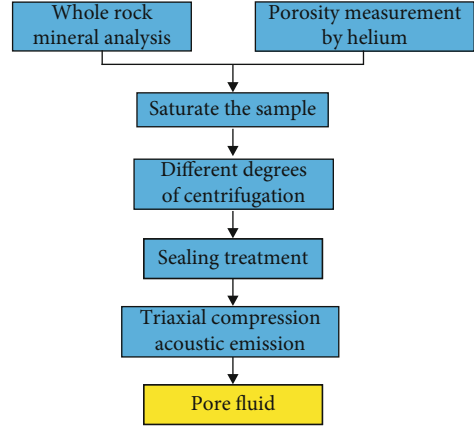


FIGURE 6: Experimental flowsheet on fluid saturation correlation between microfractures and pores.

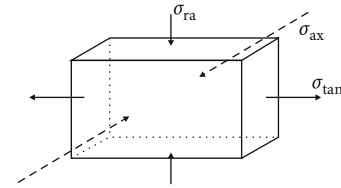


FIGURE 7: Three-dimensional stress diagram.

ples were saturated to 100% using a saturation metre and then saturated to different degrees by reconfiguration in centrifugation experiments. Then, the samples were sealed. Finally, triaxial compression experiments were performed, and AE was used to monitor fracture formation. Figure 6 shows the relationship between fractures and the pore fluid concentration.

Centrifuging is widely used to separate standard rock samples into high, medium, and low permeability. The centrifugal pressure must satisfy

$$P = 1.097 \times 9L \left(R_c - \frac{L}{2} \right) n^2, \quad (1)$$

where L is the rock length (mm), R_c is the epitrochoid radius (mm), and n is the rotating speed at the head of the centrifuge.

Triaxial compression experiments were performed, where the three-dimensional stress states of rock samples were simulated (Figure 7) to measure the maximum and minimum principal stresses. Then, the compressive strength, internal friction angle, and cohesion of the rocks were measured using multiple tests.

Three groups of rocks were placed in a saturation metre. Because all rock samples were tight sandstone, the static pressure for saturation was set to 20 MPa. Four rock samples (two samples per group) were placed in an LD5-10B centrifuge and centrifuged at 8000 rotations. After 1 h, the rock samples were removed. Then, one sample from each group was selected and placed inside the centrifuge again. When the lithology is consistent and the centrifugation time is the

TABLE 1: Parameters involved in the acoustic emission counting for the Lucaogou Formation tight sandstones in the Jimsar Sag, Junggar Basin.

Group	No. of core	Condition of water saturation (%)	Acoustic emission counting
G1	J174-1	0	50
	J174-2	30	65
	J174-3	80	100
	J174-4	100	166
G2	J22-1	0	53
	J22-2	30	74
	J22-3	90	101
	J22-4	100	169
G3	J36-1	0	56
	J36-2	30	65
	J36-3	70	107
	J36-4	100	170

same, the rock samples must show a consistent decrease in water content. The above steps were repeated successively. The centrifuged samples were then immediately sealed for the triaxial experiment. The rock samples were set in an anti-oil and antipressure plastic set that was custom-made and softened using blowing so that the samples tightly clung to the set. The set was installed according to experimental requirements. Then, the sensor was adjusted and slowly compressed. Simultaneously, the AE analyser was started. Thereafter, the corresponding rock mechanical parameters were determined. The AE curves were used to record the number of AE rings upon microfracture formation (i.e., number of AE events) (Table 1).

The main factors that affect the formation of microfractures in rocks are the contents of fragile minerals and carbonates. In this experiment, the quantitative relationship between microfractures and mineral composition was mainly studied from two aspects. First, several rock samples rich in carbonates were selected according to their lithological data and physical properties. Then, the rocks were fractured in triaxial compression experiments to form microfractures. Samples showing evident microfractures in the NMR T_2 spectrum were selected and used to analyse the quantitative relationship between the mineral composition and microfractures (Figure 8).

The main form of NMR applied to tight sandstone is usually the transverse relaxation time T_2 . Under rapid diffusion conditions, the relaxation time T_{2a} of a pore fluid can be approximated as

$$\frac{1}{T_{2a}} = \frac{1}{T_{2b}} + \rho_2 \frac{S}{V}, \quad (2)$$

where T_{2b} is the inherent relaxation time (ms) of pore fluid in a rock, ρ_2 is the surface relaxation rate in a fluid-containing pore ($\mu\text{m}/\text{ms}$), and S/V is the ratio of surface area to volume

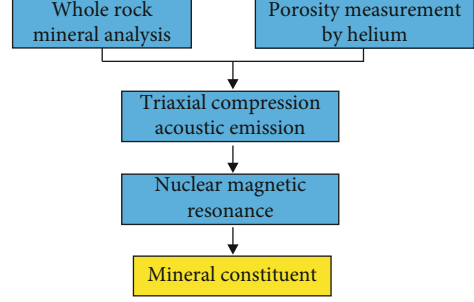


FIGURE 8: The experimental flow chart of correlation between microfractures and mineral composition.

of the corresponding pore and is inversely proportional to the pore size:

$$\frac{S}{V} = \frac{F_s}{r}, \quad (3)$$

where F_s is the pore shape factor and r is the pore radius. When the pore fluid is water or light oil, the long inherent relaxation time leads to

$$\frac{1}{T_{2a}} = \rho_2 \frac{S}{V}. \quad (4)$$

For the same rock sample, the relaxation rate ρ_2 and pore shape factor F_s can be approximated as constants. Hence, the T_2 spectra can be used to determine the distribution of rock pores because rocks with longer relaxation times correspond to larger fractures, and vice versa [52, 53].

Before the experiments, tight sandstone samples were ground and parallelled. The samples were dried in a thermostatic drying chamber at 60°C for approximately 24 h until the weight no longer changed. Then, the basic parameters of the samples were measured at a peripheral pressure of 900 psi, air pressure of 400 psi, and pulse attenuation of PDP-200. To further clarify the mineral composition, the rock samples were tested in terms of the total organic carbon, kerogen ultimate analysis, whole-rock mineral X-ray diffraction, and organic matter macerals.

4. Genetic Types of Microfractures

Microfracture formation was primarily attributed to the tectonic stress field during rock diagenesis [54, 55]. Given the small openings and invisibility of microfractures, microscopy (i.e., casting thin sections and SEM) was used to observe their developmental characteristics to explore genetic types. Microfractures were generally well developed in the Lucaogou Formation with complex genetic types, including tectonic fractures, bedding fractures, intragranular fractures, marginal fractures, corroded fractures, diagenetic contraction fractures, and organic hydrocarbon-producing high-pressure fractures. These microfractures can be broadly classified as tectonic (i.e., directional), granular, or diagenetic based on their genetic types.

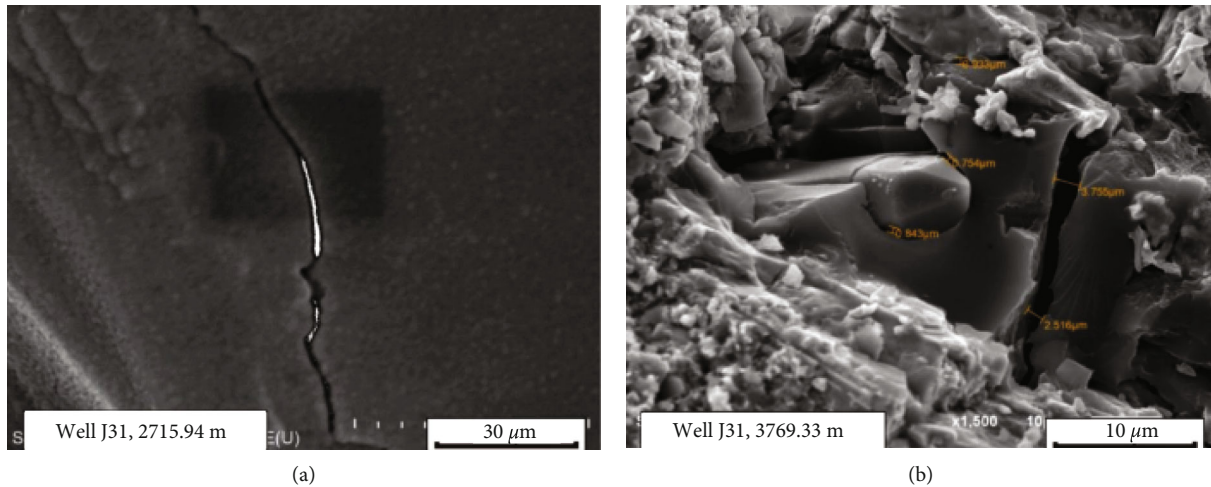


FIGURE 9: Tectonic-breaking microfractures in microscopic scale of the Lucaogou Formation in the Jimsar Sag: (a) well J31, 2715.94 m; (b) well J31, 3769.33 m.

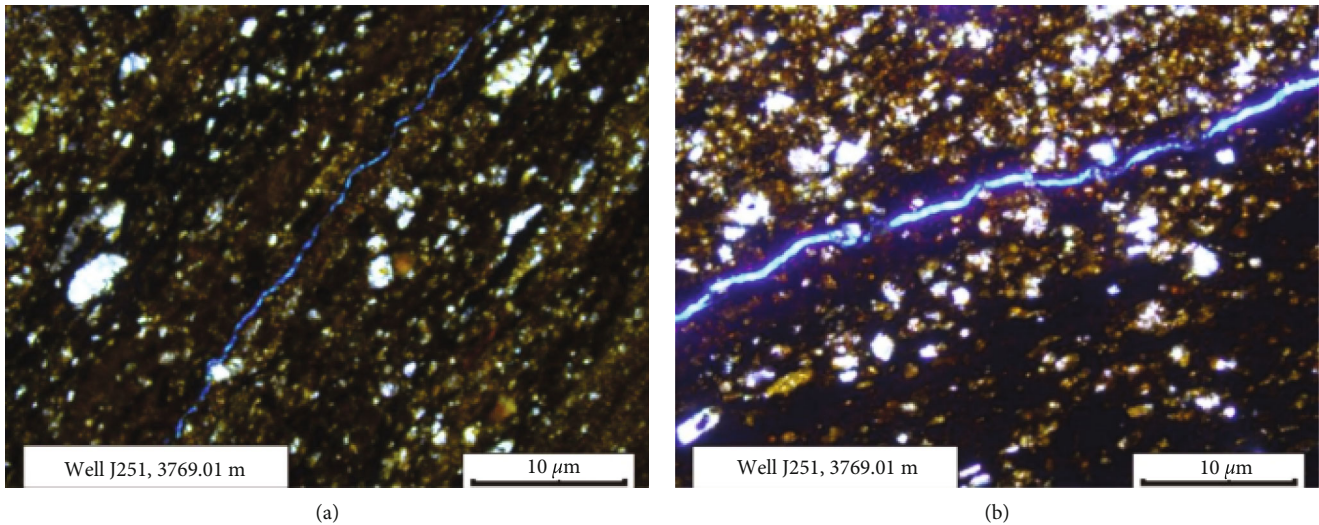


FIGURE 10: Bedding fractures in microscopic scale of the Lucaogou Formation in the Jimsar Sag: (a) well J251, 3769.01 m; (b) well J251, 3769.01 m.

4.1. Tectonic Microfractures. Small-scale high-elongation tectonic fractures are formed, and some even cut through rocks and grains. They can connect with other fractures and even form networks to improve seepage [10, 11]. Tectonic fractures cut through beddings and are straight and even with openings of $0.01\text{--}10\ \mu\text{m}$ (Figure 2). Most tectonic microfractures are filled with quartz, calcite, and dolomite and rarely with mud (Figure 2). Such tectonic fractures are formed when minerals are destroyed under stress that exceeds their fracture strength [14, 15]. Their developing planes are straight, even, and open to varying degrees. Tectonic fractures are commonly seen in quartz, feldspar, and other fragile minerals but rarely in clay minerals (Figure 9).

Bedding fractures are related to tectogenesis. Because beddings are the weak surfaces of strata, when the pressure gradient inside a closed system is greater than a critical value, a part of the bedding surface dislocates or opens to form a

fracture [52, 56]. Bedding fractures are nearly parallel to the bedding surface and cross mineral grains. They are typically manifested as one broad head and one gradually sharpening head. Bedding fractures are $0.1\text{--}5\ \mu\text{m}$ wide and $0.1\text{--}10\ \text{mm}$ long; they are mostly filled with mud, iron or quartz, feldspar, calcite, and other minerals in the later stage, with a filling degree of 80% (Figure 10).

4.2. Diagenetic Microfractures. Diagenetic microfractures result from diagenesis and show no definite orientation. They are open to varying degrees. Diagenetic microfractures exhibit irregular shapes, distributions, and sizes and are mostly branch- or cobweb-like. Common types include diagenetic contraction fractures, organic hydrocarbon-producing fractures, and corroded fractures. Diagenesis contraction fractures are found in kaolinite and other clay minerals, which contract upon dehydration because of their

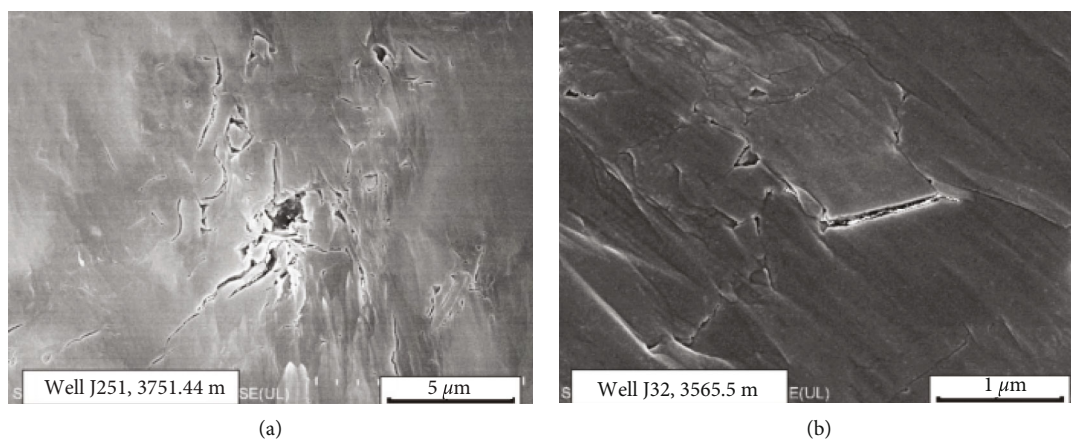


FIGURE 11: Diagenetic contraction fractures in microscopic scale of the Lucaogou Formation in the Jimsar Sag: (a) well J251, 3751.44 m; (b) well J251, 3565.5 m.

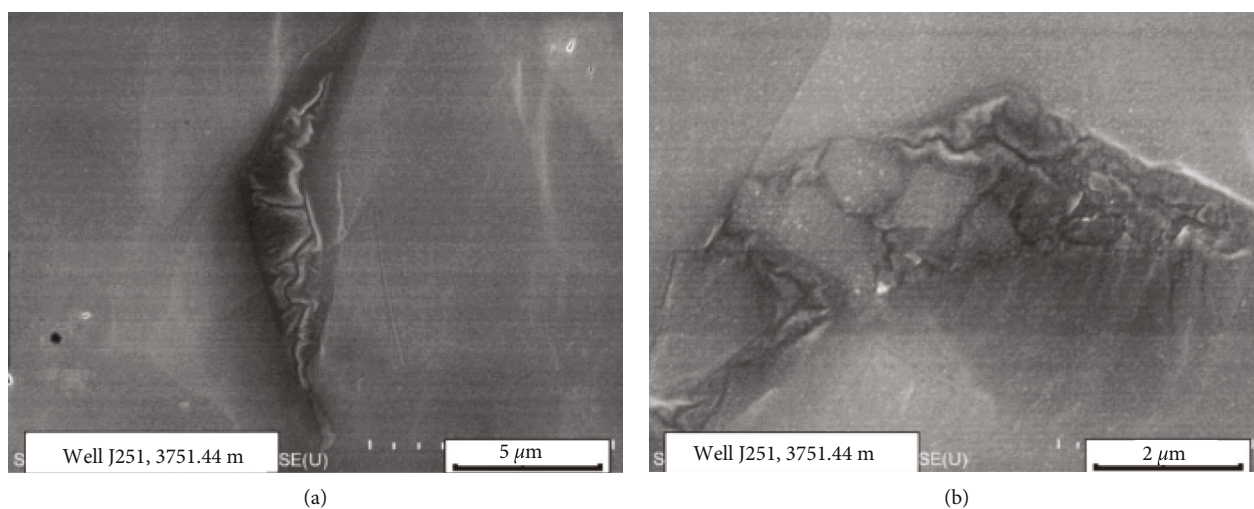


FIGURE 12: High-pressure microfractures in microscopic scale of the Lucaogou Formation in the Jimsar sag: (a) well J251, 3751.44 m; (b) well J251, 3751.44 m.

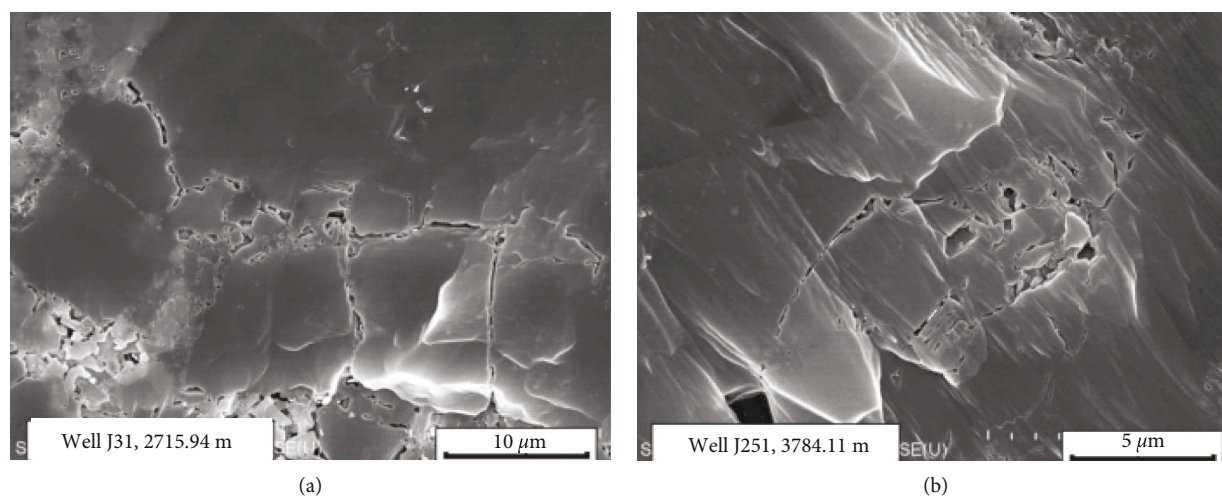


FIGURE 13: Dissolution fractures in microscopic scale of the Lucaogou Formation in the Jimsar sag: (a) well J31, 2751.94 m; (b) well J251, 3784.11 m.

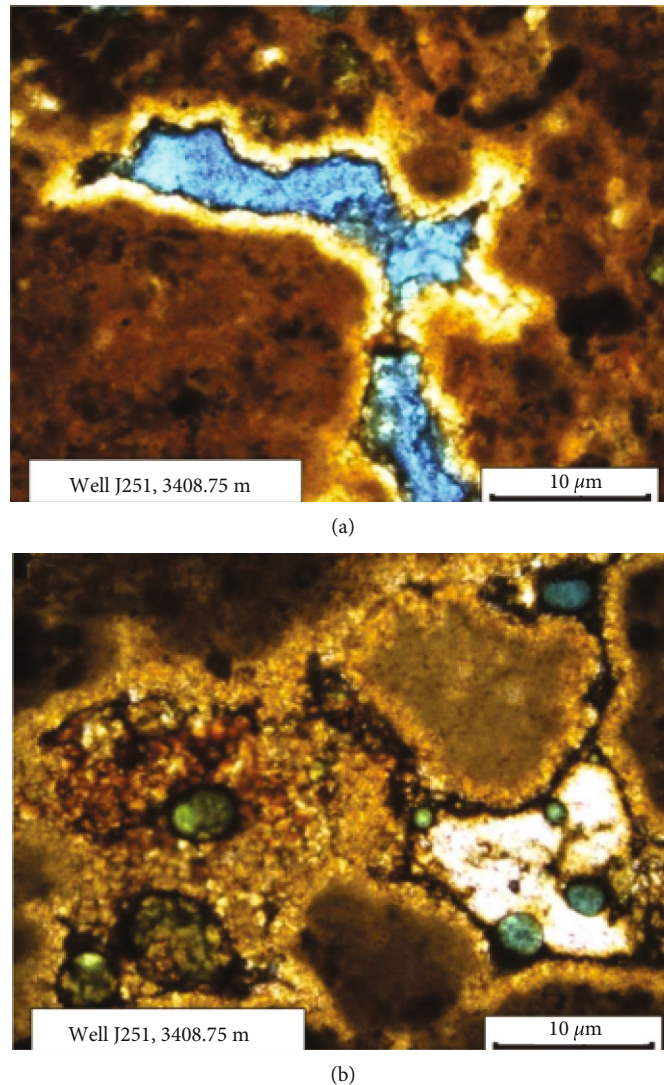


FIGURE 14: Gravel-edge fractures and corrosion fractures in microscopic scale of the Lucaogou Formation in the Jimsar Sag: (a) well J251, 3408.75 m; (b) well J251, 3408.75 m.

scale-like crystals to form fractures nearly parallel to the mineral layers [57]. High silicon reservoirs form diagenetic contraction fractures because of dehydration, mineral phase transformation, or thermodynamic contraction. Diagenetic contraction fractures are commonly seen in stratified minerals and exhibit diverse shapes, including straight or curved. They do not extend considerably but are well connected with large openings (Figure 11).

Organic hydrocarbon-producing high-pressure fractures are intragranular porous fractures that form when organic-rich argillaceous interlayers in tight reservoirs are sufficiently mature and buried sufficiently deep (Figure 12). This is probably because porous fractures are formed because of organic depletion after hydrocarbon generation from kerogen, water consumption owing to hydrocarbon generation, or increased pressure owing to hydrocarbon formation. Moreover, organic matter and adjacent minerals can form porous fractures owing to hydrocarbon formation, likely attributed to

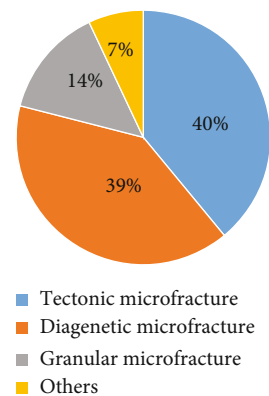


FIGURE 15: Classification diagram of genetic types of microfractures.

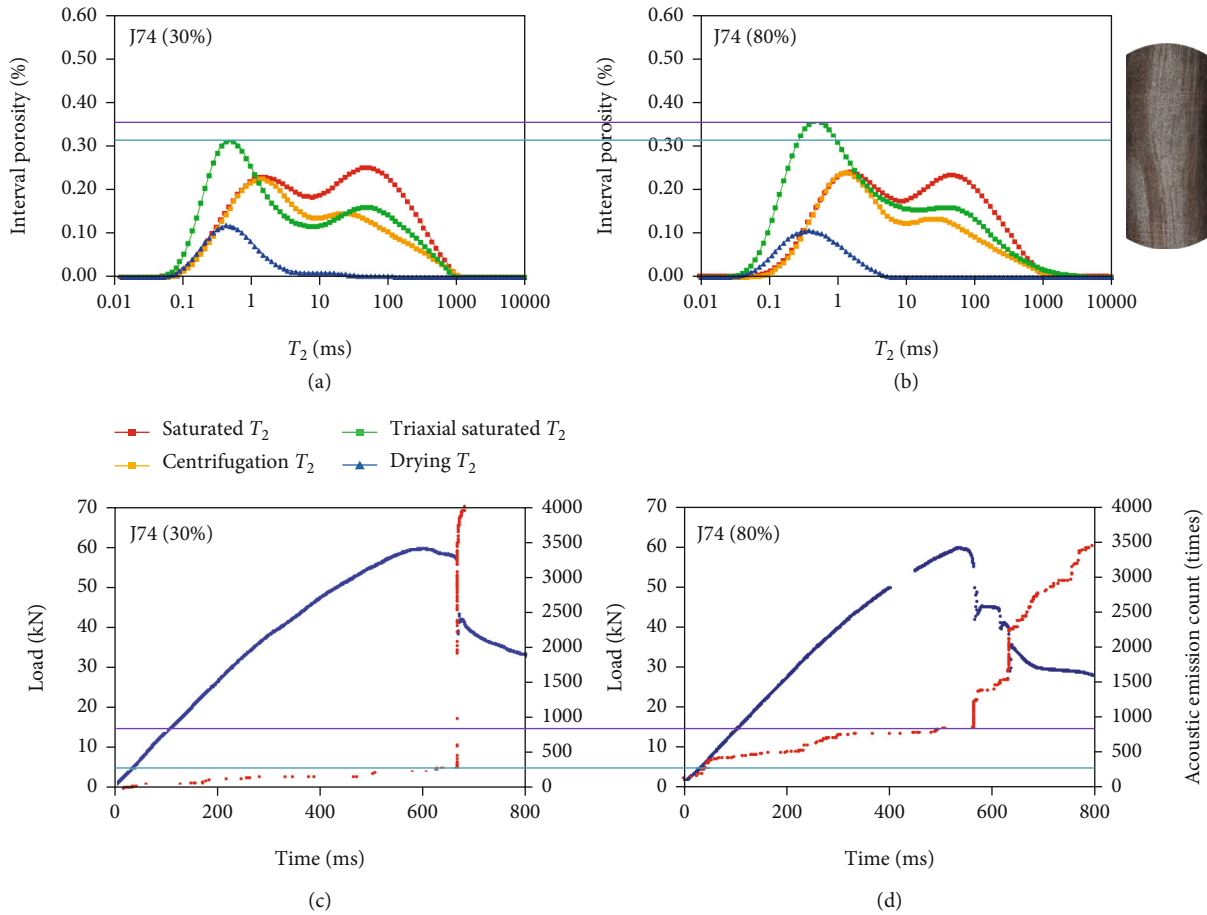


FIGURE 16: Comparison between the NMR experiment and the acoustic emission experiment of well J174 based on a variable saturation: (a) NMR experiment of well J74 with 30% water saturation; (b) NMR experiment of well J74 with 80% water saturation; (c) AE experiment of well J74 with 30% water saturation; (d) AE experiment of well J74 with 80% water saturation.

organic matter contraction or pressure increment after hydrocarbon production.

Corroded fractures are formed when organic acids or underground fluids generated from hydrocarbon formation corrode the rock [14, 16, 17, 58–60]. The organic acids formed from the thermal evolution of organic matter provide H⁺ and metallic elements for complexation, improving the solubility of minerals and affecting their stability. This leads to intragranular or intergranular corrosion. The degree of corrosion is related to the mineral type because different minerals exhibit differing levels of corrosion resistance. Calcite, dolomite, and other carbonates are the most easily corroded, followed by quartz and feldspar. Clay minerals show the highest corrosion resistance (Figure 13).

4.3. Granular Microfractures. Granular microfractures are formed along some fractured grains or particulate joints because of external forces and are mainly related to corrosion [61]. Granular microfractures mainly include intragranular and marginal fractures. Early-stage fractures are filled in the later stages and are less significant; however, once the filling corrodes, the fractures become more connected and significant [62–64]. SEM analysis revealed the intergranular fractures that formed more easily among different minerals but

not within the same mineral type (Figure 14). Owing to different crystal lattices among different minerals, they grow in different directions and thus can easily form intergranular fractures. Within the same mineral type, the formation of intergranular fractures is rare owing to consistent crystal lattice directions. Moreover, the mechanical properties differ among minerals; hence, they deform differently when subjected to the same stress, which also encourages intergranular fractures.

Generally, the Lucaogou Formation mainly developed diagenetic microfractures followed by tectonic microfractures, with little formation of granular microfractures (Figure 15). Statistical analysis of the cast sections showed that tectonic microfractures (directional microfractures) mostly developed near well J174. This indicates that besides the large-scale basin-wide geological activities, small-scale geological activities very likely occurred at this well. Diagenetic microfractures were mainly near well J34, indicating that this site is rich in organic matter and fragile minerals.

5. Results and Discussion

5.1. Relationship between Microfractures and Pore Fluid. The relationship between fractures and the pore fluid was

TABLE 2: Effect of fluids on mechanical properties of the Lucaogou Formation tight sandstones in the Jimsar Sag, Junggar Basin.

Water saturation (%)	Compressive strength (GPa)	Ratio of decrease (%)	Elastic modulus (GPa)	Ratio of decrease (%)	Poisson's ratio	Ratio of increase (%)	Group
0	156.94		29.75		0.259		G1
30	151.44	0.035	22.78	0.23	0.258	0.0039	G1
80	146.12	0.035	20.23	0.11	0.295	0.1434	G1
100	80.58	0.449	7.52	0.63	0.554	0.8780	G1
0	156.33		25.01		0.283		G2
30	146.16	0.065	21.65	0.13	0.284	0.0035	G2
90	90.22	0.321	14.30	0.34	0.289	0.0176	G2
100	80.23	0.191	8.30	0.42	0.446	0.5433	G2
0	146.21		26.35		0.214		G3
30	140.90	0.036	20.99	0.20	0.221	0.0327	G3
70	93.73	0.335	18.88	0.10	0.368	0.6652	G3
100	79.26	0.154	15.36	0.19	0.392	0.0652	G3

TABLE 3: Test data of core sample from well J34.

Sample	Nonbrittle mineral content (%)				Brittle mineral content (%)				
	Clay mineral	Chlorite	Illite	Mixed-layer illite	Quartz	Calcite	Dolomite	Feldspar	Pyrite
J37-1	44	24	59	16	43	1	2	6	4
J37-2	24	10	71	19	63	4	6	1	2
J37-3	28	11	70	19	48	7	4	12	1
J37-4	25	14	55	31	43	8	8	13	3

evaluated in terms of lithomechanical properties. The NMR T_2 spectrum of well J174 revealed additional microfractures and micropores as the water saturation increased. The same results were obtained from the AE experiments. In Figure 16, the curve of the AE count under the purple line indicates the number of microfractures, and that above the purple line indicates fractures. The AE ring count significantly increased as the water saturation increased, indicating the formation of additional microfractures.

The results of the triaxial experiments showed that the deformation parameters of rocks followed different trends depending on the degree of saturation. As the water content increased, the compressive strength and elastic modulus decreased by 45%–65% compared with the dry condition. Moreover, Poisson's ratio increased by 80% compared with the dry condition. These results indicate that the presence of a pore fluid affects the mechanical properties of rocks (Table 2).

As the pore fluid content increased, the compressive strength and elastic modulus decreased more rapidly, Poisson's ratio increased faster, and pore fluids more severely affected the mechanical properties of rocks. Contrarily, as the pore fluid content decreased, the compressive strength and elastic modulus decreased more slowly, Poisson's ratio increased more slowly, and pore fluids less severely affected the mechanical properties of rocks. The AE experiments showed that the AE ring count was proportional to the number of microfractures and significantly increased with increasing pore fluid content, indicating the formation of

additional microfractures. Furthermore, the number of microfractures showed a positive correlation with the pore fluid content.

The pore fluid content affected not only the deformation parameters but also the deformation and failure mechanisms of the rocks. The presence of pore fluid changed the rock strength and deformation because it can relieve the intergranular cohesive strength of rocks and accelerate the molecular motion of fluids. The liquid and gas filling the microfractures generate pore pressure, which partially offsets the total stress imposed on a random section on rocks, including peripheral pressure and tectonic stress. Such pressure decreases the elastic yield strength of rocks and makes them more susceptible to deformation, further affecting the formation and development of internal microfractures in the rocks. The presence of pore fluid also decreases the shear strength of rocks and makes them more susceptible to shear deformation. In summary, the pore fluid content mainly affects the mechanical properties of rocks and controls the developing degree of tectonic fractures. However, changes in the lithomechanical properties have little effect on the development of bedding fractures.

5.2. Relationship between Microfractures and Mineral Composition. Ten rock samples were selected and found to be rich in carbonate and fragile minerals (Table 3). After the samples were sealed, triaxial experiments were conducted. The rocks were compressed and saturated with water at certain degrees of mineralisation. The rock samples were

TABLE 4: NMR test results of samples from well J34.

Sample	Length (cm)	Diameter (cm)	Nuclear magnetic analysis		
			Fracture/microfracture content (%)	Water saturation (%) Saturated	200 psi
J37-1	5.082	2.539	17.33	100	52.15
J37-2	5.051	2.539	3.71	100	84.33
J37-3	5.086	2.531	9.61	100	86.58
J37-4	5.071	2.539	12.72	100	67.12

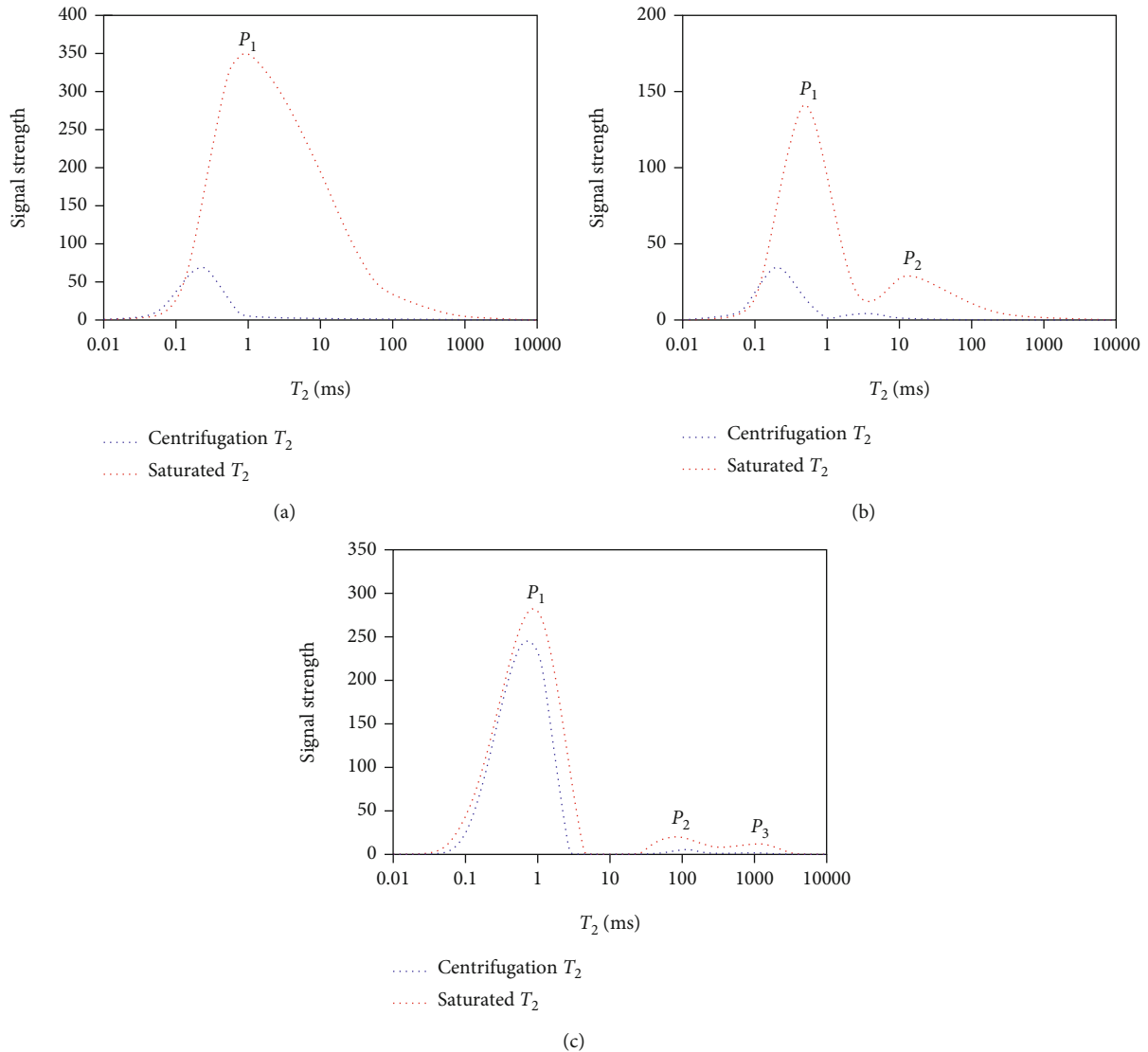


FIGURE 17: T_2 features of samples: (a) NMR of type I fractures; (b) NMR of type II fractures; (c) NMR of type III fractures.

displaced with oil and salts. According to laboratory standards, NMR was then applied to the saturated water cores. The NMR T_2 spectra were used to select rocks according to their microfracture characteristics (Figure 5) and calculate the corresponding fracture/microfracture ratio (Table 4).

The Lucaogou Formation mainly consists of five facies: sand detritus dolomite, micrite dolomite, dolomitic fine siltstone, argillaceous fine siltstone, and mudstone. The first

member of Lucaogou (Lu1) mainly shows three types of sedimentation: graded in situ mixed sedimentation, combined marginal mixed sedimentation, and graded parent-derived mixed sedimentation. The second member of Lucaogou (Lu2) mainly exhibits three types of sedimentation: mutant in situ mixed sedimentation, graded in situ mixed sedimentation, and combined marginal mixed sedimentation. The mechanical properties of the reservoir rocks were mainly

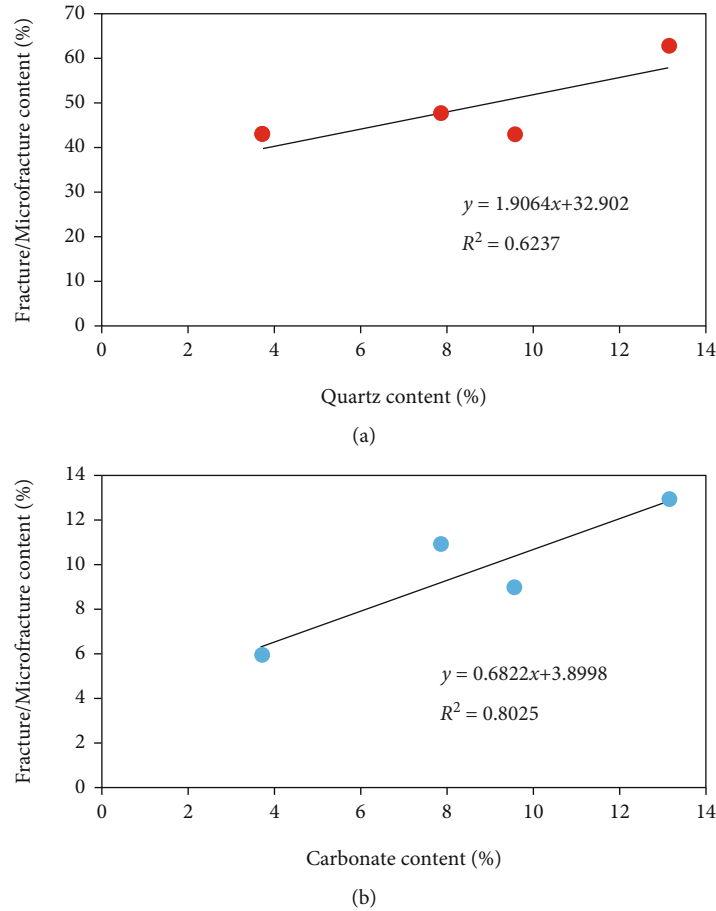


FIGURE 18: T_2 features of samples: (a) relationship between quartz content and microfractures; (b) relationship between carbonate content and microfractures.

affected by two components: (1) brittle components, such as calcareous and siliceous components, and (2) plastic components, such as argillaceous components [65].

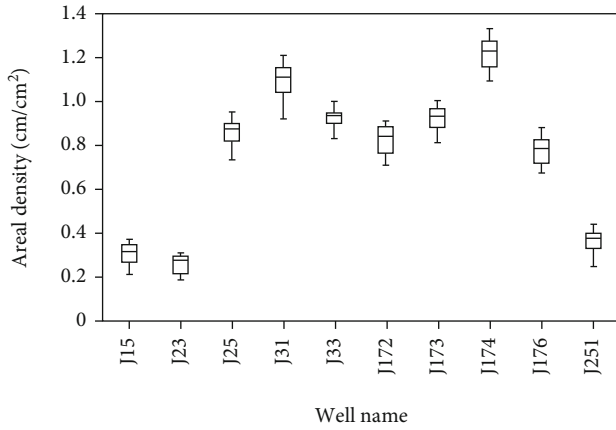
The NMR images after triaxial compression experiments showed that the compressed fractures were mainly distributed as three types. Type I showed only one peak (P_1), and the fractures were distributed in areas with a short relaxation time ($T_2 < 10$ ms), indicating that only tiny pores were formed (Figure 17(a)). Type II exhibited two peaks (P_1 and P_2) distributed in areas with relatively long and short relaxation times, respectively, suggesting the development of tiny pores and microfractures (Figure 17(b)). Type III exhibited three peaks ($P_1 - P_3$) with long relaxation times, suggesting the formation of macrofractures (Figure 17(c)). This type of fracture is difficult to observe using NMR. The presence of macrofractures increased the breakability of the rocks in the centrifugation experiments.

In tight sandstone, a higher quartz content was positively correlated with a larger fracture/microfracture ratio (Figure 18(a)). Moreover, a higher carbonate content was positively correlated with a larger fracture/microfracture ratio (Figure 18(b)). Quartz is mainly composed of SiO_2 . According to the rock rupture mechanism, when quartz grains are stressed, their margins easily form marginal frac-

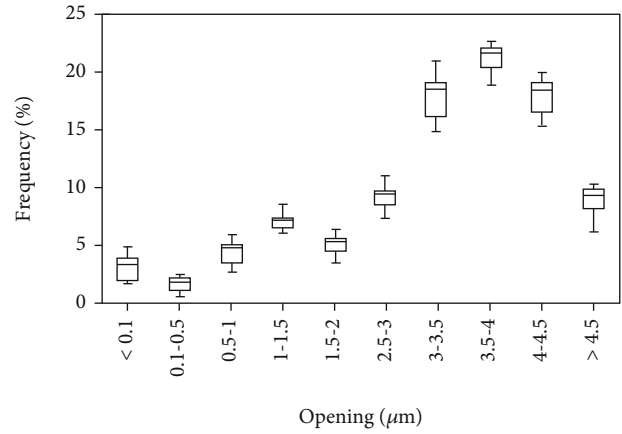
tures, which increase the pore permeability. Rocks containing a high silicon content are more brittle and can more easily form fractures. Furthermore, carbonate minerals are more prone to corrosion, forming corroded microfractures. Rocks with more carbonates can form microfractures more easily.

5.3. Relationship between Microfractures and Lithology. Sections from 10 wells in the study area were sent for granularity analysis. Combined with the lithological data, the sandstone in the study area was found to be generally fine-grained and well separated. Fine-sand and medium-sand rocks accounted for 60% and 23%, respectively. Microfractures also developed in dolomite, dolomitic mudstone, mudstone, and dolomitic fine siltstone. The types and characteristics of microfractures differed depending on lithology. Mudstone was mainly black or grey black and contained few macrofractures. It mainly developed with organic hydrocarbon-producing high-pressure fractures and corroded fractures. The dolomitic mudstone was greyish white and mainly developed with bedding fractures. The dolomitic siltstone was greyish white and mainly developed with bedding fractures and tectonic fractures.

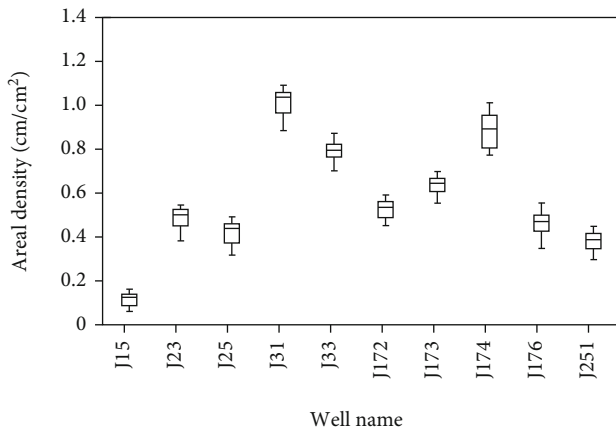
The casting thin sections and 200 SEM images from nearly 20 wells in the Lucaogou Formation were classified



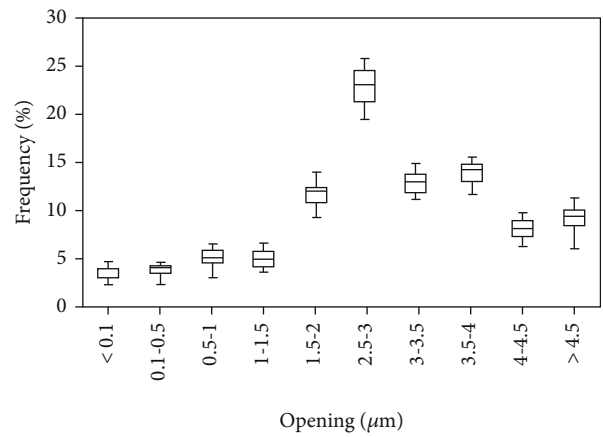
(a)



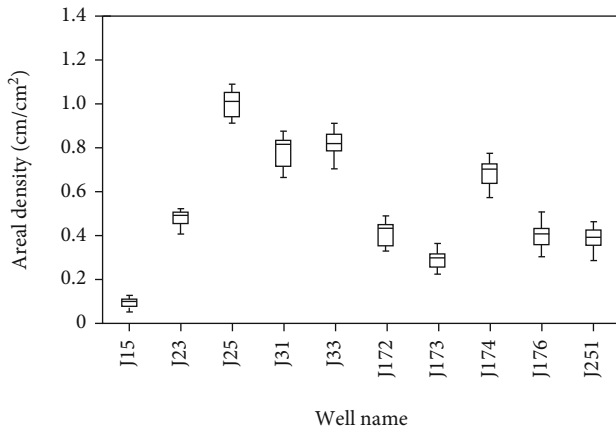
(b)



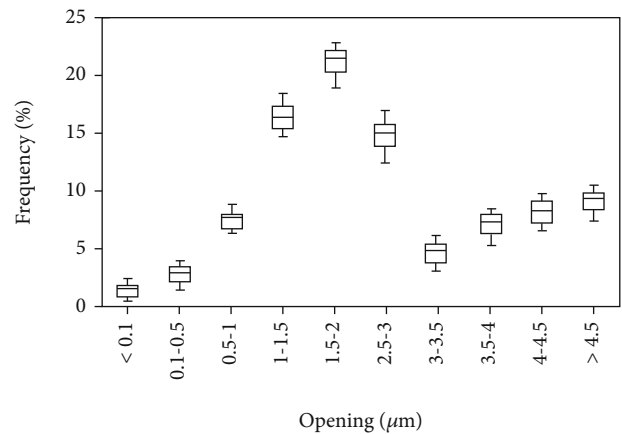
(c)



(d)



(e)



(f)

FIGURE 19: Continued.

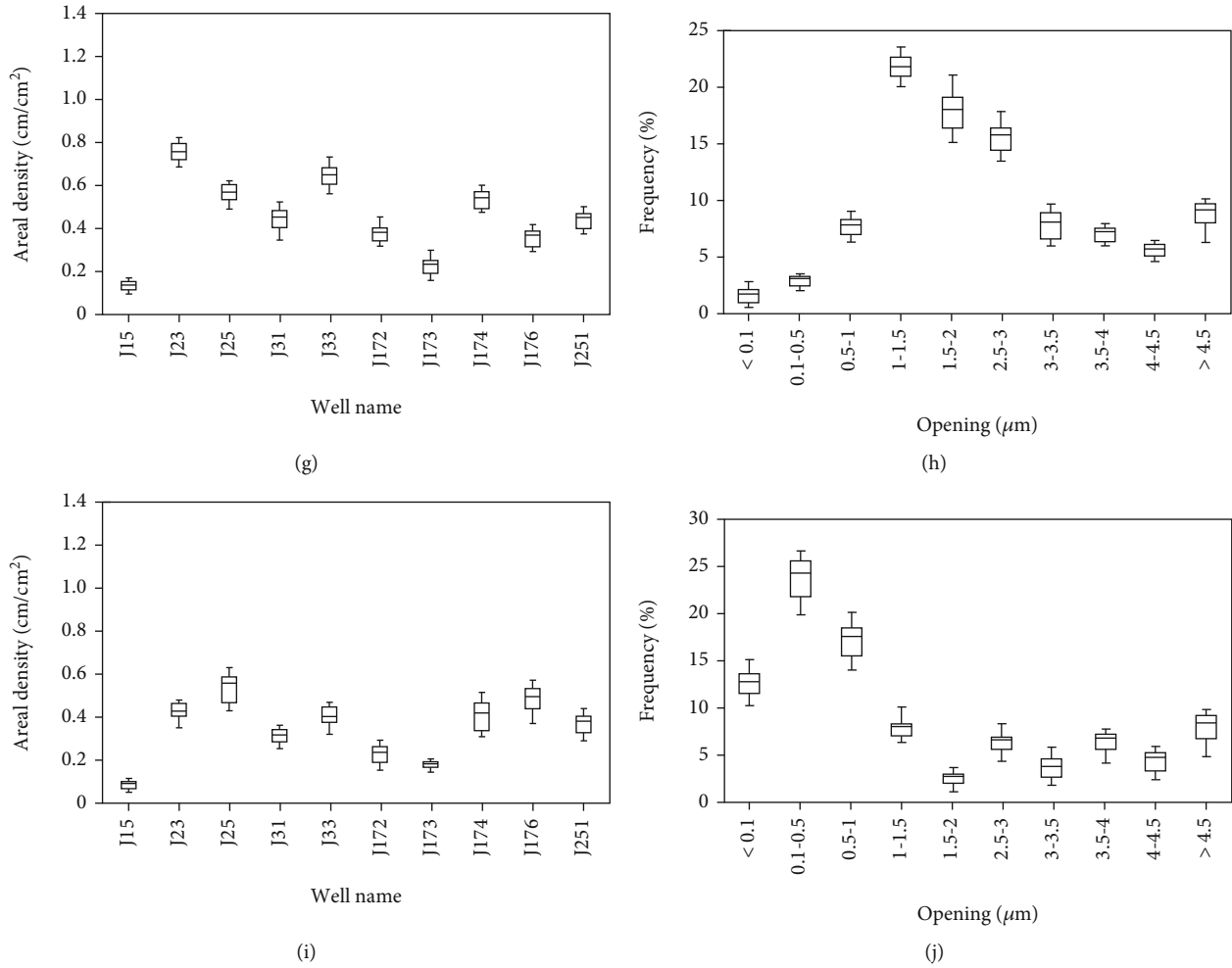


FIGURE 19: The correlation diagram of microfractures and lithology: (a) microfracture surface density of sandy dolomite; (b) microfracture frequency of sandy dolomite; (c) microfracture surface density of micritic dolomite; (d) microfracture frequency of micritic dolomite; (e) microfracture surface density of dolomitic fine sandstone; (f) microfracture frequency of dolomitic fine sandstone; (g) microfracture surface density of argillaceous siltstone; (h) microfracture frequency of argillaceous siltstone; (i) microfracture surface density of mudstone; (j) microfracture frequency of mudstone.

according to lithology, and the microfractures were statistically analysed (Figure 19). The microfractures clearly developed according to the lithology. Generally, dolomite showed the highest microfracture density, followed by dolomitic siltstone, dolomitic mudstone, and mudstone. Hence, the microfracture development was observed to be closely related to lithology.

5.4. Relationship between the Fracture Space and Stratum Thickness. The Lucaogou Formation is enriched with hydrocarbon source rocks and has two major sweet points. The upper sweet point is divided into four sublayers: STD-1, STD-2, STD-3, and STD-4. The lower sweet point is segregated into six sublayers: XTD-1, XTD-2, XTD-3, XTD-4, XTD-5, and XTD-6. Statistical results showed that when the rock mechanical parameters and stress conditions were the same, thin rock layers were more likely to form high-density microfractures than thick rock layers. Because dolomite is rich in carbonate minerals, the microfractures formed from its corrosion affected the results. Hence, the microfrac-

tures in sections collected from sandstone layers of the study area were statistically analysed. The sections from the upper and lower sweet points of the Lucaogou Formation were statistically analysed under microscopy. Up to a stratum thickness of 2.5 m, the average single-well fracture space increased with the stratum thickness and the fracture density decreased. When the stratum thickness was greater than 2.5 m, the fracture space remained constant. Lithomechanical experiments verified that when the same stress ratio was applied for a certain time, the fracture space increased with the stratum thickness.

6. Conclusions

- (1) The Lucaogou Formation mainly developed diagenetic microfractures followed by tectonic microfractures, with little development of granular microfractures. The developing degree of the microfractures showed correlations with the pore

fluid content, mineral composition, lithology, and stratum thickness

- (2) The count of AE events showed a positive correlation with the microfracture density. A higher pore fluid content indicated a lower compressive strength of the rocks and a higher likelihood of microfracture formation
- (3) NMR obtained the fracture/microfracture percentage ratio. A higher fracture/microfracture percentage ratio indicated a higher content of fragile minerals in the rock and thus a higher likelihood of microfracture development
- (4) Thin rock layers were more likely to form high-density microfractures than thick rock layers when the rock mechanical parameters and stress conditions were the same

Data Availability

The main data used to support the study is available within the article. Readers interested in the data can communicate with the corresponding authors and obtain this data by email.

Conflicts of Interest

The authors declare that they have no conflicts of interest.

Authors' Contributions

Xiangye Kong and Haowei Yuan contributed equally to this work.

Acknowledgments

This work is financially supported by grants from the National Natural Science Foundation of China (No. 42002050) and the China Postdoctoral Science Foundation Funded Project (No. 2020M680815).

References

- [1] B. M. Newberry, R. F. Nelson, and U. Ahmed, "Prediction of vertical hydraulic fracture migration using compressional and shear wave slowness," in *SPE/DOE Low Permeability Gas Reservoirs Symposium*, Society of Petroleum Engineers, 1985.
- [2] S. E. Laubach, "Subsurface fractures and their relationship to stress history in East Texas Basin sandstone," *Tectonophysics*, vol. 156, no. 1-2, pp. 37–49, 1988.
- [3] J. C. Lorenz, N. R. Warpinski, P. T. Branagan, and A. R. Settler, "Fracture characteristics and reservoir behavior of stress-sensitive fracture systems in flat-lying lenticular formations," *Journal of Petroleum Technology*, vol. 41, no. 6, pp. 615–622, 1989.
- [4] J. F. Gale, S. E. Laubach, J. E. Olson, P. Eichhubl, and A. Fall, "Natural fractures in shale: a review and new observations," *AAPG bulletin*, vol. 98, no. 11, pp. 2165–2216, 2014.
- [5] R. Wang, Z. Hu, C. Sun et al., "Comparative analysis of shale reservoir characteristics in the Wufeng-Longmaxi (O3w-S1l) and Niutitang (Є1n) Formations: a case study of wells JY1 and TX1 in the southeastern Sichuan Basin and its neighboring areas, southwestern China," *Interpretation*, vol. 6, no. 4, pp. 31–35, 2018.
- [6] D. D. Liu, C. Zhang, Q. Luo et al., "Development characteristics and controlling factors of natural fractures in Permian Lucaogou Formation tight reservoir in Jimsar Sag, Junggar Basin," *China Petroleum Exploration*, vol. 22, no. 4, p. 36, 2017.
- [7] R. G. Miller and S. R. Sorrell, *The Future of Oil Supply*, vol. 372, no. 2006, 2014 The Royal Society Publishing, 2014.
- [8] Z. Xu, P. Zhao, Z. Wang, M. Ostadhassan, and Z. Pan, "Characterization and consecutive prediction of pore structures in tight oil reservoirs," *Energies*, vol. 11, no. 10, p. 2705, 2018.
- [9] B. Yuan and D. A. Wood, "A holistic review of geosystem damage during unconventional oil, gas and geothermal energy recovery," *Fuel*, vol. 227, pp. 99–110, 2018.
- [10] H. Zhang, R. Zhang, Y. Haijun et al., "Characterization and evaluation of ultra-deep fracture-pore tight sandstone reservoirs: a case study of Cretaceous Bashijiqike Formation in Kelasu tectonic zone in Kuqa foreland basin, Tarim, NW China," *Petroleum Exploration and Development*, vol. 41, no. 2, pp. 175–184, 2014.
- [11] W. Xiaoqi, S. Liang, Z. Rukai et al., "Application of charging effects in evaluating storage space of tight reservoirs: a case study from Permian Lucaogou Formation in Jimusar Sag, Junggar Basin, NW China," *Petroleum Exploration and Development*, vol. 42, no. 4, pp. 516–524, 2015.
- [12] W. Huang, S. Lu, O. S. Hersi, M. Wang, S. Deng, and R. Lu, "Reservoir spaces in tight sandstones: classification, fractal characters, and heterogeneity," *Journal of Natural Gas Science and Engineering*, vol. 46, pp. 80–92, 2017.
- [13] B. Liu, Y. Yang, J. Li, Y. Chi, J. Li, and X. Fu, "Stress sensitivity of tight reservoirs and its effect on oil saturation: a case study of Lower Cretaceous tight clastic reservoirs in the Hailar Basin, Northeast China," *Journal of Petroleum Science and Engineering*, vol. 184, article 106484, 2020.
- [14] J. E. Olson, S. E. Laubach, and R. H. Lander, "Combining diagenesis and mechanics to quantify fracture aperture distributions and fracture pattern permeability," *Geological Society, London, Special Publications*, vol. 270, no. 1, pp. 101–116, 2007.
- [15] J. E. Olson, S. E. Laubach, and R. H. Lander, "Natural fracture characterization in tight gas sandstones: Integrating mechanics and diagenesis," *AAPG bulletin*, vol. 93, no. 11, pp. 1535–1549, 2009.
- [16] J. Gallagher Jr., M. Friedman, J. Handin, and G. Sowers, "Experimental studies relating to microfracture in sandstone," *Tectonophysics*, vol. 21, no. 3, pp. 203–247, 1974.
- [17] J.-F. Barthélémy, "Effective permeability of media with a dense network of long and micro fractures," *Transport in porous media*, vol. 76, no. 1, pp. 153–178, 2009.
- [18] D. Tiab and E. C. Donaldson, *Petrophysics: Theory and Practice of Measuring Reservoir Rock and Fluid Transport Properties*, Gulf professional publishing, 2015.
- [19] P. A. Geiser and S. Sansone, "Joints, microfractures, and the formation of solution cleavage in limestone," *Geology*, vol. 9, no. 6, pp. 280–285, 1981.
- [20] S. Yin, D. Lv, and W. Ding, "New method for assessing microfracture stress sensitivity in tight sandstone reservoirs based on acoustic experiments," *International Journal of Geomechanics*, vol. 18, no. 4, article 04018008, 2018.

- [21] W. Wawersik and C. Fairhurst, "A study of brittle rock fracture in laboratory compression experiments," *International Journal of Rock Mechanics and Mining Sciences & Geomechanics Abstracts*, vol. 7, pp. 561–575, 1970.
- [22] L. Germanovich, R. Salganik, A. Dyskin, and K. Lee, "Mechanisms of brittle fracture of rock with pre-existing cracks in compression," *Pure and Applied Geophysics*, vol. 143, no. 1, pp. 117–149, 1994.
- [23] C. Tang, H. Liu, P. Lee, Y. Tsui, and L. Tham, "Numerical studies of the influence of microstructure on rock failure in uniaxial compression—part I: effect of heterogeneity," *International Journal of Rock Mechanics and Mining Sciences*, vol. 37, no. 4, pp. 555–569, 2000.
- [24] K. Bjørlykke, "Lithological control on fluid flow in sedimentary basins," in *Fluid Flow and Transport in Rocks*, pp. 15–34, Springer, 1997.
- [25] J. Wang and S. S. Rahman, "An investigation of fluid leak-off due to osmotic and capillary effects and its impact on microfracture generation during hydraulic fracturing stimulation of gas shale," *EUROPEC*, 2015.
- [26] C. Li, D. Liu, Y. Cai, and Y. Yao, "Fracture permeability evaluation of a coal reservoir using geophysical logging: a case study in the Zhengzhuang area, southern Qinshui Basin," *Energy Exploration & Exploitation*, vol. 34, no. 3, pp. 378–399, 2016.
- [27] K. W. Shanley, R. M. Cluff, and J. W. Robinson, "Factors controlling prolific gas production from low-permeability sandstone reservoirs: implications for resource assessment, prospect development, and risk analysis," *AAPG bulletin*, vol. 88, no. 8, pp. 1083–1121, 2004.
- [28] D. Jinhu, L. He, M. Desheng, F. Jinhua, W. Yuhua, and Z. Tiyao, "Discussion on effective development techniques for continental tight oil in China," *Petroleum Exploration and Development*, vol. 41, no. 2, pp. 217–224, 2014.
- [29] J. Lai, G. Wang, Y. Ran, Z. Zhou, and Y. Cui, "Impact of diagenesis on the reservoir quality of tight oil sandstones: the case of Upper Triassic Yanchang Formation Chang 7 oil layers in Ordos Basin, China," *Journal of Petroleum Science and Engineering*, vol. 145, pp. 54–65, 2016.
- [30] L. C. Kuang, Y. Tang, and D. W. Lei, "Formation conditions and exploration potential of tight oil in the Permian saline lacustrine dolomitic rock, Junggar Basin, NW China," *Petroleum Exploration and Development*, vol. 39, no. 6, pp. 700–711, 2012.
- [31] C. Zhang, D. Zhu, Q. Luo et al., "Major factors controlling fracture development in the Middle Permian Lucaogou Formation tight oil reservoir, Junggar Basin, NW China," *Journal of Asian Earth Sciences*, vol. 146, pp. 279–295, 2017.
- [32] F. Shihu, S. Yan, X. Huaimin, F. Ruidong, L. Loujun, and X. Xiucui, "Relationship between tectonic evolution and petroleum system formation-taking the Jimsar Sag of eastern Junggar Basin as an example," *Petroleum Geology and Experiment*, vol. 29, no. 2, p. 149, 2007.
- [33] M. Wan, W. Yang, L. Liu, and J. Wang, " _Ductoagathoxylon jimsarensis_ gen. nov. et sp. nov., a gymnospermous stem from the Wuchiapingian (upper Permian) Wutonggou Formation in the Junggar Basin, northern Bogda Mountains, northwestern China," *Review of Palaeobotany and Palynology*, vol. 241, pp. 13–25, 2017.
- [34] Y. Su, M. Zha, X. Ding et al., "Pore type and pore size distribution of tight reservoirs in the Permian Lucaogou Formation of the Jimsar Sag, Junggar Basin, NW China," *Marine and Petroleum Geology*, vol. 89, pp. 761–774, 2018.
- [35] Y. Zhi, H. Lianhua, L. Senhu et al., "Geologic characteristics and exploration potential of tight oil and shale oil in Lucaogou Formation in Jimsar Sag," *China Petroleum Exploration*, vol. 23, no. 4, pp. 76–85, 2018.
- [36] L. C. Fuzhong and L. M. Weihua, "The composition of the west section of the Piedmont fault in north margin of Bogda, Xinjiang, mountains and its activity in Holocene," *Inland Earthquake*, vol. 4, 1998.
- [37] Z. Yan, L. Zhensheng, N. Feng, T. Xiaoli, and S. Yonghong, "Age, provenance and tectonic evolution of Late Paleozoic strata in Bogda Mountain, Xinjiang: evidence from detrital zircon U-Pb geochronology," *Chinese Journal of Geology*, vol. 50, no. 1, pp. 155–181, 2015.
- [38] P. C. Hackley, N. Fishman, T. Wu, and G. Baugher, "Organic petrology and geochemistry of mudrocks from the lacustrine Lucaogou Formation, Santanghu Basin, northwest China: application to lake basin evolution," *International Journal of Coal Geology*, vol. 168, pp. 20–34, 2016.
- [39] S. Tao, Y. Wang, D. Tang, D. Wu, H. Xu, and W. He, "Organic petrology of Fukang Permian Lucaogou formation oil shales at the northern foot of Bogda Mountain, Junggar Basin, China," *International Journal of Coal Geology*, vol. 99, pp. 27–34, 2012.
- [40] R. Wang, W. Ding, Y. Zhang et al., "Analysis of developmental characteristics and dominant factors of fractures in Lower Cambrian marine shale reservoirs: a case study of Niutitang formation in Cen'gong block, southern China," *Journal of Petroleum Science and Engineering*, vol. 138, pp. 31–49, 2016.
- [41] A. Ougier-Simonin, F. Renard, C. Boehm, and S. Vidal-Gilbert, "Microfracturing and microporosity in shales," *Earth-Science Reviews*, vol. 162, pp. 198–226, 2016.
- [42] J. Cui, "Oil transport in shale nanopores and micro-fractures: modeling and analysis," *Journal of Petroleum Science and Engineering*, vol. 178, pp. 640–648, 2019.
- [43] R. Zimmerman and I. Main, "Hydromechanical behavior of fractured rocks," *International Geophysics Series*, vol. 89, pp. 363–422, 2004.
- [44] B. L. Parker, J. A. Cherry, and S. W. Chapman, "Discrete fracture network approach for studying contamination in fractured rock," *AQUA mundi*, vol. 3, no. 2, pp. 101–116, 2012.
- [45] D. J. Holcomb, "Memory, relaxation, and microfracturing in dilatant rock," *Journal of Geophysical Research: Solid Earth*, vol. 86, no. B7, pp. 6235–6248, 1981.
- [46] C. H. Sondergeld and L. H. Estey, "Acoustic emission study of microfracturing during the cyclic loading of Westerly granite," *Journal of Geophysical Research: Solid Earth*, vol. 86, no. B4, pp. 2915–2924, 1981.
- [47] L. Liu, S. Ma, J. Ma et al., "Temporal and spatial distribution of microfractures in granites of different structures under triaxial compression and its significance in seismology," *Chinese Science Bulletin*, vol. 44, no. 14, pp. 1321–1325, 1999.
- [48] A. J. Mian, N. Driver, and P. T. Mativenga, "Chip formation in microscale milling and correlation with acoustic emission signal," *The International Journal of Advanced Manufacturing Technology*, vol. 56, no. 1–4, pp. 63–78, 2011.
- [49] N. Golsanami, J. Sun, Y. Liu et al., "Distinguishing fractures from matrix pores based on the practical application of rock physics inversion and NMR data: a case study from an

- unconventional coal reservoir in China,” *Journal of Natural Gas Science and Engineering*, vol. 65, pp. 145–167, 2019.
- [50] T. Sun, W. Yan, H. Wang, N. Golsanami, and L. Zhang, “Developing a new NMR-based permeability model for fractured carbonate gas reservoirs,” *Journal of Natural Gas Science and Engineering*, vol. 35, pp. 906–919, 2016.
- [51] S. Chen, D. Tang, S. Tao, X. Ji, and H. Xu, “Fractal analysis of the dynamic variation in pore-fracture systems under the action of stress using a low-field NMR relaxation method: an experimental study of coals from western Guizhou in China,” *Journal of Petroleum Science and Engineering*, vol. 173, pp. 617–629, 2019.
- [52] K. Sun, S. Zhang, and L. Xin, “Impacts of bedding directions of shale gas reservoirs on hydraulically induced crack propagation,” *Natural Gas Industry B*, vol. 3, no. 2, pp. 139–145, 2016.
- [53] G. Borgia, V. Bortolotti, and P. Fantazzini, “Magnetic resonance relaxation-tomography to assess fractures induced in vugular carbonate cores,” in *SPE Annual Technical Conference and Exhibition*, OnePetro, 1999.
- [54] K. Bjørlykke and K. Høeg, “Effects of burial diagenesis on stresses, compaction and fluid flow in sedimentary basins,” *Marine and Petroleum Geology*, vol. 14, no. 3, pp. 267–276, 1997.
- [55] A. P. Lavenue, J. Lamarche, A. Gallois, and B. D. Gauthier, “Tectonic versus diagenetic origin of fractures in a naturally fractured carbonate reservoir analog (Nerthe anticline, southeastern France) tectonic vs. diagenetic fractures in a naturally fractured reservoir,” *AAPG bulletin*, vol. 97, no. 12, pp. 2207–2232, 2013.
- [56] M. R. Gross and Y. Eyal, “Throughgoing fractures in layered carbonate rocks,” *Geological Society of America Bulletin*, vol. 119, no. 11-12, pp. 1387–1404, 2007.
- [57] X. X. Wang, J. G. Hou, and S. H. Li, “Insight into the nanoscale pore structure of organic-rich shales in the Bakken Formation, USA,” *Journal of Petroleum Science and Engineering*, vol. 191, article 107182, 2020.
- [58] K. Zhang, J. Peng, W. Liu et al., “The role of deep geofluids in the enrichment of sedimentary organic matter: a case study of the Late Ordovician-Early Silurian in the upper Yangtze region and early Cambrian in the lower Yangtze region, south China,” *Geofluids*, vol. 2020, 12 pages, 2020.
- [59] K. Zhang, J. Peng, X. Wang et al., “Effect of organic maturity on shale gas genesis and pores development: a case study on marine shale in the upper Yangtze region, South China,” *Open Geosciences*, vol. 12, no. 1, pp. 1617–1629, 2020.
- [60] Y. Qi, Y. Ju, S. Meng et al., “Geological controls on high production of tight sandstone gas in Linxing Block, Eastern Ordos Basin, China,” *Acta Geologica Sinica-English Edition*, vol. 94, no. 2, pp. 430–443, 2020.
- [61] R. Resende, L. Lamas, J. Lemos, and R. Calçada, “Micromechanical modelling of stress waves in rock and rock fractures,” *Rock mechanics and rock Engineering*, vol. 43, no. 6, pp. 741–761, 2010.
- [62] N. Odling, P. Gillespie, B. Bourguine et al., “Variations in fracture system geometry and their implications for fluid flow in fractures hydrocarbon reservoirs,” *Petroleum Geoscience*, vol. 5, no. 4, pp. 373–384, 1999.
- [63] K.-B. Min, J. Rutqvist, C.-F. Tsang, and L. Jing, “Stress-dependent permeability of fractured rock masses: a numerical study,” *International Journal of Rock Mechanics and Mining Sciences*, vol. 41, no. 7, pp. 1191–1210, 2004.
- [64] A. Baghbanan and L. Jing, “Stress effects on permeability in a fractured rock mass with correlated fracture length and aperture,” *International Journal of Rock Mechanics and Mining Sciences*, vol. 45, no. 8, pp. 1320–1334, 2008.
- [65] M. Marder and S. Gross, “Origin of crack tip instabilities,” *Journal of the Mechanics and Physics of Solids*, vol. 43, no. 1, pp. 1–48, 1995.

Research Article

Characteristics of Organic Macerals and Their Influence on Hydrocarbon Generation and Storage: A Case Study of Continental Shale of the Yanchang Formation from the Ordos Basin, China

Lei Xiao,^{1,2} Zhuo Li ^{1,2}, Yufei Hou,^{1,2} Liang Xu,^{1,2} Liwei Wang,^{1,2} and Youdong Yang^{1,2}

¹State Key Laboratory of Petroleum Resources and Prospecting, China University of Petroleum, Beijing 102249, China

²Unconventional Petroleum Research Institute, China University of Petroleum, Beijing 102249, China

Correspondence should be addressed to Zhuo Li; lizhuopaper@163.com

Received 29 January 2021; Accepted 25 June 2021; Published 15 July 2021

Academic Editor: Julie Pearce

Copyright © 2021 Lei Xiao et al. This is an open access article distributed under the Creative Commons Attribution License, which permits unrestricted use, distribution, and reproduction in any medium, provided the original work is properly cited.

Organic macerals are the basic components of organic matter and play an important role in determining the hydrocarbon generation capacity of source rock. In this paper, organic geochemical analysis of shale in the Chang 7 member of the Yanchang Formation was carried out to evaluate the availability of source rock. The different organic macerals were effectively identified, and the differences in hydrocarbon generation and pore-forming capacities were discussed from two perspectives: microscopic pore development and macroscopic hydrocarbon generation through field emission scanning electron microscopy (FE-SEM) and energy-dispersive spectrum (EDS) analyses, methane isotherm adsorption, and on-site analysis of gas-bearing properties. The results show that the source rock of the Chang 7 member has a high abundance of organic matter and moderate thermal evolution and that the organic matter type is mainly type I. Based on the morphology of the organic matter and the element and pore development, four types of hydrogen-rich macerals, including sapropelite and exinite, and hydrogen-poor macerals, including vitrinite and inertinite, as well as the submacerals, algae, mineral asphalt matrix, sporophyte, resin, semifusinite, inertodetrinite, provitrinite, euvitrinite, and vitrodetrinite, can be identified through FE-SEM and EDS. A large number of honeycomb-shaped pores develop in sapropelite, and round-elliptical stomata develop in exinite, while vitrinite and inertinite do not develop organic matter pores. The hydrogen-rich maceral is the main component of organic macerals in the Chang 7 member of the Yanchang Formation. The weight percentage of carbon is low, so it has good hydrocarbon generation capacity, and the organic matter pores are developed and contribute 97% of the organic matter porosity, which is conducive to hydrocarbon generation and storage. The amount of hydrogen-poor maceral is low, and the weight percentage of carbon is low, and the organic matter pores are not developed, which is not conducive to hydrocarbon generation and storage.

1. Introduction

Organic maceral is a component of organic matter and has an important effect on hydrocarbon generation capacity [1, 2]. The method for identifying macerals in shale is derived from coal petrology, which involves complex sample preparation and uses transmitted light fluorescence to identify different macerals [3–5]. FE-SEM is an effective method to describe and analyze shale pore types and pore structure with simple sample preparation methods and high resolution.

Maceral is clearly visible under FE-SEM. Previous research used FE-SEM to effectively identify the organic maceral of the Shahezi Formation in the Songliao Basin, China, but did not detect the sapropelite and exinite, and the identification methods were not systematic [6]. The amount of research on continental shale is relatively low, and there is less research on the organic maceral of the Ordos Basin. Previous studies have shown that there is heterogeneity in the development of organic matter pores, but they have not studied its correlation with organic maceral [7, 8]. At present,

sapropelite and exinite are generally classified as hydrogen-rich macerals, which is an important support for organic matter in the generation of oil. The higher the content of hydrogen-rich macerals, the higher the hydrocarbon generation capacity will be, while vitrinite and inertinite are classified as hydrogen-poor macerals with low hydrocarbon generation capacity [9]. There is a lack of in-depth research on the difference in hydrocarbon generation and pore-forming capacities of different macerals.

The Ordos Basin is the second largest sedimentary basin in China, and the continental shale of the Chang 7 member of the Yanchang Formation is an important source rock in the region. In this paper, the research focused on Chang 7 shale samples, and FE-SEM combined with EDS methods was used to identify each organic maceral. The contribution of each maceral to the pore-forming capacity of organic matter and the relationship between macerals and hydrocarbon generation potential and gas content were studied. The relationship between organic maceral and hydrocarbon storage capacity was examined from both the microscopic and macroscopic perspectives. This research provides theoretical support for the in-depth understanding of the hydrocarbon generation capacity of organic matter and has a positive effect on the exploration and development of continental shale gas.

2. Regional Geological Characteristics

The Ordos Basin is located in the central part of mainland China, in the western part of the North China Platform, spanning three provinces and two regions (Shanxi, Gansu, Ningxia, and Inner Mongolia). It is bounded by the Yellow River fault to the north, the Weihe River north margin fault to the south, Liupan Mountain and Yinchuan Basin to the west, and the Lishi fault zone with the Lvliang uplift to the east. The basin has experienced a series of complex tectonic movements such as Lvliang, Caledonian, Indosinian, and Yanshan, forming the geological features of the wide and gentle east and narrow west, the well-developed peripheral faults, and the simple structure in the basin [10, 11]. Based on the current structural morphology and basin evolution history, the basin can be divided into six tectonic units: the Yimeng uplift in the north, the Weibei uplift in the south, the western edge thrust belt in the west, the Jinxi folding belt in the east, and the Tianhuan depression and Yishan slope in the central region (Figure 1(a)) [12, 13]. The Triassic Yanchang Formation is one of the important oil-generating reservoirs in the basin. During the sedimentary period, the basin experienced a process of rapid development and then extinction, with the characteristics of the sedimentary evolution cycle. The continental sedimentary system of the river-lake-delta is widely developed. The Yanchang Formation can be divided into ten members from top to bottom. The upper part is composed of shale and thin siltstone, and the lower part is mainly composed of sand-shale interbeds (Figure 1(b)) [14]. In the Chang 7 member, the basin developed to its peak. The sedimentary facies were mainly deep lakes and semideep lakes, with developed organic-rich black shale and a small amount of siltstone and siltstone [15, 16].

3. Samples and Methodology

In this paper, a total of 410 shale samples from the Yanchang Formation were collected from shale gas wells of the Ordos Basin, China. Total organic content (TOC) analysis and rock pyrolysis were conducted on the 410 samples. TOC analysis was performed with a Leco CS230 carbon-sulfur analyzer. One gram of the sample was added to a crucible, and then the inorganic carbon was removed with dilute hydrochloric acid, and the sample was then rinsed with distilled water; the sample was then dried in an oven at 100°C for 12 h to perform TOC measurement. Rock-Eval analysis was carried out using an OGE-II rock pyrolyzer (RIPED, Beijing, China) under programmed heating processes. Then, the Tmax (the temperature at which the maximum number of hydrocarbons is generated) and other thermal parameters were obtained [17]. Vitrinite reflectance (Ro, %) values were identified using an MPM-80-type microspectrophotometer at a temperature of 25°C and a relative humidity of 65%. A total of 79 Ro data points were obtained. A total of 78 samples were used to quantify the organic maceral. Samples were crushed and sieved to a range size of 60~80 mesh, cemented with epoxy resin, and prepared into a 3 cm × 3 cm particle light sheet. According to the characteristics and the color, shape, and intensity of fluorescence under the Leica DM4500P polarizing microscope, the organic macerals were identified and the contents were analyzed by statistical methods.

A Zeiss Merlin field emission scanning electron microscope was used to examine samples at a temperature of 24°C and a relative humidity of 35%. Shale sections of 1 cm × 1 cm were Ar ion-milled to create an ultrasurface and then coated with carbon. The working voltage was set to 2 kV, and the working distance was 3~4 mm. The elemental composition of the mineral was determined using the EDAX ternary integrated system. Methane isotherm adsorption was measured using the FY-KT 1000 isotherm adsorption instrument at a temperature of 40°C and humidity of 2.12%. Samples were prepared by crushing and sieving to a size of 80 mesh and weighing, and 100 g portions were weighed out for moisture equilibrium treatment. The moisture equilibrium was processed for at least four days for each sample. After these pretreatments, samples were put into the apparatus for the isotherm adsorption test [18]. Eight pressure points were measured, and the time for each pressure point to reach equilibrium was not less than 12 hours. Then, the ideal gas equation of state was used to calculate the adsorption capacity of each point, and finally, the isotherm adsorption curve was obtained through regression. The total gas content was measured by on-site analysis using the gas-bearing experiment and the KD-III shale gas field analyzer developed by China University of Petroleum, Beijing.

4. Results

4.1. Organic Geochemistry

4.1.1. Om Richness. The abundance of organic matter is an important parameter for evaluating the quality of source

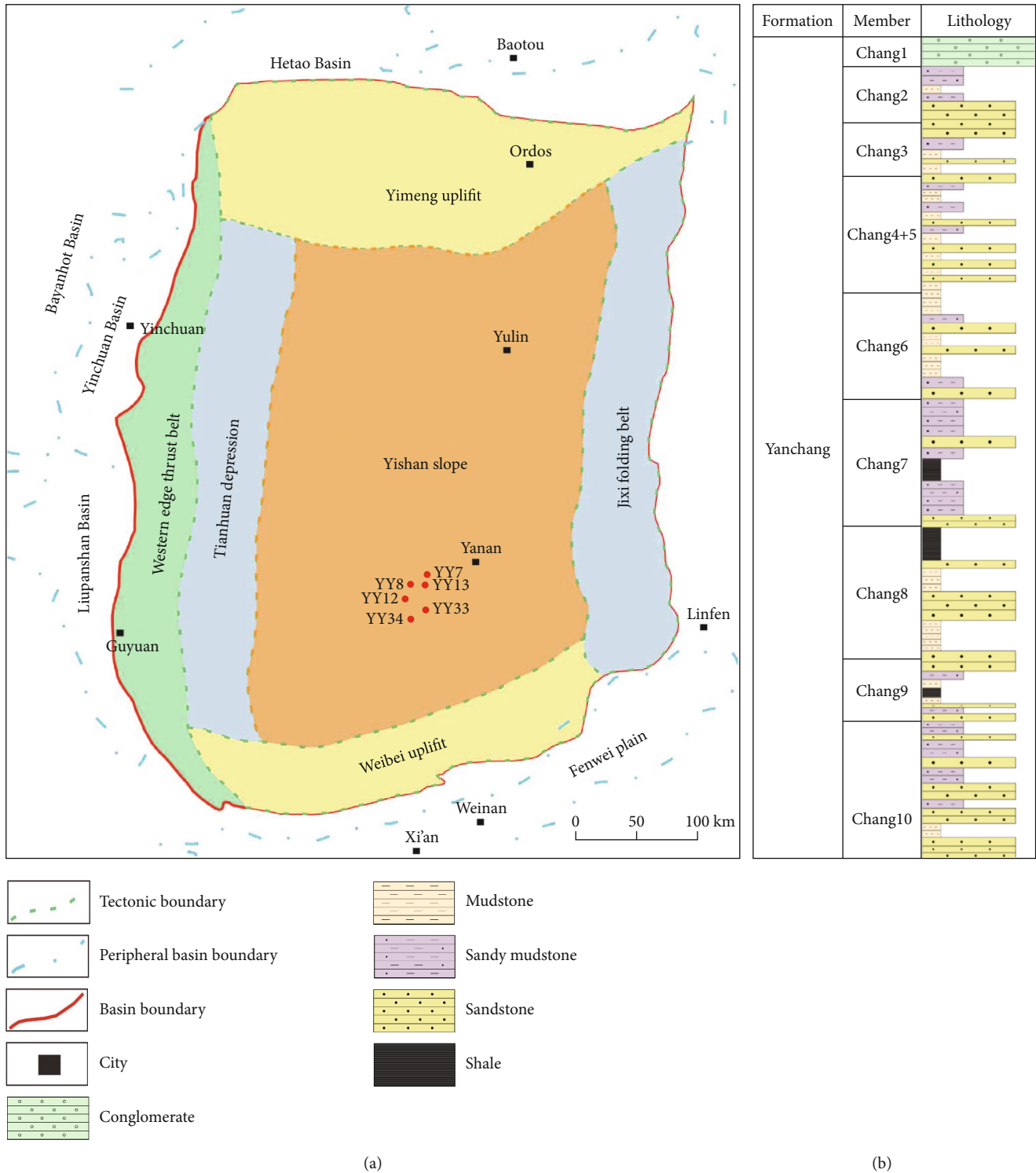


FIGURE 1: (a) The structural zones of the Ordos Basin. (b) The stratigraphic column of the Yanchang Formation in the Ordos Basin.

rocks, usually using TOC, chloroform pitch “A,” and hydrocarbon generation potential ($S_1 + S_2$). A total of 410 samples of the Chang 7 member in the Yanchang Formation were examined by TOC analysis and pyrolysis analysis. Statistics indicated that the TOC of the Chang 7 member shale was 0.2%~13%, with an average of 4.6% (Figure 2(a)); the content

of chloroform pitch “A” was 0.73%~1.75%, with an average of 1.26%; the amount of hydrocarbon generation potential was 0.6~30 mg/g, with an average of 12.9 mg/g, which had a good positive correlation with TOC, indicating that the shale of the Chang 7 member has good hydrocarbon generation potential (Figure 2(b)).

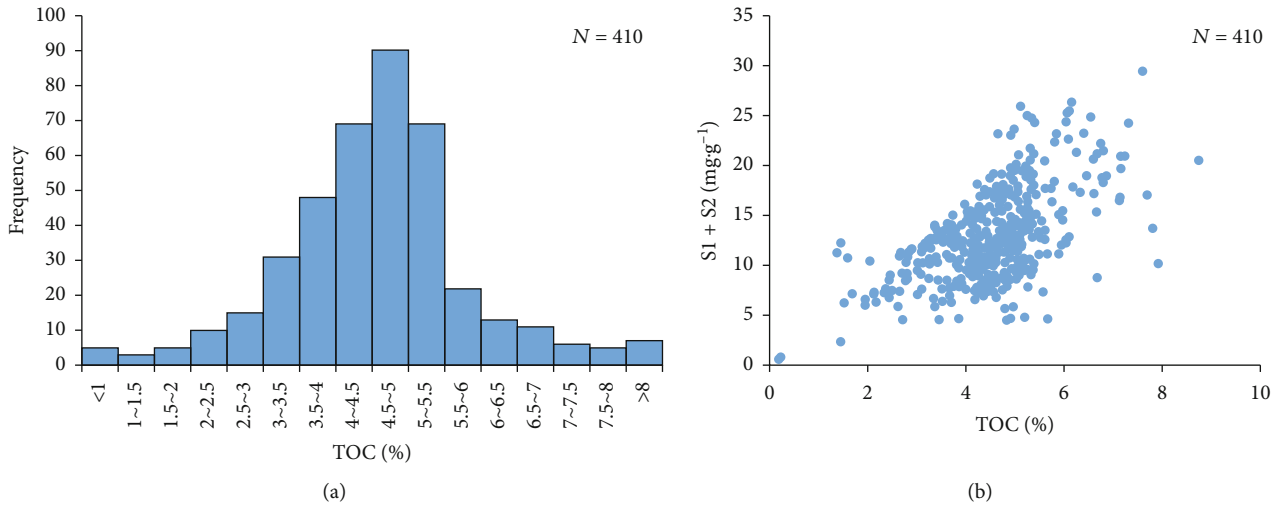


FIGURE 2: (a) The TOC frequency distribution. (b) The relationship between TOC and $S_1 + S_2$.

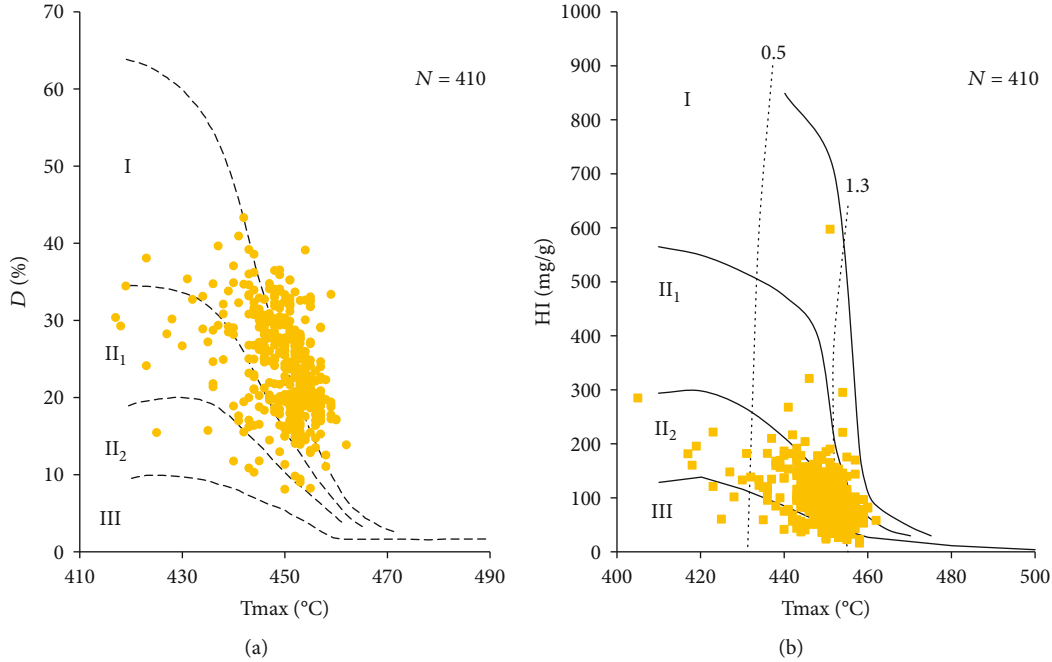


FIGURE 3: (a) Tmax- D crossplot. (b) Tmax-HI crossplot.

4.1.2. Om Type. The ability of source rock to generate hydrocarbon is not only related to the abundance of organic matter but also determined by the type of organic matter. Rock pyrolysis parameters can effectively classify the organic matter types mainly based on the crossplot of the pyrolysis parameters: maximum pyrolysis peak temperature (Tmax) and hydrogen index (HI) or degradation rate (D). Among the samples analyzed in this pyrolysis, D was 8%~43%, with an average of 24%. According to the Tmax- D crossplot (Figure 3(a)), the organic matter of Chang 7 shale was mainly type I with a small amount of type II₁; HI was 16~597 mg/g, with an average of 103 mg/g. According to the Tmax-HI crossplot (Figure 3(b)), the organic matter type was mainly type II. Most of the samples generate hydrocarbon that

migrates out of source rock, which leads to low HI, mostly less than 300 mg/g, and further affects the identification of organic matter types using the Tmax-HI crossplot. In summary, the organic matter type of the Chang 7 member in the Yanchang Formation is mainly type I, with a small amount of type II₁.

4.1.3. Thermal Maturity. The abundance and type of organic matter are the necessary basis components for source rock hydrocarbon generation, but maturity is the necessary condition for determining whether a large amount of hydrocarbon can be generated. Only when the oil generation window or the gas generation window is reached can a large amount of hydrocarbon be generated under the action of heat. At

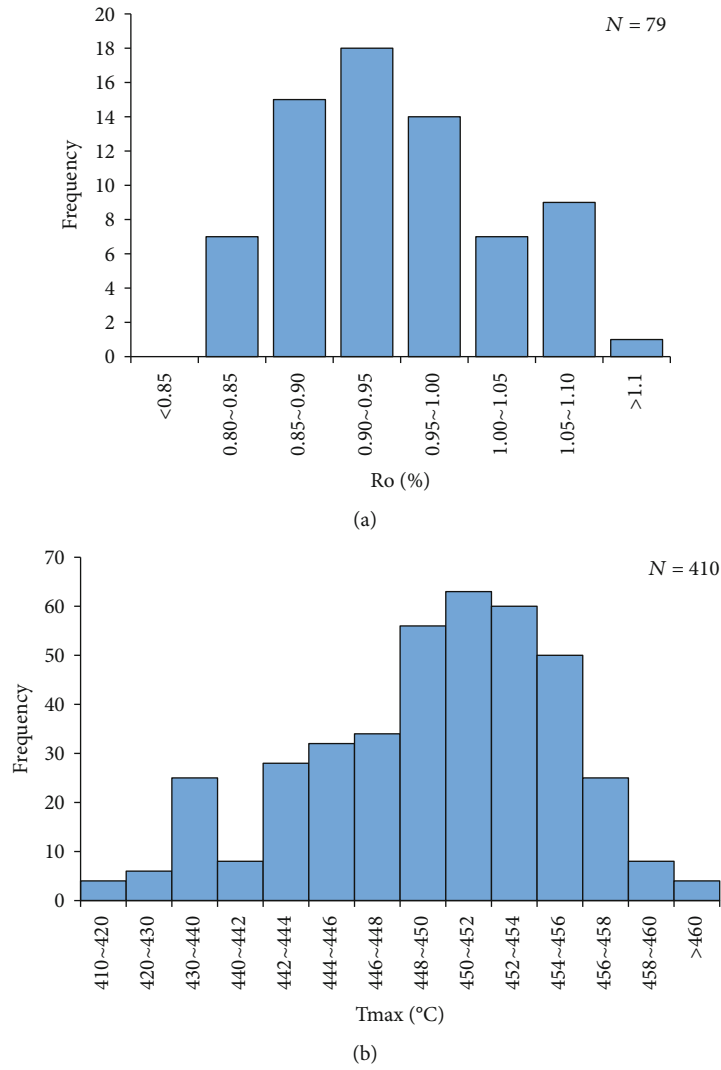


FIGURE 4: (a) The Ro frequency distribution. (b) The Tmax frequency distribution of source rocks in the Chang 7 member.

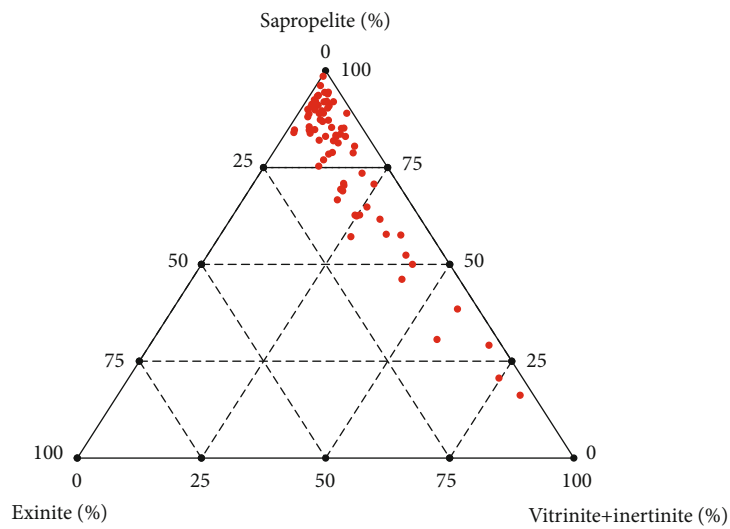


FIGURE 5: The kerogen maceral triangulation in source rocks of the Chang 7 member in the Ordos Basin.

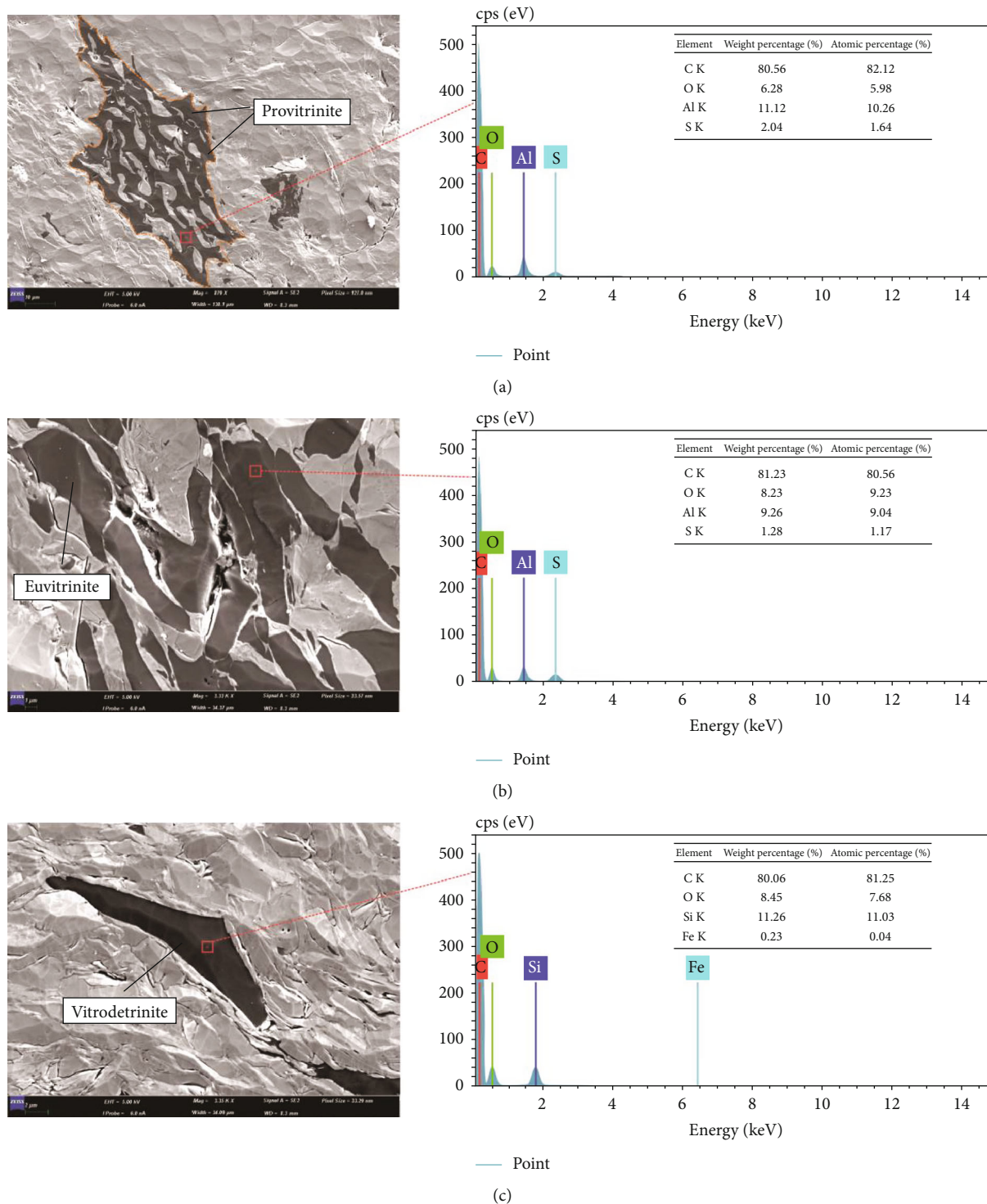


FIGURE 6: Characteristics of vitrinite under FE-SEM. (a) YY33, 1607.30 m, provitrinite. (b) YY33, 1622.80 m, euvitritinite. (c) YY34, 1396.37 m, vitrodetrinite. The EDS of the corresponding points are shown on the right.

present, the commonly used identification indexes are vitrinite reflectance (R_o) and maximum pyrolysis peak temperature (T_{max}). The analysis showed that the R_o was 0.82%~1.09%, with an average of 0.92% (Figure 4(a)); T_{max} was 349°C~462°C, with an average of 448°C (Figure 4(b)).

The Chang 7 shale is in the mature stage and mainly generates oil by kerogen pyrolysis.

4.2. Organic Macerals. The kerogen organic macerals play an important role in classifying organic matter types and

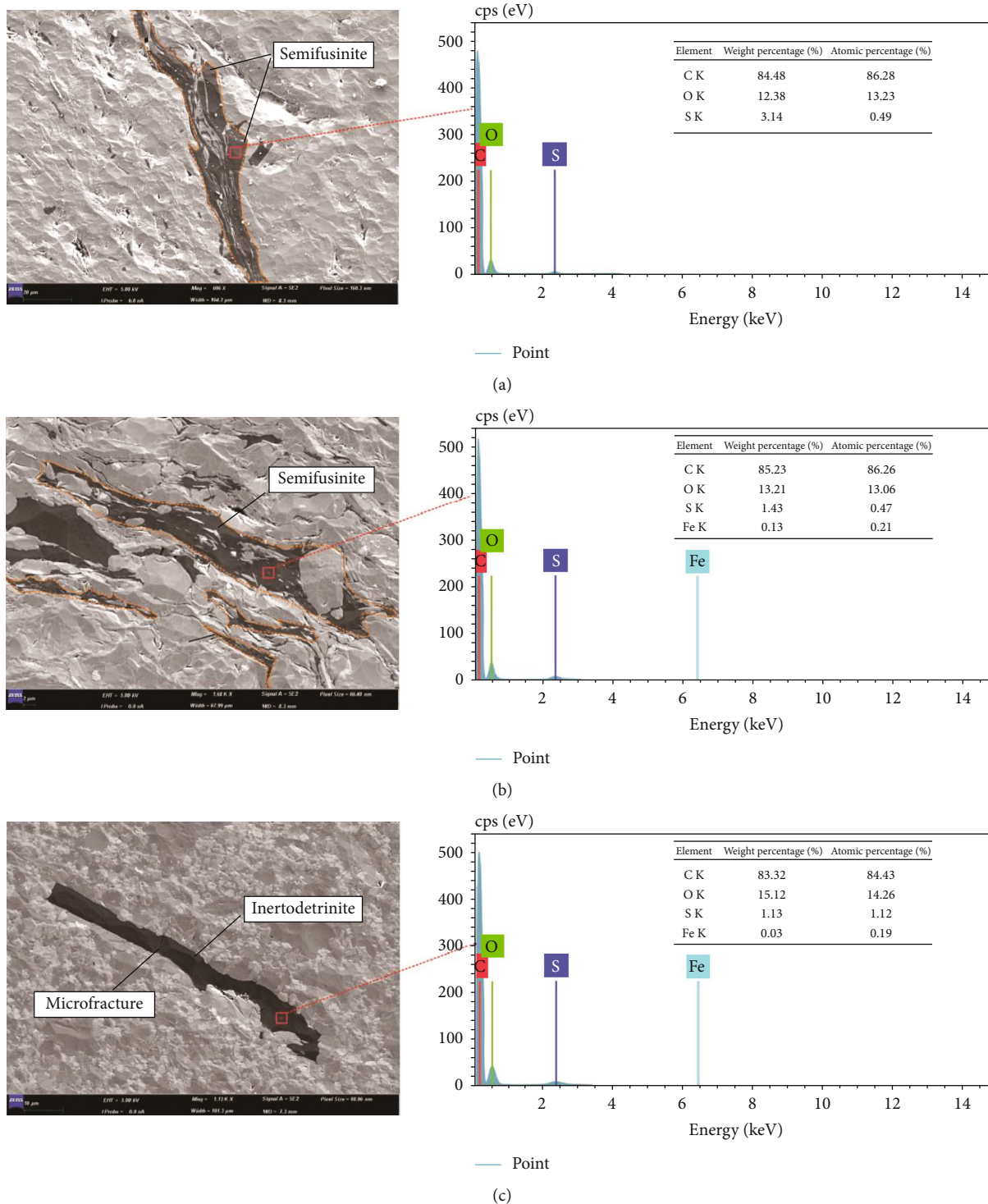


FIGURE 7: Characteristics of inertinite under FE-SEM. (a) YY33, 1622.8 m, semifusinite. (b) YY33, 1622.8 m, semifusinite. (c) YY33, 1622.8 m, inertodetrinite and microfracture. The EDS of the corresponding points are shown on the right.

revealing the hydrocarbon generation potential of source rock. There are various names and classification methods for organic maceral [19, 20]. This article refers to the Chinese standard SY/T 6414 to classify maceral. Through identification and quantitative analysis of macerals of 78 shale samples from the Chang 7 member, it was found that the organic

matter was composed of sapropelite, exinite, vitrinite, and inertinite. The relative percentage content of sapropelite was 16.2%~98.6%, with an average of 77.9%, indicating that it mainly accepted the input of organic matter such as planktonic algae and lower microorganisms; the relative percentage content of exinite was 1.2%~16%, with an average of

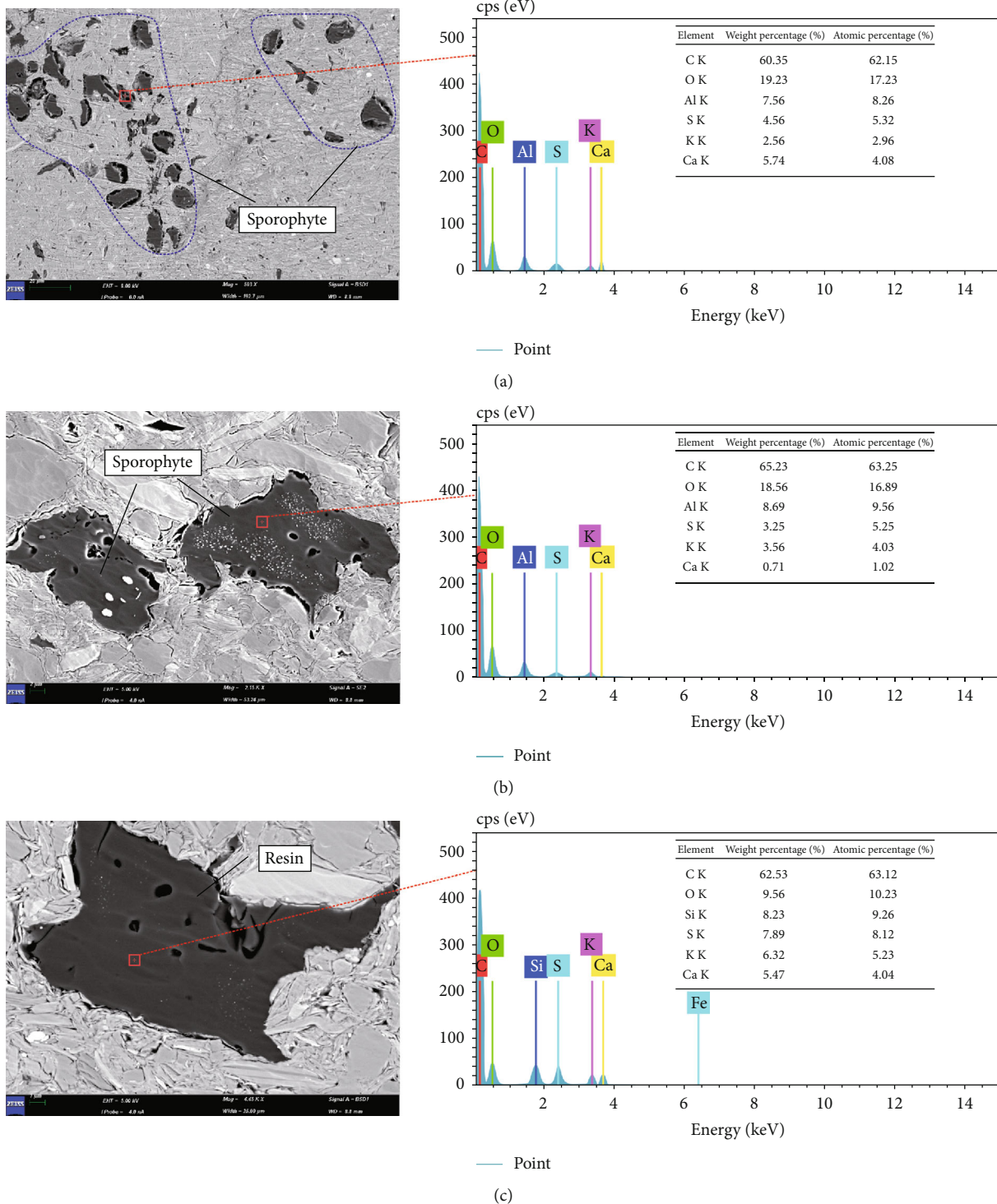


FIGURE 8: Characteristics of exinite under FE-SEM. (a) YY33, 1622.8 m, sporophyte. (b) YY33, 1622.8 m, sporophyte. (c) YY33, 1622.8 m, resin. The EDS of the corresponding points are shown on the right.

7.2%; the relative percentage of vitrinite was 0.2%~81.1%, with an average of 13.8%; the relative percentage of inertinite was 0.4%~8.9%, with an average of 1.0%. The kerogen maceral triangulation showed that sapropelite is the main component of the Chang 7 shale kerogen, and the organic matter was mainly type I (Figure 5).

4.2.1. Vitrinite. Vitrinite is the product of humification and gelation of the wood fiber tissue of higher plants [21]. Vitrinite has a darker color, smooth surface, and uniform texture, is enriched in bands or clumps, and generally does not develop pores under FE-SEM. Due to the difference in the degree of gelation, the cell structure of the original plant is

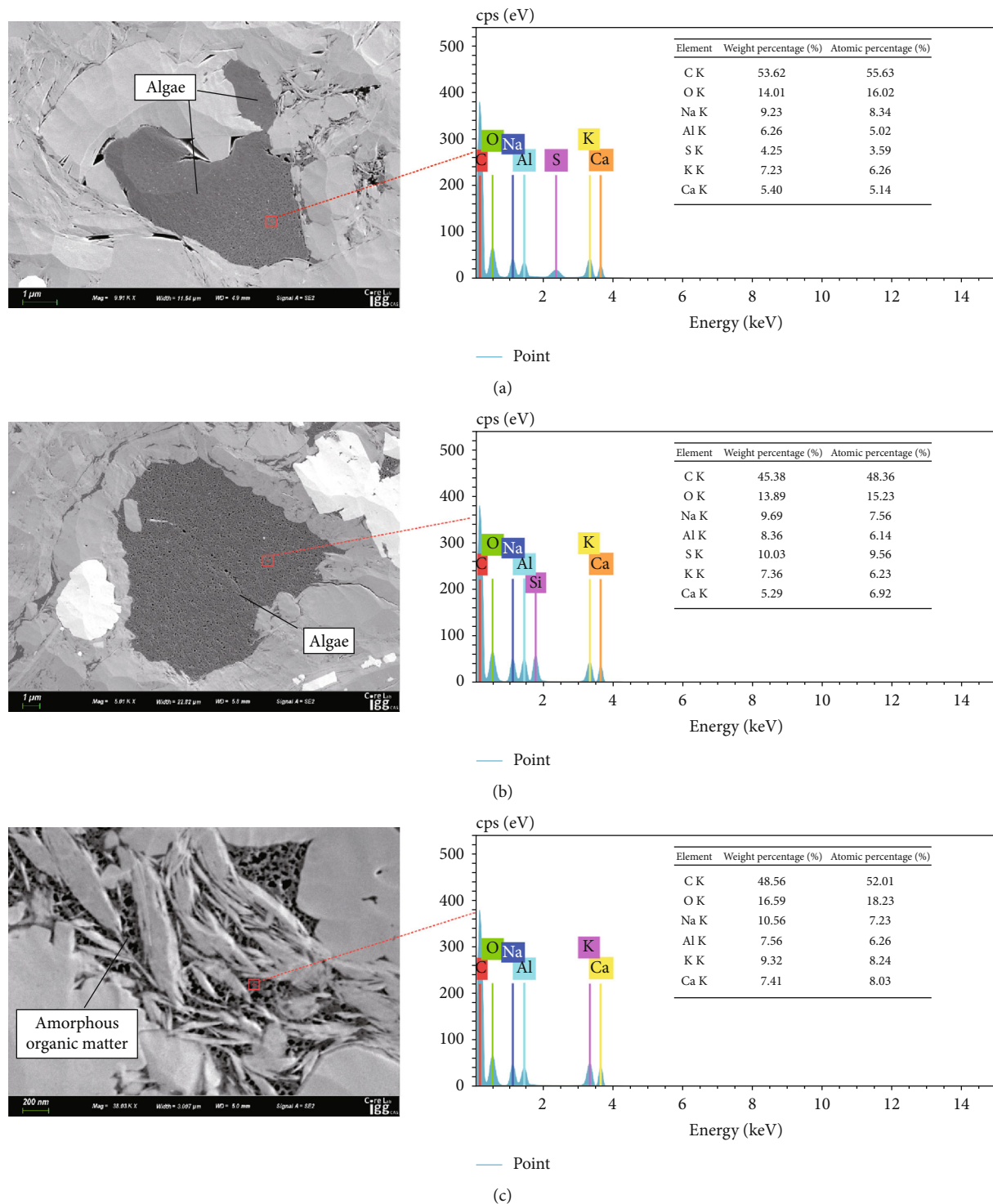


FIGURE 9: Characteristics of sapropelite under FE-SEM. (a) YY33, 1622.8 m, algae. (b) YY33, 1622.8 m, algae. (c) YY7, 1153.35 m, amorphous organic matter. The EDS of the corresponding points are shown on the right.

preserved differently. Based on this, vitrinite can be subdivided into provitrinite, euvitrinite, and vitrodetrinite. Provitritinite can be clearly observed under the electron microscope in the cell wall and cell cavity structure of the original plant. The cell wall often deforms and bends under compaction, and the cell cavity becomes different in shape

due to pressure, which is oval or arc-shaped. The interior is often filled with inorganic minerals (Figure 6(a)). The cell structure of the primitive plants of euvitrinite is not visible under strong gelation. The results showed that the euvitrinite of the Chang 7 member is mainly matrix vitrinites, which have smooth surfaces, dense texture, rich shapes, and bands

TABLE 1: Main identification features of organic macerals under FE-SEM for Chang 7 shale in the Ordos Basin.

Maceral	Submaceral	Characteristics under FE-SEM	EDS
Vitrinite	Provitrinite	Visible cell structure, distorted cell wall, cell cavity filled with inorganic minerals, undeveloped pore	C: 80%~90%
	Euvitritinite	Invisible cell structure, banded and cloddy, undeveloped pore	O: <10%
	Vitrodetrinite	Obvious protrusions, fragmentary with sharp edges, undeveloped pore	
Inertinite	Semifusinite	Swelling cell wall, combined with the surrounding matrix tightly, cell cavity filled with minerals, ribbon-shaped, underdeveloped pore	C: 80%~90%
	Inertodetrinite	Invisible cell structure, fragmentary with angular, arc-shaped, or other morphologies, transverse microcracks developed	O: >10%
Exinite	Sporophyte	Ellipsoidal, worm-like, and irregular shapes, cluster distribution round-elliptical large pores developed	C: 60%~70%
	Resin	Elliptical or irregular without cell structure, flat surface, circular-elliptical large pores developed	O: >10%
Sapropelite	Algae	Various shapes, cluster distribution, uneven surface, jagged edges, honeycomb-shaped pores developed	C: 40%~60%
	Mineral asphalt matrix	No fixed shape, unclear outline, mixed with inorganic minerals, large honeycomb pores developed	O: >10%

and clumps (Figure 6(b)). Vitrodetrinite is the detrital particles of vitrinite, mainly derived from peat-decomposed plants. The cell structure of the plant is not visible under FE-SEM, but the protrusions are obvious, often in the shape of bones and sharp edges (Figure 6(c)). EDS showed that the weight percentage of carbon in vitrinite was generally 80~90%, and the weight percentage of oxygen was generally less than 10%. Vitrinite is formed in a reducing environment and therefore has a low oxygen weight percentage [22].

4.2.2. Inertinite. Inertinite is formed by the carbonization of higher plants [23]. It is gray-black under FE-SEM, usually grid-like, ribbon-like, clump-like, and angular. The submacerals observed in samples are mainly semifusinite and inertodetrinite. Semifusinite is a component between fusinite and provitrinite. The cell wall swells strongly, and it is combined tightly with the surrounding matrix. The cell cavity is compressed and becomes smaller, filled with minerals. Semifusinite is ribbon-shaped, with underdeveloped pores (Figures 7(a) and 7(b)). Inertodetrinite is the fragments of fusinite, semifusinite, and sclerotinite. The cell structure of plants is not visible. It is gray-black, with angular, arc-shaped, and other morphologies, and it can develop transverse microcracks (Figure 7(c)). It is difficult to distinguish between vitrinite and inertinite under FE-SEM.

Inertinite and vitrinite have similar shapes and structures, which are not easy to distinguish under FE-SEM, but the two can be effectively identified with the help of EDS. EDS showed that the weight percentage of carbon in inertinite was generally 80%~90%, which was similar to vitrinite, but the weight percentage of oxygen was generally greater than 10%, which was significantly higher than vitrinite. This was mainly because the inertinite was formed in an oxidation environment, and the vitrinite was formed in a reducing environment, so the weight percentage of oxygen in inertinite was higher than that in vitrinite [22]. In addition, the inertinite had a higher protrusion, which is also an effective way to distinguish it from vitrinite.

4.2.3. Exinite. Exinite is derived from stable organs or metabolites in higher plants, such as resin and essential oil. It has good chemical stability and is not damaged by biochemical processes, so it is a good hydrocarbon generation material [21]. It had a high brightness under FE-SEM. Two submacerals, sporophyte and resin, were mainly observed in samples. Sporophyte is derived from the reproductive organs of plants and can be divided into macrospores (>0.1 mm) and microspores (<0.1 mm) according to their morphological size. Most of the microspores observed under FE-SEM have ellipsoidal, worm-like, and irregular shapes, with low-medium protrusions, often distributed in groups, with round-elliptical large pores (Figures 8(a) and 8(b)). The resin is mainly formed by plant waxes, resins, and lipids and is generally regarded as a good hydrocarbon generation material. The surface was flat, the inside is uniform, and the shape was elliptical or irregular without cell structure, and there were circular-elliptical large pores (Figure 8(c)).

Previous studies have shown that the combination of organic matter and inorganic minerals is more likely to lead to the formation of organic matter pores [24]. Compared with other inorganic minerals, clay minerals are more likely to catalyze the formation of gaseous hydrocarbons [25]. In the process of hydrocarbon expulsion and pore generation, affected by the catalysis of clay minerals, the EDS of the organic matter showed inorganic mineral elements such as Al, K, Mg, and Si. The weight percentage of carbon was found to be generally 60 to 70%, and the weight percentage of oxygen generally exceeded 10%. The influencing factors that control the development of organic matter pores are complicated. The hydrocarbon generated and organic acids may also be involved. This area requires needs further study to elucidate the mechanism.

4.2.4. Sapropelite. Sapropelite is the product of saprofication of lower aquatic organisms, such as algae [21]. Similar to exinite, it is a hydrogen-rich and oxygen-poor maceral in the source rock, which tends to generate oil. It is an excellent

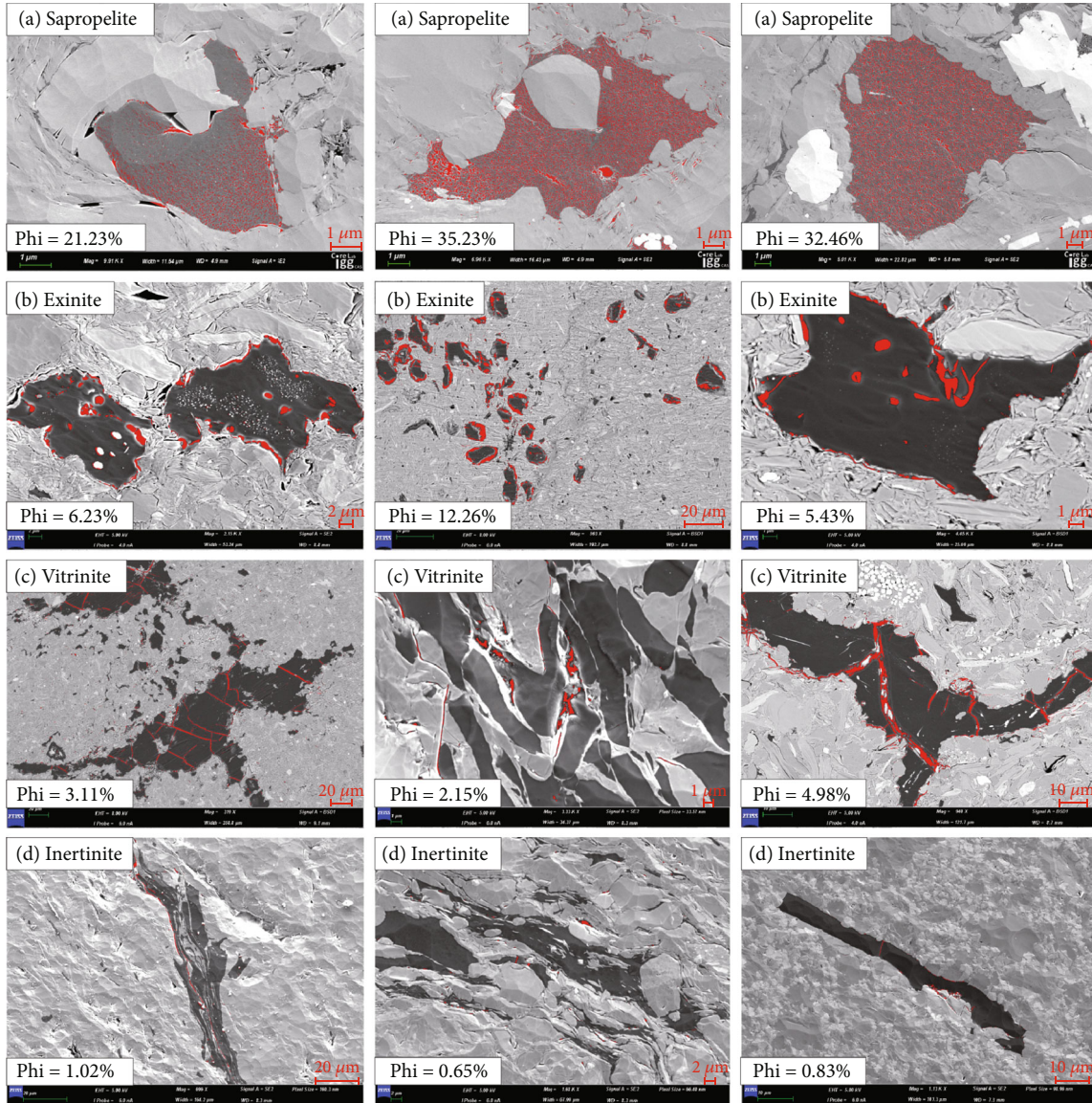


FIGURE 10: Schematic diagram of the Phi of each maceral extracted using the IPP software.

hydrocarbon generation material and the main component of the Chang 7 kerogen organic maceral. The color was lighter under FE-SEM. Two submacerals, algae and amorphous organic matter, were mainly observed in samples. Algae are the remains of single-celled or multicelled lower aquatic organisms and an important part of the hydrocarbon generation maceral. The algae had various shapes, with the characteristics of cluster distribution, uneven surface, and honeycomb-shaped pores, and the edges were often jagged under FE-SEM (Figures 9(a) and 9(b)).

Amorphous sapropelite mainly appears in the form of a mineral asphalt matrix, which is a composite of organic matter and inorganic minerals. The results showed that the mineral asphalt matrix of the Chang 7 member accounted for the absolute proportion of organic matter, with an average of more than 50%, and plays an important role in hydrocarbon generation and the evaluation of source rock. The mineral asphalt matrix had no fixed shape, an unclear outline, was

TABLE 2: The contribution of each maceral to the organic matter pores of the Chang 7 member.

Organic maceral	Weight percentage (%)	Average Phi (%)	Contribution	Percentage contribution (%)
Sapropelite	77.94	25.8	0.20109	94.96
Exinite	7.23	6.2	0.00448	2.12
Vitrinite	13.77	4.4	0.00606	2.86
Inertinite	1.06	1.1	0.00012	0.06

mixed with inorganic minerals, and developed a large number of honeycomb pores (Figure 9(c)). The sapropelite was affected by the catalysis of clay minerals during the hydrocarbon generation process. The EDS showed inorganic mineral elements such as K, Na, Mg, Al, and Si, and the weight percentage of carbon was low, generally 40~60%, and the weight

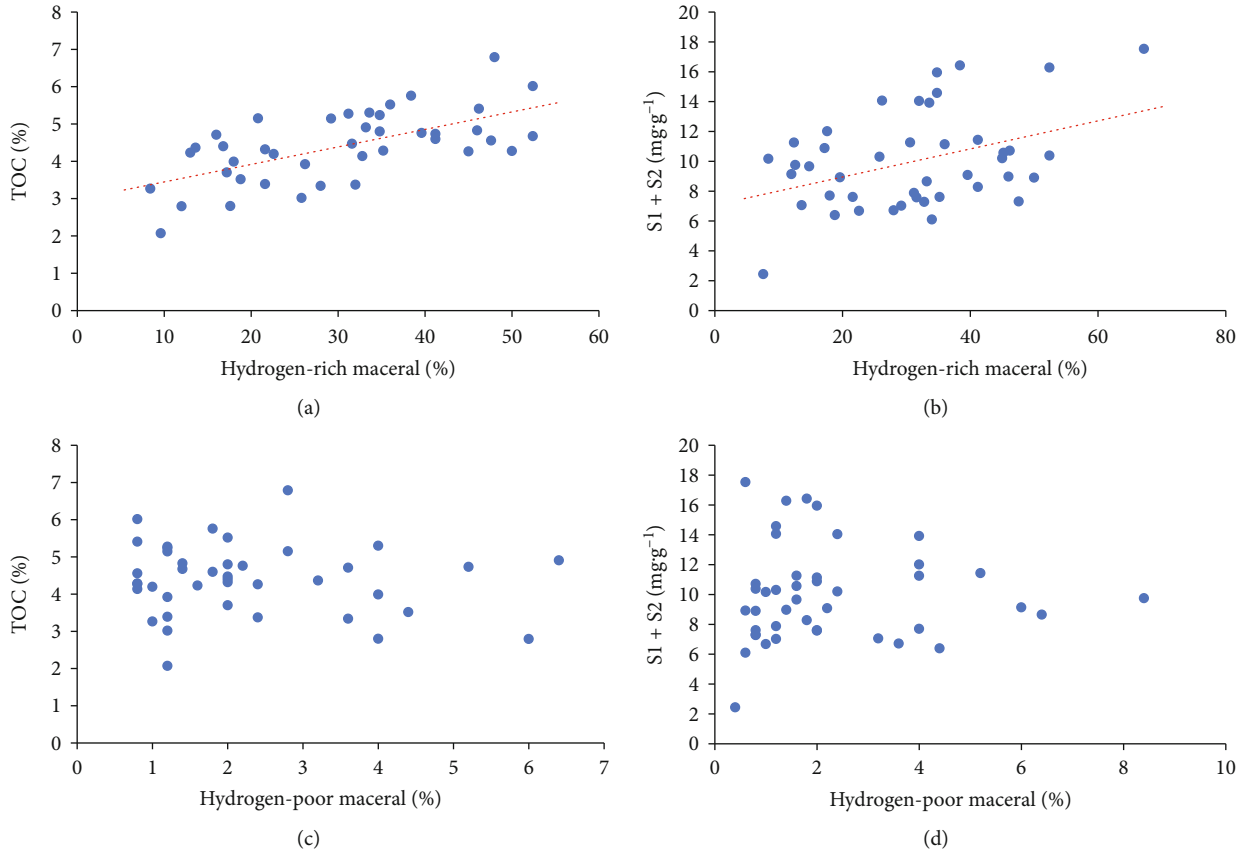


FIGURE 11: Relationships between macerals and TOC and $S_1 + S_2$.

percentage of oxygen generally exceeded 10%. The higher the weight percentage of carbon, the worse the hydrocarbon generation potential. Sapropelite had the best hydrocarbon generation potential, followed by exinite, vitrinite had a poor hydrocarbon generation potential, and inertinite had the worst generation potential.

4.2.5. Synthetic Discrimination of Organic Macerals. Based on FE-SEM and EDS, the organic macerals can effectively be identified by their morphology and elemental composition. Sapropelite and exinite had higher brightnesses, and the organic matter pores were developed. Sapropelite developed honeycomb-shaped pores, and exinite developed round-elliptical large pores. EDS showed that the oxygen of the two is greater than 10%. The carbon of sapropelite was 40%~60%, while that of exinite was 60%~70%. Vitrinite and inertinite were dark with undeveloped organic matter pores under FE-SEM. EDS showed that the carbon of the above was 80%~90%. The oxygen of vitrinite was less than 10%, while that of inertinite was greater than 10%. The higher protrusion of inertinite was also an effective auxiliary method to distinguish it from vitrinite. The identification method of each submaceral is shown in Table 1.

5. Discussion

5.1. Control of Organic Matter Porosity by Macerals. It is assumed that the organic matter pores in the shale are evenly

distributed, and the plane porosity of the entire space (Φ) on any organic matter section is equal. Therefore, the sample can be used to deduce the organic matter porosity through several scanning electron microscope pictures. The pore parameters were extracted using the Image-Pro Plus (IPP) software. First, the target area was selected; then, an appropriate gray value was set to divide the pore and matrix; and finally, the required parameters were selected. This study used Φ as the analysis parameter. Prior studies have done a lot of research on the methods to calculate organic matter porosity [26, 27]; the calculation formula is as follows:

$$\varphi_{\text{org}} = \varphi_s \times \frac{\omega_{\text{TOC}}}{100} \times \frac{\rho_s}{\rho_{\text{org}}} \times 100\%, \quad (1)$$

where φ_{org} , φ_s , and ω_{TOC} are the organic matter porosity, plane porosity of the entire space, and the weight percentage of organic matter, respectively; ρ_s represents the shale density, which is 2.6 g/cm³; and ρ_{org} represents the density of organic matter, which is 1.2 g/cm³.

Using the shale sample of 1622.8 m of YY33 as an example, the results of extracting the Φ of each maceral under FE-SEM through the IPP software are shown in Figure 10. The Φ of sapropelite was 20%~40%; the Φ of exinite was 5%~10%; the Φ of vitrinite was 2%~5%; the Φ of inertinite was <2%. According to the formula, the organic porosity of the sample was 0.97%.

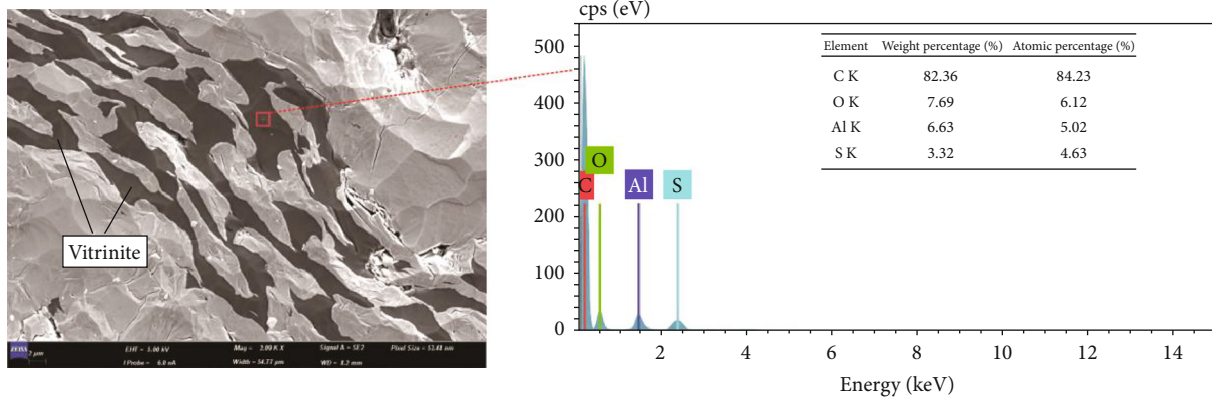
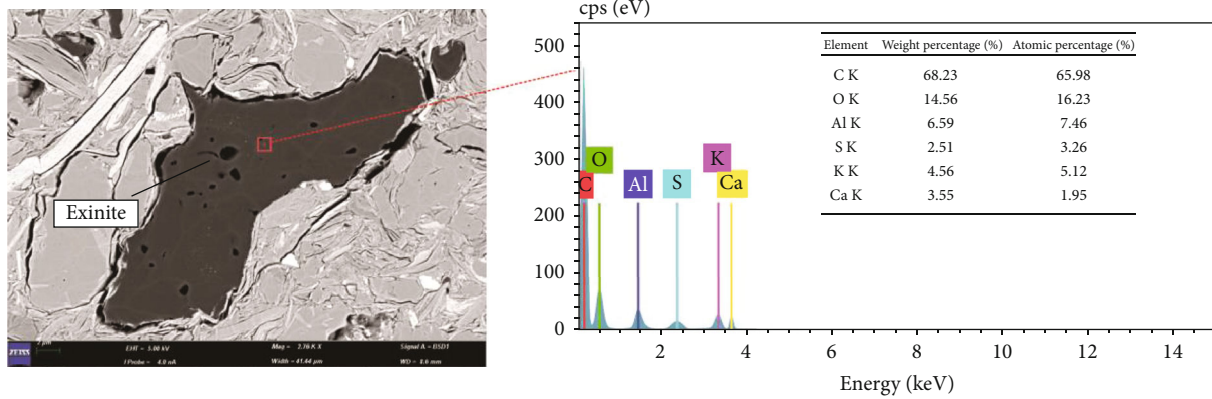
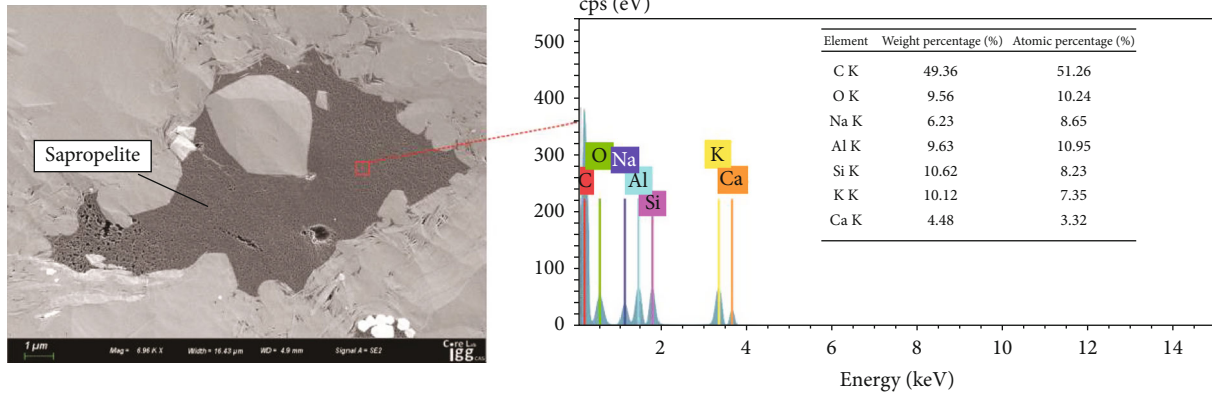


FIGURE 12: Continued.

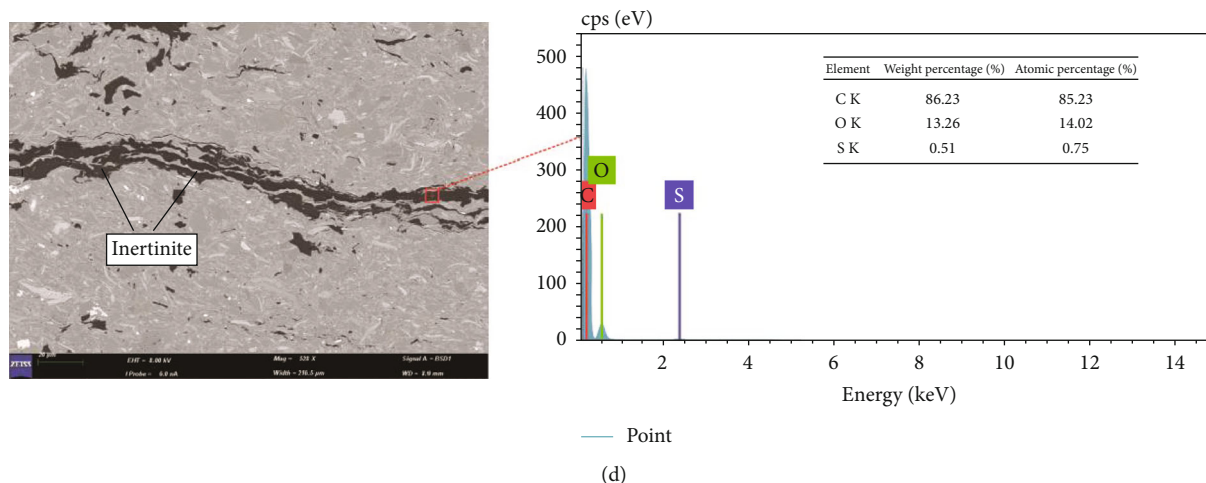


FIGURE 12: EDS of different macerals. (a) YY34, 1388.97 m, sapropelite. (b) YY8, 1451.04 m, exinite. (c) YY12, 1624.29 m, vitrinite. (d) YY13, 1206.44 m, inertinite. The EDS of the corresponding points are shown on the right.

The organic matter porosity of the Chang 7 shale samples was calculated to be between 0.44% and 1.06%, and the contribution to the total porosity was about 11% to 47%, accounting for an average of 26%. Limited by the accuracy of the software, pores smaller than 5 nm were not included, so the actual organic matter porosity should be greater. As mentioned above, observations under FE-SEM found that there were great differences in the degree of organic matter pore development of different macerals. The hydrogen-rich macerals sapropelite and exinite developed large organic matter pores, while the organic matter pores of hydrogen-poor macerals vitrinite and inertinite were relatively underdeveloped, and the content of each maceral was different, which contributed to the different degrees of organic matter porosity. Therefore, in order to quantitatively evaluate the contribution of each maceral to the organic matter porosity, the contribution of each maceral was calculated by using the mass percentage and the average Phi (a certain maceral contribution = mass percentage \times average Phi). It can be seen from Table 2 that the sapropelite provided the most organic matter pores, with a contribution percentage of 94.96%, while the inertinite provided almost no organic matter pores, with the lowest contribution of 0.06%.

5.2. Relationship between Macerals and Potential Hydrocarbon Generation. Different macerals have different capacities of hydrocarbon generation. Generally speaking, the higher the content of hydrogen-rich sapropelite and exinite, the better the capacity of hydrocarbon generation. The relative content of hydrogen-rich macerals was positively correlated with TOC and $S_1 + S_2$ (Figures 11(a) and 11(b)), which indicated that the hydrogen-rich macerals are the favorable hydrocarbon-generating macerals of Chang 7 shale. There was no obvious correlation between hydrogen-poor macerals and TOC and $S_1 + S_2$ (Figures 11(c) and 11(d)), indicating that the capacity for hydrocarbon generation is weak and that inertinite is the maceral with the lowest capacity for hydrocarbon generation. The relative content of hydrogen-poor macerals in the Chang 7 shale was relatively

low and had little influence on the capacity for hydrocarbon generation of the shale.

The carbon and hydrogen contents of organic matter are usually used to judge the hydrocarbon generation potential. The higher the weight percentage of carbon and the lower the weight percentage of hydrogen, the lower the hydrocarbon generation potential. As the EDS can only measure the weight percentage of carbon, the measured carbon level was used to judge the difference in hydrocarbon generation potential of each maceral. Using the EDS of each maceral of some samples as examples, the weight percentage of carbon in the sapropelite was 40%~60% (Figure 12(a)); the weight percentage of carbon in the exinite was 60%~70% (Figure 12(b)); the weight percentage of carbon measured in the vitrinite was 80%~90% (Figure 12(c)); the weight percentages of carbon in inertinite and vitrinite were similar, ranging from 85% to 90% (Figure 12(d)). It can be seen from sapropelite, exinite, vitrinite, and inertinite that the weight percentage of carbon increases successively, indicating that the hydrocarbon generation potential is successively worsened. This is consistent with the previous research results [6, 28].

5.3. Control of Gas Content by Macerals. Macerals are an important factor affecting the capacity of hydrocarbon generation of organic matter, and they also control the gas content of shale reservoirs. At present, there are few studies on the effect of maceral content on shale adsorption capacity. The adsorption gas content measured by the methane isotherm adsorption experiment was a comprehensive reflection of gas adsorption on the surface of organic matter and inorganic minerals. In order to accurately analyze the adsorption volume of organic matter, assuming that methane molecules are uniformly adsorbed on the surface of organic and inorganic matter pores, the adsorption volume of organic matter was calculated according to the proportion of organic matter pores out of the total pores.

According to the statistical analysis of the relationship between the macerals of Chang 7 shale in the Yanchang

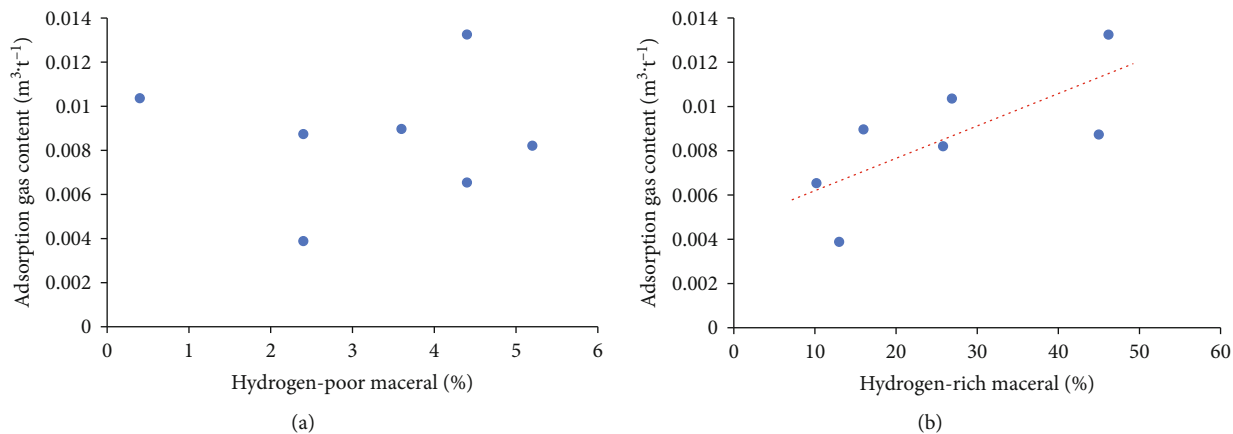


FIGURE 13: Relationships between macerals and adsorbed gas.

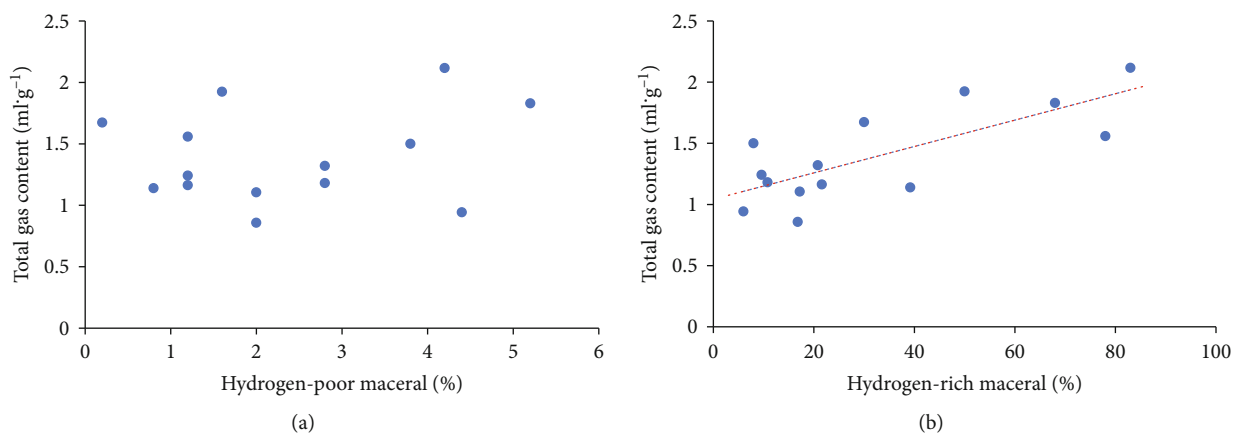


FIGURE 14: Relationships between macerals and total gas content.

Formation and the adsorption amount of organic matter, there was no significant correlation between the hydrogen-poor macerals and the adsorption amount of organic matter (Figure 13(a)). There was also a positive correlation between the hydrogen-rich macerals and the adsorption amount of organic matter (Figure 13(b)). A large number of organic matter pores are developed in hydrogen-rich macerals, which provide more surface area and more adsorption sites for gas, so the adsorption capacity is increased. However, the organic matter pores of hydrogen-poor macerals are not developed, so they are not conducive to gas adsorption.

Shale gas is the product of kerogen evolution and mainly exists in shale pores in free and adsorbed states. According to the statistical analysis of the relationship between macerals and total gas content in Chang 7 shale of the Yanchang Formation, there was no obvious correlation between hydrogen-poor macerals and total gas content (Figure 14(a)). The hydrogen-rich macerals were positively correlated with the total gas content (Figure 14(b)). Hydrogen-rich macerals have a good capacity for hydrocarbon generation, which can generate a lot of shale gas and develop more organic matter pores, providing space for the occurrence of shale gas. However, the hydrogen-poor macerals have a worse capacity for hydrocarbon generation, the organic matter pores are not developed, and the content of hydrogen-poor macerals in

Chang 7 shale was low, so it had no obvious contribution to the total gas content.

6. Conclusion

Based on our studies, the following conclusions can be drawn:

- (1) FE-SEM and EDS can effectively identify the various macerals. Based on the morphology and elements of the organic matter of the Chang 7 member, the synthetic discrimination method of organic macerals was established. Sapropelite was mainly composed of the mineral asphalt matrix, followed by algae; exinite was composed of sporophyte and resin; vitrinite had a small amount of provitrinite, euvitrinite, and vitrodetrinite; inertinite was composed of semifusinite and inertodetrinite
- (2) The sapropelite developed a large number of honeycomb pores, and the exinite developed round-elliptical stomata; a small amount of organic matter pores and microfractures were seen in vitrinite and inertinite. Further calculations showed that the sapropelite provides the most organic matter pores,

with a contribution percentage of 94.96%, and the inertinite provides almost no organic matter pores, with a contribution percentage of 0.06%

- (3) The EDS showed that the weight percentage of carbon increases successively in the order of sapropelite, exinite, vitrinite, and inertinite, which indicates that the hydrogen-rich macerals have a better hydrocarbon generation capacity, and the hydrogen-poor macerals have a lower hydrocarbon generation capacity. The hydrogen-rich macerals have a positive correlation with the organic matter adsorption gas volume and total gas content, while the hydrogen-poor macerals have no obvious correlation. Sapropelite and exinite are conducive to the generation of shale gas and develop rich organic matter pores. They can provide space for shale gas reservoirs. Vitrinite and inertinite do not develop organic matter pores and are not conducive to the generation and storage of hydrocarbons

Data Availability

The data used to support the study is available within the article.

Conflicts of Interest

The authors declare that they have no conflicts of interest.

Acknowledgments

This research was supported by the National Science and Technology Major Project of China (No. 2016ZX05034-001) and the National Natural Science Foundation of China (No. 41502123).

References

- [1] Z. Chen, G. Liu, Z. Cao et al., "Origin of solid bitumen and its significance to petroleum geology: a case study of Baikouquan formation in Mahu sag of Junggar basin," *Journal of China University of Mining & Technology*, vol. 47, no. 2, pp. 391–399, 2018.
- [2] G. J. Nowak, "Comparative studies of organic matter petrography of the late palaeozoic black shales from Southwestern Poland," *International Journal of Coal Geology*, vol. 71, no. 4, pp. 568–585, 2007.
- [3] D. Kondla, H. Sanei, C. R. Clarkson, O. H. Ardakani, X. Wang, and C. Jiang, "Effects of organic and mineral matter on reservoir quality in a Middle Triassic mudstone in the Canadian Arctic," *International Journal of Coal Geology*, vol. 153, pp. 112–126, 2016.
- [4] J. Kus, "Application of confocal laser-scanning microscopy (CLSM) to autofluorescent organic and mineral matter in peat, coals and siliciclastic sedimentary rocks – a qualitative approach," *International Journal of Coal Geology*, vol. 137, pp. 1–18, 2015.
- [5] A. Ghosh, "AuroView 2000-an optical image processing system in rank and grade analysis of coal," *Journal of the Geological Society of India*, vol. 60, no. 2, pp. 143–150, 2002.
- [6] G. Fenglin, S. Yan, L. Zhikai, L. Zhuo, Y. Yuan, and Z. Yinghan, "Development characteristics of organic pore in the continental shale and its genetic mechanism: a case study of Shahezi Formation shale in the Changling fault depression of Songliao Basin," *Acta Petrolei Sinica*, vol. 40, no. 9, pp. 1030–1044, 2019.
- [7] H. J. Guo, R. L. He, W. L. Jia et al., "Pore characteristics of lacustrine shale within the oil window in the Upper Triassic Yanchang Formation, southeastern Ordos Basin, China," *Marine and Petroleum Geology*, vol. 91, pp. 279–296, 2018.
- [8] W. M. Ji, Y. Song, Z. H. Rui, M. Meng, and H. Huang, "Pore characterization of isolated organic matter from high matured gas shale reservoir," *International Journal of Coal Geology*, vol. 174, pp. 31–40, 2017.
- [9] X. Z. Song, "Effect of false boundary of microscopic image on automatic identification of maceral group," *Coal Geology & Exploration*, vol. 47, pp. 45–50, 2019.
- [10] Q. Li, S. H. Wu, D. L. Xia, X. You, H. Zhang, and H. Lu, "Major and trace element geochemistry of the lacustrine organic-rich shales from the Upper Triassic Chang 7 Member in the southwestern Ordos Basin, China: implications for paleoenvironment and organic matter accumulation," *Marine and Petroleum Geology*, vol. 111, pp. 852–867, 2020.
- [11] C. He, L. M. Ji, A. Su et al., "Source-rock evaluation and depositional environment of black shales in the Triassic Yanchang Formation, southern Ordos Basin, north-central China," *Journal of Petroleum Science and Engineering*, vol. 173, pp. 899–911, 2019.
- [12] X. Tang, J. C. Zhang, X. Z. Wang et al., "Shale characteristics in the southeastern Ordos Basin, China: implications for hydrocarbon accumulation conditions and the potential of continental shales," *International Journal of Coal Geology*, vol. 128–129, pp. 32–46, 2014.
- [13] X. Z. Wang, S. L. Gao, and C. Gao, "Geological features of Mesozoic lacustrine shale gas in south of Ordos Basin, NW China," *Petroleum Exploration and Development*, vol. 41, no. 3, pp. 326–337, 2014.
- [14] H. Yang, X. Niu, L. Xu et al., "Exploration potential of shale oil in Chang7 Member, Upper Triassic Yanchang Formation, Ordos Basin, NW China," *Petroleum Exploration and Development*, vol. 43, no. 4, pp. 560–569, 2016.
- [15] F. J. Jiang, D. Chen, Z. F. Wang et al., "Pore characteristic analysis of a lacustrine shale: a case study in the Ordos Basin, NW China," *Marine and Petroleum Geology*, vol. 73, pp. 554–571, 2016.
- [16] J. Fu, S. Li, X. Niu, X. Deng, and X. Zhou, "Geological characteristics and exploration of shale oil in Chang 7 Member of Triassic Yanchang Formation, Ordos Basin, NW China," *Petroleum Exploration and Development*, vol. 47, no. 5, pp. 931–945, 2020.
- [17] Y. Li, D. Tang, P. Wu et al., "Continuous unconventional natural gas accumulations of Carboniferous-Permian coal-bearing strata in the Linxing area, northeastern Ordos basin, China," *Journal of Natural Gas Science and Engineering*, vol. 36, pp. 314–327, 2016.
- [18] Y. B. Yao, D. Liu, D. Tang, S. Tang, and W. Huang, "Fractal characterization of adsorption-pores of coals from North China: an investigation on CH₄ adsorption capacity of coals," *International Journal of Coal Geology*, vol. 73, no. 1, pp. 27–42, 2008.
- [19] A. C. Cook and N. R. Sherwood, "Classification of oil shales, coals and other organic-rich rocks," *Organic Geochemistry*, vol. 17, no. 2, pp. 211–222, 1991.

- [20] M. Ercegovac and A. Kostic, "Organic facies and palynofacies: nomenclature, classification and applicability for petroleum source rock evaluation," *International Journal of Coal Geology*, vol. 68, no. 1-2, pp. 70–78, 2006.
- [21] K. M. Cheng, T. G. Wang, and S. Q. Zhao, "Geochemistry and evolution characteristics of source rocks," Research Institute of Petroleum Exploration and Development, Beijing, 1989.
- [22] H. Zhang, S. J. Jiao, and G. H. Li, "Scanning electron microscopy study of unconventional oil and gas reservoirs," Geological Publishing House, Beijing, 2016.
- [23] Y. F. Jiang, L. Zhao, G. Q. Zhou et al., "Petrological, mineralogical, and geochemical compositions of Early Jurassic coals in the Yining Coalfield, Xinjiang, China," *International Journal of Coal Geology*, vol. 152, pp. 47–67, 2015.
- [24] W. M. Ji, F. Hao, H. M. Schulz, Y. Song, and J. Tian, "The architecture of organic matter and its pores in highly mature gas shales of the lower Silurian Longmaxi Formation in the upper Yangtze platform, south China," *AAPG Bulletin*, vol. 103, no. 12, pp. 2909–2942, 2019.
- [25] E. Tannenbaum and I. R. Kaplan, "Role of minerals in the thermal alteration of organic matter—I. Generation of gases and condensates under dry condition," *Geochimica et Cosmochimica Acta*, vol. 49, no. 12, pp. 2589–2604, 1985.
- [26] M. Shi, B. Yu, Z. Xue, J. Wu, and Y. Yuan, "Pore characteristics of organic-rich shales with high thermal maturity: a case study of the Longmaxi gas shale reservoirs from well Yuye-1 in southeastern Chongqing, China," *Journal of Natural Gas Science and Engineering*, vol. 26, pp. 948–959, 2015.
- [27] C. Yang, J. Zhang, X. Tang et al., "Comparative study on micro-pore structure of marine, terrestrial, and transitional shales in key areas, China," *International Journal of Coal Geology*, vol. 171, pp. 76–92, 2017.
- [28] H. Zhang, S. Jiao, Q. Pang, N. Li, and B. Lin, "SEM observation of organic matters in the Eopaleozoic shale in South China," *Oil & Gas Geology*, vol. 36, no. 4, pp. 675–680, 2015.

Research Article

Slope Belts of Paleouplifts Control the Pore Structure of Organic Matter of Marine Shale: A Comparative Study of Lower Cambrian Rocks in the Sichuan Basin

Pengfei Wang,^{1,2} Chen Zhang,^{2,3} Aoran Liu ,^{4,5} Pengfei Zhang,⁶ Yibo Qiu,⁶ Xin Li,⁷ Shanshan Yu,⁷ Shuqing Yao,¹ Sanyi Liu,¹ and Zhenxue Jiang^{2,3}

¹Geoscience Documentation Center of China Geological Survey, Beijing 100083, China

²State Key Laboratory of Petroleum Resources and Prospecting, China University of Petroleum, Beijing, China

³College of Geoscience, China University of Petroleum, Beijing, China

⁴Hebei Key Laboratory of Strategic Critical Mineral Resources, Hebei GEO University, Shijiazhuang 050031, China

⁵College of Geosciences, Hebei GEO University, Shijiazhuang 050031, China

⁶Research Institute of Exploration and Development, Sinopec Shengli Oilfield Company, Dongying 257000, China

⁷China National Offshore Oil Corporation Research Institute, Beijing 100028, China

Correspondence should be addressed to Aoran Liu; aoranliu@cug.edu.cn

Received 20 January 2021; Accepted 4 June 2021; Published 29 June 2021

Academic Editor: Henrik Drake

Copyright © 2021 Pengfei Wang et al. This is an open access article distributed under the Creative Commons Attribution License, which permits unrestricted use, distribution, and reproduction in any medium, provided the original work is properly cited.

Extensive exploration of the marine shale of the Niutitang Formation in south China has been conducted. However, exploration and development results have varied considerably in different areas. For example, the Niutitang shale in Jingyan City (Southwestern Sichuan Basin) produces a large amount of gas with a long period of stable production. In contrast, most development wells in the Niutitang shale in Chongqing City do not produce gas. Scanning electron microscopy images showed that the organic matter (OM) pore development in the Niutitang shale in Jingyan is abundant, large in size, and are well connected. In contrast, OM pores in the Niutitang shale in Chongqing are rarely observed. OM pore development of the Jingyan and Chongqing shales is mainly controlled by thermal maturity as shown by equivalent vitrine reflectance determinations. The moderate thermal maturity has resulted in the development of a large number of OM pores in the Niutitang shale in Jingyan, whereas the high thermal maturity of the Niutitang shale in Chongqing has led to the destruction of most of the OM pores. Due to the existence of ancient uplift, the shale was buried shallowly in the process of hydrocarbon generation evolution, and the shale avoided excessive thermal evolution and retained appropriate thermal maturity. In the Jingyan area, due to its location near the central uplift in the Sichuan Basin, the Niutitang shale deposited nearby avoided excessive evolution, and a large number of OM pores were retained in the reservoir.

1. Introduction

The Lower Cambrian Niutitang Formation contains highly to overly mature organic-rich black marine shales with high TOC content and type I kerogen that is widely distributed in south China [1, 2]. However, their exploration and development potential vary significantly between different areas. For example, the Niutitang shale in Chongqing City (south China) has only a short stable production of gas, low gas volumes, or even no gas production at all in some wells, and

hence no successful development [3, 4]. However, successful exploration and development of the Niutitang shale has been made in Jingyan City in Sichuan Province (south China), where commercial gas has been successfully produced from the JinYe1 well [1]. The gas produced from shale wells can reach 2.3 m³/t, with the daily gas output of 6.0 × 10⁴ m³/d [5].

Successful exploration and development of the Niutitang shale has been made in Yichang City of Hubei Province (south China) by the China Geological Survey, where commercial gas has been successfully produced from the wells

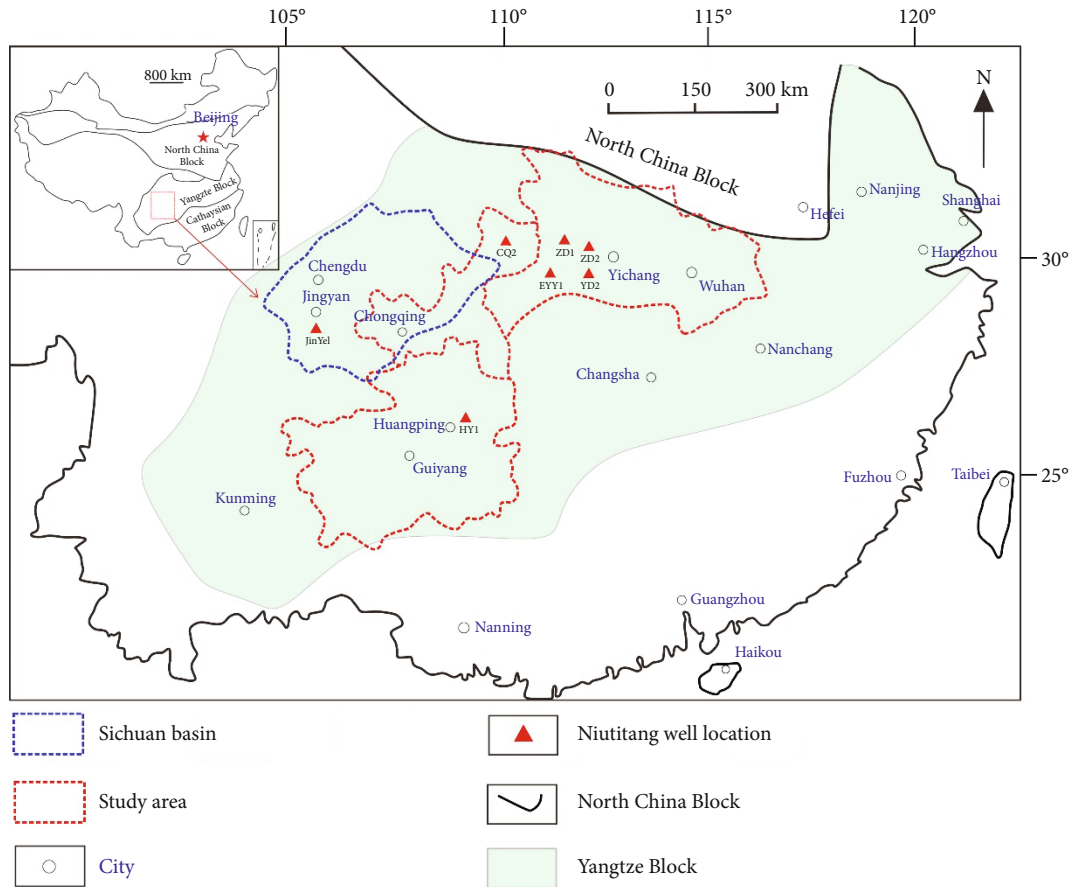


FIGURE 1: Position of the study area and Niutitang shale well distribution in Chongqing, Sichuan Basin, Hubei Province, and Guizhou Province.

EYY1 and ZD2 [6, 7]. In the EYY1 well, for example, the thickness of the Niutitang shale with gas total hydrocarbon exceeding 1.0% is 77 m [7, 8]. The gas from shale wells reaches $2.2 \text{ m}^3/\text{t}$ with a daily gas output of $7.8 \times 10^4 \text{ m}^3/\text{d}$ [5]. Furthermore, the Niutitang shale in Jingyan also showed commercial gas with a daily gas output of $6.0 \times 10^4 \text{ m}^3/\text{d}$ [4].

Successful exploration and development of the Niutitang shale has also been made in Southern Guizhou (south China), where commercial gas has been successfully produced from the HY1 well [9, 10]. The HY1 well has a gas content of $1.3 \text{ m}^3/\text{t}$ [11].

Micro- to nanometer size pores have been shown to be important storage spaces for hydrocarbon gas in shale [12, 13]. Previous studies show that different micro- to nanometer-sized pore structures present different gas storage capacities [14–16]. In particular, OM pores have been demonstrated to be effective storage spaces for gas [17, 18]. For shale reservoirs, OM pores can impact the exploration and development potential by providing space for gas to be stored and for gas to flow through [19–21].

OM pore development is affected by a variety of rock parameters, including TOC content, mineralogy, kerogen type, and thermal maturity [12, 13]. An abundant TOC content provides the source material for OM pore development [1]. Brittle minerals, such as silica, can relieve

the pressure from the overlying rock on OM pores and can provide support for the preservation of OM pores [14, 15]. Kerogen, bitumen, and pyrobitumen have distinct physical and chemical properties and can cause different styles of OM pore development [19]. Too high or too low thermal maturity is also not conducive for the development of OM pores [16].

Many studies have suggested that a number of marine shales in southern China generally have high TOC contents on average ($>2.0\%$), high siliceous mineral content, and the same kerogen type (type I), but the thermal maturity of different formations of marine shales varies considerably [18–21]. For example, several researchers have compared shales of the Lower Silurian Longmaxi Formation ($2.0\% < R_o < 3.0\%$) with those of the Lower Cambrian Niutitang Formation in Chongqing, the former of which have produced commercial gas [22, 23]. They concluded that high thermal maturity is the key reason resulting in the low gas content and low production in the Niutitang shale in Chongqing [1, 13, 14, 24–26].

Burial history and hence thermal maturity have a strong control over OM porosity development and petroleum generation [27, 28]. The OM pore evolution and petroleum generation are also closely related to the tectonic evolution [29, 30].

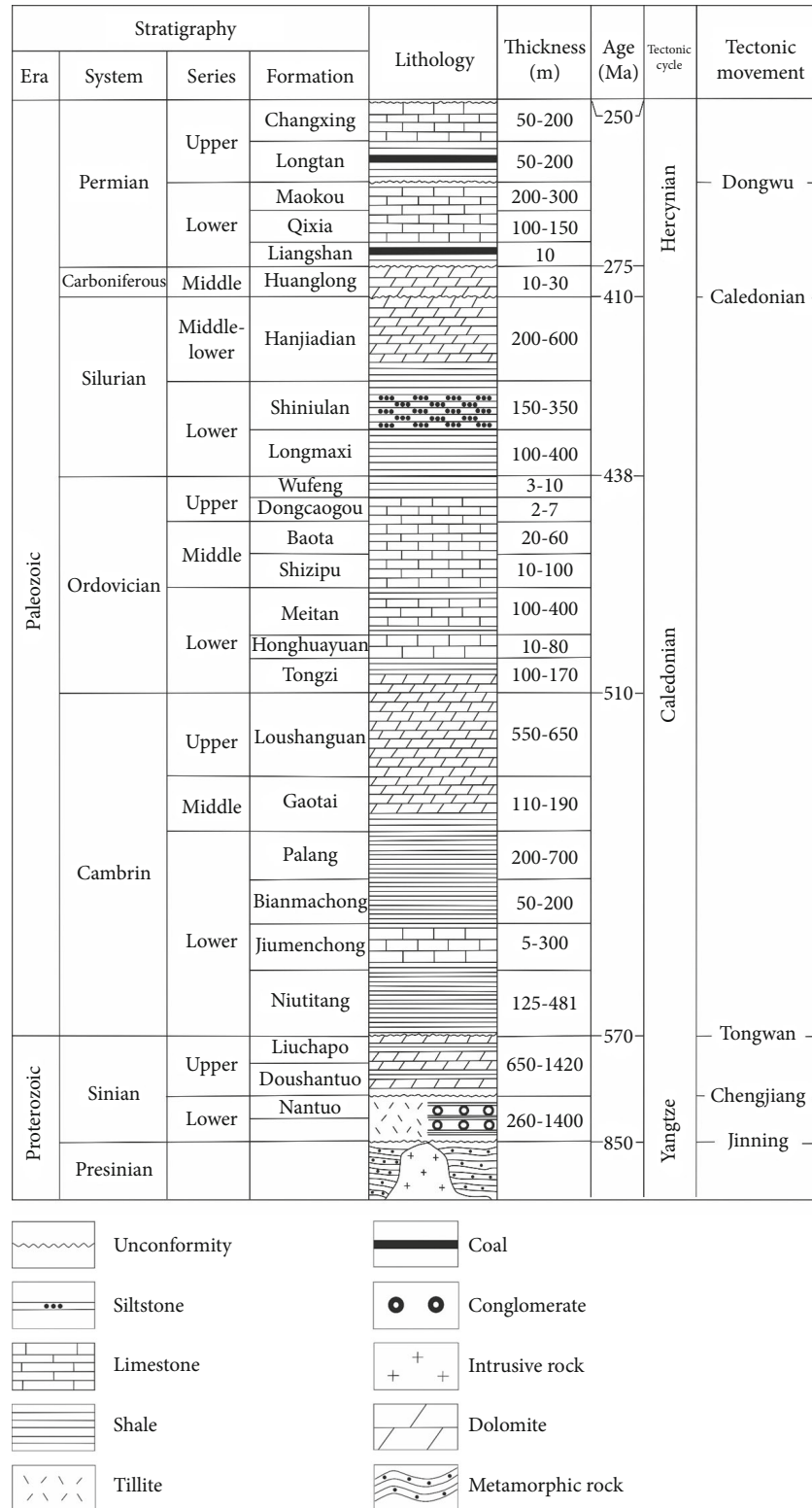


FIGURE 2: Stratigraphic sections of the study area. This figure was revised from Ref. [33].

This study used samples of the Niutitang shale from wells in the Chongqing and Jingyan areas (southwestern Sichuan Basin) as research objects (Figures 1 and 2). Combined with the regional structural characteristics, the shales of Niutitang

Formation in the Huangping area in southern Guizhou and Yichang area in western Hubei are compared. The OM pore characteristics of Niutitang shale in different exploration and development blocks in southern China were clarified, and

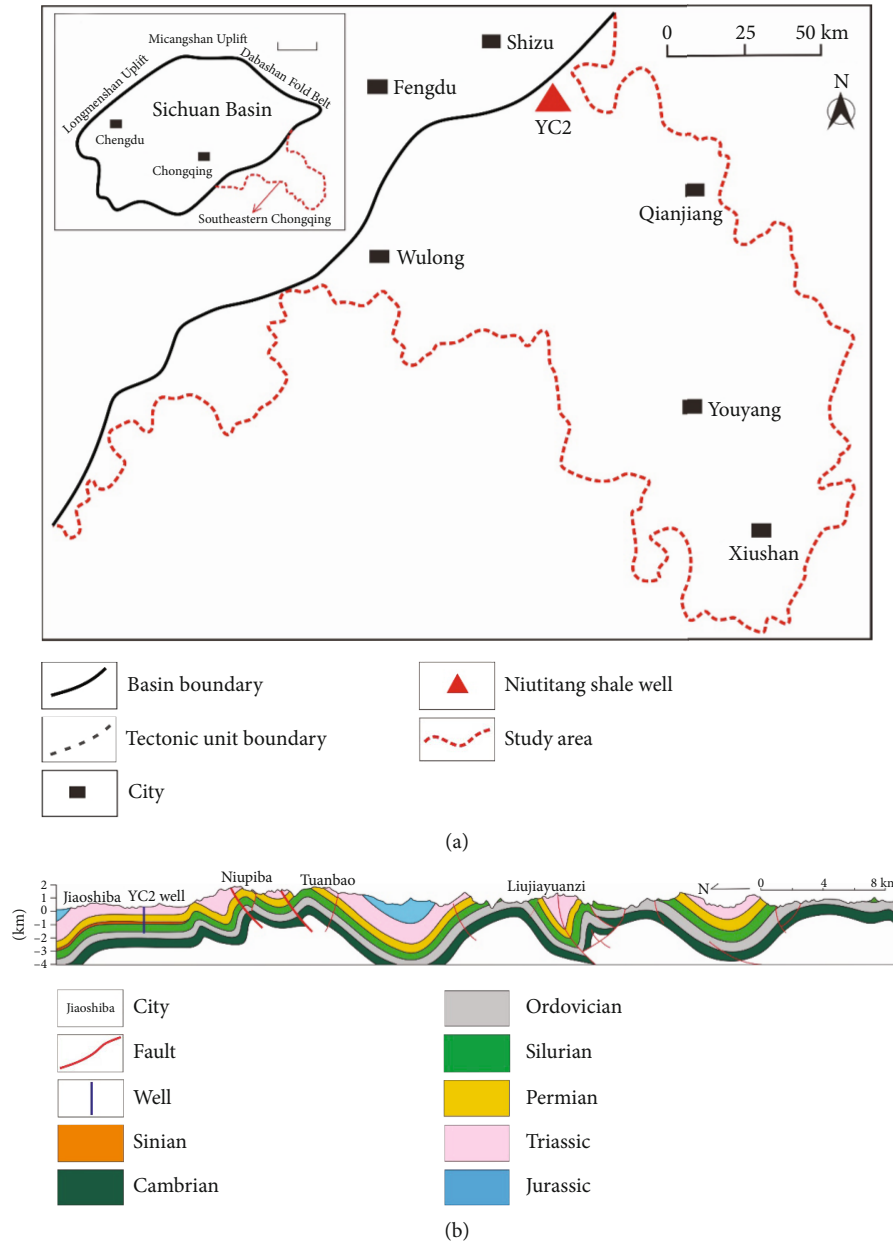


FIGURE 3: Plane and section structure of southeastern Chongqing. This figure was revised from Refs. [28, 36].

finally, the special structural characteristics were proposed as exploration targets for the efficient exploration and development of ancient marine shale in south of China.

2. Geological Setting

2.1. Chongqing Area. The Chongqing area is located in the southeastern margin of the Sichuan Basin, south China, and structurally, it is located in the southeastern part of the Yangtze Platform (Figure 3). This area has experienced three main tectonic stages since the Late Mesoproterozoic: continental margin oceanic crust changing to continental crust during the Late Proterozoic to Silurian, continental expansion during the Devonian to Middle-Late Triassic, and

Pacific plate subduction and Indian plate collision during the Mesozoic to Cenozoic [31, 32].

During the Early and Late Paleozoic, the Yangtze Platform experienced many large-scale transgression events, forming four sets of black shales during the Cambrian, the Upper Ordovician to the Lower Silurian, the Lower Permian, and the Upper Permian (Figure 2). The Niutitang shale in Chongqing was deposited during the Early Cambrian, when extensional activities resulted in the disintegration of southern Pangea and the expansion of the oceanic crust, leading to large-scale transgression [34]. The exploration target in the Chongqing area is the base section of the Niutitang Formation, which is mainly thick, black carbonaceous shale with high TOC content and siliceous minerals [35]. There is also some silty shale and a small amount of siliceous shale. These

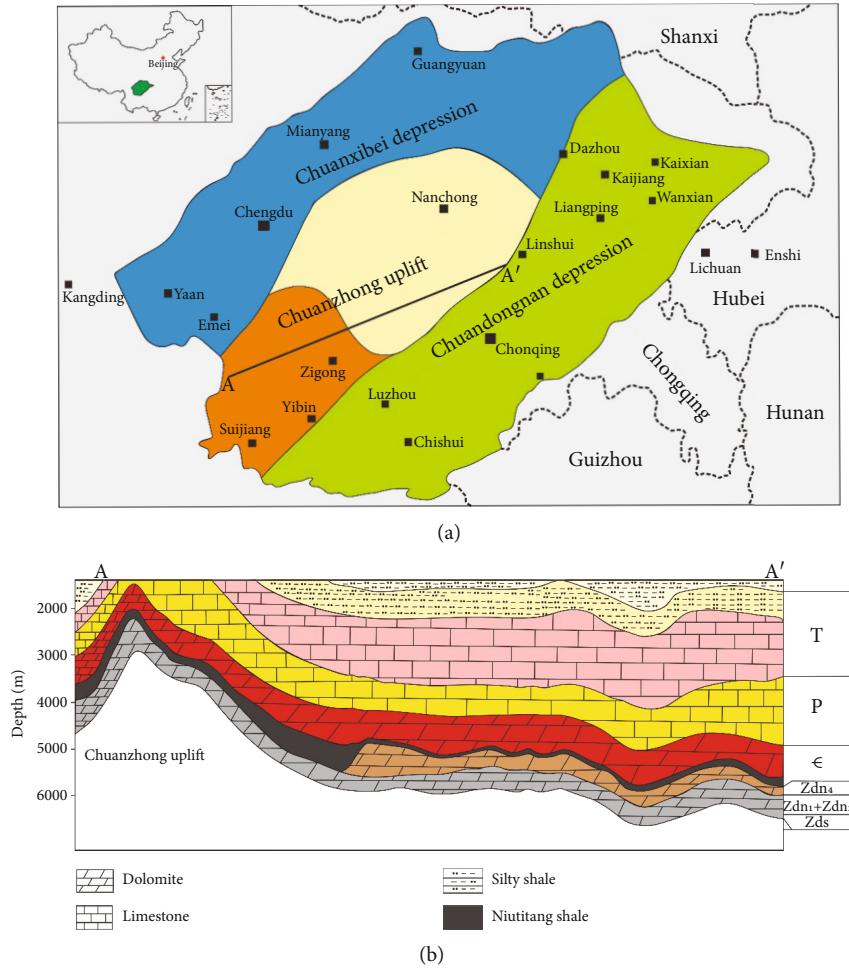


FIGURE 4: Plane and section structure of the Chuanzhong Uplift of Sichuan Basin. This figure was revised from Ref. [25].

TABLE 1: TOC content, $Eq-R_o$, and mineral composition of reservoir parameters from the Chongqing and Jingyan samples for FIB-SEM.

Sample	Well	Area	Formation	Depth (m)	TOC (%)	$Eq-R_o$ (%)	Mineral (%)				
							Quartz	Feldspar	Calcareous	Clay	Pyrites
#1	CQ2	Chongqing	Niutitang	1149	2.86	3.54	49.6	14.7	15.9	17.6	2.2
#2	JinYe1	Jingyan	Niutitang	3296.2	2.36	2.79	33.1	21	5.1	37.1	3.7

sediments were deposited on a deep-water shelf under mainly reducing conditions [28–30].

2.2. Jingyan Area. The Jingyan area is located at the southwestern margin of the Sichuan Basin, between the large Weiyuan and Tieshan anticlines (Figure 4). In the Early Cambrian, medium-deep-water shelf deposition developed in the Jingyan area, and the water column gradually deepened from NW to SE [28].

The Niutitang Formation deposited in the Jingyan area is characterized by unequal interbedding of gray-dark gray shale, silty shale, and gray-dark gray calcareous litharenite, gray siltstone, and argillaceous siltstone [3]. From bottom to top, the black shale mainly changes into an interlayer between black shale and dark gray and between gray argillaceous siltstone and gray siltstone, and the interlayer is

increased [4]. In the middle and upper part, there is a small amount of lenticular gray or siliceous nodules and a small amount of pyrite. The mineralogy is mainly quartz and clay, with minor carbonate minerals [3, 4, 20, 21].

3. Focused Ion Beam Scanning Electron Microscopy (FIB-SEM)

FIB-SEM analysis for the observation of OM pores was conducted using a FEI HELIOS NanoLab 650 (FEI Corporation, United States). Before that, samples were ground, argon ion polished, and carbon sprayed to increase electrical conductivity (Table 1). The secondary electron emission technology of FIB-SEM was also used to further identify OM pore characteristics. This technology can create bright lights around the pores, highlighting the surface

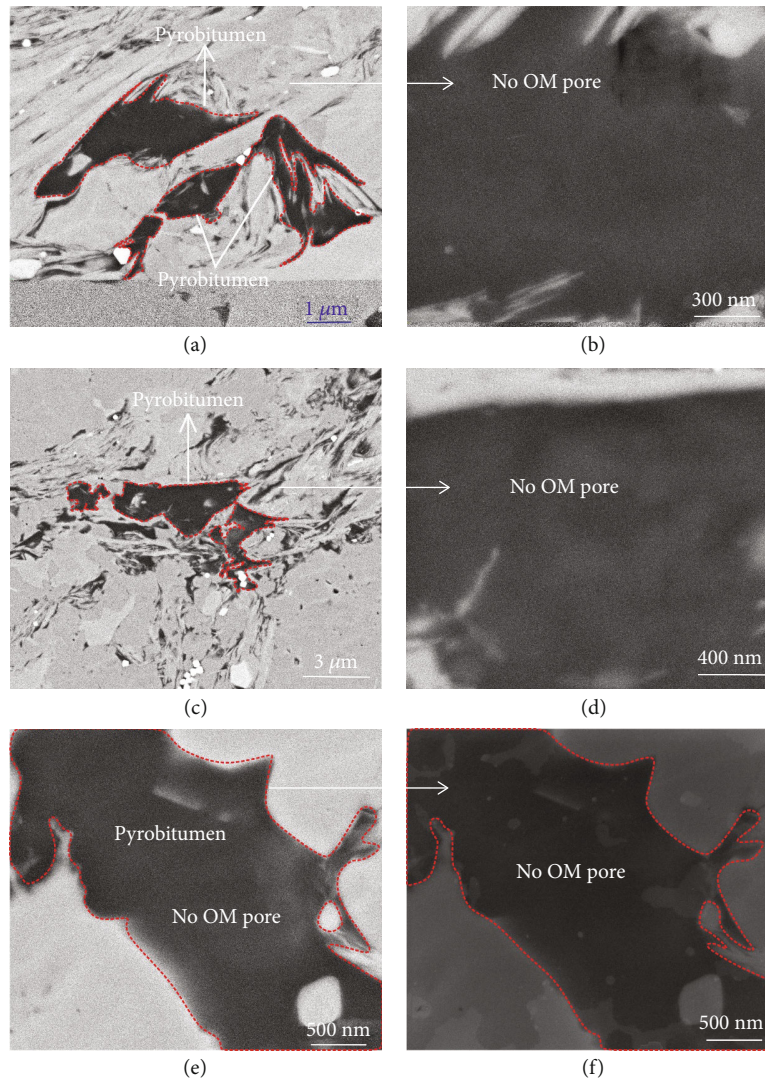


FIGURE 5: No OM pore in the pyrobitumen of Chongqing samples (CQ2 well, 1149 m). The secondary electron technique can highlight the pores in a circular layer, making them easy to identify. If no highlight is found in the pyrobitumen, there is no OM pore. The secondary electron technique proves that there is no OM pore in the pyrobitumen of the Chongqing sample.

morphology of OM pores and making them easier to identify even under low resolution.

4. Results

There are no OM pores in the pyrobitumen of the Chongqing samples, as indicated by SEM imaging (Figure 5). The secondary electronic imaging was used to highlight the morphology of any smaller-scale inner structure in these shale samples; however, none was observed in the pyrobitumen of the Chongqing samples (Figure 6). This further proves that there are no OM pores in the Chongqing samples. However, under the FIB-SEM, the pyrobitumen in the Niutitang shale in Jingyan shows a large number of OM pores (Figures 7 and 8), which are characterized by round and oval shapes, uniform distribution, and a large pore size.

5. Discussion

5.1. Comparison with Jingyan and Chongqing Areas. A large number of OM pores can not only increase the adsorption capacity for gas but also be conducive to the effective flow of gas in a shale reservoir by enhancing the connectivity [2, 17, 26]. This may be one reason why the Niutitang shale produces commercial gas in Jingyan but not in Chongqing (Figures 5–9).

Rock parameters of the Niutitang shale from Jingyan were compared with those from Chongqing. As shown in Table 2, these shale samples share very similar reservoir characteristics such as average TOC content, mineral composition, and kerogen type, but they have very different $Eq-R_o$. The Niutitang shale in Jingyan with abundant OM pores has an $Eq-R_o$ of less than 3.0%, while the Niutitang shale in Chongqing with almost no OM pores has an $Eq-R_o$ larger than 3.0%. It reveals that the formation and preservation of OM pores are likely controlled by thermal maturity [1, 26, 27].

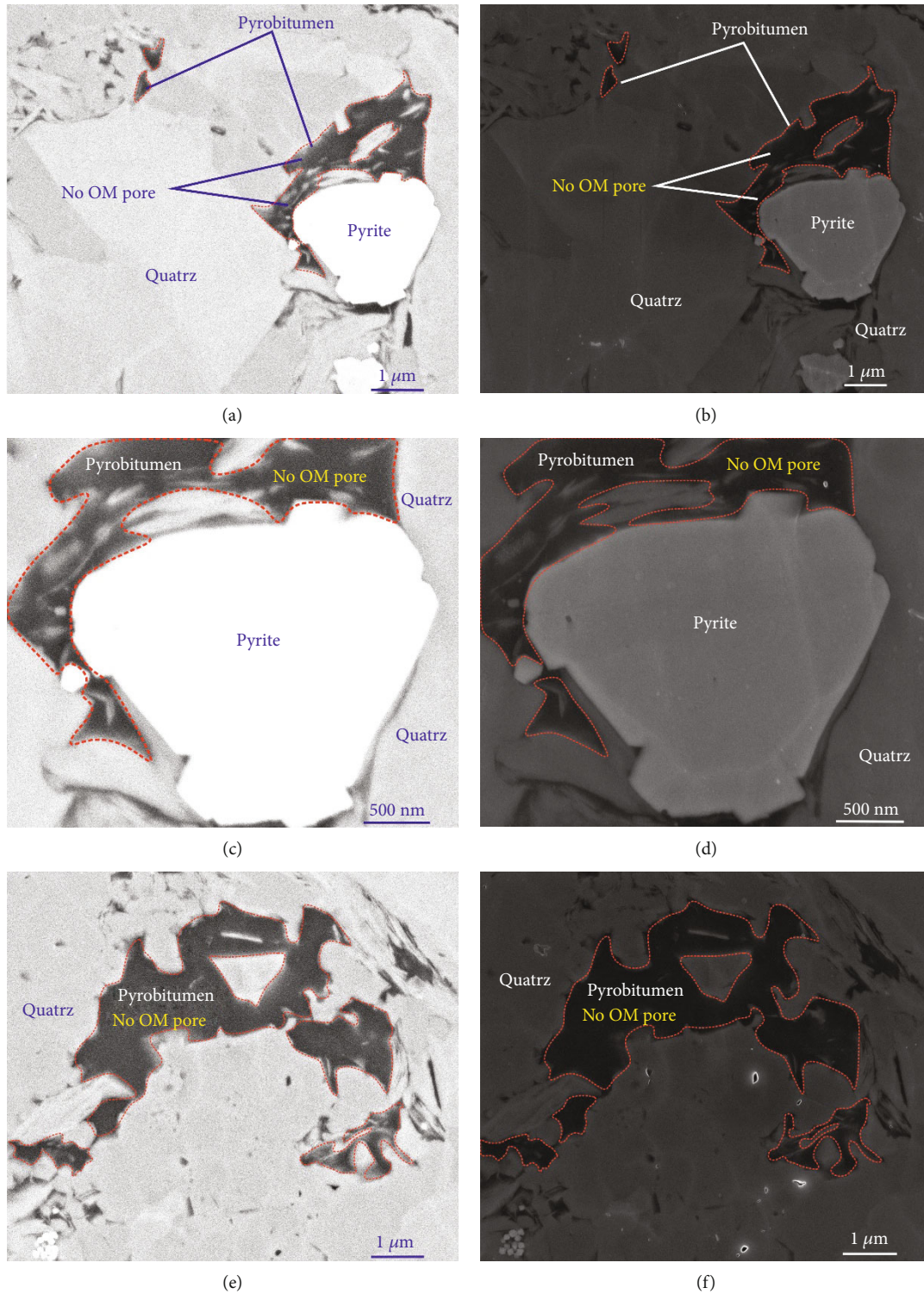


FIGURE 6: No OM pore in the pyrobitumen of Chongqing samples (CQ2 well, 1149 m). The secondary electron technique can highlight the pores in a circular layer, making them easy to identify. If no highlight is found in the pyrobitumen, there is no OM pore. The secondary electron technique proves that there is no OM pore in the pyrobitumen of the Chongqing sample.

The thermal evolution and the associated OM pore generation and hydrocarbon potential in shale are closely related to the tectonic evolution of the study areas [37, 38]. For the Chongqing study area, the maximum paleoburial depth of

the Niutitang shale is 8000 m, corresponding to an E_q-R_o exceeding 3.5% (Figure 10). A large number of OM pores in the pyrobitumen were destroyed due to excessive thermal evolution, resulting in the loss of hydrocarbon gases in shale.

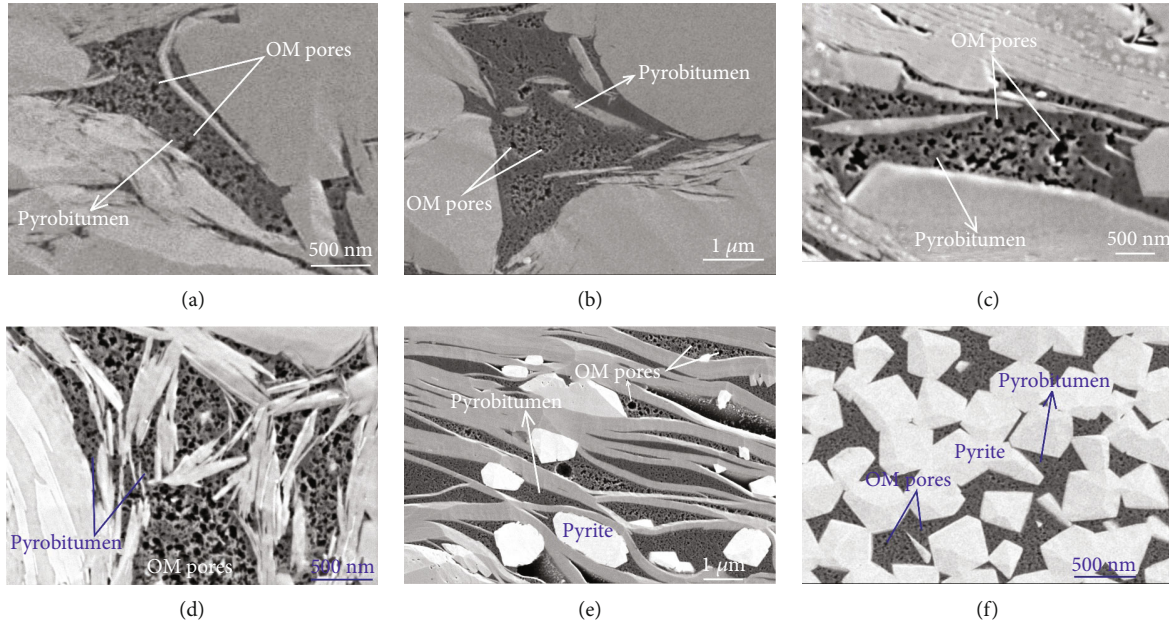


FIGURE 7: A large number of OM pores in the pyrobitumen of Jingyan samples (JinYe1 well, 3296.2 m) are shown. (a–e) OM pores in the pyrobitumen of the mineral matrix. (f) The pyrobitumen with OM pores in pyrite particles.

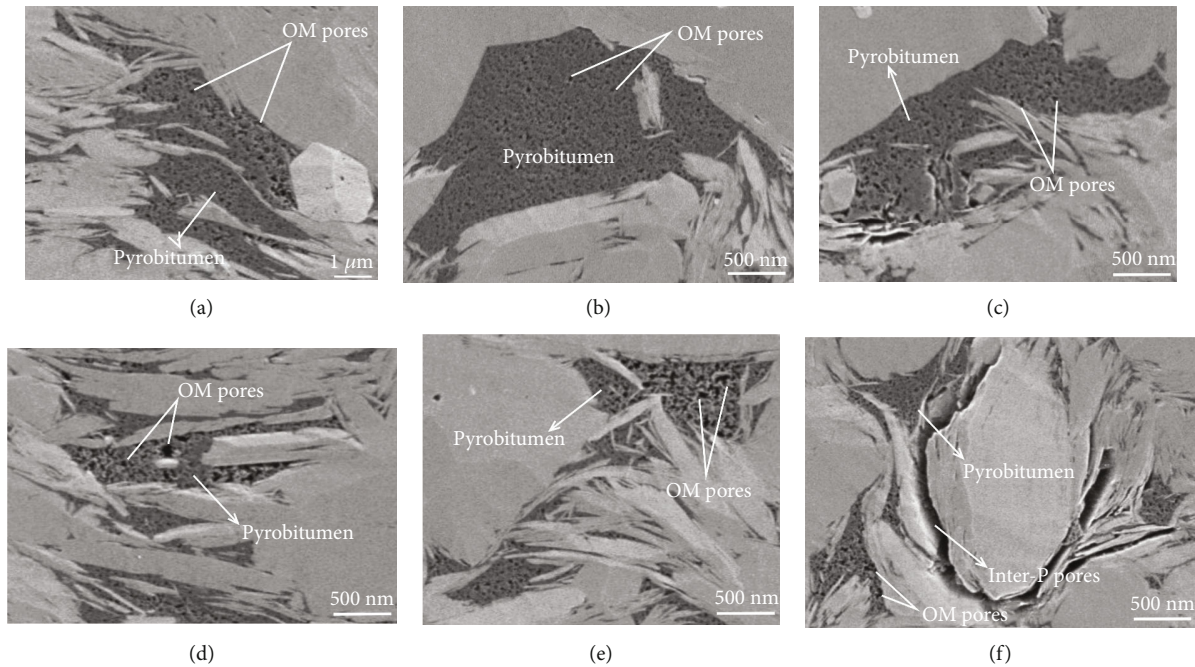


FIGURE 8: A large number of OM pores in the pyrobitumen of the Niutitang shale samples in Jingyan (JinYe1 well, 3296.2 m) are shown.

In contrast, for the Jingyan study area, the maximum paleoburial depth of the Niutitang shale is 6200 m [4], corresponding to an $Eq-R_0$ of 2.2% to 2.8% (Figure 11).

The maximum paleoburial depth of the Niutitang shale seems to be closely related to the paleostructure of the Jingyan area, which is structurally located on the wing of the Chuanzhong anticline (Figure 4). Due to the presence of the Chuanzhong paleouplift, the maximum ancient burial depth of the Niutitang shale in Jingyan is much shallower than its equivalents in south China. In contrast, the maxi-

imum paleoburial depth of the Niutitang shale in Chongqing reaches 8000 m due to a lack of such a paleouplift, and the $Eq-R_0$ of the Niutitang shale thus reaches a stage of overmaturity due to metamorphism [26, 39].

5.2. Comparison of the Niutitang Formation in Other Areas

5.2.1. Niutitang Shale in Yichang, Western Hubei.

The Yichang area is located in the center of the Middle Yangtze Platform, and it is mainly comprised of the Huangling

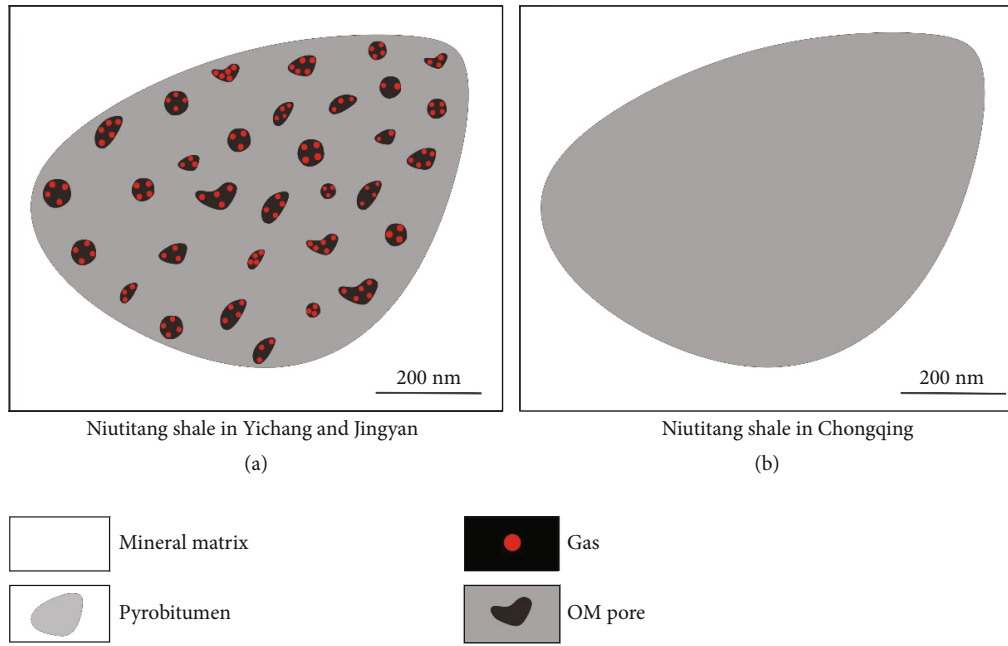


FIGURE 9: Gas adsorption models in different OM pore structures. (a) Based on the large number of OM pores, abundant gas was adsorbed in Jingyan shale samples. (b) No gas was adsorbed in Chongqing shale samples because there were no OM pores.

TABLE 2: Geological and reservoir development parameters with different gas contents and production of the Niutitang shale in Chongqing, Jingyan, Yichang, and Southern Guizhou. Parts of this table are revised from Refs. [2, 5, 7].

Formation	Area	Well	TOC (%)	Eq- R_0 (%)	Kerogern type	Porosity (%)	Pressure	Gas content (m^3/t)	Gas test production ($10^4 m^3/d$)
Niutitang	Chongqing	CQ2	2.82	3.74	I	0.16	0.7	0.18	0
	Jingyan	JinYe1	2.36	2.79	I	3.94	1.38	2.02	10.5 (HF)
	Yichang	EYY1	2.34	2.77	I	3.68	0.78	1.98	7.83
	Huangping	HY1	5.81	2.51	I	0.6	/	1.3	/

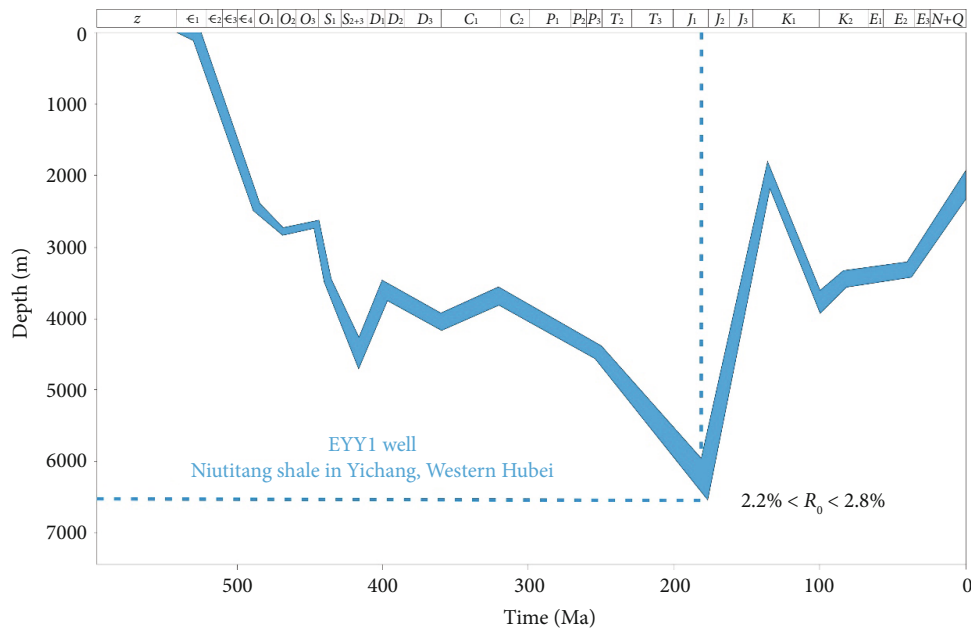


FIGURE 10: Burial history of the Niutitang shale in Yichang is based on the EYY1 well (revised from Ref. [6]). Due to the existence of the Huangling paleo uplift, the ancient burial depth of the Niutitang shale distributed in its periphery is only 6500 m.

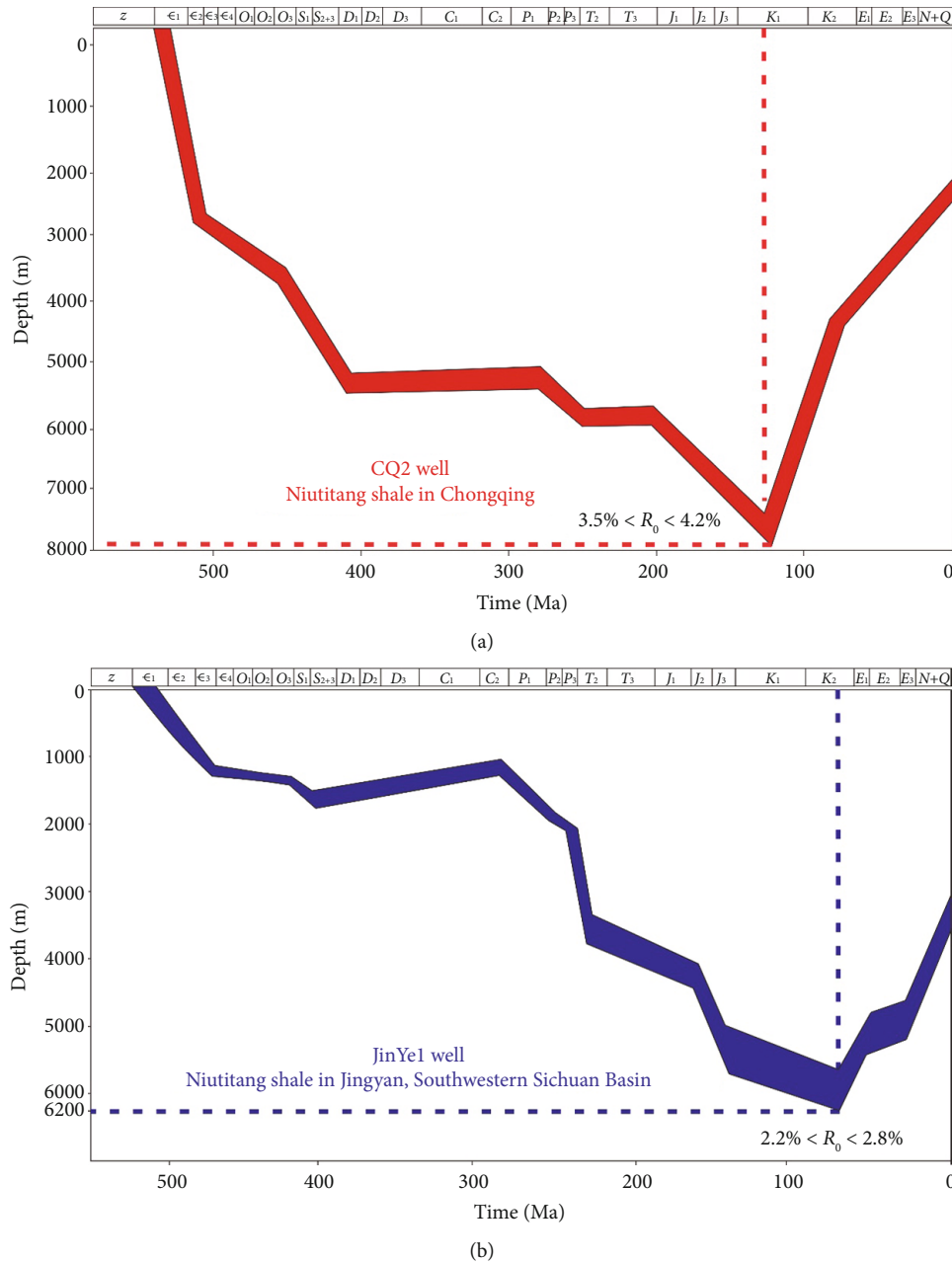


FIGURE 11: Burial history the Niutitang shale in the study area. (a) Burial history of the Niutitang shale in Chongqing based on the CQ2 well (revised from Refs. [26]). The buried depth of Chongqing reached 8000 m. (b) Burial history of the Niutitang shale in Jingyan based on the JinYe1 well (revised from Refs. [4]). Due to the existence of Sichuan Basin margin, the ancient burial depth of the Niutitang shale distributed in its periphery was only 6200 m.

paleouplift, the Yichang Slope Belt, the Zigui Depression, and many other tectonic units (Figure 12). At present, shale gas exploration has focused mainly on the Sinian Doushantuo Formation and the Niutitang Formation by the China Geological Survey, in the southeastern margin of the Huangling paleouplift [33, 39]. The Huangling paleouplift was formed during the Late Jurassic to Early Cretaceous with a monoclinical structure trending SE [40].

The Early Cambrian facies in the study area was developed as a result of the structuration in the Late Sinian period. Tectonic movement at the end of the Sinian led to the area as

a whole forming a low section in the southwest and a high section in the northeast [5]. As a result, the Niutitang Formation thickens from the northeast to the southwest. The lithofacies of the Niutitang Formation in Yichang is gray-black and black shale mixed with marl [2]. The sediments were deposited in shallow-deep and deep shelves with a thickness of 150-240 m [6, 7]. The Niutitang Formation can be roughly divided into three sections: (i) the lower section is black shale with a thin layer of silty limestone, which is a nontypical carbonate deposit at the early stage of transgression; (ii) the middle section is gray-black and black carbonaceous shale,

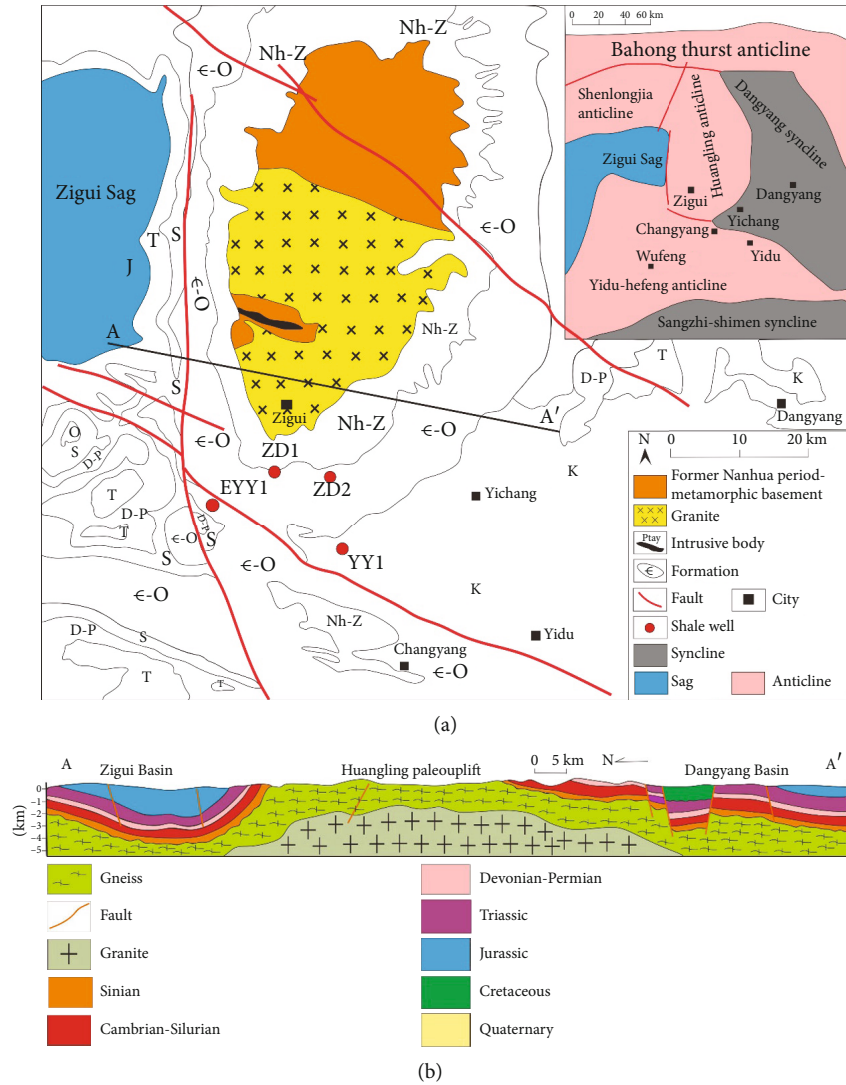


FIGURE 12: Plane and section structure of the Huangling Uplift in Hubei (revised from Refs. [5, 39]).

deposited on the outer shelf as a result of extensive transgression; and (iii) the upper section is micritic limestone which is deposited on the open platform at the high stage of transgression [2, 5, 6]. The shale with $TOC \geq 2.0\%$ is mainly developed in the middle section of the Niutitang Formation, but with thickness variations from 9 m to 140 m [23].

TOC content of the Niutitang shale in Yichang mainly ranges between 1.2% and 4.4%, with an average value of 2.3% [2, 6, 7, 40]. The $Eq-R_o$ of the Niutitang shale in Yichang is generally below 3.0%, with an average value of 2.8% [2, 6, 7]. The Niutitang shale in Yichang is dominated by quartz, clay, and carbonate. The average quartz content is 39.3% for samples from the EYY1 well, with a range of 30.2% to 50.2%. The average clay mineral content is 33.7% and has a range of 2.7% to 61.3% from samples of the YD2 well. The average carbonate mineral content is 26.2% and has a range of 8% to 39% from samples of the ZD1 well [2, 5–7].

There are a lot of OM pores inside the pyrobitumen of the Yichang shale samples. These OM pores are mostly oval and

round, with a regular morphology [2, 12, 15]. For Yichang, the maximum paleoburial depth of the Niutitang shale is 6500 m, corresponding to an $Eq-R_o$ of 2.3% to 2.8% (Figures 13 and 10).

The maximum paleoburial depth of the Niutitang shale seems to be closely related to the paleostructure of the study area, as in the case of Yichang, which is structurally located on the wing of the Huangling paleouplift [6, 40]. Due to the presence of the Huangling paleouplift, the maximum burial depth of the Niutitang shale in the Yichang area is much shallower than its peers. According to Figure 14 which is closer to the Huangling paleouplift, the $Eq-R_o$ of the Niutitang shale is lower (Figure 15). The $Eq-R_o$ average of the Niutitang shale in the ZD1 well is correspondingly 1.61% [2, 5, 7, 40].

5.2.2. Niutitang Shale in Southern Guizhou. The Southern Guizhou area is located in the south of China, bordering the Central Guizhou Uplift in the west and adjacent to the Xuefeng Mountain Uplift in the east, the Wuling Depression in the north, and the Qiannan Depression in the south

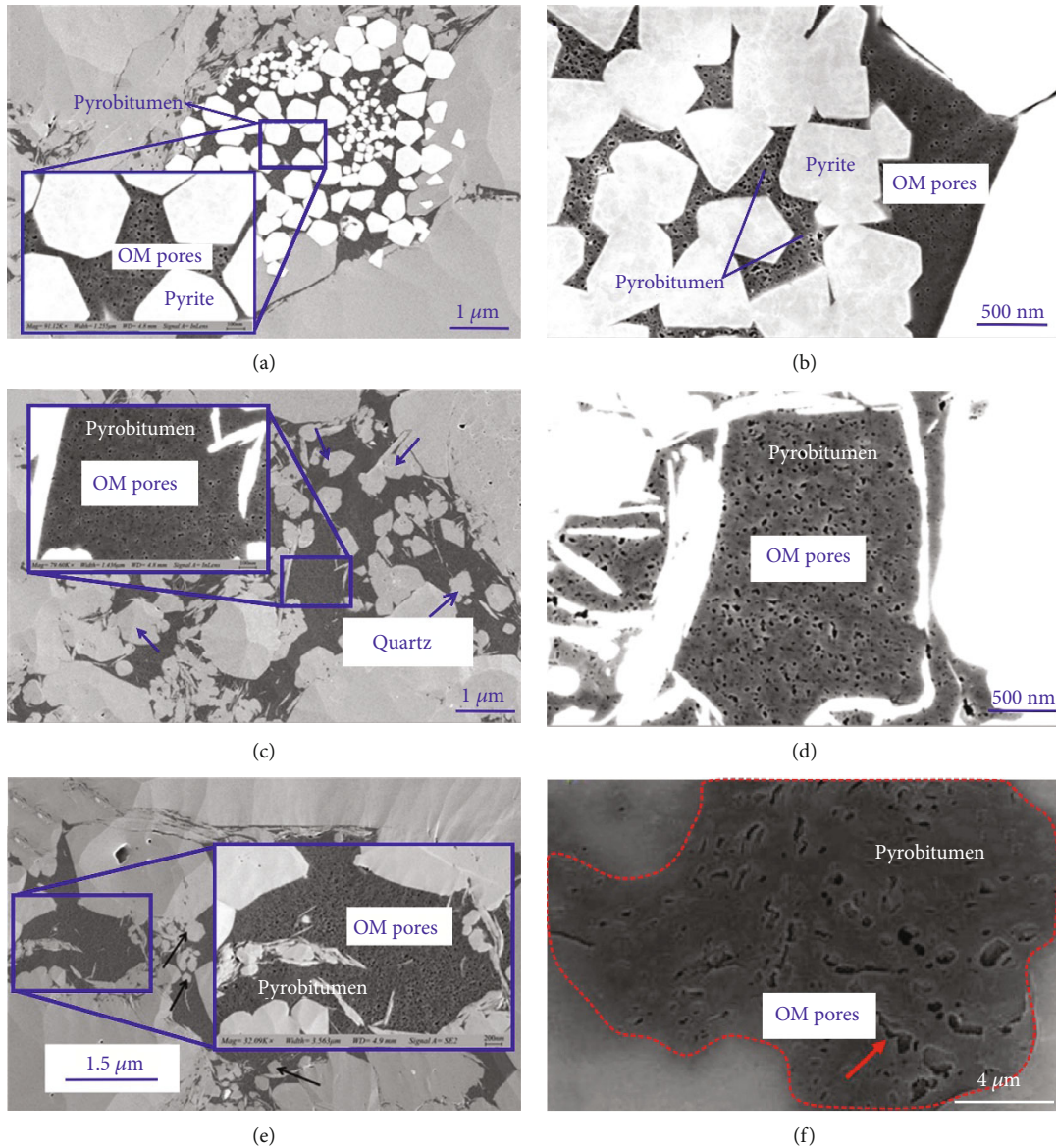


FIGURE 13: A large number of OM pores in the pyrobitumen of Yichang samples (EYY1 well, 3043 m) are shown. (a, b) The pyrobitumen with OM pores in pyrite particles. (c–f) OM pores in the pyrobitumen in the mineral matrix. Parts of this figure are revised from [2, 40].

(Figure 16). In the early Paleozoic and late Paleozoic, Southern Guizhou experienced many large-scale transgression events and formed two sets of black shales representing the Cambrian, the Upper Ordovician, and the Lower Silurian [41, 42]. The bottom of the Niutitang Formation is gray siliceous shale, the middle and lower part is gray carbonaceous shale, the upper part is dark gray argillaceous dolomite and mudstone, and the top is dark gray limestone [43, 44].

TOC content of the Niutitang shale in Southern Guizhou mainly ranges between 2.7% and 4.0%, with an average value of 3.41% [45]. The E_q-R_o of the Niutitang shale in Southern Guizhou is generally below 3.0%, with an average value of 2.4% [46, 47]. Minerals of the Niutitang shale in Southern Guizhou are also dominated by quartz, clay, and carbonate [10, 11].

There are a lot of OM pores inside the Southern Guizhou samples (Figure 17). These OM pores are mostly oval and

round, with a regular morphology. For the Southern Guizhou, the maximum paleoburial depth of the Niutitang shale is 5600 m, corresponding to an E_q-R_o of 2.2% to 2.7% (Figure 14), similar to the Yichang shale samples. The maximum paleoburial depth of the Niutitang shale seems to be closely related to the paleostructure of the Southern Guizhou area, which is structurally located on the east wing of the Qianzhong paleouplift [42, 45]. Due to the presence of the Qianzhong paleouplift, the maximum ancient burial depth of the Niutitang shale in Southern Guizhou is much shallower than its peers.

5.3. Summary. The Niutitang shale in Yichang and Guizhou has a similar thermal maturity compared with that in Jingyan. A large number of OM pores are developed in the Niutitang shale samples in Yichang and Guizhou, which is similar to the pore structure characteristics of the Niutitang

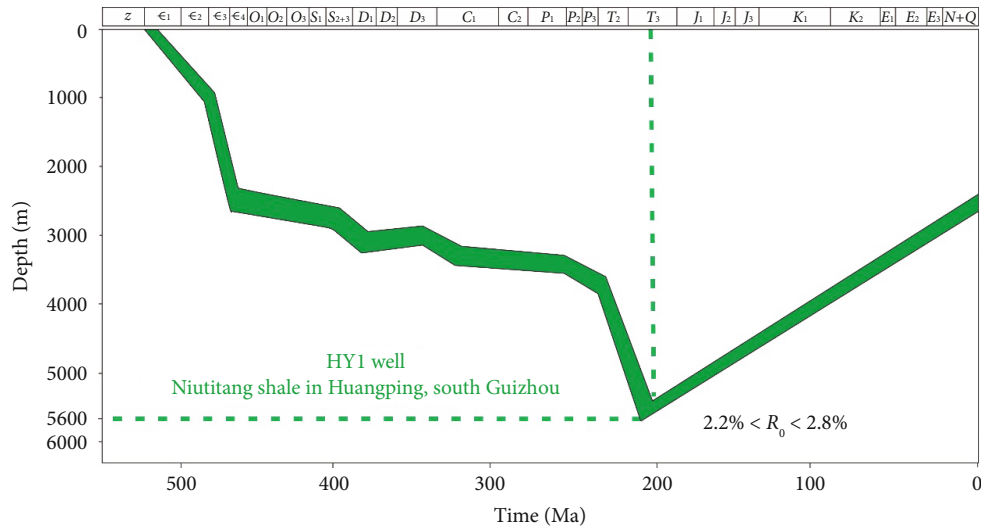


FIGURE 14: Burial history of the Niutitang shale in southern Guizhou was based on the HY1 well (revised from Ref. [9]). Due to the existence of Qianzhong paleouplift, the ancient burial depth of the Niutitang shale distributed in its periphery was only 5600 m.

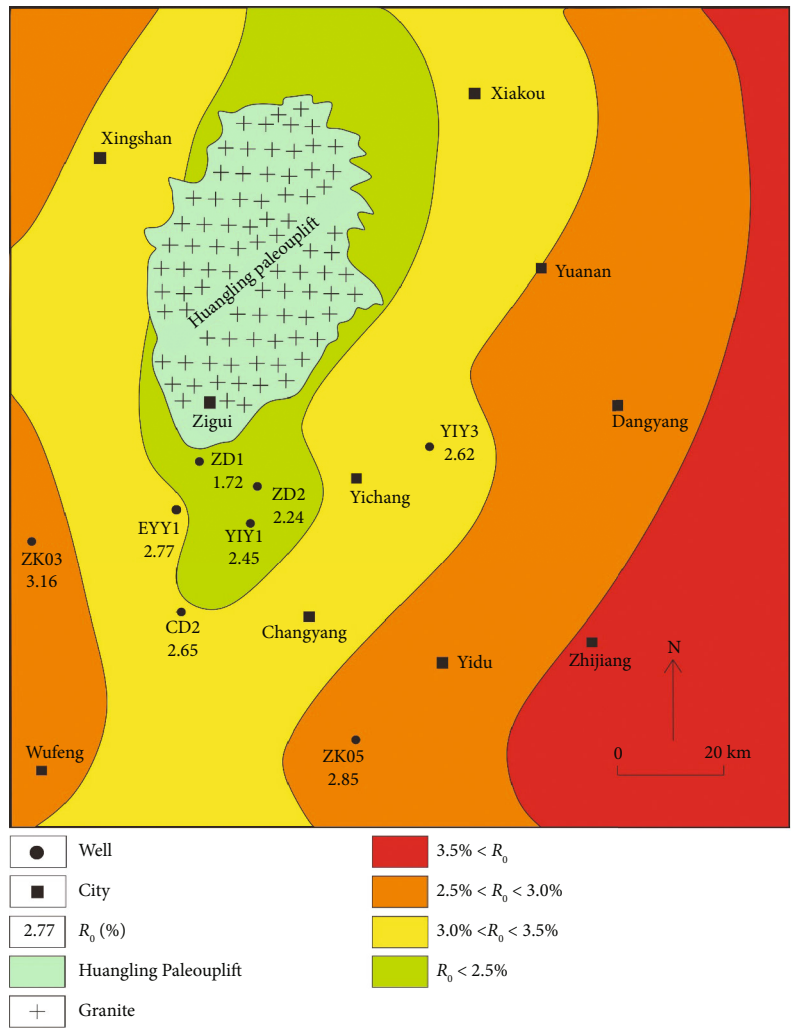


FIGURE 15: The Eq- R_0 distribution of the Niutitang shale around the Huangling paleouplift. Due to the existence of the Huangling paleouplift, the ancient burial of the Niutitang shale is lower than those of other areas in south China. The closer to the uplift, the lower the thermal maturity of the shale.

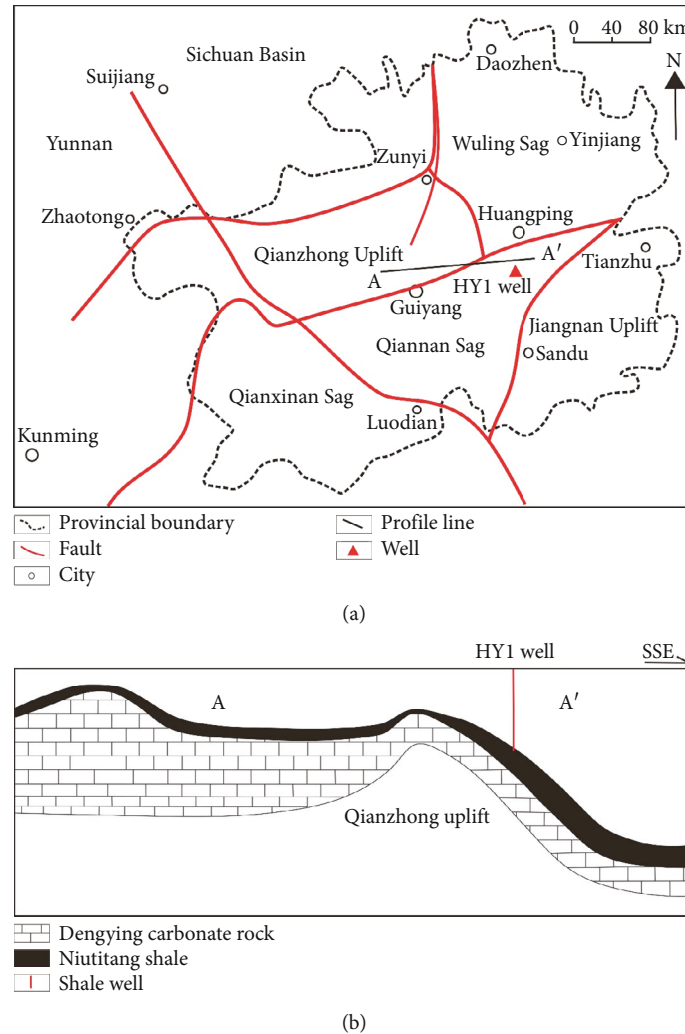


FIGURE 16: Plane and section structure of Qianzhong Uplift in Guizhou (revised from [41]).

shale in the Jingyan area. However, from the perspective of the Niutitang shale in Chongqing, its thermal maturity is much higher than that in the Jingyan, Yichang, and Guizhou regions, while there are no OM pores of the Niutitang shale in Chongqing. However, other parameters such as TOC content, mineral composition, and kerogen type of the Niutitang shale reservoirs in the four regions (Jingyan, Chongqing, Yichang, and Guizhou) have similar characteristics [2, 6, 7, 40, 42, 48–51]. Therefore, thermal maturity is the key factor to control the OM pore development.

From the perspective of tectonic evolution, the maximum burial depth of a formation controls the thermal maturity of a shale reservoir, while the burial depth is controlled by the regional tectonic pattern [1, 4, 14, 32]. According to the regional structure pattern of Jingyan, Yichang, and Guizhou, the underlying structures of the Niutitang shale are all paleouplift structures, and the target shale is distributed in the slope belt of the paleouplift [2, 4, 26, 33]. Due to the existence of the paleouplift, the maximum ancient burial depth of the Niutitang shale in Jingyan, Yichang, and Guizhou is about 6000 meters [2, 4, 5, 10], and the burial depth of the shale is moderate, avoiding excessive evolution and leaving

a large number of OM pores in the shale reservoir [1, 16]. In contrast, in the Chongqing area, due to the absence of the paleouplift structure, the maximum ancient burial depth of the Niutitang shale in this area reached 8000 meters [26], and the shale reservoir experienced excessive thermal evolution, resulting in the disappearance of a large number of OM pores, and a large volume of gas was lost due to the absence of effective storage spaces in the reservoir [49, 52, 53].

According to the successful exploration experiences of the Niutitang shale in Jingyan, Yichang, and Southern Guizhou and the failure experience of the same formation in areas like Chongqing, the exploration of the ancient marine shale reservoirs should focus on areas with moderate thermal maturity. The marine shale sedimentary in the paleouplift region has appropriate thermal maturity, so that a large number of OM pores are retained in the shale reservoir, which provides an effective space for gas occurrence, as well as a large amount of gas enrichment. Therefore, the exploration and development of marine shale with old sedimentary age (especially the lower Cambrian and older formations) should focus on the slope belt of a paleouplift (Figure 18).

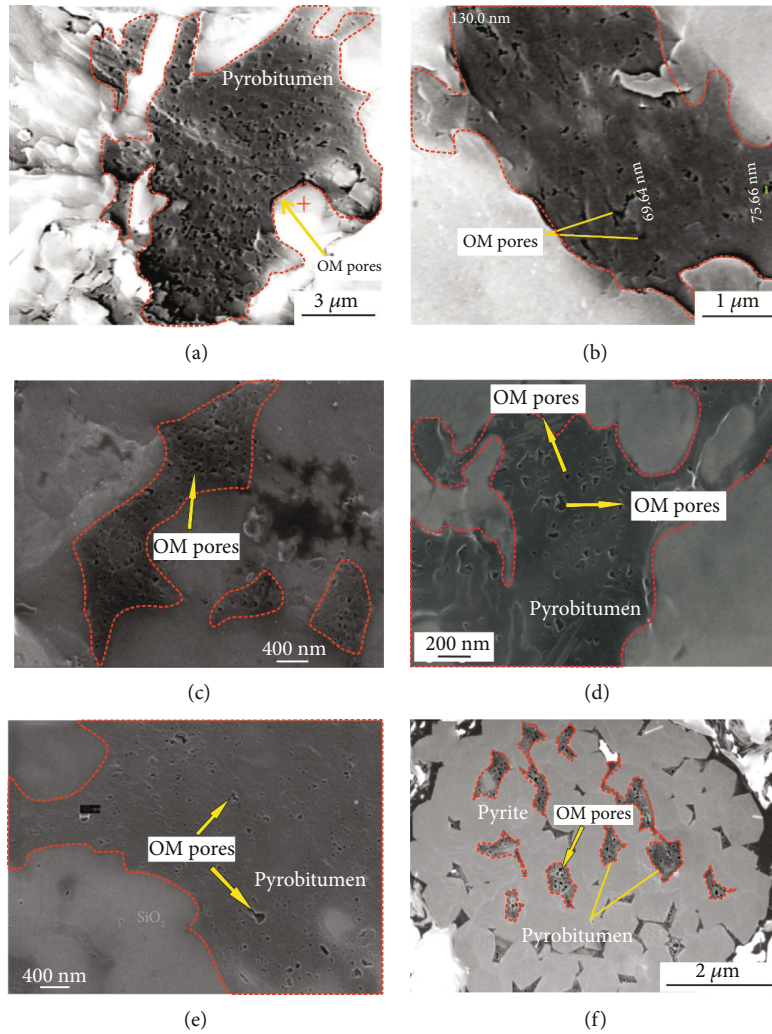


FIGURE 17: A large number of OM pores in pyrobitumen of southern Guizhou samples. (a–e) OM pores in the pyrobitumen in the mineral matrix. (f) The pyrobitumen with OM pores in pyrite particles. This figure was revised from Refs. [10, 11, 44, 46].

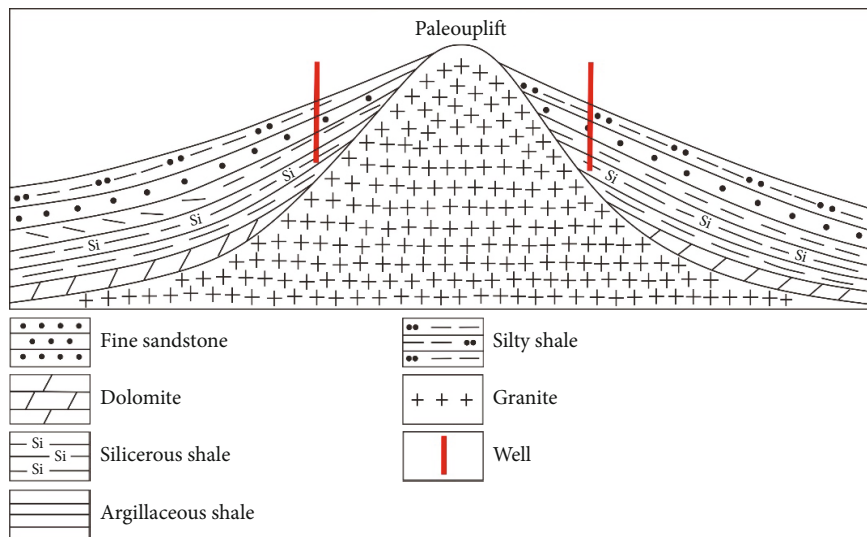


FIGURE 18: The target area for the exploration of ancient marine shale gas reservoirs. The exploration and development of ancient marine shales should focus on areas around paleouplifts.

6. Conclusions

Scanning electron microscope (SEM) and geotectonic characteristics were used to illustrate organic matter (OM) pore structure and evolution in the Lower Cambrian Niutitang shale samples with different thermal maturities in northeastern Chongqing and Jingyan of the southwestern Sichuan Basin in south China. Conclusions of this study are as follows:

- (1) The Niutitang shales in both Jingyan and Chongqing cities (south China) have similar TOC content (ranging from 1.5% to 3.0%), mineral composition (dominated by silica and clays), and kerogen type (dominated by type I) but different thermal maturity. The Niutitang shale in Jingyan has a lower thermal maturity (2.0%–3.0%) than that (3.0%–4.0%) in Chongqing
- (2) OM pore development characteristics of the Niutitang shale in Jingyan and Chongqing are quite different. The Niutitang shale in Jingyan developed a lot of large-sized OM pores. In contrast, almost no OM pores were found in the Niutitang shale in Chongqing. The OM pores in the Niutitang shale in Jingyan act as an effective storage of gas, contributing to gas enrichment
- (3) OM pore development is mainly controlled by thermal maturity. A lot of OM pores can develop in shale reservoirs when the thermal maturity (E_q-R_o) of shale is lower than 3.0%. A significant amount of OM pores will disappear when the thermal maturity exceeds 3.0%
- (4) Ancient marine shales have a relatively shallow maximum burial depth when they were deposited on the slope belt of paleouplifts, which can ensure that shale reservoirs are likely not overly mature

Data Availability

All data, models, and code generated or used during the study appear in the submitted article.

Conflicts of Interest

The authors declare that they have no conflicts of interest.

Authors' Contributions

Pengfei Wang and Chen Zhang contributed equally to this work.

Acknowledgments

The authors wish to thank all those who have supplied us with original geological data. Also, the authors thank the China Geological Survey programs (Nos. DD20190414 and 121201229000160021) for supporting this work. The authors would also like to thank Enago (<http://www.enago.cn/>) for

the English language review. This work was financially supported by grants from the National Natural Science Foundation of China (No. 42002050), the China Postdoctoral Science Foundation funded project (No. 2020M680815), and the Youth Natural Science Foundation of Hebei province (No. 2019403190.)

References

- [1] W. Zhao, J. Li, T. Yang, S. Wang, and J. Huang, "Geological difference and its significance of marine shale gases in South China," *Petroleum Exploration and Development*, vol. 43, no. 4, pp. 547–559, 2016.
- [2] G. Zhai, Y. Wang, G. Liu et al., "The Sinian-Cambrian formation shale gas exploration and practice in southern margin of Huangling paleo-uplift," *Marine and Petroleum Geology*, vol. 109, pp. 419–433, 2019.
- [3] Z. Xi, S. Tang, and J. Wang, "The reservoir characterization and shale gas potential of the Niutitang formation: case study of the SY well in northwest Hunan Province, South China," *Journal Petroleum Science and Engineering*, vol. 171, pp. 687–703, 2018.
- [4] J. Zhao, Z. Jin, Q. Hu et al., "Geological controls on the accumulation of shale gas: a case study of the early Cambrian shale in the Upper Yangtze area," *Marine and Petroleum Geology*, vol. 107, pp. 423–437, 2019.
- [5] J. Zhang, G. Zhai, D. Wang et al., "Tectonic evolution of the Huangling dome and its control effect on shale gas preservation in the north margin of the Yangtze Block, South China," *China Geology*, vol. 3, no. 1, pp. 28–37, 2020.
- [6] S. Bao, G. Zhai, Z. Zhou et al., "The evolution of the Huangling uplift and its control on the accumulation and preservation of shale gas," *China Geology*, vol. 3, pp. 346–353, 2018.
- [7] G. Zhai, J. Li, Y. Jiao et al., "Applications of chemostratigraphy in a characterization of shale gas sedimentary Microfacies and predictions of sweet spots—taking the Cambrian black shales in Western Hubei as an example," *Marine and Petroleum Geology*, vol. 109, pp. 547–560, 2019.
- [8] W. Yang, S. He, S. Iglauer et al., "Porosity characteristics of different lithofacies in marine shale: a case study of Neoproterozoic Sinian Doushantuo formation in Yichang area, China," *Journal Petroleum Science and Engineering*, vol. 187, p. 106856, 2020.
- [9] F. Chen, S. Lu, and X. Ding, "Gas generation period and quantity of organic-rich Niutitang Shale in Qiannan Depression, China," *Journal of China University of Petroleum*, vol. 40, no. 3, pp. 55–62, 2016.
- [10] W. Sun, Y. Zuo, S. Wang et al., "Pore structures of shale cores in different tectonic locations in the complex tectonic region: a case study of the Niutitang formation in Northern Guizhou, Southwest China," *Journal of Nature Gas Science and Engineering*, vol. 80, p. 103398, 2020.
- [11] W. Zeng, W. Ding, J. Zhang, Y. Li, R. Wang, and K. Jiu, "Analyses of the characteristics and main controlling factors for the micro/nanopores in Niutitang shale from China's southeastern Chongqing and northern Guizhou regions," *Earth Science Frontiers*, vol. 26, no. 3, pp. 220–235, 2019.
- [12] R. Loucks, R. Reed, M. Ruppel, and U. Hammes, "Spectrum of pore types and networks in mudrocks and a descriptive classification for matrix-related mudrock pores," *AAPG Bulletin*, vol. 96, no. 6, pp. 1071–1098, 2012.

- [13] K. Milliken, M. Rudnicki, D. Awwiller, and T. Zhang, "Organic matter-hosted pore system, Marcellus formation (Devonian), Pennsylvania," *AAPG Bulletin*, vol. 97, no. 2, pp. 177–200, 2013.
- [14] X. Guo, D. Hu, Y. Li, Z. Wei, X. Wei, and Z. Liu, "Geological factors controlling shale gas enrichment and high production in Fuling shale gas field," *Petroleum Exploration and Development*, vol. 44, no. 4, pp. 513–523, 2017.
- [15] H. Hu, F. Hao, J. Lin, Y. Lu, Y. Ma, and Q. Li, "Organic matter-hosted pore system in the Wufeng-Longmaxi (O₃w-S₁1) shale, Jiaoshiba area, Eastern Sichuan Basin, China," *International Journal of Coal Geology*, vol. 173, pp. 40–50, 2017.
- [16] Y. Hou, K. Zhang, F. Wang et al., "Structural evolution of organic matter and implications for graphitization in over-mature marine shales, south China," *Marine and Petroleum Geology*, vol. 109, pp. 304–316, 2019.
- [17] Q. Chen, Y. Kang, L. You, P. Yang, X. Zhang, and Q. Cheng, "Change in composition and pore structure of Longmaxi black shale during oxidative dissolution," *International Journal of Coal Geology*, vol. 172, pp. 95–111, 2017.
- [18] W. Ji, Y. Song, Z. Rui, M. Meng, and H. Huang, "Pore characterization of isolated organic matter from high matured gas shale reservoir," *International Journal of Coal Geology*, vol. 174, pp. 31–40, 2017.
- [19] R. Loucks and R. Reed, "Scanning-electron-microscope petrographic evidence for distinguishing organic-matter pores associated with depositional organic matter versus migrated organic matter in mudrock," *Gulf Coast Associate Geology Society Journal*, vol. 3, pp. 51–60, 2014.
- [20] P. Wang, Z. Jiang, L. Chen et al., "Pore structure characterization for the Longmaxi and Niutitang shales in the Upper Yangtze Platform, South China: evidence from focused ion beam-He ion microscopy, nano-computerized tomography and gas adsorption analysis," *Marine and Petroleum Geology*, vol. 77, pp. 1323–1337, 2016.
- [21] P. Wang, Z. Jiang, W. Ji et al., "Heterogeneity of intergranular, intraparticle and organic pores in Longmaxi shale in Sichuan Basin, South China: evidence from SEM digital images and fractal and multifractal geometries," *Marine and Petroleum Geology*, vol. 72, pp. 122–138, 2016.
- [22] R. Loucks, R. Reed, S. Ruppel, and D. Jarvie, "Morphology, genesis, and distribution of nanometer-scale pores in siliceous mudstones of the Mississippian Barnett shale," *Journal of Sedimentary Research*, vol. 79, no. 12, pp. 848–861, 2009.
- [23] K. Ma, Y. Lu, X. Liu, G. Zhai, Y. Wang, and C. Zhang, "Depositional environment and organic matter enrichment of the lower Cambrian Niutitang shale in western Hubei Province of the middle Yangtze Block, south China," *Marine and Petroleum Geology*, vol. 109, pp. 381–393, 2019.
- [24] Q. Wang, T. Wang, W. Liu et al., "Relationships among composition, porosity and permeability of Longmaxi shale reservoir in the Weiyuan Block, Sichuan Basin, China," *Marine and Petroleum Geology*, vol. 102, pp. 33–47, 2019.
- [25] W. Wang, X. Pang, Z. Chen et al., "Statistical evaluation and calibration of model predictions of the oil and gas field distributions in superimposed basins: a case study of the Cambrian Longwangmiao formation in the Sichuan Basin, China," *Marine and Petroleum Geology*, vol. 106, pp. 42–61, 2019.
- [26] P. Wang, Z. Jiang, B. Han et al., "Reservoir characteristics and controlling factor of shale gas in Lower Cambrian Niutitang Formation, South China," *Petroleum Research*, vol. 3, pp. 210–220, 2018.
- [27] W. Yang, R. Zuo, Z. Jiang et al., "Effect of lithofacies on pore structure and new insights into pore-preserving mechanisms of the over-mature Qiongzhusi marine shales in Lower Cambrian of the southern Sichuan Basin, China," *Marine and Petroleum Geology*, vol. 98, pp. 746–762, 2018.
- [28] J. Zhao, Z. Jin, Z. Jin et al., "Mineral types and organic matters of the Ordovician-Silurian Wufeng and Longmaxi shale in the Sichuan Basin, China: implications for pore systems, diagenetic pathways, and reservoir quality in fine-grained sedimentary rocks," *Marine and Petroleum Geology*, vol. 86, pp. 655–674, 2017.
- [29] H. Nie, C. Sun, G. Liu, W. Du, and Z. He, "Dissolution pore types of the Wufeng Formation and the Longmaxi Formation in the Sichuan basin, south China: implications for shale gas enrichment," *Marine and Petroleum Geology*, vol. 101, pp. 243–251, 2019.
- [30] H. Nie, D. Li, G. Liu et al., "An overview of the geology and production of the Fuling shale gas field, Sichuan basin, China," *Energy Geoscience*, vol. 1, no. 3-4, pp. 147–164, 2020.
- [31] Q. Xu, N. Qiu, W. Liu, A. Shen, and X. Wang, "Thermal evolution and maturation of Sinian and Cambrian source rocks in the central Sichuan basin, southwest China," *Journal of Asian Earth Sciences*, vol. 164, pp. 143–158, 2018.
- [32] S. Xu, R. Liu, F. Hao et al., "Complex rotation of maximum horizontal stress in the Wufeng-Longmaxi shale on the eastern margin of the Sichuan Basin, China: implications for predicting natural fractures," *Marine and Petroleum Geology*, vol. 109, pp. 519–529, 2019.
- [33] Q. Zhang, R. Littke, L. Zieger, M. Shabani, X. Tang, and J. Zhang, "Ediacaran, Cambrian, Ordovician, Silurian and Permian shales of the upper Yangtze platform, south China: deposition, thermal maturity and shale gas potential," *International Journal of Coal Geology*, vol. 216, p. 103281, 2019.
- [34] L. Zhou, Z. Kang, Z. Wang, Y. Peng, and H. Xiao, "Sedimentary geochemical investigation for paleoenvironment of the Lower Cambrian Niutitang Formation shales in the Yangtze Platform," *Journal Petroleum Science and Engineering*, vol. 159, pp. 376–386, 2017.
- [35] X. Li, Z. Jiang, P. Wang et al., "Porosity-preserving mechanisms of marine shale in Lower Cambrian of Sichuan Basin, South China," *Journal of Nature Gas Science and Engineering*, vol. 55, pp. 191–205, 2018.
- [36] P. Wang, S. Yao, C. Jin et al., "Key reservoir parameter for effective exploration and development of high-over matured marine shales: a case study from the Cambrian Niutitang formation and the Silurian Longmaxi formation, south China," *Marine and Petroleum Geology*, vol. 121, p. 104619, 2020.
- [37] Y. Wang, L. Wang, J. Wang, Z. Jiang, C. Jin, and Y. Wang, "Characterization of organic matter pores in typical marine and terrestrial shales, China," *Journal of Nature Gas Science and Engineering*, vol. 49, pp. 56–65, 2018.
- [38] Z. Lan, X. Li, X. Chu et al., "SIMS U-Pb zircon ages and Ni-Mo-PGE geochemistry of the lower Cambrian Niutitang Formation in South China: constraints on Ni-Mo-PGE mineralization and stratigraphic correlations," *Journal of Asian Earth Sciences*, vol. 137, pp. 141–162, 2017.
- [39] S. Luo, X. Chen, A. Liu, and H. Li, "Geochemical features and genesis of shale gas from the Lower Cambrian Shuijingtuo Formation shale in Yichang block, Middle Yangtze region," *Oil & Gas Geology*, vol. 40, no. 5, pp. 999–1010, 2019.

- [40] P. Zhang, "Peculiar accumulation conditions for shale gas in the Lower Cambrian in Qianzhong uplift and its periphery," *Petroleum Geology Experiment*, vol. 39, no. 2, pp. 162–179, 2017.
- [41] S. Wei, S. He, Z. Pan et al., "Characteristics and evolution of pyrobitumen-hosted pores of the overmature Lower Cambrian Shuijingtuo shale in the south of Huangling anticline, Yichang area, China: evidence from FE-SEM petrography," *Marine and Petroleum Geology*, vol. 116, p. 104303, 2020.
- [42] W. Sun, Y. Zuo, Z. Wu et al., "Pore characteristics and evolution mechanism of shale in a complex tectonic area: case study of the Lower Cambrian Niutitang Formation in Northern Guizhou, Southwest China," *Journal Petroleum Science and Engineering*, vol. 193, p. 107373, 2020.
- [43] F. Shang, Y. Zhu, Q. Hu et al., "Characterization of methane adsorption on shale of a complex tectonic area in Northeast Guizhou, China: experimental results and geological significance," *Journal of Nature Gas Science and Engineering*, vol. 84, p. 103676, 2020.
- [44] Z. Liu, B. Gao, Z. Hu, W. Du, H. Nie, and T. Jiang, "Pore characteristics and formation mechanism of high-maturity organic-rich shale in lower Cambrian Jiumenchong Formation, southern Guizhou," *Petroleum Research*, vol. 3, no. 1, pp. 57–65, 2018.
- [45] Q. Gou, S. Xu, F. Hao et al., "Full-scale pores and microfractures characterization using FE-SEM, gas adsorption, nano-CT and micro-CT: a case study of the Silurian Longmaxi Formation shale in the Fuling area, Sichuan Basin, China," *Fuel*, vol. 253, pp. 167–179, 2019.
- [46] X. Li, Z. Shen, W. Li, and H. Huang, "Exploration and development potential of Niutitang Fm shale gas in Fenggang area, North Guizhou," *Nature Gas Industry*, vol. 36, no. 12, pp. 72–79, 2016.
- [47] Z. Li, J. Zhang, D. Dong et al., "Gas-bearing property of the Lower Cambrian Niutitang Formation shale and its influencing factors: a case study from the Cengong block, northern Guizhou Province, South China," *Marine and Petroleum Geology*, vol. 120, p. 104556, 2020.
- [48] K. Zhang, C. Jia, Y. Song et al., "Analysis of Lower Cambrian shale gas composition, source and accumulation pattern in different tectonic backgrounds: a case study of Weiyuan Block in the Upper Yangtze region and Xiuwu Basin in the Lower Yangtze region," *Fuel*, vol. 263, pp. 1–15, 2020.
- [49] K. Zhang, J. Peng, W. Liu et al., "The role of deep geofluids in the enrichment of sedimentary organic matter: a case study of the Late Ordovician-Early Silurian in the upper Yangtze region and early Cambrian in the lower Yangtze region, south China," *Geofluids*, vol. 2020, Article ID 8868638, 12 pages, 2020.
- [50] K. Zhang, J. Peng, X. Wang et al., "Effect of organic maturity on shale gas genesis and pores development: a case study on marine shale in the upper Yangtze region, South China," *Open Geoscience*, vol. 12, no. 1, pp. 1617–1629, 2020.
- [51] S. Xu, Q. Gou, F. Hao, B. Zhang, Z. Shu, and Y. Zhang, "Multi-scale faults and fractures characterization and their effects on shale gas accumulation in the Jiaoshiha area, Sichuan Basin, China," *Journal of Petroleum Science and Engineering*, vol. 189, p. 107026, 2020.
- [52] Z. Liu, B. Gao, Y. Zhang, W. Du, D. Feng, and H. Nie, "Types and distribution of the shale sedimentary facies of the Lower Cambrian in Upper Yangtze area, South China," *Petroleum Exploration Development*, vol. 44, no. 1, pp. 20–31, 2017.
- [53] A. Li, W. Ding, K. Jiu, Z. Wang, R. Wang, and J. He, "Investigation of the pore structures and fractal characteristics of marine shale reservoirs using NMR experiments and image analyses: a case study of the lower Cambrian Niutitang Formation in northern Guizhou province, south China," *Marine and Petroleum Geology*, vol. 89, pp. 530–540, 2018.

Research Article

A Study on Astronomical Cycle Identification and Environmental Response Characteristics of Lacustrine Deep-Water Fine-Grained Sedimentary Rocks: A Case Study of the Lower Submember of Member 3 of Shahejie Formation in Well Fanye-1 of Dongying Sag, Bohai Bay Basin, China

Ledan Yu ¹, Jun Peng ¹, Tianyu Xu,¹ Yubin Wang,¹ and Haodong Han²

¹School of Geoscience and Technology, Southwest Petroleum University, Chengdu, Sichuan 610500, China

²Chengdu Geological Survey Center, China Geological Survey, Chengdu, Sichuan 610081, China

Correspondence should be addressed to Jun Peng; 445371976@qq.com

Received 27 January 2021; Accepted 10 June 2021; Published 28 June 2021

Academic Editor: Julie K. Pearce

Copyright © 2021 Ledan Yu et al. This is an open access article distributed under the Creative Commons Attribution License, which permits unrestricted use, distribution, and reproduction in any medium, provided the original work is properly cited.

With the further exploration and development of shale oil and gas, cycle division of fine-grained sedimentary rock strata has been increasingly highly focused on by scholars. Owing to the application of the theory of classical sequence stratigraphy based on water depth changes and its technical methods being unsatisfactory in the isochronous division and correlation of deep-water fine-grained sedimentary strata, the cycle division of fine-grained sedimentary rock strata has always been a difficult point in the study of sequence stratigraphy. In this paper, the Milankovitch cycle recorded from the study interval and the environment response characteristics were studied, with the lacustrine shale in the lower third submember of the Paleogene Shahejie Formation (lower Es3 submember) in Well Fanye-1 of the Dongying sag, Bohai Bay Basin, as the object of study, by such technical means as thin section identification and X-ray whole rock diffraction, based on such data as logging data and geochemistry, combining the methods of spectral analysis, wavelet transform, and modulus extremum. The results showed that the stratigraphic cycle thicknesses caused by long eccentricity, short eccentricity, and obliquity periods were 38.95 m, 12.98 m, and 4.10 m, respectively, and a total of 16 short eccentricity periods and 4.5 long eccentricity periods were identified in the study interval. Thus, it was further calculated that the sedimentation time was approximately 1.905 Ma, and the average sedimentation rate was estimated to be 0.105 m/ka. Studies have shown that the sedimentary environment of lacustrine fine-grained sedimentary rocks is controlled by the astronomical period, based on which the climate as a whole changes from relatively dry and cold to warm and wet when the eccentricity increases. The identification of the Milankovitch cycle of the lacustrine fine-grained sedimentary strata will provide references for the study of high frequency sequence and the division of high-resolution sequence strata, which can effectively solve the scientifically difficult isochronous division and correlation of lacustrine shale strata.

1. Introduction

Great strides have been made in the exploration of fine-grained sedimentary oil and gas in recent years, with the constantly improved fine-grained sedimentary oil and gas reservoir theory and the fast-growing well drilling and completion technology. The cycle division of fine-grained sedimentary strata is an important basic work for the exploration of fine-grained sedimentary oil and gas and has been a world-

wide problem in the study of cyclic stratigraphy [1–3]. Previous studies indicate that the high frequency cycle in fine-grained sedimentary strata is formed under the influence of the Milankovitch cycle [3–5], and the application of the theory of classical sequence stratigraphy based on water depth changes and its technical methods is not satisfactory in the isochronous division and correlation of deep-water fine-grained sedimentary strata [6–13]; the control of the fine-grained sedimentation process by Milankovitch cycle-

effected climate changes is also poorly studied. Therefore, there is a crying need for feasible methods to realize the isochronous division of fine-grained sedimentary strata and to analyze in detail the relationship between the fine-grained sedimentation process with frequent lithological changes and the paleoenvironment changes.

Cycle division of fine-grained sedimentary strata has always been a focus in the field of cyclic stratigraphy. In recent years, many scholars have tried different data and different methods to extract the Milankovitch cycle in sedimentary strata [14–22]. Wu and Liu performed the wavelet transform analysis using logging data to study the high resolution sequence lacustrine strata in the North Yellow Sea Basin [23]; Sun et al. performed the wavelet transform analysis using natural gamma ray logging data and identified the Milankovitch cycle in the upper Es4 submember in Niuye Well 1 and discussed the significance of the Milankovitch cycle to the exploration of shale oil [24]; Shi et al. studied the high frequency sequence of lacustrine fine-grained sedimentary rocks by the spectrum and mean spectrum fitting difference analysis on magnetic susceptibility data [3]; Ruhl et al. studied the carbon cycle in the Pliensbachian of Early Jurassic by astronomical tune, finding an obvious Milankovitch cycle period in the time series of concentration of the Fe element [25]; Hüsing et al. corrected the Miocene astrochronological framework in the Mediterranean region by astronomical tuning using the magnetic susceptibility of the La Vedova profile in the north of Italy and the Ca/Al data [20]; Renne et al. calibrated the astronomical chronicle of the Cretaceous–Paleogene boundary of the Zumai profile in Spain and calculated the age of cyclic strata [26]; and Nie et al. presented in their study the precipitation record of a lake in the Late Miocene, suggesting that the main short eccentricity period in the Qaidam Basin in Northern China is similar to the record of the East Asian summer monsoon in the Later Quaternary [27]. Wang et al. presented astronomically calibrated gamma-ray log and CGR curves from the clastic and carbonate successions of well GFD-1 in the Pingle Depression of South China. A high-resolution astronomical time scale and high-resolution sedimentation rate curve of the Lopingian from well GFD-1 were constructed by cyclostratigraphic analysis [28]. Chen et al. passed the power spectrum/fast Fourier transform (FFT) and gamma rays of 4 wells including Liu 8 wells of the Lower Cretaceous Xiagou Formation in the Jiuquan Basin (GR) correlation coefficient analysis of series. It reveals the existence of astronomical periods such as long eccentricity, short eccentricity, slope, and precession in the study interval [29]. Zhao et al. used spectrum analysis and wavelet transform to reveal that the Milankovitch cycles are reflected in the third reservoir of the Saertu Formation (SIII). Evidently, the astronomical orbital period had an impact on SIII [30]. In many alternative indicators used for Milankovitch cycle analysis, logging data and magnetic susceptibility data are often used in previous studies, and the studies are performed by spectral analysis method, wavelet transform method, or the combination, and these studies have played an important role in promoting enriched sequence division of fine-grained sedimentary strata. However, there are few studies on environmental

response characteristics of Milankovitch cycles. In this study, the logging data sensitive to cyclicity were still selected, and a modulus extremum analysis was further conducted on the basis of previously used spectral analysis method or wavelet transform method. This analytical method was added to mutually verify the accuracy in cycle division, thus perfecting the study methods for the Milankovitch cycle of lacustrine shale, improving the accuracy of sequence unit division and making the division results more consistent with reality. At the same time, previous studies have been less involved in the environmental responses with a very low level. Therefore, the environment response characteristics of Milankovitch cycles were further discussed in this paper based on the study of Milankovitch cycles.

A large suite of fine-grained sedimentary rocks develop in the Paleogene Shahejie Formation in Dongying sag, Bohai Bay Basin, China. This sag has abundant oil and gas resources, with a high degree of exploration [24], complete logging series, and rich geochemical test analysis data, thus being the best region for astronomical cycle identification using logging data. Achievements of many scholars in such aspects as lithofacies and sedimentary environment of this suite of fine-grained sedimentary rocks in recent years have vigorously promoted the exploration and development of shale oil and gas. However, there is a lack of a more perfect method for lacustrine shale sequence division now, and few studies focus on the relationship between the sedimentation process of lacustrine fine-grained rocks with frequent lithological changes and the paleoenvironment changes. On the basis of previous studies, the author explored the identification of the Milankovitch cycle of logging information-based fine-grained sediments and its environment response characteristics in the case of the lower Es3 submember in Well Fanye-1, predicated on Milankovitch cycle theory, based on such data as rock core observation, thin section identification, X-ray whole-rock diffraction, element geochemistry, and logging data, combining the methods of spectral analysis, wavelet transform, and modulus extremum, thus providing a widely accepted study means and method for the isochronous cycle division and correlation of fine-grained sedimentary rocks such as shale and the environmental response characteristics of the cycle and promoting the advance in cyclic stratigraphy of fine-grained sedimentary strata.

2. Geological Setting

2.1. Tectonic-Sedimentary Evolution Characteristics. Bohai Bay Basin, located in the east of China, is a Mesozoic-Cenozoic fault basin developing from the North China Plate through Paleozoic sedimentation and based on the Indosinian and Yanshanian movements (Figures 1(a) and 1(b)). Jiyang depression is located in the southeast of Bohai Bay Basin, in which four secondary sags, namely, the Chezhen sag, Zhanhua sag, Huimin sag, and Dongying sag, have developed (Figure 1(c)) [31–34]. The Dongying sag, inheriting the tectonic evolution characteristics of the Jiyang depression, has experienced four periods, namely, the initial period, development period, peak period, and decline period, and can be divided into four stages of episodic evolution, namely,

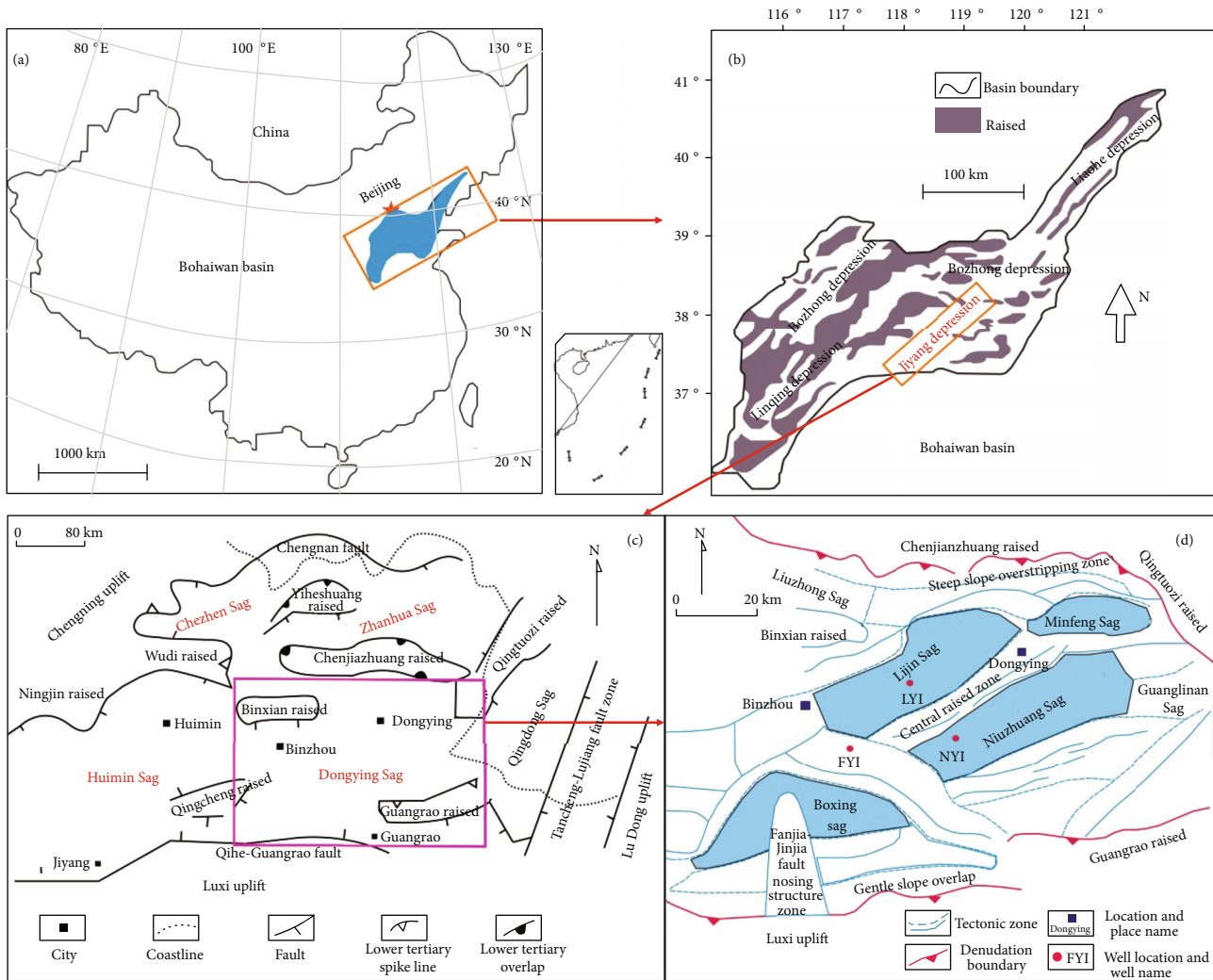


FIGURE 1: (a) Location of Bohai Bay Basin in northern China (revised by [31, 32]); (b) schematic diagram of tectonic zone of Bohai Bay Basin (revised by [31, 32]); (c) regional location and schematic diagram of tectonic zone of Jiyang depression (revised by [32]); (d) well position chart and schematic diagram of tectonic zone of Dongying sag (revised by [31–34]).

the Kongdian Formation, Es4, Es3-lower Es2 submember, and upper Es2 submember-Dongying Formation; the sedimentary center moves from south to north after each stage of extensional sedimentation, and this period is also an important period of oil and gas production. The fault depression period of tectonic evolution of the Dongying sag occurs in the Paleogene; this period is the main extensional rifting period of the sag, during which period many extensional faults develop, with strong activity, forming a typical asymmetrical dustpan-like sag style, with an exploration area of approximately 5,800 km². Many highs develop around the sag, and a series of synsedimentary normal faults inside the sag further divides the sag into four main oil-generating sub-sags (Boxing, Lijin, Niuzhuang, and Minfeng) and secondary tectonic units such as the North Steep Slope, Central Anticline Zone, and South Gentle Slope and multiple faulted tectonic zones (Figure 1(d)) [32, 33].

2.2. Strata Development Characteristics. The Dongying sag strata developing from bottom to top are Paleozoic (Pz),

Mesozoic (Mz), Paleogene (E), Neogene (N), and Quaternary (Q). Among them, Paleogene strata have a wide distribution, with a large sedimentary thickness (a maximum thickness of more than 7,000 m), which is gradually thinned and pinched out from the depocenter to the edge of the basin. Paleogene strata can be divided into the Kongdian Formation, Shahejie Formation, and Dongying Formation from bottom to top, and the Shahejie Formation can be divided into Es4, Es3, Es2, and Es1 from bottom to top (Figure 2) [32, 33, 35, 36]. Es3 is characterized by lacustrine dark grey and grey shale sedimentation, with a general thickness of 700-1,000 m and up to over 1,200 m in the central sag. Es3 can be further divided into lower Es3 submember, middle Es3 submember, and upper Es3 submember from bottom to top, respectively, of which the lower Es3 submember has interbedded layers of dark grey mudstones, oil shale, and grey brown oil shale with different thicknesses, with deep lacustrine sedimentation of a small amount of thin sand layer, grey limestone, and dolomite (Figure 2). The lower Es3 submember stratum accurately records the

Stratum					Thickness (m)	Lithology	Lithology description
System	Series	Group	Formation	Member			
Paleogene system	Eocene	Es (Shahejie formation)	Es3	M	200~600		Mainly thick gray mudstone and oil mudstone with thin sand layer
				L	100~450		Dark gray mudstone, oil mudstone, and gray-brown oil shale vary in thickness, with a small amount of thin sand layer, gray limestone, and dolomite
			Es4	U	270~350		Dark gray, gray-brown mudstone, oil shale and thin limestone, argillaceous limestone interlayer, inclusion limestone, and dolomite

	Mud-limestone		Dolomite mudstone
	Lime-limestone		Dolomites
	Lime-containing mudstone		Siltstone
	Mudstone		

FIGURE 2: Characteristics of stratum development in Dongying sag, Jiyang depression (revised by [32, 33, 35, 36]).

information of lake environment and climate changes and is an ideal carrier for Milankovitch cycle analysis.

3. Data and Experimental Methods

3.1. XRF Rock Core Scanning and X-Ray Diffraction Whole-Rock Mineral Analysis. Based on the elaborate description of rock cores of the lower Es3 submember (3,052-3,251 m) in Well Fanye-1, concentration, content, and types of various elements in the rock core samples were tested using the NITON XL3t-950 handheld mineral element analyzer (an instrument based on XRF spectroscopic analysis technology) developed by Thermo Scientific [37]. For observing the shortest cycle in the time series analysis, each cycle must be controlled by at least two points. Therefore, according to the Nyquist sampling theorem, the test density was appropriately 2.5 cm for each point and the test time was 20 s for each point to ensure the effectiveness of the collected data. In this study, such elements as Ti, Si, S, K, Ca, Fe, V, Ba, Zr, Mn, and Zn were mainly tested, and two methods were adopted, in which the mineral model was used for major elements and the soil model was used for minor elements less than 1%. Elements with an error of less than 10% in the test were selected in this paper.

X-ray whole-rock diffraction is a common method to determine the mineral composition of rocks. Rock samples were ground to powder with particle size less than 40 μm ; a test block was made with the powder and tested by the analyzer. The integral intensity of diffraction peaks of min-

erals was calculated by reference to the K value of international standard samples to obtain the mass percentages of the minerals. The experimental analysis was performed using TTR-type X-ray diffractometer, and the test conditions were according to the industrial standard SY/T5163-2010 [38].

3.2. Natural Gamma Ray Logging Data. Natural gamma ray is the intensity of gamma rays emitted during the decay of radionuclides naturally existing in strata, and the natural gamma ray intensity in the logging curve is related to the contents of ^{40}K , ^{232}Th , and ^{238}U in rocks. Such logging data have been widely used in the reconstruction of the paleoenvironment and the study of Milankovitch cycles [39, 40]. The logging data in this study were mainly obtained through the test of the CNPC Logging Engineering Co., Ltd., in which a data point was taken at an interval of 0.1 m and tested to obtain such logging data as GR, AC, SP, and resistivity.

4. Results and Discussion

4.1. Results of Milankovitch Cycle Analysis. The common methods in Milankovitch cycle study include logging spectral analysis, wavelet transform, digital filtering, and other methods, which can be used to extract the strata response information related to earth orbit parameters and thus determine the ages of strata in the millions of years and below [25, 41–44].

TABLE 1: Comparison table of natural gamma ray raw data and preprocessed data.

Depth (m)	GR/API	Denoise	Detrend	Depth (m)	GR/API	Denoise	Detrend
3051	61.436	61.908904	0.0955567	3053.2	58.013	57.811148	-3.957047
3051.1	61.614	61.880973	0.0696784	3053.3	57.739	57.548265	-4.217877
3051.2	61.962	61.700265	-0.108978	3053.4	58.012	58.065646	-3.698444
3051.3	61.748	61.34055	-0.46664	3053.5	58.737	59.093014	-2.669024
3051.4	61.026	60.929643	-0.875494	3053.6	59.625	60.081318	-1.678667
3051.5	60.443	60.617078	-1.186008	3053.7	60.369	60.446816	-1.311117
3051.6	60.514	60.520643	-1.28039	3053.8	60.8	60.481044	-1.274836
3051.7	60.978	60.775733	-1.023247	3053.9	61.044	60.637466	-1.116362
3051.8	61.453	61.353604	-0.443324	3054	61.525	61.381818	-0.369958
3051.9	62.031	62.123047	0.3281717	3054.1	62.695	63.05363	1.3039065
3052	63.047	63.13179	1.3389669	3054.2	64.923	65.440463	3.6927922
3052.1	64.507	64.409128	2.6183577	3054.3	67.811	68.30927	6.5636513
3052.2	66.004	65.723041	3.9343228	3054.4	70.531	70.709138	8.9655718
3052.3	66.955	66.844312	5.057646	3054.5	71.973	71.564115	9.8226015
3052.4	67.305	67.522101	5.7374873	3054.6	71.883	71.249998	9.5105364
3052.5	67.331	67.478868	5.6963065	3054.7	70.741	70.393862	8.6564526
3052.6	67.027	66.820185	5.0396762	3054.8	69.567	69.481237	7.7458803
3052.7	66.134	65.797358	4.0189016	3054.9	68.974	69.155916	7.4226116
3052.8	64.53	64.396162	2.6197579	3055	68.862	69.212349	7.4810974
3052.9	62.501	62.678237	0.903885	3055.1	68.84	69.146886	7.4176859
3053	60.507	60.855539	-0.916761	3055.2	68.916	69.097946	7.3707986
3053.1	58.915	59.066436	-2.703811	3055.3	69.287	69.173082	7.447987
⋮	⋮	⋮	⋮	⋮	⋮	⋮	⋮
3249.7	66.445	66.101402	8.3661231	3250.4	57.295	57.063739	-0.657174
3249.8	66.588	66.857044	9.1238178	3250.5	54.788	55.19427	-2.52459
3249.9	67.144	67.587568	9.8563937	3250.6	55.625	55.96591	-1.750897
3250	67.403	67.631191	9.902069	3250.7	59.66	60.145415	2.4306598
3250.1	66.814	66.67587	8.9488002	3250.8	65.659	65.897262	8.1845597
3250.2	64.817	64.370589	6.6455723	3250.9	71.143	70.572481	12.861831
3250.3	61.221	60.635768	2.9128035	3251	73.778	73.171648	15.46305

4.1.1. Logging Data Preprocessing. To reduce signal interference and ensure continuous stratum records and high credibility of the obtained results, a one-dimensional continuous wavelet toolkit provided by MATLAB was used in this paper to denoise and detrend the natural gamma ray logging data of the lower Es3 submember in Well Fanye-1 strata (3,051-3,251 m). Results are shown in Table 1.

In this study, the REDFIT software package in the Spectral Analysis module of Past 3.0 statistical analysis software containing various mainstream spectral analysis methods was selected for spectral analysis. Compared with other methods, the REDFIT program can be applied directly without interpolation. Meanwhile, the one-dimensional continuous wavelet toolkit provided by MATLAB was also used for wavelet analysis.

4.1.2. Theoretical Periods and Characteristics of Paleogene Earth Orbit Elements. The Milankovitch theory is a method to describe the periodical changes of the three earth orbital elements (eccentricity, obliquity, and precession) caused by

the changes in astronomical factors. In the current calculation methods of orbit elements, the representative solution was proposed by Bergen Berger and Laskar et al., and Laskar et al. provided an effective solution to the various influencing factors that have not been considered previously [45–47]. According to previous studies, the stratigraphic age of the lower Es3 submember in the Dongying sag is 30–40 Ma [48], so the solution of Laskar et al. [45] was used in this paper to calculate the theoretical values of changes in eccentricity, obliquity, and precession in 30–50 Ma at 38° north on summer solstice (June 21), thus finally calculating the proportional relationships between eccentricity, obliquity, and precession periods in the Jiyang depression in 30–50 Ma (Table 2). These proportional relationships were the key to identify the Milankovitch cycles.

4.1.3. Milankovitch Cycle Analysis

(1) Spectral Analysis. The REDFIT program in the Spectral Analysis module was selected for the spectral analysis on

TABLE 2: 30-50 Ma earth orbital parameter periods and their ratio relationship.

Parameter	Theoretical cycle (ka)				Ratio							
Eccentricity	405.00	21.667	21.525	18.407	17.397	10.510	10.348	10.186	7.837	4.253	4.090	3.260
	124.22	6.646	6.602	5.646	5.336	3.224	3.174	3.124	2.404	1.304	1.255	1.000
	99.01	5.297	5.262	4.500	4.253	2.569	2.530	2.490	1.916	1.040	1.000	
	95.24	5.095	5.062	4.329	4.091	2.471	2.433	2.395	1.843	1.000		
Obliquity	51.68	2.765	2.747	2.349	2.220	1.341	1.320	1.300	1.000			
	39.76	2.127	2.113	1.807	1.708	1.032	1.016	1.000				
	39.14	2.094	2.080	1.779	1.681	1.016	1.000					
	38.54	2.062	2.048	1.751	1.655	1.000						
Precession	23.28	1.245	1.237	1.058	1.000							
	22.00	1.177	1.169	1.000								
	18.82	1.007	1.000									
	18.69	1.000										

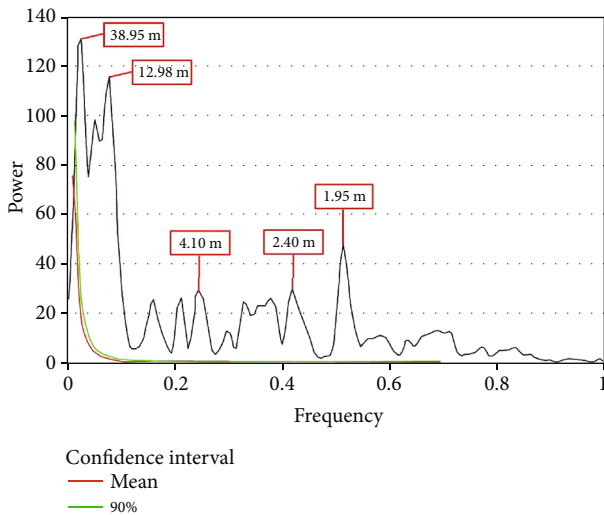


FIGURE 3: Redfit spectral analysis chart of GR curve of the lower Es3 submember in Well Fanye-1.

preprocessed natural gamma ray logging data. Pink noise curve and 90% confidence interval (CI) curve, that is, the red line and green line in Figure 3, were selected in the Significance Lines window. Figure 3 is the result chart of spectral analysis of natural gamma ray logging data in Well Fanye-1, of which the x -coordinate represents the frequency and the stratigraphic cycle thickness corresponds to the reciprocal of the dominant frequency; the y -coordinate represents spectrum energy (i.e., spectrum amplitude), namely, the significance level of a certain frequency.

The spectral analysis result of natural gamma ray data of the lower Es3 submember in Well Fanye-1 showed an obvious periodicity (Figure 3), in which the cycle thicknesses of the main peaks were 38.95 m, 12.98 m, 4.10 m, 2.40 m, 1.95 m, and other values, and the cycle thickness ratio was $38.95 : 12.98 : 4.10 : 2.40 : 1.95 = 19.974 : 6.656 : 2.103 : 1.231 : 1$, which is very close to $405 \text{ ka} : 124.22 \text{ ka} : 39.76 \text{ ka} : 23.28 \text{ ka} :$

TABLE 3: The main cycle thickness of GR curve analysis of the lower Es3 submember in Well Fanye-1 and its ratio relationship.

Frequency (1/m)	Cycle thickness (m)	Cycle thickness ratio			
0.025674	38.95	19.974	16.230	9.500	3.000
0.077022	12.98	6.656	5.408	3.166	1.000
0.243900	4.10	2.103	1.708	1.000	
0.417200	2.40	1.231	1.000		
0.513480	1.95	1.000			

TABLE 4: Comparison between dominant cycle thickness ratio and theoretical orbit period ratio.

Cycle thickness (m)	Ratio	Theoretical orbital period (ka)	
			Ratio
38.95	19.974	405	18.409
12.98	6.656	124.22	5.646
4.10	2.103	39.76	1.807
2.40	1.231	23.28	1.058
1.95	1.000	22	1.000

22 ka, the ratio of theoretical orbit periods of the Milankovitch cycle in the Paleogene (Tables 3 and 4). Therefore, the five main peaks were considered to be caused by long eccentricity (405 ka), short eccentricity (124.22 ka), obliquity (39.76 ka), and precessions (23.28 ka and 22 ka). According to the analysis, the cycle thicknesses of 38.95 m and 12.98 m corresponded to the long eccentricity period of 405 ka and the short eccentricity period of 124.22 ka, and the cycle thickness of 4.10 m corresponded to the obliquity period of 39.76 ka, while the cycle thicknesses of 2.40 m and 1.95 m corresponded to the precession periods of 23.28 ka and 22 ka. Spectral analysis results showed that the lower Es3 submember in the Well Fanye-1 may be controlled by the Milankovitch cycle, and the corresponding cycle periods and cycle thicknesses are shown in Table 4.

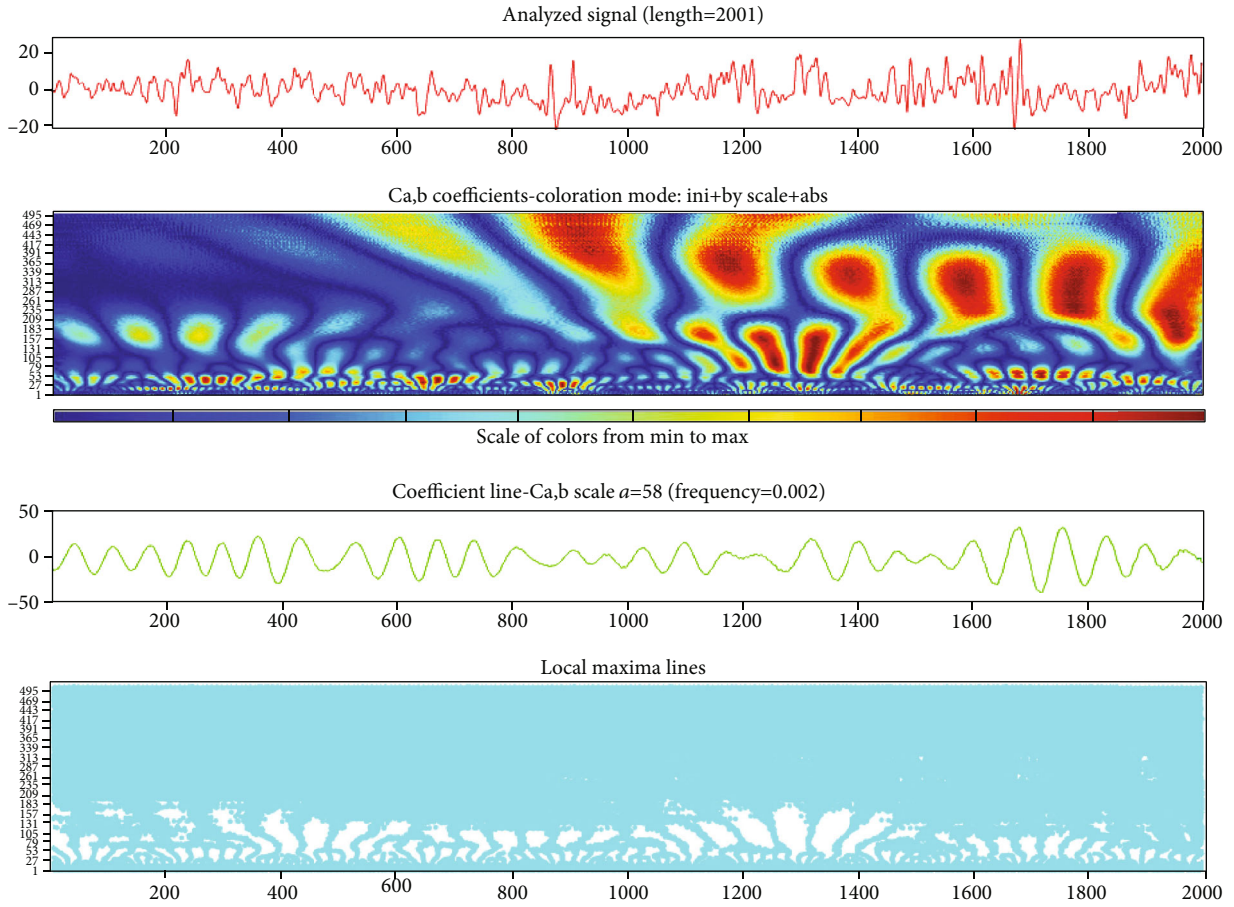


FIGURE 4: Diagram of results of one-dimensional continuous wavelet transform of the lower Es3 submember in Well Fanye-1 ($a = 512$).

(2) *Wavelet Transform.* In this paper, the one-dimensional continuous wavelet toolkit provided by MATLAB was used for wavelet analysis. The method can provide a statistical significance test to ensure the high credibility of the obtained results. One-dimensional continuous wavelet transform was performed for the natural gamma ray logging data signal of the lower Es3 submember in Well Fanye-1 using the Morlet wavelet. Results of one-dimensional continuous wavelet transform of the logging signals of the lower Es3 submember in the Well Fanye-1 at the scale of 512 ($a = 512$) are shown in Figure 4. The diagram shows, from top to bottom, the GR logging signal of the preprocessed lower Es3 submember in the Well Fanye-1, the time-frequency energy spectrum diagram (wavelet energy spectrum diagram) after the Morlet one-dimensional continuous wavelet transform, the wavelet transform coefficient curve at the current scale ($a = 512$), and the wavelet transform coefficient contour map to which time-frequency energy spectrum diagram corresponds, in which the y -coordinate represents different wavelet scales.

The wavelet coefficient matrix was extracted on the basis of wavelet analysis to calculate the modulus extremum. When searching for the extremum in the average wavelet modulus value curve, to eliminate the errors and inaccuracy caused by human identification, the formula $y = (\text{SUM}(\text{ABS}(1:n)))/n$ was self-defined in Office Excel, including sum

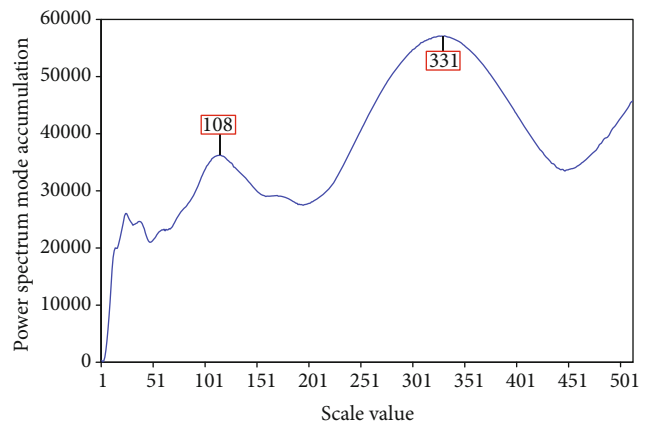


FIGURE 5: Modulus extremum diagram of wavelet analysis of GR curve of lower Es3 submember in Well Fanye-1.

function, absolute value function, and average value operation, and n in the formula is the data value at the n th column. The modulus extremum was obtained by the formula and then was determined according to the data near the extremum for whether it is a maximum or a minimum. Figure 5 shows the modulus extremum diagram of the lower Es3 submember in Well Fanye-1 obtained by matrix calculation of

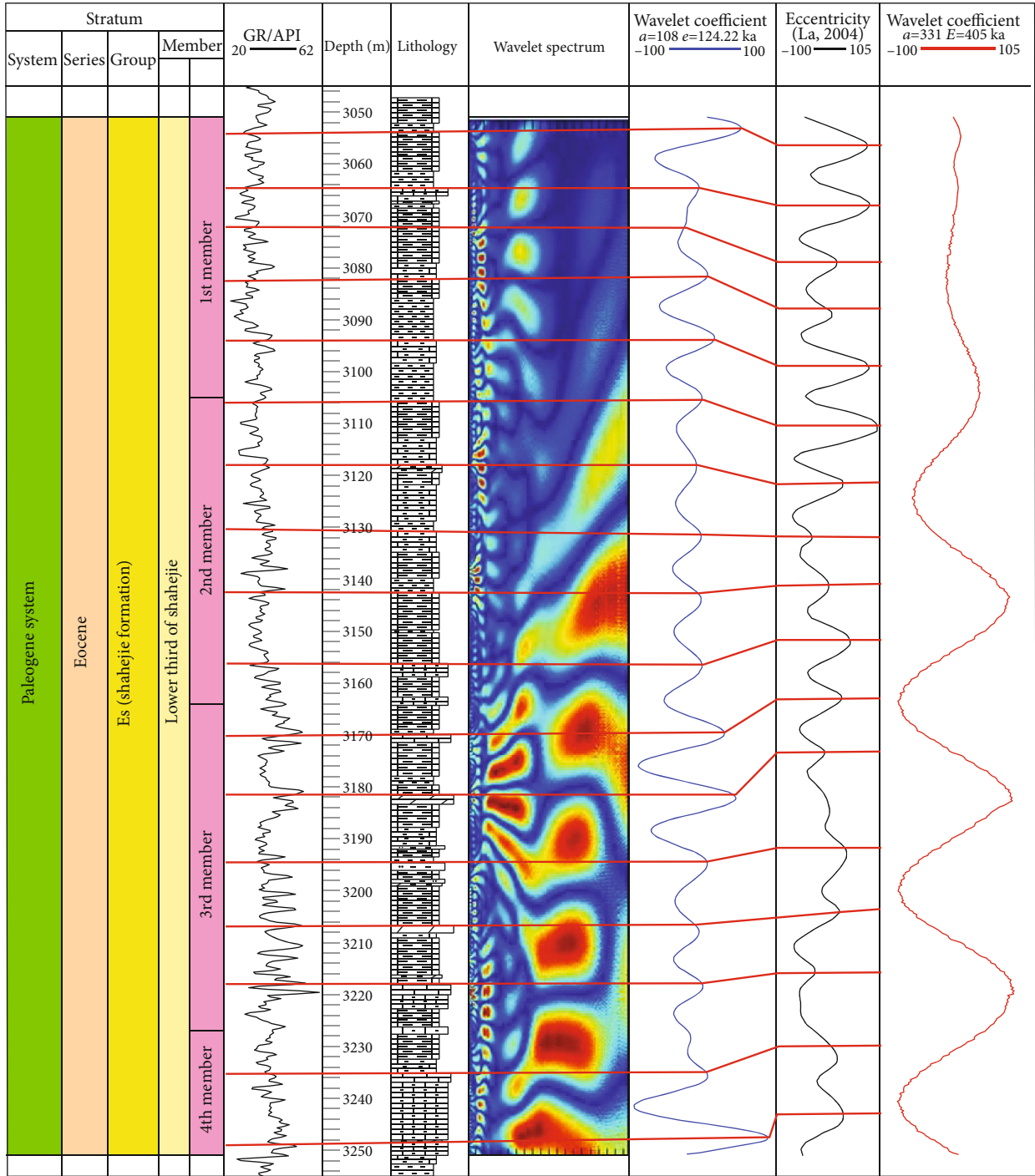


FIGURE 6: Results of cyclostratigraphy analysis of the lower Es3 submember in Well Fanye-1.

the energy spectrum of different scales, and the appropriate extremum scale is selected to analyze the wavelet period of the signal.

There are two obvious modulus maximum points in the modulus extremum diagram of wavelet analysis of the GR curve of the lower Es3 submember in Well Fanye-1, corre-

sponding to the wavelet scales of 108 and 331, and their ratio of 3.10 is almost identical to the ratio of 3.26 between the short eccentricity period (124.22 ka) and the long eccentricity period (405 ka) of the astronomical orbit period. Since the main astronomical period identified by spectral analysis also includes these two eccentricity periods, it can be concluded

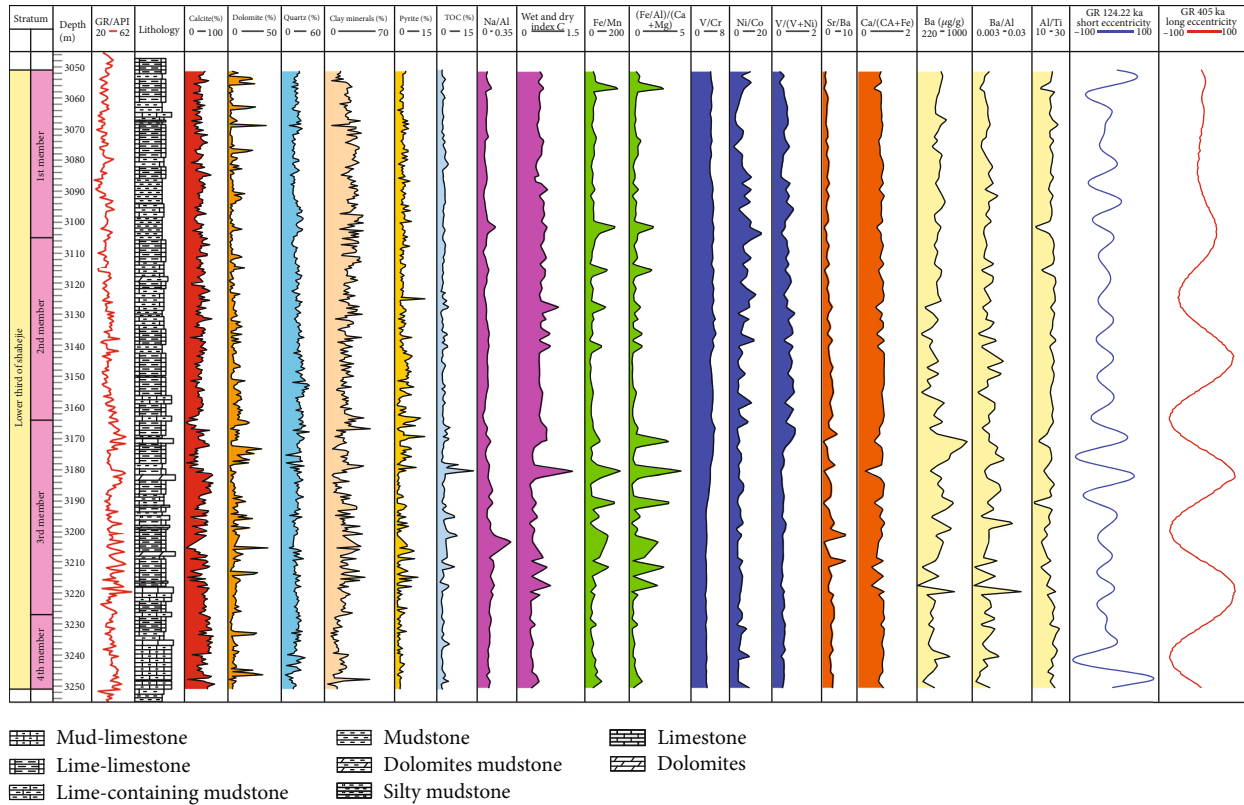


FIGURE 7: Sedimentary environment of the lower Es3 submember in Well Fanye-1 of Dongying sag and comprehensive analysis of Milankovitch cycle.

that this suite of strata has preserved obvious astronomical orbit periods and is mainly controlled by long eccentricity period and short eccentricity period. The wavelet energy spectrum diagram also shows that bright energy rings are mainly concentrated near the lines with the scales of 108 and 331, indicating that the frequency near these two scales is the dominant frequency in the signal, that is, it corresponds to the short eccentricity period of 124.22 ka at the scale of 108, and the long eccentricity period of 405 ka at the scale of 331, and their wavelet curves can be seen as the cycle curves of the long eccentricity period and short eccentricity period.

(3) *Cycle Period Analysis.* The wavelet coefficient curves at the scales (a) of 108 and 331 were extracted, respectively, based on wavelet analysis to represent the period cycle curve of the lower Es3 submember in Well Fanye-1 (Figure 6). The number of cycle periods of the two cycle curves could be directly identified from the graphical results of cycle analysis. The number of cycle periods was 16 and 4.5, respectively, and their ratio of 3.5:1 was exactly close to the ratio of 3.26:1 between the long eccentricity period (405 ka) and short eccentricity period (124.22 ka), which further confirmed that the Lower Es3 submember in Well Fanye-1 was driven by the obvious Milankovitch cycle and the main influencing factor was eccentricity.

The composite bar graph of the cyclic stratigraphic division of Well Fanye-1 was drawn based on the GR data, depth,

lithology, period curves with the scales of 108 and 331 and wavelet energy spectrum map of the Lower Es3 submember in Well Fanye-1 (Figure 6). According to the figure, the long and short eccentricity periods of the strata in the Lower Es3 submember are well preserved, and the short eccentricity cycle curve is significantly modulated by the long eccentricity cycle curve, suggesting that there is a good correspondence between the two eccentricity cycle curves and the dominant component in the energy spectrum map. Appropriately 4.5 long eccentricity periods and 16 short eccentricity periods were identified in the study interval. The strata thickness of this interval was 200 m, based on which the sedimentation time of the lower Es3 submember in Well Fanye-1 was calculated to be appropriately 1.905 Ma, and the average sedimentation rate was estimated to be 0.105 m/ka. In previous studies, the absolute age of the top of the upper Es4 submember in the Dongying sag was about 42 Ma according to the isotopic dating data of paleomagnetism and volcanic rocks [49], and thus, the absolute geological age of the top of the lower Es3 submember was determined to be 40.095 Ma. Then, a float geological age ruler for the study area lower Es3 submember can be established.

Cycle period analysis performed based on logging data and the methods of spectral analysis, wavelet transform, and modulus extremum contributes to cycle (sequence) division of fine-grained sedimentary strata, establishes the float geological age ruler, and determines the absolute age of strata at a certain depth point, thus calculating the sedimentation

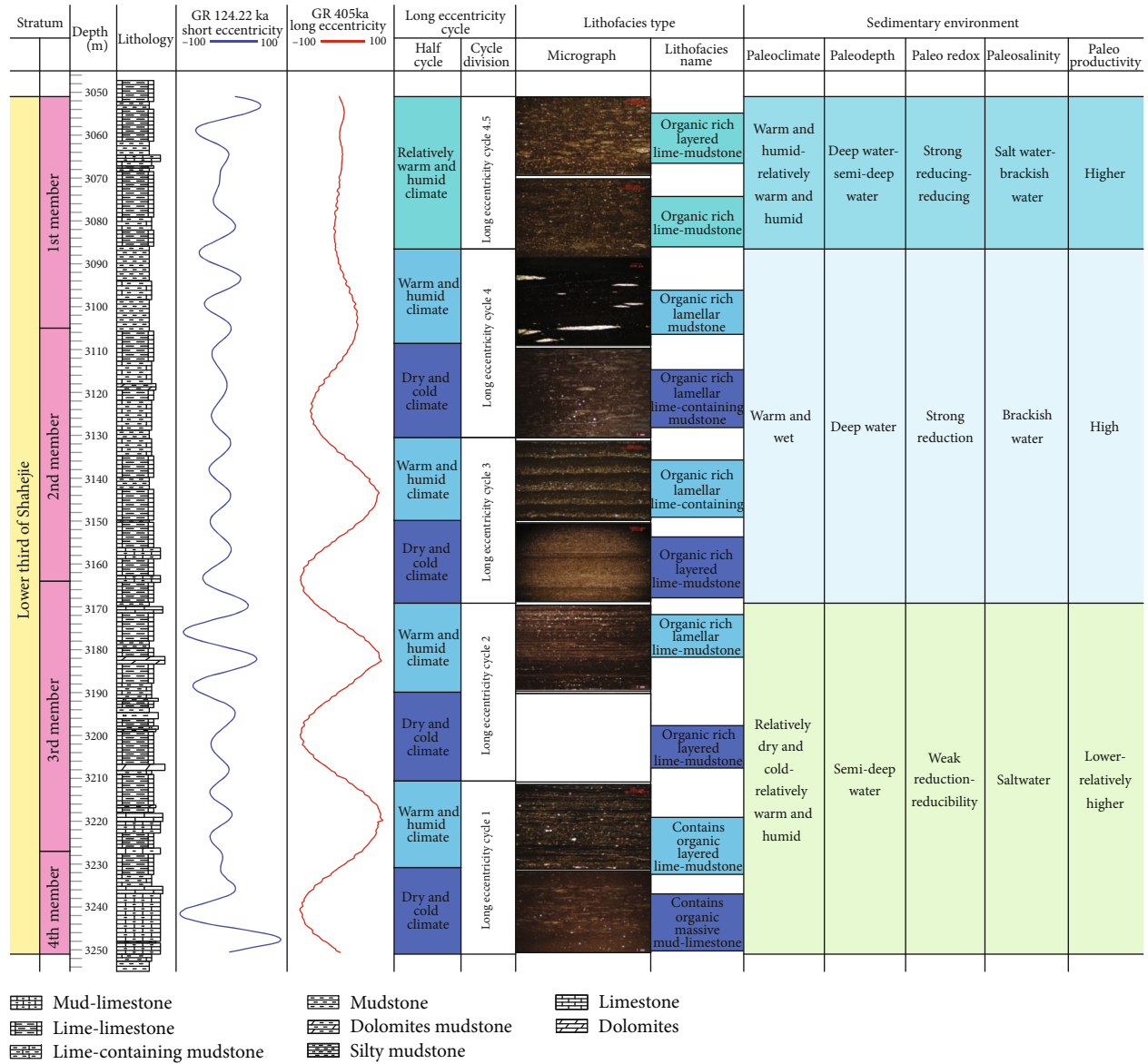


FIGURE 8: Environmental response characteristics of long eccentricity period in the lower Es3 submember in Well Fanye-1 of Dongying sag.

rate. At the same time, the isochronous division and correlation of strata provides a solution to the sequence division and correlation of shale fine-grained sedimentary strata, as well as an effective method for the fine stratigraphic division and correlation, thus promoting, enriching, and improving the theory of sequence stratigraphy and its application, and promoting the exploration and development of unconventional shale oil and gas.

4.2. Environmental Response Characteristics of the Milankovitch Cycle. Semideep lake-deep lake environment of the Dongying sag is dominated by fine-grained sedimentation. Previous studies on lacustrine fine-grained rocks have shown that the sedimentation process of lacustrine fine-grained rocks with frequent lithological changes is closely related to the changes in the paleoenvironment. The evolution of the paleoenvironment tends to lead to the changes

in the chemical composition of rocks, mineral composition, content of organic matter, rock type, and other aspects [50–58], so indicators such as geochemistry and mineral composition can be used to study the paleoclimate, paleowater depth, paleoredox conditions, paleosalinity, paleoproductivity, and other aspects [56–60]. In this paper, various indicators for the changes in the sedimentary environment were selected to further explore and confirm that the sedimentary environment of lacustrine fine-grained rocks in the lower Es3 submember of the Paleogene Shahejie Formation in Well Fanye-1 of the Dongying sag was affected by the Milankovitch cycle. The results showed that there was a good correspondence between the vertical changes of some indicators and the Milankovitch cycle.

4.2.1. Environmental Response Characteristics of Long Eccentricity Cycle. A total of 4.5 long eccentricity cycles were

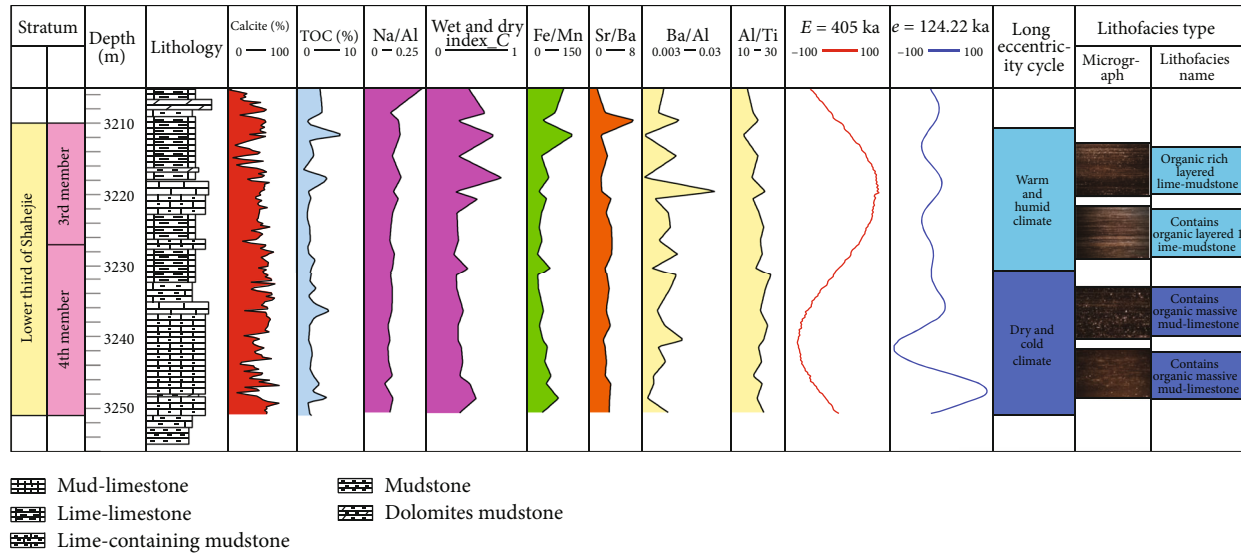


FIGURE 9: Environmental response characteristics of short eccentricity period in the lower Es3 submember in Well Fanye-1 of Dongying sag.

identified from bottom to top in the fine-grained sedimentary rock strata in the lower Es3 submember in Well Fanye-1. Based on the indicators of sedimentary environment analysis, the evolution of the sedimentary environment of the study interval is periodical (Figures 7 and 8). The environment response characteristics of the Milankovitch cycle were studied based on the results of the sedimentary environment analysis.

In a long eccentricity cycle period, eccentricity increases, due to which the amount of sunshine on the surface increases, the climate as a whole becomes warm and wet from dry and cold, and the seasonal change enhances. Thus, the long eccentricity cycle period is divided into a dry-cold climate half-period cycle and a warm-wet climate half-period cycle (Figures 7 and 8). In the warm-wet climate half-period cycle, the paleowater depth increases, the Na/Al value is low, the C value of the dry-wet index is high, the calcite content is small, the pyrite content increases, the ratios of such element combinations as Fe/Mn and $(Fe + Al)/(Ca + Mg)$ are small, the paleowater depth increases as a whole, the organic matter can be well preserved, the TOC content is relatively high, the paleoproductivity is high, the seasonal characteristics enhance, and the sedimentary structure is mainly a bedded-lamellar structure. In the dry-cold climate half-period cycle, the atmospheric precipitation decreases, the Na/Al value increases, the C value of the dry-wet index is low, the calcite content increases, the pyrite content decreases, the ratios of such element combinations as Fe/Mn and $(Fe + Al)/(Ca + Mg)$ increase, the paleowater depth decreases, the TOC content is relatively reduced, the paleoproductivity is low, and the four seasons are not distinctive, so the boundaries of different laminae formed in one year are blurred and the bedded-massive sedimentary structure develops. According to the environmental response characteristics of the Milankovitch cycle and the overall sedimentary environment analysis results, under the general background that the sedimentary environment changes from relatively dry and cold to warm and wet, the typical

types of lithofacies associations of the lower Es3 submember in Well Fanye-1 from bottom to top are massive argillaceous limestone-bearing organic matter—bedded calcareous clay-bearing organic matter—bedded calcareous clay rich in organic matter—bedded calcareous clay rich in organic matter—lamellar calcareous clay rich in organic matter—bedded lime mudstone rich in organic matter—lamellar mudstone rich in organic matter—bedded lime mudstone rich in organic matter—bedded calcareous clay rich in organic matter (Figure 8).

According to the analysis of environmental changes in the long eccentricity period and the sedimentary environment evolutionary stages, warm and wet climate is conducive to the proliferation of organisms, that is, in the interval with a high eccentricity value, the average TOC content is relatively high, the Na/Al value is low, the C value of the dry-wet index is high, the ratios of such element combinations as Fe/Mn and $(Fe + Al)/(Ca + Mg)$ are low, and the ratios of such element combinations as Ba/Al and Al/Ti are high. The relative content of calcite sensitive to the climate environment is an important source of paleoenvironmental information. When the climate tends to be dry, the water evaporates strongly and the content of carbonate minerals (mainly calcite) is high; when the climate tends to be humid, the content of carbonate minerals is low, suggesting that the calcite content is negatively correlated to the eccentricity value. The changes of the above indicators further illustrated that the climate will become warm and wet when the eccentricity increases and that the sedimentary environment of lacustrine fine-grained rocks is controlled by the Milankovitch cycle.

4.2.2. Environmental Response Characteristics of Short Eccentricity Cycle. Due to the significant modulation of the short eccentricity cycle by the long eccentricity cycle, environment response characteristics of the short eccentricity cycle were analyzed according to the different climate half-period backgrounds of the long eccentricity cycle. When

the long eccentricity is small, that is, when in the dry-cold climate half-period cycle, the overall background is that the Na/Al value and calcite content are high, the content of organic matter is low, the productivity is relatively low, and the sedimentary structure is mainly a bedded-massive structure. Under this background, in a short eccentricity cycle period, the climate changes from dry and cold to relatively warm and wet, thus causing the increase of Na/Al value, the decrease of TOC content, the gradual increase of paleoproductivity, the increase of calcite content, and the decrease of the C value of dry-wet index decreases, but the change is not significant as a whole. The typical types of lithofacies associations from bottom to top are massive argillaceous limestone bearing organic matter—bedded argillaceous limestone bearing organic matter (Figure 9); when the climate is very dry and cold (the top of the upper Es4 submember), bedded argillaceous rocks poor in organic matter often develop in the early stage of the short eccentricity cycle.

When the long eccentricity is large, that is, when in the warm-wet climate half-period cycle, the overall background is that the Na/Al value and calcite content are low, the content of organic matter is high, and the sedimentary structure is mainly a bedded-lamellar structure. Under this background, in a short eccentricity cycle period, the short eccentricity cycle becomes large, and the climate changes from relatively dry and cold to warm and wet, thus causing the decrease of Na/Al value, the increase of TOC content, the increase of paleoproductivity, the decrease of calcite content, and the increase of the C value of the dry-wet index. At the same time, the short eccentricity cycle changes, which is accordingly reflected in the lithofacies of fine-grained sedimentary rocks, that is, the sedimentary structure changes from clearly lamellar to weakly lamellar, bedded or massive. Owing to the changes of the above material composition and sedimentary structure, corresponding types of lithofacies are formed. The typical types of lithofacies associations from bottom to top are bedded calcareous clay bearing organic matter—bedded calcareous clay rich in organic matter (Figure 9).

5. Conclusions

In this paper, the Milankovitch cycle recorded from the study interval and the environment response characteristics were studied, with the lower Es3 submember of the Shahejie Formation in Well Fanye-1 of Dongying sag, Bohai Bay Basin, as the object of the study, combining the methods of spectral analysis, wavelet transform, and modulus extremum. The study concluded that

- (1) The spectral analysis, wavelet transform, and modulus extremum analyses of natural gamma ray logging data of the lower Es3 submember stratum in Fanye-1 showed that the Milankovitch cycle drove and controlled the sedimentary period of Paleogene Dongying sag
- (2) A total of about 4.5 long eccentricity periods and 16 short eccentricity periods were identified in the study

interval, based on which the sedimentation time of the lower Es3 submember in Fanye-1 was calculated to be appropriately 1.905 Ma, and the average sedimentation rate was estimated to be 0.105 m/ka

- (3) Sedimentary environment of the lacustrine fine-grained rocks was controlled by the astronomical periods. The interval with high eccentricity values generally had higher average TOC content and C value of dry-wet index and smaller content of carbonate mineral (mainly calcite), Na/Al value, and ratios of such element combinations as Fe/Mn and (Fe + Al)/(Ca + Mg). The change of each indicator further illustrated that the climate will become warm and wet when the eccentricity increases

Data Availability

All data in the article is presented in the form of tables and graphs. All the data in this article is accessible to readers.

Additional Points

Highlights. (1) Methods of spectral analysis, wavelet transform, and modulus extremum were combined to identify the Milankovitch cycle preserved in lacustrine shale strata, providing a theoretical basis and actual reference for the study of the cycle in the lacustrine deep-water fine-grained sedimentary strata. (2) Sedimentation rate of the study interval was calculated based on the absolute age of the strata determined by the isotopic dating data of paleomagnetism and volcanic rocks, facilitating the establishment of the float geological age ruler of the study area lower Es3 submember. (3) Environment response characteristics of astronomical periods were analyzed in detail, further confirming the effect of Milankovitch cycles on the evolution of the sedimentary environment of the lacustrine deep-water fine-grained sedimentary strata, thus contributing to understanding the influence of earth orbital forcing on climate and environment changes.

Conflicts of Interest

The authors declare that they have no conflicts of interest.

Acknowledgments

This study was supported by the Study on Astronomical Stratigraphic Period of Lacustrine Shale and High Resolution Sedimentary Cycle in Logging (41872166) of the National Natural Science Foundation of China and the Exploration and Development Research Institute, Shengli Oilfield Company, SINOPEC.

References

- [1] H. Wu, Q. Fang, S. Zhang, and T. Yang, "Cenozoic Milankovitch cycle and astronomical time scale," *Quaternary Sciences*, vol. 36, no. 5, p. 1055, 2016.

- [2] S. Boulila, B. Galbrun, E. Huret et al., "Astronomical calibration of the Toarcian stage: implications for sequence stratigraphy and duration of the early Toarcian OAE," *Earth and Planetary Science Letters*, vol. 386, pp. 98–111, 2014.
- [3] J. Shi, Z. Jin, Q. Liu, Z. Huang, and R. Zhang, "Quantitative classification of high-frequency sequences in fine-grained lacustrine sedimentary rocks based on Milankovitch theory," *Oil & Gas Geology*, vol. 40, no. 6, pp. 1205–1212, 2019.
- [4] X. Tan, Y. Jiang, J. Li, W. Xue, and Z. Li, "Sedimentary record and origin of high frequency cycles in the Paleogene Kongdian formation in the Jiyang depression," *Oil & Gas Geology*, vol. 36, no. 1, pp. 61–72, 2015.
- [5] D. Gao, C. Lin, M. Hu, and L. Huang, "Using spectral gamma ray log to recognize high-frequency sequences in carbonate strata: a case study from the Lianglitage formation from well T1 in Tazhong area, Tarim Basin," *Acta Sedimentologica Sinica*, vol. 34, no. 4, pp. 707–712, 2016.
- [6] R. M. Mitchum, "High frequency sequences stratigraphy," *Sedimentary Geology*, vol. 70, no. 2/4, pp. 215–307, 1991.
- [7] S. Wang and Z. Liu, "Discussion on some problems of high resolution sequence stratigraphy in the study of continental stratigraphy," *Journal of Stratigraphy*, vol. 28, no. 2, pp. 179–183, 2004.
- [8] G. Shi and Y. Liu, "Progress in the Milankovitch theory of earth climate change," *Advance in Earth Science*, vol. 21, no. 3, pp. 278–285, 2006.
- [9] J. Schnyder, J. Dejax, E. Keppens et al., "An early cretaceous lacustrine record: organic matter and organic carbon isotopes at Bernissart (Mons Basin, Belgium)," *Palaeogeography, Paleoclimatology, Paleoecology*, vol. 281, no. 1–2, pp. 79–91, 2009.
- [10] C. Huang, S. P. Hesselbo, and L. A. Hinnov, "Astrochronology of the late Jurassic Kimmeridge clay (Dorset, England) and implications for earth system processes," *Earth and Planetary Science Letters*, vol. 289, no. 1–2, pp. 242–255, 2010.
- [11] C. Huang, "The current status of cyclostratigraphy and astrochronology in the Mesozoic," *Earth Science Frontiers*, vol. 21, no. 2, pp. 048–066, 2014.
- [12] J. Yan, Y. Yan, J. Peng, C. Feng, B. Geng, and X. Li, "Log identification of astronomical cycle in lacustrine facies mud shale and its application in the lower 3rd member of Shahejie formation in Zhanhua sag," *Well Logging Technology*, vol. 41, no. 6, pp. 702–706, 2017.
- [13] J. Yan, Y. Yan, J. Peng, Z. Li, B. Geng, and F. Lai, "The research progress, significance and relationship of astrostratigraphy with cyclostratigraphy," *Lithologic Reservoirs*, vol. 29, no. 1, pp. 147–154, 2017.
- [14] F. J. Hilgen, K. F. Kuiper, W. Krijgsman, E. Snel, and E. V. Der Laan, "Astronomical tuning as the basis for high resolution chronostratigraphy: the intricate history of the Messinian salinity crisis," *Newsletters on Stratigraphy*, vol. 4, no. 2–3, pp. 231–238, 2007.
- [15] A. Holbourn, W. Kuhnt, M. Schulz, J. Flores, and N. Andersen, "Orbitally-paced climate evolution during the middle Miocene 'Monterey' carbon- isotope excursion," *Earth and Planetary Science Letters*, vol. 261, no. 3–4, pp. 534–550, 2007.
- [16] T. Westerhold and U. Rohl, "High resolution cyclostratigraphy of the early Eocene – new insights into the origin of the Cenozoic cooling trend," *Climate of the Past*, vol. 5, no. 3, pp. 309–327, 2009.
- [17] T. Westerhold, U. Rohl, T. Frederichs, S. M. Bohaty, and J. C. Zachos, "Astronomical calibration of the geological timescale: closing the middle Eocene gap," *Climate of the Past*, vol. 11, no. 9, pp. 1181–1195, 2015.
- [18] S. K. Husing, K. F. Kuiper, W. Link, F. J. Hilgen, and W. Krijgsman, "The upper Tortonian-lower Messinian at Monte dei Corvi (northern Apennines, Italy): completing a Mediterranean reference section for the Tortonian stage," *Earth and Planetary Science Letters*, vol. 282, no. 1–4, pp. 140–157, 2009.
- [19] S. K. Husing, A. Cascella, F. J. Hilgen et al., "Astrochronology of the Mediterranean Langhian between 15.29 and 14.17 Ma," *Earth and Planetary Science Letters*, vol. 290, no. 3–4, pp. 254–269, 2010.
- [20] S. K. Husing, M. H. Deenen, J. G. Koopmans, and W. Krijgsman, "Magnetostigraphic dating of the proposed Rhaetian GSSP at Steinbergkogel (upper Triassic, Austria): implications for the late Triassic time scale," *Earth and Planetary Science Letters*, vol. 302, no. 1–2, pp. 203–216, 2011.
- [21] F. M. Gradstein, J. G. Ogg, M. D. Schmitz, and G. M. Ogg, *The Geologic Time Scale 2012*, Elsevier, Amsterdam, UK, 2012.
- [22] X. Yao, Y. Zhou, and L. A. Hinnov, "Astronomical forcing of a middle Permian chert sequence in Chaohu, South China," *Earth and Planetary Science Letters*, vol. 422, pp. 206–221, 2015.
- [23] S. Wu and J. Liu, "High resolution sequence stratigraphic study basic on time-frequency analysis," *Marine Geology & Quaternary Geology*, vol. 35, no. 4, pp. 197–205, 2015.
- [24] S. Sun, H. Liu, Y. Cao, S. Zhang, Y. Wang, and W. Yang, "Milankovitch cycle of lacustrine Deepwater fine grained sedimentary rocks and its significance to shale oil: a case study of the upper Es4 member of well NY1 in Dongying sag," *Journal of China of Mining & Technology*, vol. 46, no. 4, pp. 846–855, 2017.
- [25] M. Ruhl, S. P. Hesselbo, L. A. Hinnov et al., "Astronomical constraints on the duration of the early Jurassic Pliensbachian stage and global climatic fluctuations," *Earth and Planetary Science Letters*, vol. 455, pp. 149–165, 2016.
- [26] P. R. Renne, A. L. Deino, F. J. Hilgen et al., "Time scales of critical events around the Cretaceous-Paleogene boundary," *Science*, vol. 339, no. 6120, pp. 684–687, 2013.
- [27] J. Nie, C. Garzzone, Q. Su et al., "Dominant 100,000-year precipitation cyclicity in a late Miocene lake from Northeast Tibet," *Science Advances*, vol. 3, no. 3, article e1600762, 2017.
- [28] X. Wang, X. Zhang, F. Gao, and M. Zhang, "Astronomical cycles of the late Permian Lopingian in South China and their implications for third-order sea-level change," *Journal of Ocean University of China*, vol. 19, no. 6, pp. 1331–1344, 2020.
- [29] G. Chen, W. Gang, H. Tang et al., "Astronomical cycles and variations in sediment accumulation rate of the terrestrial lower cretaceous Xiagou formation from the Jiuquan Basin, NW China," *Cretaceous Research*, vol. 109, p. 104156, 2020.
- [30] J. Zhao, K. Zhao, and J. Zhang, "Division and comparison of oil reservoirs in delta front from Milankovitch astronomical cycles," *Acta Sedimentologica Sinica*, 2021.
- [31] B. Ma, K. A. Eriksson, Y. Cao, Y. Jia, Y. Wang, and B. C. Gill, "Fluid flow and related diagenetic processes in a rift basin: evidence from the fourth member of the Eocene Shahejie formation interval, Dongying depression, Bohai Bay basin, China," *AAPG Bulletin*, vol. 100, no. 11, pp. 1633–1662, 2016.
- [32] Y. Ma, X. Du, H. Liu, and Y. Lu, "Characteristics, depositional processes, and evolution of shale Lithofacies of the upper

- submember of Es₄ in the Dongying depression,” *Earth Science*, vol. 42, no. 7, pp. 1195–1204, 2017.
- [33] J. Wu, Z. Jiang, and X. Wang, “Sequence stratigraphy characteristics of lacustrine fine-grained sedimentary rocks: a case study of the upper fourth member of Paleogene Shahejie formation, Dongying sag, Bohai Bay basin,” *Natural Gas Geoscience*, vol. 29, no. 2, pp. 199–210, 2018.
- [34] Z. Chen, W. Jiang, L. Zhang, and M. Zha, “Organic matter, mineral composition, pore size, and gas sorption capacity of lacustrine mudstones: implications for the shale oil and gas exploration in the Dongying depression, eastern China,” *AAPG Bulletin*, vol. 102, no. 8, pp. 1565–1600, 2018.
- [35] C. Lampe, G. Song, L. Cong, and X. Mu, “Fault control on hydrocarbon migration and accumulation in the tertiary Dongying depression, Bohai Basin, China,” *AAPG Bulletin*, vol. 96, no. 6, pp. 983–1000, 2012.
- [36] Z. Li, W. Yang, Y. Wang et al., “Anatomy of a lacustrine stratigraphic sequence within the fourth member of the Eocene Shahejie formation along the steep margin of the Dongying depression, eastern China,” *Bulletin*, vol. 103, no. 2, pp. 469–504, 2019.
- [37] M. Vahlenkamp, D. de Vleeschouwer, S. J. Batenburg et al., “A lower to middle Eocene astrochronology for the Mentelle Basin (Australia) and its implications for the geologic time scale,” *Earth and Planetary Science Letters*, vol. 529, p. 115865, 2020.
- [38] S. Li, R. Zhu, J. Cui, Z. Luo, H. Jiao, and H. Liu, “Sedimentary characteristics of fine-grained sedimentary rock and paleoenvironment of Chang 7 member in the Ordos Basin: a case study from well Yaoye 1 in Tongchuan,” *Acta Sedimentologica Sinica*, vol. 38, no. 3, pp. 1–13, 2019.
- [39] H. Wu, S. Zhang, G. Jiang, and Q. Huang, “The floating astronomical time scale for the terrestrial late Cretaceous Qingshankou formation from the Songliao Basin of Northeast China and its stratigraphic and paleoclimate implications,” *Earth and Planetary Science Letters*, vol. 278, no. 3–4, pp. 308–323, 2009.
- [40] M. Wang, H. Chen, C. Huang et al., “Astronomical forcing and sedimentary noise modeling of lake-level changes in the Paleogene Dongpu depression of North China,” *Earth and Planetary Science Letters*, vol. 535, article 116116, 2020.
- [41] M. Ikeda and R. Tada, “A 70 million year astronomical time scale for the deep-sea bedded chert sequence (Inuyama, Japan): implications for Triassic–Jurassic geochronology,” *Earth and Planetary Science Letters*, vol. 399, pp. 30–43, 2014.
- [42] C. Huang and L. A. Hinnov, “Astronomically forced climate evolution in a saline lake record of the middle Eocene to Oligocene, Jiangnan Basin, China,” *Earth and Planetary Science Letters*, vol. 528, article 115846, 2019.
- [43] C. Ma, S. R. Meyers, and B. B. Sageman, “Testing late Cretaceous astronomical solutions in a 15 million year astrochronologic record from North America,” *Earth and Planetary Science Letters*, vol. 513, pp. 1–11, 2019.
- [44] B. van der Meulen, P. D. Gingerich, L. J. Lourens et al., “Carbon isotope and mammal recovery from extreme greenhouse warming at the Paleocene-Eocene boundary in astronomically-calibrated fluvial strata, Bighorn Basin, Wyoming, USA,” *Earth and Planetary Science Letters*, vol. 534, p. 116044, 2020.
- [45] J. Laskar, P. Robutel, F. Joutel, M. Gastineau, A. C. Correia, and B. Levrard, “A long-term numerical solution for the insolation quantities of the earth,” *Astronomy and Astrophysics*, vol. 428, no. 1, pp. 261–285, 2004.
- [46] J. Laskar, A. Fienga, M. Gastineau, and H. Manche, “La2010: a new orbital solution for the long-term motion of the earth,” *Astronomy and Astrophysics*, vol. 532, article A89, 2011.
- [47] W. Xu and X. Xie, “A new method to calculate sedimentary rates based on Milankovitch cycles: a case study on middle section of 3rd member of Shahejie formation in well Niu38, Dongying sag, Bohai Bay basin,” *Petroleum Geology & Experiment*, vol. 34, no. 2, pp. 207–214, 2012.
- [48] Y. Yao, D. Xu, B. Li, H. Zhang, S. Zhang, and S. Yao, “High resolution cyclostratigraphic study on the third member of Shahejie formation of drill core Niu38 in the Dongying depression, Shandong Province,” *Journal of Stratigraphy*, vol. 31, no. 3, pp. 229–237, 2007.
- [49] Y. Yao, S. Xiu, X. Wei, S. Meng, Y. Ye, and X. Diao, “Researches on the ESR eochronometry in Palaeogene of Dongying depression[J],” *Petroleum Geology and Recovery Efficiency*, vol. 9, no. 2, pp. 31–34, 2002.
- [50] Z. Wang, J. Wang, X. Fu et al., “Geochemistry of the upper Triassic black mudstones in the Qiangtang Basin, Tibet: implications for paleoenvironment, provenance, and tectonic setting,” *Journal of Asian Earth Sciences*, vol. 160, pp. 118–135, 2018.
- [51] K. Zhang, J. Peng, W. Liu et al., “The role of deep geofluids in the enrichment of sedimentary organic matter: a case study of the late Ordovician-early Silurian in the upper Yangtze region and early Cambrian in the lower Yangtze region, South China,” *Geofluids*, vol. 2020, Article ID 8868638, 12 pages, 2020.
- [52] K. Zhang, J. Peng, X. Wang et al., “Effect of organic maturity on shale gas genesis and pores development: a case study on marine shale in the upper Yangtze region, South China,” *Open Geosciences*, vol. 12, no. 1, pp. 1617–1629, 2020.
- [53] K. Zhang, Y. Song, S. Jiang et al., “Mechanism analysis of organic matter enrichment in different sedimentary backgrounds: a case study of the Lower Cambrian and the Upper Ordovician-Lower Silurian, in Yangtze region,” *Marine and Petroleum Geology*, vol. 99, pp. 488–497, 2019.
- [54] K. Zhang, C. Jia, Y. Song et al., “Analysis of lower Cambrian shale gas composition, source and accumulation pattern in different tectonic backgrounds: a case study of Weiyuan block in the upper Yangtze region and Xiuwu Basin in the lower Yangtze region,” *Fuel*, vol. 263, p. 115978, 2020.
- [55] J. Peng, T. Xu, and L. Yu, “Sedimentary characteristics and controlling factors of lacustrine fine-grained rocks of the fourth member of Shahejie formation in Dongying depression. Lithologic reservoirs, 1-11,” 2020, <http://kns.cnki.net/kcms/detail/62.1195.TE.20200519.1148.002.html>.
- [56] Q. Meng, Z. Liu, A. A. Bruch, R. Liu, and F. Hu, “Palaeoclimatic evolution during Eocene and its influence on oil shale mineralisation, Fushun basin, China,” *Journal of Asian Earth Sciences*, vol. 45, pp. 95–105, 2012.
- [57] D. Bonar and M. D. Sacchi, “Denoising seismic data using the nonlocal means algorithm,” *Geophysics*, vol. 77, no. 1, pp. A5–A8, 2012.
- [58] J. Ochoa, J. M. Wolak, and M. H. Gardner, “Recognition criteria for distinguishing between hemipelagic and pelagic mudrocks in the characterization of deep-water reservoir heterogeneity,” *AAPG Bulletin*, vol. 97, no. 10, pp. 1785–1803, 2013.

- [59] S. F. Konitzer, S. J. Davies, M. H. Stephenson, and M. J. Leng, "Depositional controls on mudstone Lithofacies in a Basinal setting: implications for the delivery of sedimentary organic matter," *Journal of Sedimentary Research*, vol. 84, no. 3, pp. 198–214, 2014.
- [60] J. Zhang, Z. Jiang, X. Jiang, S. Wang, C. Liang, and M. Wu, "Oil generation induces sparry calcite formation in lacustrine mudrock, Eocene of East China," *Marine and Petroleum Geology*, vol. 71, pp. 344–359, 2016.

Research Article

Geochemical Characteristics of the Middle Devonian Dacaozi-Tanshanping Shale Strata in the Yanyuan Basin, Southwest China: Implications for Organic Matter Accumulation and Preservation

Ziya Zhang^{1,2,3}, Wei Yang^{1,2}, Xingyu Li^{1,2}, Yan Song^{1,2}, Zhenxue Jiang^{1,2}
and Qun Luo^{1,2}

¹State Key Laboratory of Petroleum Resources and Prospecting, China University of Petroleum, Beijing 102249, China

²Unconventional Petroleum Science and Technology Institute, China University of Petroleum, Beijing 102249, China

³Chinese Academy of Geological Sciences, Beijing 100037, China

Correspondence should be addressed to Wei Yang; yangwgeo@163.com and Xingyu Li; lxy18047216450@163.com

Received 30 January 2021; Accepted 4 June 2021; Published 24 June 2021

Academic Editor: Martina Zucchi

Copyright © 2021 Ziya Zhang et al. This is an open access article distributed under the Creative Commons Attribution License, which permits unrestricted use, distribution, and reproduction in any medium, provided the original work is properly cited.

How the geochemical characteristics of organic matter shale for the carbonate platform facies remain uncertain, which restricts an integrated reconstruction of the model of organic matter accumulation and preservation. Here, we present new results from element geochemical fingerprinting and integrated analyses of paleoclimate, paleoproductivity, paleoredox environment, and terrigenous input of the targeted Middle Devonian Tanshanping and Dacaozi Formations in the Ninglang-Yanyuan Basin, Southwest China. It is worth noting that although the carbonate platform connects with the open sea partially, the redox environment will not be completely controlled by relative sea level variations. Specially, the paleoclimate, paleoproductivity, and paleoredox conditions are the main controlling factors of the accumulation and preservation of organic matter. In view of the paleoclimate indexes, we suggest that both a relatively warm-humid climate characterized by intensified chemical weathering conditions and a higher terrigenous input are identified as two major drivers forcing the reductive environment in the sedimentary waterbody. Finally, a comprehensive model is established for providing new insights into the mechanism of organic matter accumulation and preservation for the carbonate platform facies. The paleoredox environment, paleoproductivity, paleoclimate, and terrigenous input are believed to have exerted a very considerable force on reconstructing the model of organic matter accumulation and preservation for the carbonate platform facies. Specially, the coupling interactions between the paleoproductivity and redox condition are thus also stressed. We found that the preservation condition is much more important than the paleoproductivity, resulting in the degree of organic matter enrichment. Even if the paleoproductivity of a sedimentary waterbody of a depositional period of the Dacaozi Formation was higher, the TOC concentrations were relatively low due to the poor preservation condition by fall of the sea level and increase of the terrigenous input. In another aspect, the better preservation condition of the Tanshanping Formation makes the TOC concentrations higher in the case of lower paleoproductivity in the sedimentary waterbody.

1. Introduction

The mud shale of the Tanshanping Formation in the Ninglang-Yanyuan area is mainly composed of clay minerals and carbonate minerals, and the mud shale of the Dacaozi Formation is mainly composed of clay minerals and siliceous minerals. As organic geochemical characteristic analysis shows, the organic matter types in the middle Devonian of

the Ninglang-Yanyuan region are type II₁ kerogen, reflecting that the maturity is high which is in the overmature dry gas phase, and the maturity increases with the increase of burial depth [1, 2]. Previous studies have proved that the Tanshanping Formation and the Dacaozi Formation are the shale-concentrated sections in the Ninglang-Yanyuan Basin, and they have been important favorable exploration layers for shale gas, which is characterized by large thickness, high

maturity, and high organic carbon content. As the development of the shale exploration in the Tanshanping Formation and the Dacaozi Formation, combined with the deployment of two-dimensional seismic data, we chose a structure favorable site (Lizihe anticline) to deploy a geological survey well called Well Yunningdi-1. Through the analysis and testing, the well drilling by the stable natural gas in the Devonian strata shows that the average total content of analytical gas is 3.25 m³/t. Specially, the total organic carbon content in the Tanshanping Formation was between 0.09% and 1.83% (with an average of 1.14%), and the organic carbon content in the Dacaozi Formation was between 0.32% and 3.48% (with an average of 1.05%).

A series of studies have reported that the Ninglang area in Yunnan is an important area for shale gas exploration and development in the complex tectonic area of Southern China. The Tanshanping Formation and the Dacaozi Formation in the Middle Devonian are components of the main source rocks. Previous studies have shown that the hydrocarbon generation capacity of shale reservoirs depends on the content, type, and thermal evolution of organic carbon [3, 4]. The development of the shale reservoir space is also affected by organic carbon content to some extent [3]. At the same time, the shale which is rich in organic matter tends to have high gas content, which indicates that the organic carbon content has a good correlation with the adsorption performance of shale [5–9]. Therefore, these important scientific issues put forward the necessity to look for more effective evidences to correctly clarify the main control factors of organic matter accumulation and preservation and the resource potential evaluation of Paleozoic shale gas in the Ninglang-Yanyuan area, Yunnan. Many scholars all over the world believe that the favorable conditions for organic matter accumulation in black shale mainly include three modes: high productivity, anoxic preservation, and the combination of the two [10–16]. The model of high productivity is a hypoxic environment which is conducive to the preservation of organic matter when high organic matter is formed under the influence of paleoclimatology, terrestrial organic matter supply, biological productivity of waterbody, and other factors by consuming oxygen in the sedimentary waterbody [17–19]. To sum up, the three models are in the final analysis to discuss the effects of the paleosedimentary environment formed by different factors on the accumulation and preservation of organic matter. Therefore, the reconstruction of the paleosedimentary environment is very important. Many scholars have used the geochemical index of shale to study the sedimentary environment of the organic rich shale [20–25].

At present, most scholars have studied the shale outcrops of the Tanshanping Formation and the Dacaozi Formation of the Devonian in the Ninglang-Yanyuan area in terms of geochemical characteristics, generation and storage characteristics, sedimentary characteristics, and shale gas geological conditions. However, the mechanism of organic matter accumulation and preservation in black shale has not been studied in the Tanshanping Formation and the Dacaozi Formation. In this paper, we took the Well Yunningdi-1 as an example, and systematic elemental geochemistry analysis

was conducted, including the analysis of main elements by X-ray fluorescence spectrometry, the measurement of trace elements and rare earth elements by inductively coupled plasma-mass spectrometry (ICP-MS), the combustion oxidation-nondispersive infrared absorption method, and the measurement of TOC concentrations by the total organic carbon analyzer and summary of its variation characteristics. Moreover, we have studied the elemental chemical characteristics and paleosedimentary environment of the Tanshanping and Dacaozi Formations. On this basis, the main controlling factors of accumulation and preservation of organic matter in shale rocks were discussed in order to provide a theoretical basis for the mechanism of accumulation and preservation of organic matter and the reconstruction of sedimentary model.

2. Geological Background

2.1. Tectonic Position. The Yanyuan Basin is located in the west of Sichuan Basin, at the junction of the Sichuan-Yunnan plateau, and is structurally located in the south-north tectonic belt between western Sichuan and eastern Tibet. Specially, the basin was sandwiched between the Songpan-Ganzi Indosinian fold belt and the Kang-Yunnan ancient land, which is part of the Zhenzhon gnappe thrust belt. The northern part of the Yanyuan Basin is controlled by the Xiaojinhe fault, which is adjacent to the Sanjiang island arc orogeny. The west side is controlled by the Guobaoshan-Yanfeng fault, which divides the Yanyuan Basin, the Yongning fault block on the west side and the Ninglang Basin on the southwest side. The east side is controlled by the Jinhe-Jinghe fault and adjacent to the Kangdian ancient land. The Lijiang Basin lies to the south of the Kang-Dian ancient land [26].

2.2. Tectonic Characteristics. The tectonic evolution of the Upper Yangtze plate is mainly controlled by the tectonic activities of the Tethys tectonic domain, which has undergone three major development stages: the proto-Tethys Oceanic basin (Z-O-S), the Guthys Oceanic basin (D-T3), and the New Tethys Oceanic basin (T3-N), reflecting the formation and evolution of the Tethys Ocean basin showed the change of becoming more and more earlier from south to north [27, 28]. Evidence of the disappearance of the New Tethys basin can be seen in the Yaluzangbu river and the Bangongcuo-Nu river Ophiolitic jumble zone in Tibet. At this time, the marine deposition in the western part of the Upper Yangtze river was terminated by the Indochina movement, which was no longer in the category of the tectonic evolution of the New Tethys Basin but was mainly located in the process of sea-land transition facies-continental sedimentary evolution. Paleozoic and Mesozoic marine sedimentary events in the western part of the Upper Yangtze Plate are bounded by the end of Silurian, and the geological period can be divided into two main periods: (1) Proto-Tethyan period of the Sinian-Early Paleozoic and (2) Late Paleozoic-Early Mesozoic Paleo-Tethyan period. Based on the observation and analysis of a large number of drilling data and outcrops, the sedimentary sequence and structural characteristics of

the Yanyuan Basin have been discussed. It is believed that the Yanyuan Basin was formed during the Miocene to Pliocene by the collision and extrusion of the Indian plate and the Eurasian plate. The emergence of this basin indirectly supported and recorded an important collision event of the Indo-Eurasian Plate in the Late Cenozoic [29]. It is important to focus on the tectonic position of the Yanyuan Basin which is in the arc structural belt in front of the Sichuan-Yunnan block, and it is the most obvious area of Cenozoic extrusion in the Qinghai-Tibet Plateau, which is sandwiched between the Xianshuihe fault and Honghe fault. The Sichuan-Yunnan block and its interior were cut by the Xiaojinhe fault, which can be divided into two secondary part blocks called the northwestern Sichuan Block and central Yunnan Block. The sliding velocities of the block boundaries are different between the blocks in northwestern Sichuan and central Yunnan, which reflects the composite motion model of the secondary blocks sliding horizontally and rotating clockwise about the vertical axis [30].

2.3. Sedimentary and Stratum Characteristics

2.3.1. The Ninglang Area. According to the “Yunnan Provincial Regional Geology Records of Ministry of Geology and Mineral Resources,” the Silurian (S) strata are mainly distributed in the Dacaozi area in the northwest and east of the Ninglang Basin, with thickness ranging from 182 m to 659 m. The Lower Silurian is mainly composed of shallow marine facies, with argillaceous limestone and gray limestone shale with a small amount of black siliceous layers. The Upper Silurian is mainly composed of lagoon facies, and a large number of carbonate rocks were developed. As for the Devonian system, Devonian strata are well developed in this area, which mainly outcrops in the Dacaozi, Xilaping, Wenxiang, and other areas, and there are deposits in the Upper, Middle, and Lower Series (Figure 1). The measurement area is divided from bottom to top as follows: The Lower Devonian Daguaping Formation (D_1d), with a thickness of 92 m~687 m, is exposed in the eastern Dacaozi and Maoniuping areas, which belongs to coastal and shallow marine facies deposition and be dominated by dark gray shale and siltstone at the top and conglomeratic sandstone at the bottom. It is worth noting that the lithology is in a regular cycle and in parallel unconformable contact with the Silurian system, reflecting an obvious depositional discontinuity. The thickness of the outcrops in the eastern part of the basin is about 91 m, and it is missing in the Xilaping area in the southeast. The Middle Devonian Dacaozi Formation (D_2d) is exposed at Dacaozi and Maoniuping in the east, with a thickness of 266 m~378 m, in which thickness is 266 m at the Dacaozi and missing at the Xilaping in the southeast. The strata of the Dacaozi Formation belong to shallow marine sedimentary facies, which is dominated by dark gray and gray biolimestone, which is interbedded with shale and integrated over the Daguaping Formation of Lower Devonian. The Middle Devonian Tanshanping Formation (D_2t) is exposed in the Dacaozi area in the east with a thickness range of 618 m~640 m, and the thickness of the Dacaozi area is 141.3 m, which belongs to shallow marine sedimentary

facies. The lithology is quite different from bottom to top. In particular, the bottom is mainly interbedded with sandstone, conglomeratic sandstone, and black shale, the upper part has experienced a transition that it has less sandy and more calcareous, and the top part is mainly grey limestone, bioclastic limestone, marl, and shale. The thickness of the Tanshanping Formation is about 617 m, and it is in a conformable contact with the Dacaozi Formation. On the whole, the Devonian strata overlay the Lower Ordovician strata. The Upper Devonian Lanniqing Formation (D_3l), with a thickness ranging from 476 m to 569 m, is exposed in the Dacaozi, Xilaping, and Luniqing areas in the east, composed of limestone at the top and dolomitic limestone at the bottom, which is integrated above the Tanshanping Formation. The Upper Devonian Gangou Formation (D_3g), with a thickness of 298 m~527 m, is exposed in the Dacaozi, Maoniuping, and other areas in the east, which belongs to shallow marine sedimentary facies, and its lithology is dominated by limestone and oolitic limestone, which is integrated over the Lanniqing Formation. Moreover, the Carboniferous system (C), with a thickness range of 266 m~964 m, is exposed in Yaoshan, Zhushan, and other areas in the northwest of China, in which lithology is dominated by dark gray bioclastic limestone and oolitic limestone, with pebbly sandstone and conglomerate at the bottom and chert nodule oolitic limestone at the top [31].

2.3.2. The Yanyuan Area. The strata in the Yanyuan Basin are all exposed from Sinianto Quaternary, except for the absence of Jurassic and Cretaceous. The strata below Triassic are all marine sediments, and the upper Permian has a set of Emei mountain basalt intrusion. The Sinian strata in the basin are exposed in the southeast margin of the basin, which only has a part of the upper Sinian strata; the lithology is mainly dolomite, and the bottom of which is marl, sandy mudstone interlayer. The Lower Paleozoic strata are exposed in the southeast and southwest sides of the basin, and the upper part of the Lower Cambrian to upper Cambrian and upper Ordovician strata are missing, so the Cambrian and Ordovician, Ordovician and Silurian are in parallel unconformable contact. The stratigraphic lithology of the Cambrian is dominated by fine silty clastic rocks, while the dolomite and limestone of the Middle and Upper Ordovician belong to a relative high level of enrichment, and the top is in parallel unconformable contact with the Silurian. As for the Lower Silurian Longmaxi Formation, it belongs to the marine deposit, which consists of graptolite-bearing siliceous argillaceous shale, intercalated argillaceous limestone, argillaceous sandstone, and sandy mudstone. The Middle Silurian is mainly argillaceous limestone, while the Upper Silurian is sand-mudstone and siliceous rock, and the Middle and Upper Silurian is locally dolomite. In terms of the Devonian system, Devonian and Silurian, Carboniferous and Devonian, and Permian and Carboniferous are in parallel unconformity contacts. The lithology of the Lower Devonian is mainly quartz sandstone, fine siltstone, limestone, siliceous rock intercalated with shale, argillaceous siltstone, and black shale. In the upward direction, the gray and sandy matter are reduced, while the argillaceous matter is increased. The Middle and Upper Devonian is dominated by carbonate deposits

	Formation			Code	Lithology	Lithologic description
	System	Series	Group			
Palaeozoic group	Carboniferous	Upper	Mapping	C ₂ mp		Gray, dark gray limestone, oolitic limestone containing chert nodules
			Huanglong	C ₂ hl		Light gray limestone with oolitic limestone
		Lower	Jianshanying	C ₁ j		Gray, dark gray bioclasts, oolitic limestone, basal conglomerate
	Devonian	Upper	Gangou	D ₃ g		Gray and light gray oolitic limestone
			Lanniqing	D ₃ l		Light gray limestone, dolomitic limestone, upper dolomite
		Middle	Tanshanping	D ₂ t		Shale, organic reef limestone, gray limestone with a small amount of dolomitic limestone and mudstone
			Dacaozi	D ₂ d		Dark gray biological limestone, shale, Alengchu zone for: sandstone, shale with limestone
			Daguaping	D ₁ d		Gray, dark gray shale, siltstone with limestone, bottom sandstone, conglomerate
		Lower	Alengchu	D ₁ a		Dark gray limestone, biological limestone
			Shanjiang	D ₁ s		Dark gray limestone, biological limestone with mud shale, calcareous limestone
	Silurian	Upper		S ₃		Gray argillaceous limestone, shale, crystalline dolomitic limestone in the east of Ninglang area
		Middle		S ₂		Gray argillaceous reticulated limestone
		Lower		S ₁		Gray, dark gray graptolite shale interbedded with siliceous rock



FIGURE 1: Comprehensive stratigraphic column of Devonian in Ninglang-Yanyuan [86].

interbedded with calcareous mudstone and argillaceous limestone, while it contains a small amount of sandstone conglomerate. Then, the Carboniferous system is mainly composed of limestone deposits with light gray limestone lithology and a large number of coral fossils. In the end, the lower Permian is dominated by sandy mudstone with local coal intercalation lines, and the middle Permian is dominated by limestone with weathering crust developed at the top, and the upper Permian is invaded by basalt with a thickness of about 2800 m. The top is dominated by fine clastic rocks with black carbonaceous shale mainly.

The Ninglang-Yanyuan Basin is located at the junction of the Songpan-Ganzi fold system and the western margin of the Yangtze platform. It is a component of the Yanyuan-Lijiangtai fold belt on the western margin of the Upper Yangtze block, adjacent to the Sanjiang tectonic belt in the west and the Kangdian ancient land in the east. Accordingly,

this study focuses on Well Yunningdi-1, which is selected as the favorable site for structural preservation in this study (Figure 2).

3. Samples and Methods

3.1. Samples. A total of 52 shale samples in the Tanshanping and Dacaozi Formations were obtained from Well Yunningdi-1 in the Ninglang-Yanyuan Basin. The depth of these shale samples was in a range of 750.28 m~1486.5 m. Specially, the data of shale gas content was provided by the Oil & Gas Resource Survey, China Geological Survey. In this study, 52 shale samples were systematically collected from the black shales of the Devonian Tanshanping and Dacaozi Formations in Well Yunningdi-1 in the Ninglang-Yanyuan Basin. In order to take the next step, pretreatment was performed firstly. After drying the

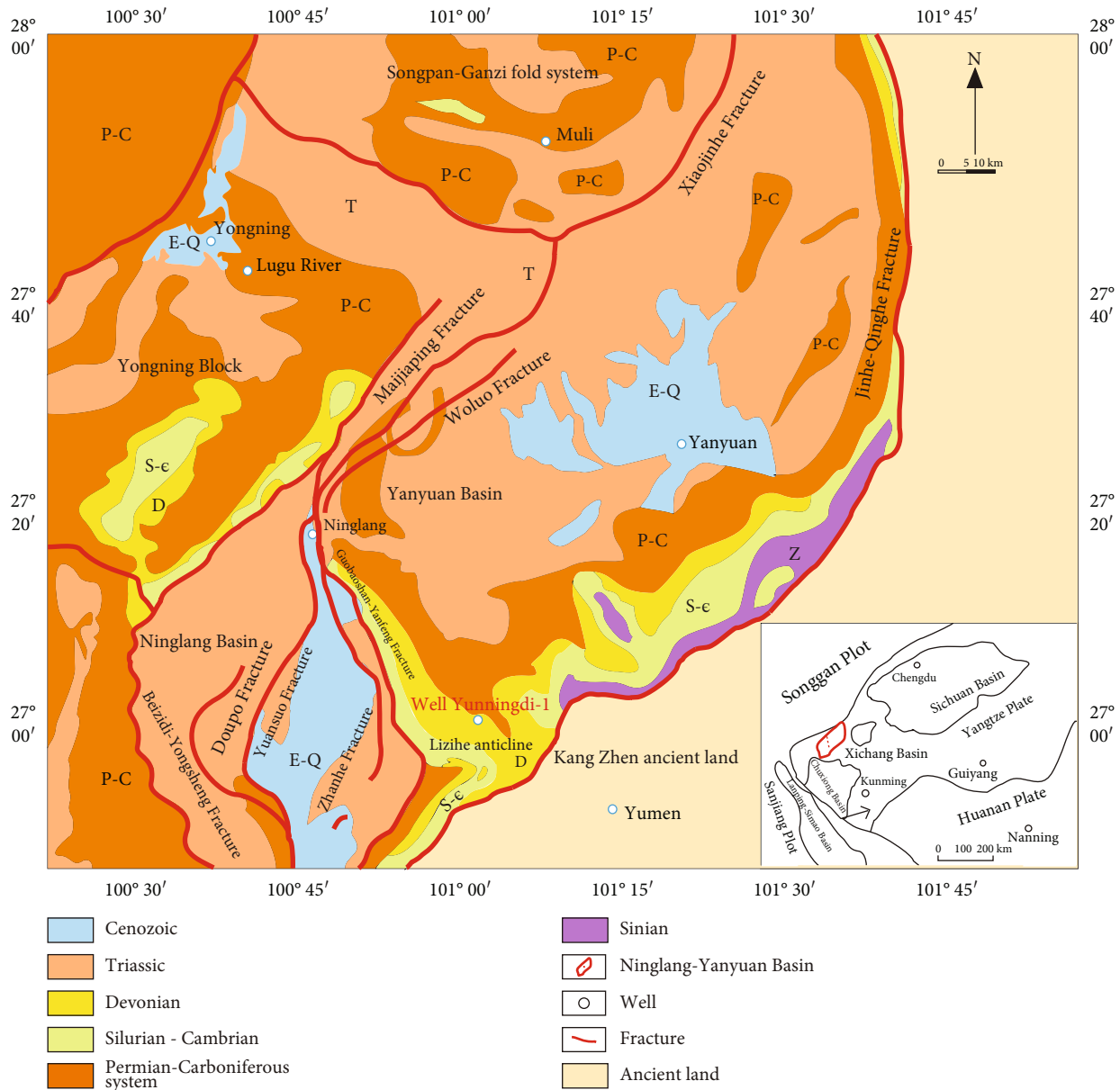


FIGURE 2: Tectonic position of the Ninglang-Yanyuan Basin and Well Yunningdi-1 (modified from reference [1]).

sample, which had been cleaned by ultrasonic waves with deionized water several times, the sample was ground to 200 mesh with agate mortar.

3.2. Analytical Methods

3.2.1. *TOC Analysis.* In this study, a total of 52 shale samples from the black shales of the Devonian Tanshanping and Dacaozi Formations were selected for TOC analysis. About 100 mg of powdered samples was prepared and then acidified with 5% HCl in a crucible when the temperature reached approximately 80°C to remove carbonates. The TOC concentration was determined using a Leco CS-230 apparatus at the Oil & Gas Resource Survey, China Geological Survey.

3.2.2. *Major Element.* All 52 samples were air-dried and crushed into powders before geochemical analysis. The con-

centration of major elements were measured at the Oil & Gas Resource Survey, China Geological Survey, using a Leeman Prodigy (USA) inductively coupled plasma-optical emission spectrometer (ICP-OES) with high-dispersion Echelle optics. Samples were prepared by dilution with tetraborate/lithium metaborate fusion and nitric dissolution processes. Chinese National Rock Standards (GSR-1 and GSR-5) and US Geological Survey (USGS) standard materials (BCR-1, AVG-2, and SCO-1) were used to correct the analytical uncertainties. Analytical precision for most of the major element oxides is more than 98%.

3.2.3. *Trace and Rare Earth Elements.* Trace element and rare earth element concentrations were determined with the Thermo Scientific Element XR Sector Field Inductively Coupled Plasma Source Mass Spectrometer (ICP-MS). Firstly,

52 test samples were added to lithium metaborate and lithium tetraborate solvent. Then, the powder samples were mixed well and dried at 105°C. Finally, ICP-MS was used to complete the test, which accuracy of for most of the trace and rare earth elements was better than 5%, with higher precision.

4. Results

4.1. Distribution of the TOC. The total organic carbon concentrations of the Tanshanping Formation and the Dacaozi Formation in Well Yunningdi-1 range from 0.10% to 3.48%, with an average of 1.08%. In particular, the total organic carbon concentrations of the Tanshanping Formation are higher than that of the Dacaozi Formation means 1.13% and 1.06%, respectively). Among them, it is worth noticing that the total organic carbon content of the organic-rich shale (1070.6~1088.6 m) in the Tanshanping Formation ranges from 0.92% to 1.43%, with an average of 1.21%. And the total organic carbon content of organic-rich shale (1320.8~1486.5 m) in the Dacaozi Formation ranges from 0.37% to approximately 3.48%, with an average of 1.14%. They were thought to be a good source rock because of the relatively high organic carbon content of these Formation shales, which has reached the standard of good source rock.

4.2. Distribution of Major Elements. The contents of major-element oxides in the shale samples from the Tanshanping Formation and the Dacaozi Formation are presented in Table 1. Table 1 shows that the main elements of the Tanshanping shale are SiO₂ (with an average of 42.55%), Al₂O₃ (with an average of 12.17%), and CaO (with an average of 11.94%), and the total content of these 3 components ranges from 48.96% to 78.34%. In addition, the concentrations of other major element oxides in the Tanshanping Formation are obviously less than 4%, which include Fe₂O₃ (with an average of 3.41%), MgO (with an average of 1.79%), K₂O (with an average of 2.87%), Na₂O (with an average of 1.26%), P₂O₅, SO₃, TiO₂, and MnO (less than 1%). It is worth noting that the main components of the organic-rich shale in the Tanshanping Formation are SiO₂ (with an average of 44.74%), Al₂O₃ (with an average of 12.95%), and CaO (with an average of 11.97%), and the total content of these three components ranges from 63.98% to 73.61%.

The main elements of the Dacaozi shale are SiO₂ (with an average of 56.07%), Al₂O₃ (with an average of 15.95%), Fe₂O₃ (with an average of 5.89%), and CaO (with an average of 4.57%). And the total content of these 4 components ranges from 80.74% to 96.92%. The concentrations of other major element oxides in the Dacaozi Formation are obviously less than 6%, which include K₂O (with an average of 5.53%), MgO (with an average of 1.54%), Na₂O (with an average of 1.44%), P₂O₅, SO₃, TiO₂, and MnO (less than 1%).

The variation trend of the mass fraction of major elements and TOC is similar to the study section of the Tanshanping Formation and the Dacaozi Formation (Figure 3). In the Tanshanping organic-rich shale, the contents of SiO₂, Al₂O₃, Fe₂O₃, Na₂O, TiO₂, and MnO decrease with the increase of TOC, while the contents of CaO and MgO increase with the increase of TOC. In the Tanshanping

organic-poor shale, the contents of SiO₂, Al₂O₃, Fe₂O₃, Na₂O, TiO₂, and MnO increase with the increase of TOC, while the contents of CaO decrease with the increase of TOC. In particular, TiO₂ content is relatively stable, and K₂O content increases with the increase of TOC in both organic-rich and organic-poor shale segments of the Tanshanping Formation. The variation trend of the mass fraction of major elements and TOC in the Dacaozi Formation is similar to that of the Tanshanping Formation.

4.3. Distribution of Trace Elements. Because the total number of samples from the Dacaozi Formation is obviously larger than the Tanshanping Formation, the Dacaozi Formation is divided into Dacaozi1 and Dacaozi2 in order to indicate the transition of burial depth. Trace and rare earth element (REE) contents were normalized to North America shale composite (NASC) (for trace elements) and chondrite (for REES) in Figures 4(a) and 4(b) [32, 33]. As shown in Figure 4 and Table 2, the shale samples of the study area were standardized by North American shale (NASC). In the samples of the Tanshanping Formation and Dacaozi Formation of Well Yunningdi-1 (52 samples studied), trace elements Zn (ranges from 0.18 to 2.26) and Sr (ranges from 0.22 to 4.45) are relatively rich, while Rb (ranges from 0.02 to 1.30) is relatively poor (Figure 4(a)). In the two shale members, the trace elements have a similar trend of change, but the relative content of the trace elements in the Tanshanping Formation fluctuates slightly more greatly than the Dacaozi Formation (Figure 4(a)). Compared with the Dacaozi1 Formation and the Dacaozi2 Formation, the contents of trace elements in some samples of the Tanshanping Formation fluctuate more greatly, and the peak values of Zn and Sr are lower, while the relative contents of Rb are lower.

4.4. Distribution of Rare Earth Elements. To begin with, the rare earth elements refer to the lanthanides from La to Lu, which exhibit similar chemical properties. Rare earth elements are good tracers and indicators, which are often used in the analysis of paleosedimentary environment of organic-rich shale [34, 35]. REE content of black shales of the Tanshanping Formation and the Dacaozi Formation in Well Yunningdi-1 in the Ninglang-Yanyuan Basin is shown in Table 3. The REE (\sum REE) concentrations of the Tanshanping Formation ranges from 6.00 to 321.24 μ g/g, with an average of 198.00 μ g/g, the average is significantly higher than the abundance of North American shale REE (173.21 μ g/g) and upper crustal abundance (146.40 μ g/g) [36, 37]. And the REE (\sum REE) concentrations of the Dacaozi Formation ranges from 103.95 to 898.57 μ g/g, with an average of 337.47 μ g/g; the value is also significantly higher than the North American shale \sum REE, which is nearly twice as much. From the data above, the REE content of the Dacaozi Formation samples is higher than that of the Tanshanping Formation samples, indicating that the shale of the Dacaozi Formation is farther from the provenance area.

The ratio of \sum LREE (light rare earth elements) to \sum HREE (heavy rare earth elements) (\sum LREE/ \sum HREE), reflecting the REE differentiation degree to some extent. The \sum LREE/ \sum HREE content of the Tanshanping Formation

TABLE 1: Concentrations of major elements (unit: wt%) in samples from the Tanshanping and Dacaozi Formations in the Ninglang-Yanyuan Basin.

Sample code	Member	Al ₂ O ₃	SiO ₂	Fe ₂ O ₃	CaO	MgO	Na ₂ O	K ₂ O	P ₂ O ₅	SO ₃	TiO ₂	MnO	CIA
Q1908705	Tanshanping	5.20	27.64	0.46	22.56	1.22	0.95	0.33	0.028	0.012	0.093	0.006	17.9096
Q1908706	Tanshanping	10.33	35.86	3.33	16.92	1.35	1.08	2.33	0.041	0.115	0.297	0.014	33.6900
Q1908709	Tanshanping	16.56	48.83	5.91	4.74	1.97	1.24	6.17	0.114	0.114	0.820	0.055	57.6821
Q1908837	Tanshanping	15.16	44.63	5.25	6.83	2.21	1.18	4.15	0.049	0.139	0.654	0.032	55.4974
Q1908712	Tanshanping	8.44	33.88	1.38	18.56	1.52	1.05	1.69	0.070	0.043	0.209	0.022	28.3799
Q1908713	Tanshanping	9.39	36.74	2.00	18.26	1.31	1.11	2.15	0.075	0.054	0.250	0.034	30.3686
Q1908714	Tanshanping	13.59	49.53	3.59	7.01	2.13	1.35	4.16	0.056	0.088	0.520	0.050	52.0566
Q1908721	Tanshanping	16.22	58.39	5.22	3.73	1.62	1.61	4.07	0.384	0.124	0.897	0.062	63.2941
Q1908723	Tanshanping	15.48	51.07	3.70	8.08	1.58	1.49	3.27	0.136	0.072	0.549	0.044	54.6782
Q1908727	Tanshanping	15.36	44.37	5.32	9.12	1.51	1.43	3.98	0.291	0.116	0.677	0.060	51.3754
Q1908734	Tanshanping	12.64	42.68	4.97	12.11	1.43	1.31	2.74	0.261	0.146	0.472	0.044	43.8976
Q1908843	Tanshanping	8.97	37.41	1.34	17.60	1.37	1.15	1.49	0.122	0.041	0.206	0.029	30.7172
Q1908844	Tanshanping	15.09	49.20	4.04	9.32	1.47	1.48	3.33	0.223	0.084	0.599	0.047	51.6402
Q1908737	Tanshanping	15.11	49.64	4.22	8.84	1.48	1.44	3.16	0.184	0.092	0.618	0.075	52.9244
Q1908847	Dacaozi	14.43	47.19	7.86	8.43	1.34	1.25	6.05	0.683	0.147	0.969	0.116	47.8553
Q1908742	Dacaozi	12.24	41.22	6.43	14.13	1.21	1.11	6.19	0.773	0.122	0.796	0.131	36.3541
Q1908849	Dacaozi	18.81	52.12	7.15	2.60	1.53	1.46	5.35	0.175	0.126	0.903	0.067	66.6623
Q1908745	Dacaozi	17.53	55.07	5.64	3.71	1.62	1.49	4.71	0.152	0.091	0.792	0.079	63.8803
Q1908746	Dacaozi	16.64	61.25	4.18	3.68	1.62	1.64	3.72	0.197	0.086	0.754	0.041	64.8141
Q1908748	Dacaozi	13.69	45.69	3.21	11.80	1.36	1.29	3.48	0.092	0.069	0.452	0.085	45.2417
Q1908751	Dacaozi	17.73	53.91	5.96	4.20	1.60	1.47	4.96	0.141	0.086	0.836	0.107	62.4997
Q1908753	Dacaozi	10.39	39.74	2.28	16.66	1.26	1.14	2.71	0.171	0.055	0.307	0.097	33.6283
Q1908756	Dacaozi	18.43	55.38	6.53	1.94	1.50	1.48	5.60	0.203	0.122	0.971	0.073	67.1236
Q1908759	Dacaozi	10.34	68.08	3.26	6.34	1.44	1.57	1.65	0.172	0.037	0.284	0.092	51.9619
Q1908761	Dacaozi	18.47	48.53	9.52	2.17	1.43	1.39	7.45	0.347	0.146	1.081	0.100	62.6328
Q1908762	Dacaozi	17.56	61.00	4.27	2.35	1.71	1.67	5.46	0.203	0.040	1.045	0.038	64.9155
Q1908765	Dacaozi	11.10	63.61	1.67	8.99	1.44	1.57	2.05	0.126	0.014	0.288	0.118	46.8225
Q1908767	Dacaozi	16.65	62.96	3.70	2.21	1.58	1.60	5.34	0.234	0.041	1.157	0.043	64.5156
Q1908768	Dacaozi	19.84	58.17	8.82	2.65	1.72	1.59	7.69	0.291	0.115	1.228	0.077	62.453
Q1908771	Dacaozi	18.91	52.84	7.47	2.00	1.56	1.48	6.95	0.240	0.111	1.168	0.036	64.4267
Q1908775	Dacaozi	16.99	64.57	3.07	2.14	1.64	1.60	4.76	0.106	0.049	0.668	0.018	66.6216
Q1908777	Dacaozi	19.36	55.03	5.85	2.25	1.60	1.49	6.30	0.115	0.068	0.967	0.060	65.8493
Q1908785	Dacaozi	16.19	57.62	5.06	3.90	1.60	1.47	5.58	0.316	0.075	0.950	0.075	59.6406
Q1908787	Dacaozi	12.86	54.84	3.96	6.89	1.45	1.39	4.25	0.382	0.072	0.751	0.190	50.6456
Q1908789	Dacaozi	12.56	56.29	4.26	12.24	2.00	1.50	4.31	0.483	0.090	0.656	0.294	41.023
Q1908798	Dacaozi	14.99	48.66	10.15	5.81	1.45	1.27	8.08	0.691	0.131	1.166	0.161	49.7102
Q1908800	Dacaozi	18.70	60.29	3.90	2.07	1.79	1.64	5.84	0.123	0.017	1.119	0.032	66.1879
Q1908801	Dacaozi	16.23	61.32	5.32	2.35	1.65	1.56	6.16	0.390	0.059	0.986	0.039	61.721
Q1908802	Dacaozi	16.89	65.21	3.37	1.93	1.57	1.64	4.28	0.055	0.050	0.893	0.024	68.2578
Q1908803	Dacaozi	17.78	56.44	5.95	2.34	1.68	1.47	7.45	0.438	0.027	1.374	0.042	61.2296
Q1908808	Dacaozi	17.71	58.80	5.21	2.31	1.61	1.50	6.68	0.374	0.057	1.102	0.031	62.7902
Q1908811	Dacaozi	12.08	46.26	11.51	4.96	1.08	1.08	11.85	1.853	0.220	1.704	0.064	40.3274
Q1908814	Dacaozi	18.83	57.96	5.53	2.19	1.74	1.60	6.04	0.239	0.040	0.121	0.025	65.6967
Q1908817	Dacaozi	8.91	71.29	4.32	5.89	1.24	1.34	0.14	0.000	0.007	0.120	0.033	54.7409
Q1908819	Dacaozi	16.64	56.06	7.55	2.60	1.52	1.43	7.03	0.591	0.134	0.975	0.081	60.0749
Q1908823	Dacaozi	16.86	64.64	6.61	2.28	1.64	1.34	0.09	0.000	0.007	0.120	0.028	81.9678
Q1908825	Dacaozi	17.66	51.95	8.77	2.15	1.50	1.36	6.93	0.369	0.133	0.992	0.098	62.8532
Q1908826	Dacaozi	17.49	53.96	8.18	1.97	1.63	1.43	5.75	0.197	0.104	0.892	0.078	65.6693

TABLE 1: Continued.

Sample code	Member	Al ₂ O ₃	SiO ₂	Fe ₂ O ₃	CaO	MgO	Na ₂ O	K ₂ O	P ₂ O ₅	SO ₃	TiO ₂	MnO	CIA
Q1908828	Dacaozi	17.62	55.90	6.54	2.14	1.66	1.44	6.46	0.311	0.058	1.136	0.039	63.7058
Q1908832	Dacaozi	16.87	59.62	5.68	2.26	1.70	1.47	5.85	0.315	0.052	0.952	0.030	63.7879
Q1908835	Dacaozi	14.01	50.90	9.14	4.53	1.41	1.18	11.22	1.405	0.009	1.755	0.070	45.2838

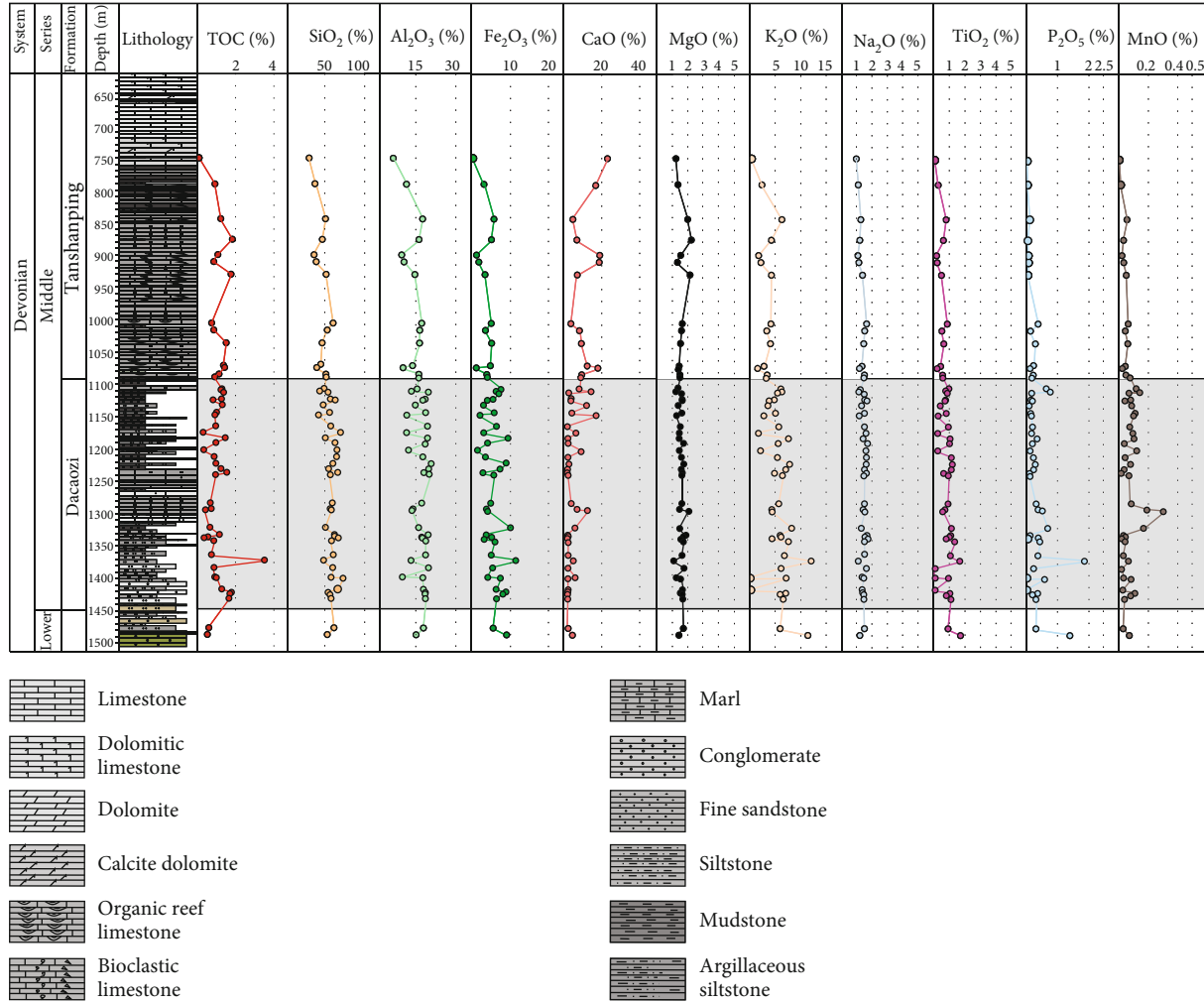


FIGURE 3: Main element and TOC content of YND-1 well in the Tanshanping Formation and Dacaozi Formation in the Ninglang-Yanyuan area (see Figure 2 for the well position).

ranges from 1.12 to 2.29, with an average of 1.85. And the $\sum\text{LREE}/\sum\text{HREE}$ content of the Dacaozi Formation ranges from 1.17 to 2.59, with an average of 2.01, and light rare earth elements are more enriched. However, the $\sum\text{LREE}/\sum\text{HREE}$ of both shale formations is smaller than that of North American shale (7.44), indicating that there was not much distance between these 2 groups and the provenance area.

The degree of differentiation of rare earth elements can be characterized by the slope of the partition curve of rare earth elements to chondrites, reflecting the higher the slope is, the slower the deposition rate is. LaN/YbN represents the slope of rare earth elements in the normalized chondrite diagram (Figure 4(b)), which can be used to evaluate the sedimental rate of shale. Meanwhile, the higher the deposition

rate is, the closer LaN/YbN is to 1. After the test, we found that the LaN/YbN of the Tanshanping Formation ranges from 0.85 to 1.37, with an average of 1.13. And the LaN/YbN of the Dacaozi Formation ranges from 0.75 to 1.58, with an average of 1.16. It is not difficult to see that the LaN/YbN of the samples of the Tanshanping Formation is closer to 1, leading the deposition rate of shale in the Tanshanping Formation is higher. What is more, the transport distance of the Tanshanping shale is shorter than that of the Dacaozi shale, which can reduce the loss of organic matter effectively.

The geochemical composition of sediments provides important information about the parent rocks from which they derived. The rare earth elements (REEs) are considered to be best indicators of provenance, as they are unlikely to

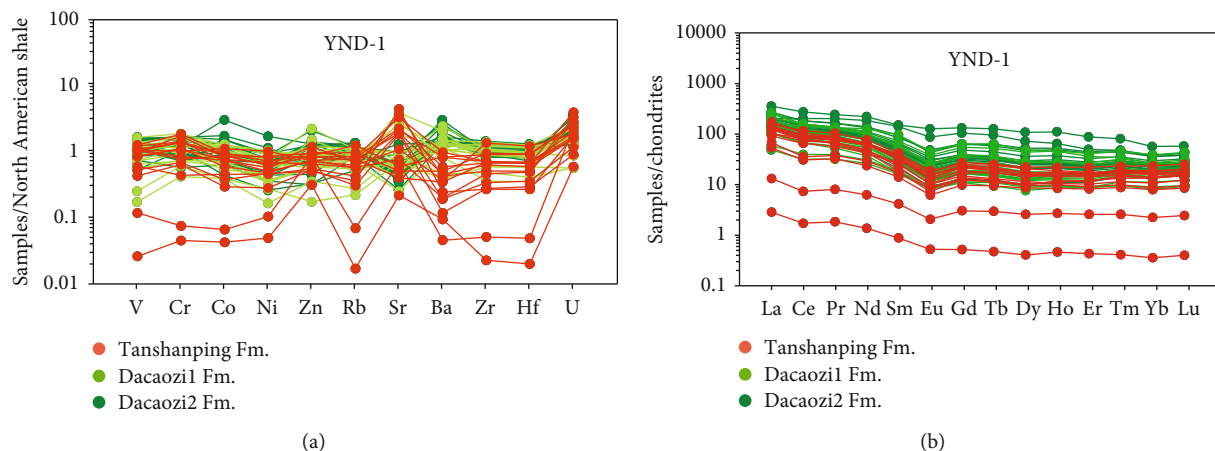


FIGURE 4: North American shale composite (NASC) normalized (for trace element) and chondrite normalized (for REE) diagrams for samples from the Middle Devonian Tanshanping Formation and Dacaozi Formation in the Ninglang-Yanyuan Basin, Southwest China.

be lost during postdepositional or sedimentary transport processes [38, 39]. In order to eliminate the serrated change of REE abundance with increasing atomic number caused by the even-odd rule of element abundance, REE concentrations were normalized to chondrite in Figure 4(b). Because it is generally accepted that there is no fractionation between LREE and HREE in chondrites, the chondrite standardization enables any separation between REE in the sample to be clearly shown.

The REE distribution pattern of shale samples from the Tanshanping Formation and the Dacaozi Formation in the study area is relatively stable and similar (Figure 4(b)). Figure 4(b) shows that LREE is relatively enriched and HREE is relatively depleted, and the distribution curve has a large slope in the light REE member, while it is flat in the heavy REE member. In addition, Ce and Eu are slightly depleted. On the whole, the REE distribution pattern is right tilted, which means LREE is enriched and HREE is flat. In another aspects, it also reflects the consistency of the provenance of the Tanshanping Formation and Dacaozi Formation in the study area.

5. Discussion

5.1. Paleoredox Condition Control on Deposition of the Tanshanping and Dacaozi Formations. Redox condition was the indispensable factor for organic matter preservation. Considering that particular self-stable and redox-sensitive elements (such as V, Cr, Co, Ni, Sc, and Zr) have been a bit affected or unaffected by diagenetic alternation due to their significantly lower correlation coefficients relative to other element contents [40, 41], the associated redox-sensitive trace elements, especially the trace-element ratios (e.g., V/Ni, Ni/Co, V/Cr, V/Sc, and V/(V + Ni)) are considered empirical indicators of paleoredox conditions. For the above reasons, the ratios of these elements (e.g., V/Ni, V/Cr, V/Sc, Ni/Co, and V/(V+Ni)) are usually considered effective proxies for distinguishing redox conditions of seawater to eliminate the underlying limitation utilizing a single trace

element. Previous studies have suggested that high ratios of these elements reflect reducing conditions.

Previous studies have demonstrated that the redox-sensitive elements were commonly enriched in the anoxic sediments, which could be used as powerful proxies for redox conditions [42]. Redox conditions have an important effect on the preservation of organic matter, the formation of sediments, and the formation and evolution of organisms. Specially, the redox condition indicators including V/Sc, V/Cr, Ni/Co, and V/(V+Ni) were widely used [43–45]. Constraints on the paleoredox conditions and paleoenvironment are provided by the above indicators, which show the discrimination of trace elements in different redox environments of shale in Well Yunningdi-1 (Figure 5). As the indexes to quantitatively evaluate the redox environment of the sedimentary waterbody, it is obvious that the sedimentary environment of the Tanshanping and Dacaozi Formations is different, suggesting that the Tanshanping Formation mainly deposited in a relatively anoxic environment.

On the whole, the redox environments changed greatly in the sedimentary history from the Dacaozi Formation to the Tanshanping Formation. The analysis of this study shows that, influenced by the paleoclimate and terrigenous input, the preservation conditions are triggered to change, reflecting on the TOC concentrations in the end, showing reasonable agreement with the decisive effect of the preservation condition of the mechanism of accumulation and preservation of the organic matter.

5.2. Paleoclimate Control on Deposition of the Tanshanping and Dacaozi Formations. Our investigations on CIA and REE further strengthened overall dysoxic to anoxic conditions of the waterbody during accumulation of the Dacaozi Formation to Tanshanping Formation, which provides the foundation for the following interpretations of the paleoclimate effect on redox environments.

The climatic conditions control the temperature, Eh, and pH of the sedimentary environment [46]. Chemical weathering is a crucial process to control the evolution of the earth surface system, by shaping landscapes, supplying nutrients

TABLE 2: Concentrations of trace elements (unit: $\mu\text{g/g}$) in samples from the Tanshanping and Dacaozi Formations in the Ninglang-Yanyuan Basin.

Sample code	Member	V	Cr	Co	Ni	Rb	Sr	Zr	Mo	Ba	Hf	U	V/Cr	Ni/Co	Th/U	V/Sc	V/(V+Ni)	Sr/Ba	Baxs	P/Ti
Q1908705	Tanshanping	15.47	7.56	1.26	7.09	9.74	208.89	10.25	2.29	26.59	0.31	6.17	2.05	5.62	0.17	6.70	0.69	7.86	26.55	0.30
Q1908706	Tanshanping	137.07	102.71	21.27	68.95	81.52	231.30	92.25	11.01	115.11	3.11	7.53	1.33	3.24	3.11	9.24	0.67	2.01	115.03	0.14
Q1908709	Tanshanping	165.26	184.98	18.04	48.76	175.08	181.33	181.43	1.38	478.90	5.76	6.79	0.89	2.70	2.92	8.32	0.77	0.38	478.78	0.14
Q1908837	Tanshanping	124.37	173.71	15.58	58.45	136.49	152.96	189.48	5.28	294.19	5.85	7.08	0.72	3.75	3.05	9.30	0.68	0.52	294.07	0.07
Q1908712	Tanshanping	56.25	63.88	5.62	19.25	43.14	551.63	55.49	0.86	68.95	1.86	2.41	0.88	3.43	3.06	7.99	0.74	8.00	68.89	0.33
Q1908713	Tanshanping	78.13	43.99	8.69	31.22	59.70	577.97	68.11	3.83	112.01	2.25	3.11	1.78	3.59	3.68	6.64	0.71	5.16	111.94	0.30
Q1908714	Tanshanping	109.32	111.71	11.31	32.65	107.96	121.50	137.41	1.52	202.22	4.17	4.23	0.98	2.89	3.50	10.05	0.77	0.60	202.11	0.11
Q1908721	Tanshanping	140.34	139.53	14.11	34.53	87.22	325.95	272.63	0.72	216.50	7.65	4.94	1.01	2.45	4.88	11.84	0.80	1.51	216.37	0.43
Q1908723	Tanshanping	135.13	137.15	16.79	42.66	104.49	579.60	126.24	1.00	264.89	3.75	4.19	0.99	2.54	3.69	11.18	0.76	2.19	264.77	0.25
Q1908727	Tanshanping	159.17	142.46	17.67	55.93	117.31	992.74	142.33	9.73	574.02	4.22	10.49	1.12	3.16	1.65	12.12	0.74	1.73	573.91	0.43
Q1908734	Tanshanping	112.28	109.49	14.55	46.75	80.03	1105.91	102.26	6.67	246.32	3.19	8.82	1.03	3.21	1.94	8.53	0.71	4.49	246.22	0.55
Q1908843	Tanshanping	69.51	68.67	7.17	31.88	50.82	1335.90	54.31	2.09	141.67	1.70	4.65	1.01	4.45	1.34	10.04	0.69	9.43	141.61	0.59
Q1908844	Tanshanping	138.81	84.27	14.16	38.81	113.76	678.97	134.54	1.89	342.83	4.30	5.39	1.65	2.74	3.14	12.11	0.78	1.98	342.71	0.37
Q1908737	Tanshanping	137.36	77.10	16.42	42.55	97.29	648.31	142.07	1.62	480.04	4.39	4.53	1.78	2.59	3.55	11.36	0.76	1.35	479.93	0.30
Q1908847	Dacaozi	141.02	139.65	18.40	40.86	122.04	560.28	181.83	1.70	622.67	5.36	5.03	1.01	2.22	4.64	9.37	0.78	0.90	622.67	0.70
Q1908742	Dacaozi	128.19	133.17	16.72	45.49	118.83	769.06	121.17	1.28	660.75	3.71	7.10	0.96	2.72	1.90	8.52	0.74	1.16	660.64	0.97
Q1908849	Dacaozi	180.03	167.36	22.38	51.96	159.87	257.43	215.42	4.00	1426.36	6.17	6.13	1.08	2.32	3.21	13.03	0.78	0.18	1426.27	0.19
Q1908745	Dacaozi	156.35	157.74	19.43	46.54	141.12	300.84	177.80	1.55	643.92	5.11	5.06	0.99	2.39	3.23	11.89	0.77	0.47	643.78	0.19
Q1908746	Dacaozi	83.54	72.78	11.57	25.03	77.00	209.36	243.36	0.71	605.66	7.13	3.67	1.15	2.16	3.80	9.20	0.77	0.35	605.53	0.26
Q1908748	Dacaozi	117.42	109.68	13.97	39.92	102.69	1169.57	125.97	1.54	1201.71	3.68	4.69	1.07	2.86	2.84	8.89	0.75	0.97	1201.58	0.20
Q1908751	Dacaozi	177.21	167.37	24.82	61.38	153.49	299.38	187.71	1.15	783.38	5.51	5.15	1.06	2.47	3.64	12.31	0.74	0.38	783.27	0.17
Q1908753	Dacaozi	95.04	91.64	10.15	31.49	71.88	864.32	72.22	0.76	484.48	2.23	3.24	1.04	3.10	2.89	10.05	0.75	1.78	484.34	0.56
Q1908756	Dacaozi	172.35	170.51	20.22	50.68	137.80	148.75	220.54	2.48	802.06	6.30	6.44	1.01	2.51	2.97	11.72	0.77	0.19	801.98	0.21
Q1908759	Dacaozi	22.65	42.21	7.48	18.67	31.21	213.97	118.14	0.76	225.70	3.71	1.52	0.54	2.50	3.18	5.62	0.55	0.95	225.56	0.61
Q1908761	Dacaozi	214.56	189.15	24.12	71.26	175.25	218.80	193.11	2.20	824.44	5.76	6.98	1.13	2.95	3.05	10.93	0.75	0.27	824.36	0.32
Q1908762	Dacaozi	118.20	114.89	13.25	29.14	116.69	124.26	252.55	0.59	766.60	7.32	4.60	1.03	2.20	3.79	9.45	0.80	0.16	766.46	0.19
Q1908765	Dacaozi	33.05	60.59	7.43	11.32	39.04	268.61	97.25	0.51	270.83	2.59	1.55	0.55	1.52	3.53	8.29	0.74	0.99	270.70	0.44
Q1908767	Dacaozi	95.96	113.46	12.11	23.15	104.28	124.51	268.45	0.57	674.62	7.57	4.35	0.85	1.91	3.79	9.31	0.81	0.18	674.53	0.20
Q1908768	Dacaozi	170.67	130.90	23.93	64.94	166.23	157.34	208.30	1.72	891.17	5.76	5.11	1.30	2.71	3.84	9.30	0.72	0.18	891.04	0.24
Q1908771	Dacaozi	175.19	93.09	23.81	44.76	159.06	166.72	281.99	0.99	855.18	7.95	6.64	1.88	1.88	3.25	9.95	0.80	0.19	855.02	0.21
Q1908775	Dacaozi	72.52	74.54	13.46	25.42	93.34	75.93	214.39	0.67	633.45	5.94	2.34	0.97	1.89	4.92	7.91	0.74	0.12	633.30	0.16
Q1908777	Dacaozi	156.78	116.68	23.30	52.99	151.86	169.14	187.90	0.99	926.44	5.36	4.69	1.34	2.27	3.94	8.94	0.75	0.18	926.31	0.12
Q1908785	Dacaozi	177.43	155.47	16.13	47.27	135.69	180.69	194.90	0.69	1648.02	5.79	5.41	1.14	2.93	3.26	15.92	0.79	0.11	1647.87	0.33
Q1908787	Dacaozi	119.68	120.84	12.59	32.08	97.13	259.97	202.79	0.60	1326.24	6.29	4.62	0.99	2.55	3.24	12.14	0.79	0.20	1326.12	0.51
Q1908789	Dacaozi	65.73	99.51	8.09	17.24	69.80	230.26	174.56	0.71	1466.94	4.38	3.85	0.66	2.13	4.40	10.89	0.79	0.16	1466.85	0.74

TABLE 2: Continued.

Sample code	Member	V	Cr	Co	Ni	Rb	Sr	Zr	Mo	Ba	Hf	U	V/Cr	Ni/Co	Th/U	V/Sc	V/(V+Ni)	Sr/Ba	Baxs	P/Ti
Q1908798	Dacaozi	165.72	81.48	27.34	56.88	156.85	282.11	187.85	1.94	928.08	5.65	8.01	2.03	2.08	2.52	9.14	0.74	0.30	927.98	0.59
Q1908800	Dacaozi	135.60	127.17	11.82	28.94	157.10	104.52	274.27	0.61	917.98	7.82	4.29	1.07	2.45	4.30	9.46	0.82	0.11	917.87	0.11
Q1908801	Dacaozi	107.37	84.22	14.21	27.74	123.22	135.11	234.60	0.55	792.74	6.88	4.12	1.27	1.95	3.92	8.93	0.79	0.17	792.60	0.40
Q1908802	Dacaozi	92.21	55.28	11.46	23.65	115.00	77.49	228.30	0.79	710.04	6.66	3.26	1.67	2.06	4.60	9.04	0.80	0.11	709.92	0.06
Q1908803	Dacaozi	158.26	76.84	18.49	41.22	149.39	161.44	222.89	1.25	1337.85	6.41	5.15	2.06	2.23	3.98	9.94	0.79	0.12	1337.72	0.32
Q1908808	Dacaozi	149.66	80.03	20.70	39.16	136.53	127.57	250.59	0.80	788.96	7.24	5.22	1.87	1.89	3.38	12.11	0.79	0.16	788.83	0.34
Q1908811	Dacaozi	139.47	116.24	54.07	110.28	105.93	369.09	191.94	2.05	778.83	5.38	6.94	1.20	2.04	2.10	7.35	0.56	0.47	778.70	1.09
Q1908814	Dacaozi	187.22	148.38	18.14	43.63	161.81	120.21	218.69	0.86	809.75	6.54	5.64	1.26	2.40	3.52	11.09	0.81	0.15	809.66	1.98
Q1908817	Dacaozi	143.57	76.71	20.77	60.50	136.56	188.79	167.92	2.69	778.06	4.85	4.71	1.87	2.91	4.37	8.73	0.70	0.24	777.91	(0.00)
Q1908819	Dacaozi	141.27	72.12	16.49	50.50	122.50	146.01	195.70	2.37	783.05	5.80	4.22	1.96	3.06	3.50	11.40	0.74	0.19	782.98	0.61
Q1908823	Dacaozi	128.65	70.10	16.29	50.09	123.92	154.75	256.60	1.82	646.15	7.47	4.76	1.84	3.07	3.48	9.67	0.72	0.24	646.02	(0.00)
Q1908825	Dacaozi	198.05	156.91	31.41	73.86	177.88	112.78	191.43	1.56	804.79	5.64	6.11	1.26	2.35	3.09	11.62	0.73	0.14	804.66	0.37
Q1908826	Dacaozi	191.23	157.70	27.62	61.27	181.75	101.74	164.83	1.37	907.78	4.95	5.24	1.21	2.22	3.38	11.37	0.76	0.11	907.65	0.22
Q1908828	Dacaozi	205.39	135.73	23.93	50.51	179.94	116.77	201.04	1.30	861.98	6.04	6.19	1.51	2.11	3.25	10.90	0.80	0.14	861.85	0.27
Q1908832	Dacaozi	181.81	76.41	22.08	45.95	157.33	110.49	191.07	0.69	1105.79	5.93	5.24	2.38	2.08	3.32	11.96	0.80	0.10	1105.66	0.33
Q1908835	Dacaozi	196.25	78.93	13.50	43.94	156.97	189.10	157.81	0.34	994.91	4.86	8.70	2.49	3.26	1.89	11.42	0.82	0.19	994.78	0.80

TABLE 3: Concentrations of rare earth elements (unit: $\mu\text{g/g}$) in samples from the Tanshanping and Dacaozi Formations in the Ninglang-Yanyuan Basin.

Sample code	Member	La	Ce	Pr	Nd	Sm	Eu	Gd	Tb	Dy	Ho	Er	Tm	Yb	Lu	REE	LREE	HREE	LREE/HREE	LaN/YbN
Q1908705	Tanshanping	4.11	5.96	0.97	3.75	0.83	0.15	0.79	0.15	0.83	0.19	0.54	0.08	0.47	0.07	29.90	15.78	14.12	1.12	0.85
Q1908706	Tanshanping	28.55	53.15	6.89	25.25	5.17	0.73	4.46	0.86	4.90	1.02	2.99	0.46	2.96	0.45	205.62	119.75	85.87	1.39	0.93
Q1908709	Tanshanping	54.32	84.91	10.80	38.39	7.15	0.95	5.60	1.00	5.59	1.19	3.56	0.58	3.95	0.61	290.17	196.52	93.64	2.10	1.33
Q1908837	Tanshanping	41.21	64.62	7.83	26.83	3.66	0.51	3.32	0.56	3.24	0.81	2.44	0.45	2.94	0.48	216.21	144.66	71.55	2.02	1.36
Q1908712	Tanshanping	16.59	25.13	3.92	14.27	2.82	0.44	2.56	0.47	2.75	0.59	1.73	0.26	1.68	0.26	105.42	63.17	42.25	1.50	0.96
Q1908713	Tanshanping	31.41	67.63	9.15	36.53	7.98	1.33	6.50	1.22	6.61	1.34	3.69	0.55	3.47	0.53	237.28	154.03	83.24	1.85	0.88
Q1908714	Tanshanping	31.98	59.16	8.19	28.38	5.33	0.71	3.90	0.65	3.68	0.74	2.16	0.34	2.26	0.37	192.13	133.74	58.39	2.29	1.37
Q1908721	Tanshanping	48.75	95.01	12.58	46.64	8.45	1.23	7.14	1.27	7.19	1.55	4.64	0.70	4.94	0.76	321.24	212.65	108.6	1.96	0.96
Q1908723	Tanshanping	38.20	61.17	8.28	29.54	4.48	0.62	3.54	0.62	3.18	0.83	2.53	0.40	2.83	0.46	206.99	142.29	64.70	2.20	1.31
Q1908727	Tanshanping	43.59	75.96	10.62	39.20	7.01	1.08	5.94	1.06	5.42	1.24	3.49	0.57	3.83	0.60	269.15	177.46	91.69	1.94	1.10
Q1908734	Tanshanping	40.34	69.82	9.67	40.02	7.76	1.11	6.09	1.09	5.56	1.21	3.14	0.50	3.34	0.50	254.86	168.72	86.14	1.96	1.17
Q1908843	Tanshanping	21.29	28.97	4.55	17.76	3.47	0.59	3.26	0.58	3.08	0.70	1.91	0.30	1.83	0.29	124.22	76.63	47.60	1.61	1.13
Q1908844	Tanshanping	44.66	76.38	9.79	37.38	6.45	0.96	5.67	0.96	5.02	1.15	3.29	0.54	3.28	0.52	258.64	175.62	83.02	2.12	1.32
Q1908737	Tanshanping	42.73	76.73	9.41	37.80	6.40	0.87	4.87	0.87	4.60	1.09	3.26	0.56	3.56	0.54	252.18	173.94	78.24	2.22	1.16
Q1908847	Dacaozi	63.58	128.09	16.57	67.88	14.58	2.65	14.20	2.60	13.99	3.23	8.60	1.38	8.19	1.30	487.72	293.35	194.4	1.51	0.75
Q1908742	Dacaozi	52.66	115.25	15.97	77.00	19.29	3.18	16.56	3.19	15.61	3.17	7.57	1.03	5.47	0.81	460.67	283.36	177.3	1.60	0.93
Q1908849	Dacaozi	58.50	98.35	12.40	47.35	8.05	1.22	6.60	1.07	5.53	1.20	3.45	0.59	3.66	0.57	315.72	225.88	89.83	2.51	1.55
Q1908745	Dacaozi	44.55	74.84	8.90	34.40	5.45	0.81	4.50	0.77	3.86	0.87	2.50	0.45	2.89	0.46	238.56	168.96	69.60	2.43	1.49
Q1908746	Dacaozi	37.69	67.76	8.12	32.31	5.45	0.86	4.62	0.81	4.09	0.92	2.72	0.47	3.00	0.49	219.47	152.19	67.28	2.26	1.22
Q1908748	Dacaozi	41.00	70.30	9.04	36.57	7.12	1.39	5.97	1.14	5.69	1.24	3.39	0.55	3.41	0.52	249.58	165.42	84.17	1.97	1.16
Q1908751	Dacaozi	52.63	85.31	10.30	39.27	6.03	0.90	5.04	0.87	4.41	1.03	3.01	0.53	3.38	0.53	274.72	194.45	80.27	2.42	1.51
Q1908753	Dacaozi	31.44	54.29	7.02	27.46	5.46	0.97	4.99	0.92	4.90	1.13	3.03	0.49	2.98	0.45	199.24	126.63	72.61	1.74	1.02
Q1908756	Dacaozi	53.50	88.45	11.01	38.96	6.57	1.05	5.72	0.99	5.07	1.15	3.47	0.60	4.10	0.66	288.61	199.55	89.06	2.24	1.27
Q1908759	Dacaozi	15.08	25.70	3.85	15.74	3.26	0.57	2.91	0.54	2.84	0.65	1.83	0.29	1.90	0.29	103.95	64.19	39.76	1.61	0.77
Q1908761	Dacaozi	78.79	119.94	15.31	59.35	12.14	1.82	10.24	1.84	9.34	1.97	5.21	0.85	5.25	0.84	417.17	287.35	129.8	2.21	1.45
Q1908762	Dacaozi	47.50	90.96	10.81	40.78	7.67	1.17	6.31	1.06	5.45	1.21	3.34	0.57	3.57	0.58	283.97	198.88	85.09	2.34	1.29
Q1908765	Dacaozi	18.54	32.08	4.70	18.54	3.66	0.64	3.11	0.58	3.00	0.68	1.85	0.29	1.69	0.28	120.83	78.16	42.67	1.83	1.06
Q1908767	Dacaozi	43.99	89.18	10.30	39.67	7.48	1.21	6.06	1.08	5.44	1.21	3.46	0.58	3.72	0.60	276.22	191.82	84.39	2.27	1.15
Q1908768	Dacaozi	56.93	102.05	12.26	46.01	8.72	1.50	7.44	1.32	6.89	1.60	4.57	0.75	4.81	0.74	341.18	227.47	113.7	2.00	1.15
Q1908771	Dacaozi	82.11	126.43	15.99	61.28	10.99	1.73	9.29	1.66	8.68	1.99	5.64	0.96	5.69	0.93	432.21	298.52	133.7	2.23	1.40
Q1908775	Dacaozi	31.99	54.55	6.33	22.34	3.42	0.58	2.85	0.47	2.47	0.60	1.85	0.34	2.35	0.37	169.28	119.21	50.07	2.38	1.32
Q1908777	Dacaozi	60.64	95.84	11.07	38.13	5.16	0.73	4.34	0.73	3.86	0.98	3.02	0.56	3.72	0.59	293.21	211.56	81.64	2.59	1.58
Q1908785	Dacaozi	52.18	87.95	11.34	43.63	8.68	1.50	7.44	1.30	6.39	1.38	3.70	0.60	3.71	0.59	299.77	205.27	94.49	2.17	1.36
Q1908787	Dacaozi	44.90	82.96	10.80	42.91	8.70	1.51	7.67	1.41	7.42	1.63	4.38	0.71	4.35	0.67	292.53	191.78	100.8	1.90	1.00
Q1908789	Dacaozi	42.25	72.90	9.10	36.12	7.28	1.23	6.66	1.22	6.34	1.44	3.95	0.65	3.93	0.60	260.86	168.88	91.99	1.84	1.04

TABLE 3: Continued.

Sample code	Member	La	Ce	Pr	Nd	Sm	Eu	Gd	Tb	Dy	Ho	Er	Tm	Yb	Lu	REE	LREE	HREE	LREE/HREE	LaN/YbN
Q1908798	Dacaozi	68.75	135.40	18.03	76.60	17.64	2.80	14.85	2.90	15.51	3.39	8.67	1.34	7.43	1.14	510.87	319.22	191.7	1.67	0.90
Q1908800	Dacaozi	52.00	86.72	10.22	37.12	5.51	0.81	4.05	0.71	3.95	0.99	3.12	0.57	3.69	0.59	270.41	192.38	78.03	2.47	1.36
Q1908801	Dacaozi	46.41	93.25	11.60	47.27	9.85	1.70	8.25	1.53	7.74	1.71	4.61	0.74	4.33	0.65	318.29	210.08	108.2	1.94	1.04
Q1908802	Dacaozi	36.70	62.21	7.17	24.05	3.92	0.61	3.18	0.57	3.11	0.72	2.21	0.41	2.69	0.42	192.54	134.65	57.89	2.33	1.32
Q1908803	Dacaozi	58.54	103.83	13.02	49.70	9.77	1.75	8.47	1.53	8.03	1.76	4.90	0.80	5.13	0.79	355.28	236.61	118.7	1.99	1.11
Q1908808	Dacaozi	48.59	94.73	12.89	53.23	11.82	2.04	9.13	1.64	7.97	1.62	4.30	0.66	3.95	0.62	328.92	223.30	105.6	2.11	1.19
Q1908811	Dacaozi	100.12	202.13	26.50	120.69	27.70	8.14	31.57	5.82	31.90	7.11	17.07	2.23	11.1	1.61	898.57	485.28	413.3	1.17	0.88
Q1908814	Dacaozi	56.86	109.78	13.74	54.03	10.32	1.63	9.05	1.53	7.78	1.70	4.61	0.76	4.74	0.77	360.64	246.35	114.3	2.16	1.16
Q1908817	Dacaozi	77.20	135.01	17.96	73.54	15.69	3.14	15.45	2.70	14.17	3.17	8.28	1.23	7.02	1.07	517.69	322.53	195.2	1.65	1.07
Q1908819	Dacaozi	50.99	96.93	12.48	49.01	9.95	1.93	9.61	1.65	8.84	2.03	5.48	0.84	4.99	0.77	351.77	221.29	130.5	1.70	0.99
Q1908823	Dacaozi	56.30	116.93	14.98	60.42	12.29	2.27	11.65	2.07	10.78	2.43	6.46	0.99	5.79	0.91	411.00	263.19	147.8	1.78	0.94
Q1908825	Dacaozi	54.32	96.23	12.46	47.93	9.33	1.56	8.43	1.44	7.40	1.62	4.56	0.76	4.53	0.70	337.94	221.82	116.1	1.91	1.16
Q1908826	Dacaozi	51.65	89.92	11.59	43.38	8.01	1.32	6.95	1.19	6.21	1.40	3.93	0.65	4.04	0.63	306.97	205.87	101.1	2.04	1.24
Q1908828	Dacaozi	59.80	113.77	13.98	54.49	10.58	1.67	9.20	1.54	7.79	1.74	4.79	0.80	5.06	0.78	376.63	254.28	122.4	2.08	1.14
Q1908832	Dacaozi	50.44	93.62	12.04	45.81	9.03	1.57	8.34	1.46	7.47	1.69	4.71	0.77	4.74	0.76	327.52	212.51	115.0	1.85	1.03
Q1908835	Dacaozi	57.49	150.23	22.11	101.48	25.87	5.63	24.86	4.39	21.44	4.20	9.69	1.32	7.05	1.06	595.93	362.81	233.1	1.56	0.79

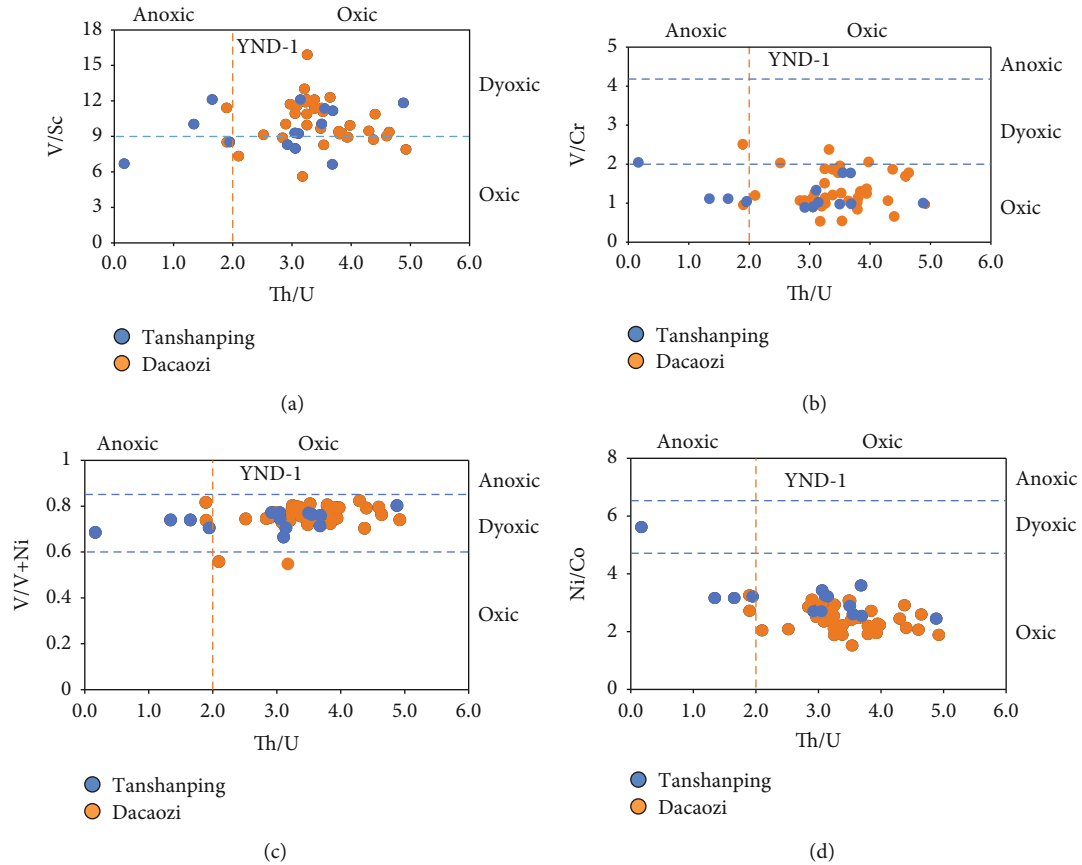


FIGURE 5: Discrimination of trace elements in different redox environments of shale in Well Yunningdi-1.

and trace elements from the lithosphere to the biosphere, and regulating global chemical cycles. In the process of sediment formation, several geochemical indexes have been proposed to assess the degree of chemical weathering [47–50], among which the chemical index of alteration (CIA) is one of the most frequently used indexes. The chemical index of alteration (CIA) is calculated as the ratio $[\text{Al}_2\text{O}_3/(\text{Al}_2\text{O}_3 + \text{CaO} + \text{Na}_2\text{O} + \text{K}_2\text{O}) * 100]$ in molecular proportions, where CaO represents Ca content in silicate minerals only. It is worth noting that the CIA has been widely used to quantify the degree of chemical weathering for (paleo-)weathering profiles and to reconstruct source region chemical weathering conditions for ancient and modern sediments [51]. In addition, the climate indexes (CIA) display the slowly warming environment, which is often used to reflect the paleoclimate conditions. It means the higher CIA values experienced relatively intense chemical weathering, which indicates a warm and humid climate [52]. It is also consistent with previous studies on the relationship between the CIA and paleoclimate which provides a better standard. As discussed in previous studies, when the value of CIA ranges from 50 to 65, it indicates arid climate. When the value of CIA ranges from 65 to 85, it indicates semiarid climate. When the value of CIA ranges from 85 to 100, it indicates warm and humid climate [53, 54]. Specially, the shale-dominated the Dacaozi Formation and Tanshanping Formation experienced a moderate to weak degree of chemical weathering as evidenced by the

significant decrease of CIA (mean 58.5 and 43.2, respectively) (Figure 6 and Table 1). Besides, the $\sum\text{REE}$ ($\sum\text{REE} = \text{Sc} + \text{Y} + \text{La} + \text{Ce} + \text{Pr} + \text{Nd} + \text{Sm} + \text{Eu} + \text{Gd} + \text{Tb} + \text{Dy} + \text{Ho} + \text{Er} + \text{Tm} + \text{Yb} + \text{Lu} + \text{Th}$) can also indicate climate conditions [55]. It is noticed that the climate became more dry-cold from the Dacaozi Formation to the Tanshanping Formation as evidenced by the significant decrease of $\sum\text{REE}$ (mean 337.5 and 198.0, respectively) (Figure 6 and Table 1).

Therefore, these considerable variations likely reflect the impact of alternating climatic conditions of warm-humid and cool-arid, which confirm a relatively intensive weathering and its associated warm-humid setting that occur during the deposition of shales of the Dacaozi Formation.

In summary, there are several lines of evidence that it is more conducive to form a higher paleoproductivity in the context of a relatively warm-humid climate which promote biological growth in the sedimentary waterbody. From the above discussion of the values (CIA, $\sum\text{REE}$) from the Dacaozi Formation to the Tanshanping Formation, we have found that although the climate is relatively warm-humid during the deposition of the Dacaozi Formation, the weak preservation condition leads to destroy the accumulation of organic matter, which shows the lower TOC concentrations in the end.

5.3. Paleoproductivity Control on Deposition of the Tanshanping and Dacaozi Formations. In particular, the initial productivity of waterbody can be characterized by the

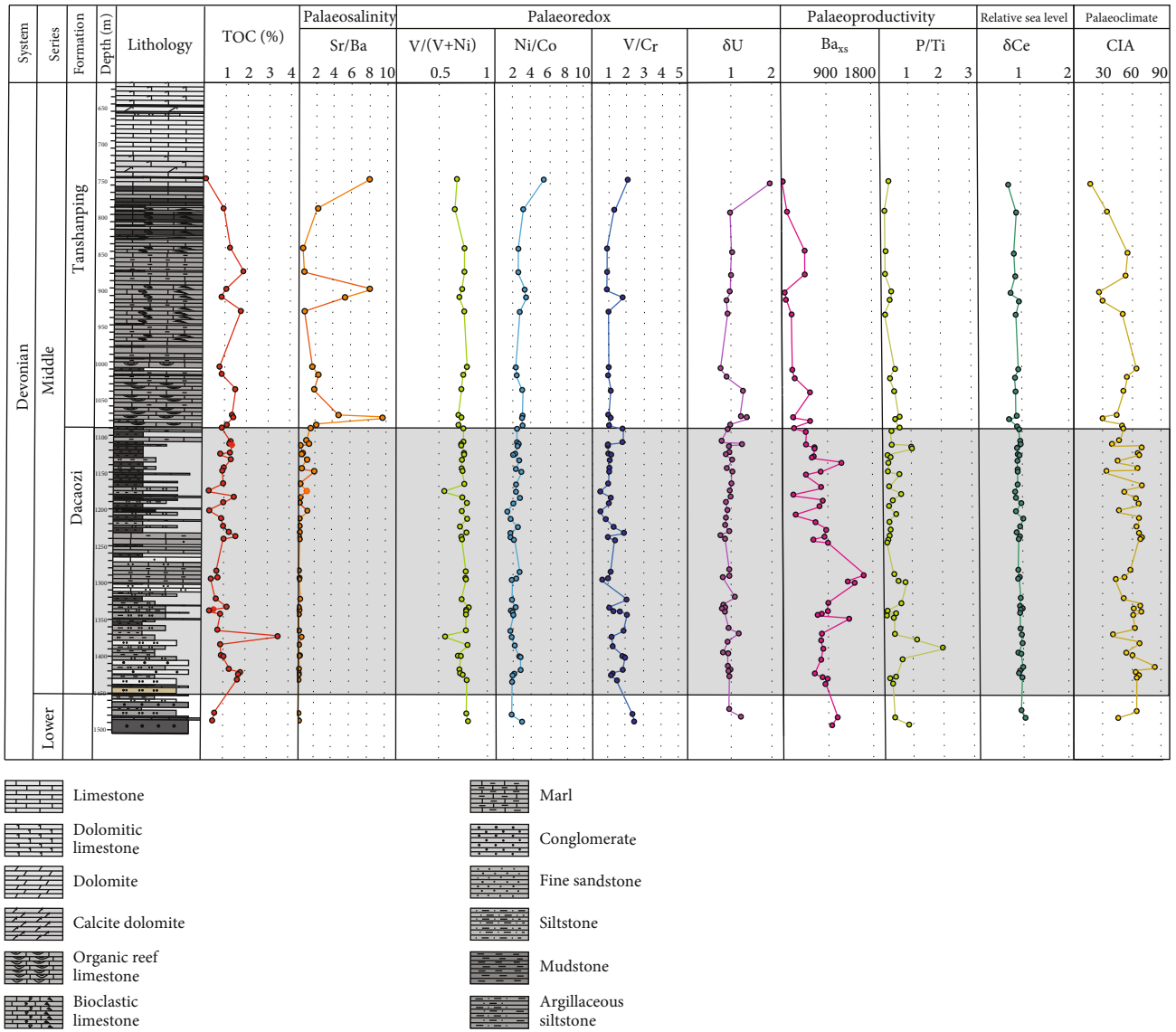


FIGURE 6: Paleoproductivity, paleoredox, paleosalinity, paleoclimate, relative sea level, and TOC content of Well Yunningdi-1 in the Tanshanping Formation and Dacaozi Formation in the Ninglang-Yanyuan area (see Figure 2 for the well position).

nutrient richness and organic carbon flux of surface water, and the change of initial productivity plays a key role in the accumulation of organic matter.

The Ba content is an indicator widely used to reflect the paleocean bioproductivity [56–60]. There is a high concentration of SO_4^{2-} ions reoxidized by H_2S on the surface of decayed organic matter. These ions will react with the Ba^{2+} in seawater to form $BaSO_4$ and result in sedimentation. Therefore, the area with a higher bioproductivity also has a higher content of $BaSO_4$ [61, 62]. The trace elements in rocks are composed of terrigenous input constituents and authigenic ones. Only the latter can reflect the characteristics of the paleosedimentary environment [63–65]. The Ba produced under the biological action is known as excess Ba (Ba_{xs}). The Late Archean Australian Shale standard is commonly used to calculate excess barium (Ba_{xs}) to characterize paleoproductivity. It is worth noticing that the higher values

of Ba_{xs} are indicators of higher paleoproductivity in the sedimentary waterbody of the Dacaozi Formation (Figure 6).

Furthermore, phosphorus (P) is considered to be one of the ultimately limited elements in marine environment, and also, it belongs to the most important nutrient elements for plankton [66] and a major component of skeletal material. Therefore, P is widely used as an indicator of paleoproductivity. Organic matter and authigenic minerals may have a dilutive effect on the absolute P content in the terrigenous detrital matter. To eliminate the effect, the P/Ti ratio is used to evaluate the paleoproductivity rather than the absolute P content [67, 68] because Ti is usually derived from the terrigenous detrital matter [69, 70]. The higher ratios of P/Ti of the Dacaozi Formation (which is higher than the P/Ti ratio of the black flint in the Ubara profile with medium productivity (with an average of 0.34)) reported in Figure 6 can also imply relatively high paleoproductivity throughout the depositional

sequence of shales, which coincides with the better provenance supply as argued above in a relatively warm-humid sedimentary setting, which provided favorable conditions for the accumulation of organic matter.

Since the depth of water controls the redox conditions and Ce depletion degree of water, Ce anomaly can also be used to indicate the relative change of the sea level. With the rise of sea level, the oxygen content of bottom water and the δCe of sediments are reduced [71].

From the above discussion, we can get a stronger idea that detailed analysis of the paleoredox conditions and further investigation of the paleoclimatic and paleoproductivity forcing mechanisms operating during sedimentation indicate that the Dacaozi organic-rich shales was deposited in the more warm-humid environments. Climatic fluctuations resulted in the difference degree of the terrigenous input of the Dacaozi and Tanshanping Formations, which coincide well with the water paleoproductivity changes and redox environmental evolution [72]. Specifically, during the deposition of the Dacaozi Formation, significant increases in the temperature and humidity led to the relatively high terrigenous inputs with more nutrient inputs. The terrigenous inputs promoted abundant planktons and favoring organic matter accumulation [73]. In addition, the shallow waterbody made it easier for sunlight to penetrate the waterbody, which coincides with the relatively high paleoproductivity. However, the preservation condition of the organic matter in the Dacaozi Formation was generally poor, as often the relative sea level was so low that it tend to accumulate more oxygen [74]. Specially, the higher terrigenous input diluted more organic matter, and the longer distance of transportation and lower deposition rate have accelerated the destruction of preservation conditions. Due to the worse preservation conditions, the TOC concentrations of the Dacaozi Formation were lower. On the contrary, we have found that the paleoproductivity during the sedimentary period of the Tanshanping Formation was lower than that of the Dacaozi Formation, reflecting the relative cold-dry climate and lower terrigenous input. It is obvious that the paleoproductivity in the waterbody was worse, and that is mainly because it did not have enough terrigenous input, reflecting the limited provenance supply. In another aspects, we found that the range of the penetration from sunlight was relatively narrow, for the sea level was relatively high. Nevertheless, the higher sea level supports a reductive and stable bottom waterbody (Figure 7). And the lower terrigenous input indicates the decrease of fresh water input, leading to be more reductive in the waterbody. In addition, it is worth to emphasis on the shorter distance of transportation during the sedimentary period of the Tanshanping Formation, which enhance the preservation ability in the sedimentary center.

6. Mechanism of Accumulation and Preservation of Organic Matter

The study area was in the sedimentary environment of the carbonate platform. The high biological productivity, anoxic, and reducing environment were conducive to the accumulation and preservation of organic matter in shale [75]. In order

to reconstruct the model of accumulation and preservation of organic matter in the carbonate platform facies, it is essential to clear up the relationship between TOC and relative sea level, paleoproductivity, and redox conditions of the unique sedimentary facies which has many unconventional features. Therefore, this study preliminarily discusses the accumulation and preservation mechanism of shale organic matter in Well Yunningdi-1 in the Ninglang-Yanyuan area by using the evolution of water redox conditions combined with the research results of sea level change, paleoproductivity, paleoclimate, and terrigenous input.

6.1. Relationship between TOC and Relative Sea Level Variations. In considering sea level variations during the sedimentary period, the relative sea level and regional paleoclimate are suggested here as two distinct factors for the influence of accumulation and preservation of organic matter at different scales.

On the one hand, the difference of the redox environment of the Tanshanping and Dacaozi Formations can be analyzed from the relative sea level. Previous studies have shown that water depth is one of the elements which controls the redox condition and Ce depletion degree. With the rise of sea level, both of the oxygen content of bottom water and the δCe of sediments decrease [71]. The value of δCe in the Tanshanping Formation is lower than that in the Dacaozi Formation (mean 0.763 and 0.824, respectively), reflecting the rise of the relative sea level. The research of the redox environment emphasized the importance of the relative sea level response in the process of deposition of the carbonate platform and throw light on whether the relative sea level variations control the redox environment of the sedimentary waterbody in the carbonate platform.

On the other hand, the anoxic environment in the sedimentary waterbody of the Tanshanping Formation is ascribed to the regional paleoclimate effect during the sedimentary period. At the same time, the terrigenous inputs promote planktons' propagation and growth.

This implies that the combined effects of relative sea level variations and regional paleoclimate driving mechanisms favored the accumulation and preservation of organic matter in the study area. To summarize, the combined impact of these factors is ultimately reflected in the TOC.

6.2. Relationship between TOC and Paleoproductivity. Based on the above researches, Ba_{xs} indicates that the paleoproductivity of the sedimentary waterbody in the Dacaozi Formation is higher than that of the Tanshanping Formation (mean 856.29 and 254.49, respectively), which are shown in Figure 6 and Table 2. Considering that the accumulation and preservation of the organic matter in the Dacaozi Formation is largely controlled by paleoproductivity due to their significantly higher correlation coefficients between TOC and paleoproductivity indexes (e.g., Pb and Ni/Al) [76], which are shown in Figures 7(d) and 8(e). In addition, the associated indexes of climate and terrigenous input (e.g., REE and CIA values) are considered important indicators of paleoproductivity. However, due to the damage of the preservation condition, there is more oxygen enrichment of

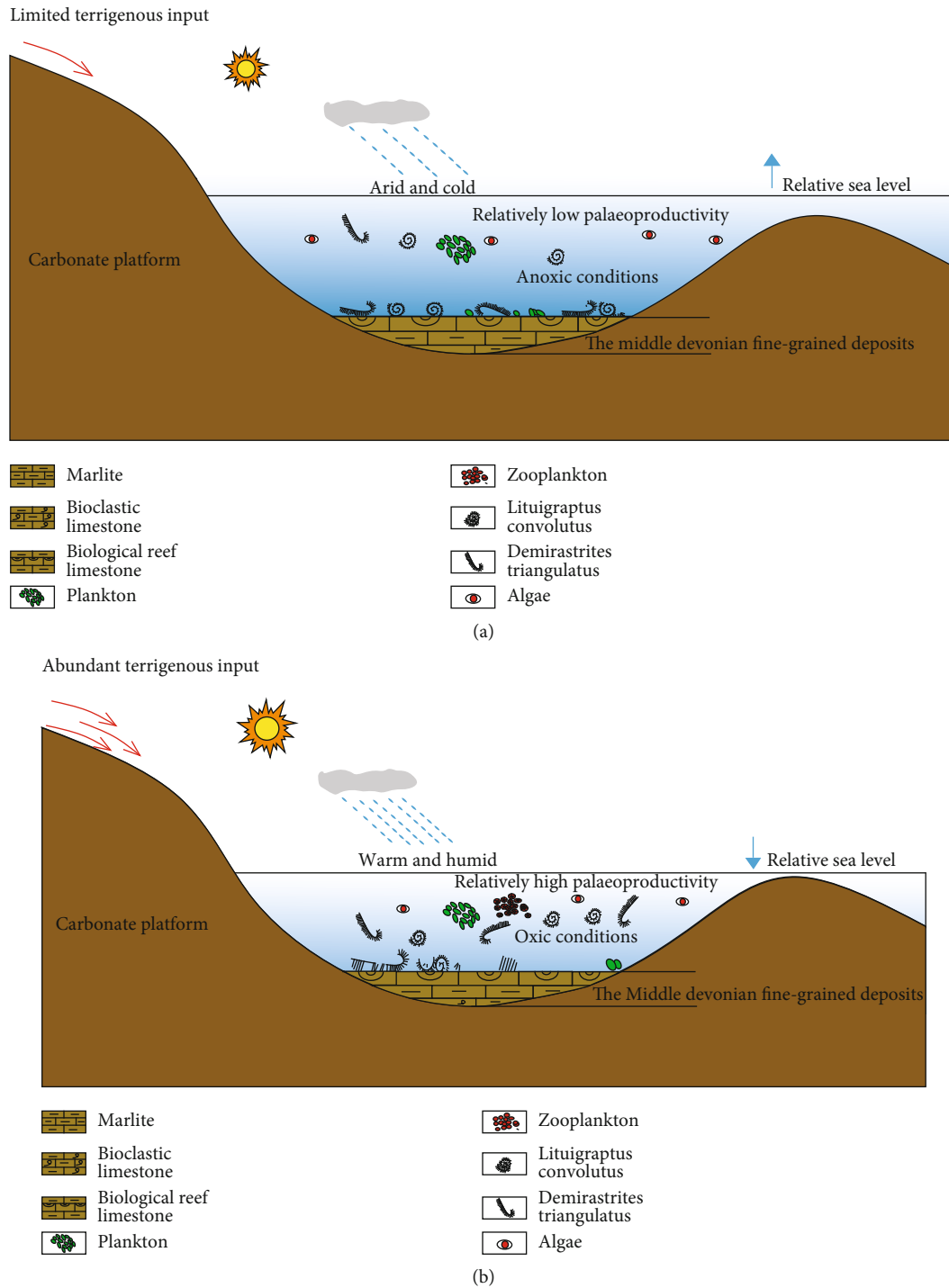


FIGURE 7: A conceptual model illustrating the influence of the changes of relative sea level, paleoredox condition, paleoproductivity condition, and paleoclimate condition on organic matter accumulation and preservation for the Tanshanping Formation and the Dacaozi Formation. (a) The Tanshanping Formation. (b) The Dacaozi Formation.

the sedimentary waterbody of the Dacaozi Formation, which led to the lower TOC concentrations of the Dacaozi Formation.

6.3. Relationship between TOC and Redox Conditions and Terrigenous Inputs. The redox conditions are crucial in the mechanism of accumulation and preservation of the organic

matter, which shown in Figure 7. As most scholars believe, this is in close agreement that the redox environment of sedimentary waterbody is not only affected by redox indexes but also affected by terrigenous input.

On the one hand, we have supported the idea that the accumulation and preservation of the organic matter in the Tanshanping Formation are largely controlled by paleoredox

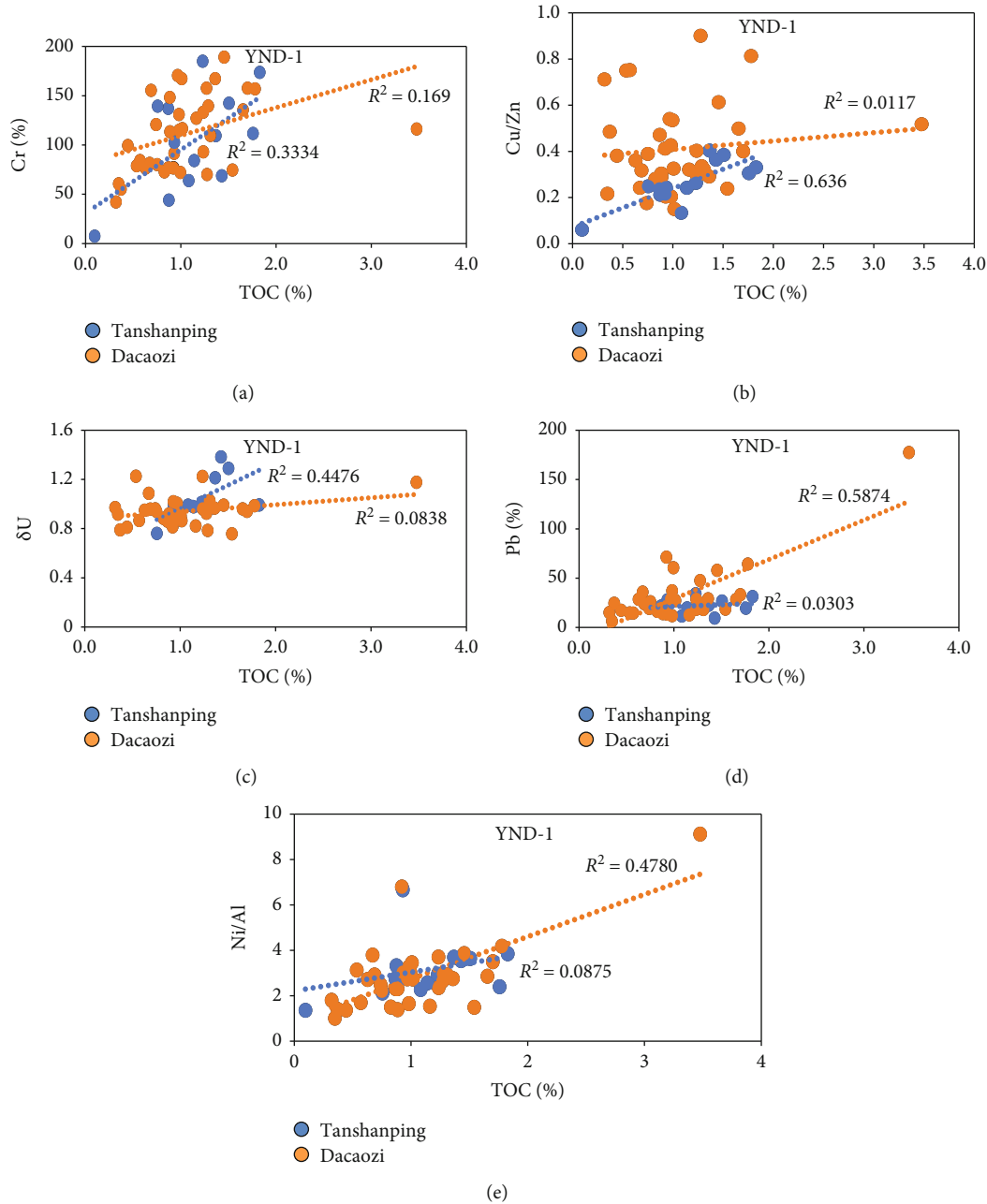


FIGURE 8: Crossplots of redox indexes (Cr, Cu/Zn, and δU) versus TOC content and paleoproductivity indexes (Pb and Ni/Al) versus TOC content of the Tanshanping and Dacaozi shales.

due to their significantly higher correlation coefficients between TOC and paleoredox indexes (e.g., Cr, Cu/Zn, and δU), which have been considered reliable redox indexes [77, 78], reflecting in Figures 8(a)–8(c).

On the other hand, terrigenous input is also considered an important element, coinciding reasonably well with the paleoproductivity and paleoredox environment.

From the above discussion, we can get a stronger idea that CIA and $\sum REE$ can reflect paleoclimate and terrigenous input together. The CIA and $\sum REE$ values of the Dacaozi Formation are higher, reflecting the relatively warm-humid

paleoclimate and higher terrigenous input. At the same time, the higher terrigenous input diluted more organic matter. According to the previous studies, both of the paleoclimate and terrigenous input led to oxidation of the sedimentary waterbody of the Dacaozi Formation. On the contrary, it was relatively dry-cold during the sedimentary period of the Tanshanping Formation, which reflects lower terrigenous input. The lower terrigenous input has effectively decreased the dilution of organic matter, leading a reductive environment of sedimentary waterbody in the Tanshanping Formation.

6.4. Model of Accumulation and Preservation of Organic Matter

6.4.1. *The Interactions between the Relative Sea Level, Paleoproductivity, Redox Condition, and Carbonate Platform Sedimentation.* As one of the key research points of the Ninglang-Yanyuan Basin, the Tanshanping and Dacaozi Formations of Well Yunningdi-1 have the following features.

According to previous studies, we have done a lot of works about the marine facies and pure continental facies. Specially, the sedimentary position of the study area is different from the previous researches, which belongs to the carbonate platform facies (Figure 7).

Unlike marine deposits, sedimentary water bodies of the carbonate platform are partially connected with the open sea, showing reasonable agreement that the accumulation and preservation of organic matter will be partially affected by the open sea (Figure 7). However, the connection area with the open sea is really limited in the sedimentary waterbody here, it will be greatly affected by other multiple factors (such as paleoclimate, paleoproductivity, terrigenous input, and redox conditions) within the sedimentary waterbody.

Aiming at the mechanism of accumulation and preservation of the carbonate platform, this paper takes the Tanshanping Formation and Dacaozi Formation as an excellent example and focuses on the analysis of the dialectical relation between the paleoproductivity and paleoredox environment and the accumulation and preservation model of shale in the study area.

In terms of paleoproductivity and redox condition, it is obvious to know that both of them affect the accumulation and preservation of organic matter. In the study on the accumulation and preservation mechanism of organic matter in the Tanshanping and Dacaozi Formations, the comprehensive results of the combined effects of paleoproductivity and redox conditions form a marked contrast.

From the above discussion, we have summarized a view. Based on the example of the Dacaozi Formation, the TOC of the study shale member is not necessarily higher in the context of higher productivity waterbody. The reason why it shows lower TOC concentrations is that the sedimentary waterbody of the Dacaozi Formation had more oxygen because of the fall of the sea level and the dilution from the terrigenous input. In another aspect, based on the example of the Tanshanping Formation, the paleoproductivity was lower, for the relatively dry-cold climate has blocked biological growth. As a complement, the range of the penetration from sunlight was relatively narrow because of the rise of the sea level. However, the waterbody was more reductive during this depositional period, because the lower terrigenous input which was reflected by the dry-cold climate indicates the decrease of fresh water input. All of the conditions guarantee a better preservation condition of organic matter. On the whole, the TOC concentrations of the study shale are not necessarily lower although the paleoproductivity is relatively poor.

6.4.2. *Depositional Model for Organic-Rich Shale of Carbonate Platform.* In terms of sedimentary facies, the Dacaozi Formation developed saline lagoon facies, which belongs to shallow

water deposits farther from the sedimentary center. During the deposition period of the Dacaozi Formation, the water energy was low, which was mainly due to weak tidal action. It is noticed that only a limited number of organisms developed in the waterbody because of the abnormal salinity of the waterbody. Based on the above factors, it can be seen that the organic matter enrichment capacity of the Dacaozi Formation was relatively poor. As for the sedimentary period during the Tanshanping Formation, it developed the reef deposit with rich reservoir performance. It developed closer to the sedimentary center. Due to the rich nutrients and clean water, there were a lot of organisms growing in the waterbody during the sedimentary period of the Tanshanping Formation.

According to the detailed analysis of the paleoredox conditions and further investigation of the multifaceted studies about relative sea level, paleoclimate, terrigenous input, and paleoproductivity during sedimentation, we have purposed the conceptual model illustrating the influences of the relative sea level variations, paleoredox condition, paleoproductivity condition, and paleoclimate condition on organic matter accumulation and preservation for the Tanshanping Formation and the Dacaozi Formation.

Detailed analysis of the paleoredox conditions and further investigation of the paleoproductivity forcing mechanisms operating during sedimentation indicate that the shales of the Dacaozi and Tanshanping Formations were deposited under the controlling of paleoredox conditions. During the deposition period of the Dacaozi Formation, which was deposited in the more warm-humid shallow water environments, we found that significant increases in the temperature and humidity led to more fresh water inputs and a high degree of chemical weathering [79–83]. The higher terrigenous inputs, promoting abundant planktons and better condition of organic matter accumulation, coincides with the higher level of penetration from sunlight. From the above factors, it is obvious to exhibit a higher paleoproductivity in the sedimentary waterbody of the Dacaozi Formation. However, the preservation condition of the organic matter in the Dacaozi Formation was poor, as often the relative sea level was so low that it tend to accumulate more oxygen. Specially, the higher terrigenous input diluted more organic matter, and the longer distance of transportation and lower deposition rate have accelerated the destruction of preservation conditions. As we can see in Figure 7(b), there were a few dead planktons left in the bottom water, in which their bodies were damaged to varying degrees because of the poor preservation condition. Due to the worse preservation conditions, the TOC concentrations of the Dacaozi Formation were lower. During our investigation of the mechanism of accumulation and preservation of organic matter in the Tanshanping Formation, the depositional model for organic-rich shale of the Tanshanping Formation has been discovered. Our previous work has summarized that the paleoproductivity during the sedimentary period of the Tanshanping Formation was lower than that of the Dacaozi Formation, which reflects the relative cold-dry climate and lower terrigenous input. As the relative sea level rise, increased water depth would decrease the mixing chance of surface oxygenated water into sediment-water interface, and increased sea level also trapped clastic flux inshore,

which reflects lower terrigenous input [84]. In addition, the range of the penetration from sunlight was relatively narrow, for the sea level was so high that it blocks sunlight from entering into the water. Nevertheless, it supports a reductive and stable bottom water because of the rise of the sea level (Figure 7(a)), showing reasonable agreement with the influence of the decrease of fresh water input which is attributed to the fall of terrigenous input. Moreover, the shorter distance of transportation of terrigenous detritus during the sedimentary period of the Tanshanping Formation enhances the preservation ability in the sedimentary center. As is shown in Figure 7(a), the number of plankton carcasses greatly increases due to the lack of oxygen in the waterbody or catastrophic events. Decomposition of these carcasses consumes large amounts of oxygen and form H_2S gas, which further ensures the anoxic condition of the bottom water [85]. It is worth noting that there are a large number of plankton carcasses in the bottom water, which were hardly destroyed by external forces because of the stable anoxic waterbody and the shorter distance of transportation of terrigenous detritus.

To sum up, the significance of establishing the accumulation and preservation model of organic matter lies in discussing the coupling interactions between the paleoproductive forces and paleoredox environment. Because of the unique features of the carbonate platform facies, the examples of the Dacaozi Formation and the Tanshanping Formation are used to illustrate: the TOC concentrations of the study shale member are not necessarily higher although the paleoproductivity is relatively high, and the TOC concentrations of the study shale is not necessarily lower although the paleoproductivity is relatively poor. The considerable fluctuations in the TOC concentrations are reasonably attributed to the redox environment of the Tanshanping and Dacaozi Formations, which determines the preservation conditions.

These findings highlight the importance of coupling between the paleoproductivity and redox environment in the more specific carbonate platforms in further research.

7. Conclusions

On the basis of our results from TOC concentrations, major, trace, and rare earth elemental fingerprints and comprehensive analyses on the special features of the carbonate platform facies in the Tanshanping and Dacaozi Formations, this current study provides a good opportunity for documenting the major controlling factors of the accumulation and preservation of organic matter and for revealing new insights into the response of the coupling interactions between the paleoproductivity and redox environment. The achievements are thus conducted to generate a comprehensive and specific depositional model for the carbonate platform facies as evident in the case of the Tanshanping and Dacaozi Formations, Ninglang-Yanyuan Basin, Southwest China, and the following conclusions have been drawn:

- (1) The variation trend of the content of major elements and TOC is similar to the study shales of the Tanshanping and Dacaozi Formations. Com-

pared to the Dacaozi Formation, the value of the trace elements (Ni/Co, V/Cr, and V/Sc) in our study confirms that the shale of the Tanshanping Formation was deposited in an reductive environment. As for the rare earth element, the shale members of the Middle Devonian Tanshanping and Dacaozi Formations are both enriched in LREE and depleted in HREE, with negative anomalies of Ce and Eu

- (2) Specially, the sedimentary position of the study area is different from the previous researches, which belongs to the carbonate platform facies. We have concluded that the main controlling factors are the paleoclimate, paleoproductivity, terrigenous input, and paleoredox conditions in the sedimentary waterbody. Aiming at the mechanism of accumulation and preservation of the carbonate platform, this paper takes the Tanshanping Formation and Dacaozi Formation as an excellent example and focuses on the analysis of the coupling interactions between the paleoproductivity and paleoredox environment. On the whole, these above features show its uniqueness, which deserved to be analyzed
- (3) Dacaozi organic-rich shales were deposited in the more warm-humid environments. In addition, the shallow waterbody made it easier for sunlight to penetrate the waterbody, which coincides with the relatively high paleoproductivity. However, the preservation condition of the organic matter was generally poor, as often the relative sea level was so shallow that it tend to accumulate more oxygen. Specially, the higher terrigenous input diluted more organic matter, leading to the destruction of preservation conditions. Due to the worse preservation conditions, the TOC concentrations of the Dacaozi Formation were lower. On the contrary, the paleoproductivity during the sedimentary period of the Tanshanping Formation was lower. Nevertheless, the higher sea level and the lower terrigenous input reduced input of fresh water and supported a reductive bottom waterbody. Through a combination of the above factors, the TOC concentrations of the Tanshanping Formation shale were relatively high
- (4) The significance of constructing the accumulation and preservation model of organic matter lies in discussing the coupling interactions between paleoproductive forces and redox environment. The examples of the Dacaozi and Tanshanping Formations are used to illustrate the following: the TOC concentrations of the study shale member are not necessarily higher although the paleoproductivity is relatively high. In the same way, the TOC concentrations of the study shale are not necessarily lower although the paleoproductivity is relatively poor. As a result, the preservation conditions have been the decisive factor in the accumulation and preservation model of organic matter of the carbonate platform

Data Availability

Some of the data are contained in a published source cited in the references. All the data in this article is accessible to the readers.

Conflicts of Interest

The authors declare that they have no conflicts of interest.

Acknowledgments

A critical review and constructive comments from Dr. Rusi Zuo undoubtedly enhanced the quality of interpretations of chemostratigraphic data and are highly appreciated. Many thanks are given to Dr. Liang Xu for his sincere help during the analysis of the major and trace elements. We are especially grateful to Dr. Rong Chen of Oil & Gas Resource Survey, China Geological Survey, for the help during TOC content analysis. This work was supported by the Science Foundation for Distinguished Young Scholars of China University of Petroleum, Beijing (No. 2462020QNXZ004) and the National Natural Science and Technology Major Project (No. 2016ZX05034-001 and 2017ZX05035-002).

References

- [1] Z. Zhang, D. Shi, L. Lan et al., "Geological characteristics and exploration directions of Devonian strata in the Ninglang-Yanyuan Basin," *Petroleum Science Bulletin*, vol. 5, no. 2, pp. 161–171, 2020.
- [2] Y. Qin, Z. Zhang, D. Shi et al., "Geochemical characteristics and geological significances of shales in the Dacaozi Formation, Ninglang Region," *Journal of Northeast Petroleum University*, vol. 44, no. 2, pp. 11–23, 2020.
- [3] K. E. Peters, "Guidelines for evaluating petroleum source rock using programmed pyrolysis," *AAPG Bulletin*, vol. 70, no. 3, pp. 318–329, 1994.
- [4] D. M. Jarvie, R. J. Hill, T. E. Ruble, and R. M. Pollastro, "Unconventional shale-gas systems: the Mississippian Barnett Shale of North-Central Texas as one model for thermogenic shale-gas assessment," *AAPG Bulletin*, vol. 91, no. 4, pp. 475–499, 2007.
- [5] D. J. K. Ross and R. Marc Bustin, "The importance of shale composition and pore structure upon gas storage potential of shale gas reservoirs," *Marine and Petroleum Geology*, vol. 26, no. 6, pp. 916–927, 2009.
- [6] S. Guo and Y. Wang, "Shale gas accumulation conditions and exploration potential of Carboniferous Banxi Formation in Ordos Basin," *Acta Petroleum Sinica*, vol. 34, no. 5, pp. 445–452, 2013.
- [7] F. Hao, H. Y. Zou, and Y. C. Lu, "Mechanisms of shale gas storage: implications for shale gas exploration in China," *AAPG Bulletin*, vol. 97, no. 8, pp. 1325–1346, 2013.
- [8] S. B. Wang, Z. G. Song, T. T. Cao, and X. Song, "The methane sorption capacity of paleozoic shales from the Sichuan Basin, China," *Marine and Petroleum Geology*, vol. 44, pp. 112–119, 2013.
- [9] C. Xie, J. Zhang, Y. Li, and X. Wang, "Characteristics and gas content of the Lower Cambriandark shale in Well Yuke 1, Southeast Chongqing," *Oil & Gas Geology*, vol. 34, no. 1, pp. 11–15, 2013.
- [10] G. J. Demaison and G. T. Moore, "Anoxic environments and oil source bed genesis," *Organic Geochemistry*, vol. 2, no. 1, pp. 9–31, 1980.
- [11] S. E. Calvert and M. R. Fontugne, "On the Late Pleistocene-Holocene sapropel record of climatic and oceanographic variability in the Eastern Mediterranean," *Paleoceanography*, vol. 16, no. 1, pp. 78–94, 2001.
- [12] J. Rinna, B. Warning, P. A. Meyers, H. J. Brumsack, and J. Rullkötter, "Combined organic and inorganic geochemical reconstruction of paleodepositional conditions of a Pliocene sapropel from the Eastern Mediterranean Sea," *Geochimica et Cosmochimica Acta*, vol. 66, no. 11, pp. 1969–1986, 2002.
- [13] B. B. Sageman, A. E. Murphy, J. P. Werne, C. A. ver Straeten, D. J. Hollander, and T. W. Lyons, "A tale of shales: the relative roles of production, decomposition, and dilution in the accumulation of organic-rich strata, Middle-Upper Devonian, Appalachian Basin," *Chemical Geology*, vol. 195, no. 1-4, pp. 229–273, 2003.
- [14] H. Mort, O. Jacquat, T. Adatte et al., "The cenomanian/turonian anoxic event at the Bonarelli level in Italy and Spain: enhanced productivity and/or better preservation?," *Cretaceous Research*, vol. 28, no. 4, pp. 597–612, 2007.
- [15] H. Y. Wei, D. Z. Chen, J. G. Wang, H. Yu, and M. E. Tucker, "Organic accumulation in the lower Chihhsia Formation (Middle Permian) of South China: constraints from pyrite morphology and multiple geochemical proxies," *Palaeogeography, Palaeoclimatology, Palaeoecology*, vol. 353-355, pp. 73–86, 2012.
- [16] Y. Li, D. Shao, H. Lv, Y. Zhang, X. Zhang, T. Zhang et al., "A relationship between element geochemical characteristics and organic matter enrichment in marine shale of Wufeng Formation-Longmaxi Formation, Sichuan Basin," *Acta Petroleum Sinica*, vol. 36, no. 12, pp. 1470–1483, 2015.
- [17] T. F. Pedersen and S. E. Calver, "Anoxia vs. productivity: what controls the formation of organic-carbon-rich sediments and sedimentary rocks?," *AAPG Bulletin*, vol. 74, no. 4, pp. 454–466, 1990.
- [18] B. J. Katz, "Controlling factors on source rock development: a review of productivity, preservation and sedimentation rate," *SEPM Special Publication*, vol. 82, pp. 7–16, 2005.
- [19] R. V. Tyson, "The productivity versus preservation controversy: cause, flaws and resolution," *Society for Sedimentary Geology*, vol. 82, pp. 17–33, 2005.
- [20] A. E. Murphy, B. B. Sageman, D. J. Hollander, T. W. Lyons, and C. E. Brett, "Black shale deposition and faunal overturn in the Devonian Appalachian Basin: clastic starvation, seasonal water-column mixing, and efficient biolimiting nutrient recycling," *Paleoceanography*, vol. 15, no. 3, pp. 280–291, 2000.
- [21] S. M. Rimmer, "Geochemical paleoredox indicators in Devonian-Mississippian black shales, Central Appalachian Basin (USA)," *Chemical Geology*, vol. 206, no. 3-4, pp. 373–391, 2004.
- [22] X. Xiong and J. Xiao, "Geochemical indicators of sedimentary environments-a summary," *Earthand Environment*, vol. 39, no. 3, pp. 405–414, 2011.
- [23] S. Li, K. Xiao, Y. Wo, S. Long, and L. Cai, "Developmental controlling factors of Upper Ordovician-Lower Silurian high quality source rocks in marine sequence, South China," *Acta Sedimentologica Sinica*, vol. 26, no. 5, pp. 872–880, 2008.

- [24] H. D. Rowe, R. G. Loucks, S. C. Ruppel, and S. M. Rimmer, "Mississippian Barnett formation, Fort Worth Basin, Texas: bulk geochemical inferences and Mo-TOC constraints on the severity of hydrographic restriction," *Chemical Geology*, vol. 257, no. 1-2, pp. 16-25, 2008.
- [25] N. Tribouillard, T. J. Algeo, F. Baudin, and A. Riboulleau, "Analysis of marine environmental conditions based on molybdenum-uranium covariation—applications to Mesozoic paleoceanography," *Chemical Geology*, vol. 324-325, pp. 46-58, 2012.
- [26] M. Zhu, H. Chen, J. Zhou, and S. Yang, "Provenance of Early Triassic in Yanyuan Basin, Upper Yangtze and its implication for the tectonic evolution," *Earth Science*, vol. 41, no. 8, pp. 1309-1321, 2016.
- [27] D. Zhong and L. Ding, "Remarkable progresses in study on deformation and kinematics of eastern Himalayan tectonic syntaxis," *Institute of Geology*, vol. 1, pp. 56-57, 1996.
- [28] S. Kuang and B. Zhang, "Tectonic subdivision of Dabie Orogenic Belt, Central China: evidence from geochemical characteristics of mantle-derived rocks since the Hercynian," *Geological Journal of China Universities*, vol. 2, pp. 129-140, 2002.
- [29] Y. Li, Z. Hou, G. Si, R. Zhou, and X. Liang, "Sedimentary characteristics and tectonic controls in Neogene Yanyuan tectonic escape Basin in southeastern Qinghai-Tibet plateau," *Mineralogy and Petrology*, vol. 3, pp. 34-43, 2001.
- [30] X. Xu, G. L. Cheng, G. H. Yu et al., "Tectonic and paleomagnetic evidence for the clockwise rotation of the Sichuan-Yunnan Rhombic Block," *Seismology and Geology*, vol. 1, pp. 61-70, 2003.
- [31] L. Fang, *Study on Reservoir Characteristics of Devonian of Well 1, Ninglang, Yunnan Province in Ninglang-Yanyuan Region*, China University of Geosciences, Beijing, 2020.
- [32] S. R. Taylor and S. M. McLennan, "The continental crust: its composition and evolution," *The Journal of Geology*, vol. 94, no. 4, pp. 57-72, 1985.
- [33] Z. Ma, Q. Chen, Z. Shi, C. Wang, W. Du, C. Zhao et al., "Geochemistry of oil shale from Chang 7 reservoir of Yanchang Formation in south Ordos Basin and its geological significance," *Geological Bulletin of China*, vol. 35, no. 9, pp. 1550-1558, 2016.
- [34] W. Xia, B. S. Yu, and M. D. Sun, "Depositional setting and enrichment mechanism of organic matter of the block shales of Niutitang Formation at the bottom of Lower Cambrian, in Well Yuke 1, Southeast Chongqing," *Mineralogy and Petrology*, vol. 35, no. 2, pp. 70-80, 2015.
- [35] S. Wang, D. Dong, Y. Wang, X. Li, and J. Huang, "Geochemical characteristics the sedimentation environment of the gas-enriched shale in the Silurian Longmaxi Formation in the Sichuan Basin," *Bulletin of Mineralogy, Petrology and Geochemistry*, vol. 34, no. 6, pp. 1203-1212, 2015.
- [36] W. V. Boynton, "Cosmochemistry of the rare earth elements: meteorite studies," *Developments in Geochemistry*, vol. 2, pp. 63-114, 1984.
- [37] S. R. Taylor and S. M. McLennan, *The Continental Crust: Its Composition and Evolution: An Examination of the Geochemical Record Preserved in Sedimentary Rocks*, Science Press, Beijing, 1985.
- [38] B. K. Nelson and D. J. DePaolo, "Comparison of isotopic and petrographic provenance indicators in sediments from Tertiary continental basins of New Mexico," *Journal of Sedimentary Research*, vol. 58, pp. 348-357, 1988.
- [39] S. M. McLennan, "Weathering and global denudation," *The Journal of Geology*, vol. 101, no. 2, pp. 295-303, 1993.
- [40] J. M. Zheng and M. Pang, *Diagenesis of Clastic Reservoir Rocks*, China University of Geosciences Press, Wuhan, 1989.
- [41] J. Zhang and L. H. Sun, "Variations in element geochemistry of detrital sediments during diagenesis: a case study of the Diaoyutai reservoir of the Suzhou City, Eastern China," *Journ of Suzhou College*, vol. 27, no. 2, pp. 36-39, 2012.
- [42] N. Tribouillard, T. J. Algeo, T. Lyons, and A. Riboulleau, "Trace metals as paleoredox and paleoproductivity proxies: an update," *Chemical Geology*, vol. 232, no. 1-2, pp. 12-32, 2006.
- [43] B. Jones and D. A. C. Manning, "Comparison of geochemical indices used for the interpretation of paleoredox conditions in ancient mudstones," *Chemical Geology*, vol. 111, no. 1-4, pp. 111-129, 1994.
- [44] J. Crusius, S. Calvert, T. Pedersen, and D. Sage, "Rhenium and molybdenum enrichments in sediments as indicators of oxic, suboxic and sulfidic conditions of deposition," *Earth and Planetary Science Letters*, vol. 145, no. 1-4, pp. 65-78, 1996.
- [45] P. A. Abanda and R. E. Hannigan, "Effect of diagenesis on trace element partitioning in shales," *Chemical Geology*, vol. 230, no. 1-2, pp. 42-59, 2006.
- [46] H. Li, J. L. Lu, R. L. Li et al., "Generation paleoenvironment and its controlling factors of Lower Cretaceous lacustrine hydrocarbon source rocks in Changling Depression, South Songliao Basin," *Earth Science*, vol. 42, no. 10, pp. 1774-1786, 2017.
- [47] H. W. Nesbitt and G. M. Young, "Early Proterozoic climates and plate motions inferred from major element chemistry of lutites," *Nature*, vol. 299, no. 5885, pp. 715-717, 1982.
- [48] H. W. Nesbitt and G. M. Young, "Prediction of some weathering trends of plutonic and volcanic rocks based on thermodynamic and kinetic considerations," *Journal of Geology*, vol. 48, pp. 1523-1534, 1984.
- [49] L. Harnois, "The CIW index: a new chemical index of weathering," *Sedimentary Geology*, vol. 55, no. 3-4, pp. 319-322, 1988.
- [50] C. M. Fedo, H. W. Nesbitt, and G. M. Young, "Unraveling the effects of potassium metasomatism in sedimentary rocks and paleosols, with implications for paleoweathering conditions and provenance," *Geology*, vol. 23, no. 10, p. 921, 1995.
- [51] X. Jian, W. Zhang, H. Liang, P. Guan, and L. Fu, "Mineralogy, petrography and geochemistry of an early Eocene weathering profile on basement granodiorite of Qaidam basin, northern Tibet: Tectonic and paleoclimatic implications," *Catena*, vol. 172, pp. 54-64, 2019.
- [52] X. Jian, P. Guan, W. Zhang, and F. Feng, "Geochemistry of Mesozoic and Cenozoic sediments in the northern Qaidam basin, northeastern Tibetan Plateau: implications for provenance and weathering," *Chemical Geology*, vol. 360, pp. 74-88, 2013.
- [53] W. Tian, C. S. Wang, and Y. S. Bai, "Shale geochemical characteristics and enrichment mechanism of organic matter of the Upper Devonian Shetianqiao Formation Shale in Lianyuan Sag, Central Hunan," *Earth Science*, vol. 44, no. 11, pp. 1794-3811, 2019.
- [54] S. M. McLennan, S. Hemming, D. K. McDaniel, and G. N. Hanson, "Geochemical approaches to sedimentation, provenance and tectonics," *Geological Society of America Special Paper*, vol. 284, pp. 21-40, 1993.

- [55] L. Chen, C. Lu, C. Zhuang, X. Che, and J. Wu, "Rare earth element records of the lower paleogene sediments in the Sanshui Basin and their paleoclimate implications," *Acta Sedimentologica Sinica*, vol. 27, no. 6, pp. 1155–1162, 2009.
- [56] K. Zhang, J. Peng, W. Liu et al., "The role of deep geofluids in the enrichment of sedimentary organic matter: a case study of the Late Ordovician-Early Silurian in the upper Yangtze region and early Cambrian in the lower Yangtze region, south China," *Geofluids*, vol. 2020, Article ID 8868638, 12 pages, 2020.
- [57] W. Ji, Y. Song, Z. Rui, M. Meng, and H. Huang, "Pore characterization of isolated organic matter from high matured gas shale reservoir," *International Journal of Coal Geology*, vol. 174, pp. 31–40, 2017.
- [58] W. Ji, F. Hao, H.-M. Schulz, Y. Song, and J. Tian, "The architecture of organic matter and its pores in highly mature gas shales of the lower Silurian Longmaxi Formation in the upper Yangtze platform, South China," *AAPG Bulletin*, vol. 103, no. 12, pp. 2909–2942, 2019.
- [59] X. Zhao, K. Qi, L. Liu, C. Gong, and W. D. McCaffrey, "Development of a partially-avulsed submarine channel on the Niger Delta continental slope: architecture and controlling factors," *Marine and Petroleum Geology*, vol. 95, pp. 30–49, 2018.
- [60] K. Zhang, C. Jia, Y. Song et al., "Analysis of lower Cambrian shale gas composition, source and accumulation pattern in different tectonic backgrounds: a case study of Weiyuan block in the upper Yangtze region and Xiuwu Basin in the lower Yangtze region," *Fuel*, vol. 263, article 115978, 2020.
- [61] K. Zhang, Z. Li, S. Jiang et al., "Comparative analysis of the siliceous source and organic matter enrichment mechanism of the upper Ordovician-lower Silurian shale in the Upper-Lower Yangtze area," *Minerals*, vol. 8, no. 7, p. 283, 2018.
- [62] K. Zhang, Z. Jiang, L. Yin et al., "Controlling functions of hydrothermal activity to shale gas content-taking lower Cambrian in Xiuwu Basin as an example," *Marine and Petroleum Geology*, vol. 85, pp. 177–193, 2017.
- [63] K. Zhang, Y. Song, S. Jiang et al., "Accumulation mechanism of marine shale gas reservoir in anticlines: a case study of the southern Sichuan Basin and Xiuwu Basin in the Yangtze region," *Geofluids*, vol. 2019, Article ID 5274327, 14 pages, 2019.
- [64] K. Zhang, Y. Song, S. Jiang et al., "Mechanism analysis of organic matter enrichment in different sedimentary backgrounds: a case study of the lower Cambrian and the upper Ordovician-lower Silurian, in Yangtze region," *Marine and Petroleum Geology*, vol. 99, pp. 488–497, 2019.
- [65] J. Peng, J. Liu, Y. Wang, and J. Liu, "Origin and controlling factors of chlorite coatings-an example from the reservoir of T₃x Group of the Baojie area, Sichuan Basin, China," *Marine and Petroleum Geology*, vol. 6, no. 4, pp. 376–382, 2009.
- [66] T. Tyrrell, "The relative influences of nitrogen and phosphorus on oceanic primary production," *Nature*, vol. 400, no. 6744, pp. 525–531, 1999.
- [67] T. J. Algeo, K. Kuwahara, H. Sano et al., "Spatial variation in sediment fluxes, redox conditions, and productivity in the Permian-Triassic Panthalassic Ocean," *Paleogeography, Paleoclimatology, Paleoecology*, vol. 308, no. 1-2, pp. 65–83, 2011.
- [68] J. C. Latimer and G. M. Filippelli, "Eocene to Miocene terrigenous inputs and export production: geochemical evidence from ODP Leg 177, Site 1090," *Paleogeography, Paleoclimatology, Paleoecology*, vol. 182, no. 3-4, pp. 151–164, 2002.
- [69] T. J. Algeo and J. B. Maynard, "Trace-element behavior and redox facies in core shales of Upper Pennsylvanian Kansas-type cyclothems," *Chemical Geology*, vol. 206, no. 3-4, pp. 289–318, 2004.
- [70] S. E. Calvert and T. F. Pedersen, "Geochemistry of recent oxic and anoxic marine sediments: Implications for the geological record," *Marine Geology*, vol. 113, no. 1-2, pp. 67–88, 1993.
- [71] P. Wilde, M. S. Quinby-Hunt, and B. D. Erdtmann, "The whole-rock cerium anomaly: a potential indicator of eustatic sea-level changes in shales of the anoxic facies," *Sedimentary Geology*, vol. 101, no. 1-2, pp. 43–53, 1996.
- [72] C. Chen, C. Mu, K. K. Zhou et al., "The geochemical characteristics and factors controlling the organic matter accumulation of the Late Ordovician-Early Silurian black shale in the Upper Yangtze Basin, South China," *Marine and Petroleum Geology*, vol. 76, pp. 159–175, 2016.
- [73] W. Yang, R. Zuo, D. Chen et al., "Climate and tectonic-driven deposition of sandwiched continental shale units: new insights from petrology, geochemistry, and integrated provenance analyses (the western Sichuan subsiding Basin, Southwest China)," *International Journal of Coal Geology*, vol. 211, article 103227, 2019.
- [74] K. J. H. Lenstra and M. van der Vegt, "The impact of sea-level rise and basin area reduction on the cyclic behavior of tidal inlet systems," *Continental Shelf Research*, vol. 214, pp. 1–14, 2021.
- [75] K. Zhang, J. Peng, X. Wang et al., "Effect of organic maturity on shale gas genesis and pores development: a case study on marine shale in the upper Yangtze region, South China," *Open Geosciences*, vol. 12, no. 1, pp. 1617–1629, 2020.
- [76] Zhang, W. Yang, and L. Xie, "Controls on organic matter accumulation in the Triassic Chang 7 lacustrine shale of the Ordos Basin, central China," *International Journal of Coal Geology*, vol. 183, pp. 38–51, 2017.
- [77] X. Fu, J. Wang, W. Feng et al., "Elemental geochemistry of the early Jurassic black shales in the Qiangtang Basin, eastern Tethys: constraints for palaeoenvironment condition," *Geological Journal*, vol. 51, no. 3, pp. 26–42, 2015.
- [78] X. Wang, Z. Jin, J. Zhao et al., "Depositional environment and organic matter accumulation of Lower Jurassic nonmarine fine-grained deposits in the Yuanba Area, Sichuan Basin, SW China," *Marine and Petroleum Geology*, vol. 116, article 104352, 2020.
- [79] J. Dai, D. Gong, Y. Ni, S. Huang, and W. Wu, "Stable carbon isotopes of coal-derived gases sourced from the Mesozoic coal measures in China," *Organic Geochemistry*, vol. 74, pp. 123–142, 2014.
- [80] J. L. Liu, Y. L. Ji, K. M. Yang et al., "Tectono-stratigraphy and sedimentary infill characteristics of Xujiache Formation in western Sichuan foreland basin," *Journal of China University of Petroleum*, vol. 39, no. 6, pp. 11–23, 2015.
- [81] E. C. Fru, C. Hemmingsson, N. Callac et al., "Atmospheric weathering of Scandinavian alum shales and the fractionation of C, N and S isotopes," *Applied Geochemistry*, vol. 74, pp. 94–108, 2016.
- [82] S. C. Xu, Z. J. Liu, P. Zhang, J. M. Boak, R. Liu, and Q. T. Meng, "Characterization of depositional conditions for lacustrine oil shales in the Eocene Jijuntun Formation, Fushun Basin, NE China," *International Journal of Coal Geology*, vol. 167, pp. 10–30, 2016.
- [83] L. N. Zhai, C. D. Wu, Y. T. Ye, S. C. Zhang, and Y. Z. Wang, "Fluctuations in chemical weathering on the Yangtze Block

during the Ediacaran-Cambrian transition: implications for palaeoclimatic conditions and the marine carbon cycle,” *Paleogeography, Paleoclimatology, Paleoecology*, vol. 490, pp. 280–292, 2018.

- [84] W. Chao, D. Tian, Z. He et al., “Major, trace-elemental and sedimentological characterization of the upper Ordovician Wufeng-lower Silurian Longmaxi formations, Sichuan Basin, south China: Insights into the effect of relative sea-level fluctuations on organic matter accumulation in shales,” *Marine and Petroleum Geology*, vol. 126, pp. 1–21, 2021.
- [85] W. Z. Zhang, H. Yang, J. H. Yang, Q. F. Kong, and K. Wu, “Petrology and element geochemistry and development environment of Yanchang formation Chang 7 high quality source rocks in Ordos Basin,” *Geochimica*, vol. 37, pp. 59–64, 2008.
- [86] Z. Ren, F. Yang, and K. Yuan, “The natural gamma energy spectrum survey and significance of Devonian in Ninglang area, Yunnan,” *Yunnan Geology*, vol. 37, no. 1, pp. 84–89, 2018.

Research Article

Evaluation of Favorable Shale Gas Intervals in Dawuba Formation of Ziyun Area, South Qian Depression

Kun Yuan ^{1,2}, Wenhui Huang,¹ Xinxin Fang ³, Ting Wang,¹ Tuo Lin,¹ and Rong Chen¹

¹School of Energy Resources, China University of Geosciences (Beijing), Beijing 100083, China

²Oil and Gas Resources Survey, China Geological Survey, Ministry of Natural Resources, Beijing 100083, China

³Institute of Geomechanics, Chinese Academy of Geological Sciences, Beijing 100081, China

Correspondence should be addressed to Kun Yuan; kunyuanogscgs@sina.com and Xinxin Fang; freestarxin@163.com

Received 16 December 2020; Revised 10 January 2021; Accepted 20 May 2021; Published 8 June 2021

Academic Editor: Kun Zhang

Copyright © 2021 Kun Yuan et al. This is an open access article distributed under the Creative Commons Attribution License, which permits unrestricted use, distribution, and reproduction in any medium, provided the original work is properly cited.

A series of qualitative descriptions and quantitative analyses was used to determine the lithofacies characteristics and recognize the favorable shale intervals of Dawuba Formation in the Ziyun area of South Qian Depression. The qualitative descriptions include core description and scanning electron microscope (SEM) observation. The quantitative analyses include X-ray diffraction, total organic content analysis, vitrinite reflectance, maceral composition, porosity, and permeability, as well as gas and element composition. The Dawuba Formation could be divided into four members. In general, the shale in the first and third members showed similarly high organic matter content with most samples in range of 2–2.5% and higher brittle mineral content with a content of quartz 40.53% and 33.21%, respectively, compared with the other two members, as well as high gas content. However, the first member shale samples exhibited much higher porosity and permeability than the third member shale samples. Furthermore, the shale gas in the first member was chiefly composed of methane (average: 83.63%), while that in the third member mainly consisted of nitrogen (average: 79.92%). Hence, the first member should be regarded as the most favorable target.

1. Introduction

In recent years, the success of shale oil and gas exploration and development in North America, such as the Barnett shale with tremendous cumulative gas production, has driven and promoted the development of shale oil and gas industry in China [1–8]. The industrial breakthroughs of shale gas exploration and development in China were achieved mainly in the Ordovician Wufeng and Silurian Longmaxi Formation marine shale reservoirs in Weiyuan, Zhaotong, and Jiaoshiba areas in the southern Sichuan Basin, where the shale gas output reached 10 billion cubic meters in 2019 [9–14]. Although the strata, pattern, mechanism, and geological factors for shale gas source and accumulation were different for different areas, such as in the Weiyuan block and Xiuwu basin [7, 8], the high-quality shale section is generally located at the top of Wufeng Formation and the bottom of Longmaxi Formation, in which the biogenic silica caused by frequent volcanic

activities hugely developed [13, 15, 16]. However, in the Lower Cambrian shales, such as the shale in Xiuwu basin, the hydrothermal silica occupied a large proportion [13, 14]. Although the massively developed reverse faults in the complex geological structure areas outside the basin damaged the sealing property of the whole reservoir and induced the hydrocarbon loss and nitrogen entry [7], China Geological Survey firstly discovered that the Sinian and Cambrian systems in these areas also obtained high-yielding industrial shale gas airflow [6]. Shale oil exploration and development in China mainly focus on the widely developed continental shale in the north, including Ordos Basin, Songliao Basin, Tarim Basin, and Bohai Bay basin [17–22]. Shale oil exploration in the 2nd member of the Kondian Formation in Cangdong Sag of Bohai Bay Basin has made great breakthroughs, and industrial oil flows have been obtained in several wells such as KN9 and GD6 × 1 [23].

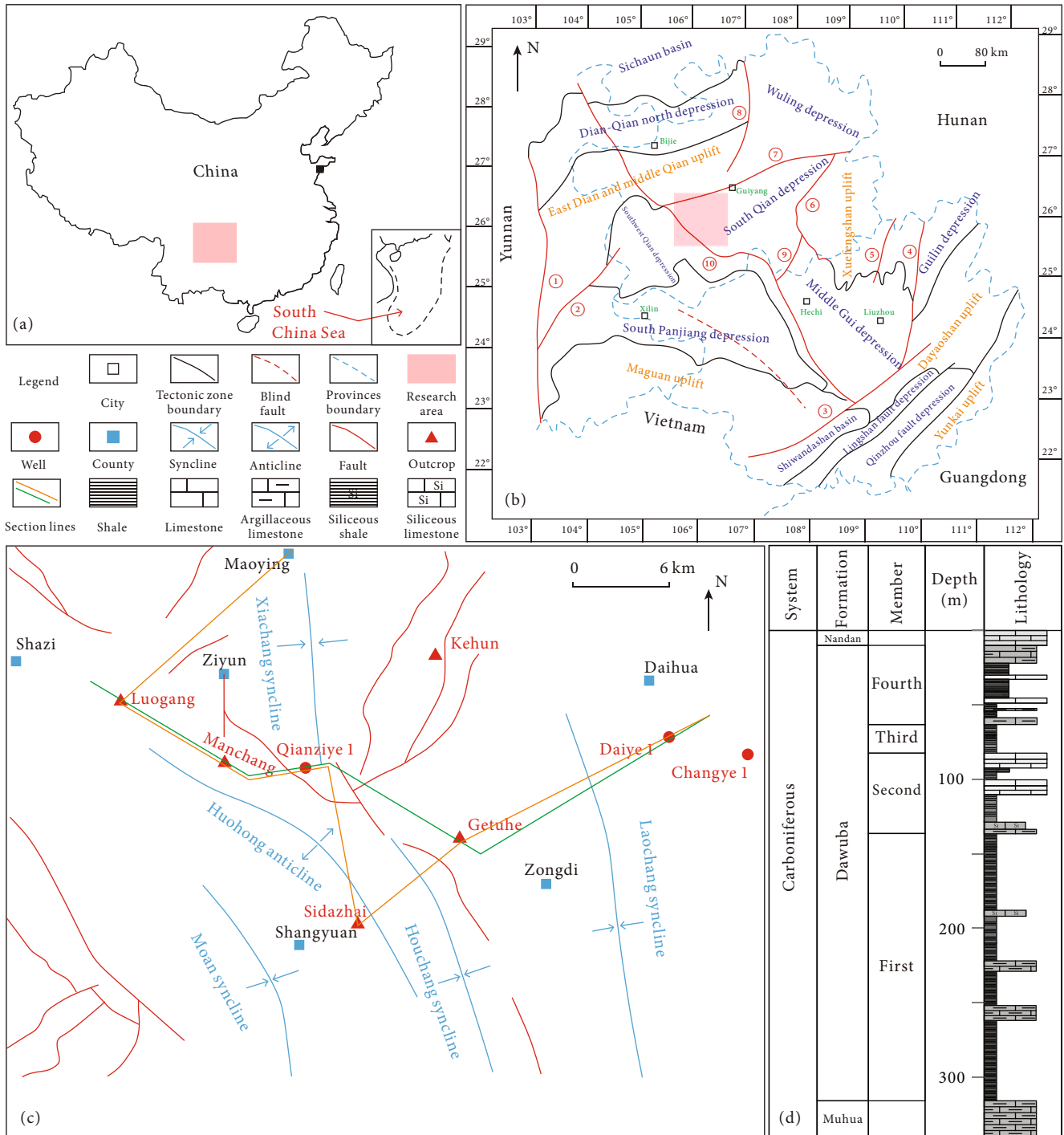


FIGURE 1: Location map of the research area (a, c, d), lithological characteristics of Dawuba Formation (b), tectonic characteristics of Ziyun area (c), and location of samples from wells and outcrops (d). ① Xiaojiang fault; ② Shizong fault; ③ Pingxiang-Dali fault; ④ Yongfu fault; ⑤ Longsheng fault; ⑥ Tongren-Sandu fault; ⑦ Guiyang-Zhenyuan fault; ⑧ Zunyi fault; ⑨ Libo fault; ⑩ Ziyun-Luodian-Nandan-Duan fault. “Dian” means Yunnan province; “Qian” means Dui Zhou province; “Gui” means Guangxi province. The yellowish-brown section line crosses the wells and outcrops used in stratigraphic correlation and the green one used in comparison of total organic carbon (TOC).

However, the constant exploration and development of shale oil and gas in new areas is still necessary, because it still cannot meet the country’s energy demand at the present stage. The Permian transitional facies shale is widely distributed in China, and only a few shale gas discoveries have been made in it of some areas [24–26]. Hence, the industry has dif-

ferent opinions on whether the Permian transitional facies shale has commercial scale shale gas. In addition, the major breakthrough in Devonian and Carboniferous shale strata has not been made in south China. The main reason is that most areas in the south belonged to the paleogeographic environment alternative distribution of interplatform and

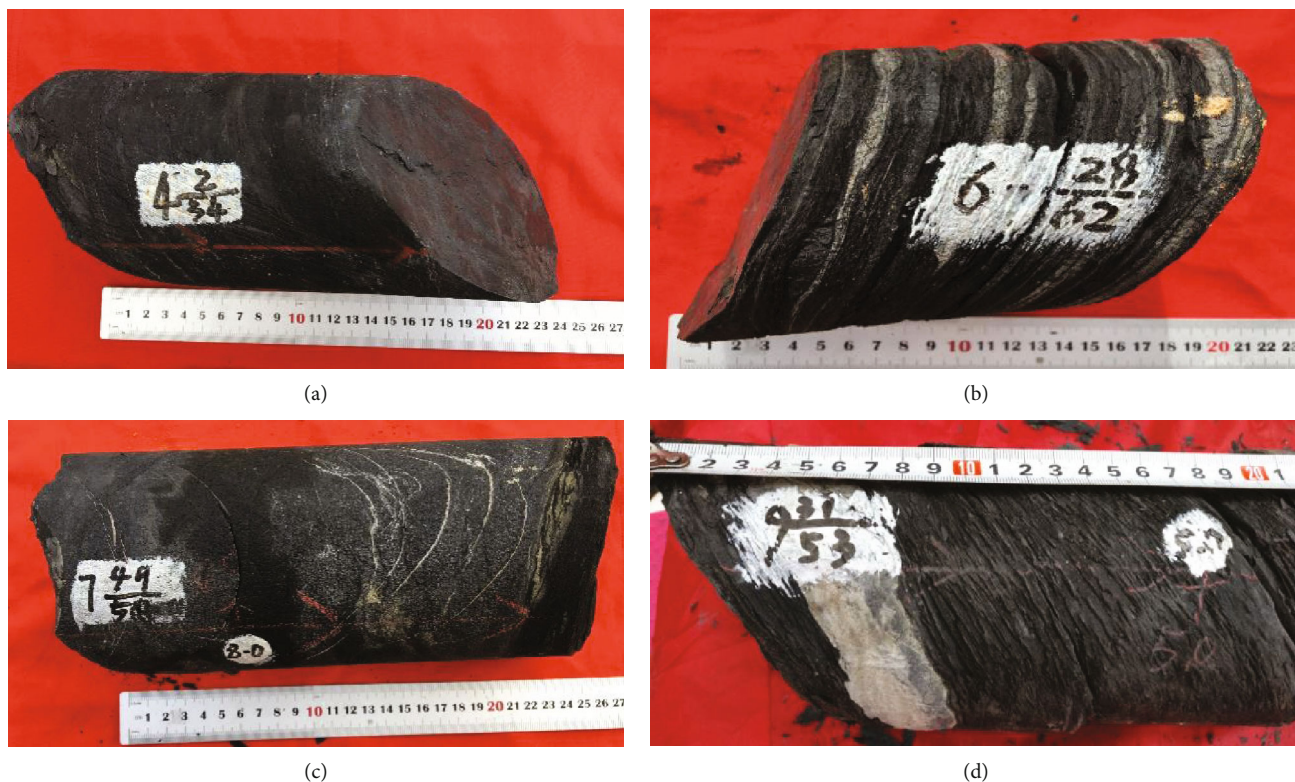


FIGURE 2: Images of shale samples from Dawuba Formation: (a) black shale sample from the fourth member of Dawuba Formation; (b) black shale with argillaceous stripe sample from the third member of Dawuba Formation; (c) black shale sample from the second member of Dawuba Formation; (d) black shale sample from the first member of Dawuba Formation.

basin during the Devonian-Carboniferous period [27]. Hence, the lithological association varies greatly, including the shale development thickness, distribution characteristics, organic geochemical characteristics, mineral composition, mechanical properties, and reservoir property of different layers [28].

In this paper, the Ziyun area of South Qian Depression is taken as the research area. Core samples of shale and mudstone in wells Qianziye 1, Changye 1, and Daiye 1, Guizhou, as well as samples collected from the surrounding outcrops, Manchang, Getuhe, Sidazhai, and Luogang, were taken as the research objects. The stratigraphic distribution characteristics, geochemical characteristics, reservoir characteristics, and gas bearing properties of Dawuba Formation were evaluated. On this basis, the sedimentary background and its effect on organic matter enrichment were discussed. Then, the favorable target layers for shale gas enrichment were optimized.

2. Geological Setting

The South Qian Depression is located in the southwest part of China (Figure 1(a)). It is a superimposed basin formed by the early Paleozoic Craton basin, the late Paleozoic passive continental margin basin, and the Mesozoic foreland basin [29–31]. The Guiyang-Zhenyuan fault zone and middle Qian uplift are the boundary in the northwest

of the depression; the Tongren-Sandu fault zone and the Xuefengshan uplift are the boundary in the east and southeast; the Ziyun-Luodian fault zone is the boundary in the southwest of the depression (Figure 1(b)).

The study area is located in the west part of South Qian Depression and confined by the Ziyun and Guiyang fault. Under the tectonic processes of multiple stresses, the Carboniferous, Permian, and Triassic strata have undergone strong structural deformation and denudation of different extent. In the Indosinian-Yanshan and Himalayan stages, strong folds and thrust nappes resulted in massive shortening deformation. The north-south compressional deformation dominated throughout the entire district (Figure 1(c)). The anticline was in box shape with mainly Devonian and Carboniferous strata. The syncline was in a groove shape with the axis being mostly destroyed by strike compressional faults and mainly consists of Triassic strata. In some areas, it was covered in unconformity with the upper Cretaceous strata.

The Dawuba Formation is about 150–250 m thick and is mainly composed of shale, silty shale with thin chert layer, and a small amount of silty sandstone, generally containing iron and phosphorus nodules and spore fossils (Figures 1(d) and 2). According to the lithological characteristics of wells Qianziye 1, Daiye 1, and Changye 1, as well as outcrops Manchang, Getuhe, Sidazhai, Luogang, and Kehun, the Dawuba Formation can be divided into four members.

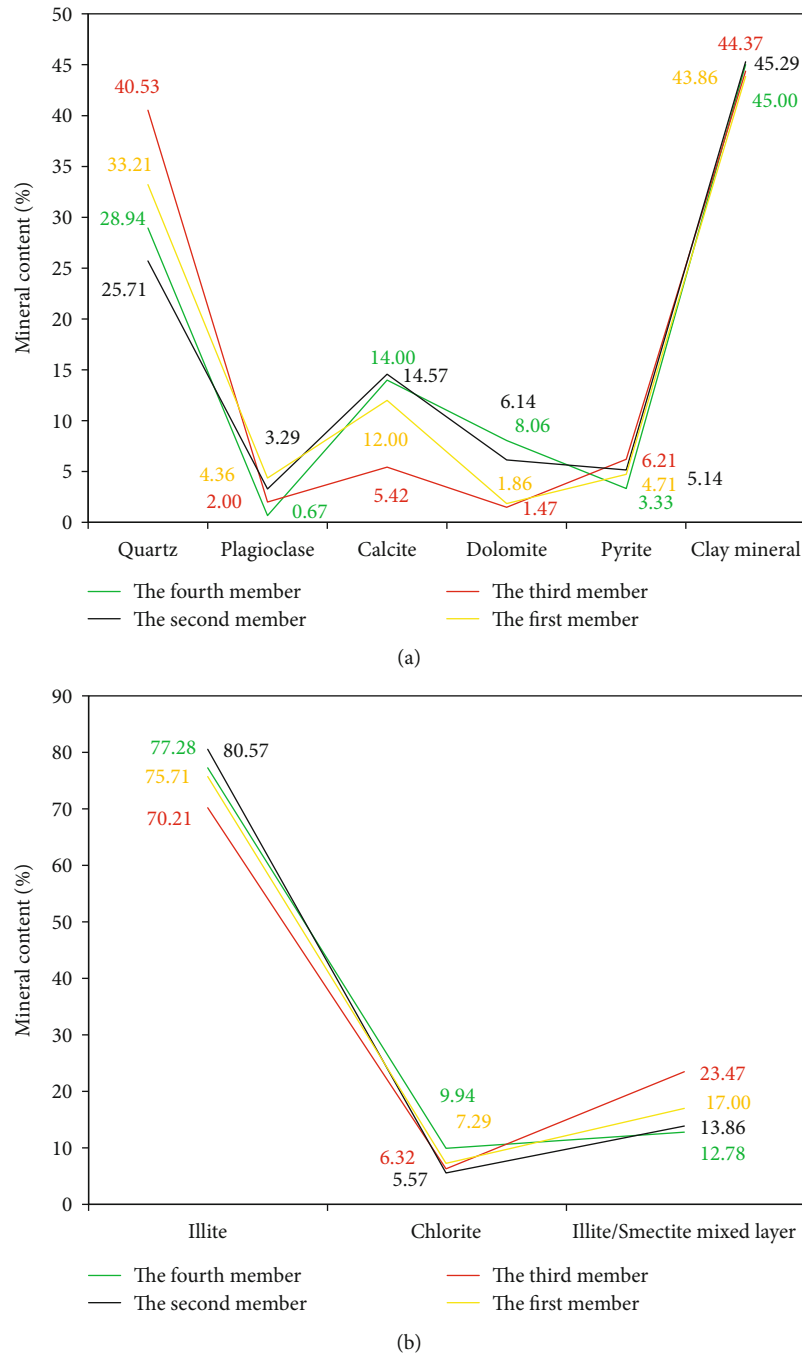


FIGURE 3: Mineral composition of the Dawuba Formation shale samples: (a) mineral composition of bulk-rock; (b) clay mineral composition.

The fourth member of Dawuba Formation is approximate 100 m thick and lithologically composed of dark shale, black mudstone, and gray mudstone sandwiched with dark gray marl limestone and gray limestone (Figure 2(a)). The third member of the Dawuba Formation is 30 m thick and lithologically consists of black shale, gray mudstone with dark gray marl limestone, and gray dolomitic siltstone (Figure 2(b)). The second member is 75 m thick and lithologically interbedded with dark gray marl and gray dolomite (Figure 2(c)). The first section of Dawuba Formation is about 150 m thick and lithologically composed of dark shale, gray black mudstone, and gray limestone (Figures 1(d) and 2(d)).

3. Sample Preparation and Methods

3.1. Lithology Analysis. Core observation and descriptions, including composition, texture, sedimentary structure, grain size, and color, were conducted to determine the lithofacies in Dawuba Formation. The mineral composition was measured by a Rigaku automated powder diffractometer (D/MAX-RA) equipped with a Cu X-ray source (40kV, 35 mA). The samples from Dawuba shale were analyzed for whole-bulk and clay fraction mineralogy by quantitative X-ray diffraction following two independent processes. First, the bulk mineral composition of the powder sample was

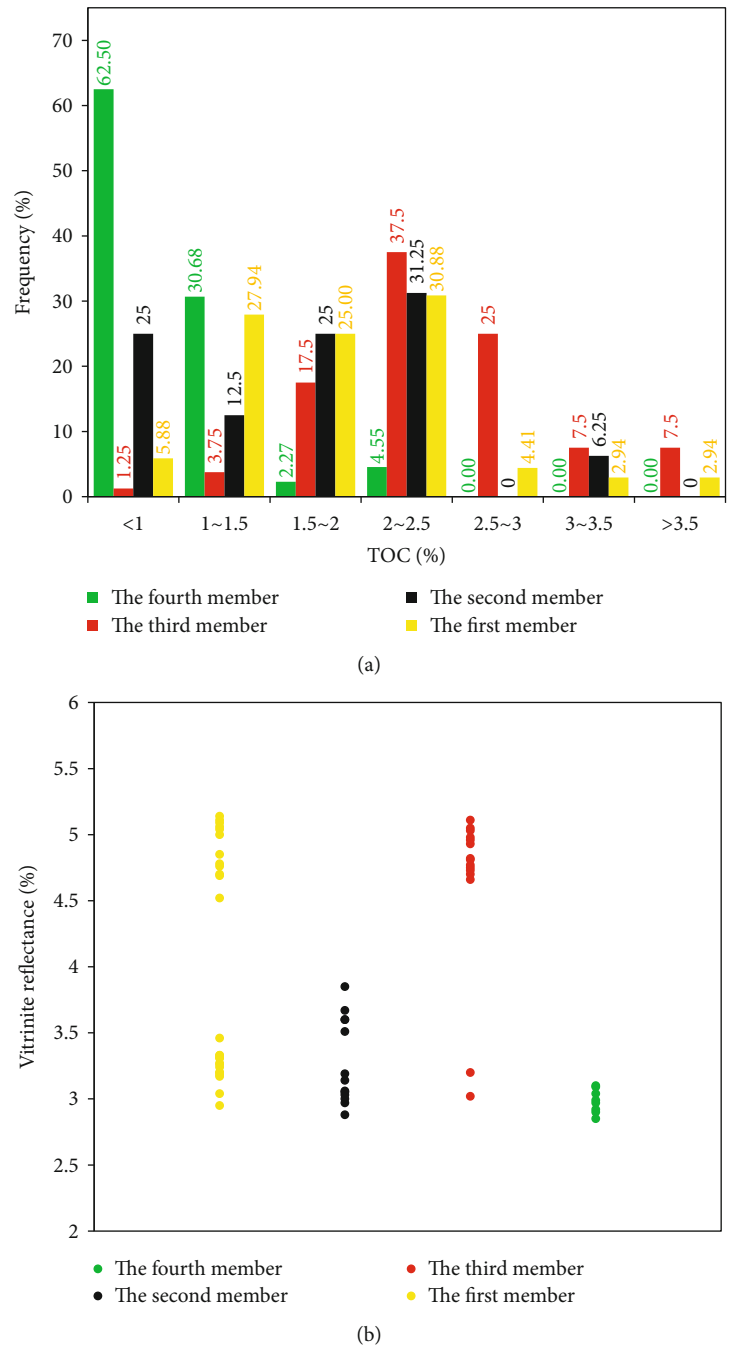


FIGURE 4: Histogram of TOC and R_o of all the Dawuba Formation shale samples: (a) histogram of TOC; (b) R_o value scope.

determined at this stage to only include the total clay content. The whole-rock samples were analyzed over an angular range of 4 to $70^{\circ}2\theta$ at a scanning speed of $1^{\circ}2\theta/\text{min}$. Second, the individual clay mineral content of the clay fractions separated from the rock powder sample was determined. The clay minerals were analyzed over an angular range of 3 to $65^{\circ}2\theta$ at a scanning speed of $1.5^{\circ}2\theta/\text{min}$. Quantification of the minerals was based on calculations of the integrated area using the Jade Five software.

3.2. Analysis of Geochemical Characteristics. The total organic carbon (TOC) analyses were conducted using labora-

tory apparatus Leco TOC (CS-230HC). The samples were immersed in 10% HCl solution for two days to remove the carbonate minerals and then washed with distilled water. Before measurement, the samples were dried in a stoving oven at 65°C for 1.5 days. The thermal maturity reflected by the experimental vitrinite reflectance (R_o) values and maceral composition of Dawuba Formation shale samples were acquired by using an oil-immersion lens and a full-automatic microscope photometer (a Leica MPV Compact II reflected-light microscope) in both reflected and fluorescent modes. Before the measurements, the equipment calibration was performed using two standard samples of

TABLE 1: The maceral composition of all the Dawuba Formation shale samples.

Sample ID	Depth/m	Member	Lithology	Sapropelinite %	Exinite %			Sum	Vitrinite %	Inertinite %	Types classification	
					Resinite	Homocollinite	Alginite		Normal vitrinite	Fusinite	Index	Type
CY1-1	751	Fourth	Black shale	0	—	59	28	87	10	3	33	II ₂
DY1-5	450	Fourth	Black shale	0	2	63	20	85	13	2	30.8	II ₂
MC-1	2750	Fourth	Black shale	0	—	63	22	85	12	3	30.5	II ₂
ZY1-1	2668	Fourth	Black shale	0	2	67	13	82	14	4	26.5	II ₂
ZY1-3	2688	Fourth	Black shale	0	4	56	18	78	17	5	21.3	II ₂
ZY1-4	2759	Fourth	Black shale	0	3	56	17	76	16	8	18	II ₂
ZY1-9	2738	Fourth	Black shale	0	—	64	17	81	16	3	25.5	II ₂
GTH-1	Outcrop	Third	Black shale	0	5	47	24	76	18	6	18.5	II ₂
LG-1	Outcrop	Third	Black shale	0	—	58	26	84	11	5	28.8	II ₂
ZY1-2	2806.50	Third	Black shale	0	—	72	13	85	11	4	30.3	II ₂
ZY1-6	2796	Third	Black shale	0	0	74	12	86	13	1	32.3	II ₂
ZY1-7	2802.60	Third	Black shale	0	—	73	11	84	14	2	29.5	II ₂
ZY1-8	2812.5	Third	Black shale	0	—	64	15	79	16	5	22.5	II ₂
GTH-2	Outcrop	Second	Black shale	0	0	55	26	81	16	3	31.8	II ₂
LG-2	Outcrop	Second	Black shale	0	1	53	29	83	14	3	31.8	II ₂
ZY1-10	2857	Second	Black shale	0	0	54	28	82	15	3	31.8	II ₂
ZY1-12	2858	Second	Black shale	0	4	53	29	86	11	3	31.8	II ₂
ZY1-13	2858.5	Second	Black shale	0	0	50	28	78	17	5	31.8	II ₂
CY1-2	880	First	Black shale	0	4	57	14	75	17	8	16.8	II ₂
CY1-3	881	First	Black shale	0	4	59	8	71	22	7	12	II ₂
DY1-1	633	First	Black shale	0	0	62	22	84	12	4	29	II ₂
DY1-2	634	First	Black shale	0	—	74	16	90	8	2	37	II ₂
KH-1	Outcrop	First	Black shale	0	—	69	16	85	11	4	30.3	II ₂
SDZ-1	Outcrop	First	Black shale	0	0	75	12	87	11	2	33.3	II ₂
SDZ-2	Outcrop	First	Black shale	0	—	80	12	92	6	2	39.5	II ₂

TABLE 1: Continued.

Sample ID	Depth/m	Member	Lithology	Sapropelinite %	Exinite %				Vitrinite % Normal vitrinite	Inertinite % Fusinite	Types classification	
					Resinite	Homocollinite	Alginite	Sum			Index	Type
ZY1-14	2871	First	Black shale	0	—	65	20	85	12	3	30.5	II ₂
ZY1-15	2877.40	First	Black shale	0	—	63	19	82	14	4	26.5	II ₂
ZY1-16	2931.95	First	Black shale	0	5	61	14	80	15	5	23.8	II ₂
ZY1-17	2882.50	First	Black shale	0	—	76	16	92	5	3	39.3	II ₂

known reflectance. Each R_o represents the average of 20-30 measuring points. Each maceral analysis covered more than 30 points.

3.3. SEM Observation. Scanning electron microscopy (SEM) was performed to provide visualization of the minerals and micropores through FEI Quanta-200F apparatus with an energy-dispersive spectrometer (EDS). Fractured surfaces generated from slightly knock with a little hammer were used in SEM observation. Ar-ion polishing was applied in SEM observation. A thin layer of Au element was applied in gilding on the fractured surfaces before observation. The operating current must be maintained to be 15 kV for stable signal output of clear images.

3.4. Porosity and Permeability Analysis. The porosity of the dry samples was determined from the grain density obtained from helium pycnometry (skeletal density), and the bulk volume of the plugs was calculated from mercury immersion (bulk density) [32]. The total porosity was calculated from the difference between the bulk and skeletal densities. The permeability was calculated from measurements with helium expansion at a constant temperature of 30°C and a range of pressures from 5 MPa to 30 MPa in a stepwise increase [33, 34]. The cylinder samples of shale with diameters of 2.5 cm and lengths of 5 cm were analyzed for porosity and permeability. These 25 samples had no factitious fractures on the surface formed. But, it is hard to identify artificial microfractures that formed interior the sample, which explains the aberrant data points of porosity and permeability analysis.

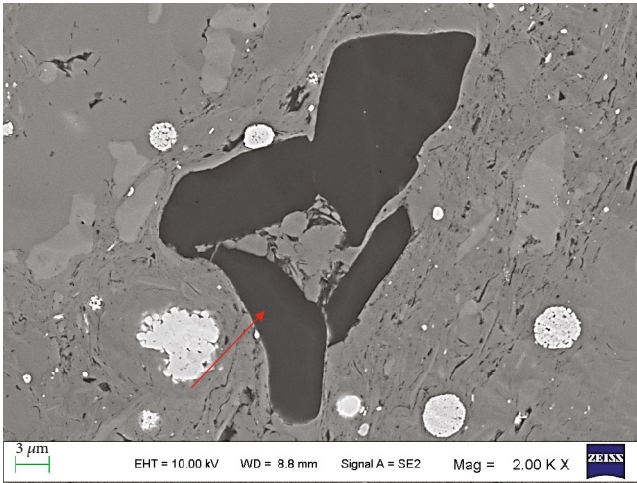
3.5. Gas Content and Component Analysis. The shale gas was collected through gas gathering system, of which the principle was water gas displacing method. The water in it is saturated salt solution. When the core sample was taken out from the drilling borehole, they were put in an air collector as soon as possible. The shale gas gathered during the unheated stage was regarded as desorbed gas. When the desorbed gas content did not increase any more, the system was heated, and the gas gathered was regarded as residual gas. The shale gas component was determined through gas chromatographic method.

3.6. Element Analysis. Trace element analysis can also be used in the study of the sedimentary environment, such as the reducibility or oxidability, salinity, and climate [35–39]. The shale samples of Dawuba Formation were used for the element analysis, which was determined with a laser-ablation microprobe linked to an inductively coupled plasma mass spectrometer (LAM-ICP-MS) at the Beijing Research Institute of Uranium Geology.

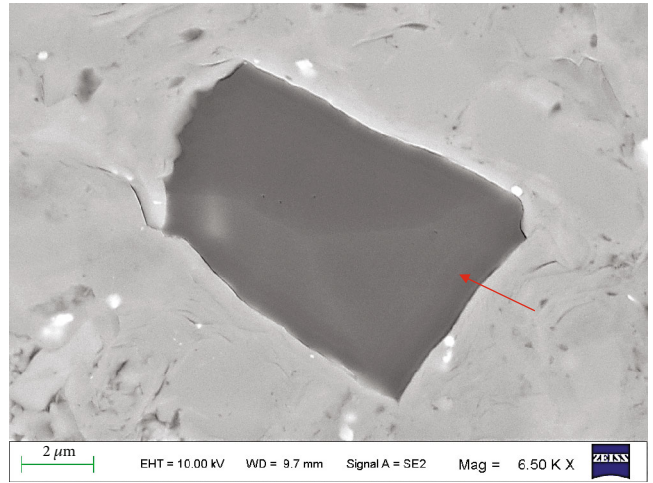
4. Results

4.1. Mineral Composition Characteristics. The Dawuba Formation shale is mainly composed of quartz and clay minerals (Figure 3). The third member shale exhibited the highest content of quartz (average 40.53%) but the lowest content of calcite (average 5.42%) (Figure 3(a)). For the shale of other three members, quartz was the dominated brittle minerals and then followed by calcite (Figure 3(a)). The contents of plagioclase, dolomite, and pyrite of all the four members were smaller than 10% (Figure 3(a)). The clay minerals were not much difference in content in shale of the four members. The clay minerals were mainly composed of illite, which reached larger than 70%, followed by illite/smectite mixed layers (average 16.78%) and chlorite (<10%) (Figure 3(b)). From the perspective of clay mineral composition, the shale of the four members in Dawuba Formation was similar to each other. Among the shale samples of Dawuba Formation, the third member shale exhibited the highest content of illite/smectite mixed layers (average 23.47%) but the lowest content of illite (average 70.21%) (Figure 3(b)).

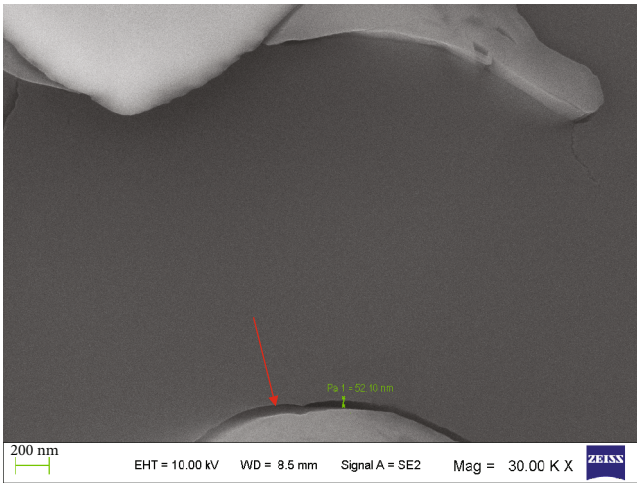
4.2. Organic Matter Characteristics. The TOC content of all the samples varies from 0.26% to 4.66%, while most samples are included in the range of 1–3% (Figure 4). Shale samples from the fourth member showed the lowest content of TOC values, while the TOC values did not show substantial difference among the shale sample from the other three members. Some shale samples in the third member show toc content larger than 3% (Figure 4). The measured vitrinite reflectance (R_o) of all the Dawuba Formation shale samples is in the range of 2.85–5.14% (Figure 4). The measured R_o of most of the samples from all the four members ranged from



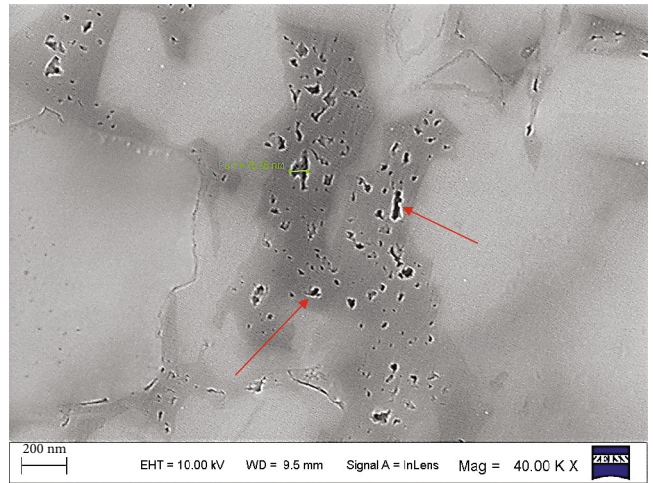
(a)



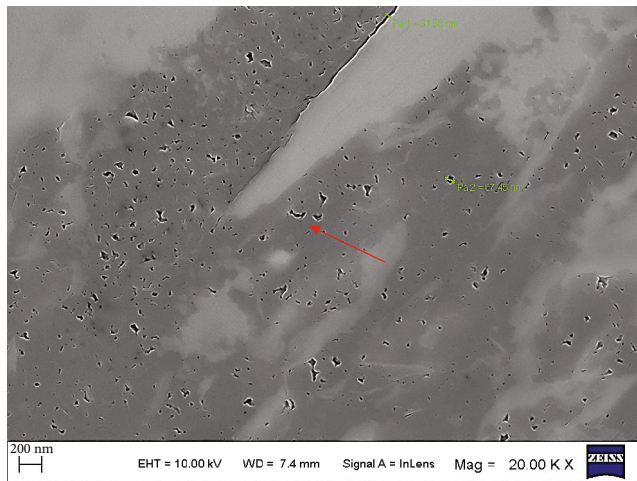
(b)



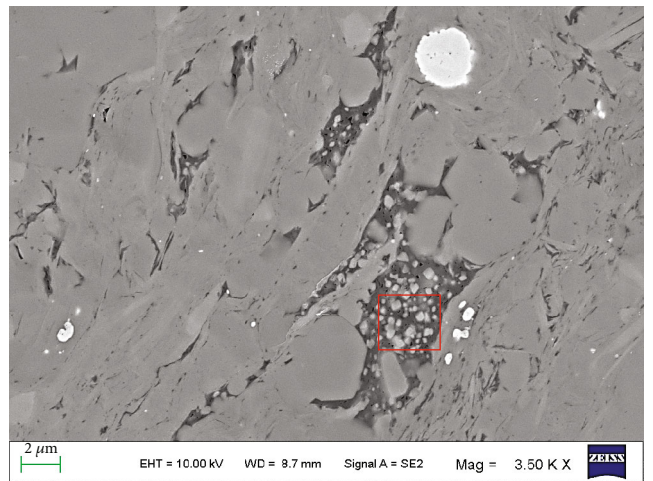
(c)



(d)

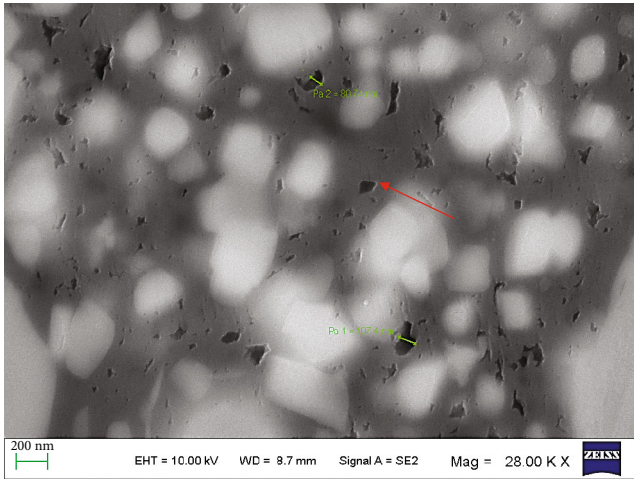


(e)

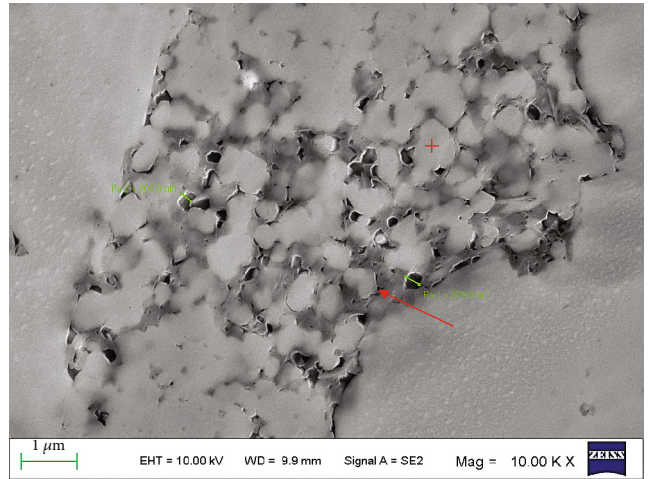


(f)

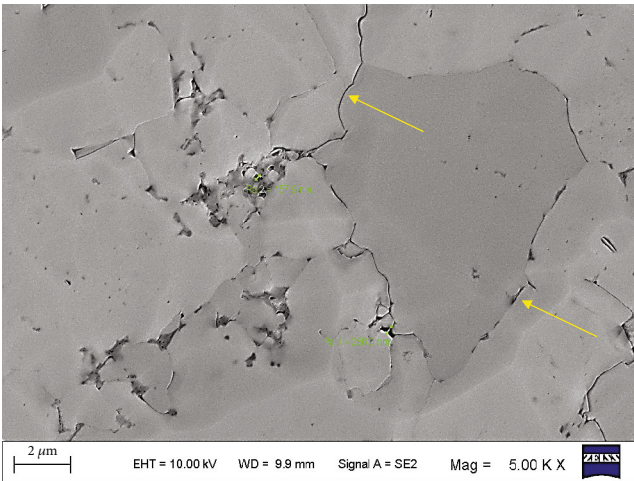
FIGURE 5: Continued.



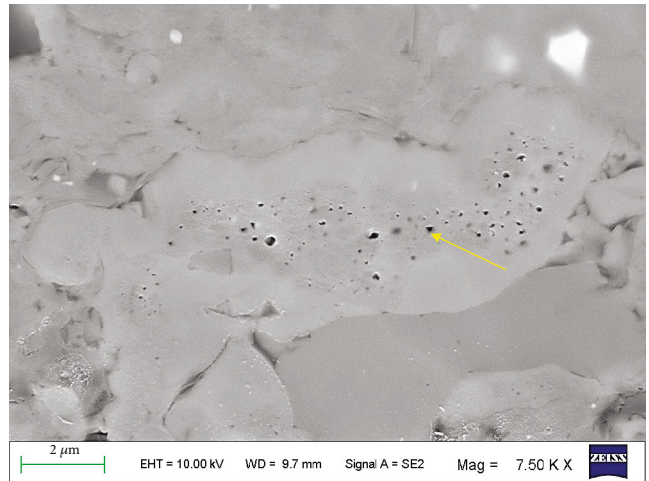
(g)



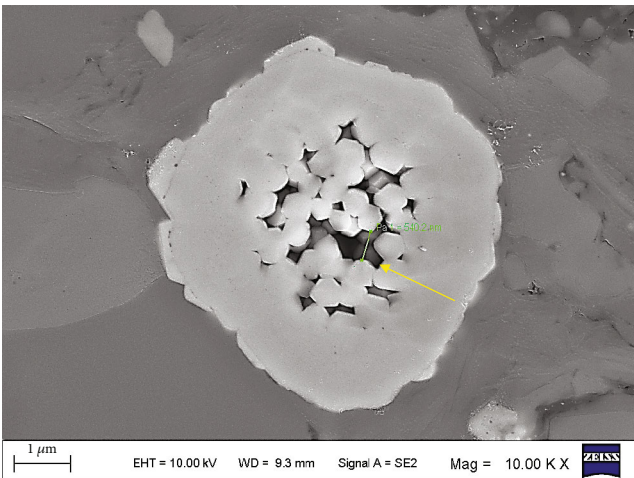
(h)



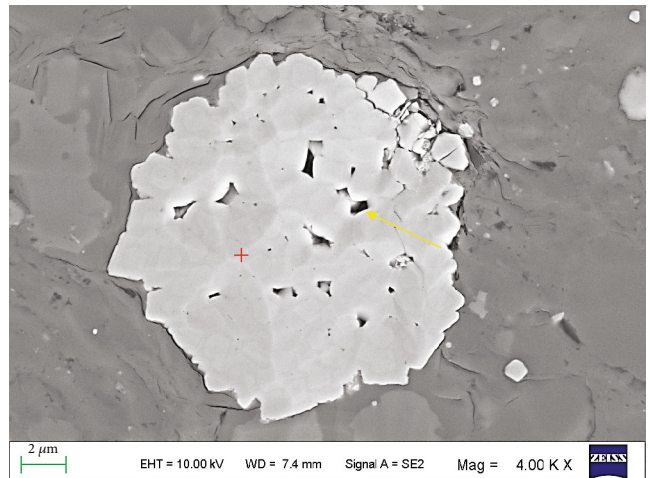
(i)



(j)

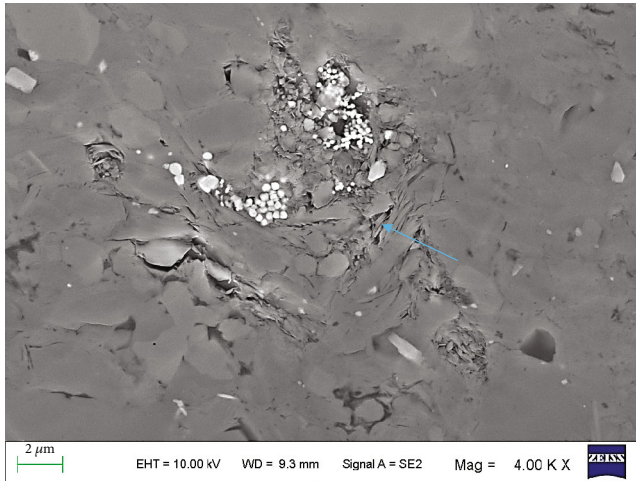


(k)

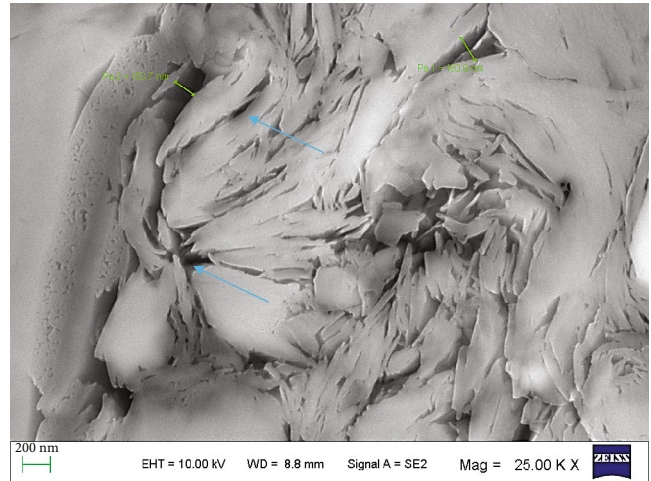


(l)

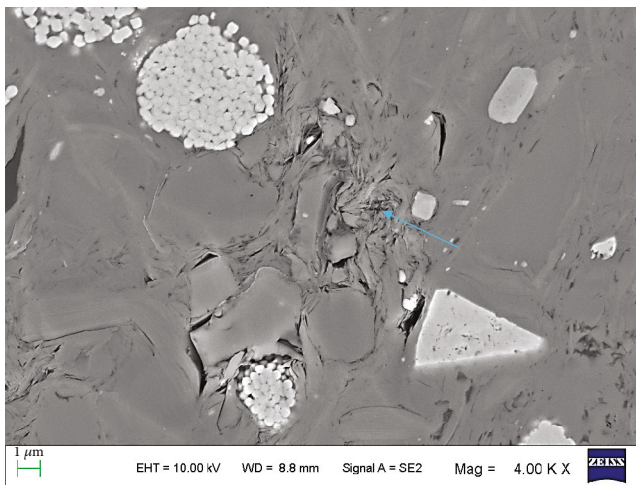
FIGURE 5: Continued.



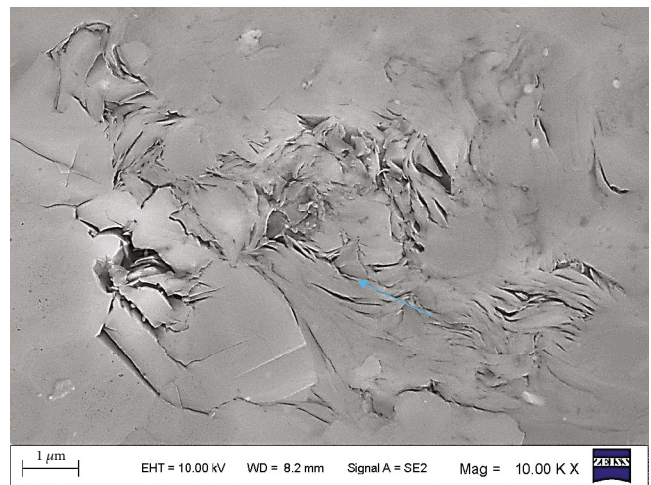
(m)



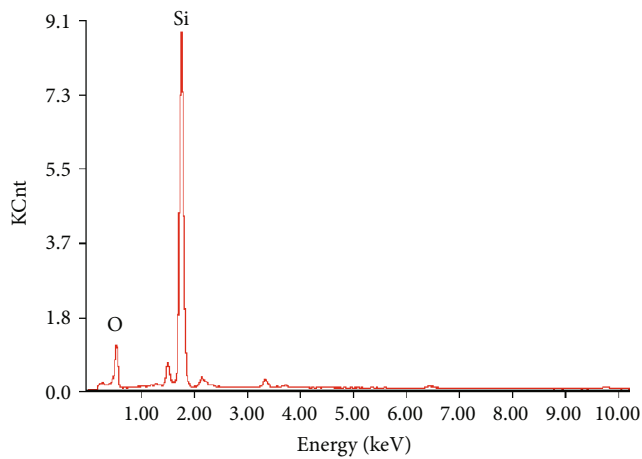
(n)



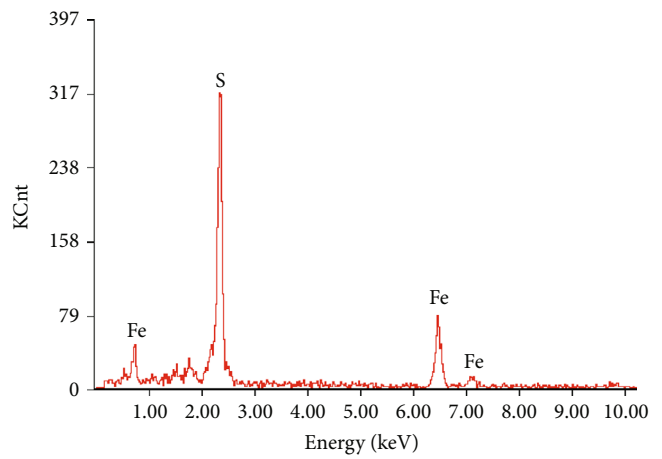
(o)



(p)



(q)



(r)

FIGURE 5: Images of SEM observation for the Dawuba Formation shale. The red arrows point to the organic matter and organic matter pores. The yellow arrows point to the pores related to quartz and pyrite. The blue arrows point to the pores among clay minerals. (a) 2946 m, the 1st member, black shale; (b, j) 2929 m, the 1st member, black shale; (c) 2811.5 m, the 4th member, black shale; (d) 2942.15 m, the 1st member, black shale; (e) 2950 m, the 1st member, black shale; (f, g) 2946.6 m, the 1st member, black shale; (h, i) 2983.3 m, the 1st member, black shale; (k, m) 2950.1 m, the 1st member, black shale; (l) 2932.95 m, the 1st member, black shale; (n, o) 2946.6 m, the 1st member, black shale; (p) 2883.5 m, the 2nd member, black shale; (q) EDS spectrum of red “+” in image (h); (r) EDS spectrum of red “+” in image (l).

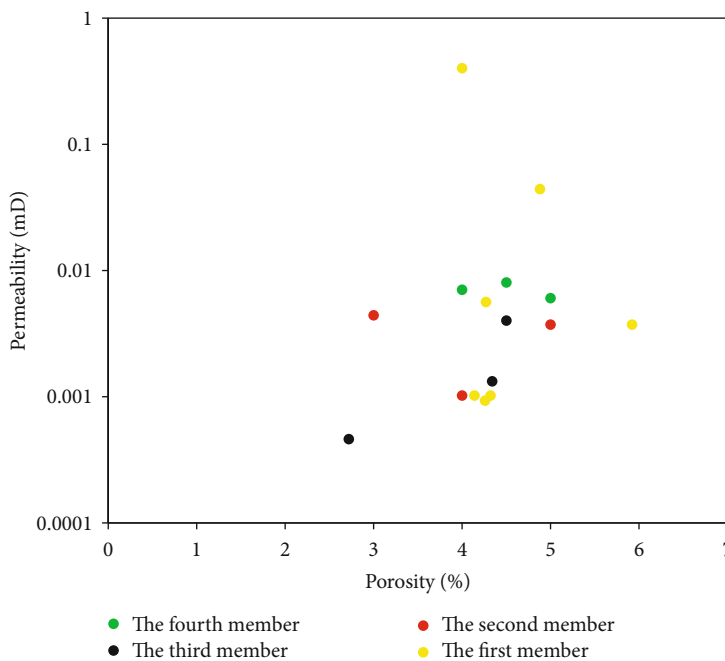


FIGURE 6: The cross plot of porosity and permeability.

2.85% to 4.0%, which means most of Dawuba Formation shale samples were in the gas-generation stage at the present time. But some R_o values of shale samples from the first and third members were larger than 4.5% (Figure 4), which means overmaturity stage. It was speculated that the high R_o was caused by magmatic hydrothermal deposit, but there was no precise evidence. Approaching to the organic matter type from the point of view of maceral composition, exinite dominated the shale samples of Dawuba Formation, which means an incline to Type II₂ organic matter (Table 1). The exinite mainly consisted of homocollinite and alginite (Table 1). The vitrinite and inertinite were not widely developed. In general, the organic matter type did not show material difference among the shale samples from the four members (Table 1).

4.3. Characterization of Pores. Compared with marine shale, organic matter pores did not hugely develop in Dawuba Formation shale (Figures 5(a)–5(c)). Cracks can be observed between organic matter and mineral particles under high magnification (Figure 5(c)). Some organic matter developed pores, which were not subrotund or elliptical as usual but elongated and irregular (Figures 5(d) and 5(e)). The organic matter symbiotic with minerals, such as pyrite and quartz, always developed pores (Figures 5(f)–5(h) and 5(p)). Interparticle pores always appear along the rims of quartz and plagioclase, as well as in the pyrite frambooids (Figures 5(i)–5(l)). Rims of detrital quartzes and plagioclase are always jagged, which leads to inter particle pores surviving consolidation and compaction. Pyrites were abundant in Dawuba Formation shale and occurred mostly as pyrite frambooids (Figures 5(k) and 5(l)). Interparticle pores exist in pyrite frambooids (Figure 5(l)). Many of interparticle pores and cracks occurred among clay minerals (Figures 5(m)–5(p)).

Some clay minerals exhibited sheet-like shapes because of compaction. Gaps occurred between these sheet-like clay minerals. For the Ar-ion polished samples, clay mineral pore types cannot be further identified and classified, because most clay minerals are not authigenic minerals of diagenetic genesis.

4.4. Porosity and Permeability. Samples with drilling orientation perpendicular to sedimentary stratification displayed relatively lower permeability than samples with drilling orientation parallel to sedimentary stratification, which explained the largest data point of the first member (Figure 6). In general, the first member shale samples possessed the inconspicuous highest porosity and permeability. Although one sample from the third member shale displayed lower permeability and porosity, totally speaking, no apparent difference of permeability and porosity occurred among the other three member shales (Figure 6). The abnormally higher permeability value for the first member shale sample may be reduced by factitious microfracture formed in sample interior during drilling process. Porosity displayed a positive correlation with the permeability for all the samples (Figure 6).

4.5. Gas-Containing Property. Through shale gas gathering system, the desorbed gas in Dawuba Formation shale ranged from 0.07 cm³/g to 1.28 cm³/g, while the residual gas varied from 0.09 cm³/g to 0.44 cm³/g. Some samples did not contain residual gas. The total shale gas content was in the scope of 0.07 cm³/g to 1.28 cm³/g (Figure 7). The first and third member shale samples presented much higher content of shale gas (Figure 7). It seems that these two member shales were favorable for development. However, the shale gas component showed different opinion through gas chromatographic

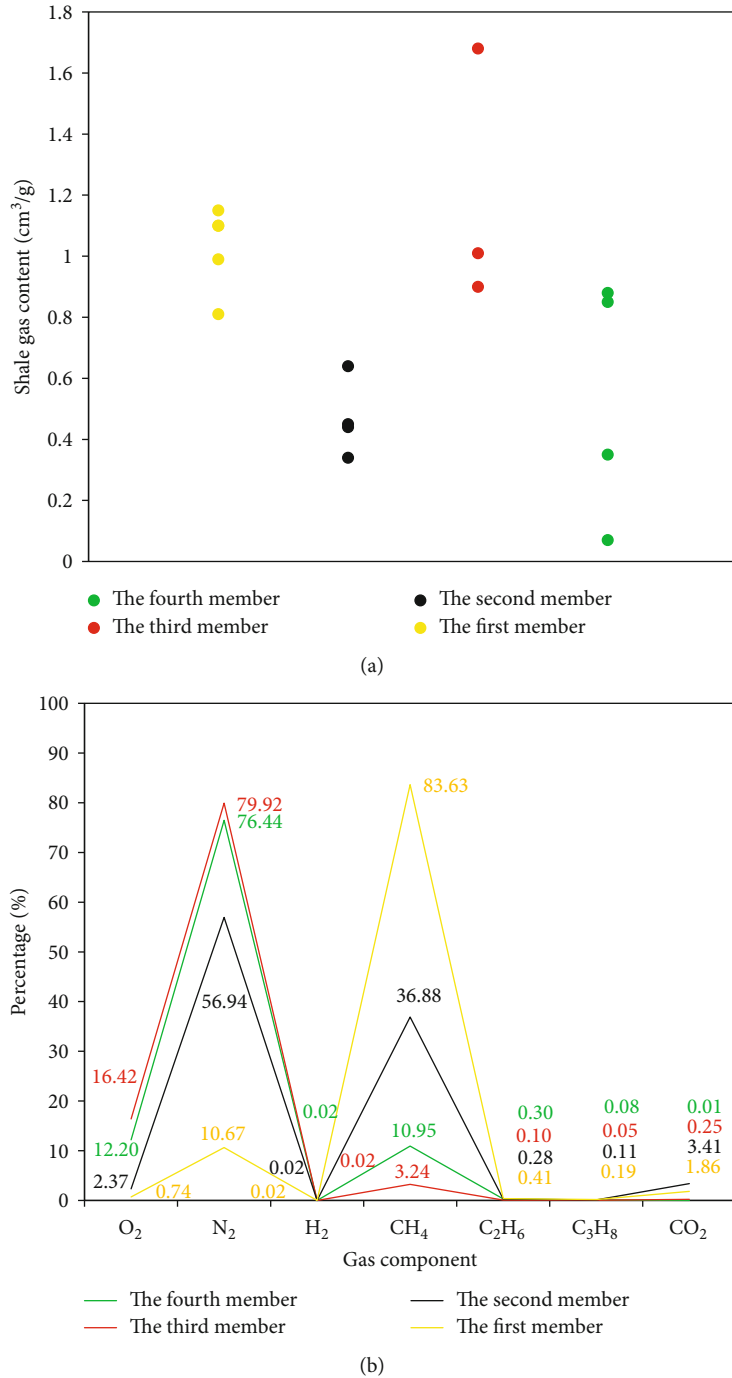


FIGURE 7: The shale gas content and components of the Dawuba Formation.

method. Only the shale gas gathered from the first member contained a large abundant of methane (83.63%), followed by the second member shale samples (36.88%) (Figure 7). The major component of shale gas in the other three member samples was nitrogen, which means no commercial production value.

4.6. Element Characteristics. The Sr/Ba is a parameter sensitively reflecting the salinity of sedimentary water because of much stronger migration ability of Sr than Ba [39, 40]. It represents fresh water sedimentary environment when the Sr/Ba

value is less than 1 [38–41], which is exactly describing most of the Dawuba Formation shale samples (Figure 8). The Sr/Cu is a parameter employed to express the dry-humid degree of sedimentary environment. The Sr/Cu values ranging from 1 to 10 represent warm-moist climate and larger than 10 reflect hot-dry climate [37, 39, 42, 43]. Sr/Cu values of most Dawuba Formation shale samples are larger than 10, which indicates hot-dry climate. However, some samples of the first member shale showed Sr/Ba and Sr/Cu values much larger than 1 and 40, respectively, which means relatively higher salinity of sedimentary water for the first

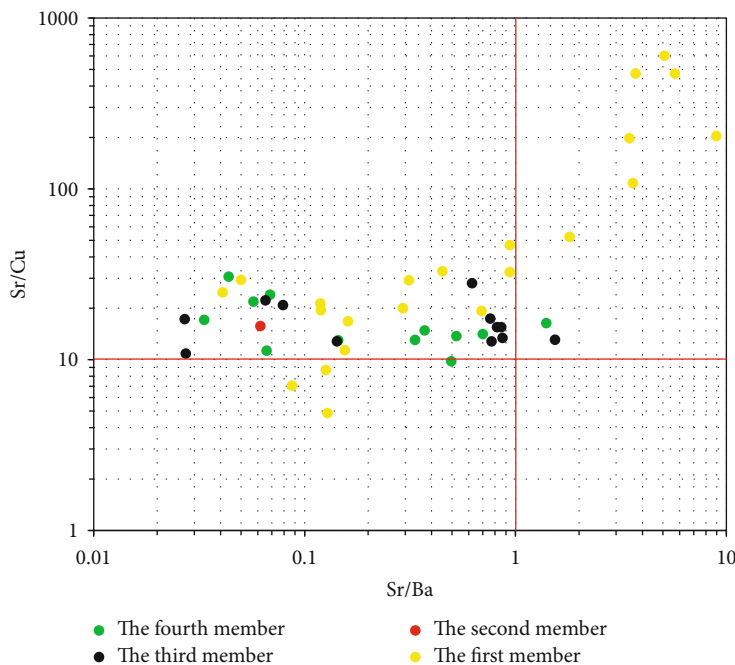


FIGURE 8: The relationship between Sr/Ba and Sr/Cu.

member shale (Figure 8). A large quantity of parameters have been used to reflect the reducibility or oxidability of sedimentary environment, such as Ce/La, Th/U, Cr/Cu, and V/Sc [36, 38, 44–46]. Compared with the other three member shales, the first member shale presented obviously much lower Ce/La, Th/U, Cr/Cu, and V/Sc values, which represented a stronger reducing environment (Figure 9). The first member shale might develop under much deeper and stratified water. Water below with more mineral ions cannot be mixed with the fresh water on top in view of density differences.

5. Discussion

5.1. Sedimentary Environment and Shale Thickness. The whole Dawuba Formation is characterized by a set of platform edge slope facies and platform basin facies deposits. The content of sand in the strata near the platform increased, while the content of silica in the strata near the basin increased [47–49]. In the early Carboniferous period, the seawater of Qinfang basin and Ailaoshan basin in the Tethys domain invaded along the sedimentary basin from southeast to northwest. The Ziyun area was stretched into a rifting basin under the action of NE-NW stress [50]. Due to the rapid transgression and insufficient material supply, the first member of the Dawuba Formation in deep water was deposited in the basin and mainly consisted of black shale and siliceous rock (Figure 10). At this time, the southwest of Ziyun area was the sedimentary center, and the shale thickness in the Ziyun area represented by Sidazhai outcrop was the largest (Figure 10). In the north, there was no deposit of shale strata because it was not within the range of the rift basin. During Ziyun tectonic movement, transgression gradually increased, and water body became shallow gradually from the trough internal to both sides. Material continued in sup-

plying from the north and north east of Ziyun area. A thin layer of silty sand rock with gray, silty mudstones, colored marl of the lithologic combination was formed, which was called the upper strata of Dawuba Formation (Figure 10). Subsequently, with the continuous uplift of the structure, the water body continued to become shallower. The thick carbonate rocks of the Nandan Formation were formed and covered over the Dawuba Formation.

The shale thickness in Ziyun area was obviously affected by sedimentary facies and gradually thickened from north-east to southwest (Figure 11), with the maximum sedimentary thickness of nearly 400 m [51]. The first and third members of the Dawuba Formation in the north of Ziyun area were dominated by organic-enriched shale, which was about 40–170 m in in the first member and less than 50 m in the third member. However, the changes of sedimentary facies occurred in the north of Maoying, and the Dawuba Formation changed from mud-shale system to limestone-marl system. To the south of Ziyun area, the thickness of the Dawuba Formation increased significantly, reaching over 300 m. The first and third members of Dawuba Formation were still intensively compose of black shale, while the second and fourth members changed from sandstone combined with mudstone and marl in the north to gray marl with thin layer siliceous rock. The thickness of Dawuba Formation in the eastern Ziyun area gradually decreased, and the stratification characteristic was fuzzy. But, the organic-enriched shale was still developed in the first and third members, and in the first member was about 70 m thick; the third member was about 20 m thick. The second member was composed of only a few meters of black shale with grey black lens marl, and the fourth member consisted of a set of grey black and dark grey silty mudstone with mud shale. It is generally concluded that the first and third members of the Dawuba Formation were

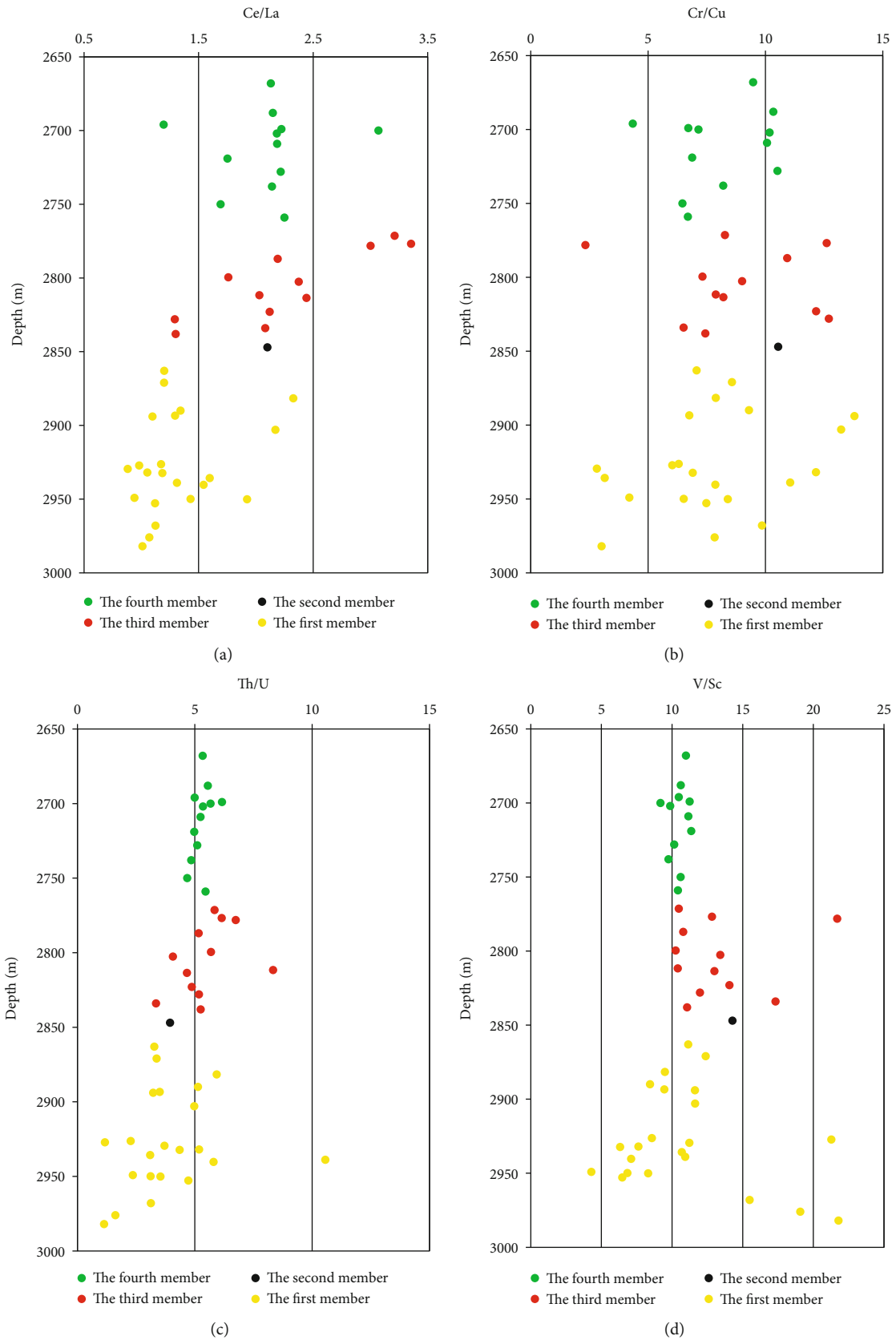


FIGURE 9: The resolution comparison of reducing environment exquisite changes for variety of parameters: (a) cross plot of Ce/La values and depth for the four member shale samples; (b) cross plot of Cr/Cu values and depth for the four member shale samples; (c) cross plot of Th/U values and depth for the four member shale samples; (d) cross plot of V/Sc values and depth for the four member shale samples.

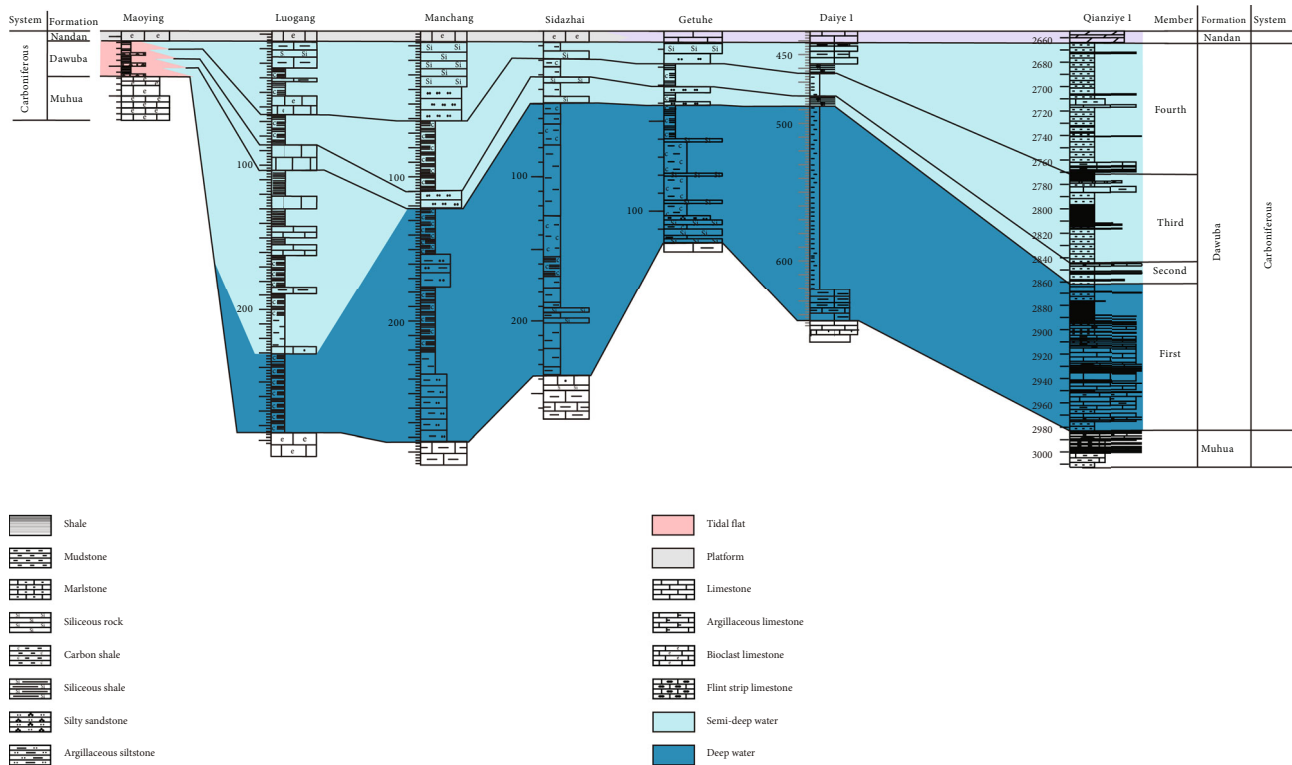


FIGURE 10: Columnar contrast map of the Dawuba Formation in Ziyun area. The section line of wells and outcrops connecting was shown in Figure 1 (the yellowish-brown one).

the most intensively and consistently organic-rich shale layers. From the perspective of lithologic characteristics, limestone and marl mostly developed at the bottom of the first member, and then, shale widely developed. In the third member, mudstone and shale developed with marl strips. The proportion of black shale in the second and fourth members of the Dawuba Formation is relatively small. Except for sandstone and siliceous rocks with continuous thickness of more than 3 meters, the proportion of shale is less than 50%.

In fact, the Dawuba Formation was deposited during a transgressive–regressive cycle, which included several sea level eustacy of small scale. The transgression began during the first member deposition period and reached its climax. During most of this transgression, the bottom waters of the first member were oxygen poor (anoxic to euxinic), allowing for preservation of the abundant organic matter. During the third member deposition period, a transgressive of smaller scale happened, but the redox conditions never fully returned to the anoxic conditions of the first member, so in general, organic-matter abundances are lower in black shale from the Upper Dawuba Formation than in black shale from the Lower Dawuba Formation.

5.2. Comparative Evaluation of the Dawuba Formation Shale.

As an important shale gas survey target in the southern Guizhou depression, the Carboniferous Dawuba Formation shale was characterized by large thickness, high TOC, and high gas-bearing content. By comparing and analyzing the shale thickness, sedimentary environment, organic geochemical characteristics, reservoir characteristics, and gas-bearing

property, the four members of the Dawuba Formation in Ziyun area were evaluated.

The fourth member of Dawuba Formation was mainly black carbonaceous mudstone mixed with siliceous rocks and limestone deposited in half deep water, and gray mudstone was developed locally. The strata thickness of the fourth member was about 20–105 m. The organic-enriched shale strata was relatively thin, merely about 2–30 m, and the continuous thickness of shale is small. The TOC was in the range of 0.38–2.26% with an average of 0.99%. The major gas component was nitrogen. The third member was one of the major shale strata with thickness of 10–70 m. It was mainly composed of black carbonaceous shale with siliceous rocks with thickness for 5–45 m. The thickness thinned gradually from south west to north east. It was deposited under semideep water and reductive environment. The TOC was in the scope of 0.97–4.25% with an average of 2.44%. The third member contained a large scale of shale gas, but the major component was nitrogen, which is the similar component as the gas in the Lower Cambrian shale of Xiuwu Basin in the Lower Yangtze [7]. It was obvious that the third member of the Carboniferous Dawuba Formation shale in the southern Guizhou depression was not sealed well as the Wufeng-Longmaxi Formation shale in Sichuan Basin [12]. The second member of the Dawuba Formation had a thin thickness, generally less than 20 m. The obvious feature is mudstone interbedded with limestone and was formed under the oxidation environment of semideep water. The shale was thin, with a thickness of less than 5 m and the single layer of shale much thinner. The content of organic carbon is

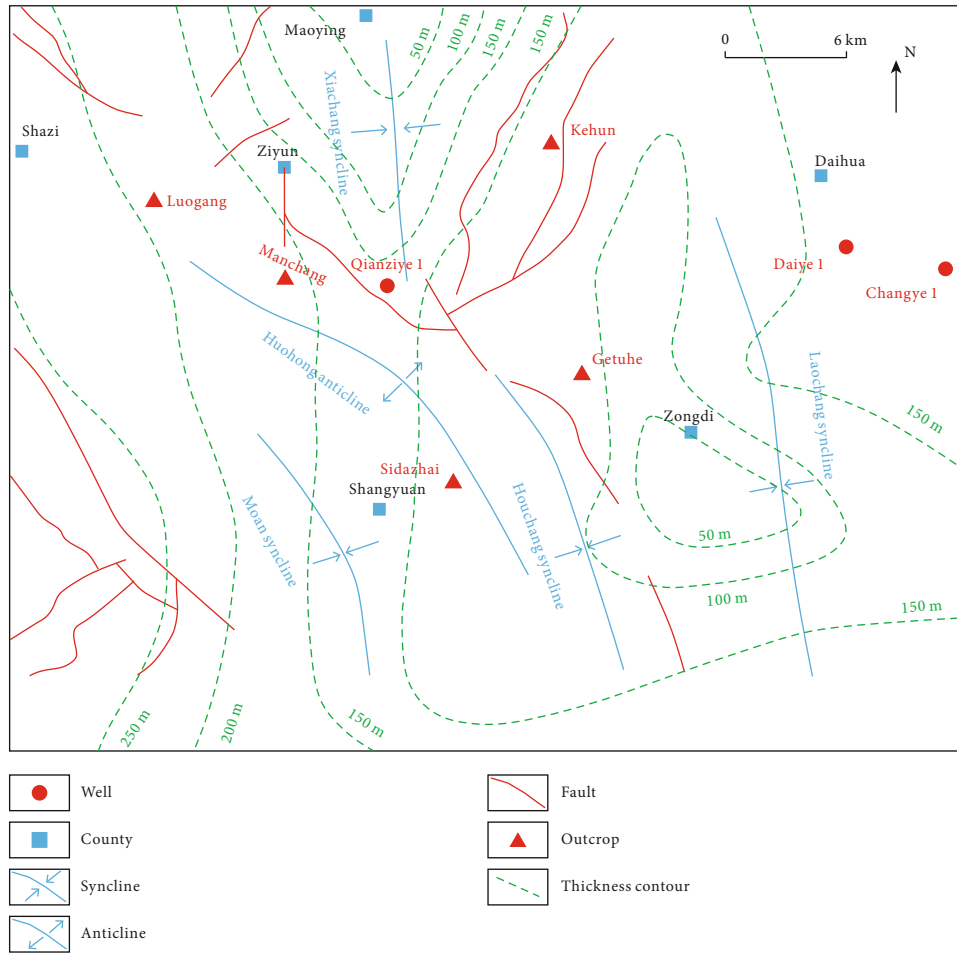


FIGURE 11: Stratum thickness contour map of Dawuba Formation.

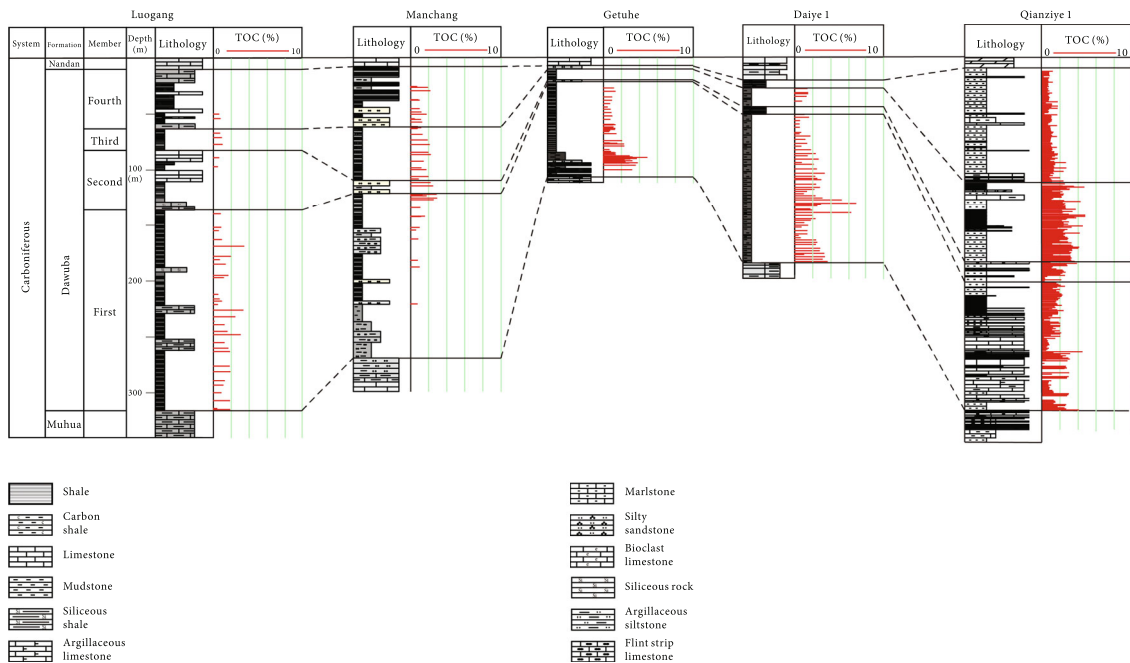


FIGURE 12: The TOC comparison of typical stratigraphic section of Dawuba Formation in Ziyun area. The section line of wells and outcrops connecting was shown in Figure 1 (the green one).

relatively low, with an average TOC of 1.59%. The shale in this member basically contains no gas. The first member of Dawuba Formation was mainly composed of organic-enriched shale with silty sand a small amount of marl limestone at the bottom. The formation thickness was usually more than 100 m, and the proportion of shale in the formation is relatively high. The elemental analysis indicated that the shale strata in the first member was formed in a relatively stagnant and reducing environment. The TOC was in the range of 0.96–4.66%, with an average of 1.92%. Moreover, the shale gas content was higher, and the shale gas mainly consisted of methane.

In general, the TOC vertically increased gradually from the fourth member to the first member of Dawuba Formation. On the plane, the organic carbon content increased gradually from north to south (Figure 12). The southern part of Ziyun area in early Carboniferous period is near the center of the rift basin, and the water is relatively deep, which is conducive to the accumulation of organic matter.

6. Conclusion

The shale intervals of the Dawuba Formation in Ziyun area of South Qian Depression were evaluated through mineral composition, organic matter character, pores, porosity, and permeability, as well as gas-containing property.

- (1) The Dawuba Formation had a stable distribution in Ziyun area and was mainly composed of platform and basin facies deposits. According to the stratigraphic development characteristics and lithofacies association law of Dawuba Formation, the Dawuba Formation was divided into four members, among which the first and third members were organic-rich shale strata
- (2) The type of shale organic matter in Dawuba Formation in Ziyun area was mostly II₂ kerogen. The TOC content ranged from 0.38 to 4.66%, with an average of 1.73%. Ro was in the range of 2.85% and 5.14%, which indicated a stage of overmature evolution. The mineral composition is mainly quartz and clay minerals, and the brittle mineral content is more than 45%, which has good compressibility. The shale gas content was in the scope of 0.07–1.68 cm³/g
- (3) The shale in the first and third members of Dawuba Formation was characterized by high TOC, high evolution degree, and high brittle mineral content, which indicated favorable shale strata. However, the shale gas in the third member mainly consisted of nitrogen, while that in the first member was chiefly composed of methane. Hence, the first member should be regarded as the most favorable target

Data Availability

The data has been included in the manuscript.

Conflicts of Interest

The authors declare that they have no conflicts of interest.

Acknowledgments

This study was supported by the China Geological Survey Projects “Geological survey of shale gas in Guizhong-Nanpanjiang area” (grant no. DD20190088). We thank Guoheng Liu at China University of Petroleum (East China) for his help in these experiments.

References

- [1] K. A. Bowker, “Barnett shale gas production, Fort Worth Basin: issues and discussion,” *AAPG Bulletin*, vol. 91, no. 4, pp. 523–533, 2007.
- [2] D. M. Jarvie, R. J. Hill, T. E. Ruble, and R. M. Pollastro, “Unconventional shale-gas systems: the Mississippian Barnett shale of north-central Texas as one model for thermogenic shale-gas assessment,” *AAPG Bulletin*, vol. 91, no. 4, pp. 475–499, 2007.
- [3] J. C. Zhang, “Exploration potential of shale gas resources in China,” *Natural Gas Industry*, vol. 28, no. 6, pp. 136–140, 2008.
- [4] C. Zou, Q. Zhao, D. Dong et al., “Geological characteristics, main challenges and future prospect of shale gas,” *Journal of Natural Gas Geoscience*, vol. 2, no. 5-6, pp. 273–288, 2017.
- [5] G. Liu, G. Zhai, C. Zou et al., “A comparative discussion of the evidence for biogenic silica in Wufeng- Longmaxi siliceous shale reservoir in the Sichuan basin, China,” *Marine and Petroleum Geology*, vol. 109, pp. 70–87, 2019.
- [6] G. Zhai, Y. Wang, G. Liu et al., “The Sinian-Cambrian formation shale gas exploration and practice in southern margin of Huangling paleo-uplift,” *Marine and Petroleum Geology*, vol. 109, pp. 419–433, 2019.
- [7] K. Zhang, C. Jia, Y. Song et al., “Analysis of Lower Cambrian shale gas composition, source and accumulation pattern in different tectonic backgrounds: a case study of Weiyuan Block in the Upper Yangtze region and Xiuwu Basin in the Lower Yangtze region,” *Fuel*, vol. 263, p. 115978, 2020.
- [8] K. Zhang, Y. Song, S. Jiang et al., “Shale gas accumulation mechanism in a syncline setting based on multiple geological factors: an example of southern Sichuan and the Xiuwu Basin in the Yangtze region,” *Fuel*, vol. 241, pp. 468–476, 2019.
- [9] T. L. Guo and H. R. Zhang, “Formation and enrichment mode of Jiaoshiba shale gas field, Sichuan Basin,” *Petroleum Exploration and Development*, vol. 41, no. 1, pp. 31–40, 2014.
- [10] C. Han, M. Han, Z. Jiang et al., “Source analysis of quartz from the Upper Ordovician and Lower Silurian black shale and its effects on shale gas reservoir in the southern Sichuan Basin and its periphery, China,” *Geological Journal*, vol. 54, no. 1, pp. 439–449, 2019.
- [11] K. Zhang, Y. Song, S. Jiang et al., “Mechanism analysis of organic matter enrichment in different sedimentary backgrounds: a case study of the Lower Cambrian and the Upper Ordovician-Lower Silurian, in Yangtze region,” *Marine and Petroleum Geology*, vol. 99, pp. 488–497, 2019.
- [12] K. Zhang, Y. Song, C. Jia et al., “Vertical sealing mechanism of shale and its roof and floor and effect on shale gas accumulation, a case study of marine shale in Sichuan basin, the Upper

- Yangtze area,” *Journal of Petroleum Science and Engineering*, vol. 175, pp. 743–754, 2019.
- [13] K. Zhang, Z. Jiang, L. Yin et al., “Controlling functions of hydrothermal activity to shale gas content-taking Lower Cambrian in Xiuwu Basin as an example,” *Marine and Petroleum Geology*, vol. 85, pp. 177–193, 2017.
- [14] K. Zhang, J. Peng, W. Liu et al., “The role of deep geofluids in the enrichment of sedimentary organic matter: a case study of the Late Ordovician-Early Silurian in the upper Yangtze region and early Cambrian in the lower Yangtze region, South China,” *Geofluids*, vol. 2020, Article ID 8868638, 12 pages, 2020.
- [15] R. Y. Wang, Z. Q. Hu, and H. K. Nie, “Comparative analysis and discussion of shale reservoir characteristics in the Wufeng-Longmaxi and Niutitang formations,” *Petroleum Geology & Experiment*, vol. 40, no. 5, pp. 639–649, 2018.
- [16] T. Dong, N. B. Harris, K. Ayranci, and S. Yang, “The impact of rock composition on geomechanical properties of a shale formation: Middle and Upper Devonian Horn River Group shale, Northeast British Columbia, Canada,” *AAPG Bulletin*, vol. 101, no. 2, pp. 177–204, 2017.
- [17] G. Liu, Z. Huang, Z. Jiang, J. Chen, F. Chen, and J. Xing, “Gas adsorption capacity calculation limitation due to methane adsorption in low thermal maturity shale: a case study from the Yanchang Formation, Ordos Basin,” *Journal of Natural Gas Science and Engineering*, vol. 30, pp. 106–118, 2016.
- [18] G. Liu, Z. Huang, F. Chen et al., “Reservoir characterization of Chang 7 member shale: a case study of lacustrine shale in the Yanchang Formation, Ordos Basin, China,” *Journal of Natural Gas Science and Engineering*, vol. 34, pp. 458–471, 2016.
- [19] Z. Huang, G. Liu, T. Li, Y. Li, Y. Yin, and L. Wang, “Characterization and control of mesopore structural heterogeneity for low thermal maturity shale: a case study of Yanchang Formation shale, Ordos Basin,” *Energy & Fuels*, vol. 31, no. 11, pp. 11569–11586, 2017.
- [20] G. Liu, B. Liu, Z. Huang et al., “Hydrocarbon distribution pattern and logging identification in lacustrine fine-grained sedimentary rocks of the Permian Lucaogou Formation from the Santanghu basin,” *Fuel*, vol. 222, pp. 207–231, 2018.
- [21] G. Liu, G. Zhai, Z. Huang et al., “The effect of tuffaceous material on characteristics of different lithofacies: a case study on Lucaogou Formation fine-grained sedimentary rocks in Santanghu Basin,” *Journal of Petroleum Science and Engineering*, vol. 179, pp. 355–377, 2019.
- [22] J. Ma, G. Liu, Z. Huang, G. Ou, T. Li, and X. Guo, “Tight tuff reservoir characteristics and its controlling factors: a comparative study of the Permian Tiaohu Formation and carboniferous Haerjiawu Formation in the Santanghu Basin, NW China,” *Journal of Petroleum Science and Engineering*, vol. 187, p. 106808, 2020.
- [23] X. ZHAO, L. ZHOU, P. U. Xiugang et al., “Geological characteristics of shale rock system and shale oil exploration breakthrough in a lacustrine basin: a case study from the Paleogene 1st sub-member of Kong 2 Member in Cangdong sag, Bohai Bay Basin, China,” *Petroleum Exploration and Development*, vol. 45, no. 3, pp. 377–388, 2018.
- [24] X. Guo, D. Hu, R. Liu, X. Wei, and F. Wei, “Geological conditions and exploration potential of Permian marine-continent transitional facies shale gas in the Sichuan Basin,” *Natural Gas Industry*, vol. 38, no. 10, 2018.
- [25] S. J. Bao, T. Lin, and H. K. Nie, “Preliminary study of the transitional facies shale gas reservoir characteristics: taking Permian in the Xiangzhong depression as an example,” *Earth Science Frontiers*, vol. 23, no. 1, pp. 44–53, 2016.
- [26] G. Y. Zhai, Y. F. Wang, and G. H. Liu, “Enrichment and accumulation characteristics and prospect analysis of the Permian marine continental multiphase shale gas in China,” *Sedimentary Geology and Tethyan Geology*, vol. 40, no. 3, pp. 102–117, 2020.
- [27] X. D. Wang and Y. Jin, “Geochemical features and sedimentary conditions of the Middle-Devonian shale in the northwestern Central-Guangxi depression,” *Journal of Stratigraph*, vol. 2, 2000.
- [28] K. Yuan, K. Y. Wang, and S. H. Gong, “Shale gas enrichment features and impacting factors in carboniferous Dawuba Formation, southern Guizhou area,” *Coal Geology of China*, vol. 3, pp. 28–34, 2018.
- [29] Z. H. Yang, Z. M. Li, and B. J. Shen, “Shale gas accumulation conditions and exploration prospect in southern Guizhou depression,” *China Petroleum Exploration*, vol. 3, pp. 24–28, 2009.
- [30] Z. Y. Xu, G. S. Yao, and Q. X. Guo, “Genetic interpretation about geotectonics and structural transfiguration of the southern Guizhou depression,” *Geotectonica et Metallogenia*, vol. 34, no. 1, pp. 20–31, 2010.
- [31] S. F. Lu, B. He, and S. J. Du, “Geological conditions and exploration prospect of shale gas in Dawuba Formation of Lower Carboniferous of Daiye-1 well in southern Guizhou Province,” *Geological Survey of China*, vol. 3, pp. 4–11, 2016.
- [32] G. R. Chalmers, R. M. Bustin, and I. M. Power, “Characterization of gas shale pore systems by porosimetry, pycnometry, surface area, and field emission scanning electron microscopy/transmission electron microscopy image analyses: examples from the Barnett, Woodford, Haynesville, Marcellus, and Doig units,” *AAPG Bulletin*, vol. 96, pp. 1099–1119, 2011.
- [33] X. Cui, R. M. Bustin, and R. Brezovski, “A new method to simultaneously measure in-situ permeability and porosity under reservoir conditions: implications for characterization of unconventional gas reservoirs,” in *Society of Petroleum Engineers, Canadian Unconventional Resources and International Petroleum Conference*, pp. 19–21, Calgary, Alberta, Canada, 2010.
- [34] A. Ghanizadeh, A. Amann-Hildenbrand, M. Gasparik, Y. Gensterblum, B. M. Krooss, and R. Littke, “Experimental study of fluid transport processes in the matrix system of the European organic-rich shales: II. Posidonia Shale (Lower Toarcian, northern Germany),” *International Journal of Coal Geology*, vol. 123, pp. 20–33, 2014.
- [35] K. Hiroto, “Ocean anoxic event at the Precambrian-Cambrian boundary. *Geology*, 29 (11). Translated by Wen F. Y., 2002,” *Marine Geology Letters*, vol. 18, no. 4, pp. 33–35, 2001.
- [36] L. Tonger, X. WH, and Y. C., “The discussion on anoxic environments and its geochemical identifying indices,” *Acta Sedimentologica Sinica*, vol. 22, no. 2, pp. 365–372, 2004.
- [37] G. Liu and D. S. Zhou, “Application of trace elements analysis in identifying sedimentary environment: taking Qianjiang Formation in the Jiangnan Basin as an example,” *Petroleum Geology and Experiment*, vol. 29, no. 3, pp. 307–310, 2007.
- [38] C. Du, B. Zhang, and S. T. Zhang, “Application and principle of element geochemistry in the evolution of lake sedimentary environment,” *Geology and Resources*, vol. 21, no. 5, pp. 487–492, 2012.

- [39] Y. H. Fan, H. J. Qu, and H. Wang, "The application of trace elements analysis to identifying sedimentary media environment: a case study of Late Triassic strata in the middle part of western Ordos Basin," *Geology in China*, vol. 39, no. 2, pp. 382–389, 2012.
- [40] R. C. Zheng and M. Q. Liu, "Study on palaeo-salinity of Chang-6 oil reservoir set in Ordos Basin," *Oil & Gas Geology*, vol. 20, no. 1, pp. 20–25, 1999.
- [41] E. Custodio, "Aquifer overexploitation: what does it mean?," *Hydrogeology Journal*, vol. 10, no. 2, pp. 254–277, 2002.
- [42] A. Leman, *Chemical Geology and Physics of Lake*, S. M. Wang, Ed., Geological Publishing House, Beijing, 1989.
- [43] H. W. Deng and K. Qian, *Sedimentary Geochemistry and Environment Analysis*, Gansu Science and Technology Press, Lanzhou, 1993.
- [44] J. R. Hatch and J. S. Leventhal, "Relationship between inferred redox potential of the depositional environment and geochemistry of the Upper Pennsylvanian (Missourian) Stark Shale Member of the Dennis Limestone, Wabaunsee County, Kansas, U.S.A.," *Chemical Geology*, vol. 99, no. 1-3, pp. 65–82, 1992.
- [45] B. J. Jones and A. C. Manning, "Comparison of geochemical indices used for the interpretation of palaeo-redox conditions in ancient mudstones," *Palaeogeography Palaeoclimatology Palaeoecology*, vol. 111, pp. 111–129, 1994.
- [46] G. M. Alberdi and R. Tocco, "Trace metals and organic geochemistry of the Machiques Member (Aptian-Albian) and La Luna Formation (Cenomanian-Campanian), Venezuela," *Chemical Geology*, vol. 160, no. 1-2, pp. 19–38, 1999.
- [47] Z. Z. Feng, Y. Q. Yang, and Z. D. Bao, "Lithofacies palaeogeography of the carboniferous in South China," *Journal of Palaeogeography*, vol. 1, pp. 75–86, 1999.
- [48] K. Yuan, R. Chen, and T. Lin, "Petrological characteristics and sedimentary environment in the southern Guizhou during the Late Carboniferous," *Petroleum Geology & Experiment*, vol. 41, no. 1, pp. 38–44, 2019.
- [49] S. F. Tian and R. D. Yang, "Lithofacies and paleogeography evolution and characteristics of shale gas accumulation in Lower Carboniferous, Guizhou, China," *Journal of Chengdu University of Technology (Science & Technology Edition)*, vol. 3, pp. 291–299, 2016.
- [50] H. D. Chen and Y. F. Zeng, "Nature and evolution of the Youjiang Basin," *Sedimentary Facies and Palaeogeography*, vol. 1, pp. 28–37, 1990.
- [51] Y. Y. An, H. B. Fu, and H. G. Chen, "Reservoir property and control factors of shale gas of Dawuba Formation, Lower Carboniferous in South Guizhou—with Changye No. 1 reservoir as an example," *Guizhou Geology*, vol. 32, pp. 181–189, 2015.

Research Article

Research on the Oil-Bearing Difference of Bedding Fractures: A Case Study of Lucaogou Formation in Jimsar Sag

Jia Lu ¹, Chen Zhang ^{2,3}, Jianhui Zeng ^{2,3} and Haowei Yuan ^{2,3}

¹Faculty of Land and Resource Engineering, Kunming University of Science and Technology, Kunming, China

²State Key Laboratory of Petroleum Resources and Prospecting, China University of Petroleum, Beijing, China

³College of Geoscience, China University of Petroleum, Beijing, China

Correspondence should be addressed to Jianhui Zeng; zengjh@cup.edu.cn

Jia Lu and Chen Zhang contributed equally to this work.

Received 28 January 2021; Accepted 18 May 2021; Published 1 June 2021

Academic Editor: Martina Zucchi

Copyright © 2021 Jia Lu et al. This is an open access article distributed under the Creative Commons Attribution License, which permits unrestricted use, distribution, and reproduction in any medium, provided the original work is properly cited.

Lucaogou formation in Jimsar sag is host to large quantities of bedding fractures which are known to play a critical role in the enrichment, accumulation, and efficient development of tight oil. In this paper, we examine and finely characterize the development of the bedding fractures found in the upper and lower sweet spots of Lucaogou formation of tight oil reservoir through field outcrop and core observation, cast thin section analysis, and imaging log recognition and investigate the factors affecting their differentiated oil-bearing by means of inclusion temperature measurement, TOC testing, physical property testing, high-pressure mercury injection, and physical simulation experiment. By comparison with the linear density, bedding fractures are more developed in the lower sweet spot. These fractures occur in parallel to the formation boundary and have small aperture. Most of bedding fractures are unfilled fractures. Among the few types of fractures found there, bedding fractures have the best oil-bearing property, but the oil-bearing can differ from one bedding fracture to another. The factors affecting the differentiated oil-bearing of bedding fractures include the temporal coupling of the formation of these fractures with the hydrocarbon generation of the source rocks and the spatial coupling of the bedding fractures with the source rocks. In terms of temporal coupling, mass hydrocarbon generation in Jimsar sag began in Late Jurassic. Inclusion temperature measurement indicates that the bedding fractures there formed in or after Early Cretaceous. Hence, by matching the mass hydrocarbon generation period of the source rocks with the formation period of the bedding fractures, we discovered that the bedding fractures formed within the mass hydrocarbon generation period, which favored the oil-bearing of these fractures. The spatial coupling is manifested in TOC, porosity, permeability, and pore throat, with TOC being the main controlling factor. For TOC, the higher the formation TOC, the better the oil-bearing property of the bedding fractures. For porosity, subject to the TOC level, if the TOC is adequate, the larger the porosity, the larger the chloroform asphalt “A,” accordingly the higher the oil content of the formation, and the better the oil-bearing property of the bedding fractures developed therein. In this sense, in terms of spatial coupling, TOC constitutes the main controlling factor of the oil-bearing property of bedding fractures.

1. Introduction

Over the past years, as the exploitation of conventional oil and gas intensifies, global oil and gas exploration and development has gradually shifted toward unconventional oil and gas resources. Tight oil, as a very important unconventional oil and gas resource, is a very realistic alternative for conventional oil [1–3]. Inside tight reservoirs, fractures not

only provide seepage channels for oil and gas migration, but also serve as important oil and gas storage spaces. They are one of the important factors affecting the oil-bearing property of tight oil reservoirs. For this reason, studying the natural fractures in tight reservoirs is highly instructive for the efficient development of tight oil reservoirs [4]. Bedding fractures are strongly associated with hydrocarbon generation and migration in tight reservoirs. Previous authors have

made extensive studies into structural fractures, but few have paid attention to bedding fractures.

Previous studies have tended to categorize bedding fractures as a part of structural fractures or diagenetic fractures [5–8]. Regarding the origin of bedding fractures, assumptions include tectonic origin [9–11], hydrocarbon generation–acid expulsion–dissolution [10, 12], pressure fracturing of authigenic fluids inside reservoirs [13, 14], and tectonic plus hydrocarbon generation–acid expulsion [15, 16]. The earliest assumption of the origin of bedding fractures in tight reservoirs was the self-generation–self-storage–postfracturing of oil and gas proposed by Wu and Yin [17], whose target formation was Upper Shaximiao formation in Xinchang of western Sichuan where the oil and gas reservoirs are tight sandstone reservoirs. At the time when natural gas enriched and accumulated in Upper Shaximiao formation, the reservoirs were conventional natural gas reservoirs. Over time, after reservoir tightening and tectonic processes, Upper Shaximiao formation became a tightly closed system. When the pressure of the natural gas and other fluids inside the formation is greater than the breaking strength of the bedding plane of tight sandstone, the bedding plane can be pressed open by the natural fluids in the closed body to form bedding fractures [18, 19]. Later on, their assumption was echoed by some other authors, who suggested that for a bedding to break open, there should exist a critical strength. Only when the stress acting on the bedding boundary is greater than this critical strength will the bedding be pressed open to form bedding fractures [20–22]. Among the many discussions supporting the tectonic origin of bedding fractures [12, 18, 20–22], one common belief is that water flow direction, lithologic alternation, sand body distribution, and sedimentary processes such as sedimentary facies control the development of beddings [20, 22], while subsequent tectonic processes, such as faulting, compression by horizontal in situ stress, and basin uplifting, caused the weak plane of the beddings to break and form bedding fractures. As to hydrocarbon generation–acid expulsion, it is commonly believed to be an auxiliary factor, since dissolved pores are present on some of the bedding planes. The hydrocarbon generation–acid expulsion of organic matter is obviously a pore adder for the formations [23]. The dissolution effect of organic acids when migrating along the bedding boundary [24] is possibly the main controlling factor for the formation of bedding fractures. The assumption of tectonic plus dissolution origin includes for the interaction among various factors. It suggests that single factors can become the main controlling factor of the formation of bedding fractures in a specific historic period or a certain block, such as fracture creation by tectonic stress, the dissolution of acid fluids, or the release of abnormally high pressure. Some authors have conducted research specific to the fractures developed in Lucaogou formation in Jimsar sag [19, 25–27]. They discovered that tectonic processes are quite weak in this area. Hence, for the formation of bedding fractures, the hydrocarbon generation–acid expulsion bedding plane of the source rocks makes play a critical role. The acidic matter generated by

the hydrocarbon generation of the source rocks may have migrated along the already formed bedding boundary. The joint action of tectonic processes with the dissolution effect of hydrocarbon generation–acid expulsion is more likely to have caused the formation of bedding fractures.

Among existing studies around bedding fractures and oil and gas migration, the opinions of most of the authors are advocating and superficial, assuming that bedding fractures are conducive to tight oil enrichment and occurrence. For example, in 2016, in a study of Chang6 reservoir in Heshui of Eros Basin, Yang and his colleagues discovered that bedding fractures, massive beddings, and graded beddings exist on millimeter scale in the tight reservoirs there; the development of bedding fractures has led to tight oil enrichment, and massive beddings are the most conducive to oil enrichment [28, 29]. In 2017, Zhang et al. noticed that bedding fractures are commonly present in tight reservoirs. Preliminary core observation also revealed that these fractures play a critical role in tight oil accumulation and enrichment. They recommended employing more effort in the research of bedding fractures, especially their aperture and closure, as well as their oil filling and enrichment efficiency [26]. They also put forward some ideas and methods in this respect for the first time. Some other authors have looked at how bedding fractures affect tight oil migration and accumulation. They deemed that the extensive development of bedding fractures increases the saturation of movable oil in tight oil reservoirs, thus contributing positively to tight oil migration and occurrence. For example, Dou et al. investigated how the Jurassic bedding fractures in Yongjin of Junggar Basin affect the reservoirs there. They concluded that bedding fractures bridge the matrix pores, provide seepage channels for oil and gas, and enhance the permeability of low-permeability reservoirs. Besides, the development of bedding fractures also helps increase the number of dissolution pores and further expands the storage spaces [30]. Bai et al. and Wang et al. yielded roughly the same conclusion in their study of the double-medium reservoirs in the tight sandstone of Chang3 member of Triassic Yanchang formation in Junggar Basin: the number of bedding fractures present has a significant impact on the saturation of movable oil. That is, the more developed the bedding fractures, the higher the saturation of the movable oil in the reservoir. Bedding fractures are a great contributor for tight oil accumulation and enrichment [31, 32]. However, despite the wide consensus that fractures make a great difference to oil and gas migration, studies specific to the relationship between bedding fractures and tight oil accumulation have rarely been read. In general, many findings have been made with respect to fractures in conventional reservoirs [33, 34] and low-permeability reservoirs [35]. The few reports on bedding fractures in tight oil reservoirs that do exist are mostly descriptive, qualitative studies, let alone research specific to the relationship between bedding fractures and tight oil accumulation, especially the oil-bearing difference and oil accumulating pattern of bedding fractures.

Lucaogou formation in Jimsar sag, Junggar Basin, has a rich stock of tight oil. In fact, it is a very important tight oil reservoir in China [19, 36, 37]. Over the past few years, industrial oil flows have been yielded from a number of

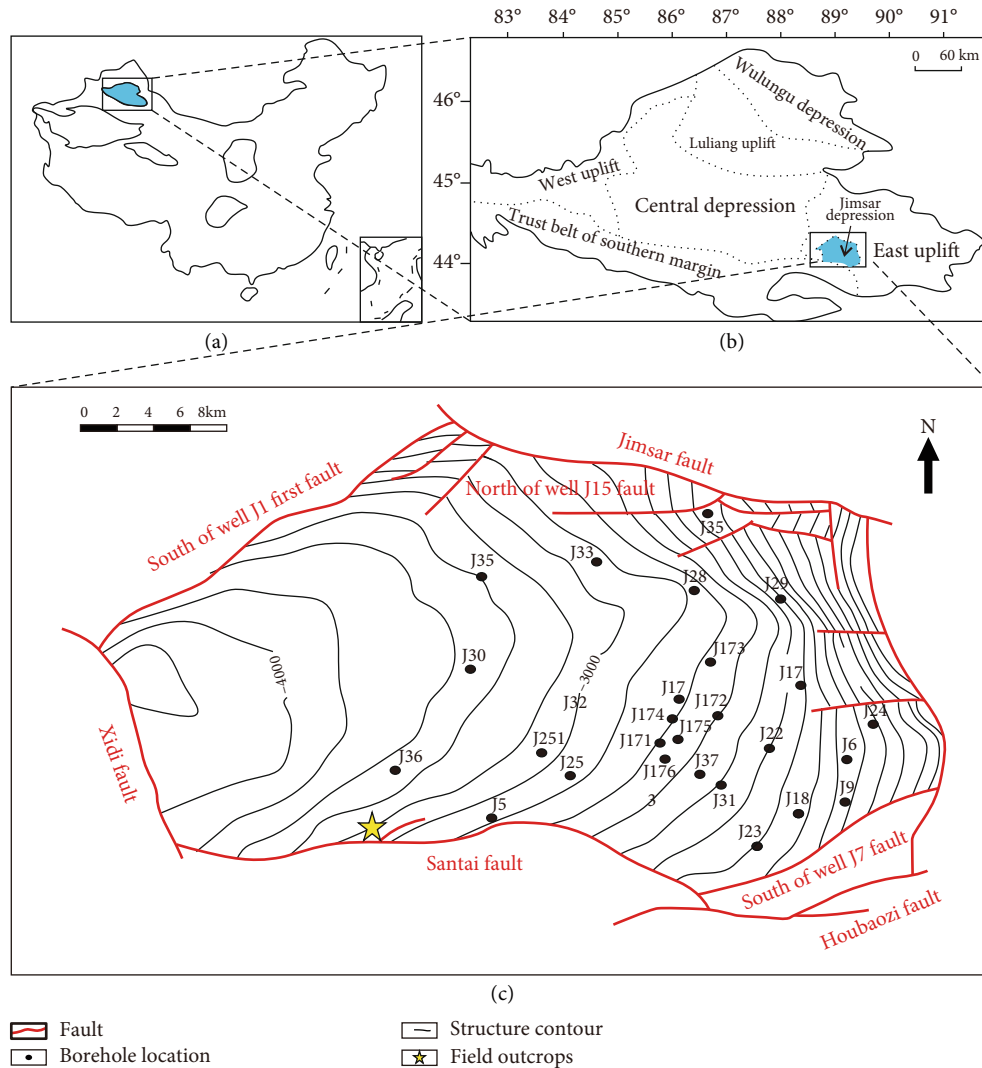


FIGURE 1: The Tectonic setting map of Jimsar sag [42].

boreholes in Jimsar sag, demonstrating vast exploration and development potential [1, 4, 19]. Tight oil reservoirs are low-porosity, low-permeability reservoirs. For the commercial development of tight oil, the enrichment and development of fractures is of fatal significance. The fractures in reservoirs, as both important oil and gas storage spaces and seepage channels, are an important determinant for the mobility of oil and gas [6, 7, 11]. The presence of natural fractures is conducive to oil and gas accumulation [1–3, 7, 8] and to the formation of sweet spots in tight oil reservoirs. Lucaogou formation in Jimsar sag is host to large quantities of bedding fractures, yet research on the relationship between the bedding fractures in tight oil reservoirs and tight oil accumulation is still quite weak [19, 20, 36]. For this reason, investigating the development characteristics and oil-bearing property of bedding fractures and their impact on tight oil accumulation is both theoretically and practically useful for understanding the development characteristics of Lucaogou formation tight oil reservoir, evaluating its development potential and feasibility, and looking for engineering development sweet spots.

In the following sections, we are going to elaborate on and finely characterize the development of bedding fractures in the upper and lower sweet spots of Lucaogou formation tight oil reservoir, discuss the factors affecting their differentiated oil-bearing, determine their oil accumulating pattern, and eventually establish the tight oil accumulation pattern of the bedding fractures in the study area.

2. Geological Setting

Junggar Basin is a typical giant inland superimposed basin located at the junction between Kazakhstan plate, Siberia plate, and Tarim plate [38–40]. It is well known for its rich oil and gas resources. Within the basin, Jimsar sag contains a large stock of tight oil that is well worth exploration and development [37, 41]. Jimsar sag is located in the southeast margin of Junggar Basin, covering an area of approximately 1300 km². Tectonically, this basin has very distinct boundary features (Figure 1). Its north, west, and south are controlled by faults, while its east transitions into Guxi uplift [37, 40, 41]. Since basin evolution began in Permian, Jimsar sag has

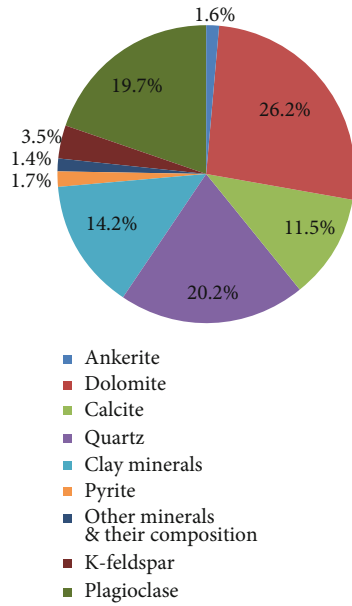


FIGURE 2: Mineral composition fan chart of Lucaogou formation.

undergone a number of tectonic movements. Among them, the one most closely related to its present tectonic architecture is the Himalayan movement in Cenozoic, when the uplifting of its east boundary turned the sag into a dustpan-like monocline that is high in the east and low in the west, with formation dip angle of 3° – 5° for the main part and no obvious faulting inside [26, 41].

From bottom to top, Lucaogou formation can be divided into two members: first member (P_{21_1}) and second member (P_{21_2}) of Lucaogou [42]. Each of the two members can be further divided into two sublayers. Inside Lucaogou formation, there are two sweet spots. The upper sweet spot lies in the second sublayer of the second member of Lucaogou ($P_{21_2^2}$). This sweet spot mainly sits in the center of the sag and the slope location in the east, covering an area of approximately 398 km^2 . Its thickness spans from 0 to 45 m with an average of 37.2 m. The lower sweet spot sits in the second sublayer of the first member of Lucaogou ($P_{21_1^1}$). This sweet spot is widely distributed across the area, covering an area of approximately 1278 km^2 . Its thickness spans from 0 to 65 m with an average of 50 m. The mineral composition of the Lucaogou formation rocks is complicated, and most of the rocks are lithologically transitional [36, 43]. High-content minerals in the Lucaogou formation rocks include dolomite, quartz, and plagioclase, which account for 26.2%, 20.2%, and 19.7%, respectively, and 66.1% together. Calcite and clay minerals account for 11.5% and 14.2%, respectively, and 25.7% together. Other minerals account for 8.2% (Figure 2). In general, the observed lithologies can be grouped into three categories: mudstone, carbonate rock, and siltstone.

The entire Lucaogou formation consists of saline lake facies dark-colored, fine-grained sediments [44]. Taking the maximum flooding surface as the boundary, the formation can be divided into an upper member (second member of Lucaogou) and a lower member (first member of Lucaogou). The upper member is a transgressive sedimentary system as a

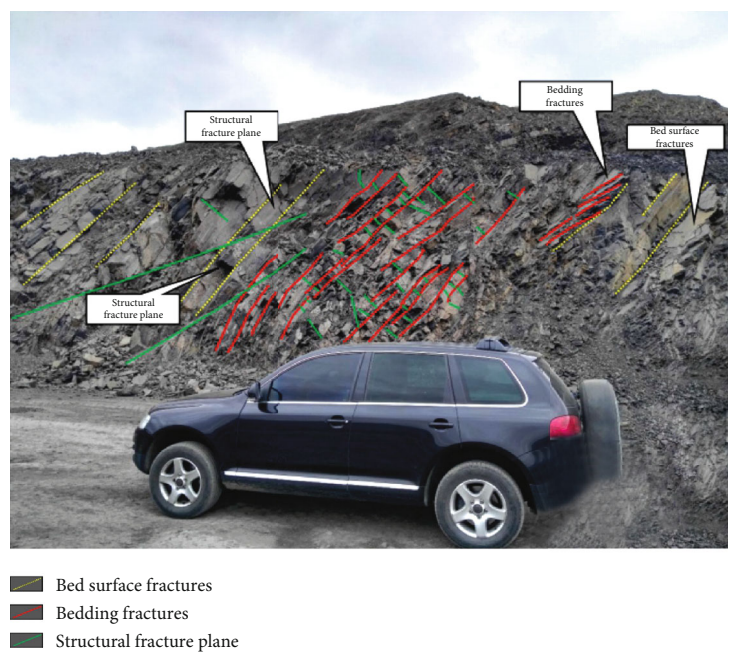
whole, while the lower member is a regressive sedimentary system as a whole. The sedimentary facies type of Lucaogou formation at large is lacustrine delta. For the second member of Lucaogou (P_{21_2}), the sediment supply mainly came from the southeast. The majority of the terrestrial clastic materials were injected from the south of the sag. The main sedimentary facies is shore-shallow lake facies. The microfacies types include sandy bar, dolomite mudflat, sandy beach, dolomite sandflat, and shallow lake mud. For the first member of Lucaogou (P_{21_1}) at large, the sediment supply came from two directions. In the south, deltaic sediments were adequately supplied. The deposited sand bodies stand in great thicknesses. The microfacies types in this member include distal bar, sheet sand, sandy beach, and shallow to semideep lake mud.

3. Characteristics of Bedding Fractures

Bedding fractures are the most frequently found type of fractures in Jimsar sag. Statistical analysis of the development characteristics, oil-bearing property, and horizontal distribution of the bedding fractures in the study area is the basis for examining these fractures. Extensive statistics, documentation, and analysis were conducted on the quantity, development characteristics, and oil-bearing property of these fractures through field outcrop observation, core observation, thin section observation, and imaging log recognition. On this basis, the overall development of the bedding fractures in the study area was identified and finely characterized.

3.1. Characteristics of Field Outcrops. Fracture observation and description on field formation outcrops is a fairly straightforward means of fracture research. It offers a systematic understanding of the vertical distribution of fractures, consequently a general idea of the development of fractures inside the formation. The study area Jimsar sag in Junggar Basin is simply structured dustpan-like sag that is faulted in the west and overlapped in the east. Without considering the influence of weathering, outcrop fractures can give a true picture of the development conditions of fractures underground. For the present study, field outcrops were observed across the oil shale section of Baoming Mining 10 km south-east of Santai county of Jimsar county, Xinjiang (Figure 1(c)). The target formation was Lucaogou formation. In general, the exposed part of the formation consists of very thick black oil shale that contains silty mudstone. The exposure dip angle is 70° – 80° . Overall, the section has undergone a level of weathering. However, our observation was mainly focused on the bedding fractures developed therein (Figure 3(a)).

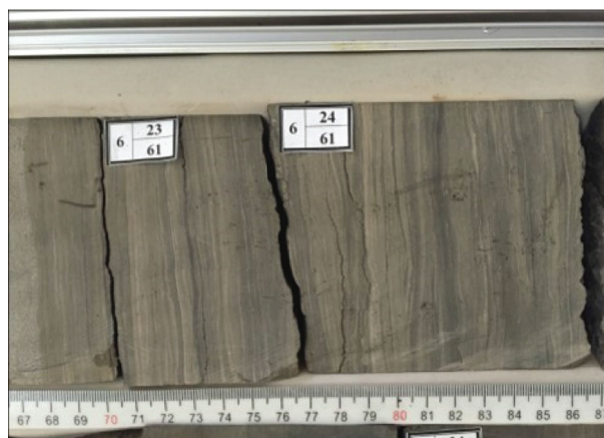
By observing the Lucaogou formation outcrop, we found that bedding fractures are the most frequently found type of fractures in Lucaogou formation—they are actually the prevailing type of fractures there. In the photographs, the fractures occurring roughly in parallel to the formation plane are mostly bedding fractures, while those straighter ones intersecting with the formation plane at large angles are mostly structural fractures (Figures 3(a) and 3(b)). The densely distributed bedding fractures and the groups of structural fractures developed there have cut the rock layers



(a)



(b)



(c)



(d)

FIGURE 3: (a) Macroscopic photograph of Lucaogou outcrop 10 km southeast of Santao town of Jimsar county, Xinjiang; (b) local photograph of Lucaogou outcrop 10 km southeast of Santai town of Jimsar county, Xinjiang; (c, d) core photographs of bedding fractures in Lucaogou formation, Jimsar sag.

into broken rhombic fragments. For the large-thickness rock layers, the cutting disruption is not so intense and the formation is more complete. Lithologically, the exposed stratum is composed of mud shale, with occasional presence of silty mudstone or dolomitic rocks. Some of the bedding fractures have been filled by gypsum or calcite. The filling thickness is very small, roughly 1–3 mm. Closer to the section, a further look at the outcrop will find that lamina is highly developed in the formation, with a density of approximately 5–10/cm (Figure 3(b)). Smaller-scale bedding fractures are also densely distributed, with approximately 4–10 bedding fractures per 10 centimeters, and most of them are half-filled or filled ones (Figure 3(b)). In summary, the most intuitive feature of the Lucaogou formation outcrop is the high development of formation beddings and the extensive presence of bedding fractures.

3.2. Characteristics of Cores. To obtain a better understanding of the development of fractures in the formation, compared with field outcrop research, direct observation, description, and statistics of fractures using formation cores are very effective methods. As cores have not been exposed to weathering denudation on earth's surface, they give a more realistic picture of fracture development in the rock layers underground. Extensive core observation was carried out in the core library of Xinjiang Oilfield. From these photographs, we can easily see that the bedding fractures typically occur in parallel or almost in parallel to the bedding plane (Figures 3(c) and 3(d)). They generally formed at the interface between strata of different lithologies, and their apertures are limited. Some of the cores are badly disrupted by bedding fractures, which cut off the cores transversely, breaking them into separate segments. The majority of the bedding fractures have poor filling property and are either unfilled or half-filled. The filling materials are generally pelite, calcite, or asphalt. The oil-bearing property of the bedding fractures is commonly good. Oil immersion and oil spotting are extensively observed.

3.3. Characteristics of Thin Sections under Microscope. 86 samples were collected from 24 exploration wells in the middle Permian Lucaogou formation in southeastern Junggar Basin, China. Generally, the bedding fractures observed in cast thin sections and scanning electron microscopy (SEM) are microscale fractures. They are therefore referred to as microfractures. Under thin sections, the bedding fractures generally occur along the lamina. Their lithology usually differs between the upper and lower layers, and they will bypass mineral particles. We can observe the bedding fractures in argillaceous siltstone, mudstone, dolomitic siltstone, and gray sandstone (Figure 4). The bedding fractures have small aperture, limited extension, and large magnification. Morphologically, these fractures are not as straight as they appear on the cores. Instead, they will make curved extension. The extent of extension is not as large, and they will pinch out. The aperture of the bedding fractures is 0.1–5 μm . The length is 0.1–10 mm. The bedding fractures are mostly unfilled ones. For the filled ones, the filling degree is roughly 20%, leaving a

large empty space (Figure 4). The filling materials include some pelite, calcite, and quartz.

On the microscale, the quantity of bedding fractures is modest. The fractures observed include not only bedding fractures, but also other types of fractures such as structural fractures and dissolution fractures. The bedding fractures observed are rated higher than pore throat in size. They constitute good oil and gas migration channels. In the study area, micro bedding fractures—a kind of microfracture—are also present. However, microfractures are a separate research hotspot, and the present study is more focused on macro bedding fractures.

4. Fine Characterization of Bedding Fractures

Fine characterization of fractures, namely, fine, detailed description of the characteristics of fractures, typically uses qualitative and quantitative parameters to characterize and reflect the development of fractures [45, 46]. As bedding fractures are fractures that formed by rupture along the beddings and occur roughly in parallel to the formation, their strike and dip angle are roughly the same as the strike and dip angle of the formation. In this consideration, our characterization of bedding fractures herein is made mainly with respect to the density, aperture, and filling property of bedding fractures.

4.1. Linear Density of Bedding Fractures. Fracture density is an important parameter for characterizing the development quantity of fractures [47, 48]. The linear density of fractures, namely, the number of fractures per unit of length, is calculated by the formula below:

$$D_{\text{lf}} = \frac{n}{l}, \quad (1)$$

where n is the number of fractures in the measured interval, l is the length of the measured interval, and D_{lf} is the linear density of fractures in the measured interval. The linear densities of the fractures present in the study area were counted and calculated. Data used for that purpose mainly included imaging log data, which are highly continuous and can provide a full, more objective view of the basic conditions of fracture development on a large scale. Fullbore Formation MicroImager (FMI) is a recently developed new logging technology. The formation information obtained with this technology is more intuitive and provides more precise measurement results [49]. In an FMI diagram, the color represents the resistivity of the borehole wall. High-resistivity portions are marked in white while low-resistivity portions are marked in black. The imaging log data are displayed as individual pictures. Therefore, the results are more intuitive and more convenient for investigation. FMI has already demonstrated satisfactory application results in determining the formation and fracture attitude and recognizing fractures, especially in the development and exploration of complicated oil and gas reservoirs [45, 47, 48, 50].

In imaging logs, fractures undulate as sinusoidal curves. However, our focus herein is mainly on bedding fractures.

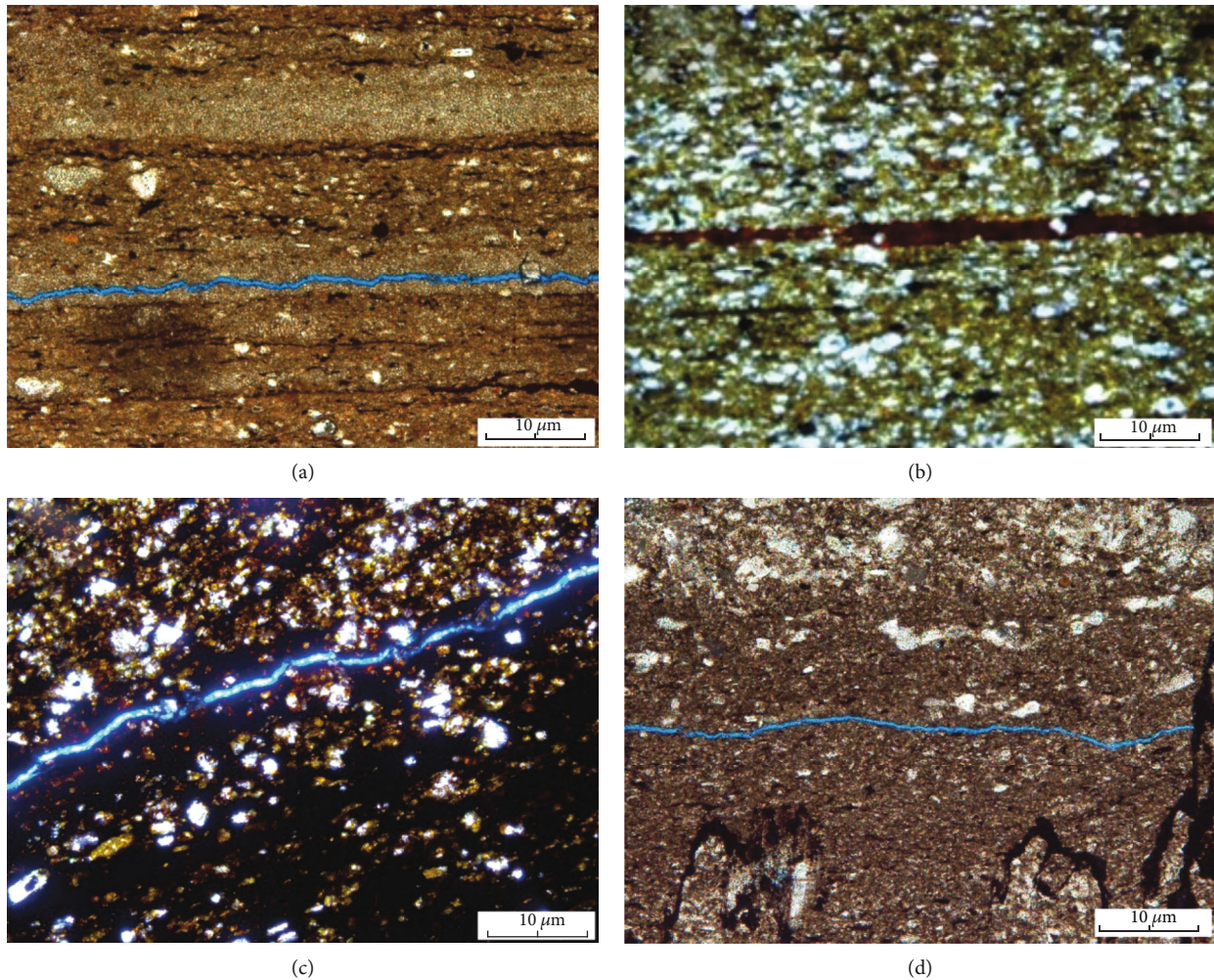


FIGURE 4: Photographs of bedding fractures in casting thin sections of rocks from Lucaogou formation in Jimsar sag. (a) Ji31, argillaceous siltstone, 2730.2 m; (b) Ji37, mudstone, 2853.9 m; (c) Ji251, dolomitic siltstone, 3769.3 m; (d) Ji251, gray sandstone, 3606.5 m.

Compared with structural fractures, the sinusoidal curve undulation of bedding fractures in imaging log diagrams is smaller. Their aperture is mostly smaller than that of structural fractures. Bedding fractures are approximately parallel to the bedding plane, while structural fractures mostly penetrate the bedding plane. On imaging log diagrams, the bedding fractures in the study area present themselves as low-angle, continuous, dense, and dark fine strips with the same attitude. They also look obviously darker than the adjacent bedding planes due to either the presence of organic matter inside them or the intrusion of drilling fluid (Figures 5(a)–5(c)).

The locations of fractures were determined according to the signatures of fractures in the imaging log data and verified against real cores (Figure 5(d)). The result showed good matching. According to the imaging log data, microscopically, Lucaogou formation is host to mainly structural fractures and bedding fractures, with bedding fractures existing in the largest quantity.

The fractures in the upper and lower sweet spots were, respectively, counted according to the imaging log recognition result. Although the bedding fractures recognized by

imaging logs were verified against real cores, there were still instances where beddings were misrecognized as bedding fractures. However, as a bedding plane is a structurally weak plane and locations with excessive beddings can easily rupture to produce bedding fractures in subsequent tectonic movement, the number of beddings in a formation is positively correlated with the number of bedding fractures therein. The number of bedding fractures measured by imaging log data is representative. It can reflect the development of bedding fractures in the formation on the macroscale.

Fractures present in the upper sweet spot were extensively recognized and counted according to the FMI data and some core data of 17 boreholes therein. Table 1 gives the counting result for the upper sweet spot. There, a total of 1468 bedding fractures were recognized. Their average linear density is 2.23/m.

Fractures present in the lower sweet spot were counted and calculated according to the FMI data and some core data of 9 boreholes therein. Table 2 gives the counting result for the lower sweet spot. A total of 1147 bedding fractures were recognized in the lower sweet spot of the study area. Their average linear density is 2.65/m.

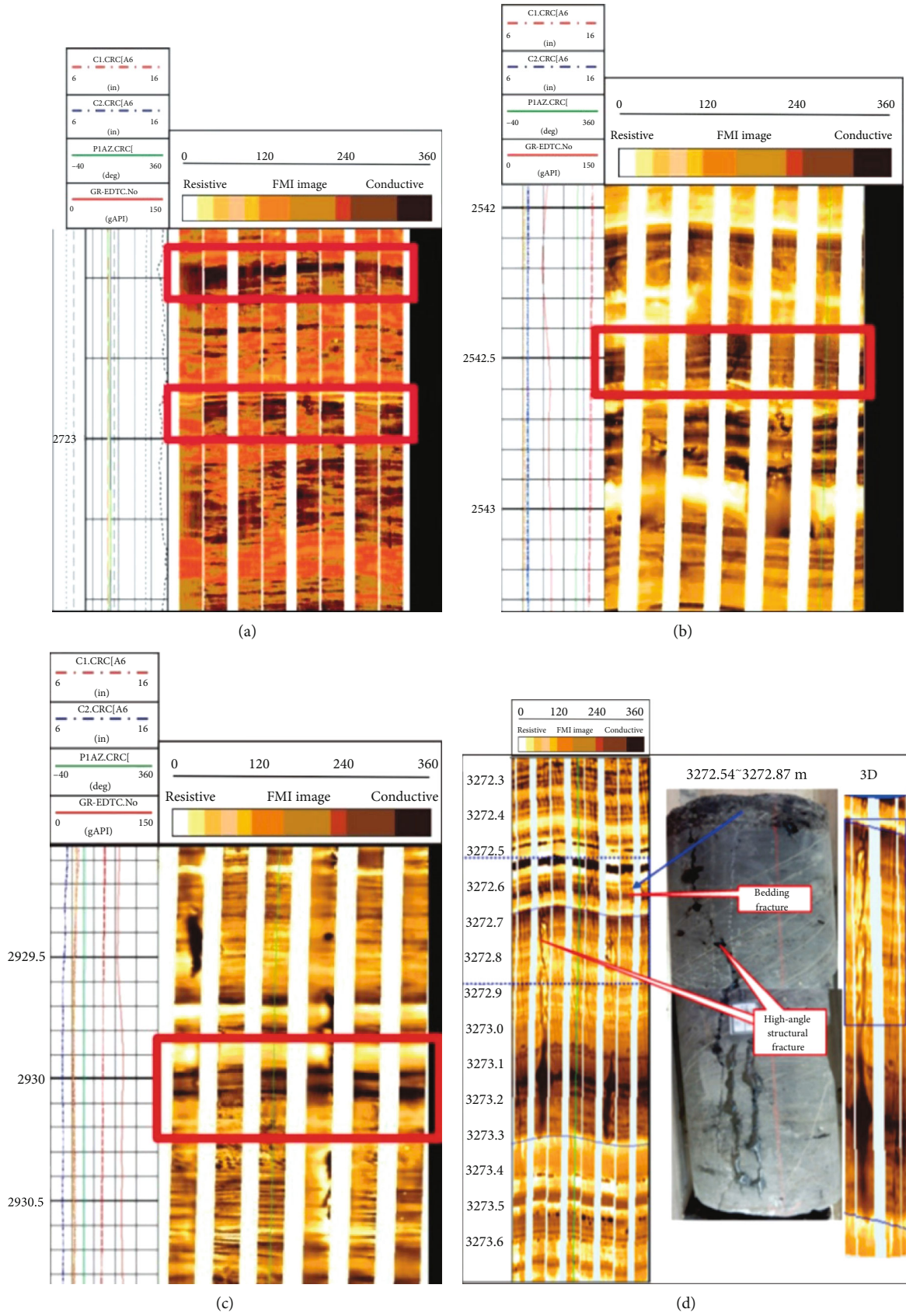


FIGURE 5: Imaging log identification diagrams of bedding fractures in Lucaogou formation in Jimsar sag. (a) Ji31, 2722.9 m; (b) Ji22, 2542.8 m; (c) Ji172, 2930 m. Note: (d) Ji174, 3272.54–3272.87 m, carbonaceous mudstone.

TABLE 1: Statistic of linear density of bedding fractures in the upper sweet spot of Lucaogou formation in Jimsar sag.

Borehole name	Statistical initial depth (m)	Statistical cutoff depth (m)	Statistical thickness (m)	No. of bedding fractures	Linear density of bedding fracture (fractures/m)
Ji172	2917.49	2955.67	38.18	117	3.06
Ji173	3077.65	3116.03	38.38	79	2.06
Ji174	3115.20	3152.40	37.20	128	3.44
Ji176	3022.64	3063.03	40.39	97	2.40
Ji22	2540.07	2575.90	35.83	59	1.65
Ji23	2318.58	2379.34	60.76	83	1.37
Ji25	3393.80	3429.70	35.90	41	1.14
Ji27	2281.84	2316.81	34.97	87	2.49
Ji29	2336.66	2370.10	33.44	96	2.87
Ji30	4018.80	4054.60	35.80	53	1.48
Ji31	2707.64	2749.24	41.60	93	2.24
Ji32	3548.61	3596.02	47.41	109	2.30
Ji33	3517.86	3568.04	50.18	64	1.28
Ji34	3651.76	3691.57	39.81	95	2.39
Ji35	3972.97	3985.13	12.16	21	1.73
Ji36	4117.00	4150.00	33.00	113	3.42
Ji37	2829.39	2871.97	42.58	133	3.12

TABLE 2: Statistic of linear density of bedding fractures in the lower sweet spot of Lucaogou formation in Jimsar sag.

Borehole name	Statistical initial depth (m)	Statistical cutoff depth (m)	Statistical thickness (m)	No of bedding fractures	Linear density of bedding fracture (fractures/m)
Ji174	3262.35	3311.55	49.20	178	3.62
Ji176	3174.41	3230.18	55.77	167	2.99
Ji30	4161.86	4203.83	41.97	89	2.12
Ji31	2874.87	2934.28	59.41	150	2.52
Ji32	3711.26	3745.53	34.27	115	3.36
Ji33	3667.37	3714.93	47.56	87	1.83
Ji34	3801.25	3861.91	60.66	151	2.49
Ji35	4041.86	4085.92	44.06	91	2.07
Ji36	4229.31	4269.44	40.13	119	2.97

Compared with the average linear density of fractures in the upper sweet spot, the linear density of fractures in the lower sweet spot is greater in general (Figure 6). That is, bedding fractures are more developed in the lower sweet spot.

The horizontal distribution of bedding fracture linear density was, respectively, predicted for the upper and lower sweet spots according to the linear densities of bedding fractures at each borehole location. As illustrated by the horizontal distribution charts of bedding fracture linear density for the two sweet spots (Figures 7(a) and 7(b)), across Jimsar sag, the predominant development area for bedding fractures falls in the central south. The development of bedding fractures is closely associated with the sedimentary beddings, which in turn are controlled by the sedimentary microfacies. Lucaogou formation is a continental deltaic sedimentary system as a whole having received quite a lot of material supply from the south. This also associates the development of bedding fractures with sedimentary environment.

4.2. Aperture of Bedding Fractures. Cores from 13 boreholes, including Ji174, were observed in the core library of Xinjiang Oilfield (Table 1). The color, lithology, type, and oil-bearing property of these core samples, as well as the type, aperture, and filling property of the fractures therein, were described and documented in great detail. As our focus was on bedding fractures, the aperture, filling property, and oil-bearing property of the bedding fractures were finely characterized (Table 3).

Next, we are going to describe the aperture distribution of the bedding fractures. Fracture aperture, namely, the distance between fracture walls, is an important measure of the seepage and storage capacity of fractures [49, 48, 50]. Due to the release of confining pressure during sample collection, the apparent aperture of the fractures is usually greater than the true aperture of fractures underground. Hence, to obtain the true aperture of fractures, an aperture correction formula will be needed to convert the apparent fracture aperture

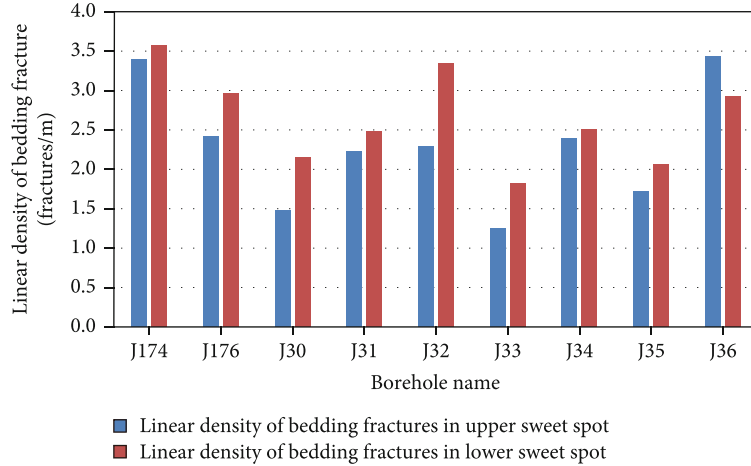


FIGURE 6: Comparing column chart of bedding fracture linear densities between the upper and lower sweet spots of Lucaogou formation in Jimsar sag.

observed in the cores into the true aperture of fractures underground. The following formula is used:

$$b_u = \frac{2b_s \cos^2\theta}{\pi}, \quad (2)$$

where b_s is the apparent aperture of fractures on the core, b_u is the true aperture of the fractures, and θ is the angle between the fracture surface and the measured surface [51, 52]. After measuring, correcting, and counting the aperture distribution of the fractures in the cores, a fan chart of the true aperture distribution of the fractures in the study area was drawn (Figure 8). From this chart, the aperture of the fractures in the tight reservoirs of Jimsar sag is quite small as a whole, with figures mostly concentrated in the 0–1.0 mm interval, which accounts for 72.13%. Fractures with aperture in the 0.5–1.0 mm interval are the greatest contributors with a share of 48.95%. Fractures with aperture greater than 1 mm are less developed.

4.3. Filling Property of Bedding Fractures. The filling property of fractures is an important measure of the effectiveness of fractures. As the filling degree of fractures increases, their effectiveness gradually reduces, and the formation porosity and permeability degrade.

After extensive core observation, the filling conditions of 617 bedding fractures were documented. By filling degree, these bedding fractures can be categorized as unfilled fractures, half-filled fractures, and fully filled fractures. By filling material, they can be categorized as calcite-filled, pelite-filled, asphalt-filled, pyrite-filled, others, and unfilled. Statistics discovered that the majority of the bedding fractures in Lucaogou formation are unfilled ones, accounting for 76.3% (Figures 9(a) and 9(b)). In the filled bedding fractures, the filling materials are primarily calcite, pelite, and asphalt.

4.3.1. Oil-Bearing Property of Bedding Fractures. From core observation of Ji174 and other boreholes, bedding fractures and structural fractures are important controlling factors for the oil-bearing property of a reservoir. Bedding fractures

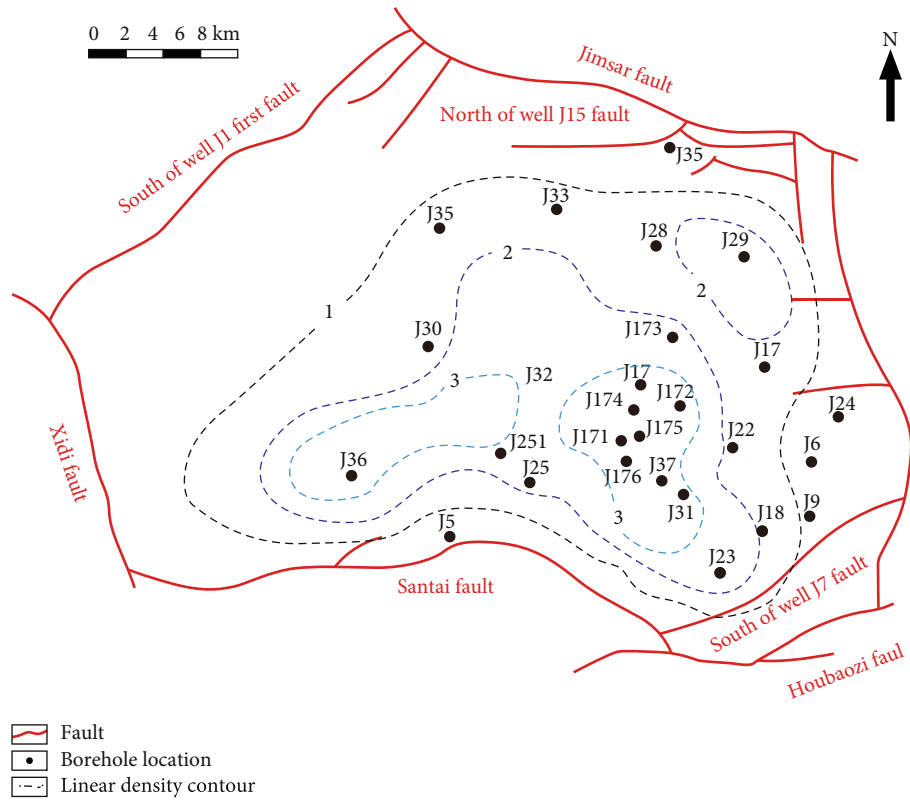
are present in the greatest quantity and with the best oil-bearing property (Figures 10(a) and 10(b)). From the photographs, we can easily see that locations with densely distributed bedding fractures have good oil-bearing property. Besides, the oil-bearing can also differ from one bedding fracture to another.

Two fracture network oil-bearing patterns were recognized in the densely fractured locations: bedding fracture network and bedding-structural fracture network (Figures 10(c) and 10(d)). Cores under both fracture network oil-bearing patterns have good oil-bearing property. In the fracture networks, we can see more distinct oil-bearing difference among bedding fractures.

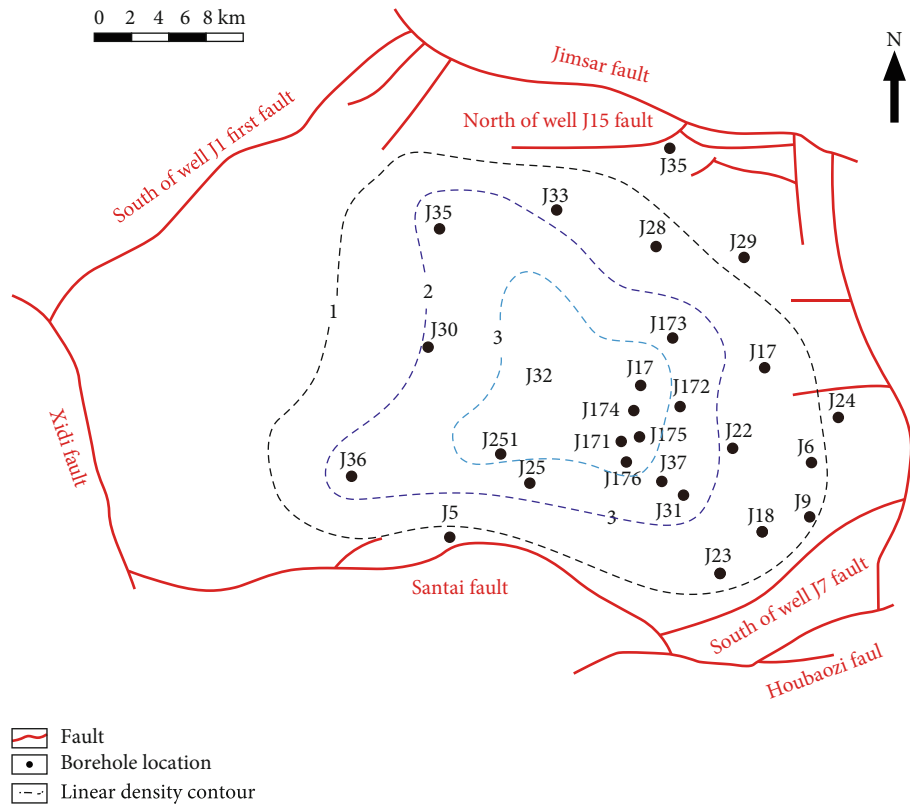
The oil-bearing grades of the observed fractures were counted. From the charts, we can easily see that bedding fractures have the best oil-bearing property whether for the oil-immersed or oil-spotted grade. Among the oil-immersed fractures, the number of bedding fractures is approximately 2.5 times that of structural fractures (Figure 11(a)). Among the oil-spotted fractures, the number of bedding fractures is approximately 1.4 times that of structural fractures (Figure 11(b)). The other types of fractures, such as water release fractures, are both poor in oil-bearing property and small in quantity. Statistics of the oil-bearing indication grades also confirms the differentiated oil-bearing among individual bedding fractures of Lucaogou formation.

5. Discussion

5.1. Definition of Factors Affecting the Differentiated Oil-Bearing of Bedding Fractures. Core observation revealed differentiated oil-bearing among individual bedding fractures, as results from the differentiated influences of factors affecting the oil-bearing of these fractures. In this section, we are going to discuss factors affecting the oil-bearing of bedding fractures from the temporal and spatial perspectives. The former mainly addresses the temporal coupling between the mass hydrocarbon generation of the source rocks of Lucaogou formation and the formation of the bedding fractures therein. The latter mainly considers the spatial coupling



(a)



(b)

FIGURE 7: (a) Linear density prediction map of bedding fractures in the upper sweet spot of Lucaogou formation in Jimsar sag. (b) Linear density prediction map of bedding fractures in the lower sweet spot of Lucaogou formation in Jimsar sag.

TABLE 3: Statistical table of number of bedding fractures observed in cores from Lucaogou formation in Jimsar sag.

Borehole name	Total coring length (m)	No. of bedding fractures
Ji23	25.41	37
Ji25	13.60	29
Ji27	4.30	4
Ji30	34.13	83
Ji31	32.18	40
Ji32	27.25	53
Ji36	3.56	6
Ji172	12.76	30
Ji173	14.92	28
Ji174	97.20	216
Ji251	45.16	91
Total	310.47	617

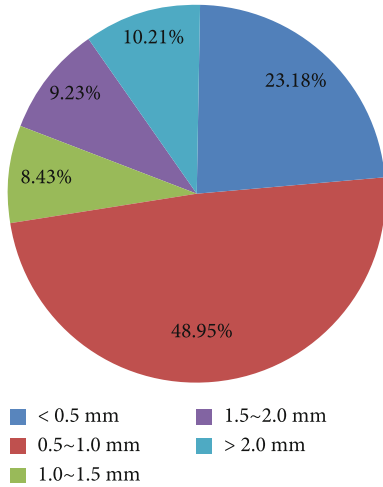


FIGURE 8: Fan chart of bedding fracture aperture distribution of Lucaogou formation in Jimsar sag.

between the development location of the bedding fractures and location of the source rocks.

5.2. Temporal Coupling. By temporal coupling, we refer to the matching of the mass hydrocarbon generation period of the source rocks of Lucaogou formation and the formation period of the bedding fractures therein in time. Here, our focus is on two periods: the mass hydrocarbon generation period of the source rocks of Lucaogou formation and the formation period of the bedding fractures therein. For purpose of examining the formation period of bedding fractures, fluid inclusion temperature measurement represents an effective method [19].

The fluid inclusions in the fracture-filling materials preserve a variety of information of the environment wherein the fracture filling materials formed [53–55], including the temperature at the time the inclusions were captured. By heating the inclusions and yielding their homogenization temperature, the paleotemperature of the fluids can be iden-

tified. At the time when inclusions formed, their phase was just single. As the burial depth changes, so do the environmental conditions, including temperature and pressure, around the inclusions. While the external environment changes, the volume of the inclusions remains the same. Hence, the phase of the fluids inside the inclusions will change with the external environment, turning the inclusions from single phase to multiphase. By heating these multiphase inclusions until they are restored to a homogeneous liquid phase, we can yield the homogenization temperature of the inclusions, which approximately represents the temperature of the fluids contained in the inclusions when they had just formed and accordingly the temperature of the formation when the inclusions formed [56, 57]. By combining this temperature with the burial history and geothermal history of Jimsar sag, the geological time of the inclusions, namely, the upper limit of the formation period of the fractures, can be determined. Further, by identifying the mass hydrocarbon generation period of the source rocks based on the hydrocarbon generation history of the source rocks in the basin, the coupling between the formation period of the bedding fractures and the mass hydrocarbon generation period of the source rocks in time can be investigated.

Inclusion temperature measurement specific to bedding fractures was performed on samples from 39 spots of the study area (Table 4). The bedding fracture filling materials are primarily calcite veins. The inclusions selected are typically large-volume, easily identifiable gas-liquid inclusions with distinct internal fluid phases. The inclusions are smaller than $1\ \mu\text{m}$ in volume. Most of the inclusions have a gas/liquid ratio between 10% and 20%. They are homogeneously captured inclusions. In the samples, they are mostly elliptical or circular in shape. After they were heated to the homogenized temperature, the air bubbles disappeared and they all turned out to be liquid phase.

The homogenization temperature of the inclusions was yielded through experiment. From the homogenization temperature distribution histogram (Figure 12(a)), the homogenization temperature of the samples spans from 60 to 95°C . For most of the samples, the homogenization temperature is between 80 and 95°C , with the largest number of samples falling in the 85°C – 90°C interval.

By combining the homogenization temperature of the inclusions with the paleogeotemperature of Jimsar sag, the formation period of the bedding fractures can be established. Regarding the paleogeotemperature of Jimsar sag, some authors have already attempted to reconstruct the geothermal history of this sag [19] (Figure 12(b)). From the diagram, we can easily see that the geotemperature of Lucaogou formation reached 80°C in Early Cretaceous. After that, it has stayed between 80 and 90°C most of the time. In light of the thermometric interval of the inclusions, the formation period for the majority of the bedding fractures should be in or after Early Cretaceous.

Regarding the mass hydrocarbon generation period of the source rocks of Jimsar sag, some authors have investigated the hydrocarbon generation history of Lucaogou formation based on the burial history and thermal history of Jimsar sag [58, 27] (Figure 12(c)). They discovered that

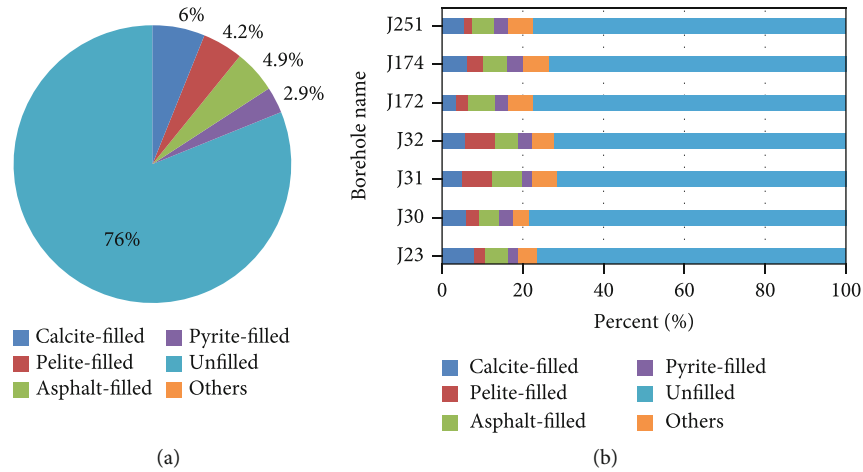


FIGURE 9: (a) Fan chart of bedding fracture filling of Lucaogou formation in Jimsar sag. (b) Stacked bar graph of bedding fracture filling condition in each borehole in Lucaogou formation in Jimsar sag.

Lucaogou formation began hydrocarbon generation in Late Triassic ($R_o = 0.5\%$) and mass hydrocarbon generation in Late Jurassic ($R_o = 0.7\%$, the portion in red). In that case, Late Jurassic should mark the beginning of mass hydrocarbon generation for the source rocks of Lucaogou formation in Jimsar sag.

By correlating the thermal history, hydrocarbon generation history of Jimsar sag with the homogenization temperature of the inclusions therein as described above, we discovered that the formation began mass hydrocarbon generation in Late Jurassic. Based on the inclusion temperature measurement result, the bedding fractures formed in or after Early Cretaceous. As Jimsar sag is simply structured, its exposure to tectonic movement has been quite modest. Hence, by matching the mass hydrocarbon generation period of the source rocks with the formation period of the bedding fractures therein, we found that the bedding fractures formed within the mass hydrocarbon generation period of the source rocks, which favored the oil-bearing of the bedding fractures.

5.3. Spatial Coupling. Regarding the factors affecting the oil-bearing property of bedding fractures, apart from the temporal coupling of the formation of these fractures with mass hydrocarbon generation of the source rocks, their spatial coupling with the source rocks is also important [59, 60]. That is, the development location of the bedding fractures in the formation matches and interacts with the location of the source rocks. Source rocks normally have a high abundance of organic matter. If the bedding rocks occur close to or right inside the source rocks, they can easily accumulate oil. Hence, TOC constitutes an affecting factor. For bedding fractures far away from the source rocks, migration will be needed for them to accumulate oil. Hence, porosity, permeability, and even the size of pore throat are affecting factors. Here, we are going to discuss the spatial coupling between bedding fractures and source rocks from the perspective of TOC, porosity, permeability, and pore throat.

5.3.1. Determination of the Oil-Bearing Indicator of Bedding Fractures. Regarding the oil-bearing property of bedding

fractures, through core observation, we can easily tell how good the oil-bearing property is for individual fractures [61, 62]. However, as the number of cores available is limited, so is the number of bedding fractures observable therein. To investigate the oil-bearing property of the bedding fractures in the entire Lucaogou formation, we have to find a proper indicator. Through correlation in terms of time, we established that in Lucaogou formation, mass hydrocarbon generation occurred before the formation of bedding fractures. In that case, the oil and gas generated should have been stored in the pores of the formation. Furthermore, after extensive core observation, we also found that if the oil-bearing property of a bedding fracture is good, that of the surrounding formation matrix will be good, too. So the oil content of the formation matrix would be an ideal indirect indicator for the oil content of the bedding fractures developed therein. In the absence of coupling with other fractures, we suggest that the greater the oil content of the matrix, the better the oil-bearing property of the bedding fractures developed therein. As the oil contained in bedding fractures is free petroleum, here we used chloroform asphalt “A” to represent the oil-bearing of bedding fractures. Chloroform asphalt “A” is the organic matter dissolved and extracted from rocks using chloroform. Generally, the mass percentage of chloroform asphalt “A” in the rock is used to represent the content of chloroform asphalt “A.”

5.3.2. TOC. After analyzing the TOC levels of the rock samples [63], we discovered that all three types of rocks are high in organic matter, with average TOC of 2.83%. For dolomite, the TOC range is 0.39%–4.65% with an average of 2.27%. For siltstone, the TOC range is 0.57%–4.16% with an average of 2.47%. For mudstone, the TOC range is 0.91%–8.50% with an average of 3.99% (Figure 13). Among the three types of rocks, the mudstone has the highest TOC.

By examining the relationship between chloroform asphalt “A” and TOC, we can easily see that overall, the chloroform asphalt “A” of the formation matrix (the oil content of the strata) is positively correlated with TOC. That is, the larger the TOC, the larger the chloroform asphalt “A,”

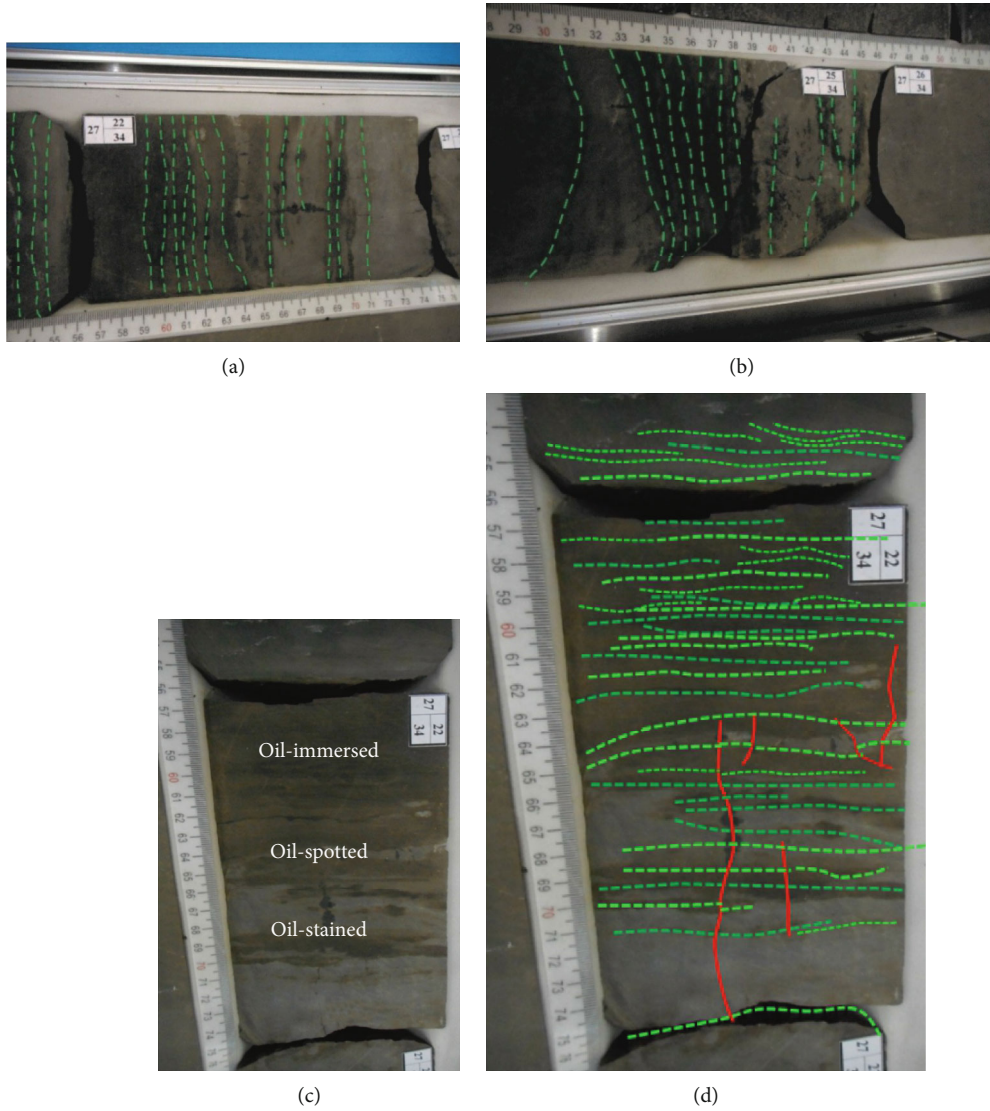


FIGURE 10: Core photographs of Lucaogou formation in Jimsar sag. (a) Ji174, 3305.8 m; (b) Ji174, 3307.2 m; (c) core photograph of Ji174, 3305.1 m; (d) interpreted core photograph of Ji174, 3305.1 m.

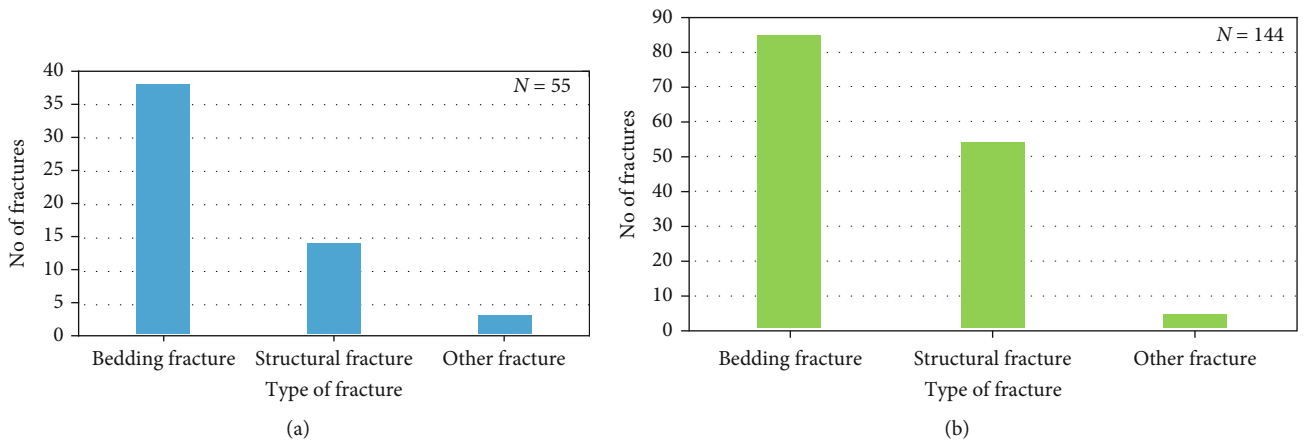


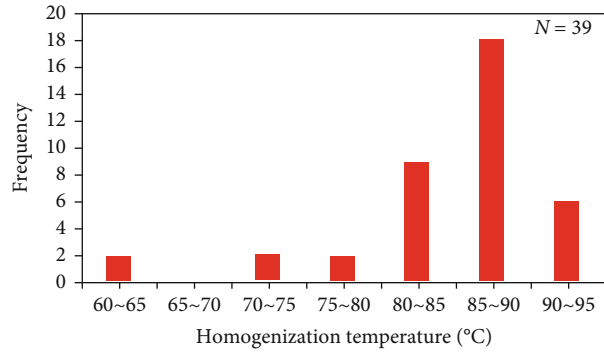
FIGURE 11: (a) Statistical chart of number of oil-immersed fractures in cores from Lucaogou formation in Jimsar sag; (b) statistical chart of number of oil-spotted fractures in cores from Lucaogou formation in Jimsar sag.

TABLE 4: Fluid inclusion parameter table of bedding fracture fillers in Lucaogou formation.

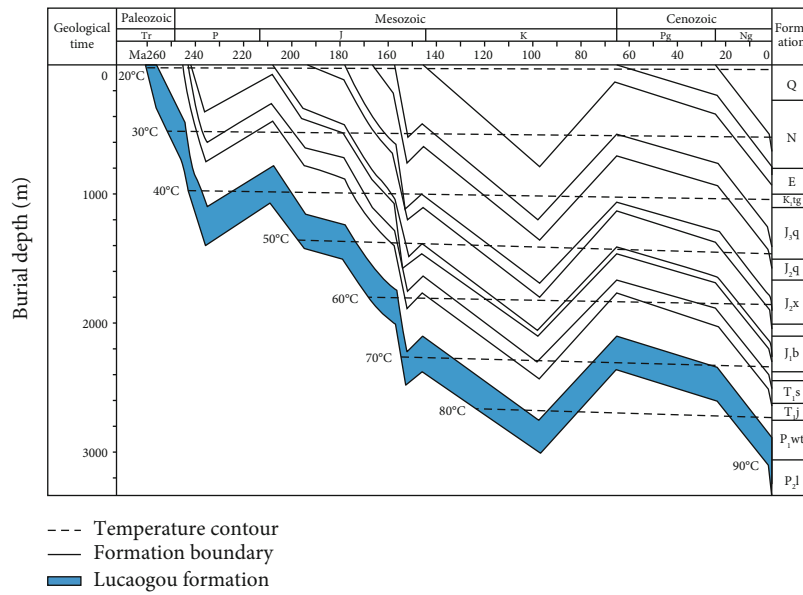
SN	Host mineral	Origin	Type	Gas/liquid ratio (%)	Homogenization Temp. (°C)
1	Calcite	Secondary	Liquid inclusion	10	86
2	Calcite	Secondary	Liquid inclusion	15	85.6
3	Calcite	Secondary	Liquid inclusion	10	74
4	Calcite	Secondary	Liquid inclusion	15	87
5	Calcite	Secondary	Liquid inclusion	10	81
6	Calcite	Secondary	Liquid inclusion	10	88.2
7	Calcite	Secondary	Liquid inclusion	15	85.9
8	Calcite	Secondary	Liquid inclusion	5	80.3
9	Calcite	Secondary	Liquid inclusion	10	89
10	Calcite	Secondary	Liquid inclusion	10	87.2
11	Calcite	Secondary	Liquid inclusion	15	92
12	Calcite	Secondary	Liquid inclusion	15	82.2
13	Calcite	Secondary	Liquid inclusion	20	91
14	Calcite	Secondary	Liquid inclusion	10	62
15	Calcite	Secondary	Liquid inclusion	20	94.2
16	Calcite	Secondary	Liquid inclusion	15	87.5
17	Calcite	Secondary	Liquid inclusion	10	80.8
18	Calcite	Secondary	Liquid inclusion	15	89.5
19	Calcite	Secondary	Liquid inclusion	15	90.5
20	Calcite	Secondary	Liquid inclusion	10	72.5
21	Calcite	Secondary	Liquid inclusion	15	88
22	Calcite	Secondary	Liquid inclusion	10	82.6
23	Calcite	Secondary	Liquid inclusion	10	87.3
24	Calcite	Secondary	Liquid inclusion	15	86.5
25	Calcite	Secondary	Liquid inclusion	10	84
26	Calcite	Secondary	Liquid inclusion	15	91
27	Calcite	Secondary	Liquid inclusion	10	89.1
28	Calcite	Secondary	Liquid inclusion	15	79.4
29	Calcite	Secondary	Liquid inclusion	10	85.5
30	Calcite	Secondary	Liquid inclusion	10	83
31	Calcite	Secondary	Liquid inclusion	15	93
32	Calcite	Secondary	Liquid inclusion	10	83.6
33	Calcite	Secondary	Liquid inclusion	5	61.5
34	Calcite	Secondary	Liquid inclusion	10	89.3
35	Calcite	Secondary	Liquid inclusion	10	76.2
36	Calcite	Secondary	Liquid inclusion	10	88.1
37	Calcite	Secondary	Liquid inclusion	15	82
38	Calcite	Secondary	Liquid inclusion	10	86.3
39	Calcite	Secondary	Liquid inclusion	15	89

accordingly the higher the oil content of the formation and the better the oil-bearing property of the bedding fractures developed therein (Figure 14). However, in the diagram, we also observed three anomalous spots (as marked by red ellipses) that show very high TOC but very low chloroform asphalt “A” (Figure 14). Moreover, the rocks of all three spots are mudstone and dolomite, which are both a type of rock with low overall porosity. Further analysis revealed that the porosity of all three spots is very low. The porosity of the

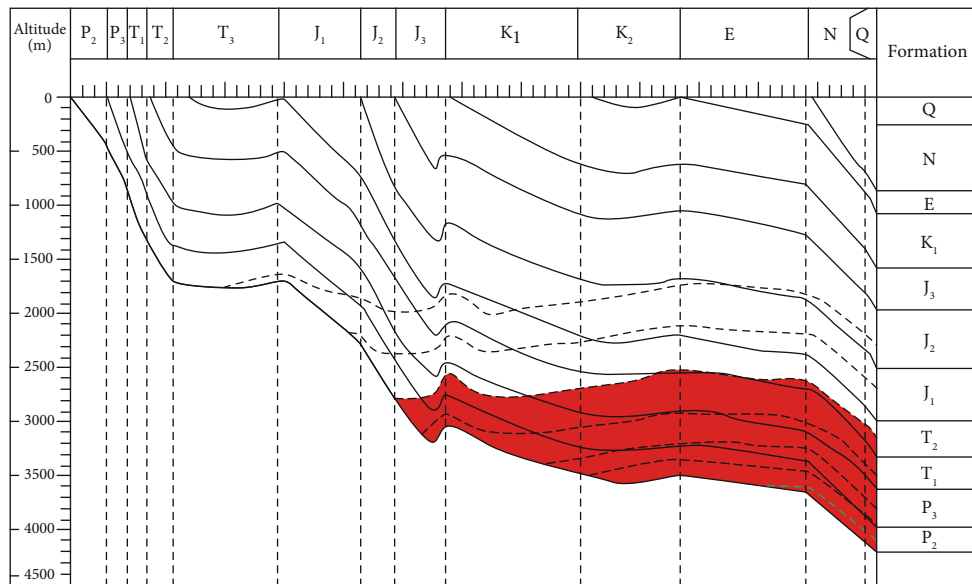
dolomite sample is 4.33%. That of the two mudstone samples is 1.25% and 3.18%, respectively. The low chloroform asphalt “A” of these spots is caused by their low porosity and limited storage spaces inside themselves, which limit their respective oil content. However, in Lucaogou formation, mudstone is the main source rock with great hydrocarbon generation potential [64]. All these spots have very high TOC. They have great hydrocarbon generation potential and the ability to generate hydrocarbon continuously. Hence, for the oil-



(a)



(b)



(c)

FIGURE 12: (a) Homogenization temperature distribution histogram of samples from Lucaogou formation. (b) Burial history and thermal history diagram of Jimsar sag. (c) Burial history and hydrocarbon generation history diagram of Jimsar sag.

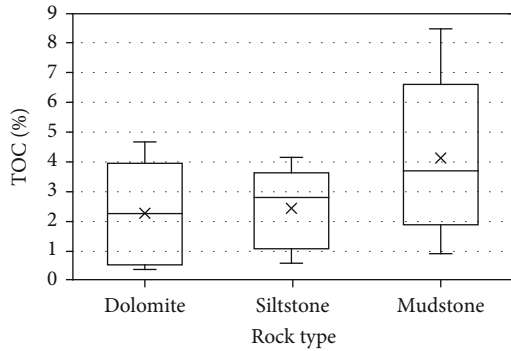


FIGURE 13: Box diagram of TOC value distribution of rock samples from Lucaogou formation.

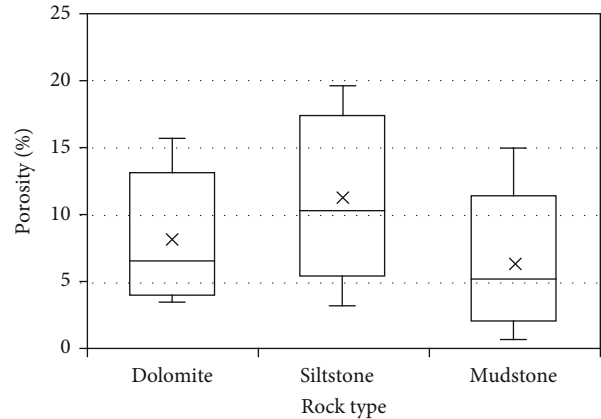


FIGURE 15: Box diagram of porosity distribution of samples from Lucaogou formation.

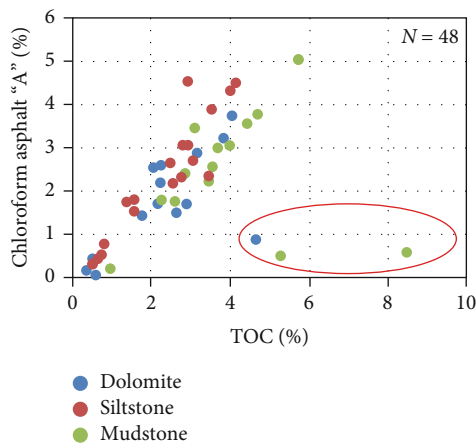


FIGURE 14: Relation diagram of chloroform asphalt “A” and TOC value of rock samples from Lucaogou formation.

bearing of bedding fractures, high TOC is a good contributor. In this sense, TOC is positively correlated with the oil-bearing property of bedding fractures.

5.3.3. *Porosity.* Pores are important storage spaces for tight oil. In this paper, we also examined the relationship between porosity and the oil-bearing property of bedding fractures. From the porosity distribution diagram, we can also see that dolomite, siltstone, and mudstone all exhibit a fairly broad porosity range, with siltstone having the highest average porosity, followed by dolomite and mudstone (Figure 15). For siltstone, the porosity range is 3.29%–19.60% with an average of 11.02%. For dolomite, the porosity range is 3.64%–15.71% with an average of 8.28%. For mudstone, the porosity range is 0.69%–14.90% with an average of 6.09%.

As discovered from analysis above, porosity affects the level of chloroform asphalt “A.” In the present study, we also investigated the relationship between chloroform asphalt “A” and porosity (Figure 16). From the relationship diagram, we can see that overall, porosity is positively correlated with chloroform asphalt “A.” That is, the larger the porosity, the larger the chloroform asphalt “A,” accordingly the higher the oil content of the formation matrix and the better the oil-bearing property of the bedding fractures developed therein. After further analysis, we also discovered a couple

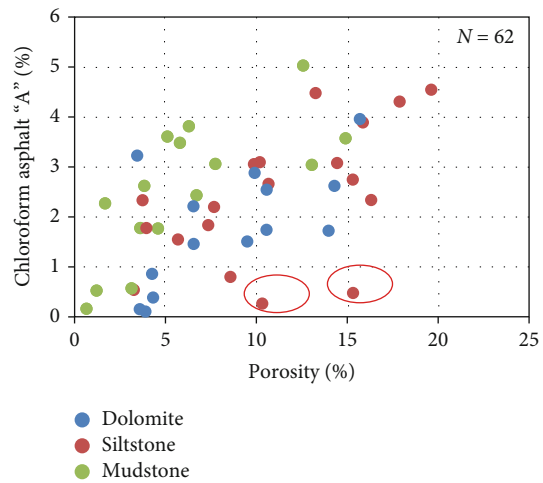


FIGURE 16: Relation diagram of chloroform asphalt “A” and porosity of rock samples from Lucaogou formation.

of anomalous spots (as marked by red ellipses) that have fairly high porosity but very low chloroform asphalt “A.” A closer look at the TOC of these spots revealed that the TOC of both spots is very low—0.61% and 0.57%, respectively, (Figure 16). This indicates that the hydrocarbon generation potential of these spots is very low, which explains why these anomalous spots should exist. The TOC is low. Their own hydrocarbon generation potential is low. The oil and gas generated could not fill up their own pores, and the tight oil outside did not migrate in. Accordingly, the oil-bearing property of the bedding fractures developed in the formation will be poor. Existence of these anomalous spots suggests that porosity is essentially controlled by TOC.

At large, the oil-bearing property of bedding fractures is positively correlated with the formation porosity, since pores are the storage spaces for tight oil. As most of the rocks in Lucaogou formation have a level of hydrocarbon generation potential and the tight oil generated will fill up the whole pores, high-porosity bedding fractures there will have good oil-bearing property. However, this does not apply to all

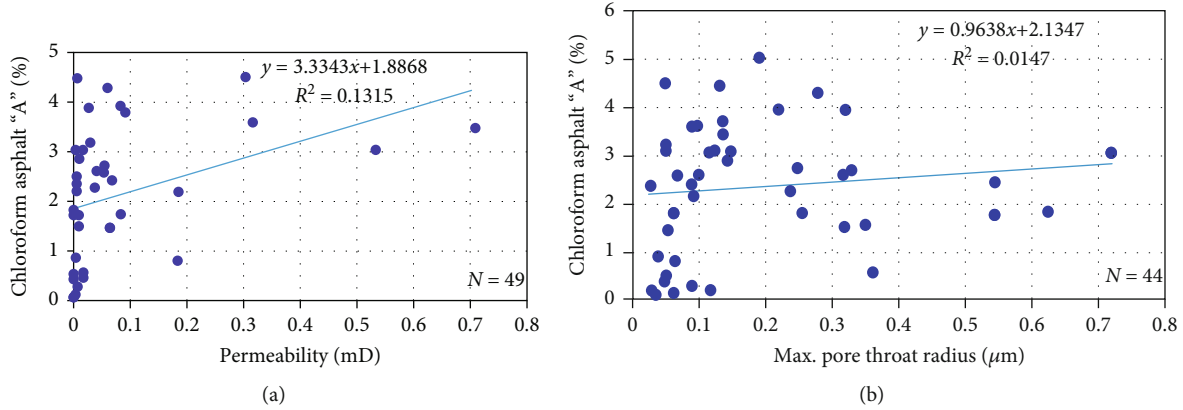


FIGURE 17: (a) Relation diagram of chloroform asphalt “A” and permeability of rock samples from Lucaogou formation. (b) Relation diagram of chloroform asphalt “A” and maximum pore throat radius of rock samples from Lucaogou formation.

bedding fractures. If the host formation has very high porosity but very low TOC, the bedding fractures will have to rely on migration to bear oil. Then, porosity and pore throat will make a difference to the oil-bearing of the bedding fractures. However, tight oil migration is not likely to happen in Lucaogou formation given its tight strata.

5.3.4. Permeability and Pore Throat. Permeability and pore throat are key parameters affecting tight oil migration. In strata with large porosity but small TOC, for tight oil to migrate into the bedding fractures, permeability and pore throat will become key factors affecting the oil-bearing of these bedding fractures. The relationship of chloroform asphalt “A” with permeability (Figure 17(a)) and with maximum pore throat radius (Figure 17(b)) was, respectively, analyzed. From the scatter diagrams, we can see that the correlation coefficient between permeability and chloroform asphalt “A” is 0.1315, and that between maximum pore throat radius and chloroform asphalt “A” is 0.0147. Chloroform asphalt “A” is almost not correlated with either permeability or pore throat. That is, permeability and pore throat make little difference to the oil-bearing of bedding fractures.

After examining the permeability and pore throat data, we discovered that samples with permeability smaller than 0.1 mD account for more than 90%. After excluding anomalous values, the average permeability is 0.07 mD, suggesting a typical tight reservoir. For the majority of the samples, the maximum pore throat radius is smaller than 0.4 μm . According to the pore throat classification criteria for low-permeability sandstone [65, 66] (Table 5), the pore throats are basically all microthroats.

According to the mercury injection statistics, for the rock samples tested, the average displacement pressure is 9.22 MPa; the average saturation median pressure is 31.72 MPa; the average maximum pore throat radius is 0.18 μm ; the average median radius is 0.08 μm . These figures strongly confirm that tight oil migration is not likely to happen in Lucaogou formation unless there is a huge pressure difference. Hence, the influence of permeability and pore throat on the oil-bearing of bedding fractures is quite modest. Only when the formation porosity is large and the TOC is

TABLE 5: Classification criteria for pore and throat in low permeability sandstone [66].

Throat size rating	Prevailing throat radius (μm)
Coarse throat	>4
Medium throat	2–4
Fine throat	1–2
Tiny throat	0.5–1
Microthroat	0.025–0.5
Adsorption throat	<0.025

small will the bedding fractures rely on migration to bear oil. Accordingly, only then will permeability and pore throat become the deciding factors for the oil-bearing of bedding fractures.

Among the factors considered for spatial coupling, for TOC, the larger the formation TOC, the better the oil-bearing of the bedding fractures. For porosity, subject to the TOC, if the TOC is adequate, the larger the porosity, the larger the chloroform asphalt “A,” accordingly the higher the oil content of the strata and the better the oil-bearing property of the bedding fractures developed therein. If the TOC is inadequate and the porosity is large, the bedding fractures will have to rely on migration to bear oil. In that case, permeability and pore throat will make a difference to the oil-bearing of the bedding fractures. However, as the strata of Lucaogou formation are tight, tight oil migration is not likely to happen there. Hence, in terms of spatial coupling, TOC is the main controlling factor for the oil-bearing property of bedding fractures.

6. Conclusions

- (1) Bedding fractures are extensively present in Lucaogou formation tight oil reservoir in Jimsar sag. In fact, they are the most frequently found type of fractures there. Statistics and calculation show that the linear density of the bedding fractures is 2.23/m for the upper sweet spot and 2.65/m for the lower sweet spot.

By comparison, bedding fractures are more developed in the lower sweet spot

- (2) The favorable area for the development of bedding fractures lies in the central south of the sag. Overall, these fractures occur in parallel to the formation boundary. Their aperture is quite small. Most of them are unfilled fractures. For the filled fractures, the filling materials mainly include calcite, petite, and asphalt. Among the few types of fractures found in Lucaogou formation, bedding fractures have the best oil-bearing property, but the oil-bearing can differ from one bedding fracture to another
- (3) The factors affecting the differentiated oil-bearing of the bedding fractures include temporal coupling and spatial coupling. In terms of temporal coupling, the majority of the bedding fractures in Lucaogou formation formed in or after Early Cretaceous, while the source rocks of this formation began mass hydrocarbon generation in Late Jurassic. By matching these two periods, we suggest that the bedding fractures formed within the mass hydrocarbon generation period of the source rocks, which favored the oil-bearing of these fractures. In terms of spatial coupling, the influencing factors include TOC, porosity, permeability, and pore throat, with TOC being the main controlling factor

Data Availability

All data, models, and code generated or used during the study appear in the submitted article.

Conflicts of Interest

The authors declare that they have no conflicts of interest.

Authors' Contributions

Jia Lu and Chen Zhang contributed equally to this work.

Acknowledgments

This work is financially supported by the grants from the National Natural Science Foundation of China (No. 42002050) and the China Postdoctoral Science Foundation Funded Project (No. 2020M680815).

References

- [1] Z. Caineng, Y. Zhi, Z. Rukai et al., "Progress in China's unconventional oil & gas exploration and development and theoretical technologies," *Acta Geologica Sinica-English Edition*, vol. 89, no. 3, pp. 938–971, 2015.
- [2] H. Wang, F. Ma, X. Tong et al., "Assessment of global unconventional oil and gas resources," *Petroleum Exploration and Development*, vol. 43, no. 6, pp. 925–940, 2016.
- [3] Y. Song, Z. Li, Z. Jiang, Q. Luo, D. Liu, and Z. Gao, "Progress and development trend of unconventional oil and gas geological research," *Petroleum Exploration and Development*, vol. 44, no. 4, pp. 675–685, 2017.
- [4] X. Tong, G. Zhang, Z. Wang et al., "Distribution and potential of global oil and gas resources," *Petroleum Exploration and Development*, vol. 45, no. 4, pp. 779–789, 2018.
- [5] X. Guo, Y. Li, R. Liu, and Q. Wang, "Characteristics and controlling factors of micropore structures of the Longmaxi Shale in the Jiaoshiba area, Sichuan Basin," *Natural Gas Industry B*, vol. 1, no. 2, pp. 165–171, 2014.
- [6] Y. Cai, D. Liu, Z. Pan, Y. Yao, and C. Li, "Mineral occurrence and its impact on fracture generation in selected Qinshui Basin coals: an experimental perspective," *International Journal of Coal Geology*, vol. 150–151, pp. 35–50, 2015.
- [7] G. Aghli, R. Moussavi-Harami, and R. Mohammadian, "Reservoir heterogeneity and fracture parameter determination using electrical image logs and petrophysical data (a case study, carbonate Asmari Formation, Zagros Basin, SW Iran)," *Petroleum Science*, vol. 17, no. 1, pp. 51–69, 2020.
- [8] J. Shi, L. Zeng, X. Zhao, Y. Zhang, and J. Wang, "Characteristics of natural fractures in the upper Paleozoic coal bearing strata in the southern Qinshui Basin, China: implications for coalbed methane (CBM) development," *Marine and Petroleum Geology*, vol. 113, p. 104152, 2020.
- [9] S. Bergbauer and D. D. Pollard, "A new conceptual fold-fracture model including prefolding joints, based on the Emigrant Gap anticline, Wyoming," *Geological Society of America Bulletin*, vol. 116, no. 3, pp. 294–307, 2004.
- [10] O. Lacombe, N. Bellahsen, and F. Mouthereau, "Fracture patterns in the Zagros Simply Folded Belt (Fars, Iran): constraints on early collisional tectonic history and role of basement faults," *Geological Magazine*, vol. 148, no. 5–6, pp. 940–963, 2011.
- [11] J. F. Gale, S. E. Laubach, J. E. Olson, P. Eichhuble, and A. Fall, "Natural fractures in shale: a review and new observations," *AAPG Bulletin*, vol. 98, no. 11, pp. 2165–2216, 2014.
- [12] Q. Wang, W. Liu, L. Pei et al., "Hydrocarbon generation from calcium stearate: insights from closed-system pyrolysis," *Marine and Petroleum Geology*, vol. 126, article 104923, 2021.
- [13] J. Parnell, P. Carey, and B. Monson, "Fluid inclusion constraints on temperatures of petroleum migration from authigenic quartz in bitumen veins," *Chemical Geology*, vol. 129, no. 3–4, pp. 217–226, 1996.
- [14] D. Feng and D. Chen, "Authigenic carbonates from an active cold seep of the northern South China Sea: new insights into fluid sources and past seepage activity," *Deep Sea Research Part II: Topical Studies in Oceanography*, vol. 122, pp. 74–83, 2015.
- [15] T. P. Harding and J. D. Lowell, "Structural styles, their plate-tectonic habitats, and hydrocarbon traps in petroleum provinces," *AAPG Bulletin*, vol. 63, no. 7, pp. 1016–1058, 1979.
- [16] B. Sanford, F. Thompson, and G. McFall, "Plate tectonics—a possible controlling mechanism in the development of hydrocarbon traps in southwestern Ontario," *Bulletin of Canadian Petroleum Geology*, vol. 33, no. 1, pp. 52–71, 1985.
- [17] Z. Wu and J. Yin, "Fracturing behaviors of FRP-strengthened concrete structures," *Engineering Fracture Mechanics*, vol. 70, no. 10, pp. 1339–1355, 2003.
- [18] X. Zhang, R. G. Jeffrey, and M. Thiercelin, "Deflection and propagation of fluid-driven fractures at frictional bedding

- interfaces: a numerical investigation," *Journal of Structural Geology*, vol. 29, no. 3, pp. 396–410, 2007.
- [19] D. Liu, C. Zhang, Z. Pan et al., "Natural fractures in carbonate-rich tight oil reservoirs from the Permian Lucaogou Formation, southern Junggar Basin, NW China: insights from fluid inclusion microthermometry and isotopic geochemistry," *Marine and Petroleum Geology*, vol. 119, p. 104500, 2020.
- [20] X. Zhang and R. G. Jeffrey, "Reinitiation or termination of fluid-driven fractures at frictional bedding interfaces," *Journal of Geophysical Research: Solid Earth*, vol. 113, no. B8, 2008.
- [21] X. Chang, Y. Shan, Z. Zhang, C. Tang, and Z. Ru, "Behavior of propagating fracture at bedding interface in layered rocks," *Engineering Geology*, vol. 197, pp. 33–41, 2015.
- [22] H. P. Lee, J. E. Olson, J. Holder, J. F. Gale, and R. D. Myers, "The interaction of propagating opening mode fractures with preexisting discontinuities in shale," *Journal of Geophysical Research: Solid Earth*, vol. 120, no. 1, pp. 169–181, 2015.
- [23] L. Jijun, W. Weiming, C. Qun, S. Yinglin, Y. Xintong, and T. Shansi, "Impact of hydrocarbon expulsion efficiency of continental shale upon shale oil accumulations in eastern China," *Marine and Petroleum Geology*, vol. 59, pp. 467–479, 2015.
- [24] H. Liu, S. Zhang, G. Song et al., "A discussion on the origin of shale reservoir inter-laminar fractures in the Shahejie Formation of Paleogene, Dongying depression," *Journal of Earth Science*, vol. 28, no. 6, pp. 1064–1077, 2017.
- [25] M. Zheng, J. Li, X. Wu et al., "Physical modeling of oil charging in tight reservoirs: a case study of Permian Lucaogou Formation in Jimsar Sag, Junggar Basin, NW China," *Petroleum Exploration and Development*, vol. 43, no. 2, pp. 241–250, 2016.
- [26] C. Zhang, D. Zhu, Q. Luo et al., "Major factors controlling fracture development in the Middle Permian Lucaogou Formation tight oil reservoir, Junggar Basin, NW China," *Journal of Asian Earth Sciences*, vol. 146, pp. 279–295, 2017.
- [27] Y. Yang, L. Qiu, M. Wan et al., "Depositional model for a salinized lacustrine basin: the permian Lucaogou formation, Jimsar sag, Junggar Basin, NW China," *Journal of Asian Earth Sciences*, vol. 178, pp. 81–95, 2019.
- [28] Y. Yang, J. Yang, G. Yang et al., "New research progress of Jurassic tight oil in central Sichuan Basin, SW China," *Petroleum Exploration and Development*, vol. 43, no. 6, pp. 954–964, 2016.
- [29] H. Yang, X. Liang, X. Niu, S. Feng, and Y. You, "Geological conditions for continental tight oil formation and the main controlling factors for the enrichment: a case of Chang 7 Member, Triassic Yanchang Formation, Ordos Basin, NW China," *Petroleum Exploration and Development*, vol. 44, no. 1, pp. 11–19, 2017.
- [30] H. Dou, S. Ma, C. Zou, and S. Yao, "Threshold pressure gradient of fluid flow through multi-porous media in low and extra-low permeability reservoirs," *Science China Earth Sciences*, vol. 57, no. 11, pp. 2808–2818, 2014.
- [31] H. Bai, X. Pang, L. Kuang et al., "Hydrocarbon expulsion potential of source rocks and its influence on the distribution of lacustrine tight oil reservoir, Middle Permian Lucaogou Formation, Jimsar Sag, Junggar Basin, Northwest China," *Journal of Petroleum Science and Engineering*, vol. 149, pp. 740–755, 2017.
- [32] Q. Wang, Y. Qin, W. Jia, Y. Wang, W. Zhang, and P. A. Peng, "Density and viscosity of tight oil from Yanchang Formation, Ordos Basin, China and the geochemical controls," *Petroleum Science and Technology*, vol. 36, no. 16, pp. 1298–1304, 2018.
- [33] G. Xiu e, "Relation between the productivity and the degree of development of the fractures in low porosity and low permeability sandshale reservoirs," *Natural Gas Industry*, vol. 23, no. 5, pp. 41–43, 2003.
- [34] O. Pal, B. Zoghbi, and W. Razzaq, "Characterization of unconventional reservoir for development and production: an integrated approach," in *Proceedings SPE Middle East Unconventional Resources Conference and Exhibition 2015, Society of Petroleum Engineers, Muscat, Oman, January 2015*.
- [35] W. Hu, Y. Wei, and J. Bao, "Development of the theory and technology for low permeability reservoirs in China," *Petroleum Exploration and Development*, vol. 45, no. 4, pp. 685–697, 2018.
- [36] Y. Yang, L. Qiu, Y. Cao, C. Chen, D. Lei, and M. Wan, "Reservoir quality and diagenesis of the Permian Lucaogou Formation tight carbonates in Jimsar Sag, Junggar Basin, west China," *Journal of Earth Science*, vol. 28, no. 6, pp. 1032–1046, 2017.
- [37] Y. Zhi, H. Lianhua, L. Senhu et al., "Geologic characteristics and exploration potential of tight oil and shale oil in Lucaogou Formation in Jimsar sag," *China Petroleum Exploration*, vol. 23, no. 4, pp. 76–85, 2018.
- [38] Y. Feng, R. G. Coleman, G. Tilton, and X. Xiao, "Tectonic evolution of the west Junggar region, Xinjiang, China," *Tectonics*, vol. 8, no. 4, pp. 729–752, 1989.
- [39] Z. Xixi, R. S. Coe, Z. Yaoxiu, W. HaoRuo, and W. Jie, "New paleomagnetic results from northern China: collision and suturing with Siberia and Kazakhstan," *Tectonophysics*, vol. 181, no. 1-4, pp. 43–81, 1990.
- [40] S.-L. Li, X.-H. Yu, C.-P. Tan, R. Steel, and X.-F. Hu, "Jurassic sedimentary evolution of southern Junggar Basin: implication for palaeoclimate changes in northern Xinjiang Uygur Autonomous Region, China," *Journal of Palaeogeography*, vol. 3, no. 2, pp. 145–161, 2014.
- [41] K. Lichun, W. Xiatian, G. Xuguang, C. Qiusheng, and J. Xiyu, "Geological characteristics and exploration practice of tight oil of Lucaogou Formation in Jimsar Sag," *Xinjiang Petroleum Geology*, vol. 36, no. 6, p. 1, 2019.
- [42] Y. Su, M. Zha, X. Ding et al., "Petrographic, palynologic and geochemical characteristics of source rocks of the Permian Lucaogou formation in Jimsar Sag, Junggar Basin, NW China: origin of organic matter input and depositional environments," *Journal of Petroleum Science and Engineering*, vol. 183, p. 106364, 2019.
- [43] X. Ding, C. Gao, M. Zha, H. Chen, and Y. Su, "Depositional environment and factors controlling β -carotane accumulation: a case study from the Jimsar Sag, Junggar Basin, northwestern China," *Palaeogeography, Palaeoclimatology, Palaeoecology*, vol. 485, pp. 833–842, 2017.
- [44] C. Liu, K. Liu, X. Wang, L. Wu, and Y. Fan, "Chemostratigraphy and sedimentary facies analysis of the Permian Lucaogou Formation in the Jimusaer Sag, Junggar Basin, NW China: implications for tight oil exploration," *Journal of Asian Earth Sciences*, vol. 178, pp. 96–111, 2019.
- [45] S. Yin, C. Han, Z. Wu, and Q. Li, "Developmental characteristics, influencing factors and prediction of fractures for a tight gas sandstone in a gentle structural area of the Ordos Basin, China," *Journal of Natural Gas Science and Engineering*, vol. 72, p. 103032, 2019.

- [46] G. Feng, X. Wang, M. Wang, and Y. Kang, "Experimental investigation of thermal cycling effect on fracture characteristics of granite in a geothermal-energy reservoir," *Engineering Fracture Mechanics*, vol. 235, p. 107180, 2020.
- [47] A. Ouenes, "Practical application of fuzzy logic and neural networks to fractured reservoir characterization," *Computers & Geosciences*, vol. 26, no. 8, pp. 953–962, 2000.
- [48] D. J. Sanderson and C. W. Nixon, "The use of topology in fracture network characterization," *Journal of Structural Geology*, vol. 72, pp. 55–66, 2015.
- [49] Z. Lianbo and L. Xiang-Yang, "Fractures in sandstone reservoirs with ultra-low permeability: a case study of the Upper Triassic Yanchang Formation in the Ordos Basin, China," *AAPG Bulletin*, vol. 93, no. 4, pp. 461–477, 2009.
- [50] L. Zeng, W. Lyu, J. Li et al., "Natural fractures and their influence on shale gas enrichment in Sichuan Basin, China," *Journal of Natural Gas Science and Engineering*, vol. 30, pp. 1–9, 2016.
- [51] C.-H. Lee, B.-W. Deng, and J.-L. Chang, "A continuum approach for estimating permeability in naturally fractured rocks," *Engineering Geology*, vol. 39, no. 1–2, pp. 71–85, 1995.
- [52] H. L. Ramandi, P. Mostaghimi, and R. T. Armstrong, "Digital rock analysis for accurate prediction of fractured media permeability," *Journal of Hydrology*, vol. 554, pp. 817–826, 2017.
- [53] P. Nazariyan Samani, M. Mirshahani, Z. Zamani, and M. Bahremani, "Carbonate cements investigation in Permian-Triassic Dalan-Kangan reservoirs: case study in Persian Gulf, Iran," *International Journal of Petroleum and Geoscience Engineering*, vol. 3, no. 2, pp. 108–115, 2015.
- [54] K. Spikes, "Overview of rock property relationships and characterization methods for selected oil and gas shales in North America," *Geohorizons*, vol. 17, no. 1, pp. 18–25, 2012.
- [55] K. Azmy and N. J. Blamey, "Source of diagenetic fluids from fluid-inclusion gas ratios," *Chemical Geology*, vol. 347, pp. 246–254, 2013.
- [56] A. M. Van den Kerkhof and U. F. Hein, "Fluid inclusion petrography," *Lithos*, vol. 55, no. 1–4, pp. 27–47, 2001.
- [57] Y.-F. Yang, N. Li, and Y.-J. Chen, "Fluid inclusion study of the Nannihu giant porphyry Mo–W deposit, Henan Province, China: implications for the nature of porphyry ore-fluid systems formed in a continental collision setting," *Ore Geology Reviews*, vol. 46, pp. 83–94, 2012.
- [58] X. Ding, J. Qu, A. Imin et al., "Organic matter origin and accumulation in tuffaceous shale of the lower Permian Lucaogou Formation, Jimsar Sag," *Journal of Petroleum Science and Engineering*, vol. 179, pp. 696–706, 2019.
- [59] L. Cai, G. Xiao, S. Lu, J. Wang, and Z. Wu, "Spatial-temporal coupling between high-quality source rocks and reservoirs for tight sandstone oil and gas accumulations in the Songliao Basin, China," *International Journal of Mining Science and Technology*, vol. 29, no. 3, pp. 387–397, 2019.
- [60] W. Zhao, X. Wang, S. Hu et al., "Hydrocarbon generation characteristics and exploration prospects of Proterozoic source rocks in China," *Science China Earth Sciences*, vol. 62, no. 6, pp. 909–934, 2019.
- [61] L. Zeng, C. Gao, J. Qi, Y. Wang, L. Li, and X. Qu, "The distribution rule and seepage effect of the fractures in the ultra-low permeability sandstone reservoir in east Gansu Province, Ordos Basin," *Science in China Series D: Earth Sciences*, vol. 51, no. S2, pp. 44–52, 2008.
- [62] S. Su, Z. Jiang, S. Xuanlong et al., "The effects of shale pore structure and mineral components on shale oil accumulation in the Zhanhua Sag, Jiyang Depression, Bohai Bay Basin, China," *Journal of Petroleum Science and Engineering*, vol. 165, pp. 365–374, 2018.
- [63] T. Barth and K. Bjørlykke, "Organic acids from source rock maturation: generation potentials, transport mechanisms and relevance for mineral diagenesis," *Applied Geochemistry*, vol. 8, no. 4, pp. 325–337, 1993.
- [64] Q. Zhen, S. Zhensheng, D. Dazhong et al., "Geological characteristics of source rock and reservoir of tight oil and its accumulation mechanism: a case study of Permian Lucaogou Formation in Jimusar sag, Junggar Basin," *Petroleum Exploration and Development*, vol. 43, no. 6, pp. 1013–1024, 2016.
- [65] P. Li, M. Zheng, H. Bi, S. Wu, and X. Wang, "Pore throat structure and fractal characteristics of tight oil sandstone: a case study in the Ordos Basin, China," *Journal of Petroleum Science and Engineering*, vol. 149, pp. 665–674, 2017.
- [66] S. Lu, J. Li, P. Zhang et al., "Classification of microscopic pore-throats and the grading evaluation on shale oil reservoirs," *Petroleum Exploration and Development*, vol. 45, no. 3, pp. 452–460, 2018.

Research Article

Petrographic Characterization and Maceral Controls on Porosity in Overmature Marine Shales: Examples from Ordovician-Silurian Shales in China and the U.S.

Lin Wei ^{1,2}, Shasha Sun ³, Dazhong Dong,³ Zhensheng Shi,³ Jia Yin,^{1,2} Shudi Zhang,^{1,2} Maria Mastalerz ^{4,5} and Xiong Cheng^{1,2}

¹School of Energy Resources, China University of Geosciences, Beijing 100083, China

²Key Laboratory of Marine Reservoir Evolution and Hydrocarbon Enrichment Mechanism, Ministry of Education, Beijing 100083, China

³Research Institute of Petroleum Exploration & Development, PetroChina, Beijing 100083, China

⁴Indiana Geological and Water Survey, Bloomington, IN 47405, USA

⁵Department of Earth and Atmospheric Sciences, Indiana University, 1001 E. 10th St., Bloomington, IN 47405, USA

Correspondence should be addressed to Shasha Sun; sunss69@petrochina.com.cn and Maria Mastalerz; mmastale@indiana.edu

Received 27 January 2021; Revised 16 March 2021; Accepted 17 April 2021; Published 1 June 2021

Academic Editor: Kun Zhang

Copyright © 2021 Lin Wei et al. This is an open access article distributed under the Creative Commons Attribution License, which permits unrestricted use, distribution, and reproduction in any medium, provided the original work is properly cited.

The pore structure characterization and its controlling factors in overmature shales are keys to understand the shale gas accumulation mechanism. Organic matter in source rocks is a mixture of various macerals that have their own specific evolutionary pathways during thermal maturation. Pores within macerals also evolve following their own path. This study focused on petrographic characterization and maceral controls on porosity in overmature marine shales in China and the United States. Shale from Ordos Basin in China was also selected as an example of overmature transitional shale for maceral comparison. Organic petrology techniques were used to identify maceral types and describe morphological features in detail; scanning electron microscopy techniques were then used to document the abundance and development of pores within macerals. Helium measurement, mercury intrusion capillary pressure, and CO₂ adsorption were especially applied to quantify the pore structure of Wufeng-Longmaxi shale from Sichuan Basin in China. The vitrinite reflectance equivalent of the studied overmature samples is ~2.4%. The macerals within the studied marine shales are composed mainly of pyrobitumen and zooclasts. At this maturity, pyrobitumen develops abundant gas-related pores, and their volume positively correlates to gas content. Three types of pyrobitumen and its related pore structure are characterized in Wufeng-Longmaxi shales. Zooclasts contribute to total organic carbon (TOC) content but little to porosity. When the TOC content is above 1.51% in Wufeng-Longmaxi samples, the TOC content positively correlates to quartz content. Organic matter strongly controls micropore development. Pores of diameter ~0.5 nm provide a significant amount of micropore volume. Clay mineral and quartz contents control micro- and macropore increments in organic-lean shales. MICP results indicate that pores within 3-12 nm and 900-2500 nm account for a major contribution to pore volume obtained. Determining the proportions of pyrobitumen to zooclasts within the total organic matter in pre-Devonian organic-rich marine shales is important in predicting porosity and gas storage capacity in high-maturity shales.

1. Introduction

Elucidating the pore network and its evolution in gas shales is a key topic in unconventional oil and gas exploration because many studies have shown that shale pore structure is one of

the most important factors controlling gas storage capacity ([1]; Jarvie et al. 2007; [2–13]). Shale pores have been divided into micropore (<2 nm), mesopore (2–50 nm), and macropore (>50 nm) based on pore size [14]. Researchers also divided pores into interparticle pore, intraparticle pore, and

organic matter (OM) pore based on pore types and position [15–20]. Previous studies suggest that various controlling factors influence the abundance of pores, such as total organic carbon (TOC) content and mineralogy [5, 16, 17, 21–23]. Quantitative assessments of pore volume and pore size distribution analyzed by scanning electron microscopy (SEM) imaging and gas adsorption techniques revealed that OM porosity is a significant component of the pore networks of shales [3, 5–7, 24–26]. Most researchers concluded that TOC content has a positive relationship with porosity in shales [4, 16, 18, 27–29]. For example, Mastalerz et al. [16] suggest that OM contributes micropores to total porosity in organic-rich marine shales. Also reported in the literature are cases that do not show a strong TOC-porosity correlation perhaps because of the presence of a significant inorganic porosity fraction [15, 18, 23, 30–36]. A growing number of researchers have suggested that porosity is influenced by mineralogy and rock fabric [17, 31, 37]. For example, Mastalerz et al. [16] observed that total porosity increases with clay and quartz content and decreases with carbonate content. Ji et al. [38] and Chen et al. [39, 40] concluded that the biogenic quartz in marine shale was typically accompanied by abundant pores, whereas the quartz in marine-continental transitional shale or continental shale had little influence on the pore structure. Milliken et al. [17] proposed higher clay content may allow the collapse of OM pores and interparticle pores, especially for deeply buried shales that have undergone immense compaction [40].

The effects of thermal maturation on porosity have recently attracted more attention because of the growing recognition that the porosity of OM is a function of thermal maturity [4, 16, 18, 27, 29, 41, 42]. For example, Curtis et al. [4] used focused ion beam milling combined with scanning electron microscopy (FIB-SEM) techniques to investigate the organic porosity within Woodford shale, finding that secondary organic porosity is absent in samples having vitrinite reflectance (VR_o) values $< 0.9\%$ but does occur in samples having $VR_o > 1.23\%$. Mastalerz et al. [16] examined the evolution of porosity with maturation in a suite of five New Albany Shale samples spanning a maturity range from immature ($VR_o = 0.35\%$) to postmature ($VR_o = 1.41\%$), observing that total porosity and total pore volume show a significant decline from immature to late mature and then regain higher values in the postmature sample. However, their data were limited to shales having VR_o values $< 1.41\%$. That study suggests that porosity change with maturity is the response to oil and gas generation. In addition, there is a growing awareness that different macerals have different pore characteristics and that the evolution of porosity with maturity is maceral-dependent [43–47]. A maceral is an organic component of coal and shale. The type, amount, and origin of macerals in shales are a function of their depositional environment. For example, the liptinite group includes oil-prone macerals containing compounds of a mainly aliphatic nature, and upon thermal evolution, they produce hydrocarbons [48, 49]. The vitrinite group originates from lignin and cellulose, partly from tannins of the woody tissues of plants [47, 50–52], and is considered to be gas-prone. Liu et al. [45] studied maceral evolution in New

Albany Shale (NAS) as an example of kerogen type II marine shale at the early mature to postmature stage. They show that amorphous organic matter (AOM) and alginite are the dominant organic components in their early mature samples, whereas solid bitumen becomes the dominant OM in samples in the oil window and even higher-maturity stages. They concluded that secondary organic nanopores developed in solid bitumen when oil and gas were generated and expelled. Vitrinite and inertinite did not contribute much to porosity. Haeri-Ardakani et al. [53] discussed OM assemblage in Utica shale samples, consisting of type II marine kerogen (i.e., chitinozoans, graptolite, and liptinite) and migrated bitumen. They also concluded that bitumen is the only organic fraction that contributed to total porosity for Utica shale samples in the oil window but not for samples in the dry gas window [43].

Pore structure is constantly changing under the combined effect of the thermal transformation of OM, and the major control on shale pores at the overmature stage (range from 1.5% to above 2.5%) remains unclear. The characterization of porosity of various macerals in marine shale has mostly been done on mature rocks where various macerals are present and easy to identify [45, 47, 53]. However, researchers also have different opinions on maceral identification in overmature shales. For example, Liu et al. [45] proposed that AOM and alginite in New Albany marine shales disappeared at the late mature stage. Hu et al. [54] identified two types of alginite in overmature Longmaxi marine shales in China. Besides, much less is known about the influence of macerals on pore characteristics in high-maturity shales. It remains unclear how the original OM evolves and how secondary products influence the overall porosity at the overmature stage. Some researchers concluded that zooclasts also contribute to porosity and, as such, are an important component in gas storage [55, 56], but how zooclasts evolve during maturation and how they differ from other macerals remain unclear. In general, detailed organic petrology studies are limited to high-maturity shales.

In this study, Late Ordovician to Early Silurian overmature shales in China and the U.S. were chosen for petrographic and porosity characterization. Most representative samples come from the most productive marine shales in Sichuan Basin in China (Figure 1), which have reached a maturity equivalent to $VR_o = \sim 2.3 - 3.0\%$ [57–61]. Many economically important high-maturity gas shales are of pre-Silurian age, and they are characterized as a different mineral and maceral composition which controls pore development [62–64]. Specifically, this investigation is aimed at studying (1) the pore type characterization in the overmature stage. Both the marine and transitional shales are selected for maceral comparison. Our study uses a combination of optical microscopy and SEM to characterize OM in postmature shales. Optical microscopy can evaluate the color, reflectance, and morphology of OM and can identify maceral types [44, 65]. SEM observations of ion-milled argon allow us to examine nanometer-scale OM-hosted pores in shales [2, 66, 67]. This investigation is also aimed at studying (2) the pore structure characterization in overmature marine shales and major control factors on porosity. We chose CO_2 gas

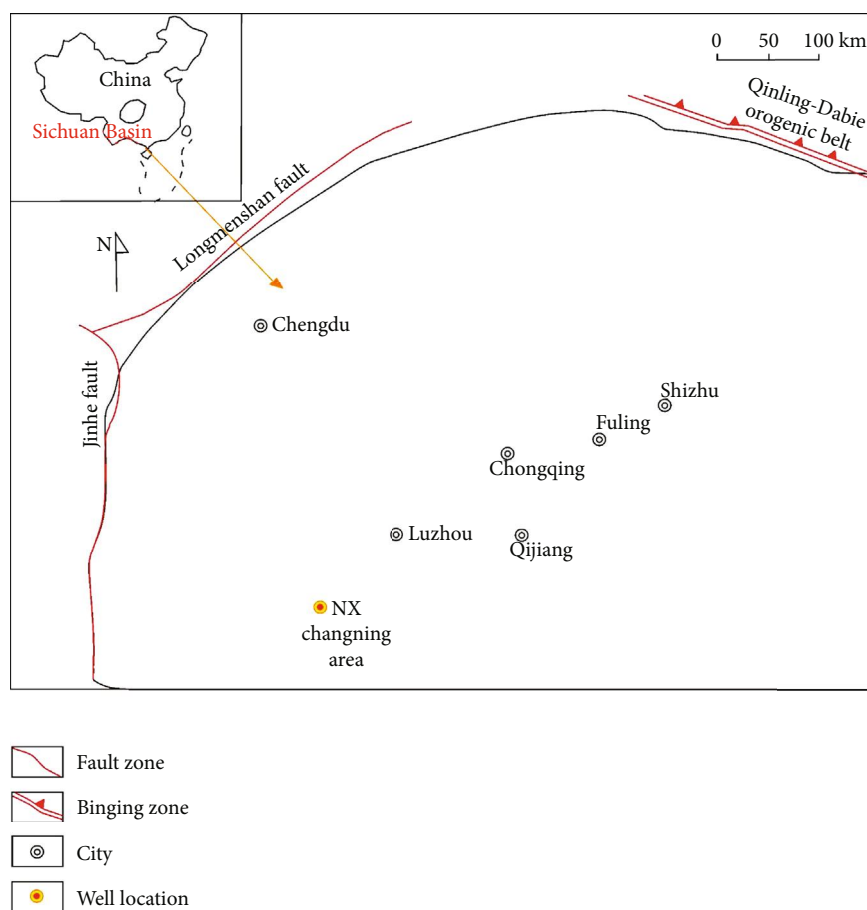


FIGURE 1: Geological background and core location (well NX is marked as a colored dot in Changning area) in Sichuan Basin in the southwest of China. Sichuan Basin is surrounded by the orogenic belt around Longmen Mountain, Jinhe Mountain, and Qinling Mountain. The study region is located in the southwest region of Sichuan Basin.

adsorption and mercury injection capillary pressure (MICP) analysis as tools of this study. Our study contributes to an understanding of maceral types and the control of SEM-detectable pores in different OM types in typical overmature pre-Paleozoic shales and aids in evaluating the pore structure control factors, occurrence, and storage of gas in overmature shale reservoirs.

2. Samples and Experimental Method

To characterize OM populations and pore structures, we used Wufeng-Longmaxi shale samples interpreted as being overmature from sedimentary basins in China. Wufeng-Longmaxi shales are from Sichuan Basin located in the southwest of China (Figure 1). Samples N1 and N12 were selected from a drilled core in Changning County, Sichuan Basin (Figures 1 and 2). The samples came from an interval of 2481 to 2576 m in depth, covering the Late Silurian to Early Ordovician time period (Table 1). Shales cover the gas-productive Wufeng-Longmaxi Formation. These sediments have been deposited on a deep-sea continental shelf and were interpreted to be overmature marine shales [34, 55, 61, 68–70]. Detailed sample information of Wufeng-Longmaxi shale is listed in Table 1.

Additional overmature shales of similar age and maturity from basins in China and the U.S. were also selected only for maceral comparison with Wufeng-Longmaxi shales. Two of them are also marine shales, and the other is marine-continental transitional shale. Marine shales include Utica shale and Xiuwu shale. Ordos shale belongs to transitional shale. The sample TRA-10 is an example of Early Silurian Utica shale from Appalachian Basin in the U.S. Utica shale is one of the most important gas-producing formations in North America [43, 53, 71–73]. A sample from Xiuwu Basin is characterized as an overmature marine shale deposit at the Ordovician time period [74]. Xiuwu shale is expected to have the highest maturity among marine shales. A shale sample from Ordos Basin is an example of a marine-continental transitional shale deposit in Carboniferous [75–77].

2.1. TOC, XRD, and Porosity Analysis of Wufeng-Longmaxi Shale. The TOC content and mineralogical composition were analyzed in the State Key Laboratory of Petroleum Resources and Prospecting at the China University of Petroleum in Beijing. The TOC contents of the shale samples were measured using a Leco CS230 carbon/sulfur analyzer. Samples were crushed to powder < 100-mesh size, and then 1 to 2 g samples were pyrolyzed up to 540°C. Samples were crushed to 300-mesh size for X-ray diffraction (XRD) analysis using a Rigaku

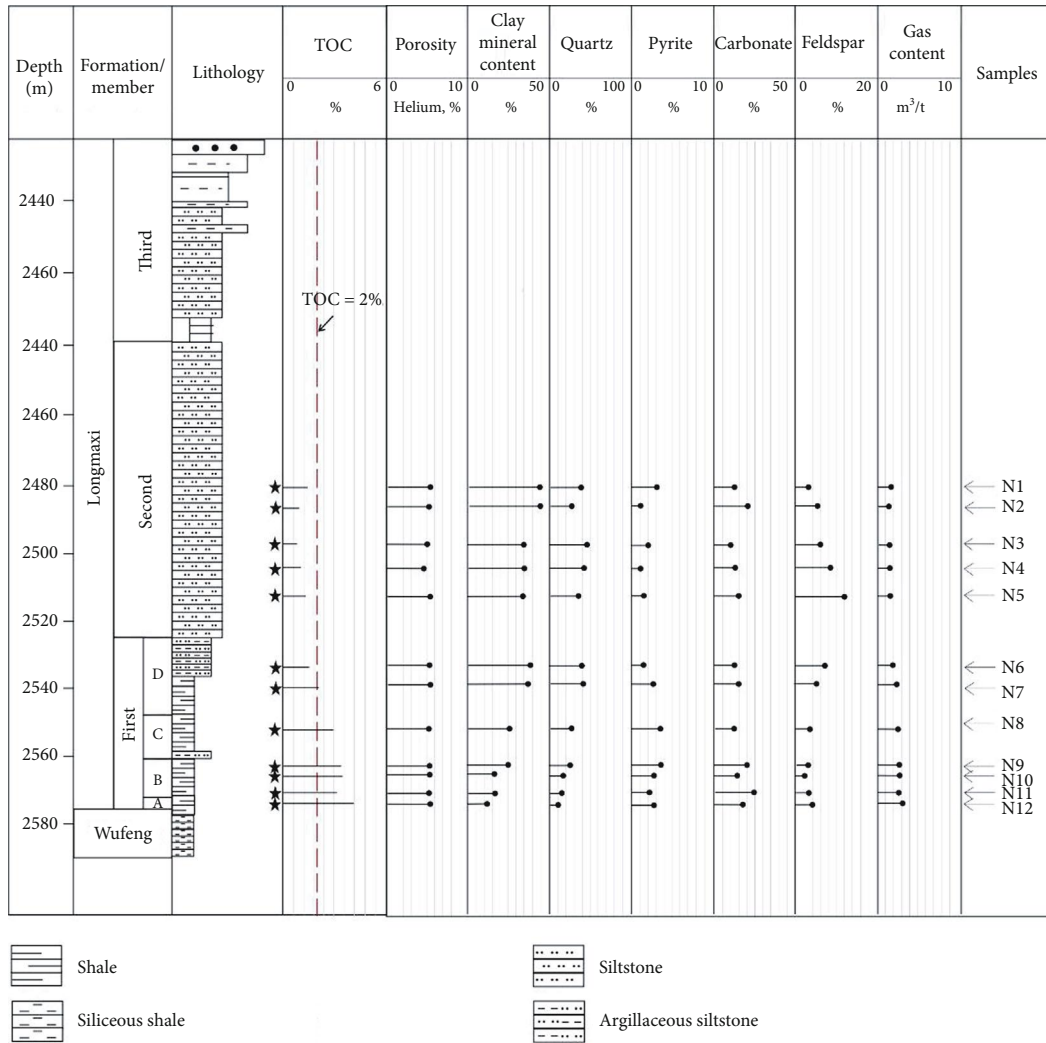


FIGURE 2: Compositional analysis, total organic carbon (TOC) content, helium porosity, and gas content of selected Wufeng-Longmaxi shale samples (N1 to N12) at different depths.

D/max-2500PC diffractometer at 40 kV and 30 mA. Crushed samples were mixed with ethanol, hand-ground, and then smear-mounted on glass slides. They were further scanned from 2° to 70° at a step of 0.02° and 2-second step time at room temperature.

The pore structure measurements were performed at Renqiu Jiechuang Petroleum Technology Corporation. Combined MICP and CO_2 adsorption were applied to quantify pore structure for different pore sizes. The pore size classification in this study follows the International Union of Pure and Applied Chemistry [78] and other recent pore studies (e.g., [79–81]).

Low-pressure gas adsorption measurements with carbon dioxide (CO_2) were conducted on a Micromeritics ASAP-2020 apparatus. The shale samples were crushed to 60-mesh size ($180 \mu\text{m}$). Detailed procedures could be found in Mastalerz et al. [16]. CO_2 gas adsorption was used to characterize micropores ($<2 \text{ nm}$ in diameter). The density functional theory (DFT) [82, 83] method was used to calculate the specific surface area and pore size distribution based on the adsorption curve.

Mercury intrusion data were collected on a Micromeritics Autopore 9520 instrument. The mercury pressure increases from 0 to 400 MPa. Pore size distribution was determined using the Washburn equation [84]. Pore throat size ranging between 3 nm ($0.003 \mu\text{m}$) and $3 \times 10^5 \text{ nm}$ ($300 \mu\text{m}$) was characterized. The mercury injection and withdrawal capillary curves were used to predict the behavior of fluids during pressure changes in reservoirs. Pore size distribution can be displayed as cumulative or log differential curves of pore volume or surface area. The log differential curves ($dV/d \log D$ or $dS/d \log D$) are widely used for comparing relative pore volumes and characteristics of pores [65, 85].

Total porosity measurements were carried out with ULTRAPORE-300 using a helium expansion method. The gas contents of the shale samples were analyzed by the Research Institute of PetroChina Southwest Oil & Gasfield Company. They were measured using direct methods, according to a procedure similar to the USBM method [86], and indirect methods following the sorption isotherm procedure described in the literature [87, 88].

TABLE 1: Lists of Wufeng-Longmaxi shale samples from Sichuan Basin and their depths, porosities, total organic carbon (TOC) contents, and mineral contents. Gas contents are also included. Gas contents include lost gas, desorbed gas, and remaining gas.

Sample ID	Depth (m)	TOC (total organic carbon content, %)	Porosity (helium, %)	Clay mineral content (%)	Quartz (%)	Pyrite (%)	Carbonate (%)	Feldspar (%)	Gas content (m ³ /t)
N1	2481	1.23	5.23	43.0	38.3	3.1	12.5	3.1	1.62
N2	2487	0.96	4.35	46.3	27.4	1.1	20.3	4.9	1.38
N3	2498	0.89	4.47	35.0	47.0	2.0	10.1	5.9	1.34
N4	2503	1.07	4.22	36.6	40.7	1.1	13.5	8.1	1.42
N5	2513	1.31	4.53	34.3	36.0	1.5	16.0	12.2	1.55
N6	2534	1.51	5.30	38.2	40.3	1.5	13.1	6.9	1.98
N7	2540	2.15	5.25	35.6	43.9	2.6	12.6	5.3	2.33
N8	2554	2.98	5.30	26.0	55.1	3.6	12.0	3.3	2.41
N9	2563	3.39	5.47	25.1	46.8	3.7	20.7	3.7	2.54
N10	2567	3.52	5.67	16.2	64.8	2.7	14.3	2.0	2.61
N11	2573	3.19	5.22	15.9	54.6	2.1	24.5	2.9	2.63
N12	2576	4.18	5.88	11.8	59.3	2.7	22.3	3.9	3.08

2.2. *Organic Petrology and Scanning Electron Microscopy (SEM) Analysis.* Each core sample was cut into $\sim 2 \times 1.5$ cm fragments. Organic petrology and SEM observations were carried out in the same area; reflected light microscopy was used to identify OM, whereas SEM was used to visualize pores, as well as to evaluate changes in the rock fabric resulting from different mineralogies.

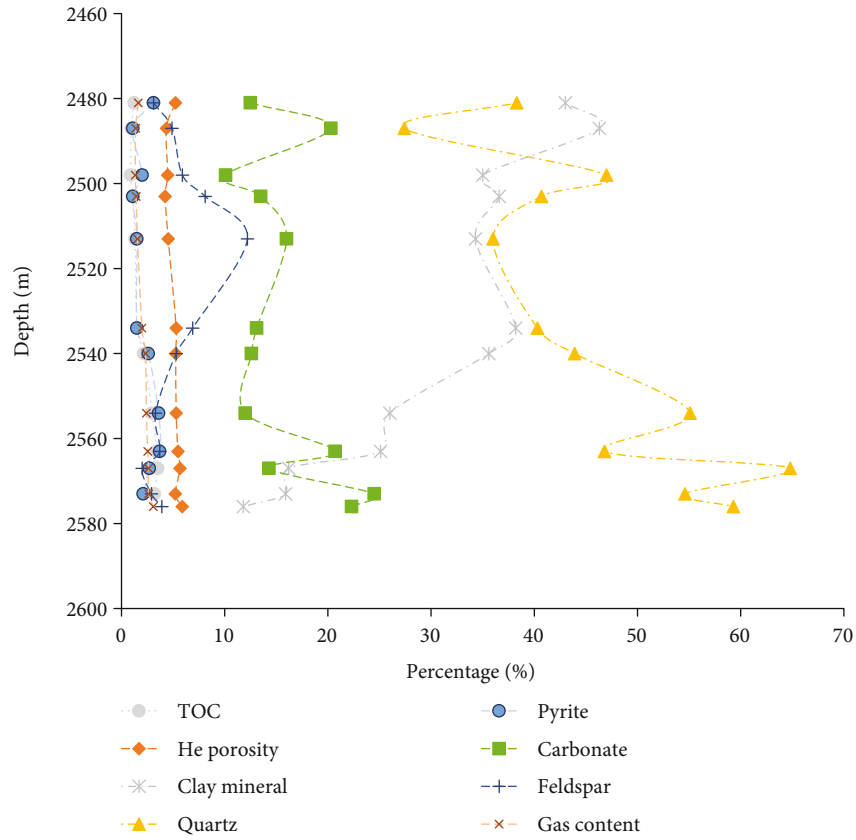
Samples were argon-ion-milled with Gatan 600 DuoMill using a custom-designed sample holder and then observed and analyzed using field emission- (FE-) SEM (Quanta 200F) in low vacuum mode at the China Petroleum Exploration Research Institution. FE-SEM was performed using a Hitachi S-4800 FE-SEM microscope with an accelerating voltage of 1.0 kV. Samples were not coated. The analyzed areas were photographed/mapped to enable the subsequent identification of the same OM particles under a microscope. All SEM images were taken under secondary electron imaging mode. Considering the heterogeneity of shales, 60 evenly spaced SEM pictures were taken within the sample to document the morphology and pore development of OM particles. In the same areas where SEM photomicrographs were taken, organic macerals were identified using reflected light microscopy (Leica DFC310 FX) at Indiana University in Bloomington, Indiana, USA. To evaluate the maturity of the samples, the reflectance of graptolite and/or pyrobitumen was measured under reflected white light and oil immersion, with 25 readings recorded.

2.3. *Micro-FTIR.* Micro-FTIR measurements were performed with a Nicolet 6700 spectrometer connected to a Nicolet Continuum microscope operating in reflectance mode. For micro-FTIR mapping, the smallest aperture size used for the area analysis is $25 \times 25 \mu\text{m}$. Details about instrumentation were presented by Wei et al. [89]. Briefly, Micro-FTIR spectra were obtained at a resolution of 4 cm^{-1} , using a gold plate as a background. The spectra cover a wavenumber range from 650 cm^{-1} to 4000 cm^{-1} . The OMNIC program was used for spectral deconvolution, curve fitting, and deter-

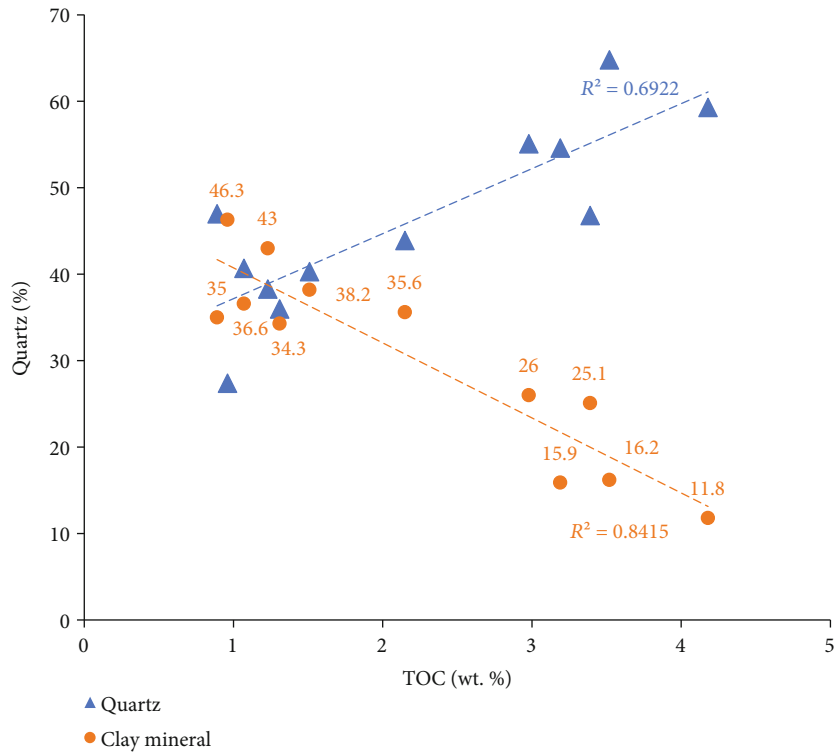
mination of peak integration areas. Reflectance micro-FTIR spectra were subjected to Kramers-Kronig transformation. Peak assignments of spectra were based on Painter et al. [90, 91] and Wang and Griffiths [92].

3. Results

3.1. *Compositional Analysis, TOC, Helium Porosity, and Gas Content of Wufeng-Longmaxi Shale.* Twelve Wufeng-Longmaxi samples from one well at different depths were chosen for this study. The analyzed TOC content, mineral composition, and helium porosity results of Wufeng-Longmaxi shale (N1 to N12) are presented in Table 1. Relationships between depths and those geochemical parameters are shown in Figures 2 and 3. In the well, the TOC content decreases upward in the section, ranging from 4.18% to 0.89%, and the gas content has a similar decreasing trend with shallower depths. Mineralogically, the quartz and clay mineral contents are the main components, accounting for $\sim 46\%$ and $\sim 30\%$, respectively, in the studied samples. The average value of carbonate content is $\sim 16\%$, and pyrite and feldspar contents are minor (a few percent, on average). Samples N1 to N7 at shallower depths have relatively lower quartz and carbonate contents but higher clay mineral content compared to samples at greater depths. Quartz content exhibits a weak positive relationship with TOC content ($R^2 = 0.69$) for all twelve studied Wufeng-Longmaxi shales (Figure 3(b)). However, quartz content is obviously correlated with TOC content in shale with clay content $< 38\%$ (approximately equal to the mean value of clay content in the twelve studied samples), while no obvious relationship is shown with increasing TOC in shales with high clay content ($> \sim 35\%$). Furthermore, clay content shows an obvious negative relationship with TOC content ($R^2 = 0.84$). The helium porosity of the samples was between 4.22% and 5.88%. The result shows that the gas yield ranged from 1.34 to $3.08 \text{ m}^3/\text{t}$ of rock. Overall, the TOC content, helium porosity, quartz and carbonate contents, and gas content increase



(a)



(b)

FIGURE 3: (a) Relationship between depth and total organic carbon (TOC) content (%), mineral content (%), helium porosity content (%), and gas content (m^3/t) of Wufeng-Longmaxi shales. (b) Crossplot of quartz content vs. TOC content. Crossplot of clay mineral content vs. TOC content. The marked numbers are contents (%) of clay minerals of Wufeng-Longmaxi shales.

with depth, especially when depth is at 2540 m and deeper. The measured mean reflectance of pyrobitumen in sample N9 at 2573 m is 2.22%, and three equations were used to calculate equivalent vitrinite reflectance (VR_o): (1) $VR_o = (0.618 \times BR_o (\text{bitumen reflectance})) + 0.4 = 1.77\%$ [93]; (2) $VR_o = (BR_o + 0.41)/1.09 = 2.41\%$ [94]; and (3) $VR_o = (BR_o - 0.059)/0.936 = 2.31\%$ [95]. Even though the values obtained range in amounts, they all indicate a postmature stage and dry gas window.

3.2. Organic Petrology and Maceral Morphology

3.2.1. Wufeng-Longmaxi Shale. Reflected light microscopy and SEM were used to identify and describe different macerals (Figures 4(a) and 4(b)). Photomicrographs of the same areas at the same scale were taken using those two methods (Figures 5 and 6). Under incident white light, a large number of gray structureless OM were observed in Wufeng-Longmaxi shale; those small OM particles (less than $10 \mu\text{m}$) are pyrobitumen. Some pyrobitumens occur as speckles disseminated in the shale matrix (Figures 4(a), 4(b), and 5(d)), and some occupy interparticle pores and microfractures (Figures 4(c) and 4(d)) or are present inside zooclasts and mineral grains (Figures 4(e) and 4(f)). We divided pyrobitumen into three types depending on morphology and pore distribution within the particle. The most abundant type is pyrobitumen I, which has no specific shape and fills in intergranular pores and cracks of minerals (Figures 4(c)–4(f)). Occasionally, larger pieces (several micrometers in size) of pyrobitumen (type II) were also observed (Figures 4(g) and 4(h)). Pyrobitumen II featured an intact shape, which does not distribute around microfractures nor surround minerals. Their shapes are not fixed due to compaction and other effects, with diameters ranging from $1 \mu\text{m}$ to more than $10 \mu\text{m}$. They have clear edge outlines. Pyrobitumen III featured a unique surface different from types I and II. The surface is not smooth but displays uniform pellets inside (Figures 4(i) and 4(j)). Pellets are easily recognized under SEM pictures. This OM is composed of small aggregates of quasispherical bacteria. The diameters of the pellets range from 300 to 400 nm. Affected by compaction, some pellets are flattened to form flat spheres.

Other organic components are fragments of structured zooclasts, including graptolite and chitinozoan (Figures 5(a)–5(d)). The graptolite fragments are grayish-white under reflected light and are characterized by biological morphologies with sharp outlines. Commonly, they are stacked or are forming laminae with a fibrous or threadlike structure (Figures 5(a), 5(b), and 6(a)–6(d)). Void space in these graptolite fragments could be filled with carbonates or quartz. Chitinozoan fragments generally have a segment or scalene shape (Figures 5(c), 6(e), and 6(f)), with a chamber confined by the cell wall. Most zooclast particles seem to be filled with minerals, and OM remains only along the edges. Wufeng-Longmaxi shale samples have the same maceral types at different depths, but the total OM content and relative proportions of pyrobitumen and zooclasts vary. Sporadically, some bodies similar in form to acritarchs could also be found (Figures 6(g) and 6(h)). An acritarch is a small microfossil

of unknown and probably varied biological affinities with varied symmetry, shape, structure, and orientation [96]. It can originate from algae, fungal spores, organic-walled cysts from unicellular protozoa, or spawns of higher organisms. Their central cavity is closed or communicates with the exterior via pores, slitlike or irregular ruptures, or circular openings (Figures 6(g) and 6(h)).

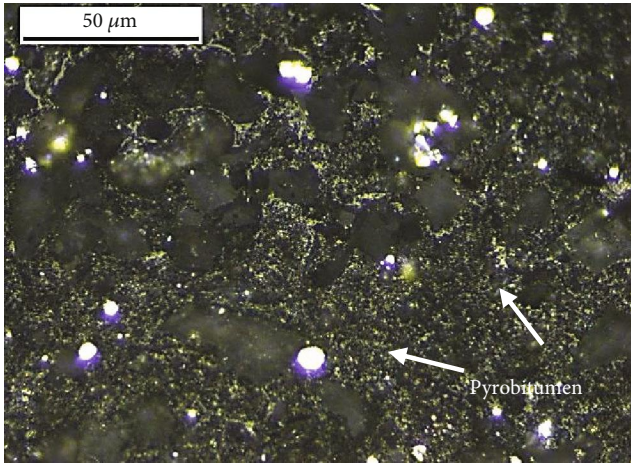
3.2.2. Utica Shale. The measured TOC content of Utica shale TRA-10 is 4.1%. Twenty-five points of graptolite reflectance (GR_o) were measured, and the mean reflectance value is 2.32%. The equivalent VR_o was calculated using the same three empirical equations with Wufeng-Longmaxi shale, and the calculated values are 1.83, 2.50, and 2.41 [93–95], indicating the dry gas window. The measured helium porosity of this sample is 3.95%.

In TRA-10, the dominant maceral is graptolite, which consists of ~95% of the whole OM. Graptolites are typically oriented in a direction parallel to the bedding plane. Some occur as large pieces (~20–50 μm) in the matrix (Figures 7(a) and 7(b)), whereas others are small (a few μm or smaller) and dispersed in the matrix (Figures 7(c) and 7(f)). The spindle shape of graptolites can also be observed (Figure 7(e)). In this sample, pyrobitumen is much less common than graptolites and occurs around mineral grains in relatively small particles of $<1 \mu\text{m}$ (Figures 7(c), 7(d), and 7(f)). Framboidal pyrite is common.

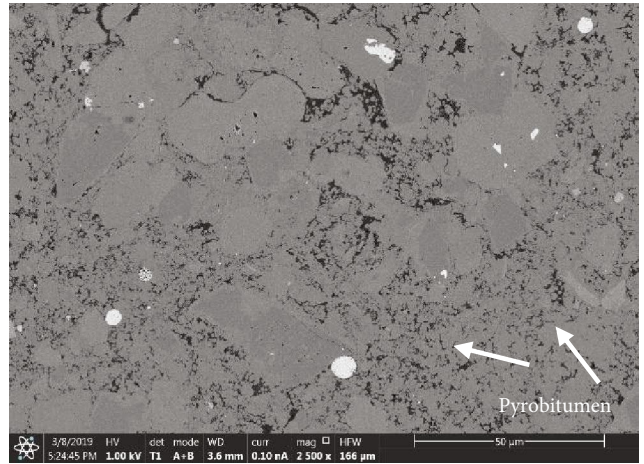
3.2.3. Ordos Shale. The measured TOC content of Ordos shale is 2.14%. Twenty-five points of vitrinite were measured, and the mean reflectance value is 1.88%, indicating the sample is at the overmature stage. Different from other overmature marine shales in this study, the OM in Ordos shale is composed of vitrinite and inertinite (Figures 8(a) and 8(b)). The vitrinite and inertinite pieces have no observable organic pores under a microscope.

3.2.4. Xiuwu Shale. In Xiuwu shale, the observed macerals are pyrobitumen and zooclast (Figures 8(c) and 8(d)). Pyrobitumen consists of ~95% of the whole OM. The measured TOC content is 2.84%, and the mean reflectance value from twenty-five points of pyrobitumen measurements is 3.32%. The equivalent VR_o was calculated using the empirical equation proposed by Landis and Castaño [94]: $VR_o = (BR_o + 0.41)/1.09 = 3.42\%$, indicating a highly overmature stage.

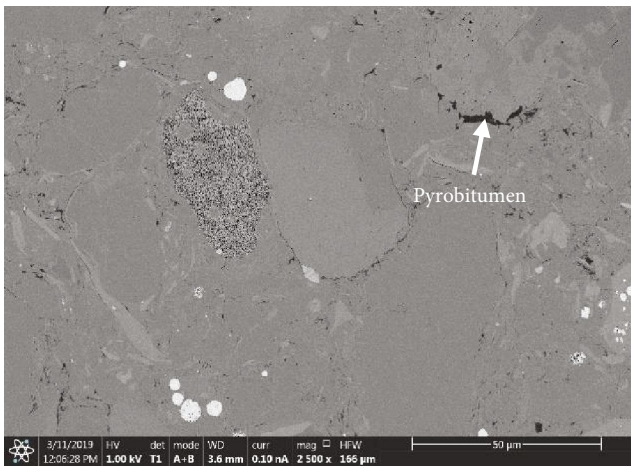
3.3. Organic Pores Analyzed by SEM. In Wufeng-Longmaxi shale samples, large pores (micrometer in size) were observed in pyrobitumen; they can be round, subround, or irregular in shape (Figures 9(a)–9(f)). The round pores have a sponge-like shape and texture (Figure 9(b)). Inside some round pores, two tail-like traces can be seen. Clay minerals generally feature a curved to highly contorted scaly and silk thread laminar structure, whereas brittle minerals had a relatively regular shape and lower brightness [58, 97, 98]. In the studied samples, relatively round and subround pores generally were observed in pyrobitumen surrounding brittle minerals (Figures 9(a)–9(d)). The pyrobitumens having deformed or irregular pores are usually filled inside or occurred near clay minerals having layered or deformed structures (Figures 9(e)



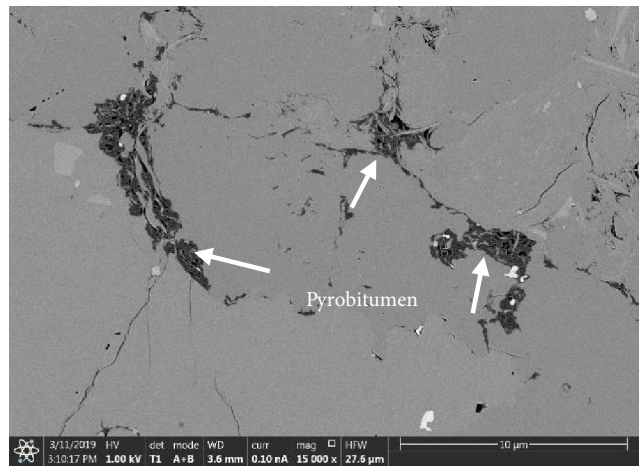
(a)



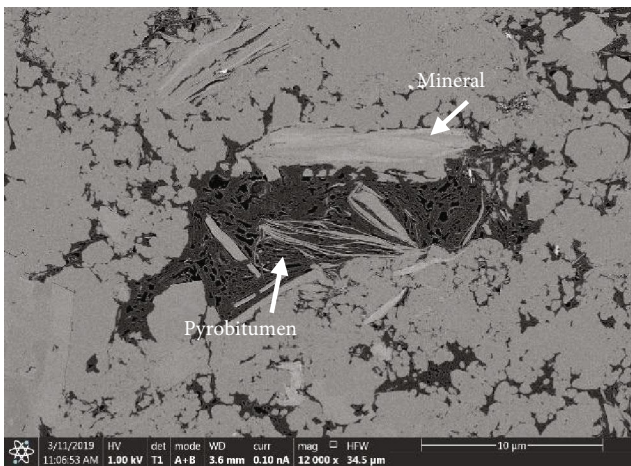
(b)



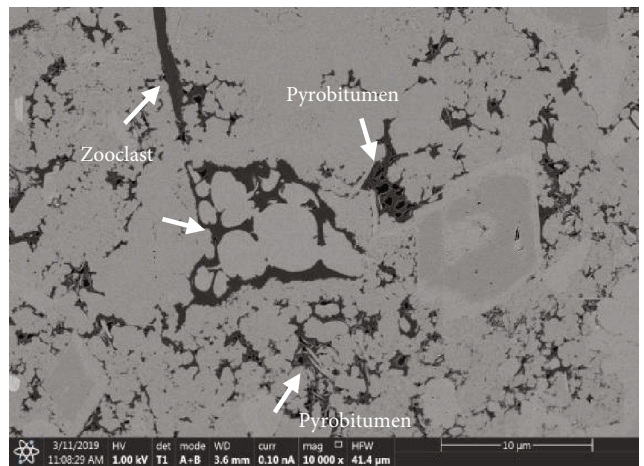
(c)



(d)



(e)



(f)

FIGURE 4: Continued.

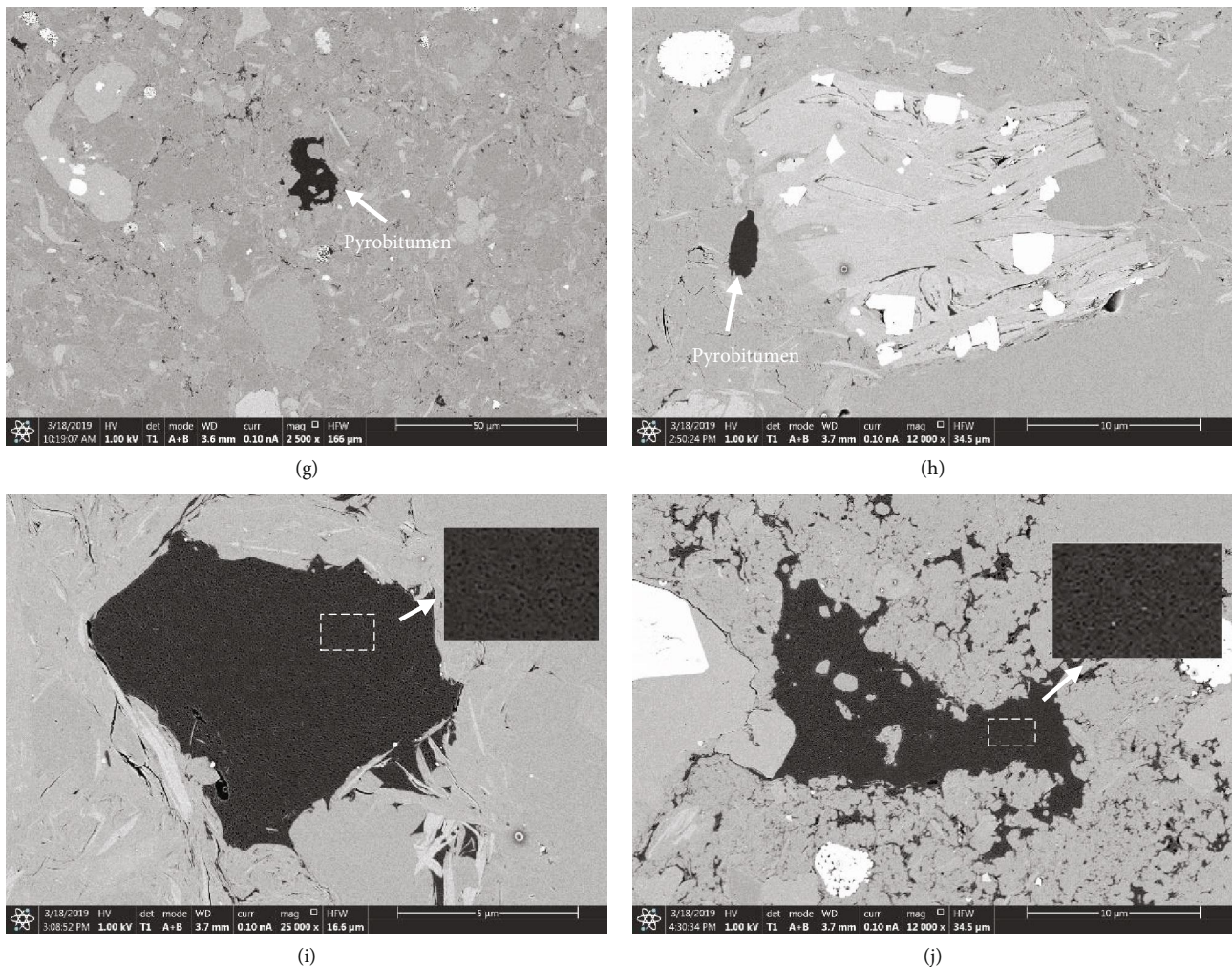


FIGURE 4: (a) Photomicrographs of groundmass pyrobitumen in Wufeng-Longmaxi shale samples under a microscope in incident white light under oil immersion. (b) Scanning electron microscopy (SEM) of the pyrobitumen disseminated in the shale matrix in the same area as (a). (c, d) Pyrobitumen accumulated in interparticle pores and microfractures. (e, f) Pyrobitumen filling the mineral outline. Zooclast and pyrobitumen distributing along the shale matrix. (g, h) Single large pyrobitumen particle of several micrometers in diameter. The larger rectangles in (i, j) are enlarged areas of the related smaller rectangles. This type of pyrobitumen consists of bacteria-like aggregates.

and 9(f)). Some pyrobitumens had irregular surfaces with abundant pores so that it was difficult to recognize them at a micrometer scale.

Pyrobitumen I has a uniform internal texture, and its pores are uniform or random (Figures 9(a)–9(f)). The pores in pyrobitumen I can be divided into two types: (1) irregular pores with spongy uniform distribution (Figure 9(b)) and (2) circular or elliptical pores (Figures 9(a) and 9(c)–9(f)). The latter has pores of different sizes that coexist. In comparison, pyrobitumen II has no observable pores within OM particles (Figures 4(g) and 4(h)). Those two types are related to hydrocarbon generation processes at the late stage. Pyrobitumen III displays a different morphology but a homogeneous internal biological structure (Figures 4(i) and 4(j)). This type of pyrobitumen consists of bacteria-like particles; the pores are significantly different from the bubble-like pores in bitumen. The pores are randomly distributed but display a homogeneous internal biological structure.

No pores could be found in graptolite or chitinozoan in the studied samples, even after enlarging images to the nanometer scale (Figures 10(a)–10(d)). It is interesting to note that SEM photomicrographs from the same Wufeng-Longmaxi shale taken on cores without any polishing (Figures 10(e)–10(h); Figure 10(f) is an amplified picture of Figure 10(e); Figure 10(h) enlarges Figure 10(g)) do show pores in graptolites at a micrometer scale. This observation is in contrast to what we observed in ion-milled samples described in this study (Figures 10(a) and 10(b)).

As described in the methods section, 60 SEM pictures were taken of each sample at different depths from Wufeng-Longmaxi shale. The studied area is the same size on each sample, which allowed us to roughly compare the different maceral contents of the samples. The OM content increases with deeper depth in the studied samples, which is also reflected by the area of dark material in the SEM images of samples (Figures 11(a)–11(h)). Pyrobitumen is

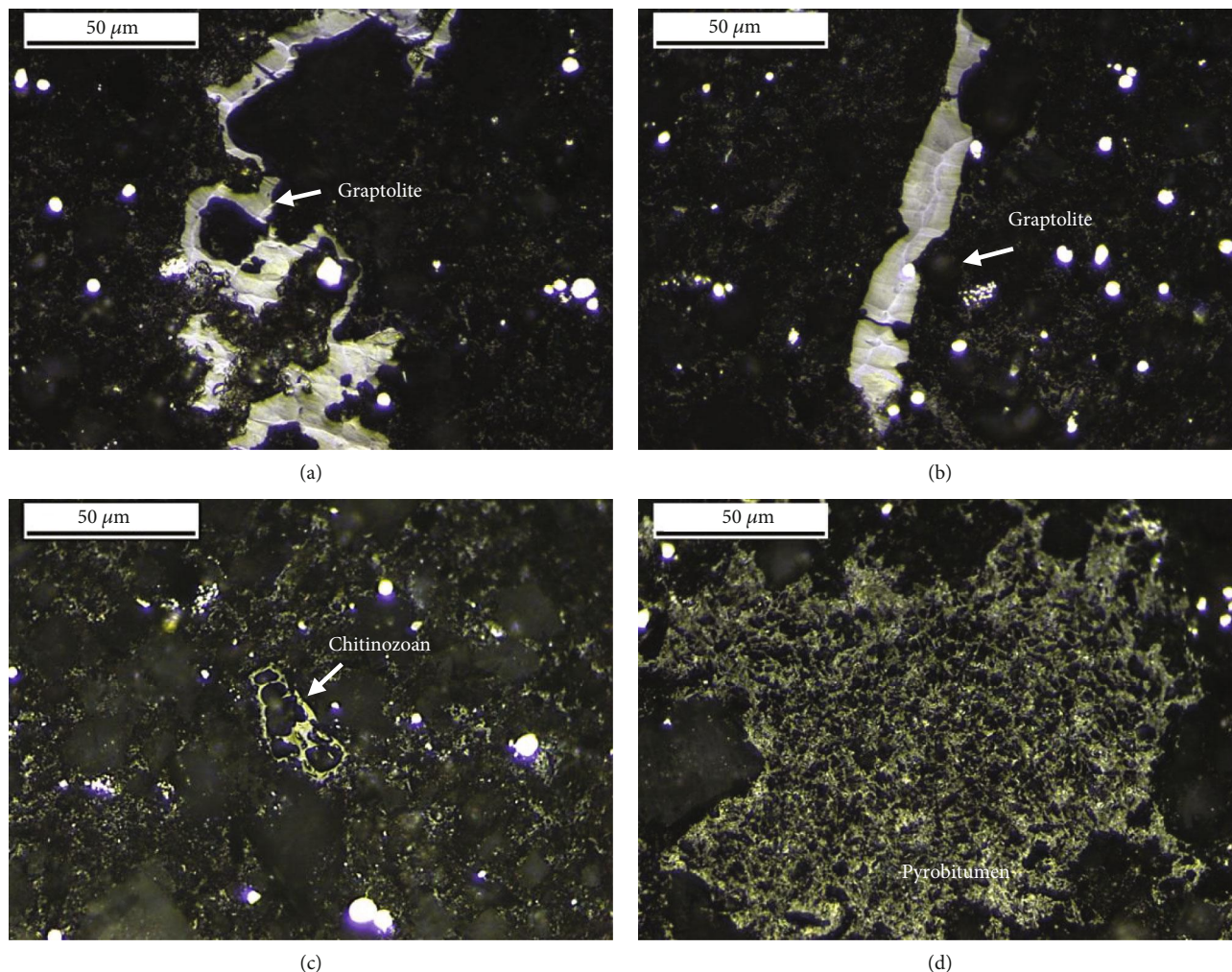


FIGURE 5: Organic petrography photomicrographs (oil immersion, white incident light) showing typical types and morphology of organic matter in Wufeng-Longmaxi shale samples. (a, b) Graptolite fragment with biological shape and fibrous structure within its cell wall. (c) Chitinozoan fragment with a segment or scalene shape. (d) Pyrobitumen of ~40 micrometers in size filling the shale matrix.

the dominant maceral in all samples, and it increases in samples from 2567 m deep and deeper. Zooclast content, including graptolite and chitinozoan, also increases with increasing pyrobitumen content.

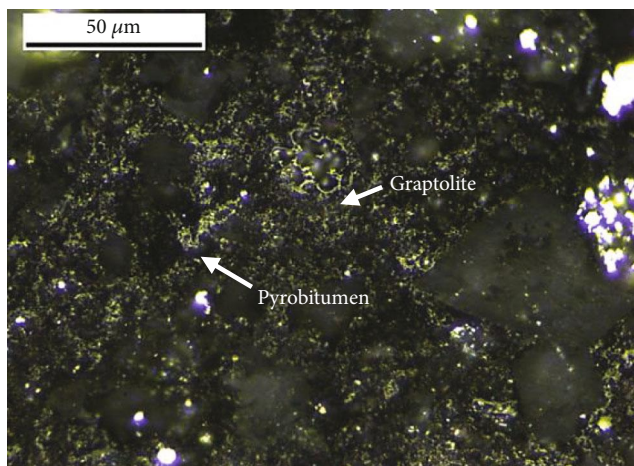
For Utica shale, in the SEM analysis at micrometer to nanoscales, most (~95%) of the analyzed graptolites had no pores detected under SEM (Figures 12(a)–12(e)). A few pores of irregular and narrow shape were found in some graptolites (Figure 12(f)). For Xiuwu shale, pyrobitumen also is featured as structureless and filling characterization. However, different from Wufeng-Longmaxi shale, those pyrobitumen pieces have already lost abundant OM pores (Figures 8(c) and 8(d)). In addition, the inertinite and vitrinite particles in Ordos shale also featured no observable organic pores inside (Figures 8(a) and 8(b)).

3.4. Pore Characterization Based on CO₂ Adsorption and MICP in Wufeng-Longmaxi Shale. Low-pressure CO₂ adsorption was applied to characterize the micropore (pore diameter < 2 nm) distribution. CO₂ adsorption isotherms of

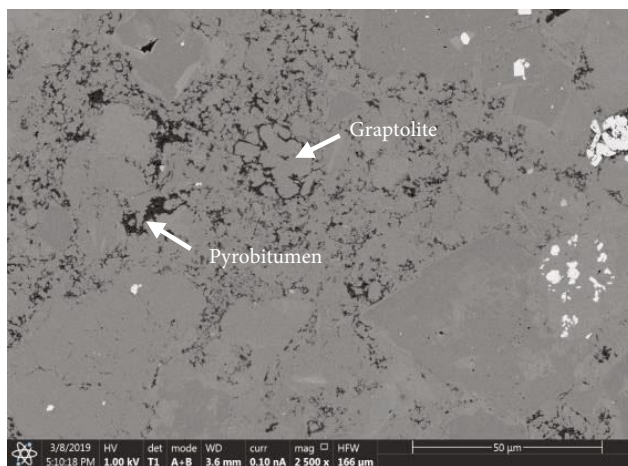
the studied shales display similar variations and trends as type I (Figure 13), which is generally characterized by microporous solids [14]. Maximum volumes of adsorbed CO₂ range from 0.893 to 2.286 cm³/g. The volume of adsorbed CO₂ increases with TOC content (Figure 13). DFT micropore volumes range from 0.001 to 0.003 cm³/g, and DFT micropore surface areas range from 3.60 to 9.89 m²/g (Table 2).

The strongest adsorption happened in shale samples N8, N9, and N10 of the highest TOC content. Sample N5 adsorbs the least amount of CO₂, whereas samples N2 to N4 adsorb intermediate volumes. Comparing samples N2 to N5, sample N5 has relatively higher TOC content and feldspar values but relatively the least clay mineral content and quartz content.

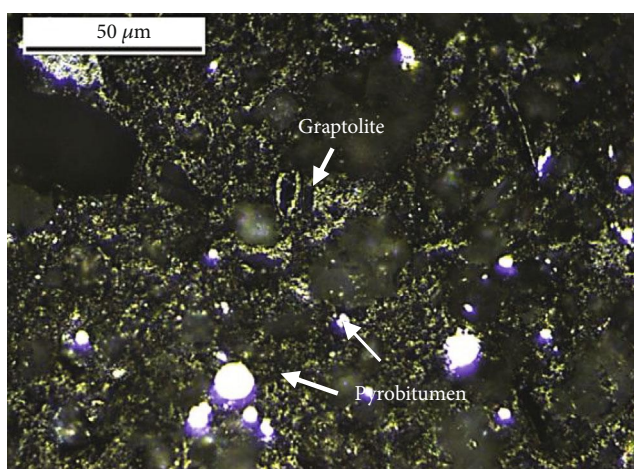
The micropore size distribution up to 1.2 nm was calculated with the DFT model (Figure 14). Pores with diameter < 1 nm have different log differential pore volumes. There are three higher $dV/d \log D$ peaks at approximately 0.40–0.50 nm, 0.55–0.60 nm, and 0.80–0.81 nm, which indicate a high abundance of micropore distributions of those pore size



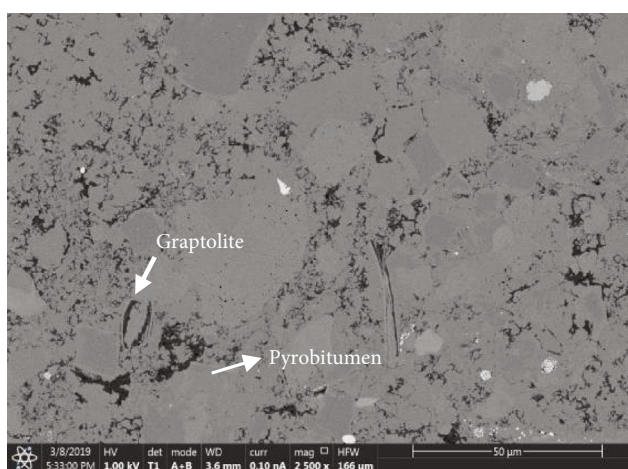
(a)



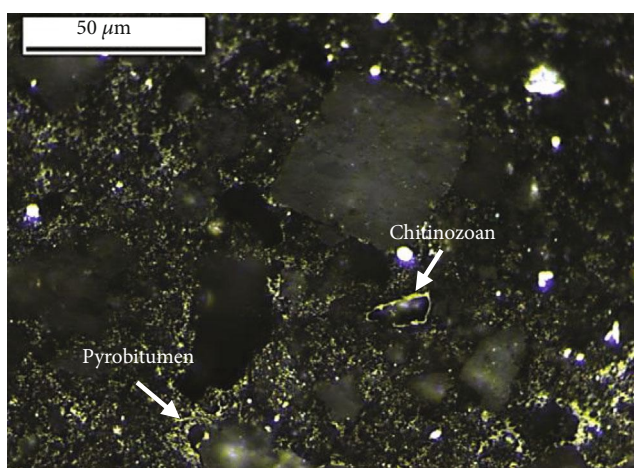
(b)



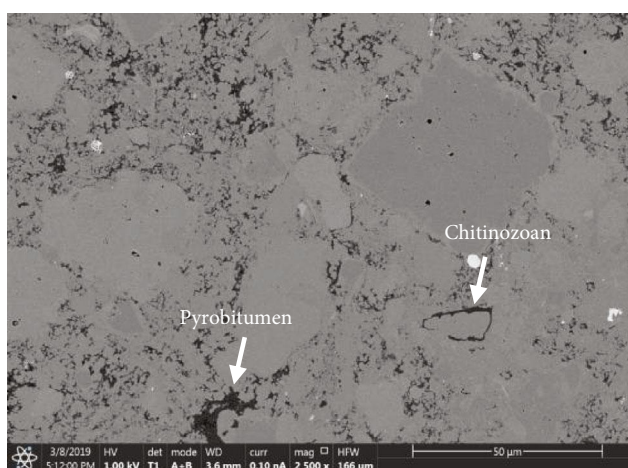
(c)



(d)



(e)



(f)

FIGURE 6: Continued.

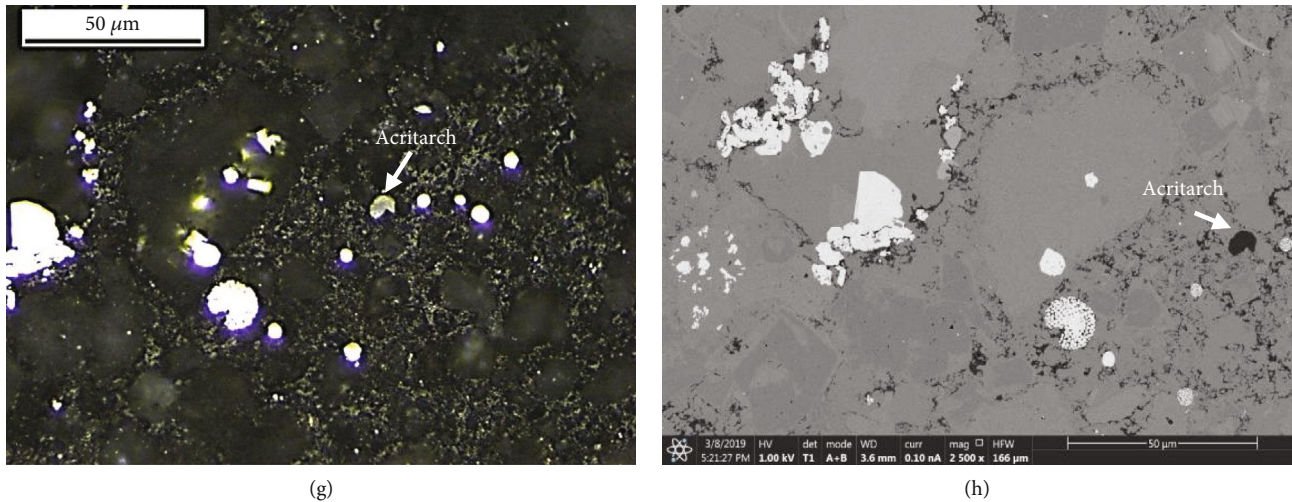


FIGURE 6: Pyrobitumen and zooclast morphology and distribution under SEM and reflected light microscopy in Wufeng-Longmaxi shale. The pairs (a, b), (c, d), (e, f), and (g, h) show the same areas on four different samples. (a–f) Pyrobitumen occurred as speckles disseminated in the shale matrix. (a–d) Graptolite fragments characterized by biological morphologies with sharp outlines. (b, c) Graptolite with a spindle shape. (e, f) Chitinozoan fragment with a scalene shape. (g, h) Acritarch body and its central cavity closed with irregular ruptures.

ranges. The peaks of log differential pore volume increase with increasing TOC content. Pores of diameter approximately 0.5 nm provide a significant amount of pore volume.

MICP was applied to quantify the pore structure of diameter > 5 nm, especially for macropore diameter > 50 nm. A certain pressure of mercury intrusion corresponds to a specific pore diameter. The volume of mercury intrusion under different pressures reflects pore volume within the corresponding pore size. The mercury intrusion curves exhibit two different trends in studied samples, which are presented in Figures 15(a) and 15(b). Samples N2 to N5 with relatively lower TOC content are examples of type I. The volume of mercury intrusion first increases (0.01–1 MPa) and is then kept stable (1–400 MPa) (Figure 15(a)). Samples N8 to N10 are another type of curve. The volume of mercury intrusion shows a rapid increase (0.01–1 MPa), a relatively stable phase (1–50 MPa), and a rapidly increasing phase (50–400 MPa) (Figure 15(b)). Maximum volumes of mercury intrusion, i.e., the total pore volumes, range from 0.007 to 0.020 cm³/g, with an average of 0.011 cm³/g. The specific surface area ranges from 1.49 to 3.83 m²/g, with an average of 2.72 m²/g.

Different mercury injection curves are closely correlated with TOC content and also indicate different pore size distributions. The relationship between pore size distribution and log differential pore volume is shown in Figure 16, which exhibits basically similar variations and trends in studied shales. It is obvious that the log differential pore volume featured distribution with two peaks at 3–12 nm and 900–2500 nm, which suggests that pores within these two intervals account for a major contribution to total pore volume obtained by MICP. Additionally, the inconsistency of pore size distribution in different samples indicates a strong heterogeneity of pore networks.

3.5. Pore Structure and Its Relationship with TOC and Mineral Composition in Wufeng-Longmaxi Shale. Pore struc-

ture parameters (i.e., pore volume and surface area) were obtained by CO₂ gas adsorption and MICP. The cumulative micropore pore volume, micropore surface area, and macropore volume show an obvious increasing trend with TOC content that changed from ~1% to ~3%, but no such change trend in the macropore surface area. For samples with TOC contents of 0.96%–1.31%, the average micropore volume is 0.00113 cm³/g, and the average micropore surface area is 3.984 m²/g. For samples with TOC contents of 2.98%–3.52%, the average value is 0.00237 cm³/g, and the average micropore surface area is 8.123 m²/g.

The quartz content has a positive influence on the micropore surface area, micropore volume, and macropore volume when the quartz content is above ~40%. Clay mineral content has a negative influence on the micropore surface area, micropore volume, and macropore volume when its content is above 30%. However, when the TOC is below ~3%, the increasing clay mineral content is positively correlated to micropore and macropore volumes.

3.6. Variations in Functional Group Abundances among Maceral Groups. The purpose of using micro-FTIR analysis was to investigate whether differences between macerals are also reflected in their chemical structures and, in particular, if chemical functional groups can differentiate between zooclasts and pyrobitumen. Micro-FTIR is capable of characterizing the chemical properties of in situ particles of macerals as small as 10–30 μm. The main difficulty with this technique is recognizing and identifying macerals under a dry objective. Therefore, only macerals of relatively large size were analyzed by FTIR, i.e., pyrobitumen in Wufeng-Longmaxi shale and graptolite in Wufeng-Longmaxi shale and Utica shale. To facilitate maceral identification, photomicrographs under reflected light microscopy were taken prior to FTIR analysis. IR signals derived from the following functional groups were of

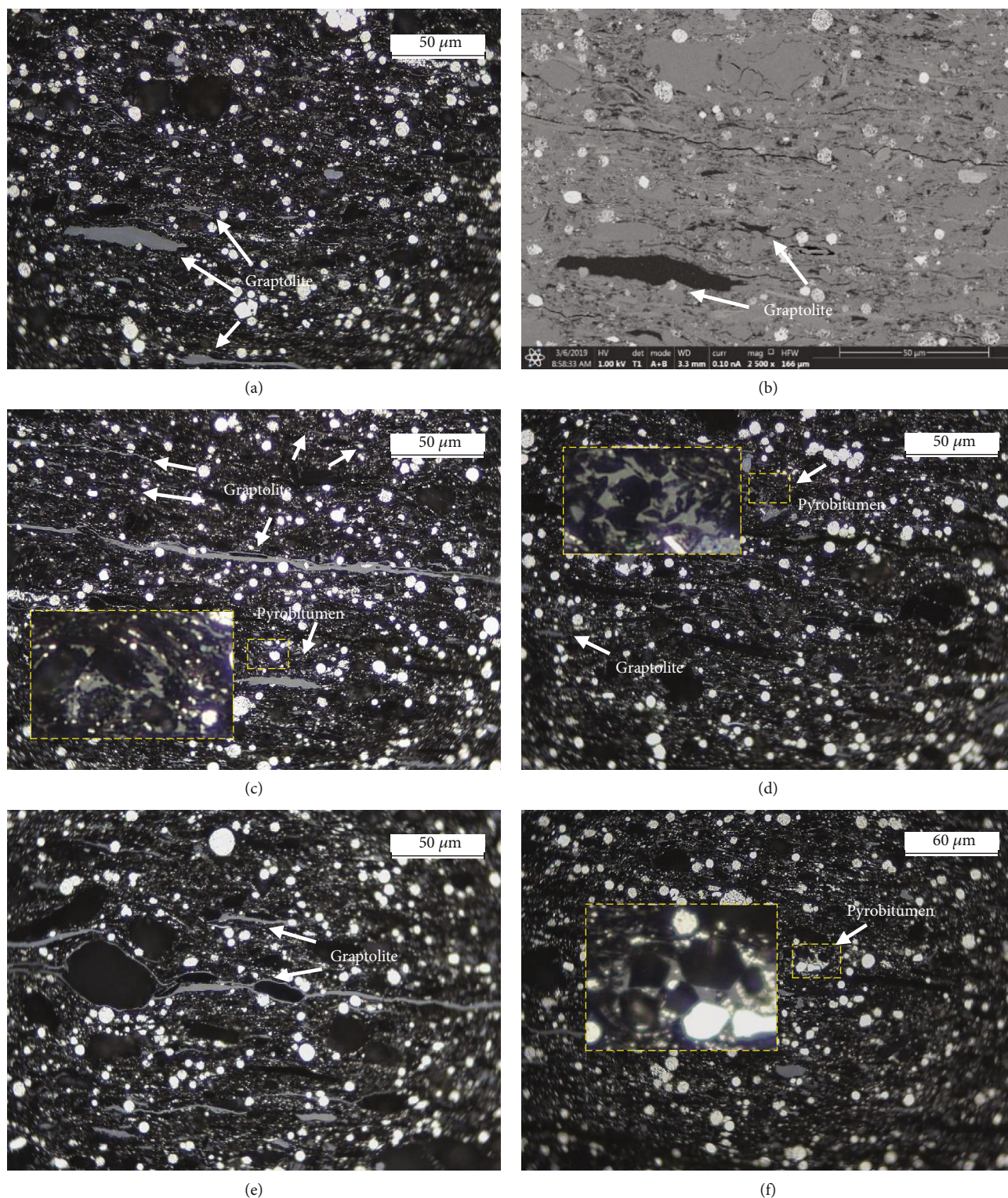


FIGURE 7: Organic petrography photomicrographs (oil immersion, white incident light) (a, c–f) and SEM images (b) showing typical maceral types (graptolite and pyrobitumen) and distributions of sample TRA-10. (a, b) The microscopy (a) and SEM (b) analysis on the same area of TRA-10. The larger rectangles in (c, d, f) are enlarged areas of the related smaller rectangles. (a, b) Typical graptolite grains occurred as large pieces and oriented in a direction parallel to the bedding plane. (c, d, f) Thinner graptolite pieces dispersed within the shale matrix. (c–f) Small pyrobitumen (less than a few micrometers) grains filled in minerals and oriented in various directions. (e) Some graptolites of a spindle or lenticular shape.

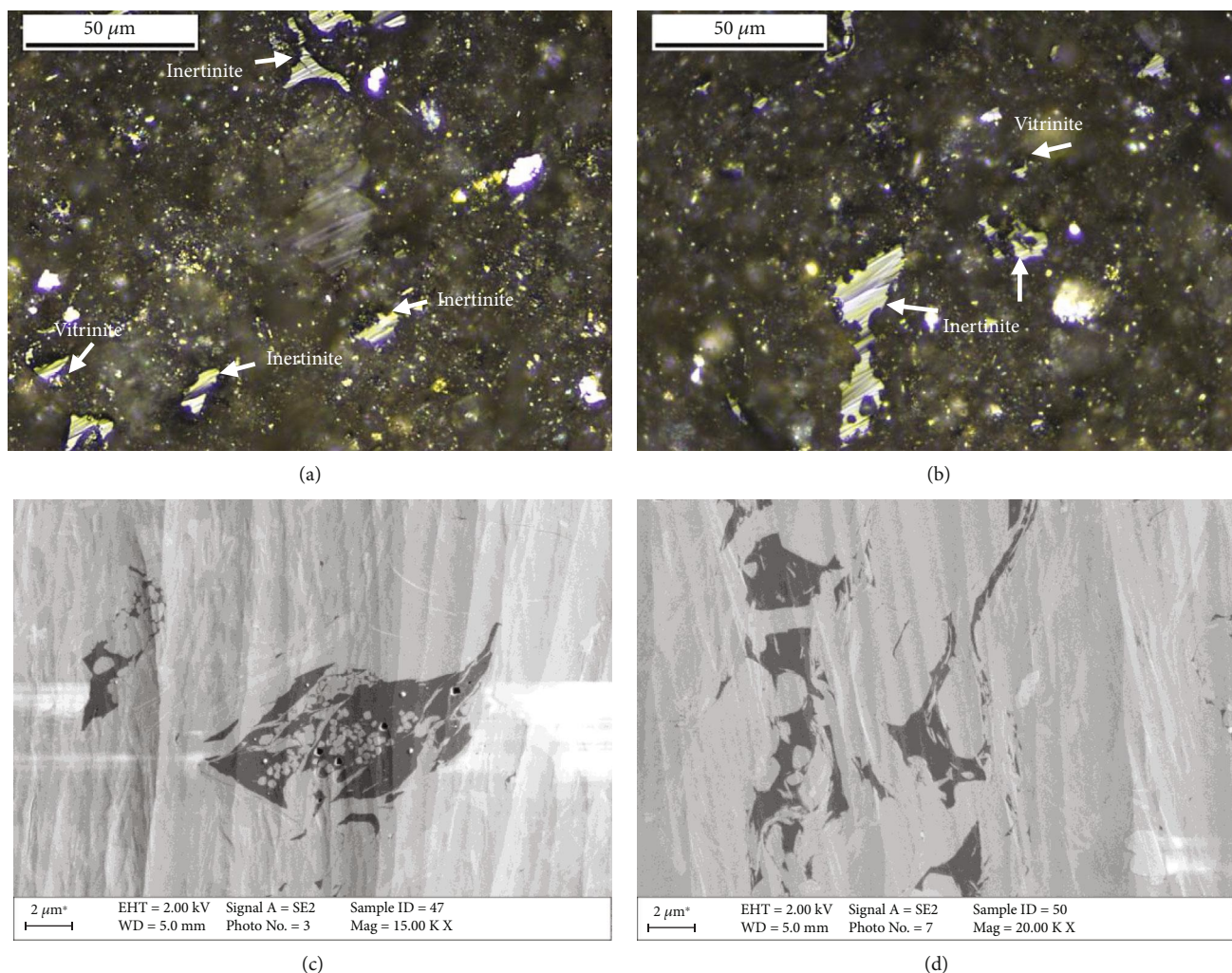


FIGURE 8: (a, b) Organic petrography photomicrographs (oil immersion, white incident light) of Ordos shale. The maceral of Ordos shale is composed of vitrinite and inertinite. (c, d) SEM images showing typical maceral types and the internal pore structure of Xiuwu shale.

particular interest to this study: (i) aromatic CH_x stretching in the $3000\text{--}3100\text{ cm}^{-1}$ region, (ii) aliphatic CH_x stretching at $2800\text{--}3000\text{ cm}^{-1}$, (iii) oxygenated groups at $1650\text{--}1800\text{ cm}^{-1}$, and (iv) aromatic $\text{C}=\text{C}$ ring stretching at $1550\text{--}1650\text{ cm}^{-1}$ [99].

The micro-FTIR spectra of pyrobitumen and graptolites in the samples studied are compared in Figure 17(a). Most analyzed particles were very small and close to the detection limits of the technique. Because of small particle sizes, the spectra are noisy; however, most functional groups were easily detectable. In this study, pyrobitumens show very weak absorbance in both aliphatic CH_x stretching at $2800\text{--}3000\text{ cm}^{-1}$ and aromatic CH_x stretching between wavenumbers $3000\text{--}3100\text{ cm}^{-1}$. They exhibit weak absorbance in oxygenated groups at $1650\text{--}1800\text{ cm}^{-1}$ and aromatic $\text{C}=\text{C}$ ring stretching at $1550\text{--}1650\text{ cm}^{-1}$. In comparison, graptolites feature more distinct aliphatic CH_x stretching at $2800\text{--}3000\text{ cm}^{-1}$ and higher absorbance of oxygenated groups at $\sim 1710\text{ cm}^{-1}$.

Previous FTIR spectra of alginite, AOM, solid bitumen, vitrinite, and inertinite studied by Wei et al. [89] on early mature Devonian New Albany Shale (marine mature shale,

kerogen type II) are shown in Figure 12(b) for comparison. We note that our study used the same experimental method as Wei et al. [89]. Compared with macerals in NAS, graptolite spectra from this study are very similar to those of vitrinite and inertinite of Wei et al. [89]; they display relatively strong peaks at $2800\text{--}3000\text{ cm}^{-1}$ and 1710 cm^{-1} . Compared to solid bitumen from NAS, the pyrobitumen of the present study has weaker absorbance of aliphatic CH_x stretching and aromatic CH_x stretching at $2800\text{--}3000\text{ cm}^{-1}$ and $3000\text{--}3100\text{ cm}^{-1}$ functionalities. The $\text{C}=\text{O}$ and aromatic $\text{C}=\text{C}$ peak intensities in pyrobitumen and solid bitumen appear similar.

4. Discussion

4.1. Compositional Controls on Porosity and Pore Structure.

Previous studies have indicated that different origins of quartz could have different influences on shale porosity. Some studies proposed that the porosity increases with increasing detrital quartz content due to the compaction weakening effect and presence of intergranular pores between quartz grains [10, 100, 101]. In addition, quartz of

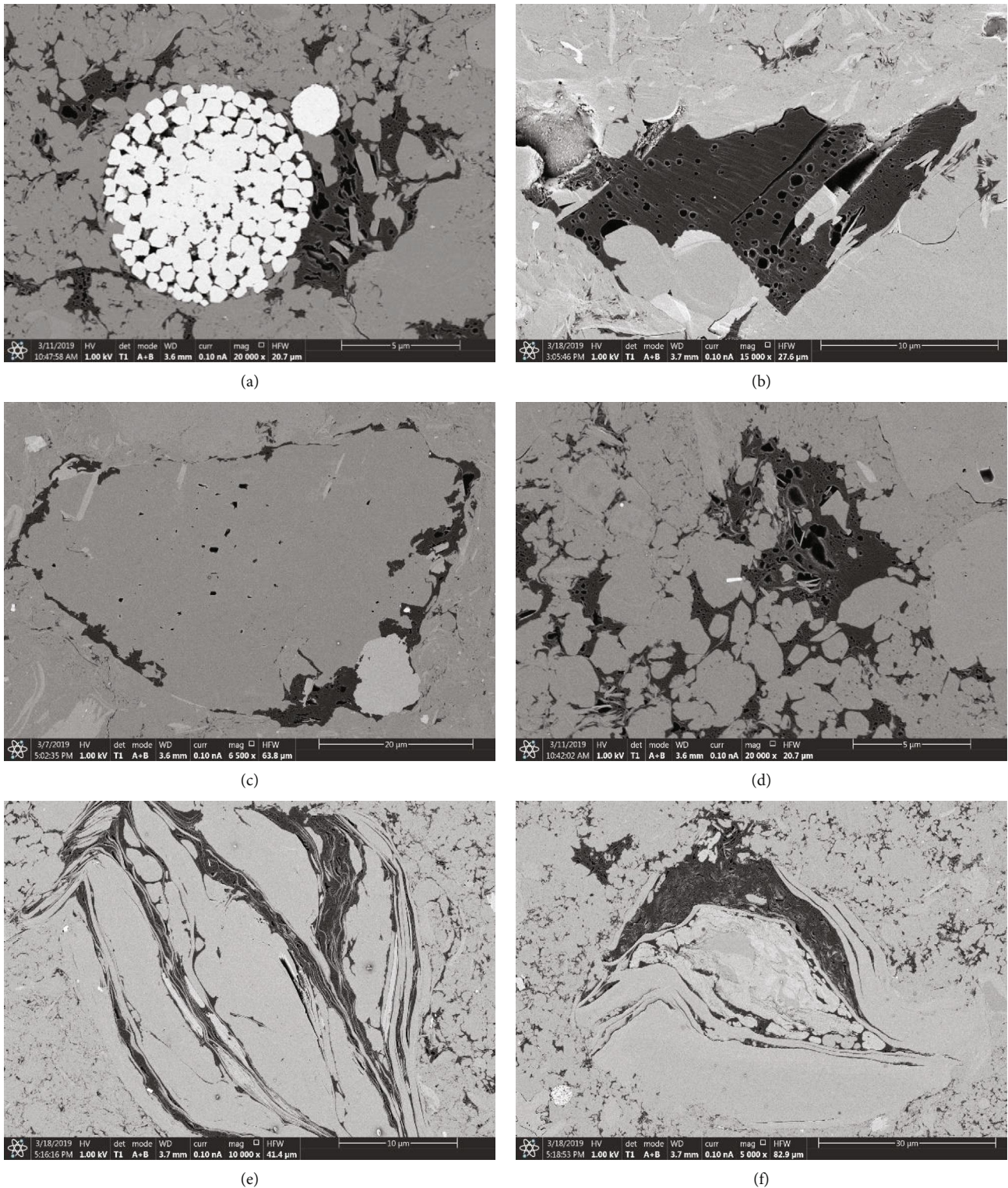
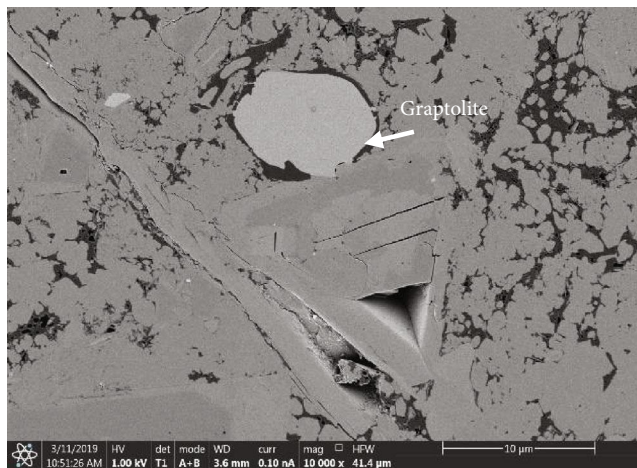


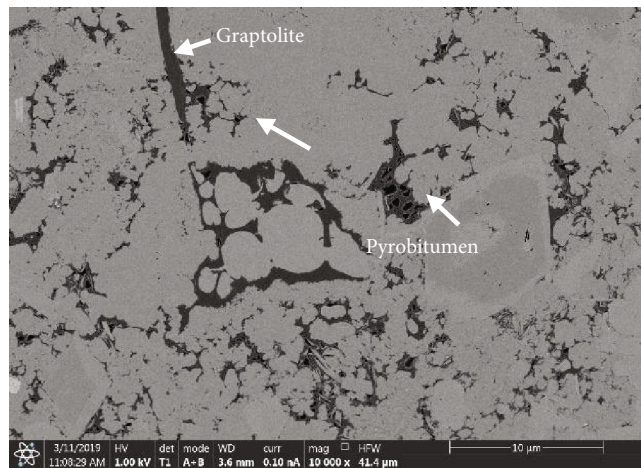
FIGURE 9: SEM images showing pyrobitumen and related pores in Wufeng-Longmaxi shale samples. (a–d) Pyrobitumen pieces with subround to round pores. Pyrobitumen is associated with minerals having a relatively regular shape and lower brightness. (b) Gas-related round pores with a tail-like structure within pyrobitumen. (e, f) Irregular or deformed pores in pyrobitumen filled with minerals of a curved to highly contorted scaly and silk thread laminar structure.

biogenic origins obviously plays a positive role in the porosity because of increasing TOC content [13, 102]. In comparison, the increasing biogenic quartz content could also decrease

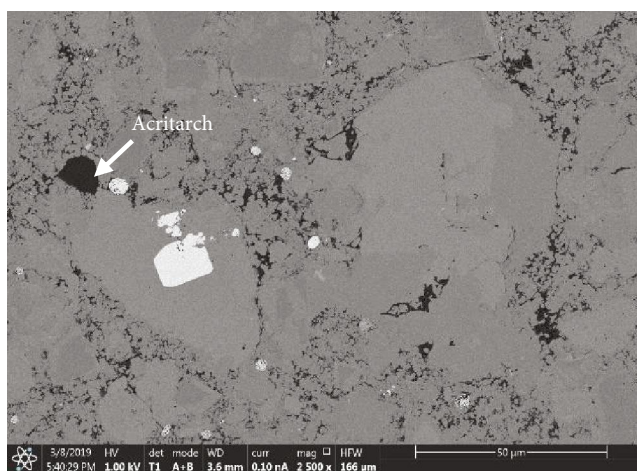
porosity due to secondary cementation of biogenic silica [103]. In our study, the quartz effect is also closely correlated to its origin. For relatively clay-poor shales (clay mineral



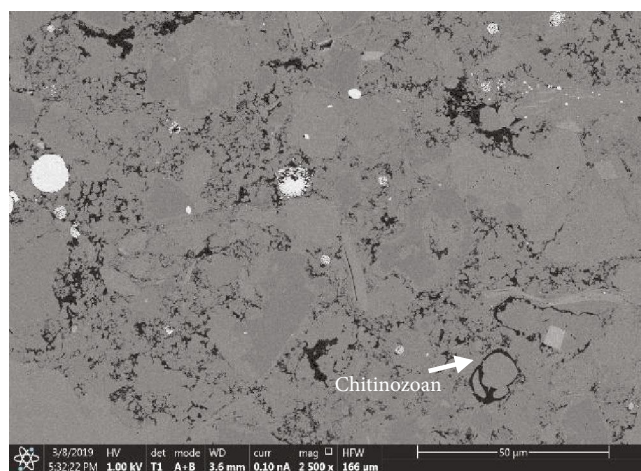
(a)



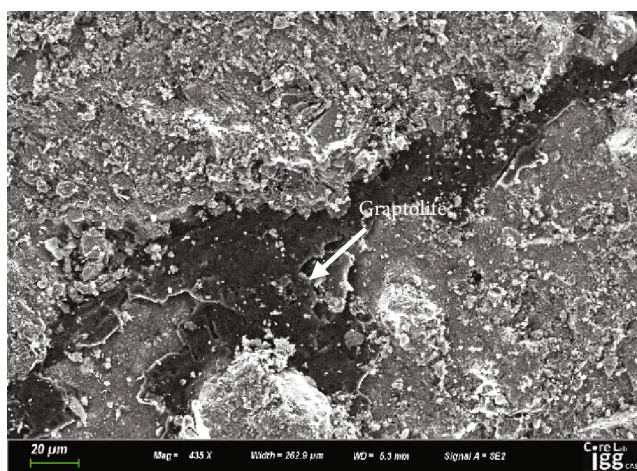
(b)



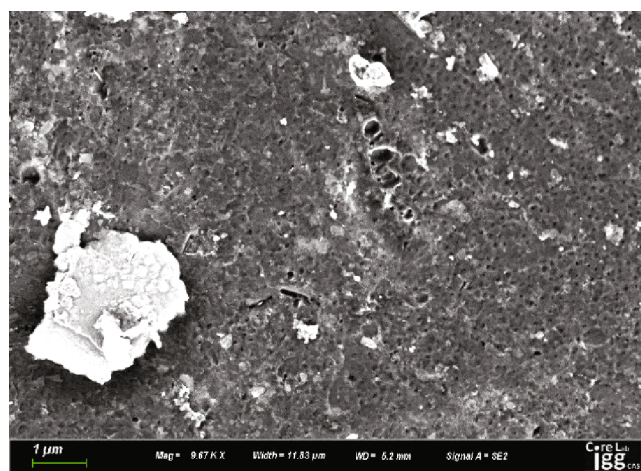
(c)



(d)



(e)



(f)

FIGURE 10: Continued.

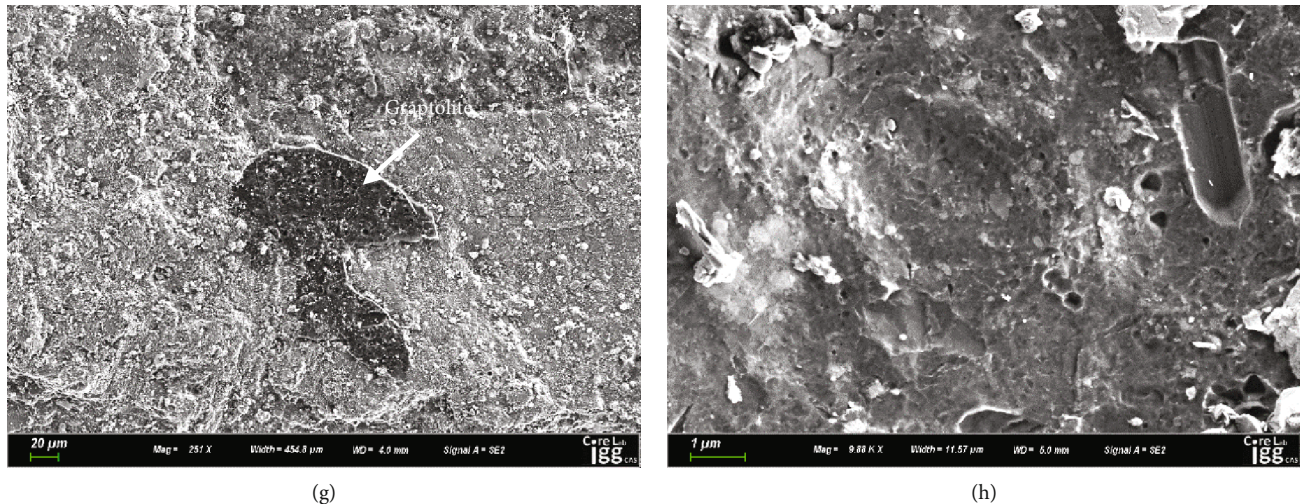


FIGURE 10: SEM images showing zooclast types and related pores in Wufeng-Longmaxi shale samples. (a–d) Zooclasts, including graptolite, chitinozoan, and acritarch, have no observable pores. (e, g) SEM images of graptolite in natural cores with no polishing. (f, h) Enlarged images of (e, g) in the arrow-pointed area, respectively.

content < 35%), quartz content is positively correlated with increasing TOC content, suggesting that the quartz in these shales is closely correlated with the biogenic origin, which is also indicated in previous studies [13, 102, 104]. For relatively clay-rich shales, quartz could mainly come from detrital input and has a weak correlation with the TOC content. Accordingly, different relationships between quartz and TOC content are attributed to the differences in their depositional environment and source input of quartz [65, 105]. In our study, there is also a positive correlation between TOC content and shale porosity parameters (pore volume and pore surface area). However, this relationship has a TOC content boundary. The existence of this boundary could result from different maceral types in OM, which would be discussed in Sections 4.2 and 4.3. When the TOC content in studied samples > 2%, the positive correlation is stronger than that in shale with TOC < 2%. The OM shows strong control than other factors in shales. In addition, the clay mineral content in shales is around 35% with the 2% boundary of TOC content. For clay-rich shales, OM and clay minerals together control pores in shales. The above different controls are due to the development of organic pores and also source input of quartz from detrital or biogenic origins. Content of biogenic quartz strongly correlates to OM and positively increases porosity compared to that of detrital quartz.

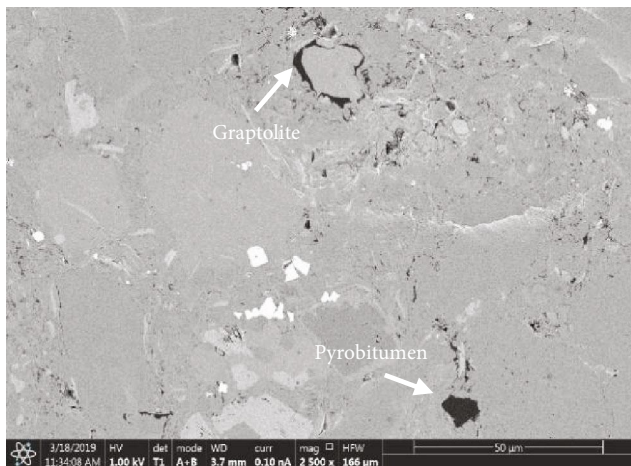
The OM plays a positive role in the micropore structure of Wufeng-Longmaxi shales. When the TOC content is above 1.5%, an obvious increase and strong positive relationship were found between TOC content, micropore volumes, and micropore surface areas, highlighting the large abundance of smaller pores within the organic fraction. However, the relationship between TOC content, macropore volumes, and macropore surface areas is not obvious. Clay mineral has a positive influence on macropores. The clay-rich shales usually have low TOC content, which reflects a significant contribution of clays to pore structure in organic-lean shales. Furthermore, pores in clays are usually well developed around quartz grains since rigid quartz grains can form pres-

sure shadows that prevent pores in clays from collapsing (Yang et al. 2016).

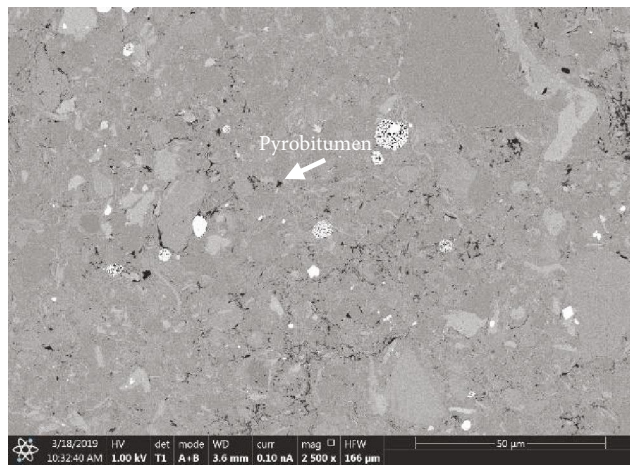
4.2. Organic Matter Types and Transformation with Maturation. The Ordovician to Early Silurian time interval represents a period of black shale deposition under stratified and anoxic bottom-water conditions in basins of China, North Africa, the Middle East, North America, and Europe [12, 53, 106, 107]. Those organic-rich shales are the source of large amounts of hydrocarbons and therefore were the subject of intensive studies on sedimentology and source rock evaluation ([5, 7, 53, 106, 107]; Yang et al. 2016). Reported major OM in these early Paleozoic sediments include AOM, algal *Tasmanites*, solid bitumen, chitinozoans, and graptolites [62–64] ranging from the early mature to postmature stage. Our study analyzed maceral composition in marine Wufeng-Longmaxi shale and Utica shale deposits of Late Ordovician-Early Silurian age from China and the U.S. Those shales feature a high maturity level at the postmature stage. The majority of the original kerogen is thermally degraded, and petrographic observations show that the pyrobitumen and zooclasts (graptolites and chitinozoans) are the dominant OM components. Pyrobitumen is dominant in Wufeng-Longmaxi shale, whereas graptolites dominated OM in Utica shale samples.

Because most prolific gas-producing shales are postmature [108–110] and organic porosity provides important storage capacity for gas [3, 5, 6, 26], understanding the characterization of OM and organic pores in postmature shales is very important in evaluating shale reservoir properties.

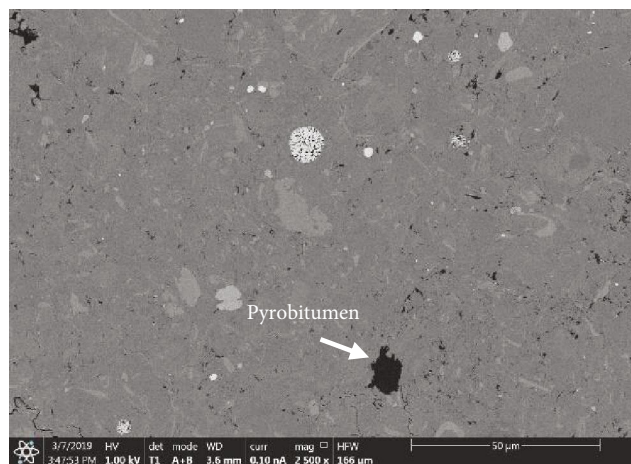
Previous studies indicate that each maceral evolves differently with maturation [27, 111]. With increasing maturity, from immature to postmature, oil-prone kerogen (AOM and alginite) first transforms to preoil bitumen and then to oil, gas, and postoil bitumen or pyrobitumen (e.g., [45]). Liu et al. [45] concluded that AOM and alginite began transforming to solid bitumen at the mature stage and that the solid bitumen network followed the original AOM network.



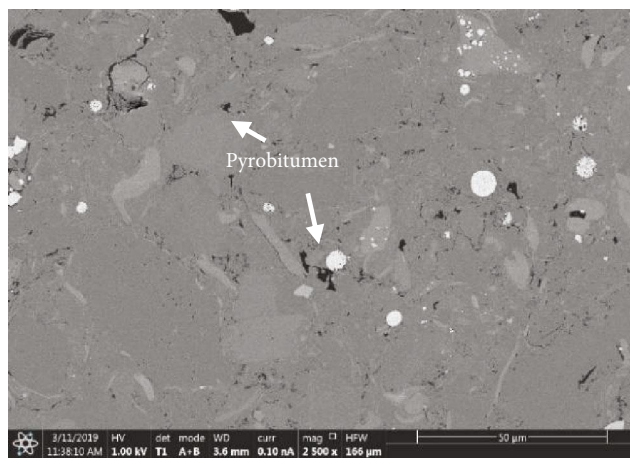
(a)



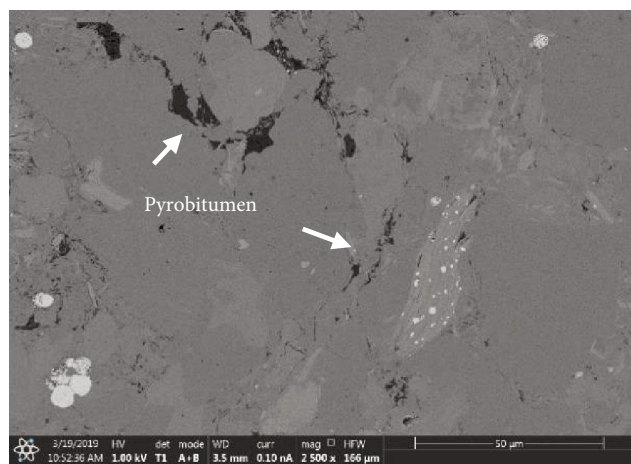
(b)



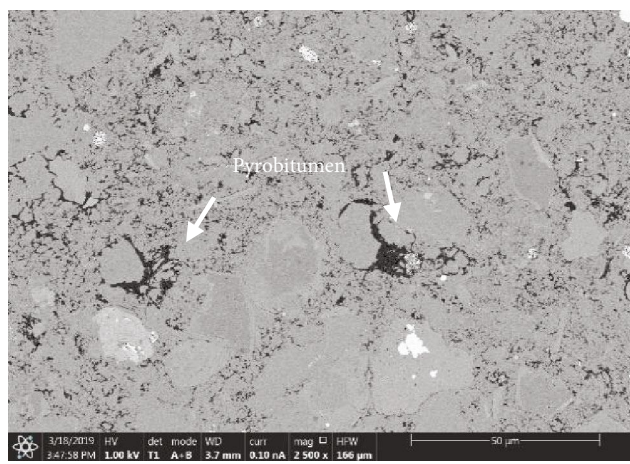
(c)



(d)



(e)



(f)

FIGURE 11: Continued.

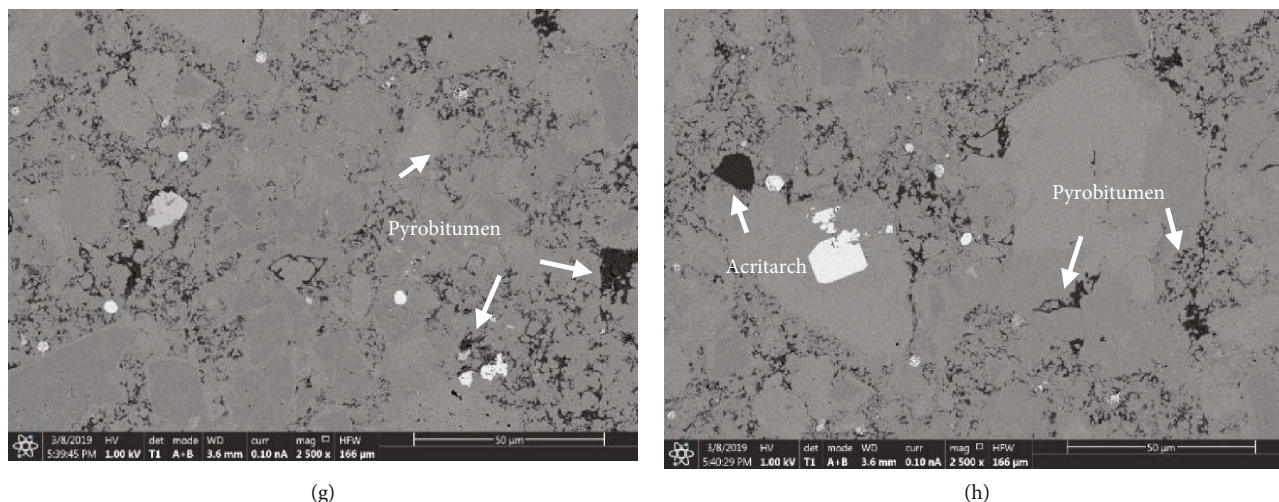


FIGURE 11: SEM images showing maceral types and related pores observed in Wufeng-Longmaxi shales. (a–h) Selected samples under SEM at depths of 2481 m, 2503 m, 2513 m, 2534 m, 2567 m, 2573 m, 2576 m, and 2577 m, respectively. The organic matter content increases with deeper depth (a–h) in the studied samples and can be reflected by the area of dark material (a–h). Pyrobitumen is the dominant maceral in samples, and its content shows an obvious increase in samples from 2567 m deep and deeper.

Cardott et al. [27] also suggested that a postoil solid bitumen network could have developed along the AOM network. Mastalerz et al. [111] proposed that the 1.5% solid bitumen reflectance (equivalent VR_o of approximately 1.33%, based on the empirical formula by Jacob [93]) could be considered the boundary between solid bitumen and pyrobitumen. In both Wufeng-Longmaxi shale and Utica shale, most pyrobitumen occurrences are very small (a few micrometers), scattered within the matrix, and porous. Compared to the solid bitumen reported from shales ranging from the early mature to postmature stage [45, 89, 98, 111, 112], pyrobitumen in our studied samples is smaller and more porous. We conclude that solid bitumen becomes more porous and scattered throughout the matrix during transformation to pyrobitumen as a result of secondary cracking. Researchers also suggest that with an increase in maturity to above 3.0%, OM could transform from amorphous carbon to crystalline graphite [70, 74]. When pyrobitumen loses its potential for generating hydrocarbons, no additional organic pores could be generated [74, 113, 114]. Wood et al. [115] proposed that the morphology of pyrobitumen resulted from its different origins in shales. Specifically, the curved margin of pore-filling pyrobitumen is a reflection of the original oil-water interface. The laminar structure within pyrobitumen was formed from increments of the viscous flow of oil into the original pore structure. The globular/granular texture was formed by the early precipitation of asphalt floccules from an unstable precursor oil phase in the central portions of large open pores. In our studied samples at the overmature stage ($VR_o = \sim 2.4\%$), the previously mentioned morphologies are not clearly reflected. Most pyrobitumens have a clear pore-filling structure and condensed morphology. We concluded particles except for zooclast as pyrobitumen and divided them into three types in this study. The first type is a migrated secondary product occupying interparticle space (between quartz, dolomite, K-feldspar, clay, and mica grains)

and cavities. The second type occurs as isolated and condensed individual pieces occupying interparticle space ($\sim 50 \mu\text{m}$), which might have been converted from oil-prone kerogen particles (AOM or alginite) in situ [45]. The third type of pyrobitumen particles having coarse surfaces might be an indicator of bacteria and fluid activity, which is also indicated in Wang et al. [85]. Different from the other pyrobitumen types, bacteria pellet-like pyrobitumen is isolated and might have a relatively weak correlation with hydrocarbon generation.

In comparison to alginite and AOM, vitrinite and inertinite (kerogen types III and IV) derived from terrestrial woody materials do not have a high hydrocarbon generation potential, so they do not show a significant change in morphology with increasing thermal maturity. Vitrinite and inertinite are present as distinct particles across the entire maturity range, as observed in Ordos shale and another study [45].

When the maturity reaches above 3%, the organic-rich shale loses its potential for hydrocarbon generation. In addition, as gas loss leads to pressure drop, the pores generated during the mature stage collapse and even disappear because they lack support [70, 74, 113]. A small amount of OM pores was preserved because of skeleton particle support [74], which is also indicated in Xiuwu shale in this study.

4.3. Maceral Pores and Their Relationship to Gas Storage. Organic matter-hosted pores are widely recognized as a significant component of the pore system in gas shales, including Wufeng-Longmaxi shale [55, 116, 117]. The strong correlation between TOC content and total porosity in studied Wufeng-Longmaxi samples supports the contribution of organic pores (Table 2). Among their macerals, pyrobitumen is the main component that hosts the organic pores detected by SEM. Pyrobitumen pores range from nanometer to micrometer in size. Some pyrobitumens with well-

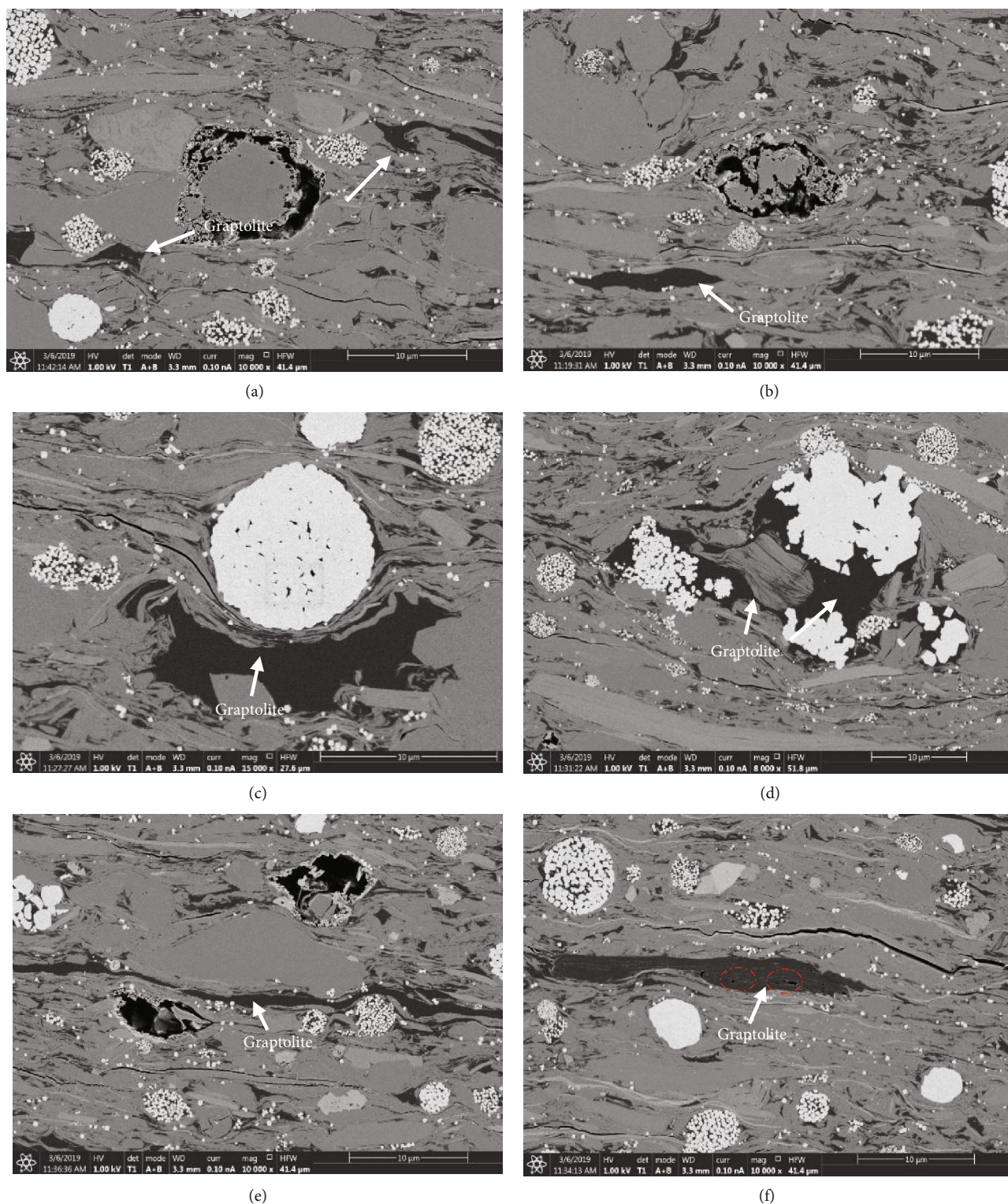


FIGURE 12: SEM images showing the typical habit and internal pore structure of organic matter in sample TRA-10. (a–f) Abundant graptolites and pyrite framboids distributed within the shale matrix. (a–c, e) Dispersed graptolite pieces without pores even enlarging current magnification. (f) A few pores of irregular and narrow shape inside graptolite grains, and the existence of such pores is not common in the studied sample.

developed nanopores were almost unidentifiable at the resolution of an optical microscope because only very thin walls remained. Subround to round pores in pyrobitumen were

considered to be formed by the devolatilization of gaseous hydrocarbons from matrix-retained bitumen or oils during thermal cracking [2, 5, 48, 54]. In our study, micrometer-

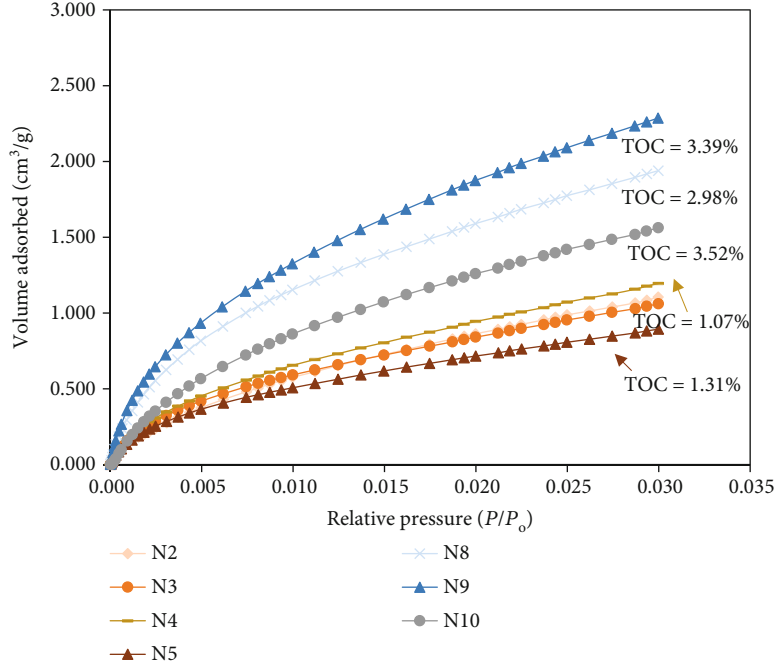


FIGURE 13: Low-pressure CO₂ adsorption isotherms of Wufeng-Longmaxi shales. Note that the largest volumes of adsorbed CO₂ occur in samples (samples N8, N9, and N10) of the highest TOC values. The TOC content is marked near the isotherm lines. P = actual gas pressure; P_0 = vapor pressure of the adsorbing gas.

TABLE 2: Micropore and macropore volumes and surface areas obtained by CO₂ gas adsorption and mercury intrusion capillary pressure (MICP) in Wufeng-Longmaxi shale. The total organic carbon content is also listed in the second column from the left side.

Sample ID	Total organic carbon (TOC) content (wt. %)	Pore volume (cm ³ /g)		Specific surface area (m ² /g)	
		Micropore	Macropore	Micropore	Macropore
N2	0.96	0.00110	0.0057	3.773	0.023
N3	0.89	0.00114	0.0053	4.084	0.025
N4	1.07	0.00127	0.0050	4.476	0.021
N5	1.31	0.00101	0.0053	3.604	0.014
N8	2.98	0.00238	0.0145	8.379	0.020
N9	3.39	0.00285	0.0056	9.887	0.027
N10	3.52	0.00187	0.0071	6.102	0.010

sized pore shapes depend on the degree of compaction. For example, pyrobitumen with round to subround pores frequently developed between quartz or carbonate grains, which suggests that brittle minerals can protect the micrometer-sized organic pores from compaction at the postmature stage. In turn, irregular pores in pyrobitumen are usually associated with deformed or layered clay minerals, which are ductile and easily compacted. To some extent, micrometer-sized pores resist compaction with the help of surrounding brittle minerals. In fact, some studies indicate that pore sizes < 100 nm are especially resistant to compaction [29, 118].

Zooclasts including graptolites and chitinozoan have zero to very limited pores in the studied samples, indicating that zooclasts did not undergo secondary transformation with maturation. Thus, for Utica shale and Wufeng-Longmaxi shale at the dry gas stage, the SEM-detected porosity contribution from graptolites and chitinozoan to

the total porosity in shale is negligible. Ardakani et al. [43] also reported that chitinozoans had no pores visible in their wall structure in Utica shale samples from southern Quebec at the mature to postmature stage (VR_0 ranging from ~1 to 2.1%). This could explain why the Utica shale sample with abundant zooclasts has lower porosity compared to the Wufeng-Longmaxi samples from a depth of ~2576 m that have low contributions of zooclasts and abundant pyrobitumen. In Wufeng-Longmaxi shale, owing to the relatively low abundance and limited pore network of zooclasts, the pyrobitumen network that hosts secondary organic nanopores plays a significant role in hydrocarbon storage and migration.

With increased depths in Wufeng-Longmaxi shale, the positive relationship between pyrobitumen, porosity, and gas content emphasizes the significance of pyrobitumen in this formation. Both pyrobitumen and zooclasts contribute

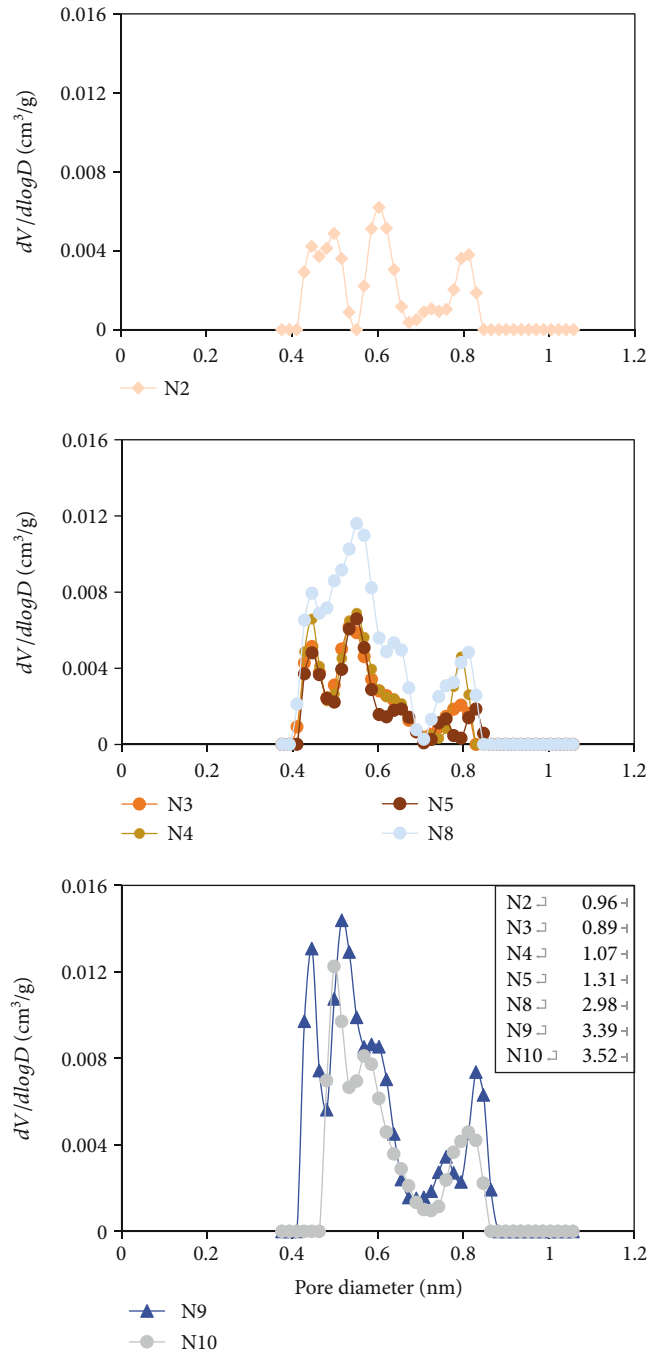


FIGURE 14: Log differential pore volume derived from low-pressure CO_2 adsorption for Wufeng-Longmaxi shales with samples of different total organic carbon (TOC) contents. The TOC content (wt. %) of each sample is marked in the rectangle in the third panel. The micropore size distribution up to 1.2 nm was calculated with the DFT model. Pores with diameter < 1 nm have different log differential pore volumes. There are three higher $dV/d \log D$ peaks at approximately 0.40–0.50 nm, 0.55–0.60 nm, and 0.80–0.81 nm.

to the TOC content, but not as much as porosity. The TOC content strongly controls pore development, especially for marine shales. Therefore, among high-maturity samples with comparable amounts of TOC, those having higher proportions of pyrobitumen and lower proportions of zooclasts will likely have a greater potential for gas storage. Because pyrobitumen is the secondary product from lipid material, we can conclude that a higher input of algae can provide not only

greater hydrocarbon-generating ability but also more space for hydrocarbon storage.

In contrast to our observations, some researchers found that submicron- to micron-sized pores were present in graptolite structures [55, 56]. For example, Luo et al. [55] found abundant organic pores in the nongranular graptolites in Wufeng-Longmaxi shale having equivalent VR_0 values ranging from 3.08 to 4.29%. They also claimed

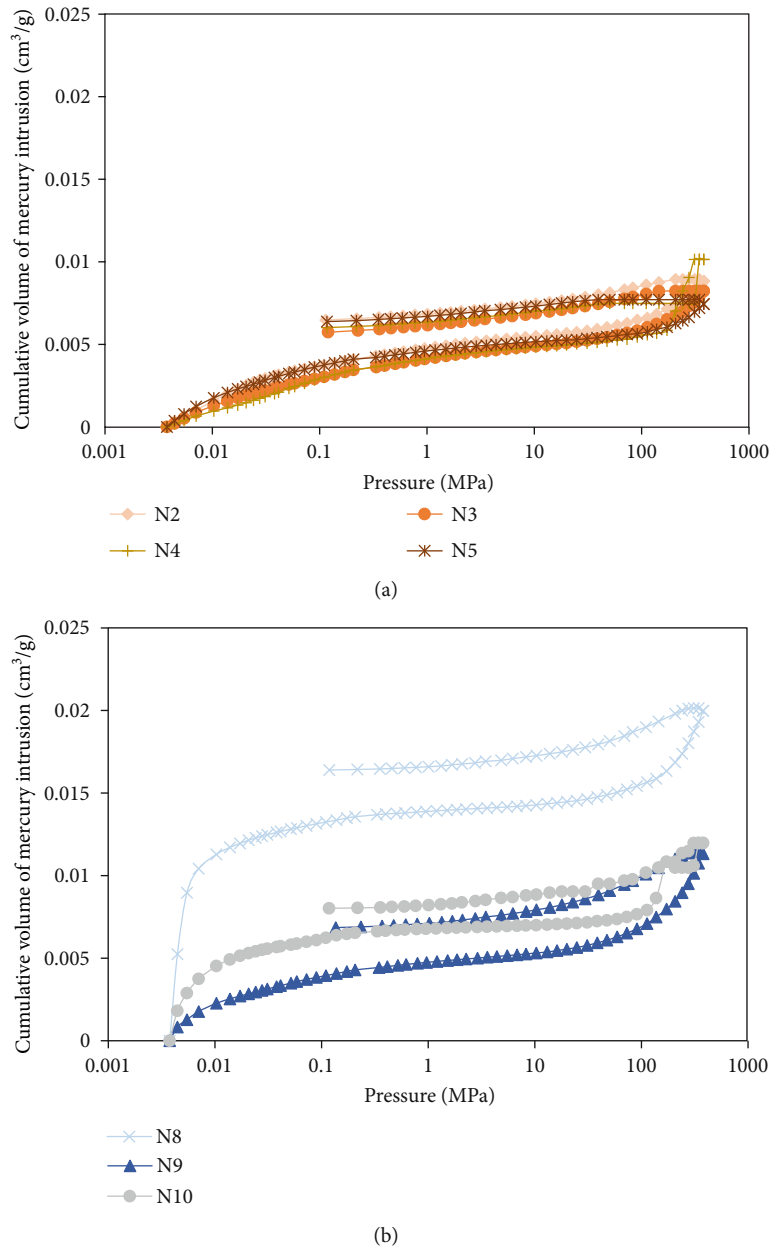


FIGURE 15: Mercury injection curves for Wufeng-Longmaxi shales. The mercury intrusion curves exhibit two different trends in studied samples, which are presented in (a, b). (a) Types of samples N2 to N5 with relatively lower TOC contents. The volume of mercury intrusion first increases (0.01–1 MPa) and is then kept stable (1–400 MPa). (b) Types of samples N8 to N10 with higher TOC contents. The volume of mercury intrusion shows a rapid increase (0.01–1 MPa), a relatively stable phase (1–50 MPa), and a rapidly increasing phase (50–400 MPa).

that graptolites account for 20 to 93% of the dispersed OM in the Wufeng-Longmaxi Formation [55]. However, the graptolites in our ion-milled Wufeng-longmaxi samples only accounted for a small portion of the whole OM (less than 20%) and have zero to very limited pores inside. This indicates that maturity above 3.0% may change the structure of graptolites. In addition, the SEM images on unpolished Wufeng-Longmaxi samples also show clear pores in large graptolite bodies in cores (Figures 10(e)–10(h)). One possible explanation of this discrepancy could be that the structure of graptolite is layered and soft and could be easily eroded with long-

term exposure, developing a pore-like structure on the surface of unpolished cores. Ion milling removed the pore-like structure in the graptolite surface and allowed observing real internal structure in shales.

4.4. Chemical Structure of Pyrobitumen and Zooclasts. Graptolites and chitinozoans are microfossils that have thin organic walls and are common in Lower Paleozoic marine rocks [53, 62, 64, 119, 120]. Previous studies of pyrolysis-gas chromatography on chitinozoan in mature shales suggest that their composition is similar to woody material (i.e.,

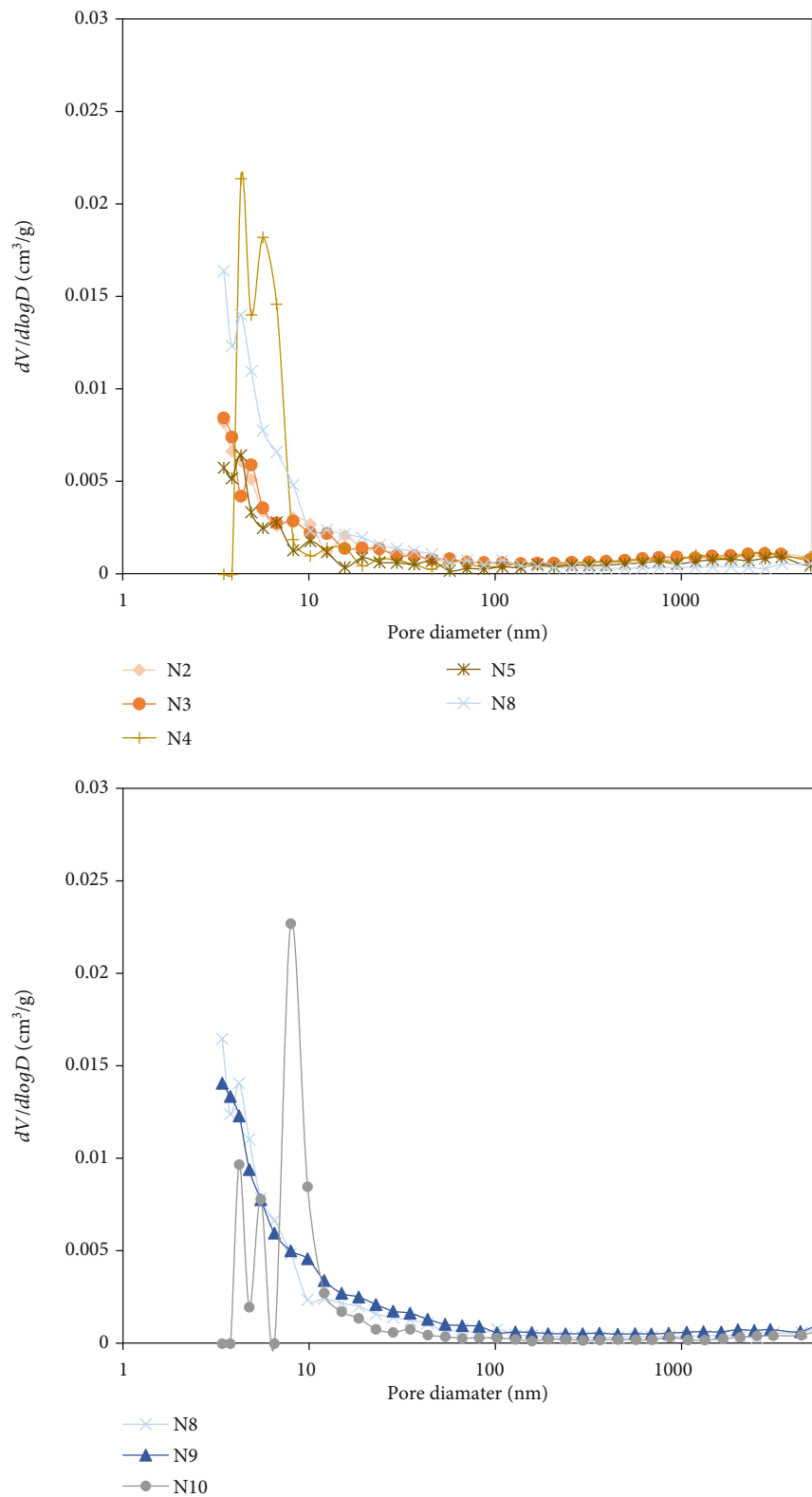


FIGURE 16: Log differential pore volume for Wufeng-Longmaxi shales derived from MICP. The x -axis marked the pore diameter in the nanometer, and the y -axis marked the log differential pore volume. Samples N8, N9, and N10 featured higher TOC contents than samples N2 to N8. The TOC contents of N8 to N10 are 2.98%, 3.39%, and 3.52%, respectively.

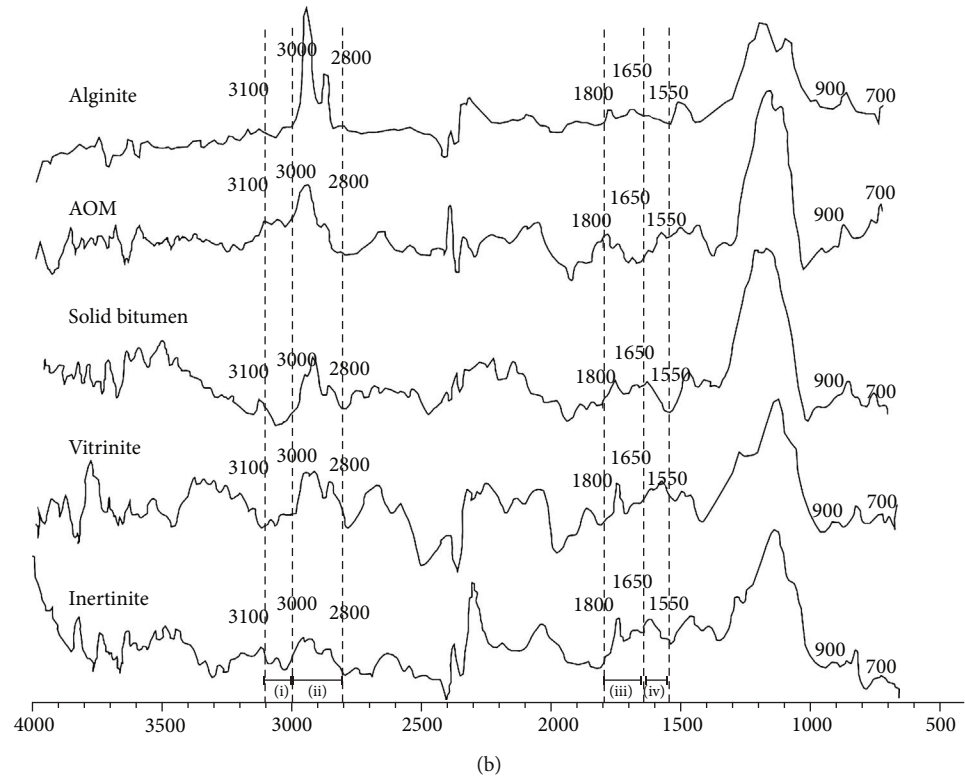
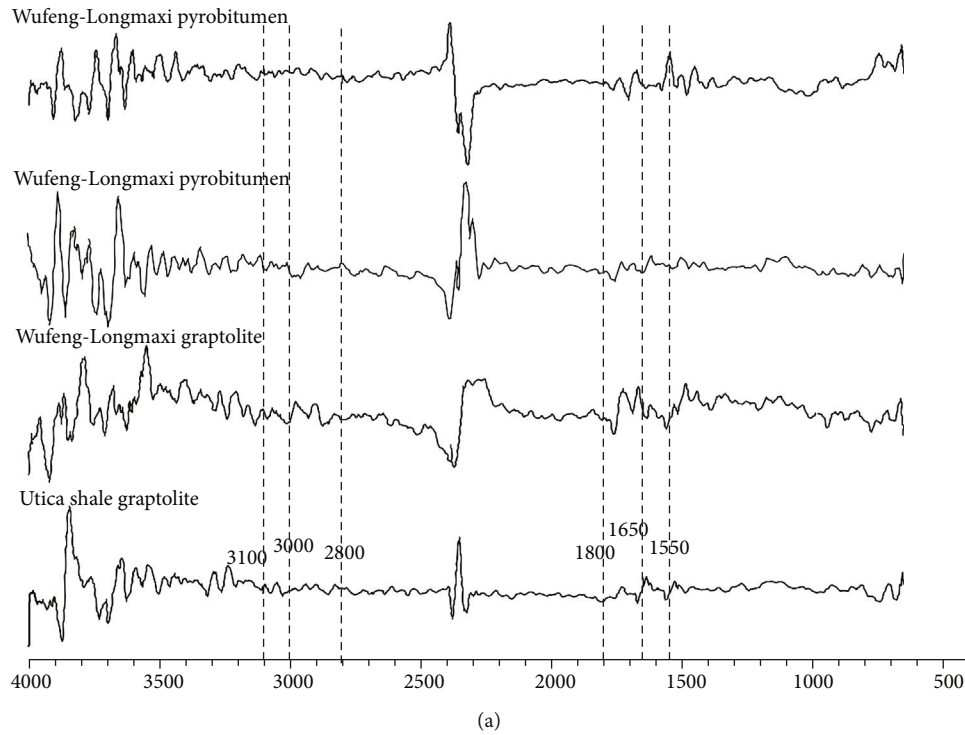


FIGURE 17: (a) Micro-FTIR spectra of pyrobitumen and graptolite in studied samples. The first two are of pyrobitumen, and the third and fourth show graptolite in Wufeng-Longmaxi shale and Utica shale, respectively. (b) Micro-FTIR spectra of alginite, AOM, solid bitumen, vitrinite, and inertinite from New Albany Shale samples ($VR_o = 0.63\%$) (adapted from [89]).

kerogen type III) and gas-prone biomacromolecules [121, 122]. Dutta et al. [123], using SEM images, suggested that chitinozoans originally are devoid of any porosity in their structure, and based on their kerogen composition, pores

are not expected to develop during thermal maturation. Our FTIR analysis further suggests that the chemical composition of graptolite periderm is indeed similar to vitrinite and inertinite, which are major components of type III kerogens;

i.e., they contain a large amount of oxygen-containing functional groups and aromatic groups [121]. Reyes et al. [122] suggested that chitinozoans and graptolites had limited or no contribution to overall hydrocarbon generation because morphological evidence of the thermal decomposition in the immature to gas generation window under SEM is unavailable. Our FTIR data show that at the maturity corresponding to $VR_o \sim 2.45\%$, pyrobitumen lost its hydrocarbon-generating potential and only some C=O and C=C groups are detected in the spectra.

5. Conclusions

In this study, postmature Ordovician to Early Silurian Wufeng-Longmaxi shale samples were collected from Sichuan Basin in South China to investigate OM types and their associated pore structures by correlative organic petrographic and SEM analyses and various porosimetry measurements. For comparison, organic petrographic and SEM analyses were performed on the age-equivalent Utica shale from the U.S., overmature marine shale from Xiuwu Basin, and marine-continental transitional shale from Ordos Basin in China.

Quartz content shows different relationships with TOC content in studied Wufeng-Longmaxi shales due to quartz origin difference. Quartz content is positively correlated with TOC content in clay-poor shales (clay mineral content $< \sim 35\%$), indicating quartz mainly of biogenic origins, whereas it exhibits no correlation with TOC in clay-rich shales, indicating quartz mainly of detrital origins. OM is the predominant controlling factor on micropores and also controls macropore development when TOC content increased to a certain level. Clay mineral and quartz contents also make different contributions to pore development.

In both Wufeng-Longmaxi shale and Utica shale, pyrobitumen and zooclasts were the dominant OM components, but their relative proportions varied. Specifically, pyrobitumen was dominant in Wufeng-Longmaxi shale, whereas zooclasts (and graptolites, in particular) were dominant in Utica shale. Pyrobitumen in Wufeng-Longmaxi shale was classified into three types according to morphological and internal structure differences. Each type of pyrobitumen owns distinct forms, and pore development within is highly heterogeneous. Specifically, pores are universally and uniformly developed in pyrobitumen I and abundantly developed in pyrobitumen III as bacteria-like aggregates but not well developed in pyrobitumen II nor graptolites. Pores developed in pyrobitumen I were most strongly influenced by hydrocarbon generation. Pyrobitumen II is a highly condensed form resulting from high compaction and high-temperature evaporation.

At the overmature maturation level ($VR_o \sim 2.4\%$), neither graptolites nor pyrobitumens have hydrocarbon-generating potential, as indicated by their aromatic nature and almost total absence of aliphatic hydrogen functionalities.

At the scale detected by SEM, most pyrobitumens were very porous, providing space for gas storage. In contrast, zero to very limited pores were documented in zooclasts, suggesting that while they contribute to the total OM content, they

do not contribute space for gas storage or migration in these rocks. The high abundance of pyrobitumen in organic matter is the main contribution to pore development. These observations suggest that the proportions of pyrobitumen to zooclasts in the total OM may play an important role in predicting organic porosity and, ultimately, storage capacity of Ordovician-Silurian shales.

The types and sources of some organic matter are indistinguishable due to overly high maturity and compaction deformation. Nevertheless, the identification of typical maceral and related pore distributions is meaningful for better understanding the generation and preservation of shale gas and pore development mechanisms.

Data Availability

The data used to support the findings of this study are available from the first author upon request.

Conflicts of Interest

We declare that we do not have any commercial or associative interest that represents a conflict of interest in connection with the work submitted.

Acknowledgments

This work was supported by the Fundamental Research Funds for China University of Geosciences (Beijing) under Award Numbers 35832019035 and 53200759769. Financial support from the National Natural Science Foundation of China under Award Number 41702133 is also greatly appreciated.

References

- [1] J. B. Curtis, "Fractured shale-gas systems," *AAPG Bulletin*, vol. 86, pp. 1921–1938, 2002.
- [2] S. Bernard, B. Horsfield, H.-M. Schulz, R. Wirth, A. Schreiber, and N. Sherwood, "Geochemical evolution of organic-rich shales with increasing maturity: a STXM and TEM study of the Posidonia Shale (Lower Toarcian, northern Germany)," *Marine and Petroleum Geology*, vol. 31, no. 1, pp. 70–89, 2012.
- [3] Y. Chen, L. Wei, M. Mastalerz, and A. Schimmelmann, "The effect of analytical particle size on gas adsorption porosimetry of shale," *International Journal of Coal Geology*, vol. 138, pp. 103–112, 2015.
- [4] M. E. Curtis, B. J. Cardott, C. H. Sondergeld, and C. S. Rai, "Development of organic porosity in the Woodford Shale with increasing thermal maturity," *International Journal of Coal Geology*, vol. 103, pp. 26–31, 2012.
- [5] R. G. Loucks and R. M. Reed, "Scanning-electron-microscope petrographic evidence for distinguishing organic-matter pores associated with depositional organic matter versus migrated organic matter in mudrocks," *Gulf Coast Association of Geological Societies Transactions*, vol. 64, p. 713, 2014.
- [6] D. Misch, F. Mendez-Martin, G. Hawranek, P. Onuk, D. Gross, and R. F. Sachsenhofer, "SEM and FIB-SEM investigations on potential gas shales in the Dniepr-Donets Basin (Ukraine): pore space evolution in organic matter during

- thermal maturation," *IOP Conference Series: Materials Science and Engineering*, vol. 109, article 012010, 2016.
- [7] M.-F. Romero-Sarmiento, M. Ducros, B. Carpentier et al., "Quantitative evaluation of TOC, organic porosity and gas retention distribution in a gas shale play using petroleum system modeling: application to the Mississippian Barnett Shale," *Marine and Petroleum Geology*, vol. 45, pp. 315–330, 2013.
- [8] M. D. Sun, B. S. Yu, Q. H. Hu et al., "Pore characteristics of Longmaxi shale gas reservoir in the northwest of Guizhou, China: investigations using small-angle neutron scattering (SANS), helium pycnometry, and gas sorption isotherm," *International Journal of Coal Geology*, vol. 171, pp. 61–68, 2017.
- [9] M. D. Sun, B. S. Yu, Q. H. Hu, R. Yang, Y. Zhang, and B. Li, "Pore connectivity and tracer migration of typical shales in South China," *Fuel*, vol. 203, pp. 32–46, 2017.
- [10] F. Yang, Z. Ning, Q. Wang, R. Zhang, and B. M. Krooss, "Pore structure characteristics of Lower Silurian shales in the southern Sichuan Basin, China: insights to pore development and gas storage mechanism," *International Journal of Coal Geology*, vol. 156, pp. 12–24, 2016.
- [11] K. Zhang, J. Peng, W. Liu et al., "The role of deep geofluids in the enrichment of sedimentary organic matter: a case study of the Late Ordovician-Early Silurian in the Upper Yangtze region and Early Cambrian in the Lower Yangtze region, South China," *Geofluids*, vol. 2020, Article ID 8868638, 12 pages, 2020.
- [12] W. Zhao, J. Li, T. Yang, S. Wang, and J. Huang, "Geological difference and its significance of marine shale gases in South China," *Petroleum Exploration and Development*, vol. 43, no. 4, pp. 547–559, 2016.
- [13] J. Zhao, Z. K. Jin, Z. J. Jin, X. Wen, and Y. Geng, "Origin of authigenic quartz in organic-rich shales of the Wufeng and Longmaxi Formations in the Sichuan Basin, South China: implications for pore evolution," *Journal of Natural Gas Science and Engineering*, vol. 38, pp. 21–38, 2017.
- [14] K. S. W. Sing, "Reporting physisorption data for gas/solid systems with special reference to the determination of surface area and porosity (Recommendations 1984)," *Pure Applied Chemistry*, vol. 57, no. 4, pp. 603–619, 1985.
- [15] R. G. Loucks, R. M. Reed, S. C. Ruppel, and U. Hammes, "Spectrum of pore types and networks in mudrocks and a descriptive classification for matrix-related mudrock pores," *AAPG Bulletin*, vol. 96, no. 6, pp. 1071–1098, 2012.
- [16] M. Mastalerz, A. Schimmelmann, A. Drobniak, and Y. Chen, "Porosity of Devonian and Mississippian New Albany Shale across a maturation gradient: insights from organic petrology, gas adsorption, and mercury intrusion," *AAPG Bulletin*, vol. 97, no. 10, pp. 1621–1643, 2013.
- [17] K. L. Milliken, M. Rudnicki, D. N. Awwiller, and T. Zhang, "Organic matter-hosted pore system, Marcellus Formation (Devonian), Pennsylvania," *AAPG Bulletin*, vol. 97, no. 2, pp. 177–200, 2013.
- [18] M. Pommer and K. Milliken, "Pore types and pore-size distributions across thermal maturity, Eagle Ford Formation, southern Texas," *AAPG Bulletin*, vol. 99, no. 9, pp. 1713–1744, 2015.
- [19] M. D. Sun, J. L. Zhao, Z. J. Pan et al., "Pore characterization of shales: a review of small angle scattering technique," *Journal of Natural Gas Science and Engineering*, vol. 78, article 103294, 2020.
- [20] M. D. Sun, L. H. Zhang, Q. H. Hu et al., "Multiscale connectivity characterization of marine shales in southern China by fluid intrusion, small-angle neutron scattering (SANS), and FIB-SEM," *Marine and Petroleum Geology*, vol. 112, article 104101, 2020.
- [21] L. T. Ko, G. L. Loucks, T. Zhang, S. C. Ruppel, and D. Shao, "Pore and pore network evolution of Upper Cretaceous Boquillas (Eagle Ford-equivalent) mudrocks: results from gold tube pyrolysis experiments," *AAPG Bulletin*, vol. 100, no. 11, pp. 1693–1722, 2016.
- [22] Q. R. Passey, K. M. Bohacs, W. L. Esch, R. Klimentidis, and S. Sinha, "From oil-prone source rock to gas-producing shale reservoir – geologic and petrophysical characterization of unconventional shale-gas reservoirs," in *CPS/SPE International Oil Gas Conference and Exhibition*, Beijing, China, 2010.
- [23] R. M. Slatt and N. R. O'Brien, "Pore types in the Barnett and Woodford gas shales: contribution to understanding gas storage and migration pathways in fine-grained rocks," *AAPG Bulletin*, vol. 95, no. 12, pp. 2017–2030, 2011.
- [24] F. Javadpour, D. Fisher, and M. Unsworth, "Nanoscale gas flow in shale gas sediments," *Journal of Canadian Petroleum Technology*, vol. 46, no. 10, pp. 55–61, 2007.
- [25] Y. Li, Y. Wang, J. Wang, and Z. Pan, "Variation in permeability during CO₂-CH₄ displacement in coal seams: part 1 - experimental insights," *Fuel*, vol. 263, article 116666, 2020.
- [26] L. Wei, M. Mastalerz, A. Schimmelmann, and Y. Chen, "Influence of Soxhlet-extractable bitumen and oil on porosity in thermally maturing organic-rich shales," *International Journal of Coal Geology*, vol. 132, pp. 38–50, 2014.
- [27] B. J. Cardott, C. R. Landis, and M. E. Curtis, "Post-oil solid bitumen network in the Woodford Shale, USA – a potential primary migration pathway," *International Journal of Coal Geology*, vol. 139, pp. 106–113, 2015.
- [28] T. Dong, S. He, M. Chen et al., "Quartz types and origins in the Paleozoic Wufeng-Longmaxi Formations, eastern Sichuan Basin, China: implications for porosity preservation in shale reservoirs," *Marine and Petroleum Geology*, vol. 106, pp. 62–73, 2019.
- [29] R. G. Loucks, R. M. Reed, S. C. Ruppel, and D. M. Jarvie, "Morphology, genesis, and distribution of nanometer-scale pores in siliceous mudstones of the Mississippian Barnett Shale," *Journal of Sedimentary Research*, vol. 79, no. 12, pp. 848–861, 2009.
- [30] O. H. Ardakani, H. Sanei, A. Ghanizadeh, M. McMechan, F. Ferri, and C. R. Clarkson, "Hydrocarbon potential and reservoir characteristics of Lower Cretaceous Garbutt Formation, Liard Basin Canada," *Fuel*, vol. 209, pp. 274–289, 2017.
- [31] N. S. Fishman, P. C. Hackley, H. A. Lowers et al., "The nature of porosity in organic-rich mudstones of the Upper Jurassic Kimmeridge Clay Formation, North Sea, offshore United Kingdom," *International Journal of Coal Geology*, vol. 103, pp. 32–50, 2012.
- [32] W. Ji, F. Hao, H. Schulz, Y. Song, and J. Tian, "The architecture of organic matter and its pores in highly mature gas shales of the Lower Silurian Longmaxi Formation in the Upper Yangtze Platform, South China," *AAPG Bulletin*, vol. 103, no. 12, pp. 2909–2942, 2019.
- [33] R. G. Loucks, R. M. Reed, S. C. Ruppel, and U. Hammes, "Preliminary classification of matrix pores in mudrocks,"

- Gulf Coast Association of Geological Societies Transactions*, vol. 60, pp. 435–441, 2010.
- [34] H. Nie, Z. Jin, and J. Zhang, “Characteristics of three organic matter pore types in the Wufeng-Longmaxi shale of the Sichuan Basin, Southwest China,” *Scientific reports*, vol. 8, no. 1, p. 7014, 2018.
- [35] J. Schieber, “Common themes in the formation and preservation of intrinsic porosity in shales and mudstones – illustrated with examples across the Phanerozoic,” in *Society of Petroleum Engineers Unconventional Gas Conference*, Pittsburgh, Pennsylvania, U.S, 2010.
- [36] K. Zhang, Y. Song, S. Jiang et al., “Shale gas accumulation mechanism in a syncline setting based on multiple geological factors: an example of southern Sichuan and the Xiuwu Basin in the Yangtze region,” *Fuel*, vol. 241, pp. 468–476, 2019.
- [37] X. Guo, Z. Qin, R. Yang et al., “Comparison of pore systems of clay-rich and silica-rich gas shales in the Lower Silurian Longmaxi Formation from the Jiaoshiba area in the eastern Sichuan Basin, China,” *Marine and Petroleum Geology*, vol. 101, pp. 265–280, 2019.
- [38] W. Ji, Y. Song, Z. Jiang et al., “Fractal characteristics of nanopores in the Lower Silurian Longmaxi shales from the Upper Yangtze Platform, South China,” *Marine and Petroleum Geology*, vol. 78, pp. 88–98, 2016.
- [39] J. Chen and X. Xiao, “Evolution of nanoporosity in organic-rich shales during thermal maturation,” *Fuel*, vol. 129, pp. 173–181, 2014.
- [40] J. Chen, F. Jiang, T. Hu et al., “Experimental investigation of the characteristics of organic matter pores in Chang 7 member lacustrine shale from the Ordos Basin due to organic matter evolution induced by hydrous pyrolysis,” *Journal of Natural Gas Science and Engineering*, vol. 35, pp. 412–424, 2016.
- [41] W. Yang, R. S. Zuo, Z. X. Jiang et al., “Effect of lithofacies on pore structure and new insights into pore-preserving mechanisms of the over-mature Qiongzhusi marine shales in Lower Cambrian of the southern Sichuan Basin, China,” *Marine and Petroleum Geology*, vol. 98, pp. 746–762, 2018.
- [42] K. Zhang, J. Peng, X. Wang et al., “Effect of organic maturity on shale gas genesis and pores development: a case study on marine shale in the Upper Yangtze region, South China,” *Open Geosciences*, vol. 12, no. 1, pp. 1617–1629, 2020.
- [43] O. H. Ardakani, H. Sanei, A. Ghanizadeh, D. Lavoie, Z. Chen, and C. R. Clarkson, “Do all fractions of organic matter contribute equally in shale porosity? A case study from Upper Ordovician Utica shale, southern Quebec, Canada,” *Marine and Petroleum Geology*, vol. 92, pp. 794–808, 2018.
- [44] G. R. L. Chalmers and R. M. Bustin, “A multidisciplinary approach in determining the maceral (kerogen type) and mineralogical composition of Upper Cretaceous Eagle Ford Formation: impact on pore development and pore size distribution,” *International Journal of Coal Geology*, vol. 171, pp. 93–110, 2017.
- [45] B. Liu, J. Schieber, and M. Mastalerz, “Combined SEM and reflected light petrography of organic matter in the New Albany Shale (Devonian-Mississippian) in the Illinois Basin: a perspective on organic pore development with thermal maturation,” *International Journal of Coal Geology*, vol. 184, pp. 57–72, 2017.
- [46] S. C. Löhner, E. T. Baruch, P. A. Hall, and M. J. Kennedy, “Is organic pore development in gas shales influenced by the primary porosity and structure of thermally immature organic matter?,” *Organic Geochemistry*, vol. 87, pp. 119–132, 2015.
- [47] J. Teng, M. Mastalerz, and L. Hampton, “Maceral controls on porosity characteristics of lithotypes of Pennsylvanian high volatile bituminous coal: example from the Illinois Basin,” *International Journal of Coal Geology*, vol. 172, pp. 80–94, 2017.
- [48] P. C. Hackley and B. J. Cardott, “Application of organic petrography in North American shale petroleum systems: a review,” *International Journal of Coal Geology*, vol. 163, pp. 8–51, 2016.
- [49] B. P. Tissot and D. H. Welte, *Petroleum Formation and Occurrence*, Springer Berlin Heidelberg, Berlin, 2nd Edition edition, 1984.
- [50] ICCP (International Commission for Coal Petrology), *International Handbook of Coal Petrography, 2nd Supplement to, Centre National de la Recherche Scientifique, Paris, 2nd Edition edition, 1975.*
- [51] Y. Li, J. Yang, Z. Pan, and W. Tong, “Nanoscale pore structure and mechanical property analysis of coal: an insight combining AFM and SEM images,” *Fuel*, vol. 260, article 116352, 2020.
- [52] R. W. T. Wilkins, J. R. Wilmshurst, N. J. Russell, G. Hladky, M. V. Ellacott, and C. Buckingham, “Fluorescence alteration and the suppression of vitrinite reflectance,” *Organic Geochemistry*, vol. 18, no. 5, pp. 629–640, 1992.
- [53] O. Haeri-Ardakani, H. Sanei, D. Lavoie, Z. Chen, and C. Jiang, “Geochemical and petrographic characterization of the Upper Ordovician Utica shale, southern Quebec, Canada,” *International Journal of Coal Geology*, vol. 138, pp. 83–94, 2015.
- [54] G. Hu, Q. Pang, K. Jiao, C. Hu, and Z. Liao, “Development of organic pores in the Longmaxi Formation overmature shales: combined effects of thermal maturity and organic matter composition,” *Marine and Petroleum Geology*, vol. 116, article 104314, 2020.
- [55] Q. Luo, N. Zhong, N. Dai, and W. Zhang, “Graptolite-derived organic matter in the Wufeng-Longmaxi Formations (Upper Ordovician-Lower Silurian) of southeastern Chongqing, China: implications for gas shale evaluation,” *International Journal of Coal Geology*, vol. 153, pp. 87–98, 2016.
- [56] Y. Ma, N. Zhong, L. Cheng et al., “Pore structure of the graptolite-derived OM in the Longmaxi shale, southeastern Upper Yangtze region, China,” *Marine and Petroleum Geology*, vol. 72, pp. 1–11, 2016.
- [57] T. Guo, “The Fuling shale gas field—a highly productive Silurian gas shale with high thermal maturity and complex evolution history, southeastern Sichuan Basin, China,” *Interpretation*, vol. 3, no. 2, pp. SJ25–SJ34, 2015.
- [58] X. Guo, Y. Li, R. Liu, and Q. Wang, “Characteristics and controlling factors of micropore structures of the Longmaxi shale in the Jiaoshiba area, Sichuan Basin,” *Natural Gas Industry B*, vol. 1, no. 2, pp. 165–171, 2014.
- [59] J. Tan, B. Horsfield, N. Mahlstedt et al., “Natural gas potential of Neoproterozoic and Lower Palaeozoic marine shales in the Upper Yangtze Platform, South China: geological and organic geochemical characterization,” *International Geology Review*, vol. 57, no. 3, pp. 305–326, 2015.
- [60] K. Zhang, C. Z. Jia, Y. Song et al., “Analysis of Lower Cambrian shale gas composition, source and accumulation pattern in different tectonic backgrounds: a case study of

- Weyuan block in the Upper Yangtze region and Xiuwu Basin in the Lower Yangtze region,” *Fuel*, vol. 263, article 115978, 2020.
- [61] C. Zou, D. Dong, Y. Wang et al., “Shale gas in China: characteristics, challenges and prospects (II),” *Petroleum Exploration and Development*, vol. 43, no. 2, pp. 182–196, 2016.
- [62] F. Goodarzi, “Organic petrography of graptolite fragments from Turkey,” *Marine and Petroleum Geology*, vol. 1, no. 3, pp. 202–210, 1984.
- [63] I. Suárez-Ruiz, D. Flores, J. G. Mendonça Filho, and P. C. Hackley, “Review and update of the applications of organic petrology: part 1, geological applications,” *International Journal of Coal Geology*, vol. 99, pp. 54–112, 2012.
- [64] V. Suchý, I. Sýkorová, M. Stejskal, J. Šafanda, Vladimír Machovič, and M. Novotná, “Dispersed organic matter from Silurian shales of the Barrandian Basin, Czech Republic: optical properties, chemical composition and thermal maturity,” *International Journal of Coal Geology*, vol. 53, no. 1, pp. 1–25, 2002.
- [65] H. Tian, L. Pan, X. Xiao, R. W. Wilkins, Z. Meng, and B. Huang, “A preliminary study on the pore characterization of Lower Silurian black shales in the Chuandong Thrust Fold Belt, southwestern China using low pressure N₂ adsorption and FE-SEM methods,” *Marine and Petroleum Geology*, vol. 48, pp. 8–19, 2013.
- [66] S. İnan, H. Al Badairy, T. İnan, and A. Al Zahrani, “Formation and occurrence of organic matter-hosted porosity in shales,” *International Journal of Coal Geology*, vol. 199, pp. 39–51, 2018.
- [67] J. Klaver, G. Desbois, R. Littke, and J. L. Urai, “BIB-SEM characterization of pore space morphology and distribution in postmature to overmature samples from the Haynesville and Bossier Shales,” *Marine and Petroleum Geology*, vol. 59, pp. 451–466, 2015.
- [68] W. Ji, Y. Song, Z. Rui, M. Meng, and H. Huang, “Pore characterization of isolated organic matter from high matured gas shale reservoir,” *International Journal of Coal Geology*, vol. 174, pp. 31–40, 2017.
- [69] W. Yang, S. He, S. Iglaer et al., “Porosity characteristics of different lithofacies in marine shale: a case study of Neoproterozoic Sinian Doushantuo Formation in Yichang area, China,” *Journal of Petroleum Science and Engineering*, vol. 187, article 106856, 2020.
- [70] W. Yang, R. S. Zuo, D. X. Chen et al., “Climate and tectonic-driven deposition of sandwiched continental shale units: new insights from petrology, geochemistry, and integrated provenance analyses (the western Sichuan subsiding basin, Southwest China),” *International Journal of Coal Geology*, vol. 211, article 103227, 2019.
- [71] Z. Chen, D. Lavoie, M. Malo, C. Jiang, H. Sanei, and O. Ardakani, “A dual-porosity model for evaluating petroleum resource potential in unconventional tight-shale plays with application to Utica shale, Quebec (Canada),” *Marine and Petroleum Geology*, vol. 80, pp. 333–348, 2017.
- [72] D. Lavoie, C. Rivard, R. Lefebvre et al., “The Utica shale and gas play in southern Quebec: geological and hydrogeological syntheses and methodological approaches to groundwater risk evaluation,” *International Journal of Coal Geology*, vol. 126, pp. 77–91, 2014.
- [73] C. Rivard, D. Lavoie, R. Lefebvre, S. Séjourné, C. Lamontagne, and M. J. Duchesne, “An overview of Canadian shale gas production and environmental concerns,” *International Journal of Coal Geology*, vol. 126, pp. 64–76, 2014.
- [74] F. Gao, Y. Song, Z. Li et al., “Pore characteristics and dominant controlling factors of overmature shales: a case study of the Wangyinpu and Guanyintang Formations in the Jiangxi Xiuwu Basin,” *Interpretation*, vol. 6, no. 2, pp. T393–T412, 2018.
- [75] Y. Li, J. Yang, Z. Pan, S. Meng, K. Wang, and X. Niu, “Unconventional natural gas accumulations in stacked deposits: a discussion of Upper Paleozoic coal-bearing strata in the east margin of the Ordos Basin, China,” *Acta Geologica Sinica (English Edition)*, vol. 93, no. 1, pp. 111–129, 2019.
- [76] Y. Wang, L. Wang, J. Wang, Z. Jiang, C. Jin, and Y. Wang, “Characterization of organic matter pores in typical marine and terrestrial shales, China,” *Journal of Natural Gas Science and Engineering*, vol. 49, pp. 56–65, 2018.
- [77] W. Yang, Q. Y. Wang, Y. H. Wang et al., “Pore characteristic responses to categories of depositional microfacies of delta-lacustrine tight reservoirs in the Upper Triassic Yanchang Formation, Ordos Basin, NW China,” *Marine and Petroleum Geology*, vol. 118, article 104423, 2020.
- [78] C. Orr, “Surface area measurement,” in *Treatise on Analytical Chemistry: Part III. Analytical Chemistry in Industry*, I. M. Kolthoff, P. J. Elving, and F. H. Stross, Eds., vol. 4, pp. 321–358, John Wiley and Sons, New York, 1977.
- [79] C. R. Clarkson and R. Marc Bustin, “Variation in micropore capacity and size distribution with composition in bituminous coal of the Western Canadian Sedimentary Basin: implications for coalbed methane potential,” *Fuel*, vol. 75, no. 13, pp. 1483–1498, 1996.
- [80] C. R. Clarkson, M. Freeman, L. He et al., “Characterization of tight gas reservoir pore structure using USANS/SANS and gas adsorption analysis,” *Fuel*, vol. 95, pp. 371–385, 2012.
- [81] M. Mastalerz, A. Drobniak, D. Strąpóć, W. Solano Acosta, and J. Rupp, “Variations in pore characteristics in high volatile bituminous coals: implications for coal bed gas content,” *International Journal of Coal Geology*, vol. 76, no. 3, pp. 205–216, 2008.
- [82] S. J. Gregg and K. S. W. Sing, *Adsorption, Surface Area, and Porosity*, Academic Press, New York, 1982.
- [83] P. A. Webb and C. Orr, *Analytical Methods in Fine Particle Technology*, Micromeritics Instrument, Norcross, 1997.
- [84] E. W. Washburn, “Note on a method of determining the distribution of pore sizes in a porous material,” *Proceedings of the National Academy of Science*, vol. 7, no. 4, pp. 115–116, 1921.
- [85] Y. Wang, L. Liu, S. Zheng, Z. Luo, Y. Sheng, and X. Wang, “Full-scale pore structure and its controlling factors of the Wufeng-Longmaxi shale, southern Sichuan Basin, China: implications for pore evolution of highly overmature marine shale,” *Journal of Natural Gas Science and Engineering*, vol. 67, pp. 134–146, 2019.
- [86] W. P. Diamond and S. J. Schatzel, “Measuring the gas content of coal: a review,” *International Journal of Coal Geology*, vol. 35, no. 1–4, pp. 311–331, 1998.
- [87] M. Gasparik, A. Ghanizadeh, P. Bertier, Y. Gensterblum, S. Bouw, and B. M. Krooss, “High-pressure methane sorption isotherms of black shales from the Netherlands,” *Energy & Fuels*, vol. 26, no. 8, pp. 4995–5004, 2012.

- [88] B. M. Krooss, F. van Bergen, Y. Gensterblum, N. Siemons, H. J. M. Pagnier, and P. David, "High-pressure methane and carbon dioxide adsorption on dry and moisture-equilibrated Pennsylvanian coals," *International Journal of Coal Geology*, vol. 51, no. 2, pp. 69–92, 2002.
- [89] L. Wei, Y. Wang, and M. Mastalerz, "Comparative optical properties of macerals and statistical evaluation of mis-identification of vitrinite and solid bitumen from early mature Middle Devonian - Lower Mississippian New Albany Shale: implications for thermal maturity assessment," *International Journal of Coal Geology*, vol. 168, pp. 222–236, 2016.
- [90] P. C. Painter, R. W. Snyder, M. Starsinic, M. M. Coleman, D. W. Kuehn, and A. Davis, "Concerning the application of FTIR to the study of coal: a critical assessment of band assignments and the application of spectral analysis programs," *Applied Spectroscopy*, vol. 35, no. 5, pp. 475–485, 1981.
- [91] P. Painter, M. Starsinic, and M. Coleman, "Determination of functional groups in coal by Fourier transform interferometry," in *Fourier Transform Infrared Spectra: Applications to Chemical Systems*, pp. 169–240, Academic press, 1985.
- [92] S. H. Wang and P. R. Griffiths, "Resolution enhancement of diffuse reflectance i.r. spectra of coals by Fourier self-deconvolution: 1. C-H stretching and bending modes," *Fuel*, vol. 64, no. 2, pp. 229–236, 1985.
- [93] H. Jacob, "Classification, structure, genesis and practical importance of natural solid oil bitumen ("migrabitumen")," *International Journal of Coal Geology*, vol. 11, no. 1, pp. 65–79, 1989.
- [94] C. R. Landis and J. R. Castaño, "Maturation and bulk chemical properties of a suite of solid hydrocarbons," *Organic Geochemistry*, vol. 22, no. 1, pp. 137–149, 1995.
- [95] R. Bertrand and M. Malo, "Source rock analysis, thermal maturation and hydrocarbon generation in Siluro-Devonian rocks of the Gaspé Belt basin, Canada," *Bulletin of Canadian Petroleum Geology*, vol. 49, no. 2, pp. 238–261, 2001.
- [96] W. R. Evitt, "A discussion and proposals concerning fossil dinoflagellates, hystrichospheres, and acritarchs, I," *Proceedings of the National Academy of Sciences of the United States of America*, vol. 49, no. 2, pp. 158–164, 1963.
- [97] Y. Ma, N. Zhong, D. Li, Z. Pan, L. Cheng, and K. Liu, "Organic matter/clay mineral intergranular pores in the Lower Cambrian Lujiaping Shale in the north-eastern part of the Upper Yangtze area, China: a possible microscopic mechanism for gas preservation," *International Journal of Coal Geology*, vol. 137, pp. 38–54, 2015.
- [98] D. Misch, D. Gross, G. Hawranek et al., "Solid bitumen in shales: petrographic characteristics and implications for reservoir characterization," *International Journal of Coal Geology*, vol. 205, pp. 14–31, 2019.
- [99] Y. Chen, M. Mastalerz, and A. Schimmelmann, "Characterization of chemical functional groups in macerals across different coal ranks via micro-FTIR spectroscopy," *International Journal of Coal Geology*, vol. 104, pp. 22–33, 2012.
- [100] Y. Wang, L. Liu, S. Li et al., "The forming mechanism and process of tight oil sand reservoirs: a case study of Chang 8 oil layers of the Upper Triassic Yanchang Formation in the western Jiyuan area of the Ordos Basin, China," *Journal of Petroleum Science and Engineering*, vol. 158, pp. 29–46, 2017.
- [101] C. Wu, J. Tuo, L. Zhang et al., "Pore characteristics differences between clay-rich and clay-poor shales of the Lower Cambrian Niutitang Formation in the northern Guizhou area, and insights into shale gas storage mechanisms," *International Journal of Coal Geology*, vol. 178, pp. 13–25, 2017.
- [102] R. Yang, S. He, D. F. Hu, D. Hu, S. Zhang, and J. Yi, "Pore characterization and methane sorption capacity of over-mature organic-rich Wufeng and Longmaxi shales in the southeast Sichuan Basin, China," *Marine and Petroleum Geology*, vol. 77, pp. 247–261, 2016.
- [103] D. J. K. Ross and R. Marc Bustin, "The importance of shale composition and pore structure upon gas storage potential of shale gas reservoirs," *Marine and Petroleum Geology*, vol. 26, no. 6, pp. 916–927, 2009.
- [104] G. R. L. Chalmers, D. J. K. Ross, and R. M. Bustin, "Geological controls on matrix permeability of Devonian gas shales in the Horn River and Liard Basins, northeastern British Columbia, Canada," *International Journal of Coal Geology*, vol. 103, pp. 120–131, 2012.
- [105] C. Yang, J. Zhang, X. Wang et al., "Nanoscale pore structure and fractal characteristics of a marine-continental transitional shale: a case study from the Lower Permian Shanxi Shale in the southeastern Ordos Basin, China," *Marine and Petroleum Geology*, vol. 88, pp. 54–68, 2017.
- [106] D. P. Le Heron, Y. Khoukhi, F. Paris, J.-F. Ghienne, and A. Le Herissé, "Black shale, grey shale, fossils and glaciers: anatomy of the Upper Ordovician-Silurian succession in the Tazzeqa Massif of eastern Morocco," *Gondwana Research*, vol. 14, no. 3, pp. 483–496, 2008.
- [107] S. Lüning, Y. M. Shahin, D. Loydell et al., "Anatomy of a world-class source rock: distribution and depositional model of Silurian organic-rich shales in Jordan and implications for hydrocarbon potential," *AAPG Bulletin*, vol. 89, no. 10, pp. 1397–1427, 2005.
- [108] H. Hu, F. Hao, J. Lin, Y. Lu, Y. Ma, and Q. Li, "Organic matter-hosted pore system in the Wufeng-Longmaxi (O₃w-S₁) shale, Jiaoshiba area, eastern Sichuan Basin, China," *International Journal of Coal Geology*, vol. 173, pp. 40–50, 2017.
- [109] N. D. Rodriguez and R. P. Philp, "Geochemical characterization of gases from the Mississippian Barnett Shale, Fort Worth Basin, Texas," *AAPG Bulletin*, vol. 94, no. 11, pp. 1641–1656, 2010.
- [110] R. M. Slatt and N. D. Rodriguez, "Comparative sequence stratigraphy and organic geochemistry of gas shales: commonality or coincidence?," *Journal of Natural Gas Science and Engineering*, vol. 8, pp. 68–84, 2012.
- [111] M. Mastalerz, A. Drobniak, and A. B. Stankiewicz, "Origin, properties, and implications of solid bitumen in source-rock reservoirs: a review," *International Journal of Coal Geology*, vol. 195, pp. 14–36, 2018.
- [112] P. C. Hackley, B. J. Valentine, and J. J. Hatcherian, "On the petrographic distinction of bituminite from solid bitumen in immature to early mature source rocks," *International Journal of Coal Geology*, vol. 196, pp. 232–245, 2018.
- [113] Y. Hou, K. Zhang, F. Wang et al., "Structural evolution of organic matter and implications for graphitization in over-mature marine shales, South China," *Marine and Petroleum Geology*, vol. 109, pp. 304–316, 2019.
- [114] R. Wang, Y. Gu, W. Ding et al., "Characteristics and dominant controlling factors of organic-rich marine shales with high thermal maturity: a case study of the Lower Cambrian Niutitang Formation in the Cen'gong block, southern China," *Journal of Natural Gas Science and Engineering*, vol. 33, pp. 81–96, 2016.

- [115] J. M. Wood, H. Sanei, O. Haeri-Ardakani, M. E. Curtis, T. Akai, and C. Currie, "Solid bitumen in the Montney Formation: diagnostic petrographic characteristics and significance for hydrocarbon migration," *International Journal of Coal Geology*, vol. 198, pp. 48–62, 2018.
- [116] J. Dai, C. Zou, S. Liao et al., "Geochemistry of the extremely high thermal maturity Longmaxi shale gas, southern Sichuan Basin," *Organic Geochemistry*, vol. 74, pp. 3–12, 2014.
- [117] S. Zhou, G. Yan, H. Xue, W. Guo, and X. Li, "2D and 3D nanopore characterization of gas shale in Longmaxi Formation based on FIB-SEM," *Marine and Petroleum Geology*, vol. 73, pp. 174–180, 2016.
- [118] K. L. Milliken and M. E. Curtis, "Imaging pores in sedimentary rocks: foundation of porosity prediction," *Marine and Petroleum Geology*, vol. 73, pp. 590–608, 2016.
- [119] F. Goodarzi, "Reflected light microscopy of chitinozoan fragments," *Marine and Petroleum Geology*, vol. 2, no. 1, pp. 72–78, 1985.
- [120] Y. Grahn and F. Paris, "Emergence, biodiversification and extinction of the chitinozoan group," *Geological Magazine*, vol. 148, no. 2, pp. 226–236, 2011.
- [121] J. Jacob, F. Paris, O. Monod et al., "New insights into the chemical composition of chitinozoans," *Organic Geochemistry*, vol. 38, no. 10, pp. 1782–1788, 2007.
- [122] J. Reyes, C. Jiang, D. Lavoie, D. K. Armstrong, M. Milovic, and R. Robinson, "Organic petrographic analysis of artificially matured chitinozoan- and graptolite-rich Upper Ordovician shale from Hudson Bay Basin, Canada," *International Journal of Coal Geology*, vol. 199, pp. 138–151, 2018.
- [123] S. Dutta, C. Hartkopf-Fröder, K. Witte, R. Brocke, and U. Mann, "Molecular characterization of fossil palynomorphs by transmission micro-FTIR spectroscopy: implications for hydrocarbon source evaluation," *International Journal of Coal Geology*, vol. 115, pp. 13–23, 2013.

Research Article

Early Paleozoic Extension-Compression Transition and Formation of a Paleo-Oil Reservoir System in the NW Sichuan Basin: Implications for Deeply Buried Hydrocarbon Accumulation

Xiao Liang ^{1,2}, Shu-gen Liu ^{1,3}, Liang-liang Wu ⁴, Bin Deng ¹, Jing Li ²,
Meng-lin Zhang ² and Xu-hang Tan ²

¹State Key Laboratory of Oil and Gas Reservoir Geology and Exploitation, Chengdu University of Technology, Chengdu, Sichuan 610059, China

²CNPC Chuanqing Drilling Engineering, Chengdu, Sichuan 610051, China

³Xihua University, Chengdu, 610039 Sichuan, China

⁴State Key Laboratory of Organic Geochemistry, Guangzhou Institute of Geochemistry, Chinese Academy of Science, Guangzhou, Guangdong 510640, China

Correspondence should be addressed to Shu-gen Liu; lsg@cdut.edu.cn

Received 6 January 2021; Revised 3 March 2021; Accepted 21 April 2021; Published 27 May 2021

Academic Editor: Kun Zhang

Copyright © 2021 Xiao Liang et al. This is an open access article distributed under the Creative Commons Attribution License, which permits unrestricted use, distribution, and reproduction in any medium, provided the original work is properly cited.

Owing to multiple tectonic events after the Late Triassic, the northern segment of the western Sichuan depression (NSWSCD) has a complex geological history of significant uplift and deeply buried. With abundant oil and gas play in the NSWSCD, the study of paleo-oil reservoir systems and early hydrocarbon accumulation in this area is of great significance for deep marine hydrocarbon distribution prediction in complex structural settings. Analysis on the northern section of the Mianyang-Changning Intracratonic Sag (MY-CN IS) and the Tianjingshan Paleouplift (TJS PU), the two Early Paleozoic tectonic units are laterally superimposed. Combined the reservoir bitumen of the Sinian Dengying Fm firstly, the biomarker (TT_{23}/tT_{24} , S_{21}/S_{22} , etc.) and Organic $\delta^{13}C$ (lighter than 30‰) characteristics indicate that the Sinian-Jurassic paleo-oil system in the TJS PU area is the main source of Lower Cambrian organic-rich black shale. This is closely related to the superimposition and combination effects of the intracratonic sag and paleouplift. Therefore, this study establishes a geological-geochemical accumulation model through a combination of R_o and fluid inclusion data. The No. 1 fault is an important zoning fault in the NSWSCD, which significantly controls the division of the oil-gas zone. The process of paleo-oil reservoir destroyed directly only exists in the frontal deformation zone. The deep marine strata of the eastern No. 1 fault demonstrate the four-center hydrocarbon accumulation processes, which include oil generation, gas generation, gas storage, and gas preservation. The superdeep Dengying Fm has long-term exploration potential in the NSWSCD.

1. Introduction

Typical dual thrust belt and foreland basin structures are well developed in the western Sichuan Basin [1]. The western Sichuan depression (WSCD) is a foreland depression that has been influenced by Indosinian, Yanshan, and Himalayan tectonic events. Since the Indosinian Orogeny, the typical multistage basin evolution and tectonic movement characteristics in the WSCD have been largely controlled by the formation and evolution of the Longmenshan Thrust Belt

(LMS TB) on the western margin [2, 3]. Both of these are relatively consistent in the present tectonic pattern [4, 5]. With the complex tectonic-sedimentary evolutionary process, researches concentrated on the unconformities between continental strata, lithofacies records, and paleo-structural preceding the Late Triassic [6, 7].

The northern segment of the western Sichuan depression (NSWSCD) has one of the longest histories of oil and gas exploration in the Sichuan Basin [8, 9]. Among the petroleum geological features, there are abundant oil and gas that

play in the Tianjingshan area. In addition, the discovery of a sizeable Anyue gas field in the middle of the Sichuan Basin and the development of the Early Cambrian Mianyang-Changning Intracratonic Sag (MY-CN IS) also indicate advantageous exploration prospects for deeply buried marine hydrocarbon in the WSCD [10, 11]. However, the oil and gas exploration of the deeply buried Dengying and Qixia formation has become increasingly difficult nowadays [12]. Preliminary research indicates that the widespread distribution of the paleo-oil reservoir system in the NSWSCD closely relates to the formation and evolution of the MY-CN IS and the Tianjingshan Paleouplift (TJS PU) in the Early Paleozoic. The prediction of deep hydrocarbon accumulation under the suddenly deformed basin-mountain system of the NSWSCD should also be relevant to paleo-oil reservoirs and deep-superdeep gas reservoirs in the frontal-deformation zone and depression areas. Therefore, the paltry amount of data available on tectonic-sedimentary processes between the Late-Sinian and the Early-Triassic highlights the lack of research on the geology of the deep petroleum system.

This study covers a detailed description of tectonic-sedimentary evolution during the Early Paleozoic in the NSWSCD. The sources of the paleo-oil reservoirs (oil seeps/bitumens) from the Sinian-Jurassic strata in the TJS PU area were assessed. Additionally, related studies on oil-source correlation, thermal burial history, and deep hydrocarbon accumulation processes were considered. This allows for a better understanding of the extension-compression transition and the processes responsible for the formation of the paleo-oil reservoir system in the northwestern Sichuan Basin. Furthermore, the oil-gas migration model and implications for deeply buried hydrocarbon predictions were clarified.

2. Geological Setting

2.1. Stratigraphy, Palaeogeography, and Age Constraints. Owing to the differences in tectonic background and deformation stage, level, and strength, the LMS TB has typical segmentation characteristics of the southern, middle, and northern sections. The structural deformation of the WSCD also shows a certain trend of segmentation characteristics. Combined with oil and gas exploration, the WSCD is divided into southern, middle, and northern segments [13, 14]. The 150 km long and 50 km wide northern segment of the western Sichuan depression (NSWSCD) stretches from Jiangyou-Tongkou in the south to Guangyuan in the north (Figure 1). The development of the LMS TB and the WSCD influences the marine strata that are generally buried at depths that exceed 7000 m. Given the relative ancient geological age (>250 Ma), this study determines that the deeply buried marine strata were deposited from the Late Sinian, after the initial formation of the cratonic basin, to the Middle-Late Triassic that occurred before the evolution of the intra-continental foreland basin (Figure 2).

The Sichuan Basin had a complex tectonic history of supercontinental and multistage extensional events in the Late Proterozoic (pre-Late Sinian) before the construction of the craton. The amalgamated North China Block (NCB) and the Yangtze and Cathaysia blocks (South China Block,

SCB) were a part of the Rodinia supercontinent during the Late Mesoproterozoic and Early Neoproterozoic (1.0–0.8 Ga, Figure 1(a)). The SCB was separated gradually from Rodinia during the Late Neoproterozoic (830–720 Ma) through oceanic crust subduction [15–17] and related superplume events [18, 19]. The evidence of superplume events includes a large number of outcrops of Upper Proterozoic basic-ultrabasic intrusions, pyroclitics, and metamorphic complexes on the western margin of the SCB. The multistage process of extension and compression in the SCB is named the Xingkai taphrogenesis and is associated with the breakup of the Rodinia supercontinent [10, 20].

The Xingkai taphrogenesis started in the Middle-Late Proterozoic. The western margin of the Yangtze Plate exhibits typical rift-derived characteristics, with a set of 803 ± 12 Ma continental volcanic rocks (the Suxiong Fm), continental conglomerates, and sandstones that were assigned to the Nanhua Kaijianqiao, Lieguli, Chengjiang, and Luliang formations [21, 22]. Tectonic tension was sustained up to the Early Sinian. When the climate began to warm-up after the Nanhuan glacial period, the Yangtze block entered a depositional stage. The deposition of black mudstones and the rapid transgression of the Yangtze Craton formed the Doushantuo Fm (Zn_2dn) and the clasolite and carbonatite marine sequences [23, 24]. The development of an overlying carbonate platform sequence and fine silica-carbon clasolite led to the deposition of the Dengying Fm (Zn_2dn), which completely shaped the Sichuan Craton before the Late Sinian [25]. The Upper Sinian Dengying Formation in the Upper Yangtze area has a preserved thickness of 600–1000 m and can be divided into four categories on the basis of lithology, structure, and the abundance of cyanobacteria [26].

Paraconformities developed between the second (Zn_2dn^2) and the third (Zn_2dn^3) members of the Dengying Fm and Lower Cambrian-Dengying Fm during the Tongwan I and II episodes. Paleogeographic differentiation began to occur in the Upper Yangtze and surrounding areas during the depositional period of the Zn_2dn^2 – Zn_2dn^3 [27]. The thickness of Zn_2dn^3 is inconsistent in the NSWSCD. The black shale has only been preserved in certain areas, and pebbly sandstones dominate the Hujiaba section in Ningqiang. Whether or not the WSCD was still subject to tectonic tension during the deposition of Zn_2dn^3 remains controversial. One view suggests that the Zn_2dn^3 was only deposited in either the restricted basin [28, 29], interplatform basin, or deep shelf [30]. Another view is that the initial tectonic tension began during Zn_2dn^3 deposition, which includes the formation of either the Chengdu-Luzhou Aulacogen [31, 32] or the Mianzhu-Changning Intracratonic Sag [33]. The most widely accepted view suggests that large-scale tensile processes began in the Early Cambrian, which is consistent with the WSCB of the Upper Yangtze area. This was primarily characterized using the formation of the MY-CN IS, which was also the main indicator of the Xingkai taphrogenesis II episode.

The initial extension during the Late Sinian Dengying period was proceeded by the Sichuan Craton that underwent a period of weak extension in the Early Cambrian. The thickness of the Lower Cambrian Maidiping and the Qiongzhusi formations in the NSWSCD shows that the northern

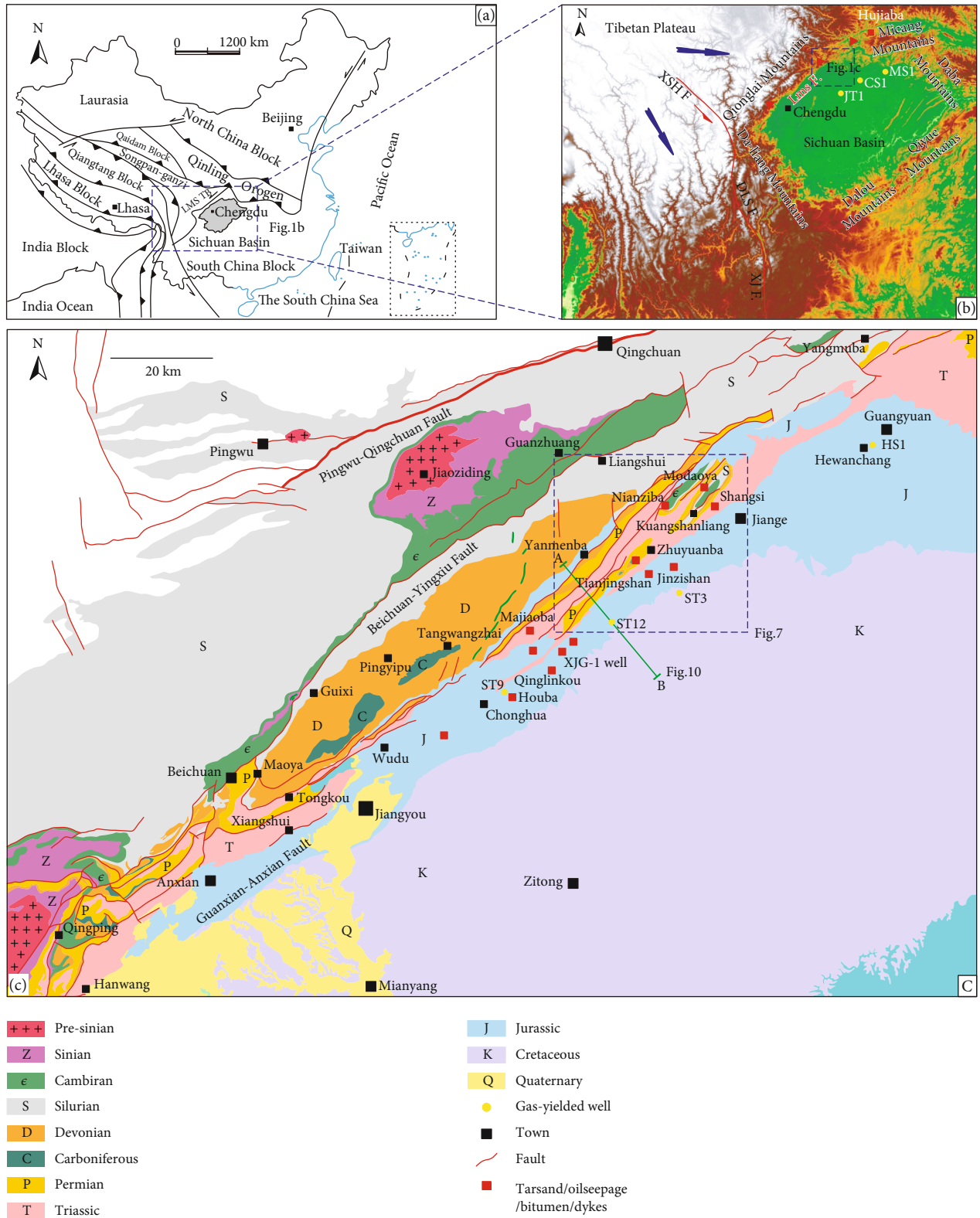


FIGURE 1: (a) Simplified map of China that shows the location of the Sichuan Basin (gray). (b) Simplified digital elevation map that shows the location of the Sichuan Basin on the eastern boundary of the Tibetan Plateau. The northern segment of the western Sichuan depression (NSWSCD) is at the basin-mountain junction [1] of the Longmenshan Thrust Belt (LMS TB). The blue box represents the main study area. (c) 1:200,000 geological map of the NSWSCD, which shows the distribution of oil and gas plays (red frame) in the Houba, Qinglinkou, Tianjingshan, Shangsisi, and Nianziba areas.

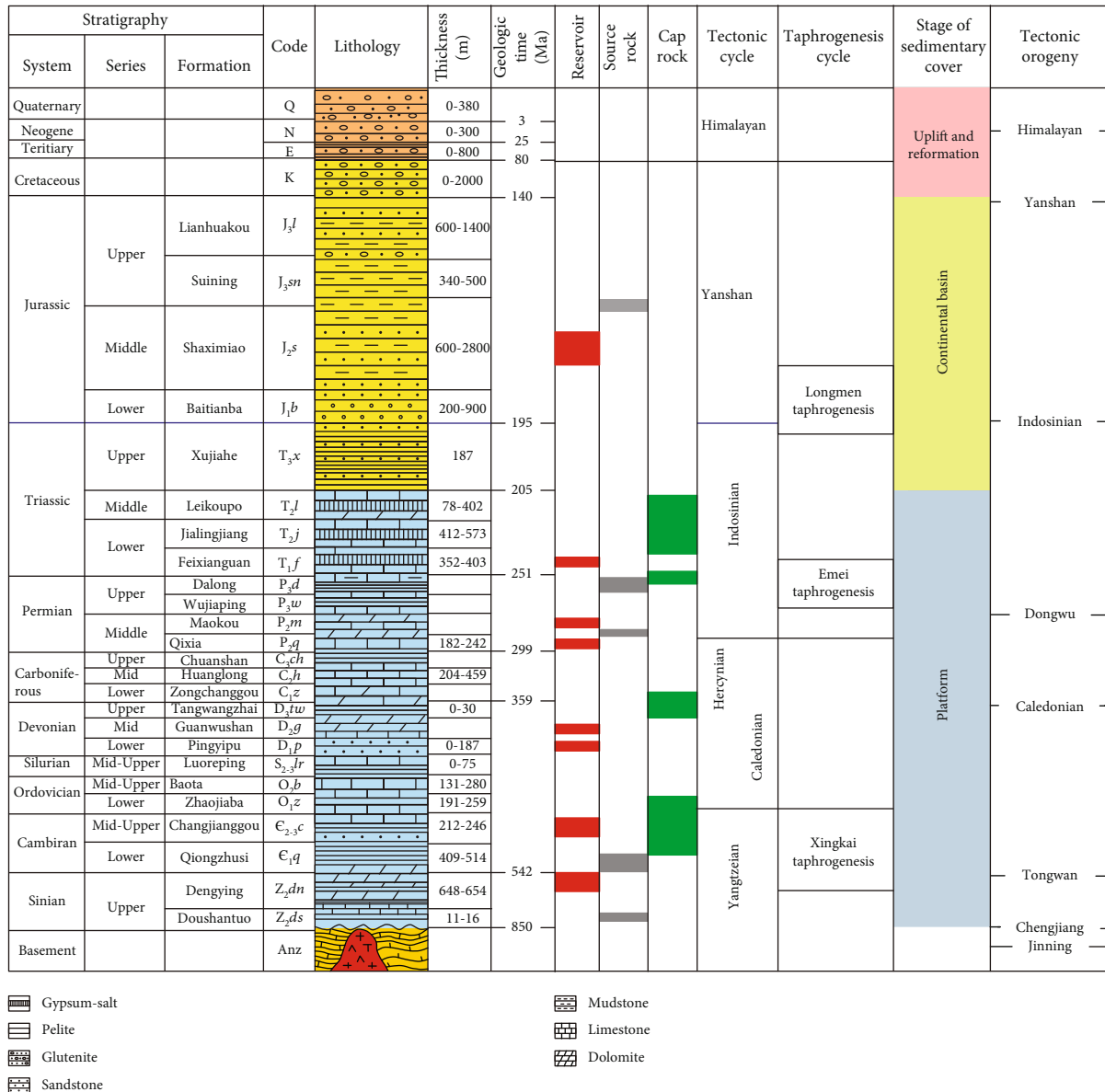


FIGURE 2: Generalized stratigraphic column of the western Sichuan depression (WSCD). Simplified stratigraphic units with major marker beds, age constraints, and tectonic orogenic events from the Sinian (Ediacaran) Doushantuo Fm, Dengying Fm, and Lower Cambrian Qiongzhusi Fm to the middle Permian Qixia Fm in the WSCD.

segment of the MY-CN IS also experienced an initial extension period during the deposition of the Maidiping Fm. This included extension peaking during the deposition of the Qiongzhusi Fm [34].

2.2. Paleo-Oil Reservoir Evaluation: Review. Although statistical records are incomplete, more than 200 oil seeps, heavy oil, tar sands, and solid bitumen veins are identified in this area [35]. The widespread distribution of paleo-oil reservoirs in the NSWSCD indicates a large-scale hydrocarbon migration and accumulation process in this region.

Petroleum geologists have performed numerous studies on the significance and scale [36–39], oil-to-source correlation [40–49], and petroleum generation timing [50–52] of paleo-oil reservoirs in the NSWSCD. Additionally, there

exists a lack of effective reconciliation of geologic history, classification, and level of contribution from Sinian and Cambrian source rocks [44, 49]. This is caused by the possibility of a mixed Upper Paleozoic source [41, 51] and the timing controversy of petroleum generation at 550, 440, or 180 Ma, which is based on Re-Os isotopic dating [50–52].

3. Oil-Source Correlation of Tianjingshan Paleo-Petroleum System

3.1. Marine Source Rocks and the Distribution of Paleo-Oil Reservoirs

3.1.1. Source Rocks. According to detailed geological analysis, the potential source rocks in the NSWSCD include the upper

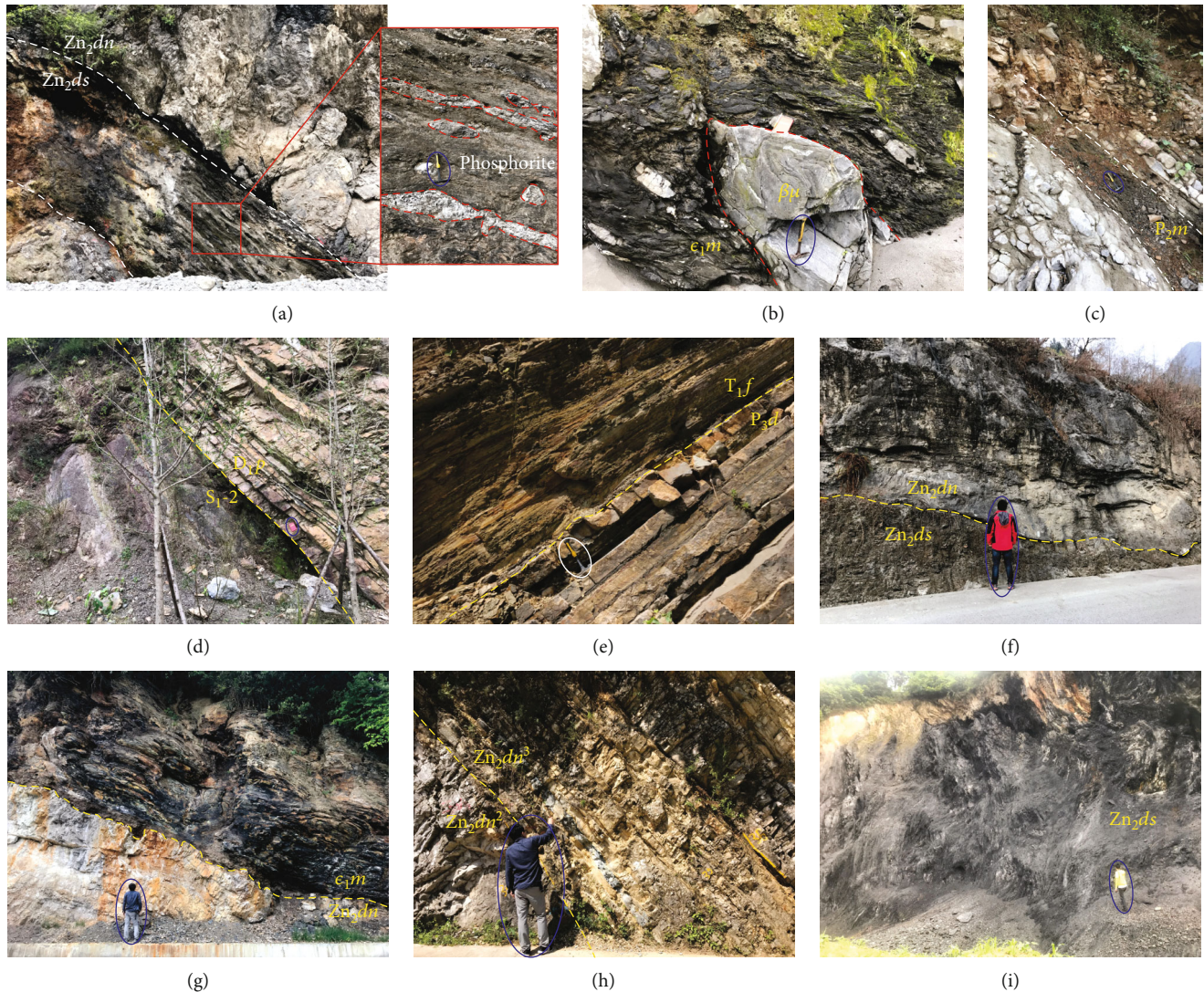


FIGURE 3: Lithofacies photos of source rocks in the Longmenshan-Michangshan area. (a) Paraconformity of the Doushantuo Fm and Dengying Fm, Qingping, Hanwang. The top of the Doushantuo Fm has interbedded black mudstones and phosphorite. (b) QP-6 is the Lower Cambrian Maidiping Fm with diabase dyke intrusion, at Qingping, Hanwang. (c) GY-7 is the nodular limestone interbedded with thin black shale, which has oil intrusion, at Changjianggou, Shangsi. (d) Paraconformity between the Lower-Middle Silurian gray shale and the Lower Devonian Pingyipu Fm, at Yanmenba, Jiangyou. (e) HY-GYCJG/CJG-11, P/T Boundary, and paraconformity between the Upper Permian Dalong Fm and the Lower Triassic Feixianguan Fm, at Changjianggou, Shangsi. (f) Suspected paraconformity between the Doushantuo and Dengying formations, which has bitumen infill at the boundary, at Guanzhuan, Qingchuan. (g) E/C Boundary and paraconformity between the Dengying and Qingzhusi formations, at Daba, Guangwushan. (h) Conformable contact of the third (clasolite) and second (dolomite) members of the Dengying Fm, at Hujiaba, Ningqiang. (i) Black shale of the Doushantuo Fm, at Nanping and Da'an, Ningqiang.

Sinian Doushantuo Fm, the third member of the upper Sinian Dengying Fm, the Lower Cambrian Qiongzhusi Fm, the Silurian Longmaxi Fm, the interbedded mudstones of the Middle Permian Qixia-Maokou Fm, and the Upper Permian Dalong Fm.

The Lower Cambrian Maidiping Fm-Qiongzhusi Fm (ϵ_1m-q) source rock that is controlled by the MY-CN IS is particularly thick and is widely distributed in the NSWSCD area. In addition to the good outcrops of black shale that occur in the Mianzhu, Qingchuan, and Nanjiang areas, the deeply buried Lower Cambrian source rocks have been dis-

covered by the Jiaotan-1 (JT-1), Mashen-1 (MS-1), and Chuanshen-1 (CS-1) wells (Figures 3(a) and 3(i)).

The organic-rich black shale of the Sinian Doushantuo Fm mainly developed in the second member, which was deposited on the shoreland-continental shelf during extensive transgression [53]. The Doushantuo Fm is thicker toward the edges than in other parts of the Sichuan Basin. Furthermore, the Doushantuo Fm is more developed in the northeast and southeast margins than in the other margins of the Sichuan Basin. The thickness in the northeast Sichuan Basin is 30–90 m. The outcropped mudstone of the Ziyang



FIGURE 4: Paleo-oil reservoir distribution of the Tianjingshan Paleouplift area. (a) Bitumen under the Ediacaran-Cambrian unconformity, located at Dengying Fm, Hujiaba, Ningqiang. (b) CJG-10 is the oil seeps from micrite Feixianguan Fm, located at Changjianggou and Shangsi. (c) GY-7 is the oil seep in stylolite and fractured limestone, located at Changjianggou, Shangsi. (d) TB-8 is the siltstone with large bitumen dyke intrusion, located at Changjianggou Fm, the Nianziba structure. (e) CJG-12 is dry oil seep in dolomite, which is located at Devonian-Permian, Jianfeng. (f) NZB-04 is oil seep in siltstone, which is located at Changjianggou Fm, Jianfeng. (g) TJS-01 is oil seep in siltstone, which is located at Pingyipu Fm and Tianjingshan. (h) QLK-01 is tar sand and oil sand, which is located at Shaximiao Fm, Huangjinkou. (i) HB-01 is the oil pool of the Xinjiagou-1 well, which is located at Shaximiao Fm, Qinglinkou.

section is ~96 m. However, the thickness in the southeast is 30–60 m, with the mudstone of the Songlin section ~65 m. The Doushantuo Fm is particularly thin in the interior of the Sichuan Basin, which is generally 10–30 m. The first, second, and third members of the Doushantuo Fm are missing in most areas and have not been verified using sufficient cores.

The potential source rock for the Tianjingshan paleo-reservoir prevents the exposure of the Doushantuo Fm in the TJS PU area. The possible superdeep burial in the NSWSCD has led to no wells being found in this area. The Qingping section is located in the transitional area between the middle and northern segments of the WSCD. The Qingping section is a black

siliceous mudstone-shale interbedded phosphorite that overlies the Doushantuo Fm (Figure 3(a)). The total organic carbon (TOC) value is 5.17, but the lithology is relatively thin (5 m) and is not exposed elsewhere in the WSB.

Thin (2 m) black mudstone, which is similar to the Doushantuo Fm, also crops out in the Qingping section. The third member of the Sinian Dengying Fm is thick in the Ningqiang (Hujiaba) section. However, the third member contains thick sets of terrigenous clastic rock (Figure 3(h)). The third member of Sinian Dengying Fm, which has thin mudstones and variable lithofacies, should not be considered an important hydrocarbon-generating layer in the NSWSCD. Additionally, the Ordovician and Silurian have variable periods of hiatus in this study area. When compared with the widely distributed organic-rich shale of the Wufeng-Longmaxi Fm in the central and southern Sichuan Basin, the Silurian in the NSWSCD is dominated by gray shale (Figure 3(d)), and the lower black shale of the Silurian sequence is absent. The black mudstones are also developed in the Middle Permian Qixia and Maokou Fm but are very thin (Figure 3(c)). Therefore, the formation also cannot represent the main source of rock. The Upper Permian Longtan Fm (P_3l) transforms into the Wujiaping Fm (P_3w) in this area, which has depositional characteristics suggestive of melanic deep-water silicalite. Notably, during the Late Permian and Early Triassic, the formation and evolution of the Guangwang, Kaijiang, and Liangping Intracratonic Sag led to the development of the Dalong Fm (P_3d) source rock in the Guangyuan area of the NSWSCD (Figure 3(e)). Thick and widely distributed black siliceous mudstones crop out in the Changjianggou section (Guangyuan area, northern NSWSCD). These are potentially important hydrocarbon generation formations for the Tianjingshan paleo-oil reservoirs.

3.1.2. Paleo-Oil Reservoirs. The reservoirs of the Dengying Fm in the NSWSCD are well developed. Furthermore, the large-scale paleo-oil reservoir of the Dengying Fm is well-matched with the Lower Cambrian source rocks. Numerous bitumen fillings can be seen in the pores of the Hujiaba (Ningqiang) and Yangba (Nanjiang) sections (Figure 4(a)). The widely distributed bitumen in the Dengying Fm can be linked to paleo-oil reservoirs in the TJS PU area. The frontal and deformation zone of the NSWSCD (TJS PU area) has a highly dense distribution of paleo-oil reservoirs (oil and gas plays). According to the division of the northern, middle, and southern segments of the TJS PU, the paleo-reservoir in the northern segment of the TJS PU contains mainly solid bitumen veins or oil seeps in the Changjianggou Fm. This is located at the core of the Nianziba-Kuangshanliang structure (Figures 4(d) and 4(f)). Additionally, the oil seeps in the monoclinic Qixia-Maokou-Feixianguan Fm of the Changjianggou (Shangsi) section (Figures 4(b) and 4(e)). There are Pingyipu Fm oil seeps between the layers of the overlying Middle-Upper Cambrian and in the upside of the Permian and Triassic, which is located in the middle segment of the TJS PU (Figure 4(c)). There is also intermediate Lower Devonian Pingyipu Fm oil seep in the southern and northern segments. Specific analysis of the time-space sequence in this area is important. Among the samples

taken from the southern TJS PU were Jurassic oil sands from the Houba area and heavy oil samples from the Xinjiagou-1 well (Figures 4(h) and 4(i)). The southeast flank of the Shuigentou-Wuhudong structure shows a monoclinic surface structure. The heavy oil samples from the XJG-1 well can show variations in the maturity and degree of biodegradation of the surface tar sand samples.

3.2. Materials and Methods. More than 20 samples were collected for the oil-to-source correlation that was based on TOC, R_o , GC-MS, and $\delta^{13}C$ analyses. These include two bitumen samples from the Sinian Dengying Fm, bitumen, and oil-seep sample from the Lower Cambrian Changjianggou Fm. Furthermore, samples in the upper formations are oil-seep sample from the Lower Devonian Pingyipu Fm, two oil-seep samples taken from the Middle Permian Qixia-Maokou Fm, and two tar sand/oil-seep samples from the Middle Jurassic Shaximiao Fm. Moreover, included two source rock samples from the Sinian Doushantuo Fm, three source rock samples were taken from the Lower Cambrian Maidiping-Qiongzhusi Fm, the Upper Permian Dalong Fm, and Lower Triassic Feixianguan Fm (Table 1).

Organic geochemistry experiments on source rock and paleo-oil reservoir samples were conducted at the Guangzhou Institute of Geochemistry, Chinese Academy of Science. According to the temperature conversions of 7500 m/170°C and 8000 m/190°C in the ST-6 and CS-1 wells, respectively, the TJS PU area has a low geothermal gradient of 2.0–2.2°C/0.1 km. Additionally, most samples in the NW Sichuan Basin have suitable maturity for biomarker analysis. The sample pretreatments mainly use the Soxhlet extraction (Soxh) method, whereas others use the Hydropyrolysis (HyPy) method for comparison.

Hydropyrolysis experiments were performed in a fixed bed reactor using high pressure (15 MPa, 4 L/min) hydrogen gas with a catalyst of ammonium dioxodithiomolybdate $[(NH_4)_2MoO_2S_2]$ [54, 55]. The HyPy method using biomarker geochemistry can reduce the thermal maturation effect on biomarkers ($R_o \leq 2.4\%$) and migrated hydrocarbons to a great extent. The covalently bound biomarkers released by HyPy are useful in the study of biomarker geochemistry and oil-source correlation on highly overmature source rocks [56]. The advantages of HyPy and its additional details are described in Liao et al. and Wu et al. [56, 57]. The saturated and aromatic hydrocarbon fractions were analyzed using GC-MS. The stable carbon isotope analysis of kerogen and extract GC-C-IRMS measured fractions (bulk $\delta^{13}C$ values). The standard deviation of GC-C-IRMS for each compound was less than 0.3%.

3.3. Oil-to-Source Correlation

3.3.1. Geochemical Characteristics of Potential Source Rocks

(1) Doushantuo Formation. The mudstone of Doushantuo Fm in the eastern margin of the Sichuan Basin has an average TOC of 1.51%, which is consistent with sapropel-type kerogen and an average carbon isotope value of -30.90% . The equivalent R_o of the Doushantuo Fm generally reaches 3.46–3.82%, which indicated the postmature stage [58]. The

TABLE 1: Characteristics of source rock and paleo-oil reservoir samples.

Category	Sample	Formation	Description	Sample point	R_o	TOC	Method (Soxh/HyPy)
Source rock	ZYSL-120	Doushantuo/ Zn_2ds	Mudstone	Songlin, Zunyi	3.50	1.20	√/√
	QP-6	Maidiping/ ϵ_1m	Siliceous-mud rock	Qingping, Hanwang	R_b 1.56	12.95	√/√
	CS1-8140	Qiongzhusi/ ϵ_1q	Siliceous-mud rock	CS-1 well	R_b 1.52	2.56	√/√
	NJ-S-2	Guojiaba/ ϵ_1g	Mudstone	Yangba, Nanjiang	4.05	4.05	√/√
	GYCJG	Dalong/ P_3d	Mudstone	Changjianggou, Shangsi	0.58	8.75	√/√
	YB-1	Dengying/ Zn_2dn	Reservoir bitumen	Yangba, Nanjiang	R_b 3.26	—	√/√
Paleo-oil reservoir	NZB-4	Changjianggou/ $\epsilon_{1-2}c$	Oil-seepage	Jianfeng	R_b 0.26	—	√/×
	TB-8	Changjianggou/ $\epsilon_{1-2}c$	Solid bitumen vein	Nianziba	0.51	—	√/√
	TJS-1	Pingyipu/ D_1p	Oil-seepage	Tianjingshan	R_b 0.65	—	√/√
	CJG-12	Qixia/ P_2q	Oil-seepage	Jianfeng	—	—	√/×
	GY-7	Maokou/ P_2m	Oil-seepage	Changjianggou, Shangsi	—	—	√/×
	CJG-10	Feixianguan/ T_1f	Oil-seepage	Changjianggou, Shangsi	0.94	—	√/×
	QLK-1	Shaximiao/ J_2s	Tar sand	Qinglinkou	R_b 0.41	—	√/√
	HB-1	Shaximiao/ J_2s	Oil	Xinjiagou-1 well	1.03	—	√/√

GC-MS results of HyPy for saturates of the Doushantuo Fm with a high thermal maturity still have an indistinguishable hump (UCM). Terpanes and regular steranes are also missing.

(2) *Dalong Formation*. Controlled by the Guangwang-Kaijiang-Liangping Intracratonic Sag, the Upper Permian Dalong Fm (P_3d) is marine gray-black siliceous rock interbedded with black shales. The Upper Permian Dalong Fm is mainly found in the Guangyuan area. The thickness of the Dalong Fm ranges from 17 to 40 m. High TOC values (4.58–8.75%) in the Changjianggou section indicate that the Dalong Fm has considerable petroleum potential for the Permian Qixia-Maokou Fm and Triassic Feixianguan Fm.

The C_{23} -tricyclic terpane/ C_{24} -tetracyclic terpane (TT_{23}/tT_{24}) ratios of the Dalong Fm range from 1.2 to 1.6 [56]. The values of gammacerane/ C_{30} - $\alpha\beta$ hopane (Gam/ H_{30}) are only 0.09. The distributions of C_{27} - C_{29} $\alpha\alpha\alpha R$ steranes in the Dalong Fm show similar “V” shapes ($C_{27} > C_{29} > C_{28}$, Figure 5). The maturity-related parameters such as $20S/(20S + 20R)$ and $\beta\beta/(\alpha\alpha + \beta\beta)$ for C_{29} -regular steranes ($C_{29} - \beta\beta/[\alpha\alpha + \beta\beta]$ and $C_{29} - \beta\beta/[\alpha\alpha + \beta\beta]$) are 0.45 and 0.56, respectively. C_{23} -tricyclic terpane/ C_{30} - $\alpha\beta$ hopane (TT_{23}/H_{30}) ranges from 0.10 to 0.30. $Ts/(Ts + Tm)$ range from 0.17–0.22. The ratios of $C_{27}\beta\alpha(20R)/C_{27}\alpha\alpha(20R)$ -steranes range from 0.08 to 0.15. These maturity parameters were consistent with the maturity of the Dalong Fm in the TJS PU area (R_o 0.58%). This is lower than those in the eastern segment of the Kaijiang-Liangping Intracratonic Sag (NE Sichuan Basin). The uplift of the Longmen Mountains causes the Dalong Fm in the Guangyuan area to be in the early stages of oil generation. It may only charge the stratigraphically adjacent formation (Permian-Triassic) because of the limited extent and relatively low maturity.

(3) *Maidiping-Qiongzhusi Formation*. The kerogens of the Qiongzhusi Fm in the WSB are dominated by micrinite (more than 95%), with less than 5% content of marine vitrinite and intertinite. The Lower Cambrian source rocks in the NSWCD generally have high TOC values and maturity. This creates significant petroleum potential for the Sinian Dengying Fm and the Upper Paleozoic [59]. The TOC value of the silicate-mudstone in the CS-1 well (burial depth 8140 m) is 2.56. The thickness of the Qiujiabe Fm (equivalent to the Maidiping Fm) in the Qingping section is 142 m. This was tested using 26 equidistant samples with average TOC and R_o^b values of 12.95% and 2.31%. The thickness of the exposed Qingchuan section is 80 m, and the average TOC for 15 equidistant samples was 2.2%. The adjacent north Sichuan basin shows that the Guojiaba Fm (equivalent to the Qiongzhusi Fm) of the Yangba and Daba sections also has high TOC values of 2.87–3.79%.

The GC-MS of two superdeep samples (8140 m and 7894 m from the CS-1 well) show the complete distribution of n -alkanes. Steranes originate from the sterols of eukaryotic organisms [60]. The stable distribution of C_{27} - C_{29} regular steranes in the generative windows can effectively distinguish oils from the same source rock with different organic phases [61, 62]. The distributions of C_{27} - C_{29} steranes in the CS-1 well have a similar “L-V” shape of $C_{27} \geq C_{27} > C_{28}$ (Figure 5). This is similar to the Dalong Fm. The C_{23} -tricyclic terpane/ C_{24} -tetracyclic terpane (TT_{23}/tT_{24}) ratios of the 8140 m sample are 2.74. The $C_{29} - 20S/(20S + 20R)$ and $\beta\beta/(\alpha\alpha + \beta\beta)$ rise from 0 to ~0.5 (0.52–0.55 endpoint) and from 0 to ~0.7 (0.67–0.71 endpoint), respectively, with the increase in isomerization [60, 62]. The $C_{29} - 20S/(20S + 20R)$ are approximately 0.41–0.42, and $C_{29} - \beta\beta/(\alpha\alpha + \beta\beta)$ is approximately 0.36 (Table 2), which is significantly similar to the north Sichuan Basin. The north Sichuan Basin ranges

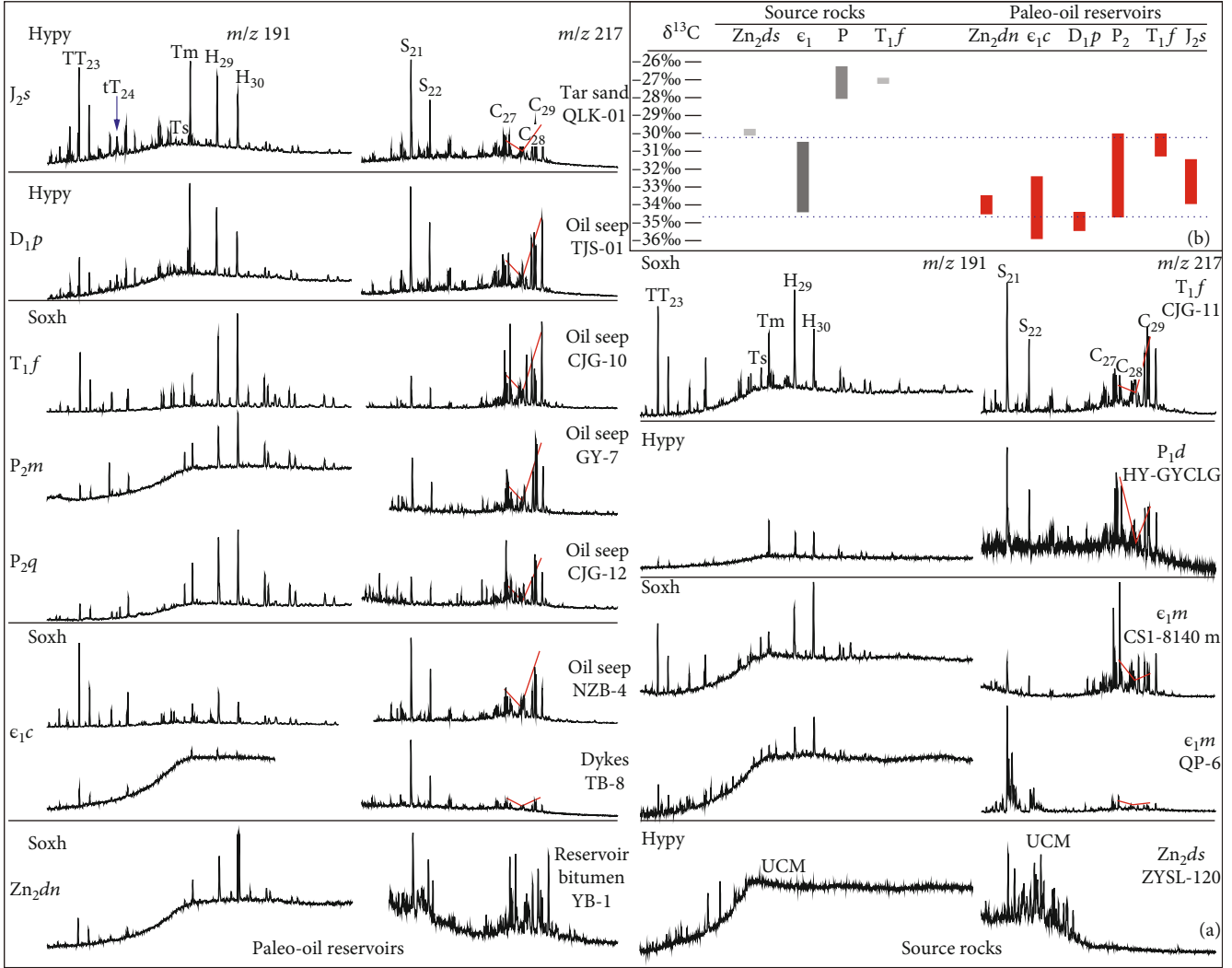


FIGURE 5: The GC-MS and $\delta^{13}\text{C}$ characteristic of paleo-oil reservoirs and source rocks in the Tianjingshan Paleouplift area. (a) The GC-MS shows that the distribution of the C_{27} – C_{29} regular steranes ($\text{C}_{29} > \text{C}_{27} > \text{C}_{28}$) is similar in both the Sinian Dengying and Jurassic Shaximiao formations. The paleo-oil reservoirs show that the $\text{TT}_{23}/\text{tT}_{24}$ values can also possibly correlate with the source rocks. (b) The distribution interval of the $\delta^{13}\text{C}$ correlation shows that the source for the paleo-oil reservoirs is mainly the Lower Cambrian.

TABLE 2: Biomarker parameters of source rock and paleo-oil reservoir.

Biomarker parameters	Source rock					Paleo-oil reservoir							
	ϵ_{1m+q} CS1-8140	QP-6	P_{2d} GY-S-8	T_{1f}^1 CJG-11	Zn_{2dn}^4 YB-1	ϵ_{1c} TB-8	ϵ_{1c} NZB-4	D_{1p} TJS-1	P_{2q} CJG-12	P_{2m} GY-7	T_{1f} CJG-10	J_2^s QLK-1	J_2^s HB-01
$\text{TT}_{23}/\text{tT}_{24}$	2.74	/	1.1	2.57	3.37	2.68	2.78	2.73	2.48	3.46	1.9	3.70	3.32
$\text{TT}_{23}/\text{H}_{30}$	0.7	0.67	0.28	1.25	0.29	1.96	2.4	1.8	0.14	0.17	0.39	1.53	1.8
$\text{H}_{29}/\text{H}_{30}$	0.78	0.74	0.91	1.49	0.79	1.78	1.42	1.45	0.88	0.71	0.75	1.39	1.17
$\text{Ts}/\text{Ts} + \text{Tm}$	0.5	0.5	0.17	0.29	0.12	0.27	0.23	0.27	0.33	0.41	0.31	0.49	0.48
$\text{C}_{29} - 20\text{S}/(20\text{S} + 20\text{R})$	0.4	0.42	0.44	0.48	0.46	0.44	0.46	0.46	0.46	0.47	0.37	0.49	0.46
$\text{C}_{29} - \beta\beta/(\alpha\alpha + \beta\beta)$	0.37	0.36	0.52	0.51	0.27–0.44	0.58	0.58	0.56	0.56	0.57	0.3	0.59	0.6
$\text{S}_{21}/\text{S}_{22}$	3.75	2.28	1.19	2.46	2.77	2.62	1.99	2.08	2.34	2.49	2.37	2.39	2.63
$\text{S}_{21} + \text{S}_{22}/\text{C}_{27} + \text{C}_{28} + \text{C}_{29}$	0.43	0.12	0.33	0.36	0.19	0.96	0.35	0.42	0.13	0.19	0.1	0.33	0.44
$\text{C}_{27}/(\text{C}_{27} + \text{C}_{28} + \text{C}_{29})$	37	38	39	23	27	29	24	23	29	23	28	28	27
$\text{C}_{28}/(\text{C}_{27} + \text{C}_{28} + \text{C}_{29})$	31	32	31	25	31	30	27	23	23	21	32	22	22
$\text{C}_{29}/(\text{C}_{27} + \text{C}_{28} + \text{C}_{29})$	32	30	30	52	42	44	49	54	48	56	40	50	51

from 0.31 to 0.40 using Soxh and HyPy [48]. These deeply buried maturity parameters for the CS-1 well samples were consistent with a relatively low maturity, which is according to the R_o (1.5%). Therefore, the deeply buried Lower Cambrian source rocks in the NSWCD (CS-1 well) may not have reached the high-overmature stage owing to overpressure suppression.

3.3.2. Geochemical Characteristics of Paleo-Oil Reservoirs

(1) *Terpanes and Regular Steranes.* The Dengying Fm reservoir and the Lower Cambrian source rocks are typical hydrocarbon accumulation units of ancient geological age. The maturity-related parameters such as the $C_{29} - 20S/(20S + 20R)$ and $C_{29} - \beta\beta/(\alpha\alpha + \beta\beta)$ of the Dengying Fm bitumen in the Yangba section range from ~ 0.42 to 0.46 and ~ 0.27 to 0.44 , which does not reach the endpoint of isomerization. The maturity of the Dengying reservoir bitumen is similar to the Cambrian-Jurassic paleo-oil reservoir (R_o 0.5–1.0%) in the TJS PU area. Tricyclic terpanes are common in petroleum and source rock extracts, possibly originate from prokaryotic cell membranes [63], and can be related to Tasmanites [64–67]. The cell structure observation of Tasmanite using optical microscopy shows that tricyclic terpanes first occurred in the Upper Cambrian and were extremely abundant in some Paleozoic strata [68–70]. Tricyclic terpanes are also present in the Upper Permian Dalong Fm in the Tianjingshan structure. Generally, the C_{23} member is the dominant compound in tricyclic terpanes in crude oils, especially those from marine sources [71]. Moreover, tricyclic terpanes are more resistant to biodegradation than hopanes and can occur in severely biodegraded oil even when the hopanes have been destroyed [72]. The tetracyclic terpanes were derived from the thermal or microbial rupture of hopanes or precursor hopanoids [60]. Tetracyclic terpanes are more resistant to biodegradation than the hopanes [68]. These terpanes are present in a few samples from the TJS PU area. C_{24} tetracyclic terpane (tT24) is more common than its homologs. Oils sourced from terrestrial organisms have relatively high concentrations of tT₂₄ [73].

The TT_{23}/tT_{24} ratio can indicate the type of organic matter. Relatively high values for the TT_{23}/tT_{24} ratio usually imply a large input from marine organic matter [74, 75]. The TT_{23}/tT_{24} ratios are in the range of 3.0–3.5 in the Qiongzhusi Formation [48], whereas they fall to 1.1–1.6 in the Dalong Formation. However, oils sourced from terrestrial organic matter have a relatively low TT_{23}/tT_{24} ratio value. The NW Sichuan Basin has the Qiongzhusi Formation that was deposited in the open sea during the Lower Cambrian [76]. The decreased TT_{23}/tT_{24} ratio from the Qiongzhusi Fm to the Dalong Fm is consistent with increased terrestrial organic matter input, which can be observed in the composition of macerals. Meanwhile, Wang et al. [41] also identified the characteristics of gravity current deposition in the Dalong Fm in the Sichuan Basin [77]. Therefore, the decrease of the TT_{23}/tT_{24} ratio shows a sufficient correlation with the variation in the sedimentary environment. The TT_{23}/tT_{24} ratios of the Lower Cambrian paleo-oil reservoir (~ 2.7 – 3.2), the

Lower Devonian Pingyipu Fm oil seep (~ 2.7), the Permian Qixia-Maokou Fm oil seep (~ 2.5 – 3.5), the Jurassic Shaximiao Fm tar sand and oil (~ 3.3 – 3.7), and the Qiongzhusi Formation (~ 2.7 – 3.2) are all approximately similar. However, these differ from the Dalong Fm (~ 1.1 – 1.6). Therefore, it appears that the Lower Cambrian source rocks most likely correlate with the Sinian-Cambrian bitumen, Devonian-Permian, and Jurassic oil seeps.

Pregnane and homopregnane are highly resistant to biodegradation [78]. They are derived from the hormones pregnanol and pregnanone and the thermal cracking of C_{27} – C_{29} regular steranes [79]. The pregnane/homopregnane (S_{21}/S_{22}) ratios of the Sinian Dengying Fm and Jurassic Shaximiao Fm paleo-oil reservoir are very similar (~ 2.0 – 2.7). These ratios are also similar to that of the Lower Cambrian (~ 2.3 – 2.5) but higher than the Dalong Fm (~ 1.1 – 1.2). This provides additional evidence that the oil seeps and bitumens in the TJS PU area were derived from the same source rock. The paleo-oil reservoir was severely biodegraded. Particularly, the absence of acyclic isoprenoids in the bitumen from the Dengying and Changjianggou formations indicates that those paleo-oil reservoirs rank 5–6 on the PM biodegradation scale [58]. The distributions of the C_{27} – C_{29} regular steranes ($C_{29} > C_{27} > C_{28}$) in extracts are similar, which was also reported by Huang and Wang (2008) and Rao et al. (2008) [41, 42].

(2) *Bulk $\delta^{13}C$ Values of Kerogen and Extract Fractions.* Stable carbon isotopic compositions have been widely used for correlating oil with source rocks [61, 80]. The $\delta^{13}C$ value of oil (bitumen) depends on the original organic matter from which the oil was expelled [81]. A negative shift of bulk $\delta^{13}C$ values between kerogen and oil/bitumen of less than 3‰ usually suggests a possible correlation [60, 82]. The bulk $\delta^{13}C$ values of the Precambrian Doushantuo Fm in the Yichang and Zunyi areas range from -27.9‰ to -30.7‰ . The bulk $\delta^{13}C$ values of Lower Cambrian kerogen in the NW Sichuan basin are between -31.0‰ and -34.0‰ . However, the bulk $\delta^{13}C$ values of the Middle-Upper Permian and Lower Triassic kerogen range from -26.0‰ to -28.0‰ , which are much higher than those of the Cambrian kerogen (Figure 5(b)).

The bulk $\delta^{13}C$ values of the Lower Cambrian oil seep and the solid bitumen veins from the Nianziba anticline are -34‰ to -36.0‰ . The bulk $\delta^{13}C$ value of the Devonian Pingyipu Fm paleo-oil reservoir in Tianjingshan (Middle TJS PU area) is -34.95‰ . The $\delta^{13}C$ values of the Qixia, Maokou, and Feixianguan Fm range from -30‰ to -34‰ . The $\delta^{13}C$ values of the saturates, aromatics, resins, and asphaltenes of the Jurassic tar sands and oil in the Qinglinkou-Huangjinkou area (Southern TJS PU area) are in the range of -31.5‰ – 34.0‰ . Generally, oils from Paleozoic marine sources have bulk $\delta^{13}C$ values lighter than -30‰ , which gradually became heavier (rich in ^{13}C) in the following (Permian-Triassic) geologic periods [83]. The Tianjingshan structure shows that paleo-oil reservoirs in different strata (Sinian, Cambrian, Devonian, Permian, Triassic, and Jurassic) have very low $\delta^{13}C$ values (commonly $< -34.0\text{‰}$), which confirmed that those oil seeps and bitumen are mainly from the Lower Cambrian source rocks.

4. Petroleum System Interpretation and Discussion

4.1. Tectonic-Controlled (Intracratonic Sag and Paleouplift) of Early Hydrocarbon Accumulation

4.1.1. *Northern Segment of the Mianyang-Changning Intracratonic Sag.* Along with a full analysis of the regional structural characteristics of China, the formation mechanism of the North China Rift and the structural background of the eruption of the Emeishan Basalt in the southwestern margin of the Sichuan Basin were reported. Therefore, Luo proposed the taphrogenesis theory and proposed that there had been three large-scale taphrogeny in the Chinese mainland since the Late Proterozoic subsequently [84], which include the Xingkai, Emei, and North China [20]. These were closely related to the formation and distribution of oil and gas.

The Early Cambrian MY-CN IS has received extensive attention since being discovered along with the genesis of the Rodinia and Gondwana supercontinents being proposed [10]. The MY-CN IS extends from the original Tethys Ocean into the Sichuan Basin of the Upper Yangtze Craton, which trends along the NNW-SSE. Both sides of the Weiyuan and Gaoshiti structure in the middle segment of the MY-CN IS are used as boundaries. Therefore, intracratonic sag can be divided into three segments. The southern segment spans from Dazu, Yibin, and Longchang to Changning, and the northern segment stretches over Yanting, Langzhong, and Guangyuan area. Currently, the middle-north segment of the WSCD coincides with the northern segment of the MY-CN IS. However, because of the greater burial depth of the Sinian Dengying Formation and the Lower Paleozoic, the investigation of the structural features of the northern segment of the intracratonic sag is difficult.

Based on the preliminary analysis of the two-dimensional seismic profile in the Shuangyushi-Shejianhe area, the deeply buried Devonian-Permian structure is located just above the eastern boundary of the MY-SC IS, and scarp features are distinct. The Late Sinian-Early Cambrian tectonic and sedimentary characteristics of the NSWSCD are similar to that of the Gaoshiti-Moxi structure in the central Sichuan Basin. This study has sufficiently used high-precision contiguous 3D seismic and some 2D seismic data (from Sinopec and Petro-China) in addition to drilling and field outcrop data. This was performed using the thickness description method of the Lower Cambrian Maidiping and Qiongzhusi formations that was first discovered in the MY-CN IS (Figure 6(a)).

The boundary on the west side of the northern segment is approximately perpendicular to the original Tethys Ocean and is distributed along the Chengdu-Weiyuan area. The boundary characteristics of the reflected thickness are clear. The eastern part of the northern segment has great depth, is widely distributed, and is more prominent owing to the depositional control of the deep formations in the NSWSCD. The east side of the northern segment lies along the Shehong-Santai-Yanting-Langzhong-Jiangyou-Guangyuan line, and the distance between scarps is wider. The thickness differentiation of the Qiongzhusi Fm decreases gradually after passing Shehong. The continuous feature of the Dengying Fm is

apparent in the seismic profile below the steeper scarp (I). Similar to that of the central Sichuan Basin, tension faults are not well developed in the northern segment of the MY-CN IS. The clarity of boundary features is relatively reduced. The NSWSCD is in the center of the northern segment of the MY-CN IS, where the Lower Cambrian is thick. The Lower Cambrian marine dolomite is approximately 1000 m thick and is the sedimentary center of the black organic-rich shale from the Maidiping-Qiongzhusi Fm.

4.1.2. *Stratigraphic Context of the Tianjingshan Paleouplift Area.* Paleouplifts are areas of positive structural relief that form on the Earth's surface owing to the interaction of internal and external geodynamic processes through the geologic time [85]. According to pre-Devonian sedimentary paleomorphology, the study states that there is a paleouplift structure in the northwest of the Sichuan Basin. This was subject to tectonic evolution in the sag and platform areas, which was controlled by the Longmenshan deep faults. This structure was named the TJS PU, with Cambrian-Ordovician denudation in the core of the area [86]. Paleouplifts can control early oil and gas accumulation of ancient deep petroleum systems. The TJS PU is located on the northern side of the Leshan-Longnvsi paleouplift and has a relatively small area. Therefore, a few studies consider the TJS PU to be part of the Caledonian Paleouplift [87].

The TJS PU is poorly constrained in time-space. Outcropping strata are scarce in this area and have poor quality seismic data owing to the complex structural background and lack of Sinian-Cambrian drilling in the region. This caused the precise structural boundary of the TJS PU to be difficult to determine. Controversy also exists regarding the initial uplift time. A few studies believe that the TJS PU formed in the Early Cambrian, which is based on observations of the lithological characteristics of the Lower Cambrian Changjianggou Fm [85, 88].

The 1:200,000 regional survey report originally divides the Changjianggou Fm into three members. Revised in 1962, the lower two members still belong to the Changjianggou Fm. However, the upper member belongs to the Modaoya Fm. When the distinct lithologies and lithofacies in this area are considered, drilling has not revealed the relationship of the contact between the top of the Dengying Fm and the bottom of the Lower Cambrian. Whether the Yunnan stratigraphic system should be adopted to correspond the Changjianggou-Modaoya Fm to the Qiongzhusi-Canglangpu Fm is still questionable, respectively. Furthermore, this study corresponds to the Modaoya Fm to the middle-upper part of the Lower Cambrian such as the Yanwangyan Fm in the northern Sichuan Basin. Therefore, the initial uplift time of the TJS PU is slightly different from a few other studies. The TJS PU is vertically superimposed on the MY-CN IS, which is roughly on the west side of scarp (I) in the northern segment of the Early Cambrian MY-CN IS. Based on the stratal relationships and outcrop chronostratigraphy, the TJS PU can also be divided into several zones (Figure 7).

The preserved tectonic features of the N. TJS PU are characterized by two anticlinal structures (the Kuangshanliang and Nianziba structures), which can be traced further

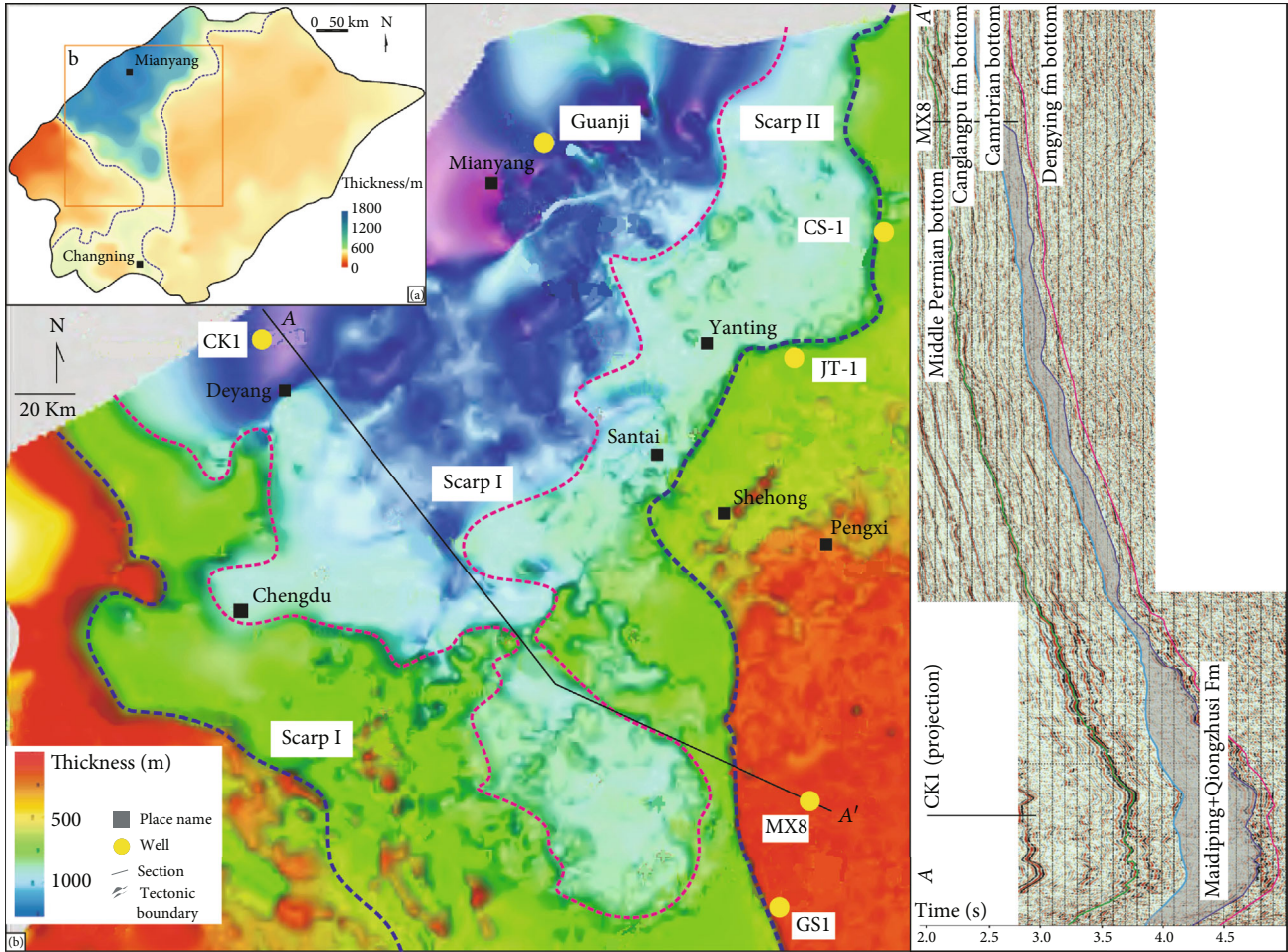


FIGURE 6: Structural characteristics of the northern segment of the Mianyang-Changning intracratonic sag (MY-CN IS). (a) Earlier research results showed that the north segment of the western Sichuan Basin coincides with the northern segment of the MY-CN IS. The relatively rough thickness figure of the Lower Cambrian is from Liu et al. [10]. (b) Latest thickness map of the Lower Cambrian Maudiping Fm and Qiongzhusi Fm from this study. The thickness of the Qiongzhusi Fm has decreased gradually after passing Shehong.

north to Sanliba, Baolun, and Guangyuan area. Finally, the N. TJS PU gradually transects the southwest limb of the Michangshan Paleouplift in the Chaotian. The complete outcrops in the N. TJS PU are found in the current Nianziba structure, which has paraconformable stratigraphic contacts. Combined with the middle and upper part of the Changjianggou Fm, the Middle Ordovician Baota Fm overlies on the third member of the Changjianggou Fm. This includes an overlap from the Middle Silurian Luoreping Fm. Paraconformities also occur in the Lower-Middle Devonian Guanwushan Fm and between the Upper Permian and Lower-Middle Carboniferous in this area. The ages of the missing strata between the Baota and Changjianggou Fm and the Luojiang and Baota Fm are 50 Ma in the Nianziba structure. A weakly compressive tectonic regime from the Caledonian orogeny caused the north segment of the TJS PU to undergo episodic sedimentation-uplift processes during the Early Paleozoic. The relatively stable deposition during the Devonian proceeded with the Lower and Middle Carboniferous strata being developed in a few areas of the northern segment. The Permian Liangshan Fm directly overlies the Devo-

nian under the Kuangshanliang-Nianziba structure, which has a hiatus in time of 60 Ma (Figure 8).

The present-day topography of the middle segment of the TJS PU varies slightly. The surface structural features of the middle segment are characterized by two tightly closed anticlinal structures with a linear strike that trends from the northeast to the southwest. The limbs are oriented at 30° – 60° . The Ordovician-Silurian is not represented in the middle segment of the TJS PU. The missing strata represent a time gap of 110 Ma. The siliceous conglomerate at the top of the Changjianggou Fm is an unconformable contact with the overlying Devonian Pingyipu Fm. The stratigraphic characteristics of the Early Paleozoic sequence indicate that the middle segment of the TJS PU was uplifted and denuded without associated deposition during the Caledonian period. When compared to the northern segment, geological mapping has only identified the entire Devonian and Carboniferous sequence in the middle segment of the TJS PU because of the limited thickness of the stratigraphy. The section still indicates stratal development in the Lower and Middle Devonian near Yanmenba. Similar to the northern segment, the

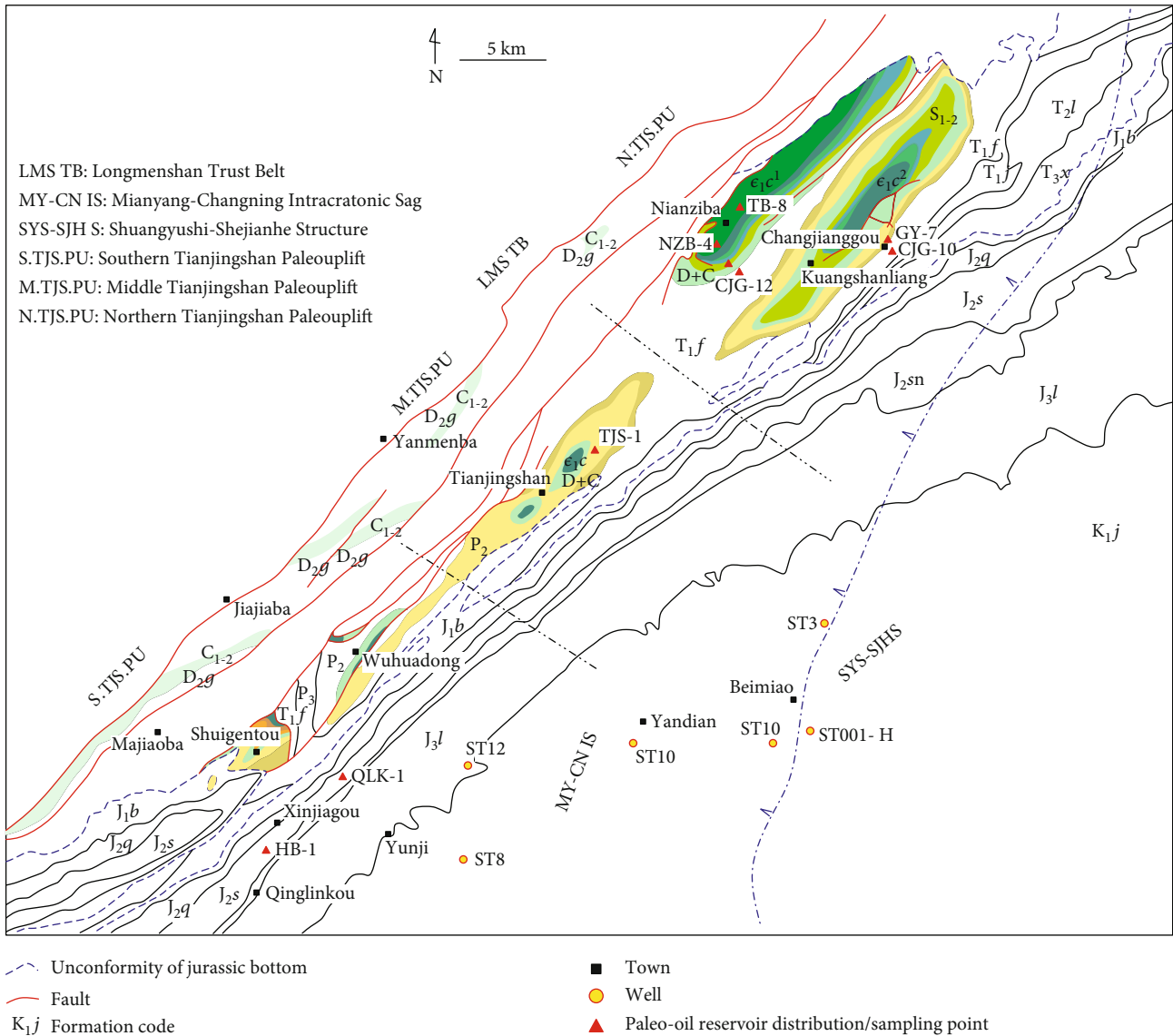


FIGURE 7: Surface geological characteristics and paleo-oil reservoir distribution in the TJS PU area. The Tianjingshan Paleouplift can be divided into south, middle, and north segment. Nowadays, the Tianjingshan structure belt (Tianjingshan Paleouplift area) is overlapping on the Mianyang-Changning Intracratonic Sag.

Upper Carboniferous strata are missing in this area. Large-scale transgression of the entire basin in the Early Permian caused that unconformities occurred between the Middle Carboniferous and the Middle-Upper Permian in the middle TJS PU. The Triassic strata were subject to deformation through folding during the Mesozoic. The conglomerate of the Lower Jurassic Baitianba Fm overlies the Permian-Triassic with an angular unconformable contact.

The southern segment is currently located along Shuigentou-Wuhuadong (Houba-Erlangmiao), which is north of Jiangyou, and appears as an anticline structure that gradually slopes in a southwesterly direction. The surface geology of the southern segment shows a sequence of the middle member from the bottom to the top of the Changjianggou Fm, Lower-Middle Devonian, Lower Carboniferous Zongchanggou Fm, and Permian, respectively. The Paleozoic

sequence in the southern segment is also missing the Middle-Upper Cambrian, Ordovician, and Silurian, which indicates that deposition had not occurred in the area for some time owing to uplift and denudation before the Devonian. The discovery of the Devonian during multidrilling at the Shuangyushi structure was followed by the original undivided Lower-Middle Carboniferous strata in the area that was reassigned to the Lower Carboniferous Zongchanggou Fm. The preserved thickness is only 6 m. This indicates that the Carboniferous in the southern segment of the TJS PU is missing 15 Ma and 32 Ma of strata at the top and bottom, respectively.

4.1.3. Early Paleozoic Extension-Compression Transition. The Yunan movement in the Early Cambrian to Early Ordovician caused a sequence of marine conglomerates and sandstones (the Changjianggou Fm) that was deposited on the top of

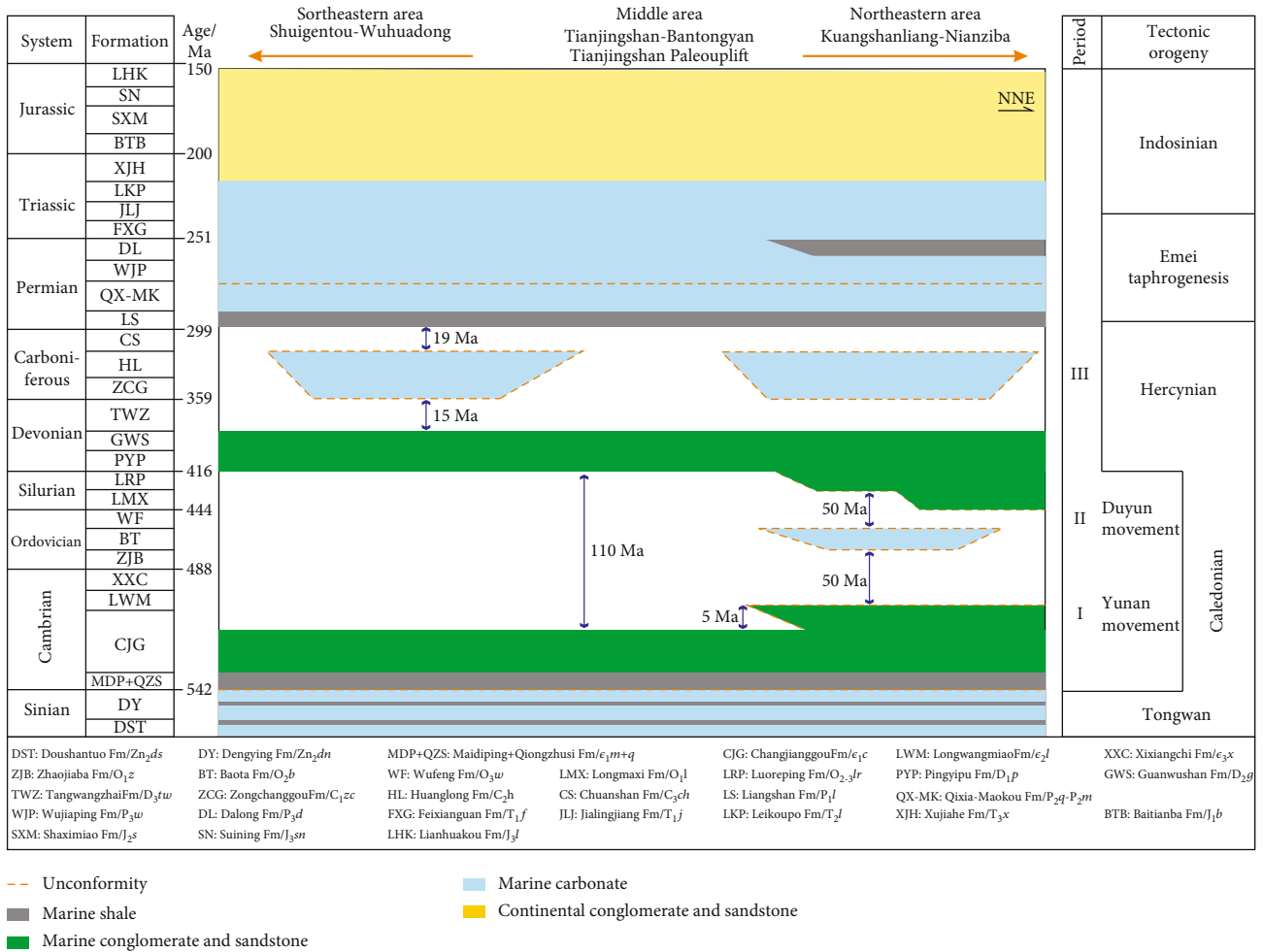


FIGURE 8: Stratigraphic contact of the southern-middle-northern Tianjingshan Paleouplift (TJS PU). Among them, a wide range of Middle Cambrian-Silurian strata is missing, which is mainly in the southern and middle TJS PU. The siliceous conglomerate at the top of the Changjianggou Fm is an unconformable contact with the overlying Devonian Pingyipu Fm, which has a hiatus in time of 110 Ma.

the Lower Cambrian black mudstone in the NSWSCD. However, the Lower Ordovician hiatus may indicate that the Longmenshan ancient land (the TJS PU and the Longmenshan island chain) has been uplifted. The evolution of the TJS PU entered the episodic stage (I) (Figure 9(b)). Therefore, the Caledonian TJS PU must have formed before the Leshan-Longnsvi Paleouplift in central Sichuan.

The Upper Yangtze area reentered a widespread transgressive period at the beginning of the middle Ordovician. The NSWSCD reaccepted stable sediments from sand-mud tidal flats. The transgression intensified in the Middle Ordovician and limestone that was deposited in the northwestern Sichuan Basin. A few studies suggest that during the Late Ordovician and Early Silurian, the Duyun movement, which is evident in southern Guizhou [89], was also essential in the formation of the Caledonian Paleouplift in the Sichuan Basin [90]. Furthermore, the Duyun movement contributed to the development of the Baota Fm karst reservoir in the northwestern Sichuan Basin. The NSWSCD inherited the tectonic-sedimentary framework of the Ordovician during the Early Silurian. The sedimentary system appears as a gently dipping homoclinal sequence of carbonate-terrigenous strata [91]. A

detailed investigation of the surface geology showed that a set of relatively deep-water black shales that belonged to the shelf facies occurred at the bottom of the Silurian in northern Wangcang [92]. There is also a thin layer of oolitic limestone higher up, which has undergone high-energy sorting and transport [93]. Furthermore, 150 m of reef deposits was discovered in the Lower-Middle Silurian in the Chaotian-Guangyuan area.

The Lower-Middle Silurian is difficult to identify in the Tianjingshan area with sets of gray-green silt-shale interbedded siltstone, which is located in the middle of the NSWSCD. The Luoreping Fm depositional environment was a sand-mud flat to gentle slope or intertidal zone. The Upper Yangtze area had uplifted significantly owing to the Late Caledonian movement (i.e., Guangxi movement) by the end of the Silurian. The Leshan-Longnsvi area in the central Sichuan area was the core of the uplift. Denudation of the Ordovician-Silurian strata provided a large supply of terrestrial detritus for the Devonian sedimentary rocks in the western Sichuan area. The Tianjingshan area underwent discontinuous uplift (Figure 9(c)) during this period. The continuous differential uplifting of the TJS PU area exposed the strata and created unevenly distributed

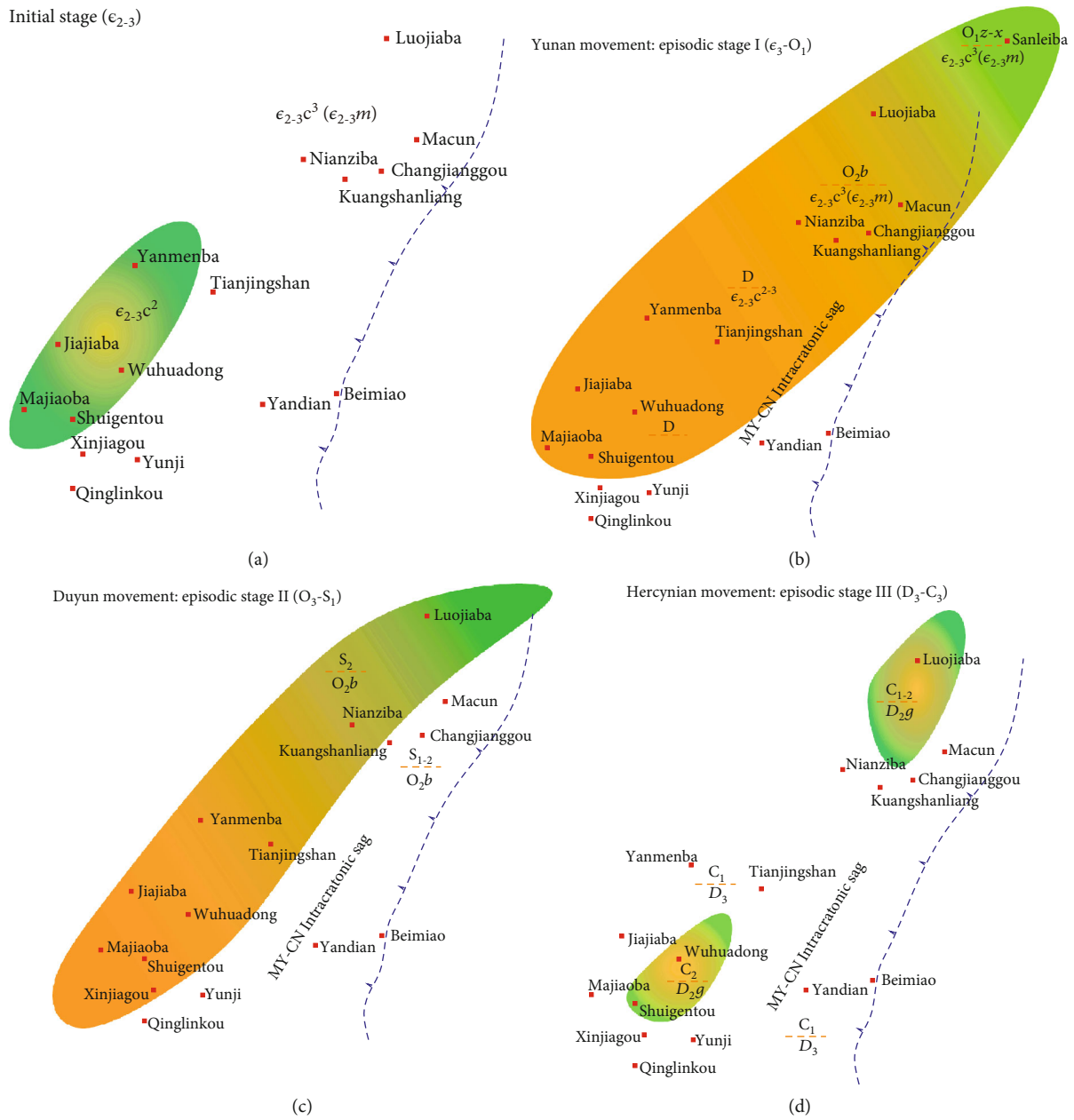


FIGURE 9: Relationship between the TJS PU and MY-CN IS in different time periods. (a) The prototype of the TJS PU is thought to have formed in the Late Cambrian; (b) corresponding to the Yunan movement, the TJS PU reached its maximum extent; (c) in the Caledonian, the TJS PU was still approximately 10–20 km away from the MY-CN IS; (d) the TJS PU area is reflected and dominated by regression of cyclical sea-level variation in the Hercynian.

unconformities. The current exposure of the Kuangshanliang-Nianziba structure shows that the nodular limestone of the Upper Ordovician Baota Fm has unconformable contact with the lower Changjiangkou Fm and upper Lower Silurian. The significant uplift in the mid-southern segment of the TJS PU caused the Middle-Upper Cambrian, Middle-Upper Ordovician, and Lower Silurian to become nearly absent.

The TJS PU evolved into episode III during the Devonian-Carboniferous Hercynian orogeny. Furthermore, the Tianjingshan area has a deeply buried depositional framework that is consistent with uplift and depression. Devonian lithologies are poorly represented in the paleoup-

lift area, with the Middle and Lower Carboniferous overlying the Middle Devonian Guanwushan Fm. A large Devonian sedimentary basin occurs on the western side of the TJS PU. The sand-mud flat depositional environment in an asymmetric NE-oriented rift basin in the Tangwangzhai-Yangtianwo area represents the center of Devonian subsidence [94]. The NSWSCD transformed into a semienclosed bay environment in the Carboniferous on the western margin of the Yangtze Plate. This was dominated by a limited and semilimited platform to open-platform carbonate sequence [95]. The Carboniferous in the mid-southern segment of the TJS PU is also relatively complete, whereas the

northern segment lacks Upper Carboniferous deposition. Significant regression in cyclical sea-level variations is indicated in the TJS PU area from the Middle Carboniferous Huanglong Fm to the Upper Carboniferous Chuanshan Fm (Figure 9(d)).

The Paleozoic stratigraphic contacts indicate that the tectonic core of the TJS PU migrated from south to north. The early core of the paleouplift was approximately located in the Shuigentou-Tianjingshan-Bantongyan area of the mid-southern segment. A later increase in uplift and denudation amplitude in the northern segment caused that the structural high moved from the mid-southern to the northern segment. The TJS PU and the MY-CN IS overlapped laterally. The area of the TJS PU was relatively larger in the Late Cambrian and Early Ordovician, and Late Ordovician and Early Silurian of episodes I and II, respectively. The Nianziba-Kuangshanliang area in the northern segment overlapped vertically onto the intracratonic sag. The core of the paleouplift was only approximately 10–20 km away from scarp I on the eastern side of the MY-CN IS during multistage sea-level rise and fall processes (Figure 9). The Changjiangkou and Pingyipu Fm in the paleouplift area remained on a regional high until the Middle-Late Triassic. This is the optimal accumulation area for early generation oil and gas that is derived from high-quality Cambrian source rocks in the northern segment of the MY-CN IS. The formation and structural relationship of the TJS PU with the MY-CN IS led to the development of the intracratonic sag, paleo-uplift complex, and joint model that controls the early accumulation of oil and gas in the NSWSCD. The northern segment of the MY-CN has controlled the development of high-quality source rocks of the Lower Cambrian Maidiping and Qiongzhusi Fm. However, the evolution of the paleouplift coincided spatiotemporally with the superior source rocks. The source rocks and reservoir characteristics in the NSWSCD provided the optimal conditions for hydrocarbon accumulation in the region.

4.2. The Multistyle and Stage Hydrocarbon Accumulation Characteristics under Complex Geological Background

4.2.1. Deeply Buried-Strong Uplift Characteristics and Oil-Gas Zoning. Studies of the Dengying Fm-Longwangmiao Fm gas reservoirs (i.e., the Gaoshiti-Moxi structure in the middle Sichuan Basin) have realized the importance of the preservation conditions, which were concluded as four-center accumulation processes of original gas generation centers (paleo-oil reservoirs), the transition of gas storage centers, and the current gas-holding centers (present gas reservoirs) [96–98].

Two important faults were evolved at the junction of the NSWSCD and the LMS TB, which are the Majiaoba fault (MJB F) and the frontal hidden fault (i.e., No. 1 fault), after the Late Triassic. The Majiaoba fault is a zone that comprises of several thrust faults and single faults that often have limited extension. This is the boundary fault between the LMS TB and the NSWSCD. The Majiaoba fault mainly developed along the clasolite of the Upper Triassic Xujiahe Fm. The area to the west of the fault is mainly composed of pre-Jurassic strata. The oil and gas preservation conditions have been destroyed completely after undergoing extreme deformation.

The east of the fault is mainly composed of Jurassic and younger strata, which include minor deformation. The No. 1 fault is predominantly buried and primarily developed together with the continental clasolite formations from the Jurassic. The No. 1 fault is also known as the Guangyuan-Dayi (hidden) Fault. The No. 1 fault developed inside the Upper Yangtze block, which is the extended result of thrust movement from the LMS TB to the foreland. The frontal and deformation zone of the NSWSCD remained involved in the deformation to varying degrees. The angle of the dip of the strata decreases rapidly in the easternmost No. 1 fault area.

When the NSWSCD is considered, the No. 1 fault is also a boundary fault that is characterized by deeply buried and strong uplift (Figure 10). According to the main structural events after the Late Triassic, the formation and evolution of the No. 1 fault have been an important influence on the early accumulation effect of the paleo-oil reservoir in the TJS PU. The No. 1 fault also divided the oil-gas zone after the Late Triassic. The current Middle Permian top structural map of the NSWSCD shows that the two subzones have typical burial depth differences owing to the influence of the thrust belt on extension and deformation. The burial depth of the Paleozoic (Cambrian-Middle Permian) in the hanging-wall of the No. 1 fault (i.e., frontal deformation zone in the NSWSCD) is generally maintained at 2500–4000 m after being affected by the rapid uplift and erosion processes of the LMS TB after the Late Triassic. Numerous residual paleo-oil reservoirs dominate the surface. The evolution process of the paleo-oil reservoir system in the Tianjingshan Tectonic Belt (frontal deformation zone) of the NSWSCD has led to the following formations: first, the Early Tianjingshan Paleouplift oil reservoir (Dengying Fm-Changjianggou Fm-Lower Devonian); second, the adjustment and reconstruction of the subdamaged secondary oil reservoir (Qixia Fm-Feixianguan Fm) with multistage and lateral-vertical migration; third, the complete destruction of the residual oil reservoirs (Upper Cambrian solid bitumen-Jurassic tar sand) in the Himalayan period (Figure 11). Therefore, only the hydrocarbon accumulation process from the paleo-oil reservoirs has been maintained during the destruction of the paleo-oil reservoirs in the frontal deformation zone of NSWSCD.

4.2.2. Multistyle and Stage Characteristics of Deep Hydrocarbon Accumulation. Based on the inheritance and innovation of source control theory, which has a multisource supply of high-quality Cambrian source rock as the core, the contrasting relationship between cap strength and trap closure height are the main factors that control oil and gas distribution. The superimposed basin is an important attribute of the Sichuan Basin. The oil and gas accumulation process in the NSWSCD of the Sichuan superimposed basin includes the following processes. First, the coupling process of paleo-oil reservoir formation and destruction in the frontal deformation zone, gas reservoir formation, and adjustment processes in the target deeply buried Upper Proterozoic Sinian Dengying Fm. Second, the current exploration and development of the Upper Paleozoic Middle Permian Qixia Fm.

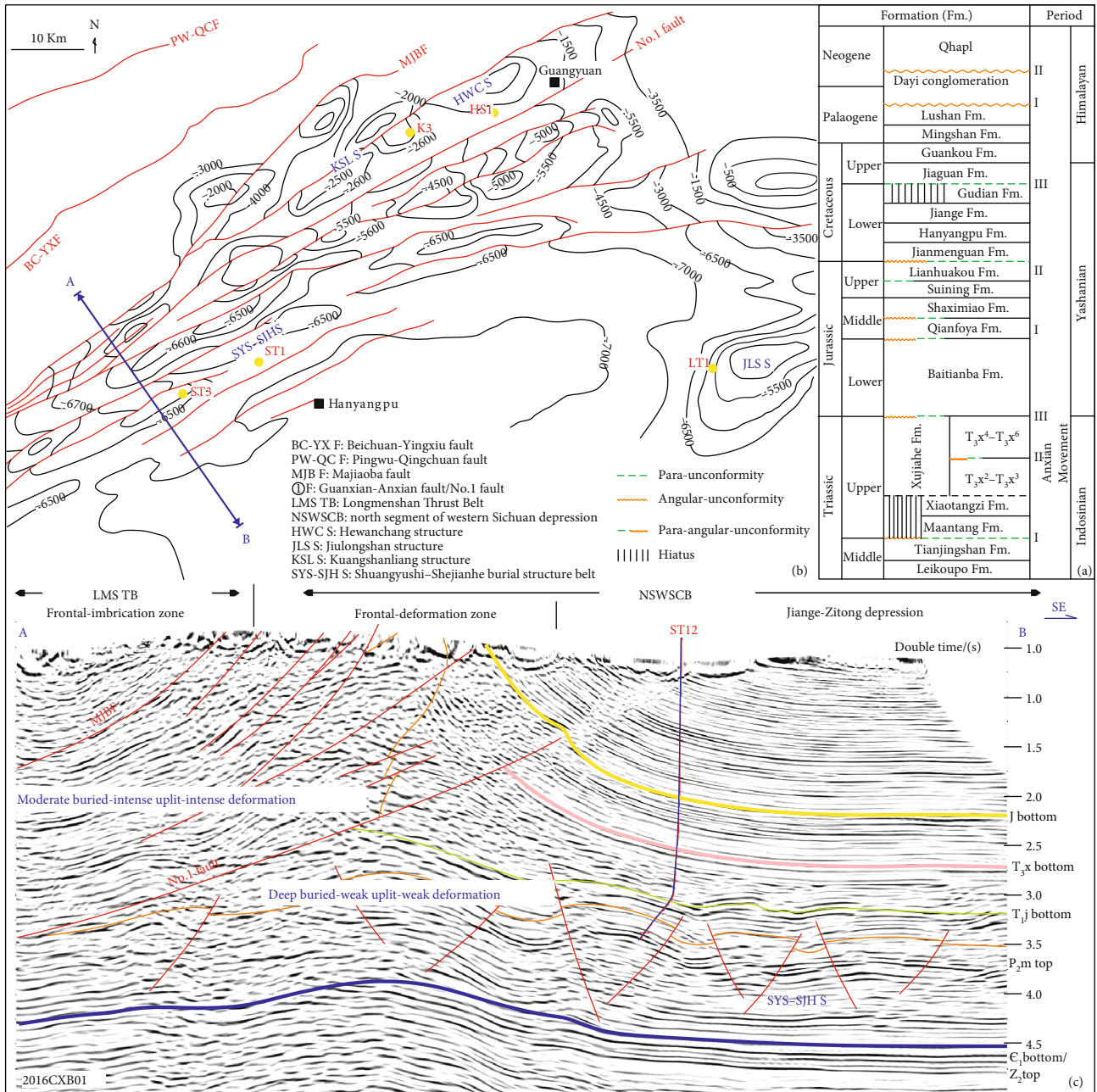


FIGURE 10: (a) The NSWSCD has experienced three stages (eight periods) of tectonic movements since the Late Triassic. (b) The structural map (Middle Permian top) showing that the NSWSCD has developed a series of subsurface structures (HWC S, SYS-SJH S, and JLS S). (c) NW-SE section shows that the No. 1 fault has divided the NSWSCD into the frontal and deformation zone, and the Jiange-Zitong depression, which has different structural histories after the Late Triassic.

Third, other oil and gas-bearing processes used for reservoir formation.

(1) *Multistyle Characteristics.* The deep marine hydrocarbon accumulation in the NSWSCD can be divided into two categories. The first is the primary oil-gas reservoir model, which includes the Lower Cambrian source rocks that are mature enough for hydrocarbon expulsion. This has the migration of the side generation to the side of the reservoir (Dengying Fm), upper generation to the lower reservoir (Dengying Fm), or lower generation to the upper reservoir (the overly-

ing Longwangmiao Fm, the Qixia-Makou Fm, and other paleo-oil reservoirs). The paleo-oil reservoirs were cracked in situ in the later stages. Typical thermally cracked bitumen allows for the paleo-oil reservoirs that formed the current gas reservoir. The primary reservoir and primary gas reservoir model is located near the eastern boundary of the MY-CN IS and the NSWSCD. This includes scarp (I) of the deeply buried Shuangyushi-Shejianhe structure and scarp II of the Langzhong-Jiulongshan-Yuanba area, which has a pivotal role in oil and gas exploration in the Dengying, Longwangmiao, and Qixia-Maokou Formations.

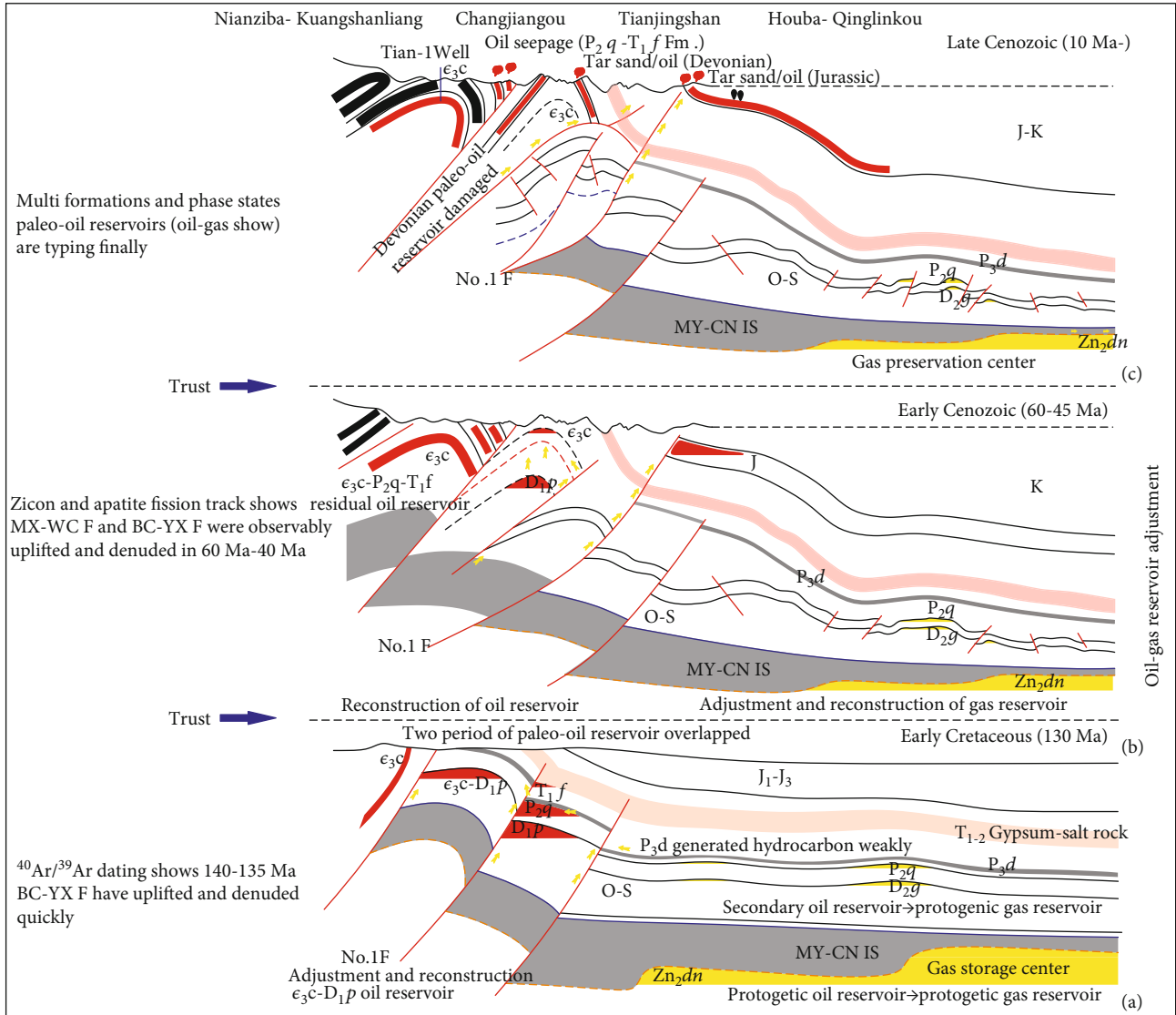


FIGURE 11: Model of deeply buried hydrocarbon accumulation and oil-gas zoning in the NSWCD. (a) With a complete thermal cracking process, the gas storage center may have formed in the Dengying Fm at the eastern boundary of the MY-CN IS. (b) The oil reservoir and deeply buried gas reservoir were adjusted and reconstructed continuously on both sides of the No. 1 fault. (c) Paleo-oil reservoir (oil seeps, tar sand, and bitumen dykes) and deeply buried gas reservoirs formed from the Late Cenozoic.

The second category is the secondary reservoir and the primary gas reservoir model. The weak adjustment and transformation of local uplift, denudation, and thrusting causes the primary paleo-oil reservoir to mainly consist of the Dengying Fm that was partially damaged during the Indosinian period. The partial paleo-oil reservoirs had migrated into the upper Guanwushan Fm, Qixia-Makou Fm, and Feixianguan Fm, which has relatively shallow burial depths. This was achieved through secondary migration that uses the fracture-to-fracture system to form the secondary reservoirs. If later tectonic activity is relatively stable, the secondary reservoir will not be damaged again. The bitumen in the reservoir will undergo thermal cracking with oil cracked in situ to form a primary gas reservoir. The rapid and pronounced uplift and denudation process in the Yanshanian-Hishanian period caused the secondary oil reservoirs to be destroyed completely. The crude oil migrated to the shallow

surface to form residual paleo-oil reservoirs such as oil seeps, oil sands, heavy oil, and solid bitumen veins. The gas reservoirs of the Guanwushan and Qixia-Maokou Fm in the Shuangyushi-Shejianhe structure belt of the NSWCD (on the east side of the No. 1 fault) belong to the secondary reservoir and primary gas reservoir model. Notably, the local Permian and Triassic gas reservoirs in the northern part of the NSWCD may also have individual source rocks within the Dalong Fm source rocks because of the Guangwang, Kaijiang, and Liangping intracratonic sag. Therefore, the Devonian-Permian gas reservoirs in the Hewanchang-Jiulongshan area can be a combination of either primary oil and gas reservoirs or secondary oil and primary gas reservoirs.

(2) *Multistage Characteristics.* The combination of the multiple unconformities, fault-based migration system, and



FIGURE 12: Deeply buried reservoir characteristics of the Dengying and Qixia formations. (a) CS-1 well that is located between 8161.07 and 8161.20 m and consists of algal-laminae stromatolite dolomite (Zn_2dn^4). (b) CS-1 well that is located between 8162.04 and 8162.15 m and consists of algal-dolarenite and algal irregular nodule dolomite (Zn_2dn^4). (c) CS-1 well that is located between 8160.29 and 8160.36 m and consists of karst holes that are formed near the unconformity at the top of the Dengying Fm (Zn_2dn^4). (d) CS-1 well that is located between 8157.96 and 8158.07 m and consists of karst holes that are formed by strong paleokarst weathering at the top of the Dengying Fm (Zn_2dn^4). (e) CS-1 well that is located between 8157.18 and 8157.34 m and consists of fine crystalline dolomite with bitumen and saddle-shaped dolomite that fills in super large intercrystalline pores and intercrystalline dissolved pores. The traces of bitumen that are notably disturbed and broken (Zn_2dn^4) into 5×10 m pieces. (f) ST-3 well, which is located between 7433.72 and 7433.85 m, consists of dolomitic leopard limestone (P_2q). (g) ST-12 well that is located between 7065.48 and 7065.63 m and consists of the bedrock is micrite. Gray leopard dolomiticrite that is formed after partial dolomitization (P_2q). (h) ST-12 well that has characteristics of methane-bearing inclusion in coarse-grain dolomite of the Qixia Fm. (i) ST-12 well that is located between 7050.24 and 7050.34 m and consists of gray micrite with developed fractures (P_2q^2). (j) ST-12 well that is located between 7057.50 and 7057.72 m and consists of micrite with corrosion pores and a large amount of bitumen infill. (k) ST-12 well that is located between 7059.22 and 7059.28 m and consists of two-stage dolomitization, the early stage is dolomiticrite and later recrystallized to form gray-white, medium-coarse, and grained dolomite (P_2q^2).

inclusion homogenization temperature data (Dengying and Qixia formations) corresponds to structural deformation and evolution periods. Furthermore, this combination led to the constraints of thermal burial histories that were used to establish deep marine hydrocarbon accumulation processes in the NSWSCD. Early burial and recrystallization processes created first-generation dolomiticrites with relatively rare microbial calcic-shell concretions in the Dengying Fm. The pores of the Dengying Fm microbial dolomite are well developed and filled with fourth-generation saddle-shaped, coarse-grained dolomite, and a small amount of mesocrystalline dolomite in the two ultradeep samples of the CS-1 well. According to the observation of the mineral generation rela-

tionship between the pores and bitumen infills in the Dengying Fm, the filling sequence can be expressed as first-generation dolomiticrite, second-generation mesocrystalline dolomite, third-generation bitumen, and fourth-generation saddle-shaped dolomite (Figures 12(b) and 12(e)). The fourth-generation dolomite of the Dengying Fm in the NSWSCD is more common, which primarily occurs as saddle-shaped monocrystalline dolomite. Bitumen is a typical result of the thermal cracking of oil and is formed in the gas window during deeply buried. Fluid inclusions in the saddle-shaped dolomite are relatively abundant, distributed in the cleavage, and the growth annulus of the crystals. Given the association with third-generation bitumen, the fourth-

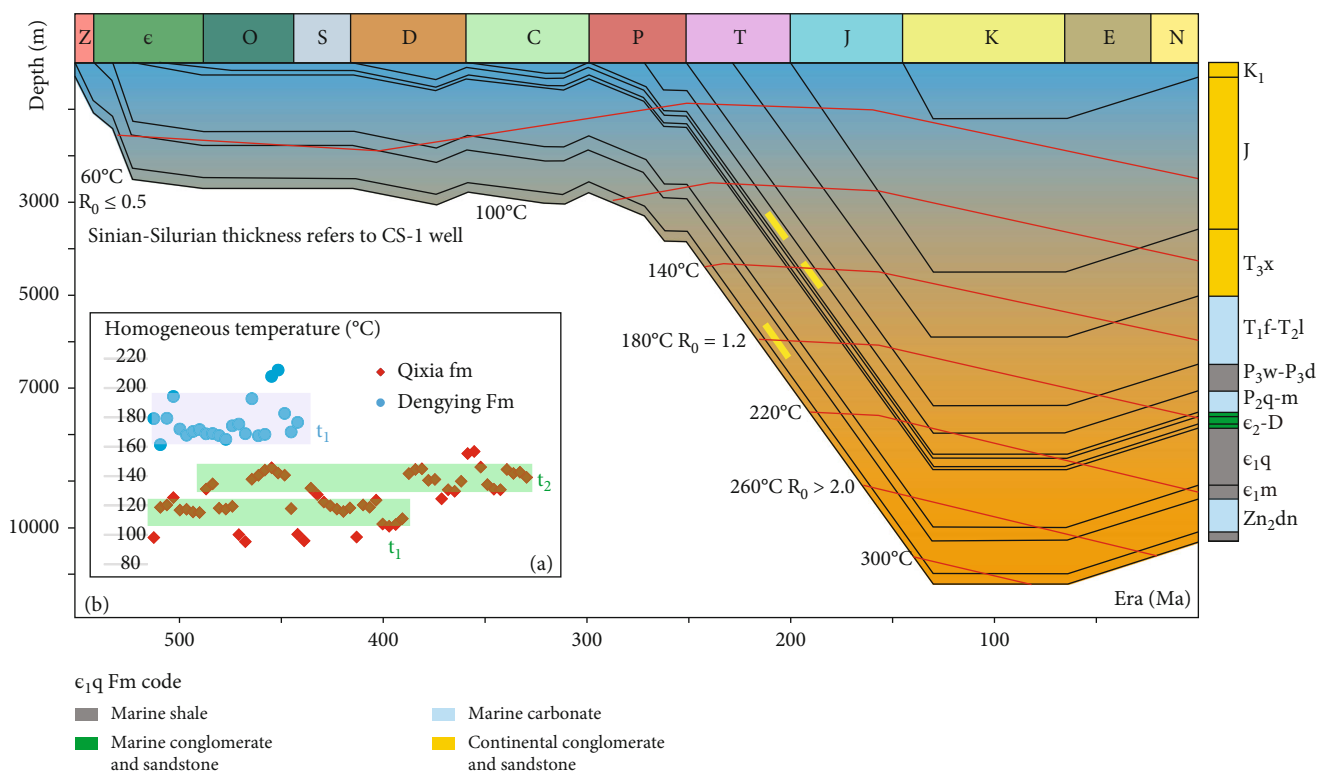


FIGURE 13: (a) The inclusion T_h of the Dengying Fm is 167–176°C. The Qixia Fm has two sets of peaks at 115–125°C and 135–145°C, respectively. (b) Thermal burial evolution that is combined with R_0 and fluid inclusion characteristics indicates that the gas (oil-cracked) charging period of the NSWSCD that mainly occurred in the Middle-Late Triassic to Early Jurassic.

generation dolomite is the primary target for inclusion temperature measurement. The homogenization temperature recorded by the fluid inclusions in the Dengying Fm is set at 167–176°C. According to the thermal burial model, the top of the Dengying Fm is approximately 5200 m deep in the Lower-Middle Triassic. The fluids were consistent over a cracking period of the previously charged oil in the Sinian Dengying Fm.

The abundance of inclusions in the deeply buried Qixia Fm is relatively limited from the ST-12 well in the NSWSCD. According to the statistical observation of the core, the edge of the hole in the Qixia Fm contains either first-generation dolomiticrite, second-generation bitumen, third-generation saddle-shaped dolomite, or third-generation mesocrystalline dolomite (Figure 12(h)). The second-generation bitumen is a typical thermally cracked bitumen. The filling order shows that the saddle-shaped and mesocrystalline dolomite occurred later than the thermally cracked bitumen, which indicated that the fluid filling in this period occurred after the gas generation window. The dolomite reservoirs of the Qixia Fm have mainly powdered crystal dolomite in the (pre) oil generation window. The inclusions in this period are very small, with a lack of tawny oil inclusions. The primary or secondary oil reservoirs are relatively weakly charged in the Qixia Fm. The minerals formed after the gas generation window were mainly either coarse-grained dolomite or saddle-shaped dolomite.

Raman spectroscopy analysis of fluid inclusions in coarse-grained dolomite of the Qixia Fm shows that some gaseous phases of some of the SAH aqueous inclusions have noticeable characteristic CH_4 peaks, which indicates that these hydrocarbon inclusions should be pure liquid methane-bearing. The dolomite with coexisting SAH aqueous and methane-bearing inclusions was selected to measure the homogenization temperatures and to obtain density and salinity values. The ST-12 well (burial depth in the Qixia Fm ranging 7061.83–7083.50 m) has 58 inclusions in the 6 samples (CXB01–CXB06), has homogenization temperatures ranging 95.4–156.8°C, and has freezing point temperatures from -9.6 to -5°C . The calculated salinity and the density range are 7.86%–13.51% and 0.99–1.03 g/cm³, respectively. The inclusions of the Qixia Fm have two sets of peaks at 115–125°C and 135–145°C (Figure 13). This can represent the main oil and gas filling process in the Middle-Late Triassic and Late Triassic to Early Jurassic (Figure 13). Subsequently, a temperature range of 115–125°C approximately corresponds to vertical gas charging that originated from underlying strata (probably the Dengying Fm). Additionally, 135–145°C can represent the gas generation (oil-cracking) window of the secondary (or protogenic) oil reservoir.

4.2.3. Four-Center Accumulation Processes of Deeply Buried Dengying and Qixia Fm. Currently, the deep marine hydrocarbon system in the NSWSCD is controlled by the composite action of the intracratonic sag, paleouplift, and basin-

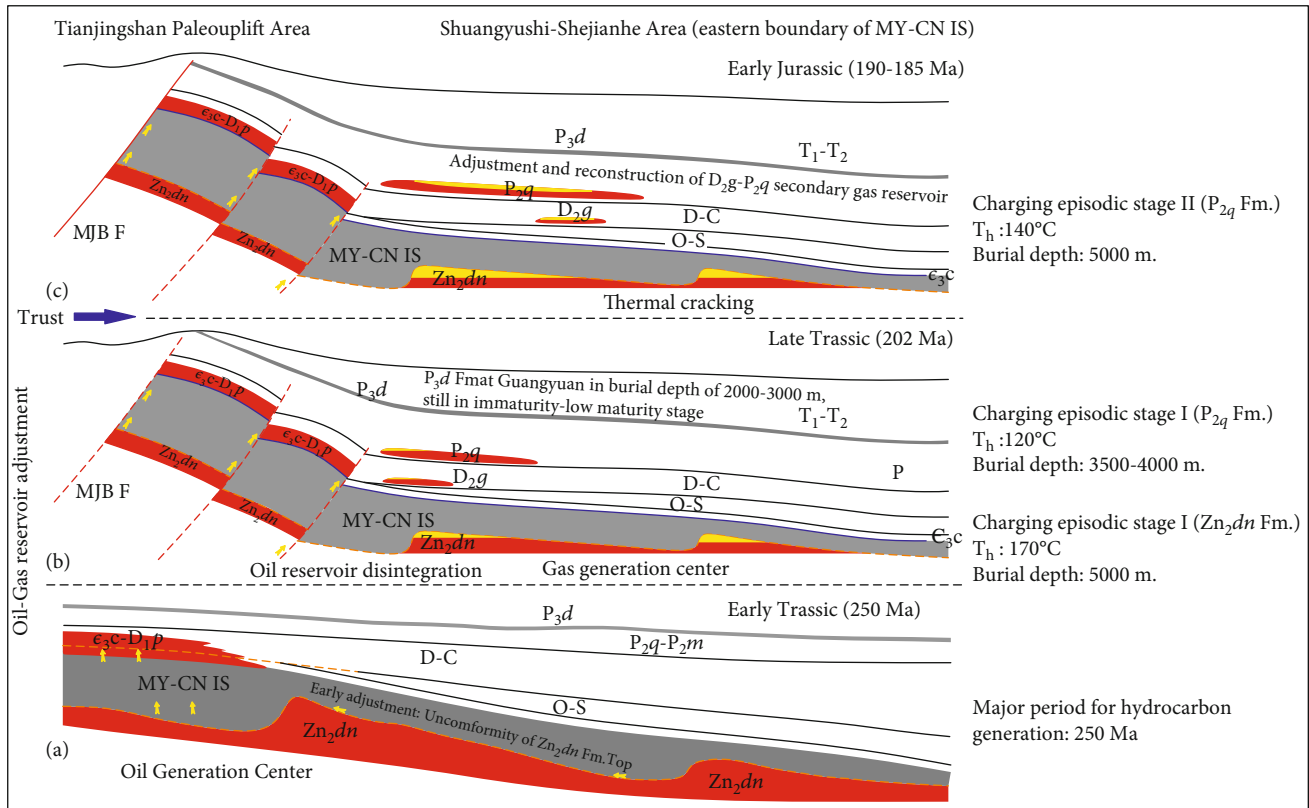


FIGURE 14: The early formation and evolution processes of the paleo-oil reservoir in the Tianjingshan Paleouplift (TJS PU) area. (a) The Early Triassic shows that the TJS PU area is still at the structural high for oil accumulation in the NSWSCD. (b) The oil reservoir disintegrating (Dengying Fm) in the Late Triassic shows that the gas generation center formed gradually in the Shuangshi-Shejianhe area. (c) A burial depth of 5000 m and temperature of 140°C shows that the second gas charging of the Qixia Fm was coupled with gas reservoir adjustment and reconstruction in the Early Jurassic.

mountain structure. Initial uplift and denudation occurred in the Tianjingshan area in the middle of the Early Cambrian. The formation of the TJS PU eventually caused the generated oil to migrate to the high part of the paleouplift area, which formed a paleo-oil reservoir under suitable trap conditions. The TJS PU area controlled early protogenetic hydrocarbon migration, accumulation, and distribution in the Dengying Fm and Cambrian-Devonian before the Triassic (Figure 14). The Shuangyushi-Shejianhe area and the east platform margin of the MY-CN IS (to the east of the No. 1 fault) were the enrichment zones for the adjusted paleo-oil reservoirs during the Indosinian period. Furthermore, these represent the best preservation conditions for the transformation from gas generation to gas storage center (Figure 11(a)).

The main body of the WSCD was shaped gradually after the Early Cretaceous. The rapid settlement of the western Sichuan foreland basin has increased the burial depth of the deep marine strata below the Lower Triassic in the footwall of the No. 1 fault. The construction of the margin-plate and basin-mountain system created the burial depths of the Shuangyushi-Shejianhe structure and the eastern platform margin of the MY-CN IS area (east of the No. 1 fault), which are greater than 8000m. The paleo-oil reservoirs were completely cracked to form the paleo-gas reservoir during

deep burial and high-temperature processes. The Dengying, Canglangpu, Guanwushan, and Qixia Fm have visible bitumen infills in the Shuangyushi-Shejianhe structural belt. Furthermore, the east side of the northern segment of the MY-CN IS is an oil-cracked gas reservoir. This process has facilitated the adjustment from gas generation to gas storage center (Figure 11(a)). The margin-plate and basin-mountain boundary of the WSCB has an important influence on the preservation of deep marine hydrocarbons and the final distribution of current gas reservoirs. Uplift since the late Cretaceous-Cenozoic has had negligible impact on the deep marine strata to the east of the No. 1 fault in the NSWSCD. The final shape of the Shuangyushi-Shejianhe structure belt is the resultant gas-rich region, which has a final transition process from gas storage to a gas preservation center (Figure 11(c)).

5. Conclusions

- (1) This study analyzes the oil-to-source correlation of Sinian-Jurassic multilayered paleo-oil reservoirs in the Tianjingshan Tectonic Belt. Notably, the paleo-oil reservoirs are the main source of Cambrian organic matter-rich black shale, which established the concept of the Tianjingshan paleo-oil reservoir system

- (2) The Early Paleozoic Mianyang-Changning intracratonic sag and the Tianjingshan Paleouplift units have a laterally superimposed relationship. The reservoir-forming combination of high-quality source rocks and dominant hydrocarbon charging area developed in the northern segment of the western Sichuan Basin. This shows the early accumulation effects of regional marine petroleum on tectonic-controlled conditions
- (3) The northern segment of the western Sichuan depression that was affected by multistage tectonic events, recorded a complex tectonic history with strong uplift and deeply buried since the Late Triassic. The formation and evolution of the No. 1 fault have been an important criterion for the division of the oil-gas zonation in the Tianjingshan Paleouplift area
- (4) The preservation conditions of the foreland frontal-deformation zone (i.e., hanging-wall of the No. 1 fault) have been entirely destroyed. Furthermore, only a hydrocarbon accumulation process of paleo-oil reservoir destruction remains. The deeply buried Dengying and Qixia formations to the east of the No. 1 fault have the four-center accumulation conditions, which include the hydrocarbon generation center, gas generation center, gas storage center, and gas preservation center. The superdeep Dengying Fm has necessary petroleum geologic conditions for the discovery of a large-scale gas reservoir in the NSWSCD

Data Availability

Some or all data, models, or codes used during the study were provided by a third party. Direct requests for these materials may be made to the provider as indicated in Acknowledgments.

Conflicts of Interest

The authors declare that they have no conflicts of interest.

Acknowledgments

This work was supported by the National Natural Science Foundation of China (No. 441572111 and No. 41972150). We are grateful to the editors and experts for their constructive comments.

References

- [1] S. G. Liu, B. Deng, Z. W. Li, and W. Sun, "The texture of sedimentary basin-orogenic belt system and its influence on oil-gas distribution: a case study from Sichuan basin," *Acta Petrologica Sinica*, vol. 27, no. 3, pp. 621–635, 2011.
- [2] J. Q. Wang, "Relationship between tectonic evolution and the foreland hydrocarbon in the Longmen Mountains," *Acta Geoscientia Sinica*, vol. 15, no. 3/4, pp. 167–179, 1994.
- [3] K. L. Deng, "Indosinian progressive deformation and its chronogenesis in Longmengshan structural belt," *Oil & Gas Geology*, vol. 28, no. 4, pp. 485–490, 2007.
- [4] Z. W. Li, S. G. Liu, J. Lin, C. Tang, B. Deng, and W. Sun, "Structural configuration and its genetic mechanism of the west Sichuan depression in China," *Journal of Chengdu University of Technology (Science & Technology Edition)*, vol. 36, no. 6, pp. 645–653, 2009.
- [5] S. G. Liu, Z. W. Li, J. X. Cao et al., "4-D textural and structural characteristics of Longmen intracontinental composite orogenic belt, southwest China," *Chinese Journal of Geology*, vol. 44, no. 4, pp. 1151–1180, 2009.
- [6] S. G. Liu, *The Formation and Evolution of Longmenshan Thrust Zone and West Sichuan Foreland Basin*, Press of Chengdu University of Science and Technology University, Chengdu, 1993.
- [7] Z. W. Guo, K. L. Deng, and Y. H. Han, *The Formation and Development of Sichuan Basin*, Geological Publishing House, Beijing, 1996.
- [8] W. H. Song, "On nappe structure at northern sector of Longmen Mountain and its oil and gas prospects," *Natural Gas Industry*, vol. 9, no. 3, pp. 12–16, 1989.
- [9] C. G. Tong and S. Q. Hu, "Prospective value of oil and gas in the foothill belt of the north Longmen Mountains," *Journal of Chengdu University of Technology*, vol. 2, pp. 1–8, 1997.
- [10] S. G. Liu, W. Sun, Z. L. Luo et al., "Xingkai taphrogenesis and petroleum exploration from upper Sinian to Cambrian strata in Sichuan Basin, China," *Journal of Chengdu University of Technology (Science & Technology Edition)*, vol. 40, no. 5, pp. 511–520, 2013.
- [11] Y. Zhong, Y. L. Li, X. B. Zhang et al., "Features of extensional structures in pre-Sinian to Cambrian strata, Sichuan Basin, China," *Journal of Chengdu University of Technology (Science & Technology Edition)*, vol. 40, no. 5, pp. 498–510, 2013.
- [12] X. Liang, S. G. Liu, Q. W. Mo et al., "The characteristics of marine hydrocarbon accumulation and its exploration prospects in the northern section of western Sichuan depression, China," *Journal of Chengdu University of Technology (Science & Technology Edition)*, vol. 45, no. 1, pp. 53–67, 2018.
- [13] Z. W. Li, H. D. Chen, S. G. Liu, M. C. Hou, and B. Deng, "Differential uplift driven by thrusting and its lateral variation along the Longmenshan belt, western Sichuan, China: evidence from fission track thermochronology," *Chinese Journal of Geology (Scientia Geologica Sinica)*, vol. 45, no. 4, pp. 944–968, 2010.
- [14] Z. Li, S. Liu, H. Chen, D. Sun, J. Lin, and C. Tang, "Structural superimposition and conjunction and its effects on hydrocarbon accumulation in the western Sichuan depression," *Petroleum Exploration and Development*, vol. 38, no. 5, pp. 538–551, 2011.
- [15] M.-F. Zhou, D.-P. Yan, A. K. Kennedy, Y. Li, and J. Ding, "SHRIMP U-Pb zircon geochronological and geochemical evidence for Neoproterozoic arc-magmatism along the western margin of the Yangtze block, south China," *Earth and Planetary Science Letters*, vol. 196, no. 1–2, pp. 51–67, 2002.
- [16] J. H. Zhao and M. F. Zhou, "Neoproterozoic adakitic plutons in the northern margin of the Yangtze block, China: partial melting of a thickened lower crust and implications for secular crustal evolution," *Lithos*, vol. 104, no. 1–4, pp. 231–248, 2008.
- [17] V. E. Andrushevich, M. H. Engel, J. E. Zumberge, and L. A. Brothers, "Secular, episodic changes in stable carbon isotope

- composition of crude oils," *Chemical Geology*, vol. 152, pp. 59–72, 1998.
- [18] X. H. Li, "U-Pb zircon ages of granites from the southern margin of the Yangtze block: timing of Neoproterozoic Jinning orogeny in SE China and implications for Rodinia assembly," *Precambrian Research*, vol. 97, no. 1-2, pp. 43–57, 1999.
- [19] J. Wang and Z. X. Li, "History of Neoproterozoic rift basins in south China: implications for Rodinia break-up," *Precambrian Research*, vol. 122, no. 1–4, pp. 141–158, 2003.
- [20] Z. L. Luo, "A discussion of Taphrogenesis and hydrocarbon distribution," *Acta Geoscientica Siniaca*, vol. 3, pp. 93–101, 1984.
- [21] X. Z. Cui, X. S. Jiang, J. Wang et al., "Filling sequence and evolution model of the Neoproterozoic rift basin in Central Yunnan Province, south China: response to the breakup of Rodinia supercontinent," *Acta Sedimentologica Sinica*, vol. 32, no. 3, pp. 399–409, 2014.
- [22] Z. D. Gu and Z. C. Wang, "The discovery of Neoproterozoic extensional structures and its significance for gas exploration in the Central Sichuan Block, Sichuan Basin, south China," *Scientia Sinica (Terrae)*, vol. 44, no. 10, pp. 2210–2220, 2014.
- [23] H. F. Liu, J. M. Li, X. Q. Li, L. Q. Liu, X. J. Li, and S. H. Hu, "Evolution of cratonic basins and carbonate–evaporite sedimentary sequence hydrocarbon systems in China," *Journal of Geosciences*, vol. 20, no. 1, pp. 1–18, 2016.
- [24] Q. Yu, C. L. Mu, H. Q. Zhang, Q. Y. Tan, X. S. Xu, and J. F. Yan, "Sedimentary evolution and reservoir distribution of northern upper Yangtze plate in Sinian–Early Paleozoic," *Acta Petrologica Sinica*, vol. 27, no. 3, pp. 672–680, 2011.
- [25] S. G. Liu, W. Sun, Y. Zhong et al., "Evolutionary episodes and their characteristics within the Sichuan marine craton basin during Phanerozoic Eon," *Acta Petrologica Sinica*, vol. 33, no. 4, pp. 1058–1072, 2017.
- [26] J. M. Song, P. Luo, S. G. Liu et al., "The deposition and reservoir characteristics of Dengying formation in western Sichuan Basin, China," *Journal of Chengdu University of Technology (Science & Technology Edition)*, vol. 45, no. 1, pp. 27–44, 2018.
- [27] M. C. Hou, F. C. Xing, S. L. Xu et al., "Paleogeographic patterns of E–C transition period in the upper Yangtze and the geodynamic mechanism," *Acta Sedimentologica Sinica*, vol. 35, no. 5, pp. 902–917, 2017.
- [28] J. J. Liu, W. Li, B. M. Zhang et al., "Sedimentary palaeogeography of the Sinian in upper Yangtze region," *Journal of Palaeogeography*, vol. 17, no. 6, pp. 735–753, 2015.
- [29] H. Zhou, W. Li, B. M. Zhang et al., "Formation and evolution of upper Sinian to lower Cambrian intraplatformal basin in Sichuan Basin," *Acta Petrologica Sinica*, vol. 36, no. 3, pp. 310–323, 2015.
- [30] F. C. Xing, M. C. Hou, L. B. Lin, S. L. Xu, and H. R. Hu, "The records and its dynamic genesis discussion of tectonic movement during the late Sinian and the early Cambrian of Sichuan Basin," *Earth Science Frontiers*, vol. 22, no. 1, pp. 115–125, 2015.
- [31] J. H. Du, C. N. Zou, C. C. Xu et al., "Theoretical and technical innovations in strategic discovery of a giant gas field in Cambrian Longwangmiao Formation of central Sichuan paleo-uplift, Sichuan Basin," *Petroleum Exploration and Development*, vol. 41, pp. 268–277, 2014.
- [32] C. N. Zou, J. H. Du, C. C. Xu et al., "Formation, distribution, resource potential and discovery of the Sinian–Cambrian giant gas field, Sichuan Basin, SW China," *Petroleum Exploration and Development*, vol. 41, pp. 278–293, 2014.
- [33] G. Q. Wei, W. Yang, J. H. Du et al., "Geological characteristics of the Sinian–Early Cambrian intracratonic rift, Sichuan Basin," *Natural Gas Industry*, vol. 35, no. 1, pp. 24–35, 2015.
- [34] S. G. Liu, Y. G. Wang, W. Sun et al., "Control of intracratonic sags on the hydrocarbon accumulations in the marine strata across the Sichuan Basin, China," *Journal of Chengdu University of Technology (Science & Technology Edition)*, vol. 43, pp. 1–23, 2016.
- [35] S. Q. Xu, Q. Zeng, D. H. Tang, and G. R. Zhang, "Analysis on reservoir forming conditions of Houba oil sands in Jiangyou area," *Natural Gas Exploration & Development*, vol. 28, no. 3, pp. 1–4, 2005.
- [36] W. Zhou, H. C. Deng, D. Z. Qiu, and R. C. Xie, "The discovery and significance of the Devonian paleo-reservoir in Tianjingshan structure of the northwest Sichuan, China," *Journal of Chengdu University of Technology (Science & Technology Edition)*, vol. 34, no. 4, pp. 413–417, 2007.
- [37] X. M. Sun, Q. W. Xu, Y. D. Wang, J. X. Tian, S. Q. Wang, and J. Y. Du, "Reservoir forming characteristics and main controlling factors of oil sandstones in the northern Longmen Mountain thrust zone of the northwest of Sichuan," *Journal of Jilin University (Earth Science Edition)*, vol. 40, no. 4, pp. 886–896, 2010.
- [38] X. L. Shan, H. H. Luo, X. M. Sun, Y. Y. Zhang, and J. Yi, "Main factors of Houba Jurassic large oil sands reservoir in Sichuan Basin," *Journal of Jilin University (Earth Science Edition)*, vol. 40, no. 4, pp. 897–904, 2010.
- [39] X. F. Yang, X. Z. Wang, S. N. Zhang et al., "Sedimentary characteristic and oilsands prediction in the upper Shaximiao formation, Houba area, northwestern Sichuan Basin," *Geological Science and Technology Information*, vol. 33, no. 3, pp. 112–117, 2014.
- [40] G. X. Liu, S. D. Wang, W. L. Pan, and J. X. Lv, "Characteristics of Tianjingshan destroyed oil reservoir in Guangyuan area, Sichuan," *Marine Origin Petroleum Geology*, vol. 8, no. 1, pp. 103–107, 2003.
- [41] S. Y. Wang, Q. Ming, Z. Y. He, and L. Huang, "Study on forming process and geochemical character of the crude oil in fracture of the limestone in northwest of Sichuan," *Journal of Natural Gas Geoscience*, vol. 17, no. 4, pp. 579–581, 2006.
- [42] H. M. Dai, W. L. Liu, Y. M. Yang, Y. G. Li, and Y. Duan, "The origin of Jurassic oil-soaked sandstone in the piedmont zone of north Longmenshan, the Sichuan Basin," *Petroleum Geology & Experiment*, vol. 36, no. 6, pp. 604–608, 2007.
- [43] D. Rao, J. Z. Qin, G. E. Teng, and M. Z. Zhang, "Source analysis of oil seepage and bitumen originating from marine layer strata in Guangyuan area, the northwest Sichuan Basin," *Petroleum Geology & Experiment*, vol. 30, no. 6, pp. 596–605, 2008.
- [44] D. F. Huang and L. S. Wang, "Geochemical characteristics of bituminous dike in Kuangshanliang area of the northwestern Sichuan Basin and its significance," *Acta Petrologica Sinica*, vol. 29, no. 1, pp. 23–28, 2008.
- [45] C. Liu, H. L. Zhang, A. J. Shen, Z. F. Qiao, X. F. Ni, and X. X. Zhao, "Geochemistry characteristics and origin of the Devonian oil-sandstone in the northwest of Sichuan Basin," *Acta Petrologica Sinica*, vol. 31, no. 2, pp. 253–258, 2010.
- [46] C. Liu, Q. X. Guo, and H. L. Zhang, "The discovery and geological significance of petroleum of Triassic Feixianguan

- Formation in northwest Sichuan Basin,” *Natural Gas Geoscience*, vol. 22, no. 4, pp. 692–699, 2011.
- [47] M. Luo, A. S. Geng, Z. W. Liao, and X. L. Shan, “The organic geochemical characteristics and genesis study of Houba oil sand in the Sichuan Basin, China,” *Geochimica*, vol. 40, no. 3, pp. 280–288, 2011.
- [48] L. L. Wu, Y. H. Liao, Y. X. Fang, and A. S. Geng, “The study on the source of the oil seeps and bitumens in the Tianjingshan structure of the northern Longmen Mountain structure of Sichuan Basin, China,” *Marine and Petroleum Geology*, vol. 37, no. 1, pp. 147–161, 2012.
- [49] G. L. Wang, T. G. Wang, K. Y. Han, and S. B. Shi, “Organic geochemical characteristics and origin of solid bitumen and oil sands in northwestern Sichuan,” *Petroleum Geology and Experiment*, vol. 36, no. 6, pp. 731–735, 2014.
- [50] C. B. Shen, S. David, L. F. Mei et al., “Advances in the study of Re–Os geochronology and tracing of hydrocarbon generation and accumulation,” *Journal of Mineralogy and Petrology*, vol. 31, no. 4, pp. 87–93, 2011.
- [51] J. Wang, L. Tenger, L. B. Ma et al., “Definition of petroleum generating time for Lower Cambrian bitumen of the Kuangshanliang in the west Sichuan Basin, China: evidence from Re–Os isotopic isochron age,” *Natural Gas Geoscience*, vol. 27, no. 7, pp. 1290–1298, 2016.
- [52] X. Ge, C. Shen, D. Selby et al., “Petroleum-generation timing and source in the northern Longmen Shan thrust belt, southwest China: implications for multiple oil-generation episodes and sources,” *AAPG Bulletin*, vol. 102, no. 5, pp. 913–938, 2018.
- [53] Z. C. Wang, J. J. Liu, H. Jiang et al., “Lithofacies paleogeography and exploration significance of Sinian Doushantuo depositional stage in the middle–upper Yangtze region, Sichuan Basin, SW China,” *Petroleum Exploration and Development*, vol. 46, no. 1, pp. 39–51, 2019.
- [54] G. D. Love, C. E. Snape, A. D. Carr, and R. C. Houghton, “Release of covalently-bound alkane biomarkers in high yields from kerogen via catalytic hydroxyprolysis,” *Organic Geochemistry*, vol. 23, no. 10, pp. 981–986, 1995.
- [55] I. P. Murray, G. D. Love, C. E. Snape, and N. J. L. Bailey, “Comparison of covalently-bound aliphatic biomarkers released via hydroxyprolysis with their solvent-extractable counterparts for a suite of Kimmeridge clays,” *Organic Geochemistry*, vol. 29, no. 5–7, pp. 1487–1505, 1998.
- [56] L. L. Wu, Y. H. Liao, Y. X. Fang, and A. S. Geng, “The comparison of biomarkers released by hydroxyprolysis and by Soxhlet extraction from source rocks of different maturities,” *Chinese Science Bulletin*, vol. 57, no. 32, pp. 3067–3077, 2012.
- [57] Y. Liao, Y. Fang, L. Wu, A. Geng, and C. S. Hsu, “The characteristics of the biomarkers and $\delta^{13}\text{C}$ of *n*-alkanes released from thermally altered solid bitumens at various maturities by catalytic hydroxyprolysis,” *Organic Geochemistry*, vol. 46, pp. 56–65, 2012.
- [58] G. Q. Wei, Z. H. Wang, J. Li, W. Yang, and Z. Y. Xie, “Characteristics of source rocks, resource potential and exploration direction of Sinian and Cambrian in Sichuan Basin,” *Journal of Natural Gas Geoscience*, vol. 28, no. 1, pp. 1–13, 2017.
- [59] K. Zhang, C. Jia, Y. Song et al., “Analysis of lower Cambrian shale gas composition, source and accumulation pattern in different tectonic backgrounds: a case study of Weiyuan block in the upper Yangtze region and Xiuwu Basin in the lower Yangtze region,” *Fuel*, vol. 263, p. 115978, 2020.
- [60] K. E. Peters, C. C. Walters, and J. M. Moldowan, *The Biomarker Guide, Biomarkers and Isotopes in Petroleum Exploration and Earth History*, Cambridge University Press, New York, 2005.
- [61] W. K. Seifert, J. M. Moldowan, and G. J. Demaison, “Source correlation of biodegraded oils,” *Organic Geochemistry*, vol. 6, pp. 633–643, 1984.
- [62] W. K. Seifert and J. M. Moldowan, “Use of biological markers in petroleum exploration,” in *Methods in Geochemistry and Geophysics*, R. B. Johns, Ed., pp. 261–290, Elsevier, New York, 1986.
- [63] G. Ourisson, P. Albrecht, and M. Rohmer, “Predictive microbial biochemistry – from molecular fossils to prokaryotic membranes,” *Organic Geochemistry*, vol. 7, no. 7, pp. 236–239, 1982.
- [64] J. K. Volkman, M. R. Banks, K. Denwer, and F. R. Aquino Neto, “Biomarker composition and depositional setting tasmanite oil shale from northern Tasmania, Australia,” *14th International Meeting on Organic Geochemistry*, 1989, Paris, September 1989, 1989.
- [65] F. R. A. Neto, J. Triguíis, D. A. Azevedo, R. Rodrigues, and B. R. T. Simoneit, “Organic geochemistry of geographically unrelated tasmanites,” *Organic Geochemistry*, vol. 18, no. 6, pp. 791–803, 1992.
- [66] D. A. Azevedo, F. R. Aquino Neto, B. R. T. Simoneit, and A. C. Pinto, “Novel series of tricyclic aromatic terpanes characterized in Tasmanian tasmanite,” *Organic Geochemistry*, vol. 18, no. 1, pp. 9–16, 1992.
- [67] P. F. Greenwood, K. R. Arouri, and S. C. George, “Tricyclic terpenoid composition of *tasmanites* kerogen as determined by pyrolysis GC-MS,” *Geochimica et Cosmochimica Acta*, vol. 64, no. 7, pp. 1249–1263, 2000.
- [68] F. R. Aquino Neto, J. M. Trendel, A. Restle, J. Connan, and P. A. Albrecht, “Occurrence and formation of tricyclic and tetracyclic terpanes in sediments and petroleum,” in *Advances in Organic Geochemistry 1981*, pp. 659–676, J. Wiley and Sons, New York, 1983.
- [69] H. Tappan, *The Pale Biology of Plant Protists*, Freeman W H and Company, San Francisco, 1980.
- [70] S. Dutta, P. F. Greenwood, R. Brocke, R. G. Schaefer, and U. Mann, “New insights into the relationship between *tasmanites* and tricyclic terpenoids,” *Organic Geochemistry*, vol. 37, no. 1, pp. 117–127, 2006.
- [71] J. Connan, A. Restle, and P. Albrecht, “Biodegradation of crude oil in the Aquitaine basin,” *Physics and Chemistry of the Earth*, vol. 12, pp. 1–17, 1980.
- [72] W. K. Seifert and J. M. Moldowan, “The effect of biodegradation on steranes and terpanes in crude oils,” *Geochimica et Cosmochimica Acta*, vol. 43, no. 1, pp. 111–126, 1979.
- [73] R. P. Philp and T. D. Gilbert, “Biomarker distributions in oils predominantly derived from terrigenous source material,” in *Advances in Organic Geochemistry 1985*, D. Leythaeuser and R. Ötter, Eds., pp. 73–84, Pergamon Press, 1986.
- [74] F. R. A. Neto, A. Restle, J. Connan, P. Albrecht, and G. Ourisson, “Novel tricyclic terpanes (C_{19} , C_{20}) in sediments and petroleum,” *Tetrahedron Letters*, vol. 23, no. 19, pp. 2027–2030, 1982.
- [75] J. Connan, J. Bouroullac, D. Dessort, and P. Albrecht, “The microbial input in carbonate-anhydrite facies of a sabkha palaeoenvironment from Guatemala: a molecular approach,” *Organic Geochemistry*, vol. 10, no. 1–3, pp. 29–50, 1986.

- [76] S. G. Liu, S. Liu, W. Sun et al., "Tectonic and sedimentary features of the northern Mianyang–Changning intracratonic sag, Sichuan, China," *Journal of Chengdu University of Technology (Science & Technology Edition)*, vol. 45, no. 1, pp. 1–13, 2018.
- [77] Y. G. Wang, Y. C. Wen, H. T. Hong et al., "Petroleum geological characteristics of deep water deposits in Upper Permian–Lower Triassic trough in Sichuan basin and adjacent areas," *Oil & Gas Geology*, vol. 27, no. 5, pp. 702–714, 2006.
- [78] L. M. Wenger and G. H. Isaksen, "Control of hydrocarbon seepage intensity on level of biodegradation in sea bottom sediments," *Organic Geochemistry*, vol. 33, no. 12, pp. 1277–1292, 2002.
- [79] J. W. De Leeuw and M. Bass, "Early diagenesis of steroids," in *Biological Markers in the Sedimentary Record*, R. B. Johns, Ed., pp. 102–127, Elsevier, Amsterdam, 1986.
- [80] Y. Fang, Y. Liao, L. Wu, and A. Geng, "Oil-source correlation for the paleo-reservoir in the Majiang area and remnant reservoir in the Kaili area, south China," *Journal of Asian Earth Sciences*, vol. 41, no. 2, pp. 147–158, 2011.
- [81] M. Bjorøy, K. Hall, P. Gillyon, and J. Jumeau, "Carbon isotope variations in *n*-alkanes and isoprenoids of whole oils," *Chemical Geology*, vol. 93, no. 1–2, pp. 13–20, 1991.
- [82] D. R. Wang, *Stable Isotope Geochemistry of Oil and Gas*, Publishing House of Oil Industry, Beijing, 2000.
- [83] W. J. Stahl, "Carbon and nitrogen isotopes in hydrocarbon research and exploration," *Chemical Geology*, vol. 20, pp. 121–149, 1977.
- [84] Z. L. Luo, "The influence of Taphrogenesis from late Paleozoic Era in southern China on petroleum and other deposits," *Sichuan Geological Journal*, vol. 2, no. 1, pp. 1–22, 1981.
- [85] D. F. He and S. L. Wu, "The "past and present" of the Tianjingshan palaeo–uplift: discussion on structural restoration of paleo–uplift," *Earth Science Frontiers*, vol. 26, no. 1, pp. 86–101, 2019.
- [86] G. M. Zhai, *Petroleum Geology of China: Vol. 10*, Petroleum Industry Press, Beijing, 1989.
- [87] W. H. Song, "Some new knowledge of Caledonian paleo–uplift in Sichuan Basin," *Natural Gas Industry*, vol. 9, no. 3, pp. 12–16, 1987.
- [88] G. H. Li, G. Yang, L. Li et al., "Formation and evolution of Tianjingshan paleo–uplift, northwestern margin of Sichuan Basin," *Natural Gas Exploration and Development*, vol. 41, no. 4, pp. 1–7, 2019.
- [89] K. F. Yu and S. D. Wang, "Duyun movement in South Guizhou Province and its paleostructure, and their significance in petroleum geology," *Guizhou Geology*, vol. 12, pp. 225–232, 1995.
- [90] D. S. Sun, S. J. Li, D. Y. Zhu, D. W. Zhang, Y. J. Wo, and Z. L. He, "Unconformity of the Duyun movement in the Sichuan Basin and its significance of petroleum geology," *Oil & Gas Geology*, vol. 5, pp. 721–728, 2015.
- [91] T. S. Zhang and F. H. Hou, "Reefs discovered in the lower–middle Silurian, northwest Sichuan," *Journal of Southwestern Petroleum Institute*, vol. 2, pp. 139–140, 1989.
- [92] D. Y. Liu, X. Chen, and T. R. Zhang, "Memoirs of Nanjing Institute of Geology and Palaeontology," *Academia Sinica, Stratigraphy*, vol. 1, pp. 161–170, 1964.
- [93] S. Qin, T. Zhang, W. B. Su, W. Wang, and C. Ma, "Characteristics and implications of the oolitic limestones from the Silurian succession in Wangcang, Sichuan, South China," *Earth Science–Journal of China University of Geosciences*, vol. 36, no. 1, pp. 43–52, 2011.
- [94] W. J. Liu, R. C. Zheng, and X. H. Li, "Reconstruction of palaeogeography and palaeotectonics of a Devonian sedimentary basin in the Longmenshan area, Sichuan," *Acta Geologica Sinica*, vol. 73, no. 2, pp. 109–119, 1999.
- [95] J. X. Qin, Y. F. Zeng, Z. X. Huang, and Y. Wu, "Carboniferous sequence stratigraphy and sea–level changes in the Majiaoba District, Sichuan," *Sedimentary Facies and Palaeogeography*, vol. 16, no. 1, pp. 19–33, 1996.
- [96] S. G. Liu, C. Qin, W. Sun et al., "The coupling formation process of four centers of hydrocarbon in Sinian Dengying Formation of Sichuan Basin," *Acta Petrologica Sinica*, vol. 28, no. 3, pp. 879–888, 2012.
- [97] S. G. Liu, W. Sun, J. M. Song et al., "Tectonics–controlled distribution of marine petroleum accumulations in the Sichuan Basin, China," *Earth Science Frontiers*, vol. 22, no. 3, pp. 146–160, 2015.
- [98] X. Liang, S. G. Liu, S. B. Wang, B. Deng, S. Zhou, and W. Ma, "Analysis of the oldest carbonate gas reservoir in China–new geological significance of the Dengying gas reservoir in the Weiyuan Structure, Sichuan Basin," *Journal of Earth Science*, vol. 30, no. 2, pp. 348–366, 2019.

Research Article

Three-Dimensional Morphology and Connectivity of Organic Pores in Shale from the Wufeng and Longmaxi Formations at the Southeast Sichuan Basin in China

Tao Jiang ^{1,2,3,4}, Zhijun Jin,^{1,2,3,5} Zongquan Hu,^{1,2,3} Wei Du,^{1,2,3} Zhongbao Liu,^{1,2,3} and Jianhua Zhao^{1,2,3,6}

¹State Key Laboratory of Shale Oil and Gas Enrichment Mechanisms and Effective Development, Beijing 100083, China

²Key Laboratory of Shale Oil/Gas Exploration and Production, SINOPEC, Beijing 100083, China

³Petroleum Exploration and Production Research Institute, SINOPEC, Beijing 100083, China

⁴SinoProbe Center, Chinese Academy of Geological Sciences and China Geological Survey, Beijing 100037, China

⁵Institute of Energy, Peking University, Beijing 100871, China

⁶School of Geosciences, China University of Petroleum (East China), Qingdao 266580, China

Correspondence should be addressed to Tao Jiang; jiangt813@cags.ac.cn

Received 22 January 2021; Accepted 22 April 2021; Published 17 May 2021

Academic Editor: Kun Zhang

Copyright © 2021 Tao Jiang et al. This is an open access article distributed under the Creative Commons Attribution License, which permits unrestricted use, distribution, and reproduction in any medium, provided the original work is properly cited.

Organic pores play an important role in shale reservoirs. Organic pores occur where shale gas was produced and accumulated. However, there is little scientific understanding of the distribution and connectivity of organic pores. Organic pore types and their structural characteristics were studied using a total organic carbon (TOC), thin section, focused ion beam scanning electron microscope (FIB-SEM), and nano-CT. The samples were from the Wufeng Formation in the Upper Ordovician and Longmaxi Formations from the lower Silurian. The results show that organic matter is mainly concentrated in the Wufeng Formation and the bottom of the Longmaxi Formation and that the middle and upper parts of the Longmaxi Formation contain a low amount of organic matter. The shale of the Wufeng-Longmaxi Formation has high maturity, and its organic pores are well developed. There are three types of organic pores: algae, graptolite, and pyrobitumen pores. The pore connectivity of shale with a high organic content is better than that of shale with a low organic content. The volume of the organic pores accounts for more than 50% of the volume of the organic matter. Majority of the organic pores have an aperture smaller than 100 nm and are round, nearly circular, and elliptical in morphology. Most of the organic pores in a shale formation are developed in pyrobitumen, and most of the larger organic pores are concentrated at the center of solid pyrobitumen. The organic pores in pyrobitumen have the best connectivity and are the most favorable reservoir spaces and migration channels for shale gas, which is a crucial point of reference for future research of shale gas.

1. Introduction

In recent years, shale gas has undergone significant development as an unconventional resource [1]. With the success of industrial shale gas development in the United States, the research and development of shale gas have become important for increasing global oil and gas resources [2]. With rising energy demand, increasing pressure on energy, and growing environmental awareness, it is urgently necessary to explore and develop shale gas resources. China is the third

country after the United States and Canada to develop and utilize shale gas resources. To date, China has made significant progress in the research and development of shale gas [3–7]. In Jiaoshiba Chongqing, the first large-scale shale gas field in China was built and has reached 100 billion cubic meters [8].

Organic pores are widely developed in shale that is rich in organic material and are an important part of the shale reservoir space [9]. Shale gas can be stored in a free phase in organic pores and can be adsorbed onto the surface of

organic matter in an adsorbed phase [10]. The porosity of the organic matter directly determines the distribution of the gas [7]. The type and maturity of organic matter are the geological conditions used to judge the commercial developmental value of shale gas [11]. Therefore, the study of organic pores is important for shale gas research and the evaluation of shale gas as a resource.

There are many types of pores in shale. There are primary pores, such as matrix cracks and intergranular pores, and there are secondary pores, such as organic pores, dissolved pores, and organic microfractures [12]. Organic pores are important because they are one of the largest reservoir spaces. Organic pores have various shapes, and they can be elliptical, circular, or irregular polygons, but are primarily in the form of ellipses, with pore sizes between 5 and 200 nm [13–15]. Well-developed organic pores have good connectivity, forming interconnected pore networks that can contain large shale gas reservoirs. Pores in two adjacent organic materials or in different parts of the same organic material can be different [16, 17]. In addition, there are many forms of organic matter in shale, mainly occurring in the presence of clay and brittle minerals. Pores can comprise up to 50% of the volume of the organic matter. The formation of organic pores is a product of the maceral content of organic matter and the degree of host shale maturity. Some maceral generates hydrocarbons and a large number of pores as its maturity increases [18, 19]. When the maturity of the organic matter (R_o) is less than 0.90%, organic pores are not well developed. In the gas window, liquid hydrocarbons begin to crack, and organic pores begin to develop [20]. Loucks et al. [19] and Slatt et al. [12] indicated that organic pores formed when $R_o = 0.60\%$. The maturation of organic pores can be divided into three stages: the formation period ($0.60\% < R_o \leq 2.00\%$), the development period ($2.00\% < R_o \leq 3.50\%$), and the destruction period ($R_o > 3.50\%$). The density of organic pores is a function of the TOC content, maturity, and the type of organic matter such as maceral or pyrobitumen [21–23].

Currently, there is no detailed description or classification scheme for organic pores in shale. What characteristic differences may exist between different types of shale remains unclear. It is necessary to know the connectivity of organic pores in shale formations. In particular, the current understanding of the three-dimensional morphology and connectivity of pores in different types of organic matter is insufficient. Therefore, various organic pores in shale were analyzed to classify the types of organic matter present and the morphology and connectivity characteristics. The present study augments our understanding of shale gas storage space and will assist in the research and development of shale gas.

2. Geological Background

The Sichuan Basin is located at the northwestern edge of the Yangtze Platform [24]. The basin has experienced two stages: the Craton stage (from the Early Paleozoic to Middle Triassic) and the foreland basin stage (from the Late Triassic to Cenozoic) [25]. The Sichuan Basin began to

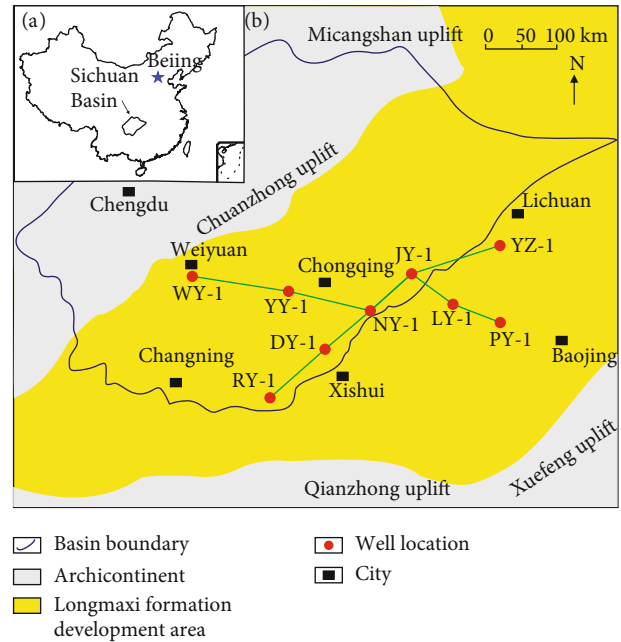


FIGURE 1: Tectonic setting and location of the southeast Sichuan Basin. (a) Location of the Sichuan Basin in China. (b) Tectonic setting of the southeast Sichuan Basin.

form during the early Indosinian Movement and, eventually, formed a diamond-shaped sedimentary basin after the Himalayan movement (Figure 1). The Sichuan Basin is surrounded by a contiguous range of mountains. The Sichuan Basin is a complex, superimposed basin with terrestrial and marine sediments [26]. The shale deposits in the central Sichuan Basin are thin, and the shale deposits in the eastern, southeastern, and southwestern Sichuan Basin are relatively thick.

The southeast Sichuan Basin is composed mainly of ejective folds that consist of high-steep anticlines, loose synclines, and fault zones [26]. The basement of the southeast Sichuan Basin is composed of Presinian metamorphic rocks. The Devonian, Carboniferous, Cretaceous, and Paleogene rock strata were absent from the entire area. During the Early-Middle Ordovician, the area transformed from an open sea to a restricted sea surrounded by uplifts, resulting in a low-energy and anoxic sedimentary environment [27, 28]. During the Early Silurian, the southeastern Sichuan Basin was a semiocluded stagnant basin with a deep shelf environment. A black, organic-material-rich shale was deposited, forming the best layer for shale gas investigation in the region [29, 30].

The lower section of the Wufeng-Longmaxi Formation is primarily composed of a black graptolite shale, and the upper section is primarily a gray argillaceous siltstone [31]. During the Longmaxi's Formation period, the Sichuan Basin was shallow and has graptolite shale deposits and a short deposit range compared with that of the Wufeng's Formation period [32]. The Wufeng-Longmaxi Formation in the southeast Sichuan Basin is relatively thick, and the terrigenous detrital content increases from the lower to the upper section. At present, the Wufeng Formation and the lower Longmaxi Formation are the main shale gas reservoirs [33].

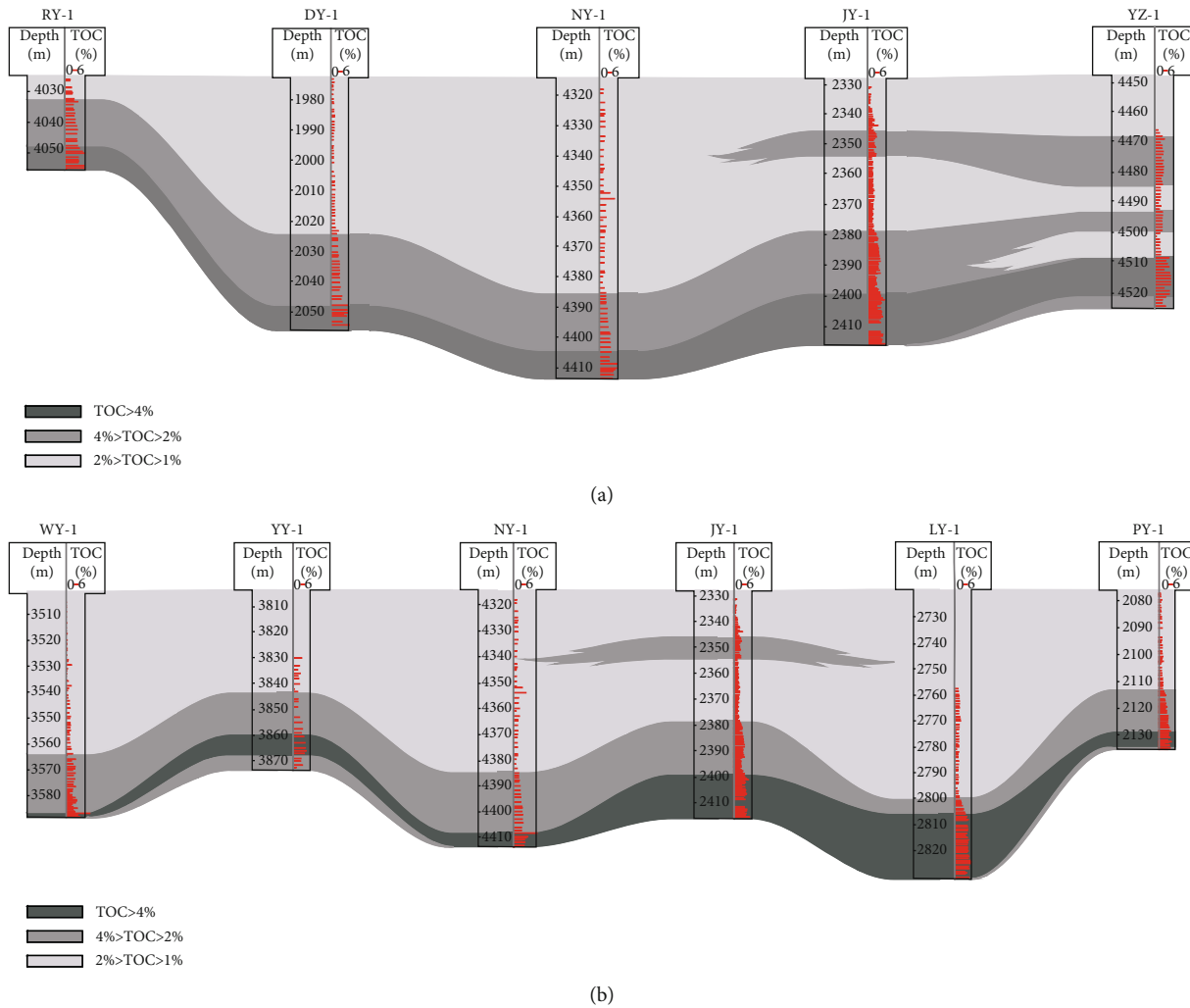


FIGURE 2: Comparison sections of the TOC content of the Wufeng-Longmaxi Formation shale in the southeast Sichuan Basin. (a) Section of the TOC content from northeast to southwest. (b) Section of the TOC content from east to west.

3. Sampling and Experimental Methods

The total organic carbon (TOC) content was tested with a Leco analyzer. The inorganic carbon in the sample was removed with diluted hydrochloric acid and then burned in a high-temperature oxygen oven to convert all the organic carbon to carbon dioxide. The TOC content was then measured by an infrared detector. The type and maturity of organic matter were observed under a LABORLUX 12 POL fluorescence microscope. Samples larger than 4 mm were cemented with a nonfluorescent cement to a microscope slide and observed using the microscopes oil immersion lens. A high-pressure mercury vapor or xenon lamp was used as the excitation source, and then, a blue or ultraviolet light was used to excite the filter. Organic matter with fluorescence was isolated and tested. The reflectance of the graptolite was determined. Then, the type and maturity of the organic material were obtained.

The two-dimensional micromorphology, structural characteristics, and three-dimensional connectivity of the samples were studied using an FEI Quanta 200F focused

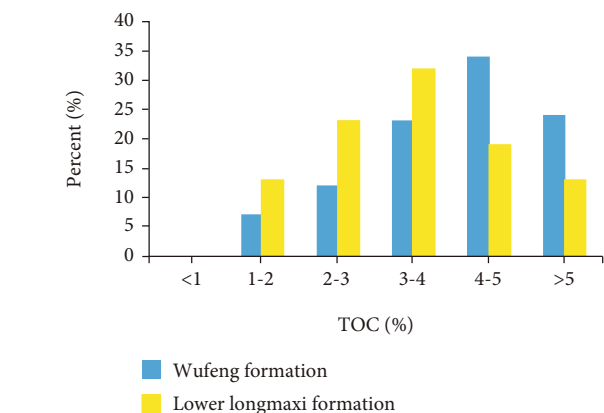


FIGURE 3: TOC distribution of the shale in the Wufeng-Longmaxi Formation at the southeast Sichuan Basin.

ion beam scanning electron microscope (FIB-SEM) in the high-vacuum scanning mode. The electron image was obtained from the secondary electron signal of the sample

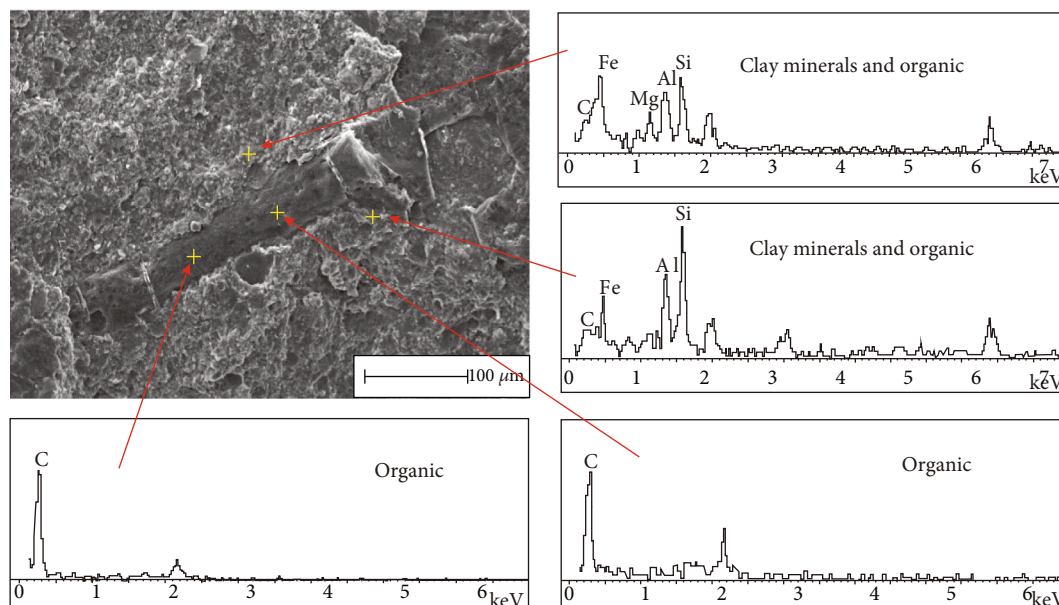


FIGURE 4: Graptolite photographs and energy spectrum of the Wufeng-Longmaxi Formation shale in the southeast Sichuan Basin. The fragment is graphitic, that is, mainly composed of carbon. The fragment is encased in clay minerals and carbonate minerals.

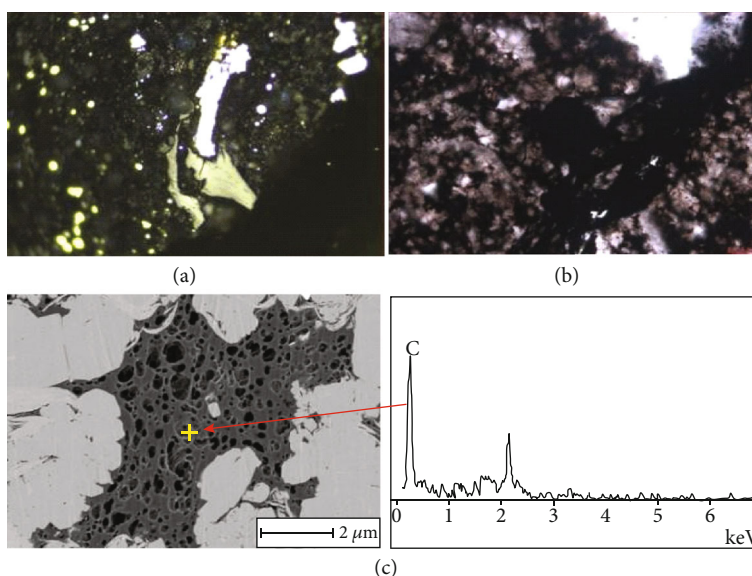


FIGURE 5: Pyrobitumen morphology photograph and energy spectrum of the Wufeng-Longmaxi Formation shale in the southeast Sichuan Basin. (a) Fluorescence microscope photo. (b) Polarized light microscope photo. (c) SEM photo and energy spectrum characteristics.

surface through an ion beam generated by a liquid metal (Ga) ion source. The sample was observed to have dimensions of $4.5 \mu\text{m} \times 8 \mu\text{m} \times 8 \mu\text{m}$. The surface of the sample was polished with a JEOL IB-09010 argon ion sample polishing machine. Pores with apertures larger than 5 nm could be observed by the FIB-SEM, and ImageJ was used to calculate the face rate based on gray recognition.

A Zeiss Metrotom nano-CT was used to study the three-dimensional characteristics of the samples. Sixty-five micrometer diameter cylinder samples were selected. The

resolution of the nano-CT in the present study was 65 nm. Therefore, pores larger than 65 nm could be imaged. The working principle is that the X-ray source and the detection receiver scan the samples synchronously. When each scan was completed, the scanning rack rotated to the next angle and then performed the next scan. Through digital image processing and three-dimensional reconstruction of the CT single-image and CT image sequences, the porosity of the samples was calculated, and an image was obtained of the three-dimensional distribution and connectivity of pores.

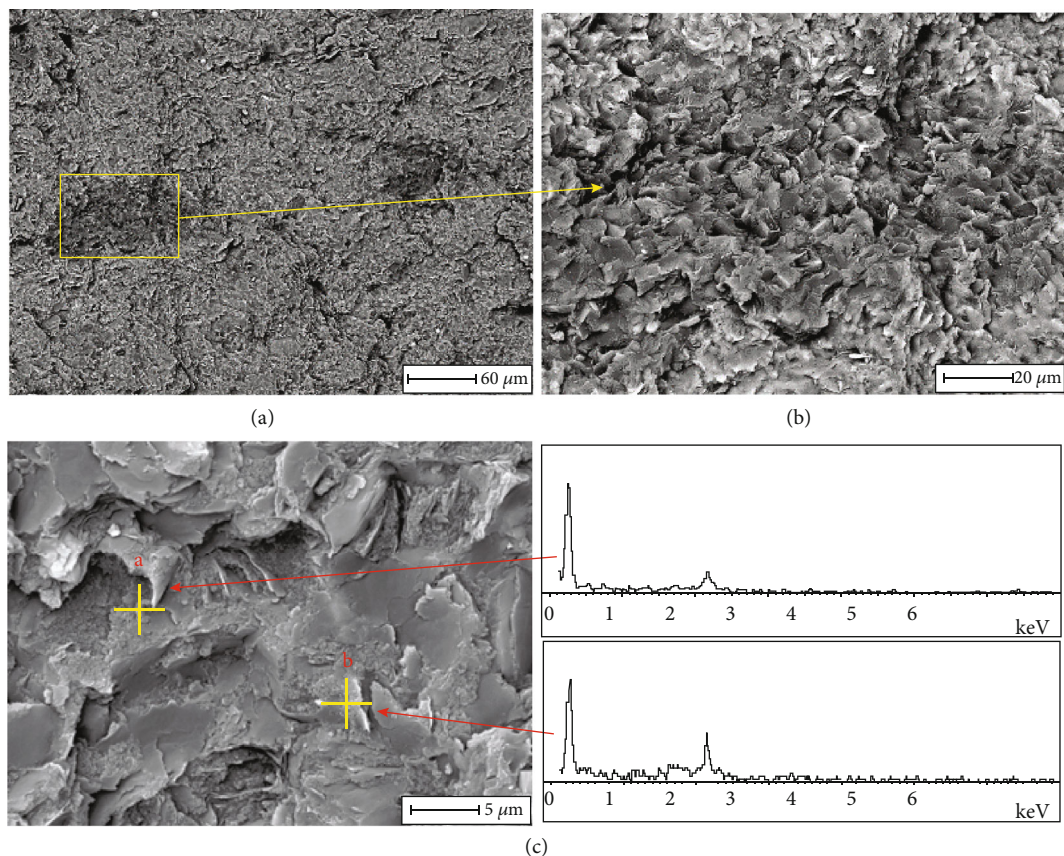


FIGURE 6: Algae morphological photograph and energy spectrum of the Wufeng-Longmaxi Formation shale in the southeast Sichuan Basin. (a) The dark part is algae. (b) Amplification of (a). (c) Amplification of (b). The algae are mainly carbonaceous and energy spectrum characteristics.

4. Results

4.1. Organic Matter Characteristics

4.1.1. Organic Matter Content. The organic matter in the southeast Sichuan Basin has many different characteristics in both the horizontal and vertical space [34]. The thickness of the TOC > 2% shale varies significantly from northeast to southwest (Figure 2(a)). From the northeast to the southwest, the thickness gradually declines. The thickest area is around the JY-1 well in the northeast, approximately 40 m thick, while the shale with TOC > 2% in the southwestern area is less than 20 m thick. The JY-1 well area and LY-1 well area have the thickest shale from east to west (Figure 2(b)). In the vertical direction, the TOC > 4% shale is mainly concentrated at the Wufeng Formation and at the bottom of the Longmaxi Formation, and the TOC content gradually decreases from the bottom to the top in the Longmaxi Formation. The average TOC content of the Wufeng Formation is 4.3%, while the average TOC content of the bottom of the Longmaxi Formation is 3.2% (Figure 3).

4.1.2. Organic Matter Type. Based on light microscopy and FIB-SEM observations, the majority of organic matter in the southeast Sichuan Basin is algae, pyrobitumen, and graptolite.

A small amount of biodebris was also observed, such as acritarchs, chitinozoans, and sponge spicules (Figures 4–6). Most of the graptolite has a thin, dense carbonaceous structure (Figure 4), and its pores are poorly developed. There are contraction fractures between the graptolite and surrounding minerals. Energy spectrum analysis showed that the graptolite is mainly carbonaceous.

Pyrobitumen generally fills the space between mineral particles and has no fixed form (Figure 5). Compared with the dense structure of graptolite, pyrobitumen has a loose structure and more well-developed pores (Figure 5(c)). Energy spectrum analysis showed that the main elemental composition of pyrobitumen is also carbonaceous (Figure 5(d)).

Algae are generally secondary components that postdate hydrocarbon generation and are covered with lamellate clay minerals. The clay minerals do not have a fixed orientation and look like petals (Figure 6). The algae are also relatively loose, and energy spectrum analysis showed that the elemental composition of the algae is mainly carbonaceous (Figure 6(c)).

Energy spectrum analysis showed that the biodebris contains mostly phosphorus and calcium, with a relatively complete structure and morphology (Figure 7; [35]). The biodebris is relatively dense, and its pores are either not developed or only a few nanoscale micropores are developed.

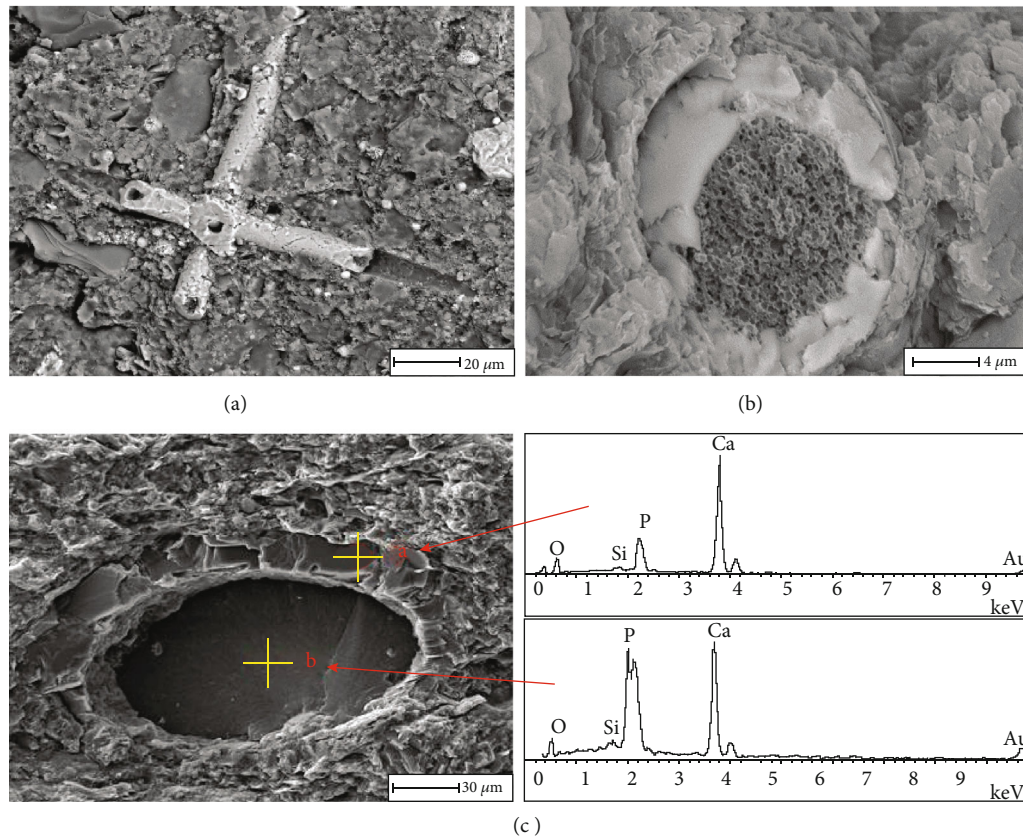


FIGURE 7: Biodetritus morphology photograph and energy spectrum of the Wufeng-Longmaxi Formation shale in the southeast Sichuan Basin. (a) Sponge spicule. (b) Sponge spicule (cross section). (c) Biotritus with calcium and phosphorus.

4.1.3. Organic Matter Maturity. The microscopic organic components that indicate the maturity of the black shale in the Wufeng-Longmaxi Formation in the southeast Sichuan Basin are mainly three types: pyrobitumen, biodetritus (predominantly graptolite), and vitrinite-like maceral (VLM). The black shale of the Wufeng-Longmaxi Formation is abundant in graptolite, with obvious morphological features. In the present study, the reflectance of the graptolite was measured. Based on 18 samples from 12 wells, the R_o is between 2.22% and 3.13%, with an average of 2.71% [36, 37], indicating that the shale has a high degree of maturity (Figure 8).

4.2. Organic Pore Characteristics

4.2.1. Algae Pores. The pores in the organic matter of the Wufeng-Longmaxi Formation shale are generally well developed, but the pores in different types of organic matter show significant variability. The cell structure of the algae is poorly preserved, and most of it have been degraded and heavily micronized. This type of organic matter has a distinct shape, and the inorganic minerals produced by the internal metasomatism have an obvious biological structure. The organic matter pores inside the algae mostly have a local concentration, and the surface porosity is approximately 15% (Figure 9).

4.2.2. Graptolite Pores. Generally, graptolite is poorly preserved and displays a fixed, rigid shape. Fractures can form

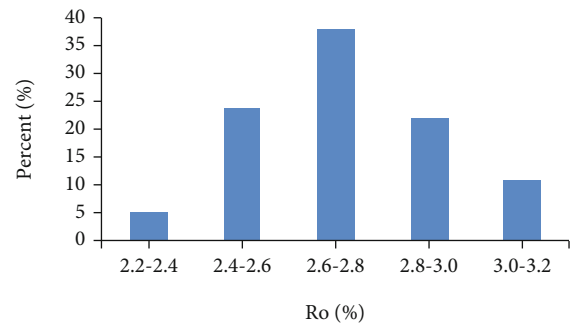


FIGURE 8: Equivalent vitrinite reflectance distribution of the Wufeng-Longmaxi Formation shale in the southeast Sichuan Basin.

between the graptolite and inorganic minerals. Small quantities of inorganic minerals are observed inside the graptolite, and the pores are poorly developed, with 5% surface porosity (Figure 10).

4.2.3. Pyrobitumen Pores. Pyrobitumen does not have a fixed shape and fills the spaces in the inorganic mineral particles of the clay layers. The pores are well developed in the pyrobitumen, with a 30% surface porosity (Figure 11). The pore shape within the pyrobitumen is controlled by the morphology of the pyrobitumen. The pores are mainly concentrated in the center of the pyrobitumen. The pore morphology is mostly

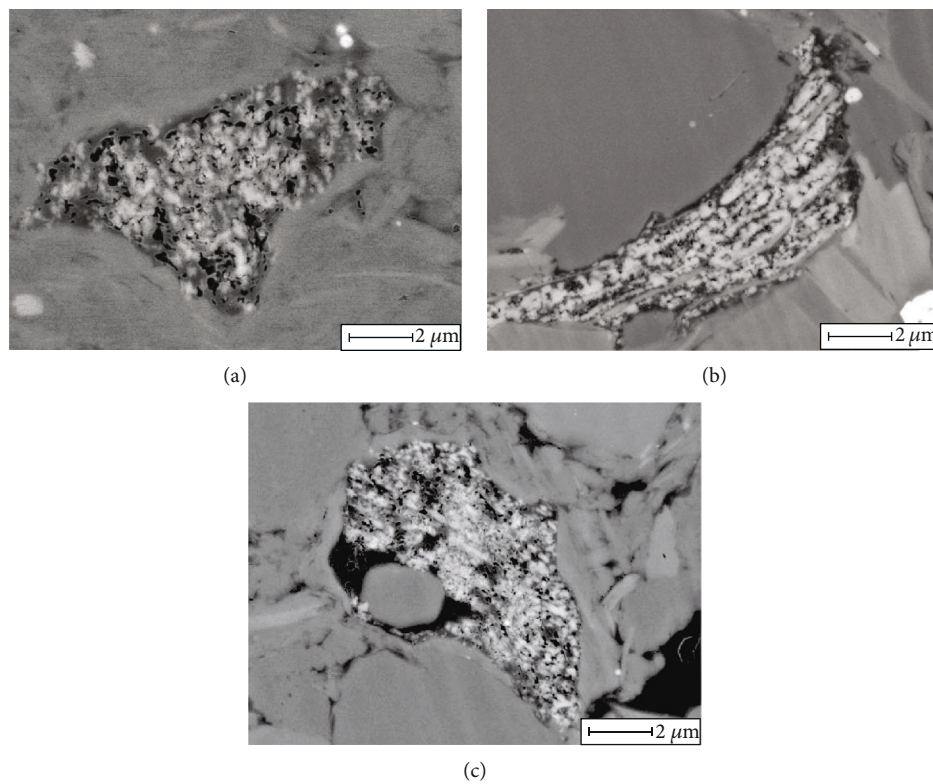


FIGURE 9: Pore characteristics of the algae in the Wufeng-Longmaxi Formation shale at the southeast Sichuan Basin.

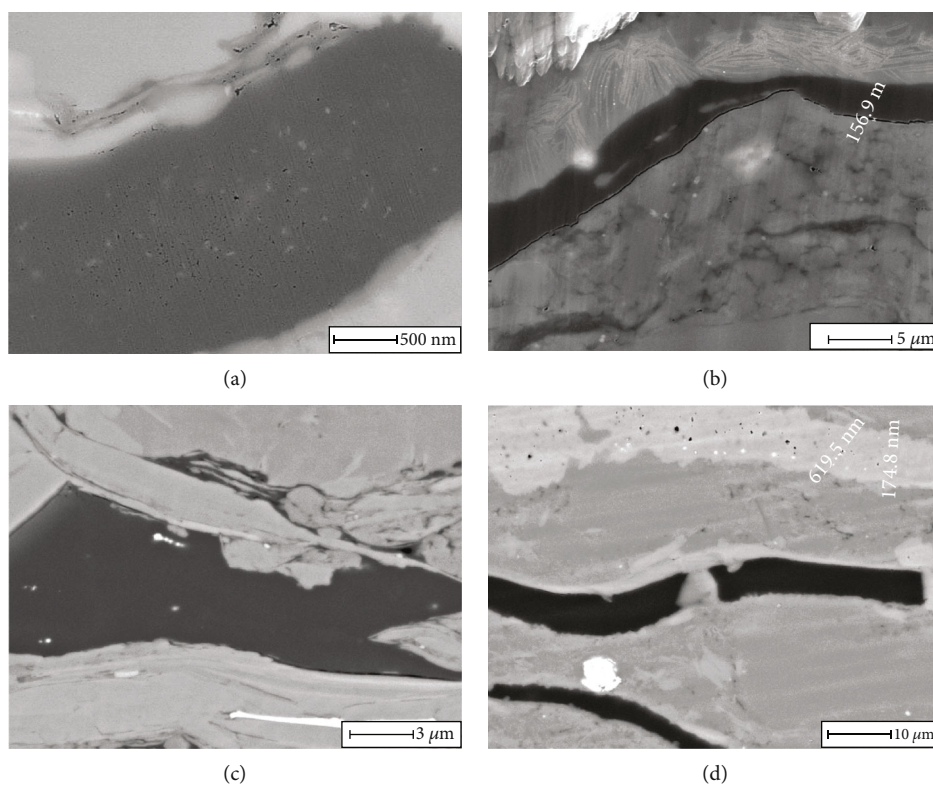


FIGURE 10: The pore characteristics of graptolite in the Wufeng-Longmaxi Formation shale at the southeast Sichuan Basin.

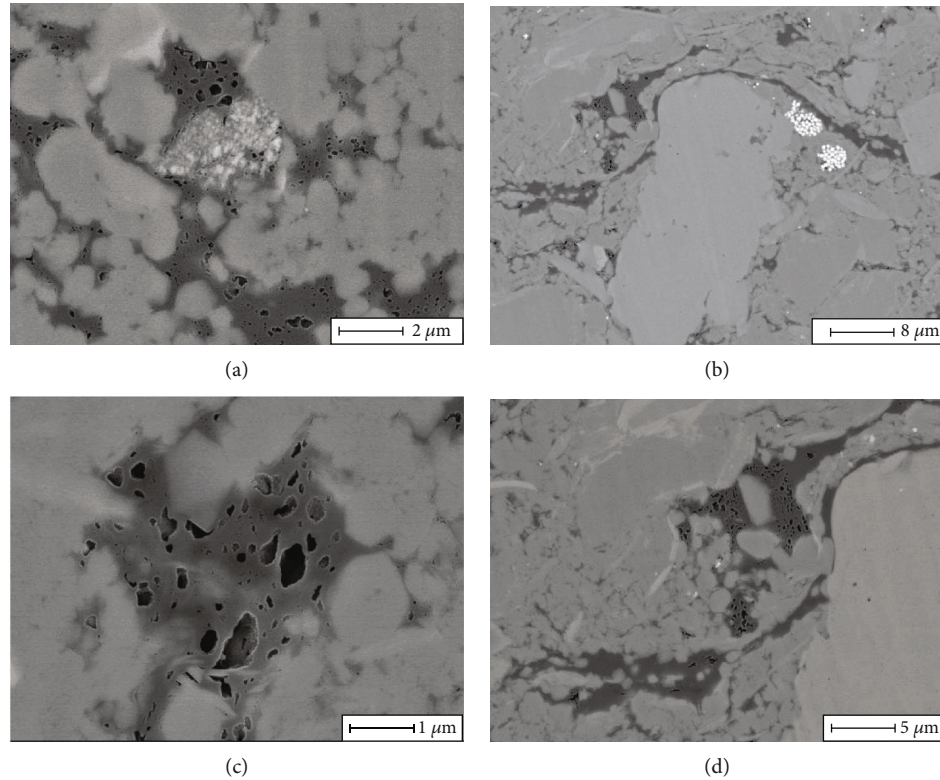


FIGURE 11: The pore characteristics of pyrobitumen in the Wufeng-Longmaxi Formation shale at the southeast Sichuan Basin.

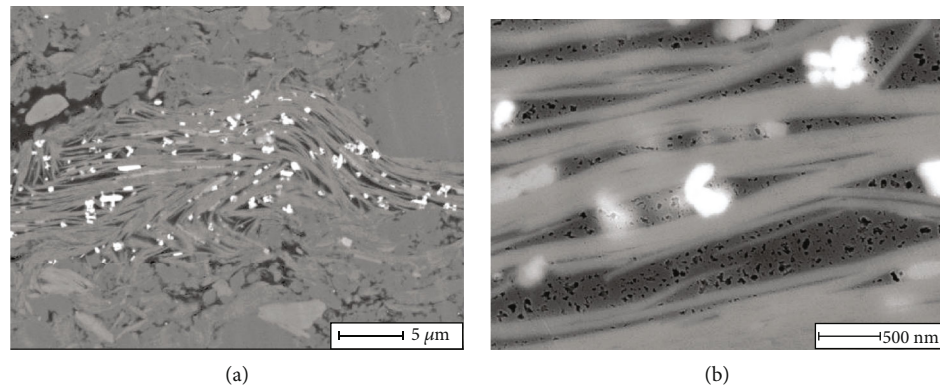


FIGURE 12: Pyrobitumen in the clay mineral layers, with pores mainly smaller than 50 nm.

ellipsoidal or semiround, with a 10-300 nm long axis and a 2-100 nm short axis. The pores are less developed at the edges of the pyrobitumen, especially at the throat area adjacent to the inorganic minerals. The morphology of the pyrobitumen is mainly long strips or flat, with an aspect ratio greater than 5 : 1. The long axis direction of the pores agrees with the long axis direction of the pyrobitumen (Figure 11). The pyrobitumen portion contained pores ranging in size from 5 to 50 nm (Figure 12; [38]). These pyrobitumen pores are the main body of organic pores in the Wufeng-Longmaxi Formation shale.

5. Discussion

5.1. Morphology and Connectivity of Organic Pores. The pores in the shale exist in three dimensions. Nano-CT scans can

display the internal mineral composition and pore structure in 3D [39]. The connectivity of the organic-material-rich shale at the bottom of the Wufeng-Longmaxi Formation is medium-poor, and the pore size is small (Figure 13). The continuity of organic matter in three-dimensional space is good, and a large number of pores have developed in these well-connected organic materials. Figure 13(b) shows the organic pores in different regions using multiple colors. Areas with the same color indicate that the nanopores in the organic matter of this part are connected. These different-sized pores form a complex spatial network structure. The pores in the sample are mainly circular, and the shape of the pores is sill-like, sheet-like, and tubular, with moderate connectivity. The throat is needle-shaped and partially sill-like (Figure 13(c)). The sample had a total of more

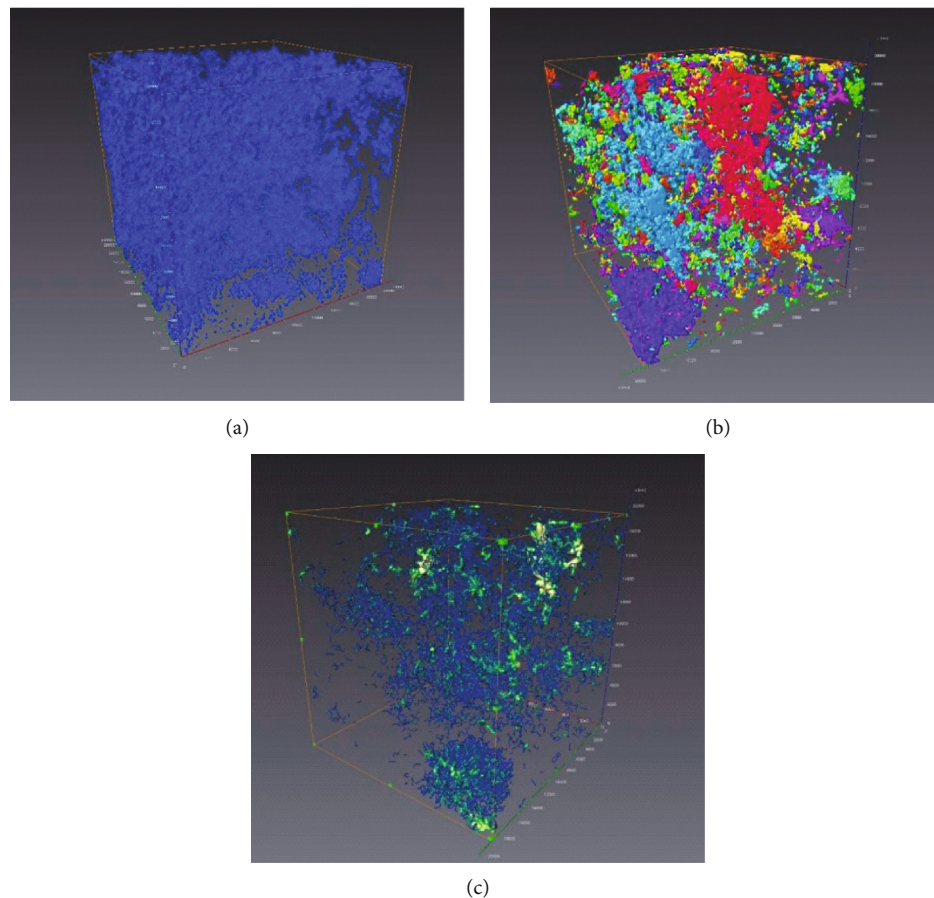


FIGURE 13: Organic pore characteristics of the organic-material-rich shale based on nano-CT. The TOC is 5.7%. (a) The blue part is organic matter. (b) Interconnected pores in the organic matter. (c) Throat distribution in the organic matter.

than 7400 organic pores, with a total volume of $4.6 \times 10^{11} \text{ nm}^3$, which accounted for 5.7% of the total sample volume of $8 \times 10^{12} \text{ nm}^3$. The sample had 5120 organic pores (larger than 65 nm), and the total volume of the organic pores was $2.6 \times 10^{11} \text{ nm}^3$, which accounted for 3% of the total volume of the sample and 56.6% of the total organic matter volume.

The organic-material-poor shale in the middle and upper parts of the Wufeng-Longmaxi Formation has poor connectivity (Figure 14). The continuity of the organic matter in three-dimensional space is poor, and the connected organic pore range is obviously reduced (Figure 14(b)). The same characteristics are also visible in the organic throat distribution. The pores of the sample were mainly elongated (similar to intergranular pores) and flake-shaped with poor connectivity. The throat was needle-shaped (Figure 14(c)). The sample had a total of 2698 organic pores with an overall volume of $1.2 \times 10^{11} \text{ nm}^3$, which accounted for approximately 1.6% of the total sample volume of $8 \times 10^{12} \text{ nm}^3$. The sample had 1067 organic pores, which accounted for 0.9% of the total volume of the sample.

According to the 3D FIB-SEM data, the organic pores in the Wufeng-Longmaxi Formation shale with long axes < 100 nm accounted for approximately 89% of the total organic pores, while the organic pores with long axes > 200 nm accounted for less than 4% of the total organic pores

(Figure 15). Organic pores have a relatively high proportion of small pores [40]. It was determined that the majority of the organic pores in the sample were less than 50 nm, and a large number of the small pores had developed inside the organic matter.

The organic pores with aspect (long – to – minor axis) ratios > 4 only comprise approximately 15% of the total organic pores, and more than 50% of the pores have aspect ratios < 2 (Figure 16). The morphological characteristics of the organic pores obtained by three-dimensional FIB-SEM are similar to those obtained by two-dimensional FIB-SEM: the shapes of the organic pores are primarily rounded, nearly circular, or elliptical.

5.2. Role of Pyrobitumen Pores. The majority of organic matter in the Wufeng-Longmaxi shale are migrated organic matter of amorphous form, uniform color, and nanometer-scale internal pores [41]. The migrated organic matter was injected into the mineral pores (mainly intergranular) in the form of liquid hydrocarbon during the shale oil generation stage [42]. If the TOC content in the shale is 5% by weight, the organic matter density is approximately 50% of the shale density. The organic matter then accounts for nearly 10% of the pore volume of the shale, while the organic matter contains approximately 20%-40% of the

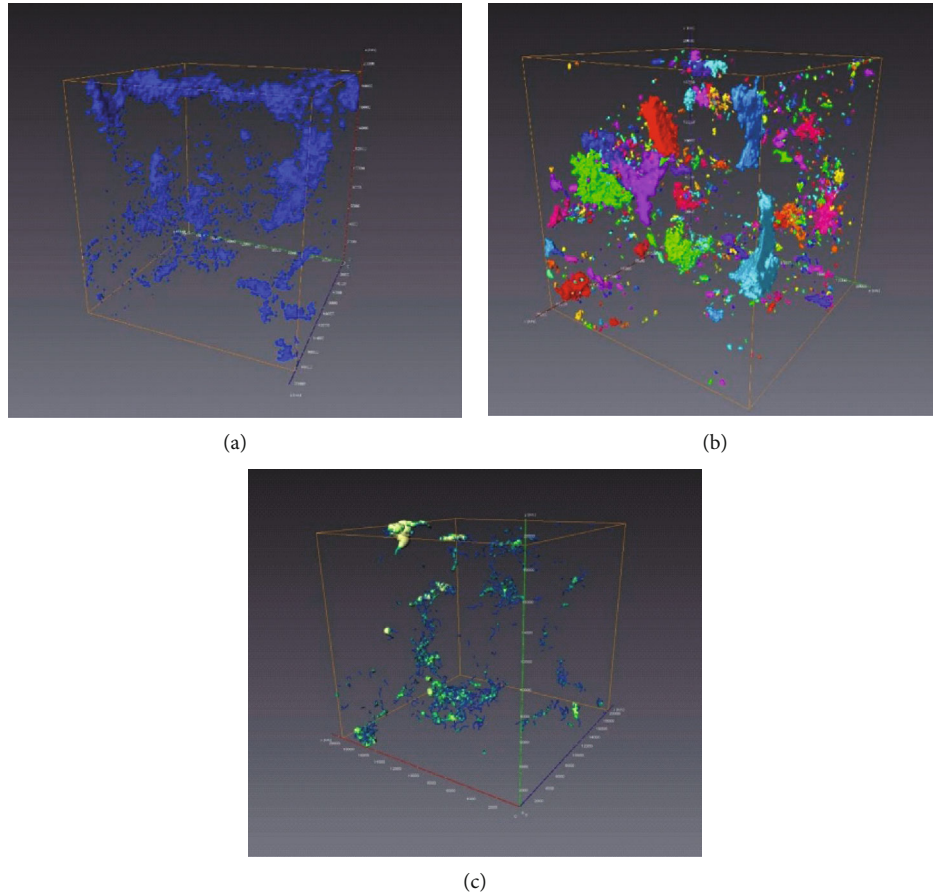


FIGURE 14: Organic pore characteristics of the shale based on the nano-CT. TOC is 1.6%. (a) The blue part is organic matter. (b) Interconnected pores in the organic matter. (c) Throat distribution in the organic matter.

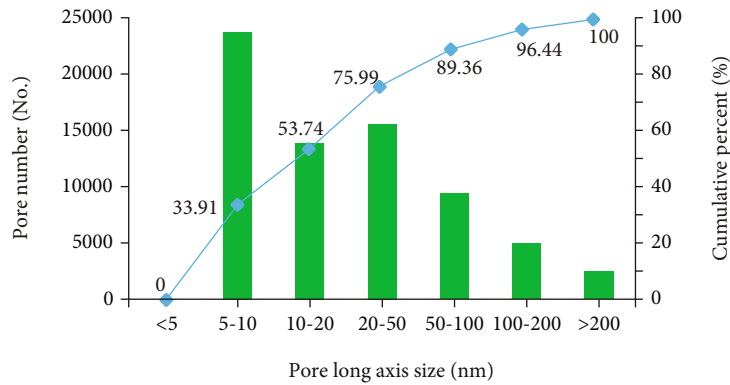


FIGURE 15: Characteristics of the long axis of organic pores based on 3D FIB-SEM data. The majority of long axes are shorter than 100 nm.

volume occupied by organic pores. Therefore, the organic matter has an organic matter porosity of 2%-4% of the total volume of the shale. Due to its low porosity and poor permeability, it was difficult for liquid hydrocarbon to migrate out of the shale [43]. The remaining hydrocarbon separated into light hydrocarbon (primarily methane) and heavy hydrocarbon (primarily solid pyrobitumen) [44]. The pyrobitumen pores were formed during the process of gas and liquid separation.

Based on the analysis of 832 pyrobitumen enclaves in 16 samples, it was determined that the pyrobitumen pores are primarily ellipsoidal or near-circular. The long-to-minor axis ratios of the pyrobitumen pores are similar. The aspect ratios are concentrated at <3, and less than 10% of the long-to-minor axis ratios are >3 (Figure 17).

The pores in the center of the pyrobitumen are mostly rounded, and the aspect ratios are concentrate close to 1. The pores close to the throat between inorganic minerals

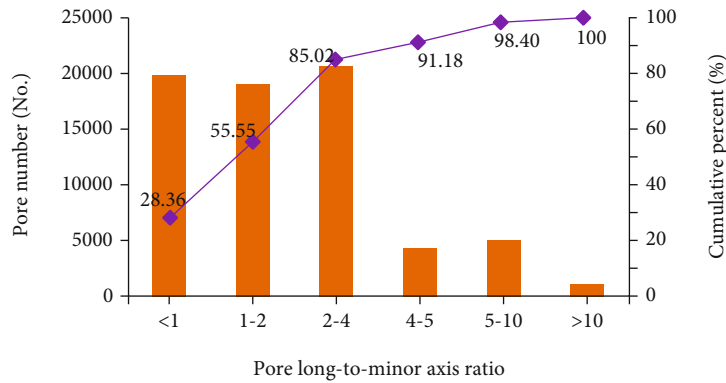


FIGURE 16: Characteristics of the aspect ratio of the organic pores based on 3D FIB-SEM data.

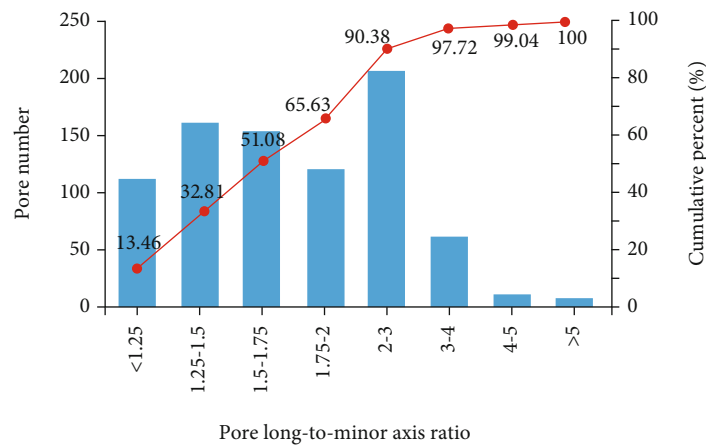


FIGURE 17: Characteristics of the aspect ratios of the pyrobitumen pores based on 2D FIB-SEM data.

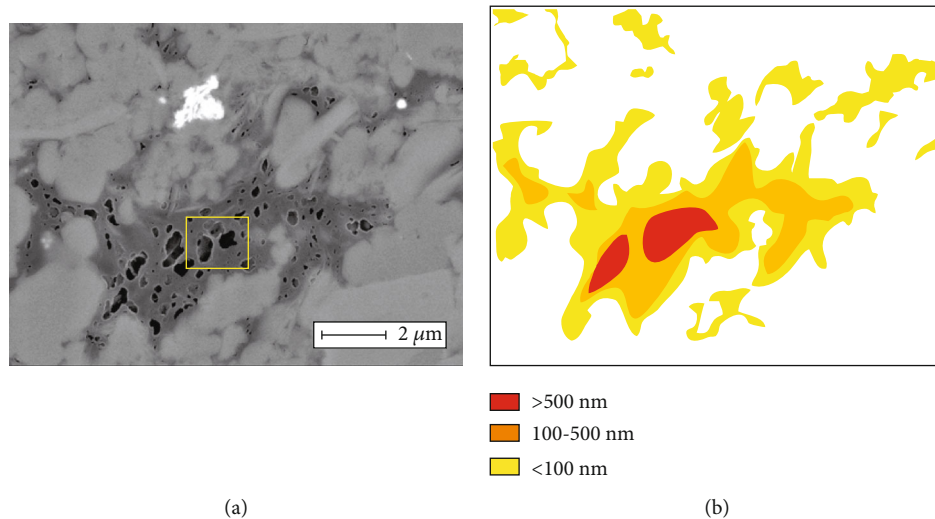


FIGURE 18: Characteristics of the pyrobitumen pores based on 2D FIB-SEM data. (a) The large pores are concentrated at the center of the pyrobitumen. (b) Pattern of figure (a).

are flat shaped or in long strips for the most part, with long-to-minor axis ratios higher than 3. The larger the volume of a single pyrobitumen enclave, the more developed the pyrobitumen pores and the larger the pore size. Additionally, the

large pores are concentrated at the center of the pyrobitumen (Figure 18).

For example, Figure 18(a) shows that one 9 μm long pyrobitumen portion has abundant nanopores, and its surface

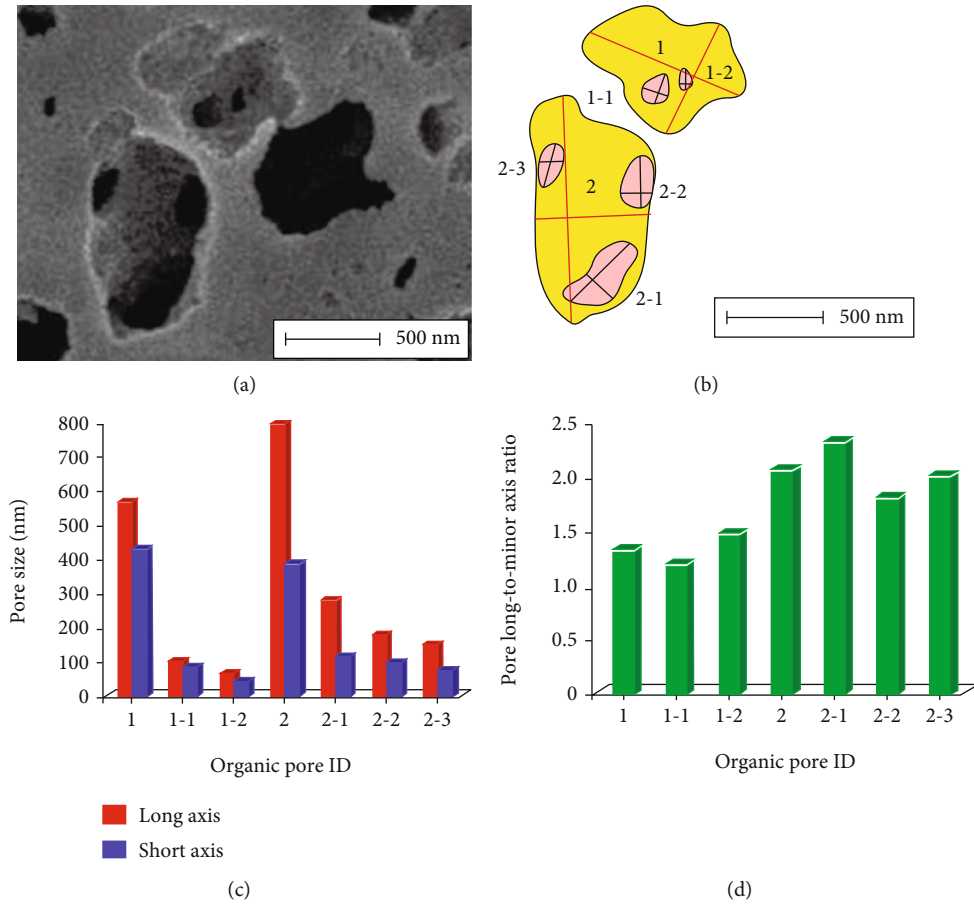


FIGURE 19: Pores in the pyrobitumen based on 2D FIB-SEM data. (a) Magnification of Figure 18(a) showing good pore connectivity. (b) Pattern of figure (a). (c) Statistics of the long axis and short axis of pyrobitumen pores. (d) Proportional distribution of the long and short axes of pyrobitumen pores.

porosity is approximately 30% (Figure 18(a)). From the edge of the pyrobitumen to the center, the size of the pores has a pronounced increasing trend, from a majority of less than 100 nm near the edge, increasing to 500 nm further in, and increasing to greater than 500 nm at the center of the pyrobitumen. This trend may indicate that most of the gas are generated at the center of the organic matter concentrations (Figure 18(b)). The long axis direction of the pores is generally coordinated with the extension direction of the pyrobitumen. Especially in narrow pyrobitumen enclaves, the long axis direction of the pores is consistent with the extension direction of the pyrobitumen, indicating that pyrobitumen deformation has occurred on the internal pyrobitumen pores.

The pyrobitumen pores are not completely isolated from each other and have good connectivity. The large pores are generally interconnected by small pores (Figure 19(a)). In the No.1 pore, there are 2 secondary nanopores, and their aspect ratios are all lower than 1.5 (Figures 19(b)–19(d)). In the No.2 pore, there are 3 secondary nanopores, and their aspect ratios are all greater than 1.5 (Figures 19(b)–19(d)). The relationship between the large pyrobitumen pores and the secondary pyrobitumen pores indicates that they were generated by similar processes. During the formation and accumulation of shale gas, small secondary pores may accumulate within large pores, increasing the size of the larger pores.

6. Conclusion

The distribution of organic matter in the southeast Sichuan Basin has distinct variations both horizontally and vertically. The TOC > 4% shale is mainly concentrated at the Wufeng Formation and at the bottom of the Longmaxi Formation. The organic materials are primarily algae (secondary components), pyrobitumen, and graptolite, with a small amount of biotritus, such as acritarch, chitinozoa, and sponge spicule. The Wufeng-Longmaxi Formation shale has a high degree of thermal evolution, and its R_o is between 2.22% and 3.13%, with an average of 2.71%.

There are three main types of organic pores: algae pores, graptolite pores, and pyrobitumen pores. The cell structure of algae pores is poorly preserved but displays an apparent biological structure. Algae pores are locally concentrated. Graptolite is generally poorly preserved and has a fixed, rigid shape. Small quantities of inorganic minerals can be found inside the graptolite. The pyrobitumen does not have a fixed shape and fills the spaces between inorganic mineral particles and clay layers. The pyrobitumen pores are well developed, as determined by the overall morphology of the pyrobitumen enclaves.

The pores in the organic-material-rich shale are primarily circular, nanoscale pores. The majority of throats are

needle shaped, and the organic pores may account for more than 50% of the total organic matter volume. The organic matter in the organic-material-poor shale has poor continuity in three-dimensional space. The pores are mostly long and narrow, and the majority of throats are needle shaped. The organic pores may account for less than 1% of the total sample volume.

The majority of the pyrobitumen pores are ellipsoidal or near-circular, with aspect ratios concentrated at <3 . The pores in the center of the pyrobitumen are mostly rounded, and the aspect ratios are predominantly close to 1. The pores close to the throat between the inorganic minerals are largely flat or in the shape of long strips, and their aspect ratios are mostly greater than 3. The large pores are concentrated in the center of the pyrobitumen, and the pyrobitumen pores are generally well connected.

Data Availability

The experimental data used to support the findings of this study are included within the manuscript.

Conflicts of Interest

The authors' declare that they have no conflicts of interest.

Acknowledgments

This study was supported by the National Natural Science Foundation of China (Grant No. 41872124) and the National Science and Technology Major Project (No. 2017ZX05036004). Thanks are due to Guangxiang Liu, Bo Gao, Haikuan Nie, Quanyou Liu, Tong Zhu, Ruyue Wang, and Pengwei Wang who participate in the project and give much critical suggestion and help on the thesis. We sincerely appreciate all anonymous reviewers and the handling editor for their critical comments and constructive suggestions.

References

- [1] A. Vengosh, R. B. Jackson, N. Warner, T. H. Darrah, and A. Kondash, "A critical review of the risks to water resources from unconventional shale gas development and hydraulic fracturing in the United States," *Environmental Science & Technology*, vol. 48, no. 15, pp. 8334–8348, 2014.
- [2] S. Balasubramanian, P. Chen, and S. Bose, "Recent advances in enhanced oil recovery technologies for unconventional oil reservoirs," *Paper presented at the Offshore Technology Conference*, 2018, Houston, TX, USA, April 2018, 2018.
- [3] C. Han, Z. Jiang, M. Han, M. Wu, and W. Lin, "The lithofacies and reservoir characteristics of the Upper Ordovician and Lower Silurian black shale in the Southern Sichuan Basin and its periphery, China," *Marine and Petroleum Geology*, vol. 75, pp. 181–191, 2016.
- [4] T. Jiang, Z. Jin, G. Liu et al., "Source analysis of siliceous minerals and uranium in early Cambrian shales, South China: Significance for shale gas exploration," *Marine and Petroleum Geology*, vol. 102, pp. 101–108, 2019.
- [5] X. Qiu, C. Liu, G. Mao, Y. Deng, F. Wang, and J. Wang, "Major, trace and platinum-group element geochemistry of the Upper Triassic nonmarine hot shales in the Ordos basin, Central China," *Applied Geochemistry*, vol. 53, pp. 42–52, 2015.
- [6] J. Wu, C. Liang, Z. Jiang, and C. Zhang, "Shale reservoir characterization and control factors on gas accumulation of the lower Cambrian Niutitang shale, Sichuan Basin," *Geological Journal*, vol. 54, no. 3, pp. 1604–1616, 2018.
- [7] K. Zhang, J. Peng, W. Liu et al., "The role of deep geofluids in the enrichment of sedimentary organic matter: a case study of the late Ordovician-Early Silurian in the upper Yangtze region and early Cambrian in the lower Yangtze region, South China," *Geofluids*, vol. 2020, Article ID 8868638, 12 pages, 2020.
- [8] Z. He, Z. Hu, H. Nie, S. Li, and J. Xu, "Characterization of shale gas enrichment in the Wufeng Formation-Longmaxi Formation in the Sichuan Basin of China and evaluation of its geological construction-transformation evolution sequence," *Journal of Natural Gas Geoscience*, vol. 2, no. 1, pp. 1–10, 2017.
- [9] F. Wang and R. M. Reed, "Pore networks and fluid flow in gas shales," in *SPE Annual Technical Conference and Exhibition*, New Orleans, LA, USA, October 2009.
- [10] T. Zhang, G. S. Ellis, S. C. Ruppel, K. Milliken, and R. Yang, "Effect of organic-matter type and thermal maturity on methane adsorption in shale-gas systems," *Organic Geochemistry*, vol. 47, pp. 120–131, 2012.
- [11] S. Chen, Y. Zhu, H. Wang, H. Liu, W. Wei, and J. Fang, "Shale gas reservoir characterisation: a typical case in the southern Sichuan Basin of China," *Energy*, vol. 36, no. 11, pp. 6609–6616, 2011.
- [12] R. M. Slatt and N. R. O'Brien, "Pore types in the Barnett and Woodford gas shales: contribution to understanding gas storage and migration pathways in fine-grained rocks," *AAPG Bulletin*, vol. 95, no. 12, pp. 2017–2030, 2011.
- [13] M. E. Curtis, C. H. Sondergeld, R. J. Ambrose, and C. S. Rai, "Microstructural investigation of gas shales in two and three dimensions using nanometer-scale resolution imaging," *AAPG Bulletin*, vol. 96, no. 4, pp. 665–677, 2012.
- [14] X. Tang, Z. Jiang, Z. Li et al., "The effect of the variation in material composition on the heterogeneous pore structure of high-maturity shale of the Silurian Longmaxi formation in the southeastern Sichuan Basin, China," *Journal of Natural Gas Science and Engineering*, vol. 23, pp. 464–473, 2015.
- [15] F. Yang, Z. Ning, D. Kong, and H. Liu, "Pore structure of shales from high pressure mercury injection and nitrogen adsorption method," *Natural Gas Geoscience*, vol. 24, no. 3, pp. 450–455, 2013.
- [16] G. R. Chalmers, R. M. Bustin, and I. M. Power, "Characterization of gas shale pore systems by porosimetry, pycnometry, surface area, and field emission scanning electron microscopy/transmission electron microscopy image analyses: examples from the Barnett, Woodford, Haynesville, Marcellus, and Doig units," *AAPG Bulletin*, vol. 96, no. 6, pp. 1099–1119, 2012.
- [17] H. Tian, L. Pan, T. Zhang, X. Xiao, Z. Meng, and B. Huang, "Pore characterization of organic-rich Lower Cambrian shales in Qiannan Depression of Guizhou Province, Southwestern China," *Marine and Petroleum Geology*, vol. 62, pp. 28–43, 2015.
- [18] D. M. Jarvie, R. J. Hill, T. E. Ruble, and R. M. Pollastro, "Unconventional shale-gas systems: the Mississippian Barnett shale of north-Central Texas as one model for thermogenic

- shale-gas assessment," *AAPG Bulletin*, vol. 91, no. 4, pp. 475–499, 2007.
- [19] R. G. Loucks, R. M. Reed, S. C. Ruppel, and D. M. Jarvie, "Morphology, genesis, and distribution of nanometer-scale pores in siliceous mudstones of the Mississippian Barnett shale," *Journal of Sedimentary Research*, vol. 79, no. 12, pp. 848–861, 2009.
- [20] M. E. Curtis, C. H. Sondergeld, and C. S. Rai, *Relationship between organic shale microstructure and hydrocarbon generation*, Society of Petroleum Engineers, The Woodlands, TX, USA, 2013.
- [21] T. Cao, Z. Song, S. Wang, and J. Xia, "Characterization of pore structure and fractal dimension of Paleozoic shales from the northeastern Sichuan Basin, China," *Journal of Natural Gas Science and Engineering*, vol. 35, pp. 882–895, 2016.
- [22] X. Liang, T. Zhang, Y. Yang et al., "Microscopic pore structure and its controlling factors of overmature shale in the lower Cambrian Qiongzhusi Fm, northern Yunnan and Guizhou provinces of China," *Natural Gas Industry*, vol. 34, no. 2, pp. 18–26, 2014.
- [23] K. Zhang, J. Peng, X. Wang et al., "Effect of organic maturity on shale gas genesis and pores development: a case study on marine shale in the upper Yangtze region, South China," *Open Geosciences*, vol. 12, no. 1, pp. 1617–1629, 2020.
- [24] C. Zou, J. Du, C. Xu et al., "Formation, distribution, resource potential, and discovery of Sinian-Cambrian giant gas field, Sichuan Basin, SW China," *Petroleum Exploration and Development*, vol. 41, no. 3, pp. 306–325, 2014.
- [25] S. Chen, C. J. L. Wilson, and B. A. Worley, "Tectonic transition from the Songpan-Garzê Fold Belt to the Sichuan Basin, southwestern China," *Basin Research*, vol. 7, no. 3, pp. 235–253, 1995.
- [26] T. Guo, "Evaluation of highly thermally mature shale-gas reservoirs in complex structural parts of the Sichuan Basin," *Journal of Earth Science*, vol. 24, no. 6, pp. 863–873, 2013.
- [27] T. Guo and H. Zhang, "Formation and enrichment mode of Jiaoshiha shale gas field, Sichuan Basin," *Petroleum Exploration and Development*, vol. 41, no. 1, pp. 31–40, 2014.
- [28] C. Liang, Z. Jiang, Y. Cao, J. Zhang, and L. Guo, "Sedimentary characteristics and paleoenvironment of shale in the Wufeng-Longmaxi Formation, North Guizhou Province, and its shale gas potential," *Journal of Earth Science*, vol. 28, no. 6, pp. 1020–1031, 2017.
- [29] J. Wu, C. Liang, Z. Hu et al., "Sedimentation mechanisms and enrichment of organic matter in the Ordovician Wufeng Formation-Silurian Longmaxi formation in the Sichuan Basin," *Marine and Petroleum Geology*, vol. 101, pp. 556–565, 2018.
- [30] C. Zou, D. Dong, S. Wang et al., "Geological characteristics and resource potential of shale gas in China," *Petroleum Exploration and Development*, vol. 37, no. 6, pp. 641–653, 2010.
- [31] Z. Jiang, L. Guo, and C. Liang, "Lithofacies and sedimentary characteristics of the Silurian Longmaxi shale in the southeastern Sichuan Basin, China," *Journal of Palaeogeography*, vol. 2, no. 3, pp. 238–251, 2013.
- [32] S. Liu, W. Ma, L. Jansa, W. Huang, X. Zeng, and C. Zhang, "Characteristics of the shale gas reservoir rocks in the lower silurian longmaxi formation, East Sichuan basin, China," *Energy Exploration & Exploitation*, vol. 31, no. 2, pp. 187–219, 2013.
- [33] C. Zou, D. Dong, Y. Wang et al., "Shale gas in China: characteristics, challenges and prospects (II)," *Petroleum Exploration and Development*, vol. 43, no. 2, pp. 182–196, 2016.
- [34] J. Liu, Y. Yao, D. Elsworth, D. Liu, Y. Cai, and L. Dong, "Vertical heterogeneity of the shale reservoir in the lower Silurian Longmaxi Formation: analogy between the southeastern and northeastern Sichuan Basin, SW China," *Minerals*, vol. 7, no. 8, p. 151, 2017.
- [35] H. K. Nie, Z. J. Jin, and J. C. Zhang, "Characteristics of three organic matter pore types in the Wufeng-Longmaxi Shale of the Sichuan Basin, Southwest China," *Southwest China. Scientific Reports*, vol. 8, no. 1, article 7014, 2018.
- [36] C. Cao, Q. Shang, and Y. Fang, "The study of graptolite reflectance as the indicator of source rock maturation in Ordovician and Silurian of Tarim Basin, Ordos, Jiangsu areas," *Acta Palaeontologica Sinica*, vol. 39, no. 1, pp. 151–156, 2000.
- [37] H. Jacob, "Classification, structure, genesis and practical importance of natural solid oil bitumen ("migrabitumen")," *International Journal of Coal Geology*, vol. 11, no. 1, pp. 65–79, 1989.
- [38] H. K. Nie, Z. J. Jin, C. X. Sun, Z. L. He, G. X. Liu, and Q. Y. Liu, "Organic matter types of the Wufeng and Longmaxi Formations in the Sichuan Basin, South China: implications for the formation of organic matter pores," *Energy & Fuels*, vol. 33, no. 9, pp. 8076–8100, 2019.
- [39] X. Tang, Z. Jiang, S. Jiang, and Z. Li, "Heterogeneous nanoporosity of the Silurian Longmaxi Formation shale gas reservoir in the Sichuan Basin using the QEMSCAN, FIB-SEM, and nano-CT methods," *Marine and Petroleum Geology*, vol. 78, pp. 99–109, 2016.
- [40] R. G. Loucks, R. M. Reed, S. C. Ruppel, and U. Hammes, "Spectrum of pore types and networks in mudrocks and a descriptive classification for matrix-related mudrock pores," *AAPG Bulletin*, vol. 96, no. 6, pp. 1071–1098, 2012.
- [41] C. A. Rios and O. M. Castellanos, "Microstructural characterization of pore types in unconventional gas reservoirs utilizing FEG-SEM: an example from the Galemba member of the cretaceous La Luna Formation, Middle Magdalena Valley Basin (Colombia)," *Revista de la Academia Colombiana de Ciencias Exactas, Fisicas y Naturales*, vol. 40, no. 154, pp. 161–175, 2016.
- [42] R. G. Loucks and R. M. Reed, "Scanning-electron-microscope petrographic evidence for distinguishing organic-matter pores associated with depositional organic matter versus migrated organic matter in mudrock," *GCAGS Journal*, vol. 3, pp. 51–60, 2014.
- [43] Y. Yang and A. C. Aplin, "A permeability-porosity relationship for mudstones," *Marine and Petroleum Geology*, vol. 27, no. 8, pp. 1692–1697, 2010.
- [44] R. Sassen, "Geochemical and carbon isotopic studies of crude oil destruction, bitumen precipitation, and sulfate reduction in the deep Smackover Formation," *Organic Geochemistry*, vol. 12, no. 4, pp. 351–361, 1988.

Research Article

Quantitative Characterization and Determination of the Main Factors That Control Fracture Development in the Lower Paleozoic Shale in Southeastern Chongqing, China

Zhiping Zhang,^{1,2} Xiangye Kong ,³ Qing Chen ,⁴ Ye Zhang,^{1,2} Zhi Deng,^{1,2} Chuan Yu,¹ Zhian Lei,⁵ Haijie Zhang,⁵ Xiaofeng Wang,⁶ Guanghua Yao,⁷ Licheng Yang,⁸ and Xianfeng Tan ⁴

¹National and Local Joint Engineering Research Center of Shale Gas Exploration and Development, Chongqing Institute of Geology and Mineral Resources, Chongqing 401120, China

²Key Laboratory of Shale Gas Exploration, Ministry of Natural Resources, Chongqing Institute of Geology and Mineral Resources, Chongqing 401120, China

³State Key Laboratory of Petroleum Resources and Prospecting, China University of Petroleum, Beijing 102249, China

⁴Chongqing Key Laboratory of Complex Oil and Gas Exploration and Development, Chongqing 401331, China

⁵Chongqing Shale Gas Exploration and Development Company Limited, Chongqing 401121, China

⁶Chongqing Institute of Geological Survey, Chongqing 401122, China

⁷China Huaneng Group Co., Ltd. Chongqing Branch, Chongqing 401122, China

⁸PetroChina Southwest Oil and Gasfield Company, Chongqing 401122, China

Correspondence should be addressed to Xiangye Kong; kongxiangyecup@163.com and Qing Chen; chenqing0144@126.com

Received 24 January 2021; Revised 9 April 2021; Accepted 19 April 2021; Published 6 May 2021

Academic Editor: Kun Zhang

Copyright © 2021 Zhiping Zhang et al. This is an open access article distributed under the Creative Commons Attribution License, which permits unrestricted use, distribution, and reproduction in any medium, provided the original work is properly cited.

The Longmaxi and Niutitang Formations are typical shale reservoirs in southeastern Chongqing. Since the Paleozoic, southeastern Chongqing has experienced multistage tectonic movement and diagenesis, resulting in the formation of a large number of natural fractures. In shale reservoirs, fractures not only provide seepage channels for oil and gas migration but also play an important role in the oil and gas reservoir space. Natural fractures provide a flow path from source rock to reservoir during oil filling and connect hydraulic fractures, matrix pores, and boreholes during production. Therefore, identifying the main factors that control the development of natural fractures in the Longmaxi and Niutitang Formations in southeastern Chongqing has a guiding significance for the efficient development of shale reservoirs in this area. By considering the Longmaxi and Niutitang Formation shales as case studies, using field outcrops, drilling cores, and other data, and conducting X-ray diffraction (XRD) analysis as well as total organic carbon (TOC) measurements, the quantitative parameter characteristics and main factors that control the development of natural fractures in reservoir shales were examined in detail. The results obtained showed that there are three types of fractures in the lower Paleozoic shale in southeastern Chongqing, which are structural, diagenetic, and abnormal high-pressure fractures. Among them, the fractures in the Longmaxi Formation shale, which are relatively abundant, predominantly consist of low-angle and high-angle inclined fractures, while the Niutitang Formation predominantly consists of high-angle fractures. Additionally, the investigation of fracture size and fracture density, as well as correlation analyses, showed that the fractures of the Lower Paleozoic shale are predominantly micro fractures that play a key role in improving reservoir seepage. It was also noted that the development of fractures is affected by several factors, including tectonic stress, mineral composition, organic carbon content, and rock thickness. The degree of fracture development was found to be positively correlated with brittle mineral and quartz contents, and high organic matter contents also significantly favored the formation micro fractures.

1. Introduction

Since the 21st century, owing to a significant increase in the demand for energy, interest in unconventional oil and gas resources has increased significantly [1–6]. Natural fractures including structural fracture, diagenetic fracture, and abnormally high-pressure fracture are the dominant seepage channels for oil and gas filling and can connect hydraulic fractures and matrix holes with wellbores during the oil and gas production process [7, 8]. Fractures are common in some shales, which may be the local factors affecting the growth of hydraulic fracture height [9]. Fractures are mainly concentrated in the shale with low clay content, and the abundance and size of outcrop fractures vary greatly [9]. In the subsurface, shales may consist of complex, stratified fractured, and nonfractured rocks [9]. Therefore, to evaluate the distribution of shale oil and gas sweet spots, it is necessary to study the development of natural fractures [10–12]. This is of great significance and may help to minimize drilling and completion costs.

Sichuan-Chongqing area is the key target for shale gas exploration and development in China [13, 14]. The southeastern Chongqing has experienced the superimposed transformation of multistage tectonic activities, which have made its stratigraphic relationships and structural characteristics more complex [15, 16], and simultaneously, it consists of a large number of natural structural fractures. Complex diagenesis, hydrocarbon generation, and expulsion have also had an important impact on the opening of bedding fractures in this area [17, 18]. These natural fractures are one of the important factors responsible for the differences in the oil and gas properties of shale reservoirs in southeastern Chongqing. Previous studies on shale oil and gas in southeastern Chongqing have been primarily focused on regional structure, reservoir lithology, pore structure, and sedimentary characteristics [19, 20]. The reservoir properties of the Longmaxi Formation in this region are rich and have the greatest potential for gas production because of total organic carbon (TOC) enrichment, higher thermal maturity, and improved fracture potential [20]. There are several stages of hydrocarbon generation, migration, and accumulation in this formation [19]. However, research on natural fractures is relatively scarce, and the main factors that control their development are still unclear; this limits the efficient development of tight oil in the study area. In this regard, by using field outcrops, drilling cores, and other data and conducting X-ray diffraction (XRD) analysis as well as TOC measurements, this study focuses on the main factors that control shale fracture development in the Longmaxi and Niutitang Formations in southeastern Chongqing, to provide a new reference for marine shale gas exploration, prediction, and optimization in South China.

2. Geological Setting

Southeastern Chongqing is located in the upper Yangtze platform and belongs to the East Sichuan fold belt in the southeast of the Sichuan Basin [21, 22]. The west of this area is bounded by the Huayingshan deep fault, which is connected to the central Sichuan structural area. The eastern part is

bounded by the Qiyue fault and is adjacent to the fault fold belt in Western Hubei [21]. From southeast to northwest are the Shizhu syncline, Fangdoushan anticline, and Wanxian syncline [23] (Figure 1). The inner part of the fault fold belt in which the anticline is narrow and the stratum is steep and tight, is predominantly linear, with an inverted wing. Usually, two wings lie asymmetrically, and thrust faults are often developed in the core part. Additionally, the syncline axis is wide and the stratum is gentle.

In southeastern Chongqing, there are no upper Silurian and Devonian strata. Almost all the strata are Carboniferous. In some areas, there are Middle Triassic Series, and in most areas, there are Jurassic, Cretaceous, Paleogene, and Neogene strata. Additionally, the Paleozoic strata are mainly exposed [24, 25]. On the surface of the Jiaoshiba structure, only the Huanglong Formation of the Carboniferous system is preserved, while the Devonian system is absent. Other marine strata are relatively intact. The Niutitang Formation of the Lower Cambrian disagrees with the Dengying Formation, with gray green shale or black carbonaceous shale at the bottom and siliceous rock intercalated with carbonaceous shale at the upper part [25–28]. The Longmaxi Formation of the Lower Silurian system is composed of black shale, silty shale, and light gray and yellow siltstone, which are high-quality shale intervals for shale gas exploration and development.

3. Data and Methods

The identification and observation of outcrop fractures mainly included three observation points (Pengshui, Youyang, and Xiushan) and six cores (Yuancan-9, Xiuye-6, Youdi-2, Youye-1, Xiuqian-1, and Youcan-1). Parameters, such as fracture strike and dip, were measured using a compass, and parameters, such as fracture length and opening, were directly measured using a meter rule. A total of 1486 pairs of fracture occurrence data points were sampled. Simultaneously, the TOC contents of 17 shale samples from Well Yuancan-7 were determined using a Leco CS-230 carbon at the Sichuan Coalfield Geology Bureau, and the XRD patterns of 41 shale samples from Well Yuancan-8 were determined using Bruker D8 Advance at the State Key Laboratory of Oil and Gas Reservoir Geology and Exploitation (Chengdu University of Technology, China) under temperature and humidity conditions of 25°C and 50%, respectively.

4. Results

4.1. Fracture Types and Development Characteristics

4.1.1. Structural Fracture. This type of structure refers to the fracture caused by regional or local tectonic stress, which is mainly controlled by in situ stress and is closely related to fracture tectonic deformation. The structural fractures in the Longmaxi and Niutitang Formations in southeastern Chongqing, which are mainly vertical or high-angle structures, are the most developed in the field outcrop. It was observed that the regional structural joint surfaces are straight, penetrating deep and extending long, perpendicularly to the surface layer, or intersecting with the

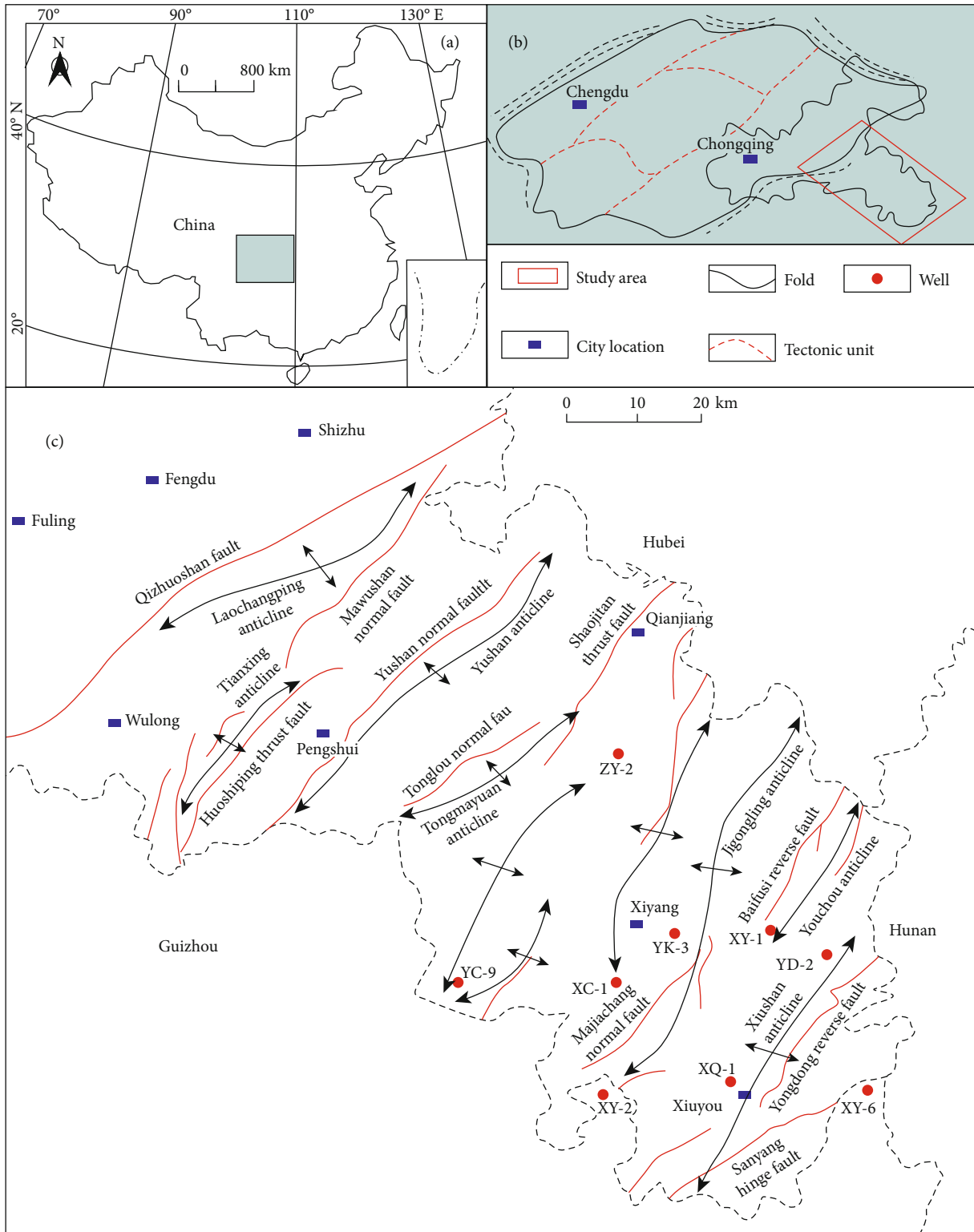


FIGURE 1: Distribution map of folds and fault systems in the target layer of southeastern Chongqing.

rock surface at a large angle [29–32]. The high-angle shear fractures on the outcrop are characterized by multistage fractures cutting each other in the plane, extending long in the longitudinal direction, and often cutting through the rock strata. Additionally, the same group of fractures showed

good equidistance (Figure 2(a)). According to the relationship between fractures and shale layers, mainly two types of shear fractures exist in the Longmaxi and Niutitang Formations in southeastern Chongqing, the high-angle through layer fractures, which are approximately perpendicular to



FIGURE 2: Shale fracture development characteristics in the target layer of southeastern Chongqing.

the bedding plane, and the low-angle slip fractures, which are approximately parallel to the bedding plane or the tensile fractures formed by the locally derived tensile stress under the compressive stress environment.

It was observed that the high-angle shear fractures on the core have straight fracture surfaces, small fracture spacings, and high fracture development degrees, and the same group of fractures showed similar spacings, and the fractures of different groups cut each other. The openings of high-angle shear fractures, which are often filled with quartz, calcite, pyrite, and other minerals, changed significantly, and the other fractures showed smaller openings and higher filling degrees (Figures 2(d) and 2(c)).

The fracture surface of the low-angle slippage fracture is not smooth and is often filled with quartz, calcite, and other minerals (Figure 2(e)), and on the fracture surface, there are scratches and steps. Additionally, the developed tension fractures in the target layer in the study area were mainly formed under the influence of the compression background and sometimes appeared simultaneously with the conjugate shear fractures. Tension fractures are mainly distributed above the neutral fold planes, and most of them are located in the hinge area. In the Niutitang Formation shale in southeastern Chongqing, the degree of opening of the fractures,

which changes significantly, is large. Additionally, it was observed that the fracture surface, which is often filled with quartz, calcite, and other minerals and has a short fracture extension length (Figure 2(f)), is not straight.

4.1.2. Diagenetic Fracture. This type of structure is defined as a dilatational or tensile fracture with a decrease in the total volume of the rock. Diagenetic fractures are a type of near-horizontal fractures caused by pressure solution, compaction, and pressure release [33–35]. These fractures, which are developed in the outcrop shale of the Longmaxi Formation, are predominantly horizontal foliation fractures and bedding slip joints. The bedding structure of shale with foliate or lamellar bedding is the weakest mechanical structural plane, and its antiweathering ability is weak. Owing to weathering, leaching, and denudation for a long time, it is easily peeled off or it slides along the bedding plane and the existing fracture surface, forming a large number of bedding joints and layer slip joints (Figure 2(b)). The Lower Paleozoic shales are usually composed of a series of thin shales formed under strong hydrodynamic conditions. Mechanical compaction and water loss shrinkage bring about the shale fracture along the foliation, forming foliation fractures (Figures 2(g) and 2(h)).

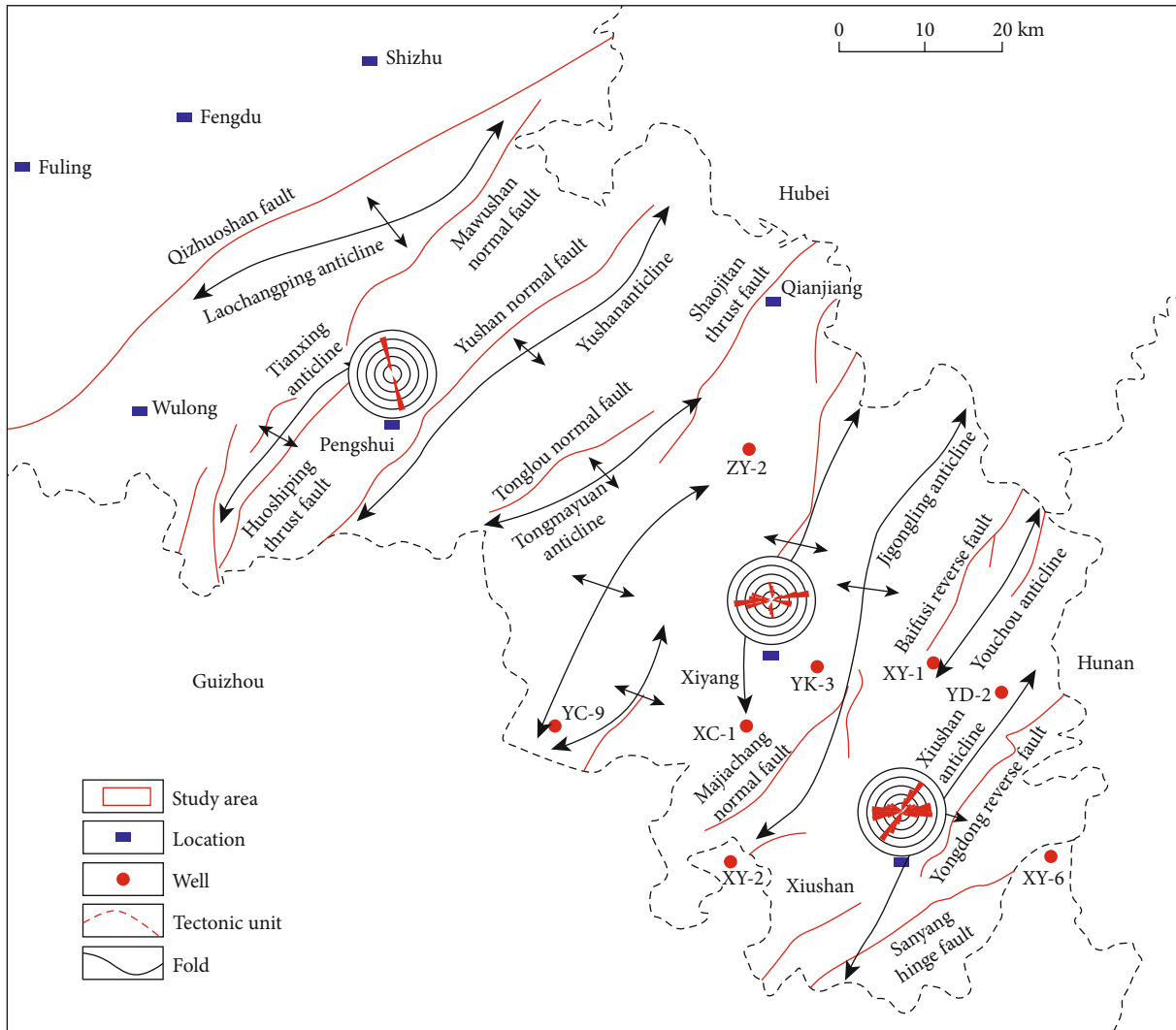


FIGURE 3: Strike rose diagrams of black shale fractures in the target layer of southeastern Chongqing.

4.1.3. *Abnormally High-Pressure Fractures.* Abnormal high-pressure fractures are mainly drainage fractures, which are converted from a principal stress to tensile stress under the action of extremely high fluid pressure, resulting in fracture clusters with bending directions and different openings. Abnormally high shale pressures primarily result from three aspects: (1) the abnormal gas pressure formed in the process of organic matter evolution, which is related to organic matter content and is controlled by the thermal evolution degree of organic matter [36, 37]; (2) the black thick-layered organic matter-rich shale, which is under compaction due to rapid sedimentation [38]; or (3) the closed state, within which an abnormally high fluid pressure is generated owing to the combination of the dehydration and hydrothermal pressurization of clay minerals. When the abnormally high fluid pressure exceeds the rock fracture strength, fractures are formed. Abnormally high-pressure fractures are usually distributed in areas with relatively high organic matter content, where the maturity of the organic matter is also relatively high. These fractures are characterized by an irregular shape,

a short extension, and their occurrence varies significantly (Figure 2(i)).

4.2. *Characterization of Fracture Parameters*

4.2.1. *System and Occurrence of Fracture.* According to the rose diagram of the fracture strike corresponding to the target layer in the survey area, there are mainly three stages of structural fractures in southeastern Chongqing. These are the near EW, NE (strike N30°E), and near SN directions (Figure 3). The plane-cutting relationship of the fractures on the outcrop shows that a group of structural fractures in the near SN direction limit the two groups of fractures to the near EW and NE directions, indicating that the group of structural fractures close to the near SN direction was formed first. Simultaneously, a group of structural fractures in the near EW direction limit the expansion of a group of structural fractures in the NE direction, indicating that the group of fractures in the near EW direction formed earlier than the group of fractures in the NE

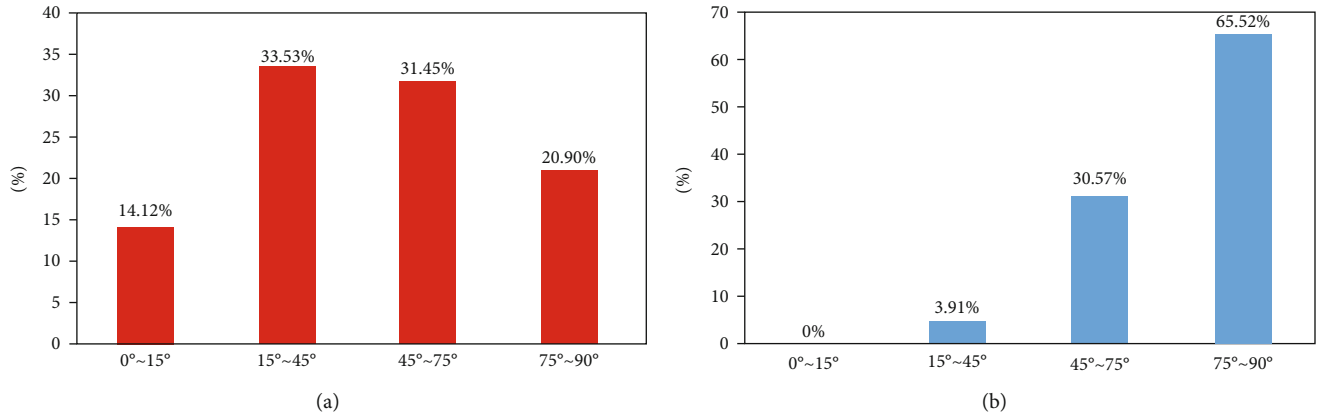


FIGURE 4: Distribution frequency diagram of shale fracture dip angle in the target layer, i.e., Longmaxi Formation (a) and Niutitang Formation (b), of southeastern Chongqing.

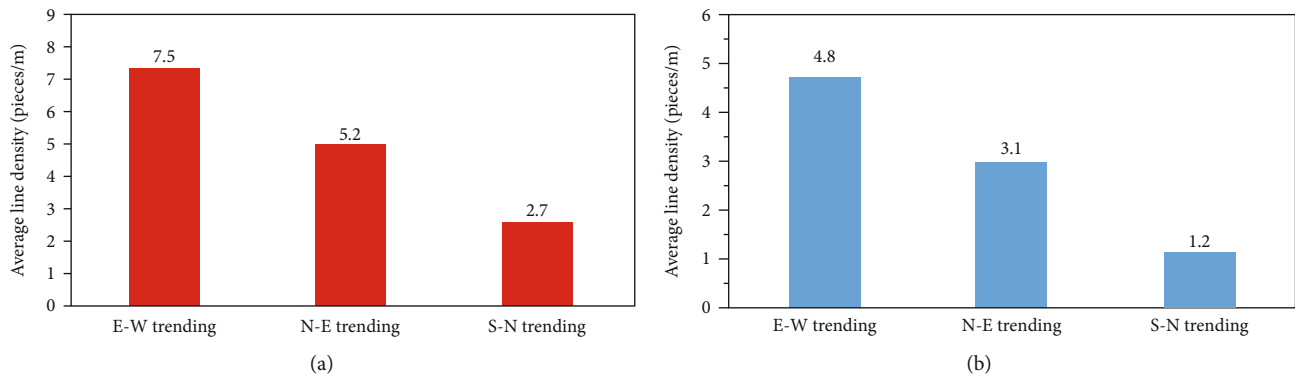


FIGURE 5: Shale fracture density distribution map in the target layer, i.e., Longmaxi Formation (a) and Niutitang Formation (b), of southeastern Chongqing.

direction; i.e., the fractures trending in the NE direction were formed last. In the Youyang survey area, structural fractures in the near EW and near SN directions showed distinct development advantages, while in the Xiushan survey area, those in the near EW and NE directions showed distinct development advantages (Figure 3).

According to the statistical results obtained following the measurement of the fracture dip angles in the study area, most of the fractures in the Longmaxi Formation shale are predominantly inclined with low angles (15°-45°) and high angles (45°-75°), and only a few are vertical and horizontal (i.e., inclined at 75°-90° and 0°-15°, respectively). It was observed that 20.90, 31.45, 33.53, and 14.12% of these fractures are inclined at angles in the ranges 75°-90°, 45°-75°, 15°-45°, and 0°-15°, respectively, as shown in Figure 4(a). It was also observed that vertical fractures, high-angle cutting fractures, and low-angle oblique fractures are developed in the Niutitang Formation shale, while horizontal fractures are rare. Among these fractures, 65.52 and 49.4% (approximately half of the total) are inclined at angles in the ranges 75°-90° and >81°, respectively. Additionally, a total of 30.57 and 3.9% of these fractures are inclined at angles in the ranges 45°-75° and 15°-45°, respectively, while horizontal fractures (0°-15°) are absent. These results show that the

shale fractures of the Niutitang Formation are mainly high-angle fractures, followed by oblique fractures, and low-angle fractures, while horizontal fractures are not developed (Figure 4(b)).

4.2.2. Fracture Density. The calculation method of fracture density can be seen previous study in detail [39]. It was observed that the fracture densities corresponding to the three dominant directions of the target layer in the study area are different. The average linear density of the fractures, i.e., the number of fractures in per unit area, in the near SN, NE, and near EW directions in the Longmaxi Formation is approximately 2.7, 5.2, and 7.5 pieces/m, respectively (Figure 5(a)). For the Niutitang Formation, they are approximately 1.2, 3.1, and 4.8 pieces/m, respectively (Figure 5(b)). This finding indicates that the fractures in the shale of the target layer in southeastern Chongqing are mainly NE and near EW fractures, with the most developed and least developed being the near EW and near SN fractures, respectively. Moreover, the Longmaxi Formation was found to be better than the Niutitang Formation. The two sets of shale fractures in southern Chongqing, which are more significant in terms of shale gas enrichment and development, are greater in number than those in conventional sandstone reservoirs.

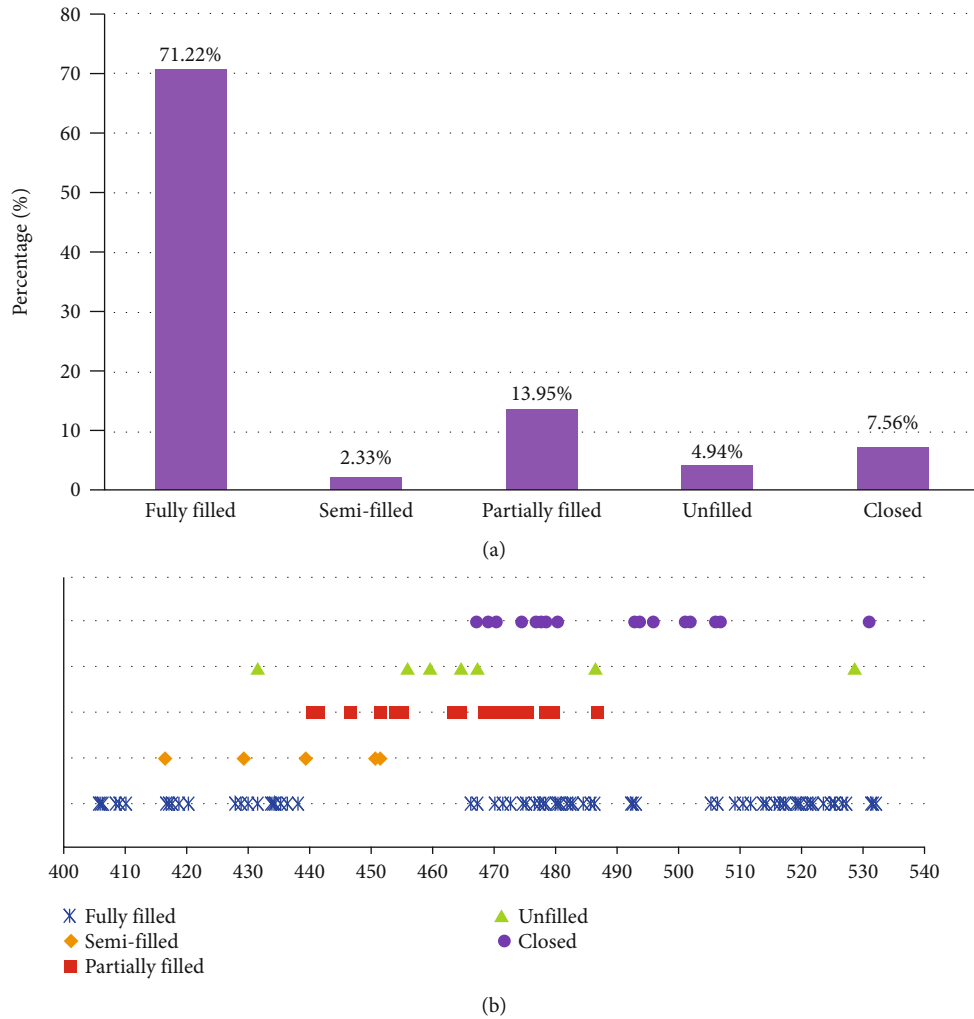


FIGURE 6: Statistics of fracture filling in the target layer of southeastern Chongqing.

4.2.3. *Fracture Filling.* The fracture surface morphologies of approximately 160 m long cores from Well Yucan-8 in the Longmaxi Formation and Well Xiuqian-1 in the Niutitang Formation were observed and described in detail. Overall, it was observed that more than 87% of the fractures are filled, approximately 5% are unfilled, and approximately 8% are closed. Most of the filling joints are fully filled, while a few are partially filled or semifilled (Figure 6(a)). The filling mineral is mainly calcite, and occasionally, it is pyrite (Figure 6(b)). Vertically, taking Well Xiuqian-1 as an example, the length of the observed core was found to be approximately 130 m, and it was observed that the fully filled fractures are generally developed in other depth sections except for the well section at a depth range of 440–460 m. Some of the filled fractures were mainly observed in the well section at a depth range of 440–480 m. The unfilled fractures were found to be concentrated within a depth range of 455–465 m, and the closed fractures were observed at two well depth ranges of 460–480 and 490–505 m. Additionally, semi-filled fractures were scattered at depths of 415, 429, 439, and 450 m (Figure 7). Overall, the shale fracture filling degree corresponding to Well Xiuqian-1 in the Niutitang Formation,

which has adverse effects on shale gas reservoirs and seepage, is relatively high.

5. Discussion

The shale reservoirs of the Longmaxi and Niutitang Formations in southeastern Chongqing have strong heterogeneity, and the degree of fracture development in the different regions of the study area is very different [40, 41]. Based on mineral composition, TOC content, and layer thickness, the factors that influence shale fracture development in the Longmaxi and Niutitang Formations in southeastern Chongqing were comprehensively studied.

5.1. *Mineral Composition.* Mineral composition can affect the degree of the fracture development; i.e., both carbonates and quartz contribute to the increase of crack density. According to the results of the XRD analysis of the 789–860 m section of Well Yucan-8, the brittle mineral in this section is predominantly quartz, and based on quartz content and fracture statistics data, the relationship between fracture development in Well Yucan-8 in the Longmaxi Formation shale and quartz

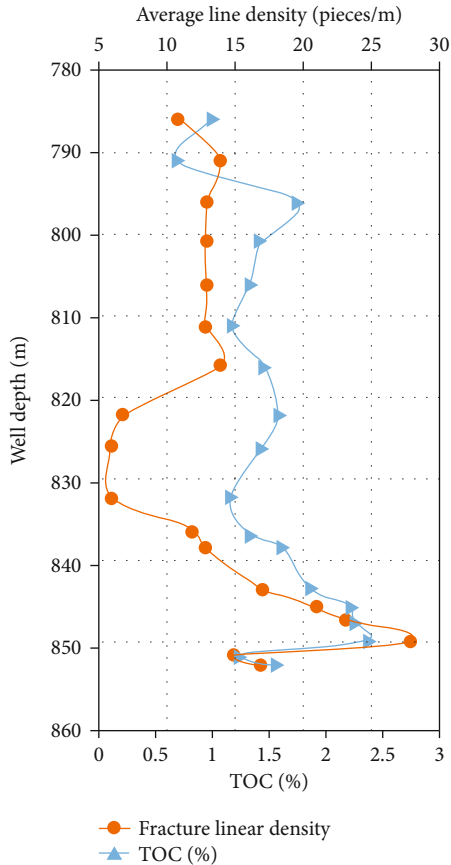


FIGURE 7: Relationship between TOC and shale fracture development in Well Yucan-7 of the Longmaxi Formation in southeastern Chongqing.

content was obtained (Figure 8). Thus, it is observed that there is a certain degree of positive correlation between quartz content and fracture linear density; i.e., the higher the quartz content, the greater the fracture linear density.

5.2. Organic Matter Content. The influence of TOC on fracture development is mainly reflected by the distribution of organic matter [32], the consumption of organic components and water for kerogen hydrocarbon generation, and hydrocarbon generation pressurization. The higher the organic matter content, the more obvious the banding and the easier it is for micro fractures to develop in or around the organic matter band. According to the statistical results corresponding to the relationship between organic carbon content and the degree of shale gas development in various regions of the world, the higher the organic carbon content, the greater the number of micro pores in the shale matrix, and the greater the number of micro fractures formed, the higher the number of shale gas reservoirs [32].

Based on statistics corresponding to the fracture linear density and TOC of Well Yucan-7 in the study area (Figure 7), the organic matter content in the 786–836 m well section is below 1.6% and has little influence on fracture density and the fracture development. Additionally, low TOC contents, which showed no obvious change trend, were

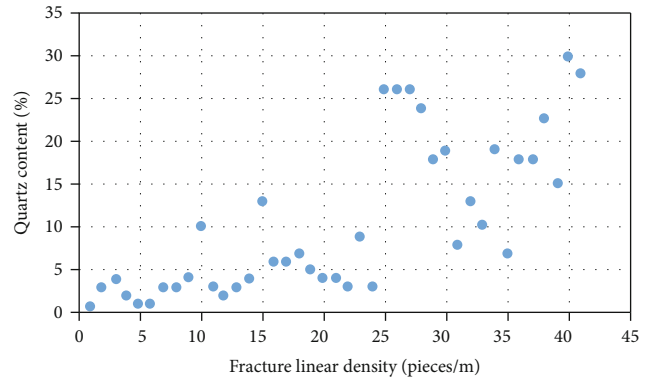


FIGURE 8: Relationship between shale fracture development and quartz content in Well Yucan-8 of the Longmaxi Formation in southeastern Chongqing.

observed. However, within the 838–849 m well section, TOC and fracture density showed a distinct correlation. It was observed that changes in organic matter contents in the range 1.6–2.5% have a significant effect on fracture density. Specifically, when TOC changes from 1.63 to 2.38%, the fracture linear density increases from 13 to 28 pieces/m.

This is primarily due to the high sea level that characterized the beginning of the shale deposition. Nutrient-rich upwelling carried the remains of animals and plants from the deep sea, making the biological yield high and forming the still water deep slope basin facies with a strong reduction environment. It was observed that the organic matter is well preserved and is enriched. The sediments primarily consisted of semipelagic ooze (from shallow water shelf) and biological skeleton debris. Siliceous organisms, such as radiolarians, were found to be buried, an observation that is closely related to the high organic matter content. However, marine organic matter-rich shales with high organic carbon contents and high silicon contents are prone to fracture. Thus, a positive correlation was observed between organic carbon content and shale fracture development. For the Longmaxi Formation shale, at TOC values < 1.6%, the relationship between the fracture development degree and organic carbon content is not distinct. However, when TOC ranges between 1.6 and 2.5%, the relationship between the fracture development degree and organic carbon content is distinct. Thus, the overall change trend is consistent, and the degree of fracture development is good.

5.3. Formation Thickness. Generally, thin-layer rocks are more prone to fracturing than their thicker counterparts, and fracture spacing is positively correlated with the thickness of the formation [42]. Previous studies have shown that the smaller the stratum thickness, the higher the degree of fracture development under the same geomechanical environment. According to statistics corresponding to fracture development in Well Yushen-1 in the Longmaxi Formation shale, the fracture development degree is negatively correlated with formation thickness; i.e., the degree of fracture development decreases as the formation thickness increases (Figure 9).

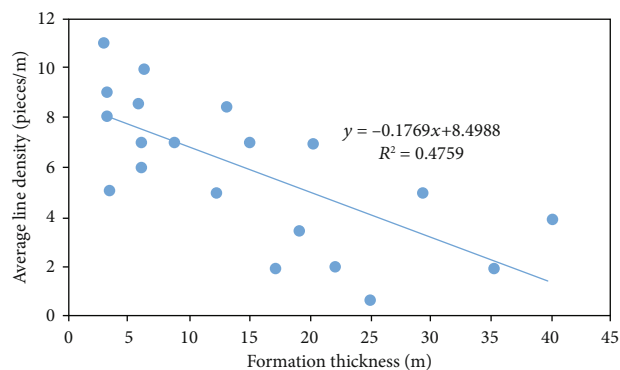


FIGURE 9: Relationship between shale fracture development and stratum thickness in the Longmaxi Formation in Yushenjing District, southeastern Chongqing.

6. Conclusions

The fractures in the Longmaxi and Niutitang Formation shales can be divided into structural, diagenetic, and abnormal high-pressure fractures. Additionally, the structural fractures can be further divided into tensile and shear fractures depending on their mechanical properties. The shear fractures can be classified as high-angle through layer fractures and low-angle slip fractures based on their relationship with the shale layers. However, diagenetic fractures can be divided into horizontal foliation fractures, bedding plane slip joints, and high-angle shrinkage fractures depending on their relationship with the shale layers.

The fractures in the Longmaxi Formation shale in southeastern Chongqing are predominantly low-angle and high-angle inclined fractures that are partially vertical or horizontal. In the Niutitang Formation shale, they are predominantly high-angle fractures, followed by oblique fractures, and a few low-angle fractures, with horizontal fractures absent.

Furthermore, it was also observed that the fractures in the Longmaxi and Niutitang Formations in southeastern Chongqing are predominantly micro fractures with small fracture openings. The underground opening of shale reservoirs restored to underground confining pressure is mainly in the range 0–350 μm . Compared with shale matrix pores, it was observed that the reservoir effect of fractures is relatively small and primarily improves the seepage of ultralow-permeability reservoirs. Additionally, high-angle macro structural fractures are the main seepage fractures of the target layer.

The results obtained showed that the degree of fracture development is positively correlated with the brittle mineral and organic carbon content of the rocks. Additionally, higher quartz contents resulted in a greater fracture linear density, and higher organic carbon contents resulted in an increase in the number of the micro pores and micro fractures formed in the shale matrix. Besides, the fracture development degree is negatively correlated with formation thickness; i.e., the degree of fracture development decreases as the formation thickness increases.

Data Availability

The main data used to support the study is available within the article. If readers are interested in the data, they can communicate with the corresponding author and obtain these data by email.

Conflicts of Interest

The authors declare that they have no conflicts of interest.

Acknowledgments

We greatly thank all the teachers in Chongqing University of Science and Technology for the analysis and guidance of experimental samples. This work was financially supported by the National Natural Science Foundation of China (Grant Numbers 42072140 and 41502150), Natural Science Foundation Project of Chongqing, Chongqing Science and Technology Commission (CQ CSTC) (Grant Numbers cstc2018jcyjAX0523 and cstc2020jcyj), the Performance Incentive and Guidance Project for Scientific Research Institutions in Chongqing (Grant Number cstc2020jxjX0002), Special Project of performance incentive and guidance for scientific research institutions in Chongqing (Grant Number cstc2019jxj190001), and the Preproject of Chongqing Shale Gas Exploration and Development Company Limited (Grant Number CYS-FW-2020-0047). We thank our scientific research team for their help and guidance in the field investigation.

References

- [1] B. E. Law and J. B. Curtis, "Introduction to unconventional petroleum systems," *American Association of Petroleum Geologists Bulletin*, vol. 86, no. 11, pp. 1851–1852, 2002.
- [2] X. Wang, J. Hou, S. Li et al., "Insight into the nanoscale pore structure of organic-rich shales in the Bakken Formation, USA," *Journal of Petroleum Science and Engineering*, vol. 191, p. 107182, 2020.
- [3] C. Zou, Z. Yang, S. Tao et al., "Continuous hydrocarbon accumulation over a large area as a distinguishing characteristic of unconventional petroleum: the Ordos Basin, North-Central China," *Earth-Science Reviews*, vol. 126, pp. 358–369, 2013.
- [4] C. Zou, Z. Yang, J. Dai et al., "The characteristics and significance of conventional and unconventional Sinian-Silurian gas systems in the Sichuan Basin, central China," *Marine and Petroleum Geology*, vol. 64, pp. 386–402, 2015.
- [5] J. Qiao, R. Littke, L. Zieger, Z. Jiang, and R. Fink, "Controls on gas storage characteristics of Upper Paleozoic shales from the southeastern Ordos Basin," *Marine and Petroleum Geology*, vol. 117, article 104377, 2020.
- [6] J. Qiao, A. Baniasad, L. Zieger, C. Zhang, Q. Luo, and R. Littke, "Paleo-depositional environment, origin and characteristics of organic matter of the Triassic Chang 7 Member of the Yan-chang Formation throughout the mid- western part of the Ordos Basin, China," *International Journal of Coal Geology*, vol. 237, article 103636, 2021.
- [7] J. F. W. Gale, R. M. Reed, and J. Holder, "Natural fractures in the Barnett Shale and their importance for hydraulic fracture treatments," *AAPG Bulletin*, vol. 91, no. 4, pp. 603–622, 2007.

- [8] Y. Cho, O. G. Apaydin, and E. Ozkan, "Pressure-dependent natural-fracture permeability in shale and its effect on shale-gas well production," *SPE Reservoir Evaluation & Engineering*, vol. 16, no. 2, pp. 216–228, 2013.
- [9] J. F. Gale, S. E. Laubach, J. E. Olson, P. Eichhubl, and A. Fall, "Natural fractures in shale: a review and new observations," *AAPG Bulletin*, vol. 98, no. 11, pp. 2165–2216, 2014.
- [10] S. Zhang, "Tectonic stress field modeling and fracture prediction in T3x~(2-4) strata in Xiaoquan-Xinchang area, western Sichuan depression," *Oil & Gas Geology*, vol. 25, no. 1, pp. 70–74, 2004.
- [11] W. Zeng, W. Ding, J. Zhang et al., "Fracture development in Paleozoic shale of Chongqing area (South China). Part two: numerical simulation of tectonic stress field and prediction of fractures distribution," *Journal of Asian Earth Sciences*, vol. 75, pp. 267–279, 2013.
- [12] K. Jiu, W. Ding, and Y. Li, "Structural features in northern Guizhou area and reservoir fracture of lower Cambrian shale gas," *Natural Gas Geoscience*, vol. 23, no. 4, pp. 797–803, 2012.
- [13] R. Wang, W. Ding, Y. Zhang et al., "Analysis of developmental characteristics and dominant factors of fractures in Lower Cambrian marine shale reservoirs: a case study of Niutitang formation in Cen'gong block, southern China," *Journal of Petroleum Science and Engineering*, vol. 138, pp. 31–49, 2016.
- [14] R. Wang, Z. Hu, C. Sun et al., "Comparative analysis of shale reservoir characteristics in the Wufeng-Longmaxi (O3w-S11) and Niutitang (E1n) formations: a case study of the Wells JY1 and TX1 in southeastern Sichuan Basin and its periphery, SW China," *Interpretation*, vol. 6, no. 4, pp. SN31–SN45, 2018.
- [15] Y. Li, W. Sun, X. W. Liu, D. W. Zhang, Y. C. Wang, and Z. Y. Liu, "Study of the relationship between fractures and highly productive shale gas zones, Longmaxi Formation, Jiaoshiba area in eastern Sichuan," *Petroleum Science*, vol. 15, no. 3, pp. 498–509, 2018.
- [16] S. Han, J. Zhang, C. Wang, and X. Tang, "Elemental geochemistry of lower Silurian Longmaxi shale in southeast Sichuan Basin, South China: Constraints for Paleoenvironment," *Geological Journal*, vol. 53, no. 4, pp. 1458–1464, 2018.
- [17] C. Ou and C. Li, "3D discrete network modeling of shale bedding fractures based on lithofacies characterization," *Petroleum Exploration and Development*, vol. 44, no. 2, pp. 336–345, 2017.
- [18] C. Peng, "Mechanism of interaction between hydraulic fractures and weak plane in layered shale," *Petroleum Drilling Techniques*, vol. 84, no. 3, pp. 181–196, 2014.
- [19] T. Guo and H. Zhang, "Formation and enrichment mode of Jiaoshiba shale gas field, Sichuan Basin," *Petroleum Exploration and Development*, vol. 41, no. 1, pp. 31–40, 2014.
- [20] S. Chen, Y. Zhu, H. Wang, H. Liu, W. Wei, and J. Fang, "Shale gas reservoir characterisation: a typical case in the southern Sichuan Basin of China," *Energy*, vol. 36, no. 11, pp. 6609–6616, 2011.
- [21] K. Zhang, C. Jia, Y. Song et al., "Analysis of Lower Cambrian shale gas composition, source and accumulation pattern in different tectonic backgrounds: a case study of Weiyuan block in the upper Yangtze region and Xiuyu Basin in the Lower Yangtze region," *Fuel*, vol. 263, article 115978, 2020.
- [22] K. Zhang, J. Peng, W. Liu et al., "The role of deep geofluids in the enrichment of sedimentary organic matter: a case study of the Late Ordovician-Early Silurian in the upper Yangtze region and early Cambrian in the lower Yangtze region, south China," *Geofluids*, vol. 2020, Article ID 8868638, 12 pages, 2020.
- [23] Y. Zhang, S. Dong, J. Li, and W. Shi, "Mesozoic multi-directional compressional tectonics and formation-reformation of Sichuan Basin," *Geology in China*, vol. 38, no. 2, pp. 233–250, 2011.
- [24] K. Zhang, J. Peng, X. Wang et al., "Effect of organic maturity on shale gas genesis and pores development: a case study on marine shale in the upper Yangtze region, South China," *Open Geosciences*, vol. 12, no. 1, pp. 1617–1629, 2020.
- [25] Y. Wang, D. Dong, X. Li, J. Huang, S. Wang, and W. Wu, "Stratigraphic sequence and sedimentary characteristics of Lower Silurian Longmaxi Formation in Sichuan Basin and its peripheral areas," *Natural Gas Industry B*, vol. 2, no. 2-3, pp. 222–232, 2015.
- [26] Q. Li, S. Shao, and X. Xia, "Characterization and geological model of fractured shale reservoir in eastern China," *Egu General Assembly*, vol. 14, p. 6672, 2012.
- [27] W. Li, H. Yu, and H. Deng, "Stratigraphic division and correlation and sedimentary characteristics of the Cambrian in central-southern Sichuan Basin," *Petroleum Exploration and Development*, vol. 39, no. 6, pp. 725–735, 2012.
- [28] L. Wei, R. Fan, P. Jia et al., "Sequence stratigraphy and lithofacies paleogeography of the Middle-Upper Cambrian Xixiangchi Group in the Sichuan Basin and its adjacent area, SW China," *Petroleum Exploration and Development*, vol. 46, no. 2, pp. 238–252, 2019.
- [29] B. Marc-André, M. Yan, and D. Stead, "The role of tectonic damage and brittle rock fracture in the development of large rock slope failures," *Geomorphology*, vol. 103, no. 1, pp. 30–49, 2009.
- [30] Z. Ji, J. Dai, B. Wang, and H. Liu, "Multi-parameter quantitative calculation model for tectonic fracture," *Journal of China University of Petroleum (Edition of Natural Ence)*, vol. 34, no. 1, pp. 24–28, 2010.
- [31] L. Rivera and H. Kanamori, "Spatial heterogeneity of tectonic stress and friction in the crust," *Geophysical Research Letters*, vol. 29, no. 6, pp. 12-1–12-4, 2002.
- [32] W. Zeng, J. Zhang, W. Ding et al., "Fracture development in paleozoic shale of Chongqing area (South China). Part one: fracture characteristics and comparative analysis of main controlling factors," *Journal of Asian Earth Sciences*, vol. 75, no. 5, pp. 251–266, 2013.
- [33] D. Li, W. Jiao, F. Yue, X. Xiang, and L. Pan, "Natural fractures and their effects on reservoir reconstruction in Lower Cambrian shale, southeast Chongqing, China," *Energy Exploration & Exploitation*, vol. 33, no. 6, pp. 769–783, 2015.
- [34] R. Marrett and S. E. Laubach, "Diagenetic controls on fracture permeability and sealing," *International Journal of Rock Mechanics and Mining Sciences*, vol. 34, no. 3-4, pp. 204.e1–204.e11, 1997.
- [35] O. Abiola and R. Mileva, "Diagenetic influence on fracture conductivity in tight shale and CO2 sequestration," *Energy Procedia*, vol. 63, pp. 5021–5031, 2014.
- [36] L. Zeng, W. Lyu, J. Li et al., "Natural fractures and their influence on shale gas enrichment in Sichuan Basin, China," *Journal of Natural Gas Science and Engineering*, vol. 30, pp. 1–9, 2016.
- [37] Y. Feng, W. Jiao, and S. Guo, "Controlling factors of fracture distribution of shale in Lower Cambrian Niutitang Formation in southeast Chongqing," *Coal Geology & Exploration*, vol. 43, no. 6, pp. 39–44, 2015.

- [38] J. Tremosa, H. Gailhanou, C. Chiaberge et al., “Effects of smectite dehydration and illitisation on overpressures in sedimentary basins: a coupled chemical and thermo-hydro-mechanical modelling approach,” *Marine and Petroleum Geology*, vol. 111, pp. 166–178, 2020.
- [39] D. Liu, C. Zhang, Z. Pan et al., “Natural fractures in carbonate-rich tight oil reservoirs from the Permian Lucaogou Formation, southern Junggar Basin, NW China: insights from fluid inclusion microthermometry and isotopic geochemistry,” *Marine and Petroleum Geology*, vol. 119, article 104500, 2020.
- [40] W. Gao, J. Iqbal, D. Xu, H. Sui, and R. Hu, “Effect of brittle mineral size on hydraulic fracture propagation in shale gas reservoir,” *Geofluids*, vol. 2019, Article ID 9147048, 14 pages, 2019.
- [41] P. G. Meredith, “Fracture and failure of brittle polycrystals: an overview,” in *Deformation Processes in Minerals Ceramics & Rocks*, Springer, 1990.
- [42] H. McQuillan, “Small-scale fracture density in asfari formation of southwest Iran and its relation to bed thickness and structural setting,” *AAPG Bulletin*, vol. 12, pp. 2367–2385, 1973.

Research Article

Characteristics and Origin of Methane Adsorption Capacity of Marine, Transitional, and Lacustrine Shales in Sichuan Basin, China

Xianglu Tang¹, Wei Wu², Guanghai Zhong², Zhenxue Jiang¹, Shijie He¹, Xiaoxue Liu¹, Deyu Zhu¹, Zixin Xue¹, Yuru Zhou¹, and Jiajing Yang²

¹State Key Laboratory of Petroleum Resources and Prospecting, China University of Petroleum, Beijing 102249, China

²Shale Gas Research Institute, Southwest Oil & Gas Field Company, PetroChina, Chengdu 610000, China

Correspondence should be addressed to Xianglu Tang; tangxl@cup.edu.cn and Zhenxue Jiang; zhenxue_jiang@sina.com

Received 9 November 2020; Revised 27 November 2020; Accepted 8 April 2021; Published 21 April 2021

Academic Editor: Reza Rezaee

Copyright © 2021 Xianglu Tang et al. This is an open access article distributed under the Creative Commons Attribution License, which permits unrestricted use, distribution, and reproduction in any medium, provided the original work is properly cited.

Adsorbed gas is an important component of shale gas. The methane adsorption capacity of shale determines the composition of shale gas. In this study, the methane adsorption capacity of marine, transitional, and lacustrine shales in the Sichuan Basin was analyzed through its isothermal adsorption, mineral composition, water content, etc. The results show that the methane adsorption capacity of marine (Qiongzhusi Formation and Longmaxi Formation), transitional (Longtan Formation), and lacustrine (Xujiahe Formation and Ziliujing Formation) shales is significantly different. The Longtan Formation has the strongest methane adsorption capacity. This is primarily related to its high organic matter and organic matter type III content. The methane adsorption capacity of the lacustrine shale was the weakest. This is primarily related to the low thermal evolution degree and the high content of water-bearing clay minerals. Smectite has the highest methane adsorption capacity of the clay minerals, due to its crystal structure. The water content has a significant effect on methane adsorption largely because water molecules occupy the adsorption site. Additionally, the temperature and pressure in a specific range significantly affect methane adsorption capacity.

1. Introduction

As a clean fossil resource, natural gas has always been an important energy source for the world's industrial and economic development. As one of the important types of natural gas, shale gas is an abundant resource, and the shale revolution has changed the global oil and gas supply [1–3]. North America and China are the primary regions of commercial shale gas development. In 2019, the production of shale gas in the United States reached $7151 \times 10^8 \text{ m}^3$, accounting for 62.0% of the total gas production, the highest production in North America. China's shale gas production reached $154 \times 10^8 \text{ m}^3$ in 2019. The Sichuan Basin is an important petroliferous basin where China's shale gas exploration and development has made the most rapid progress and the earliest commercial development [4, 5].

Shale gas is divided into adsorbed gas, free gas, and dissolved gas. Adsorbed gas and free gas are the primary forms of shale gas [6]. Adsorbed gas is a popular focus of shale gas research, largely because the control factors of adsorbed gas are complex. According to the different adsorption forces, adsorption can be divided into two types: chemical adsorption and physical adsorption. Physical adsorption is VDW (Van der Waals' force) adsorption, which is produced by the interaction force between the adsorbate and adsorbed molecules. It includes the dispersion force, electrostatic force, and induction force. Physical adsorption is the principal type of adsorption for shale gas [7].

Adsorbed gas and free gas codetermine the scale of shale gas accumulation, and the dominant position of the two changes with the accumulation conditions, shale, gas molecules, etc. [8]. The adsorption starts quickly, and the adsorbed gas molecules are then easily desorbed from the

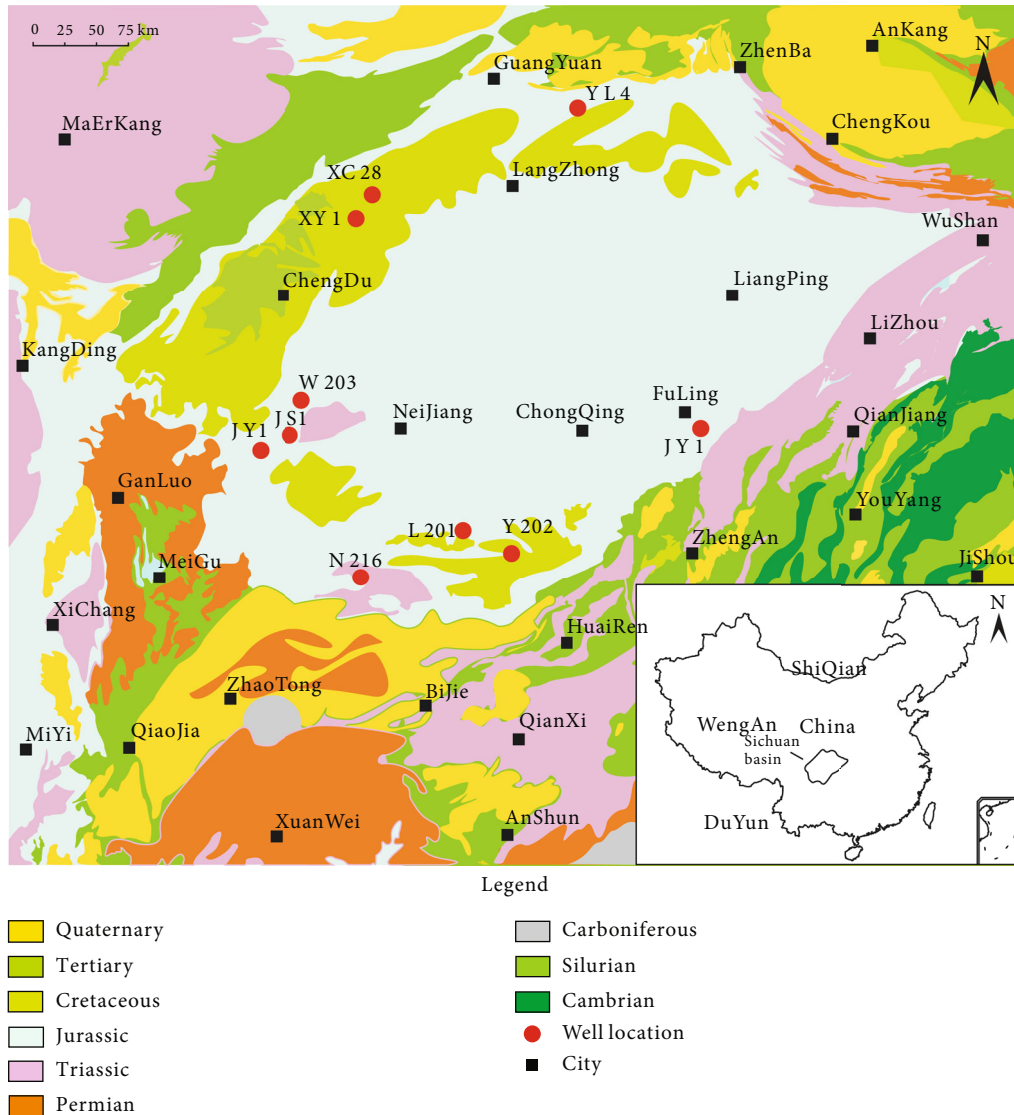


FIGURE 1: Stratum characteristics and sampling locations in the Sichuan Basin. Shales are primarily developed in the Cambrian Qiongzhusi Formation, the Ordovician Wufeng Formation, the Silurian Longmaxi Formation, the Permian Longtan Formation, the Triassic Xujiage Formation, and the Jurassic Ziliujing Formation. A total of 10 wells and 152 samples were selected for analysis.

surface of the shale particles and enter the dissolved and free phases. When the adsorption and desorption speeds are equal, the adsorption reaches a dynamic equilibrium. With the massive generation of natural gas, the internal pressure of the shale rises, causing gaps and discharge, and free gas enters the sandstone to form conventional gas reservoirs [9].

Unlike conventional gas reservoirs, shale has a high content of adsorbed gas [10, 11]. Therefore, it is necessary to conduct a detailed study on the adsorption capacity of shale to determine the various factors that affect its adsorption capacity. The adsorption capacity of shale is primarily related to the organic carbon content, mineral composition, reservoir temperature, formation pressure, shale water content, gas component, shale density, and pore structure [12–16]. When the formation pressure is low, gas adsorption requires a higher binding energy. When the pressure increases, the required binding energy decreases, and the rate of increase

of the gas adsorption capacity declines [17]. Reservoir temperature has a great influence on methane adsorption capacity. The higher the temperature, the lower the methane adsorption capacity. The shale gas in the Upper Jurassic Gordondale Formation in northeastern Canada has a methane adsorption capacity of 0.05–2.00 cm³/g at 60 MPa and 30°C [18]. Additionally, there is a positive relationship between organic carbon content and methane adsorption capacity [19]. While both clay minerals and kerogen adsorb gas, the adsorption capacity of kerogen is stronger than that of clay. Although the adsorption capacity of clay is relatively weak, it still contains a large amount of gas and cannot be ignored [20, 21]. Only when the water content is large (higher than 4%) is the gas adsorption capacity of shale significantly reduced, and the gas adsorption capacity of samples saturated with water was 40% lower than that of dry samples [18].

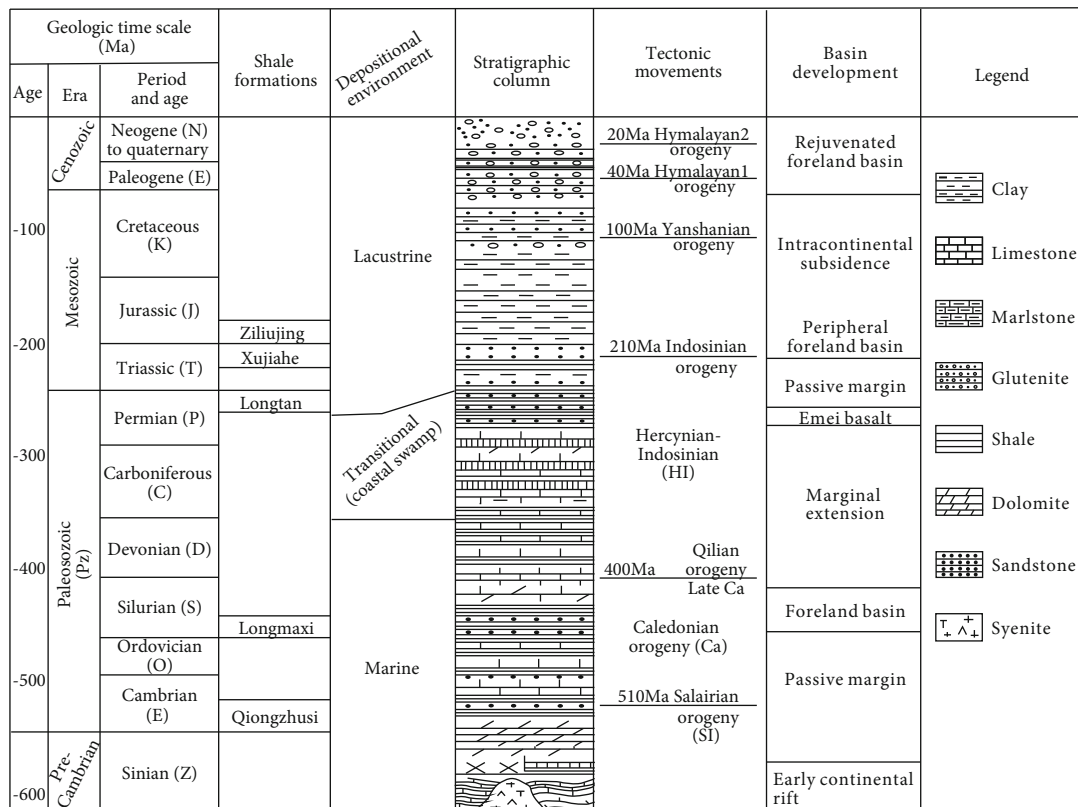


FIGURE 2: Structural evolution and Stratigraphic histogram of Sichuan Basin. The Qiongzhusi Formation, Wufeng Formation, Longmaxi Formation, Longtan Formation, Xujiache Formation, and Ziliujing Formation shales are primarily developed in the Sichuan Basin.

There are multiple sets of shale formations in the Sichuan Basin, China. The occurrence status of marine shale, transitional shale, and lacustrine shale gas is not clear, and the influence of shale reservoir parameters and the external environment on shale gas adsorption capacity has not been determined. The microscopic mechanisms of shale gas adsorption have not been clarified, which hinders the understanding of shale gas formation. Thus, we selected typical marine shale (Qiongzhusi Formation with 27 samples, Longmaxi Formation with 54 samples), transitional shale (Longtan Formation with 37 samples), and lacustrine shale (Xujiache Formation with 19 samples, Ziliujing Formation with 15 samples) in the Sichuan Basin for methane adsorption capacity analysis (Figure 1). In order to guide shale gas exploration and development, the primary controlling factors of methane adsorption capacity were determined through the analysis of shale composition, water content, temperature, and pressure.

2. Geological Setting

The Sichuan Basin is part of the Upper Yangtze Plate and is a petroliferous basin surrounded by complex fold belts. There are six sets of potential shale gas layers in the Sichuan Basin. From old to new, they are the Lower Cambrian Qiongzhusi Formation Shale, Upper Ordovician Wufeng Formation Shale, Lower Silurian Longmaxi Formation Shale, Permian Longtan Formation Shale, Triassic Xujiache Formation Shale, and Lower Jurassic Ziliujing Formation Shale. Among them, the Lower Cambrian, Upper Ordovician, and Lower Silurian

are marine shale, the Permian is transitional shale, and the Upper Triassic and Lower Jurassic are lacustrine shales. These shales have reached the standard of effective gas sources, especially the marine shale, which has many layers and a wide distribution, and have entered a high and overmature stage, with a higher gas generation rate [22–24].

The evolution of the Sichuan Basin goes through five stages, namely, the Presinian basement formation stage, the Sinian–Middle Triassic kratogen basin stage, the Late Triassic foreland basin stage, the Early Jurassic–Late Cretaceous depression basin stage, and the Cenozoic tectonic basin stage (Figure 2). The Sinian–Middle Triassic is dominated by platform-type marine carbonate rocks, interbedded with transitional facies argillaceous sediments, with a thickness of 4000–6000 m. After the Indosinian period, seawater exited the area resulting in a terrestrial environment [25]. The basin began to enter the foreland and depression stages. The Upper Triassic and above strata were dominated by clastic rocks with a thickness of 2000–6000 m.

The Qiongzhusi and Longmaxi Formation shales are a set of deep-water shelf black carbonaceous shales [26]. The Longtan Formation transitional shale is thick and has many layers. The lithology is a set of shale strata with black shale as the foundation and frequent interbeds of siltstone, limestone, and coal seams. The sedimentary facies of the Triassic Xujiache Formation and the Lower Jurassic Ziliujing Formation are large-scale black shale strata of lacustrine deposits, dominated by shore-shallow lake deposits, with a shale thickness of 40–120 m, and the distribution is stable. The primary

TABLE 1: Characteristics of shale in different formation in the Sichuan Basin.

Deposition type	Formation	Number of samples	Organic matter type	TOC (%)	Ro (%)	Quartz (%)	Feldspar (%)	Carbonate minerals (%)	Clay minerals (%)
Lacustrine shale	Ziliujing Formation	13	Mainly type II ₁ and II ₂ , partly type III	0.7–3.9 2.1	1.6–1.8 1.7	15.3–78.8 25.3	4.2–23.4 8.2	1.3–38.6 22.4	21.6–78.1 44.1
	Xujiahe Formation	17	Mainly type II ₁ and II ₂ , partly type III	0.7–5.9 2.2	1.2–1.5 1.3	12.1–53.0 35.9	0.4–6.3 3.9	0.6–67.0 14.2	15.1–57.3 46.0
Transitional shale	Longtan Formation	35	Mainly type III, followed by II ₂	0.5–13.0 4.8	1.3–2.0 1.6	10.9–71.7 28.9	2.0–24.8 11.6	2.3–86.6 21.3	5.1–77.8 38.2
Marine shale	Longmaxi Formation	52	Mainly type I, part II ₁	0.4–5.6 1.8	2.1–2.9 2.4	28.7–76.3 42.2	4.2–19.3 9.8	8.3–33.3 16.7	26.7–53.0 31.3
	Qiongzhusi Formation	25	Mainly I, II ₁ type	0.9–9.9 4.5	3.2–3.6 3.3	26.2–70.6 44.1	3.5–26.1 10.3	2.5–16.5 12.1	23.8–54.5 33.6

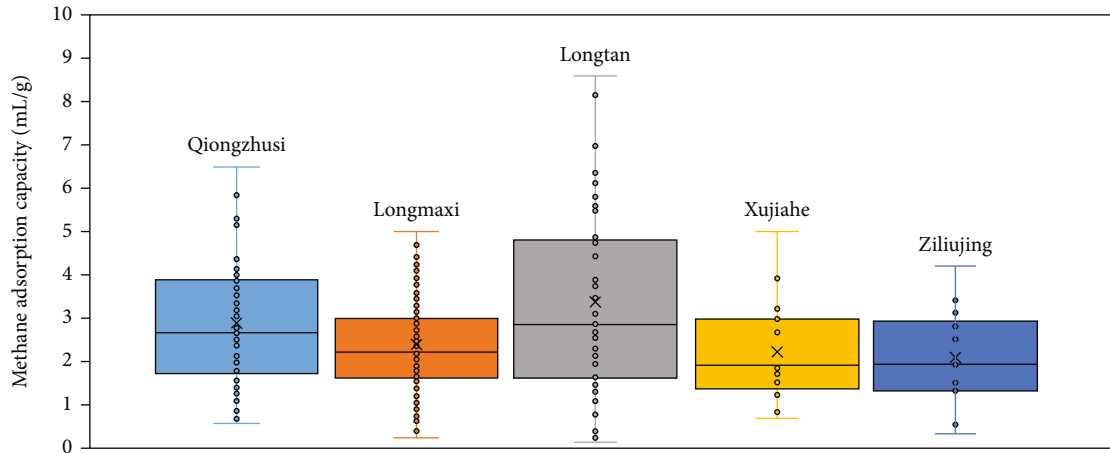


FIGURE 3: Methane adsorption capacity of different types of shale. All 5 sets of shales have high methane adsorption capacity, among which the Longtan Formation Shale has the strongest methane adsorption capacity, followed by the Qiongzhusi Formation and the Longmaxi Formation.

lithology is thin gray-black shale, siltstone, and thin green marl. Climbing ripple bedding, wavy sand bedding, and horizontal bedding are common sedimentary structures.

3. Experimental Methods

3.1. Methane Isothermal Adsorption. The detection equipment used for methane isotherm adsorption is a ZJ466 HP Static III magnetic levitation balance high-pressure gas adsorption isotherm instrument. The resolution of the magnetic levitation balance is 0.01 mg, the environmental condition is 23.5°C, and the maximum test pressure is 30 MPa. First, sample particles of 0.18–0.43 mm were placed in a sealed chamber, and the methane adsorption was tested under different pressures at a constant temperature. The weight change recorded by the magnetic levitation balance was used to obtain the mass of methane gas, calculate the shale adsorption characteristic parameters according to the Langmuir theoretical

model, and draw the adsorption isotherm curve. Five sets of shales with 152 samples were tested. Additionally, each component of shale, including organic matter, quartz, feldspar, carbonate minerals, smectite, illite/smectite, illite, and chlorite, was tested for methane adsorption capacity.

3.2. Organic Matter Content, Type, and Maturity. Organic matter content was tested using a C-S determining apparatus. Dilute hydrochloric acid was used to remove the inorganic carbon in the sample, and then it was burned in high-temperature oxygen to convert the total organic carbon into carbon dioxide. The organic carbon was checked by an infrared detector, and the total organic carbon content was determined. The sample was powdered with a particle size of less than 0.2 mm. The organic matter type was tested using a biological microscope with transmitted light and reflected fluorescence functions to identify the microscopic components of kerogen in shale and calculate the percentage of each

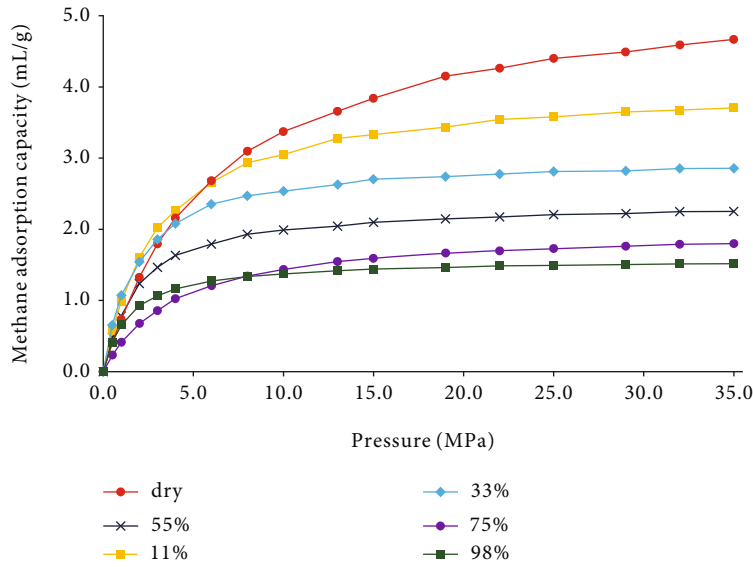


FIGURE 4: Methane adsorption isotherms of shale under different humidity conditions. As the humidity increases, the methane adsorption capacity of the sample decreases.

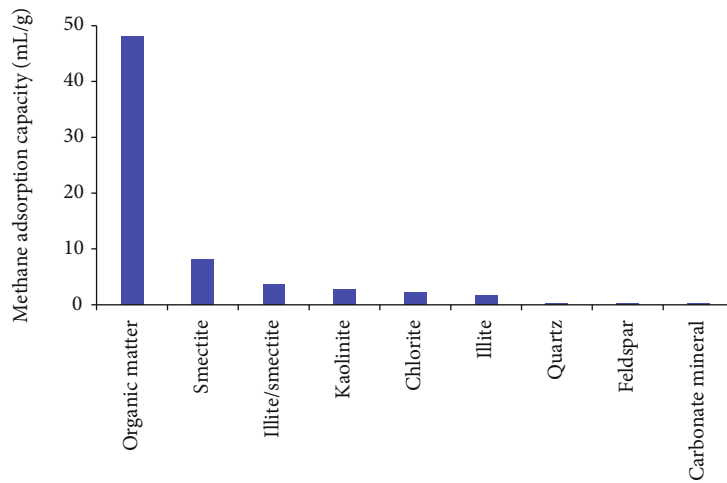


FIGURE 5: Methane adsorption capacity of different components. Organic matter has a significantly higher methane adsorption capacity than other components. Brittle minerals have the lowest adsorption capacity.

microscopic component according to their different weighting coefficients and calculate the type index and divide the kerogen into four types: I, II₁, II₂, and III. The maturity of organic matter was obtained by the vitrinite reflectance method. Vitrinite reflectance refers to the percentage of the intensity of the reflected light from the polished surface of the vitrinite at a wavelength of 546 nm ± 5 nm. It is obtained through the photoelectric effect principle by converting the reflected light intensity into current intensity through a photomultiplier tube and comparing it with the current intensity generated by a standard sample with known reflectivity under the same conditions.

3.3. Mineral Composition. The mineral composition was obtained using an X-ray diffractometer. Each mineral crystal has a specific X-ray diffraction pattern. The content of

a certain mineral in the sample is proportional to the intensity of its diffraction peak. The test voltage was 40kV, the current was 40 mA, the target was Cu, and the measuring angle range was 5°-70°. First, the sample was dried at 60°C, and then the sample was crushed to less than 40 μm. The powder was placed on a frosted glass plate, pressed to shape, and tested.

3.4. Humidity. Shales with different water contents were obtained through a balanced water experiment and were used to analyze the influence of water content on methane adsorption capacity. During the equilibrium water experiment, the moisture content in the sample principally depends on the humidity of the environment. The higher the relative humidity, the higher the water content in the environment, and the higher the water content adsorbed

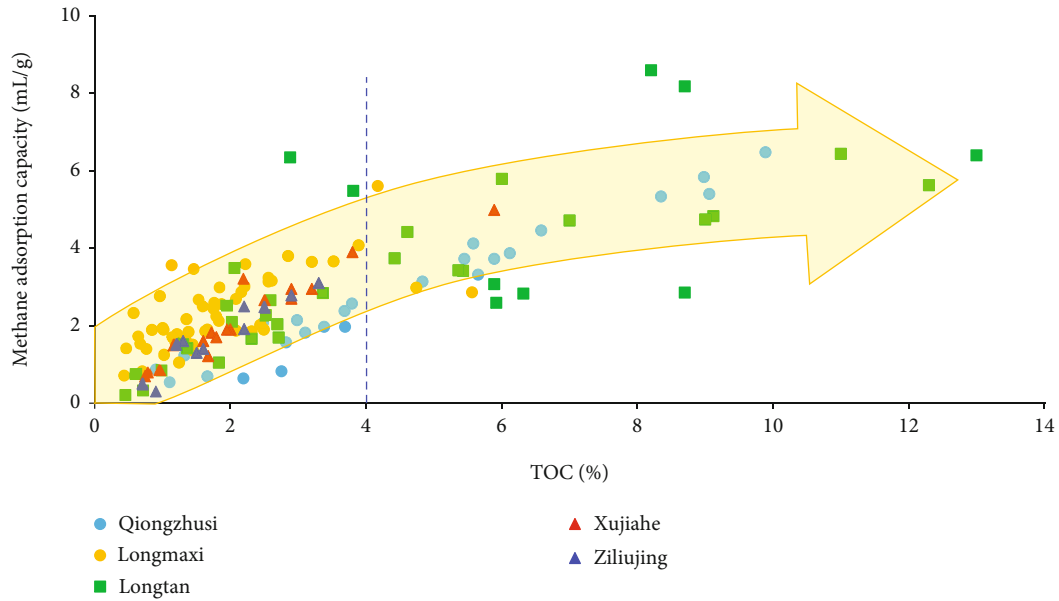


FIGURE 6: Relationship between methane adsorption capacity and TOC of different types of shale. With the increase of TOC content, methane adsorption capacity increases gradually. After TOC > 0.4%, the increase range decreases.

in the sample pores, the higher the water saturation. Conversely, if the relative humidity of the environment is low, the moisture in the sample will also evaporate. Therefore, there is a one-to-one correspondence between the humidity in the environment and the moisture content in the sample. In order to get samples with different degrees of saturation, different solutes were used. In this experiment, five solutes, namely, zinc chloride, magnesium chloride, sodium bromide, sodium chloride, and magnesium sulfate, were selected, corresponding to samples with a humidity of 11%, 33%, 55%, 75%, and 98%, respectively. The temperature of the experiment was 30°C. Shale samples as well as organic matter and single minerals such as smectite, illite, chlorite, and kaolinite in the shale were tested.

4. Results

4.1. Characteristics of Shale. The geochemical characteristics of shale in different strata in the Sichuan Basin are quite different (Table 1). The total organic carbon (TOC) varies widely, ranging from 0.4% to 13.0%. Generally, the Qiongzhusi and Longtan formations have higher TOC values, followed by the Longmaxi Formation, Xujiache Formation, and Ziliujing Formation. The maturity, R_o , is 1.2%–3.6%, and the order of values is usually Qiongzhusi Formation > Longmaxi Formation > Longtan Formation, Xujiache Formation, and Ziliujing Formation. There are obvious differences in the types of organic matter. The marine shales were primarily type I and II₁, the transitional shales were type III, and the lacustrine shales were type II₁ and II₂. The marine shale is dominated by dark shale, and its minerals are primarily quartz, clay, carbonate minerals, and other types of minerals. The clay mineral

content in lacustrine shale is higher, with an average content of over 40%.

4.2. Methane Adsorption Capacity

4.2.1. Methane Adsorption Capacity of Shale under the Same Humidity Conditions. The methane adsorption capacity of the Qiongzhusi Formation is in the range of 1–4 mL/g, with an average of 2.87 mL/g, indicating a high adsorption capacity (Figure 3). The methane adsorption capacity of the Longmaxi Formation is in the range of 1–4 mL/g, with an average of 2.38 mL/g, also indicating a strong adsorption capacity. The methane adsorption capacity of the Longtan Formation is widely distributed, the peak value ranges from 1–4 mL/g, and there are many samples greater than 4 mL/g, with an average of 3.36 mL/g, the strongest adsorption capacity. The range of the methane adsorption capacity of Xujiache Formation shale is 1–3 mL/g, with an average of 2.19 mL/g, indicating that the adsorption capacity of the Xujiache Formation shale is relatively weak. The range of methane adsorption capacity of the Ziliujing group is 1–3 mL/g, with an average of 2.07 mL/g, showing relatively weak adsorption capacity. A comprehensive comparison shows that the Longtan Formation transitional shale has the strongest adsorption capacity, followed by the Qiongzhusi Formation and Longmaxi Formation marine shales, and the Xujiache Formation and Ziliujing Formation lacustrine shale have the weakest adsorption capacity.

4.2.2. Methane Adsorption Capacity of Shale under Different Humidity Conditions. Experiments on the methane adsorption capacity of shale under different levels of humidity, from absolute drying to 98% humidity control, showed the increase in water content reduced the methane adsorption

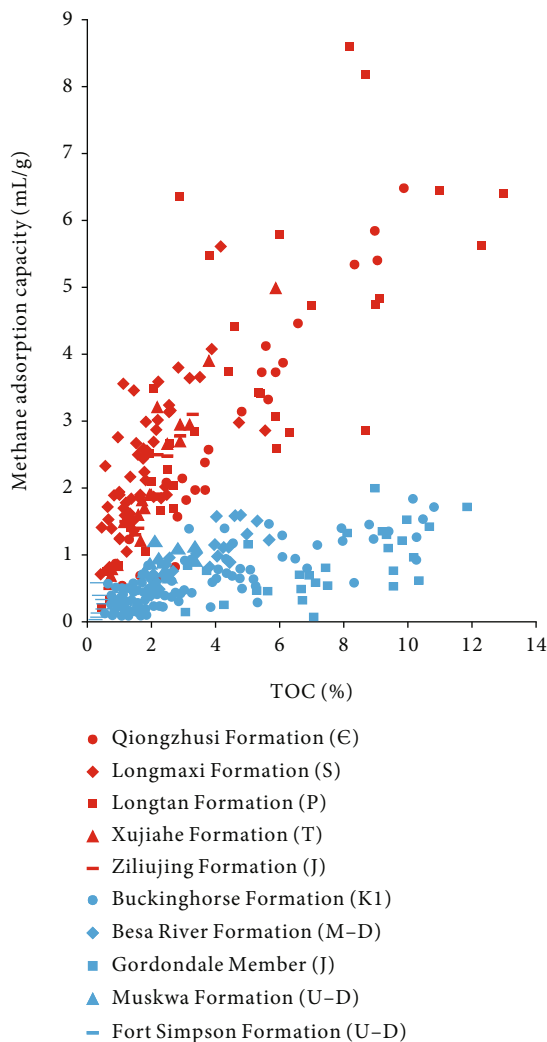


FIGURE 7: Comparison of shale adsorption capacities of Sichuan Basin and North America. The adsorption capacity of 5 sets of shales in Sichuan Basin is higher than that in North America. (Part of data is from Reference [12, 14]). Red points represented shale adsorption capacities of Sichuan Basin, and blue points represented that of North America. Besides, the era of different Formation was labelled in following parentheses.

capacity of shale (Figure 4). When the humidity increases to 98%, the shale adsorption capacity drops from 4.90 mL/g to 1.35 mL/g, and the adsorption capacity of the dry sample drops to 28%.

4.2.3. Methane Adsorption Capacity of Different Shale Components. Testing the methane adsorption capacity of a single component of shale shows that the methane adsorption capacity of different components varies greatly. The adsorption capacity of organic matter was the strongest, reaching 48 mL/g. Among the clay minerals, smectite has the strongest adsorption capacity, followed by illite/smectite, kaolinite, chlorite, and illite. Brittle minerals such as quartz and feldspar have the weakest methane adsorption capacity, with an average of only 0.2 mL/g (Figure 5). Therefore, the difference in methane adsorption capacity of different com-

ponents jointly determines the methane adsorption capacity of shale.

5. Discussion

5.1. Shale Components

5.1.1. Organic Matter Content. The methane adsorption capacity of the five sets of shales shows a significant positive correlation (nonlinear) with organic matter content, but the correlation coefficients of the five sets of shales are different (Figure 6). When $\text{TOC} < 4\%$, the adsorption capacity was positively correlated with organic matter. When $\text{TOC} > 4\%$, the adsorption capacity did not increase significantly with the increase in organic matter, indicating that the adsorption capacity had a certain upper limit. Therefore, the organic carbon content is an important factor in controlling shale gas adsorption. The increase in organic carbon content will improve the methane adsorption capacity of shale for two primary reasons: first, the shale with a higher organic carbon value has a greater gas potential, so it has a higher gas content per unit volume of shale. Second, owing to the characteristics of kerogen, micropores can be developed, the surface is oil-wet, and the adsorption capacity of gaseous hydrocarbons is relatively strong. At the same time, the dissolution of gaseous hydrocarbons in amorphous and structural-matrix bituminites has a nonnegligible contribution [27]. In the five sets of shales, the Qiongzhusi and Longtan formations tend to have higher TOC levels to match their strong shale gas adsorption capacity.

The Sichuan Basin shale has similar adsorption characteristics to the North American shale, and its organic carbon content is positively correlated with methane adsorption capacity [28, 29]. However, the shale in Sichuan shows a stronger methane adsorption capacity. The methane adsorption capacity of shales in Sichuan and shales in North American can be up to three times worse. The Sichuan Basin shale TOC is about 3 times as high as that of the North American shale, which is more favorable for gas adsorption (Figure 7).

This may be related to the type and maturity of organic matter. The organic matter of the Longtan Formation, Xujiahe Formation, and Ziliujing Formation shales in the Sichuan Basin are primarily composed of types II and III, which have strong adsorption capacity. This is because the III kerogen type, relative to the I and II kerogen, has a high content of aromatic hydrocarbons and enhances the adsorption capacity of shale [30]. Additionally, the vitrinite relative to the other ingredients has a stronger adsorption ability, and III kerogen contains a higher concentration of vitrinite, thus, enhancing the adsorption ability of the shale. The Longmaxi and Qiongzhusi shales, of the same organic type as North American shales, are highly thermally evolved with more developed organic pores, leading to increased adsorption capacity [4, 28, 31].

5.1.2. Organic Matter Maturity. The relationship between the adsorption capacity and maturity of the five shale formations in the Sichuan Basin shows that when $R_o < 3\%$, the methane adsorption capacity per TOC of each formation gradually

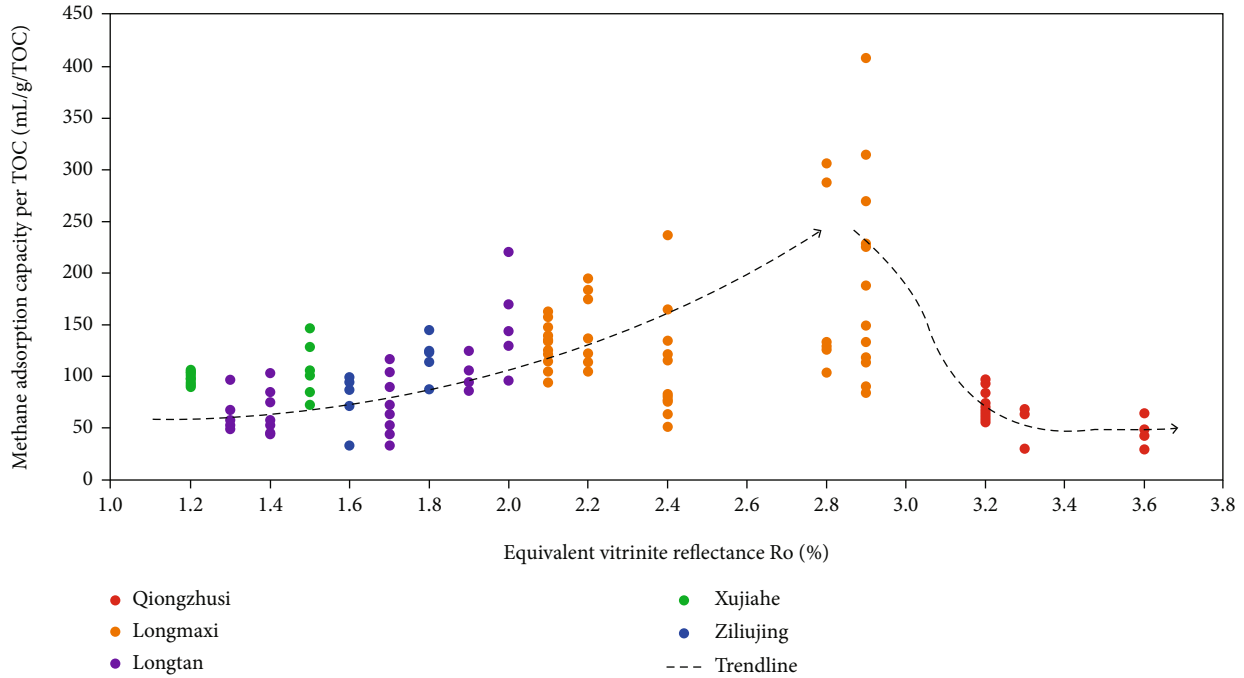


FIGURE 8: Relationship between methane adsorption capacity per TOC and maturity of different types of shale. With the increase of maturity, the adsorption capacity first increased and then decreased.

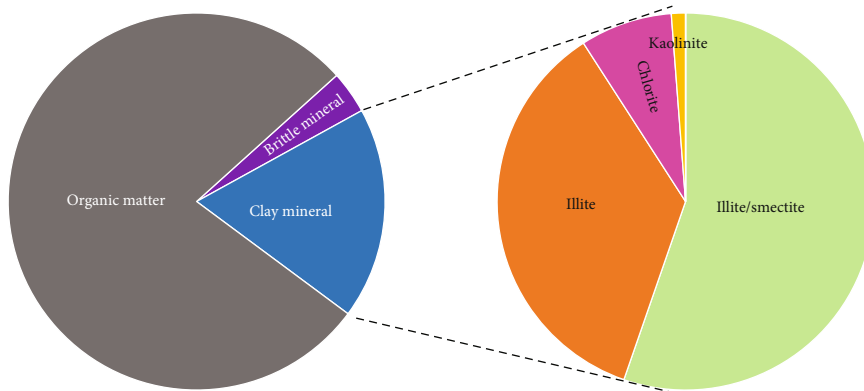


FIGURE 9: Theoretical calculation of adsorbed gas proportion. The adsorption capacity of organic matter was the highest, followed by clay minerals, and the adsorption capacity of brittle minerals was the lowest.

increases with an increase in maturity (Figure 8). The Qiongzhusi Formation R_o is greater than 3% with relatively high maturity and showed a gradual decrease in methane adsorption capacity per TOC as maturity increased. The adsorption capacity per TOC of shale in the Longmaxi Formation was significantly higher, which may be related to its appropriate thermal evolution degree ($2\% < R_o < 3\%$).

The effect of maturity on shale adsorption capacity is primarily influenced by the development of organic matter pores. With the increase in maturity, the methane adsorption capacity of shale increases [32]. Under similar conditions of organic matter content and type, the methane adsorption capacity of overmature shale was higher than that of the high mature shale. The reason for this is that the increase in maturity creates more organic pores in shale, thus, producing

more micropores and mesopores and increasing the methane adsorption capacity of shale. When the maturity is too high, the adsorption capacity and maturity will be negatively correlated, and the methane adsorption capacity decreases.

5.1.3. Clay Minerals. Using the methane adsorption capacity of organic matter and minerals and the composition content of shale, the contribution of each shale component to the methane adsorption capacity of shale as a whole can be calculated. According to theoretical calculations, 3.0% TOC, 26.6% clay minerals, and 67.4% brittle minerals represent a typical composition of the shales in the Longmaxi Formation [33]. In each gram of shale, organic matter can absorb 2.9 mL methane, and clay minerals can absorb 0.7 mL methane, accounting for 19.4% of the total amount of adsorbed gas

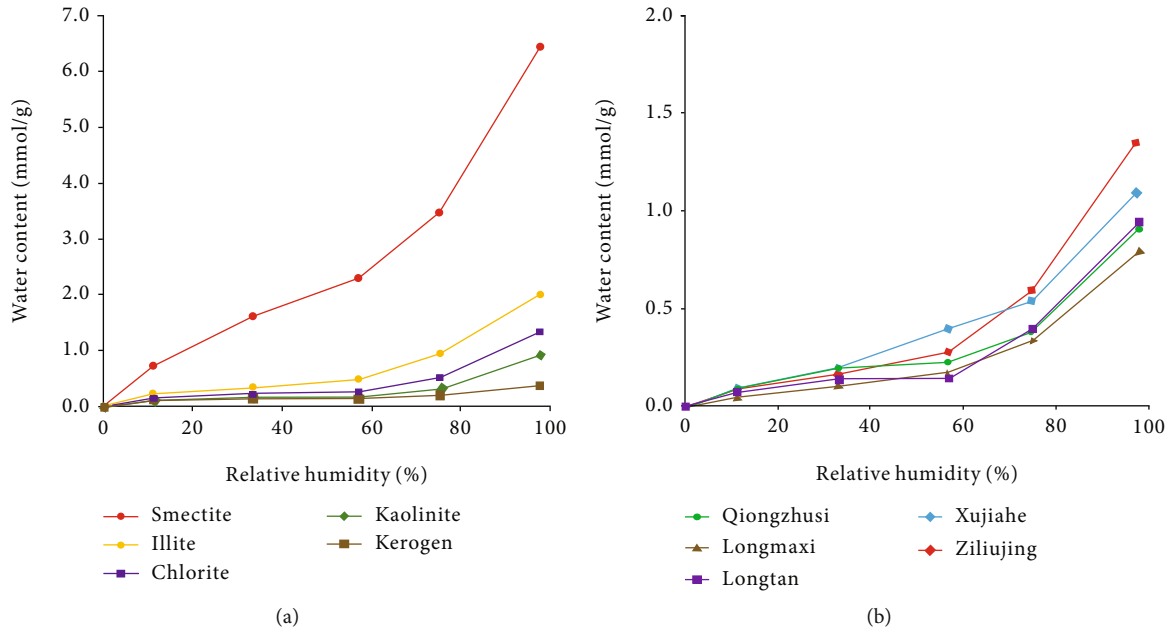


FIGURE 10: Water absorption capacity of different clay minerals and different shales. (a) The relationship between the water content of clay minerals and the relative humidity. (b) The relationship between water content of shale and relative humidity.

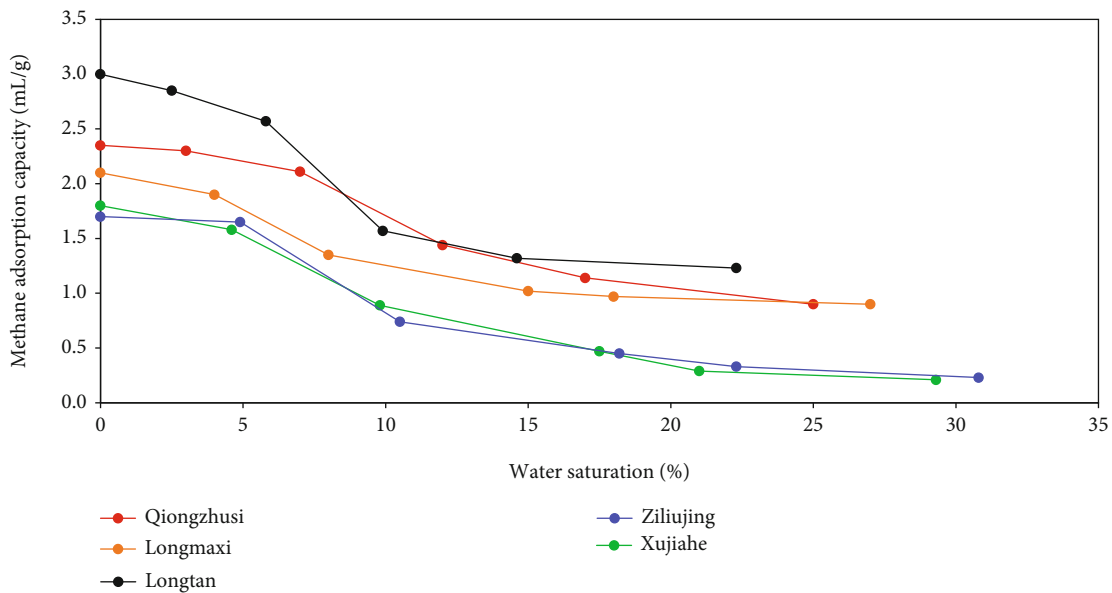


FIGURE 11: The influence of water saturation of different types of shale on the methane adsorption capacity.

(Figure 9). Therefore, the methane adsorption capacity of clay minerals cannot be ignored. The clay minerals in shale primarily consist of illite, smectite, illite/smectite, kaolinite, and chlorite. Because the clay mineral content, chemical characteristics, and pore structure are different, they contributed differently to the absorption ability of shale. The Mississippi shale shows that illite has the largest specific surface area, followed by smectite, and kaolinite is the smallest [34]. Under dry conditions, the adsorption capacity of clay minerals is consistent with the order of the specific surface area, and the order of clay minerals gas adsorption capacity is smectite > kaolinite > illite. The methane isothermal adsorp-

tion experiment was performed on dried samples of each single mineral at 65°C, and the adsorption capacity of clay minerals was obtained in the order of smectite > illite/smectite > kaolinite > chlorite > illite [35].

5.2. *Water Content.* Hydrophilicity is an important characteristic of clay minerals [36]. Clay minerals have different lattice structures and different water-absorbing swelling capabilities. Smectite has the strongest water swelling properties and is stronger than both illite and kaolinite. This is because the traction between the oxygen layers in the smectite crystal layer is very small, and the water molecules easily

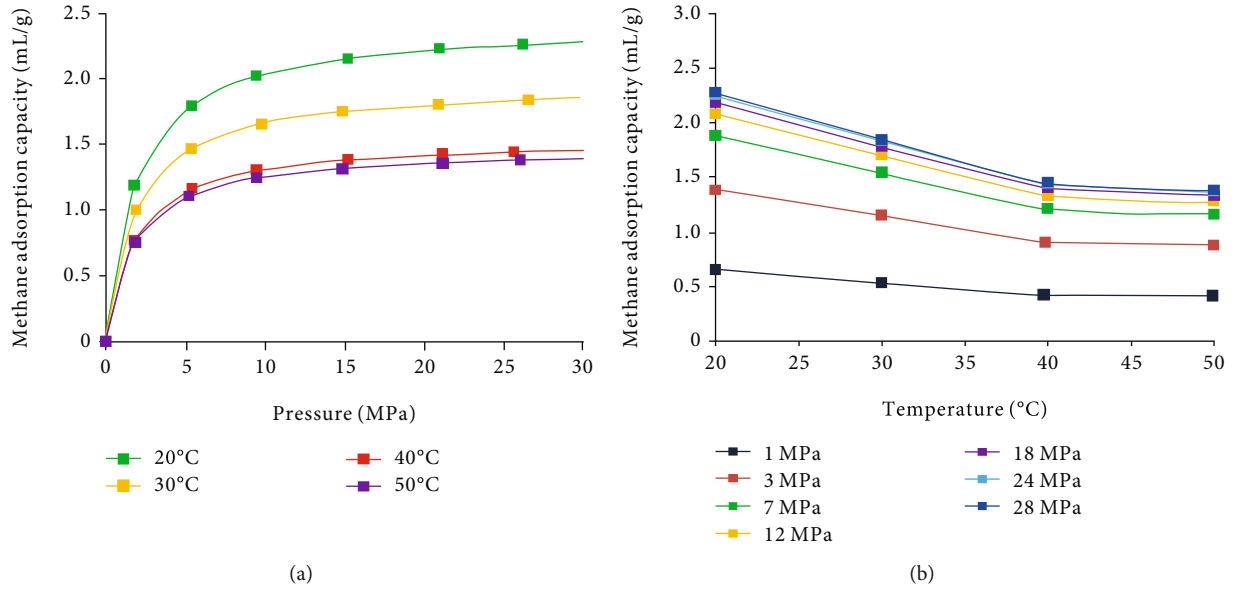


FIGURE 12: Effect of pressure and temperature on methane adsorption capacity. (a) As the pressure increases, the methane adsorption capacity gradually increases, and the increasing trend decreases after 5 MPa. (b) As the temperature increases, the methane adsorption capacity gradually decreases, and after 40°C, the increase rate decreases.

fit between the layers, which causes the crystal layer expansion to follow the vertical plane. At the same time, a small part of Si^{4+} in the tetrahedral layer of the crystal lattice is replaced by Al^{3+} , P^{5+} , etc., and the octahedral layer is often replaced by Mg^{2+} , Fe^{3+} , Zn^{2+} , Li^+ , etc. This increases the distance between the crystal layers and allows more water molecules to enter the crystal layers, causing the mineral to expand. The crystal structure of illite is similar to that of smectite. The difference is that the hydration ability of illite is small, making it difficult for water molecules to enter between the layers and for illite to expand. The presence of hydrogen bonds between the kaolinite crystal layers makes the cells tightly connected, thus, limiting the entrance of water molecules. The results of a quantitative study on the water absorption capacity of the mineral component of the shale of the Xujiahe Formation in the Sichuan Basin show that the water absorption capacity is highest in smectite, followed by illite, chlorite, kaolinite, and kerogen. At the same time, according to the water content at various levels of humidity, the corresponding water content can be calculated, and then, by combing the porosity, the water saturation can be calculated (Figure 10).

After the clay minerals absorb water, the surface adsorption sites are occupied by water molecules, reducing the adsorption capacity of the clay minerals [37]. At the same time, because clay minerals have the characteristics of water swelling, the increase in the interlayer spacing during expansion reduces the pore volume and connectivity, reducing the space for free gas of clay minerals. The relationship between the adsorption capacity and water saturation of shale in different layers in the Sichuan Basin shows that the adsorption capacity of lacustrine shale, such as the Xujiahe Formation and the Ziliujing Formation, has decreased the most significantly due to the abundance of clay minerals (Figure 11).

5.3. Temperature and Pressure. In addition to the surface properties of shale, the adsorption capacity of shale is affected by temperature and pressure [38, 39]. At a constant temperature, the adsorption gas content of the same sample increases with an increase in pressure, which also proves that there is a positive correlation between pressure and adsorption capacity. However, it can be seen from the shape of the adsorption curve that the increase in pressure has a limited effect on the content of adsorbed gas (Figure 12). In the beginning stage (pressure increases from 0 to 5 MPa), the increase in pressure has the most obvious effect on the content of adsorbed gas, and the slope of the curve is larger. After that, the increase in pressure caused the content of adsorbed gas to increase more slowly. After the pressure increased to 10 MPa, the influence of pressure on the amount of adsorbed gas in shale was significantly reduced, and the amount of adsorbed gas remained fundamentally unchanged; the control effect of pressure on the content of adsorbed gas gradually disappeared (Figure 12). When the pressure is low, the gas adsorption needs to reach a higher binding energy, and the adsorption gas content increases with the pressure. When the pressure increases continuously, the required binding energy decreases continuously, and the gas adsorption rate decreases accordingly [31]. For the same sample under the same pressure, a decrease in temperature causes a higher adsorption content. Specifically, when the temperature increases from 20°C to 40°C, the slope of the adsorption capacity decline is evident. When the temperature exceeds 40°C, the amplitude of the decrease gradually lessens (Figure 12). This is because gas adsorption is an exothermic process. As the temperature increases, the exothermic process is suppressed and the amount of adsorbed gas decreases.

6. Conclusion

- (1) The five sets of shales had different methane adsorption capacities and the order was Longtan Formation > Qiongzhusi Formation and Longmaxi Formation > Xujiache Formation and Ziliujing Formation
- (2) The methane adsorption capacity was positively correlated with TOC, while negatively correlated with humidity. And in a specific range, it was positively correlated with pressure, while negatively correlated with temperature
- (3) The methane adsorption capacity first increased and then decreased as maturity increased. For clay minerals, the methane adsorption capacity of smectite was the highest, followed by illite/smectite, kaolinite, chlorite, and illite. While the brittle minerals such as quartz and feldspar had the weakest adsorption capacity for methane

Data Availability

The data used to support the findings of this study are available from the corresponding author upon request.

Conflicts of Interest

The authors declare that there are no conflicts of interest regarding the publication of this paper.

Acknowledgments

The National Natural Science Foundation of China (41802153 and 41728004) and the Key Project of National Science and Technology (2017ZX05035-002) provided funds for this study. We acknowledge support received from the Southwest Oil & Gas Field Company and the Jiangnan Oilfield Company. We express our appreciation for their approval to publish the data.

References

- [1] W. L. Auping, E. Pruyt, S. Jong, and J. H. Kwakkel, "The geopolitical impact of the shale revolution: exploring consequences on energy prices and rentier states," *Energy Policy*, vol. 98, pp. 390–399, 2016.
- [2] K. Zhang, C. Jia, Y. Song et al., "Analysis of lower Cambrian shale gas composition, source and accumulation pattern in different tectonic backgrounds: a case study of Weiyuan block in the upper Yangtze region and Xiuwu Basin in the lower Yangtze region," *Fuel*, vol. 263, 2020.
- [3] T. Jiang, Z. Jin, G. Liu et al., "Source analysis of siliceous minerals and uranium in early Cambrian shales, South China: significance for shale gas exploration," *Marine and Petroleum Geology*, vol. 102, pp. 101–108, 2018.
- [4] X. Tang, Z. Jiang, S. Jiang et al., "Characteristics, capability, and origin of shale gas desorption of the Longmaxi Formation in the southeastern Sichuan Basin, China," *Scientific Reports*, vol. 9, no. 1, pp. 1–12, 2019.
- [5] Y. Ma, X. Cai, and P. Zhao, "China's shale gas exploration and development: understanding and practice," *Petroleum Exploration and Development*, vol. 45, no. 4, pp. 589–603, 2018.
- [6] Y. Pang, M. Y. Soliman, H. Deng, and X. Xie, "Experimental and analytical investigation of adsorption effects on shale gas transport in organic nanopores," *Fuel*, vol. 199, pp. 272–288, 2017.
- [7] Y. Shuai, S. Yu-Ming, Z. Lian-Hui, X. Run-Cheng, and W. Lei, "Research of shale gas isothermal adsorption quantity and equal amount adsorption heat," *Science Technology and Engineering*, vol. 13, no. 29, pp. 8572–8578, 2013.
- [8] B. Zhang, B. Shan, Y. Zhao, and L. Zhang, "Review of formation and gas characteristics in shale gas reservoirs," *Energies*, vol. 13, no. 20, p. 5427, 2020.
- [9] X. Tang, Z. Jiang, S. Jiang, L. Cheng, and Y. Zhang, "Characteristics and origin of in-situ gas desorption of the Cambrian Shuijingtuo Formation shale gas reservoir in the Sichuan Basin, China," *Fuel*, vol. 187, pp. 285–295, 2017.
- [10] Z. Pan and L. D. Connell, "Reservoir simulation of free and adsorbed gas production from shale," *Journal of Natural Gas Science & Engineering*, vol. 22, pp. 359–370, 2015.
- [11] Y. Liu, J. Zhang, and X. Tang, "Predicting the proportion of free and adsorbed gas by isotopic geochemical data: a case study from lower Permian shale in the southern North China basin (SNCB)," *International Journal of Coal Geology*, vol. 156, pp. 25–35, 2016.
- [12] P. Li, Z. Jiang, M. Zheng, H. Bi, and L. Chen, "Estimation of shale gas adsorption capacity of the Longmaxi Formation in the upper Yangtze Platform, China," *Journal of Natural Gas Science and Engineering*, vol. 34, pp. 1034–1043, 2016.
- [13] W. Ji, F. Hao, H.-M. Schulz, Y. Song, and J. Tian, "The architecture of organic matter and its pores in highly mature gas shales of the lower Silurian Longmaxi Formation in the upper Yangtze platform, South China," *AAPG Bulletin*, vol. 102, no. 12, pp. 2909–2942, 2019.
- [14] K. Xi, Y. Cao, K. Liu et al., "Authigenic minerals related to wettability and their impacts on oil accumulation in tight sandstone reservoirs: an example from the lower Cretaceous Quantou Formation in the southern Songliao Basin, China," *Journal of Asian Earth Sciences*, vol. 178, pp. 173–192, 2019.
- [15] K. Liu, L. Wang, M. Ostadhassan, J. Zou, B. Bubach, and R. Rezaee, "Nanopore structure comparison between shale oil and shale gas: examples from the Bakken and Longmaxi Formations," *Petroleum Science*, vol. 16, no. 1, pp. 77–93, 2019.
- [16] Y. F. Li, W. Sun, X. W. Liu, D. W. Zhang, Y. C. Wang, and Z. Y. Liu, "Study of the relationship between fractures and highly productive shale gas zones, Longmaxi Formation, Jiaoshiha area in eastern Sichuan," *Petroleum Science*, vol. 15, no. 3, pp. 498–509, 2018.
- [17] U. Raut, M. Famá, B. D. Teolis, and R. A. Baragiola, "Characterization of porosity in vapor-deposited amorphous solid water from methane adsorption," *Journal of Chemical Physics*, vol. 127, no. 20, 2007.
- [18] D. J. K. Ross and R. M. Bustin, "Impact of mass balance calculations on adsorption capacities in microporous shale gas reservoirs," *Fuel*, vol. 86, no. 17–18, pp. 2696–2706, 2007.
- [19] J. K. Hill and P. A. Wheeler, "Organic carbon and nitrogen in the northern California current system: comparison of offshore, river plume, and coastally upwelled waters," *Progress in Oceanography*, vol. 53, no. 2–4, pp. 369–387, 2002.

- [20] A. L. Cheng and W. L. Huang, "Selective adsorption of hydrocarbon gases on clays and organic matter," *Organic Geochemistry*, vol. 35, no. 4, pp. 413–423, 2004.
- [21] O. P. O. Cancino, D. P. Mancilla, M. Pozo, E. Pérez, and D. Bessieres, "Effect of organic matter and thermal maturity on methane adsorption capacity on shales from the middle Magdalena Valley Basin in Colombia," *Energy & Fuels*, vol. 31, no. 11, pp. 11698–11709, 2017.
- [22] S. Chen, Y. Zhu, H. Wang, H. Liu, W. Wei, and J. Fang, "Shale gas reservoir characterisation: a typical case in the southern Sichuan Basin of China," *Energy*, vol. 36, no. 11, pp. 6609–6616, 2011.
- [23] J. Tan, P. Weniger, B. Krooss et al., "Shale gas potential of the major marine shale formations in the upper Yangtze platform, South China, part II: methane sorption capacity," *Fuel*, vol. 129, pp. 204–218, 2014.
- [24] Y. Zhang, Z. He, S. Jiang et al., "Factors affecting shale gas accumulation in overmature shales case study from lower Cambrian shale in western Sichuan Basin, South China," *Energy & Fuels*, vol. 32, no. 3, pp. 3003–3012, 2018.
- [25] J.-n. Peng, D.-y. Wang, G.-x. Liu, M. Zhang, and F.-l. Li, "Carbon isotopic composition and genetic types of natural gas in the Sichuan Basin, China," *Acta Geochimica*, vol. 36, no. 1, pp. 102–111, 2017.
- [26] J. P. Zhang, S. H. Tang, and D. X. Guo, "Shale gas favorable area prediction of the Qiongzhusi Formation and Longmaxi Formation of lower Palaeozoic in Sichuan Basin, China," *Geological Bulletin of China*, vol. 30, no. 2, pp. 357–363, 2011.
- [27] G. R. Chalmers, R. M. Bustin, and I. M. Power, "Characterization of gas shale pore systems by porosimetry, pycnometry, surface area, and field emission scanning electron microscopy/transmission electron microscopy image analyses: examples from the Barnett, Woodford, Haynesville, Marcellus, and Doig units," *AAPG Bulletin*, vol. 96, no. 6, pp. 1099–1119, 2012.
- [28] T. Zhang, G. S. Ellis, S. C. Ruppel, K. Milliken, and R. Yang, "Effect of organic-matter type and thermal maturity on methane adsorption in shale-gas systems," *Organic Geochemistry*, vol. 47, no. 6, pp. 120–131, 2012.
- [29] A. M. M. Bustin and R. M. Bustin, "Importance of rock properties on the producibility of gas shales," *International Journal of Coal Geology*, vol. 103, pp. 132–147, 2012.
- [30] M. Yamamoto and Y. Watanabe, "Kerogen and biomarker compositions of uranium-rich coaly shales from Miocene sequence at Kanamaru, Japan," *Bulletin. Geological Survey of Japan*, vol. 61, pp. 325–336, 2005.
- [31] Y. Pang, Y. Tian, M. Y. Soliman, and Y. Shen, "Experimental measurement and analytical estimation of methane absorption in shale kerogen," *Fuel*, vol. 240, pp. 192–205, 2019.
- [32] H. Hu, T. Zhang, J. D. Wiggins-Camacho, G. S. Ellis, M. D. Lewan, and X. Zhang, "Experimental investigation of changes in methane adsorption of bitumen-free Woodford shale with thermal maturation induced by hydrous pyrolysis," *Marine & Petroleum Geology*, vol. 59, pp. 114–128, 2015.
- [33] Y. M. Wang, D. Z. Dong, H. Yang et al., "Quantitative characterization of reservoir space in the lower Silurian Longmaxi Shale, southern Sichuan, China," *Science China Earth Sciences*, vol. 57, no. 2, pp. 313–322, 2014.
- [34] D. J. K. Ross and R. M. Bustin, "The importance of shale composition and pore structure upon gas storage potential of shale gas reservoirs," *Marine & Petroleum Geology*, vol. 26, no. 6, pp. 916–927, 2009.
- [35] L. Ji, J. Qiu, Y. Xia, and T. Zhang, "Micro-pore characteristics and methane adsorption properties of common clay minerals by electron microscope scanning," *Acta Petrologica Sinica*, vol. 33, no. 2, pp. 249–256, 2012.
- [36] C. J. van Oss, "The hydrophilicity and hydrophobicity of clay minerals," *Clays and Clay Minerals*, vol. 43, no. 4, pp. 474–477, 1995.
- [37] J. Li, X. Li, X. Wang et al., "Water distribution characteristic and effect on methane adsorption capacity in shale clay," *International Journal of Coal Geology*, vol. 159, pp. 135–154, 2016.
- [38] V. Sharma and A. Sircar, "Multi-technique characterization of shale reservoir quality parameters," *Journal of Natural Gas Science and Engineering*, vol. 75, 2019.
- [39] A. Hildenbrand, B. M. Krooss, A. Busch, and R. Gaschnitz, "Evolution of methane sorption capacity of coal seams as a function of burial history – a case study from the Campine Basin, NE Belgium," *International Journal of Coal Geology*, vol. 66, no. 3, pp. 179–203, 2006.

Research Article

Characteristics of Hydration Damage and Its Influence on Permeability of Lamellar Shale Oil Reservoirs in Ordos Basin

Pengfei Zhao ¹, Xiangyu Fan,^{1,2} Qianguai Zhang ^{1,2}, Bowei Yao,¹ Mingming Zhang,¹ Liang He,¹ Yu Qiang,¹ and Jinhua Liu¹

¹Southwest Petroleum University, Chengdu 610500, China

²National Key Laboratory of "Oil and Gas Reservoir Geology and Development Engineering", Southwest Petroleum University, Chengdu 610500, China

Correspondence should be addressed to Pengfei Zhao; zpf2017@stu.swpu.edu.cn and Qianguai Zhang; qianguai.zhang@polymtl.ca

Received 22 December 2020; Revised 9 January 2021; Accepted 23 March 2021; Published 21 April 2021

Academic Editor: Keni Zhang

Copyright © 2021 Pengfei Zhao et al. This is an open access article distributed under the Creative Commons Attribution License, which permits unrestricted use, distribution, and reproduction in any medium, provided the original work is properly cited.

The continental shale oil reservoir has low permeability, high clay content, rich lamellar structure, and strong heterogeneity, which makes the reservoir vulnerable to hydration damage. In order to study characteristics of hydration damage and its influence on permeability of lamellar shale oil reservoirs, a series of experiments such as high-pressure mercury injection, steady gas permeability, rock thin section identification, and scanning electron microscope were carried out with the downhole core in Ordos Basin as the experimental object. The effects of water and water-based drilling fluid on pore size distribution, permeability, and rock microstructure were analyzed. Results show that the pore size of the reservoir is mainly nanoscale, and the pore size of shale changes most dramatically in the stage of hydration for 12-24 hours, while that of tuff changes most dramatically in 24-48 hours. The permeability increases rapidly with hydration time and then tends to be stable, among which the permeability of samples with lamellar structure in the direction parallel to the lamellar structure is most easily affected by hydration and changes fastest. Hydration leads to the formation of new pores, new fractures, and the expansion of existing fractures in rocks, especially in the strata containing large amounts of terrigenous clastic, lamellar structure, and pyrite. The new seepage channel increases the permeability of rock, and the soil powder and plugging particles in drilling fluid are easy to form protective mud cake in these places. These protective mud cakes not only change the microstructure of rock but also inhibit the influence of hydration on the pore space and permeability of rock, which play an effective role in preventing the mineral shedding on the rock surface, reducing the increase of micropores and delaying hydration.

1. Introduction

Shale oil is a kind of unconventional oil resources with great potential. It has large reserves and wide distribution in the world, which may become an important substitute for conventional oil in the future [1, 2]. The United States has changed from an oil-importing country to an oil-exporting country benefit from the successful commercial exploration and production of marine-sourced shale oil, which has aroused great attention to shale oil in the world [3, 4]. China is rich in shale oil reserves, and shale oil is mainly distributed in lacustrine basin. In recent years, the distribution characteristics, geochemical characteristics, and geological environment of shale oil reservoirs have been initially recognized

through the exploration and research of Ordos Basin [5], Jiangnan Basin [6], Bohai Bay Basin [7], Songliao Basin [8], and Jungar Basin [9]. However, due to the complex geological environment, strong heterogeneity, and high clay content of continental shale oil reservoir, drilling is difficult, which limits the efficient and safe development of shale oil in China [10].

Compared with oil-based drilling fluid, water-based drilling fluid (WBM) has lower cost and better environmental protection, and is widely used in drilling engineering [11]. There is high clay mineral content and complex pore structure in shale oil reservoir, which leads to hydration reaction when drilling with water-based drilling fluid [12]. The hydration reaction will lead to the increase of porosity, the

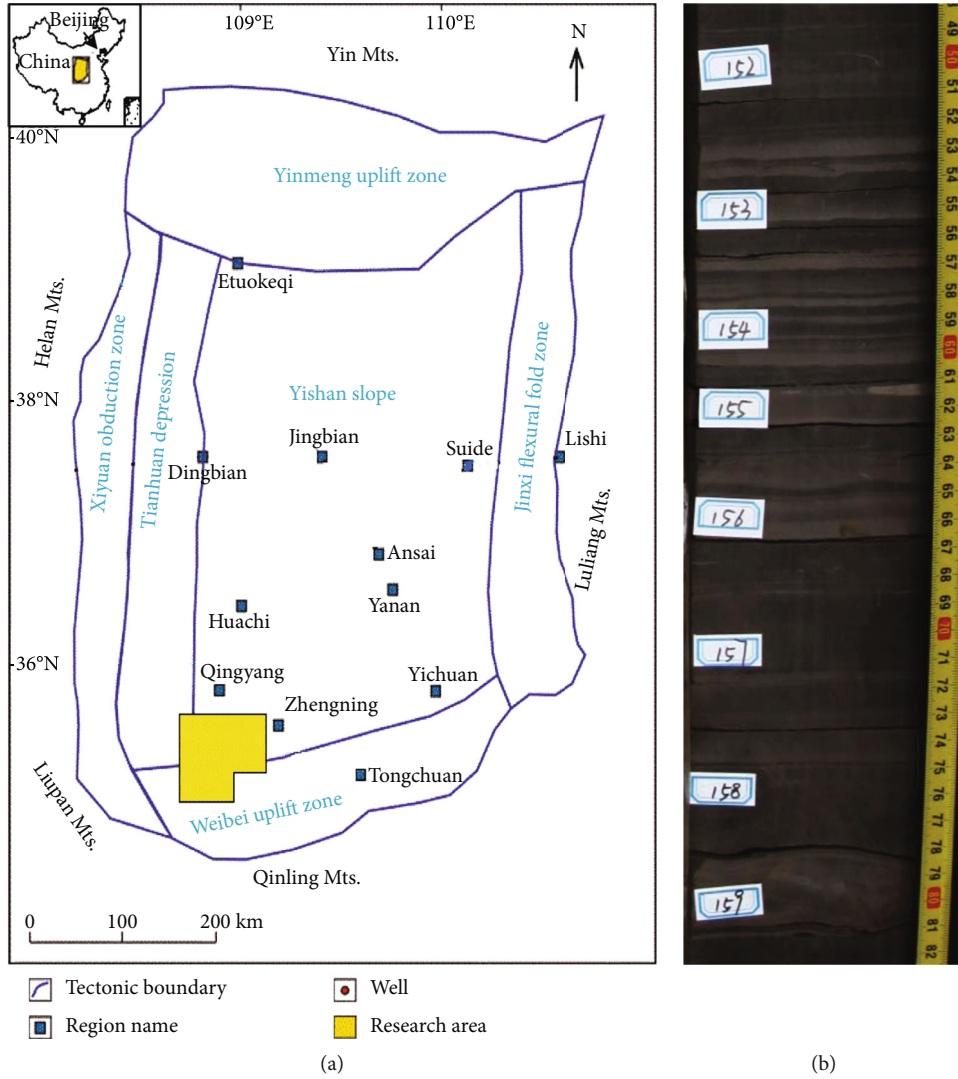


FIGURE 1: Continued.



(c)

FIGURE 1: (a) Geographical location characteristics of Ordos Basin and study area (modified after [33]). (b) Lamellar sandstone and bedding fractures in shale. (c) Bedding and structural fractures in tuff.

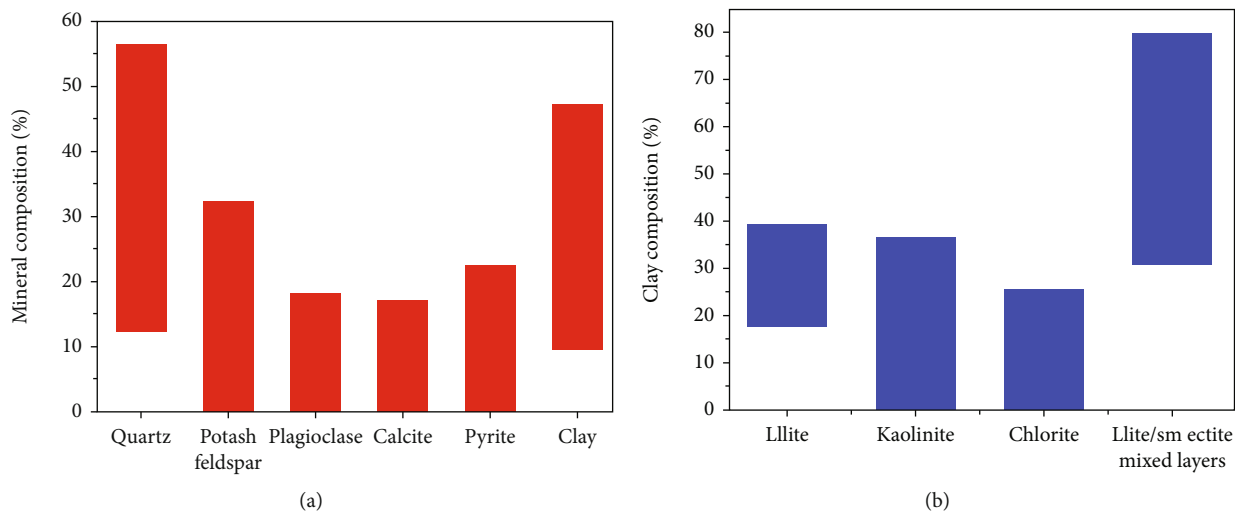


FIGURE 2: Clay and mineral composition in work area (modified after [34]). (a) Content fluctuation range of different minerals. (b) Content fluctuation range of different clay.

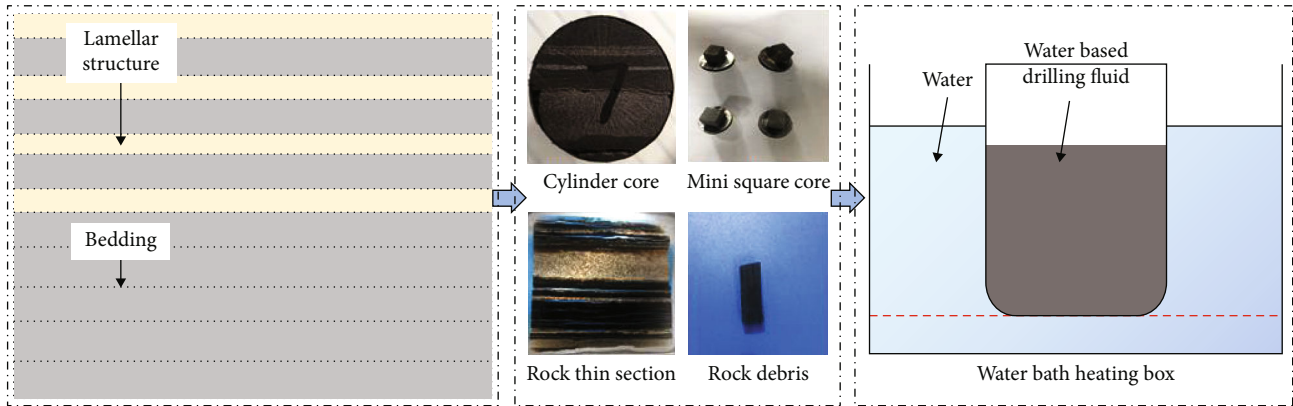


FIGURE 3: Samples preparation and hydration process.

looseness of internal structure, and the decrease of rock strength. Shale has obvious bedding structure, and micro-cracks are usually developed along the bedding, which provides a good channel for hydration [13]. The expansion stress produced by hydration will concentrate on the crack tip, which will cause fracture expansion and deformation and cause damage to the rock interior, such as borehole instability [14].

Through the experimental study of shale outcrop and core samples of Longmaxi formation in southern Sichuan Basin, Liu et al. analyzed the variation law of shale expansion stress under the influence of oil and water, and concluded that water-based drilling fluid is easy to cause wellbore instability [15]. Shi et al. used X-ray CT technology to observe the microstructure changes and crack propagation during the hydration process of hard brittle shale and concluded that secondary fracture failure caused by self-absorption is one of the main reasons for wellbore instability in hard brittle shale formation [16]. Ma and Chen carried out CT scanning on outcrop shale under different soaking time, and established a qualitative description method of shale hydration damage based on microstructure change [17]. Wang et al. carried out nuclear magnetic resonance (NMR) test on shale samples from Xi Feng formation after hydration damage and established a method to quantitatively explain shale hydration damage based on nuclear magnetic resonance [18]. Hydration damage not only changes rock structure and strength but also affects the permeability. Permeability reflects the migration ability of reservoir, which is one of the important parameters to evaluate reservoir. The permeability of unconventional reservoirs is very low, and the permeability of shale oil reservoirs is generally a few millidarcy [19]. Shale is dense, and its permeability is mainly provided by internal microfractures. Due to the bedding structure of shale, fractures are easy to distribute along the bedding, resulting in obvious anisotropy of shale permeability. N. R. Backeberg et al. studied the anisotropic permeability of shale by the nano-CT and found that the anisotropic permeability of shale is related to the anisotropy of initial fracture [20]. Ma et al. studied the permeability of Longmaxi shale and concluded that the permeability is related to the gas tested. Under the methane and nitrogen test, the permeability

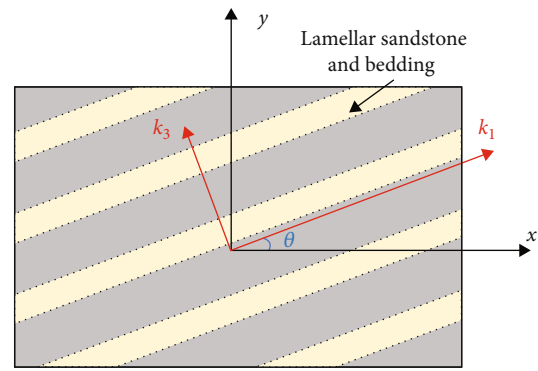


FIGURE 4: Relationship between permeability direction and lamellar structure in shale oil reservoir.

anisotropy ratio ranges from 5.2 to 510.5 [21]. They studied the influence of temperature and bedding direction on shale permeability by using high temperature triaxial steady-state permeability test system and obtained shale permeability anisotropy and its reasons under different temperatures and bedding directions [22]. It is more and more important for oil exploration and development to study the permeability variation characteristics of unconventional reservoirs under the influence of multiple factors.

As for the hydration damage of shale oil reservoir and its influence on permeability, the following contents need to be supplemented. First of all, the existing research object of hydration damage is usually the outcrop core of marine strata [23, 24]. Because of the difference of geological environment and lithologic composition, the research results cannot reflect the hydration damage law of continental oil shale reservoir. Secondly, high-quality continental source rocks in China often coexist with tuff, which is an important feature of shale oil reservoir [25]. Tuff is a volcanic rock which is easy to hydrate. Tuff must be considered in the study of hydration damage and permeability characteristics of shale oil reservoir, which is lack of existing research. Finally, different from the bedding structure within the same lithology, the laminar structure is formed by overlapping of different lithology. Continental shale oil contains lamellar structure, which makes it more heterogeneous than marine shale [26].

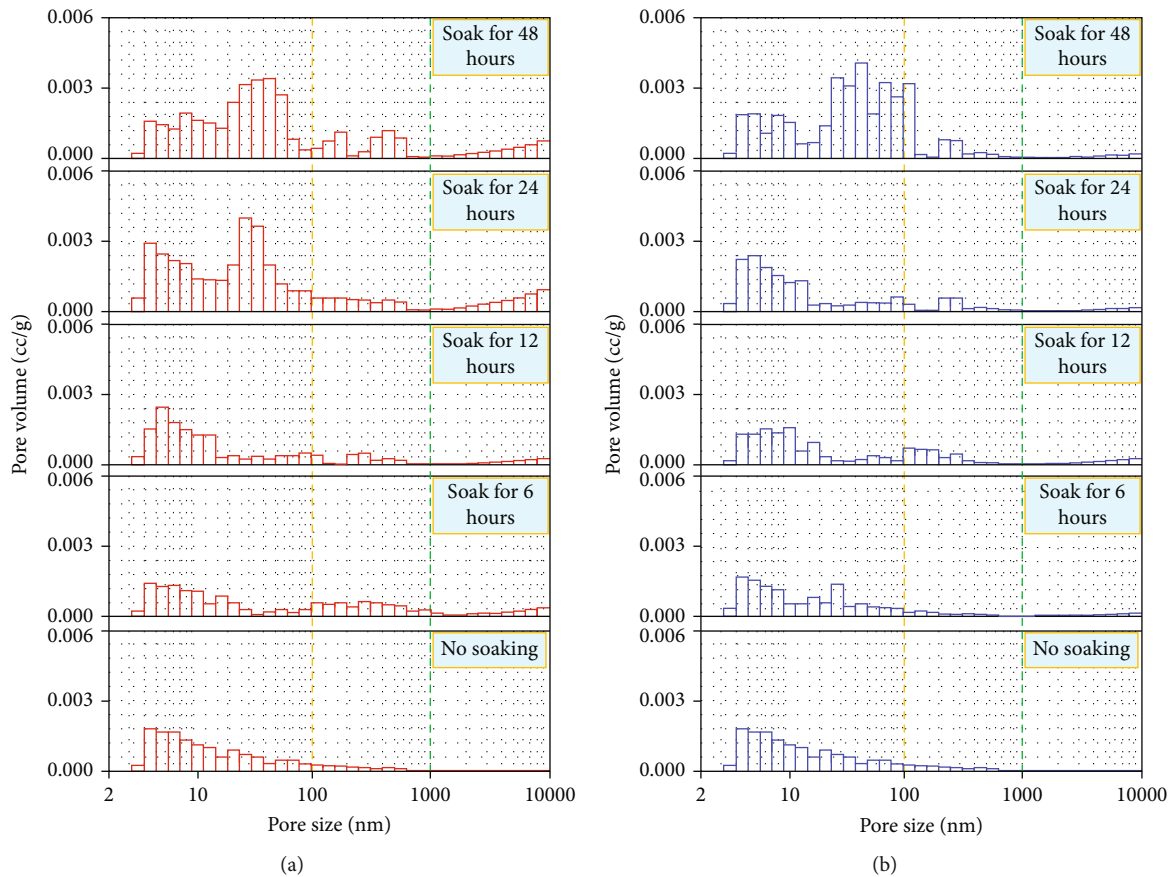


FIGURE 5: Influence of fluid invasion on shale's pore size distribution. (a) Relationship between pore distribution and water soaking time. (b) Relationship between pore distribution and water-based drilling fluid soaking time.

In this study, the downhole core in the Triassic Chang 7 Member of Southern Ordos Basin was taken as the experimental object, and the lamellar structure was analyzed by macroscopic core description, rock thin section identification, and scanning electron microscope. The pore size distribution and permeability of rock under different fluid invasion time were tested by high pressure mercury injection experiment and steady gas permeability experiment. Characteristics of hydration damage and its influence on permeability can be obtained by analyzing experimental results, which can provide support for drilling and completion operation and selection of water-based drilling fluid for lamellar shale oil reservoirs.

2. Samples and Methods

2.1. Basic Geochemical Properties. Ordos Basin is the second largest sedimentary basin in China, which is rich in mineral resources. After investigation, it is found that high-quality source rocks are developed in the Triassic Chang 7 Member, and the total organic carbon (TOC) content of the reservoir reaches 17.41% [27]. Some organizations have studied the source rock development, lithology characteristics, and pore distribution of shale oil reservoir in Chang 7 member. It is proved that the shale oil in Chang 7 member of Ordos Basin

has great potential for exploitation, and several shale oil test areas have been established in the basin [28–31]. It is proved that the shale oil in Chang 7 member of Ordos Basin has great potential for exploitation, and several shale oil test areas have been established in the basin [32].

The samples in the study were taken from the BC block in the southwest of the basin (Figure 1(a)). The structure in the area is high in the southeast and low in the northwest, with developed faults. Small anticlines, fault anticlines, and nose uplifts developed locally. The core of the exploration well shows that the reservoir contains a large number of thin sandstone lamina structure, and parallel laminar fractures are developed in the shale (Figure 1(b)). The lower part contains tuff, in which bedding and structural fractures are developed (Figure 1(c)). The content of terrigenous clasts is high in the reservoir, especially in the lamellar shale section.

Zhao et al. tested the mineral composition of rocks in the work area by X-ray diffraction experiment and found that the mineral types are complex, the content of quartz and clay is high, the brittle minerals are more, and the range of mineral content fluctuation is large [34] (Figure 2).

2.2. Samples and Drilling Fluid. The rocks were collected from the depth of 1434–1447 m in the research area. On the basis of the full diameter core, the lamellar structure and

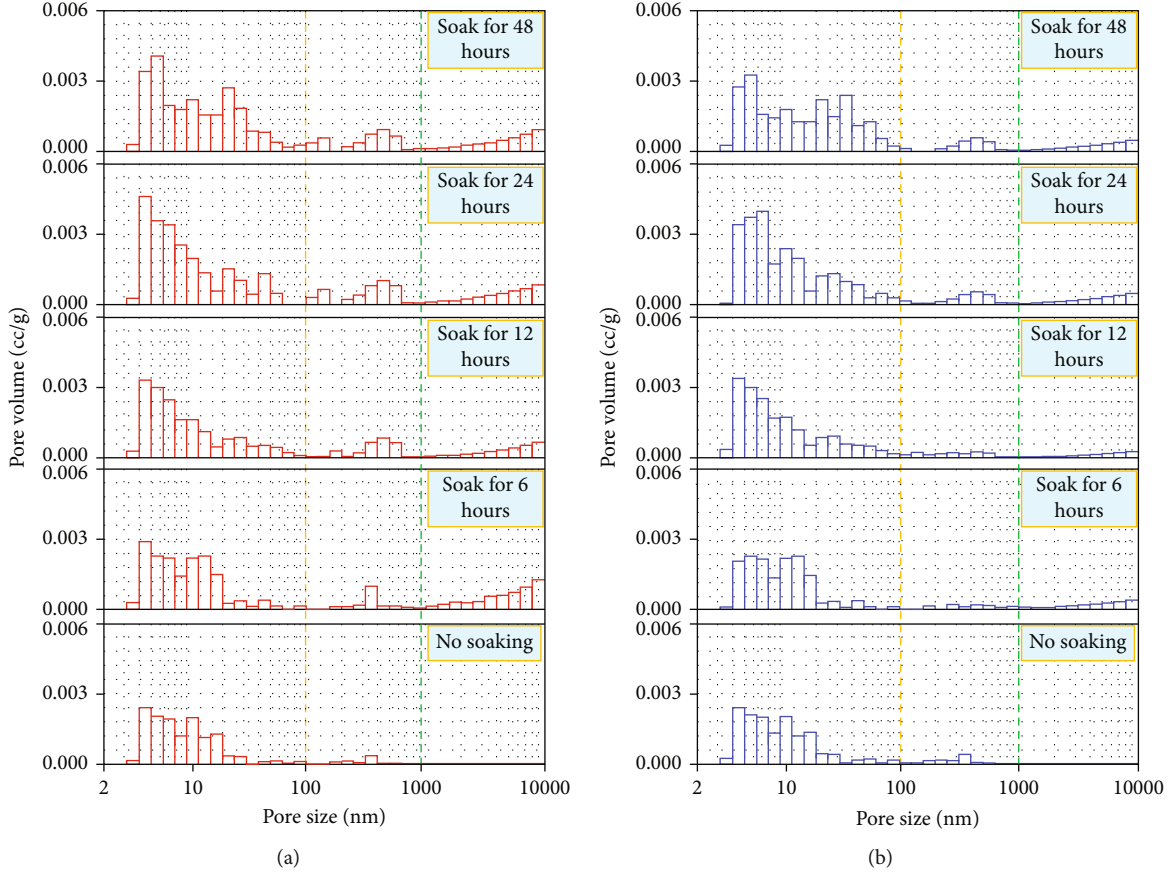


FIGURE 6: Influence of fluid invasion on tuff's pore size distribution. (a) Relationship between pore distribution and water soaking time. (b) Relationship between pore distribution and water-based drilling fluid soaking time.

bedding sections were taken, respectively, to prepare samples of different specifications (Figure 3). Cylinder cores with angles of 0° , 45° , and 90° from lamina were drilled for permeability test. After grinding and spraying metal, microsquare cores were used for scanning electron microscope. Rock thin sections with a thickness of $30\text{--}100\ \mu\text{m}$ were used for microscope. The long strip rock debris with large specific surface area are the samples for mercury injection experiment.

The hydration damage of rock in formation was simulated by soaking the samples in water and water-based drilling fluid at 80°C . The water-based drilling fluid contained potassium sodium silicate and amino group inhibitor for inhibit hydration and was equipped with nanosized silica and asphalt for plugging. The apparent viscosity of drilling fluid is $20\ \text{mPa}\cdot\text{s}$, and the apparent viscosity of drilling fluid is $20\ \text{mPa}\cdot\text{s}$. The particle size of drilling fluid ranges from $0.02\ \mu\text{m}$ to $200\ \mu\text{m}$, which is concentrated in $1.38\ \mu\text{m}$.

2.3. Pore Size Distribution Test. The pressure that forces non-wetting liquid to enter the pore depends on the radius of the pore, so mercury injection experiment can be used to test the pore size distribution in rock [35]. Mercury injection method is widely used in reservoir pore distribution because of its simple principle, wide testing range, and high precision [36]. The Poremaster-60 produced by Quantachrome Instru-

ments Company was used for the mercury injection experiment. Before the experiment, the instrument was calibrated with aluminum oxide standard sample. 106 pressure points were tested for each sample, and each point was stabilized for 30 seconds.

The pore radius (R_i) can be calculated when the pressure is P_i . According to the amount of mercury injected (Q_i), the content (C_i) of pores with different radius (R_i) can be obtained. The calculation equation is given as

$$\begin{cases} R_i = \frac{K}{P_i}, \\ C_i = \begin{cases} Q_1 & i = 1, \\ Q_i - \sum_1^{i-1} Q_n, & i \geq 2, \end{cases} \end{cases} \quad (1)$$

where R_i is the pore diameter at different test points, P_i is the pressure at different test points, C_i is the pore volume at different test points, Q_i is the mercury injection amount at different test points, and K is the constant of test calibration.

2.4. Permeability Test and Permeability Anisotropy Calculation. According to Darcy's law, the seepage velocity

TABLE 1: The influence of lithology, structure, sampling angle, fluid environment, and soaking time on permeability.

No.	Lithology	Structure	Sampling angle (°)	Soaking fluid	Permeability after soaking (mD)				
					0 h	12 h	24 h	36 h	48 h
1	Shale	Lamellar structure	0	Water	4.27	6.93	7.08	7.15	7.15
2				WBDF	3.67	4.55	5.12	5.20	5.18
3			45	Water	1.98	2.57	2.67	2.83	2.83
4				WBDF	1.56	2.01	2.12	2.22	2.19
5			90	Water	0.51	0.57	0.61	0.67	0.61
6				WBDF	0.33	0.36	0.37	0.39	0.38
7		Bedding structure	0	Water	1.48	1.51	1.64	1.70	1.71
8				WBDF	1.41	1.47	1.56	1.54	1.55
9			45	Water	1.14	1.21	1.25	1.24	1.26
10				WBDF	0.77	0.79	0.87	0.85	0.85
11			90	Water	0.36	0.39	0.39	0.39	0.40
12				WBDF	0.29	0.30	0.31	0.32	0.32
13	Tuff	Lamellar structure	0	Water	3.61	4.99	5.27	5.29	5.31
14				WBDF	3.71	4.49	4.67	4.61	4.65
15			45	Water	1.77	2.33	2.51	2.54	2.57
16				WBDF	2.24	2.91	2.87	2.89	2.97
17			90	Water	0.67	0.73	0.75	0.79	0.76
18				WBDF	0.65	0.69	0.71	0.70	0.71
19		Bedding structure	0	Water	0.89	1.09	1.20	1.23	1.24
20				WBDF	0.91	0.98	0.95	0.97	0.99
21			45	Water	0.51	0.56	0.58	0.59	0.60
22				WBDF	0.69	0.72	0.75	0.76	0.75
23			90	Water	0.45	0.49	0.51	0.52	0.53
24				WBDF	0.55	0.59	0.58	0.59	0.60

of flow through porous media is directly proportional to cross-sectional area, pressure difference, and permeability and inversely proportional to liquid viscosity and length of porous media [37]. In anisotropic lamellar shale oil reservoirs, the three-dimensional expression of Darcy formula is as follows.

$$\begin{cases} v_x = -\frac{1}{\mu} \left(k_{xx} \frac{\partial P}{\partial x} + k_{xy} \frac{\partial P}{\partial y} + k_{xz} \frac{\partial P}{\partial z} \right), \\ v_y = -\frac{1}{\mu} \left(k_{yx} \frac{\partial P}{\partial x} + k_{yy} \frac{\partial P}{\partial y} + k_{yz} \frac{\partial P}{\partial z} \right), \\ v_z = -\frac{1}{\mu} \left(k_{zx} \frac{\partial P}{\partial x} + k_{zy} \frac{\partial P}{\partial y} + k_{zz} \frac{\partial P}{\partial z} \right), \end{cases} \quad (2)$$

where v_i is seepage velocity, μ is liquid viscosity, k_{ij} is permeability tensor, and P is formation pressure. The Gasperm permeameter produced by VINCI was used in the experiment, and the temperature was 20°C, and the confining pressure was 230 psi during the experiment. Due to a large number of lamellar sandstone and obvious bedding in shale, the shale oil reservoir has significant anisotropy (Figure 4).

Yang et al. deduced that the permeability in any direction can be calculated by formula (3). By testing K_1 and K_3 , the permeability at any angle with the lamellar structure could be calculated [38].

$$\begin{cases} k_{xx} = k_1 \cos^2 \theta + k_3 \sin^2 \theta = \frac{k_1 + k_3}{2} + \frac{k_1 - k_3}{2} \cos 2\theta, \\ k_{xy} = k_{yx} = (k_1 - k_3) \cos \theta \sin \theta = \frac{k_1 - k_3}{2} \sin 2\theta, \\ k_{yy} = k_1 \sin^2 \theta + k_3 \cos^2 \theta = \frac{k_1 + k_3}{2} - \frac{k_1 - k_3}{2} \cos 2\theta, \end{cases} \quad (3)$$

where k_1 is the permeability parallel to the laminar direction, k_3 is the permeability perpendicular to the laminar direction, and θ is the angle between the permeability direction and lamellar structure. Fluid invasion not only changes the permeability of rocks but also affects their permeability anisotropy. The permeability anisotropy of lamellar shale oil reservoir is expressed by the permeability ratio of bedding and vertical lamina, and the change rate of permeability anisotropy is calculated by formula (4).

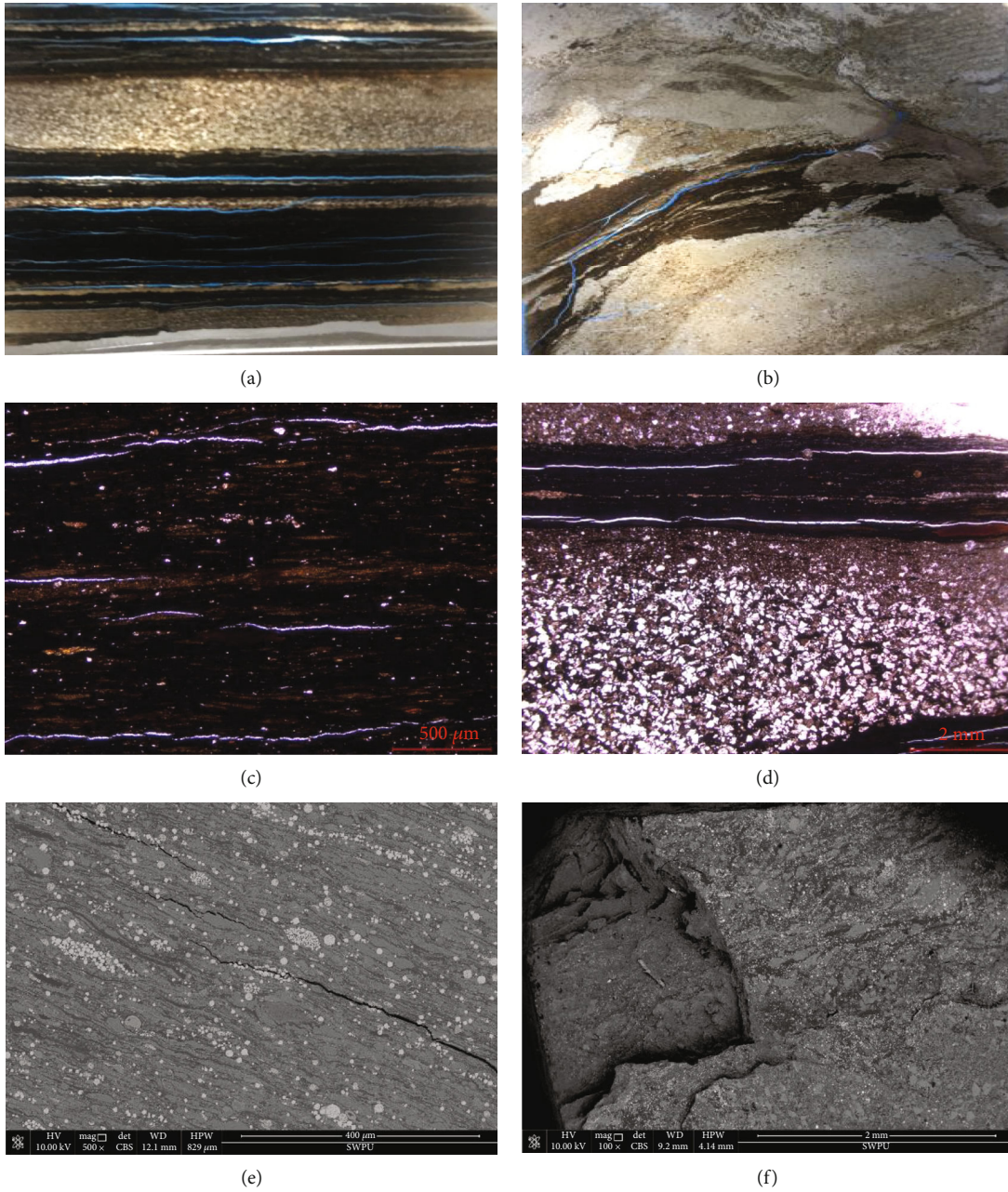


FIGURE 7: Microstructure of laminas and beddings. (a) Fracture networks formed by superimposition of shale and sandstone laminas. (b) Deformed laminas and dendritic fractures in transition section between shale and tuff. (c) Fractures in beddings. (d) Fractures in laminas. (e) The direction of mineral arrangement and organic matter band were consistent with fractures. (f) There was obvious delamination phenomenon at the edge of the sample when the observation surface was parallel to the lamellar plane.

$$PA_t = \frac{k_{t1}/k_{t3} - k_1/k_3}{k_1/k_3} \times 100\%, \quad (4)$$

where PA_t is the change rate of permeability anisotropy after different soaking time, k_{t1} is the permeability parallel to the laminar direction after different soaking time, and k_{t3} is the permeability perpendicular to the laminar direction after different soaking time.

2.5. Rock Microstructure Test. The distribution of fractures and pores can be clearly observed under the microscope through the thin section of rock injected with color glue, which is an effective method to observe the rock microstructure [39]. The rock with obvious surface features were selected to make thin sections and observed under the DM2700P microscope of Leica Instrument Co., Ltd.

Scanning electron microscope (SEM) is an important method to observe tight reservoir, which can display the

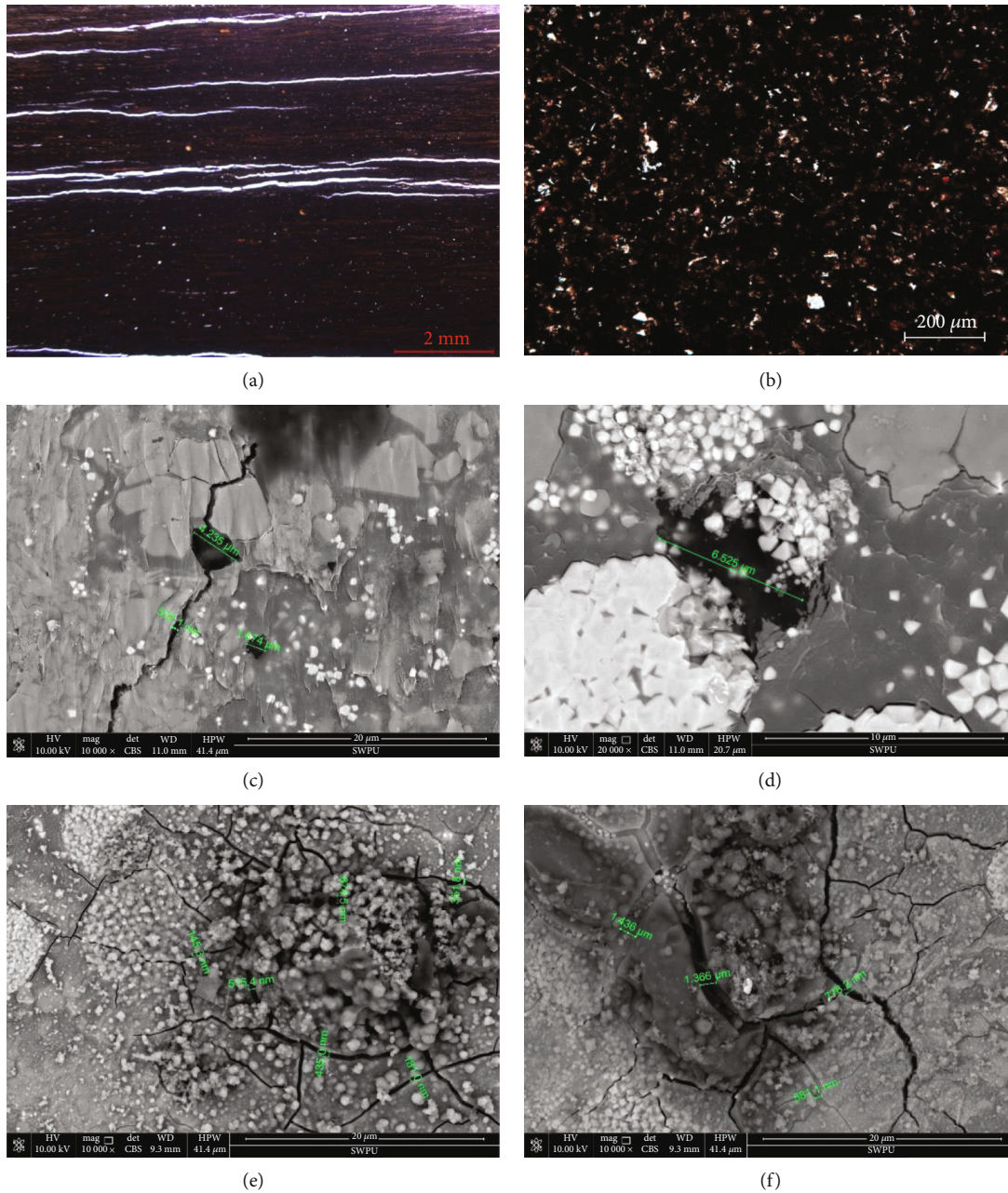


FIGURE 8: Microstructure of laminas and beddings after soaking. (a) Rock thin section after soaking in water. (b) Rock thin section after soaking in water-based drilling fluid. (c) The mineral on the rock surface fell off after soaking in water. (d) The pyrite coated with organic matter fell off after soaking in water. (e) Bentonite and solid particles in drilling fluid formed mud cake around pyrite. (f) The mud cake cracked after drying and dehydrating.

structural characteristics of rocks at a high magnification [40]. After polishing, metal spraying, soaking, and drying, micro-square cores were observed under the FEI Quanta 650 FEG field emission scanning electron microscope.

3. Results

3.1. Pore Size Distribution. In order to facilitate the description and study, the pores above 1 μm were classified as large pores, the pores with 100-1000 nm were classified as medium pores, and the pores below 100 nm were classified as small

pores. Figure 5 shows the pore size distribution of shale after soaking in water/water-based drilling fluid for 6 h, 12 h, 24 h, and 48 h. The pores of nonsoaked shale were mainly small and medium pores, and the pore volume decreased step by step with the increase of pore size. After soaking in water for 6 hours, large pores increased significantly, and the medium pores increased a little. After soaking in water for 6 to 12 hours, the pore volume of small pores increased significantly. After soaking in water for 12 to 24 hours, the pores of all sizes increased, and the increase of small pores was the most obvious. After soaking in water for 24 to 48 hours, the

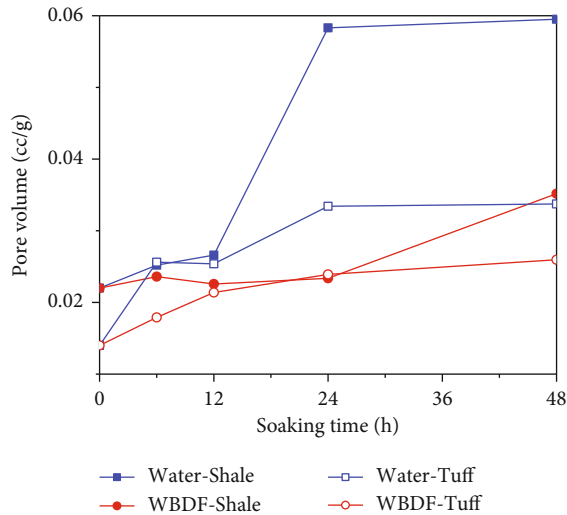


FIGURE 9: Variation curve of pore volume of shale and tuff with soaking time in different fluids.

total pore volume of shale was almost unchanged, and the transformation of pores with different sizes, such as the increase of 4-10 nm pores and the decrease of 10-100 nm pores, was the main feature of this stage.

The effect of water-based drilling fluid on pore size distribution is quite different from that of water-based drilling fluid. After soaking in water-based drilling fluid for 6 hours, the pores of shale were basically unchanged, which proves that drilling fluid had obvious inhibition effect on the growth of large pore at the initial stage of soaking. After soaking in water-based drilling fluid for 6 to 12 hours, large pores and the medium pores increased a little. After soaking in water-based drilling fluid for 12 to 24 hours, the small pores increased obviously, but the increase was smaller than that of the samples soaked in water. After soaking in water-based drilling fluid for 24 to 48 hours, the small pores increase greatly. The increase of total pore volume was the most obvious in this stage, while that of the sample soaked in water was basically unchanged.

Figure 6 shows the influence of fluid invasion on tuff's pore size distribution. The pore size of nonsoaked tuff was mainly concentrated in 4-12 nm. After soaking in water for 6 hours, the large pores increased significantly, and small pores around 10 nm also increased slightly. After soaking in water for 6 to 12 hours, the medium pores and small pores larger than 10 nm increased. After soaking in water for 12 to 48 hours, the pore volume of medium and large pores was basically unchanged, while that of small pores was increased. Under the influence of water, the large pores of tuff increased most obviously in the first 6 hours, the medium pores increased most obviously in 6 to 12 hours, and the small pores increased most obviously in 12 to 24 hours. The water-based drilling fluid also affected the pore size distribution of tuff caused by hydration. In the initial 6 hours of drilling fluid soaking, a small number of large pores appeared in the tuff, but the growth rate was less than that of the sam-

ples soaked in water. The tuff in water showed obvious medium pore's growth in 6-12 hours, while the tuff in water-based drilling fluid showed the same, but smaller growth after 12 hours of soaking.

By comparing the effects of water and water-based drilling fluid on the pore size distribution, it can be concluded that water-based drilling fluid can inhibit the growth of large pores and medium pores obviously in the experiment. The pore size changes of samples in water-based drilling were later than those in water, which proves that water-based drilling fluid delayed the hydration of rocks.

3.2. Permeability and Its Anisotropy. The permeability test results showed that the reservoir permeability was generally lower than 5 mD (Table 1). The k_1/k_3 of shale and tuff with lamellar structure could reach 11.1 and 5.7, while the values were 4.8 and 1.9 in shale and tuff without lamellar structure, which indicated that the permeability anisotropy of shale with lamellar structure was the strongest. The permeability is vector, and the lamellar structure makes the permeability of shale oil reservoir obviously anisotropic. The permeability of samples with lamellar structure was higher than that of samples without lamellar structure, and this phenomenon was most prominent when the sampling angle is 0° .

The soaking time and the type of fluid would change the original permeability of samples. Compared with water, water-based drilling fluid reduced the increase of permeability by inhibiting the growth of pores. According to the experimental results, the permeability of samples changed obviously in the initial 24 hours after soaking and tended to be stable after soaking 48 hours. The results show that the permeability of the samples could be increased by increasing the lamina, soaking in water, increasing the soaking time, and reducing the angle between the permeability direction and the lamina or bedding, and the effects of increasing the lamina and changing the permeability direction were the most obvious.

3.3. Microstructure. The density of laminas in rock thin sections was high, and shale laminas and sandstone laminas overlapped each other to form fracture networks (Figure 7(a)). In the lithology of the transition section between shale and tuff, the content of argillaceous and tuffaceous was high, which would form deformed laminas and dendritic fractures (Figure 7(b)). Under the microscope, it can be seen that there were considerable fractures in the lamellar rock (Figure 7(c)) and bedding rock (Figure 7(d)), and the fractures in the lamellar rock were generally longer and wider than those in the bedding rock. Under the SEM, it could be seen that the direction of mineral arrangement and organic matter band in the rock were consistent with fractures (Figure 7(e)), which proved that the orderly deposition of minerals had an impact on the fracture extension direction. When the observation surface of the sample was parallel to the lamellar plane, there were few fractures on the observation surface but were obvious delamination at the edge of the sample (Figure 7(f)), which proved that the fractures were concentrated on the lamellar and bedding planes.

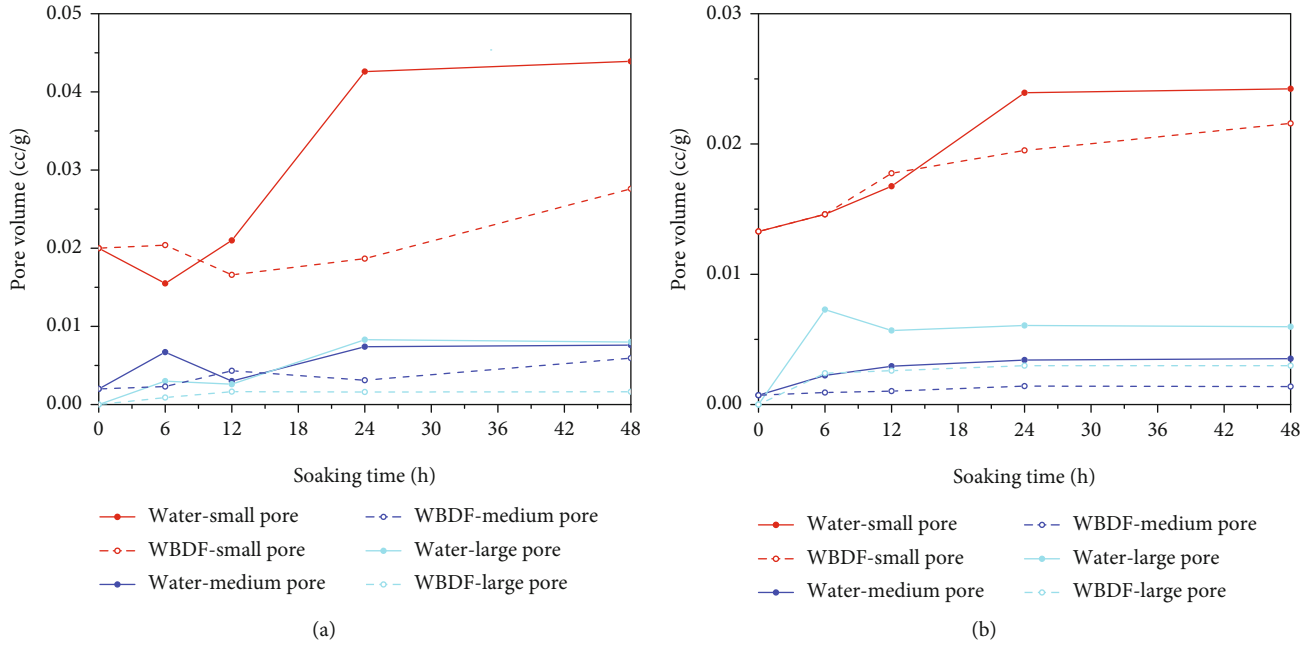


FIGURE 10: Variation curve of pore volume of different pore sizes with soaking time in different fluids. (a) Shale. (b) Tuff.

Figure 8 shows the microstructure of the sample after soaking in water and water-based drilling fluid for 24 hours and drying in a blower at 80°C for 12 hours. There were still a large number of fractures in the rock thin section after soaking in water (Figure 8(a)). After soaking in water-based drilling fluid, the surface of rock thin section was filled with bentonite, and no obvious fracture was found under the low magnification (Figure 8(b)). Under the SEM with a higher magnification, it was found that the mineral exfoliation occurred on the surface of the sample after soaking in water (Figure 8(c)), especially around pyrite wrapped by clay and organic matter (Figure 8(d)). After soaking in water-based drilling fluid, bentonite and plugging particles accumulated in the surface with high permeability to form plugging mud cake, and the mud cake cracked after drying and dehydrating (Figures 8(e) and 8(f)).

4. Discussion

4.1. Change of Pore Size Distribution Caused by Hydration Damage. Figure 9 is the variation curve of pore volume of shale and tuff after soaking in water and water-based drilling fluid. After soaking for 48 hours, the pore volume of shale and tuff in water increased by 170.5% and 140.9%, respectively, while that in water-based drilling fluid increased by 59.8% and 89.2%. After soaking for 6 hours, the pore growth of shale and tuff in water-based drilling fluid was smaller than those in water, while the pore growth of shale and tuff in the two fluids was close after soaking for 12 hours. After soaking for 24 hours, the pore volume of shale in water-based drilling fluid was much smaller than that in water, while this phenomenon occurred in tuff after soaking for 48 hours. The experimental results show that shale has stronger

hydration reaction than tuff at the initial stage of immersion, while the effect of hydration on tuff is longer.

Further study on the change of pore size in the hydration process showed that the change of the small pore was the most obvious, especially in shale (Figure 10). The growth rates of the small and medium pore of shale in water were 119.5% and 28.1% after 48 hours soaking, while those in water-based drilling fluid were 38.1% and 19.6%. At the same time, the increase of the large pore in water-based drilling fluid was 79.6% less than that in water, which showed that water-based drilling fluid had obvious inhibition effect on small and large pores in shale (Figure 10(a)). The growth rates of the small and medium pore of tuff in water were 82.4% and 391.2% after 48 hours soaking, while those in water-based drilling fluid were 62.4% and 92.9%. At the same time, the increase of the large pore in water-based drilling fluid was 50.2% less than that in water, which showed that water-based drilling fluid had obvious inhibition effect on medium and large pores in tuff (Figure 10(b)). According to the observation results of microstructure, large pores mainly formed by mineral shedding and fracture extension, which proved that water-based drilling fluid had obvious effect on strengthening mineral particles on rock surface and preventing fracture extension.

4.2. Effect of Hydration on Permeability Anisotropy of Lamellar Shale Oil Reservoir. The change of permeability with soaking time under different lithology, rock structure, fluid environment, and sampling angle is shown in Figure 11. The permeability of lamellar samples gradually tended to be stable after soaking for 12 hours, which was earlier than that of bedding samples. This phenomenon proved that hydration had a rapid effect on the permeability of lamellar samples. During the soaking process, the increase

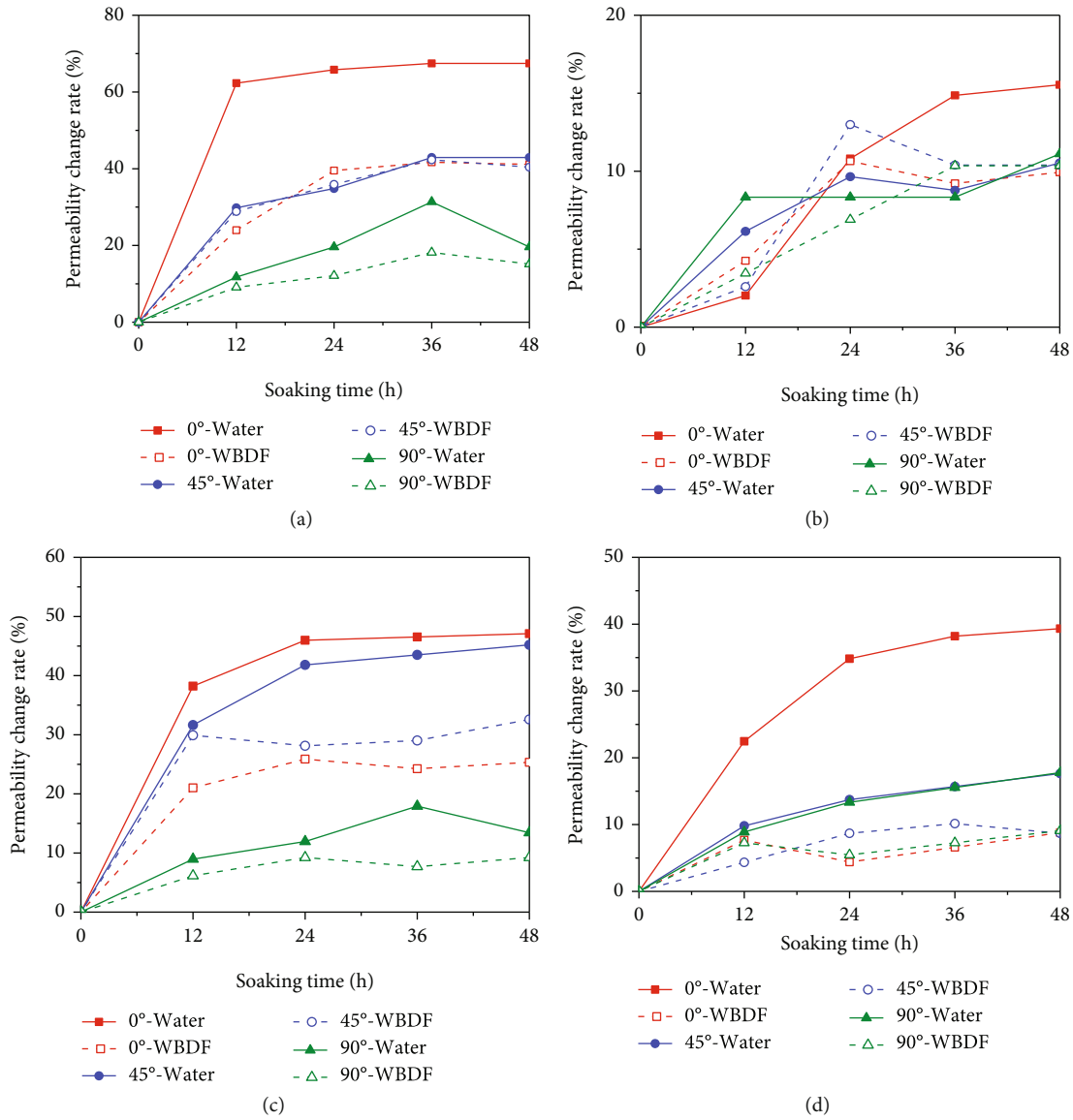


FIGURE 11: Variation curve of permeability with soaking time under different lithology, rock structure, fluid environment, and sampling angle. (a) Lamellar shale. (b) Bedding shale. (c) Lamellar tuff. (d) Bedding tuff.

of permeability in water-based drilling fluid was smaller than that water, and the difference was most obvious when the permeability direction was parallel to the lamina or bedding. The permeability of lamellar samples increased more than that of bedding samples, especially in shale, which proved that lamellar structure aggravated the influence of fluids on rock permeability.

The permeability was positively correlated with the soaking time in general, because the pore volume increased with the increase of soaking time, which was consistent with the results of the mercury injection experiment. The permeability of some samples decreased slightly with the increase of soaking time in some stages, which might lead by repeated shedding and adhesion of clay, mineral debris, and plugging particles in the permeability channel due to the continuous soaking and drying process.

According to formula (4), the influence of lithology, rock structure, and fluid environment was calculated as shown in Figure 12. The results show that the permeability change rate of lamellar samples was larger than that of samples without lamellar structure, whether immersed in water or water-based drilling fluid. Under the same lithology, rock structure, and soaking time, the permeability anisotropy of samples in water-based drilling fluid was smaller than that in water, which proved that the hydration could increase the permeability anisotropy of shale oil reservoir rock, and the influence can be reduced by adding inhibitor and plugging materials in the drilling fluid. Compared with rock structure and fluid environment, the influence of lithology on permeability anisotropy was not obvious.

Lu et al. studied the effect of hydration on the bedding shale by SEM. They found that after soaking in distilled

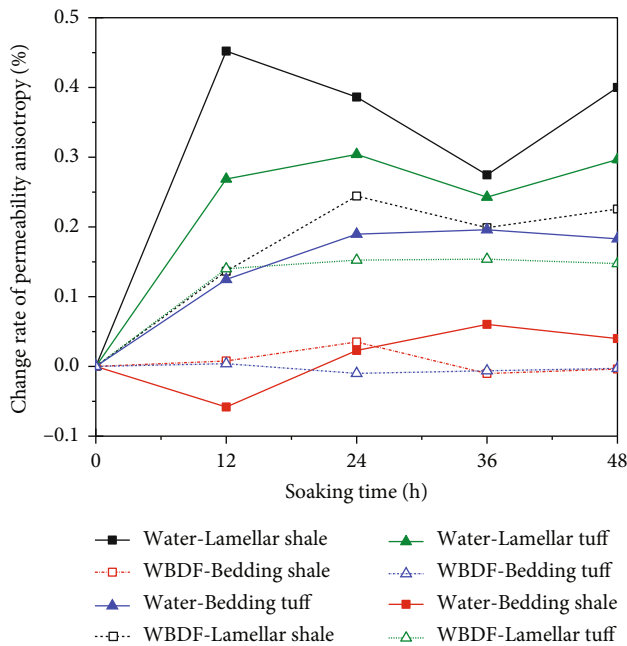


FIGURE 12: Variation curve of permeability anisotropy with soaking time under different lithology, rock structure, and fluid environment.

water, the width of microcracks parallel to bedding would increase, but there was no significant change in vertical bedding direction [41]. Through the experimental study, it is concluded that lamellar shale has similar properties and is more obvious than bedding shale.

4.3. Effect of Hydration on Rock Microstructure. The change of physical parameters of rock is the macroscopic manifestation of microstructure change. The results of rock thin section and scanning electron microscope showed that there were a lot of fractures near the lamellar structure, which were caused by the weak cementation between different lithology [42]. The fractures in the lamellar rock were longer and wider than those in bedding rocks. The larger fractures increased the contact area between fluid and rock and accelerated the hydration process, resulting in the permeability of lamellar rock tended to be stable earlier than that of bedding rock. The content of continental clastic rock is high in continental lamellar shale oil reservoirs. After soaking, minerals on the surface of the rock fell off and formed pores, which is the reason for the increase of large pores in the initial stage of soaking.

There are a lot of berry pyrite wrapped by clay in the lamellar shale oil reservoir of Ordos Basin. Hydration resulted in clay swelling and pyrite shedding, which increased the permeability channel of fluid. The solid particles and soil powder in the water-based drilling fluid were easy to be accumulated in the pores and fractures to form protective mud cake, which could reduce the mineral shedding and seal the pores and fractures.

5. Conclusion

To study characteristics of hydration and its influence on permeability of lamellar shale oil reservoirs, the influence of

water and water-based drilling fluid on pore size distribution, permeability, and microstructure of rock was tested by taking the core of lamellar shale oil reservoir in Ordos Basin. Several conclusions are drawn as follows:

- (1) The pores are mainly in nanoscale, which are concentrated below 100 nm. After soaking in water for 48 hours, the pore volume of shale increases by 170.5%, which is most obvious in 12-24 hours, and the pore volume of tuff increases by 140.9%, which is most obvious in 24-48 hours. Water-based drilling fluid can inhibit the growth of pores and delay the hydration of rocks
- (2) The permeability of lamellar rocks is generally higher than that of bedding rocks. Hydration can increase the permeability of rocks, which is most obvious when the permeability direction is parallel to the laminar/bedding direction. Hydration not only increases permeability but also enhances permeability anisotropy of rocks, especially lamellar rocks
- (3) Hydration leads to the formation of new pores, new fractures, and the expansion of existing fractures in rocks, especially in the strata containing large amounts of terrigenous clastic, lamellar structure, and pyrite. The new seepage channel increases the permeability of rock, and the soil powder and plugging particles in drilling fluid are easy to form protective mud cake in these places
- (4) Compared with bedding rock, lamellar rock has stronger anisotropy and more fracture, and its permeability is easier affected by hydration. It is helpful for the efficient and safe development of continental shale oil to find out the occurrence and characteristics of lamina and put forward corresponding drilling and development plans

Data Availability

All laboratory data used to support the findings of this study are included within the article.

Conflicts of Interest

The authors declare that they have no conflicts of interest.

Acknowledgments

This work was funded by the National Science and Technology Program during the 13 Five-year Plan Period (Grant no. 2017ZX05049) and the National Natural Science Foundation of China (Grant nos. 51774246 and 51474185).

References

- [1] C. Zou, G. Zhang, Z. Yang et al., "Geological concepts, characteristics, resource potential and key techniques of unconventional hydrocarbon: on unconventional petroleum geology,"

- Petroleum Exploration and Development*, vol. 40, pp. 385–399+454, 2013.
- [2] S. Hu, W. Zhao, L. Hou et al., “Development potential and technical strategy of continental shale oil in China,” *Petroleum Exploration and Development*, vol. 47, no. 4, pp. 877–887, 2020.
 - [3] U.S. Energy Information Administration, *How Much Shale (Tight) Oil is Produced in the United States?*, 2020, <https://www.eia.gov/tools/faqs/faq.php?id=847&t=6>.
 - [4] Q. Zhou, Z. Jin, G. Yang, N. Dong, and Z. Shang, “Shale oil exploration and production in the U. S.: status and outlook,” *Oil and Gas Geology*, vol. 40, pp. 469–477, 2019.
 - [5] D. Li, R. Li, Z. Zhu et al., “Rare earth elements geochemistry characteristics and their geological implications of lacustrine oil shale from Chang 7 oil layer in southern Ordos Basin, China,” *Geological Journal*, vol. 52, pp. 119–131, 2017.
 - [6] X. Nie, J. Lu, R. R. Djaroun, P. Wang, J. Li, and C. Zhang, “Oil content prediction of lacustrine organic-rich shale from wire-line logs: a case study of intersalt reservoirs in the Qianjiang Sag, Jiangnan Basin, China,” *Interpretation*, vol. 8, no. 3, pp. -SL79–SL88, 2020.
 - [7] Q. Hu, Y. Zhang, X. Meng, Z. Li, Z. Xie, and M. Li, “Characterization of micro-nano pore networks in shale oil reservoirs of Paleogene Shahejie Formation in Dongying Sag of Bohai Bay Basin, East China,” *Petroleum Exploration and Development*, vol. 44, no. 5, pp. 720–730, 2017.
 - [8] B. Liu, J. Shi, X. Fu et al., “Petrological characteristics and shale oil enrichment of lacustrine fine-grained sedimentary system: a case study of organic-rich shale in first member of Cretaceous Qingshankou Formation in Gulong Sag, Songliao Basin, NE China,” *Petroleum Exploration and Development*, vol. 45, no. 5, pp. 884–894, 2018.
 - [9] S. Zhang, C. Liu, L. Hao et al., “Paleoenvironmental conditions, organic matter accumulation, and unconventional hydrocarbon potential for the Permian Lucaogou Formation organic-rich rocks in Santanghu Basin, NW China,” *International Journal of Coal Geology*, vol. 185, pp. 44–60, 2018.
 - [10] Z. Jin, Z. Bai, B. Gao, and M. Li, “Has China ushered in the shale oil and gas revolution?,” *Oil and Gas Geology*, vol. 40, pp. 558–570, 2019.
 - [11] H. Zhong, Z. Qiu, W. Huang, and J. Cao, “Poly (oxypropylene)-amidoamine modified bentonite as potential shale inhibitor in water-based drilling fluids,” *Applied Clay Science*, vol. 67–68, pp. 36–43, 2012.
 - [12] H. She, Z. Hu, Z. Qu, Y. Zhang, and H. Guo, “Determination of the hydration damage instability period in a shale borehole wall and its application to a Fuling shale gas reservoir in China,” *Geofluids*, vol. 2019, Article ID 3016563, 17 pages, 2019.
 - [13] P. Zhao, X. Fan, Q. Zhang et al., “The effect of hydration on pores of shale oil reservoirs in the third submember of the Triassic Chang 7 member in Southern Ordos Basin,” *Energies*, vol. 12, no. 20, article 3932, 2019.
 - [14] X. Li, X. Yan, and Y. Kang, “Investigation of drill-in fluids damage and its impact on wellbore stability in Longmaxi shale reservoir,” *Journal of Petroleum Science and Engineering*, vol. 159, pp. 702–709, 2017.
 - [15] X. Liu, J. Xiong, L. Liang, C. Luo, and A. Zhang, “Analysis of the wettability of Longmaxi Formation shale in the south region of Sichuan Basin and its influence,” *Natural Gas Geoscience*, vol. 25, pp. 1644–1652, 2014.
 - [16] B. Shi, B. Xia, Y. Lin, and J. Xu, “CT imaging and mechanism analysis of crack development by hydration in hard-brittle shale formations,” *Acta Petrolei Sinica*, vol. 33, pp. 137–142, 2012.
 - [17] T. Ma and P. Chen, “Study of meso-damage characteristics of shale hydration based on CT scanning technology,” *Petroleum Exploration and Development*, vol. 41, no. 2, pp. 249–256, 2014.
 - [18] P. Wang, Z. Qu, and E.-M. Charalampidou, “Shale hydration damage captured by nuclear magnetic resonance,” *Journal of Dispersion Science and Technology*, vol. 40, no. 8, pp. 1129–1135, 2019.
 - [19] W. Zhao, S. Hu, L. Hou et al., “Types and resource potential of continental shale oil in China and its boundary with tight oil,” *Petroleum Exploration and Development*, vol. 47, no. 1, pp. 1–11, 2020.
 - [20] N. R. Backeberg, F. Iacoviello, M. Rittner et al., “Quantifying the anisotropy and tortuosity of permeable pathways in clay-rich mudstones using models based on X-ray tomography,” *Scientific Reports*, vol. 7, no. 1, article 14838, 2017.
 - [21] Y. Ma, Z. Pan, N. Zhong et al., “Experimental study of anisotropic gas permeability and its relationship with fracture structure of Longmaxi Shales, Sichuan Basin, China,” *Fuel*, vol. 180, pp. 106–115, 2016.
 - [22] G. Wang, D. Yang, and Z. Kang, “Experimental study on anisotropic permeability of oil shale under high temperature and triaxial stress,” *Chinese Journal of Rock Mechanics and Engineering*, vol. 39, pp. 1129–1141, 2020.
 - [23] J. Gui, T. Ma, P. Chen, H. Yuan, and Z. Guo, “Anisotropic damage to hard brittle shale with stress and hydration coupling,” *Energies*, vol. 11, p. 196, 2018.
 - [24] Q. Zhang, X. Fan, P. Chen, T. Ma, and F. Zeng, “Geomechanical behaviors of shale after water absorption considering the combined effect of anisotropy and hydration,” *Engineering Geology*, vol. 269, article 105547, 2020.
 - [25] C. Zou, Z. Ynag, J. Cui et al., “Formation mechanism, geological characteristics and development strategy of nonmarine shale oil in China,” *Petroleum Exploration and Development*, vol. 40, no. 1, pp. 15–27, 2013.
 - [26] K. Xi, K. Li, Y. Cao et al., “Laminae combination and shale oil enrichment patterns of Chang 7₃ sub-member organic-rich shales in the Triassic Yanchang Formation, Ordos Basin, NW China,” *Petroleum Exploration and Development*, vol. 47, no. 6, pp. 1342–1353, 2020.
 - [27] Z. Li, G. Tao, M. Li et al., “Discussion on prospecting potential of shale oil in the 3rd sub-member of the Triassic Chang 7 member in Binchang block, southwestern Ordos Basin,” *Oil and Gas Geology*, vol. 40, pp. 558–570, 2019.
 - [28] G. Chen, W. Gang, Y. Liu et al., “High-resolution sediment accumulation rate determined by cyclostratigraphy and its impact on the organic matter abundance of the hydrocarbon source rock in the Yanchang Formation, Ordos Basin, China,” *Marine and Petroleum Geology*, vol. 103, pp. 1–11, 2019.
 - [29] H. Cao, X. Shan, P. Sun, H. Chi, and S. Du, “Geochemical characteristics of oil shale in the Triassic Chang7 subsection, southern Ordos basin, China, and palaeo-environment reconstruction,” *Neues Jahrbuch für Mineralogie, Abhandlungen*, vol. 193, pp. 45–57, 2016.
 - [30] W. Yuan, G. Liu, L. Xu, X. Niu, and C. Li, “Petrographic and geochemical characteristics of organic-rich shale and tuff of the Upper Triassic Yanchang Formation, Ordos Basin, China:

- implications for lacustrine fertilization by volcanic ash,” *Canadian Journal of Earth Science*, vol. 56, no. 1, pp. 47–59, 2019.
- [31] Z. Xu, L. Liu, B. Liu et al., “Geochemical characteristics of the Triassic Chang 7 lacustrine source rocks, Ordos Basin, China: implications for paleoenvironment, petroleum potential and tight oil occurrence,” *Journal of Asian Earth Science*, vol. 178, pp. 112–138, 2019.
- [32] Z. Huang, Y. Hao, S. Li et al., “Oil-bearing potential, mobility evaluation and significance of shale oil in Chang 7 shale system in the Ordos Basin: a case study of well H317,” *Geology in China*, vol. 47, pp. 210–219, 2020.
- [33] J. Cui, R. Zhu, Z. Luo, and S. Li, “Sedimentary and geochemical characteristics of the Triassic Chang 7 member shale in the southeastern Ordos Basin, Central China,” *Petroleum Science*, vol. 16, no. 2, pp. 285–297, 2019.
- [34] P. Zhao, X. Fan, Q. Zhang, M. Zhang, and B. Yao, “Effects of hydration on physical properties and rock microstructure of shale oil reservoir in the Triassic Chang 7 member of Southern Ordos Basin,” *Energy Sources, Part A: Recovery, Utilization, and Environmental Effects*, pp. 1–19, 2020.
- [35] F. Wang, K. Yang, J. You, and X. Lei, “Analysis of pore size distribution and fractal dimension in tight sandstone with mercury intrusion porosimetry,” *Results in Physics*, vol. 13, article 102283, 2019.
- [36] M. M. Labani, R. Rezaee, A. Saeedi, and A. Hinai, “Evaluation of pore size spectrum of gas shale reservoirs using low pressure nitrogen adsorption, gas expansion and mercury porosimetry: a case study from the Perth and Canning Basins, Western Australia,” *Journal of Petroleum Science and Engineering*, vol. 112, pp. 7–16, 2013.
- [37] G. Sheng, F. Javadpour, and Y. Su, “Dynamic porosity and apparent permeability in porous organic matter of shale gas reservoirs,” *Fuel*, vol. 251, pp. 341–351, 2019.
- [38] T. Yang, P. Jia, and W. Shi, “Seepage-stress coupled analysis on anisotropic characteristics of the fractured rock mass around roadway,” *Tunnelling and Underground Space Technology*, vol. 43, pp. 11–19, 2014.
- [39] S. Fang, J. He, F. Hou et al., “Reservoirs pore space types and evolution in M-5(5) to M-5(1) submembers of Majiagou Formation of Middle Ordovician in central gasfield area of Ordos basin,” *Acta Petrologica Sinica*, vol. 25, pp. 2425–2441, 2009.
- [40] X. Tang, Y. Zhu, and Y. Liu, “Investigation of shale nano-pore characteristics by scanning electron microscope and low-pressure nitrogen adsorption,” *Journal of Nanoscience and Nanotechnology*, vol. 17, no. 9, pp. 6252–6261, 2017.
- [41] Y. H. Lu, L. P. Zeng, Y. Jin et al., “Effect of shale anisotropy on hydration and its implications for water uptake,” *Energies*, vol. 12, no. 22, article 4225, 2019.
- [42] B. Liu, Y. F. Lu, Y. L. Meng et al., “Petrologic characteristics and genetic model of lacustrine lamellar fine-grained rock and its significance for shale oil exploration: A case study of Permian Lucaogou Formation in Malang sag, Santanghu Basin, NW China,” *Petroleum Exploration and Development*, vol. 42, no. 5, pp. 656–666, 2015.

Research Article

A Comparative Study of the Micropore Structure between the Transitional and Marine Shales in China

Pengfei Jiao ¹, Genshun Yao,¹ Shangwen Zhou ^{1,2,3}, Zhe Yu,^{1,2,3} and Shiluo Wang^{1,2,3}

¹PetroChina Research Institute of Petroleum Exploration & Development, Beijing 100083, China

²National Energy Shale Gas R&D (Experiment) Center, Langfang 065007, China

³Key Lab of Unconventional Oil & Gas, CNPC, Langfang 065007, China

Correspondence should be addressed to Shangwen Zhou; zhousw10@petrochina.com.cn

Received 24 January 2021; Revised 9 March 2021; Accepted 25 March 2021; Published 8 April 2021

Academic Editor: Zhiye Gao

Copyright © 2021 Pengfei Jiao et al. This is an open access article distributed under the Creative Commons Attribution License, which permits unrestricted use, distribution, and reproduction in any medium, provided the original work is properly cited.

To compare the micropore structure of marine-continental transitional shale with marine shale, organic geochemical, field emission scanning electron microscopy, and low-temperature nitrogen adsorption experiments were conducted on shale samples from the Shanxi Formation in the eastern Ordos Basin and the Longmaxi Formation in the southern Sichuan Basin. The results show that Shanxi Formation shale has a smaller specific surface area and pore volume than Longmaxi Formation shale; therefore, the transitional shales fail to provide sufficient pore spaces for the effective storage and preservation of natural gas. Both the transitional and marine shales are in an overmature stage with high total organic carbon content, but they differ considerably in pore types and development degrees. Inorganic pores and fractures are dominantly developed in transitional shales, such as intragranular pores and clay mineral interlayer fractures, while organic nanopores are rarely developed. In contrast, organic pores are the dominant pore type in the marine shales and inorganic pores are rarely observed. The fractal analysis also shows that pore structure complexity and heterogeneity are quite different. These differences were related to different organic types, i.e., type I of marine shale and type III of transitional shale. Marine Longmaxi shale has experienced liquid hydrocarbon cracking, gas generation, and pore-forming processes, providing good conditions for natural gas to be preserved. However, during the evolution of transitional Shanxi shale, gas cannot be effectively preserved due to the lack of the above evolution processes, leading to the poor gas-bearing property. The detailed comparison of the micropore structure between the transitional and marine shales is of great importance for the future exploitation of marine-continental transitional shale gas in China.

1. Introduction

After the shale gas successes in North America, China's shale gas exploration and development has achieved great achievements in marine shales, especially in the southern Sichuan Basin [1–4]. In 2020, China reported total shale gas production of 20 billion cubic meters. Marine shale gas in China is mainly developed in the Upper Ordovician Wufeng-Lower Silurian Longmaxi Formation, where the depositional environment is stable and changes progressively from deep-sea shelf facies to shallow-sea shelf facies, featuring large thickness, vast distribution, and good continuity [5, 6]. Previous studies have covered the depositional sediment, reservoir

characteristics, and main constraints for the enrichment and high yield of the marine shale in the Sichuan Basin, especially about its pore development and relating mechanisms [7–9]. In the Sichuan Basin, Wufeng-Longmaxi Formation marine shale features high TOC, with the organic maturity generally in the high maturity stage to the overmature stage and the organic type commonly being type I or type II₁, promising good hydrocarbon-generating potential [10–12]. The mineral contents are principally quartz minerals and secondarily clay minerals. Carbonate minerals are relatively developed, and pyrite is developed in many layers. Shale has good brittleness, which is beneficial to hydrofracturing operation [13, 14].

The field emission scanning electron microscope (FE-SEM) images indicate that the marine shale has organic nanopores of various shapes: irregular organic matter pores are mainly developed in the primary organic matter, and the spongy and dense round bubble pores are mainly developed in the solid bitumen [15–17]. The image quantitative analysis method can be used to extract organic pores in FE-SEM images and count their pore size distribution (PSD) and surface porosity (SP), and it is found that mesopores (2 nm–50 nm) and micropores (<2 nm) are mainly developed in marine shale [18–20]. The shape of the low-temperature nitrogen adsorption (LTNA) curve shows that the Longmaxi shale is dominated by ink bottle pores and parallel plate pores [21]. There are many factors affecting the development of organic matter pores in marine shale. It is generally believed that the higher the organic carbon content, the more developed the organic pores [22, 23]. Various minerals also have different effects on the development of organic matter pores [24–27]. As to the genesis of the organic nanopores, it is assumed that they mainly come from gas generation by kerogen pyrolysis [28, 29] and raw oil (bitumen) cracking [30–32].

Compared with marine shale, less attention has been paid to marine-continental transitional shale, which is mostly found in delta facies where rapid microfacies changes have caused the marine-continental transitional shale to be thinner and less continuous, making it more difficult to be developed [33, 34]. However, the transitional shale gas resources are large, about $19.8 \times 10^{12} \text{ m}^3$ [35], and marine-continental transitional shale will be the future research highlight for shale gas exploration and development in China. The establishment of a complete set of the marine-continental transitional shale gas theory will fill the gap of the unconventional oil and gas theory. At present, the organic geochemistry, mineral composition, and micropore structure characteristics of marine-continental transitional shale in the Longtan Formation of the Sichuan Basin and the Shanxi Formation of the Ordos Basin have been studied. The research shows that the transitional shale has high TOC, its organic maturity varies from place to place, and it is usually in the high maturity stage, and the kerogen type is mainly type III or type II₂ [36]. Clay minerals are the main components, most of which are montmorillonite or illite/smectite mixed layers [37–39].

Four types of pores are developed in the transitional facies shale, which are clay mineral pores, organic matter pores, brittle mineral pores, and microfractures. Clay mineral pores are dominant, followed by brittle mineral pores and organic matter pores [40, 41]. The LTNA curve shape of the transitional shale is similar to that of the marine shale, indicating that the mesopores with the ink bottle shape and parallel plate shape are mainly developed [42, 43]. It can be found that the main pore development types of marine shale and marine-continental transitional shale are very different. Some scholars think that it is caused by different types of kerogen [44, 45]. Some researchers believe that the clay mineral content is the main factor affecting the pore development of marine-continental transitional shale [46].

Although some basic studies have been carried out on the marine-continental transitional shale and the micropore structure characteristics have been preliminarily understood, few scholars have compared and analyzed the pore development characteristics of the two types of shale. In particular, the reason for their differences has not been deeply analyzed, which is very important for the future exploration of transitional shales. In the present study, we investigated the micropore structure characteristics of marine-continental transitional shale from the Shanxi Formation in the eastern Ordos Basin by FE-SEM and LTNA tests and FHH fractal analysis. And we also made some comparisons between transitional shales and marine shales, focusing on the pore development of marine-continental transitional shale and its geological significance.

2. Geological Settings

The Ordos Basin, located in the west of the North China plate, is composed of six secondary structural units: Yimeng uplift, Tianhuan depression, Northern Shanxi slope, Western margin thrust belt, Weibei uplift, and West Shanxi flexural belt [47]. The Permian strata in the eastern margin of the Ordos Basin were developed in marine-continental transitional facies deposits, which can be divided into Shanxi, Benxi, and Taiyuan Formations. The Shanxi Formation is dominated by delta facies, while the Benxi and Taiyuan Formations were developed in delta, lagoon, tidal flat, and shallow shelf deposits from north to south. In the vertical directions, mudstone is distributed alternately with coal and sandstone, and pure mudstone is rarely developed. The thickness of mudstone in Benxi, Taiyuan, and Shanxi Formations is about 10–30 m, 20–30 m, and 70–100 m, respectively. Therefore, the mudstone of the Shanxi Formation is preferred as the research object of marine-continental transitional shale in this area. The studied shale samples are from the Daning-Jixian block in the southern end of the West Shanxi flexural belt and the southern margin of the Yishan slope, Ordos Basin (Figure 1). Its tectonic setting is relatively gentle and simple, and the fault is not developed, which is characterized by “one uplift and one depression and two slopes.” In the Shan-2 member of the Daning-Jixian block, the mudstone thickness is primarily ranging from 40 m to 70 m.

The Sichuan Basin is located on the western edge of the Upper Yangtze Platform, surrounded by many orogenic belts [48]. The marine Longmaxi Formation in the Sichuan Basin is dominated by shelf facies with stable sedimentary facies belts and wide distribution. The deep-water shelf sediments are developed in the southern and northeastern Sichuan Basin. The studied shale samples from the Longmaxi Formation in the Taiyang-Dazhai block belong to deep-water shelf sediments, located in the low fold structural belt of the southern Sichuan Basin, which presents a structural pattern of “three sags, one uplift,” i.e., Luobu-Daba syncline, Yunshanba syncline, Baiyangping syncline, and Taiyang anticline (Figure 2). The shale thickness of the Taiyang-Dazhai block is about 100–170 m, which is larger than that of the Daning-Jixian block.

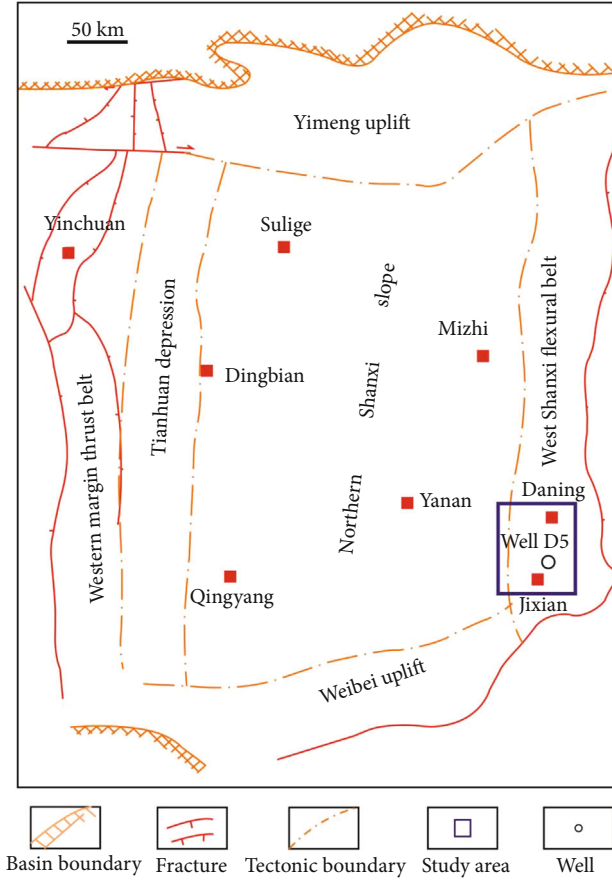


FIGURE 1: Daning-Jixian block in the eastern Ordos Basin.

3. Samples and Experiments

3.1. Samples. A total of 32 shale samples were collected from the Shanxi Formation of well D5 in the eastern Ordos Basin (16 samples) and from the Longmaxi Formation of well Y5 in the southern Sichuan Basin (16 samples). The locations of the 2 wells are shown in Figures 1 and 2, respectively. Well D5 is located in the Daning-Jixian block, and well Y5 is situated in the Taiyang-Dazhai block. These samples will be tested as follows.

3.2. Field Emission Scanning Electron Microscopy (FE-SEM). The shale samples were imaged with an FEI Helios 650 field emission scanning electron microscope (FE-SEM). Backscattering electron (BSE) mode images well discriminate different minerals and organic matters (voltage 5 kV, current 1.6 nA, and maximum resolution 2 nm), while secondary electron (SE) mode images can well distinguish organic matters and pores (voltage 10 kV, current 0.4 nA, and maximum resolution 2 nm) [49]. The shale samples were cut into approximately 1 cm thick pieces that are parallel between the upper and lower parts. The observation surface was ground with 400-, 800-, 1000-, and 2000-mesh sandpaper to mirror-smooth, then polished again with diamond water, cleaned, and kept in a 105°C incubator for 2 days. The observation surface of the sample was then polished and carbon-

plated with a PECS II 685 argon ion polisher to make the observation surface smoother and enhance the electrical conductivity of the sample.

3.3. Low-Temperature Nitrogen Adsorption (LTNA). The surface area and porosity analyzer ASAP 2420 produced by Micromeritics Company was used to conduct LTNA experiments on shale samples crushed to 200-mesh sandpaper at 77 K. The saturated vapor pressure p_0 of N_2 is 0.11117 MPa, and the maximum equilibrium pressure of the experiment is the atmospheric pressure (0.1013 MPa) to deliver a wide N_2 adsorption and desorption isothermal line ($p/p_0 = 0.0095 - 0.995$, where p is the equilibrium pressure). The Barrett-Joyner-Halenda (BJH) method can be used to analyze the mesopore distribution and calculate the average pore size and PV [50]. The SSA of the sample can be derived by the Brunauer-Emmett-Teller (BET) process [51, 52]. The average pore size, total pore volume, and specific surface area of the two shales were compared and analyzed to further characterize their differences.

3.4. Fractal Method. The FHH fractal approach features a simple model expression and operation principle, and it follows the classic theory of multilayer adsorption [53]. The multilayer adsorption on the surface of mesopores in shale can be explained by the following expression:

$$\theta = \frac{V}{V_m} = k \cdot \left(-\ln \frac{p}{p_0} \right)^{-f(D)} = k \cdot \left(\ln \frac{p_0}{p} \right)^{-f(D)}, \quad (1)$$

where θ is the surface coverage of adsorbed molecules; V is the adsorption quantity at the equilibrium pressure, cm^3/g ; V_m is the maximum adsorption capacity of the monolayer, cm^3/g ; p is the equilibrium pressure, MPa; and p_0 is the saturated vapor pressure of the adsorbate, MPa. k is the characteristic constant, and $f(D)$ is the expression of fractal dimension D of mesopores. Take the logarithm on both sides of Equation (1) to get

$$\ln V = -f(D) \cdot \ln \ln \frac{p_0}{p} + \ln V_m + \ln k. \quad (2)$$

In Equation (2), $\ln V$ is linear to $\ln \ln(p_0/p)$, and $-f(D)$ is the slope of a linear equation. According to Ismail and Pfeifer [54], at the beginning of N_2 adsorption, the number of adsorbed molecular layers is less, and the relation of $f(D)$ with fractal dimension D conforms to the following expression:

$$f(D) = \frac{3-D}{3}. \quad (3)$$

When there are more molecular layers, capillary condensation will take place. Then, the relation of $f(D)$ with fractal dimension D conforms to the following equation:

$$f(D) = 3 - D. \quad (4)$$

So, the fractal dimension analysis of mesopores was made

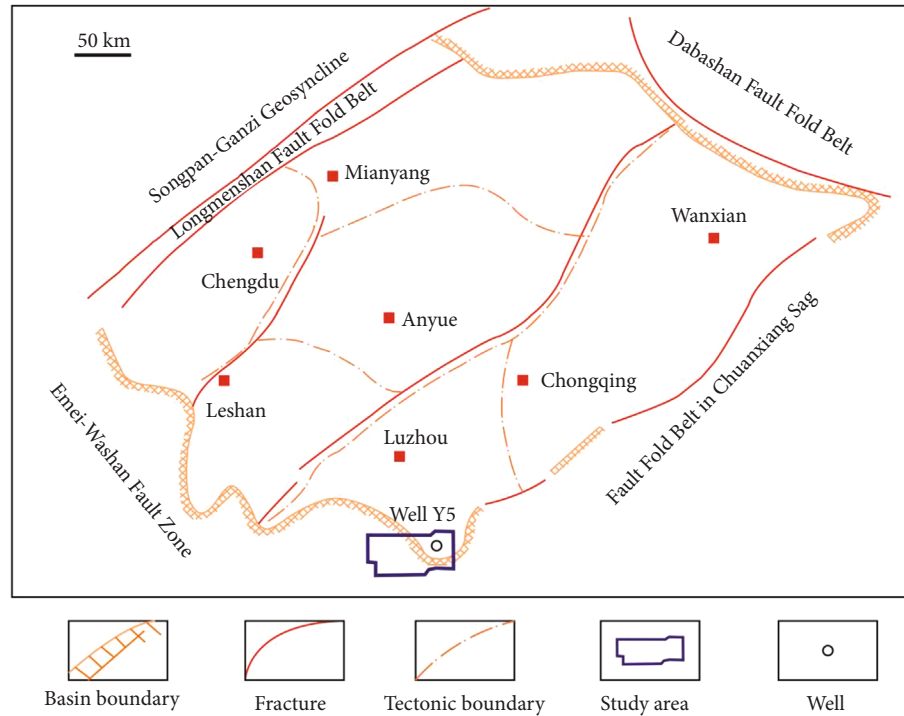


FIGURE 2: Taiyang-Dazhai block in the south of the Sichuan Basin.

over two stages: initial N_2 adsorption when there are fewer adsorbed molecular layers and later N_2 adsorption when there are more adsorbed molecular layers and capillary condensation takes place.

4. Results

4.1. Organic Geochemistry and Mineral Compositions. The TOC values of the transitional shale are 0.45%–15% with an average of 3.92%. About 60% of the transitional shale samples have TOC content greater than 2%. The organic maturity is 1.92%–2.60% with an average of 2.36%, suggesting a gas-generating peak stage. As the organic type is type III, it mainly produces gas. Among the marine shale samples, the TOC is 1.07%–6.18% with an average of 2.89%. The organic maturity is 2.47%–2.79% with an average of 2.59%, suggesting an overmature gas-generating stage. The organic type is mainly type I and partially type II₁.

Shanxi Formation shale has a relatively high clay mineral content and quartz content, with an average of 47.81% and 40%, respectively, but they fluctuate greatly. Only very few samples contain carbonate minerals (Figure 3(a)). Kaolinite is the main clay mineral, followed by illite and smectite mixed layers; illite content is low; some samples contain a small amount of chlorite. Longmaxi Formation shale has slightly lower clay minerals than quartz minerals, with an average of 29.40% for clay minerals and 34.60% for quartz minerals. Carbonate minerals are very developed with an average of 27.80% (Figure 3(b)). The clay minerals are mostly illite/smectite mixed layers and secondarily illite. Chlorite is well developed, and kaolinite is not found.

4.2. Pore Morphology from FE-SEM. After argon ion polishing and carbon plating on shale samples, their SEM images were obtained by FE-SEM. The SE mode images can clearly distinguish organic matters and organic pores. Organic matters are darker than other minerals and grayish-black in color. The halo generated on the edge of organic pores can well determine the size of the organic pores. In Shanxi Formation shale, the organic matters are typically loose lumps. A small amount of organic matter locally developed dense bubble pores of different sizes (Figure 4(a)). Most of the organic matters contain a few angular organic pores (Figure 4(b)). In addition, some organic matter developed marginal fractures or a small number of angular pores in the part contacting with minerals (Figure 4(c)). The quartz and feldspar minerals mostly contain angular and elliptical intragranular pores (Figure 4(d)). Dissolution pores can be seen in a few calcite and feldspar minerals. Inside the pyrite framboids, angular intercrystalline pores are frequently encountered (Figure 4(e)). Clay minerals represent the main mineral type for Shanxi Formation shale, and they are predominantly smectite and illite/smectite mixed layers; hence, slit clay mineral pores and clay mineral interlayer fractures are very developed (Figure 4(f)). Marine-continental transitional shale mainly features various types of inorganic pores, with slit clay mineral pores and clay mineral interlayer fractures being the most developed, followed by brittle mineral intragranular pores.

Unlike Shanxi Formation shale, there are numerous nanoscale organic pores with pore size mostly ranging from dozens up to hundreds of nanometers inside the organic matters of Longmaxi Formation shale. Most of the organic matters contain large amounts of bubble pores about

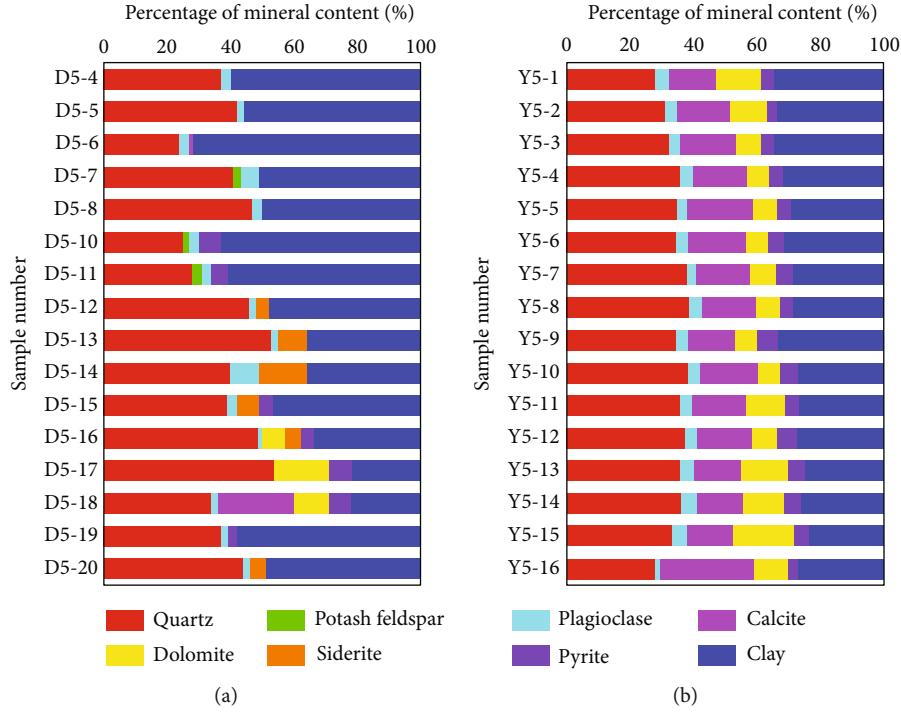


FIGURE 3: Mineral percentage content bar chart of (a) Shanxi Formation shale and (b) Longmaxi Formation shale.

100 nm in size (Figure 5(a)), and fused macropores composed of a number of bubble pores contacted together are very common. Irregular primary pores are developed in a few organic matters. Pyrite is well developed in marine shale, which is associated with organic matter. Organic pores inside these organic matters are very developed and relatively small in size (Figure 5(c)). As to mineral matrix pores, in addition to angular intragranular pores in brittle minerals like quartz, feldspar, and calcite (Figure 5(d)), slit-shaped or wedge-shaped intergranular pores are often observed on the edge of some brittle minerals (Figure 5(e)). Inside strawberry pyrite, around 20 μm in diameter, angular intercrystalline pores are often detected (Figure 5(f)). Longmaxi Formation shale mainly features organic bubble pores, followed by brittle mineral intragranular and intergranular pores. On the contrary, clay mineral pores are not well developed.

4.3. Analysis of Low-Temperature Nitrogen Adsorption. The marine shale and the marine-continental transitional shale display similar nitrogen adsorption isothermal patterns. The curve is an anti-S type as a whole, belonging to the typical type IV isotherm, and the hysteresis loop is equivalent to type H3 [21, 43] (Figure 6). At the beginning of adsorption, micropore filling and single-layer adsorption are completed quickly [55], and the adsorption quantity increases steeply. When the relative pressure increases to 0.8, the adsorption curve is relatively mild, suggesting the entry into a multilayer adsorption stage, and the adsorption quantity increases slowly by almost one time. When the relative pressure further increases to 1, capillary condensation takes place, the adsorption quantity quickly rises and is unsaturated. The maximum

adsorption quantity of the marine shale is greater than that of the marine-continental transitional shale.

On the desorption branch, when the relative pressure decreases from 1 to 0.8, the gas in the half-open mesopores or macropores is quickly desorbed along the original path, causing the adsorption quantity to drop steeply. Then, the adsorption quantity drops slowly until the relative pressure decreases to nearby 0.5, when sudden evaporation causes the adsorption quantity to drop steeply again. After that, the adsorption curve almost coincides with the desorption curve. A hysteresis loop on the isotherm suggests the existence of mesopores in the sample. Obvious capillary condensation on the adsorption branch occurs at a pressure nearby 0.8 with no adsorption saturation, indicating that there are parallel plate pores with four edges open. Yet sudden evaporation takes place on the desorption branch at the relative pressure of 0.5, implying that there are thin bottleneck pores or ink bottle pores [35].

4.4. Analysis of Fractal. According to the FHH mesoporous fractal model, a scatter plot with the logarithm of the N_2 adsorption amount under a relative pressure ($\ln V$) as the horizontal axis and the double logarithm of the reciprocal of the relative pressure ($\ln \ln(p/p_0)$) as the vertical axis is shown in Figure 7. Since capillary condensation begins to appear when the relative pressure is greater than 0.5 (corresponding to the hysteresis loop), the adsorption data were divided into a low-pressure section with the relative pressure smaller than 0.5 and a high-pressure section with the relative pressure of 0.5-1, corresponding to Equations (3) and (4),

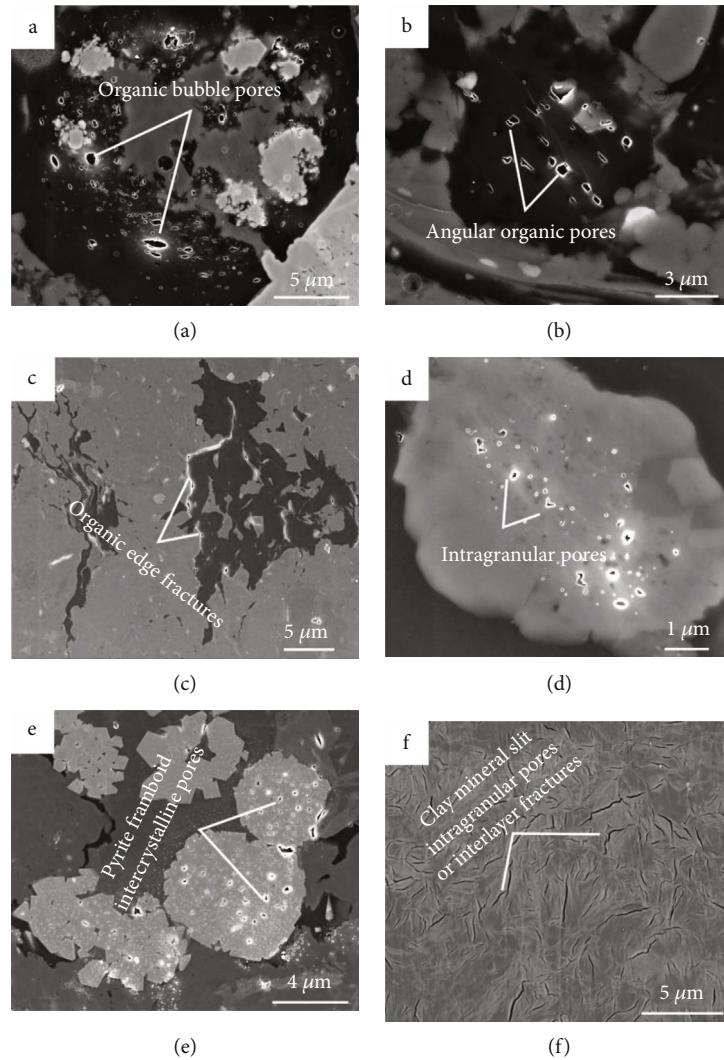


FIGURE 4: Different types of nanoscale pores in the marine-continental transitional shale. (a) Organic bubble pores. (b) Angular organic pores. (c) Organic edge fractures. (d) Intragranular pores. (e) Pyrite framboid intercrystalline pores. (f) Clay mineral slit intragranular pores or interlayer fractures.

respectively. For transitional shale, the fractal dimension in the low-pressure segment (D_1) is 1.7646–1.9944 with an average of 1.8670, and that in the high-pressure segment (D_2) is 2.5936–2.6716 with an average of 2.6368. For marine shale, D_1 is 2.0253–2.1666 with an average of 2.0779 and D_2 is 2.7260–2.7819 with an average of 2.7515 (Table 1).

5. Discussion

5.1. Pore Structure Characteristic Comparison. PSD curves derived from the BJH adsorption method can be used to determine the PSD of mesopores and some of the macropores. PSD curves can be plotted in two ways. Their ordinates are $dV/d(D)$ and $dV/d \log(D)$, respectively. Given that both shales contain few large pores and the second method can highlight the distribution of large pores, the second method was selected (Figure 8). The two shales differ obviously in PSD. In Shanxi Formation shale, the PSD curves vary considerably from one sample to another, but their general trend is

quite the same, suggesting that transitional shale is highly heterogeneous. In Longmaxi Formation shale, the PSDs of mesopores are tight while those of macropores are loose, indicating that marine shale is less heterogeneous, but macropore development differs obviously among different layers. Comparison of the two shales shows that in terms of mesopores, marine shale is more developed than transitional shale, especially pores 2 nm–4 nm in size. For macropores, the two shales do not differ much, except that the change rate of pore volume in Shanxi Formation shale increases faster with the increase of pore size.

The BET specific surface area (SSA) and BJH total pore volume (PV) were compared to further investigate the pore structure differences between transitional shale and marine shale. For Shanxi Formation shale, the SSA is 2.1 m²/g–12.4 m²/g with an average of 9.1 m²/g, the PV is 0.0049 ml/g–0.0314 ml/g with an average of 0.0245 ml/g, and the average pore diameter is 13.6 nm. In terms of Longmaxi Formation shale, the SSA is 19.3 m²/g–28.2 m²/g with

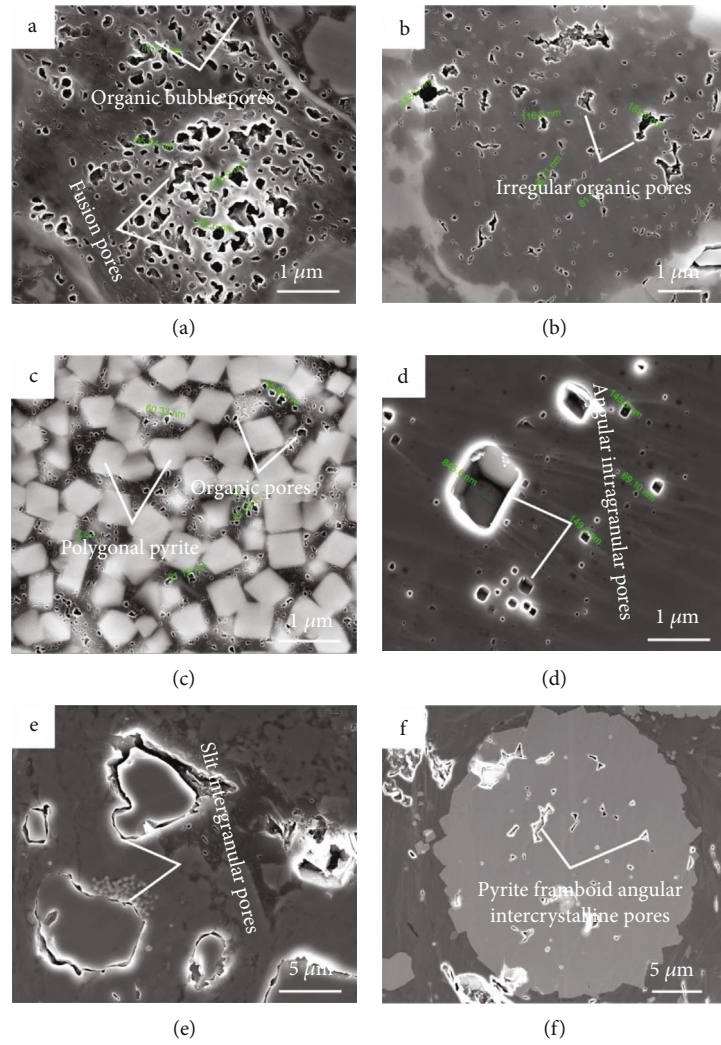


FIGURE 5: Different types of nanoscale pores in the marine shale. (a) Organic bubble pores. (b) Irregular organic pores. (c) Organic pores filled in pyrite particles. (d) Angular intragranular pores. (e) Slit intergranular pores. (f) Pyrite framboid angular intercrystalline pores.

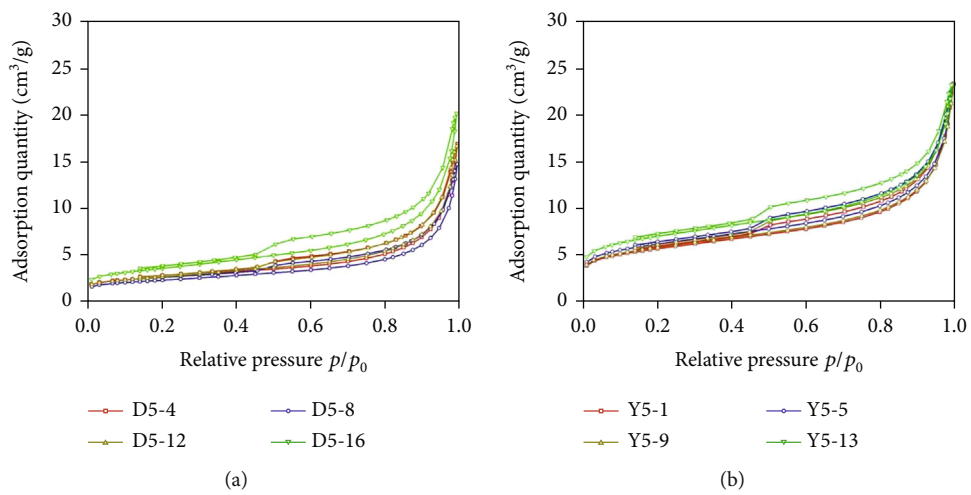


FIGURE 6: Typical sample N_2 isothermal adsorption graph of (a) Shanxi Formation shale and (b) Longmaxi Formation shale.

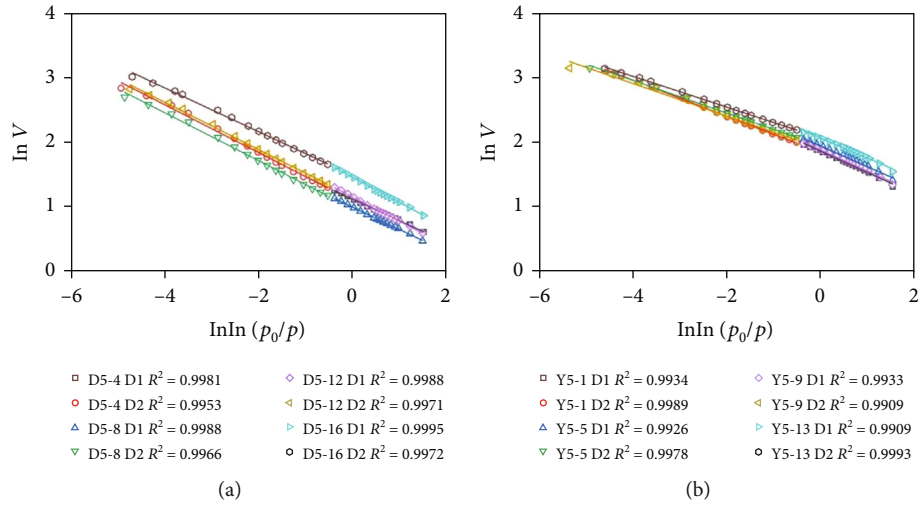


FIGURE 7: Typical sample mesopore fractal of (a) Shanxi Formation shale and (b) Longmaxi Formation shale.

TABLE 1: Mesopore fractal dimension comparison.

Sample ID	Relative pressure (0-0.5)		Relative pressure (0.5-1)		Sample ID	Relative pressure (0-0.5)		Relative pressure (0.5-1)	
	$f(D)$	D_1	$f(D)$	D_2		$f(D)$	D_1	$f(D)$	D_2
D5-4	0.3352	1.9944	0.3712	2.6288	Y5-1	0.2778	2.1666	0.2769	2.7231
D5-5	0.3521	1.9437	0.3862	2.6138	Y5-3	0.3249	2.0253	0.274	2.726
D5-6	0.3456	1.9632	0.3285	2.6715	Y5-5	0.3195	2.0415	0.2515	2.7485
D5-7	0.3809	1.8573	0.4064	2.5936	Y5-7	0.3213	2.0361	0.2695	2.7305
D5-10	0.3970	1.8090	0.3613	2.6387	Y5-9	0.3264	2.0208	0.2499	2.7501
D5-12	0.3771	1.8687	0.3663	2.6337	Y5-11	0.3187	2.0439	0.2499	2.7501
D5-14	0.3825	1.8525	0.3719	2.6281	Y5-13	0.3082	2.0754	0.2369	2.7631
D5-16	0.3907	1.8279	0.3393	2.6607	Y5-14	0.2963	2.1111	0.2308	2.7692
D5-18	0.4118	1.7646	0.3575	2.6425	Y5-15	0.2935	2.1195	0.2273	2.7727
D5-20	0.4039	1.7883	0.3439	2.6561	Y5-16	0.2870	2.1390	0.2181	2.7819

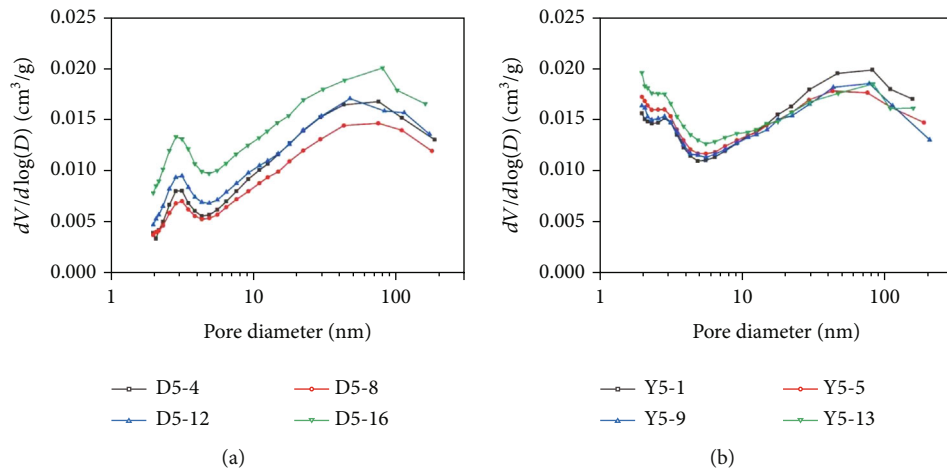


FIGURE 8: Typical sample PSD graph of (a) Shanxi Formation shale and (b) Longmaxi Formation shale.

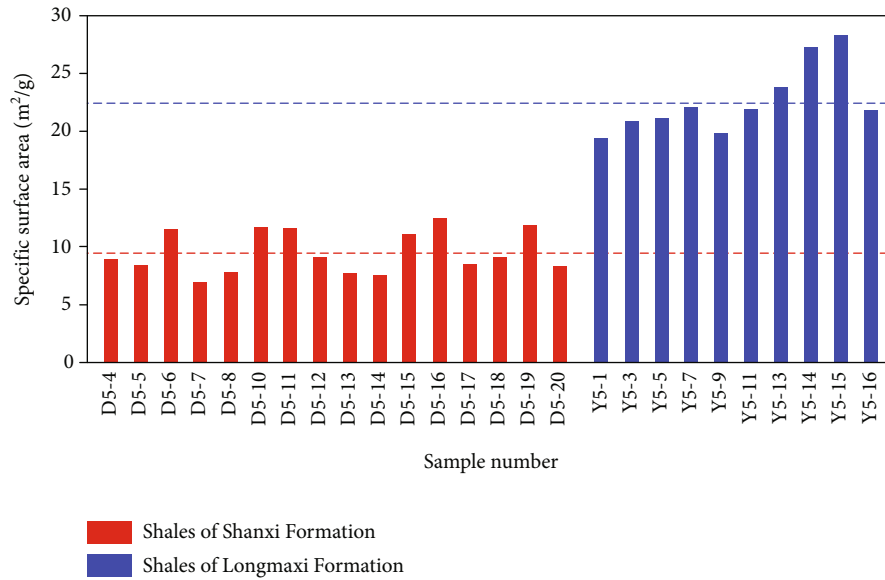


FIGURE 9: Comparative analysis results of the specific surface area between the two types of shale.

an average of $22.6 \text{ m}^2/\text{g}$, the PV is 0.0269 ml/g – 0.0349 ml/g with an average of 0.0325 ml/g , and the average diameter is 9.5 nm . The results indicate that the two shales differ considerably in the pore structure. The SSA provided by most of the transitional shale samples is smaller than $10 \text{ m}^2/\text{g}$, which is about $1/2$ of that of marine shale samples (Figure 9). The PV of Shanxi Formation shale is mostly in the 0.020 ml/g – 0.030 ml/g range, while that of Longmaxi Formation shale is mostly larger than 0.030 ml/g (Figure 10). It suggests that smaller-sized pores are more developed in marine shale than in transitional shale, whereas the distribution of larger-sized pores does not differ much, which is consistent with our comparison of PSD.

5.2. Fractal Characteristic Comparison. The values of D_1 and D_2 represent the complexity of the pore structure corresponding to the low-pressure section and high-pressure section, respectively. Comparing the two fractal parameters of marine shale and marine-continental transitional shale, it is obvious that the D_1 and D_2 values of marine-continental transitional shale are smaller than those of marine shale (Figures 11 and 12), indicating that the complexity of the pore structure of marine-continental transitional shale is lower than that of marine shale. Because the transitional shale is dominated by mineral matrix pores, the marine shale is mainly composed of organic pores. Generally, the pore walls of organic pores are rougher than those of mineral matrix pores [56]. The fluctuation range of D_1 and D_2 of Shanxi Formation shale is larger than that of Longmaxi Formation shale, which indicates that the heterogeneity of Shanxi Formation shale is strong.

Further analysis of the relationship between the pore structure and the fractal dimension of marine-continental transitional shale and marine shale shows that the D_1 value has no obvious relationship with the specific surface area, but the D_2 value has a good positive correlation with the specific surface area (Figure 13). This is because the nitrogen

adsorption in the low-pressure section involves a short micropore filling process, and the corresponding mesopore range in the low-pressure section is very small, which affects the result of the D_1 value. The more complex the mesopore structure corresponding to the high-pressure section, the larger the specific surface area and D_2 value will be.

5.3. Pore-Forming Mechanism Comparison and Its Geological Significance. Marine shale features well-developed organic pores and less-developed inorganic pores. Its geochemical data can verify that this shale has very good hydrocarbon-generating potential. The generation of gaseous hydrocarbon accompanies the entire process of organic matter evolution, including biogenic gas in the premature stage, pyrolysis gas (wet gas) in the mature stage, and cracked gas in the overmature stage (dry gas) [28–32]. The vitrinite reflectance of organic matter is mostly higher than 2.5% in Longmaxi Formation shale, indicating an overmature stage. In this stage, the liquid hydrocarbon and heavy gaseous hydrocarbon are cracked strongly to produce methane and bitumen. When the bitumen is not solidified, the pressure of the natural gas itself supports the bubble pores. Because the thickness of the marine shale is large, the natural gas is not easy to migrate out of the shale, and the bubble pores are the most affected by the deformation (Figure 14(b)). After the bitumen solidifies, these bubble pores are supported and protected by the solid bitumen skeleton and become the storage space of gaseous hydrocarbon [57].

The pore types of marine-continental transitional shale are different from those of marine shale, dominated by clay mineral slit pores and interlayer fractures and less developed organic matter pores. Organic geochemical analysis shows that the marine-continental transitional shale is also in the over mature stage, but the type III organic matter means that the marine-continental transitional shale directly generates gaseous hydrocarbon in the form of kerogen degradation, and only a small amount of liquid hydrocarbon is generated,

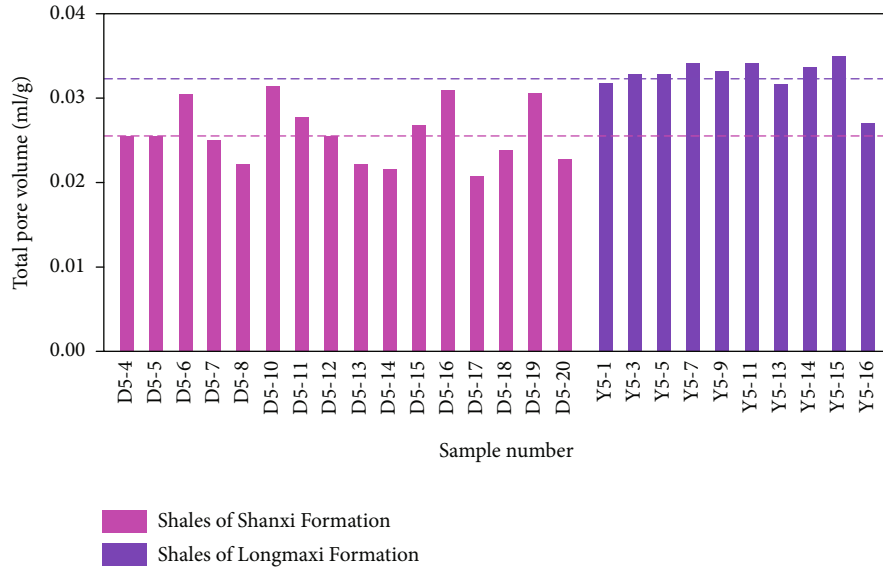


FIGURE 10: Comparative analysis results of the total pore volume between the two types of shale.

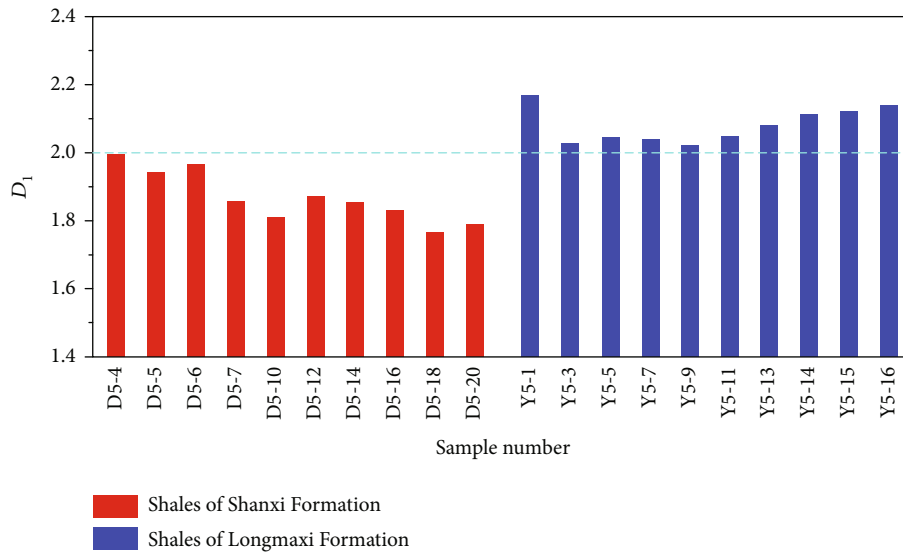


FIGURE 11: Comparative analysis results of the D_1 value between the two types of shale.

then cracking to generate gaseous hydrocarbon. Therefore, there are only a few organic matter bubble pores in the transitional shale [58, 59]. It can be seen that the type of organic matter is one of the influencing factors of pore development.

The on-site gas content test shows that the field gas content of shale samples in well D5 is $0.21 \text{ m}^3/\text{t}$ – $3.71 \text{ m}^3/\text{t}$ with an average of $1.39 \text{ m}^3/\text{t}$, and that in well Y5 is $1.88 \text{ m}^3/\text{t}$ – $6.18 \text{ m}^3/\text{t}$ with an average of $2.92 \text{ m}^3/\text{t}$. The gas hydrocarbon content of transitional shale is lower than that of marine shale, but in the sandstone layer adjacent to the Shanxi Formation shale layer, the gas content is comparable to that of the shale layer, suggesting that part of the gaseous hydrocarbon produced from the shale layer has been migrated to the sandstone layer. This is because the depositional environment of Shanxi Formation shale in the eastern Ordos Basin is deltaic facies featuring frequent sand-mud alternation

and high hydrocarbon expulsion efficiency in the stratum. Large amounts of the natural gas produced from the shale can easily be migrated into the adjacent tight sandstone to form conventional gas reservoirs (Figure 14(a)). A large number of connected clay mineral slit-like pores and inter-layer fractures provide migration channels so that natural gas can migrate to adjacent sandstone, resulting in the organic matter pores not being preserved. At the same time, the mineral matrix pores of shale also provide space for shale gas preservation. Therefore, the sedimentary environment is also an important factor affecting the pore development of marine-continental transitional shale [34, 60].

Although a large amount of natural gas in the shale layer migrated to the adjacent sandstone layer, the average gas content of the shale reservoir is still $1.39 \text{ m}^3/\text{t}$, which not only indicates that there are a large number of mineral matrix

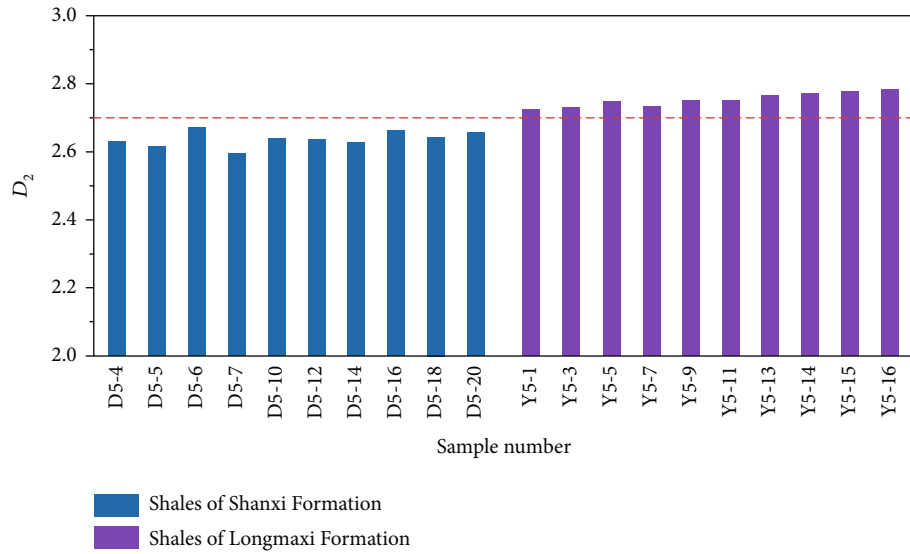


FIGURE 12: Comparative analysis results of the D_2 value between the two types of shale.

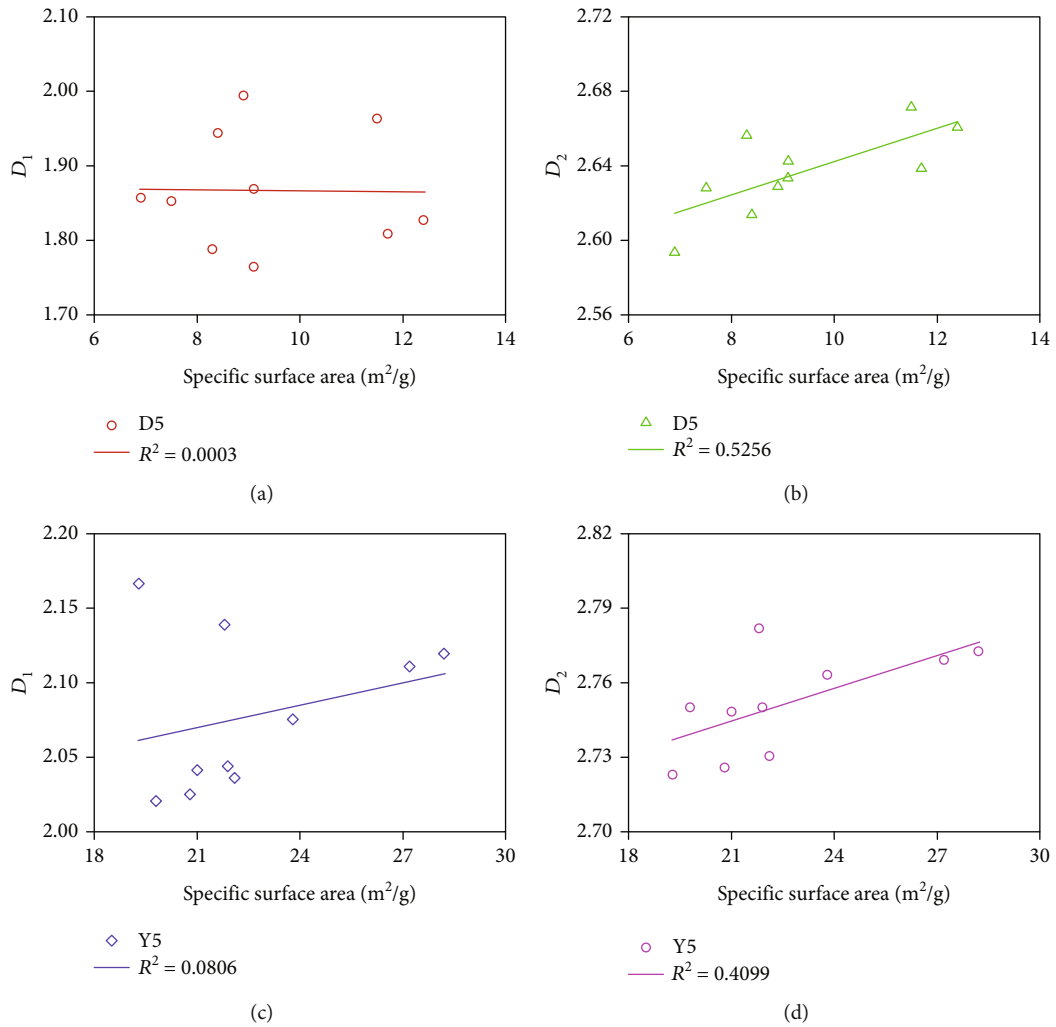


FIGURE 13: Relationship between the fractal dimension and the specific surface area of (a, b) Shanxi Formation shale and (c, d) Longmaxi Formation shale.

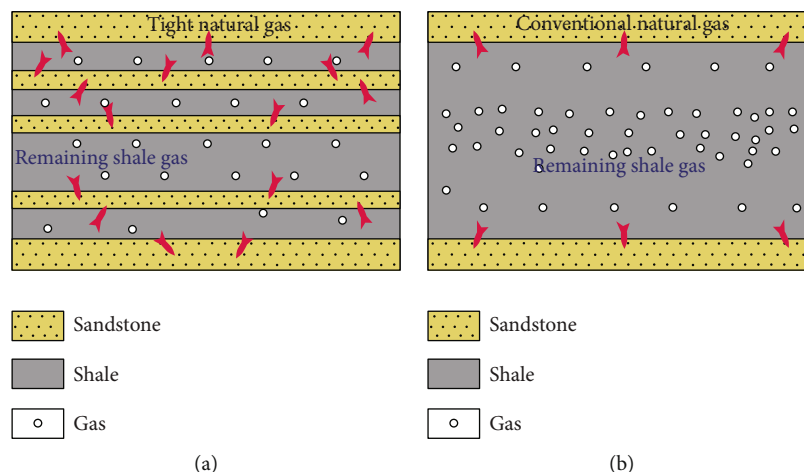


FIGURE 14: Hydrocarbon expulsion model of (a) Shanxi Formation shale and (b) Longmaxi Formation shale.

pores to provide storage space but also indicates that the adjacent single shale and single sandstone provide better sealing conditions for each other when the hydrocarbon concentration reaches a certain value so as to prevent the further transportation of natural gas. Therefore, the exploration target of the Shanxi Formation in the eastern Ordos Basin should not be limited to shale strata only. It is suggested that the combination of interbedded mudrock and sandstone can be taken as the key exploration target for the Shanxi Formation marine-continental transitional stratum in the eastern Ordos Basin.

6. Conclusions

- (1) The clay minerals of the Shanxi Formation are more developed than quartz minerals, dominated by clay mineral slit pores and interlayer fractures, followed by brittle mineral intragranular pores. The quartz contents of Longmaxi Formation shale are higher than clay contents, mainly composed of organic matter nanopores, and mineral matrix pores are less developed
- (2) The shapes of the nitrogen adsorption curves of the marine and transitional shales are similar, showing parallel plate pores and ink bottle pores. Longmaxi Formation shale with more mesopores has a larger SSA and a more complex pore structure
- (3) The type of organic matter (type I or III) and the sedimentary environment are important influencing factors of the development of organic nanopores. Mineral matrix pores with good connectivity can also affect the formation of organic pores to a certain degree
- (4) The transitional shale features frequent sand-mud alternation and cannot completely preserve gaseous hydrocarbon. Its exploration target can be focused on the combination of interbedded mudrock and sandstone

Data Availability

The data used to support the findings of this study are included within the article.

Conflicts of Interest

The authors declare that they have no conflicts of interest.

Acknowledgments

This study was funded by the National Science and Technology Major Project (No. 2017ZX05035002-002).

References

- [1] C. Zou, Q. Zhao, D. Dong et al., "Geological characteristics, main challenges and future prospect of shale gas," *Journal of Natural Gas Geoscience*, vol. 2, no. 5-6, pp. 273–288, 2017.
- [2] X. Guo, Y. Li, B. Tenger et al., "Hydrocarbon generation and storage mechanisms of deep-water shelf shales of Ordovician Wufeng Formation-Silurian Longmaxi Formation in Sichuan Basin," *Petroleum Exploration and Development*, vol. 47, no. 1, pp. 193–201, 2020.
- [3] Z. Jiang, Y. Song, X. Tang et al., "Controlling factors of marine shale gas differential enrichment in southern China," *Petroleum Exploration and Development*, vol. 47, no. 3, pp. 417–628, 2020.
- [4] C. Zou, D. Dong, Y. Wang et al., "Shale gas in China: characteristics, challenges and prospects (I)," *Petroleum Exploration and Development*, vol. 42, no. 6, pp. 689–701, 2015.
- [5] X. Ma, H. Wang, S. Zhou, Z. Feng, H. Liu, and W. Guo, "Insights into NMR response characteristics of shales and its application in shale gas reservoir evaluation," *Journal of Natural Gas Science and Engineering*, vol. 84, article 103674, 2020.
- [6] Y. Ma, M. Fan, Y. Lu et al., "Geochemistry and sedimentology of the Lower Silurian Longmaxi mudstone in southwestern China: implications for depositional controls on organic matter accumulation," *Marine and Petroleum Geology*, vol. 75, pp. 291–309, 2016.

- [7] X. Guo, "Controlling factors on shale gas accumulations of Wufeng-Longmaxi Formations in Pingqiao shale gas field in Fuling area, Sichuan Basin," *Natural Gas Geoscience*, vol. 30, no. 1, pp. 1–10, 2019.
- [8] S. Liu, W. Ma, L. Jansa, W. Huang, X. Zeng, and C. Zhang, "Characteristics of the shale gas reservoir rocks in the Lower Silurian Longmaxi Formation, East Sichuan Basin, China," *Acta Petrologica Sinica*, vol. 27, no. 8, pp. 2239–2252, 2011.
- [9] C. Liang, Z. Jiang, C. Zhang, L. Guo, Y. Yang, and J. Li, "The shale characteristics and shale gas exploration prospects of the Lower Silurian Longmaxi Shale, Sichuan Basin, South China," *Journal of Natural Gas Science and Engineering*, vol. 21, pp. 636–648, 2014.
- [10] M. Sun, B. Yu, Q. Hu, S. Chen, W. Xia, and R. Ye, "Nanoscale pore characteristics of the Lower Cambrian Niutitang Formation Shale: a case study from Well Yuke 1 in the Southeast of Chongqing, China," *International Journal of Coal Geology*, vol. 154–155, pp. 16–29, 2016.
- [11] T. Cao, Z. Song, S. Wang, X. Cao, Y. Li, and J. Xia, "Characterizing the pore structure in the Silurian and Permian shales of the Sichuan Basin, China," *Marine and Petroleum Geology*, vol. 61, pp. 140–150, 2015.
- [12] J. Shu, Y. Peng, B. Gao et al., "Geology and shale gas resource potentials in the Sichuan Basin, China," *Energy Exploration and Exploitation*, vol. 34, no. 5, pp. 689–710, 2016.
- [13] S. Chen, Y. Zhu, H. Wang, H. Liu, W. Wei, and J. Fang, "Characteristics and significance of mineral compositions of Lower Silurian Longmaxi Formation Shale gas reservoir in the southern margin of Sichuan Basin," *Acta Petrologica Sinica*, vol. 32, no. 5, pp. 775–782, 2011.
- [14] X. Wang, C. Mou, X. Ge et al., "Mineral component characteristics and evaluation of black rock series of Longmaxi Formation in Southern Sichuan and its periphery," *Acta Petrologica Sinica*, vol. 36, no. 2, pp. 150–162, 2015.
- [15] H. Zhang, X. Jin, J. Wu, Q. Yang, and L. Hao, "Nano-pores of organic matter in Longmaxi Formation shale in Sichuan Basin," *Coal Geology & Exploration*, vol. 46, no. 3, pp. 47–53, 2018.
- [16] H. Nie, Z. Jin, C. Sun, Z. He, G. Liu, and Q. Liu, "Organic matter types of the Wufeng and Longmaxi Formations in the Sichuan Basin, South China: implications for the formation of organic matter pores," *Energy Fuels*, vol. 33, no. 9, pp. 8076–8100, 2019.
- [17] R. G. Loucks and R. M. Reed, "Scanning-electron-microscope petrographic evidence for distinguishing organic-matter pores associated with depositional organic matter versus migrated organic matter in mudrocks," *Gulf Coast Association of Geological Societies*, vol. 3, pp. 51–60, 2014.
- [18] J. Rouquerol, D. Avnir, C. W. Fairbridge et al., "Recommendations for the characterization of porous solids (technical report)," *Pure & Applied Chemistry*, vol. 66, no. 8, pp. 1739–1758, 1994.
- [19] H. Hu, F. Hao, J. Lin, Y. Lu, Y. Ma, and Q. Li, "Organic matter-hosted pore system in the Wufeng-Longmaxi (O₃w-S₁1) shale, Jiaoshiba area, Eastern Sichuan Basin, China," *International Journal of Coal Geology*, vol. 173, pp. 40–50, 2017.
- [20] K. Jiao, S. Yao, C. Liu et al., "The characterization and quantitative analysis of nanopores in unconventional gas reservoirs utilizing FESEM-FIB and image processing: an example from the Lower Silurian Longmaxi Shale, upper Yangtze region, China," *International Journal of Coal Geology*, vol. 128–129, pp. 1–11, 2014.
- [21] K. Liu, M. Ostadhassan, and L. Kong, "Multifractal characteristics of Longmaxi Shale pore structures by N₂ adsorption: a model comparison," *Journal of Petroleum Science and Engineering*, vol. 168, pp. 330–341, 2018.
- [22] F. Wang, J. Guan, W. Feng, and L. Bao, "Evolution of overmature marine shale porosity and implication to the free gas volume," *Petroleum Exploration and Development*, vol. 40, no. 6, pp. 819–824, 2013.
- [23] L. Wu, Y. Lu, S. Jiang, Y. Lu, X. Liu, and H. Hu, "Pore structure characterization of different lithofacies in marine shale: a case study of the Upper Ordovician Wufeng-Lower Silurian Longmaxi Formation in the Sichuan Basin, SW China," *Journal of Natural Gas Science and Engineering*, vol. 57, pp. 203–215, 2018.
- [24] T. Cao, M. Deng, Z. Song, G. Liu, Y. Huang, and A. S. Hursthouse, "Study on the effect of pyrite on the accumulation of shale oil and gas," *Natural Gas Geoscience*, vol. 29, no. 3, pp. 404–414, 2018.
- [25] X. Tang, Z. Jiang, Z. Li et al., "The effect of the variation in material composition on the heterogeneous pore structure of high-maturity shale of the Silurian Longmaxi Formation in the southeastern Sichuan Basin, China," *Journal of Natural Gas Science and Engineering*, vol. 23, pp. 464–473, 2015.
- [26] S. Chen, Y. Han, C. Fu, H. Zhang, Y. Zhu, and Z. Zuo, "Micro and nano-size pores of clay minerals in shale reservoirs: implication for the accumulation of shale gas," *Sedimentary Geology*, vol. 342, pp. 180–190, 2016.
- [27] Y. Wang, D. Dong, H. Yang et al., "Quantitative characterization of reservoir space in the Lower Silurian Longmaxi Shale, Southern Sichuan, China," *Science China: Earth Sciences*, vol. 57, no. 2, pp. 313–322, 2014.
- [28] L. T. Ko, R. G. Loucks, T. Zhang, S. C. Ruppel, and D. Shao, "Pore and pore network evolution of upper Cretaceous Boquillas (Eagle Ford-equivalent) mudrocks: results from gold tube pyrolysis experiments," *AAPG Bulletin*, vol. 100, no. 11, pp. 1693–1722, 2016.
- [29] L. T. Ko, R. G. Loucks, S. C. Ruppel, T. Zhang, and S. Peng, "Origin and characterization of Eagle Ford pore networks in the South Texas upper Cretaceous shelf," *AAPG Bulletin*, vol. 101, no. 3, pp. 387–418, 2017.
- [30] S. Bernard, R. Wirth, A. Schreiber, H. M. Schulz, and B. Horsfield, "Formation of nanoporous pyrobitumen residues during maturation of the Barnett Shale (Fort Worth Basin)," *International Journal of Coal Geology*, vol. 103, pp. 3–11, 2012.
- [31] H. Liu, X. Li, and S. Zhou, "Phenomenon of bubble evolving into pore occurred in black shale and its geological significance," *Natural Gas and Oil*, vol. 36, no. 6, pp. 60–64, 2018.
- [32] S. C. Löhner, E. T. Baruch, P. A. Hall, and M. J. Kennedy, "Is organic pore development in gas shales influenced by the primary porosity and structure of thermally immature organic matter?," *Organic Geochemistry*, vol. 87, pp. 119–132, 2015.
- [33] C. Yang, J. Zhang, S. Han et al., "Compositional controls on pore-size distribution by nitrogen adsorption technique in the Lower Permian Shanxi Shales, Ordos Basin," *Journal of Natural Gas Science and Engineering*, vol. 34, pp. 1369–1381, 2016.
- [34] J. Liu, K. Liu, and X. Huang, "Effect of sedimentary heterogeneities on hydrocarbon accumulations in the Permian Shanxi Formation, Ordos Basin, China: insight from an integrated

- stratigraphic forward and petroleum system modelling,” *Marine and Petroleum Geology*, vol. 76, pp. 412–431, 2016.
- [35] L. Kuang, D. Dong, W. He et al., “Geological characteristics and development potential of transitional shale gas in the east margin of the Ordos Basin, NW China,” *Petroleum Exploration and Development*, vol. 47, no. 3, pp. 435–446, 2020.
- [36] Z. Wei, G. Wang, Y. Wang et al., “Geochemical and geological characterization of marine-continental transitional shale: a case study in the Ordos Basin, NW China,” *Acta Geologica Sinica*, vol. 94, no. 3, pp. 809–821, 2020.
- [37] C. Xue, J. Wu, L. Qiu et al., “Lithofacies classification and its controls on the pore structure distribution in Permian transitional shale in the northeastern Ordos Basin, China,” *Journal of Petroleum Science and Engineering*, vol. 195, article 107657, 2020.
- [38] X. Tang, H. Zhang, W. Ding et al., “The reservoir property of the Upper Paleozoic marine-continental transitional shale and its gas-bearing capacity in the Southeastern Ordos Basin,” *Earth Science Frontiers*, vol. 23, no. 2, pp. 147–157, 2016.
- [39] P. Zhang, Y. Huang, J. Zhang, H. Liu, and J. Yang, “Fractal characteristics of the Longtan Formation transitional shale in northwest Guizhou,” *Journal of China Coal Society*, vol. 43, no. 6, pp. 1580–1588, 2018.
- [40] D. Zhao, Y. Guo, C. Ren, and Y. Li, “Development characteristics and affecting factors of nanopores in transitional shale reservoirs: an example of the Shanxi Formation,” *Journal of Northeast Petroleum University*, vol. 42, no. 5, pp. 1–15, 2018.
- [41] J. Zhang, X. Li, Y. Wang, Q. Fu, Y. Cai, and H. Niu, “Accumulation conditions and reservoir characteristics of marine-terrestrial facies coal measures shale gas from Longtan Formation in South Sichuan Basin,” *Journal of China Coal Society*, vol. 40, no. 8, pp. 1871–1878, 2015.
- [42] S. Tang, J. Zhang, D. Elsworth et al., “Lithofacies and pore characterization of the Lower Permian Shanxi and Taiyuan shales in the southern North China Basin,” *Journal of Natural Gas Science and Engineering*, vol. 36, pp. 644–661, 2016.
- [43] F. Xiong, Z. Jiang, P. Li et al., “Pore structure of transitional shales in the Ordos Basin, NW China: effects of composition on gas storage capacity,” *Fuel*, vol. 206, pp. 504–515, 2017.
- [44] T. Cao, Q. Cao, H. Liu, M. Deng, and G. Liu, “Geochemical characteristics and adsorption capacity of marine-continental transitional mudrock in eastern Sichuan Basin,” *Journal of China Coal Society*, vol. 45, no. 4, pp. 241–252, 2020.
- [45] E. Deng, J. Jin, R. Wang, F. Shi, and L. Wang, “Characteristics of microscopic pore and gas storage on shale in Permian Longtan Formation, Northern Guizhou,” *Science Technology and Engineering*, vol. 17, no. 24, pp. 190–195, 2017.
- [46] Z. Xi, S. Tang, J. Li, and L. Li, “Investigation of pore structure and fractal characteristics of marine-continental transitional shale in the east-central of Qinshui Basin,” *Natural Gas Geoscience*, vol. 28, no. 3, pp. 366–376, 2017.
- [47] Z. P. Sun, Y. L. Wang, Z. F. Wei et al., “Shale gas content and geochemical characteristics of marine-continental transitional shale: a case from the Shanxi Formation of Ordos Basin,” *Journal of China University of Mining & Technology*, vol. 46, no. 4, pp. 859–868, 2017.
- [48] Q. Gou, S. Xu, F. Hao, F. Yang, Z. Shu, and R. Liu, “The effect of tectonic deformation and preservation condition on the shale pore structure using adsorption-based textural quantification and 3D image observation,” *Energy*, vol. 219, p. 119579, 2021.
- [49] S. Zhou, G. Yan, H. Xue, W. Guo, and X. Li, “2D and 3D nanopore characterization of gas shale in Longmaxi Formation based on FIB-SEM,” *Marine and Petroleum Geology*, vol. 73, pp. 174–180, 2016.
- [50] S. Brunauer, P. H. Emmett, and E. Teller, “Adsorption of gases in multimolecular layers,” *Journal of the American Chemical Society*, vol. 60, no. 2, pp. 309–319, 1938.
- [51] E. P. Barrett, L. G. Joyner, and P. H. Halenda, “The determination of pore volume and area distributions in porous substances. I. Computations from nitrogen isotherms,” *Journal of the American Chemical Society*, vol. 73, no. 1, pp. 193–380, 1951.
- [52] S. Zhou, D. Zhang, H. Wang, and X. Li, “A modified BET equation to investigate supercritical methane adsorption mechanisms in shale,” *Marine and Petroleum Geology*, vol. 105, pp. 284–292, 2019.
- [53] J. Liu, D. Lu, and P. Li, “Nano-scale dual-pore-shape structure and fractal characteristics of transitional facies shale matrix,” *Journal of Natural Gas Science and Engineering*, vol. 68, article 102907, 2019.
- [54] M. K. Ismail and P. Pfeifer, “Fractal analysis and surface roughness of nonporous carbon fibers and carbon blacks,” *Langmuir*, vol. 10, no. 5, pp. 1532–1538, 1994.
- [55] S. Zhou, Y. Ning, H. Wang, H. Liu, and H. Xue, “Investigation of methane adsorption mechanism on Longmaxi shale by combining the micropore filling and monolayer coverage theories,” *Advances in Geo-Energy Research*, vol. 2, no. 3, pp. 269–281, 2018.
- [56] X. Shao, X. Pang, Q. Li et al., “Pore structure and fractal characteristics of organic-rich shales: a case study of the Lower Silurian Longmaxi shales in the Sichuan Basin, SW China,” *Marine and Petroleum Geology*, vol. 80, pp. 192–202, 2017.
- [57] X. Li, G. Chen, Z. Chen et al., “An insight into the mechanism and evolution of shale reservoir characteristics with over-high maturity,” *Natural Gas Geoscience*, vol. 27, no. 3, pp. 407–416, 2016.
- [58] T. Zhang, G. S. Ellis, S. C. Ruppel, K. Milliken, and R. Yang, “Effect of organic-matter type and thermal maturity on methane adsorption in shale-gas systems,” *Organic Geochemistry*, vol. 47, pp. 120–131, 2012.
- [59] J. Zhao, J. Zhang, and G. Gao, *Geology of Natural Gas*, Petroleum Industry Press, Beijing, 2013.
- [60] H. Liu, H. Wang, H. Zhang, W. Zhao, Y. Liu, and D. Liu, “Geological characteristics and exploration countermeasures of shale gas in the Shanxi Formation of the Ordos Basin,” *Acta Geologica Sinica*, vol. 94, no. 3, pp. 905–915, 2020.

Research Article

Organic-Inorganic Geochemical Characteristics of the Upper Permian Pusige Formation in a High-Saline Lake Basin, Tarim Basin: Implications for Provenance, Paleoenvironments, and Organic Matter Enrichment

Jingbin Wang ^{1,2,3}, Zhiliang He ^{1,2,4}, Dongya Zhu ^{2,3}, Zhiqian Gao,¹ Xiaowei Huang,^{1,2,3} and Quanyou Liu^{2,3}

¹China University of Geosciences (Beijing), Beijing 100083, China

²State Key Laboratory of Shale Oil and Gas Enrichment Mechanisms and Effective Development, Beijing 100083, China

³Petroleum Exploration and Production Research Institute, SINOPEC, Beijing 100083, China

⁴Department of Science and Technology, SINOPEC, Beijing 100728, China

Correspondence should be addressed to Jingbin Wang; 476559034@qq.com

Received 6 January 2021; Revised 27 February 2021; Accepted 3 March 2021; Published 7 April 2021

Academic Editor: Kun Zhang

Copyright © 2021 Jingbin Wang et al. This is an open access article distributed under the Creative Commons Attribution License, which permits unrestricted use, distribution, and reproduction in any medium, provided the original work is properly cited.

The third member (M3) of the Upper Permian Pusige Formation is a prominent organic-rich lacustrine mudstone sequence within the Yecheng-Hetian Sag, Tarim Basin, hosting major petroleum resources. However, its depositional history and organic matter (OM) enrichment mechanism have received little attention. Therefore, various organic and inorganic geochemical analyses were performed on thirty-four core samples from the Well DW1, to elucidate their depositional paleoenvironments, provenance, and tectonic setting, as well as the controlling factors of OM enrichment. Results showed that the M3 mudstones are classified as poor- to fair-quality hydrocarbon source rocks with mature type II-III kerogen, considering their low organic geochemical parameters. Paleosalinity indexes (e.g., Beq, Sr/Ba, and B/Ga) indicated the typical high-saline lacustrine water body, in which redox state was the oxic-dysoxic as suggested by multiple indicators. Many paleoclimate and weathering proxies suggest a dominant semiarid condition and low weathering degree in the Yecheng-Hetian Sag, which led to that weathered felsic rocks from the West Kunlun Orogen to the southwest of basin were quickly transported into the lake basin. Detrital materials carrying nutrient elements finally promoted the development of relatively high paleoproductivity indicated by fairly high P/Ti and Ba/Al ratios. The negative relationship between P/Ti and total organic carbon (TOC) indicates that paleoproductivity was not the main controlling factor. The correlations among TOC and P/Ti and other multiple proxies suggest that the OM enrichment can be interpreted as both the “preservation model” and “dilution model.” Although the water body was relatively oxygen-riched, high sedimentation rate could largely shorten the exposure time of OM with oxygen, thus decreased the decomposition of OM. In particular, the high-saline, stratified lake water may also restrain the degradation of OM. Furthermore, detrital dilution exerted a potential effect on TOC abundances. On the basis of the above results, a developing model was established to decipher the formation mechanism of OM in these M3 mudstones.

1. Introduction

In recent decades, much attention has been drawn to the formation mechanism of organic matter (OM) in both marine and lacustrine fine-grained sediments. Three fundamental models have been put forward, including (i) higher organic

productivity, (ii) enhanced OM preservation (associated with oxygen-deficiency condition in bottom water and sedimentation rate), and (iii) OM dilution (minimal detrital material input) [1–11]. However, the main controlling factors on the formation of organic-rich sediments remain to be controversial. This is because that in most cases, the formation of OM

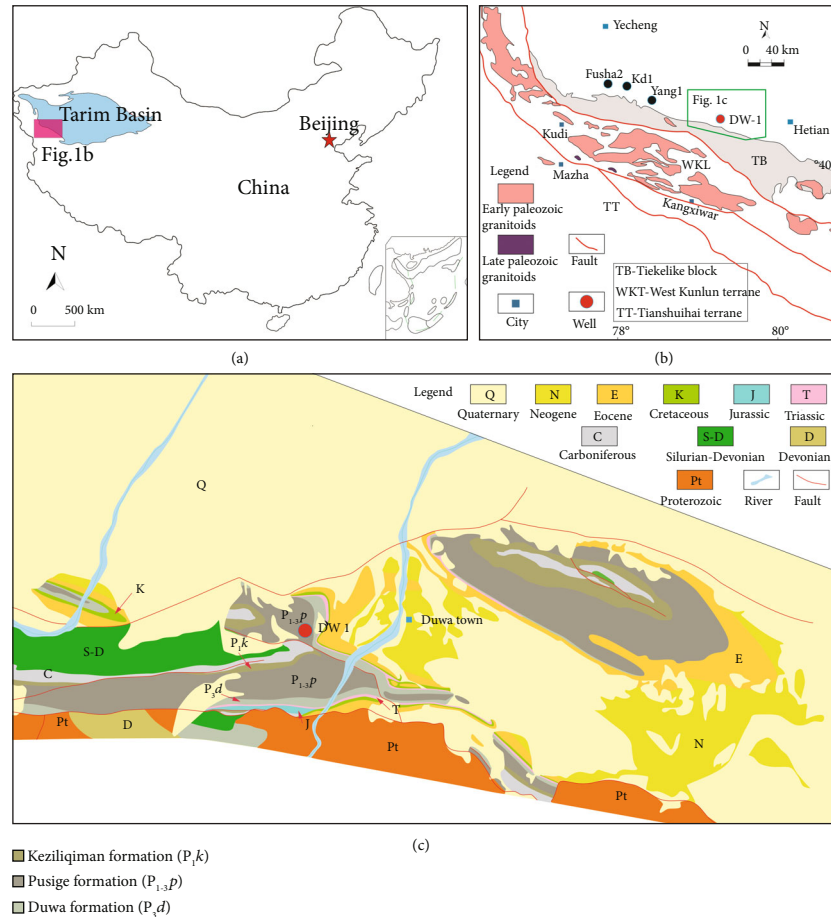


FIGURE 1: (a) Location of the Tarim Basin and the study area within Northwest China. (b) Sketch map showing major structural units and distribution of Paleozoic granitoids within the West Kunlun Orogen, and location of the investigated Well DW1 in the southwest of Tarim Basin (modified after Jiang et al. [37]; Wang et al. [39]). (c) Simplified geological map showing the distribution of the Pusige Formation strata in the Hetian area (modified after Henan Institute of Geological Survey [42]).

is the result of the complicated, nonlinear interactions among these controlling factors, and also each basin has its own specific factors [1, 4, 12, 13].

Organic-rich mudstones in lacustrine basins can be regarded as favorable hydrocarbon source rocks or direct unconventional petroleum resources (e.g., shale oil and shale gas) [14, 15]; however, their formation processes are much more complicated than those in marine basins, since terrigenous influx and paleoclimate can exert a substantial influence on the evolution of restricted lacustrine basins [16, 17]. Fortunately, continuous geochemical data of lacustrine sediments are used to reconstruct the depositional paleoenvironments at that time, which contributes to a better understanding of OM enrichment in lacustrine basins [9, 12, 18–20].

The Yecheng-Hetian Sag is currently one of the most potential petroliferous areas in the Tarim Basin [21–26]. The Permian organic-rich marls (Qipan Formation) and lacustrine mudstones (Pusige Formation) are two sets of important source rocks because of their widespread distributions in the study area and relatively high organic geochemical properties [23–25]. According to the results of the oil-source correlation results [21, 23, 24], the lacustrine mud-

stones in the third member (M3) of the Upper Permian Pusige Formation studied herein are potentially the dominant hydrocarbon source rocks for the Kekeya oil/gas field and Well KD-1. The Pusige Formation sediments were just developed during one basin-mountain transition process that basin type was transferred from the Carboniferous-late Early Permian retroarc extensional basin to late Late Permian typical foreland basin. Previous studies mainly focused on their stratigraphic sequences, paleontology, sedimentary facies, and hydrocarbon source rock evolution [27–31]. However, few studies have been made regarding the depositional paleoenvironments (e.g., paleoclimate, weathering, sedimentation rate, and water-mass properties), provenance attribute, and tectonic setting during the deposition of Pusige Formation, which limits the understanding of controlling factors for OM accumulation within the mudstones in the Yecheng-Hetian Sag.

Therefore, in this study, many reliable organic parameters and inorganic elemental indicators were well screened to clarify the depositional paleoenvironments, provenance characters, and mechanism of OM enrichment, as well as the developing model of these Permian Pusige Formation lacustrine mudstones. This study not only provides a more

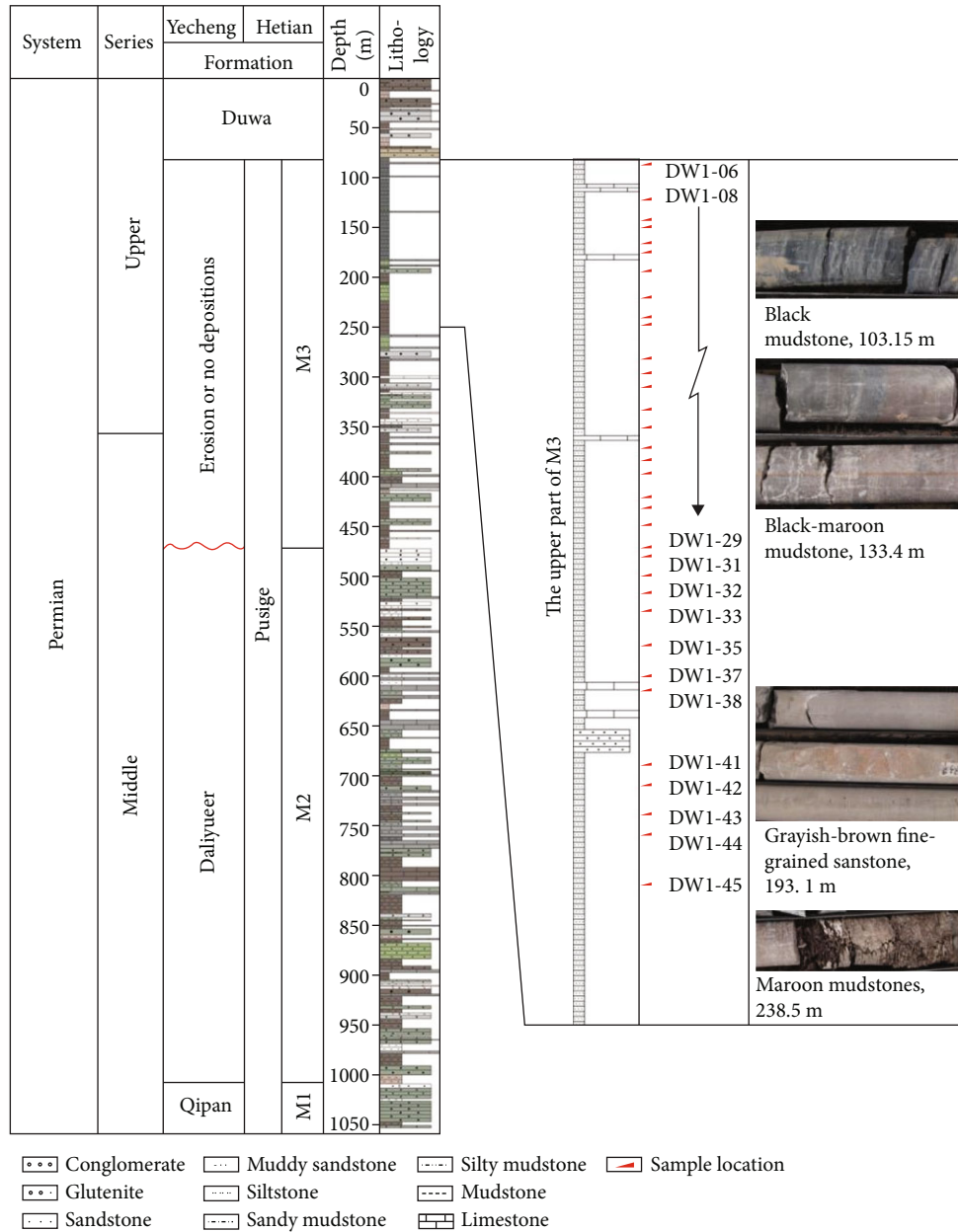


FIGURE 2: Permian stratigraphy in Yecheng-Hetian Sag, and the generalized stratigraphic column for the Pusige Formation and the sampling locations of the M3 mudstones in Well DW1.

comprehensive cognition of the depositional history for Pusige Formation sediments and guide the future petroleum explorations in Southwestern Tarim Basin but also acts as a reference for OM enrichment in other high-saline lake basins.

2. Geological Setting

Tarim Basin is a typical superimposed polycyclic intracratonic basin developed on the Precambrian basements [22, 32–34]. The Southwestern Tarim Basin is sandwiched between the Tianshan Mountain to the north and Kunlun Mountain to the southwest. The investigations of tectonic cycles, basin prototype, stratigraphic sequence, and geomor-

phologic recovery suggest that the sedimentary and tectonic evolution of the southwestern Tarim Basin is closely correlated to the uplift and extrusion of the West Kunlun Orogen [22, 32–34]. Six tectonic-stages can be identified, namely, the Stage I: Sinian-Ordovician passive continental margin stage; Stage II: Silurian-Middle Devonian peripheral foreland basin; Stage III: Late Devonian-Early Permian passive continental margin stage; Stage IV: Late Permian-Triassic back-arc foreland basin; Stage V: Jurassic-Paleogene intracontinental depression; and Stage VI: Neogene-Quaternary compound foreland basin. The investigated Permian continental sediments were just deposited at the transition of Stage III and IV. In addition, following the opening and closure of the Tethys oceans, many Paleozoic intrusive plutons were widely

formed within the Kegang, Kudi, Mazha, and Kangxiwar regions (Figure 1), which are mainly composed of granite and granodiorite associated with continental island arc- and continental margin-related tectonic settings [35–40].

The Yecheng-Hetian Sag is a subtectonic unit located in the southwestern Tarim Basin. The evolution of the Permian sedimentary basin is thought to be directly controlled by the closure of the Kangxiwar Paleo-Tethys [27, 41]. Kangxiwar Paleo-Tethys is particularly one of the key regions to investigate the geological evolution of West Kunlun Orogen and Tarim plate. At the beginning of the Early Carboniferous, open marine platform facies, commenced with a large-scale transgression that represents one of the greatest sea-level rises in geological history, covered extensively in Yecheng-Hetian Sag and developed marine carbonate rocks with thousands of meters in thickness until the late Early Permian [41]. At the beginning of the late Early Permian, the Kangxiwar Paleo-Tethys moved intensively northward towards the Tarim Plate with a relatively high angle, leading to an enhanced uplift and the intense regression of sea-level in the Hetian region relative to the Yecheng region [27–29, 41]. As a result, depositional systems in the Yecheng and Hetian regions show remarkable differences [27]. A marine environment was still dominated in the Yecheng region, whereas continental clastic depositions began to be widely developed in the Hetian region (Figure 1(c)) [42]. Two stratigraphic successions were then established and include the Keziliqiman, Qipan, and Daluyueer formations in Yecheng region, and the Keziliqiman, Pusige, and Duwa formations in the Hetian region from Early to Late Permian (Figure 2) [27]. Notably, the Pusige Formation spans the Lower, Middle, and Upper series of the Permian [31] and can be informally divided into three continuous members: Member 1 (M1), Member 2 (M2), and Member 3 (M3) [23, 25, 29, 30].

The investigated Well DW1 was an important exploratory well, which was located in the west of Duwa town (Figure 1(c)) [42]. This well explored the Pusige Formation and Duwa Formation strata, with a total thickness of 1 050 m (Figure 2). The lithology included the conglomerate, sandstone, siltstone, and mudstone interbedded with some gypsum and limestone layers, which were likely deposited in fan-delta to shore-shallow-deep lacustrine facies [23, 28, 29]. In the upper part of M3, black-gray, maroon, and gray-green mudstones are the dominant lithofacies, with a total thickness of approximately 170 m in this profile. This mudstone section can be correlated with other drilling wells (e.g., Yang 1 and Fusha 2) and outcrops (e.g., Duwa and Wuluwusitang), which were deposited in the semideep lacustrine facies based on the sedimentary structures (e.g., horizontal bedding), fossils (e.g., fish skeleton) and lithofacies [23, 28]. The M3 black mudstones are widely distributed within the Yecheng-Hetian Sag with a vertical thickness up to 565.0 m [23].

3. Samples and Methods

A total of thirty-four core samples were collected from the mudstone section (82.0–223.0 m) in Well DW1, with an

average spacing of 3.4 m (Figure 2), and then subjected to various geochemical analyses.

TOC and total sulfur (S) were determined using a Leco CS-400 apparatus. Prior to analysis, powdered samples (approximately 100 mesh) were dissolved by dilute HCl (~8%) to remove carbonate minerals (inorganic carbon) for 12 hours. Rock-Eval pyrolysis was conducted on the powdered samples using a Rock-Eval VI instrument. The free hydrocarbon S_1 was measured at 300°C, and generated hydrocarbon S_2 was identified at a temperature of 600°C. Potential generation index (PG, $S_1 + S_2$) and hydrocarbon index (HI, $S_2 \times 100/\text{TOC}$) were calculated to reveal the hydrocarbon generation potential. These experiments were performed at the Yangtze University, China.

Major elements were detected by a wavelength dispersive X-ray fluorescence spectrometer at Beijing Research Institute of Uranium Geology (China). Sample was firstly heated in a muffle furnace at 105°C for 4 hours, and then, anhydrous lithium tetraborate (~5.2 g), lithium fluoride (~0.4 g), and ammonium nitrate (~0.3 g) were added to dissolve at 1150°C for another 15 minutes, in order to measure major oxides and loss on ignition. To determine trace elements, powdered samples (~25 mg) were dissolved in a mixture of hydrofluoric acid (1 ml) and nitric acid (0.5 ml) in a tightly sealed Teflon bomb at 185°C for 24 hours. The dissolved samples were diluted to 25 ml in a clean bottle for trace element analyses using a Finnigan MAT high-resolution inductively coupled plasma mass spectrometer. The relatively analytical precision is better than 5.0%. The detailed procedures and experimental parameters for major and trace element analyses are followed by the Chinese National Standard GB/T 14506-28-2010 and GB/T 14506-30-2010, respectively.

4. Results

4.1. Bulk Geochemical Characteristics. The results of TOC, S, and Rock-Eval pyrolysis are given in Table 1. All the samples have relatively low TOC values of 0.2–1.11% with an average of 0.45% ($n = 30$), displaying less variability upward from the bottom of this profile (Figure 3). Pyrolysis parameters S_1 and S_2 can represent the hydrocarbon generation potential of the organic matter [43]. The PG ($S_1 + S_2$) and HI values are distinctly low, varying from 0.02 to 0.30 mg HC/g rock (average = 0.11 mg HC/g rock), and 5.0 to 49.0 mg HC/g TOC (average = 17.8 mg HC/g TOC), respectively. For the kerogen types of organic matter, these samples are commonly dominated by type II kerogen and following type III kerogen, as evidenced by the bulk geochemical and biomarker parameters studied by Du et al. [23] and Wang et al. [25]. On the cross-plot of S_2 versus TOC (Figure 4) [44], the studied samples in Well DW1 are classified as the poor to fair-quality source rocks with mature characters (Figure 4). However, equivalent black mudstones of the M3 in other drilling wells (e.g., Yang1 and Fusha2) show relatively higher TOC, PG, and HI contents than those in Well DW1, which can be generally regarded as poor to good-quality source rocks (Figure 4) [23].

TABLE 1: TOC, S, and Rock-Eval pyrolysis data of the M3 lacustrine mudstones in the Yecheng-Hetian Sag.

Samples	Depth/m	TOC/%	S/%	TOC/S	S ₁ (mg HC/g rock)	S ₂ (mg HC/g rock)	PG (mg HC/g rock)	HI (mg HC/g TOC)
DW1-06	82.25	0.48	0.13	3.46	0.02	0.04	0.06	8
DW1-08	89.15	0.31	0.10	3.18	0.03	0.03	0.06	10
DW1-09	93.05	0.24	0.09	3.64	0.02	0.05	0.07	21
DW1-10	94.45	0.59	0.10	3.78	0.01	0.18	0.19	31
DW1-11	97.65	0.32	0.08	4.52	0.01	0.02	0.03	6
DW1-12	99.75	0.39	0.32	1.19	0.01	0.02	0.03	5
DW1-13	103.15	0.53	0.09	4.44	0.02	0.04	0.06	8
DW1-14	108.25	0.40	0.30	1.30	0.01	0.07	0.08	17
DW1-15	112.15	0.27	0.11	3.49	0.01	0.05	0.06	18
DW1-16	113.55	0.44	0.16	2.46	0.01	0.05	0.06	11
DW1-17	119.90	0.67	0.62	0.63	0.01	0.25	0.26	37
DW1-18	123.00	0.35	0.09	4.50	0.06	0.06	0.12	17
DW1-19	125.65	0.57	0.15	2.69	0.02	0.07	0.09	12
DW1-20	130.00	0.28	0.08	5.31	0.01	0.04	0.05	14
DW1-21	133.55	1.11	0.88	0.47	0.02	0.27	0.29	24
DW1-22	137.55	0.70	0.65	0.65	0.02	0.14	0.16	20
DW1-23	139.90	0.30	0.07	5.75	0.01	0.03	0.04	10
DW1-24	142.30	0.45	0.18	2.47	0.06	0.19	0.25	43
DW1-25	147.00	0.73	0.07	6.08	0.03	0.17	0.20	23
DW1-26	149.10	0.27	0.08	5.71	0.01	0.03	0.04	11
DW1-27	152.35	0.20	0.20	2.30	0.01	0.03	0.04	15
DW1-28	156.80	0.47	0.09	4.91	0.04	0.10	0.14	21
DW1-29	158.55	0.36	0.08	6.00	0.00	0.02	0.02	6
DW1-31	162.35	0.74	0.15	3.11	0.06	0.11	0.17	15
DW1-32	165.60	0.33	0.08	6.26	0.01	0.03	0.04	9
DW1-33	169.25	0.59	0.36	1.39	0.01	0.29	0.30	49
DW1-35	175.85	0.26	0.08	6.08	0.01	0.03	0.04	11
DW1-37	181.85	0.20	0.08	6.27	0.01	0.03	0.04	15
DW1-38	184.75	0.39	0.09	6.04	0.01	0.03	0.04	8
DW1-45	222.40	0.59	0.43	3.22	0.03	0.24	0.27	40

Abbreviations: TOC: total organic carbon; S: total sulfur; S₁: free hydrocarbons; S₂: hydrocarbons generated; PG: potential generation index; S₁ + S₂; HI: hydrocarbon index, S₂ × 100/TOC.

Moreover, the S contents of these lacustrine mudstones range from 0.07% to 0.88% with a median of 0.20%. The TOC/S ratios, which reflect the vertical changes in paleosalinity during the deposition [45, 46], are lower than 10.0, vary between 1.01 and 9.97.

4.2. Major Elements. Major element concentrations of the studied lacustrine mudstones are listed in Table 2. SiO₂, Al₂O₃, and CaO are the predominant oxides, with their contents ranging from 36.93% to 55.45%, 10.31% to 16.32%, and 4.44% to 16.35%, respectively. The second abundant oxides are the TFe₂O₃ (3.66-6.419%), MgO (2.51-5.37%), K₂O (1.92-3.32%), and Na₂O (1.07-2.77%), while contents of other oxides (e.g., TiO₂, P₂O₅, and MnO) are generally lower than 1.0%. When normalized to the Post-Archaean Australia Shale (PAAS) [47], these samples show uniform distribution patterns (Figure 5(a)). The contents of CaO, MgO, and Na₂O are strongly enriched, whereas others, such as the SiO₂,

Al₂O₃, MnO, K₂O, TiO₂, TFe₂O₃, and P₂O₅, are substantially depleted relative to those of the PAAS. In the well, these major element compositions in each sample are relatively uniform and exhibit slight vertical fluctuations.

4.3. Trace Elements. Some specific trace element concentrations of the studied samples are shown in Table 3. In the descending order of average concentration, trace elements include Sr (~519 ppm), Ba (~346 ppm), B (~147 ppm), Zr (~128 ppm), Rb (~112 ppm), V (~90.9 ppm), Zn (~78.4 ppm), Cr (~69.2 ppm), Ni (~41.3 ppm), Cu (~28.4 ppm), Co (~14.9 ppm), Sc (~12 ppm), Th (~9.91 ppm), Hf (~3.91 ppm), U (~3.51 ppm), and Mo (~0.76 ppm). Vertically, these trace elements do not also display distinctive changing trends along with the depths in the profile. Enrichment factor (EF) has been used to characterize the relative enrichment degree of trace elements [19]. Aluminium (Al) is often used as a normalized element due to

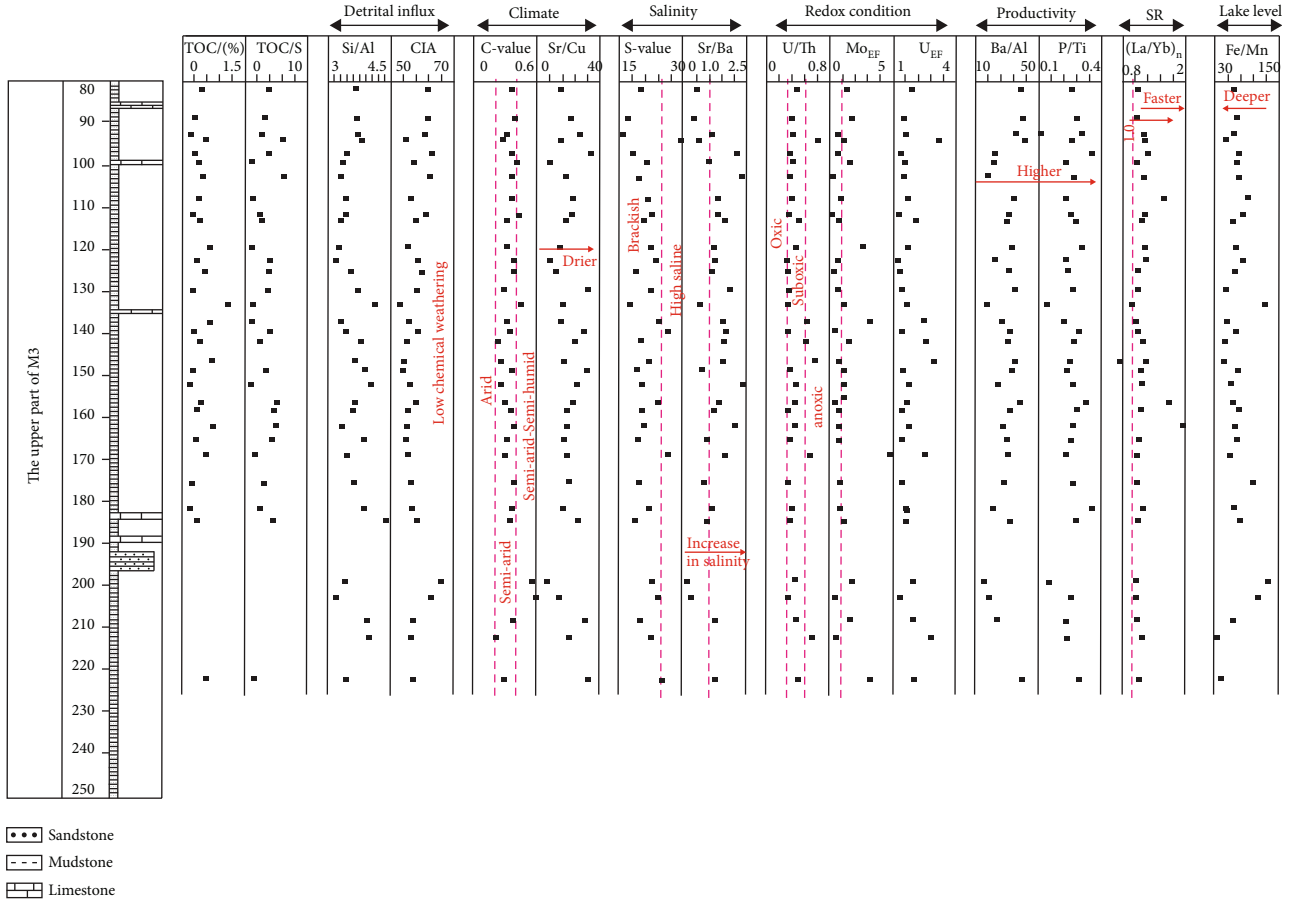


FIGURE 3: Stratigraphic variations of TOC contents, TOC/S ratio, and geochemical proxies of detrital influx, climate, salinity, redox condition, productivity, sedimentation rate (SR), and paleowater depth for these M3 mudstones in Well DW1.

its relatively high abundance and stability during weathering, transportation, and diagenesis. EF_{element} was calculated using the following equation:

$$EF_{\text{element}} = (\text{element}/\text{Al})_{\text{sample}} / (\text{element}/\text{Al})_{\text{background}}$$

where the background values refer to those of PAAS in the present study [47]. $EF < 1.0$ indicates a depletion, whereas $EF > 1.0$ or greater corresponds to a distinct enrichment relative to the PAAS. The EF results are shown in Figure 5(b), showing enrichment or depletion of trace elements with varying degrees. Remarkably, Sr is strongly enriched, with EF values varying from 2.72 to 7.5. In contrast, other trace elements, such as B ($EF = 1.8\text{--}2.93$), Zn ($EF = 1.01\text{--}2.08$), U ($EF = 1.14\text{--}3.15$), Hf ($EF = 1.06\text{--}1.64$), Ni ($EF = 0.78\text{--}1.53$), Sc ($EF = 1.07\text{--}1.38$), Th ($EF = 0.97\text{--}1.32$), Rb ($EF = 0.91\text{--}1.34$), Co ($EF = 0.7\text{--}1.83$), Cr ($EF = 0.82\text{--}1.35$), V ($EF = 0.71\text{--}1.13$), Zr ($EF = 0.79\text{--}1.27$), Cu ($EF = 0.39\text{--}1.57$), and Ba ($EF = 0.46\text{--}1.2$), show roughly narrow EF values being close to 1.0, suggesting slight enrichment or depletion. However, Mo element exhibits a wide range of EF values (0.27–5.0), which indicates various degrees of depletion to enrichment.

Total REE ($\sum\text{REE}$) contents range between 116.3 ppm and 201.3 ppm (Table 4), with an average of 134.8 ppm. However, most of the $\sum\text{REE}$ concentrations are not above

150 ppm, lower than that of PAAS (183.0 ppm) [47]. $\sum\text{REE}$ contents are positively correlated with Al_2O_3 (Figure 6(a)), suggesting typical detrital sources that were not affected by chemical alteration and sedimentary sorting. The $\sum\text{LREE}/\sum\text{HREE}$ (L/H) ratio varies from 7.4 to 12.5, reflecting a moderate enrichment in LREE relative to HREE. When normalized to the chondrite (Figure 7) [48], samples are characterized by fractionated LREE patterns [$(\text{La}/\text{Sm})_{\text{N}} = 3.91$ on average], flat HREE patterns [$(\text{Gd}/\text{Yb})_{\text{N}} = 1.37$], obvious Eu negative anomalies ($\text{Eu}/\text{Eu}^* = 0.61\text{--}0.7$), and weak Ce negative anomalies ($\text{Ce}/\text{Ce}^* = 0.92\text{--}0.97$).

5. Discussion

5.1. Sedimentary Recycling and Diagenesis. Sedimentary recycling and diagenesis can affect the redistribution of major and trace elements in sediments [49, 50]. Index of Compositional Variability [$\text{ICV} = (\text{CaO} + \text{Na}_2\text{O} + \text{K}_2\text{O} + \text{TFe}_2\text{O}_3 + \text{MgO} + \text{MnO} + \text{TiO}_2) / \text{Al}_2\text{O}_3$, all in weight percentages (%)] was defined as an index to evaluate the recycling process and compositional maturity of rocks [50]. An ICV value > 1.0 indicates that sediments were likely sourced from the first-cycle materials in active

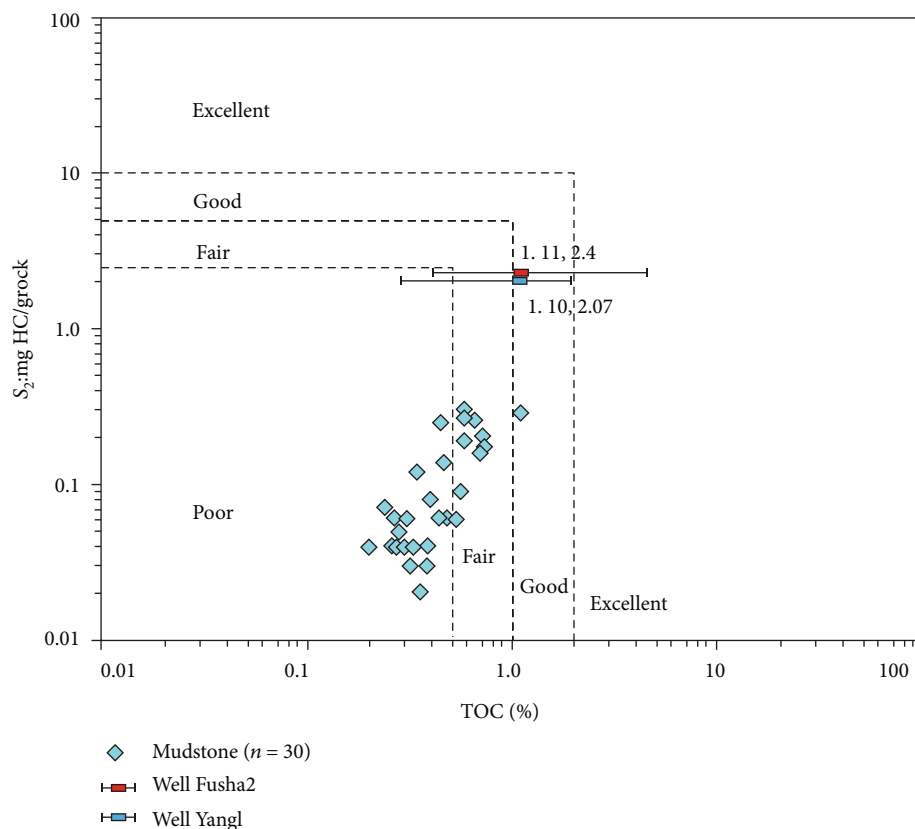


FIGURE 4: Cross-plot of TOC versus pyrolysis S_2 for the M3 mudstones in Well DW1 within the Yecheng-Hetian Sag, showing poor- to fair-quality hydrocarbon generation potential [44].

tectonic settings with a low degree of sediment recycling, while an ICV value < 1.0 is suggestive of either recycled weathered materials in cratonic environments or first-cycle products but enhanced by intense weathering. All the studied samples except for DW1-41 have high ICV values from 1.21 to 2.17, which implies that they are compositionally immature, and received first-recycling detrital materials in an active tectonic setting.

Moreover, cross-plot of Th/Sc against Zr/Sc ratios is widely used to constrain the degree of recycling and sorting [49]. The Th/Sc and Zr/Sc ratios of the samples vary between 0.74 and 1.12 averaging 0.82 and between 8.99 and 15.49 averaging 10.64 (Table 2). These data were plotted away from the trending line of mineral sorting and recycling (Figure 8(a)). Similarly, the Al_2O_3 -(CaO^*+Na_2O)- K_2O (A-CN-K; all in molar percentages) ternary diagram can also be applied to deduce the postdepositional diagenetic and metasomatic processes and parental rock composition [51–53]. On the A-CN-K diagram (Figure 8(b)), all the samples plot above the plagioclase-potash feldspar joint, and fall between the granodioritic and granitic rocks. The predicted weathering trend of these studied samples is subparallel to the A-CN boundary and does not display any implication toward the K_2O apex, revealing insignificant potash-metasomatism during burial diagenesis.

Furthermore, although REEs in sediments are generally not easily mobile during weathering and transportation, diagenetic exchanges after the depositions would cause the

apparent enrichment of Ce, depletion of Eu, and decrease in $(Dy/Sm)_N$ ratio [54]. Negative correlations between Ce/Ce^* and Eu/Eu^* or $(Dy/Sm)_N$ may be the result of diagenetic alterations. However, no detectable negative covariations between the Ce/Ce^* and Eu/Eu^* and $(Dy/Sm)_N$ ratio are observed in these lacustrine mudstones (Table 4), suggesting minor secondary chemical alterations.

In summary, the geochemical data of lacustrine mudstones, to a large extent, represent their original chemical compositions of the source rocks and could be used to identify their provenance, paleoclimate, and water conditions as the following texts.

5.2. Provenance and Tectonic Setting. Geochemical data of fine-grained sediments have been widely employed to investigate the source-rock lithotypes and their tectonic settings, due to their robust chemical behaviors during weathering, transportation, and diagenesis [55–62]. The ratios of Al_2O_3/TiO_2 (Al/Ti) and TiO_2/Zr (Ti/Zr) are often invariable and represent the chemical compositions of their parental rocks [61]. Al/Ti ratios > 21 and Ti/Zr ratios < 55 are indicative of felsic rocks, whereas mafic rocks have Al/Ti ratios lower than 8 and Ti/Zr ratios more than 200. For the studied samples, Al/Ti and Ti/Zr values range from 21 to 25 and 35 to 49, respectively, indicating a relatively stable provenance supply that consists principally of felsic rocks (Figures 9(a) and 9(b)). The above interpretation is inferred in the A-CN-K and Zr/Sc versus Th/Sc diagrams, in which provenance was

TABLE 2: Major element concentrations (as %) for the M3 lacustrine mudstones in the Yecheng-Hetian Sag.

Samples	Depth/m	SiO ₂ /%	TiO ₂ /%	Al ₂ O ₃ /%	MnO /%	MgO /%	CaO/%	Na ₂ O /%	K ₂ O/%	P ₂ O ₅ /%	TFe ₂ O ₃ /%	Ti/Al	CIA	ICV	P/Ti	Ba/Al
DW1-06	82.25	41.33	0.51	11.29	0.08	5.29	12.85	1.17	2.88	0.13	5.33	0.045	61.8	1.83	0.26	39.06
DW1-08	89.15	43.36	0.53	11.74	0.08	5.01	12.32	1.27	2.83	0.15	5.52	0.045	61.8	1.75	0.28	38.93
DW1-09	93.05	39.69	0.49	10.68	0.08	4.70	14.99	1.16	2.80	0.15	5.18	0.046	60.9	2.14	0.31	34.83
DW1-10	94.45	39.19	0.49	10.31	0.09	5.30	15.18	1.92	2.05	0.13	4.61	0.048	54.7	2.16	0.26	41.32
DW1-11	97.65	40.18	0.49	11.66	0.07	5.23	13.82	1.07	3.07	0.17	5.57	0.042	63.0	1.89	0.35	22.30
DW1-12	99.75	44.79	0.56	13.25	0.07	4.71	10.36	2.14	2.54	0.13	5.22	0.043	57.5	1.43	0.23	21.89
DW1-13	103.15	40.42	0.51	12.18	0.08	5.00	13.32	1.21	3.09	0.14	5.55	0.042	62.4	1.79	0.27	18.14
DW1-14	108.25	46.18	0.59	13.54	0.06	3.74	10.97	2.43	2.31	0.13	5.03	0.043	56.3	1.47	0.23	34.05
DW1-15	112.15	42.44	0.53	12.46	0.07	5.36	12.19	1.58	2.51	0.13	5.92	0.042	61.1	1.66	0.25	30.74
DW1-16	113.55	40.38	0.51	12.18	0.08	5.09	13.60	1.89	2.36	0.14	5.01	0.042	58.1	1.76	0.27	30.05
DW1-17	119.90	43.49	0.53	13.27	0.07	3.76	12.32	2.42	2.39	0.16	4.93	0.040	55.7	1.59	0.30	32.63
DW1-18	123.00	42.95	0.54	13.52	0.07	4.16	11.36	1.97	2.84	0.13	5.27	0.040	58.6	1.51	0.23	22.12
DW1-19	125.65	42.25	0.52	11.83	0.08	5.37	12.64	1.62	2.45	0.12	5.52	0.044	59.7	1.75	0.24	30.77
DW1-20	130.00	39.70	0.49	10.67	0.09	5.23	15.27	1.53	2.46	0.13	4.70	0.046	58.1	2.10	0.26	35.24
DW1-21	133.55	55.20	0.65	13.43	0.04	2.61	6.74	2.77	2.58	0.09	4.89	0.049	53.0	1.24	0.14	17.05
DW1-22	137.55	41.03	0.54	12.44	0.09	5.24	13.04	2.22	2.30	0.12	4.73	0.043	55.9	1.67	0.22	26.61
DW1-23	139.90	39.88	0.49	11.54	0.08	5.37	13.84	1.61	2.63	0.14	5.32	0.042	58.6	1.89	0.29	31.20
DW1-24	142.30	40.60	0.49	10.65	0.09	4.56	15.92	2.00	1.92	0.13	4.20	0.046	55.1	2.14	0.27	30.99
DW1-25	147.00	39.27	0.49	10.73	0.10	4.92	15.40	2.07	2.05	0.12	4.34	0.045	54.3	2.09	0.25	34.76
DW1-26	149.10	43.62	0.54	11.21	0.08	4.57	12.90	2.02	2.69	0.13	5.60	0.049	54.0	1.96	0.23	33.45
DW1-27	152.35	42.99	0.49	10.68	0.07	4.47	14.70	1.75	2.35	0.13	4.35	0.046	56.2	2.05	0.26	24.06
DW1-28	156.80	40.43	0.50	11.01	0.08	5.15	14.68	1.62	2.39	0.16	4.81	0.045	58.2	2.00	0.32	37.33
DW1-29	158.55	42.14	0.52	11.66	0.07	4.57	12.57	1.94	2.81	0.15	5.43	0.045	55.3	1.85	0.28	31.99
DW1-31	162.35	42.07	0.54	12.68	0.08	5.15	11.75	2.32	2.45	0.14	5.20	0.042	55.2	1.60	0.26	27.68
DW1-32	165.60	44.39	0.53	11.52	0.07	4.05	12.78	2.02	2.53	0.13	5.03	0.046	55.1	1.85	0.25	29.69
DW1-33	169.25	39.77	0.52	11.54	0.08	5.24	14.60	2.05	2.21	0.12	4.82	0.045	55.8	1.92	0.23	30.94
DW1-35	175.85	46.41	0.55	12.86	0.05	3.50	10.75	2.09	2.95	0.14	5.27	0.043	56.1	1.58	0.26	28.15
DW1-37	181.85	45.30	0.53	11.71	0.08	4.22	11.71	1.80	2.75	0.19	5.48	0.045	56.8	1.76	0.36	21.09
DW1-38	184.75	47.46	0.52	10.82	0.07	3.63	12.73	1.59	2.32	0.14	5.03	0.048	58.3	1.92	0.27	30.59
DW1-41	199.20	55.45	0.68	16.32	0.04	2.51	4.44	2.31	2.92	0.10	4.71	0.042	66.0	0.86	0.15	15.69
DW1-42	203.00	48.45	0.63	15.13	0.06	3.49	7.54	1.64	3.32	0.16	6.49	0.042	62.7	1.21	0.25	18.70
DW1-43	208.50	45.75	0.56	11.66	0.09	3.57	12.24	1.81	2.54	0.13	5.51	0.048	57.2	1.83	0.23	23.33
DW1-44	212.65	42.72	0.52	10.71	0.11	3.46	16.21	1.81	2.11	0.12	3.66	0.048	56.5	2.15	0.23	—
DW1-45	222.40	36.93	0.46	10.78	0.12	5.28	16.35	1.77	2.09	0.13	4.72	0.043	57.1	2.17	0.29	39.70

Abbreviation: “—” means invalid data.

mainly composed of the granodioritic and granitic rocks (Figure 8).

Other binary diagrams, such as La/Sc versus Co/Th and Hf versus La/Th, are also used to evaluate the source-rock compositions [59, 62, 63]. In the present study, these immobile elements show strong positive relationships with terrigenous Al₂O₃ and TiO₂ (Tables 2 and 3), preserving useful geochemical information of the parental rocks. Most of the studied samples are plotted within the felsic fields but possibly mixed with minor intermediate rocks and old sediments (Figures 9(c) and 9(d)). Typically, sediments derived from the felsic provenance are characterized by relatively low \sum REE contents, strong fractionated REE, and distinct negative Eu anomalies, whereas contradict REE features are

always indicative of the mafic rocks [59, 64]. The chondrite-normalized patterns further support a predominant felsic provenance with distinctive negative Eu anomalies ($\text{Eu}/\text{Eu}^* = 0.61\sim 0.7$; Table 4).

To further constrain the tectonic setting of source rocks, several discrimination diagrams were used in this study [56, 57, 65]. For example, on the cross-plot of K₂O/Na₂O versus SiO₂/Al₂O₃, these samples are scattered into the fields of active continental margin (ACM) and continental island arc (CIA) (Figure 10(a)). Further, the ternary discrimination diagrams of La-Th-Sc, Th-Sc-Zr/10, and Th-Co-Zr/10 were applied to decipher the tectonic settings [57]. Almost all the samples fall within the field of continental island arc (CIA) but adjacent to the ACM area (Figures 10(b)–10(d)).

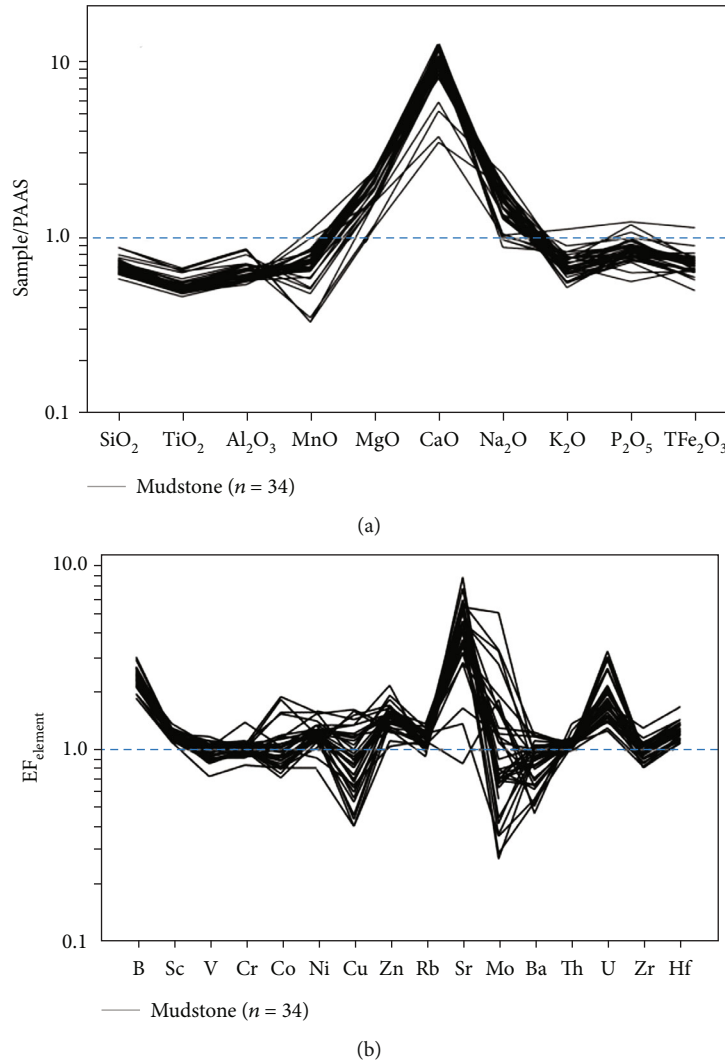


FIGURE 5: The Post-Archean Australian Shale- (PAAS-; Taylor and McLennan, [47]) normalized patterns of major elements (a) and enrichment factor (EF; b) of some selected trace elements for the M3 mudstones in Well DW1.

Moreover, according to the criteria of Bhatia [56], the contents of La, Ce, REE, $(La/Yb)_N$, and Eu/Eu^* (Table 4) of the studied samples are much more similar with the continental island arc (dissected magmatic arc) than the ACM tectonic setting.

Paleocurrent data indicate that the provenance during the deposition of the Pusige Formation was the West Kunlun Orogen located on the southwest of the study area [34]. The above results have indicated that the study area received detritus from a predominant felsic provenance consisting of granodiorite and granite with continental island arc-related tectonic signatures. By coincidence, previous studies have reported that large-scale Paleozoic granodiorite and granite are widely distributed within the West Kunlun Orogen (Figure 1(b)), which were formed under continental island arc (mostly) and active continental margin-related tectonic settings [35–39]. Chondrite-normalized REE patterns of some Paleozoic felsic plutons from the Kudi, Mazha, and Kangxiwar regions to the southwest of the study area can be compared with those of lacustrine mudstones (Figure 7)

[35–39]. Thus, it is credible that the dominant provenance for the study area during the Permian was the West Kunlun Orogen to the southwest.

5.3. *Paleoweathering and Paleoclimate Implications.* Chemical Index of Alteration (CIA) is commonly employed to quantitatively evaluate the paleoweathering conditions [49, 51–53] and calculated using the following equation:

$$CIA = [Al_2O_3 / (Al_2O_3 + CaO^* + Na_2O + K_2O)] \times 100, \quad (1)$$

where all elements are presented as molar ratios, of which CaO^* only represents silicate minerals (excluding calcite, dolomite, and apatite), and is calibrated using the method of McLennan et al. [49]. As discussed in Section 5.1, none of the studied samples were not influenced by sedimentary sorting, recycling, and diagenesis, and thus, CIA values are credible to examine the chemical weathering intensity in the study area. CIA values of the studied samples range between 53.0 and 66.0 with an average of 57.9 (Table 2),

TABLE 3: Trace element concentrations (as ppm) and relevant parameters for the M3 lacustrine mudstones in the Ye Cheng-Hetian Sag.

Samples	B	Sc	V	Cr	Co	Ni	Cu	Mo	Zn	Ga	Rb	Sr	Ba	Th	U	Zr	Hf	C- value	S- value	B _{eq}	Rb/Sr	Sr/Cu	Sr/Ba	Cu/Zn	U/Th	Co/Th	B/Ga	Ti/Zr
DW1-06	157	11.7	84.7	68.6	20.7	45.0	29.4	0.708	94.9	15.1	121	423	441	9.3	3.48	120	3.66	0.37	19.59	272.6	0.29	14.39	0.96	0.31	0.37	2.23	10.4	43
DW1-08	138	11.0	81.2	65.9	11.0	37.4	18.4	1.160	78.3	15.0	119	382	457	9.4	2.93	123	3.73	0.39	16.78	243.8	0.31	20.76	0.84	0.23	0.31	1.17	9.2	43
DW1-09	130	12	87.6	66.7	13.1	40.4	18.8	0.354	74.2	14.6	121	503	372	9.0	2.87	117	3.54	0.31	15.64	232.1	0.24	26.76	1.35	0.25	0.32	1.45	8.9	42
DW1-10	156	10.6	88.3	59.2	13.2	35.2	29.6	0.687	70.2	12.9	84	433	426	8.3	5.33	111	3.34	0.28	30.13	380.5	0.19	14.63	1.02	0.42	0.65	1.60	12.1	44
DW1-11	156	11.5	77.3	64.9	9.9	36.4	16.3	0.414	70.9	14.8	126	557	260	9.2	2.63	112	3.37	0.36	17.78	254.1	0.23	34.17	2.14	0.23	0.29	1.08	10.5	44
DW1-12	148	13.1	91.1	73.7	18.2	58.1	55.0	1.08	76.6	16.7	116	387	290	10.7	3.49	139	4.06	0.40	21.42	291.3	0.30	7.04	1.33	0.72	0.33	1.70	8.9	41
DW1-13	167	12.2	98.9	71.2	12.6	40.8	29.0	0.184	73.3	15.6	126	509	221	9.5	2.90	113	3.73	0.36	19.36	270.2	0.25	17.55	2.30	0.40	0.30	1.32	10.7	45
DW1-14	135	12.5	92.0	71.8	14.7	43.8	32.3	0.624	75.3	16.0	104	739	461	11.8	3.72	132	3.94	0.36	21.51	292.2	0.14	22.88	1.60	0.43	0.32	1.25	8.4	44
DW1-15	152	12.0	84.8	68.6	12.9	40.3	27.3	0.175	85.0	15.4	106	593	383	9.3	2.56	116	3.48	0.42	22.54	302.8	0.18	21.72	1.55	0.32	0.27	1.38	9.9	46
DW1-16	133	13.1	100.0	73.4	14.3	43.2	36.8	0.500	78.5	16.0	109	643	366	10.0	4.17	119	3.54	0.32	20.49	281.8	0.17	17.47	1.76	0.47	0.42	1.44	8.3	43
DW1-17	144	12.9	94.1	70.0	14.9	50.2	45.0	1.890	124	15.9	107	630	433	10.0	3.70	116	3.73	0.32	22.39	301.3	0.17	14.00	1.45	0.36	0.37	1.49	9.1	45
DW1-18	177	13.0	109.0	78.8	12.9	39.3	54.9	0.511	73.1	16.9	131	441	299	11.0	2.69	121	4.04	0.37	23.40	311.6	0.30	8.03	1.47	0.75	0.24	1.17	10.5	45
DW1-19	129	12.0	92.9	67.7	21.9	52.8	43.6	0.223	85.8	16.2	112	519	364	9.9	2.62	129	3.81	0.38	18.68	263.3	0.22	11.90	1.43	0.51	0.26	2.21	8.0	40
DW1-20	147	10.4	76.4	65.6	10.1	36.4	22.9	0.389	66.0	13.1	104	746	376	8.5	2.48	126	3.76	0.28	22.15	298.8	0.14	32.58	1.98	0.35	0.29	1.19	11.2	39
DW1-21	128	12.2	76.2	63.8	12.8	30.3	14.0	0.827	66.0	16.3	117	228	229	13.7	3.68	189	5.81	0.45	17.19	248.1	0.51	16.29	1.00	0.21	0.27	0.93	7.9	35
DW1-22	148	13.3	102.0	73.1	16.0	42.4	38.0	2.080	69.5	16.0	108	578	331	10.1	5.14	130	4.31	0.31	24.39	321.7	0.19	15.21	1.75	0.55	0.51	1.58	9.3	41
DW1-23	179	12.0	91.0	66.5	11.3	38.1	22.1	0.267	84.0	15.0	115	658	360	9.4	2.68	122	3.76	0.34	26.20	340.3	0.17	29.77	1.83	0.26	0.28	1.20	11.9	40
DW1-24	106	10.5	83.9	83.9	13.1	36.9	24.4	0.877	71.4	13.3	87	573	330	9.0	4.47	110	3.55	0.24	19.93	276.0	0.15	23.48	1.74	0.34	0.49	1.45	8.0	45
DW1-25	122	10.8	90.0	60.8	9.6	38.3	37.2	0.411	72.3	13.4	90	643	373	8.7	5.16	110	3.33	0.25	22.03	297.6	0.14	17.28	1.72	0.51	0.60	1.11	9.1	44

TABLE 3: Continued.

Samples	B	Sc	V	Cr	Co	Ni	Cu	Mo	Zn	Ga	Rb	Sr	Ba	Th	U	Zr	Hf	C- value	S- value	B _{eq}	Rb/Sr	Sr/Cu	Sr/Ba	Cu/Zn	U/Th	Co/Th	B/Ga	Ti/Zr
DW1-26	142	10.7	76.7	63.9	12.2	37.4	13.4	0.634	73.1	14.2	104	419	375	9.3	2.72	131	3.91	0.36	18.74	263.9	0.25	31.27	1.12	0.18	0.29	1.31	10.0	42
DW1-27	130	11.3	80.6	64.1	23.8	47.3	24.2	0.602	70.3	14.6	103	606	257	8.3	3.06	121	3.38	0.26	19.98	276.6	0.17	25.04	2.36	0.34	0.37	2.86	8.9	41
DW1-28	152	11.4	85.1	67.8	13.7	42.0	30.1	0.237	87.0	14.5	108	672	411	8.9	3.00	119	3.78	0.29	24.02	318.0	0.16	22.33	1.64	0.35	0.34	1.55	10.5	42
DW1-29	157	12.5	97.3	74.2	12.1	41.2	28.8	0.402	79.1	15.5	120	539	373	9.8	2.77	131	4.09	0.35	20.25	279.4	0.22	18.72	1.45	0.36	0.28	1.24	10.1	40
DW1-31	139	12.7	114.0	72.1	17.8	45.6	39.8	0.462	84.7	16.6	111	736	351	10.3	3.73	129	3.98	0.36	20.67	283.7	0.15	18.49	2.10	0.47	0.36	1.73	8.4	42
DW1-32	136	12.2	82.2	67.3	12.1	39.0	24.0	0.422	78.5	14.8	112	410	342	9.3	2.74	130	4.09	0.32	19.22	268.8	0.27	17.08	1.20	0.31	0.30	1.30	9.2	41
DW1-33	150	11.9	90.0	67.8	13.4	40.9	34.5	3.050	79.9	15.0	101	644	357	9.0	4.81	124	3.59	0.29	26.11	339.4	0.16	18.67	1.80	0.43	0.53	1.48	10.0	42
DW1-35	160	12.8	86.0	70.0	12.9	40.6	21.0	0.502	72.6	16.7	131	423	362	10.7	2.99	131	4.02	0.37	19.45	271.2	0.31	20.14	1.17	0.29	0.28	1.21	9.6	42
DW1-37	161	11.5	83.5	67.1	14.4	41.0	21.3	0.477	77.4	16.0	121	337	247	9.8	3.13	127	4.07	0.38	21.56	292.7	0.36	15.82	1.36	0.28	0.32	1.47	10.1	42
DW1-38	122	11.1	80.3	67.2	13.2	39.3	15.9	0.658	74.9	14.2	107	413	331	9.0	2.77	136	4.03	0.34	18.65	262.9	0.26	25.97	1.25	0.21	0.31	1.47	8.6	38
DW1-41	179	15.5	140.0	86.9	19.6	42.1	27.6	1.530	73.9	22.0	151	144	256	15.4	5.28	186	5.76	0.55	22.90	306.5	1.05	5.22	0.56	0.37	0.34	1.27	8.1	37
DW1-42	210	15.1	111.0	86.9	32.7	51.3	15.8	0.282	91.1	19.6	151	211	283	13.1	3.41	161	5.31	0.59	23.86	316.3	0.72	13.35	0.75	0.17	0.26	2.50	10.7	39
DW1-43	140	11.9	101.0	70.7	15.7	41.2	13.2	1.010	75.7	15.5	115	405	272	9.8	3.69	137	4.33	0.37	19.88	275.6	0.28	30.68	1.49	0.17	0.38	1.60	9.0	41
DW1-44	126	9.7	84.9	55.1	14.8	34.4	41.6	0.307	79.3	12.7	90	850	—	8.6	4.95	106	3.19	0.20	22.13	298.6	0.11	20.43	—	0.52	0.58	1.72	9.9	49
DW1-45	137	11.0	75.2	56.3	13.2	35.6	20.6	1.820	80.0	13.8	96	640	428	8.9	3.57	112	3.51	0.27	24.98	327.8	0.15	31.07	1.50	0.26	0.40	1.48	9.9	41
DW1-06	157	11.7	84.7	68.6	20.7	45.0	29.4	0.708	94.9	12.1	423	441	9.3	3.48	120	3.66	0.37	19.59	272.6	0.29	14.39	0.96	0.31	0.37	2.23	10.26	0.79	43
DW1-08	138	11.0	81.2	65.9	11.0	37.4	18.4	1.16	78.3	11.9	382	457	9.4	2.93	123	3.73	0.39	16.78	243.8	0.31	20.76	0.84	0.23	0.31	1.17	11.18	0.85	43
DW1-09	130	12.0	87.6	66.7	13.1	40.4	18.8	0.354	74.2	12.1	503	372	9.0	2.87	117	3.54	0.31	15.64	232.1	0.24	26.76	1.35	0.25	0.32	1.45	9.75	0.75	42
DW1-10	156	10.6	88.3	59.2	13.2	35.2	29.6	0.687	70.2	8.4	433	426	8.3	5.33	111	3.34	0.28	30.13	380.5	0.19	14.63	1.02	0.42	0.65	1.60	10.47	0.78	44

TABLE 3: Continued.

Samples	B	Sc	V	Cr	Co	Ni	Cu	Mo	Zn	Ga	Rb	Sr	Ba	Th	U	Zr	Hf	C- value	S- value	B _{eq}	Rb/Sr	Sr/Cu	Sr/Ba	Cu/Zn	U/Th	Co/Th	B/Ga	Ti/Zr
DW1-11	156	11.5	77.3	64.9	9.9	36.4	16.3	0.414	70.9	126	557	260	9.2	2.63	112	3.37	0.36	17.78	254.1	0.23	34.17	2.14	0.23	0.29	1.08	9.74	0.80	44
DW1-12	148	13.1	91.1	73.7	18.2	58.1	55.0	1.08	76.6	116	387	290	10.7	3.49	139	4.06	0.40	21.42	291.3	0.30	7.04	1.33	0.72	0.33	1.70	10.61	0.82	41
DW1-13	167	12.2	98.9	71.2	12.6	40.8	29.0	0.184	73.3	126	509	221	9.5	2.90	113	3.73	0.36	19.36	270.2	0.25	17.55	2.30	0.40	0.30	1.32	9.26	0.78	45
DW1-14	135	12.5	92.0	71.8	14.7	43.8	32.3	0.624	75.3	104	739	461	11.8	3.72	132	3.94	0.36	21.51	292.2	0.14	22.88	1.60	0.43	0.32	1.25	10.56	0.94	44
DW1-15	152	12.0	84.8	68.6	12.9	40.3	27.3	0.175	85	106	593	383	9.3	2.56	116	3.48	0.42	22.54	302.8	0.18	21.72	1.55	0.32	0.27	1.38	9.67	0.78	46
DW1-16	133	13.1	100.0	73.4	14.3	43.2	36.8	0.5	78.5	109	643	366	10.0	4.17	119	3.54	0.32	20.49	281.8	0.17	17.47	1.76	0.47	0.42	1.44	9.08	0.76	43
DW1-17	144	12.9	94.1	70.0	14.9	50.2	45.0	1.89	124	107	630	433	10.0	3.70	116	3.73	0.32	22.39	301.3	0.17	14.00	1.45	0.36	0.37	1.49	8.99	0.78	45
DW1-18	177	13.0	109.0	78.8	12.9	39.3	54.9	0.511	73.1	131	441	299	11.0	2.69	121	4.04	0.37	23.40	311.6	0.30	8.03	1.47	0.75	0.24	1.17	9.31	0.85	45
DW1-19	129	12.0	92.9	67.7	21.9	52.8	43.6	0.223	85.8	112	519	364	9.9	2.62	129	3.81	0.38	18.68	263.3	0.22	11.90	1.43	0.51	0.26	2.21	10.75	0.83	40
DW1-20	147	10.4	76.4	65.6	10.1	36.4	22.9	0.389	66	104	746	376	8.5	2.48	126	3.76	0.28	22.15	298.8	0.14	32.58	1.98	0.35	0.29	1.19	12.12	0.82	39
DW1-21	128	12.2	76.2	63.8	12.8	30.3	14.0	0.827	66	117	228	229	13.7	3.68	189	5.81	0.45	17.19	248.1	0.51	16.29	1.00	0.21	0.27	0.93	15.49	1.12	35
DW1-22	148	13.3	102.0	73.1	16.0	42.4	38.0	2.08	69.5	108	578	331	10.1	5.14	130	4.31	0.31	24.39	321.7	0.19	15.21	1.75	0.55	0.51	1.58	9.77	0.76	41
DW1-23	179	12.0	91.0	66.5	11.3	38.1	22.1	0.267	84	115	658	360	9.4	2.68	122	3.76	0.34	26.20	340.3	0.17	29.77	1.83	0.26	0.28	1.20	10.17	0.78	40
DW1-24	106	10.5	83.9	83.9	13.1	36.9	24.4	0.877	71.4	87	573	330	9.0	4.47	110	3.55	0.24	19.93	276.0	0.15	23.48	1.74	0.34	0.49	1.45	10.48	0.86	45
DW1-25	122	10.8	90.0	60.8	9.6	38.3	37.2	0.411	72.3	90	643	373	8.7	5.16	110	3.33	0.25	22.03	297.6	0.14	17.28	1.72	0.51	0.60	1.11	10.19	0.80	44
DW1-26	142	10.7	76.7	63.9	12.2	37.4	13.4	0.634	73.1	104	419	375	9.3	2.72	131	3.91	0.36	18.74	263.9	0.25	31.27	1.12	0.18	0.29	1.31	12.24	0.87	42
DW1-27	130	11.3	80.6	64.1	23.8	47.3	24.2	0.602	70.3	103	606	257	8.3	3.06	121	3.38	0.26	19.98	276.6	0.17	25.04	2.36	0.34	0.37	2.86	10.71	0.74	41
DW1-28	152	11.4	85.1	67.8	13.7	42.0	30.1	0.237	87	108	672	411	8.9	3.00	119	3.78	0.29	24.02	318.0	0.16	22.33	1.64	0.35	0.34	1.55	10.44	0.78	42
DW1-29	157	12.5	97.3	74.2	12.1	41.2	28.8	0.402	79.1	120	539	373	9.8	2.77	131	4.09	0.35	20.25	279.4	0.22	18.72	1.45	0.36	0.28	1.24	10.48	0.78	40

TABLE 3: Continued.

Samples	B	Sc	V	Cr	Co	Ni	Cu	Mo	Zn	Ga	Rb	Sr	Ba	Th	U	Zr	Hf	C- value	S- value	B _{eq}	Rb/Sr	Sr/Cu	Sr/Ba	Cu/Zn	U/Th	Co/Th	B/Ga	Ti/Zr
DW1-31	139	12.7	114.0	72.1	17.8	45.6	39.8	0.462	84.7	111	736	351	10.3	3.73	129	3.98	0.36	20.67	283.7	0.15	18.49	2.10	0.47	0.36	1.73	10.16	0.81	42
DW1-32	136	12.2	82.2	67.3	12.1	39.0	24.0	0.422	78.5	112	410	342	9.3	2.74	130	4.09	0.32	19.22	268.8	0.27	17.08	1.20	0.31	0.30	1.30	10.66	0.76	41
DW1-33	150	11.9	90.0	67.8	13.4	40.9	34.5	3.05	79.9	101	644	357	9.0	4.81	124	3.59	0.29	26.11	339.4	0.16	18.67	1.80	0.43	0.53	1.48	10.42	0.76	42
DW1-35	160	12.8	86.0	70.0	12.9	40.6	21.0	0.502	72.6	131	423	362	10.7	2.99	131	4.02	0.37	19.45	271.2	0.31	20.14	1.17	0.29	0.28	1.21	10.23	0.84	42
DW1-37	161	11.5	83.5	67.1	14.4	41.0	21.3	0.477	77.4	121	337	247	9.8	3.13	127	4.07	0.38	21.56	292.7	0.36	15.82	1.36	0.28	0.32	1.47	11.04	0.85	42
DW1-38	122	11.1	80.3	67.2	13.2	39.3	15.9	0.658	74.9	107	413	331	9.0	2.77	136	4.03	0.34	18.65	262.9	0.26	25.97	1.25	0.21	0.31	1.47	12.25	0.81	38
DW1-41	179	15.5	140.0	86.9	19.6	42.1	27.6	1.53	73.9	151	144	256	15.4	5.28	186	5.76	0.55	22.90	306.5	1.05	5.22	0.56	0.37	0.34	1.27	12.00	0.99	37
DW1-42	210	15.1	111.0	86.9	32.7	51.3	15.8	0.282	91.1	151	211	283	13.1	3.41	161	5.31	0.59	23.86	316.3	0.72	13.35	0.75	0.17	0.26	2.50	10.66	0.87	39
DW1-43	140	11.9	101.0	70.7	15.7	41.2	13.2	1.01	75.7	115	405	272	9.8	3.69	137	4.33	0.37	19.88	275.6	0.28	30.68	1.49	0.17	0.38	1.60	11.51	0.82	41
DW1-44	126	9.7	84.9	55.1	14.8	34.4	41.6	0.307	79.3	90	850	—	8.6	4.95	106	3.19	0.20	22.13	298.6	0.11	20.43	—	0.52	0.58	1.72	10.96	0.89	49
DW1-45	137	11.0	75.2	56.3	13.2	35.6	20.6	1.82	80	96	640	428	8.9	3.57	112	3.51	0.27	24.98	327.8	0.15	31.07	1.50	0.26	0.40	1.48	10.18	0.81	41

Abbreviation: “—” means invalid data.

TABLE 4: Rare earth element (REE) concentrations (as ppm) and associated parameters of the M3 lacustrine mudstones in the Ye Cheng-Hetian Sag.

Samples	La	Ce	Pr	Nd	Sm	Eu	Gd	Tb	Dy	Ho	Er	Tm	Yb	Lu	\sum REE	L/H	Eu/Eu*	Ce/Ce*	(La/Sm) _N	(Gd/Yb) _N	(Dy/Sm) _N	(La/Yb) _n
DW1-06	26.5	50.2	6.07	23.6	4.48	0.836	3.72	0.685	3.69	0.722	2.01	0.309	2.31	0.357	125.5	8.09	0.62	0.95	3.72	1.30	0.50	1.11
DW1-08	27.4	51.6	6.17	24.0	4.58	0.936	4.29	0.706	3.75	0.754	2.05	0.332	2.43	0.329	129.3	7.83	0.64	0.96	3.76	1.42	0.50	1.09
DW1-09	29.2	53.3	6.32	24.1	4.48	0.881	3.86	0.681	3.76	0.713	1.93	0.343	2.34	0.294	132.2	8.50	0.64	0.94	4.10	1.33	0.51	1.21
DW1-10	26.0	49.1	5.90	22.6	4.30	0.842	3.84	0.637	3.49	0.689	1.94	0.314	2.05	0.323	122.0	8.19	0.63	0.95	3.80	1.51	0.49	1.23
DW1-11	25.9	50.3	6.06	23.4	4.45	0.935	3.69	0.621	3.86	0.678	1.97	0.353	1.96	0.308	124.5	8.26	0.70	0.97	3.66	1.52	0.53	1.28
DW1-12	27.7	52.4	6.33	24.3	4.62	0.972	4.23	0.704	4.23	0.824	2.30	0.369	2.49	0.359	131.8	7.50	0.67	0.95	3.77	1.37	0.55	1.08
DW1-13	26.1	48.9	5.80	22.2	4.20	0.836	3.43	0.611	3.59	0.700	1.86	0.323	2.06	0.312	120.9	8.38	0.67	0.96	3.91	1.34	0.52	1.23
DW1-14	44.0	77.2	8.82	32.5	5.81	1.180	5.02	0.851	4.89	0.866	2.48	0.421	2.70	0.404	187.1	9.61	0.66	0.94	4.76	1.50	0.51	1.58
DW1-15	26.7	50.9	6.06	23.3	4.41	0.864	3.92	0.651	3.83	0.710	2.00	0.340	2.11	0.311	126.1	8.09	0.63	0.96	3.81	1.50	0.53	1.23
DW1-16	27.2	51.4	6.08	23.5	4.42	0.887	3.73	0.651	3.73	0.697	2.01	0.322	2.22	0.297	127.1	8.31	0.66	0.96	3.87	1.36	0.51	1.19
DW1-17	28.5	53.3	6.46	25.2	4.81	0.956	4.09	0.704	3.94	0.740	2.19	0.392	2.24	0.349	133.9	8.14	0.65	0.95	3.73	1.47	0.50	1.23
DW1-18	28.1	53.2	6.30	24.2	4.57	0.940	3.89	0.690	3.79	0.712	2.20	0.337	2.16	0.328	131.4	8.32	0.68	0.96	3.87	1.45	0.50	1.26
DW1-19	27.2	51.2	6.11	23.7	4.51	0.882	3.99	0.669	4.14	0.736	2.33	0.419	2.39	0.358	128.6	7.56	0.63	0.96	3.79	1.35	0.56	1.10
DW1-20	25.4	47.6	5.68	21.9	4.10	0.837	3.38	0.579	3.57	0.668	1.85	0.331	2.24	0.304	118.4	8.17	0.68	0.95	3.90	1.22	0.53	1.10
DW1-21	34.5	65.7	7.76	30.0	5.95	1.110	5.05	0.913	5.13	1.030	3.00	0.518	3.46	0.452	164.6	7.42	0.61	0.97	3.65	1.18	0.52	0.97
DW1-22	26.3	49.7	5.92	22.9	4.32	0.895	3.75	0.677	4.04	0.675	2.11	0.366	2.43	0.343	124.4	7.65	0.68	0.96	3.83	1.25	0.57	1.05
DW1-23	26.7	50.1	5.97	23.2	4.40	0.858	3.98	0.672	3.91	0.681	2.04	0.331	2.33	0.325	125.5	7.80	0.62	0.96	3.82	1.38	0.54	1.11
DW1-24	27.0	50.0	5.94	23.0	4.31	0.866	3.64	0.665	3.42	0.674	2.01	0.324	2.20	0.398	124.4	8.34	0.66	0.95	3.94	1.34	0.48	1.19
DW1-25	25.5	47.5	5.66	21.9	4.17	0.856	3.43	0.599	3.36	0.653	1.86	0.328	1.98	0.287	118.1	8.45	0.69	0.95	3.85	1.40	0.49	1.25
DW1-26	27.4	51.2	6.13	23.7	4.53	0.912	3.86	0.668	3.88	0.686	2.04	0.337	2.30	0.362	128.0	8.06	0.66	0.95	3.80	1.35	0.52	1.15
DW1-27	25.0	46.5	5.60	21.5	4.11	0.866	3.45	0.617	3.34	0.704	1.95	0.340	2.06	0.287	116.3	8.12	0.70	0.95	3.83	1.35	0.49	1.18
DW1-28	33.8	60.3	6.88	26.1	4.72	0.975	4.08	0.699	3.66	0.712	2.01	0.353	1.95	0.301	146.5	9.65	0.67	0.95	4.50	1.69	0.47	1.68
DW1-29	28.3	53.4	6.42	25.1	4.81	0.957	3.92	0.704	4.11	0.751	2.07	0.365	2.38	0.359	133.6	8.12	0.67	0.95	3.70	1.33	0.52	1.15
DW1-31	54.1	84.4	9.02	32.5	5.36	1.020	4.32	0.695	3.98	0.729	1.99	0.389	2.52	0.306	201.3	12.49	0.64	0.92	6.35	1.38	0.45	2.08
DW1-32	29.1	53.7	6.41	24.7	4.68	0.939	3.87	0.681	3.78	0.732	2.23	0.361	2.55	0.342	134.1	8.22	0.67	0.95	3.91	1.22	0.49	1.11
DW1-33	26.1	48.7	5.77	22.3	4.28	0.841	3.64	0.641	3.70	0.677	1.99	0.350	2.35	0.301	121.6	7.91	0.65	0.96	3.84	1.25	0.52	1.08
DW1-35	28.8	55.2	6.62	25.3	4.88	0.926	4.14	0.710	4.00	0.751	2.39	0.379	2.64	0.347	137.1	7.93	0.63	0.96	3.71	1.27	0.50	1.06
DW1-37	28.1	54.3	6.57	26.2	5.08	0.989	4.44	0.760	4.26	0.759	2.36	0.361	2.28	0.343	136.8	7.79	0.63	0.96	3.48	1.57	0.51	1.19
DW1-38	26.2	49.6	5.91	23.2	4.39	0.898	4.05	0.663	3.59	0.692	2.11	0.356	2.37	0.326	124.4	7.78	0.65	0.96	3.75	1.38	0.50	1.07
DW1-41	39.0	74.2	8.75	33.9	6.42	1.270	5.20	0.930	5.60	1.010	3.19	0.541	3.59	0.487	184.1	7.96	0.67	0.97	3.82	1.17	0.53	1.05
DW1-42	33.2	63.4	7.73	31.0	6.27	1.270	5.37	0.906	5.26	0.909	2.93	0.464	3.04	0.430	162.2	7.40	0.66	0.95	3.33	1.43	0.51	1.06
DW1-43	26.5	49.3	5.94	23.0	4.49	0.917	3.91	0.638	3.73	0.703	2.10	0.412	2.41	0.303	124.4	7.75	0.66	0.95	3.71	1.31	0.50	1.07
DW1-44	26.0	47.0	5.47	21.0	3.97	0.755	3.38	0.563	3.41	0.628	1.88	0.341	2.10	0.268	116.8	8.29	0.63	0.95	4.12	1.30	0.52	1.20
DW1-45	25.2	47.6	5.69	22.2	4.29	0.852	3.64	0.577	3.40	0.739	2.03	0.318	2.17	0.281	119.0	8.05	0.65	0.96	3.70	1.35	0.48	1.13

Abbreviations: L/H, \sum REE/ \sum REE; Eu/Eu* = $Eu_N / [(Sm_N \times Gd_N)^{1/2}]$; Ce/Ce* = $Ce_N / [(La_N \times Pr_N)^{1/2}]$; "N" refers to the chondrite-normalized values [48]; "n" refers to the North American Shale Composite (NASC, Gromet et al., 1984).

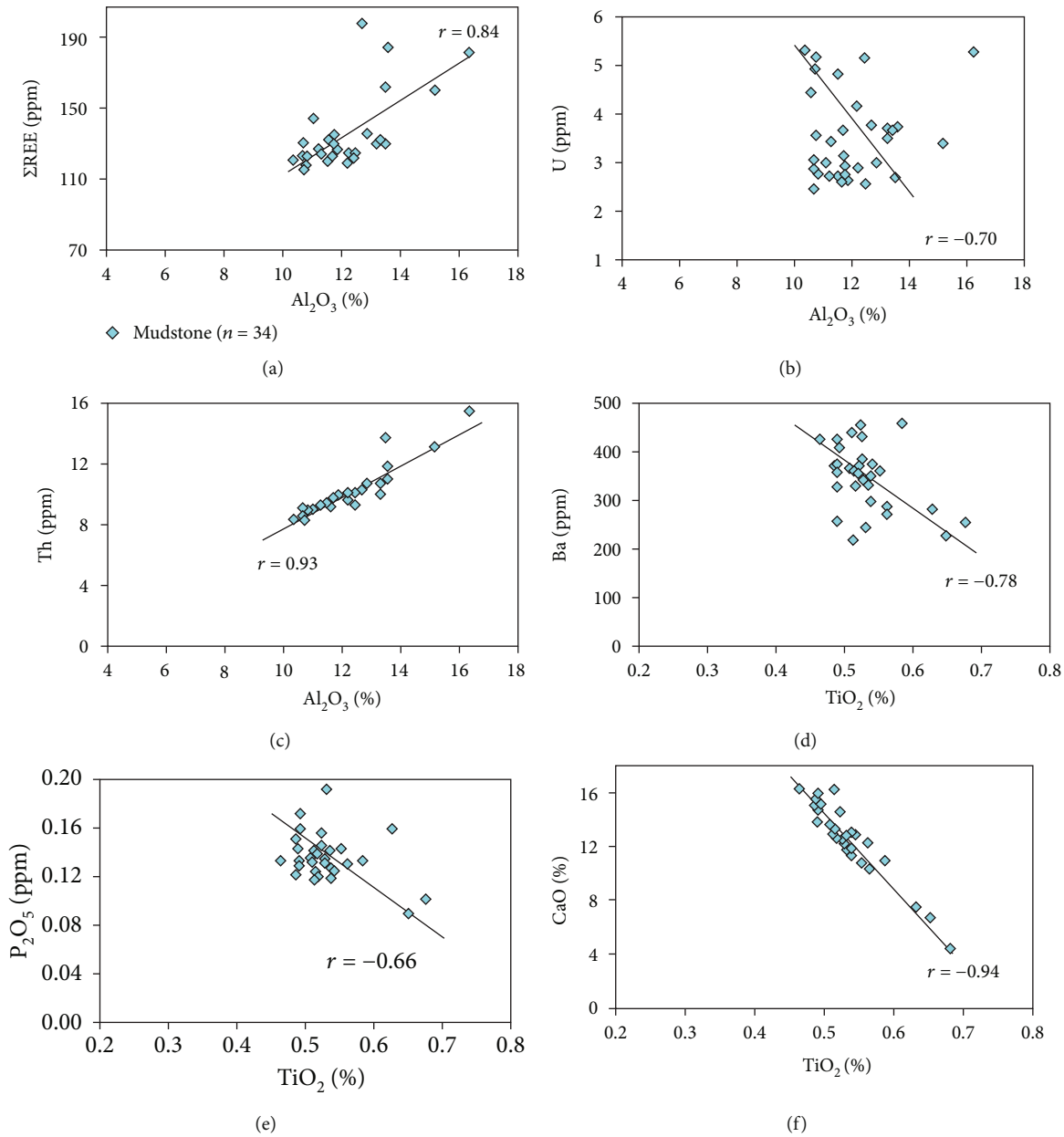


FIGURE 6: Correlations between Al_2O_3 and ΣREE (a), U (b) and Th (c), and between TiO_2 and Ba (d), P_2O_5 (e) and CaO (f) for the M3 mudstones in Well DW1.

which are lower than that of PAAS (CIA = 70.4) [47]. These low CIA data indicate a low paleoweathering condition. This CIA value can be corrected in the A-CN-K diagram (Figure 8(b)), in which these samples are plotted between 50.0 and 65.0.

In general, CIA is also used to reconstruct the paleoclimatic conditions [49, 51, 66]. A CIA value > 80~100 is indicative of a hot climate, > 70~80 indicates a warm and humid climatic setting, and > 50~70 corresponds to a relatively cool and arid paleoclimate. Therefore, the low CIA values (53.0~65.0) in the present study indicate a low chemical weathering with cool and arid paleoclimatic condition.

Previous studies have documented that Fe, Mn, V, Cr, Co, and Ni are relatively enriched under the humid condi-

tions, whereas Ca, K, Sr, Na, Mg, and Ba, being associated with saline mineral precipitates, are comparatively concentrated under arid climatic conditions [67–70]. Taken into consideration of their geochemical behaviors, the C-value was then proposed as an indicator for inferring the paleoclimate [7, 67, 71]. The C-value was defined as follows:

$$C - \text{value} = \frac{\sum(\text{Fe} + \text{Mn} + \text{Cr} + \text{Ni} + \text{V} + \text{Co})}{\sum(\text{Ca} + \text{Mg} + \text{Sr} + \text{Ba} + \text{K} + \text{Na})}. \tag{2}$$

The C-value of 0~0.2, 0.2~0.4, 0.4~0.6, 0.6~0.8, and 0.8~1.0 corresponds to arid, semiarid, semiarid to

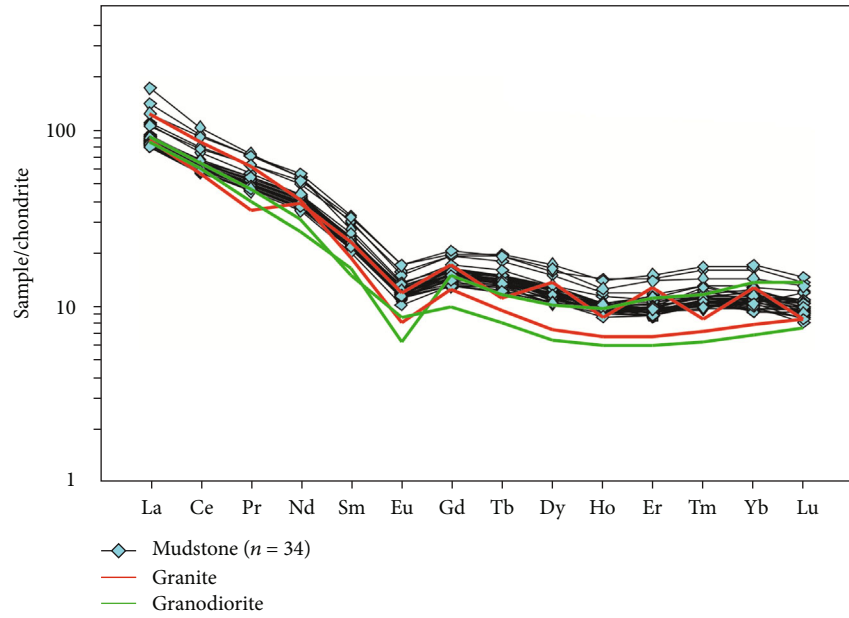


FIGURE 7: Chondrite-normalized [48] REE spider plots of the M3 mudstones in Well DW1. Red and green lines represent the chondrite-normalized patterns of Paleozoic granite and granodiorite for comparisons, respectively [35, 38]; (Zhang et al., 2016).

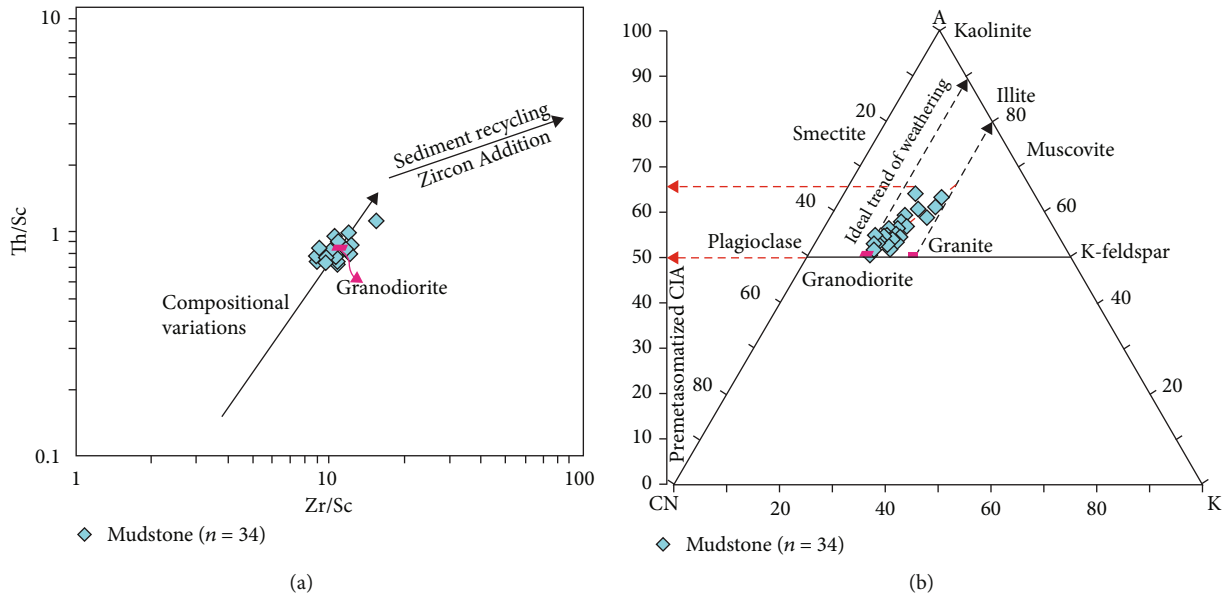


FIGURE 8: (a) Cross-plot of Zr/Sc versus Th/Sc (after McLennan et al., [49]) showing minimal influence of heavy mineral sorting and recycling. (b) Al_2O_3 -(CaO^*+Na_2O)- K_2O (A-CN-K) ternary diagram (modified after Nesbitt and Young, 1982, 1984) for M3 mudstones. A= Al_2O_3 , CN= CaO^*+Na_2O , K= K_2O (all in molar percentages). Black dashed lines with arrows represent the ideal weathering trends of granodiorite and granite [51]. Red dashed lines with arrows show the premetasomatized CIA values for the samples.

semihumid, semihumid, and humid climatic conditions, respectively [72]. C-values for all the studied samples vary from 0.2 to 0.59 averaging 0.35 (Table 2). As most C-values are restricted between 0.2 and 0.4, this suggests a relatively stable semiarid paleoclimate during the depositions. Other samples with relatively moderate C-values (>0.4-0.6) are indicative of semiarid to semihumid climatic conditions (Figure 11(a)).

Besides, ratios of Sr/Cu and Rb/Sr can also be employed for characterizing the paleoclimatic changes [67–69]. The Sr/Cu ratio will increase, while the Rb/Sr ratio decreases under drier and/or hotter climatic conditions. Sr/Cu and Rb/Sr ratios for all the studied samples range from 5.22 to 34.17 and 0.11 to 1.05, respectively. The statistically high Sr/Cu (>5.0) and low Rb/Sr (<0.4) ratios reflect a relatively arid climatic conditions (Figures 11(a) and 11(b)). From

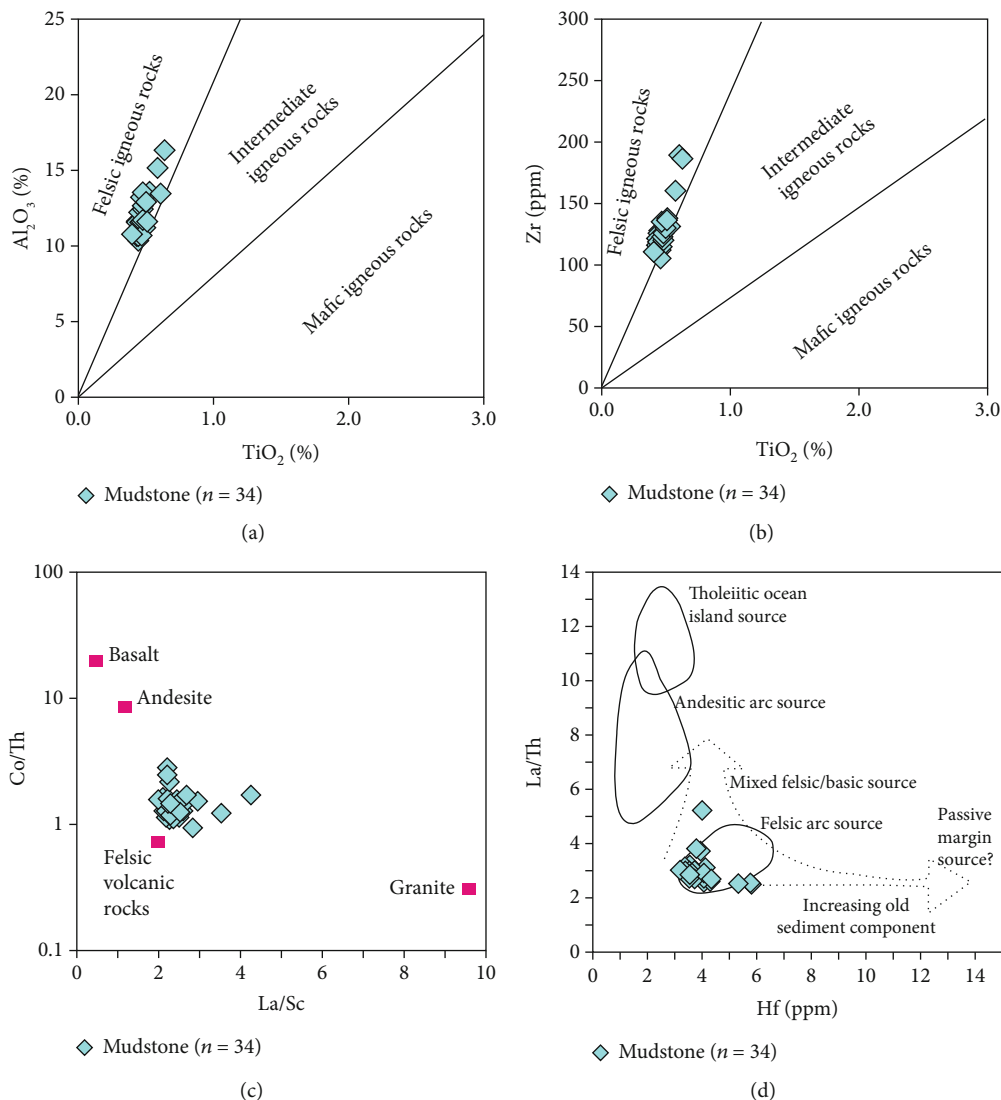


FIGURE 9: Provenance discrimination cross-plots of the M3 mudstones. (a) TiO₂ versus Al₂O₃ [61]. (b) TiO₂ against Zr [61]. (c) La/Sc versus Co/Th [62]. (d) Hf against La/Th [63].

the bottom to top in the M3 section, the paleoclimate exhibits a relatively stable semiarid condition (Figure 3).

5.4. Paleoredox, Paleosalinity, and Primary Productivity

5.4.1. Paleoredox Condition. Redox state is generally divided into four gradients: oxic (>2 ml O₂ L⁻¹), dysoxic (2-0 ml O₂ L⁻¹ ml_{O₂}/L_{H₂O}), anoxic (0 ml O₂ L⁻¹), and euxinic (0 ml O₂ L⁻¹, H₂S > 0) conditions [13, 20, 73]. Recently, many redox proxies have been established to interpret redox conditions in water columns [12, 18–20].

In general, under reducing water columns, U (VI) is more easily reduced to U (IV), which will accelerate the removal of U from the water column to sediments (especially when organic materials exist) [20]. In contrast, insoluble Th (IV) is unaffected by the redox changes. In the present study, U and Th elements display negative ($r = -0.70$) and positive ($r = 0.93$) correlations with Al₂O₃ (Figures 6(b) and 6(c)), and to a certain extent, using U/Th ratio to study the redox

states are also suitable. Some authors suggest that a U/Th ratio <0.27, 0.27-0.5, and >0.5 corresponds to oxidizing, dysoxic, and anoxic environments, respectively [74–76]. These samples exhibit moderate U/Th values (0.24~0.65; Table 3), but most values are distributed in the range of 0.27~0.49 ($n = 26$), implying dominant oxic-dysoxic bottom water conditions (Figure 3).

Another quantitative index for the redox state is the Cu/Zn ratio [77–79]. With a decrease in oxygen fugacity, vertical zonation from Cu enrichment towards Zn enrichment can develop in water columns during depositions [79]. A Cu/Zn ratio < 0.21, 0.21-0.38, 0.38-0.5, 0.5-0.63, and > 0.63 represents anoxic, weak anoxic, weak anoxic to weak oxidizing (viz., anoxic to oxidizing transition), weak oxidizing, and oxidizing conditions, respectively [79]. Cu/Zn values for all the studied samples range from 0.17 to 0.75 (Table 3) and reflect an undulatory anoxic-oxic water condition. However, most of the Cu/Zn values vary between 0.21 and 0.50 ($n = 25$), suggesting weak anoxic-weak oxidizing (dysoxic) water

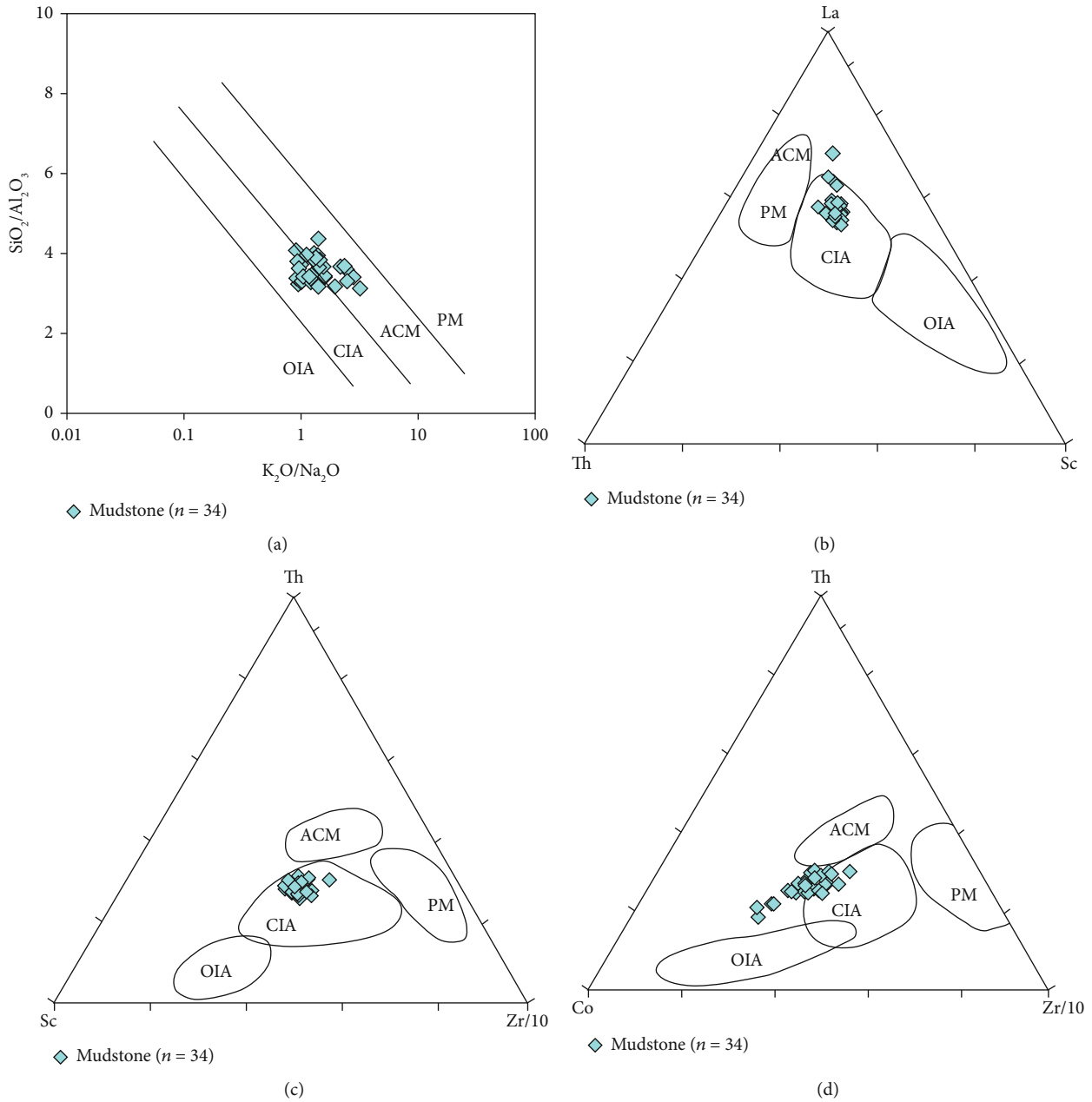


FIGURE 10: Tectonic setting discrimination diagrams for the M3 mudstones. (a) $\text{SiO}_2/\text{Al}_2\text{O}_3$ versus $\text{K}_2\text{O}/\text{Na}_2\text{O}$ (after Roser and Korsch, [65]). (b), (c), and (d) La-Th-Sc, Th-Sc-Zr/10, and Th-Co-Zr/10 [57], respectively. Abbreviations: OIA: oceanic island arc; CIA: continental island arc; ACM: active continental margin; PM: passive margin.

columns. Other samples ($n = 9$) show Cu/Zn values lower than 0.21 or higher than 0.5, which are indicative of some episodes of anoxic or oxidizing water environments, respectively.

Algeo and Tribouillard [19] investigated the covariations in U and Mo enrichment factors in some modern low-oxygen marine basins and established three Mo-U covariation patterns associated with different specific redox conditions and enrichment processes like “unrestricted marine,” “particulate shuttle,” and “strongly restricted basin” [19, 80]. These $\text{Mo}_{\text{EF}}\text{-U}_{\text{EF}}$ covariation patterns have successfully been applied to reconstruct the redox environments in both

ancient oceans and lakes [80, 81]. The U_{EF} values for all the studied samples are greater than 1.0, varying between 1.21 and 3.15 with an average of 1.88, revealing a relatively stable enrichment of U in these mudstones. In contrast, Mo_{EF} displays a wide range of 0.27–5.0 averaging 1.19, suggesting variable degrees of depletion or enrichment. Relatively low Mo_{EF} leads to the $(\text{Mo}/\text{U})_{\text{sample}}$ ratio to be 0.1–0.3 times of seawater for most studied samples. When plotted into a cross-plot of U_{EF} versus Mo_{EF} , U_{EF} exhibits a positive correlation with Mo_{EF} (Figure 12), suggesting relatively less fluctuation of redox conditions during the depositions. Additionally, Mo and U accumulation may not be influenced

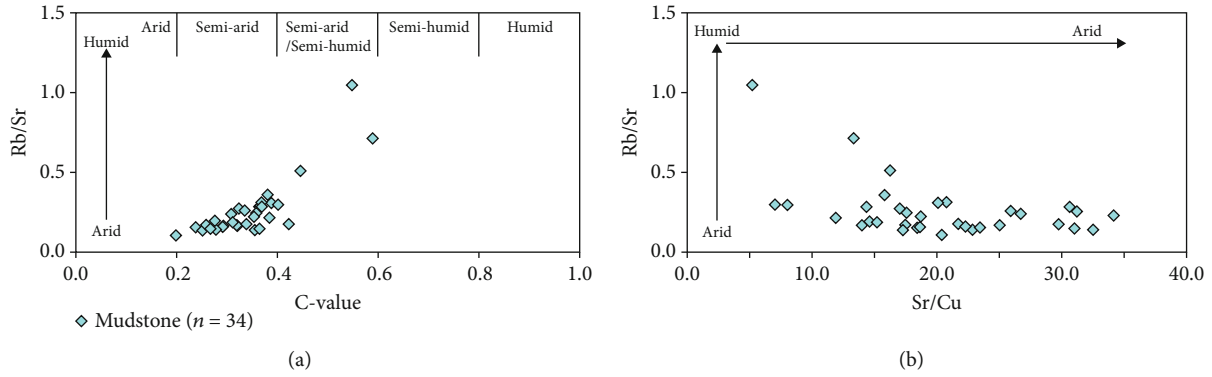


FIGURE 11: Cross-plots of Rb/Sr versus C-value (a) and Rb/Sr versus Sr/Cu (b) for the M3 mudstones, showing a dominant semiarid paleoclimate.

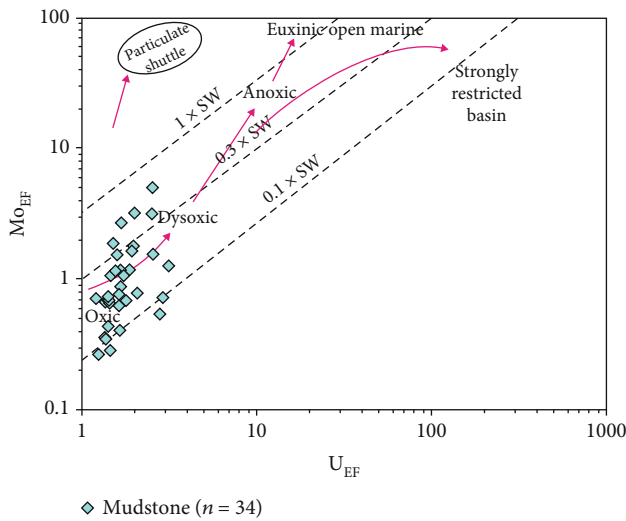


FIGURE 12: U_{EF} versus Mo_{EF} covariation pattern for the mudstones (modified after Algeo and Tribouillard, [18]; Tribouillard et al., [80]), showing oxic-dysoxic water conditions. Diagonal dashed lines refer to Mo/U molar ratios of the Seawater (SW).

by an active particulate shuttle, but are largely controlled by oxic to dysoxic conditions (Figure 12). In dysoxic waters close to the Fe (III)-Fe (II) transition, soluble U (VI) can be largely reduced to insoluble U (IV) and, then, preferentially incorporated into the sediments over Mo element (especially in the presence of OM) [29, 81]. This is consistent with that the level of U enrichment is greater than that of Mo enrichment in most samples. However, the Mo accumulation in these mudstones may not be due to the coprecipitation or absorption onto the Mn-Fe oxyhydroxides but may have been captured by sulfurized OM or Fe-S phase with different enrichment degrees under dysoxic conditions and subsequently converted into particle-reactive thiomolybdate ions ($MoO_x^{2-x}S_{4-x}$, $x = 0-3$) [20]. This inference is further indicated by the obvious positive relationships between Mo_{EF} and TOC and S (Figure 3).

5.4.2. Paleosalinity. Salinity is a fundamental feature of water-masses that is useful for paleoenvironment reconstruction in ancient oceans and lakes. Paleosalinity in this study was esti-

mated using Sr/Ba, B, TOC/S, and biomarker parameters. The Sr/Ba ratio typically increases along with enhanced water salinity [46, 82–86]. Sr/Ba values of all the samples range from 0.56 to 2.36, and only five samples have relatively low Sr/Ba values that are lower than 1.0 (Table 3), suggesting typical marine or high-saline environments but interspersed with several episodes of brackish water. According to the reassessment of Wei and Algeo [46], the TOC/S ratio is much more accurate than the Sr/Ba ratio in predicting paleosalinity, and ratios of >10, 2-10, and <2 are broadly suggestive of freshwater, brackish, or marine, and marine facies, respectively. About 27% of the studied samples have TOC/S values lower than 2.0, while other samples show moderate TOC/S values of 2.39–9.97. These data possibly suggest a dominant brackish water column but with some episodes of a marine (or high saline) environment. The above inference is slightly different from the high-saline-dominated paleosalinity derived from Sr/Ba ratios; however, it corresponds to the results from the B proxy as discussed below.

The B concentration and relevant indicators can provide a quantitative assessment of paleosalinity [82–84]. The proxy of equivalent B (B_{eq}) is usually calculated using the method of Walker and Price [85], and values of $<200 \times 10^{-6}$, $200 \times 10^{-6} \sim 300 \times 10^{-6}$, and $>300 \times 10^{-6}$ are indicative of freshwater, brackish water, and marine or high-saline facies. Furthermore, Adams et al. [82] proposed another indicator of S-value to estimate the paleosalinity of ancient water-masses, as

$$S - \text{value} = 0.0977 \times B_{eq} - 7.043, \quad (3)$$

where the S-value represents the paleosalinity (‰). In general, the calculated S-value $< 10\text{‰}$ indicates a freshwater environment, $>10-25\text{‰}$ is suggestive of a brackish condition, and $>25-35\text{‰}$ reflects a high-saline water (or marine) water. The studied samples have relatively high B_{eq} and S-values, ranging from 232.1×10^{-6} to 380.5×10^{-6} and from 15.6‰ to 30.1‰, respectively (Table 3). These data reflect a relatively stable, stratified brackish water column with some episodes of high-saline condition during the lacustrine mudstone deposition (Figure 3). Additionally, B/Ga ratio can also be a common index to evaluate the paleosalinity, and B/Ga ratio for <3.0 , $3.0\sim 6.0$, and >6.0 is indicative of

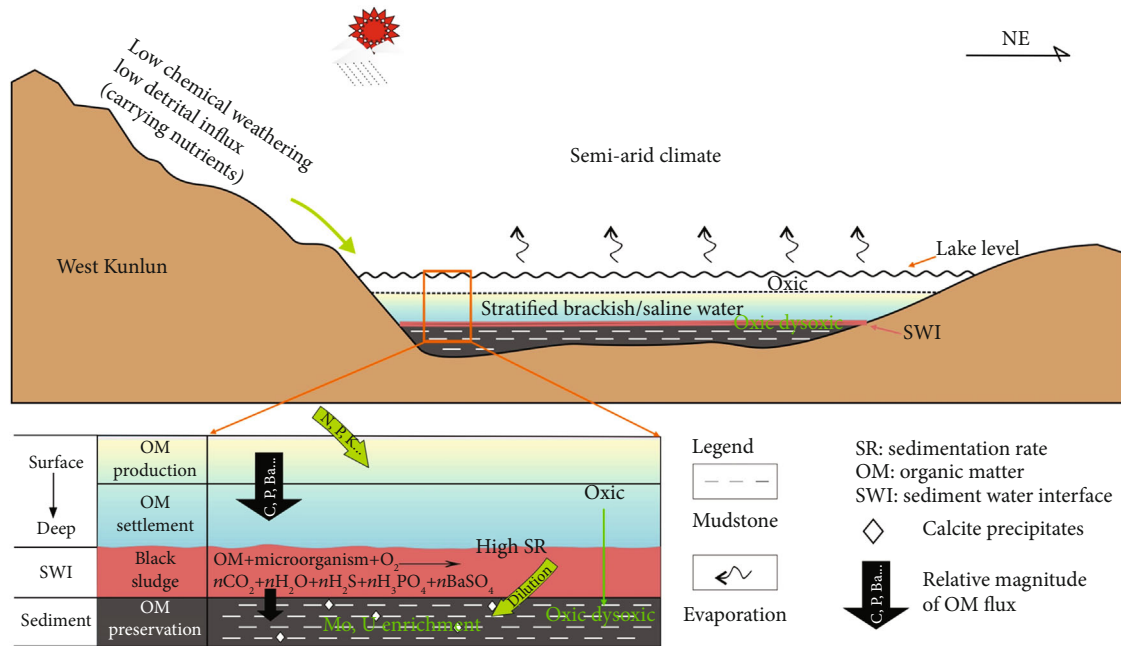


FIGURE 13: The Sketch map of the sedimentary environments and developing model of the OM enrichment for the M3 mudstones in the Yecheng-Hetian Sag.

freshwater, brackish, and marine facies, respectively [46]. These samples have higher B/Ga ratios, ranging from 7.85 to 12.09 (average 9.6), pointing out the typical marine facies. Considering the fact that this period was the regressive lacustrine deposition, we thus interpret that the higher B/Ga ratios represent the high-saline water body, consistent with the above inferences.

Moreover, some biomarker parameters, such as pristine/phytane (Pr/Ph) and gammacerane/ C_{30} hopane (G/C_{30}), are also effectively applied to infer the paleosalinity [87]. Relatively high G/C_{30} ($G/C_{30}=0.18-0.3$) and low Pr/Ph ratios (Pr/Ph=0.06-0.62), along with their negative correlations reported in our previous study [25], also suggest relatively high-saline water conditions.

Overall, the relatively high-saline paleosalinity might result from the strong evaporation induced by drier and/or hotter climate in a relatively closed lake during the M3 deposition period [88], as indicated by the positive or negative correlations between C-value, Sr/Cu, Sr/Ba, B_{eq} , and S-value (Figure 3).

5.4.3. Primary Productivity. The primary productivity is a crucial indicator to reveal the degree of OM enrichment. Several geochemical proxies, such as TOC, organic phosphorus (P_{org}), and biogenic barium (Ba_{bio}), are often useful for evaluating the paleoproductivity during the formation of organic-rich sediments (as discussed by Schoepfer et al. [9]). Although the TOC content provides the most direct implication for paleoproductivity, the application of this index is limited in the present study due to relatively high thermal maturation (which can largely accelerate the loss of organic carbon). Phosphorus is regarded as a fundamental nutrient element for all organisms and can originate from detrital and organic phosphorus sources [9]. However, in

organic-rich sediments, detrital P can be neglected because of its low proportion (<20%) in total P, based on statistical analysis [9, 75]. Therefore, the P_{org} content is approximately equivalent to the measured P. Similarly, biogenic barium (Ba_{bio}) is also associated with the sinking flux of OM and is another important proxy of primary productivity [9, 20]. The Ba and P contents exhibit relatively negative correlations with TiO_2 ($r = -0.78$ and -0.66 , respectively) (Figures 6(d) and 6(e)), to a large extent, reflecting the organic origins. The Ti- and Al-normalized indicators (e.g., P/Ti and Ba/Al) can be used to eliminate the impact of terrigenous fractions [75], and thereafter, the primary productivity can be effectively evaluated using these indicators. The P/Ti and Ba/Al ratios of the samples show relatively narrow ranges of 0.14-0.36 (0.26 on average) and 15.69-41.32 (29.24 on average) (Table 2). In terms of the P/Ti ratio, this ratio for the studied samples is higher than that of PAAS (P/Ti=0.13) [47], and Permian Lucaogou Formation fine-grained rocks (P/Ti=0.16 on average) with high TOC contents (~4.22% on average) in the Santanghu Basin [88], implying a relatively high primary productivity with stable vertical variations during the M3 deposition period.

5.5. Enrichment Mechanism and Developing Model of Organic Matter. The accumulation, preservation, and enrichment of OM are usually affected by several fundamental factors, such as paleoclimate, primary productivity, detrital influx, redox states, sedimentation rate, and sea/lake-level [1-7]. However, each sedimentary environment may have its specific elements; and therefore, the enrichment mechanism of OM cannot be explained by a single controlling factor. In this study, the covariations between various controlling factors and TOC and P/Ti will be used to evaluate the controlling factors on the enrichment process of OM.

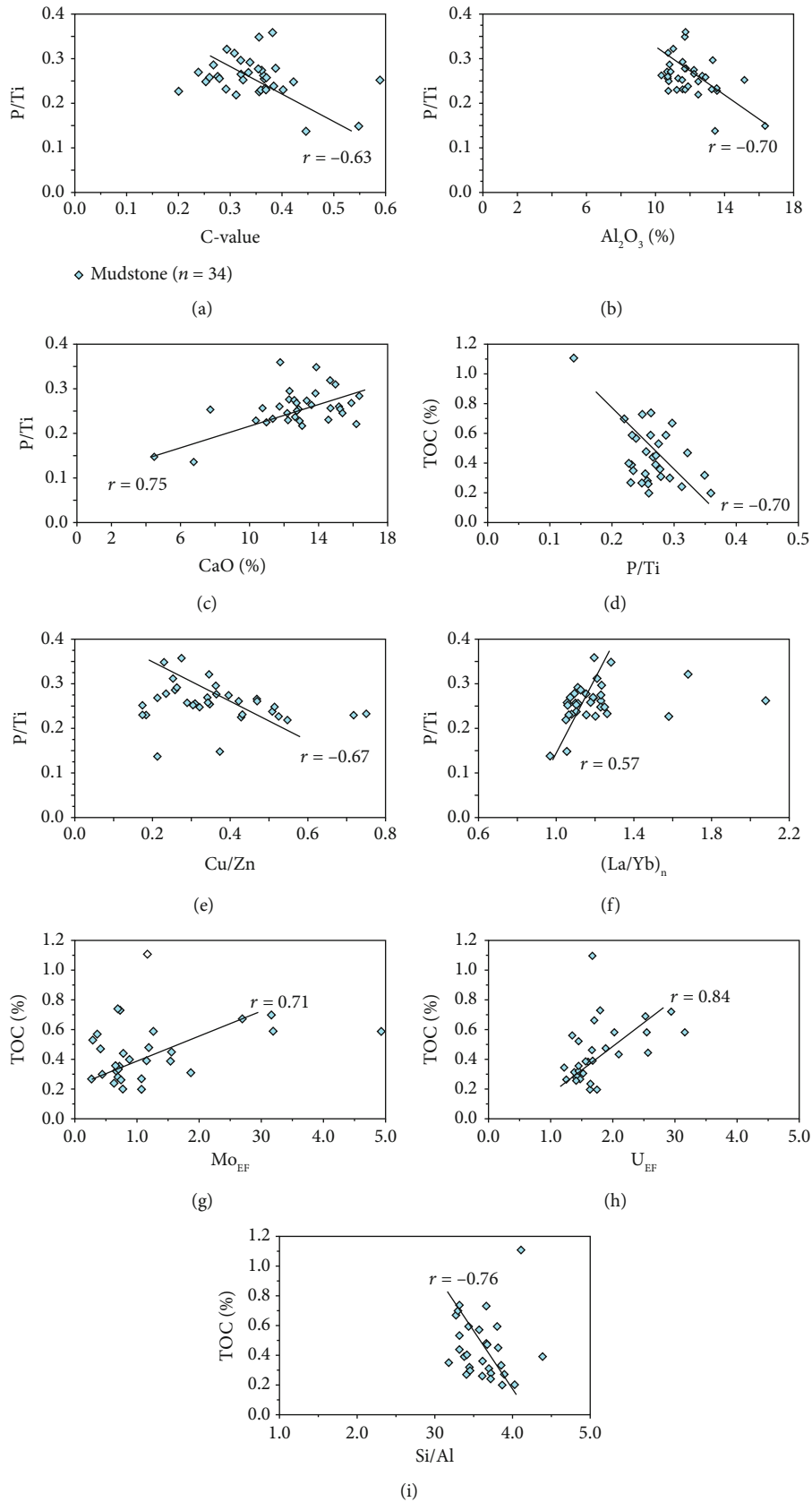


FIGURE 14: Relationships between different indexes for the M3 mudstones, reflecting controlling factors for the OM enrichment. (a) C-value versus P/Ti. (b) Al_2O_3 versus P/Ti. (c) CaO versus P/Ti. (d) TOC versus P/Ti. (e) Cu/Zn versus P/Ti. (f) $(La/Yb)_n$ versus P/Ti. (g) Mo_{EF} versus TOC. (h) U_{EF} versus TOC. (i) Si/Al versus TOC. “r” represents correlation coefficient.

The northward subduction of Kangxiwar Paleo-Tethys downwards the Tarim Plate at the beginning of the late Early Permian ended the marine sedimentation and developed such thick (> 2 000 m) continental clastic depositions in the Hetian region. Along with the gradual release of tectonic stress, the Permian sedimentary basin entered a relatively stable period of tectonic setting, provenance supply, and depositional environments during the M3 deposition period (Figure 13). This is supported that most geochemical parameters exhibit weak fluctuations upward from the bottom to top in the Well DW1 (Figure 3). Under such stable sedimentary backgrounds, the semiarid and low weathering dominated conditions resulted in low detrital influx input with carrying a certain amount of soluble nutrients, promoting the relatively high primary OM generation, as supported by the negative relationships between P/Ti and C-value, and Al_2O_3 ($r = -0.63$ and -0.70 , respectively; Figures 14(a) and 14(b)). The CaO contents are negatively or positively correlated with Ti and P/Ti ($r = -0.94$ and 0.75 , respectively; Figures 6(f) and 14(c)). This illustrates that CaO possibly derived from the authigenic carbonate precipitation due to the low annual precipitation and strong evaporation, which were closely associated with the formation process of OM in M3 lacustrine mudstones.

Unlike typical positive correlations between the primary productivity index (e.g., P/Ti) and TOC contents in most studies [17, 75], TOC contents in the present study display a negative relationship with the P/Ti ratio ($r = -0.70$; Figure 14(d)). This result may suggest that the preservation conditions instead of primary productivity are much more important for the enrichment of OM and, also, reflect that the primary OM inevitably experienced some degree of post-depositional oxidation. Fe/Mn ratio can be generally used as a common index for the relative paleowater depth [88, 89]. As shown in Figure 3, under relatively deep-waters (low Fe/Mn ratio), the TOC contents, primary productivity, and paleosalinity are relatively higher, and the redox state is relatively more reducing (but not up to dysoxic level) relative to the relatively shallow-waters (high Fe/Mn ratio). Therefore, we assumed that when primary OM reached below the sediment-water interface (SWI), most of them were progressively decomposed through the consumption of oxygen and then released CO_2 into the water columns (Figure 13). As a result, oxic-dysoxic water columns, instead of that prevailed prior to sediment depositions [20], were gradually developed above and below the SWI. Meanwhile, related authigenic carbonates were then precipitated below the SWI as mentioned above. The primary productivity index (e.g., P/Ti ratio) is negatively related with Cu/Zn ratio, and TOC contents ($r = -0.67$ and -0.7 , respectively; Figures 14(d) and 14(e)) can support the above-mentioned conclusion: the relatively high primary productivity corresponds to the relatively more reducing conditions and relatively lower TOC contents. In this circumstance, this process may not only have preserved some amounts of organic carbon below the SWI but also accelerated the removal of U and Mo towards into the sediments with various enrichment degrees (indicated by the strong positive covariations between TOC and Mo_{EF} and U_{EF} ($r = 0.71$ and 0.84 , respectively; Figures 14(h) and 14(i)).

Sedimentation rate (SR) and detrital influx may also play potential effects on OM enrichment. Ti, Si, and Zr are mainly derived from aluminosilicate and heavy minerals, and Al-normalized ratios are effective indicators for evaluating the degree of detrital influx [6]. A good negative relationship between the TOC and detrital indicator of Si/Al ratio ($r = -0.76$; Figure 14(i)) suggests the obvious dilution effect of detrital materials in TOC abundance. The $(\text{La}/\text{Yb})_n$ (where “n” represents the North American Shale Composition, NASC [90]) is regarded as a potential proxy to reflect the SR, and $(\text{La}/\text{Yb})_n \geq 1.0$ represents a rapid SR [75, 90]. The $(\text{La}/\text{Yb})_n$ values vary from 0.97 to 2.08 (average 1.2; Table 4), revealing a high SR during the M3 deposition period. The positive correlation between $(\text{La}/\text{Yb})_n$ and P/Ti ($r = 0.57$; Figure 14(f)) reflect that high SR contributes to the preservation of primary OM materials, rather than dilution. However, the high SR exerted a weak effect on TOC abundance because no relationship between them was observed in the present study. That can be interpreted that high SR further shortened the exposure time of OM with oxygen [9, 10] and, thus, largely decreased the decomposition of OM under oxic-dysoxic water conditions (Figure 13). Likewise, the relatively high-saline, stratified water columns may also exert a certain effect on the preservation of primary OM by restraining the degradation of OM [75], as the paleoclimate and paleosalinity are closely related with each other (Figure 3).

In summary, the enrichment mechanism of OM of the M3 lacustrine mudstones can be regarded as the combination of “preservation model” and “detrital dilution model.” Favorable stratified, high-saline, and oxic-dysoxic water conditions, together with high SR, were conducive to the preservation of OM, and the relatively high detrital influx diluted the TOC abundance.

6. Conclusions

- (1) The M3 lacustrine mudstones are characterized by the relatively low TOC, S_1 , S_2 , and HI values and are estimated to be poor- to fair-quality hydrocarbon source rocks with mature type II-III kerogen
- (2) Geochemical results showed that M3 mudstones had a relatively stable felsic dominated provenance formed in continental island arc and ACM tectonic settings from the West Kunlun Orogen to the southwest of the Yecheng-Hetian Sag. The depositional environment was the stratified, high-saline water body with oxic-dysoxic conditions, and paleoclimate was inferred as the predominant semiarid climate with some episodes of semihumid condition
- (3) Paleoproductivity was not the main controlling factor, and the OM enrichment in these M3 mudstones should be attributed to the preservation conditions and detrital dilution. High sedimentation rate, together with the high-saline, stratified, oxic-dysoxic lake water largely preserved the OM, while detrital dilution exerted a direct effect on TOC abundances in this study

Data Availability

The data can be found in the manuscript.

Conflicts of Interest

The authors declare that they have no conflicts of interest.

Acknowledgments

Thanks are due to Dr. Youxing Yang and Prof. Zhihong Kang for their help and providing data. This study was financially supported by the National Key Research and Development Program of China (Grant No. 2019YFA0708504), National Natural Science Foundation of China (U19B6003), and the Frontier Project of the Chinese Academy of Sciences (XDA14010201).

References

- [1] M. A. Arthur and B. B. Sageman, "Marine black shales: depositional mechanisms and environments of ancient deposits," *Annual Review of Earth and Planetary Sciences*, vol. 22, no. 1, pp. 499–551, 1994.
- [2] G. J. Demaison and G. T. Moore, "Anoxic environments and oil source bed genesis," *AAPG Bulletin*, vol. 64, pp. 1179–1209, 1980.
- [3] T. Dong, N. B. Harris, and K. Ayranci, "Relative sea-level cycles and organic matter accumulation in shales of the Middle and Upper Devonian Horn River Group, northeastern British Columbia, Canada: insights into sediment flux, redox conditions, and bioproductivity," *Geological Society of America Bulletin*, vol. 130, pp. 859–880, 2017.
- [4] G. G. Lash and D. R. Blood, "Organic matter accumulation, redox, and diagenetic history of the Marcellus Formation, southwestern Pennsylvania, Appalachian basin," *Appalachian Basin Marine & Petroleum Geology*, vol. 57, pp. 244–263, 2014.
- [5] H. Mort, O. Jacquat, T. Adatte et al., "The Cenomanian/Turonian anoxic event at the Bonarelli Level in Italy and Spain: enhanced productivity and/or better preservation?," *Cretaceous Research*, vol. 28, no. 4, pp. 597–612, 2007.
- [6] A. E. Murphy, B. B. Sageman, D. J. Hollander, T. W. Lyons, and C. E. Brett, "Black shale deposition and faunal overturn in the Devonian Appalachian Basin: clastic starvation, seasonal water-column mixing, and efficient biolimiting nutrient recycling," *Paleoceanography*, vol. 15, no. 3, pp. 280–291, 2000.
- [7] T. F. Pedersen and S. E. Calvert, "Anoxia vs. productivity: what controls the formation of organic-carbon-rich sediments and sedimentary rocks?," *AAPG Bulletin*, vol. 74, pp. 454–466, 1990.
- [8] J. H. He, W. Ding, Z. Jiang, K. Jiu, A. Li, and Y. Sun, "Mineralogical and chemical distribution of the Es3L oil shale in the Jiyang Depression, Bohai Bay Basin (E China): implications for paleoenvironmental reconstruction and organic matter accumulation," *Marine & Petroleum Geology*, vol. 81, pp. 196–219, 2017.
- [9] S. D. Schoepfer, J. Shen, H. Y. Wei, R. V. Tyson, E. Ingall, and T. J. Algeo, "Total organic carbon, organic phosphorus, and biogenic barium fluxes as proxies for paleomarine productivity," *Earth-Science Reviews*, vol. 149, pp. 23–52, 2015.
- [10] R. V. Tyson, "Sedimentation rate, dilution, preservation, and total organic carbon: some results of a modelling study," *Organic Geochemistry*, vol. 32, no. 2, pp. 333–339, 2001.
- [11] R. V. Tyson, "The "productivity versus preservation" controversy: cause, flaws, and resolution," in *The Deposition of Organic-Carbon-Rich Sediments: Models, Mechanisms, and Consequences*, N. B. Harris, Ed., vol. 82, pp. 17–33, Society for Sedimentary Geology (SEPM) Special Publication, 2005.
- [12] S. M. Rimmer, J. A. Thompson, S. A. Goodnight, and T. Robl, "Multiple controls on the preservation of organic matter in Devonian–Mississippian marine black shales: geochemical and petrographic evidence," *Palaeogeography Palaeoclimatology Palaeoecology*, vol. 215, no. 1–2, pp. 125–154, 2004.
- [13] R. V. Tyson and T. H. Pearson, "Modern and ancient continental shelf anoxia: an overview," *Geological Society, London, Special Publications*, vol. 58, no. 1, pp. 1–24, 1991.
- [14] J. B. Curtis, "Fractured shale-gas systems," *AAPG Bulletin*, vol. 86, pp. 1921–1938, 2002.
- [15] B. J. Katz and F. Lin, "Lacustrine basin unconventional resource plays: key differences," *Marine and Petroleum Geology*, vol. 56, pp. 255–265, 2014.
- [16] Z. Tan, S. Lu, W. Li et al., "Climate-driven variations in the depositional environment and organic matter accumulation of lacustrine mudstones: evidence from organic and inorganic geochemistry in the Biyang depression, Nanxiang Basin, China," *Energy & Fuels*, vol. 33, no. 8, pp. 6946–6960, 2019.
- [17] H. Liang, G. Xu, F. Xu, Q. Yu, J. Liang, and D. Wang, "Paleoenvironmental evolution and organic matter accumulation in an oxygen-enriched lacustrine basin: a case study from the Laizhou Bay Sag, southern Bohai Sea (China)," *International Journal of Coal Geology*, vol. 217, article 103318, 2020.
- [18] T. J. Algeo and N. Tribouillard, "Environmental analysis of paleoceanographic systems based on molybdenum-uranium covariation," *Chemical Geology*, vol. 268, no. 3–4, pp. 211–225, 2009.
- [19] J. L. Morford, W. R. Martin, and C. M. Carney, "Uranium diagenesis in sediments underlying bottom waters with high oxygen content," *Geochimica et Cosmochimica Acta*, vol. 73, no. 10, pp. 2920–2937, 2009.
- [20] N. Tribouillard, T. J. Algeo, T. Lyons, and A. Riboulleau, "Trace metals as paleoredox and paleoproductivity proxies: an update," *Chemical Geology*, vol. 232, no. 1–2, pp. 12–32, 2006.
- [21] D. J. Hou, D. J. Xiao, Y. J. Tang, J. Z. Zhu, and X. Q. Li, "Geochemical characterization of mixing natural gas in Kekeya field, Tarim Basin, China," *Natural Gas Geoscience*, vol. 14, no. 6, pp. 474–479, 2003.
- [22] W. S. Hu, Y. S. Chen, A. C. Xiao, X. F. Liu, and S. G. Liu, "Tectonic evolution and petroleum system in the southwest depression of Tarim Basin," *Petroleum & Exploration Development*, vol. 24, no. 1, pp. 14–17, 1997.
- [23] Z. Du, C. Zeng, H. Qiu, and Y. Yang, "Key formations of the Permian hydrocarbon source rocks and oil-source correlation of Well KD1 in Yecheng Depression of southwestern Tarim Basin," *Journal of Jilin University (Earth Science Edition)*, vol. 46, no. 3, pp. 651–660, 2016.
- [24] Q. Wang, P. A. Peng, J. Zeng et al., "Oil source of condensates from Well Kedong 1 and crude oil from Kekeya in Yecheng depression," *Geochimica*, vol. 43, no. 5, pp. 469–476, 2014.
- [25] J. B. Wang, Z. Q. Gao, Z. H. Kang, Y. X. Yang, D. Wei, and N. T. Qin, "The sedimentary environment and geochemical characteristics of the source rocks in the Pusige formation in Hetian Sag, southwestern Tarim Basin," *Natural Gas Geoscience*, vol. 28, no. 11, pp. 1723–1734, 2017.


- [26] X. M. Xiao, Q. H. Zeng, H. Tian, R. W. T. Wilkins, and Y. C. Tang, "Origin and accumulation model of the AK-1 natural gas pool from the Tarim Basin, China," *Organic Geochemistry*, vol. 36, no. 9, pp. 1285–1298, 2005.
- [27] Y. C. Ding, "Strata division and correlation of Carboniferous-Permian in western Tarim Basin," *Journal of Xinjiang Petroleum Institute*, vol. 7, no. 1, pp. 1–11, 1995.
- [28] X. G. Li, "Characteristics of sequence stratigraphy and sedimentary system of Permian-Lower Triassic in Hetian area, Xinjiang province," *Xinjiang Geology*, vol. 29, no. 2, pp. 183–188, 2011.
- [29] N. Liu, H. F. Zhang, S. C. Xiu, and Q. I. Xun, "Depositional environment in late Carboniferous-Early Permian in southern Hetian area of southwest Tarim Basin," *Xinjiang Petroleum Geology*, vol. 22, no. 4, pp. 316–319, 2001.
- [30] M. M. Meng, Z. H. Kang, H. J. Qiu, S. Z. Li, and B. Bin, "Controlling factors of Permian hydrocarbon source rocks in the southwest depression of Tarim Basin," *Bulletin of Mineralogy, Petrology Geochemistry*, vol. 35, no. 2, pp. 344–352, 2016.
- [31] H. C. Zhu, "Discovery of Late Permian spores and pollen from the Pusige Formation of Pishan, Xinjiang," *Journal of Stratigraphy*, vol. 21, no. 3, pp. 119–223, 1997.
- [32] H. Dengfa, J. Chengzao, L. Desheng, Z. Chaojun, M. Qinren, and S. Xin, "Formation and evolution of polycyclic superimposed Tarim Basin," *Oil & Gas Geology*, vol. 26, no. 1, pp. 64–77, 2005.
- [33] Z. He, M. Gao, and M. Zheng, "Regional tectonic framework and evolution of superimposed basins in northwestern China," *Earth Science Frontiers*, vol. 22, no. 3, pp. 227–240, 2015.
- [34] Y. Q. Zhang, *The Coupling of Southwest Sag of Tarim Basin and West Kunlun Orogen*, [M.S. thesis], China University of Geosciences, Beijing, 2006.
- [35] J. T. Cui, J. C. Wang, X. W. Bian et al., "Zircon SHRIMP U-Pb dating of Early Paleozoic granite in the Menggubao-Pushou area on the northern side of Kangxiwar, West Kunlun," *Geological Bulletin of China*, vol. 26, no. 6, pp. 710–719, 2007.
- [36] J. T. Cui, J. C. Wang, X. W. Bian, H. P. Zhu, and K. J. Yang, "Geological characteristics of Early Paleozoic amphibolite and tonalite in northern Kangxiwar, West Kunlun, China and their Zircon SHRIMP U-Pb dating," *Geological Bulletin of China*, vol. 25, no. 12, pp. 1441–1449, 2006.
- [37] Y. H. Jiang, R. Y. Jia, Z. Liu, S.-Y. Liao, P. Zhao, and Q. Zhou, "Origin of Middle Triassic high-K calc-alkaline granitoids and their potassic microgranular enclaves from the western Kunlun orogen, northwest China: a record of the closure of Paleo-Tethys," *Lithos*, vol. 156–159, no. 1, pp. 13–30, 2013.
- [38] B. Q. Li, J. X. Yao, W. H. Ji et al., "Characteristics and zircon SHRIMP U-Pb ages of the arc magmatic rocks in Mazar, southern Yecheng, West Kunlun Mountains," *Geological Bulletin of China*, vol. 25, no. 1–2, pp. 124–132, 2006.
- [39] C. Wang, L. Liu, S. P. He et al., "Early Paleozoic magmatism in west Kunlun: constraints from geochemical and zircon U-Pb-Hf isotopic studies of the Bulong granite," *Chinese Journal of Geology*, vol. 48, no. 4, pp. 997–1014, 2013.
- [40] Z. H. Huishan, H. E. Shiping, and J. I. Wenhua, "Implications of late Cambrian granite in Tianshuihai massif for the evolution of proto-Tethy ocean: evidences from zircon geochronology and geochemistry," *Acta Geologica Sinica*, vol. 90, no. 10, pp. 2582–2602, 2016.
- [41] X. J. Zhuang, L. X. Xiao, and J. Yang, "Sedimentary facies in southwestern region of Tarim Basin," *Xinjiang Geology*, vol. 20, no. z1, pp. 78–82, 2002.
- [42] Henan Institute of Geological Survey, *1:250000 Scale Yecheng-Hetian Regional Geological Survey Report (in Chinese)*, Henan Institute of Geological Survey, 2004.
- [43] K. E. Peters and M. R. Cassa, "Applied source rock geochemistry," in *The Petroleum System—from Source to Trap*, L. B. Magoon and W. G. Dow, Eds., vol. 60, pp. 93–120, American Association of Petroleum Geologists AAPG Memoir, Tulsa, Oklahoma, 1994.
- [44] J. H. Dembicki, "Three common source rock evaluation errors made by geologists during prospect or play appraisals," *AAPG Bulletin*, vol. 93, no. 3, pp. 341–356, 2009.
- [45] R. A. Berner and R. Raiswell, "C/S method for distinguishing freshwater from marine sedimentary rocks," *Geology*, vol. 12, no. 6, pp. 365–368, 1984.
- [46] W. Wei and T. J. Algeo, "Elemental proxies for paleosalinity analysis of ancient shales and mudrocks," *Geochimica et Cosmochimica Acta*, vol. 287, pp. 341–366, 2019.
- [47] S. R. Taylor and S. M. McLennan, "The continental crust: its composition and evolution: an examination of the geochemical record preserved in sedimentary rocks," Blackwell, Oxford University, Oxford, 1985.
- [48] W. V. Boynton, "Geochemistry of the rare earth elements: meteorite studies," *Rare Earth Element Geochemistry*, P. Henderson, Ed., pp. 63–114, 1984.
- [49] S. M. McLennan, S. Hemming, D. K. Mcdaniel, and G. N. Hanson, "Geochemical approaches to sedimentation, provenance, and tectonics," in *Processes Controlling the Composition of Clastic Sediments*, M. J. Johnsson and A. Basu, Eds., pp. 21–40, Geological Society of America, Boulder, CO, USA, 1993.
- [50] R. Cox, D. R. Lowe, and R. L. Cullers, "The influence of sediment recycling and basement composition on evolution of mudrock chemistry in the southwestern United States," *Geochimica et Cosmochimica Acta*, vol. 59, no. 14, pp. 2919–2940, 1995.
- [51] C. M. Fedo, H. W. Nesbitt, and G. M. Young, "Unraveling the effects of potassium metasomatism in sedimentary rocks and paleosols, with implications for paleoweathering conditions and provenance," *Geology*, vol. 23, no. 10, pp. 921–924, 1995.
- [52] H. W. Nesbitt and G. M. Young, "Early proterozoic climates and plate motions inferred from major element chemistry of lutes," *Nature*, vol. 299, no. 5885, pp. 715–717, 1982.
- [53] H. W. Nesbitt and G. M. Young, "Prediction of some weathering trends of plutonic and volcanic rocks based on thermodynamic and kinetic considerations," *Geochimica et Cosmochimica Acta*, vol. 48, no. 7, pp. 1523–1534, 1984.
- [54] G. Shields and P. Stille, "Diagenetic constraints on the use of cerium anomalies as palaeoseawater redox proxies: an isotopic and REE study of Cambrian phosphorites," *Chemical Geology*, vol. 175, no. 1–2, pp. 29–48, 2001.
- [55] M. R. Bhatia, "Plate tectonics and geochemical composition of sandstones," *Journal of Geology*, vol. 91, no. 6, pp. 611–627, 1983.
- [56] M. R. Bhatia, "Rare earth element geochemistry of Australian Paleozoic graywackes and mudrocks: provenance and tectonic control," *Sedimentary Geology*, vol. 45, no. 1–2, pp. 97–113, 1985.
- [57] M. R. Bhatia and K. A. Crook, "Trace element characteristics of graywackes and tectonic setting discrimination of sedimentary basins," *Contributions to Mineralogy Petrology*, vol. 92, no. 2, pp. 181–193, 1986.

- [58] R. L. Cullers, "The controls on the major- and trace-element evolution of shales, siltstones and sandstones of Ordovician to tertiary age in the Wet Mountains region, Colorado, USA," *Chemical Geology*, vol. 123, no. 1, pp. 107–131, 1995.
- [59] R. L. Cullers and V. N. Podkovyrov, "The source and origin of terrigenous sedimentary rocks in the Mesoproterozoic Ui group, southeastern Russia," *Precambrian Research*, vol. 117, no. 3–4, pp. 157–183, 2002.
- [60] R. Feng and R. Kerrich, "Geochemistry of fine-grained clastic sediments in the Archean Abitibi greenstone belt, Canada: implications for provenance and tectonic setting," *Geochimica et Cosmochimica Acta*, vol. 54, no. 4, pp. 1061–1081, 1990.
- [61] K. I. Hayashi, H. Fujisawa, H. D. Holland, and H. Ohmoto, "Geochemistry of ~1.9 Ga sedimentary rocks from northeastern Labrador, Canada," *Geochimica et Cosmochimica Acta*, vol. 61, no. 19, pp. 4115–4137, 1997.
- [62] D. J. Wronkiewicz and K. C. Condie, "Geochemistry of Archean shales from the Witwatersrand Supergroup, South Africa: source-area weathering and provenance," *Geochimica et Cosmochimica Acta*, vol. 51, no. 9, pp. 2401–2416, 1987.
- [63] C. J. Allègre and J. F. Minster, "Quantitative models of trace element behavior in magmatic processes," *Earth Planetary Science Letters*, vol. 38, no. 1, pp. 1–25, 1978.
- [64] S. Gao and K. H. Wedepohl, "The negative Eu anomaly in Archean sedimentary rocks: implications for decomposition, age and importance of their granitic sources," *Earth Planetary & Science Letters*, vol. 133, no. 1–2, pp. 81–94, 1995.
- [65] B. P. Roser and R. J. Korsch, "Determination of tectonic setting of sandstone-mudstone suites using SiO₂ content and K₂O/Na₂O ratio," *Journal of Geology*, vol. 94, no. 5, pp. 635–650, 1986.
- [66] L. J. Feng, X. L. Chu, and Q. R. Zhang, "CIA (chemical index of alteration) and its application in the Neoproterozoic clastic rocks," *Earth Science Frontiers*, vol. 10, no. 4, pp. 539–544, 2003.
- [67] J. Cao, M. Wu, Y. Chen et al., "Trace and rare earth element geochemistry of Jurassic mudstones in the northern Qaidam Basin, northwest China," *Chemie der Erde-Geochemistry*, vol. 72, no. 3, pp. 245–252, 2012.
- [68] W. Getaneh, "Geochemistry provenance and depositional tectonic setting of the Adigrat sandstone northern Ethiopia," *Journal of African Earth Sciences*, vol. 35, no. 2, pp. 185–198, 2002.
- [69] Z. D. Jin and E. L. Zhang, "Paleoclimate implications of Rb/Sr ratios from lake sediments," *Science and Technology Engineering*, vol. 2, no. 3, pp. 20–22, 2002.
- [70] K. Tanaka, F. Akagawa, K. Yamamoto, Y. Tani, I. Kawabe, and T. Kawai, "Rare earth element geochemistry of Lake Baikal sediment: its implication for geochemical response to climate change during the Last Glacial/Interglacial transition," *Quaternary Science Reviews*, vol. 26, no. 9–10, pp. 1362–1368, 2007.
- [71] J. B. Wang, Z. L. He, and D. Y. Zhu, "Geochemical characteristics, depositional environment, and provenance attitude of the Middle Jurassic Yangye Formation lacustrine mudstones in Kashi Sag, south-western Tarim Basin," *Geological Journal*, vol. 55, no. 4, pp. 2976–2994, 2020.
- [72] Z. Y. Zhao, J. H. Zhao, and H. J. Wang, "Distribution characteristics and applications of trace elements in Junggar Basin," *Natural Gas Exploration Development*, vol. 30, no. 2, pp. 30–32, 2007.
- [73] T. J. Algeo and J. S. Liu, "A re-assessment of elemental proxies for paleoredox analysis," *Chemical Geology*, vol. 540, 2020.
- [74] H. Kimura and Y. Watanabe, "Oceanic anoxia at the Precambrian-Cambrian boundary," *Geology*, vol. 29, no. 11, pp. 995–998, 2001.
- [75] Z. Wang, J. Wang, X. Fu et al., "Organic material accumulation of Carnian mudstones in the North Qiangtang Depression, eastern Tethys: controlled by the paleoclimate, paleoenvironment, and provenance," *Marine & Petroleum Geology*, vol. 88, pp. 440–457, 2017.
- [76] P. B. Wignall and R. J. Twitchett, "Oceanic anoxia and the end Permian mass extinction," *Science*, vol. 272, no. 5265, pp. 1155–1158, 1996.
- [77] T. Hu, X. Q. Pang, S. Jiang et al., "Impact of paleosalinity, dilution, redox, and paleoproductivity on organic matter enrichment in a saline lacustrine rift basin: a case study of Paleogene organic-rich shale in Dongpu depression, Bohai Bay Basin, Eastern China," *Energy & Fuels*, vol. 32, no. 4, pp. 5045–5061, 2018.
- [78] Y. Q. Guo, F. Yu, Y. Li et al., "Geochemical characteristics of sedimentary environment on He 8 Member of Shihezi Formation in eastern Ordos Basin," *Chinese Journal of Geology*, vol. 51, no. 3, pp. 872–890, 2016.
- [79] S. Q. Mei, "Application of rock chemistry in the study of Pre-sinian sedimentary environment and the source of uranium mineralization in Hunan Province," *Hunan Geology*, vol. 7, no. 3, pp. 25–34, 1988.
- [80] N. Tribouillard, T. J. Algeo, F. Baudin, and A. Riboulleau, "Analysis of marine environmental conditions based on molybdenum–uranium covariation: applications to Mesozoic paleoceanography," *Chemical Geology*, vol. 324–325, pp. 46–58, 2012.
- [81] L. Zhai, C. Wu, Y. Ye, S. Zhang, and Z. An, "Marine redox variations during the Ediacaran-Cambrian transition on the Yangtze Platform, South China," *Geological Journal*, vol. 53, pp. 58–79, 2016.
- [82] T. D. Adams, J. R. Haynes, and C. T. Walker, "Boron in Holocene illites of the Dovey estuary, Wales, and its relationship to palaeosalinity in cyclothem," *Sedimentology*, vol. 4, no. 3, pp. 189–195, 1965.
- [83] E. L. Couch, "Calculation of paleosalinities from boron and clay mineral data," *AAPG Bulletin*, vol. 55, no. 10, pp. 1829–1837, 1971.
- [84] C. T. Walker, "Evaluation of boron as a paleosalinity indicator and its application to offshore prospects," *AAPG Bulletin*, vol. 52, no. 5, pp. 751–766, 1968.
- [85] C. T. Walker and N. B. Price, "Departure curves for computing paleosalinity from boron in illites and shales," *AAPG Bulletin*, vol. 47, pp. 833–841, 1963.
- [86] R. C. Zheng and M. Q. Liu, "Study on palaeosalinity of Chang-6 oil reservoir set in Ordos Basin," *Oil & Gas Geology*, vol. 20, no. 1, pp. 20–25, 1999.
- [87] K. E. Peters, C. C. Walters, and J. M. Moldowan, *The Biomarker Guide*, Cambridge University Press, Cambridge, UK, 2nd edition, 2005.
- [88] Y. S. Pan, Z. L. Huang, T. L. Li, X. Guo, X. Xu, and X. Chen, "Environmental response to volcanic activity and its effect on organic matter enrichment in the Permian Lucaogou Formation of the Malang Sag, Santanghu Basin, Northwest China," *Palaeogeography Palaeoclimatology Palaeoecology*, vol. 560, article 110024, 2020.

- [89] Z. H. Chen, M. Zha, and Q. Jin, "Mineral elemental response to the evolution of terrestrial brine faulted-basin: a case study in the Paleogene of Well Haoke-1, Dongying Sag," *Acta Sedimentologica Sinica*, vol. 26, no. 6, pp. 925–932, 2008.
- [90] T. Tenger, W. H. Liu, and Y. C. Xu, "Comprehensive geochemical identification of highly evolved marine hydrocarbon source rocks: organic matter, paleoenvironment and development of effective hydrocarbon source rocks," *Chinese Journal of Geochemistry*, vol. 25, pp. 333–340, 2006.

Research Article

Pore Space Reconstruction of Shale Using Improved Variational Autoencoders

Yi Du,¹ Hongyan Tu,² and Ting Zhang ²

¹College of Engineering, Shanghai Polytechnic University, Shanghai 201209, China

²College of Computer Science and Technology, Shanghai University of Electric Power, Shanghai 200090, China

Correspondence should be addressed to Ting Zhang; tingzh@shiep.edu.cn

Received 28 January 2021; Revised 25 February 2021; Accepted 5 March 2021; Published 18 March 2021

Academic Editor: Hai-Kuan Nie

Copyright © 2021 Yi Du et al. This is an open access article distributed under the Creative Commons Attribution License, which permits unrestricted use, distribution, and reproduction in any medium, provided the original work is properly cited.

Pore space reconstruction is of great significance to some fields such as the study of seepage mechanisms in porous media and reservoir engineering. Shale oil and shale gas, as unconventional petroleum resources with abundant reserves in the whole world, attract extensive attention and have a rapid increase in production. Shale is a type of complex porous medium with evident fluctuations in various mineral compositions, dense structure, and low hardness, leading to a big challenge for the characterization and acquisition of the internal shale structure. Numerical reconstruction technology can achieve the purpose of studying the engineering problems and physical problems through numerical calculation and image display methods, which also can be used to reconstruct a pore structure similar to the real pore spaces through numerical simulation and have the advantages of low cost and good reusability, casting light on the characterization of the internal structure of shale. The recent branch of deep learning, variational auto-encoders (VAEs), has good capabilities of extracting characteristics for reconstructing similar images with the training image (TI). The theory of Fisher information can help to balance the encoder and decoder of VAE in information control. Therefore, this paper proposes an improved VAE to reconstruct shale based on VAE and Fisher information, using a real 3D shale image as a TI, and saves the parameters of neural networks to describe the probability distribution. Compared to some traditional methods, although this proposed method is slower in the first reconstruction, it is much faster in the subsequent reconstructions due to the reuse of the parameters. The proposed method also has advantages in terms of reconstruction quality over the original VAE. The findings of this study can help for better understanding of the seepage mechanisms in shale and the exploration of the shale gas industry.

1. Introduction

The demand for oil and gas resources is soaring in the whole world with the fast development of economy. Faced with huge energy demands, the world's conventional oil and gas production is relatively insufficient, so people begin to pay more attention to unconventional oil and gas resources. Shale oil and shale gas are two kinds of unconventional resources with wide distributions and considerable potentials. However, because of the complex geological conditions of shale reservoirs, it is necessary to figure out the internal structures including the distribution of pore space in shale before any large-scale engineering exploitation [1–3].

Shale is a typical porous medium with low porosity, low permeability, and anisotropy, making the exploration and

exploitation of shale oil and gas difficult. Some macroscopic properties of shale (such as porosity, permeability, etc.) depend on its microstructures, so it is quite useful to reconstruct a 3D microscopic shale model describing the statistical and topological properties of the pore structure. An important step for building such a model is to reconstruct the internal microstructure of pore space with the characteristics of real shale. The general pore space reconstruction methods are divided into physical experimental methods and numerical reconstruction methods [4–10].

Commonly used physical experimental methods are the scanning electron microscope (SEM) [4], the focused ion beam SEM (FIB-SEM) [5], the CT-scanning method [6], and the atomic force microscope SEM (AFM-SEM) [7]. With the help of the above experimental methods and physical

equipment, some important parameters and variation characteristics such as the variation in permeability during $\text{CO}_2\text{-CH}_4$ displacement in coal seams [11] can be effectively obtained and studied. Generally speaking, these physical methods normally are fast and their imaging quality mostly is quite good, but the imaging costs are usually quite high and experimental samples are difficult to prepare due to the fragile structure of some porous media like shale, leading to the limitation of physical experimental methods for wide application [12].

Some traditional numerical reconstruction methods extract the statistical information (such as porosity and variogram) of the 2D pore structures as constraints to complete reconstruction. For example, the early reconstruction methods such as the simulated annealing method [8], the process-based method [9], and the sequential indicator simulation method [10] use the low-order statistical information for 3D reconstruction. Then, some methods such as the multiple-point statistics (MPS) [13] used for the reconstruction of porous media focus on the reconstruction through the high-order statistical information describing the correlation between multiple points of the pore structures. It is quite obvious that the methods like MPS using high-order information have the advantages in depicting complex pores and the reconstructions are more similar to the realistic pore structures. However, this also makes it a big challenge for the branches of MPS and some improved MPS methods (e.g. direct sampling (DS) [14], filter-based simulation (FILTERSIM) [15], and single normal equation simulation (SNE-SIM) [13]) to perform reconstruction due to more hardware burdens for CPU and memory as well as a lengthy computational time.

Recently, many engineering and scientific researchers have benefited from the fast development of deep learning thanks to its robust extraction capabilities for characteristics, leading to the possibility of deep learning extracting the structural characteristics of porous media for pore space reconstruction [16]. Compared to the traditional reconstruction methods, there are two important advantages introduced by deep learning and its branches. The first one is the training time which can be greatly reduced due to the acceleration of GPU (Graphics Processing Unit) and the reuse of model parameters. Because of the frameworks (e.g., Tensorflow and PyTorch) provided by the public deep learning communities, these deep learning methods can be used by common users even without knowing the complicated assignment and design of parallelization for GPU. The detailed work about GPU is performed using the APIs of the frameworks like the black-box mechanism, which makes it easier for the general public. The second advantage relies on the strong ability of deep learning extracting characteristics from training images (TIs), improving the similarity between reconstructions and the TIs to obtain higher reconstruction quality.

As one of the important technologies in deep learning, the autoencoder is an unsupervised learning algorithm whose output can realize the learning and represent of the characteristics of input data. The concept of autoencoder was first put forward in [17]. Hinton et al. [18] derived a fast greedy

algorithm based on the autoencoder by using the complementary prior method to generate the deep autoencoder. Vincent et al. [19] added noise to the input data to improve the robustness of the algorithm to form a denoising autoencoder.

Based on variational bayes (VB) inference, the variational autoencoder (VAE) model [20] is a deep latent generation model and widely used in image generation, but it often suffers from the complicated expression model leading to the low quality of generated images. In information theory, Fisher information has always been an important tool to describe information behavior in information systems [21]. Fisher introduced Fisher information in the context of statistical estimation, which can describe the behavior of the dynamic system accurately [22]. Recent studies have reported that VAE is difficult to balance the information control between the encoder and the decoder in its structure [23]. For example, when the decoder is too expressive, latent variables generated by the encoder are almost ignored. Therefore, this paper applies the information theory specifically the Fisher information to improve VAE for the reconstruction of shale.

Compared to the traditional methods, our method can reuse the parameters obtained in the first training or reconstruction, so the subsequent reconstructions can be largely accelerated without the repeatedly training process existing in the traditional methods, which is a practical contribution for a large-quantity reconstruction mission. In addition, the combination with Fisher information also helps to improve the reconstruction quality of pore space compared to VAE.

The sketch of the research technical route of this paper is shown in Figure 1. The remainder of this paper is organized below. The main idea of the proposed method is given in Section 2. Section 3 gives a detailed procedure of the proposed method in this paper. Section 4 gives experimental results and comparison with some other methods. Section 5 provides conclusions.

2. The Main Idea of the Proposed Method

2.1. The Introduction of VAE. In VAE, two models of probability density distribution are established using two neural networks: one is called the encoder, used for the variational inference of original input data to generate the variational probability distribution of the latent variable z ; the other is the decoder, reconstructing the data by generating the approximate probability distribution of the original data according to the variational probability distribution of the generated latent variable z .

The typical structure of VAE is shown in Figure 2, in which “+” and “*,” respectively, represent the addition and multiplication of elements; X is the input dataset and X' is the reconstructed result. X usually is quite high-dimensional and used as the training data, whose internal characteristics are learned by the encoder. VAE uses stochastic gradient descent (SGD) to optimize the loss function [20]. SGD is a simple and effective optimization method that updates parameters until losses are within acceptable limits. Although SGD can handle random input, it cannot handle

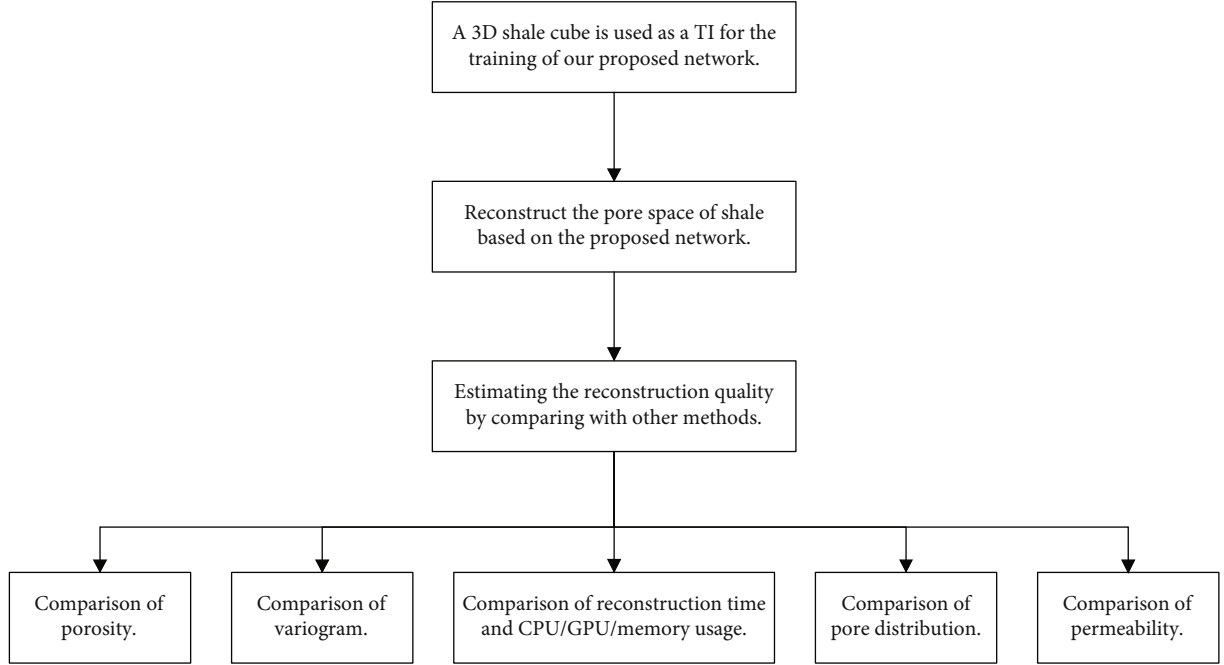


FIGURE 1: The sketch of the research technical route of this paper.

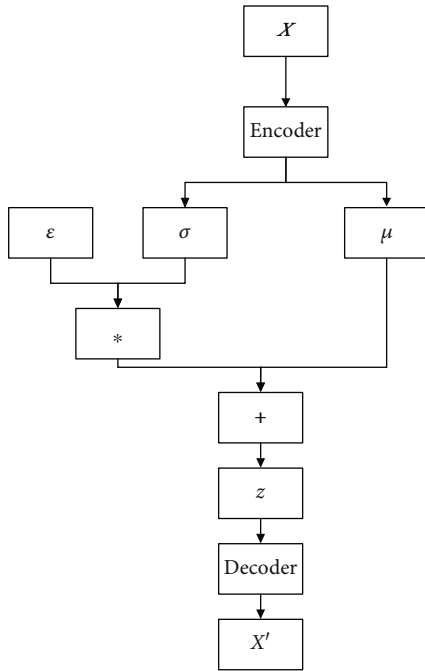


FIGURE 2: A typical VAE structural image.

random operation. Hence, VAE needs to “reparameterized” for optimization by introducing an auxiliary parameter ε , which is obtained by sampling from the standard normal distribution $N(0, 1)$. The latent variable z can be expressed by Equation (1) [24]:

$$z = \mu + \sigma_* \varepsilon, \quad (1)$$

where σ and μ are, respectively, the standard deviation and mean of Gaussian distribution calculated from the encoder. Suppose x is the input vector and x' is the output vector. The encoder model $q_\varphi(z|x)$ parameterized by φ is introduced into the encoder network to replace the undetermined real posterior distribution $P_\theta(z|x)$ since the distribution of z is unknowable. Kullback-Leibler (KL) divergence [25] is used to measure the similarity between $q_\varphi(z|x)$ and $P_\theta(z|x)$. The constraint parameters φ and θ are repeatedly trained and optimized to minimize the KL divergence, meaning that the evidence lower bound (ELBO) function $L(\theta, \varphi; X)$ is maximized, which is defined as follows:

$$L(\theta, \varphi; X) = \underbrace{E_{q_\varphi(z|x)} \text{lb} P_\theta(x' | z)}_{\text{Reconstruction item}} - D_{\text{KL}}(q_\varphi(z|x) | P_\theta(z)), \quad (2)$$

where D_{KL} represents the KL divergence, lb is a base-2 logarithm, $P_\theta(x' | z)$ is the probability distribution of a θ -parameterized decoder, and $P_\theta(z)$ represents the probability distribution of the latent variable z . Finally, z is input into the decoder model to obtain the final reconstruction X' . It seems Equation (2) has a penalty item (KL divergence) and a reconstruction item.

2.2. Fisher Information and Shannon Entropy. As can be seen from the $L(\theta, \varphi; X)$ in Equation (2), only the KL divergence is considered a penalty item for regularization, so it is difficult to balance between the representation of

the latent variable z and the likelihood maximization of the reconstructed results [23]. Since the representation of the VAE encoder network is controlled by the divergence error but there is no control exerted on the VAE decoder network, some schemas based on information theory were used to solve this problem; e.g., a constraint item based on Shannon entropy is introduced in ELBO to ensure that latent variables can learn sufficient data characteristics, thus improving the quality of representation learning [26]. However, Shannon information is usually difficult to be processed in calculation, and only approximate substitutes can be obtained in previous studies.

For a continuous probability distribution function (PDF), Shannon entropy is a measure of “global characteristics,” which is less sensitive to changes in the distribution of local details of a small area. Fisher information is quite different from Shannon entropy [21]. The former is a measure of the gradient content of the distribution, so it is also quite sensitive to small local details. Let the Shannon entropy and Fisher information of input data X be $H(X)$ and $J(X)$, respectively. Shannon entropy is usually converted into the form of entropy weight [22]:

$$N(X) = \frac{\exp(2H(X))}{2\pi \exp(1)}, \quad (3)$$

where \exp represents the exponential function with base e . When X represents a random vector and Fisher information $J(X)$ represents a Fisher information matrix, the relation between $N(X)$ and the trace of $J(X)$ writes [22, 27]

$$N(X) \cdot \text{tr}(J(X)) = K, \quad K \geq 1, \quad (4)$$

where K is a constant and $\text{tr}(\bullet)$ represents the trace of a matrix. As shown in Equation (4), Fisher information and Shannon entropy are intrinsically related and have the nature of uncertainty, in which the higher Fisher information is, the lower Shannon entropy is [27], but the calculation of Fisher information is usually easier than Shannon entropy. Hence, Fisher information is considered to be complementary for Shannon entropy and used in this paper.

2.3. The Proposed Improved VAE. In this section, Fisher information is used to balance the encoder and decoder of the VAE model. According to Equation (4), it can be found that there is a relationship between Fisher information $J(X)$ and Shannon entropy weight $N(X)$. Shannon entropy is usually difficult to be processed in calculation [28], so Fisher information instead of Shannon entropy is used to calculate information and two new penalty items of Fisher information are added for $L(\theta, \varphi; X)$. The improved method of VAE is called information variational autoencoder (IVAE) hereafter, which not only includes the KL divergence as a penalty item but also includes Fisher information as two penalty items in the encoding stage and the decoding stage, respectively, i.e. IVAE maximizes $L(\theta, \varphi; X)$ under the con-

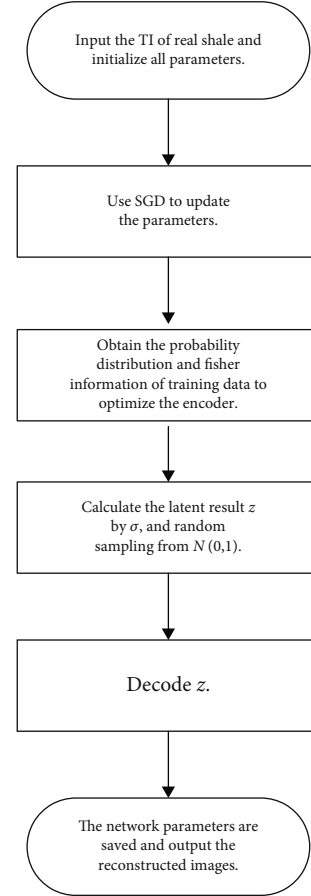


FIGURE 3: The flowchart of the proposed method.

straint of Fisher information. The new $L(\theta, \varphi; X)$ of IVAE writes

$$L(\theta, \varphi; X) = \underbrace{E_{q_\varphi(z|x)} \text{lb} P_\theta(x' | z)}_{\text{Reconstruction item}} - D_{\text{KL}}(q_\varphi(z|x) | P_\theta(z)) - \underbrace{\lambda_z | \text{tr}(J(z)) - F_z}_{\text{PI-1}} - \underbrace{\lambda_{x'} | \text{tr}(J(x')) - F_{x'}}_{\text{PI-2}}. \quad (5)$$

Compared with $L(\theta, \varphi; X)$ shown in Equation (2), Equation (5) adds two more penalty items (PI-1 and PI-2) that adjust the encoder and decoder, respectively: PI-1 controls Fisher information of the encoder network, and PI-2 controls Fisher information of the decoder network. λ_z and $\lambda_{x'}$ are adjustment coefficients. Both $F_{x'}$ and F_z are positive constants, representing the expected Fisher information values in the decoder and the encoder, respectively, meaning that Fisher information in the decoder and encoder can be controlled by $F_{x'}$ and F_z . The larger $F_{x'}$ and F_z are, the more likely the distribution is estimated by the θ - and φ -parameterized model; otherwise, the smaller $F_{x'}$ and F_z show that

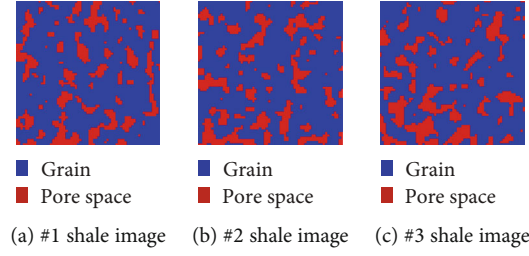


FIGURE 4: Some shale cross-section images from real volume data.

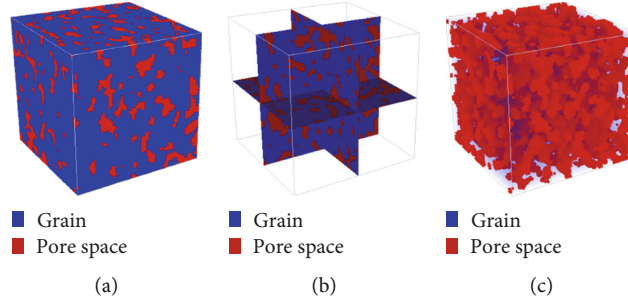


FIGURE 5: TI of shale: (a) exterior; (b) cross-sections ($X = 32, Y = 32,$ and $Z = 32$); (c) pore space.

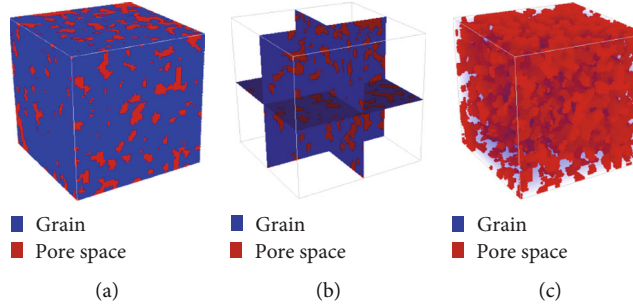


FIGURE 6: A reconstructed image using IVAE: (a) exterior; (b) cross-sections ($X = 32, Y = 32,$ and $Z = 32$); (c) pore space.

the influence of Shannon information is enhanced. Fisher information estimation can be directly calculated according to its definition [28].

The optimization procedures of the model are discussed, respectively, for the encoder network and the decoder network in the following section. Take the encoder network as an example. If the Fisher information is only considered in the encoder network, set $\lambda_x' = 0$ in Equation (5). Meanwhile, the KL divergence is considered, but the reconstruction item in Equation (5) is not considered. The ELBO of the encoder network, denoted as $L_e(\theta, \varphi; X)$, contains the error item of KL divergence and information error item:

$$L_e(\theta, \varphi; X) = -D_{\text{KL}}(q_\varphi(z|x) | P_\theta(z)) - \lambda_z |\text{tr}(J(z)) - F_z|, \tag{6}$$

where the posterior distribution $q_\varphi(z|x)$ obeys the normal distribution and $P_\theta(z)$ obeys the standard normal distribu-

tion. Therefore, the KL divergence in Equation (6) is calculated as [20] follows:

$$D_{\text{KL}}(q_\varphi(z|x) | P_\theta(z)) = -\frac{1}{2} ((1 + \ln(\sigma^2)) - (\mu)^2 - (\sigma)^2). \tag{7}$$

According to the definition, $\text{tr}(J(z))$ in Equation (6) can be obtained [25]:

$$\text{tr}(J(z)) = \int_z \left(\frac{\partial}{\partial z} q_\varphi(z|x) \right)^2 = \frac{1}{\sigma^2}. \tag{8}$$

Equations (7) and (8) are substituted into Equation (6), and then $L_e(\theta, \varphi; X)$ writes

$$L_e(\theta, \varphi; X) = \frac{1}{2} ((1 + \ln(\sigma^2)) - (\mu)^2 - (\sigma)^2) - \lambda_z \left| \frac{1}{\sigma^2} - F_z \right|. \tag{9}$$

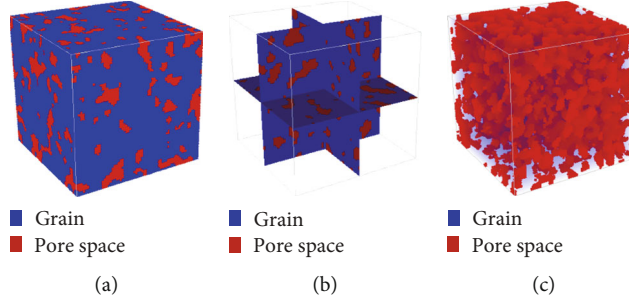


FIGURE 7: A reconstructed image using VAE: (a) exterior; (b) cross-sections ($X = 32$, $Y = 32$, and $Z = 32$); (c) pore space.

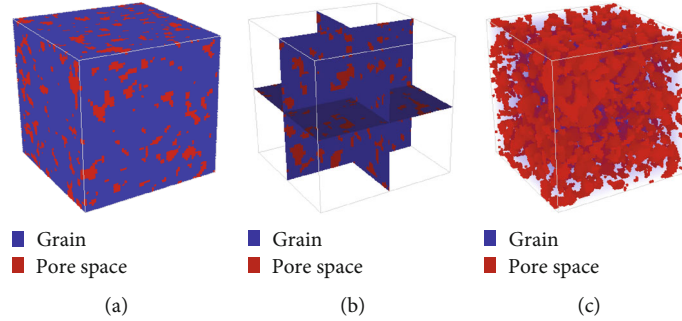


FIGURE 8: A reconstructed image using SNESIM: (a) exterior; (b) cross-sections ($X = 32$, $Y = 32$, and $Z = 32$); (c) pore space.

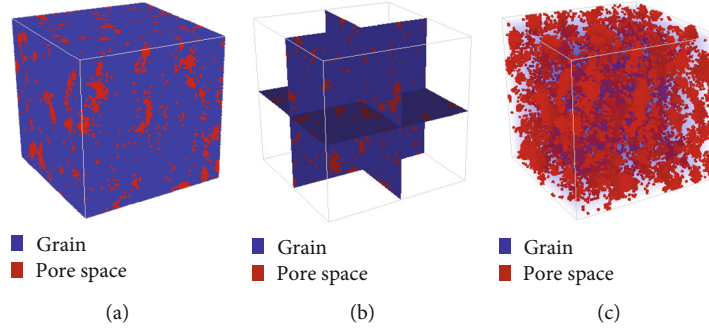


FIGURE 9: A reconstructed image using DS: (a) exterior; (b) cross-sections ($X = 32$, $Y = 32$, and $Z = 32$); (c) pore space.

Similarly, Fisher information is used in ELBO at the decoder network, denoted as $L_d(\theta, \varphi; X)$. Now, the reconstruction item in Equation (5) is considered, but the KL divergence is not considered. Then, set $\lambda_z = 0$ in Equation (5), and $L_d(\theta, \varphi; X)$ writes

$$L_d(\theta, \varphi; X) = \underbrace{E_{q_\varphi(z|x)} \text{lb} P_\theta(x' | z)}_{\text{Reconstruction item}} - \lambda_x' \left| \text{tr} \left(J(x') \right) - F_x' \right|. \quad (10)$$

As shown in Equation (2), the original VAE only considers KL divergence and a reconstruction item, while IVAE includes a reconstruction item and three penalty items (KL divergence, PI-1, and PI-2) related to the Fisher information and KL divergence, as shown in Equation (5). IVAE balances both the likelihood estimation and the dependence between input data and latent variables

TABLE 1: Porosities of the TI and the reconstructed images (shown in Figures 6–9) using IVAE, SNESIM, VAE, and DS.

	TI	SNESIM	VAE	DS	IVAE
Porosity	0.2690	0.2101	0.2334	0.1543	0.2665

TABLE 2: Average and variance of the porosities of 20 reconstructed shale images using IVAE, SNESIM, VAE, and DS.

	SNESIM	VAE	DS	IVAE
Average of porosity	0.2178	0.2382	0.1682	0.2673
Variance of porosity	0.0024	0.0023	0.0027	0.0013

through the new penalty items, making the new model include KL divergence and Fisher information together so as to improve the reconstruction quality.

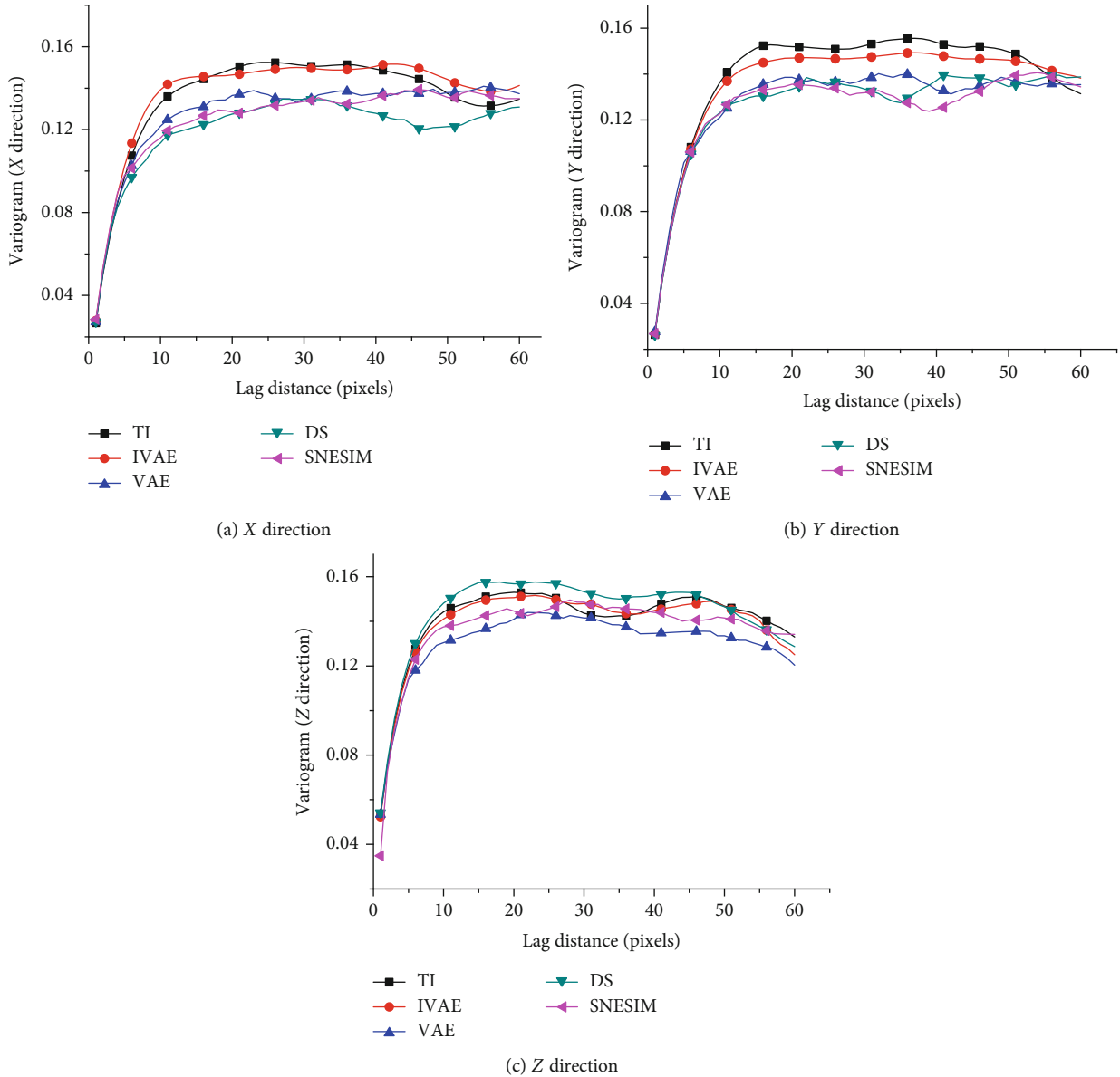


FIGURE 10: The variogram curves of TI and average variogram curves of 20 reconstructed images by IVAE, SNESIM, VAE, and DS in three directions.

3. The Procedure of the Proposed Method

The steps of the proposed method are as follows:

Step 1. Input the TI of real shale and initialize all parameters.

Step 2. Use SGD to update the parameters.

Step 3. Use the designed deep neural network to iteratively fit the training data, and then the probability distribution and information content of the training data are obtained. Optimize the encoder network according to Equation (6).

Step 4. The random sampling results from $N(0, 1)$ as well as σ and μ obtained from the encoder network are substituted into Equation (1) to calculate the latent result z . Once the

training error reaches the thresholds, the network parameters of the encoder are saved.

Step 5. Take the latent result z as the input of the decoder network, which is iteratively optimized according to Equation (10) to obtain z . The final decoding result from decoder is the final reconstruction result, and the network parameters of the decoder are saved.

The flowchart of the above procedures is shown in Figure 3.

4. Experimental Results and Analyses

In this section, the experiments were implemented with an Intel Core i7-9700k 4.1 GHz CPU, 16GB memory, and GeForce

TABLE 3: Difference degrees (DDs) between the TI and the reconstructions of IVAE, SNESIM, VAE and DS measured by variogram differences in the X, Y, and Z directions.

Directions	Difference degrees (DDs)			
	DD (TI, SNESIM)	DD (TI, DS)	DD (TI, VAE)	DD (TI, IVAE)
X	0.0569	0.0776	0.0445	0.0112
Y	0.0745	0.0579	0.0453	0.0159
Z	0.0471	0.0201	0.0645	0.0056

RTX2070s GPU with 8GB video RAM to evaluate the effectiveness of IVAE in the pore space reconstruction of shale by the metrics of porosity, variogram curves, permeability, distribution of pores, and CPU/GPU/memory performance. The experimental software framework for IVAE is Tensorflow-GPU.

4.1. Training Data. To estimate the effectiveness of the proposed method in the pore space reconstruction of shale, the real shale volume data with the resolution of 64 nanometers obtained by nano-CT scanning were used as the test data for the following tests. Figure 4 shows three cross-sections (64×64 pixels) of the shale image with two facies: grain and pore space.

Note that in 2D conditions the basic image unit is pixel while in 3D conditions the unit of 3D images is voxel. Before applying any reconstruction methods, a 3D cube with $64 \times 64 \times 64$ voxels was used as the TI, extracted from the original shale volume data. Figures 5(a)–5(c) are the exterior ($64 \times 64 \times 64$ voxels), cross-sections ($X = 32$, $Y = 32$, and $Z = 32$) and pore space of the TI (porosity = 0.2690).

4.2. Reconstructions Using IVAE, VAE, SNESIM, and DS. In the section, IVAE, VAE, and two typical reconstruction methods—SNESIM and DS—were, respectively, used to reconstruct shale for comparison. The main parameters of IVAE are initialized as follows: learning rate is 0.001, the number of training epochs is 4000, batch size is 64, $\lambda_z = \lambda_x' = 0.1$, and $F_x' = F_z = 5$. Figure 6 is the reconstruction by IVAE. Figures 7–9 are, respectively, the reconstructed images using VAE, SNESIM, and DS. All the reconstructed images are $64 \times 64 \times 64$ voxels. It can be found that the results of the four reconstruction methods all have similar long-connected pore spaces with the TI.

4.3. Comparison of Porosity. Porosity of shale indicates the shale’s ability to store fluids and is one of the characteristics for evaluating reconstruction quality. The definition of porosity ϕ is as follows:

$$\phi = \frac{V_p}{V}, \quad (11)$$

where V is the total volume and V_p is the pore volume.

The porosities of the TI and the images shown in Figures 6–9 are displayed in Table 1. It is seen that the porosity of the IVAE-reconstructed image is closest to that of the TI. To obtain an average performance in porosity, IVAE, VAE, SNESIM, and DS were performed for another 20 times to, respectively, achieve 20 reconstructed images

TABLE 4: Permeability of the TI and average permeabilities of 20 reconstructed images in three directions using IVAE, SNESIM, VAE, and DS.

Direction	Permeability ($10^{-3} \mu\text{m}^2$)				
	TI	SNESIM	DS	VAE	IVAE
X	6.123	5.591	6.582	6.210	5.901
Y	5.234	6.354	5.819	6.021	5.721
Z	7.318	8.728	6.789	9.129	6.980

TABLE 5: The pore number in the TI and the average pore numbers in the reconstructions of IVAE, SNESIM, VAE, and DS.

	TI	SNESIM	DS	VAE	IVAE
Pore number	206	184	178	195	204

TABLE 6: The maximum, minimum, and average pore diameters in the TI and the reconstructions of IVAE, SNESIM, VAE, and DS.

	TI	SNESIM	DS	VAE	IVAE
Average (voxel)	5.87	5.38	6.21	5.69	5.83
Min (voxel)	3.38	4.93	4.79	3.61	3.45
Max (voxel)	23.32	22.83	18.92	23.52	22.88

($64 \times 64 \times 64$ voxels). As shown in Table 2, the porosity of 3D images reconstructed by IVAE is closest to that of the TI, and the variance is smallest, indicating a high reconstruction quality and low fluctuation.

4.4. Comparison of Variogram. Variogram is widely used to evaluate the variability of spatial structures in different direction [29], which is defined as follows:

$$\gamma(h) = \frac{1}{2} \mathbb{E} \{ [Z(x+h) - Z(x)]^2 \}, \quad (12)$$

where \mathbb{E} is the mathematical expectation, h is the lag distance between two positions: $x+h$ and x , and $Z(x)$ means the property value at the position x . If the variogram curves of two geological bodies are similar in a certain direction, it means that the spatial structures of the two geological bodies are similar in this direction; otherwise, it means that their structures are quite different. In this section, the variogram curves of TI and average variograms of 20 reconstructed images by IVAE, SNESIM, VAE, and DS were, respectively, calculated in the three directions of X, Y, and Z, as shown in Figure 10. In general, the variogram curves of IVAE are closest to those of the TI.

In order to quantitatively measure the difference of variogram curves between the TI and the reconstruction of each method, a difference degree (DD) is defined as follows:

$$\text{DD}(\text{TI, re}) = \sum_{h=1}^n (X_h - x_h)^2, \quad (13)$$

TABLE 7: The time consumption and average usage of CPU, GPU, and memory by IVAE, SNESIM, VAE, and DS for 20 reconstructions.

	SNESIM	DS	VAE	IVAE
Average CPU usage (%)	23.1	33.7	37.5	39.8
Average GPU usage (%)	None	None	62.8	65.0
Average memory usage (MB)	532	738	4398	4627
Time for the first reconstruction (s)	2239	18611	6728	6627
Time for the other 19 reconstructions (s)	42602	353292	501	490

where TI and r_e , respectively, represent the TI and the reconstruction method and X_h and x_h represent the variogram value of the TI and the reconstructed image when the distance is h . A smaller DD means a smaller difference between the TI and the reconstruction. DDs between the TI and the reconstructions of IVAE, SNESIM, VAE, and DS measured by variogram differences in the X, Y, and Z directions are shown in Table 3. It seems that reconstructed images by IVAE are closest to the TI.

4.5. Permeability Estimation Using the Lattice Boltzmann Method. The permeability of shale means the ability of allowing fluid to pass through shale and often is related to porosity, geometry of pores in the direction of liquid penetration, and other factors. A 3D 19-velocity model of the Lattice Boltzmann Method (LBM), called D3Q19, was used to compute the permeabilities of reconstructed shale. There are altogether 19 velocity vectors defined in this model. The conditions of no-slip velocity are reached by the bounce-back scheme. Since the reconstructed results are cubic in our experiments, two parallel faces are open and the other four are sealed when supposing the fluids are perpendicularly passing through the two open parallel faces. Hence, there are altogether three directions for the computation of permeabilities using the Darcy's law. The detailed procedures and equations can be referred to [29, 30].

The data of the TI and the reconstructed images were, respectively, used as the input files of LBM simulation to calculate the permeabilities of those models with the size of $64 \times 64 \times 64$ voxels. As shown in Table 4, the permeability of the TI and the average permeabilities of 20 reconstructed images using IVAE, SNESIM, VAE, and DS in three directions were computed by LBM. The permeability values of the reconstructed images using IVAE are quite close to those of the TI, displaying the good reconstruction quality of IVAE.

4.6. Distribution and Numbers of Pores. The diameter of a pore is defined as follows:

$$\text{Diameter} = \sqrt[3]{\frac{6V}{\pi}}, \quad (14)$$

where V is the volume of a pore. The 3D shale images reconstructed by IVAE, SNESIM, VAE, and DS are imported into the software Avizo [31] to analyze the number of pores and the pore size. Table 5 shows the pore number in the TI and the average pore numbers in the reconstructions of these methods. Table 6 shows the maximum, minimum and average pore diameters in the TI and the reconstructions of

IVAE, SNESIM, VAE, and DS. From Tables 5 and 6, it is seen that IVAE has shown the best reconstruction quality since the reconstruction of IVAE has the most similar pore number and average pore diameter with those of the TI.

4.7. Comparison of Reconstruction Time and CPU/GPU/Memory Usage. Since the pore space reconstruction of shale is quite CPU-intensive and normally uses large memory, the reconstruction time and CPU/GPU/memory usage of IVAE, SNESIM, VAE, and DS are compared in this section. As for the computational hardware platforms, these four methods are different. SNESIM and DS are typical CPU-based reconstruction methods, while IVAE and VAE can be performed by both CPU and GPU. Table 7 shows the time consumption and the average usage of CPU, GPU, and memory by IVAE, SNESIM, VAE, and DS for 20 reconstructions.

In Table 7, the time for 20 reconstructions is divided into two parts: the time for the first reconstruction and the time for the other 19 reconstructions. The former means the time used for the first reconstruction of the traditional reconstruction methods (SNESIM and DS) and deep learning methods (VAE and IVAE). The latter is the time consumed for the other 19 reconstructions by IVAE, SNESIM, VAE, and DS.

Deep learning methods normally benefit from the ability of saving model parameters during training. Therefore, the reconstruction process after the first model training that is finished in the first reconstruction only needs to reuse the saved parameters and takes much less time to reconstruct images. Hence, as typical deep learning methods, VAE and IVAE require much longer training time to set up the training model before reconstruction, usually consuming more time in the first reconstruction than the time used for the subsequent reconstruction. On the contrary, SNESIM and DS need to rescan the TI from scratch for each reconstruction because they only store training modes in memory. When a reconstruction process is over, training data of SNESIM and DS in memory will be cleared, resulting in the repeated processes of scanning the TI and extracting characteristics from the TI in the subsequent reconstruction.

Since VAE and IVAE can save and reuse the parameters after the first reconstruction, each subsequent reconstruction only needs to input the parameters and complete the reconstruction very soon. Hence, as shown in Table 7, although VAE and IVAE spend more time on the first reconstruction than SNESIM, the time for the subsequent reconstructions decreases largely. From an overall point of view, VAE and IVAE have great advantages in the speed of multiple reconstructions over the other CPU-based reconstruction

methods. As for the overall performance of time consumption and average use of CPU/GPU/memory, VAE and IVAE are evenly matched and each one has its own strengths.

5. Summary and Conclusions

The properties of shale such as low porosity, low permeability, and complex inner structures are the main reasons challenging the exploitation of shale reservoirs. The establishment of a 3D pore space model of shale can help to analyze the characteristics of shale, improving the producing efficiency of shale resources. Main conclusions, including the advantages and disadvantages (or limitations) of our method, are as follows:

- (1) A real 3D shale cube acquired by nano-CT scanning was used as the TI, providing the necessary real structural information of pore space for pore space reconstruction, so the reconstructed structures have similar structures with the real shale
- (2) Traditional numerical reconstruction methods need to repeatedly scan the TI to extract the statistical information in reconstruction, leading to consuming more time in repeated reconstructions. The proposed method shows the advantage in shale reconstruction in terms of both speed and quality by reusing the saved models after the first reconstruction or training
- (3) Our method combines VAE and Fisher information together for the pore space reconstruction of shale, using new penalty terms related to Fisher information in the encoder and the decoder, respectively, so our method performs better than the original VAE in the reconstruction quality, also verified by the real experiments
- (4) Our method still has some disadvantages or limitations. First, compared to traditional reconstruction methods, our method has higher CPU/memory usage and consumes much more time in the first reconstruction. Second, our method is established on the framework of Tensorflow-GPU, so a GPU is necessary for our method, increasing the hardware cost of reconstruction

Nomenclature

VAE:	Variational autoencoder
TI:	Training image
SEM:	Scanning electron microscope
MPS:	Multiple-point statistics
DS:	Direct sampling
FILTERSIM:	Filter-based simulation
SNESIM:	Single normal equation simulation
GPU:	Graphics Processing Unit
z :	Latent variable
X :	Input dataset
X' :	Reconstructed result
SGD:	Stochastic gradient descent

ε :	Auxiliary parameter
σ :	Standard deviation of Gaussian distribution
μ :	Mean of Gaussian distribution
x :	Input vector
x' :	Output vector
$q_\varphi(z x)$:	Encoder model
$P_\theta(z x)$:	Real posterior distribution
φ :	Constraint parameter
θ :	Constraint parameter
$L(\theta, \varphi; X)$:	Evidence lower bound function
D_{KL} :	KL divergence
lb:	Base-2 logarithm
$P_\theta(x' z)$:	Probability distribution of a θ -parameterized decoder
$P_\theta(z)$:	Probability distribution of the latent variable z
ELBO:	Evidence lower bound
PDF:	Probability distribution function
$H(X)$:	Shannon entropy of input data X
$J(X)$:	Fisher information of input data X
exp:	Exponential function with base e
K :	A constant
tr():	The trace of a matrix
IVAE:	Information variational autoencoder
PI-1:	Penalty item
PI-2:	Penalty item
λ_z :	Adjustment coefficient
$\lambda_{x'}$:	Adjustment coefficient
$F_{x'}$:	The expected Fisher information value in the decoder
F_z :	The expected Fisher information value in the encoder
$L_e(\theta, \varphi; X)$:	Evidence lower bound of the encoder network
$L_d(\theta, \varphi; X)$:	Evidence lower bound of the decoder network
KL:	Kullback-Leibler
ϕ :	Porosity
V :	Total volume
V_p :	Pore volume
\mathbb{E} :	Mathematical expectation
h :	Lag distance
$Z(x)$:	Property value at the location x
DD:	Difference degree
re:	Reconstruction method
X_h :	The variogram value of the TI when the distance is h
x_h :	The variogram value of the reconstructed image when the distance is h
LBM:	Lattice Boltzmann Method
AFM:	Atomic force microscope.

Data Availability

The data used to support this study are available from the corresponding author upon request.

Conflicts of Interest

The authors declare that they have no conflict of interest.

Acknowledgments

This work is supported by the National Natural Science Foundation of China (Nos. 41702148 and 41672114).

References

- [1] D. J. Ross and R. M. Bustin, "The importance of shale composition and pore structure upon gas storage potential of shale gas reservoirs," *Marine and Petroleum Geology*, vol. 26, no. 6, pp. 916–927, 2009.
- [2] T. Boersma and C. Johnson, "The shale gas revolution: U.S. and EU policy and research agendas," *Review of Policy Research*, vol. 29, no. 4, pp. 570–576, 2016.
- [3] S. B. Chen, Y. M. Zhu, G. Y. Wang, H. L. Liu, and J. H. Fang, "Structure characteristics and accumulation significance of nanopores in Longmaxi shale gas reservoir in the southern Sichuan basin," *Journal of China Coal Society*, vol. 37, no. 3, pp. 438–444, 2012.
- [4] C. E. Krohn and A. H. Thompson, "Fractal sandstone pores: automated measurements using scanning-electron-microscope images," *Physical Review B*, vol. 33, no. 9, pp. 6366–6374, 1986.
- [5] L. Tomutsa, D. Silin, and V. Radmilovic, "Analysis of chalk petrophysical properties by means of submicron-scale pore imaging and modeling," *SPE Reservoir Evaluation and Engineering*, vol. 10, no. 3, pp. 285–293, 2007.
- [6] T. Ma and P. Chen, "Study of meso-damage characteristics of shale hydration based on CT scanning technology," *Petroleum Exploration and Development*, vol. 41, no. 2, pp. 249–256, 2014.
- [7] Y. Li, J. H. Yang, Z. J. Pan, and W. S. Tong, "Nanoscale pore structure and mechanical property analysis of coal: an insight combining AFM and SEM images," *Fuel*, vol. 260, p. 116352, 2020.
- [8] L. Duczmal and R. Assuncao, "A simulated annealing strategy for the detection of arbitrarily shaped spatial clusters," *Computational Statistics & Data Analysis*, vol. 45, no. 2, pp. 269–286, 2004.
- [9] P. E. Øren and S. Bakke, "Process based reconstruction of sandstones and prediction of transport properties," *Transport in Porous Media*, vol. 46, no. 2/3, pp. 311–343, 2002.
- [10] C. V. Deutsch, "A sequential indicator simulation program for categorical variables with point and block data: BlockSIS," *Computers & Geosciences*, vol. 32, no. 10, pp. 1669–1681, 2006.
- [11] Y. Li, Y. B. Wang, J. Wang, and Z. J. Pan, "Variation in permeability during CO₂-CH₄ displacement in coal seams: part 1 - experimental insights," *Fuel*, vol. 263, p. 116666, 2020.
- [12] Q. Wang and R. Li, "Research status of shale gas: a review," *Renewable and Sustainable Energy Reviews*, vol. 74, pp. 715–720, 2017.
- [13] S. Strebelle, "Conditional simulation of complex geological structures using multiple-point statistics," *Mathematical Geology*, vol. 34, no. 1, pp. 1–21, 2002.
- [14] G. Mariethoz and P. Renard, "Reconstruction of incomplete data sets or images using direct sampling," *Mathematical Geosciences*, vol. 42, no. 3, pp. 245–268, 2010.
- [15] T. Zhang, P. Switzer, and A. Journel, "Filter-based classification of training image patterns for spatial simulation," *Mathematical Geology*, vol. 38, no. 1, pp. 63–80, 2006.
- [16] L. Mosser, O. Dubrule, and M. J. Blunt, "Reconstruction of three-dimensional porous media using generative adversarial neural networks," *Physical Review E*, vol. 96, no. 4, article 043309, 2017.
- [17] D. E. Rumelhart, G. E. Hinton, and R. J. Williams, "Learning representations by back-propagating errors," *Nature*, vol. 323, no. 6088, pp. 533–536, 1986.
- [18] G. E. Hinton, S. Osindero, and Y. W. Teh, "A fast learning algorithm for deep belief nets," *Neural Computation*, vol. 18, no. 7, pp. 1527–1554, 2006.
- [19] P. Vincent, H. Larochelle, Y. Bengio, and P. A. Manzagol, "Extracting and composing robust features with denoising auto-encoders," in *Proceedings of the 25th International Conference on Machine Learning*, pp. 1096–1103, Helsinki, Finland, 2008.
- [20] D. P. Kingma and M. Welling, "Auto-encoding variational bayes," in *International Conference on Learning Representations*, pp. 14–27, Banff, Canada, 2014.
- [21] R. A. Fisher, "Theory of statistical estimation," *Proceedings of the Cambridge Philosophical Society*, vol. 22, no. 5, pp. 700–725, 1925.
- [22] C. Vignat and J. F. Bercher, "Analysis of signals in the Fisher-Shannon information plane," *Physics Letters A*, vol. 312, no. 1–2, pp. 27–33, 2003.
- [23] R. B. Samuel, V. Luke, V. Oriol, M. D. Andrew, and B. Samy, "Generating sentences from a continuous space," 2015, <https://arxiv.org/abs/1511.06349>.
- [24] D. J. Rezende and S. Mohamed, "Variational inference with normalizing flows," *Computer Science*, vol. 34, no. 6, pp. 421–427, 2015.
- [25] M. J. James, "Kullback-leibler divergence," *International Encyclopedia of Statistical Science*, pp. 720–722, 2011.
- [26] X. Chen, D. P. Kingma, T. Salimans et al., *Variational Lossy Autoencoder*, International Conference on Learning Representation, 2016.
- [27] A. Dembo, T. M. Cover, and J. A. Thomas, "Information theoretic inequalities," *IEEE Transactions on Information Theory*, vol. 37, no. 6, pp. 1501–1518, 1991.
- [28] A. J. Stam, "Some inequalities satisfied by the quantities of information of Fisher and Shannon," *Information and Control*, vol. 2, no. 2, pp. 101–112, 1959.
- [29] T. Zhang, Y. Du, T. Huang, J. Yang, F. Lu, and X. Li, "Reconstruction of porous media using ISOMAP-based MPS," *Stochastic Environmental Research and Risk Assessment*, vol. 30, no. 1, pp. 395–412, 2016.
- [30] H. Okabe and M. J. Blunt, "Pore space reconstruction using multiple-point statistics," *Journal of Petroleum Science and Engineering*, vol. 46, no. 1–2, pp. 121–137, 2005.
- [31] M. B. Bird, S. L. Butler, C. D. Hawkes, and T. Kotzer, "Numerical modeling of fluid and electrical currents through geometries based on synchrotron X-ray tomographic images of reservoir rocks using Avizo and COMSOL," *Computers & Geosciences*, vol. 73, pp. 6–16, 2014.

Research Article

Pore Properties of the Lacustrine Shale in the Upper Part of the Sha-4 Member of the Paleogene Shahejie Formation in the Dongying Depression in East China

Ziyi Wang ^{1,2,3}, Liuping Zhang ^{1,2}, Yuan Gao ⁴, Wenxiu Yang ⁵, Yongshi Wang ⁶,
Huimin Liu ⁶, Zhaoyang Li ^{1,2,7} and Shanshan Zhou ^{1,2,3}

¹Key Laboratory of Petroleum Resources Research, Institute of Geology and Geophysics, Chinese Academy of Sciences, Beijing 100029, China

²Innovation Academy for Earth Science, Chinese Academy of Sciences, Beijing 100029, China

³University of Chinese Academy of Sciences, Beijing 100049, China

⁴Beijing Center for Physical and Chemical Analysis, Beijing 100089, China

⁵Roxar Software Solutions, Emerson Process Management, Lysaker 1366, Norway

⁶Shengli Oilfield Company of Sinopec, Dongying 257051, China

⁷China Institute of Disaster Prevention, Sanhe 065201, China

Correspondence should be addressed to Liuping Zhang; lpzhang_int@sina.com

Received 31 December 2020; Revised 5 February 2021; Accepted 23 February 2021; Published 16 March 2021

Academic Editor: Kun Zhang

Copyright © 2021 Ziyi Wang et al. This is an open access article distributed under the Creative Commons Attribution License, which permits unrestricted use, distribution, and reproduction in any medium, provided the original work is properly cited.

Lacustrine shales hold a huge potential oil resource in China. Pore properties (pore volume, diameter, specific surface area, and fractal dimensions) and their relationships with geological factors (mineralogy, insoluble organic carbon, burial depth, and vitrinite reflectance) are critical for evaluating shale oil resource. However, the factors controlling pores for lacustrine shale oil remain unclear, as the relationships between pore properties of Soxhlet-extracted samples and geological factors have not been studied using multivariate analytical methods. In this paper, the samples from the lacustrine shale in the upper part of the Sha-4 Member of the Paleogene Shahejie Formation in the Dongying Depression were tested with a set of experiments including Soxhlet (solvent) extraction, X-ray diffraction mineral analysis, insoluble organic carbon, vitrinite reflectance, and low-pressure CO₂ and N₂ adsorption experiments. The micropore volume varies from 0.003 cm³/g to 0.045 cm³/g. The relationships of pore properties with geological factors were studied with partial least square regression analysis (PLSR analysis, a powerful multivariate regression analysis). The results of the PLSR analyses indicate that clay minerals and carbonates are two key factors affecting the pore properties of the lacustrine shale. Compared with marine shales, more clay minerals in the lacustrine shale make them become more important for controlling pores than organic matter. The PLSR results also illustrate that the shale with higher pore volume contains more clay minerals and fewer carbonates and thus is unfavorable for hydraulic fracturing. Therefore, the shale with high micropore volume may be unfavorable for shale oil production. The shale with the modest micropore volume (~0.036 cm³/g), relatively high content of brittle minerals (~71 wt%), and low clay mineral content (~29 wt%) is conducive to both oil storage and hydraulic fracturing for the development of the Es₄U shale oil in the Dongying Depression in East China.

1. Introduction

The shale revolution in the USA has changed the global energy landscape with profound impact on international economies [1, 2], which has led to the assessment and explo-

ration of shale oil and gas in basins worldwide. It has been conservatively estimated that China has shale oil resources of 40.3 × 10⁹ tons, and lacustrine shale holds the vast majority of the shale oil resources in China (40.2 × 10⁹ tons) [3]. However, the studies of lacustrine shale oil reservoirs are very

limited, compared with many studies of marine shale gas reservoirs [4–10]. As a result, the pore properties of lacustrine shale and especially their controlling factors are still unclear. The pore properties help determine the petroleum storage and transport properties of shale reservoirs. Therefore, the studies of the pore properties of lacustrine shale and their controlling factors are of great importance.

Compared with conventional reservoirs (e.g., sandstones), shale reservoirs have complex pore structures. Pores in shale are divided into micropores (with diameter < 2 nm), mesopores (with diameter of 2–50 nm), and macropores (with diameter > 50 nm) [11]. Among the techniques for quantitative analysis of shale pore systems [4, 12–14], low-pressure gas adsorption (LPGA) is important in the measurement of pore properties over a wide range of pore sizes. Low-pressure N₂ adsorption is frequently used to analyze mesopore characteristics in shale reservoirs [15]. One of reasons is that mesopores are usually much more than micropores and macropores in shale reservoirs [16]. The others are that pore volume (*V*), pore size distribution (PSD), specific surface area (*S*), and fractal dimensions can be calculated from a N₂ adsorption isotherm [17–19]. However, N₂ adsorption is less accurate in characterizing micropores due to the limitation arising from N₂ molecule and pore throat sizes. A CO₂ molecule has a higher thermal energy at the experimental temperature (273.15 K) and, as a result, can penetrate smaller pores more easily than a N₂ molecule (at 77.35 K) [20]. Low-pressure CO₂ adsorption can be used to analyze micropores. Therefore, both N₂ and CO₂ techniques need to be used to study pore properties in shale.

For shales in the oil window, residual oil in pores dramatically affects the results of pore properties obtained from the N₂ and CO₂ techniques. Removing the residual oil in shale samples via the Soxhlet (solvent) extraction can solve this problem in the analysis of LPGA [21–23]. However, published data on shale pore properties in the oil window are rarely obtained from solvent-extracted samples [24–29]. Therefore, there is an urgent need to restudy pore properties of shale in the oil window and their controlling factors, based on the solvent extraction.

The geological factors controlling pore properties are usually studied using the bivariate cross-plots and univariate regression analysis [23, 25, 30, 31]. But in most cases, the correlation coefficients of pore properties with geological factors are very low (0.33–0.86) [23, 25, 30, 31]. The reason is that the pore properties are controlled or affected by multiple factors in most cases. Therefore, multivariate regression analysis is necessary. The traditional multivariate regression analysis can develop the multiple regression models but may not work well with the independent variables that are correlated to each other [32, 33]. In this case, the traditional method is not applicable to studying the relationships of pore properties with geological factors because the geological factors as independent variables are often correlated to each other. Partial least square regression (PLSR) is a multivariate analytical method that can process the correlated independent variables. PLSR has been used to analyze correlations between pore properties and geological factors, based on seven shale samples [12, 27, 28]. But the residual oil in samples was not

extracted before testing pore properties [12, 27, 28]. The potential geological factors did not include burial depth and Ro [12, 27, 28], and the importance of the geological factor (descriptor) for a dependent variable (one of pore properties; response) was not evaluated with the parameter of variable importance in projection (VIP) [12, 27, 28, 33, 34]. As a result, the established correlations between the pore properties and the geological factors of the Soxhlet-extracted samples from shale oil reservoirs may be unreliable, and the geological factors controlling pore properties of shale oil reservoirs are still unclear. Therefore, PLSR analysis needs to be used with VIP evaluation when the univariate correlation relationships are poor between pore properties of the Soxhlet-extracted samples and geological factors.

The Dongying Depression is located in the southern part of the Bohai Bay Basin in East China [35]. The lacustrine shale in the upper part of the Sha-4 Member (Es₄U) of the Paleogene Shahejie Formation displays a great potential for shale oil exploration and development in this depression [22], with total organic carbon (TOC) content of 0.5–11.2 wt% [36], Ro values of 0.5–1.3% [37], thickness up to 400 m [38], and the area of about 3000 km² for the shale thicker than 50 m. In this work, the pore properties in fifteen Soxhlet-extracted samples of the Es₄U shale were analyzed using N₂ and CO₂ adsorption techniques. These samples were also analyzed for geological factors including mineral composition, Ro, and IOC. The relationships between pore properties and geological factors show poor correlations in the bivariate cross-plots and the results of univariate regression analyses. The partial least square regression was then used. The high correlation coefficients (0.72–0.94) show reliability of the PLSR analyses. The importance of the geological factors (descriptors) for the pore properties (responses) was evaluated with VIP scores. The results illustrate that clay minerals and carbonates with high VIP scores are two key factors that affect pore properties of the lacustrine shale. The reason is that many pores in shale samples are developed between clay minerals but some are filled with carbonates. As the shale with higher volumes of micro- and mesopores contains more clay minerals and fewer carbonates, this shale is unfavorable for production via hydraulic fracturing. The analysis of the shale pore evolution helped us find the shale with the modest micromesopore volume, brittle mineral, and clay mineral contents which is conducive to the development of the Es₄U shale oil.

2. Geological Setting

The Dongying Depression of the Bohai Bay Basin in eastern China is a lacustrine basin with a faulted margin in the north and a ramp margin in the south (see Figure 1 in Liu et al. [39] and Figure 1). The Paleogene and Neogene successions in the depression consist of clastics with subordinate lacustrine carbonates and evaporites, and they mainly comprise four formations from bottom to top: the Paleogene Shahejie (Es) and Dongying (Ed) Formations and the Neogene Guantao (Ng) and Minghuazhen (Nm) Formations (see the strata column (Figure 2) in Zhang et al. [35]). The Shahejie Formation is further divided into the Sha-4 (Es₄), -3 (Es₃), -2 (Es₂),

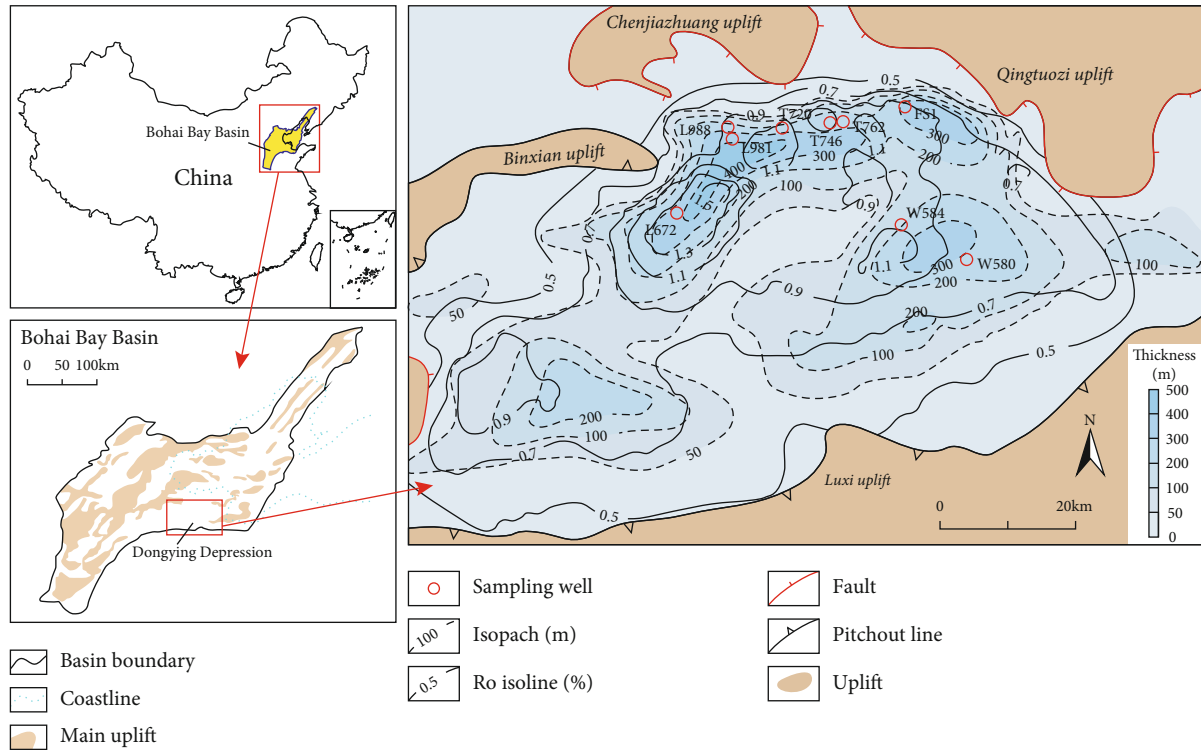


FIGURE 1: Outline map of the Dongying Depression, showing the isopachs (m) of the Es_4U shale (data from Zhang et al. [43]), the Ro (%) contours of the bottom boundary of the Es_4U shale (data from the database of Sinopec Shengli Oilfield Company) and the locations of sampling wells.

and -1 (Es_1) Members from bottom to top. The shale in the upper part of the Sha-4 Member (Es_4U) is an important source rock in the Dongying Depression [22]. The thickness of Es_4U shale is up to 400 m [38]. The area with thickness greater than 50 m (154 m on average) occupies about 3000 km² and is mainly located in the central-north part of the Dongying Depression (Figure 1). The thick Es_4U shale is good source rock, mainly containing type I kerogen and followed by type II kerogen, and has TOC content of 0.5–11.2%, Ro values of 0.5–1.3%, and hydrocarbon generation potential (free and cracked hydrocarbon, i.e., $S_1 + S_2$) values of 0.62–76.51 mg/g [29, 36–38, 40]. The average oil saturation of Es_4U shale within the oil window (samples with depths greater than 3000 m in Zhang et al. [41]) is 45.8%. The paleosalinity was high during the Es_4U deposition [42], facilitating the development of carbonates (see the strata column in Zhang et al. [35]).

3. Samples and Methods

3.1. Samples. To reveal the pore properties of the main bodies of the shale, fifteen core samples of the Es_4U shale were selected from nine wells (Figures 1 and S1), based on the sample locations in Es_4U , and observation of rock textures and carbonate content in specimens (Table S1). These samples were divided into two types according to the rock textures: laminated shale (13 samples) and massive mudstone (2 samples; see Table S1). The laminated shale is dark, gray, and brown in color and includes horizontal and low-angle parallel laminations. They are mainly composed

of interlaminated and interbedded mudstone and carbonates. The carbonates are mainly calcite (Figure 2(a)). In addition, several shale samples contain silty sands (Figure 2(b)). Massive mudstone is dark to gray. Its structure is shown in Figure 2(c).

3.2. Soxhlet Extraction. Approximately 20–40 g of each sample was crushed to the powder finer than 60 mesh [23, 44] and processed with Soxhlet extractors and 300 ml [44] of a dichloromethane/methanol mixture (DCM/MeOH, 93:7 vol/vol) for 72 h [23, 44]. The water bath temperature of the extraction was 48°C. The complete extraction of residual oil was guaranteed by the observation that solvent in the siphon and thimble-holder becomes colorless [45]. The Soxhlet-extracted samples were placed in beakers and dried under a fume hood. Each dried sample was split into four aliquots. Three of them were grounded into the powder finer than 100 mesh.

3.3. Microscopy. The particles of the original (Soxhlet-unextracted) and Soxhlet-extracted shale samples were embedded in Araldite 502 resin and polished into the fluorescent thin sections. Whether there is residual oil in the shale samples was checked by fluorescence observation of thin section through an Olympus BX-51 optical microscope equipped with a mercury lamp (USH102D), an excitation filter (UMNU2, 360–370 nm), and a longpass emission filter (LP400, >400 nm) [46].

Thin sections were also polished with argon ions by using a Leica EM TIC 3X with an acceleration voltage of 5 kV and a

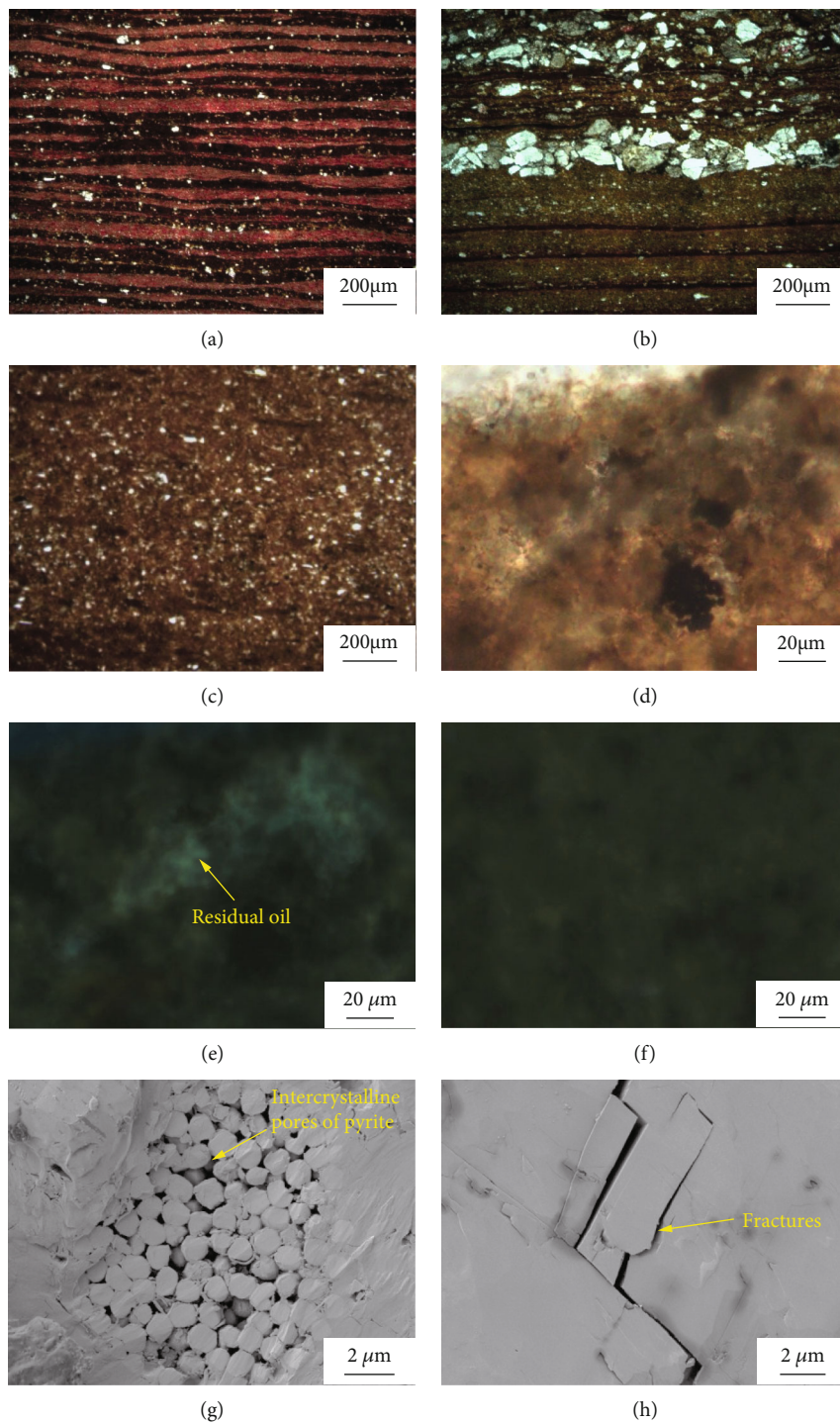
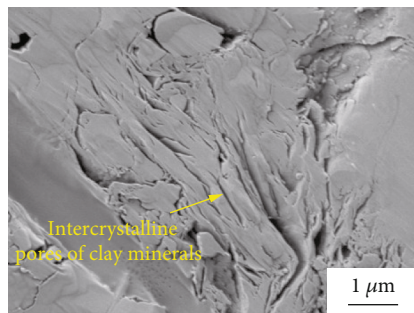


FIGURE 2: Continued.



(i)

FIGURE 2: Thin-section photomicrographs of the Es₄U shale samples in the Dongying Depression: (a) monopolarization photo of the interlaminated mudstone and calcite (dyed red by Alizarin red) in the shale sample DYS2 of the FS1 well at 3688.0 m (burial depth = 3679.4 m); (b) monopolarization photo of the silty sands in the laminated shale sample DYS12 of the T746 well at 3545.2 m (burial depth = 3538.7 m); (c) monopolarization photo of the massive structure in the mudstone sample DYS11 of the T720 well at 3677.3 m (burial depth = 3666.9 m); (d) monopolarization photo of the sample DYS9 of the L988 well at 3979.3 m (burial depth = 3966.1 m); (e) ultraviolet fluorescence photo of the original sample DYS9 showing the residual oil in the shale; (f) ultraviolet fluorescence photo of the Soxhlet-extracted sample showing most residual oil in the sample DYS9 was removed; (g) SEM image showing inkbottle-shaped pores between pyrites in the sample DYS10 of the L988 well at 4131.9 m (burial depth = 4117.1 m); (h) SEM image showing slit-shaped pores (fractures) in the sample DYS3 of the FS1 well at 3819.6 m (burial depth = 3810.9 m); (i) SEM image showing narrow slit-shaped pore between clay minerals in the sample DYS11.

current of 2 mA for 2 h to create an advanced smooth surface for electron microscope observation [47]. After coating with gold at a thickness of 2 nm on the surface, the thin sections were observed by an scanning electron microscope (SEM, Zeiss Crossbeam 540) with field emission gun [47]. The acceleration voltage was 1.2 kV.

3.4. X-Ray Diffraction, Insoluble Organic Carbon Content, and Vitrinite Reflectance Methods. One ground aliquot was tested for mineral composition by using a Rigaku D/max-2500PC X-ray diffractometer. The method and analytical conditions are documented in Zhang et al. [48]. Another ground aliquot of each sample was tested for insoluble organic carbon (IOC) [49]. IOC is the total organic carbon content of the samples after removal of soluble organic matter by Soxhlet extraction with DCM/MeOH. The Soxhlet-extracted samples finer than 100 mesh were analyzed for IOC with a LECO CS230 carbon/sulfur analyzer [44]. The kerogen in the other ground aliquot of each sample, separated from the shale sample and polished into a thin section, was tested using a J&M TIDAS MSP 400 microspectrophotometer for vitrinite reflectance (Ro) [50].

3.5. Low-Pressure Gas Adsorption. Low-pressure N₂ and CO₂ adsorption experiments were conducted in turn using a Micromeritics ASAP 2020 surface area analyzer. One of the Soxhlet-extracted aliquots was sieved to obtain particles between 60 and 80 mesh. Four grams of each sieved sample was degassed at 383.15 K in vacuum (pressure < 0.01 torr) for 20 h to remove residual volatile material before the measurements. The N₂ and CO₂ adsorption isotherms were measured at 77.35 K and 273.15 K, respectively. The tested ranges of relative equilibrium adsorption pressure (the ratio of adsorption equilibrium pressure to saturated vapor pressure, denoted by P/P_0) in N₂ and CO₂ adsorption experiments were set as 0.005–0.980 and 0.0005–0.0300, respectively.

Experiments were regarded to reach equilibration when the ratio of the pressure variation to the average pressure per time interval (60 s) was less than 0.01%. Using the density functional theory (DFT) [17, 51], the pore volumes (V) and pore size distributions (PSD) were analyzed from the N₂ and CO₂ adsorption data. Based on the international standard ISO 9277:2010 [52], the specific surface areas (S , ratio of the total surface of a sample to its mass) were calculated with the Brunauer-Emmett-Teller (BET) model [18] from the N₂ adsorption data under the relative equilibrium pressures ranging from 0.05 to 0.30. The average pore diameter was customarily calculated under the assumption that all pores are cylindrically shaped, equivalent to quadrupling the quotient of the N₂ adsorption pore volume and specific surface area [53].

The specific surface areas tested by CO₂ adsorption were not reported in this paper, due to large uncertainties in the area occupied by an adsorbed CO₂ molecule in the pores of molecular dimensions and the CO₂-measured monolayer capacity (the amount of gas molecules of a complete, close-packed monolayer covered on the solid surface) [24, 54].

3.6. Fractal Analysis. Fractal geometry has been applied to the irregularity of porous media [55]. In this study, the fractal FHH (Frenkel-Halsey-Hill) model [19] was utilized to analyze the fractal dimensions from the N₂ adsorption data. Based on the FHH model, there are two methods for calculation of fractal dimensions, using the van der Waals force regime or capillary condensation regime [56]. The method based on the capillary condensation regime is used in this paper, as it is suitable for fractal analysis of porous medium [57]. It can be described as follows:

$$\ln V = K \cdot \ln [\ln (P_0/P)] + C, \quad (1)$$

$$D = K + 3, \quad (2)$$

where K is the slope of the line of $\ln V$ vs. $\ln [\ln (P_0/P)]$, V is the adsorbed nitrogen volume (cm^3/g) at the equilibrium pressure P (Pa), P_0 (Pa) is the saturated vapor pressure of nitrogen at 77.35 K; C is a constant (dimensionless), and D (dimensionless) is the fractal dimension. The details are described in Yao et al. [57]. If a $\ln V$ vs. $\ln [\ln (P_0/P)]$ line shows two segments with different slopes, two kinds of fractal dimensions (D_1 and D_2) need to be calculated also using Equations (1) and (2). The fractal dimension D_1 , calculated with the adsorption data at $P/P_0 < 0.45$, reflects the complexity of pore surfaces, and D_2 , calculated with the adsorption data at $P/P_0 > 0.45$, represents the complexity of pore space structures [58].

3.7. Partial Least Square Regression. Partial least square regression (PLSR) was employed for establishing the relationships of pore property parameters with geological factors in this study. The pore properties, including micropore volume (V_{mic}), mesopore volume (V_{mes}), micromesopore volume ($V_{\text{mic-mes}}$, sum of V_{mic} and V_{mes}), specific surface area (S), average pore diameter (APD), and fractal dimensions (D_1 and D_2), with the appropriate forms (e.g., $\ln V_{\text{mes}}$ and $\ln S$; see Section 4.3 for details) used as dependent variables (responses) in the PLSR analyses, and the geological factors (mineralogy, IOC, burial depth, and $\ln \text{Ro}$) as independent variables (descriptors). Each variable (descriptor or response) was firstly standardized through subtracting its mean and dividing by its standard deviation. Using the PLSR analysis, orthogonal (uncorrelated to each other) components and linear combinations of descriptors are first set up:

$$F_i = \sum_{j=1}^n a_j x_j, \quad (3)$$

where F_i is the i th component ($i = 1, 2, \dots, m$), x_j is the j th standardized descriptor ($j = 1, 2, \dots, n$), and a_j is a coefficient. Then, the regression linear equation of a standardized response versus one or several orthogonal components is established:

$$y = \sum_{i=1}^m b_i F_i + C_1, \quad (4)$$

where y is the standardized response, b_j is a coefficient, and C_1 is a residual. The linear equation of a response versus descriptors is obtained from Equations (3) and (4):

$$y = \sum_{j=1}^n c_j x_j + C_2, \quad (5)$$

where c_j is a coefficient and C_2 is a residual. The components in PLSR are constructed through maximizing the information of the descriptors to efficiently predict the standardized responses [59]. The number of the components was determined by cross-validation (CV) [60]. The predicted value of the fitting model of an unstandardized response is equal to the mean plus the result of multiplying the predicted value

of a standardized response and standard deviation (i.e., inverse standardization). The means and standard deviations used for the inverse standardization are equal to those that were used for the standardization of the responses.

In PLSR analyses, the variable importance in projection (VIP) of a descriptor to a response is used to quantitatively describe the importance of a descriptor for a response and is computed from the weights of descriptors in components and correlation coefficients of descriptors with components [33, 61]. Larger VIP indicates more importance of a descriptor for a response. The descriptors with VIP values greater than one (the average of square VIP values) show the above-average importance for the prediction of the response and are considered to be the relatively important descriptors [33, 34].

4. Results and Discussion

4.1. Mineral Composition, Insoluble Organic Carbon, and Thermal Maturity. The results of the XRD analysis for the mineral composition are listed in Table S1. The mineral composition of massive mudstone samples is not evidently different from that of laminated shale samples. The samples from the top, middle, and bottom of the Es_4U shale do not show evident difference in mineral composition either. These samples are not statistically analyzed separately according to their texture types and locations in Es_4U . Clay minerals range from 6 wt% (sample DYS14) to 53 wt% (sample DYS12) with an average of 30.1 wt%. Quartz content varies from 3 wt% (sample DYS14) to 48 wt% (sample DYS13), and the average is 23.6 wt%. Feldspar content is between 4 wt% (sample DYS14) and 37 wt% (sample DYS3), and its average is 18.0 wt%. Calcite content varies widely from 3 wt% (sample DYS7) to 85 wt% (sample DYS14) with an average of 15.7 wt% and dolomite from 0 wt% (sample DYS2) to 54 wt% (sample DYS4) (10.4 wt% on average). The abundant carbonates arose from the high paleosalinity during the Es_4U deposition [42].

Carbonates are negatively related to clay minerals and quartz (Figures S2(a) and S2(b)). Comparison of brittle mineral (including carbonates, quartz, and feldspar) content of shales in different areas is helpful for shale evaluation. In this study, we compared the brittle mineral content of Es_4U shale in the Dongying Depression with those of Chang-7 shale in the Ordos Basin, from which commercial flows of oil have already been produced using horizontal drilling and hydraulic fracturing techniques. The content of brittle minerals in the Es_4U shale is 68.3 wt% on average (from 47 wt% to 94 wt%), higher than that of the lacustrine Chang-7 (49.1 wt%) [23]. Relatively high brittle mineral content in the Es_4U shale is favorable for hydraulic fracturing.

The other shales were studied with Soxhlet-unextracted samples (see Section 4.2.2 for details), such as the Bakken shale in the Williston Basin and Kong-2 shale in the Cangdong Depression [25–28]. The results about the pores in these studies cannot be compared with the pores in the Soxhlet-extracted samples in our study. We did not compare the brittle mineral content in the Soxhlet-unextracted

samples with those in the Soxhlet-extracted samples in our study, as this comparison is not helpful to study the pore properties of the Es₄U shale.

The IOC content of the Es₄U shale ranges from 1.14 wt% (sample DYS14) to 5.52 wt% (sample DYS8), with an average of 2.30 wt% (Table S1). The IOC content of the Es₄U shale is lower than that of the Chang-7 shale (average IOC = 6.93 wt% [23]) but higher than the TOC values of the lacustrine Qianfoya shale (on average 1.21 wt%) from which commercial flows of oil have also already been produced using horizontal drilling and hydraulic fracturing techniques [62]. The relatively abundant organic matter in the Es₄U shale in the Dongying Depression is a result of high paleoproductivity, warm humid climate, and deep-water environment during deposition [38].

The measured Ro values are listed in Table S1. Sample DYS13 was not tested due to insufficient vitrinite. Its Ro value was calculated by using the regression equation of the measured Ro values versus the burial depth (Figure S3). These measured and calculated Ro values vary from 0.60% (sample DYS14) to 1.29% (sample DYS7) (Table S1), with an average of 0.83%. This is very similar to Chang-7 shale whose Ro values vary from 0.64% to 1.34%, with an average of 0.88% [23]. Most Es₄U shale samples are in the oil window (Ro = 0.6 – 1.0%) and some in the gas condensate-wet gas window (Ro = 1.0 – 1.3%) according to U.S. EIA [63] and Dembicki [64].

4.2. Pore Properties. Before low-pressure gas adsorption experiments for shale pores, the effect of residual oil removal was checked with the thin sections of all original (Soxhlet-unextracted) and Soxhlet-extracted shale samples. Figures 2(d)–2(f) are the thin-section photomicrographs of the sample DYS9. Ultraviolet fluorescence photos indicate there is residual oil with yellow-green fluorescence in the unextracted sample (Figure 2(e)), but the residual oil is hardly observed in the Soxhlet-extracted sample (Figure 2(f)). Therefore, most of the residual oil in our samples was removed. Then, all of fifteen Soxhlet-extracted samples were analyzed using low pressure CO₂ and N₂ adsorption.

4.2.1. CO₂ and N₂ Adsorption Isotherms. The total adsorbed CO₂ volumes in the CO₂ adsorption experiments range from 0.15 cm³/g to 2.07 cm³/g at standard temperature and pressure (STP). The CO₂ adsorption isotherms of all samples are convex in shape when plotted against the relative pressure (P/P_0) (Figure S4) and belong to type I, which displays the features of micropores, according to the IUPAC (International Union of Pure and Applied Chemistry) classification [11]. In the N₂ adsorption experiments, the total adsorbed N₂ volumes vary from 2.12 cm³/g to 29.61 cm³/g at STP. The N₂ adsorption isotherms of all shale samples belong to type IV with hysteresis loops (Figure 3), showing the features of mesopores [11]. These hysteresis loops display rapid increases of desorption branches at relative pressures of about 0.45. These features of the CO₂ and N₂ adsorption isotherms indicate that the samples from the Es₄U all contain micro- and mesopores.

To further check the effect of the residual oil removal, three original samples (DYS3, DYS10, and DYS11) were also analyzed. Both total adsorbed CO₂ and N₂ volumes were evidently increased after the Soxhlet extraction (Figures 3 and S4). This indicates that the pore space occupied by residual oil is indeed released.

The N₂ hysteresis loops are categorized into types H1, H2, H3, and H4 according to the IUPAC classification [11]. For the Soxhlet-extracted samples from the Es₄U shale, all hysteresis loops are not similar to that of type H1, but those loops of five samples (33.3%, 5/15) are similar to type H2 (Table S2) whose desorption branch never plots parallel to the adsorption branch, with an inflexion at a relative pressure of 0.5, as shown in Figure 3(a). The pores in samples with the hysteresis loops of type H2 are mainly inkbottle-shaped (narrow necks and wide bodies) [11] and are usually intergranular, intercrystalline, and organic pores [24, 65]. Figure 2(g) shows the intercrystalline pores of pyrite, an example of an inkbottle-shaped pore. Type H3 loop is characterized by parallel adsorption-desorption branches above medium relative pressure (~0.5) and steeply increasing isotherms near the saturated vapor pressure (i.e., $P/P_0 = 1$) (Figure 3(b)). The pores in samples with the hysteresis loops of the type H3 loop are mainly slit-shaped [11]. The hysteresis loops of eight samples (53.3%, 8/15) are kin to type H3 (Table S2). The type H4 loop is similar to type H3 at low-medium relative pressure, but the isotherms increase slowly at high relative pressure (see Figure 3(c)). The pores in samples with the type H4 loop are mainly narrow slit-shaped [11]. The hysteresis loops of two samples (13.3%, 2/15) are similar to that of type H4 (Table S2). The (narrow) slit-shaped pores are usually the pores between plate-like particles (e.g., clay sheets) and fractures [24, 65]. Figures 2(h) and 2(i) show the fractures and pores between clay minerals, respectively. Fractures usually are wider than narrow slit-shaped pores between plate-like particles [40]. The samples mainly containing slit-shaped pores are significantly more than the narrow slit-shaped pore-dominated samples, probably because there develop massive fractures in the Es₄U shales. The hydrocarbon flow capability of different types of pores is discussed together with the fractal characteristics in Section 4.2.3.

4.2.2. Pore Parameters and Pore-Size Distribution. The pore parameters discussed here include micropore volume, mesopore volume, specific surface area, and average pore diameter. Mesopore volume, specific surface area, and average pore diameter were calculated using the methods introduced in Section 3.5 and data from N₂ and CO₂ adsorption experiments. The results are listed in Table S2.

The micro- and mesopore volumes and specific surface area for the three pairs of original and Soxhlet-extracted samples are listed in Table S2. Figure 4 shows the distribution curves of micropores (0.3–2 nm in diameter) and mesopores (2–50 nm in diameter) in the original and Soxhlet-extracted samples in Es₄U. The amount of the pores with the diameter less than 10 nm increase significantly. Therefore, the average pore diameter decreases after the Soxhlet extraction (Table S2).

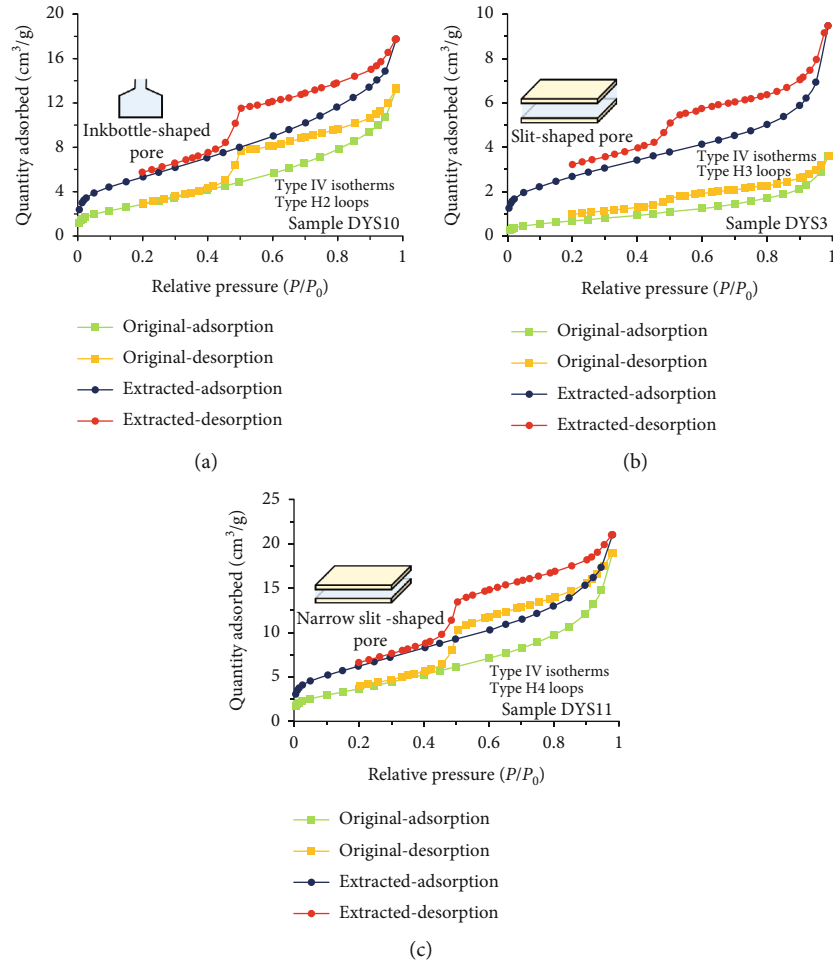


FIGURE 3: N_2 adsorption-desorption isotherms of original and Soxhlet-extracted samples from the Dongying Es_4U shale with typical types of hysteresis loops: (a) sample DYS10, (b) sample DYS3, and (c) sample DYS11.

For the Soxhlet-extracted shale samples in Es_4U , the micropore volumes (Table S2) vary from $0.0006 \text{ cm}^3/\text{g}$ (sample DYS14) to $0.0071 \text{ cm}^3/\text{g}$ (sample DYS6) ($0.0038 \text{ cm}^3/\text{g}$ on average). The mesopore volumes range from $0.0028 \text{ cm}^3/\text{g}$ (sample DYS14) to $0.0381 \text{ cm}^3/\text{g}$ (sample DYS15) with an average of $0.0181 \text{ cm}^3/\text{g}$. The mesopore volume is much higher than the micropore volume. The micromesopore volume (sum of micropore and mesopore volumes) varies from $0.003 \text{ cm}^3/\text{g}$ to $0.045 \text{ cm}^3/\text{g}$ with an average of $0.022 \text{ cm}^3/\text{g}$. The specific surface areas, tested by N_2 adsorption, range from $1.04 \text{ m}^2/\text{g}$ (sample DYS14) to $30.55 \text{ m}^2/\text{g}$ (sample DYS15) with an average of $12.56 \text{ m}^2/\text{g}$. The average pore diameters of the samples, obtained from the N_2 adsorption data, are between 4.97 nm (sample DYS1) and 12.46 nm (sample DYS13) with an average of 7.25 nm . The average pore diameter and specific surface areas were not calculated using the CO_2 adsorption data, due to their large uncertainties (see subsection 3.5).

To understand the pores in the Es_4U shale, the pore parameters of the Es_4U shale need to be compared with those of other shales. But in most of previous studies, the shale samples were analyzed without solvent extraction [24–28]. As a result, the pore data from these previous studies whose samples were not extracted cannot be compared with data

in this study, due to the pore parameter values before and after Soxhlet extraction change (e.g., samples DYS3, DYS10, and DYS11 in Table S2). However, the samples from the lacustrine Chang-7 shale in the Erdos Basin were analyzed using low-pressure N_2 and CO_2 adsorption methods, after the solvent extraction [23, 44]. The Chang-7 shale has the average micropore volume of $0.0035 \text{ cm}^3/\text{g}$, mesopore volume of $0.0113 \text{ cm}^3/\text{g}$, specific surface area of $4.99 \text{ m}^2/\text{g}$, and average pore diameter of 17.54 nm [23, 44]. Compared with the Soxhlet-extracted samples from the Chang-7 shale, the Es_4U shale has significantly higher micro- and mesopore volumes ($0.0038 \text{ cm}^3/\text{g}$ and $0.0181 \text{ cm}^3/\text{g}$ on average, respectively), but the average pore diameter is lower. The average oil saturation of mature Es_4U shale (45.8%) [41] is close to that in the Chang-7 shale (44.63%) [66]. The Es_4U shale is much thicker (see Section 3.1) and has more brittle minerals (see Section 4.1) than the Chang-7 shale (with thickness mostly lower than 100 m [67]). The roof and floor of the Chang-7 shale are tight sandstone [68], whereas the roof and floor of the Es_4U shale are mudstone, shale, and gypsum [38, 69]. All the characteristics of shale reservoirs except the average pore diameter display that the Dongying Es_4U shale is favorable for the development of shale oil and may achieve higher oil flow than the commercial oil flow

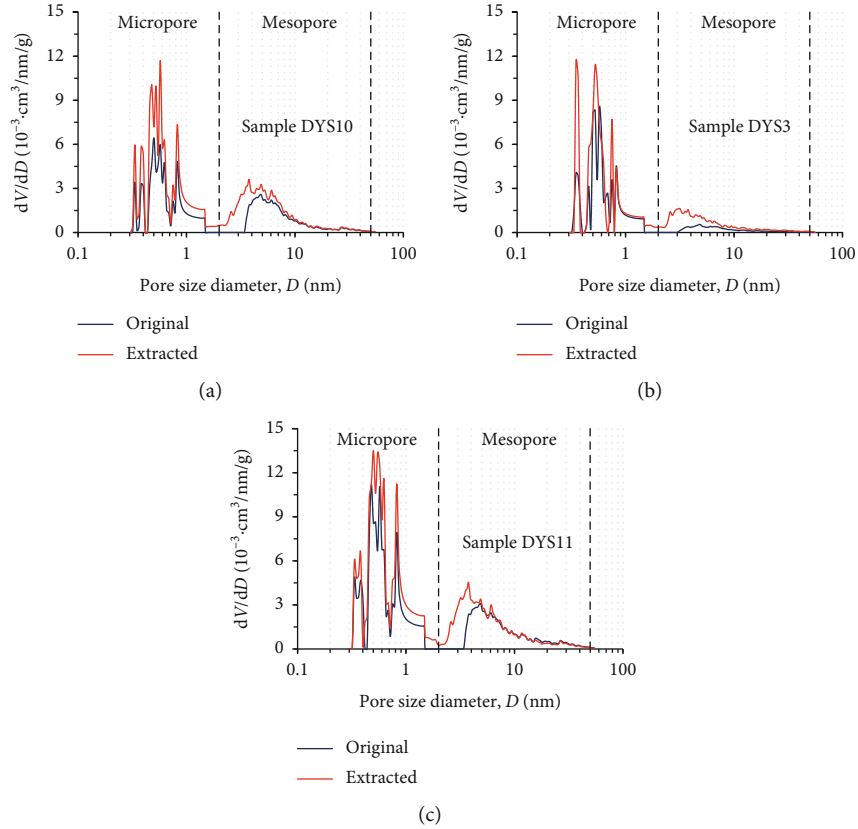


FIGURE 4: Pore size distribution of the original and Soxhlet-extracted samples from the Dongying Es₄U shale: (a) sample DYS10, (b) sample DYS3, and (c) sample DYS11. V : volume; D : diameter; dV/dD : the derivative of volume.

from the Chang-7 shale in the Ordos Basin. But the influence of the average pore diameter on the oil flow needs to be studied further.

4.2.3. Fractal Dimensions. The fractal dimension values of the Soxhlet-extracted samples from the Es₄U shale were calculated using the FHH method [19] applied to the N₂ adsorption data (see Section 3.6 for details). The $\ln V$ vs. $\ln [\ln (P_0/P)]$ lines of all samples show two segments divided at the relative pressure of 0.45 (as displayed in Figure 5(a)). The correlation coefficients (R) of these segments with different slopes are all higher than 0.97 (Table S2), indicating that the fractal characteristics are evident. From these two segments, two kinds of fractal dimensions (D_1 and D_2) were calculated for each sample. The values of the fractal dimension D_1 , calculated with the adsorption data at $P/P_0 < 0.45$ (region 1 in Figure 5(a)), range from 2.25 (sample DYS4) to 2.50 (sample DYS1) (2.42 on average). In region 1, the monolayer adsorption is dominant, and thus, the D_1 reflects the complexity of pore surfaces [58]. The D_2 values, calculated with the adsorption data at $P/P_0 > 0.45$ (region 2 in Figure 5(a)), are from 2.54 (sample DYS14) to 2.80 (sample DYS1) with an average of 2.71. In region 2, nitrogen molecules fill the pore space with multilayer adsorption, and thus, the D_2 reflects the complexity of pore space structures [58]. Higher D_1 and D_2 indicate that the samples have rougher pore surfaces and more complicated

pore space structures, respectively [24]. Therefore, pores with low D_1 and D_2 values are favorable for oil flow.

Figure 5(b) illustrates the average values of the fractal dimensions of the pores in the samples with the hysteresis loops of types H2, H3, and H4 that mainly contain inkbottle-, slit-, and narrow slit-shaped pores, respectively [11]. Slit-shaped pores with better openness have less curvature internal surface and simpler network of pores than inkbottle-shaped and narrow slit-shaped pores and thus have a higher hydrocarbon flow capacity [70]. In the Es₄U shale, the slit-shaped pore-dominated samples are the most (53.3%) and are favorable for hydrocarbon flow. The shale samples mainly containing slit-shaped pores have lower D_1 and D_2 values than those mainly containing inkbottle- and narrow slit-shaped pores (Figure 5(b)). One reason is that inkbottle-shaped pores have more complex pore surfaces and space structures than slit-shaped pores. The other reason is that although slit-shaped pores and narrow slit-shaped pores are similar in shape, the aggregation of small pores has more complicated pore surfaces and space structures than that of the relatively large pores. Therefore, inkbottle- and narrow slit-shaped pores (types H2 and H4) have higher values of fractal dimensions than slit-shaped pores and display certain similarities in fractal dimensions. These illustrate that the classification of the hysteresis loop types corresponds to the values of fractal dimensions and thus is reliable.

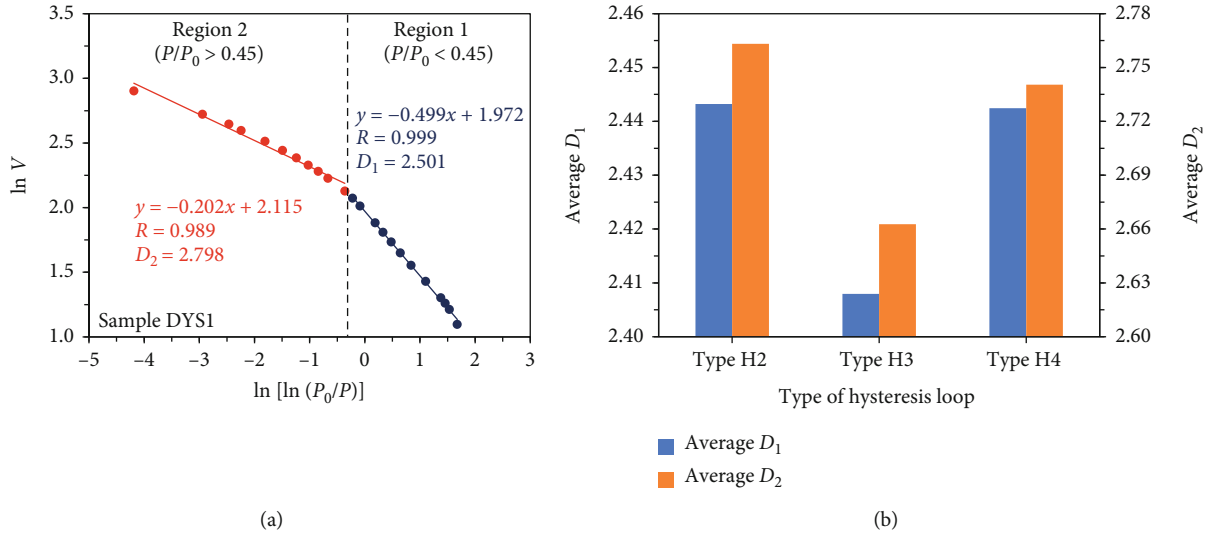


FIGURE 5: Plot of $\ln V$ vs. $\ln[\ln(P_0/P)]$ from the N_2 adsorption isotherm of the Soxhlet-extracted sample DYS1 (a) and average fractal dimensions of the pores in the Soxhlet-extracted samples with the hysteresis loops of types H2, H3, and H4 that mainly contain ink-bottle-, slit-, and narrow slit-shaped pores, respectively (b). The data are listed in Table S2.

4.2.4. Correlations between Pore Parameters. Figures 6(a) and S5(a) show that the average pore diameter is negatively correlated with both mesopore volume and specific surface area. Therefore, the quantity increase of relatively small pores in the shale is an important factor leading to the increases of mesopore volume and specific surface area in Figure 6(b). Furthermore, the samples with the hysteresis loops of types H2, H3, and H4 show the similar correlation relationships between the mesopore volume and the specific surface area (Figure 6(b)), suggesting that the influence of the geometrical shapes of the pores on the mesopore volume and specific surface area is relatively weak and masked by the strong influence of the pore quantity.

Figure 6(c) shows that the average pore diameter has a significantly negative correlation with fractal dimension D_2 ($R = 0.98$). The reason is that the aggregation of small pores has more complicated pore space structures than that of the relatively large pores. Moreover, small pores have more curvature internal surface. Therefore, the average pore diameter is also negatively related to the D_1 (Figure 6(d)), which is also supported by the positive correlation between D_1 and D_2 (Figure S5(b)). Because of the correlations between the average pore diameter, specific surface area, and mesopore volume (Figures 6(a), 6(b), and S5(a)), D_1 and D_2 are also positively correlated to the specific surface area and mesopore volume (Figures S5(c)–S5(f)). As mentioned above, the samples with the relatively high mesopore volume and specific surface area usually have higher percentage of relatively small pores and thus have higher D_1 and D_2 .

In summary, the increase of small pores in the shale leads to the increases of the pore volumes, specific surface area, and fractal dimensions (D_1 and D_2) and the decrease of the average pore diameter. But the correlations of D_1 with average pore diameter ($R = 0.52$, Figure 6(d)) and D_2 ($R = 0.52$, Figure S5(b)) are not very evident. This may suggest that the D_1 of the E_s4U shale is also affected by other factors, such as mineral composition, burial depth, and R_o (see below).

4.3. Geological Factors Controlling Shale Pores. We analyzed the relationships of geological factors with pore properties using cross-plots and univariate regression analyses. The pore properties are pore volume, diameter, specific surface area, and fractal dimensions. The geological factors (i.e., variables) include insoluble organic carbon (IOC), burial depth, vitrinite reflectance (R_o), and content of clay minerals, quartz, feldspar, carbonates (sum of calcite, dolomite, and siderite), calcite, and dolomite (Table S1). There are correlations between the pore parameters and geological factors, as shown in Figures 6(e)–6(h) and S5(g)–S5(l), but most of the correlation coefficients are low. Similar weak correlations have been found in many other shales [23, 25, 31].

In fact, pore formation is usually controlled or affected by multiple geological factors. Therefore, PLSR analyses (see Section 3.7 for details) need to be conducted to reveal multivariate correlations. Before the PLSR analyses, some pore parameters and geological factors were transformed into a logarithmic form in this work. Univariate regression analyses show that the logarithms of the pore volumes are correlated with the average pore diameter (Figure 6(a)) and fractal dimensions D_1 (Figure S5(d)) and D_2 (Figure S5(f)), as well as the clay minerals and carbonates (Figures 6(e), 6(f), S5(g), and S5(h)). Therefore, the pore volumes were transformed into the logarithmic form. The mesopore volume has remarkable positive correlation with the specific surface area (Figure 6(b)). The logarithm of the specific surface area was taken as a dependent variable. Considering that shale porosity (total pore volume \times apparent density) has an exponential relationship with the burial depth under equilibrium compaction [71] and that the log of R_o increases linearly with burial depth (Figure S3), we transformed R_o into the logarithmic form.

4.3.1. Geological Factors Controlling Micropore Volume. The log of the micropore volume ($\ln V_{mic}$) was set as a response (dependent variable) in the PLSR analysis. The descriptors

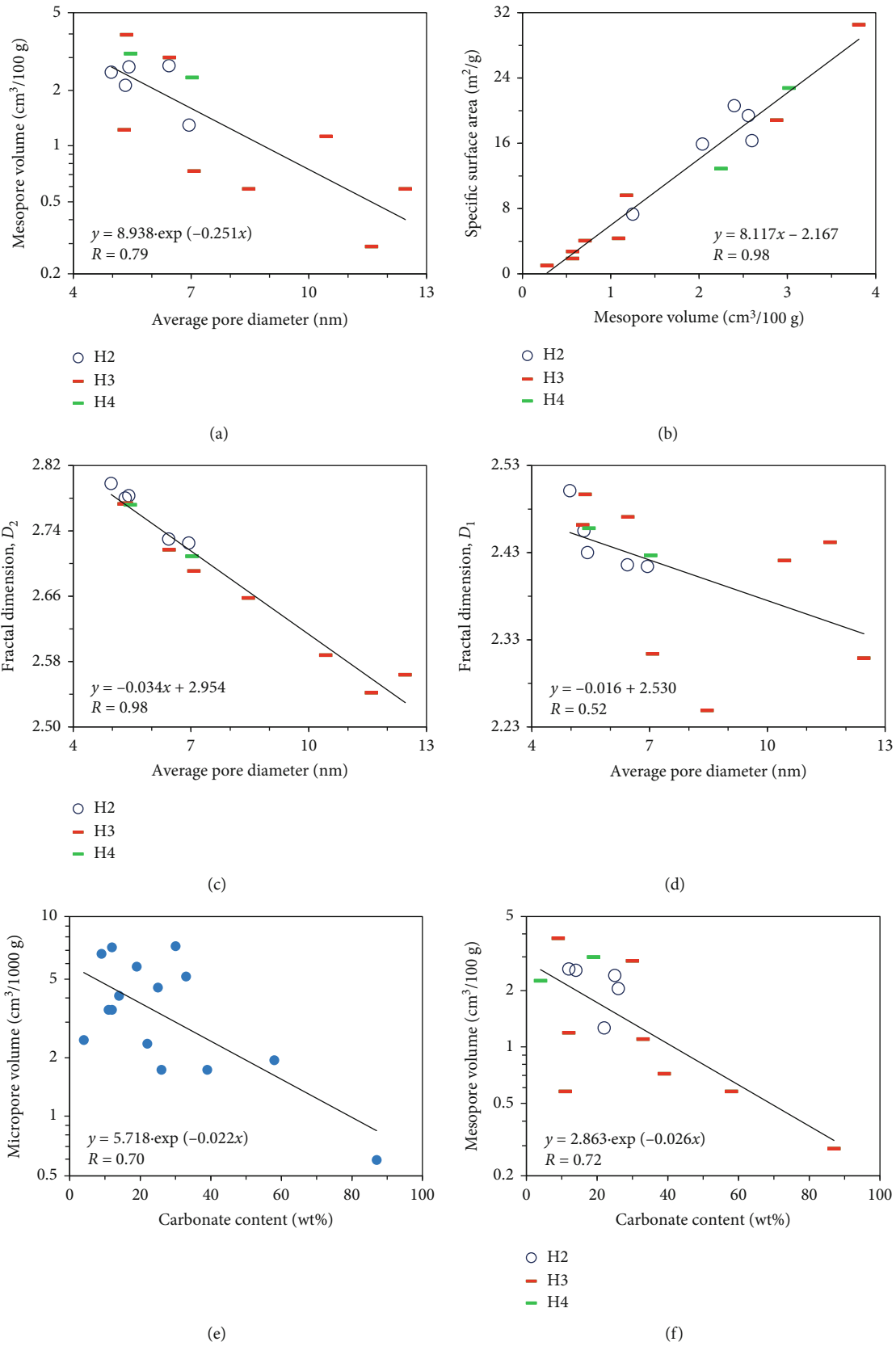


FIGURE 6: Continued.

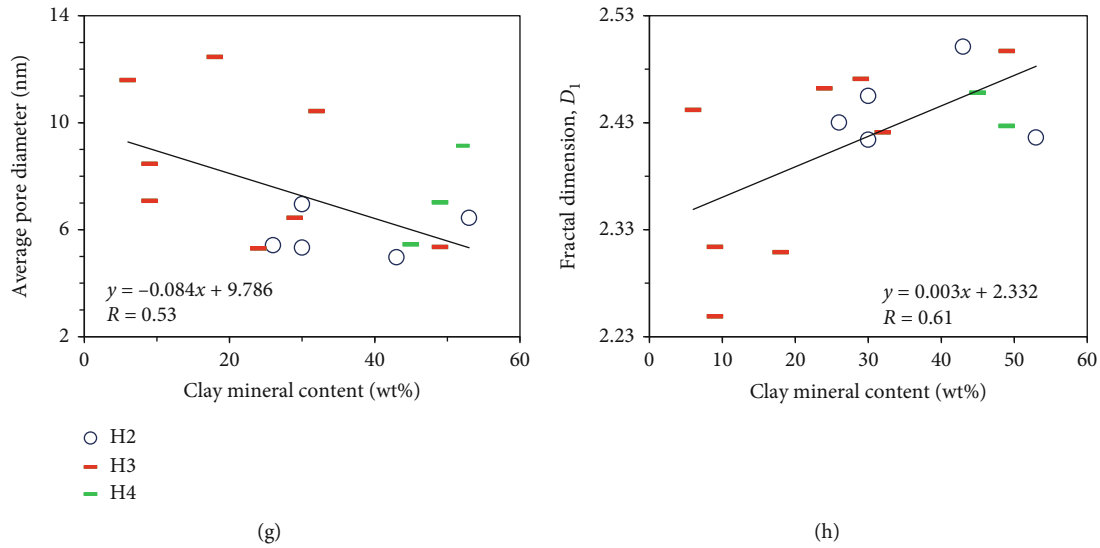


FIGURE 6: Correlation relationships between pore property parameters and between geological factors and pore property parameters for the Soxhlet-extracted samples from the Es₄U shale: (a–d) between pore parameters (mesopore volume, specific surface area, average pore diameter, and fractal dimensions D_1 and D_2); (e–h) between pore parameters (micro- and mesopore volumes, average pore diameter, and fractal dimension D_1) and mineral content (carbonates and clay minerals). The samples with the hysteresis loops of types H2, H3, and H4 mainly contain inkbottle-, slit-, and narrow slit-shaped pores, respectively. The data are listed in Tables S1 and S2.

(independent variables) include burial depth, mineral contents, IOC, and $\ln Ro$. The results of the PLSR analysis, including standardized coefficients (coefficients in regression equations obtained from standardized data) and VIP (variable importance in projection, see Section 3.7) values of the descriptors, are listed in Table S3. The predicted values of the PLSR fitting model of $\ln V_{mic}$ were computed through the inverse standardization (see Section 3.7) of the regression values obtained from the standardized coefficients of the multivariate regression equation in Table S3 and the standardized data. These standardized data were calculated from the data in Tables S1 and S2. The results are listed in Table S4. The relationship between the experimental and predicted values of the V_{mic} have a much higher correlation coefficient ($R = 0.91$, Figure 7(a)) than those of univariate regression analyses ($R = 0.69 - 0.70$, Figure 6(e) and S5(g)).

The standardized coefficients of the multivariate regression equation and VIP values (Figure 8(a) and Table S3) of the PLSR fitting model of $\ln V_{mic}$ indicate that the micropore volume is mainly correlated positively to clay minerals, quartz, and IOC but negatively to the variables of carbonates and calcite, with the VIP values higher than 1 (see Section 3.7 for details). Pyrite, feldspar, dolomite, burial depth, and $\ln Ro$ are subordinate variables in the multivariate regression equation with the VIP values lower than 1 (also see Section 3.7 for details). Micropores can be developed between clay minerals [72] and are affected by diagenesis although clay minerals are mainly terrigenous. From the early middle diagenetic stage, smectite illitization can increase intercrystalline pores [30, 73]. Besides, some pores along cleavage planes of clay minerals can be produced by the mineral distortion due to compaction [72]. Carbonates are unfavorable to pore development when carbonates fill pores [74]. At the middle diagenetic stage,

the acid fluid produced from the organic-rich shale in the Es₄U shale can dissolve some carbonates, but subsequently, the cementation of carbonates occurred when the solution became saturated again due to shale usually is a relatively closed system [30, 40]. Quartz grains probably play a supporting role in compaction or are negatively related to carbonates (Figure S2(b)). The positive correlation of micropore volume with IOC supports that some micropores can be produced from organic matters (mainly kerogen) with thermal maturation [31]. The eight Soxhlet-extracted samples from the Chang-7 lacustrine shale in the Ordos Basin also show a positive relation of the micropore volume with the IOC [23]. This correlation with IOC illustrates that organic pores are an important part of micropores. But, it is worth noting that for the Es₄U shale in the Dongying Depression, the VIP value of IOC (1.14) is evidently lower than those of the carbonates (1.50) and clay minerals (1.46), which indicate that the inorganic factors are more important for controlling micropores than IOC in the Es₄U shale.

4.3.2. Geological Factors Controlling Mesopore Volume and Specific Surface Area. Table S3 also shows the standardized coefficients and VIP values of the descriptors obtained from the PLSR analysis of the log of the mesopore volume ($\ln V_{mes}$). The predicted values of the PLSR fitting model of $\ln V_{mes}$ (Table S4) were calculated through the inverse standardization (see Section 3.7) of the regression values obtained from the standardized data and standardized coefficients of the multivariate regression equation in Table S3. The relationship between the experimental and predicted values of V_{mes} (Figure 7(b)) has a much higher correlation coefficient ($R = 0.94$) than those of univariate regression analyses ($R = 0.72 - 0.85$, Figures 6(f) and S5(h)). The VIP values and standardized coefficients of the

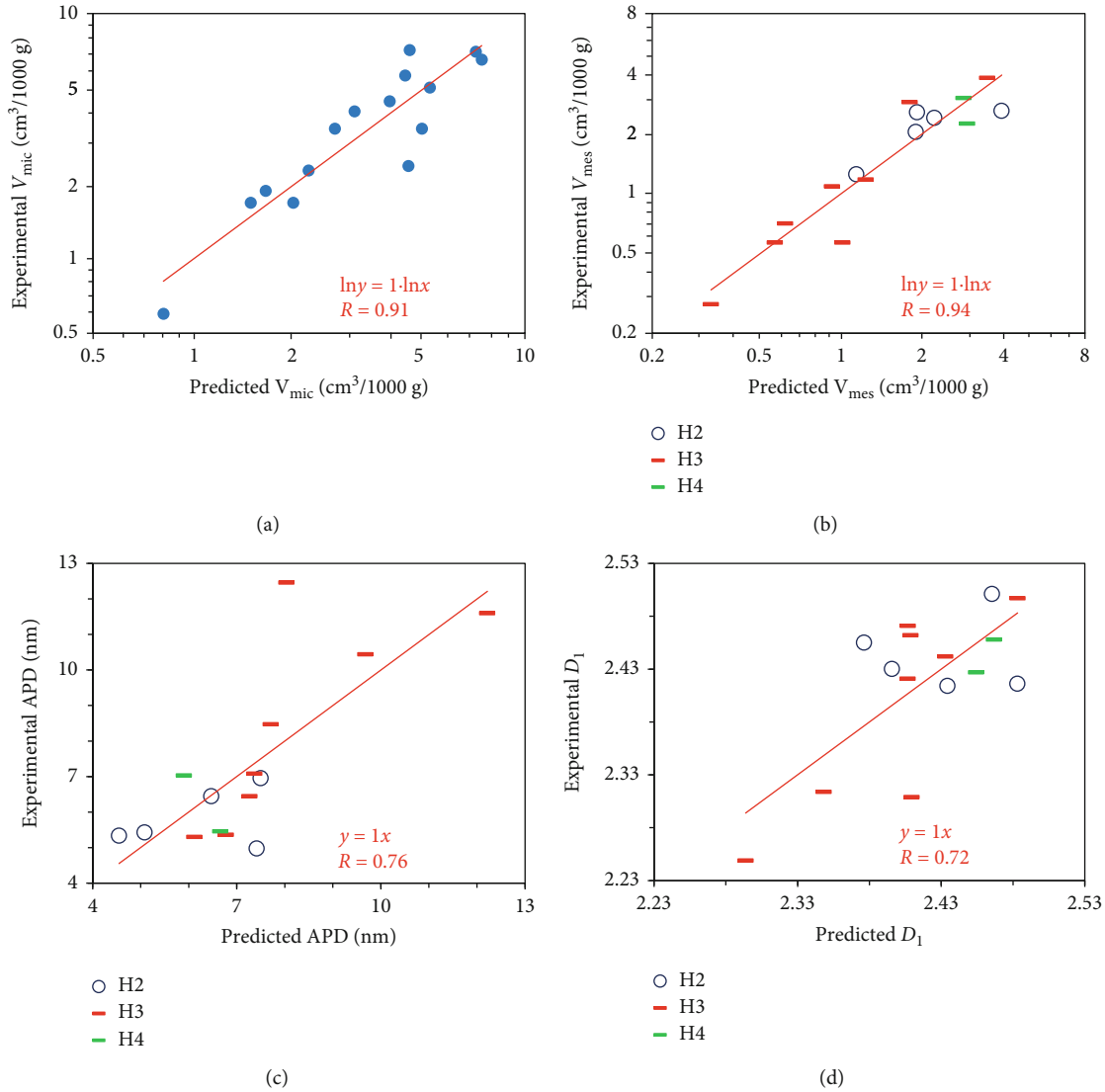


FIGURE 7: Correlation relationships between experimental and predicted pore property parameters (V_{mic} , V_{mes} , APD, and D_1) in the PLSR fitting models. V_{mic} : micropore volume; V_{mes} : mesopore volume; APD: average pore diameter; D_1 : fractal dimension D_1 . The samples with the hysteresis loops of types H2, H3, and H4 mainly contain inkbottle-, slit- and narrow slit-shaped pores, respectively. The data are listed in Tables S2 and S4.

multivariate regression equation (Figure 8(a) and Table S3) of the PLSR fitting model of $\ln V_{mes}$ indicate that the mesopore volume is mainly correlated positively to clay minerals and negatively to carbonates and calcite, with the VIP values higher than 1 (see Section 3.7 for details). This correlation with clay minerals and carbonates is similar to the model of $\ln V_{mic}$, but IOC is only a subordinate factor for mesopore volume (Figure 8(a)). The uncorrelated relationship with IOC coincides with the fact that the mesopores of the Es_4U samples with the hysteresis loops of types H3 and H4 are dominant (Figure 7(b)), which are mainly inorganic pores (see Section 4.2.1). The difference in the relationships of micropore and mesopore volumes with IOC suggests that organic pores are very subordinate in mesopores but are important in micropores. As mentioned above, carbonates are unfavorable to pore development

when they fill pores. Pores between clay minerals can be increased by diagenesis, such as smectite illitization and distortion of clay minerals due to compaction [30, 72, 73]. Therefore, the mesopore volume is mainly correlated to carbonates and clay minerals. Quartz, pyrite, burial depth, feldspar, dolomite, and $\ln Ro$ are all subordinate variables (factors) in the multivariate regression equation with the VIP values lower than 1 (see Section 3.7 for details), except for IOC.

In the Sichuan Basin and Williston Basin, the mesopore volumes of the Longmaxi (thirteen samples) and Bakken (eight samples) marine shales are all related to TOC content or Ro [25, 31]. These correlations are different from that for the Es_4U lacustrine shale in the Dongying Depression. One of the reasons probably is that terrigenous minerals in the lacustrine shale are more abundant than those in the marine

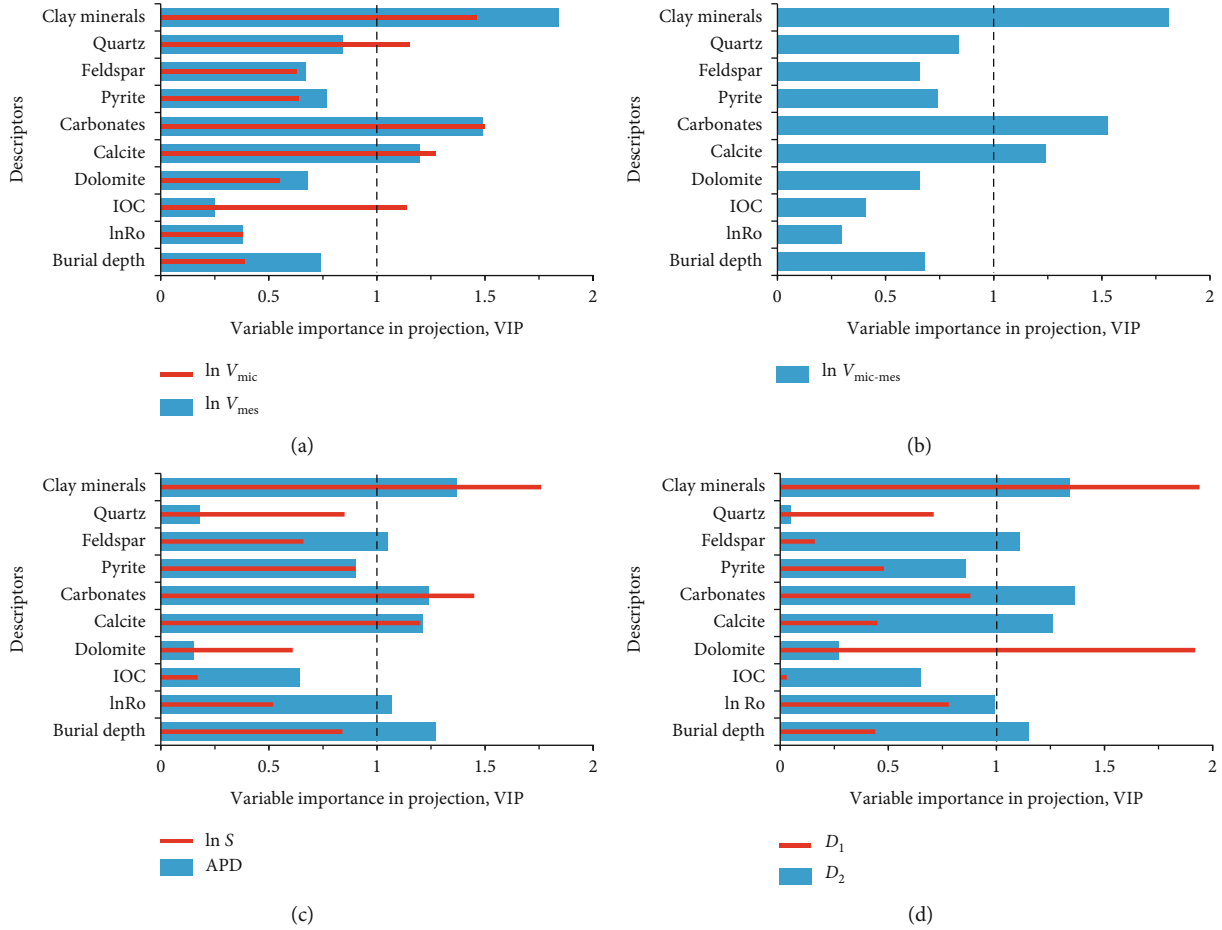


FIGURE 8: Variable importance in projection (VIP) of geological factors for the PLSR fitting models of pore properties. V_{mic} : micropore volume; V_{mes} : mesopore volume; $V_{mic-mes}$: micromesopore volume, sum of V_{mic} and V_{mes} ; S : specific surface area; APD: average pore diameter; D_1 and D_2 : fractal dimensions. The data are listed in Table S3.

shales so that the mineral composition of the lacustrine shale becomes more important for controlling pores than organic matter.

The log-transformed specific surface area ($\ln S$) and micromesopore volume ($\ln V_{mic-mes}$) were also analyzed with PLSR. The specific surface area and micromesopore volume all have significantly positive correlations with the mesopore volume (Figure 6(b) and S5(m)), due to the mesopore volume being related to the specific surface area (see Section 4.2.4 for details) and being much higher than the micropore volume (Table S2). The standardized coefficients of the multivariate regression equations in the PLSR fitting models of $\ln V_{mic-mes}$ and $\ln S$ are close to those in the $\ln V_{mes}$ model (Table S3). The clay minerals, carbonates, and calcite also have VIP values higher than 1 (Figures 8(b) and 8(c) and Table S3) and are the relatively important factors for characterizing $\ln V_{mic-mes}$ and $\ln S$ (see Section 3.7 for details). These features are the same as those in the PLSR fitting model of $\ln V_{mes}$.

In summary, the PLSR fitting models have higher correlation coefficients than those of univariate regression for analyzing the correlations of pore volumes with the multiple geological variables (factors), supporting that the pore vol-

umes are controlled or affected by multiple geological factors. The mesopore and micromesopore volumes as well as the specific surface area of the Dongying Es_4U shale are mainly controlled by the mineral composition that are determined by sedimentation and diagenesis. The micropore volume is mainly correlated positively to clay minerals, quartz, and IOC but negatively to the variables of carbonates and calcite. The difference in the relationships of micropore and mesopore volumes with IOC suggests that organic pores are very subordinate in mesopores but are important in micropores. The shale with high clay mineral and low carbonate content has more micromesopores for hydrocarbon storage but may be unfavorable for hydraulic fracturing. In contrast, although the pore volumes in the shale with abundant carbonates are low, the high content of carbonates facilitates fracture forming. Therefore, pore volumes and brittle minerals in the Es_4U shale need to be synthetically taken into account in the “sweet spot” selection and determination.

4.3.3. Geological Factors Controlling Geometrical Parameters of Mesopores. The geometrical parameters of pores including average pore diameter (APD) and fractal dimensions D_1 and D_2 were set as the responses for the PLSR analyses. The

standardized coefficients and VIP values of geological factors in the PLSR fitting model of the APD are listed in Table S3. The relationship between the experimental and predicted values of APD, computed through the inverse standardization of the regression values of the standardized data, have a higher correlation coefficient ($R = 0.76$, Figure 7(c)) than those of univariate regression analyses ($R = 0.42 - 0.53$, Figures 6(g) and S5(i)–S5(k)). APD is mainly correlated negatively to the clay minerals, feldspar, burial depth, and $\ln Ro$ and positively to the carbonates and calcite, based on the VIP values higher than 1 (Figure 8(c) and Table S3). The reason for the negative correlations of APD with clay minerals and feldspar is probably that mesopores between crystal palettes of clays and cleavages in feldspar grains are usually small. The average pore diameter decreases with the increasing burial depth, due to the compaction. As the burial depth is correlated to $\ln Ro$ (Figure S3), APD is also correlated negatively to $\ln Ro$.

The standardized coefficients and VIP values higher than 1 in the PLSR fitting model of D_2 (Figure 8(d) and Table S3) indicate that clay minerals, burial depth, carbonates, calcite, and feldspar are relatively important factors. $\ln Ro$ has a VIP value close to 1. If $\ln Ro$ is also considered as a relatively important variable, the main geological factors controlling D_2 are similar to those controlling APD. But the effects of these geological factors on the response (D_2 or APD) are the opposite, as APD has a negative correlation with D_2 (Figure 6(c)).

Figure 8(d) and Table S3 also show the standardized coefficients and VIP values of the PLSR analysis for D_1 . The relationship between the experimental and predicted values of the PLSR fitting model of D_1 has a higher correlation coefficient ($R = 0.72$, Figure 7(d)) than those of univariate regression analyses ($R = 0.61$, Figures 6(h) and S5(l)). The dolomite and clay minerals with VIP values higher than 1 (Figure 8(d) and Table S3) have relatively important influences on D_1 (see Section 3.7 for details). As mentioned above, the developed clay minerals lead to the increase of surface area and surface roughness of pores. But the dolomite in the Es_4U shale is mainly self-structured crystals with the flat surface [75]. Therefore, D_1 is mainly correlated positively to clay minerals and negatively to dolomite.

In summary, average pore diameter and fractal dimensions are also controlled by multiple geological factors and their PLSR fitting models have higher correlation coefficients than those of univariate regression. The average pore diameter and fractal dimension D_2 of the Es_4U shale are mainly controlled by multiple geological factors including clay minerals, feldspar, burial depth, $\ln Ro$, carbonates, and calcite, while the fractal dimension D_1 is mainly correlated positively to clay minerals and negatively to dolomite. The most important factor is the content of clay minerals that affect both pore size and fractal dimensions.

4.4. Pore Evolution. As inorganic pores are dominant in the Es_4U solvent-extracted samples, absolute pore volumes were directly used to analyze the pore evolution, instead of TOC- or IOC-normalized pore volumes [76]. The cross-plots of micropore and mesopore volumes, specific surface area,

average pore diameter, and fractal dimensions with Ro and burial depth are shown in Figure 9. The burial depth was calculated with the regression equation in Figure S3, so that the uniform cross-plots in Figure 9 can be drawn by using both Ro and burial depth.

Over the range of 0.6–1.3% Ro , Figures 9(a)–9(f) all display scatter features. However, the envelope curves of micropore and mesopore volumes as well as specific surface area and average pore diameter show a bimodal distribution with two peaks at 0.7% and 0.9% Ro (Figures 9(a)–9(d)). The bimodal distribution of envelope curves of fractal dimensions D_1 and D_2 are not remarkable. The mesopore volume, specific surface area, and average pore diameter of the samples with the hysteresis loop of types H3 and H4 are bimodal, but those of the samples with the hysteresis loop of type H2 are substantially unchanged with the increasing burial depth and Ro (Figures 9(b)–9(d)). Most organic pores are ink-bottle-shaped pores that mainly occur in the samples with the hysteresis loop of type H2. Therefore, the mesopore evolution is not mainly controlled by organic matter transformation. These phenomena are different from the pore evolution model reflected by the marine New Albany shale [77] showing the unimodal trend over the similar maturity range ($Ro = 0.55 - 1.15\%$). The unimodal trend was interpreted as the result of organic matter transformation [77]. The pore evolution model from the marine New Albany shale [77] cannot be used to interpret the pore evolution of the lacustrine Es_4U shale in the Dongying Depression. The main reasons probably are that the Es_4U shale is lacustrine and that organic pores in the Es_4U shale are not main contributors to the volume values of micro- and mesopores. In Figures 9(a)–9(c) the micro- and mesopore volumes as well as the specific surface area of the sample with the Ro value near 0.6% are very low, as are clay mineral and quartz content (Figures S6(a) and S6(b)). But carbonates comprise more than 80% (Figure S6(c)). The high carbonate content may lead to low pore volumes and specific surface areas. The average pore diameter is high, probably due to the fractures (i.e., slit-shaped pores) and less compaction.

When the thermal maturity reaches 0.7% Ro , the envelope curves of all micro- and mesopore volumes as well as specific surface area display peaks (Figures 9(a)–9(c)). At this stage, kerogen was generating hydrocarbons, and the clay minerals are dehydrating, resulting in high pressures which prompted the formation of fractures in the Es_4U shale [73, 78]. Simultaneously, organic acids were produced from the organic-rich shale which can dissolve carbonates and feldspar [78]. These processes probably result in the increases of pore volumes and specific surface area (Figures 9(a)–9(c)) and a high average pore diameter (Figure 9(d)). There are only the samples with the hysteresis loop of type H3 near the first peaks of the mesopore volume, specific surface area, and average pore diameter envelopes (Figures 9(b)–9(d)). Fractures may be developed in this type of samples [40] and are favorable for the development of shale oil. One of the reasons for the high average pore diameter and mesopore volume probably is that the shale is not completely compacted, and so high pore volumes can be retained. Another reason is that fewer carbonates and more clay minerals and

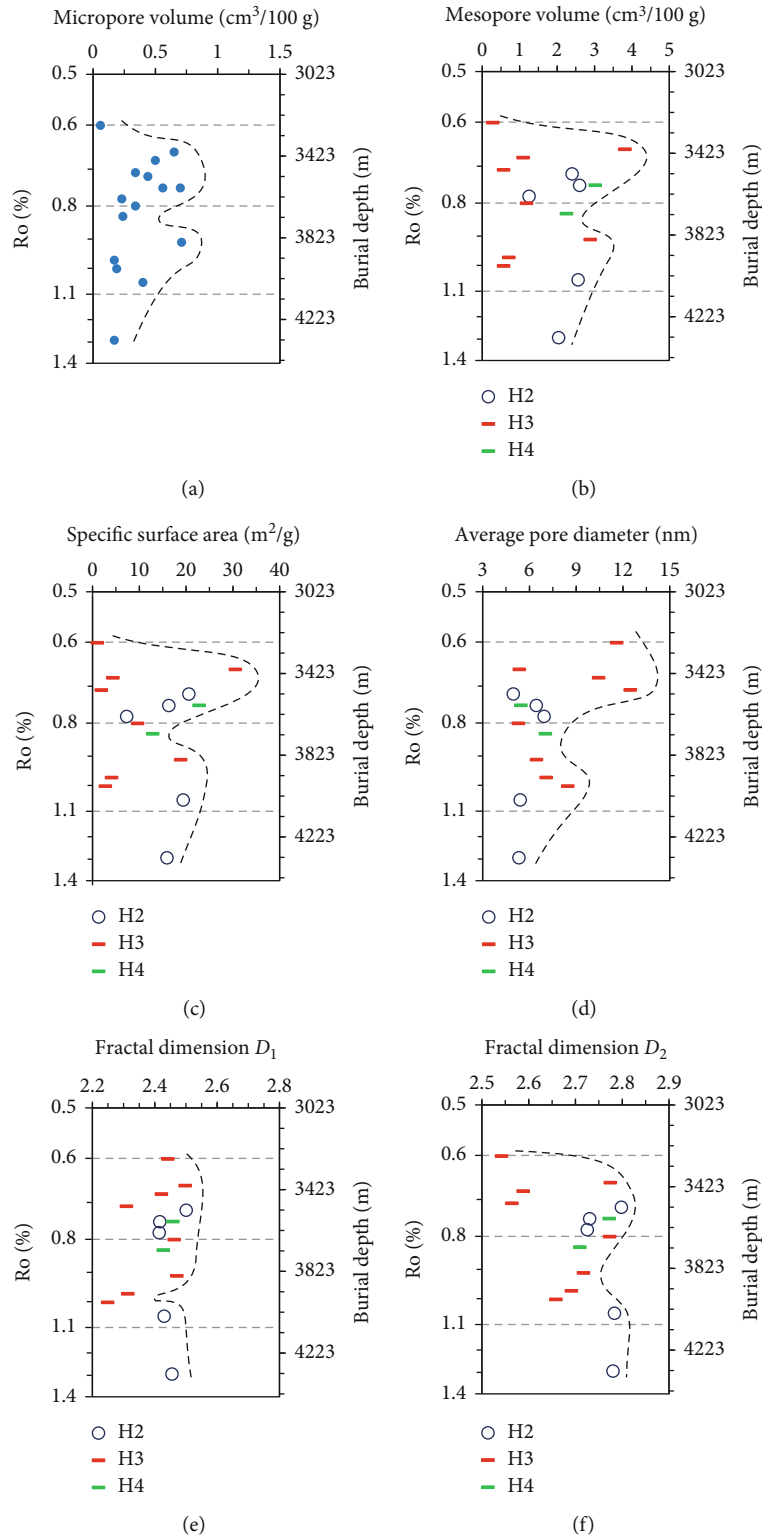


FIGURE 9: Cross-plots of main pore property parameters with Ro and burial depth for the Es₄U shale. The samples with the hysteresis loops of types H2, H3, and H4 mainly contain inkbottle-, slit-, and narrow slit-shaped pores, respectively. The data are listed in Tables S1 and S2.

quartz in these samples (Figure S6) are favorable for pore development. This is supported by the correlations that indicate micro- and mesopore volumes are all correlated positively to clay minerals and quartz and negatively to carbonates, as mentioned above.

Over the range of 0.85–0.90% Ro, the envelope curves for micro- and mesopore volumes, specific surface area, and average pore diameter, as well as carbonates, increase with increasing Ro (Figures 9(a)–9(d) and S6(c)). The high micro- and mesopore volumes as well as the specific surface area of

the sample at the second peak ($R_o = 0.9\%$) of these envelopes (Figures 9(a)–9(c)) may arise from the fracture formation after the carbonate cementation. This is supported by the high carbonate content and type H3 loop. The authigenic carbonates in the Es_4U shale of the Dongying Depression were mainly formed during the period of 28.1–4.6 Ma [30, 78]. The Bohai Bay Basin, including the Dongying Depression, was subjected to the tectonic movement since the Neogene (24.6 Ma to present), which may have resulted in the formation of fractures in the Es_4U shale with the relatively high content of carbonates [79–81]. The sample (No. DYS6) at the second peaks of the micro- and mesopore volumes as well as APD envelope curves has modest micropore volume ($0.036\text{ cm}^3/\text{g}$) and brittle mineral (71 wt%) and clay mineral content (29 wt%) (Tables S1 and S2) and may reflect a good shale reservoir for development.

Over the range from 0.95% to 1.3% R_o (3904–4335 m), the envelope curves for the micro- and mesopore volumes and specific surface as well as the average pore diameter of the Soxhlet-extracted samples from the lacustrine Es_4U shale all display the decreasing trends with the increasing R_o and burial depth (Figures 9(a)–9(d)). One reason probably is the strong compaction. With the increase of the depth, the carbonates and quartz in the shale become fewer but soft clay minerals increase (Figure S6). This variation in mineral composition makes the rocks easily compacted under a high pressure. In the process of compaction, pores between clay minerals must be reduced greatly, and some fractures in carbonates may also be reduced or closed.

5. Conclusions

In this study, low-pressure gas (N_2 and CO_2) adsorption methods were applied to shale samples from the upper part of the Sha-4 Member of the Paleogene Shahejie Formation (Es_4U) in the Dongying Depression, after the Soxhlet extraction of residual oil. On the basis of the results and discussion, the following conclusions have been reached:

- (1) The mesopore volume is much higher than the micropore volume in the Soxhlet-extracted samples. The Soxhlet-extracted samples of the Es_4U shale have an average micropore volume of $0.0038\text{ cm}^3/\text{g}$ and an average mesopore volume of $0.0182\text{ cm}^3/\text{g}$, higher than those of the Soxhlet-extracted samples of Chang-7 shale in the Ordos Basin. In the Es_4U shale, the samples with type H3 hysteresis loop make up the most (53.3%) in the studied samples. Furthermore, our samples from the Es_4U shale in the Dongying have an average brittle mineral (quartz, feldspar, and carbonates) content of 68.3 wt%, higher than that reported for the Chang-7 shale. Therefore, relatively high oil flow from the Es_4U shale may potentially be achieved through horizontal drilling and hydraulic fracturing. However, the relationships of micro- and mesopore volumes with brittle minerals in the Es_4U shale particularly need to be taken into account in the “sweet spot” selection and determination
- (2) PLSR (partial least square regression) analysis with VIP (variable importance in projection) evaluation is a powerful tool for the analyses of the main factors controlling shale pores. The PLSR results show that micro- and mesopore volumes, specific surface area, and the fractal dimension are mainly correlated positively to clay minerals and negatively to carbonate content. The increase in abundance of relatively small mesopores, related to clay minerals, is the main reason for high mesopore volume, with the high specific surface area and the fractal dimension reflecting the complexity of pore space structures. As a result, the samples with the relatively high mesopore volume for hydrocarbon storage have a high percentage of relatively small mesopores, complicated pore space structures, high content of clay minerals, and less carbonates. The shale represented by these samples may be unfavorable for shale oil development due to low oil flow, even if hydraulic fracturing is conducted. Therefore, the shale with the modest pore volumes and brittle and clay minerals may be conducive to the development of the Es_4U shale oil
- (3) Organic pores in the Es_4U shale mainly exist as micropores but are not a main contributor to mesopore volume. As the mesopore volume is much higher than the micropore volume, organic pores are not important for the storage space in the Soxhlet-extracted samples from the Es_4U shale. Probably because of this, the IOC (insoluble organic carbon) is not a main factor controlling micropores in the lacustrine shale in the Dongying Depression
- (4) Over the maturity range of 0.6–1.3% R_o , the envelope curves of the pore volumes, specific surface area, and average pore diameter with the maturity show bimodal distributions with two peaks at 0.7% and 0.9% R_o . The samples at the first peak (0.7% R_o) have high pore volumes, specific surface area, and diameters with more clay minerals and less carbonates. The sample DYS6 from well L672 at the second peak ($R_o = 0.9\%$) has relatively high micropore volume ($0.036\text{ cm}^3/\text{g}$), specific surface area ($18.85\text{ m}^2/\text{g}$), and average pore diameter (6.45 nm) with modest brittle mineral (71 wt%) and clay mineral content (29 wt%) and may reflect the shale favorable for shale oil development

Data Availability

The experimental data used to support the findings of this study are included within the manuscript and the supplementary materials.

Conflicts of Interest

The authors declare that there are no conflicts of interest regarding the publication of this paper.

Acknowledgments

We would like to express our gratitude to Messieurs Guanghua Jia, Zhenyi Li, and Juyuan Li in sampling and data retrieval as well as Dr. Zhongming Du and Jialong Liu in SEM observation. This work was supported by the Major Project of Institute of Geology and Geophysics, CAS (grant number IGGCAS-201903) and the Strategic Priority Research Program of the Chinese Academy of Sciences (grant number XDB10020203).

Supplementary Materials

Contain Tables S1–S4 and Figures S1–S6, showing the pore properties, mineral composition, insoluble organic carbon (IOC), vitrinite reflectance (Ro), and results of correlation analyses as well as the integrated column chart of a sampling well. (*Supplementary Materials*)

References

- [1] International Energy Agency, *Oil 2019*, Paris, 2019, <https://www.iea.org/reports/oil-2019>.
- [2] W. L. Auping, E. Pruyt, S. de Jong, and J. H. Kwakkel, “The geopolitical impact of the shale revolution: exploring consequences on energy prices and rentier states,” *Energy Policy*, vol. 98, pp. 390–399, 2016.
- [3] Y. Li, D. Zhang, J. Zhang et al., *Investigation and Evaluation of Shale Gas Resource Potential and Optimization for Selecting Exploration Favorable Zones in China*, Science Press, Beijing, 2016.
- [4] S. P. Ojha, S. Misra, A. Tinni, C. Sondergeld, and C. Rai, “Pore connectivity and pore size distribution estimates for Wolfcamp and Eagle Ford shale samples from oil, gas and condensate windows using adsorption-desorption measurements,” *Journal of Petroleum Science and Engineering*, vol. 158, pp. 454–468, 2017.
- [5] R. G. Loucks and S. C. Ruppel, “Mississippian Barnett shale: lithofacies and depositional setting of a deep-water shale-gas succession in the Fort Worth basin, Texas,” *American Association of Petroleum Geologists Bulletin*, vol. 91, no. 4, pp. 579–601, 2007.
- [6] M. Godec, G. Koperna, R. Petrusak, and A. Oudinot, “Potential for enhanced gas recovery and CO₂ storage in the Marcellus shale in the eastern United States,” *International Journal of Coal Geology*, vol. 118, pp. 95–104, 2013.
- [7] R. Heller and M. Zoback, “Adsorption of methane and carbon dioxide on gas shale and pure mineral samples,” *Journal of Unconventional Oil and Gas Resources*, vol. 8, no. C, pp. 14–24, 2014.
- [8] K. Zhang, J. Peng, X. Wang et al., “Effect of organic maturity on shale gas genesis and pores development: a case study on marine shale in the upper Yangtze region, South China,” *Open Geosciences*, vol. 12, no. 1, pp. 1617–1629, 2020.
- [9] K. Zhang, C. Jia, Y. Song et al., “Analysis of lower Cambrian shale gas composition, source and accumulation pattern in different tectonic backgrounds: a case study of Weiyuan block in the upper Yangtze region and Xiuyu basin in the lower Yangtze region,” *Fuel*, vol. 263, article 115978, 2020.
- [10] F. Yang, Z. Ning, Q. Wang, R. Zhang, and B. M. Krooss, “Pore structure characteristics of lower Silurian shales in the southern Sichuan basin, China: insights to pore development and gas storage mechanism,” *International Journal of Coal Geology*, vol. 156, pp. 12–24, 2016.
- [11] K. S. W. Sing, D. H. Everett, R. A. W. Haul et al., “Reporting physisorption data for gas/solid systems with special reference to the determination of surface area and porosity (recommendations 1984),” *Pure and Applied Chemistry*, vol. 57, no. 4, pp. 603–619, 1985.
- [12] K. Liu, M. Ostadhassan, L. Sun et al., “A comprehensive pore structure study of the Bakken shale with SANS, N₂ adsorption and mercury intrusion,” *Fuel*, vol. 245, pp. 274–285, 2019.
- [13] Z. Li, X. Shen, Z. Qi, and R. Hu, “Study on the pore structure and fractal characteristics of marine and continental shale based on mercury porosimetry, N₂ adsorption and NMR methods,” *Journal of Natural Gas Science and Engineering*, vol. 53, pp. 12–21, 2018.
- [14] C. R. Clarkson, N. Solano, R. M. Bustin et al., “Pore structure characterization of North American shale gas reservoirs using USANS/SANS, gas adsorption, and mercury intrusion,” *Fuel*, vol. 103, pp. 606–616, 2013.
- [15] C. Huang, Y. Ju, H. Zhu et al., “Nano-scale pore structure and fractal dimension of Longmaxi shale in the upper Yangtze region, South China: a case study of the Laifeng–Xianfeng block using HIM and N₂ adsorption,” *Minerals*, vol. 9, no. 6, p. 356, 2019.
- [16] S. Rani, B. K. Prusty, and S. K. Pal, “Characterization of shales from Damodar valley coalfields for CH₄ recovery and CO₂ sequestration,” *Environmental Technology and Innovation*, vol. 18, p. 100739, 2020.
- [17] D. D. Do and H. D. Do, “Pore characterization of carbonaceous materials by DFT and GCMC simulations: a review,” *Adsorption Science and Technology*, vol. 21, no. 5, pp. 389–423, 2003.
- [18] S. Brunauer, P. H. Emmett, and E. Teller, “Adsorption of gases in multimolecular layers,” *Journal of the American Chemical Society*, vol. 60, no. 2, pp. 309–319, 1938.
- [19] P. Pfeifer, M. Obert, and M. W. Cole, “Fractal BET and FHH theories of adsorption: a comparative study,” *Proceedings of the Royal Society of London. A. Mathematical and Physical Sciences*, vol. 423, no. 1864, pp. 169–188, 1989.
- [20] H. Han, Y. Cao, S. J. Chen et al., “Influence of particle size on gas-adsorption experiments of shales: an example from a Longmaxi shale sample from the Sichuan basin, China,” *Fuel*, vol. 186, pp. 750–757, 2016.
- [21] J. J. Valenza II, N. Drenzek, F. Marques, M. Pagels, and M. Mastalerz, “Geochemical controls on shale microstructure,” *Geology*, vol. 41, no. 5, pp. 611–614, 2013.
- [22] X. Li, J. Cai, H. Liu, X. Zhu, Z. Li, and J. Liu, “Characterization of shale pore structure by successive pretreatments and its significance,” *Fuel*, vol. 269, article 117412, 2020.
- [23] H. Han, P. Liu, Z. Ding et al., “The influence of extractable organic matter on pore development in the late Triassic Chang 7 lacustrine shales, Yanchang formation, Ordos basin, China,” *Acta Geologica Sinica*, vol. 92, no. 4, pp. 1508–1522, 2018.
- [24] Y. Li, Z. Wang, Z. Pan, X. Niu, Y. Yu, and S. Meng, “Pore structure and its fractal dimensions of transitional shale: a cross-section from east margin of the Ordos basin, China,” *Fuel*, vol. 241, pp. 417–431, 2019.
- [25] Y. Liu, B. Shen, Z. Yang, and P. Zhao, “Pore structure characterization and the controlling factors of the Bakken formation,” *Energies*, vol. 11, no. 11, article 2879, 2018.

- [26] K. Chen, X. Liu, J. Liu, C. Zhang, M. Guan, and S. Zhou, "Lithofacies and pore characterization of continental shale in the second member of the Kongdian formation in the Cangdong sag, Bohai Bay basin, China," *Journal of Petroleum Science and Engineering*, vol. 177, pp. 154–166, 2019.
- [27] K. Liu, M. Ostadhassan, J. Zhou, T. Gentzis, and R. Rezaee, "Nanoscale pore structure characterization of the Bakken shale in the USA," *Fuel*, vol. 209, pp. 567–578, 2017.
- [28] K. Liu, L. Wang, M. Ostadhassan, J. Zou, B. Bubach, and R. Rezaee, "Nanopore structure comparison between shale oil and shale gas: examples from the Bakken and Longmaxi formations," *Petroleum Science*, vol. 16, no. 1, pp. 77–93, 2019.
- [29] Z. Chen, W. Jiang, L. Zhang, and M. Zha, "Organic matter, mineral composition, pore size, and gas sorption capacity of lacustrine mudstones: implications for the shale oil and gas exploration in the Dongying depression, eastern China," *AAPG Bulletin*, vol. 102, no. 8, pp. 1565–1600, 2018.
- [30] H. Liu, S. Zhang, G. Song et al., "Effect of shale diagenesis on pores and storage capacity in the Paleogene Shahejie formation, Dongying depression, Bohai Bay basin, east China," *Marine and Petroleum Geology*, vol. 103, pp. 738–752, 2019.
- [31] X. Shao, X. Pang, Q. Li et al., "Pore structure and fractal characteristics of organic-rich shales: a case study of the lower Silurian Longmaxi shales in the Sichuan basin, SW China," *Marine and Petroleum Geology*, vol. 80, pp. 192–202, 2017.
- [32] S. Wold, M. Sjostrom, and L. Eriksson, "PLS-regression?: a basic tool of chemometrics," *Chemometrics and Intelligent Laboratory Systems*, vol. 58, no. 2, pp. 109–130, 2001.
- [33] H. Wang, Z. Wu, and J. Meng, *Partial Least-Squares Regression—Linear and Nonlinear Methods*, National Defense Industry Press, Beijing, 2006.
- [34] S. Favilla, C. Durante, M. L. Vigni, and M. Cocchi, "Assessing feature relevance in NPLS models by VIP," *Chemometrics and Intelligent Laboratory Systems*, vol. 129, pp. 76–86, 2013.
- [35] L. Zhang, G. Bai, and Y. Zhao, "Data-processing and recognition of seepage and microseepage anomalies of acid-extractable hydrocarbons in the south slope of the Dongying depression, eastern China," *Marine and Petroleum Geology*, vol. 57, pp. 385–402, 2014.
- [36] Z. Li, X. Wang, R. Zhu, and Z. Zhai, "Geochemical evaluation of shale oil in lower Es3 and upper Es4 in Jiyang depression," *Xinjiang Petroleum Geology*, vol. 36, no. 5, pp. 510–514, 2015.
- [37] S. Zhang, L. Zhang, Z. Li, and Y. Hao, "Formation conditions of Paleogene shale oil and gas in Jiyang depression," *Petroleum Geology and Recovery Efficiency*, vol. 19, no. 6, pp. 1–5, 111, 2012.
- [38] C. Liang, Y. Cao, Z. Jiang, J. Wu, S. Guoqi, and Y. Wang, "Shale oil potential of lacustrine black shale in the Eocene Dongying depression: implications for geochemistry and reservoir characteristics," *AAPG Bulletin*, vol. 101, no. 11, pp. 1835–1858, 2017.
- [39] L. Liu, X. Shang, Y. Wang et al., "Controlling factors on oil and gas accumulation and accumulation modes of the Paleogene red bed in the south slope of the Dongying depression, China," *Energy Exploration & Exploitation*, vol. 30, no. 6, pp. 941–956, 2012.
- [40] H. Liu, S. Zhang, Y. Bao, Z. Fang, S. Yao, and Y. Wang, "Geological characteristics and effectiveness of the shale oil reservoir in Dongying sag," *Oil and Gas Geology*, vol. 40, no. 3, pp. 512–523, 2019.
- [41] L. Zhang, Y. Bao, J. Li, Z. Li, R. Zhu, and J. Zhang, "Movability of lacustrine shale oil: a case study of Dongying sag, Jiyang depression, Bohai Bay basin," *Petroleum Exploration and Development*, vol. 41, no. 6, pp. 703–711, 2014.
- [42] H. Liu, S. Zhang, G. Song et al., "A discussion on the origin of shale reservoir inter-laminar fractures in the Shahejie formation of Paleogene, Dongying depression," *Journal of Earth Science*, vol. 28, no. 6, pp. 1064–1077, 2017.
- [43] L. Zhang, Z. Li, J. Li, R. Zhu, and X. Sun, "Feasibility analysis of existing recoverable oil and gas resource in the Palaeogene shale of Dongying depression," *Natural Gas Geoscience*, vol. 23, no. 1, pp. 1–13, 2012.
- [44] H. Han, Z. Ding, C. Dong et al., "Fractal characteristics of bulk-mudrock, washed, and kerogen samples of Chang 7 member mudrocks from the Ordos basin, China," *Journal of Petroleum Science and Engineering*, vol. 170, pp. 592–606, 2018.
- [45] W. Kuang, M. Lu, I. Yeboah et al., "A comprehensive kinetics study on non-isothermal pyrolysis of kerogen from Green River oil shale," *Chemical Engineering Journal*, vol. 377, article 120275, 2019.
- [46] X. Zhao, L. Zhang, F. Jin et al., "Hydrocarbon charging and accumulation history in the Niudong buried hill field in the Baxian depression, eastern China," *Marine and Petroleum Geology*, vol. 88, pp. 343–358, 2017.
- [47] J. Wu, Y. Yuan, S. Niu, X. Wei, and J. Yang, "Multiscale characterization of pore structure and connectivity of Wufeng-Longmaxi shale in Sichuan basin, China," *Marine and Petroleum Geology*, vol. 120, article 104514, 2020.
- [48] L. Zhang, Z. Chen, Z. Li et al., "Structural features and genesis of microscopic pores in lacustrine shale in an oil window: a case study of the Dongying depression," *AAPG Bulletin*, vol. 103, no. 8, pp. 1889–1924, 2019.
- [49] C. I. Fialips, B. Labeyrie, V. Burg et al., "Quantitative mineralogy of Vaca Muerta and alum shales from core chips and drill cuttings by calibrated SEM-EDS mineralogical mapping," in *Proceedings of the 6th Unconventional Resources Technology Conference*, pp. 4132–4144, Houston, Texas, July 2018.
- [50] F. Wang and S. Guo, "Influential factors and model of shale pore evolution: a case study of a continental shale from the Ordos basin," *Marine and Petroleum Geology*, vol. 102, pp. 271–282, 2019.
- [51] A. V. Neimark, Y. Lin, P. I. Ravikovitch, and M. Thommes, "Quenched solid density functional theory and pore size analysis of micro-mesoporous carbons," *Carbon*, vol. 47, no. 7, pp. 1617–1628, 2009.
- [52] IOS 9277, *Determination of the Specific Surface Area of Solids by Gas Adsorption — BET Method*, International Organization for Standardization, 2010.
- [53] J. H. De Boer, "The shape of capillaries," in *The Structure and Properties of Porous Materials*, D. H. Everett and F. S. Stone, Eds., pp. 68–92, Butterworths, London, 1958.
- [54] O. P. Mahajan, "CO₂ surface area of coals: the 25-year paradox," *Carbon*, vol. 29, no. 6, pp. 735–742, 1991.
- [55] C. E. Krohn, "Fractal measurements of sandstones, shales, and carbonates," *Journal of Geophysical Research*, vol. 93, no. B4, pp. 3297–3305, 1988.
- [56] P. Pfeifer, Y. J. Wu, M. W. Cole, and J. Krim, "Multilayer adsorption on a fractally rough surface," *Physical Review Letters*, vol. 62, no. 17, pp. 1997–2000, 1989.
- [57] Y. Yao, D. Liu, D. Tang, S. Tang, and W. Huang, "Fractal characterization of adsorption-pores of coals from North China: an investigation on CH₄ adsorption capacity of coals," *International Journal of Coal Geology*, vol. 73, no. 1, pp. 27–42, 2008.

- [58] F. Jiang, D. Chen, J. Chen et al., "Fractal analysis of shale pore structure of continental gas shale reservoir in the Ordos basin, NW China," *Energy and Fuels*, vol. 30, no. 6, pp. 4676–4689, 2016.
- [59] P. Leflaive, G. D. Pirngruber, A. Faraj, P. Martin, G. V. Baron, and J. F. M. Denayer, "Statistical analysis and partial least square regression as new tools for modelling and understanding the adsorption properties of zeolites," *Microporous and Mesoporous Materials*, vol. 132, no. 1–2, pp. 246–257, 2010.
- [60] S. Rännar, P. Geladi, F. Lindgren, and S. Wold, "A PLS kernel algorithm for data sets with many variables and few objects. Part II: cross-validation, missing data and examples," *Journal of Chemometrics*, vol. 9, no. 6, pp. 459–470, 1995.
- [61] G. Ji, Z. Yang, and W. You, "PLS-based gene selection and identification of tumor-specific genes," *IEEE Transactions on Systems, Man and Cybernetics Part C: Applications and Reviews*, vol. 41, no. 6, pp. 830–841, 2011.
- [62] Q. Wang, R. Liu, X. Wei, K. Ni, and H. Gao, "Geologic condition of shale gas accumulation in continental facies and main controlling factors of enrichment and high production: taking Yuanba district as an example," *Fault-Block Oil & Gas Field*, vol. 20, no. 6, pp. 698–703, 2013.
- [63] US Energy Information Administration (EIA), *Technically Recoverable Shale Oil and Shale Gas Resources: An Assessment of 137 Shale Formations in 41 Countries Outside the United States*, 2013, <https://www.eia.gov/analysis/studies/worldshalegas/pdf/overview.pdf>.
- [64] H. Dembicki Jr., "Three common source rock evaluation errors made by geologists during prospect or play appraisals," *AAPG Bulletin*, vol. 93, no. 3, pp. 341–356, 2009.
- [65] C. Yang, J. Zhang, X. Tang et al., "Comparative study on micro-pore structure of marine, terrestrial, and transitional shales in key areas, China," *International Journal of Coal Geology*, vol. 171, pp. 76–92, 2017.
- [66] W. Yang, X. Liu, Z. Xu, and E. Li, "Shale oil resources assessment for the member Chang 7 in Ansai area of Ordos basin," *Marine Geology Frontiers*, vol. 35, no. 4, pp. 48–56, 2019.
- [67] L. Dong, S. An, and B. Wang, "Relationship between distribution of hydrocarbon source rocks and oil-gas enrichment of Yanchang formation, Triassic, Ordos basin," *Unconventional Oil & Gas*, vol. 1, no. 1, pp. 17–21, 2014.
- [68] Z. Yang, J. Zeng, F. Han et al., "Characterization of microscopic pore texture of Chang 6-Chang 8 members tight sandstone reservoirs in the southwestern part of Ordos basin, China," *Natural Gas Geoscience*, vol. 28, no. 6, p. 909–191, 2017.
- [69] Y. Gao, "Characteristics and distribution of salt lake source rocks from lower submember of 4th member of Shahejie formation, north Dongying depression," *Petroleum Geology and Recovery Efficiency*, vol. 21, no. 1, pp. 10–15+111, 2014.
- [70] J. Xiong, X. Liu, and L. Liang, "An investigation of fractal characteristics of marine shales in the Southern China from nitrogen adsorption data," *Journal of Chemistry*, vol. 2015, Article ID 303164, 12 pages, 2015.
- [71] R. William and H. M. King, "Role of fluid pressure in mechanics of overthrust faulting II. Overthrust belt in geosynclinal area of western Wyoming in light of fluid-pressure hypothesis," *Bulletin of the Geological Society of America*, vol. 70, pp. 749–780, 1959.
- [72] R. G. Loucks, R. M. Reed, S. C. Ruppel, and U. Hammes, "Spectrum of pore types and networks in mudrocks and a descriptive classification for matrix-related mudrock pores," *AAPG Bulletin*, vol. 96, no. 6, pp. 1071–1098, 2012.
- [73] J. Li, "Pore characteristics and their evolution in Paleogene mud shales, Dongying sag, Bohai Bay basin," *Petroleum Geology & Experiment*, vol. 37, no. 5, pp. 566–574, 2015.
- [74] M. Wang, W. Xie, K. Huang, and X. Dai, "Fine characterization of lithofacies and pore network structure of continental shale: case study of the Shuinan formation in the north Jiaolai basin, China," *Journal of Petroleum Science and Engineering*, vol. 175, pp. 948–960, 2019.
- [75] Y. Liu, Z. Lu, M. Feng, J. Wang, T. Tian, and J. Chao, "Micro-pore characteristics of shale oil reservoirs of the Shahejie formation in the Dongying sag, Bohai Bay basin," *Acta Geologica Sinica*, vol. 91, no. 3, pp. 629–644, 2017.
- [76] T. Topór, A. Derkowski, P. Ziemiański, J. Szczeniowski, and D. K. McCarty, "The effect of organic matter maturation and porosity evolution on methane storage potential in the Baltic basin (Poland) shale-gas reservoir," *International Journal of Coal Geology*, vol. 180, pp. 46–56, 2017.
- [77] M. Mastalerz, A. Schimmelmann, A. Drobniak, and Y. Chen, "Porosity of Devonian and Mississippian New Albany shale across a maturation gradient: insights from organic petrology, gas adsorption, and mercury intrusion," *AAPG Bulletin*, vol. 97, no. 10, pp. 1621–1643, 2013.
- [78] S. Zhang, "Diagenesis and mechanism of shale reservoir pore increase and reduction in Dongying sag," *Journal of China University of Mining & Technology*, vol. 47, no. 3, pp. 562–578, 2018.
- [79] G. Zhu, D. Wang, G. Liu, M. Niu, and C. Song, "Evolution of the Tan-Lu fault zone and its responses to plate movements in West Pacific basin," *Chinese Journal of Geology*, vol. 39, no. 1, pp. 36–49, 2004.
- [80] S. Bao, "Fracture diversity of continental shale under horizontal geostress: a case study of the Paleogene shale in Jiyang depression," *Acta Petrolei Sinica*, vol. 40, no. 7, pp. 777–785, 2019.
- [81] Z. Hou and S. Chen, "Diagenesis evolution characteristics of shale in upper Es4 to lower Es3 members in Dongying sag and its influence on the formation of reservoir," *Petroleum Geology and Recovery Efficiency*, vol. 26, no. 1, pp. 119–128, 2019.

Research Article

Experimental Studies on Shale Cracks and Permeability Evolution Based on Acoustic Emission Monitoring

Hao Chen ^{1,2} Hongkui Ge ^{1,2} Xiaoqiong Wang ^{1,2} Jianbo Wang ³ and Shan Wu ⁴

¹Unconventional Oil and Natural Gas Institute, China University of Petroleum, Beijing 102249, China

²State Key Laboratory of Petroleum Resources and Prospecting, China University of Petroleum, Beijing 102249, China

³China University of Petroleum, Beijing at Karamay, Karamay 834000, China

⁴Department of Earth and Space Sciences, Southern University of Science and Technology, Shenzhen 518055, China

Correspondence should be addressed to Hongkui Ge; gehongkui@163.com

Received 13 December 2020; Revised 11 January 2021; Accepted 23 January 2021; Published 11 February 2021

Academic Editor: Kun Zhang

Copyright © 2021 Hao Chen et al. This is an open access article distributed under the Creative Commons Attribution License, which permits unrestricted use, distribution, and reproduction in any medium, provided the original work is properly cited.

The matrix permeability of shale reservoirs is extremely low. Therefore, massive volume fracturing is needed to form a complex crack network and get adequate sufficient capacity during the well completion. After fracturing, the effective stimulated reservoir volume (ESRV) is vital for developing shale reservoirs, mainly determined by stimulated reservoir volume (SRV) and the increase in permeability. Microseismic monitoring is widely used in the field to describe the crack shape and determine the SRV, to evaluate the stimulation effect. However, no studies have been conducted on the relationship between microseismic parameters and permeability. Thereby, we conducted uniaxial compression tests on Longmaxi shale samples and measured their changes in porosity and permeability before and after loading combining the microseismic monitoring under a laboratory scale (acoustic emission (AE)). Results show that porosity has little influence on the permeability before and after loading, while the propagation and connection of cracks are the most critical factors. As the loading stress increases, the crack volume and sample connectivity both grow. Besides, for the Longmaxi shale, when the stress is loaded to 30~50% of uniaxial compressive strength (UCS), the cracks start to propagate steadily (dilation), the permeability begins to increase rapidly, and percolation occurs, which indicates that the dilation point is closely related to the percolation threshold. The AE rate and accumulative ringing number both increase when it is larger than the percolation threshold value. The variation of AE characteristics can be used to identify the percolation threshold. Finally, the graphic model including AE parameters, crack, and permeability evolution is established based on the experimental results, which could help us understand the relationship between microseismic parameters and permeability and provide a methodological basis for the ESRV evaluation in the field.

1. Introduction

As a typical unconventional gas resource, shale gas reservoirs have extremely low porosity and permeability [1–3]. Large-scale hydraulic fracturing is required during the development to form a complex crack network and achieve efficient exploitation of shale gas [4–6]. Microseismic monitoring based on seismological theory is an effective method to describe the hydraulic crack formation, which is applied in the field to evaluate the characteristics of the fracturing network and SRV size [7–9]. Regions with signals around the cracks are treated as SRV in microseismic monitoring, yet not all cracks within the SRV have percolation capacity [10]. Therefore,

ESRV would be overestimated. Numerous field data and studies have shown that SRV is not the only factor that affects the stimulation; crack density and conductivity are also critical [11–13]. Hydraulic fracturing requires a specific stimulated volume and crack density to form the effective connections between natural cracks and bedding, cracks, and micro-nanopores with oil and gas storage, to increase reservoir permeability and achieve the ESRV.

During hydraulic fracturing, microcracks are generated in the reservoir matrix in addition to artificial cracks. According to the percolation theory, when microcracks reach the critical size, the reservoir changes from impermeable to permeable, which is called percolation, and the critical value

is the percolation threshold [14, 15]. After that, the permeability increases rapidly. Hence, understanding the crack evolution, identifying the percolation threshold, and establishing the relationship between microseismic characteristics and percolation threshold are essential to the fracturing evaluation.

Previous studies have been conducted on the crack geometry and density based on seismic data [12, 16, 17], but the relationship between microseismic crack and permeability has not been established due to the untestable permeability in the field. AE monitoring is microseismic monitoring on the laboratory scale, which is widely used to study the failure process of rocks and hydraulic fracturing in the laboratory [18–23].

Extensive experiments have been conducted to study the AE characteristics, crack, and permeability propagation of shale. There are mainly three types of researches. The first type is to study the crack evolution and failure mechanism under different loading patterns based on AE. The brittle failure of shale occurs during loading progress [24], and the bedding planes of shale have a significant effect on its mechanical behavior [25]. Tensile cracks along with the bedding dominate the failure of shale with the axis parallel to the bedding. The shale with the axis vertical to the bedding fails with complex fracture as it is affected by both shear and tensile cracks [19, 26]. The AE activities may be the response of the microstructural changes caused by the closure and development of pores and cracks at elevated stress [27]. The crack initiation occurred at approximately 30% of the UCS [24]. For shale with fluid, the failure is dominated by shear crack by analyzing the b -value of AE [28, 29]. The second type is to study the permeability variation with stress. Shale permeability increases under uniaxial stress damage, and the permeability variation is similar to that of stress damage [30]. In true triaxial stress conditions, the permeability decreases with the increase in principal stress. Still, the permeability variations caused by changing each principal stress are different. The permeability exhibits obvious bedding dependence, and the maximum decrease in permeability with increasing stress occurs in the direction vertical to the bedding [31–33]. The third type involves AE characteristics, cracks, and permeability evolution. Zhu et al. studied the influence of natural cracks on permeability and mechanical properties by AE energy. The orientation of natural fractures is closely related to permeability, AE events, and volume-strain value [34]. Based on percolation theory and AE data, Sakhaee-Pour and Agrawal established the model to predict the permeability evolution. A connected fracture is formed when the number of AE events per unit volume is larger than the threshold value. And the permeability remains close to the matrix when the number of AE events per unit volume is smaller than the threshold value [35].

Although plenty of researches have been conducted on shale mechanics, crack propagation, permeability, and AE activities, there is still a lack of comprehensive study on all the above parameters. In this paper, a series of experiments were carried out on shale to study the mechanical properties, AE characteristics, porosity, and permeability. Based on experimental data, the relationship between crack propaga-

tion, permeability, AE characteristics, and stress is obtained and the percolation threshold is identified. Furthermore, the connectivity of cracks acquired from the AE location is discussed to reveal the evolution mechanism of permeability. These results can provide a theoretical basis for ESRV estimation, thereby guiding the effective development of unconventional reservoirs.

2. Experimental Method

2.1. Sample Preparation. In this study, samples were taken from the marine sedimentary shale outcrop of the Lower Silurian Longmaxi Formation in Chongqing, SW China, as shown in Figures 1(a) and 1(b). The Longmaxi shale is bedding developed and rich in clay minerals and organic matter [36, 37]; see Figure 1(d) for the sample's mineral composition. Samples were taken from the same rock to reduce variability and cored successively in adjacent positions with coring direction paralleling the bedding direction. According to the international standard for rock mechanics experiment [38], six cylindrical shale samples were prepared. Each cylindrical sample has a nominal length of 50 mm and a diameter of 25 mm, and the sample parallelism was less than ± 0.02 mm to meet the loading requirements. See Table 1 for the basic properties of the samples.

2.2. Experimental Apparatus. The sample porosity and permeability were measured in the State Key Laboratory of Petroleum Resources and Prospecting in the China University of Petroleum (Beijing). A KXD-III helium porosimeter based on double Boyle's law was adopted to measure the porosity. It is an effective method for shale porosity measurement in recent years [39, 40]. Figure 2 shows the illustration of the porosimeter. The test procedure is shown as follows: Firstly, the sample and calibration block were put into the sample cell and then close all valves, and the calibration block is used to reduce the dead volume of the sample cell. Secondly, open valve 1 to let gas enter the reference cell, close valve 1, when the pressure got stable, and record the pressure p_1 , volume V_1 , and temperature T_1 . Finally, open valve 2 till the pressure is stable, and record p_2 , V_2 , and T_2 . The calculation equation is given by

$$\frac{(p_1 + p_0)V_{rc} + p_0(V_{sc} - V_b - V_c + V_p)}{T_1} = \frac{(p_2 + p_0)(V_{rc} + V_{sc} - V_b - V_c + V_p)}{T_2}, \quad (1)$$

$$V_p = \frac{T_2((p_1 + p_0)V_{rc} + p_0(V_{sc} - V_b - V_c)) - T_1(p_2 + p_0)(V_{rc} + V_{sc} - V_b - V_c)}{T_1(p_2 + p_0) - T_2p_0}, \quad (2)$$

where p_0 is the atmospheric pressure and A_{rc} and V_{sc} represent the reference cell and sample cell volume, respectively. V_c is the volume of the calibration block. V_b and V_p denote the bulk volume and porosity volume of the sample, respectively. The sample porosity (ϕ) is given by

$$\phi = \frac{V_p}{V_b} \times 100\%. \quad (3)$$

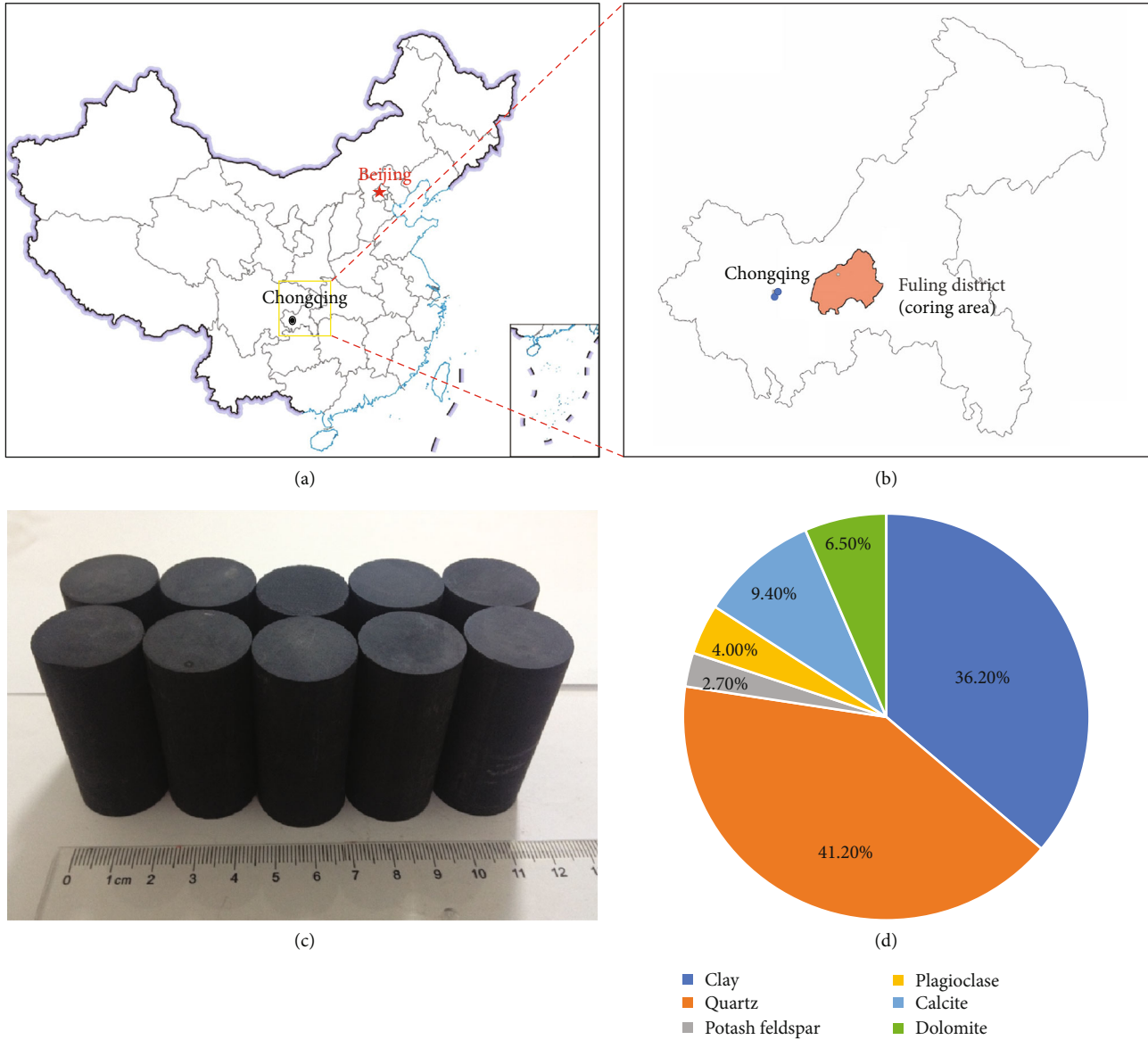


FIGURE 1: Experimental materials: (a) geographical location; (b) coring area; (c) samples; (d) mineral composition.

TABLE 1: Basic physical properties of the samples.

Sample	Length (mm)	Diameter (mm)	Mass (g)	Density (g/cm ³)	<i>p</i> -wave velocity (m/s)
Shale 1	50.30	24.28	59.20	2.54	3934
Shale 2	50.44	24.34	59.63	2.54	4042
Shale 3	51.20	24.25	59.93	2.53	4130
Shale 4	50.41	24.29	59.36	2.54	4066
Shale 5	50.34	24.22	58.92	2.54	4003
Shale 6	50.86	24.25	59.80	2.54	4058

As the shale permeability is extremely low, a YRD-CP200 pulse permeameter was adopted in this study. The pulse-decay method is a simple and accurate way to measure ultra-

low permeability. Its testing principle is shown in Figure 3. The sample was jacketed into the core holder, and then, close all valves. Open valve 1, valve 2, and valve 3, and the sample is saturated with nitrogen; maintain the upstream pressure p_u and downstream pressure p_d consistent for a while. Then, open the microleakage valve, and decrease the downstream pressure with a small Δp to cause an instantaneous additional pressure difference between the upstream and downstream ends. As the fluid flows in the sample, the upstream pressure p_u decays exponentially till a new equilibrium pressure p_f is reached. The permeability k can be obtained through the measurement of the time it takes the fluid to flow through the sample and the exponential change in fluid pressure over time, which is given by

$$k = \alpha \mu c_g \frac{L}{A} V_u. \tag{4}$$

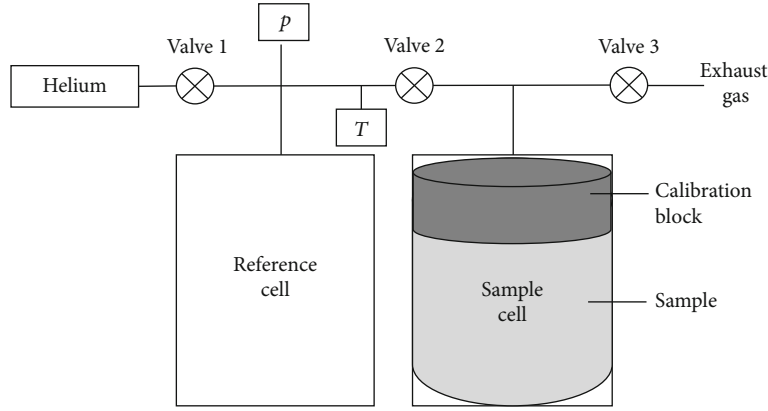


FIGURE 2: Schematic diagram of the porosimeter.

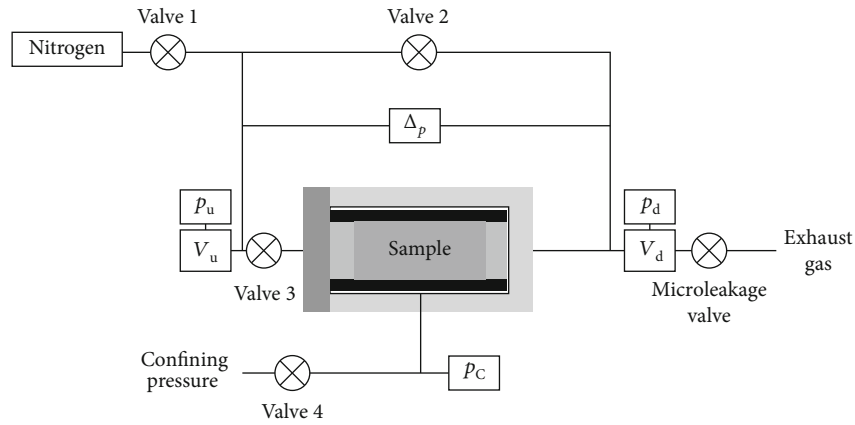


FIGURE 3: Schematic diagram of the pulse permeameter.

The attenuation index α can be obtained from the exponential attenuation of the fluid pressure:

$$p_u - p_f = \Delta p \frac{V_u}{V_u + V_d} e^{-\alpha t}, \quad (5)$$

where V_u and V_d denote the upstream and downstream container volume and α is the attenuation index. μ is the nitrogen viscosity. c_g is the compressibility of nitrogen. L and A are the length and cross-sectional area of the sample, respectively. During the test, the system automatically records data once for every 0.002 MPa attenuation of upstream pressure, and the final permeability is obtained by linear regression.

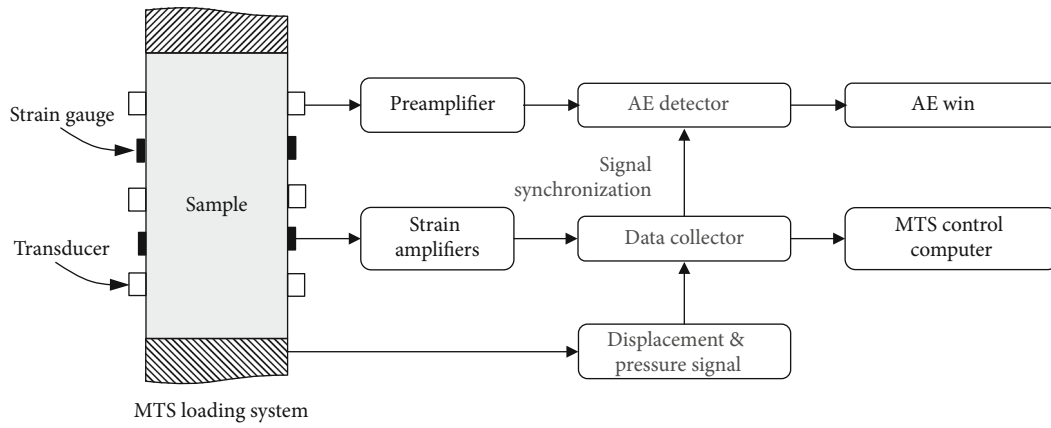
Samples were dried at 65°C for 24 hours before the porosity and permeability testing. The porosity was measured without confining pressure and under a pore pressure of 0.8 MPa and test temperature of 20°C. The permeability was measured under a confining pressure of 10 MPa and pore pressure of 6 MPa, and the test temperature was 20°C.

The mechanics and AE tests were conducted in the Institute of Geophysics, China Earthquake Administration, with the MTS-1000 kN loading system and PCI-2 acoustic emission system, as shown in Figure 4. The maximum loading of the MTS system is 1000 kN. The PCI-2 AE system from

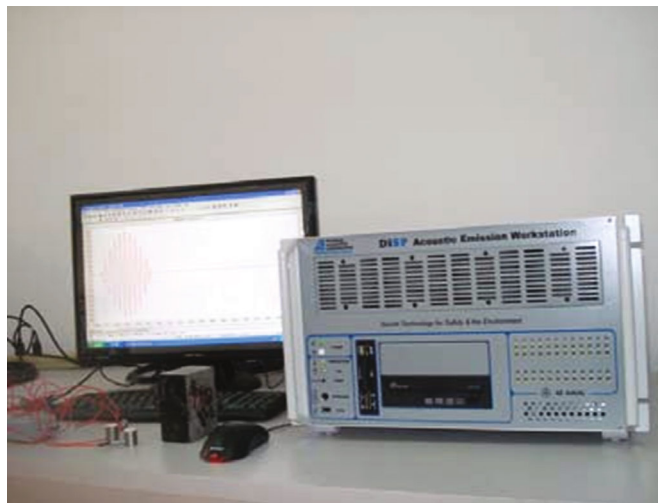
American Physical Acoustics Company (PAC) can collect 20 characteristic parameters such as AE event, AE energy, and ringing. The sampling rate is up to 40 MHz. Also, there are eight external parameters, which can introduce the MTS stress value and the strain value of the strain gauge into the AE acquisition system to keep the records time-synchronized. The two systems work simultaneously which could achieve the synchronous test of AE and mechanical parameters.

Nanotransducers with the size of $\Phi 8\text{mm} \times 8\text{mm}$ and bandwidth of 50~750 kHz were used in this study. Six nanotransducers coated with coupling agents were placed symmetrically on the cylindrical sample to record the AE event's parameters and waveform and locate their position in real time. See Figure 5 for the transducer arrangement. Stress-controlled uniaxial loading was used in this experiment. Samples were tested under a 2 MPa/min rate of stress loading. And the AE sampling rate was 5 MHz, while the threshold value was 45 dB.

2.3. Experimental Methodology. AE location, mechanical properties, and permeability of the rock are tested in this study. Due to the limitation of sample size, the strain gauges and transducers cannot be arranged in the same sample.



(a)



(b)



(c)

FIGURE 4: Schematic diagram of the test system of AE mechanics: (a) schematic diagram of the MTS-PCI-2 system; (b) PCI-2 AE system; (c) MTS loading system.

Meanwhile, the existing equipment cannot conduct AE location and permeability testing simultaneously. Therefore, the parallel experiment method is used in this research.

The test procedure consists of the following steps: (1) The samples were dried at 65°C for 24h, and then, the basic parameters such as size, porosity, and permeability were

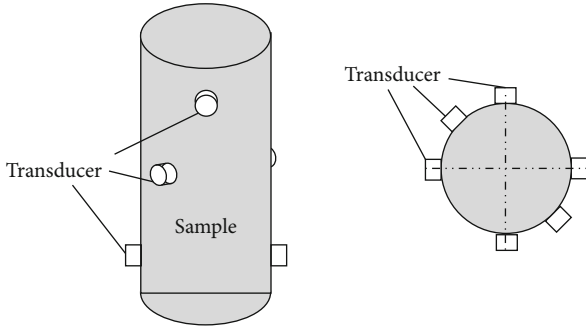


FIGURE 5: Illustration of the transducer arrangement.

measured. (2) Shale 6 was loaded under uniaxial stress until rupture, and then, the uniaxial compressive strength (UCS) of shale 6 was obtained. (3) To ensure the samples' integrity, shales 1-5 were loaded under uniaxial stress to about 15%, 35%, 50%, 70%, and 85% of the UCS of shale 6. Stop loading before the samples break, and record the stress and AE signals during the loading. (4) The porosity and permeability of shales 1-5 were measured. See Table 2 for the sample parameters that got tested.

3. Results

3.1. Shale Mechanical Properties. The stress-strain curve of shale 6 is shown in Figure 6, which is a typical brittle failure, and the maximum axial strain is about 0.4%. Many researchers have conducted comprehensive studies on the stress-strain curve [41–44]. According to the rock brittle failure theory proposed by Brace and Bieniawski, the stress-strain curve under uniaxial loading can be divided into five stages. In stage I, the curve is convex downward due to the closure of initial cracks. The microcracks are gradually compacted, and the strain change gradually slows down as the stress increases till it reaches the crack closing stress σ_{cc} . This stage could reflect the development of preexisting cracks. In stage II, the curve is a straight line with a stable slope, reflecting the rock's linear elastic deformation. Young's modulus and Poisson's ratio are both obtained in this stage. Stage III begins when the stress reaches the crack initiation stress σ_{ci} , and the slope starts to go down while the curve is convex upward. In this stage, cracks propagate stably, and new cracks are generated. The radial strain-stress and volumetric strain-stress curves become nonlinear. Rock dilation happens in this stage, and σ_{ci} is the dilation stress. Stage IV is the accelerated growth stage of cracks. As the stress reaches crack damage stress σ_{cd} , the volumetric strain is no longer reduced by compression but starts to expand, and the crack density increases significantly inside the rock. The last stage (stage V) is the postrupture stage. Shale strength drops instantly as the failure stress σ_f (UCS) is reached.

For shale 6, there are no prominent stable propagation stage and accelerated growth stage, and basically, no residual strength exists in the postpeak stage. And it is a typical brittle failure. From the stress-strain curve, the elastic

modulus is 32.87 GPa, Poisson's ratio is 0.17, and the UCS is 122.69 MPa.

3.2. AE Characteristics. AE is a kind of transient elastic wave generated by the rapid release of an internal energy source inside the material [45]. AE accompanies crack propagation during the loading progress. A certain voltage is set artificially as a specific threshold voltage. The wave that exceeds the threshold voltage will form a rectangular impulse and is considered a ringing count [46]. The ringing counts could reflect the total amount and frequency of AE activities. The ringing counts per unit pressure are defined as the AE rate. For shales 1-5, the variation law of accumulative ringing counts and AE rate with stress is shown in Figures 7(a)–7(e). For shale 1 and shale 2, the loading stress is relatively low, only a few AE signals are generated, AE activity is weak, and AE rate is low, while the accumulative ringing counts are small. The AE characteristics of shale 3, shale 4, and shale 5 during initial loading are consistent with those of shale 1 and shale 2. When the loading stress is between 45 and 60 MPa, AE activity begins to increase and AE rate and accumulative ringing counts increase significantly. Statistics show that the accumulated ringing counts of five samples increase as the maximum loading stress rises exponentially when the loading stress exceeds 60 MPa (see Figure 7(f)). Besides, the accumulative AE number of some samples would leap during the loading process, which indicates the generation of relatively large cracks inside the rocks [45].

A local change of material identified by several probes is considered an AE event. The spatial distribution of AE events can reflect the crack propagation inside the samples. The double-difference algorithm can effectively reduce the AE location error [47, 48] and can process the experimental data and obtain the AE event location. The AE event cannot reflect all cracks' position but can reflect the general area [49]. The location results shown in Figure 8 indicate that the AE event number increases as the loading stress increases. For shale 1 and shale 2, the AE event number is relatively small due to the lower loading stress and increased significantly as for shale 3 to shale 5. The ringing counts are much higher for shale 5, yet due to the bad connection of some transducers, the sensitivity decreases, which leads to bad AE location results and less locatable events. The AE location results of five samples are entirely discrete, which indicates that the cracks generated inside the rocks are random before shale rupture.

3.3. Permeability and Porosity before and after Loading. The sample porosity and permeability before and after loading are shown in Table 3. Results indicate that the permeability increases after loading, while the porosity changes very little. The permeability and porosity data are correlated, showing that the correlation is not good (see Figure 9).

The sample porosity and permeability data after loading are divided by the initial porosity and permeability data to obtain the dimensionless permeability k_D and porosity ϕ_D . The dimensionless permeability of the five samples increases as the maximum loading stress increases. While the maximum loading stress is low, the dimensionless permeability

TABLE 2: Details of the sample parameters that got tested.

Sample no.	Maximum loading stress (MPa)	Sample parameters					
		Initial porosity and permeability	Porosity and permeability after loading	AE	Stress	Strain	
Shale 1	20.96	√	√	√	√	×	
Shale 2	42.43	√	√	√	√	×	
Shale 3	61.40	√	√	√	√	×	
Shale 4	86.77	√	√	√	√	×	
Shale 5	100.00	√	√	√	√	×	
Shale 6	122.69 (fractured)	√	×	×	√	√	

Note: √ represents that the parameter was tested and × represents that the parameter was not tested.

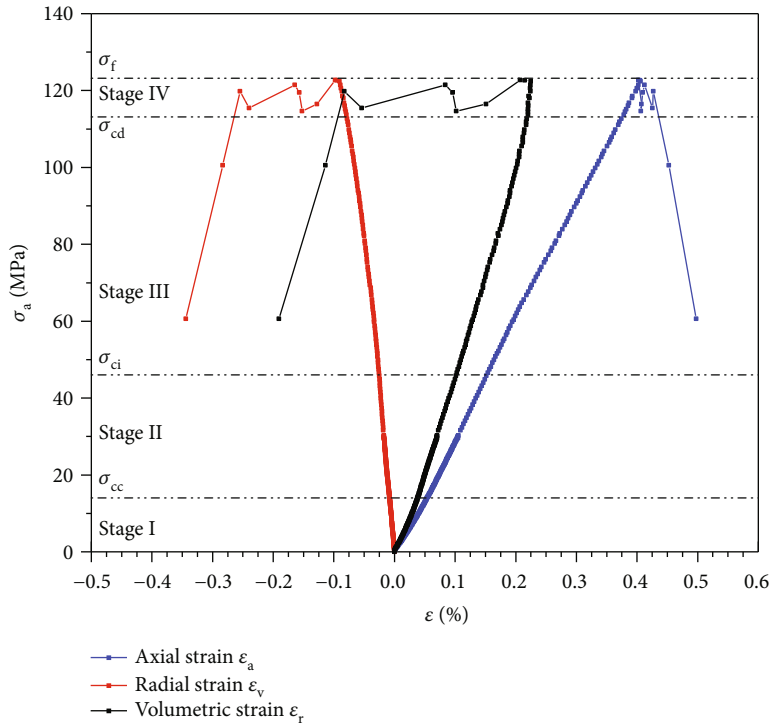


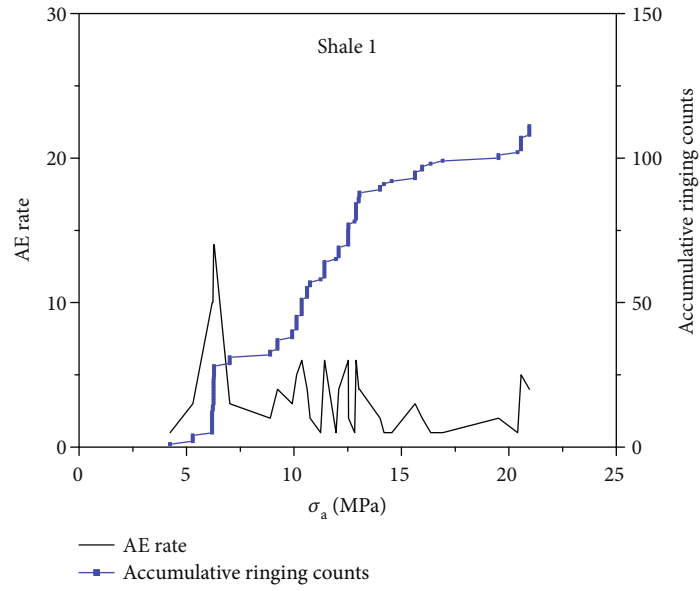
FIGURE 6: The stress-strain curve of shale 6. σ_a is the axial stress. ϵ is the strain. σ_{cc} is the crack closure stress. σ_{ci} is the crack initiation stress. σ_{cd} is the crack damage stress. σ_f is the failure stress. Stage I: initial crack closure. Stage II: linear elastic region. Stage III: stable crack propagation. Stage IV: unstable crack propagation.

changes very little. While the maximum loading stress is larger than 40 MPa, the dimensionless permeability increases exponentially and rapidly (see Figure 10). The percolation threshold of the samples appears between 40 and 60 MPa. The porosity of all the samples remains unchanged before and after the testing, indicating that the variation of the whole porosity contributes little to the increase in shale permeability before fracturing.

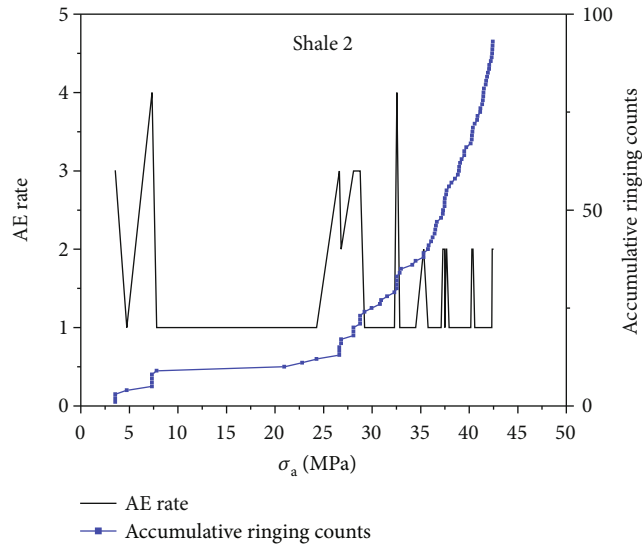
4. Discussions

4.1. Percolation Behavior of Shale during Uniaxial Loading. The ratio of the minimum to the maximum diameter of

rock pores is called the aspect ratio, according to which pores can be divided into nearly spherical holes and narrow-long cracks. The effect of cracks on rock porosity is small, but it can significantly affect the permeability [50, 51]. Based on the percolation theory, continuous flow channels initially exist in the rock, yet there are not enough connected cracks to form a network. Therefore, rock permeability is extremely low. As the loading progresses, the crack number increases gradually. The size of the connected group inside the formation shows nonlinear growth. A noticeable permeability jump occurs at the percolation threshold, while the formation permeability increases rapidly.

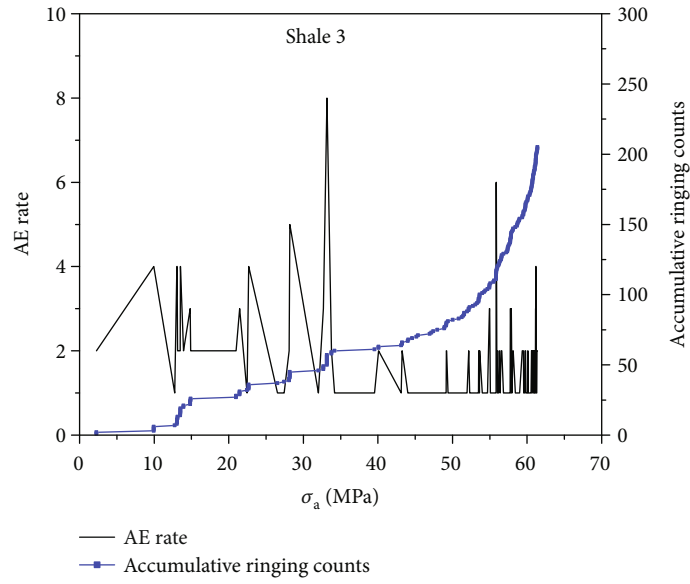


(a)

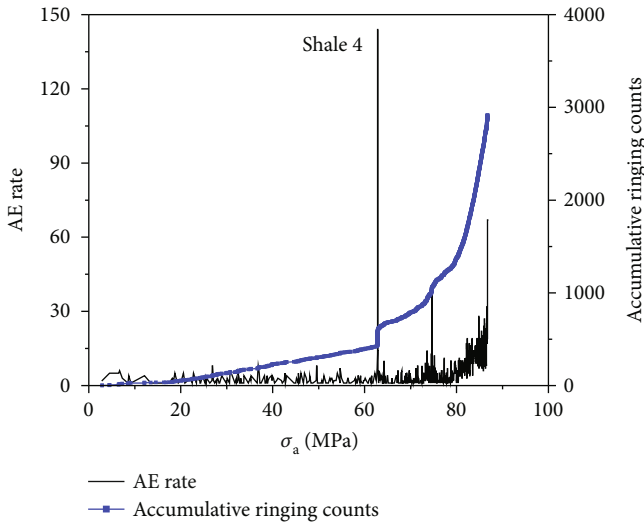


(b)

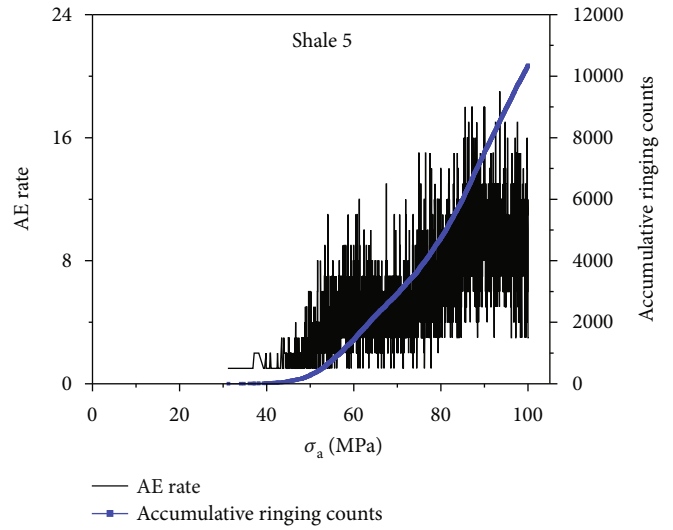
FIGURE 7: Continued.



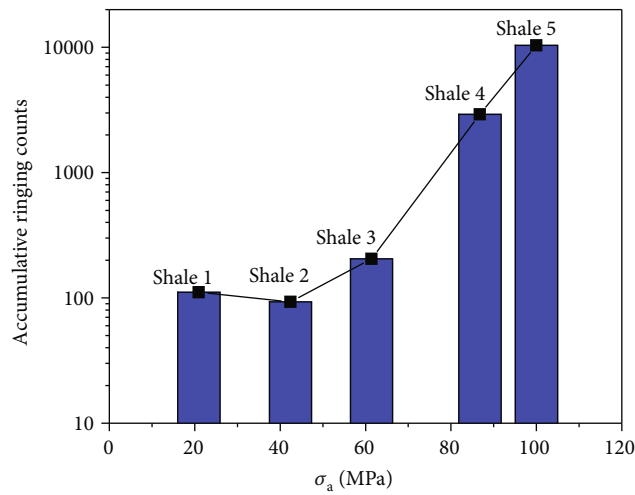
(c)



(d)



(e)



(f)

FIGURE 7: AE rate and accumulative ringing counts under loading stress.

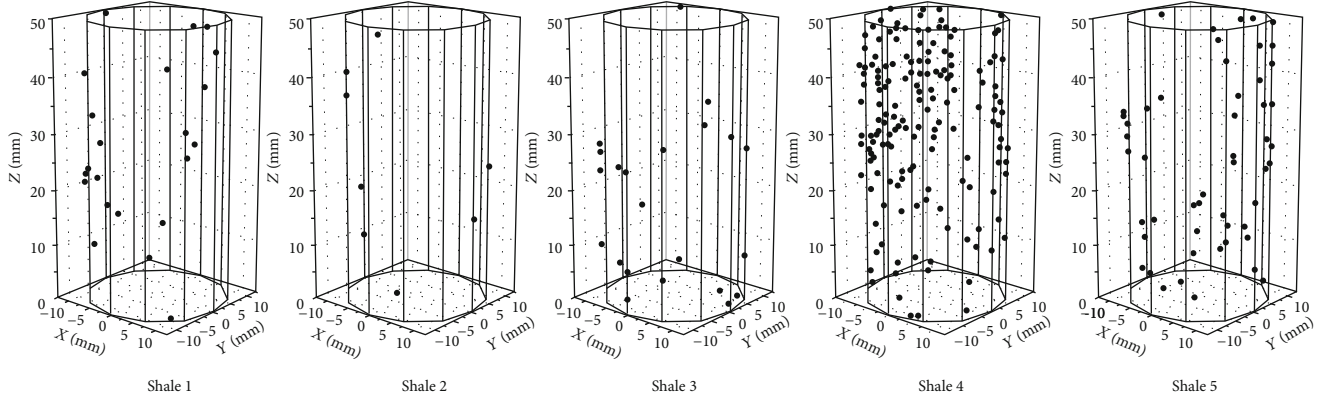


FIGURE 8: AE location results of the samples.

TABLE 3: The permeability and porosity before and after loading.

Sample	Before loading		After loading	
	Porosity ϕ (%)	Permeability k (m ²)	Porosity ϕ (%)	Permeability k (m ²)
Shale 1	3.56	2.12×10^{-19}	3.71	2.22×10^{-19}
Shale 2	3.74	2.28×10^{-19}	3.70	2.50×10^{-19}
Shale 3	4.02	1.67×10^{-18}	4.11	2.73×10^{-18}
Shale 4	3.34	1.25×10^{-19}	3.38	2.94×10^{-19}
Shale 5	2.95	1.82×10^{-19}	2.99	8.25×10^{-19}
Shale 6	3.64	1.12×10^{-19}		

The evolution laws of shale mechanics, AE characteristics, porosity, and permeability under uniaxial stress can be observed from Figures 6–10. As the axial stress is loaded to 40–60 MPa, the shale permeability increases significantly to the percolation threshold, and percolation occurs. The AE ringing counts and AE rate are very low before the percolation threshold is reached; the stress-strain curve is in the linear elastic stage. In contrast, the AE ringing counts and AE rate increase significantly after the percolation threshold is reached, and the stress-strain curve is nonlinear. The percolation threshold corresponds to the dilation point, and the porosity changes very little before and after loading. In this paper, assume that the mechanics of shale 6 represent the mechanics of all the samples. The Longmaxi shale's percolation threshold is 30–50% of UCS, which corresponds to the initial dilation stress σ_{ci} .

4.2. Percolation Mechanism: Generation and Connection of Cracks. Based on the rock brittle failure theory, Martin and Chandler proposed a method to calculate the crack volume deformation [43]. The volumetric strain of the rock ε_v is obtained by

$$\varepsilon_v = \frac{\Delta V}{V} = \varepsilon_a + 2\varepsilon_r, \quad (6)$$

where ΔV is the volume deformation of the rock. V is the

rock volume. ε_a and ε_r are the axial and radial strain, respectively. According to the elastic modulus E and Poisson's ratio ν calculated from the linear elastic stage in the rock stress-strain curve, the elastic volumetric strain of the rock ε_{ve} can be written by

$$\varepsilon_{ve} = \frac{1 - 2\nu}{E} \sigma_a. \quad (7)$$

The crack volumetric strain ε_{vc} can be described as

$$\varepsilon_{vc} = \varepsilon_v - \varepsilon_{ve}. \quad (8)$$

We can see the crack evolution during the loading process from the crack volumetric strain-axial strain curve, as shown in Figure 11. σ_{cc} and σ_{ci} are the stresses corresponding to the initial and end position of the parallel section in the curve, respectively. Cracks could close quickly under very small loading stress before σ_{cc} . Between σ_{cc} and σ_{ci} , the crack volume remains the same. And massive cracks are generated while the loading stress is larger than σ_{ci} . The dimensionless permeability is negatively correlated with the crack volumetric strain, as shown in Figure 12. From the figure, σ_{cc} is 14 MPa while σ_{ci} is 46 MPa, and the percolation threshold is also around σ_{ci} . When the axial strain is 14 MPa, the initial crack porosity obtained is 0.010%. The maximum crack porosity near rupture is 0.049%. Both are far less than the porosity before and after loading which is 3.64%. The crack volume accounts for less than 2% of the total pore volume.

Succolarity is one of the essential parameters in fractal geometry theory. For porous medium, succolarity represents the fluid flow capacity inside the medium, which can be used to characterize the connectivity of the porous medium in different directions [52]. In this paper, we created a cube grid in three-dimensional coordinates, and each AE event represents a crack. The grids with cracks are connected, while the grids without cracks are not. By applying virtual fluid pressure in different directions, the succolarity values in six directions are obtained by calculating the proportion of the grid number with fluid flow to the total grid number using the gliding box counting method. A detailed description of the 3D succolarity calculation method can be found in Xia et al. [53].

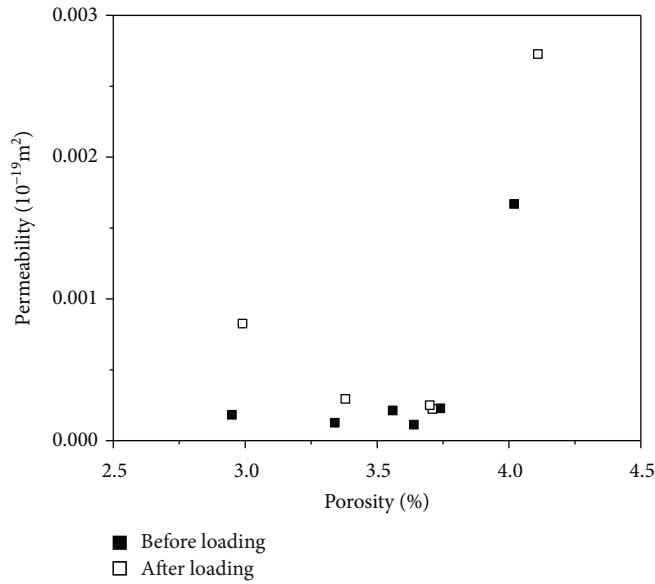


FIGURE 9: Relationship between permeability and porosity.

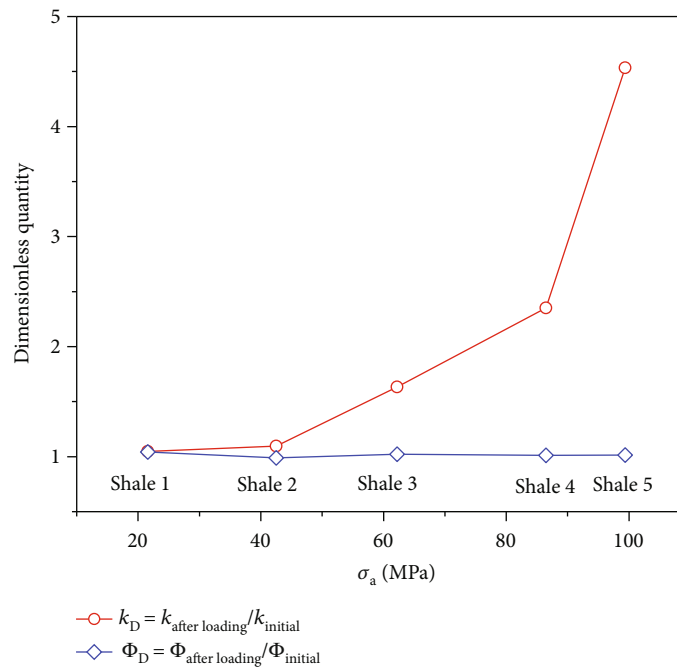


FIGURE 10: The dimensionless permeability and porosity under stress.

In this paper, coordinates established during the succolarity calculation are consistent with the AE location coordinates.

The succolarity values of shales 1-4 in six directions are shown in Figure 13(a). Due to the sample differences, the correlation between succolarity and maximum loading stress is not good but shows an overall upward trend, and the succolarity value increases significantly from shale 3 to shale 4. In order to eliminate the influence of sample differences, shale 4 was analyzed separately. The accumulative AE events of shale 4 and their locations under

different stresses (20, 40, 60, and 86 MPa) were analyzed separately, as shown in Figure 14. Figure 13(b) shows the succolarity-stress curves of shale 4. The succolarity values in $Y+$ and $Z-$ directions remain zero, which indicates that there are no cracks in the two directions or the cracks generated are disconnected. Succolarity improves in the other four directions as the stress increases and shows a good correlation. The succolarity improves remarkably when the stress is between 40 and 60 MPa, which means that the crack connectivity is significantly enhanced in this

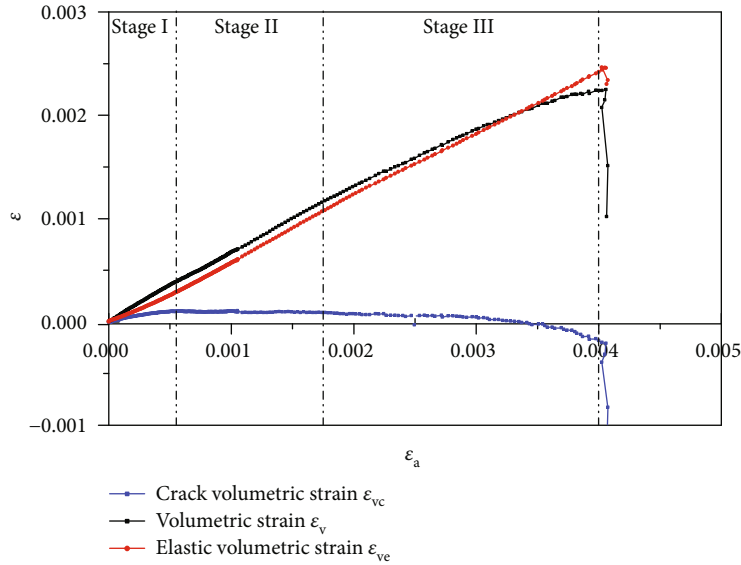


FIGURE 11: Calculated crack volumetric strain.

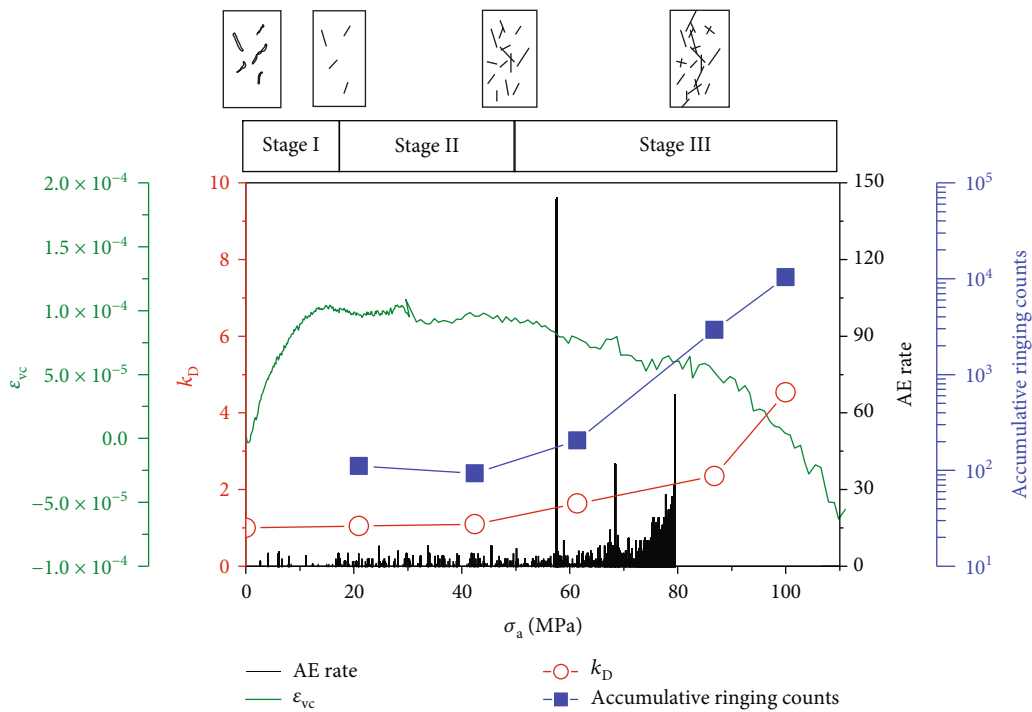


FIGURE 12: The model diagram of AE characteristics, crack propagation, and permeability evolution.

stress interval. It is consistent with the interval where σ_{ci} and percolation threshold occur.

The calculation of crack volumetric strain could reflect the crack generation process under stress, while the crack connectivity can be obtained through the statistics of sample succolarity. Combining both, we can obtain the generation and connection of cracks during the loading, which is also the main mechanism affecting the percolation threshold.

Figure 12 shows the change of mechanics, AE characteristics (accumulative ringing counts and AE rate), porosity, and permeability of shale under uniaxial loading. According to the loading stress, the curve can be divided into three stages. In stage I and stage II, the initial cracks are closed, the AE ringing counts and AE rate are low, and the porosity and permeability remain unchanged. As the stress loaded reaches σ_{ci} , the

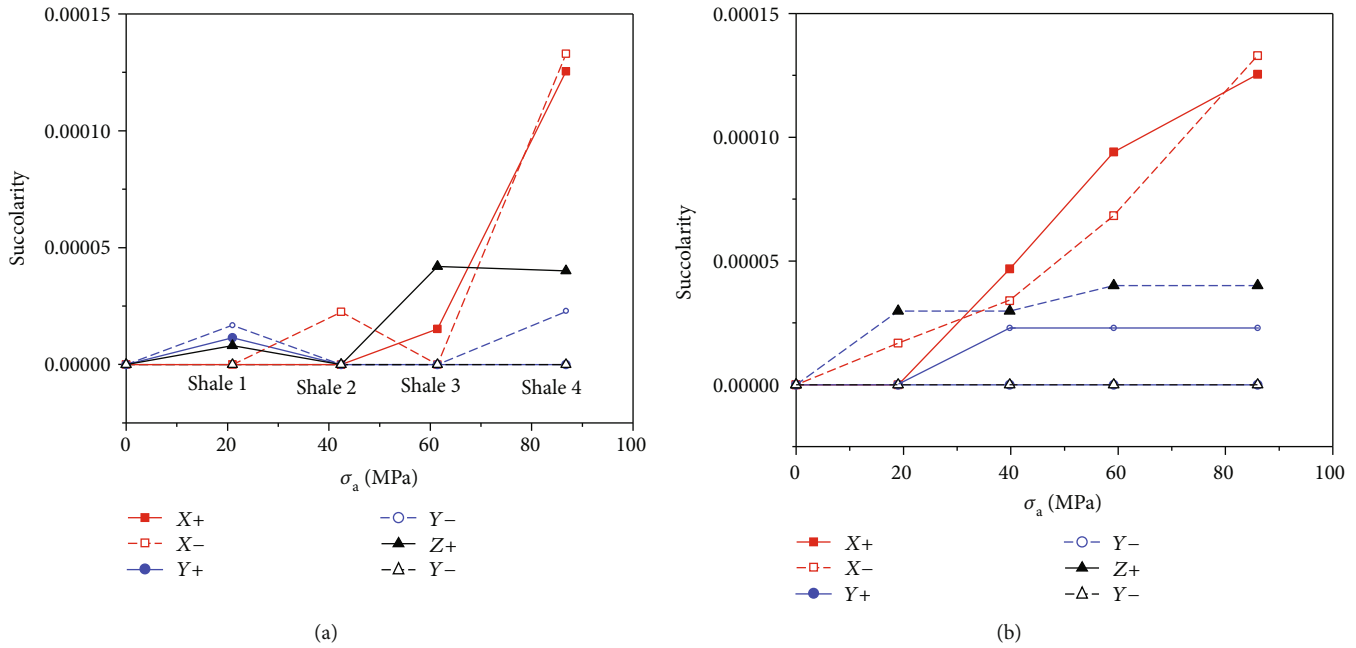


FIGURE 13: The succolarity-stress curve: (a) shales 1-4; (b) shale 4 under different stresses.

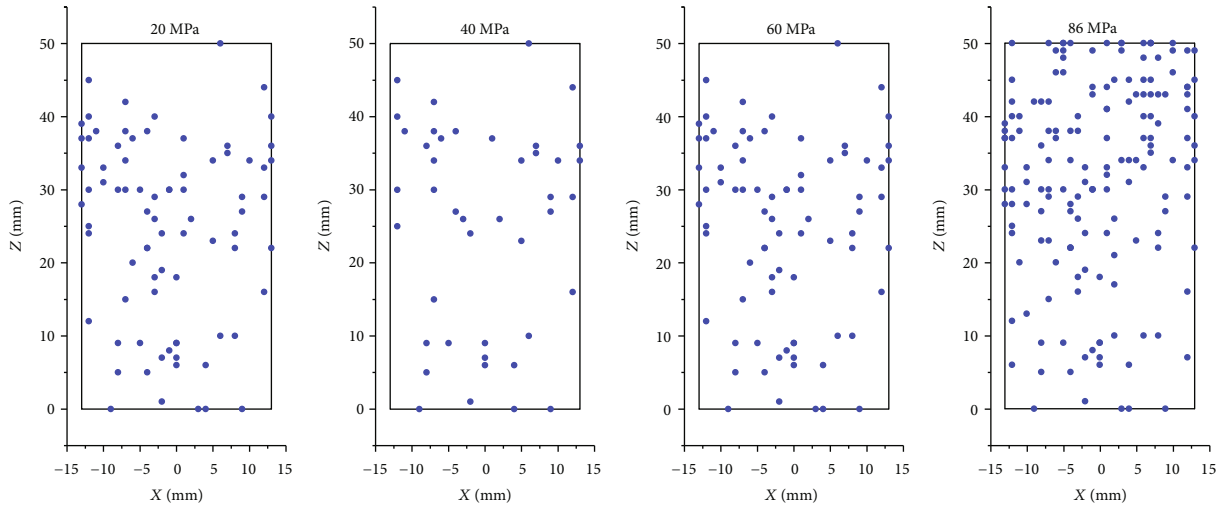


FIGURE 14: The projections of AE locations under different stresses of shale 4.

generation of new cracks leads to a significant increase in the AE rate and permeability.

Based on the above analysis, we established a graphic model of cracks, permeability, and AE characteristics and then discussed the generation mechanisms of the percolation threshold. The study could help understand the relationship between AE characteristics, crack propagation, and permeability, thus improving the microseismic monitoring accuracy of hydraulic fracturing.

5. Conclusions

In this paper, we studied the AE characteristics (AE rate, accumulative ringing counts, and AE localization), crack vol-

ume based on stress-strain calculation, crack connectivity obtained from succolarity, and permeability evolution. The main conclusions are obtained as follows:

- (1) The sample porosity is unchanged before and after 5loading, while the permeability changes significantly, and the porosity has little effect on permeability during the loading. Although cracks account for less than 2% of the pore volume, their generation and connection are the main control mechanisms of permeability evolution, which can be characterized by the crack volume calculated from stress-strain and succolarity gained by AE location, respectively

- (2) The cracks begin to propagate stably at the dilation point (30-50% of UCS). Meanwhile, the succolarity and crack volume start to increase rapidly, and the permeability threshold appears. The sample dilatancy is the main micromechanism of the percolation threshold
- (3) The AE rate and accumulative ringing counts are relatively low when the loading stress is smaller than the stress at the percolation threshold but increases significantly while the stress is larger than that. Therefore, AE characteristics can be used to identify the range of percolation threshold roughly

Data Availability

The data used to support the findings of this study are available from the corresponding author upon request.

Conflicts of Interest

The authors declare that there is no conflict of interest regarding the publication of this paper.

Acknowledgments

We would like to express our gratitude to Jianchao Cai for his useful discussion and Lili Song for helping in the AE experiments. This work was supported by the National Science and Technology Major Project (2017ZX05039-004) and the Strategic Cooperation Technology Projects of CNPC and CUPB (ZLZX2020-01).

References

- [1] C. H. Sondergeld, R. J. Ambrose, C. S. Rai, and J. Moncrieff, "Micro-structural studies of gas shales," in *SPE Unconventional Gas Conference*, Society of Petroleum Engineers, 2010.
- [2] H. H. Liu, P. G. Ranjith, D. T. Georgi, and B. T. Lai, "Some key technical issues in modelling of gas transport process in shales: a review," *Geomechanics and Geophysics for Geo-Energy and Geo-Resources*, vol. 2, no. 4, pp. 231–243, 2016.
- [3] R. Sander, Z. Pan, and L. D. Connell, "Laboratory measurement of low permeability unconventional gas reservoir rocks: a review of experimental methods," *Journal of Natural Gas Science and Engineering*, vol. 37, pp. 248–279, 2017.
- [4] T. Guo, S. Zhang, Z. Qu, T. Zhou, Y. Xiao, and J. Gao, "Experimental study of hydraulic fracturing for shale by stimulated reservoir volume," *Fuel*, vol. 128, pp. 373–380, 2014.
- [5] C. Zou, D. Dong, S. Wang et al., "Geological characteristics and resource potential of shale gas in China," *Petroleum Exploration and Development*, vol. 37, no. 6, pp. 641–653, 2010.
- [6] B. Roychoudhuri, T. T. Tsotsis, and K. Jessen, "An experimental investigation of spontaneous imbibition in gas shales," *Journal of Petroleum Science and Engineering*, vol. 111, pp. 87–97, 2013.
- [7] M. K. Fisher, C. A. Wright, B. M. Davidson et al., "Integrating fracture-mapping technologies to improve stimulations in the Barnett shale," *SPE Production and Facilities*, vol. 20, no. 2, pp. 85–93, 2005.
- [8] S. C. Maxwell, T. I. Urbancic, C. Demerling, and M. Prince, "Real-time 4D passive seismic imaging of hydraulic fracturing," in *Proceedings of the SPE/ISRM Rock Mechanics in Petroleum Engineering Conference*, pp. 298–307, Irving, Texas, 2002.
- [9] Z. Wei and Z. Siyu, "Application of surface microseismic monitoring technology in shale gas well fracturing of South Sichuan," *Reservoir Evaluation and Development*, vol. 4, pp. 71–74, 2014.
- [10] M. Y. Cui, Y. Z. Liu, N. L. Xiu et al., "Analysis of factors affecting the formation of effective stimulated reservoir volume (ESRV)," *Oil Drilling & Production Technology*, vol. 36, pp. 82–87, 2014.
- [11] M. J. Mayerhofer, E. P. Lolon, N. R. Warpinski, C. L. Cipolla, D. Walser, and C. M. Rightmire, "What is stimulated reservoir volume?," *SPE Production and Operations*, vol. 25, no. 1, pp. 89–98, 2010.
- [12] S. C. Maxwell, C. Waltman, N. R. Warpinski, M. J. Mayerhofer, and N. Boroumand, "Imaging seismic deformation induced by hydraulic fracture complexity," *SPE Reservoir Evaluation and Engineering*, vol. 12, no. 1, pp. 48–52, 2009.
- [13] Q. Zhang, Y. Su, W. Wang, and G. Sheng, "A new semi-analytical model for simulating the effectively stimulated volume of fractured wells in tight reservoirs," *Journal of Natural Gas Science and Engineering*, vol. 27, pp. 1834–1845, 2015.
- [14] J. E. Ramirez, E. Molina-Gayosso, J. Lozada-Lechuga, L. M. Flores-Rojas, M. I. Martínez, and A. F. Téllez, "Percolation strategy to improve the production of plants with high pathogen susceptibility," *Physical Review E*, vol. 98, pp. 1–10, 2018.
- [15] M. Colombier, F. B. Wadsworth, L. Gurioli et al., "The evolution of pore connectivity in volcanic rocks," *Earth and Planetary Science Letters*, vol. 462, pp. 99–109, 2017.
- [16] M. J. Mayerhofer, E. P. Lolon, J. E. Youngblood, and J. R. Heinze, "Integration of microseismic fracture mapping results with numerical fracture network production modeling in the Barnett shale," in *SPE Annual Technical Conference and Exhibition*, vol. 2, pp. 976–983, San Antonio, Texas, USA, 2006.
- [17] R. Meek, B. Suliman, H. Bello, and R. A. Hull, "Well space modeling, SRV prediction using microseismic, seismic rock properties and structural attributes in the Eagle Ford Shale of South Texas," in *Unconventional Resources Technology Conference (URTeC)*, pp. 1601–1608, San Antonio, Texas, USA, 2015.
- [18] B. Liu, Y. Ma, G. Zhang, and W. Xu, "Acoustic emission investigation of hydraulic and mechanical characteristics of muddy sandstone experienced one freeze-thaw cycle," *Cold Regions Science and Technology*, vol. 151, pp. 335–344, 2018.
- [19] Z. Moradian, A. Seiphoori, and B. Evans, "The role of bedding planes on fracture behavior and acoustic emission response of shale under unconfined compression," in *51st US Rock Mechanics / Geomechanics Symposium 2017 2017*, vol. 5, pp. 3328–3336, San Francisco, California, USA, 2017.
- [20] N. Li, S. Zhang, Y. Zou et al., "Acoustic emission response of laboratory hydraulic fracturing in layered shale," *Rock Mechanics and Rock Engineering*, vol. 51, no. 11, pp. 3395–3406, 2018.
- [21] H. Zhai, X. Chang, Y. Wang, X. Lei, and Z. Xue, "Analysis of acoustic emission events induced during stress unloading of a hydraulic fractured Longmaxi shale sample," *Journal of Petroleum Science and Engineering*, vol. 189, p. 106990, 2020.

- [22] J. Tan, J. Xie, L. Li, Q. Lyu, J. Han, and Z. Zhao, "Multifractal analysis of acoustic emissions during hydraulic fracturing experiments under uniaxial loading conditions: a Niutitang shale example," *Geofluids*, vol. 2020, Article ID 8845292, 19 pages, 2020.
- [23] Z. Moradian, H. H. Einstein, and G. Ballivy, "Detection of cracking levels in brittle rocks by parametric analysis of the acoustic emission signals," *Rock Mechanics and Rock Engineering*, vol. 49, no. 3, pp. 785–800, 2016.
- [24] F. Amann, E. A. Button, K. F. Evans, V. S. Gischig, and M. Blümel, "Experimental study of the brittle behavior of clay shale in rapid unconfined compression," *Rock Mechanics and Rock Engineering*, vol. 44, no. 4, pp. 415–430, 2011.
- [25] Y. Wang, C. H. Li, and Y. Z. Hu, "Experimental investigation on the fracture behaviour of black shale by acoustic emission monitoring and CT image analysis during uniaxial compression," *Geophysical Journal International*, vol. 213, no. 1, pp. 660–675, 2018.
- [26] P. Hou, F. Gao, Y. Ju et al., "Experimental investigation on the failure and acoustic emission characteristics of shale, sandstone and coal under gas fracturing," *Journal of Natural Gas Science and Engineering*, vol. 35, pp. 211–223, 2016.
- [27] X. Li, X. Lei, Q. Li, and X. Li, "Experimental investigation of Sinian shale rock under triaxial stress monitored by ultrasonic transmission and acoustic emission," *Journal of Natural Gas Science and Engineering*, vol. 43, pp. 110–123, 2017.
- [28] D. Liu, Z. Wang, X. Zhang, Y. Wang, X. Zhang, and D. Li, "Experimental investigation on the mechanical and acoustic emission characteristics of shale softened by water absorption," *Journal of Natural Gas Science and Engineering*, vol. 50, pp. 301–308, 2018.
- [29] F. Meng, H. Ge, W. Yan, X. Wang, S. Wu, and J. Wang, "Effect of saturated fluid on the failure mode of brittle gas shale," *Journal of Natural Gas Science and Engineering*, vol. 35, pp. 624–636, 2016.
- [30] C. Yan, Y. Cheng, F. Deng, and J. Tian, "Permeability change caused by stress damage of gas shale," *Energies*, vol. 10, no. 9, p. 1350, 2017.
- [31] M. Li, G. Yin, J. Xu, J. Cao, and Z. Song, "Permeability evolution of shale under anisotropic true triaxial stress conditions," *International Journal of Coal Geology*, vol. 165, pp. 142–148, 2016.
- [32] C. Liu, G. Yin, M. Li et al., "Shale permeability model considering bedding effect under true triaxial stress conditions," *Journal of Natural Gas Science and Engineering*, vol. 68, p. 102908, 2019.
- [33] Y. Chen, C. Jiang, G. Yin, D. Zhang, H. Xing, and A. Wei, "Permeability evolution under true triaxial stress conditions of Longmaxi shale in the Sichuan Basin, Southwest China," *Powder Technology*, vol. 354, pp. 601–614, 2019.
- [34] H. Y. Zhu, L. Tao, Q. Y. Liu, Z. D. Lei, S. Jiang, and J. D. McLennan, "Fracture characteristics and change of permeability under the influence of natural fractures: experimental study of Wufeng-Longmaxi shale," *SPE Reservoir Evaluation & Engineering*, vol. 21, no. 2, pp. 225–237, 2018.
- [35] A. Sakhaee-Pour and A. Agrawal, "Integrating acoustic emission into percolation theory to predict permeability enhancement," *Journal of Petroleum Science and Engineering*, vol. 160, pp. 152–159, 2018.
- [36] K. Zhang, J. Peng, W. Liu et al., "The role of deep geofluids in the enrichment of sedimentary organic matter: a case study of the late Ordovician-Early Silurian in the upper Yangtze region and early Cambrian in the lower Yangtze region, south china," *Geofluids*, vol. 2020, Article ID 8868638, 12 pages, 2020.
- [37] K. Zhang, J. Peng, X. Wang et al., "Effects of thermal evolution of organic matter on the genesis of shale gas and the development of organic matter pores: a case study of marine shale in the upper Yangtze region, South China," *Open Geosciences*, vol. 12, no. 1, pp. 1617–1629, 2020.
- [38] R. Ulusay, *The ISRM Suggested Methods for Rock Characterization, Testing and Monitoring: 2007-2014*, Springer International Publishing, 2014.
- [39] F. Yang, Z. Ning, Q. Wang, R. Zhang, and B. M. Krooss, "Pore structure characteristics of lower Silurian shales in the southern Sichuan Basin, China: insights to pore development and gas storage mechanism," *International Journal of Coal Geology*, vol. 156, pp. 12–24, 2016.
- [40] L. Pan, X. Xiao, H. Tian et al., "A preliminary study on the characterization and controlling factors of porosity and pore structure of the Permian shales in lower Yangtze region, Eastern China," *International Journal of Coal Geology*, vol. 146, pp. 68–78, 2015.
- [41] W. F. Brace, B. W. Paulding, and C. Scholz, "Dilatancy in the fracture of crystalline rocks," *Journal of Geophysical Research*, vol. 71, no. 16, pp. 3939–3953, 1966.
- [42] Z. T. Bieniawski, "Mechanism of brittle fracture of rock: part III—fracture in tension and under long-term loading," *International Journal of Rock Mechanics and Mining Sciences & Geomechanics Abstracts*, vol. 4, no. 4, pp. 425–430, 1967.
- [43] C. D. Martin and N. A. Chandler, "The progressive fracture of Lac du Bonnet granite," *International Journal of Rock Mechanics and Mining Sciences & Geomechanics Abstracts*, vol. 31, no. 6, pp. 643–659, 1994.
- [44] F. Amann, Ö. Ündül, and P. K. Kaiser, "Crack initiation and crack propagation in heterogeneous sulfate-rich clay rocks," *Rock Mechanics and Rock Engineering*, vol. 47, no. 5, pp. 1849–1865, 2014.
- [45] X. Wang, H. Ge, D. Wang, J. Wang, and H. Chen, "A comprehensive method for the fracability evaluation of shale combined with brittleness and stress sensitivity," *Journal of Geophysics and Engineering*, vol. 14, no. 6, pp. 1420–1429, 2017.
- [46] F. Xiangqian, H. Shaowei, L. Jun, and W. Congjie, "Acoustic emission properties of concrete on dynamic tensile test," *Construction and Building Materials*, vol. 114, pp. 66–75, 2016.
- [47] F. Waldhauser and W. L. Ellsworth, "A double-difference earthquake location algorithm: method and application to the Northern Hayward Fault, California," *Bulletin of the Seismological Society of America*, vol. 90, no. 6, pp. 1353–1368, 2000.
- [48] S. Wu, T. Li, H. Ge, X. Wang, N. Li, and Y. Zou, "Shear-tensile fractures in hydraulic fracturing network of layered shale," *Journal of Petroleum Science and Engineering*, vol. 183, article 106428, 2019.
- [49] J. P. Liu, Y. H. Li, and Y. J. Yang, "Study on characteristics of percolation in rock failure process via acoustic emission locating technique," *Dongbei Daxue Xuebao/Journal of Northeastern University*, vol. 31, pp. 1769–1772, 2010.
- [50] P. M. Benson, P. G. Meredith, and A. Schubnel, "Role of void space geometry in permeability evolution in crustal rocks at elevated pressure," *Journal of Geophysical Research: Solid Earth*, vol. 111, no. B12, pp. 1–14, 2006.

- [51] Y. Guéguen and A. Schubnel, “Elastic wave velocities and permeability of cracked rocks,” *Tectonophysics*, vol. 370, no. 1-4, pp. 163–176, 2003.
- [52] R. H. C. De Melo and A. Conci, “Succolarity: defining a method to calculate this fractal measure,” in *Proceedings of IWSSIP 2008 - 15th International Conference on Systems Signals and Image Processing*, vol. 1, pp. 291–294, Bratislava, Slovakia, 2008.
- [53] Y. Xia, J. Cai, E. Perfect, W. Wei, Q. Zhang, and Q. Meng, “Fractal dimension, lacunarity and succolarity analyses on CT images of reservoir rocks for permeability prediction,” *Journal of Hydrology*, vol. 579, article 124198, 2019.

Research Article

Genesis of Dolomite in Middle Permian Maokou Formation in Eastern Sichuan: Constraints from *In Situ* Geochemistry, Sr-Mg Isotopes, and Fluid Inclusions

Yanxia Jiang,^{1,2} Xianfeng Tan ,³ Chengjiang Zhang,¹ Wei Jiang,⁴ Jia Wang,³ Long Luo ,³ Dongping Tan,³ Wei Wang,² and Zhifu Xiong²

¹College of Earth Science, Chengdu University of Technology, Chengdu 610059, China

²Sinopec Exploration Company, Chengdu 610041, China

³Chongqing Key Laboratory of Complex Oil and Gas Exploration and Development, Chongqing 401331, China

⁴School of Earth Science and Engineering, Nanjing University, Nanjing 210046, China

Correspondence should be addressed to Xianfeng Tan; xianfengtan8299@163.com

Received 26 October 2020; Revised 31 December 2020; Accepted 8 January 2021; Published 29 January 2021

Academic Editor: Kun Zhang

Copyright © 2021 Yanxia Jiang et al. This is an open access article distributed under the Creative Commons Attribution License, which permits unrestricted use, distribution, and reproduction in any medium, provided the original work is properly cited.

The dolostone reservoir of the Middle Permian Maokou Formation in Eastern Sichuan has good prospects for oil and gas exploration. Study of dolomitizing genesis of the Maokou Formation is essential for predicting the distribution of the dolostone reservoir. Petrography, *in situ* geochemistry, Sr-Mg isotopes, and fluid inclusions were carried out on samples from the Maokou Formation in Eastern Sichuan in order to discuss the dolomitizing process. Based on mineral and textural characteristics, dolomites were divided into four components: partially clouded dolomite (PCD), mosaic-like dolomite (MLD), cloudy-centered and clear-rimmed dolomite (CACD), and saddle dolomite (SDD). Results indicate that the Maokou Formation in Eastern Sichuan mainly experienced two stages of dolomitization. PCD, MLD, and cloudy-centered dolomite (CCD) were formed during the early dolomitization. They all show turbid crystal planes and bright orange-red CL and have similar trace element contents, ⁸⁷Sr/⁸⁶Sr ratios, and rare-earth patterns, indicating that they might be formed in the same fluid. This is a period when dolomitizing fluids mainly migrated along pores or microcracks and replaced protogenetic calcites, which occurred in the shallow burial stage of the Maokou Formation before the Late Permian. Clear-rimmed dolomite (CRD) and SDD were formed in the late stage of dolomitization. They all have clean crystal planes and darkly red CL. CRD of the ERY profile has trace element contents, ⁸⁷Sr/⁸⁶Sr ratios, and rare-earth patterns similar to SDD of the HLCH profile and Well TL6, inferring that both may be formed in the same fluid. Combined with high SrO contents and homogenous temperatures of fluid inclusions of CRD and SDD and Mg-isotopic compositions, they were generated by hydrothermal dolomitization. The hydrothermal fluid stage is related to the movement of the Emeishan Large Igneous Province, which was made up of basaltic magmatic fluids mixing with the surface water. The hydrothermal fluid mainly migrated upwards along structural fractures or faults and filled in structural fractures, occurring in the Late Permian to Middle-Late Triassic.

1. Introduction

The genesis of dolomite has been a perplexing problem for geologists [1]. Over the past two hundred years, many dolomitizing models have been proposed, such as the sabha model, the seepage-reflux model, the evaporative-pump model, the mixed-water model, and the microbial exchange model [2–7]. In the past two decades, more and more geologists

paid attention to the hydrothermal dolomitization model due to lots of reports of deeply buried dolostones [8–10]. For instance, Niu et al. [11] argued that the Lower Ordovician dolomite in the southwest Tarim Basin was dolomitized by hydrothermal fluids mainly migrating along the fracture system. Nevertheless, hydrothermal dolostones are products of the multistage dolomitization and may have undergone complicated diagenetic processes [12–14]. Therefore, it is

very difficult to accurately identify sources and properties of hydrothermal fluids. Nonetheless, geochemistry and stable isotope composition of carbonate minerals or rocks are closely associated to the diagenetic environment and provide important information regarding paleosalinity, paleotemperature, and paleoclimate. Therefore, the composition of stable isotopes is of great significance to the diagenetic environment of carbonate rocks, and is also important for distinguishing the genesis of dolomite [15–18]. And distribution of major and trace elements in strata reflects changes of the diagenetic environment to a certain extent [19–22].

In Eastern Sichuan, a 23-meter-thick dolostone reservoir of the Maokou Formation was discovered in Well TL6 with a daily output of about $11.08 \times 10^4 \text{ m}^3$ industrial gas flow obtained, indicating that the dolostone reservoir in the Maokou Formation in Eastern Sichuan has good prospects for oil and gas exploration [23]. Understanding the dolomitizing mechanism is essential for predicting the spatial distribution of the dolostone reservoir in the Maokou Formation in Eastern Sichuan. The dolomite development zone of the Maokou Formation in Eastern Sichuan is extended towards to the NW-SE direction and overlaps with the No. 15 basement fault belt in the geographic space (Figure 1(b)). Thus, some scholars proposed that hydrothermal fluids generated by the Emei taphrogeny are the main factor for forming dolomites of the Maokou Formation in Eastern Sichuan [23–26]. For example, Zhang et al. [24] argued that the saddle-shaped dolomite and matrix dolomite of the Maokou Formation filling in the pores and fractures in Eastern Sichuan were formed by contemporaneous multistage hydrothermal fluids altering protogenetic calcites. Nonetheless, distinct dolomitizing genetic models have also been proposed by different scholars including the burial model [27], the mixed-water model [28], and the hot-water model [29–31]. Previous studies were mainly based on a single field profile, petrography or bulk-rock geochemistry, and fluid inclusion, whereas they lack comprehensive evidence from various aspects and demonstration from *in situ* geochemistry. Consequently, by integrating multiple field profiles, *in situ* geochemistry, Sr-Mg isotopes, and fluid inclusions, this study is able to discuss in detail dolomitizing stages, Mg^{2+} sources, dolomitizing time, models, and lateral differences of the Middle Permian Maokou Formation in Eastern Sichuan, which enables providing references for predicting the distribution of the dolostone reservoir.

2. Geological Settings

2.1. Structural Background. The study area has the domain of $26 \times 10^3 \text{ km}^2$ and is located on the eastern part of Sichuan Basin and belongs to the high-steep structural zone in Eastern Sichuan, close to the Huayingshan fault zone and the Daba Mountain [32] (Figure 1(a)). Basement rocks are composed of Archean intermediate-basic rocks and Proterozoic gneisses, developing two sets of basement faults in NE and NW directions [33] (Figure 1(b)). Eastern Sichuan experienced multitectonic cycles in geological history. Since the Maokou Period, Eastern Sichuan has undergone the Tungwu Movement and the Yanshan-Himalaya Movement, and the

tectonic environment has successively transformed from a rift basin and an intracontinental depression basin to the Huayingshan high-steep structural belt [34]. Sichuan Basin was dominated by a gentle-slope carbonate platform facies in the Maokou Period [35]. The Emei taphrogeny caused dispersion of the carbonate platform, the crustal extension, and differential uplift of fault blocks in the middle-upper Yangtze region and facilitated reactivating basement faults [36, 37].

2.2. Stratigraphic and Sedimentary Background. The Kaijiang-Liangping area rapidly sank to form a relatively deep-water environment affected by the Tungwu Movement which was an outside gentle-slope facies. The Tailai area belonged to a middle gentle-slope facies with extensively contiguous bioclastic beaches [23]. Hence, the main body of the Maokou Formation in Eastern Sichuan is a set of marine carbonate rocks which was weakly influenced by terrigenous materials. At present, the thickness of the residual strata of the Maokou Formation ranges from 90 to 400 m; the thicker locations are mainly concentrated at southwest and northwest Sichuan, and the strata gradually becomes thinner towards the northeast [26] (Figure 1(b)). The Maokou Formation in Eastern Sichuan is divided into three members from bottom to top. Member 1 consists of dark-gray augen limestone and grey-black micritic limestone (Figure 2). Thin-layered and lenticular siliceous rocks containing a large number of chert nodules are developed in Member 1 (Figure 2). The calcareous shales exist in the lower part of Member 1, interlaying between augen limestones and siliceous rocks (Figure 2). Member 2 is made up of dark-gray micrite bioclastic limestones and granular limestones (Figure 2). Member 3 is composed of dolostone, siliceous dolostone, and bioclastic limestone. The top is eroded and bauxite mudstones are developed, showing parallel unconformity contact with the overlying Wujiaping Formation or Longtan Formation (Figures 2 and 3(a)). Fine-grained dolostones and siliceous rocks contain multiple mineral assemblages related to hydrothermal fluids, such as microcrystallized quartz+dolomite, saddle dolomite+megacrystalline calcite, coarse-grained dolomite+calcite+sphalerite, and pyrite+marcasite.

3. Analytic Methods

3.1. Sampling. In order to discuss the lateral changes of dolomitization in the Middle Permian Maokou Formation, samples were collected from the ERY profile, the HLCH profile, and Well TL6 (Figure 2). The three profiles extend along the NW-SE direction, consistent with the distribution of dolostones in the Maokou Formation (Figure 1(b)). A total of 25 samples were collected (Figure 2). The strata involve Member 1 and Member 3, including dolomites and limestones. To guarantee the accuracy of analytic results, the collected samples are all fresh and organic poor. All samples are equipped with thin sections, and typical samples are selected for *in situ* geochemistry and Sr-Mg isotope analyses. Analyses of *in situ* major and trace elements, *in situ* Sr isotope, and single mineral solution Mg isotope were carried out at the State Key Laboratory of Continental Dynamics at Northwest University.

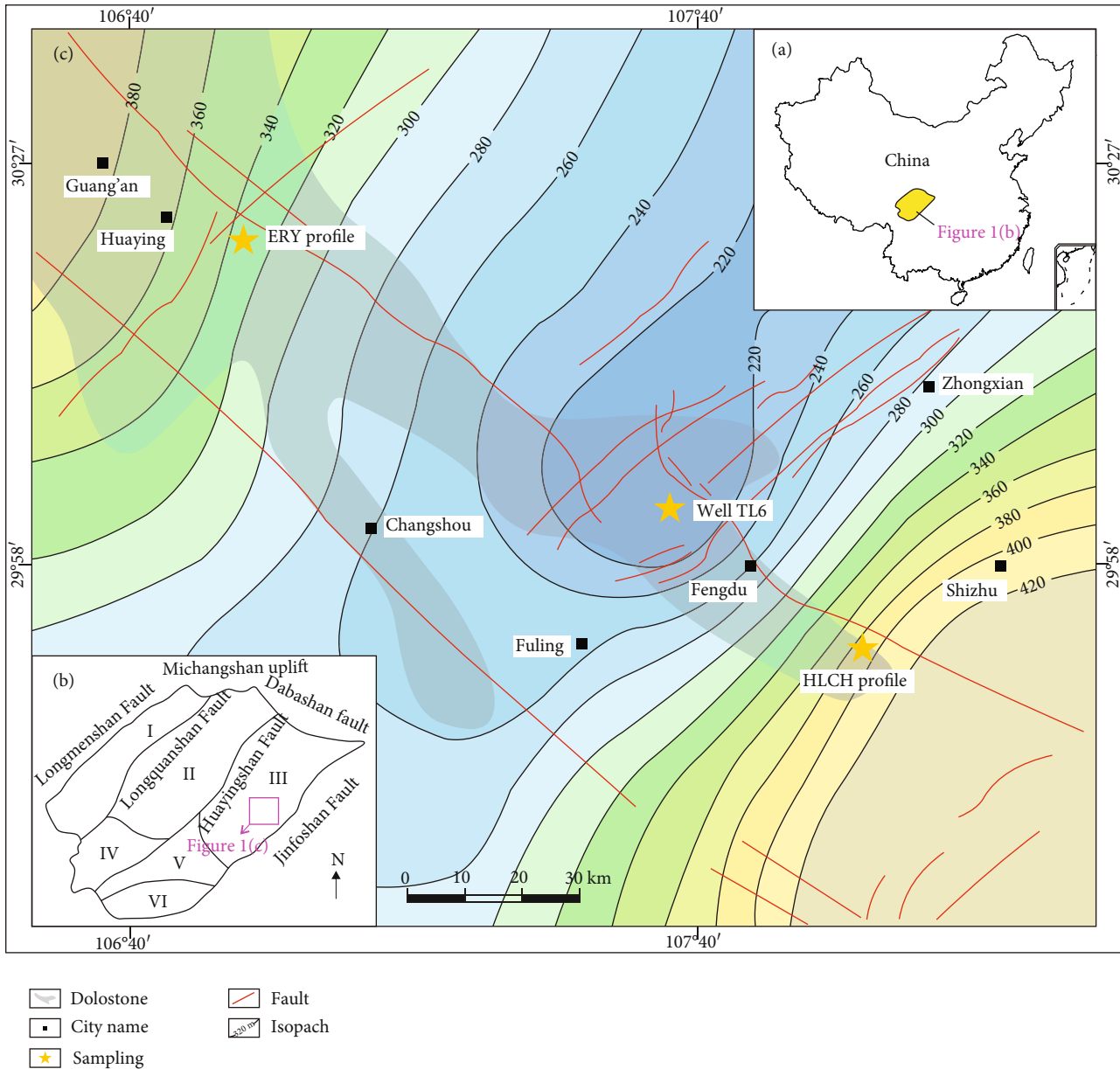


FIGURE 1: (a) Location of the Sichuan Basin in Chinese territory. (b) Geographic location of the study area in Eastern Sichuan. (c) Locations of sampling profiles [34]. I—structural zone in Western Sichuan; II—structural zone in Central Sichuan; III—structural zone in Eastern Sichuan; IV—structural zone in Southwestern Sichuan; V—structural zone in Southern Sichuan; VI—structural area of Sichuan-Yunnan-Guizhou.

3.2. *Major Elements.* Analyses of major elements of different minerals were carried out at the State Key Laboratory of Continental Dynamics at Northwest University. The *in situ* major elements are detected with the JXA-8230 electron probe produced by JEOL. The experimental electron beam acceleration voltage is 15 kV, the current is 10 nA, and the electron beam spot diameter is 2~5 μm .

3.3. *Trace Elements.* Analyses of trace elements of different minerals were carried out at the State Key Laboratory of Continental Dynamics at Northwest University. LA-ICP-MS was used for *in situ* trace element analyses. The ICP-MS used was the GeoLas Pro produced by Coherent Lambda Physik, and

the LA used was Agilent 7500a produced by Agilent, with an average power of 4 W and a beam spot diameter of 32 μm .

3.4. *Sr-Mg Isotopes.* Analyses of *in situ* Sr isotope and solution Mg isotope for minerals were carried out at the State Key Laboratory of Continental Dynamics at Northwest University. *In situ* Sr isotope and solution Mg isotope detection adopted the Nu Plasma II multicollector inductively coupled plasma mass spectrometer (MC-LA-ICP-MS) produced by the Nu Company in the United Kingdom. Standard samples are seawater, BHVO-2, and BCR-2. The quality inspection process is to test the standard sample and the sample 3 times, respectively, referring to Yuan [38] for the detailed analysis process.

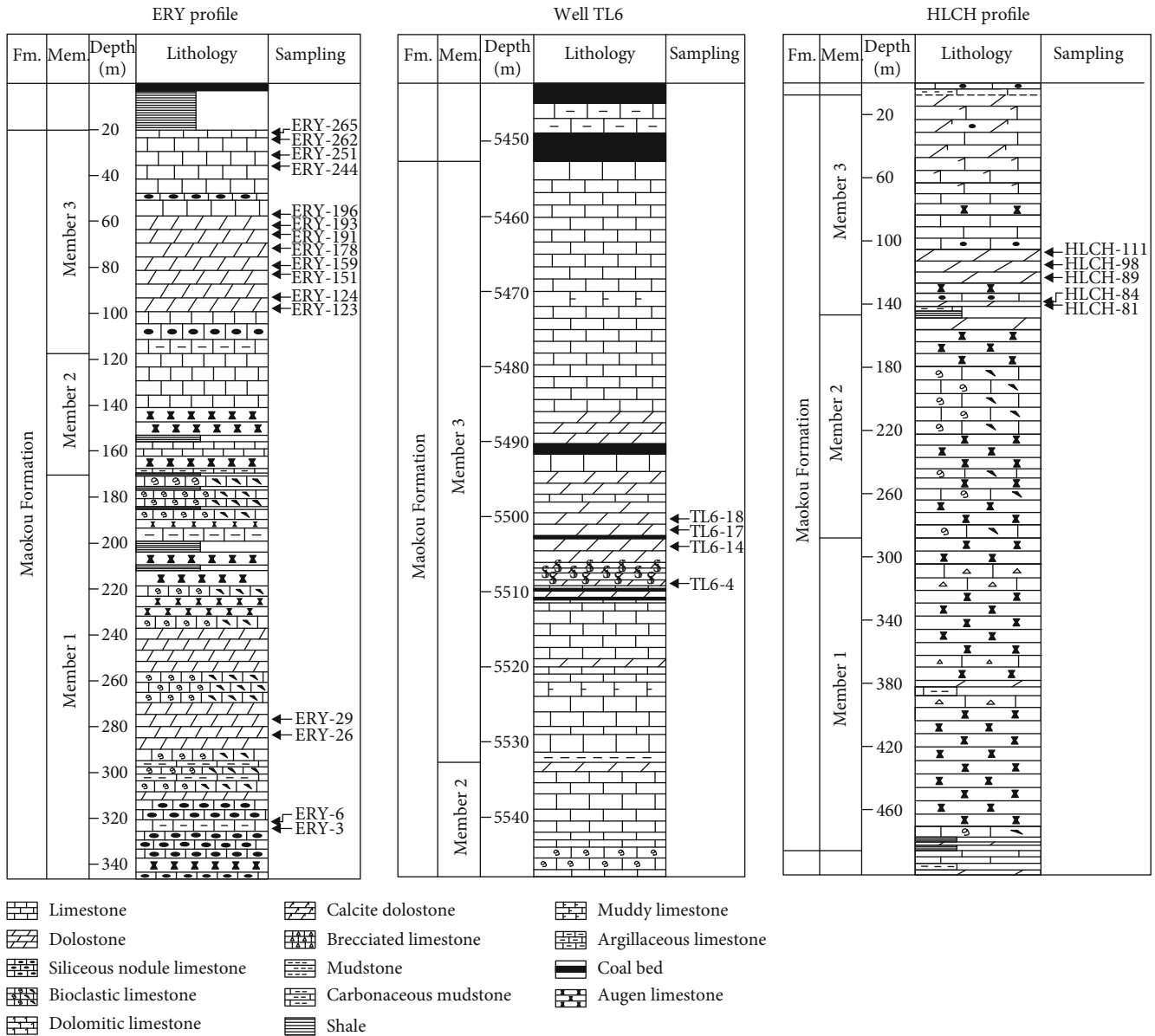


FIGURE 2: The comprehensive stratigraphic columns showing lithology and sampling sites of the Maokou Formation.

3.5. Cathodoluminescence and Fluid Inclusions. Analyses of cathodoluminescence (CL) and homogenous temperatures of fluid inclusions were completed at the Experimental Inspection Center of Xi'an Institute of Geology and Mineral Resources. CL detection uses the CL8200MK5 CL microscope with a 12~15kV beam and a current intensity of 420~430 mA on the nonstained halves of thin sections. Homogenous temperatures of fluid inclusions were measured by the THMSG 600 geological inclusion measurement system, which is composed of geological cold and hot stage and polarizing microscope with a range of -196°C to 600°C. Homogenization temperatures using the equation of Bodnar in 1993 in terms of the H₂O-NaCl system were measured with a precision (reproducibility) of ±1. To limit the possibility of measuring deformed aqueous inclusions, only primary inclusions from the same field of view were measured during

a single heating or freezing run. Heating runs were conducted before freezing runs to reduce the possibility of inclusion stretching by freezing.

4. Results

4.1. Petrographic Features

4.1.1. Petrology

(1) *Limestone.* Limestones include augen limestone (Figure 3(b)), micrite limestone, spherulitic limestone, bioclastic limestone (Figure 3(c)), conglomerate limestone (Figure 3(d)), dolomite limestone (Figure 3(e)), chert nodule limestone (Figure 3(f)), breccia limestone, and argillaceous limestone. The bottom of the Maokou Formation is dominated

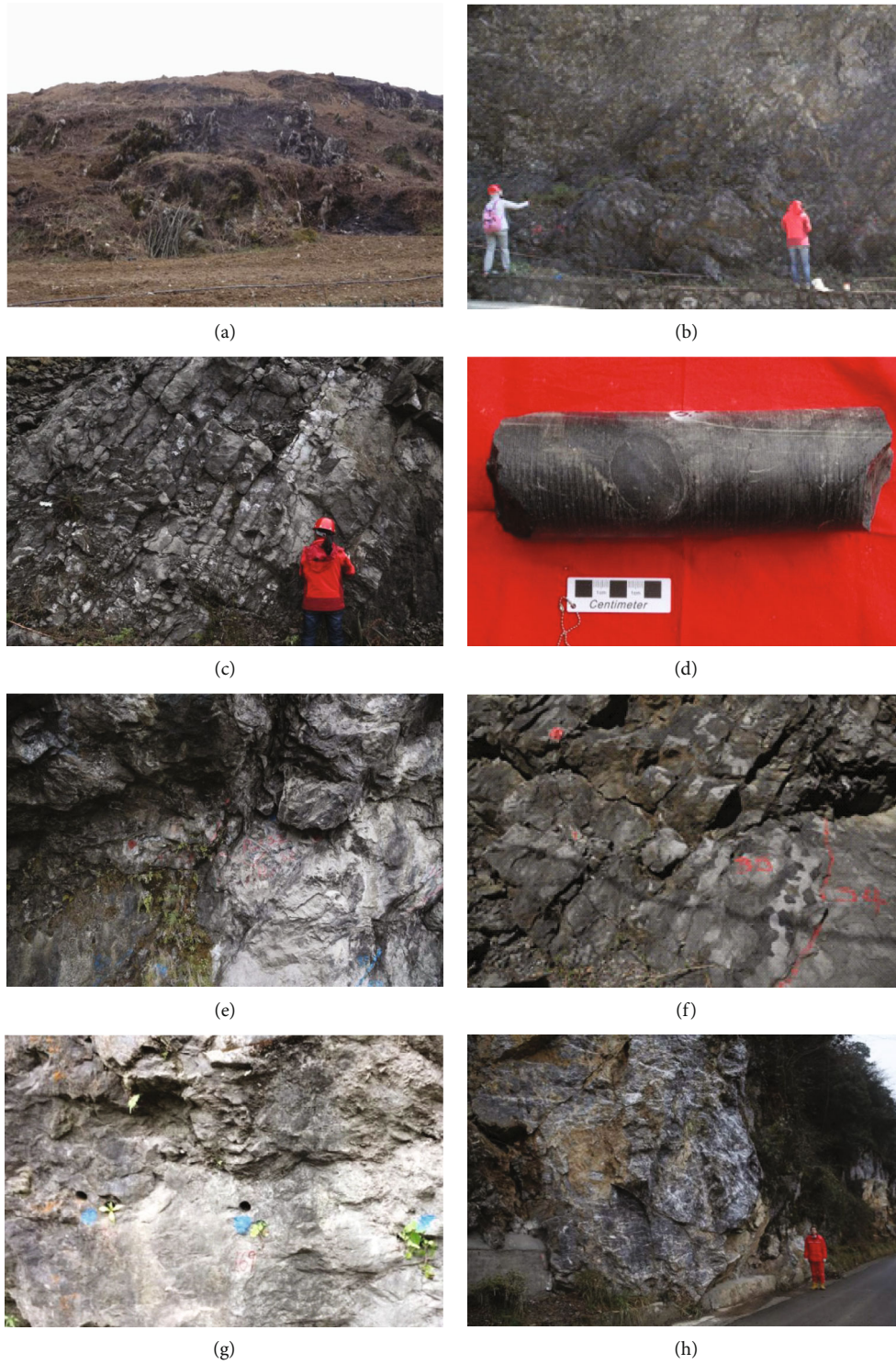


FIGURE 3: Continued.

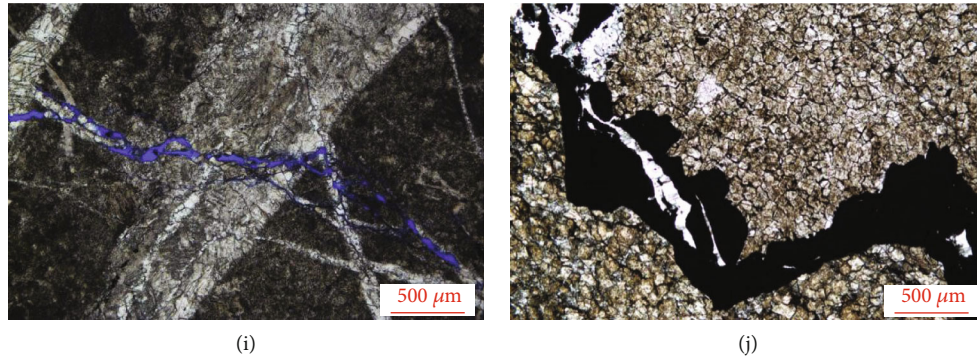


FIGURE 3: (a) Karst limestone; on top of Member 3 of the Maokou Formation in the HLCH profile. (b) Darkly grey augen limestone; Member 2 of the Maokou Formation in the HLCH profile. (c) Dolomite-bearing bioclastic limestone; Member 2 of the Maokou Formation in the ERY profile. (d) Gravel limestone; Well TL6. (e) Nubby dolomitic limestone; Member 2 of the Maokou Formation in the ERY profile. (f) Paramoudras-bearing bioclastic limestone; Member 2 of the Maokou Formation in the HLCH profile. (g) Fine-grained dolostone; Member 3 of the Maokou Formation in the ERY profile. (h) Reticulate carbonate veins; Member 3 of the Maokou Formation in the HLCH profile. (i) Two phases of carbonate veins in the HLCH profile. (j) Residual hydrocarbons in carbonate veins; Well TL6.

by dark-gray micrite limestones and spherulitic limestones and transforms upwards into sparry bioclastic limestones. Bioclastic limestones occurred in Member 2 containing few organic matter, namely, Crinoidea and Textulariina. Dolomitized limestones exist in each member of the Maokou Formation with partially clouded characteristics and dolomite contents < 40%. Dolomite-bearing limestones are distributed in Member 1 with dolomite contents < 10%. Bioclastic spherulitic limestones were developed anywhere. Their matrix contains fine veins and leaching dissolved pores of about 2%. Sparry biospherulitic limestones are distributed on top of Member 3, containing fusulinid and carbonate veins. Dissolved pores are commonly filled by calcite.

(2) *Dolostone*. Dolostones are the most important type of Member 3 and the dominating reservoir in the study area. Rock types include fine-grained dolomite, siliceous dolomite, and calcitized dolomite. Both the ERY and HLCH profiles have undergone different degrees of dolomitization from Member 1 to Member 3. Member 1 and Member 2 only developed lamellar fine-grained dolomite, while Member 3 developed thickened middle-grained dolomite (Figure 3(g)). Less dolostones contain a small amount of residual biological debris located at the boundary between Member 1 and Member 2. And the dolomite has an anhedral shape. Both drilling cores and field profiles developed netted fractures and were filled by carbonate veins (Figure 3(h)). There are at least two stages of carbonate veins. Field and microscope observations show that the second-stage carbonate veins cut the first-stage carbonate veins off (Figure 3(i)). Residual hydrocarbons filling in the carbonate veins can be observed (Figure 3(j)).

4.1.2. *Textural Components of Dolomite*. According to the microscopic characteristics of drilling cores and field samples, dolomites with granular texture can be divided into four components on the basis of clouding degree, microtexture, CL, and geochemical compositions: partially clouded dolomite, cloudy-centered and clear-rimmed dolomite, mosaic-like dolomite, and saddle dolomite, respectively.

(1) *Partially Clouded Dolomite*. Partially clouded dolomite (PCD) is mainly a fine-silty crystal with a subhedral-euhedral texture. The crystal plane is turbid and colorless or light yellow-brown. They are scattered in the matrix, and the original texture is still clear (Figure 4(a)). Moreover, they are the main components of micrite bioclastic limestones or sprite bioclastic limestones, which are predominately distributed in Member 1 and Member 2. The CL is brightly orange-red (Figure 4(b)), different from the dark-red calcite core. Under the BSE (backscattered electron) condition, partial dolomitization can obviously be seen (Figure 5(a)). The residual protogenetic calcite is mottled and is distributed in the dolomite rim and core.

(2) *Cloudy-Centered and Clear-Rimmed Dolomite*. Cloudy-centered and clear-rimmed dolomite (CACD) is mainly a fine-medium crystal with a euhedral texture and mainly occurs in fine-grained dolostones. Its core has a turbid crystal plane, and its edge has a clean crystal plane, with a typically cloudy-centered and clear-rimmed texture (Figure 4(c)), which is one of the main components of Member 3. The CL of clear-rimmed dolomite (CRD) is darkly orange-red, and the CL of cloudy-centered dolomite (CCD) is brightly orange-red (Figure 4(d)). The turbid crystal plane of CCD is still clear under the BSE condition, and the core-rim texture is exhibited visibly in contrast with CRD (Figure 5(c)).

(3) *Mosaic-Like Dolomite*. Mosaic-like dolomite (MLD) is a fine-silty crystal with a subhedral-anhedral and equigranular or inequigranular texture and is mainly found in fine-grained dolostones. They are in close contact with each other with turbid and yellowish brown crystal planes (Figure 4(e)). Furthermore, it is one of the main components of Member 3. The CL is brightly orange-red (Figure 4(f)). A turbid crystal plane can be seen likewise under the BSE condition (Figure 5(b)).

(4) *Saddle Dolomite*. Saddle dolomite (SDD) develops in the carbonate veins (Figure 4(g)). It is dominated by a medium-coarse grain, some of which is curved and fills in

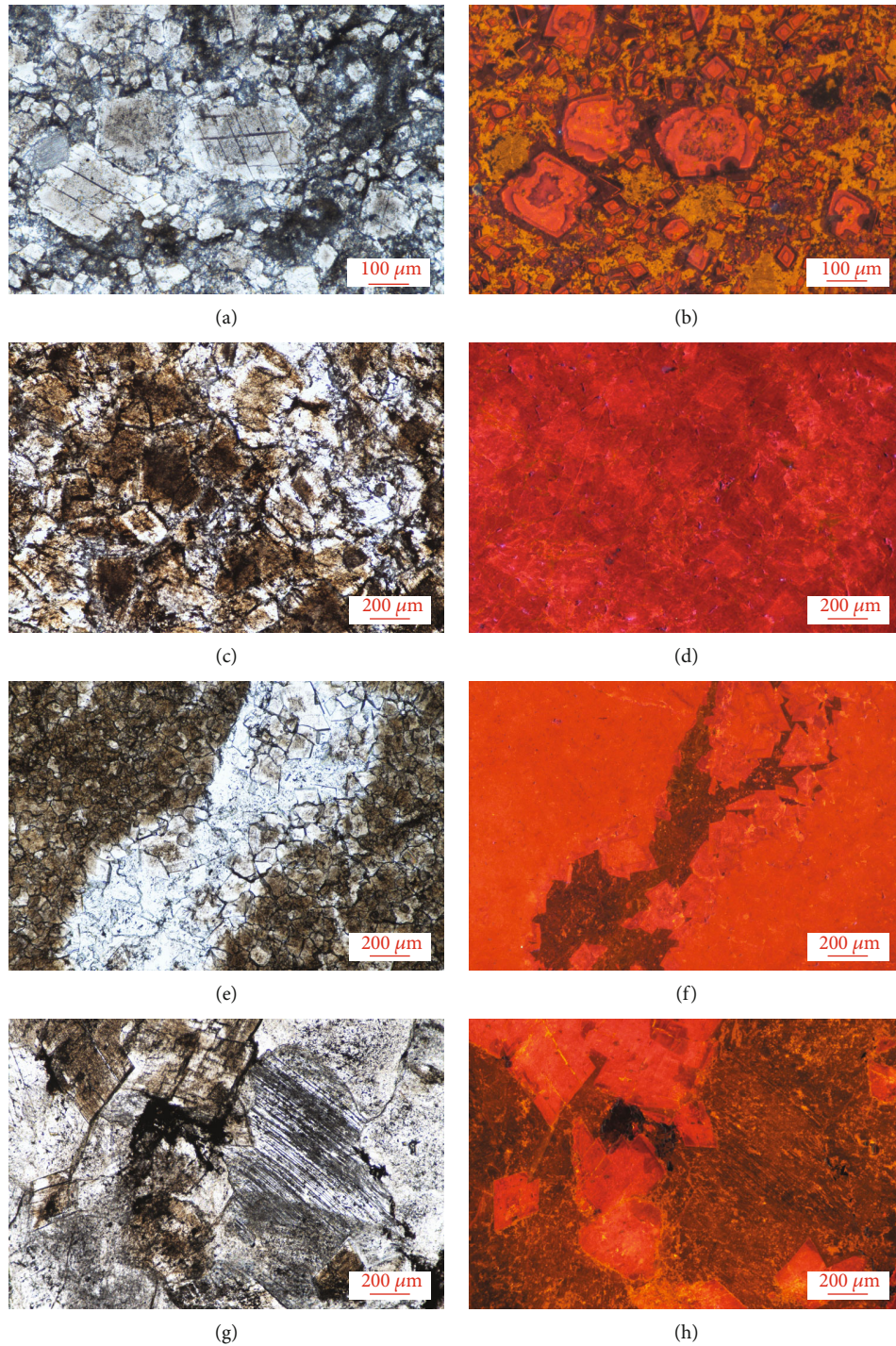


FIGURE 4: (a) PCD reserves the texture of protogenetic calcite in the HLCH profile. (b) PCD shows brightly orange-red CL in the HLCH profile. (c) CACD in the ERY profile. (d) CCD shows brightly orange-red CL, but CRD shows darkly red CL in the ERY profile. (e) MLD and carbonate vein with coarse-grained calcite in the core and SDD in the rim in the HLCH profile. (f) MLD shows brightly orange-red CL and SDD shows darkly red CL, but CGC is colorless in the HLCH profile. (g) CGC and SDD in the HLCH profile. (h) SDD shows darkly red CL, but CGC is colorless in the HLCH profile.

tensile structural fractures (Figure 4(e)). Carbonate veins are composed of coarse-grained calcite (CGC) and SDD. The vein wall is SDD, and the vein center is CGC (Figure 4(e)). The CL of SDD shows a darkly orange-red color (Figures 4(f) and 4(h)), different from MLD. Under the

BSE condition, the crystal plane is still clean and in linear contact with the CGC (Figure 5(d)).

4.2. *Major Elements.* Different dolomite components have clear compositional zoning and geochemical differences

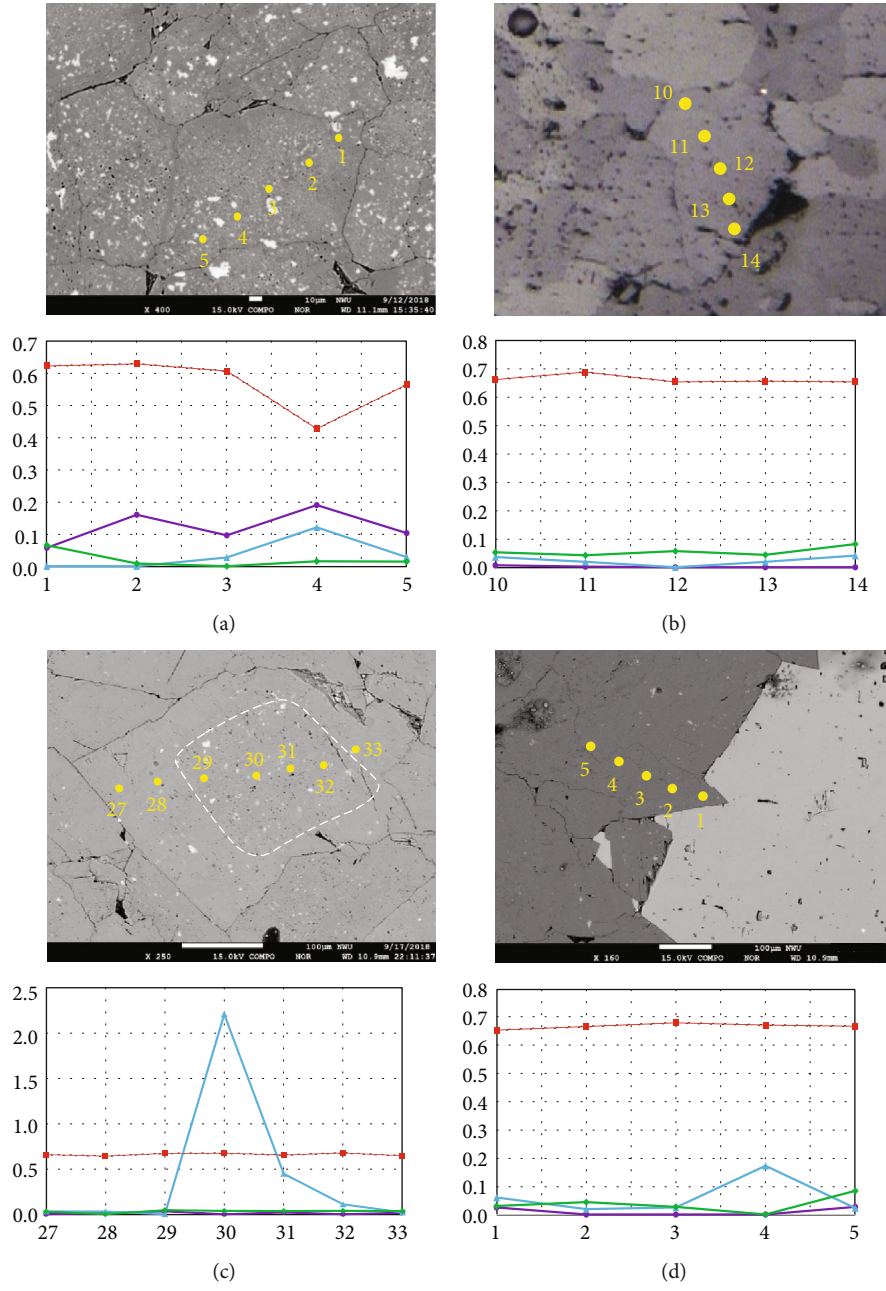


FIGURE 5: Continued.

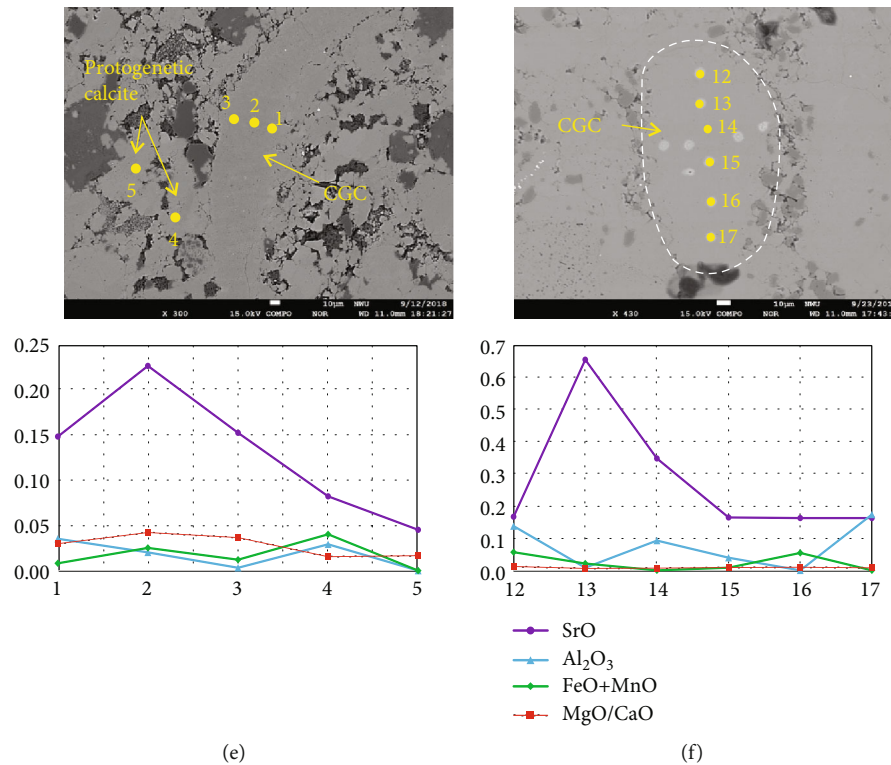


FIGURE 5: (a) Partially clouded dolomite in the BSE and ERY-3 profiles. (b) Mosaic-like dolomite in the BSE and HLCH-89 profiles. (c) Cloudy-centered and clear-rimmed dolomite in the BSE and ERY-151 profiles. (d) Saddle dolomite in the BSE and HLCH-98 profiles. (e) CGC and protogenetic calcite in the BSE and ERY-6 profiles. (f) CGC in the BSE and ERY-29 profiles. CGC: coarse-grained calcite.

(Figure 5). The MgO/CaO ratios of PCD show large variations. Where there are more protogenetic calcite residues, MgO/CaO ratios are significantly low corresponding to high Al₂O₃ contents. SrO contents progressively decrease from core to rim, whereas FeO+MnO contents did not change considerably (Figure 5(a)). MLD has no obvious changes in MgO/CaO ratios and Al₂O₃, SrO, and FeO+MnO contents. But the Al₂O₃, SrO, and FeO+MnO contents of MLD are lower than those of PCD, and the MgO/CaO ratios are higher than PCD (Figure 5(b)). The MgO/CaO ratios and SrO and FeO+MnO contents of CCD and CRD have no apparent variations, but their Al₂O₃ contents show a large change and a gradual decrease from core to rim (Figure 5(c)). The MgO/CaO ratios of CCD and CRD are between those of PCD and MLD, while the SrO and FeO+MnO contents of the former are lower than the latter. The MgO/CaO ratios of SDD did not vary markedly, whereas its core has higher Al₂O₃ but lower SrO and FeO+MnO contents than those of the rim (Figure 5(d)). The Al₂O₃, SrO, and FeO+MnO contents of the rim of SDD are analogous to protogenetic calcite (Figure 5(e)). By contrast, the CGC in the vein core has the characteristics of high SrO, low Al₂O₃, and FeO+MnO contents (Figures 5(e) and 5(f)), while the surrounding protogenetic calcite shows relatively higher Al₂O₃ and FeO+MnO and lower SrO contents and MgO/CaO ratios (Figure 5(e)).

4.3. Trace Elements. According to trace element compositions of different dolomite components, the same component has a large range of Sr, Ba, Na, Fe, and Mn contents and

Rb/Sr ratios. MLD has Sr values of 45.15~843.3 ppm (parts per million; denoting concentration), Ba values of 0.39~99.91 ppm, and Rb/Sr ratios of 0.38~1039. The Fe+Mn and Na contents of MLD show a positive correlation with Rb/Sr ratios (Figures 6(b)–6(d)). CCD contains Rb/Sr values of 31.5~128 and Na contents of 553~4011 ppm (Figure 6(b)). CRD has Na and Fe+Mn contents of 488~527 ppm and 151~215 ppm and Rb/Sr values of 35.5~90.4, respectively. Both CCD and CRD show a positive correlation between Fe+Mn and Rb/Sr (Figure 6(e)). The Na contents of CCD are positively correlated with Rb/Sr ratios, but those of CRD are reversed (Figures 6(b) and 6(c)). SDD has Na, Sr, and Fe+Mn contents of 27.1~360 ppm, 42.3~840 ppm, and 54~850 ppm, respectively (Figures 6(c), 6(e), and 6(g)). The Sr contents of CGC show a significant variation from 66.2 to 1123 ppm, and its Na contents range from 1.42 to 139 ppm (Figures 6(c) and 6(g)). MLD of the HLCH profile contains lower Sr but higher Fe+Mn and Na contents and Rb/Sr ratios than those of the ERY profile (Figures 6(b)–6(e)). The Sr contents of SDD in the HLCH profile and Well TL6 are lower than those of the ERY profile (Figure 6(g)). The Fe+Mn contents of SDD in the HLCH and ERY profiles are lower than those of Well TL6 (Figure 6(e)). Nonetheless, the Ni+Co contents and Rb/Sr values of Well TL6 are similar to those of the HLCH and ERY profiles (Figure 6(h)).

Under the normalized condition of the post-Archean Australian shale (PAAS), all dolomite components show weakly depleted LREE and HREE but slightly enriched

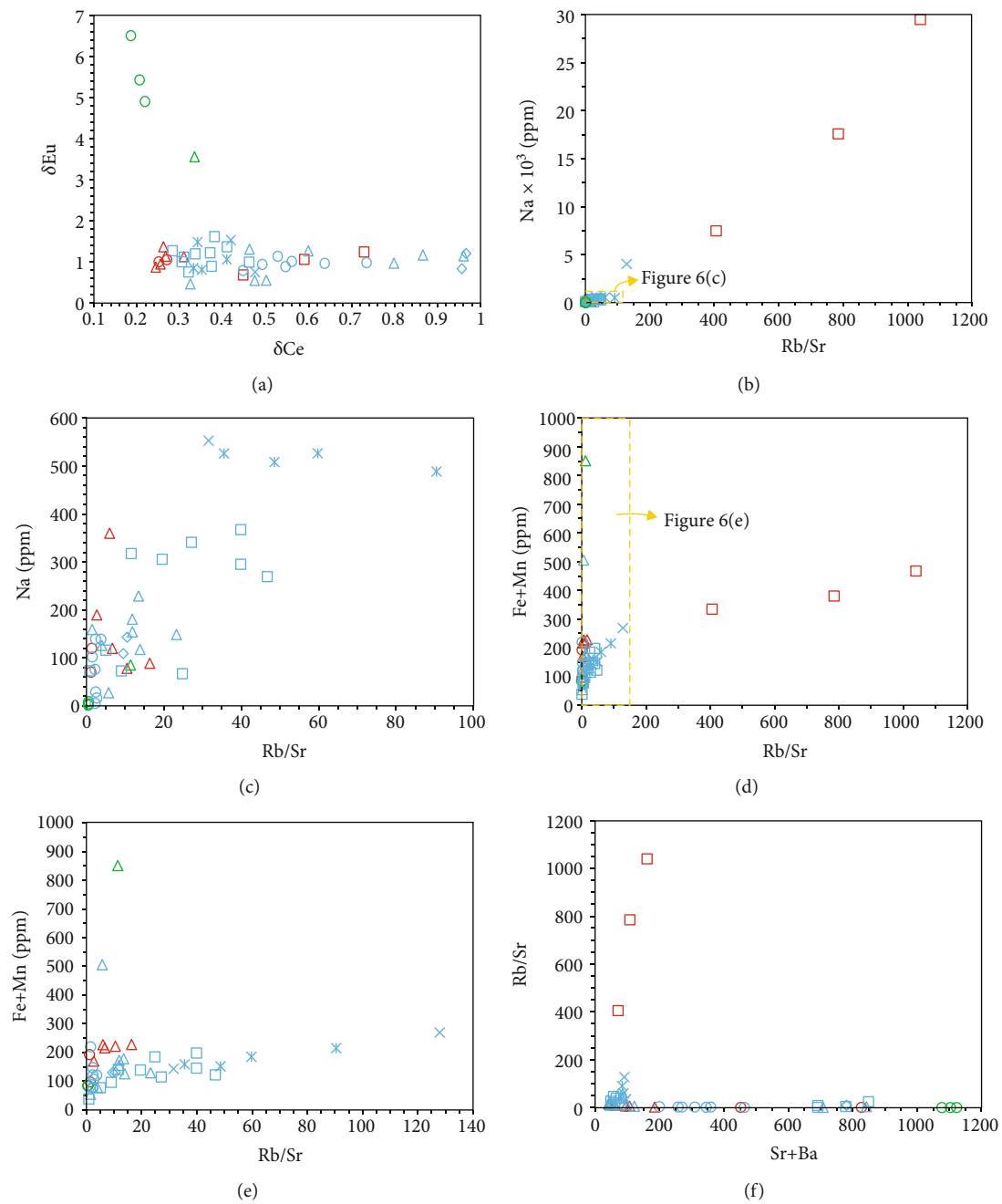


FIGURE 6: Continued.

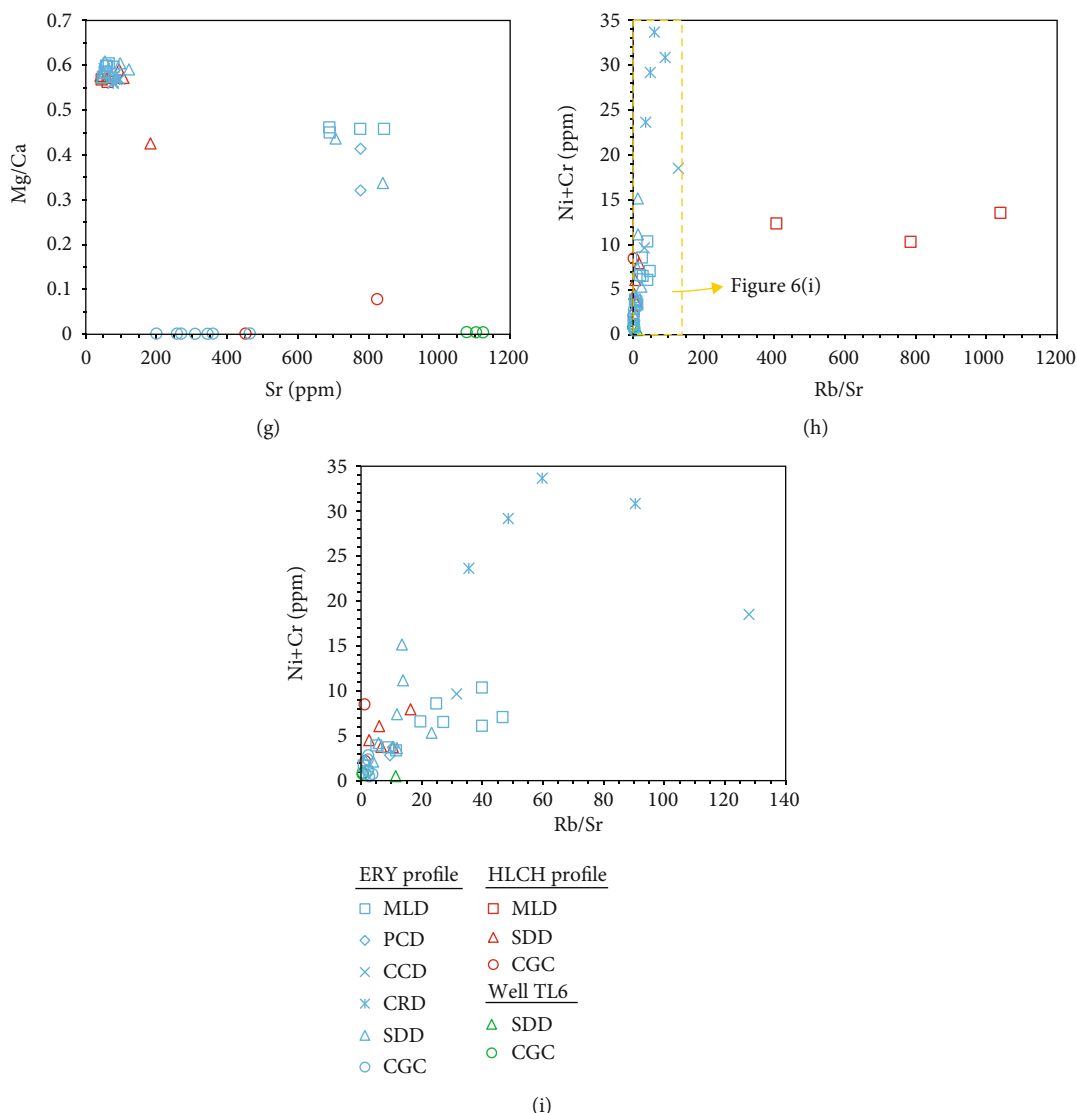


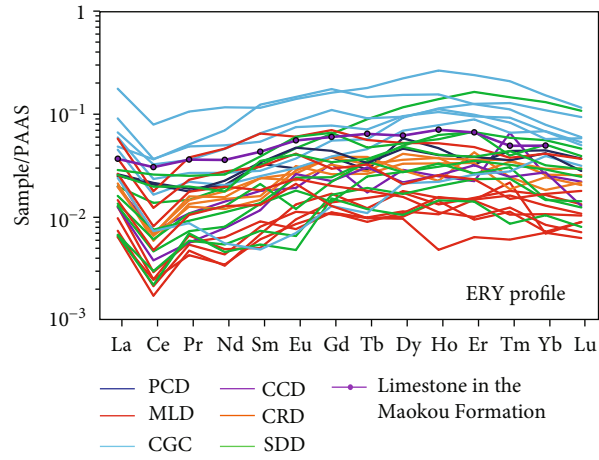
FIGURE 6: Binary diagrams of trace elements and ratios. PCD: partially clouded dolomite. MLD: mosaic-like dolomite. CCD: cloudy-centered dolomite. CRD: clear-rimmed dolomite. SDD: saddle dolomite. CGC: coarse-grained calcite.

MREE (Figure 7). Compared with the HLCH and ERY profiles, SDD and CGC in Well TL6 show obviously positive Eu anomalies and negative Ce anomalies, but CGC in Well TL6 displays more intensely depleted HREE (Figure 7(e)). MLD has higher total rare-earth contents (Σ REE) than SDD in the HLCH profile (Figure 7(c)). MLD has lower Σ REE than SDD in the ERY profile (Figure 7(a)). CGC of different profiles contains higher Σ REE (Figure 7). Under the normalized condition of the upper continental crust (UCC), spider diagrams of all dolomite components show U, La, Sr, and Y enrichment and Nb, Pb, and Ti depletion (Figure 7). MLD of the HLCH profile is enriched in Rb, Ba, Zr, and Hf, distinct from other components (Figure 7(d)).

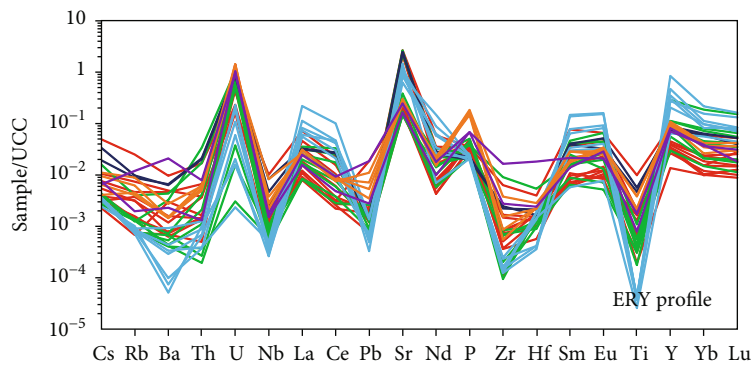
4.4. Sr-Mg Isotopes. In this study, 7 samples were selected for *in situ* Sr isotope analyses of dolomite. The $^{87}\text{Sr}/^{86}\text{Sr}$ values of SDD in the HLCH profile range from 0.707864 to 0.715535 with an average value of 0.710378 (Figure 8(a)). PCD in the

ERY profile has $^{87}\text{Sr}/^{86}\text{Sr}$ values of 0.707407~0.708054 with an average value of 0.707631 (Figure 8(a)). MLD in the ERY profile has $^{87}\text{Sr}/^{86}\text{Sr}$ values ranging from 0.707406 to 0.707605 with an average value of 0.707544 (Figure 8(a)). The $^{87}\text{Sr}/^{86}\text{Sr}$ values of CRD in the ERY profile range from 0.708095 to 0.712091 with an average value of 0.709482 (Figure 8(a)). CCD of the ERY profile has $^{87}\text{Sr}/^{86}\text{Sr}$ values of 0.707503~0.707808 with an average value of 0.707682 (Figure 8(a)). SDD of Well TL6 contains $^{87}\text{Sr}/^{86}\text{Sr}$ values ranging from 0.708060 to 0.708062 with an average value of 0.708061 (Figure 8(a)). The $^{87}\text{Sr}/^{86}\text{Sr}$ values of CGC in Well TL6 range from 0.708024 to 0.709714 with an average value of 0.708715 (Figure 8(a)).

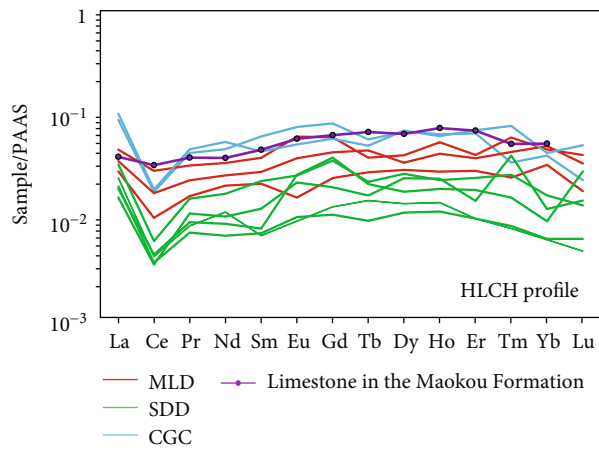
A total of 4 single mineral samples were selected for solution Mg isotope analyses. The reference values of the standard samples are $\delta^{26}\text{Mg}_{\text{BHV0-2}} = -0.20 \pm 0.07\text{‰}$ and $\delta^{26}\text{Mg}_{\text{SW}} = -0.83 \pm 0.09\text{‰}$, which are all within the error range. The $\delta^{25}\text{Mg}_{\text{DSM}}$ and $\delta^{26}\text{Mg}_{\text{DSM}}$ values of all samples



(a)



(b)



(c)

FIGURE 7: Continued.

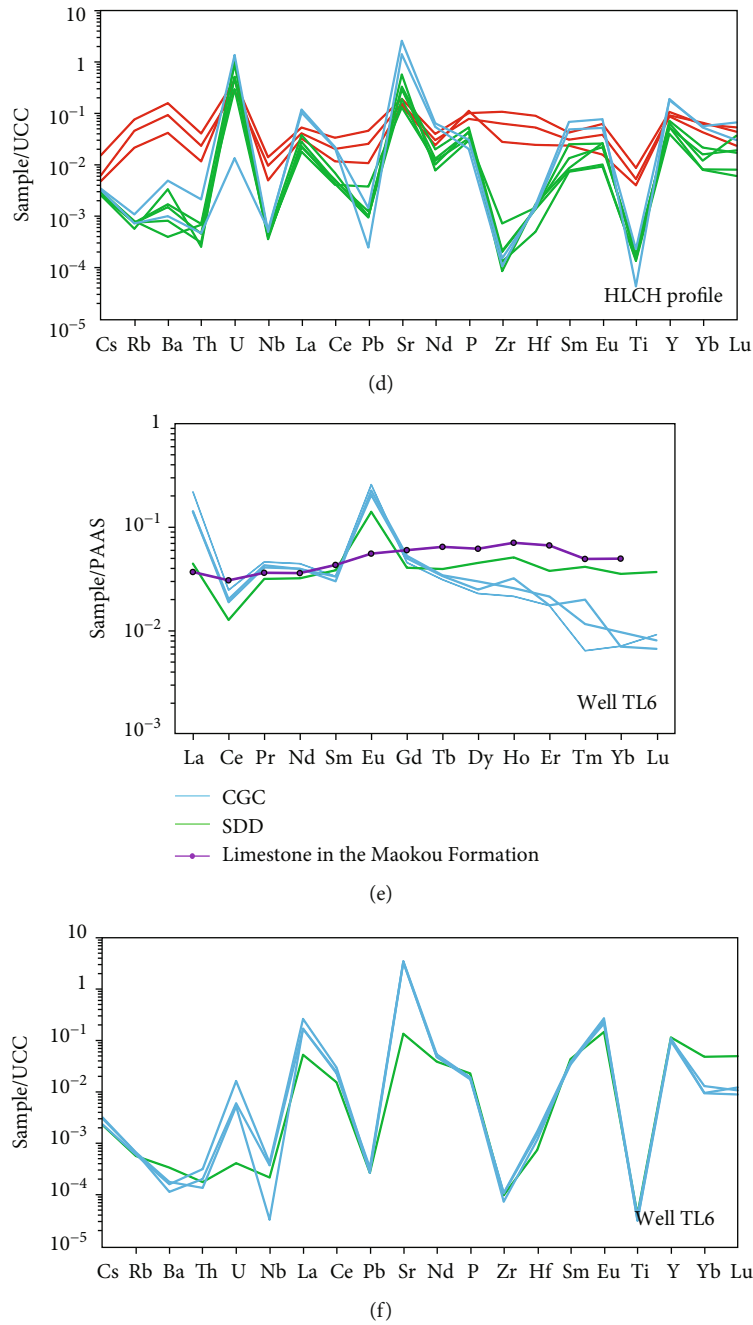
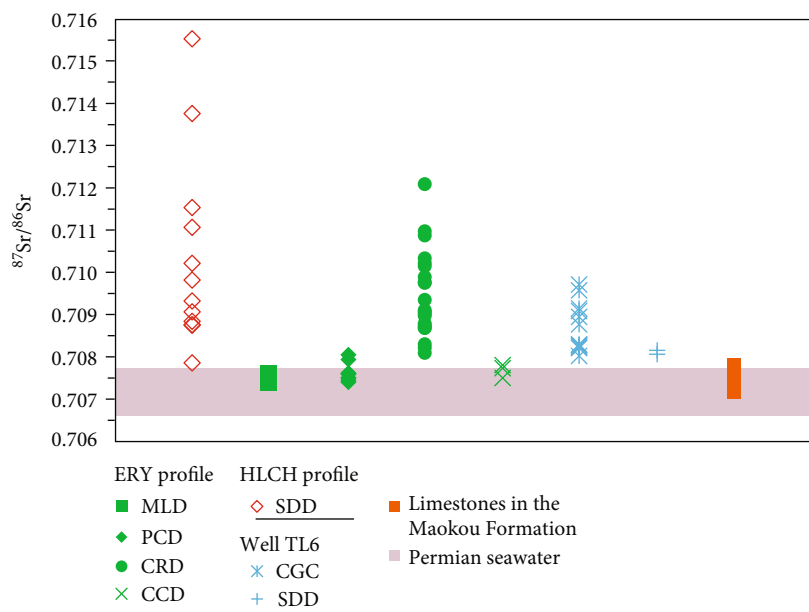


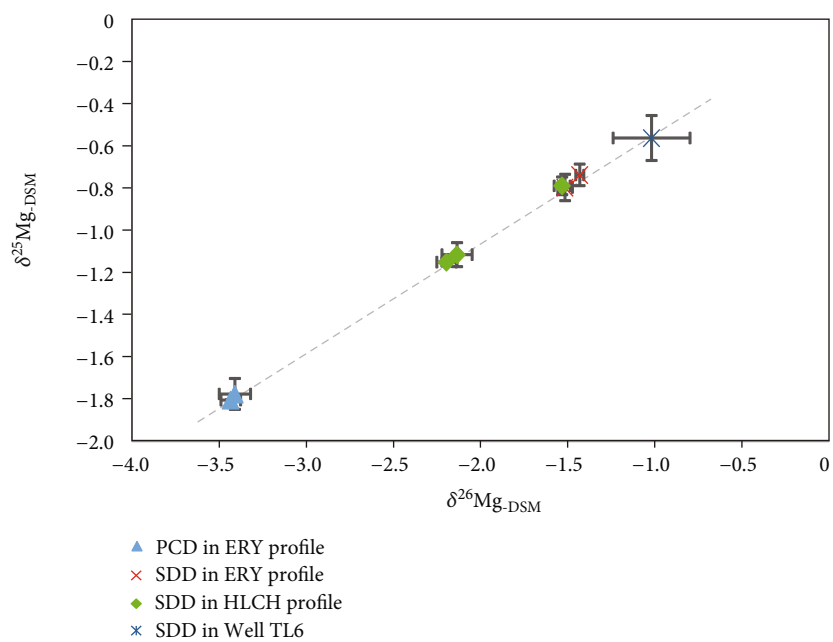
FIGURE 7: Post-Archean Australian Shale- (PAAS-) normalized rare-earth element (REE) patterns and Upper Continental Crust- (UCC-) normalized trace element spidergrams. The limestone in the Maokou Formation was from Li et al. [41]. PAAS data were from Mclennan et al. [62]. UCC data were from Rudnick and Gao [63].

fall on the mass fractionation line well (Figure 8(b)), indicating that the homoisotope interference can be ignored during the mass spectrometry analysis. PCD of the ERY profile has the lightest $\delta^{26}\text{Mg}_{\text{-DSM}}$ ranging from -3.43‰ to -3.41‰ (Figure 8(b)). The $\delta^{26}\text{Mg}_{\text{-DSM}}$ values of SDD in the ERY profile are -1.51‰~-1.43‰ (Figure 8(b)). SDD in the HLCH profile has $\delta^{26}\text{Mg}_{\text{-DSM}}$ values of -2.20‰~-1.53‰ (Figure 8(b)). The $\delta^{26}\text{Mg}_{\text{-DSM}}$ values of SDD in Well TL6 is -1.02‰. The $\delta^{26}\text{Mg}_{\text{-DSM}}$ values of PCD are significantly lower than that of SDD (Figure 8(b)).

4.5. Homogenous Temperature of Fluid Inclusions. Crystallization temperatures of different dolomite components can be referred to based on the homogenization temperature of fluid inclusion. Due to the influence of fluid density and viscosity, there are relatively more fluid inclusions in SDD than other components (Figure 9(a)). The fluid inclusion in CCD is rectangular in shape and has an isolated protogenetic brine inclusion (Figure 9(b)). Because it is difficult to find fluid inclusions in CCD, the unique homogenous temperature measured is 57.4°C (Figure 10). Fluid inclusions in CRD are



(a)



(b)

FIGURE 8: Continued.

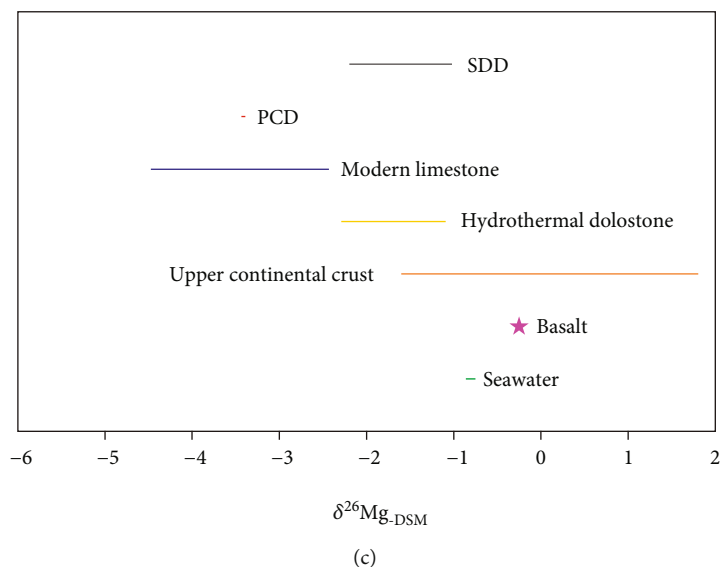


FIGURE 8: (a) *In situ* Sr isotope compositions of different dolomite components of the Maokou Formation in Eastern Sichuan. (b) Correlation of $\delta^{25}\text{Mg}_{\text{DSM}}$ and $\delta^{26}\text{Mg}_{\text{DSM}}$ of different dolomite components of the Maokou Formation in Eastern Sichuan. (c) Comparison of Mg isotope compositions. Sr isotope compositions of limestones in the Maokou Formation were cited from Liu et al. [42]. $^{87}\text{Sr}/^{86}\text{Sr}$ ratios of Permian seawater were from Huang et al. [64]. $\delta^{26}\text{Mg}_{\text{DSM}}$ values of seawater were from Chang et al. [65] and Pearson et al. [66]. $\delta^{26}\text{Mg}_{\text{DSM}}$ values of basalt were cited from Teng et al. [67]. $\delta^{26}\text{Mg}_{\text{DSM}}$ values of upper continental crust were cited from Teng et al. [68]. $\delta^{26}\text{Mg}_{\text{DSM}}$ values of hydrothermal dolostone were from Lavoie et al. [69]. $\delta^{26}\text{Mg}_{\text{DSM}}$ values of modern limestone were cited from Geske et al. [70] and Huang et al. [71].

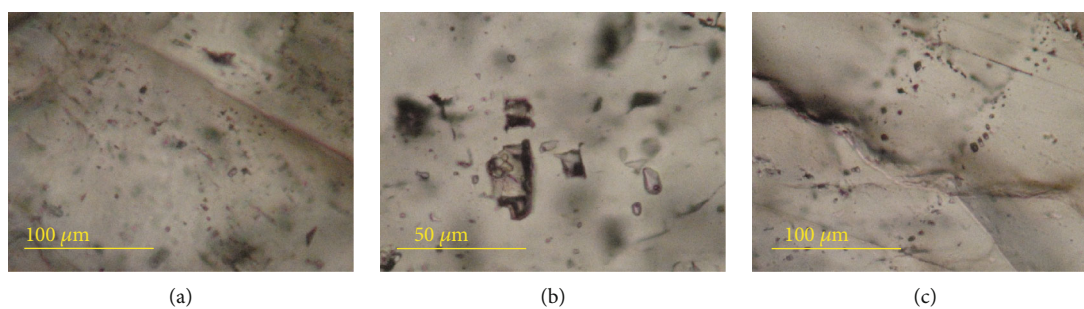


FIGURE 9: Fluid inclusions: (a) protogenetic brine inclusions in saddle dolomite, (b) rectangular or elliptical and isolated protogenetic brine inclusions in cloudy-centered dolomite, and (c) isolated protogenetic brine inclusions in coarse-grained calcite.

rectangular or elliptical and have isolated protogenetic brine inclusions with homogenous temperatures of 106.8~169.7°C (Figures 9(c) and 10). Fluid inclusions in SDD have various shapes (Figure 9(a)), such as rectangular, elliptical, and quadrilateral, and belong to isolated protogenetic brine inclusions with homogenous temperatures of 102.7~231.6°C (Figure 10). CGC contains many fluid inclusions, such as quadrilateral, triangular, rectangular, and elliptical, which are isolated protogenetic brine inclusions (Figure 9(c)). The homogenous temperatures of fluid inclusions of many groups in CGC vary from 103.7 to 298.3°C (Figure 10).

5. Discussion

5.1. Dolomitizing Situation. Anomalous degrees of δCe and δEu enable reflecting the redox situation during dolomitizing. Under PAAS normalization, all dolomite components

and CGC exhibit negative Ce anomalies (Figure 6(a)). Compared with the limestone in the Maokou Formation, all components and CGC show more intensely negative Ce anomalies, except for CCD (Figure 6(a)). Besides, there is no noticeable Eu anomaly in dolomite components and coarse-crystalline calcites except for SDD and coarse-crystalline calcites in Well TL6 (Figure 6(a)), indicating that they were possibly formed in an open oxidizing environment. However, different dolomite components have different negative Ce anomalies, and the same component also shows varying δCe values (Figure 6(a)), suggesting that the redox condition is constantly changing during the dolomitizing process. CCD has slightly higher δCe values of 0.42~0.48 than CRD and MLD in the ERY profile, inferring that the latter were formed in a stronger oxidizing environment. Likewise, SDD and CGC of the ERY profile have higher δCe values than MLD and CRD, implying that the dolomitizing

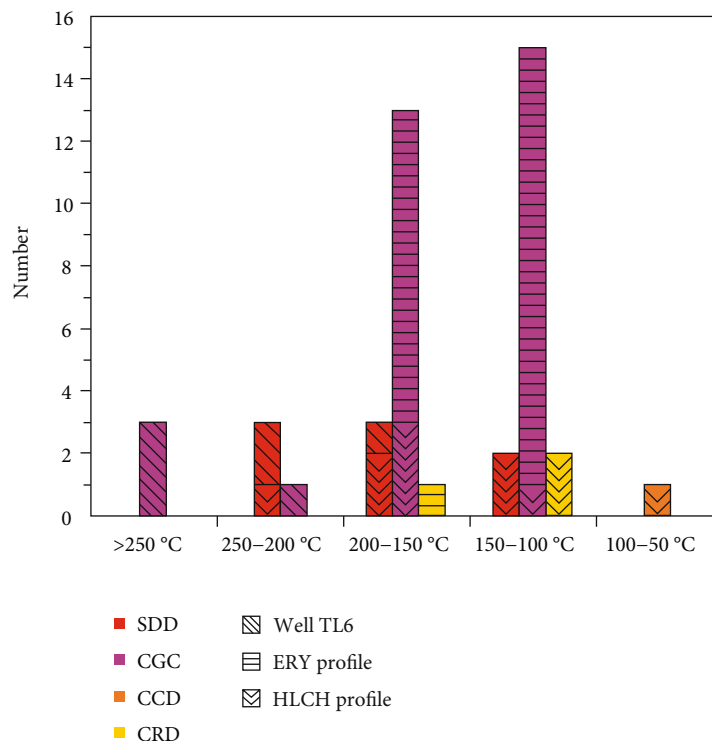


FIGURE 10: Frequency distribution histogram of homogenous temperatures of fluid inclusions in different dolomite components of the Maokou Formation in Eastern Sichuan.

condition turns to a weaker oxidizing environment. Nevertheless, SDD and CGC have stronger negative Ce anomalies than MLD in the HLCH profile, suggesting that the fluid environment has changed again. And these clues further point out that different profiles have distinct redox environments at the same dolomitizing stage. For instance, MLD of the ERY profile has lower δCe values than that of the HLCH profile, and SDD and CGC of the ERY profile have higher δCe values than those of the HLCH profile, suggesting that there are local differences of redox conditions during dolomitization.

SDD and CGC in Well TL6 have significantly positive Eu and negative Ce anomalies. There are two reasons for the characteristic occurrence: (1) Hydrothermal fluid participated in the dolomitizing process. (2) A closed reducing environment took place. Hydrothermal fluids contain apparently higher ΣREE than seawater and river water and show outstanding positive Eu anomalies, so dolomite and calcite produced from hydrothermal fluids have higher ΣREE than primitive limestones [39, 40]. ΣREE of SDD and CGC in Well TL6 is 5.17-13.17 ppm with an average value of 9.39 ppm, which is higher than ΣREE of the limestone in the Maokou Formation [41] (6.73 ppm). Combined with significantly negative Ce anomalies of SDD and CGC in Well TL6, it is inferred that the obviously positive Eu anomalies may be caused by the participation of hydrothermal fluids. Therefore, SDD and CGC in Well TL6 may be formed in an open oxidizing environment. However, δCe values of PCD (0.95~0.97) in the ERY profile are higher than the limestone in the Maokou Formation [41] (0.84), suggesting a weakly reducing environment.

Na contents can reflect the fluid salinity of a mineral-forming environment. MLD has higher Na contents than SDD and CGC in the HLCH profile (Figure 6(b)), indicating that the former was formed in a high-salinity environment. The ERY profile also has the same characteristics as the HLCH profile (Figure 6(c)). Nonetheless, PCD has lower Na contents than the other components, implying that different dolomite components were formed in distinct salinity environments. SDD and CGC of Well TL6 have the lowest Na contents (Figure 6(c)), probably related to the involvement of hydrothermal fluids.

5.2. Dolomitizing Stages and Sources of Mg^{2+}

5.2.1. The Early Stage.

Petrographic observations reveal that PCD, MLD, and CCD show turbid crystal planes (Figures 4(a), 4(c), and 4(e)) and bright orange-red CL (Figures 4(b), 4(d), and 4(f)), whereas CRD and SDD have clean crystal faces and darkly red CL (Figures 4(c), 4(d), 4(g), and 4(h)), indicating that the former and the latter may be products of different fluids. According to the geochemical features, there are similar $^{87}\text{Sr}/^{86}\text{Sr}$ values among PCD, MLD, CCD, and limestones of the Maokou Formation plotted in the range of Permian seawater [42] (Figure 8(a)), although MgO/CaO and Rb/Sr ratios and $\text{Fe}+\text{Mn}$ contents of PCD are lower than those of MLD and CCD in the ERY profile (Figures 5(a) and 6(e)). Combined with analogue REE distribution patterns and spider diagrams among PCD, MLD, and CCD (Figures 7(a) and 7(b)), it is inferred that the three may be formed in different periods of the same

fluid. Sr+Ba contents and REE distribution patterns of PCD in the ERY profile are similar to the limestone in the Maokou Formation [41], and the original calcite texture remains in PCD, suggesting that PCD were possibly formed earlier than MLD and CCD.

MgO/CaO values and Al₂O₃ contents of MLD have no obvious variations, different from those of CCD (Figure 5(b)), pointing to internal homogenous compositions of MLD. MLD in the ERY profile has lower Rb/Sr values and Fe+Mn contents than CCD, but it has higher values than PCD (Figure 6(e)). Moreover, MLD in the ERY profile was divided into two groups in terms of Sr contents and Mg/Ca values (Figure 6(g)). The one with high Sr content and low Mg/Ca is similar to PCD, while the other one with low Sr content but high Mg/Ca overlaps with CCD. This evidence supports the inference that PCD, MLD, and CCD of the ERY profile were formed at different periods of the same fluid. In Figure 5(c), the Al₂O₃ contents of CCD gradually decrease from core to rim. The low MgO/CaO values of PCD also correspond to high Al₂O₃ contents (Figure 5(a)). And the protogenetic calcite likewise exhibits the same characteristic (Figure 5(e)), implying that the dolomitizing fluid is attributed to surface fluids. Furthermore, compared with MLD and CCD of the ERY profile, PCD has lower Na contents and higher δCe values, indicating that the dolomitizing situation transforms from the lowly saline and weakly reduced condition to the highly saline and strongly oxidizing condition. Alteration of the Rb/Sr values and Fe+Mn contents among PCD, MLD, and CCD in the ERY profile may be caused by the dolomitizing diagenesis (Figures 6(d) and 6(e)). Wang et al. [43] proposed that the progressively strong metasomatic dolomitization of penecontemporaneous brine will result in Sr contents decreasing and Mn contents increasing in dolomite. Therefore, PCD, MLD, and CCD in the ERY profile were formed in the process of the brine replacing protogenetic calcites. And MLD should be formed earlier than CCD. Cr+Ni contents of PCD, MLD, and CCD show a positive correlation with Rb/Sr ratios in the ERY profile (Figure 6(h)), while their $\delta^{26}\text{Mg}$ and $^{87}\text{Sr}/^{86}\text{Sr}$ values do not reflect signals of mantle-derived material (Figures 8(a) and 8(c)). There is no fact for high field strength elements enriching in spider diagrams (Figure 7). These characteristics support that the high-salinity brine is mainly composed of seawater mixing with a few mantle-derived fluids. Compared with MLD of the ERY profile, MLD of the HLCH profile shows higher Rb/Sr ratios and Fe+Mn, Cr+Ni, and Na contents. Although MLD of the HLCH profile has similar REE distribution patterns to the limestone in the Maokou Formation, the spider diagrams show evidently enriched Zr, Hf, and Ti (Figure 7(d)), suggesting that dolomitizing fluids in the HLCH profile may be derived from high-salinity brine with the mixing of more mantle-derived fluids.

5.2.2. The Late Stage. Both CRD and SDD have clean crystal planes and darkly red CL (Figures 4(c), 4(d), 4(g), and 4(h)). CRD of the ERY profile has analogue $^{87}\text{Sr}/^{86}\text{Sr}$ values similar to SDD of the HLCH profile and Well TL6 (Figure 8(a)), implying that they were generated in the same fluids. CRD contains higher Rb/Sr values and Cr+Ni and Na contents

(Figures 6(c) and 6(h)) but lower Fe+Mn contents and δCe values (Figures 6(a) and 6(e)) than those of SDD in the ERY profile. In Figure 7(a), SDD of the ERY profile enriches HREE, different from CRD. Reversely, CRD contains higher Ba, P, Zr, Hf, and Ti contents than SDD in the ERY profile (Figure 7(b)). And $^{87}\text{Sr}/^{86}\text{Sr}$ values of CRD are higher than CCD in the ERY profile (Figure 8(a)). These facts suppose that CRD of the ERY profile was produced in a mixture of surface fluids and mantle-derived fluids, consistent with high homogenous temperatures of fluid inclusions (Figure 10). The signature that CRD in the ERY profile has high Rb/Sr values and Na contents but low Fe+Mn contents indicates that ΣHREE and δCe values should be inherited from CCD. Also, homogenous temperatures of fluid inclusions of CRD are higher than those of CCD but lower than those of SDD (Figure 10). Because CRD was formed after CCD, the temperature of dolomitizing fluids in the Maokou Formation in Eastern Sichuan should increase progressively. Consequently, SDD was generated after CRD.

SDD shows low Rb/Sr values and Sr contents, which may be associated with the distribution coefficient of Sr in calcite and dolomite. Since the ionic radius of Sr is close to Ca but quite different from Mg, it is generally believed that Sr can replace Ca in calcite or dolomite but cannot substitute Mg in dolomite [44]. In Figures 5(e) and 5(f), CGC contains higher SrO contents than SDD and CRD. Therefore, most of the Sr elements in the fluid enter into the calcite lattice rather than dolomite. SDD has high SrO contents and homogenous temperatures of fluid inclusions and $\delta^{26}\text{Mg}$ values similar to that of Early Silurian hydrothermal dolomite in southern Quebec, Canada (Figure 8(c)), indicating a hydrothermal dolomitizing model. Likewise, hydrothermal-related minerals in the Maokou Formation, such as pyrite and sphalerite, also support the hydrothermal dolomitization model [24]. Oxygen isotope has the thermal fractionation effect, so the high temperature will cause the $\delta^{18}\text{O}$ value of calcite and dolomite to become more negative [45]. Chen et al. [46] and Zhang et al. [24] reported that SDD in the Maokou Formation has negative $\delta^{18}\text{O}$ values ranging from -6.9‰ to -7.6‰, indicating that SDD is indeed affected by hydrothermal fluids. CRD shows similar REE distribution patterns to SDD in the ERY profile (Figure 7(a)), although they both have several geochemical differences. CRD of the ERY profile has similar $^{87}\text{Sr}/^{86}\text{Sr}$ values to that of SDD of the HLCH profile and Well TL6 (Figure 8(a)). This evidence indicates that magmatic fluids do not change chemical compositions but only improve the temperature. Hydrothermal fluids forming SDD may be mixed with more surface water, which results in a reduction of the Cr+Ni contents and an increase of the Fe+Mn contents of SDD. Besides, Lottermoser [47] argued that ΣREE of minerals crystallizing from fluids predominantly depends on ΣREE of the fluid. Thus, SDD in Well TL6 exhibits distinctive positive Eu anomalies (Figure 6(a)) which are possibly related to the type of rocks through which surface water flows. As mentioned above, two phases of intersecting carbonate veins can be observed in the field (Figure 3(i)), but SDD or CGC does not show significant geochemical and isotopic differences. Hence, CRD and two phases of carbonate veins may be generated at

different periods of contemporaneous hydrothermal fluids, analogue to multipulsing Mg^{2+} metasomatism during the ascent of mantle-derived fluids [48].

5.3. Dolomitizing Time. Residual hydrocarbons filling in pores between MLD and SDD and fractures can be observed in dolostones or calcareous dolostones of the Maokou Formation in Eastern Sichuan (Figure 3(j)), suggesting that oil and gas filling occurred later after the formation of SDD. Jiang et al. [49] proposed that source rocks of the Maokou Formation had produced plenty of hydrocarbons in Middle-Late Triassic via recovering the burial history of Well GC2. So, the dolomitizing time of the Maokou Formation was at least earlier than Middle-Late Triassic. Petrographic observations show that carbonate veins filled in the fractures (Figure 3(h)), testifying that SDD, one of the components of carbonate veins, has to crystallize before the fractures. The seismic profile of Well GC2 revealed that tensile basement faults disappeared in coarse-grained dolostones in the Upper Permian Wujiaping Formation [46]. Liu et al. [50] reported that the Huayingshan fault zone is a regional basement fault formed in the Proterozoic Jinning Stage and was reactivated in the Late Permian Dongwu Stage induced by the basalt eruption in the middle of the Huayingshan structure. Therefore, SDD in carbonate veins should be formed after Late Permian. CRD is also of hydrothermal origin but is not distributed in the cracks. Combined with homogenous temperatures of fluid inclusions slightly lower than those of SDD, the formation time of CRD is the same as SDD. Moreover, the Emei taphrogeny occurred after the deposition of the Maokou Formation according to previous studies [34–37], which caused generating the supergene karst system on top of the Maokou Formation. Hence, the late stage of dolomitization in the Maokou Formation took place synchronous with or later than the karst system, because SDD exists by filling in the pores or cracks.

The textural relationship that CRD envelops CCD supports that PCD, MLD, and CCD were formed before CRD and SDD (Figure 4(c)). Additionally, PCD, MLD, and CCD are distributed in the matrix and are relevant with the high-salinity brine, implying that they were produced before the fractures. According to the paleotemperature gradient profile of Sichuan Basin established by Wang et al. [51], the paleotemperature gradient is $3.53^{\circ}\text{C}/\text{hm}$ in Eastern Sichuan during Late Permian-Early Triassic. The Maokou Formation was situated in the buried depth of 930 m when CCD had been generated by assuming that the surface temperature was 25°C . At present, it is generally considered that the burial depth ranging from 500 to 1000 m is a shallow burial stage [52]. Consequently, PCD, MLD, and CCD were formed in the shallow burial stage of the Maokou Formation earlier than Late Permian. Hao et al. [53] reported that the early stage of dolomitization in the Maokou Formation happened at least 257 Ma via U-Pb isotope dating, compatible with the above inference and earlier than the exposure period of the Maokou Formation.

5.4. Dolomitizing Model. In the past 30 years, many scholars have proposed a variety of dolomitizing models for the gen-

esis of dolostones in the Maokou Formation in Sichuan Basin, including the burial model [27], the mixed-water model [28], the basalt-leaching model [54], the hot-water model [29–31], and the tectonic hydrothermal model [24, 42, 45, 46, 55]. However, the dolomitizing model of the Maokou Formation in different regions of Sichuan Basin may be various. As for the Maokou Formation in Eastern Sichuan, the hot-water model proposed by Wang et al. [29] and Li et al. [30] lacks sufficient evidence. For example, it is unreasonable that the hot-water model was considered only based on SDD, positive Eu anomalies, and a $\text{Fe} - \text{Mn} - (\text{Cu} + \text{Ni} + \text{Co}) \times 10$ triangular discriminant diagram. First, hydrothermal dolomites also have these signatures [24, 42, 45]. Second, PCD and MLD do not have these characteristics in this study.

As mentioned above, PCD, MLD, and CCD of the Maokou Formation in Eastern Sichuan were formed in the shallow burial stage before Late Permian. PCD is the main component of fine-grained dolostones of Member 1 and Member 2, while MLD and CCD are mainly distributed in the middle-coarse-grained dolostones of Member 3, indicating that at the shallowly buried stage, the lower layer of Maokou Formation was less dolomitized, but the upper layer was stronger. These features support that dolomitizing fluids should originate from the surface rather than the underground. Hence, we think that PCD, MLD, and CCD were formed at different stages of dolomitizing high-salinity brines, and high-salinity brines were principally derived from closed seawater mixing with little mantle-derived fluids. The seawater primarily migrated along pores, and the mantle-derived fluid may predominately seep upward via microcracks and pores (Figure 11(a)).

CRD and SDD have obvious hydrothermal characteristics and enrich high field strength elements Nb, Zr, Hf, and Ti and compatible elements Cr and Ni (Figures 6(h) and 7) with high homogenous temperatures of fluid inclusions (Figure 10). Furthermore, Emeishan basalts are exposed locally on the top of the Maokou Formation [56]. Therefore, we speculate that hydrothermal fluids may be related to the Emei mantle plume simultaneously. Nowadays, it is generally believed that the Emei mantle plume had a large-scale thermal effect [57]. Zhu et al. [58] reported that the heat flow value of strata in Sichuan Basin slowly increased from 290 Ma (Hercynian) and reached a maximum in ca. 259 Ma; then, it was reduced to the current temperature gradient until 230 Ma. Moreover, Sichuan Basin was in a tensional environment and developed lots of basement faults with the characteristics of high angle, short distance, large scale, and long extension [59–61]. There is a NE-SW trending Huayingshan fault zone and many NW-SE trending basement faults in Eastern Sichuan [23]. The Huayingshan fault zone is a large-scale basement fault in the Proterozoic Jinning Stage and was reactivated to result in the basaltic eruption around the Huayingshan structural axis in the Late Permian Dongwu Stage [50], identical to observations of basalt outcropped locally on the top of the Maokou Formation in Eastern Sichuan [56]. Davies and Smith [9] pointed out that hydrothermal fluid activities are specially developed in specific structures such as extensional faults, deep and

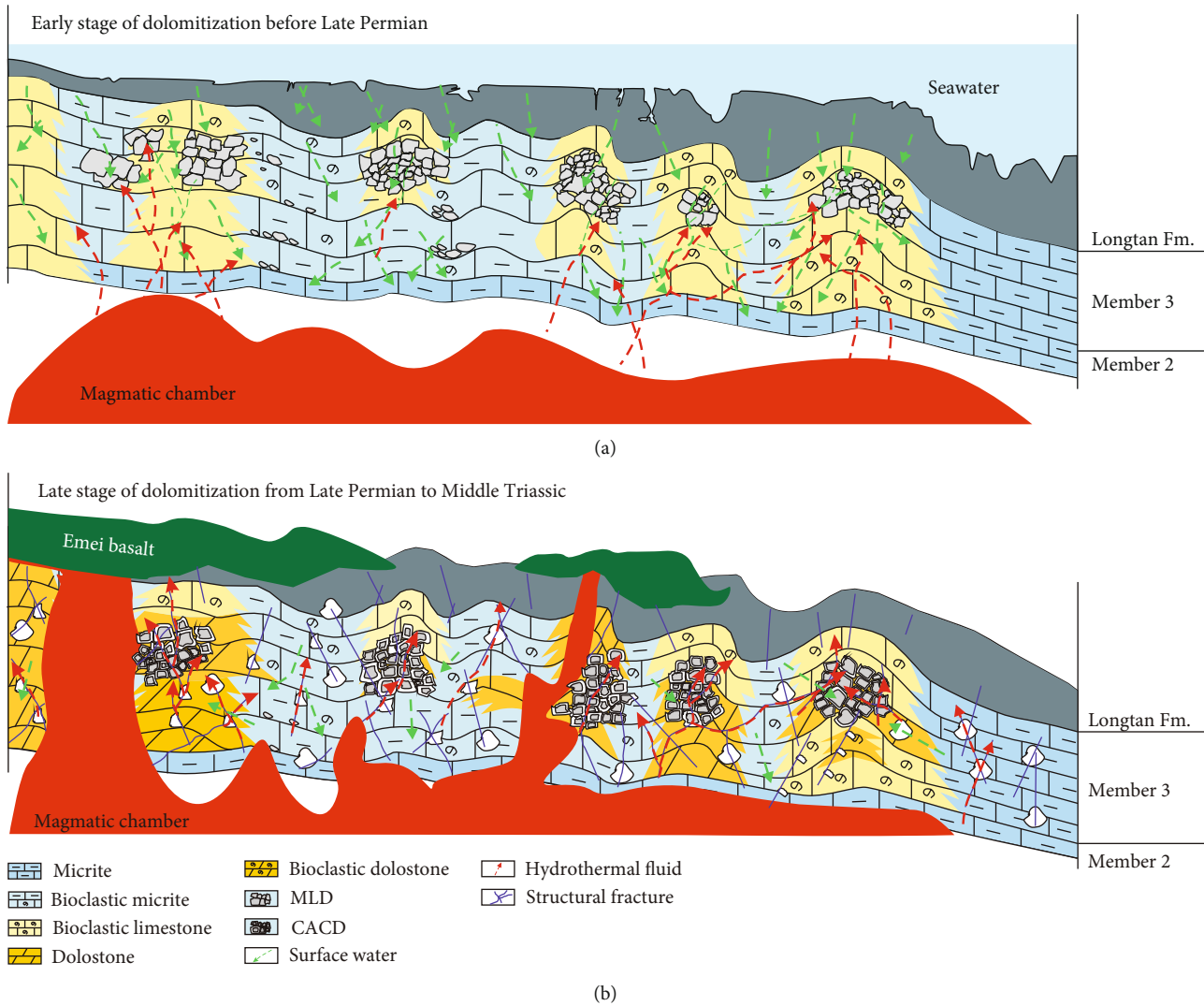


FIGURE 11: Dolomitizing model of the Middle Permian Maokou Formation in Eastern Sichuan. MLD: mosaic-like dolomite. CACD: clear-rimmed dolomite.

large strike-slip faults, tensional faults, torsional faults, and intersections of deep and large strike-slip faults. Thus, the fracture system provides an important channel for hydrothermal fluids in Eastern Sichuan and is the first choice for large-scale upward migration of Mg-rich fluids (Figure 11(b)). These speculations enable understanding the high homogenous temperatures of high-fluid inclusions and carbonate veins filling in fractures.

Consequently, dolostones in Maokou Formation in Eastern Sichuan were mainly formed by two stages of dolomitizing fluids. The early stage was high-salinity brine which mainly migrated along pores. The late stage was relevant to the activity of the Emei mantle plume and belonged to hydrothermal fluids which primarily migrated upward along structural fractures or faults and filled in structural fractures.

6. Conclusions

In this study, the integration of multiple field profiles, *in situ* geochemistry, Sr-Mg isotopes, and fluid inclusions was

carried to discuss the dolomitizing process and lateral differences of Middle Permian Maokou Formation in Eastern Sichuan. According to textural signatures, dolomites were subdivided into four components: partially clouded dolomite (PCD), mosaic-like dolomite (MLD), cloudy-centered and clear-rimmed dolomite (CACD), and saddle dolomite (SDD). Their *in situ* geochemical differences are essential to distinguish the genesis of dolomites. The conclusions can be summarized as follows:

- (1) PCD, MLD, and cloudy-centered dolomite (CCD) were formed during the early dolomitization in terms of similar textural and geochemical features. They all show turbid crystal planes and bright orange-red CL and have similar $^{87}\text{Sr}/^{86}\text{Sr}$ ratios and rare-earth patterns. Dolomitization of the early stage happened via high-salinity brines with a mixture of seawater and little mantle-derived fluids replacing protogenetic calcites which mainly migrated along pores in the shallow burial stage before Late Permian.

However, the high-salinity brine in the ERY profile consists of mixing seawater and a little mantle-derived fluid. The HLCH profile might undergo mixing high-salinity brine and more mantle-derived fluid and the more intensely diagenetic process

- (2) CRD and SDD were formed in the late stage of dolomitization. They all have clean crystal planes and darkly red CL. SDD contains slightly lower Cr and Ni contents and slightly higher Fe and Mn contents than those of CRD, and its $\delta^{26}\text{Mg}$ values are analogous to Early Silurian hydrothermal dolomite in southern Quebec, Canada. Combined with high SrO contents and homogenous temperatures of fluid inclusions of CRD and SDD, they were generated by hydrothermal dolomitization. Dolomitizing fluids mainly migrating along structural fractures or faults and filling in structural fractures occurring from Late Permian to Middle-Late Triassic are hydrothermal fluids which are associated with activities of the Emei mantle plume and composed of a mixture of magmatic fluids and surface water

Data Availability

The data used to support the findings of this study are included within the article.

Conflicts of Interest

The authors declare that they have no conflicts of interest.

Acknowledgments

The authors gratefully thank the Sinopec Exploration Company for providing core samples and geological data. This study was jointly supported by the National Natural Science Foundation of China (Grant numbers 42072140, 41672113, and 41902153), the Chongqing Natural Science Foundation of China (Grant numbers cstc2020jcyj and mxxmX0217), and the Foundation of Chongqing Education Commission (Grant number KJQN202001517).

References

- [1] H. G. Machel, "Concepts and models of dolomitization: a critical reappraisal," *Geological Society, London, Special Publications*, vol. 235, no. 1, pp. 7–63, 2004.
- [2] I. Friedman and J. E. Sanders, "Origin and occurrence of dolostone," in *Carbonate Rocks*, G. V. Chilingar, H. J. Bissel, and R. W. Fairbridge, Eds., pp. 267–348, Elsevier, Amsterdam, 1967.
- [3] K. J. Hsu and J. Schneider, "Progress report on dolomitization—hydrology of Abu Dhabi Sabkhas, Arabian Gulf," in *The Persian Gulf*, pp. 409–422, Springer, 1973.
- [4] J. E. Adams and M. L. Rhodes, "Dolomitization by seepage refluxion," *AAPG Bulletin*, vol. 44, pp. 1912–1920, 1960.
- [5] K. Badiozamani, "The Dorag dolomitization model—application to the Middle Ordovician of Wisconsin," *SEPM Journal of Sedimentary Research*, vol. 43, no. 4, pp. 965–984, 1973.
- [6] P. A. Baker and M. Kastner, "Constraints on the formation of sedimentary dolomite," *Science*, vol. 213, no. 4504, pp. 214–216, 1981.
- [7] C. Vasconcelos, J. A. McKenzie, S. Bernasconi, D. Grujic, and A. J. Tiens, "Microbial mediation as a possible mechanism for natural dolomite formation at low temperatures," *Nature*, vol. 377, no. 6546, pp. 220–222, 1995.
- [8] D. Chen, H. Qing, and C. Yang, "Multistage hydrothermal dolomites in the middle Devonian (Givetian) carbonates from the Guilin area, South China," *Sedimentology*, vol. 51, no. 5, pp. 1029–1051, 2004.
- [9] G. R. Davies and L. B. Smith Jr., "Structurally controlled hydrothermal dolomite reservoir facies: an overview," *AAPG Bulletin*, vol. 90, no. 11, pp. 1641–1690, 2006.
- [10] E. Azomani, K. Azmy, N. Blamey, U. Brand, and I. al-Aasm, "Origin of Lower Ordovician dolomites in eastern Laurentia: controls on porosity and implications from geochemistry," *Marine and Petroleum Geology*, vol. 40, pp. 99–114, 2013.
- [11] J. Niu, W. H. Huang, and F. Liang, "Geochemical characteristics and genesis of Lower Ordovician dolomite in the southwest Tarim Basin, Northwest China," *Episodes*, vol. 42, no. 1, pp. 33–54, 2019.
- [12] J. M. Gregg and K. L. Shelton, "Dolomitization and dolomite neomorphism in the back reef facies of the Bonnetterre and Davis formations (Cambrian), southeastern Missouri," *SEPM Journal of Sedimentary Research*, vol. 60, no. 4, pp. 549–562, 1990.
- [13] I. S. Al-Aasm and J. J. Packard, "Stabilization of early-formed dolomite: a tale of divergence from two Mississippian dolomites," *Sedimentary Geology*, vol. 131, no. 3–4, pp. 97–108, 2000.
- [14] M. Liu, Y. Xiong, C. Xiong et al., "Evolution of diagenetic system and its controls on the reservoir quality of pre-salt dolostone: the case of the Lower Ordovician Majiagou Formation in the central Ordos Basin, China," *Marine and Petroleum Geology*, vol. 122, p. 104674, 2020.
- [15] L. A. Derry, M. D. Brasier, R. M. Corfield, A. Y. Rozanov, and A. Y. Zhuravlev, "Sr and C isotopes in Lower Cambrian carbonates from the Siberian craton: a paleoenvironmental record during the "Cambrian explosion"," *Earth and Planetary Science Letters*, vol. 128, no. 3–4, pp. 671–681, 1994.
- [16] L. A. Derry, L. S. Keto, S. B. Jacobsen, A. H. Knoll, and K. Swett, "Sr isotopic variations in upper proterozoic carbonates from Svalbard and East Greenland," *Geochimica et Cosmochimica Acta*, vol. 53, no. 9, pp. 2331–2339, 1989.
- [17] S. J. Huang, "A study on carbon and strontium isotopes of late Paleozoic carbonate rocks in the upper Yangtze platform," *Acta Geologica Sinica*, vol. 71, no. 1, pp. 45–53, 1997.
- [18] N. P. James and P. W. Choquette, "Diagenesis 9. Limestones—the meteoric diagenetic environment," *Geoscience Canada*, vol. 11, no. 4, pp. 162–194, 1984.
- [19] D. W. Morrow, "Diagenesis I. Dolomite—part I. The chemistry of dolomitization and dolomite precipitation," *Geosciences Canada*, vol. 9, pp. 5–13, 1982.
- [20] U. Brand and J. Veizer, "Chemical diagenesis of a multicomponent carbonate system—1. Trace elements," *SEPM Journal of Sedimentary Research*, vol. 50, no. 4, pp. 1219–1236, 1980.
- [21] L. Zhu, Z. Wang, Q. Feng, B. Zhang, L. Wei, and Z. Yu, "Genesis of dolomite in the upper assemblage of the Ordovician Majiagou Formation in the southeastern Sulige gas field, Ordos Basin, China: evidence from C, O, and Sr isotopes and

- major and trace elements," *Energy Exploration & Exploitation*, vol. 38, no. 6, pp. 2729–2751, 2020.
- [22] R. Jia and D. Liu, "The relationship between dolomitization and organic matter occurrence in Lower Paleozoic carbonate in the Ordos Basin," *Chinese Science Bulletin*, vol. 45, no. S1, pp. 41–46, 2000.
- [23] D. Hu, L. Wang, R. Huang, J. Duan, Z. Xu, and L. Pan, "Characteristics and main controlling factors of the Middle Permian Maokou dolomite reservoirs in the eastern Sichuan Basin," *Natural Gas Industry*, vol. 39, no. 6, pp. 13–21, 2019.
- [24] T. Zhang, J. Lin, Y. Han, Z. Wang, J. Qin, and R. Zhang, "Pattern of hydrothermal dolomitization in the Middle Permian Maokou Formation, eastern Sichuan Basin, and its alteration on reservoirs herein," *Oil & Gas Geology*, vol. 41, no. 1, pp. 132–143, 2020.
- [25] X. Tang, X. Tan, H. Liu et al., "Characteristics and development mechanism of dolomite and dolomitic quartzite reservoirs of the Middle Permian Maokou Formation in eastern Sichuan Basin," *Oil & Gas Geology*, vol. 37, no. 5, pp. 731–743, 2016.
- [26] D. Li, H. Chen, H. Chen et al., "Relationship between reservoir development in the Middle Permian Maokou Formation and paleostructure evolution in the Sichuan Basin," *Oil & Gas Geology*, vol. 37, no. 5, pp. 756–763, 2016.
- [27] Y. He and Z. Feng, "Origin of fine- to coarse-grained dolostones of Lower Permian in Sichuan Basin and its peripheral regions," *Journal of Jiangnan Petroleum Institute*, vol. 4, no. 18, pp. 15–20, 1996.
- [28] Y. Zhang, "Dolomitization in Permian rocks in Sichuan Basin," *Acta Petrolei Sinica*, vol. 3, no. 1, pp. 29–33, 1982.
- [29] H. Wang, H. Shen, D. Huang et al., "Origin and distribution of hydrothermal dolomites of the Middle Permian in the Sichuan Basin," *Natural Gas Industry*, vol. 34, no. 9, pp. 25–32, 2014.
- [30] Y. Li, H. Shen, X. Shi, H. Wang, S. Chen, and X. Yuan, "Distribution and origin of dolomites in Maokou Formation, Eastern and Central Sichuan Basin," *Natural Gas Exploration & Development*, vol. 36, no. 4, pp. 1–3, 2013.
- [31] G. Yang, H. Wang, H. Shen et al., "Characteristics and exploration prospects of Middle Permian reservoirs in the Sichuan Basin," *Natural Gas Industry*, vol. 35, no. 7, pp. 10–16, 2015.
- [32] K. Zhang, C. Jia, Y. Song et al., "Analysis of Lower Cambrian shale gas composition, source and accumulation pattern in different tectonic backgrounds: a case study of Weiyuan Block in the Upper Yangtze region and Xiuwu Basin in the Lower Yangtze region," *Fuel*, vol. 263, article 115978, 2020.
- [33] Z. Luo, "New recognition of basement in Sichuan Basin," *Journal of Chengdu University of Technology*, vol. 25, no. 2, pp. 191–200, 1998.
- [34] S. Liu, B. Deng, Z. Li, and W. Sun, "The texture of sedimentary basin-orogenic belt system and its influence on oil/gas distribution," *Acta Petrologica Sinica*, vol. 27, no. 3, pp. 621–635, 2011.
- [35] Y. B. Zhang, "Sequence stratigraphy and depositional models of the Middle Permian in Sichuan Basin," Chengdu University of Technology: PhD thesis, 2011.
- [36] Y. Wang and Y. Jin, "The formation of dolomite and paleo-karst of the Lower Permian series in Sichuan Basin and the relation to the Emei taphrogenesis," *Journal of Chengdu University of Technology*, vol. 24, no. 1, pp. 12–20, 1997.
- [37] J. Su, S. Zhang, H. Yang, G. Zhu, J. Chen, and B. Zhang, "Control of fault system to formation of effective carbonate reservoir and the rules of petroleum accumulation," *Acta Petrolei Sinica*, vol. 31, no. 2, pp. 196–203, 2010.
- [38] H. Yuan, "State Key Laboratory of Continental Dynamics, Northwest University," *Rock and Mineral Analysis*, vol. 31, no. 6, pp. 1090–1092, 2012.
- [39] A. Michard, F. Albarède, G. Michard, J. F. Minster, and J. L. Charlou, "Rare-earth elements and uranium in high-temperature solutions from East Pacific Rise hydrothermal vent field (13°N)," *Nature*, vol. 303, no. 5920, pp. 795–797, 1983.
- [40] A. Michard and F. Albarede, "The REE content of some hydrothermal fluids," *Chemical Geology*, vol. 55, no. 1-2, pp. 51–60, 1986.
- [41] Q. Li, S. Xu, H. Chen et al., "Geochemical characteristics and palaeo-environmental implication of Middle Permian Maokou Formation in Wangcang region, Sichuan Basin, China," *Journal of Chengdu University of Technology*, vol. 45, no. 3, pp. 268–281, 2018.
- [42] H. Liu, T. Ma, X. Tan et al., "Origin of structurally controlled hydrothermal dolomite in epigenetic karst system during shallow burial: an example from Middle Permian Maokou Formation, central Sichuan Basin, SW China," *Petroleum Exploration and Development*, vol. 43, no. 6, pp. 1000–1012, 2016.
- [43] L. Wang, W. Hu, X. Wang et al., "Variation of Sr content and $^{87}\text{Sr}/^{86}\text{Sr}$ isotope fractionation during dolomitization and their implications," *Oil & Gas Geology*, vol. 37, no. 4, pp. 464–472, 2016.
- [44] Z. Li, E. Xu, M. Fan et al., "Geochemical characteristics and formation of dolostones from the Changxing Formation at Puguang gas field in Sichuan Basin," *Geochimica*, vol. 39, no. 4, pp. 371–380, 2010.
- [45] J. Wang, Y. Gu, Y. Tao, Z. Qiang, S. Qiang, and C. Jiang, "The model of dolomitization jointly controlled by two-episode fluids in Maokou Formation in Central Sichuan Basin," *Acta Sedimentologica Sinica*, vol. 34, no. 2, pp. 236–249, 2016.
- [46] X. Chen, W. Zhao, L. Zhang et al., "Discovery and exploration significance of structure-controlled hydrothermal dolomites in the Middle Permian of the central Sichuan Basin," *Acta Petrolei Sinica*, vol. 33, no. 4, pp. 562–569, 2012.
- [47] B. G. Lottermoser, "Rare earth elements and hydrothermal ore formation processes," *Ore Geology Reviews*, vol. 7, no. 1, pp. 25–41, 1992.
- [48] Y. He, B. Liu, and S. Qin, "Study on the dolomitization and dolostone genesis," *Acta Scientiarum Naturalium Universitatis Pekinensis*, vol. 46, no. 6, pp. 1010–1020, 2010.
- [49] Q. Jiang, S. Hu, Z. Wang, T. Wang, Q. Li, and X. Zhai, "Genesis of medium-macro-crystalline dolomite in the Middle Permian of Sichuan Basin," *Oil & Gas Geology*, vol. 35, no. 4, pp. 503–510, 2014.
- [50] H. Liu, Z. Sun, Z. Li et al., "Syn depositional tectonic activities in the Huayingshan fracture belt during the Triassic Jialing River phase and its implication on sedimentation and reservoir development," *Journal of Stratigraphy*, vol. 34, no. 3, pp. 312–320, 2010.
- [51] Y. Wang, X. Yu, Y. Yang, and J. Zhang, "Applications of fluid inclusions in the study of paleo-geotemperature in Sichuan Basin," *Earth Science - Journal of China University of Geosciences*, vol. 23, no. 3, pp. 69–72, 1998.
- [52] S. N. Ehrenberg, O. Walderhaug, and K. Bjørlykke, "Carbonate porosity creation by mesogenetic dissolution: reality or illusion?," *AAPG Bulletin*, vol. 96, no. 2, pp. 217–233, 2012.

- [53] Y. Hao, Q. Y. Yao, H. Tian, M. F. Gu, M. She, and Y. Wang, "Sedimentary characteristics and reservoir-controlling factors of the Permian Maokou Formation in Sichuan Basin," *Marine Origin Petroleum Geology*, vol. 25, no. 3, pp. 202–209, 2020.
- [54] Z. Jin and Z. Feng, "Origin of Dolostones of the Lower Permian in East Yunnan-West Sichuan: dolomitization through leaching of basalts," *Acta Sedimentologica Sinica*, vol. 17, no. 3, pp. 383–389, 1999.
- [55] Y. Jiang, Y. Gu, K. Li, S. Li, M. Luo, and B. He, "Space types and origins of hydrothermal dolomite reservoirs in the Middle Permian strata, Central Sichuan Basin," *Natural Gas Industry*, vol. 38, no. 2, pp. 16–24, 2018.
- [56] J. Liu, H. Zheng, B. Liu et al., "Petrology and geochemical characteristics of dolomite in the Middle Permian Maokou Formation, central Sichuan," *Petroleum Research*, vol. 2, no. 4, pp. 366–377, 2017.
- [57] C. Zhang, J. Liu, X. Liu, Z. Yang, Y. Li, and D. Wu, "Primary discussion on ore-forming effect of Emei Igneous Province," *Mineralogy and Petrology*, vol. 24, no. 1, pp. 5–9, 2004.
- [58] C. Zhu, M. Xu, Y. Yuan et al., "Palaeo-geothermal response and record of the effusing of Emeishan basalts in Sichuan basin," *Chinese Science Bulletin*, vol. 6, no. 55, pp. 474–482, 2010.
- [59] Z. Li, M. Pan, D. Xiao, G. Chen, Z. Lu, and D. Ying, "Studies of extension-compression tectonic dynamic setting in Sichuan Basin," *Acta Scientiarum Naturalium Universitatis Pekinensis*, vol. 37, no. 1, pp. 87–93, 2001.
- [60] W. Li, J. Liu, S. Deng, B. Zhang, and H. Zhou, "The nature and role of Late Sinian-Early Cambrian tectonic movement in Sichuan Basin and its adjacent areas," *Acta Petrologica Sinica*, vol. 36, no. 5, pp. 546–556, 2015.
- [61] J. Yin, Z. Gu, and Q. Li, "Characteristics of deep-rooted faults and their geological significances in Dachuanzhong area, Sichuan Basin," *Oil & Gas Geology*, vol. 34, no. 3, pp. 376–382, 2013.
- [62] S. M. McLennan, "Rare earth elements in sedimentary rocks: influence of provenance and sedimentary processes," *Geochemistry and Mineralogy of Rare Earth Elements, Reviews in Mineralogy*, vol. 21, pp. 169–200, 1989.
- [63] R. L. Rudnick and S. Gao, "Composition of the continental crust," *The Crust*, vol. 3, pp. 1–64, 2003.
- [64] S. J. Huang, Y. Huang, Y. F. Lan, and K. K. Huang, "A comparative study on strontium isotope composition of dolomites and their coeval seawater in the Late Permian-Early Triassic, NE Sichuan basin," *Acta Petrologica Sinica*, vol. 27, no. 12, pp. 3831–3842, 2011.
- [65] V. T. C. Chang, A. Makishima, N. S. Belshaw, and R. K. O'Nions, "Purification of Mg from low-Mg biogenic carbonates for isotope ratio determination using multiple collector ICP-MS," *Journal of Analytical Atomic Spectrometry*, vol. 18, no. 4, pp. 296–301, 2003.
- [66] N. J. Pearson, W. L. Griffin, O. Alard, and S. Y. O'Reilly, "The isotopic composition of magnesium in mantle olivine: records of depletion and metasomatism," *Chemical Geology*, vol. 226, no. 3–4, pp. 115–133, 2006.
- [67] F. Z. Teng, W. Y. Li, S. Ke et al., "Magnesium isotopic composition of the Earth and chondrites," *Geochimica et Cosmochimica Acta*, vol. 74, no. 14, pp. 4150–4166, 2010.
- [68] F. Z. Teng, "Magnesium isotope geochemistry," *Reviews in Mineralogy and Geochemistry*, vol. 82, no. 1, pp. 219–287, 2017.
- [69] D. Lavoie, S. Jackson, and I. Girard, "Magnesium isotopes in high-temperature saddle dolomite cements in the Lower Paleozoic of Canada," *Sedimentary Geology*, vol. 305, pp. 58–68, 2014.
- [70] A. Geske, R. H. Goldstein, V. Mavromatis et al., "The magnesium isotope ($\delta^{26}\text{Mg}$) signature of dolomites," *Geochimica et Cosmochimica Acta*, vol. 149, pp. 131–151, 2015.
- [71] K. J. Huang, B. Shen, X. G. Lang et al., "Magnesium isotopic compositions of the Mesoproterozoic dolostones: implications for Mg isotopic systematics of marine carbonates," *Geochimica et Cosmochimica Acta*, vol. 164, pp. 333–351, 2015.

Retraction

Retracted: Enrichment Factors and Resource Potential Evaluation of Qingshankou Formation Lacustrine Shale Oil in the Southern Songliao Basin, NE China

Geofluids

Received 2 June 2022; Accepted 2 June 2022; Published 12 December 2022

Copyright © 2022 Geofluids. This is an open access article distributed under the Creative Commons Attribution License, which permits unrestricted use, distribution, and reproduction in any medium, provided the original work is properly cited.



Geofluids and the authors have retracted the article. “Enrichment Factors and Resource Potential Evaluation of Qingshankou Formation Lacustrine Shale Oil in the Southern Songliao Basin, NE China” [1]. The data presented is the result of a collaboration by Jilin Oilfield, China Geological Survey and Northeast Petroleum University. The authors did not obtain permission from all data owners before publication, and therefore the article has been retracted and removed. The retraction and removal has been approved by the Chief Editor of the journal. The authors agree to the retraction and the notice.

References

- [1] L. Luo, D. Tan, X. Zha et al., “Enrichment Factors and Resource Potential Evaluation of Qingshankou Formation Lacustrine Shale Oil in the Southern Songliao Basin, NE China,” *Geofluids*, vol. 2021, Article ID 6645467, 20 pages, 2021.

Research Article

Impact of Geological Factors on Marine Shale Gas Enrichment and Reserve Estimation: A Case Study of Jiaoshiba Area in Fuling Gas Field

Siyu Yu ^{1,2}, Xixin Wang ^{1,2}, Shaohua Li,^{1,2} Yuming Liu ³, Liming Xiao ^{1,2}, Xin Liu ^{1,2}, Wen Zhao ⁴ and Jiaen Zhang ⁵

¹Key Laboratory of Exploration Technologies for Oil and Gas Resources, Yangtze University, Wuhan 430100, China

²School of Geosciences, Yangtze University, Wuhan 430100, China

³College of Geosciences, China University of Petroleum, Beijing 102249, China

⁴China Petrochemical Press, Beijing 100029, China

⁵Daqing Oilfield Co. Ltd. Downhole Service Sub-Company, Daqing 163000, China

Correspondence should be addressed to Xixin Wang; wangxixin86@hotmail.com

Received 6 November 2020; Revised 10 December 2020; Accepted 19 December 2020; Published 4 January 2021

Academic Editor: Kun Zhang

Copyright © 2021 Siyu Yu et al. This is an open access article distributed under the Creative Commons Attribution License, which permits unrestricted use, distribution, and reproduction in any medium, provided the original work is properly cited.

Geological factors are key elements to control shale gas enrichment and influence the accurate estimation of shale gas reserve. However, the impact of the main geological factors, such as porosity, mineralogy, and organic matter, on marine shale gas enrichment and reserve calculation has not yet been fully clarified. Herein, we measured gas adsorption, porosity, mineralogical composition, and total organic carbon content of the marine shale samples from the Jiaoshiba area of Fuling gas field in Sichuan Basin, South China, and investigate the relationships between the geological factors and the adsorbed gas content. The results show that adsorbed gas content is positively correlated with total organic carbon and porosity; the larger specific surface area of samples with more clay minerals essentially contributes to shale gas enrichment. Additionally, the sealing of faults imposes a significant impact on shale gas accumulation. The probability volume method was applied to calculate the shale gas reserve. The reserves of P_{90} (the most pessimistic reserve), P_{50} (the most likely reserve), and P_{10} (the most optimistic reserve) were calculated, respectively, which provides useful information to reduce the risk in shale gas development.

1. Introduction

Shale gas, as a new type of clean energy, has recently influenced the world's energy supply pattern because of the large reserves and wide distribution around the world [1]. The shale gas production of the USA is $6669 \times 10^8 \text{ m}^3$, accounting for 63.4% of the total natural gas production [2, 3]. The recoverable resources of shale gas in China are about $2600 \times 10^{10} \text{ m}^3$, and the resource potential is also huge [4, 5]. The accumulation mechanism of shale gas is complex and has the characteristics of self-generation, self-storage, and self-protection [6, 7]. Thus, the accurate evaluation of the scale and quantity is relatively difficult. According to the different characteristics of shale gas reserves, taking appropriate

resource assessment methods is of great significance for the future exploration and development of shale gas.

Many different geological factors control shale gas enrichment, such as porosity, pore structure, total organic carbon (TOC), clay, and the structural characteristics of strata [8, 9]. The marine shale gas in South China is more complex because of the heterogeneity of shale organic matter content, mineral composition, and other evolutionary conditions [10–12]. At present, the geological factors controlling shale gas enrichment in southern China are still unclear [13, 14]. The research about the relationship between shale gas supply, gas storage, gas preservation, structural style, and spatial-temporal matching of reservoir formation is urgently needed [15–18].

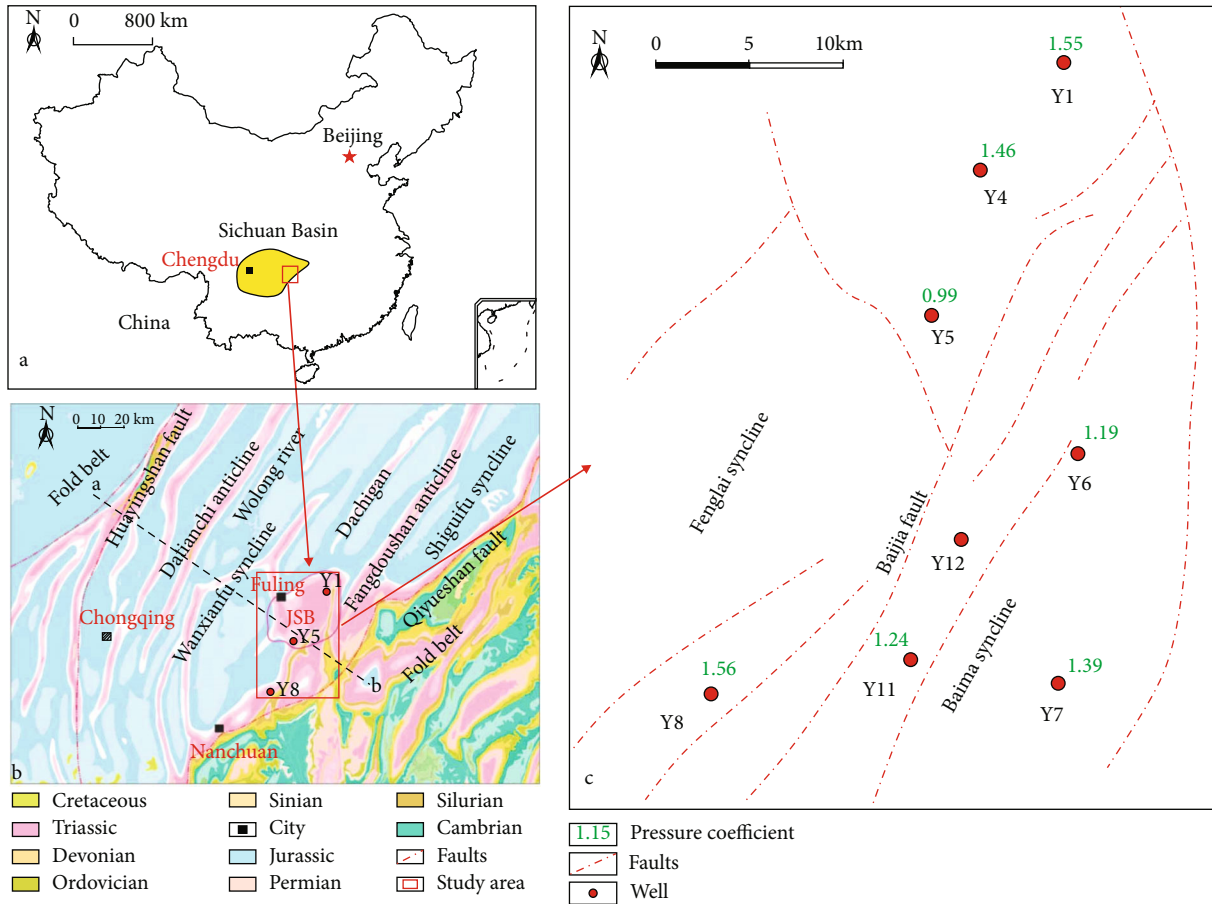


FIGURE 1: (a) Sichuan Basin; (b) the regional location of Fuling shale gas field; (c) Faults distribution in the JSB area (modified after [30]).

The volume method is generally used for resource calculation [19, 20]. However, due to the complicated accumulation mechanism of natural gas in unconventional reservoirs, shale gas reservoirs usually do not have a clear physical boundary, and the related parameters in the calculation of reserves are difficult to determine. Therefore, the probabilistic volume method is currently an ideal method for shale gas reserve assessment [21–23]. Shale gas resource evaluation method and evaluation parameter assignment have been explored [24]. The principle and method of calculating shale gas resources by volume method are described in detail [25]. Zhang et al. applied the probabilistic volume method to evaluate shale gas resources based on the current situation of shale gas exploration and development in China [26]. According to the principle of the probabilistic volume method [27, 28], the parameters for reserve calculation were selected, assigned, analyzed, and characterized, which not only reflects the uncertainty in the calculation but also ensures accuracy within a certain risk range.

In this study, the relationships between various geological factors and adsorbed gas content were established, and the main geological factors controlling shale gas enrichment were investigated. In the process of reserves calculation, only 18 tests were required to calculate the probability distribution of shale gas reserves using the orthogonal test design method, which greatly improved the efficiency of the calculation and

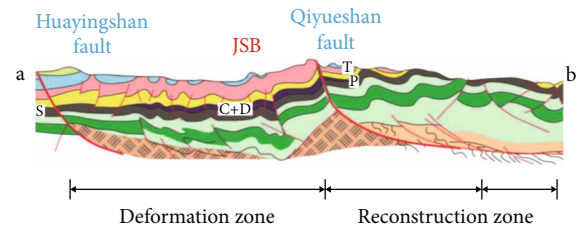


FIGURE 2: The profile of the structural deformation area of Sichuan Basin (modified after [30]).

provided a basis for the formulation of development plans and reduced development risks.

2. Geological Setting

The Fuling Shale Gas Field is located in the east of the Sichuan Basin (Figure 1(a)), west of the Qiyueshan Fault, and Chuandong barrier-type fold-thrust belt. The main shale gas reservoirs are found in the Jiaoshiba (JSB) area, which is a NE-trending anticline with diamond-shaped controlled by two groups, NE-trending faults and NS-trending faults (Figure 1(b)). The top of the JSB area has a gentle slope without faults, while the two wings of the structure show a steep dip angle and well-developed faults. The partition

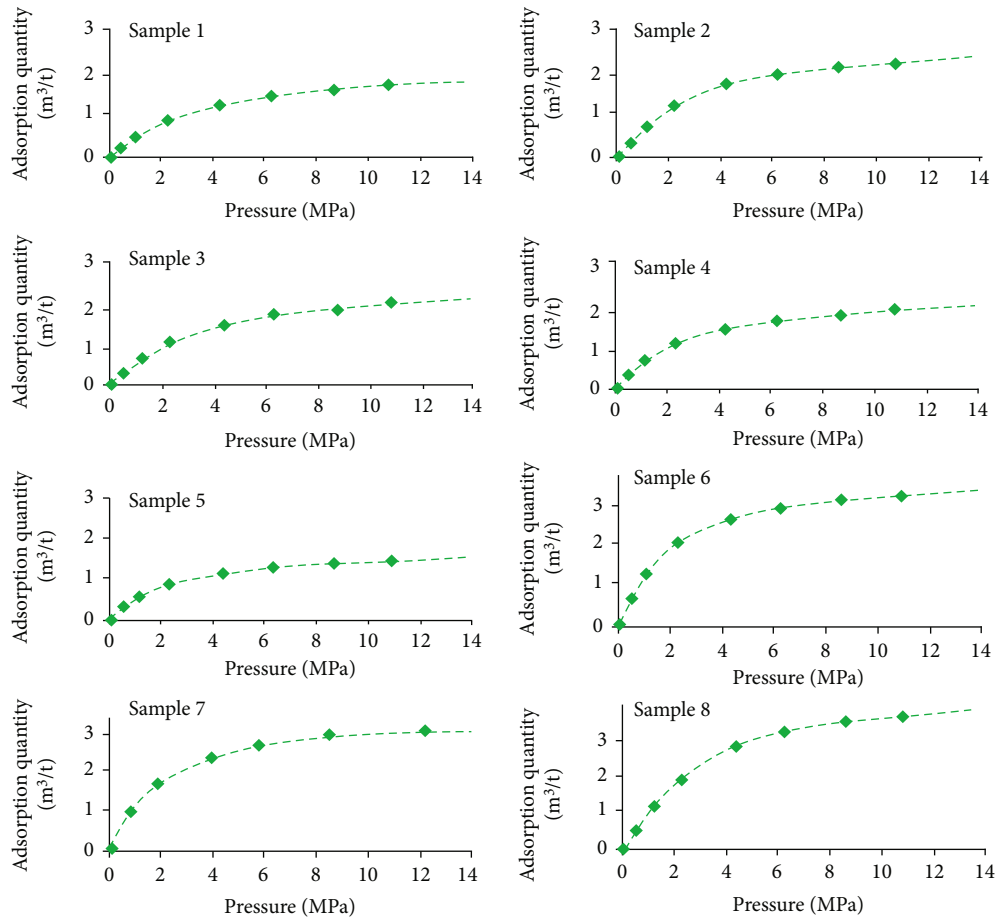


FIGURE 3: Adsorption isotherms of eight shale samples from Wufeng-Longmaxi Formation, JSB area in Fuling gas field.

deformation zone inside the basin is developed in the west of the Qiyueshan fault zone. The Qiyueshan fault zone has good vertical and horizontal continuity. It is characterized by the development of low-microamplitude fold structural styles with little tectonic erosion. The section position of Figure 2 is shown in Figure 1(b). Figure 2 shows that the JSB area, located in such a tectonic background, has well-developed Mesozoic and Paleozoic stratigraphy, which provides good conditions for oil and gas preservation.

The drilled wells showed that the sedimentary environment of Wufeng-Longmaxi Shale varies upward gradually from a deep-water continental shelf to a shallow-water continental shelf environment. The continuous thickness of the shale with a TOC content of more than 2% is over 30 m in Wufeng-Longmaxi Formations. Eight exploration wells from the Y1 well to the Y8 well and nearly 200 development wells were conducted in the main body of the JSB area. The organic-rich shale in the JSB area is well distributed on the plane. The thickness of the high-quality shale reservoir varies from 38 m to 48 m. The lithology of the top gas formation in the JSB area is mainly composed of gray-black clay silty shale, gray-black silty clay mixed shale, and silty clay rock with bands or agglomerate pyrite [29]. The high-quality shale reservoir at the bottom of Wufeng-Longmaxi Formations has the characteristics of high clay content, low siltstone content, high carbon content, and well-developed fractures.

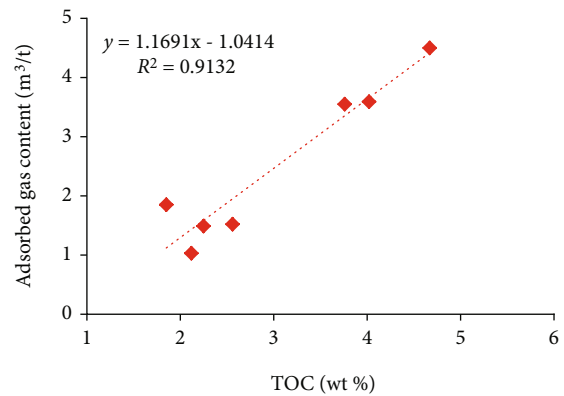


FIGURE 4: Relationship between TOC and adsorbed gas content of samples from Wufeng-Longmaxi Formation, JSB area in Fuling gas field.

3. Samples and Methods

3.1. *Samples.* Eight shale samples were collected from the lower part of Wufeng-Longmaxi Formations. The samples were divided into several parts for different experiments. First, the density of shale samples that were cut into cylinders was measured using the volumetric method. Porosity measurement was performed by ULTRA PORO300 Porosity,

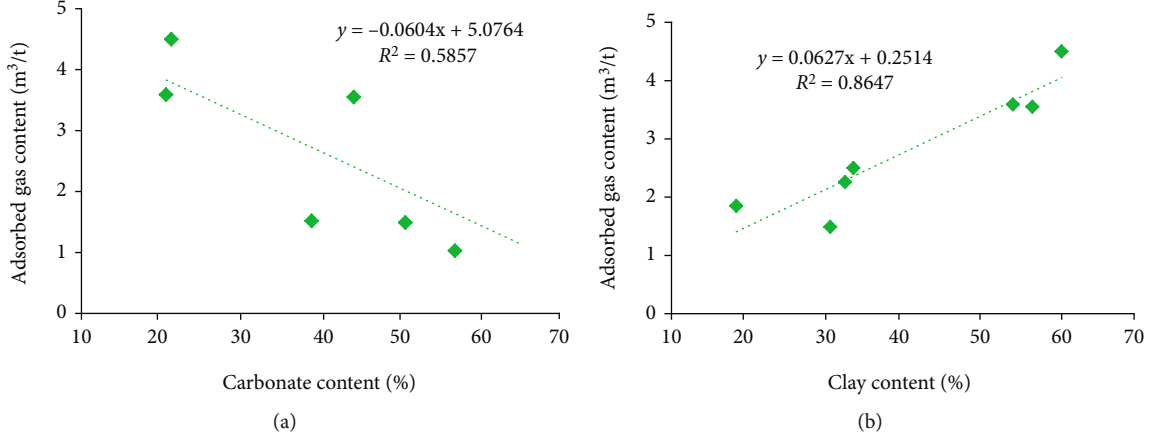


FIGURE 5: The relationship between (a) carbonate content, (b) carbonate minerals content, and adsorbed gas content.

following the standard GB/T 29172-2012 of China (GB/T 29172-2012). The pure calcium carbonate (0.2g) and the shale sample powder (0.2g) were mixed with enough dilute hydrochloric acid, respectively. The carbonate content of shale samples can be obtained by comparing the pressure of carbon dioxide.

3.2. Experiment and Calculation Methods. The samples, which were crushed into ~ 150 mesh using SPEX 8000 M Mixer/Mill, were mixed with ethanol and then laid on glass slides. Dmax-2500 X-ray diffractometer (XRD) was used to test the clay content. Before the TOC test, the inorganic carbon in the samples was removed using hydrochloric acid (4%-4.13%). The Cornerstone™ carbon-sulfur analyzer that combusts a 130 mg sample of powdered shale samples was used to test the TOC content at 704.4°C [3, 31].

Isothermal adsorption experiments were conducted by using GAI-100 high-accuracy isotherm instrument and AJP-100 volume calibrator. The maximum working pressure of GAI-100 is 10000 Psi (69 MPa), and the accuracy of the pressure sensor is 0.05%. The eight samples were crushed into 50-80 mesh size, and the adsorbed moisture and capillary water in the samples were removed at around 120°C for approximately 24 h. The isotherms were obtained under pressure ranging from 0.01 to 14 MPa at 177°C. The accuracy of the temperature sensor is 0.1°C. The maximum adsorption volume can be calculated by the software automatically using Langmuir theory [32, 33].

According to the basic principle of the probabilistic volume method, the amount of shale gas resources is the probability product of shale mass and natural gas (gas content) contained in mud shale per unit mass. The calculation formula is as follows:

$$Q_t = 0.01 \times S \cdot H \cdot \rho \cdot q. \quad (1)$$

Q_t is the amount of shale gas resources (10^8 m^3); S is the area of gas shale (km^2); H is the effective thickness of shale (m); ρ is the shale density (t/m^3); q is the gas content (m^3/t).

The shale gas content is a key parameter in the calculation and evaluation of shale gas resources. And it is a param-

eter with a large range of numerical values and is difficult to obtain accurately. Therefore, shale gas content can be obtained by using the decomposition method. The mode of occurrence of natural gas could be free, adsorbed, or dissolved, which can be calculated by different methods, as follows:

$$Q_t = q_a + q_f + q_d. \quad (2)$$

q_a is the adsorption gas content (m^3/t), q_f is the free gas content (m^3/t), and q_d is the dissolved gas content (m^3/t).

At present, the main method to obtain adsorption gas content is the isothermal adsorption experiment. The samples were placed in the environment of approximate underground temperature, and the maximum adsorbed gas was measured under different pressure conditions as follows:

$$Q_a = 0.01 \times S \cdot H \cdot \rho \cdot q_a, \quad (3)$$

$$q_a = V_L \cdot P / (P_L + P). \quad (4)$$

q_a is the adsorption gas content (m^3/t), V_L is the Langmuir volume (m^3), P_L is the Langmuir pressure (MPa), and P is the stratum pressure (MPa).

The free gas content (q_f) can be obtained by porosity (including pore and fracture volume) and gas saturation [34], as follows:

$$Q_f = 0.01 \times S \cdot H \cdot \rho \cdot q_f, \quad (5)$$

$$q_f = \phi_g \cdot S_g / B_g. \quad (6)$$

ϕ_g is the porosity (%), S_g is the gas saturation (%), and B_g is the volume factor, which is used to convert the volume of underground natural gas into the volume under standard conditions.

Natural gas in shale can be dissolved in the formation water, kerogen, asphaltene, or crude oil to varying degrees. Because the natural gas content dissolved in kerogen and

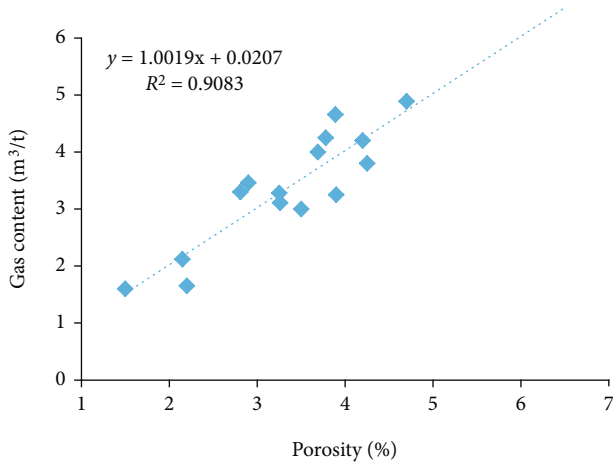


FIGURE 6: Relationship between porosity and adsorbed gas content.

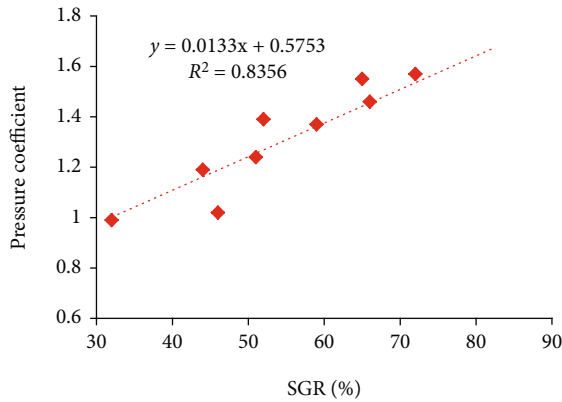


FIGURE 7: The relationship between SGR index and pressure coefficient.

asphaltenes is tiny, and the formation water is not the main fluid of shale, the dissolved gas content can be ignored in gas content analysis.

4. Results and Discussion

4.1. Relationship between the TOC and Adsorption Gas Content. The isotherms of the samples were shown in Figure 3, indicating that the lower part of the shale in Wufeng-Longmaxi Formations had good adsorption performance, and the content of adsorbed gas in the shales has a positive correlation with pressure. Wufeng-Longmaxi Shale in the study area is mainly developed in shallow water and deep-water continental shelf sedimentary environments. The continuous thickness of the shale with TOC content larger than 2% is over 30 m. The organic matter in the shale not only controls the pore structure but also significantly controls the adsorbed gas content in the shale. Figure 4 shows that the adsorbed gas content in shale samples increases with the content of TOC. This is because the presence of organic carbon generates more organic pores and larger specific surface area in the samples, which can increase the adsorbed gas content [35–37]. The relationships have been suggested

TABLE 1: Five factors and three levels orthogonal table.

Shale density	TOC	Porosity	Gas saturation	Shale gas volume coefficient
-1	-1	-1	-1	-1
0	0	0	0	0
1	1	1	1	1

TABLE 2: The calculation results of shale gas reserves of 18 tests.

No.	ρ	TOC	φ	S_g	B_{gi}	G_a (10^8m^3)	G_f (10^8m^3)	G_t (10^8m^3)
1	1	1	1	1	1	55.37	81.74	137.11
2	1	0	0	0	0	54.63	71.52	126.15
3	1	-1	-1	-1	-1	54.39	61.30	115.69
4	0	1	1	0	0	54.83	75.10	130.93
5	0	0	0	-1	-1	54.09	64.53	118.62
6	0	-1	-1	1	1	53.85	73.95	127.80
7	-1	1	0	1	-1	54.28	86.04	140.32
8	-1	0	-1	0	1	53.55	64.71	118.26
9	-1	-1	1	-1	0	53.30	64.37	117.67
10	1	1	-1	-1	0	55.37	58.24	113.61
11	1	0	1	1	-1	54.63	90.34	144.97
12	1	-1	0	0	1	54.39	68.12	122.51
13	0	1	0	-1	1	54.83	58.39	113.22
14	0	0	-1	1	0	54.09	77.65	131.74
15	0	-1	1	0	-1	53.85	79.05	132.90
16	-1	1	-1	0	-1	54.28	71.52	125.80
17	-1	0	1	-1	1	53.55	61.30	114.85
18	-1	-1	0	1	0	53.30	81.74	135.04

in previous studies on shales from some North American basins [38, 39].

4.2. Relationship between Clay, Carbonate Content, and Adsorbed Gas Content. Figure 5(a) shows the relationship between the carbonate content and the adsorbed gas content in the shale samples. It can be seen that as the content of carbonate increases, the content of adsorbed gas in the sample decreases; this is because the presence of carbonate minerals occupies the pore space, which reduces the specific surface area of the shale samples and content of adsorbed gas. However, as shown in Figure 5(b), as the clay mineral content increases, the adsorbed gas content in the samples gradually increases. This is because the presence of clay minerals increases the pores and their related specific surface area of the samples [14, 31, 40, 41], which can absorb more natural gas in the shale.

4.3. Relationship between Porosity and Adsorbed Gas Content. The porosity of Wufeng-Longmaxi Shale gas reservoirs in the JSB area of the Fuling gas field is between 1.45% and 6.38%, with an average of about 3.65%. The overall porosity is relatively high, which provides good conditions for natural gas storage. Figure 6 shows a positive correlation between porosity and gas content in the samples; that means

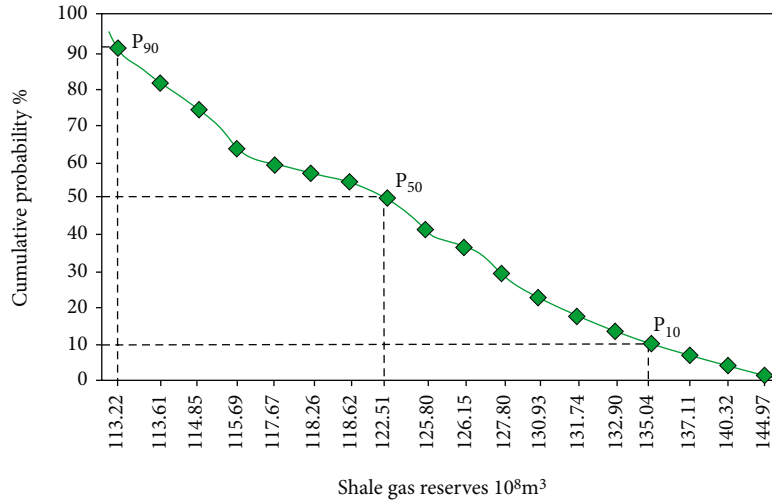


FIGURE 8: Cumulative probability distribution of shale gas reserves in JSB area.

that porosity has a significant control effect on the gas content of the shale. The porosity of gas reservoirs in the lower part of Wufeng-Longmaxi Formations is significantly higher than that of the upper part. The TOC in the lower part is significantly higher than that of the upper gas layer. This could be the main reason for the significant difference in the total amount of adsorbed gas and free gas between the lower part and upper part of Wufeng-Longmaxi Formations.

4.4. Relationship between Regional Tectonic Deformation and Shale Gas Content. The intense tectonic movement promoted many large faults, making the shale gas preservation conditions in the Fuling area vary greatly. The strength of structural deformation in the Fuling area is gradually weakened from east to west. The scale of the faults in the Baima syncline belt is very large. As a result, the pressure coefficient in the east is about 1.2, and the pressure coefficient in some areas with few faults exceeds 1.3, reflecting the poor preservation conditions in the eastern tectonic belt. The pressure coefficient of Fenglai syncline and JSB anticline is larger than 1.2, and some areas (Y8 and Y10 well area) exceed 1.5, reflecting that the overall gas preservation of the West Belt is in good condition, as shown in Figure 1(c).

Also, fault sealing has a significant control effect on the shale gas content [3]. In this study, the shale gouge ratio (SGR) index is used to evaluate the fault sealability quantitatively [42–44]. SGR index refers to the proportion of mud that is squeezed into the fault zone due to various mechanisms or dynamics (Formula (7)). A larger SGR indicates the better lateral sealing of faults. It can be seen from the relationship between the SGR index and the pressure coefficient of a single well, the better the fault sealing, the greater the pressure coefficient, indicating more gas content in the shale reservoirs (Figure 7).

$$\text{SGR} = \frac{\sum_{i=1}^n (H_i \times S_i)}{H} \times 100\%. \quad (7)$$

n is the number of broken stratum, H_i is the thickness of

broken stratum, S_i is the clay content of broken stratum, and H is the total thickness of broken strata.

4.5. Reserve Calculation

4.5.1. Parameter Optimization and Assignment. Based on the above analysis, TOC, the shale gas density, porosity, gas saturation, and original natural gas volume coefficient are selected as the main parameters for calculating shale gas reserves in the study area. To calculate shale gas reserves based on three-dimensional geological models, the construction model, the shale density model, the TOC model, the porosity model, and the gas saturation model were established by using the Sequential Gaussian method.

The value of shale density was analyzed statistically from samples. The minimum value was 2.4 g/cm³, the maximum value was 2.8 g/cm³, and the average value was 2.6 g/cm³. The density is mainly distributed in 2.55–2.65 g/cm³. The -1% model, the benchmark model, and the +1% model are regarded as the pessimistic value, the possible value, and the optimistic value, respectively. TOC, porosity, and the original natural gas volume coefficient are also taken from three equal percentage levels. The -5% model, the benchmark model, and the +5% model are regarded as the pessimistic value, the possible value, and the optimistic value. The -10% model, the benchmark model, and the +10% model of the gas saturation are regarded as the pessimistic value, the possible value, and the optimistic value.

4.5.2. Calculation of Shale Reserves Based on Probability Volume Method. Three levels of pessimism (-1), possibility (0), and optimism (1) were selected for each type of uncertain parameters affecting shale gas reserves. A factor level table was established for the calculation, as shown in Table 1.

If the five factors in the three levels are fully designed, we must establish 243 models and calculate the reserves. In this study, the experimental design method was used to analyze the uncertain parameters that affect the reserve. Only 18 tests were required to calculate the probability distribution of

shale gas reserves, which greatly improved the calculation efficiency. Also, the geological factors that affect the calculation of reserves can be quantitatively evaluated through the analysis of variance. The adsorbed gas (G_a) and the free gas (G_f) are calculated, respectively, and then the total reserves (G_t) are calculated, as shown in Table 2.

The geological process and its products can be regarded as random events; that means various geological observations have random variables. Thus, the method of probability statistics can be used to study the regularity of geological variable changes. The method of orthogonal test design is used to evaluate the uncertainty of geological variables, and the cumulative probability distribution curve of shale gas reserves was obtained (Figure 8). The reserves of P_{90} , P_{50} , and P_{10} were chosen by using the method of queuing probabilistic reserves [45]. The reserves of P_{90} , P_{50} , and P_{10} correspond to the most pessimistic reserve, the most likely, and the most optimistic reserve, respectively. To reduce the risk in shale gas development, the three possible values of shale gas reserves should be fully considered.

5. Conclusion

In this paper, the adsorbed gas content, porosity, mineralogical composition, and total organic carbon content of shale samples from the Jiaoshiba area, Sichuan Basin were investigated using a series of experiments. The following conclusions were obtained:

- (1) The main factors controlling the shale gas enrichment of the Fuling gas field are TOC, carbonate content, clay minerals, and porosity. Shales with higher TOC, clay, and porosity have more adsorption gas
- (2) Fault sealing has a significant control effect on the enrichment of shale gas. The better the sealing of faults, the greater the pressure coefficient of strata, indicating more shale gas accumulated in the formations
- (3) The reserves of P_{90} , P_{50} , and P_{10} correspond to the most pessimistic reserve, the most likely, and the most optimistic reserve, respectively. To reduce the risk in shale gas development, the three possible values of shale gas reserves should be fully considered. The corresponding geological model can be selected for shale gas numerical simulation to evaluate the impact of geological uncertainty on development quantitatively and reduce the risk in shale gas development

Data Availability

All the data can be obtained from the corresponding author.

Conflicts of Interest

The authors declare that they have no conflicts of interest.

Acknowledgments

This work is supported by Open Fund of Key Laboratory of Exploration Technologies for Oil and Gas Resources (Yangtze University), the National Natural Science Foundation of China (42002147 and 41872129), and Open Foundation of Top Disciplines in Yangtze University and the National Science.

References

- [1] J. Zhijun, C. Xunyu, L. Jinlian, Z. Yu, and C. Zhe, "The recent exploration progress and resource development strategy of China Petroleum and Chemical Corporation," *China Petroleum Exploration*, vol. 23, pp. 14–25, 2018.
- [2] Z. Jiang, Y. Song, X. Tang et al., "Controlling factors of marine shale gas differential enrichment in southern China," *Petroleum Exploration and Development*, vol. 47, pp. 661–673, 2000.
- [3] X. Wang, J. Hou, S. Li et al., "Insight into the nanoscale pore structure of organic-rich shales in the Bakken Formation, USA," *Journal of Petroleum Science and Engineering*, vol. 191, article 107182, 2020.
- [4] S. Jiang, X. Ta, and O. Steve, "Enrichment factors and current misunderstanding of shale oil and gas, case study of shales in U.S., Argentina and China," *Earth Science*, vol. 42, pp. 1083–1091, 2017.
- [5] G. Zhai, Y. Wang, S. Bao et al., "Major factors controlling the accumulation and high productivity of marine shale gas and prospect forecast in the southern China," *Earth Science*, vol. 42, pp. 1057–1068, 2017.
- [6] C. Zou, Q. Zhao, D. Dong et al., "Geological characteristics, main challenges and future prospect of shale gas," *Journal of Natural Gas Geoscience*, vol. 2, no. 5-6, pp. 273–288, 2017.
- [7] C. Sondergeld, K. Newsham, J. Comisky, M. Rice, and C. Rai, "Petrophysical considerations in evaluating and producing shale gas resources," in *SPE unconventional gas conference*, p. 2010, Pittsburgh, Pennsylvania, USA, February 2010.
- [8] G. L. Sheng, Y. L. Su, and W. D. Wang, "A new fractal approach for describing induced-fracture porosity/permeability/ compressibility in stimulated unconventional reservoirs," *Journal of Petroleum Science and Engineering*, vol. 179, pp. 855–866, 2019.
- [9] R. Wang, S. Sang, J. Jin et al., "Characteristics and significance of heterogeneity of sea-land transitional facies shale gas reservoir in North Guizhou, China," *Geosciences Journal*, vol. 23, 2019.
- [10] X. Wang, L. Zhang, and G. Chao, "The heterogeneity of lacustrine shale gas reservoir in Yanchang Formation, Xiasiwan area, Ordos Basin," *Acta Geologica Sinica English Edition*, vol. 89, no. s1, pp. 99–101, 2015.
- [11] Y. Guo and D. Zhao, "Analysis of micro-scale heterogeneity characteristics in marine shale gas reservoir," *Journal of China University of Mining and Technology*, vol. 44, pp. 300–307, 2015.
- [12] K. Wawrzyniak-Guz, J. A. Jarzyna, M. Zych, M. Bała, P. I. Krakowska, and E. Puskarczyk, "Analysis of the heterogeneity of the Polish shale gas formations by factor analysis on the basis of well logs," in *78th EAGE Conference and Exhibition 2016*, Vienna, Austria, 2016.
- [13] X. LI, S. CHEN, X. WANG, Y. ZHU, M. CHANG, and C. UWAMAHORO, "Pore structure heterogeneity of the

- Xiamaling Formation shale gas reservoir in the Yanshan area of China: evaluation of geological controlling factors,” *Acta Geologica Sinica - English Edition*, vol. 93, no. 3, pp. 588–603, 2019.
- [14] X. X. Wang, J. G. Hou, S. H. Song et al., “Combining pressure-controlled porosimetry and rate-controlled porosimetry to investigate the fractal characteristics of full-range pores in tight oil reservoirs,” *Journal of Petroleum Science and Engineering*, vol. 171, pp. 353–361, 2018.
- [15] T. Zhang, H. W. Yin, G. U. Dong et al., “Structural deformation characteristics and shale gas preservation of Lower Yangtze region,” *Journal of the China Coal Society*, vol. 38, pp. 883–889, 2013.
- [16] B. Kulga and T. Ertekin, “Numerical representation of multi-component gas flow in stimulated shale reservoirs,” *Journal of Natural Gas Science and Engineering*, vol. 56, pp. 579–592, 2018.
- [17] J. Sun and B. Luo, “Structural deformation and its influences on gas storage in Fuling shale gas play, the Sichuan Basin,” *Oil & gas geology*, vol. 37, pp. 809–818, 2016.
- [18] H. Nie, Z. He, R. Wang et al., “Temperature and origin of fluid inclusions in shale veins of Wufeng–Longmaxi Formations, Sichuan Basin, south China, implications for shale gas preservation and enrichment,” *Journal of Petroleum Science and Engineering*, vol. 193, article 107329, 2020.
- [19] Y. Ran, M. Lannerstad, M. Herrero, C. E. van Middelaar, and I. J. M. de Boer, “Assessing water resource use in livestock production: a review of methods,” *Livestock Science*, vol. 187, pp. 68–79, 2016.
- [20] H. B. Pratama and M. C. Supijo, “Experimental design and response surface method in geothermal energy: a comprehensive study in probabilistic resource assessment,” *Geothermics*, vol. 87, article 101869, 2020.
- [21] W. Ren and H. C. Lau, “Analytical modeling and probabilistic evaluation of gas production from a hydraulically fractured shale reservoir using a quad-linear flow model,” *Journal of Petroleum Science and Engineering*, vol. 184, p. 106516, 2020.
- [22] F. T. Murat and S. Caglar, “A new fully probabilistic methodology and a software for assessing uncertainties and managing risks in shale gas projects at any maturity stage,” *Journal of Petroleum Science and Engineering*, vol. 168, pp. 107–118, 2018.
- [23] L. Xue, Y. Liu, T. Nan, Q. Liu, and X. Jiang, “An efficient automatic history matching method through the probabilistic collocation based particle filter for shale gas reservoir,” *Journal of Petroleum Science and Engineering*, vol. 190, p. 107086, 2020.
- [24] Q. Xiaosong, H. Mingyi, H. Zhonggui, Y. Ying, and C. Quansheng, “Evaluation methods and parameter assignments of shale gas resources: a case study of the Wufeng–Longmaxi Formation in the Middle Yangtze region,” *Geology in China*, vol. 41, pp. 2091–2098, 2014.
- [25] W. Z. Xu, *Principle and Method of Shale Gas Resources Calculation by Volume Method-Case of ES2 Formation in LF Fault Depression*, p. 7, 2019.
- [26] J. Zhang, L. Lin, Y. Li et al., “Methods and techniques for shale gas resource evaluation: probabilistic volume method,” *Earth Science Frontiers*, vol. 19, pp. 184–192, 2012.
- [27] A. A. Kaufman, “Methods in geochemistry and geophysics principles of the gravitational method volume 41 chapter 3 principles of measurements of the gravitational field,” *Methods in Geochemistry & Geophysics*, vol. 41, pp. 161–215, 2007.
- [28] G. S. Kruglik, “Derivation of the equations of probabilistic method with account taken of the identity principle,” *Vesci Akad. Navuk BSSR Ser. Fiz.-Tehn. Navuk*, vol. 3, pp. 45–50, 1963.
- [29] Z. Shu, D. Fang, A. Zheng et al., “Geological characteristics and development potential of upper shale gas reservoirs of the 1st member of Longmaxi Formation in Jiaoshiba area, Sichuan Basin,” *Natural Gas Geoscience*, vol. 31, pp. 393–402, 2020.
- [30] X. S. Guo, “Controlling factors on shale gas accumulations of Wufeng–Longmaxi Formations in Pingqiao shale gas field in Fuling area, Sichuan Basin,” *Natural Gas Geoscience*, vol. 30, pp. 1–10, 2019.
- [31] K. Liu, M. Ostadhassan, and X. M. Xu, “A comparison study of the unloading behavior in shale samples in nanoindentation experiments using different models,” *Journal of Petroleum Science and Engineering*, vol. 186, p. 106715, 2020.
- [32] D. Avnir and M. Jaroniec, “An isotherm equation for adsorption on fractal surfaces of heterogeneous porous materials,” *Langmuir*, vol. 5, no. 6, pp. 1431–1433, 1989.
- [33] P. I. Ravikovitch, A. Vishnyakov, R. Russo, and A. V. Neimark, “Unified approach to pore size characterization of microporous carbonaceous materials from N₂, Ar, and CO₂ adsorption isotherms,” *Langmuir*, vol. 16, no. 5, pp. 2311–2320, 2000.
- [34] J. C. Zhang, L. M. Lin, Y. X. Li et al., “The method of shale gas assessment: probability volume method,” *Earth Science Frontiers*, vol. 19, pp. 184–191, 2012.
- [35] X. Shao, X. Pang, Q. Li et al., “Pore structure and fractal characteristics of organic-rich shales: a case study of the lower Silurian Longmaxi shales in the Sichuan Basin, SW China,” *Marine and Petroleum Geology*, vol. 80, pp. 192–202, 2017.
- [36] G. L. Sheng, H. Zhao, Y. L. Su et al., “An analytical model to couple gas storage and transport capacity in organic matter with noncircular pores,” *Fuel*, vol. 268, p. 117288, 2020.
- [37] C. R. Clarkson, N. Solano, R. M. Bustin et al., “Pore structure characterization of North American shale gas reservoirs using USANS/SANS, gas adsorption, and mercury intrusion,” *Fuel*, vol. 103, pp. 606–616, 2013.
- [38] D. J. K. Ross and R. M. Bustin, “The importance of shale composition and pore structure upon gas storage potential of shale gas reservoirs,” *Marine and Petroleum Geology*, vol. 26, no. 6, pp. 916–927, 2009.
- [39] G. R. Chalmers, R. M. Bustin, and I. M. Power, “Characterization of gas shale pore systems by porosimetry, pycnometry, surface area, and field emission scanning electron microscopy/transmission electron microscopy image analyses: examples from the Barnett, Woodford, Haynesville, Marcellus, and Doig unit,” *AAPG Bulletin*, vol. 96, no. 6, pp. 1099–1119, 2012.
- [40] Y. Han, D. Kwak, S. Choi, C. Shin, Y. Lee, and H. Kim, “Pore structure characterization of shale using gas physisorption: effect of chemical compositions,” *Minerals*, vol. 7, no. 5, p. 66, 2017.
- [41] X. X. Wang, Y. M. Liu, J. G. Hou et al., “The relationship between synsedimentary fault activity and reservoir quality - a case study of the Ek1 formation in the Wang Guantun area, China,” *Interpretation*, vol. 8, no. 3, pp. sm15–sm24, 2020.
- [42] T. Fristad, A. Groth, G. Yielding, and B. Freeman, “Quantitative fault seal prediction: a case study from Oseberg Syd,” *Norwegian Petroleum Society Special Publications*, vol. 7, pp. 107–124, 1997.

- [43] D. Harris, G. Yielding, P. Levine, G. Maxwell, P. T. Rose, and P. Nell, "Using Shale Gouge Ratio (SGR) to model faults as transmissibility barriers in reservoirs: an example from the Strathspey Field, North Sea," *Petroleum Geoscience*, vol. 8, no. 2, pp. 167–176, 2002.
- [44] P. Bretan, G. Yielding, and H. Jones, "Using calibrated shale gouge ratio to estimate hydrocarbon column heights," *AAPG Bulletin*, vol. 87, no. 3, pp. 397–413, 2003.
- [45] X. Bao, S. H. Li, C. Zhang, B. Qiao, J. Li, and H. M. Di, "Application of probability volume method based on experimental design to calculation of shale gas reserves," *Fault block oil gas field*, vol. 24, pp. 678–681, 2017.

Research Article

Coevolutionary Dynamics of Organic-Inorganic Interactions, Hydrocarbon Generation, and Shale Gas Reservoir Preservation: A Case Study from the Upper Ordovician Wufeng and Lower Silurian Longmaxi Formations, Fuling Shale Gas Field, Eastern Sichuan Basin

Zhijun Jin ^{1,2}, Haikuan Nie,^{1,2} Quanyou Liu,^{1,2} Jianhua Zhao,³ Ruyue Wang ^{1,2},
Chuanxiang Sun,^{1,2} and Guanping Wang⁴

¹State Key Laboratory of Shale Oil and Gas Enrichment Mechanisms and Effective Development, Beijing 100083, China

²Sinopec Petroleum Exploration and Production Research Institute, Beijing 100083, China

³College of Geosciences, China University of Petroleum, Qingdao 266580, China

⁴School of Energy Resources, China University of Geosciences, Beijing 100083, China

Correspondence should be addressed to Zhijun Jin; jinzj1957@pku.edu.cn

Received 3 October 2020; Revised 15 November 2020; Accepted 2 December 2020; Published 22 December 2020

Academic Editor: Loupasakis Constantinos

Copyright © 2020 Zhijun Jin et al. This is an open access article distributed under the Creative Commons Attribution License, which permits unrestricted use, distribution, and reproduction in any medium, provided the original work is properly cited.

Shale gas deposits are self-sourced, self-accumulating, and self-preserving in the Upper Ordovician Wufeng Formation and Lower Silurian Longmaxi Formation of the Fuling Shale Gas Field in the eastern Sichuan Basin. They were both seemingly mixed by secondary oil cracking and kerogen cracking gases during the high maturation window. The reservoir space primarily consists of mineral pores and organic matter (OM) pores, and the shale gas was mainly trapped by a high-pressure system. In this study, the Fuling O_{3w}-S_{1l} Shale Gas Field in the eastern Sichuan Basin was used as a case study to discuss the coevolutionary process and organic-inorganic interactions of hydrocarbon generation, accumulation, and preservation. The results indicate that the processes and mechanisms of organic-inorganic interactions and coevolution of hydrocarbon generation and reservoir preservation are quite different among the shale graptolite zones (GZ) with respect to hydrocarbon generation, types and characteristics of shale gas reservoirs, seal characteristics, and their spatiotemporal relations. In the WF2-LM4 GZ, the favorable OM, biogenic authigenic quartz and organic-inorganic interactions are highly coupled, leading to the high level of coevolution demonstrated within the field, as well as to the favorable conditions for shale gas accumulation. Conversely, the overlying LM5-LM8 GZ seemingly exhibits early densification and late charge and has a reverse mode of reservoir development (i.e., low degree of coevolution). These two coevolutionary processes were conducive to the development of a high degree of spatiotemporal matching between the reservoir (i.e., WF2-LM4 GZ) and the seal (i.e., LM5-LM8 GZ). This is due to underlying differences in their coevolutionary histories. The synthetic work presented here on the coevolutionary processes and mechanisms of formation for organic-inorganic interactions and hydrocarbon generation and reservoir preservation reveals insights into the driving mechanisms of shale gas enrichment, providing a basis for effectively predicting favorable enrichment intervals for shale gas worldwide.

1. Introduction

During the past 10 years, most of the research on shale gas reservoirs has focused on source rock [1–3], reservoir types, porosity, and pore structure [4–11]. Most importantly, the

pores within organic matter (OM) are widely recognized as a significant component of pore systems in gas-bearing shales [9, 10, 12–18]. A greater potential for gas storage and flow exists in higher total organic carbon (TOC) content intervals, depending on the abundance and connectivity of the OM

pores [8, 16, 19]. Therefore, shale gas reservoirs are mainly evaluated using TOC content, thermal maturity, rock mineralogy, rock brittleness, and porosity and permeability [1, 2, 20]. However, the combination of pore types, especially with respect to their components, characteristics, and organic-inorganic interactions during the evolution of the shale reservoir, are less well known. This has restricted our understanding of the diagenetic and pore evolution histories, and the accuracy with which we may evaluate reservoir potential. The pore formation and the evolutionary histories and proportion of OM porosity are the key information needed to ascertain the effectiveness of exploration as well as the associated production capacity of shale gas reservoirs.

Porosity-related variances are directly related to differences in the amount and character of the OM and mineralogical composition [21–23]. The pore formation history is composed of the inorganic-organic interactions between OM (i.e., hydrocarbon generating organisms and/or bitumen) and inorganic matter (i.e., minerals such as quartz, feldspar, pyrite, and calcite). Organic-inorganic interactions in sandstones have been documented [24–26], and many important insights have been gained on the growth of minerals, the preservation of the pores that are affected by hydrocarbon charge [27, 28], and the effects of minerals on the hydrocarbon generation of OM [29]. Meanwhile, the driving processes behind diagenetic pathways in shales [10, 30, 31], the nature of pores in shales, and the controls on porosity evolution remain poorly known [17]. Additionally, this does not take into consideration the effects of hydrocarbon generation and expulsion processes on mineral diagenesis, mineral pore evolution, and the relationship between organic (hydrocarbon generation) and inorganic (reservoir evolution) coevolutionary processes.

The petroleum retained along with kerogen and shale mineralogy may be a critical factor in shale gas generation [32], but their coevolutionary dynamics are little known. More attention is needed to develop our understanding of the coevolutionary processes that drive organic-inorganic interactions, hydrocarbon generation, and reservoir development of shale gas reservoir [20]. OM and inorganic minerals are not considered as unidirectional, simple, and determinate in their relations, but rather as a kind of interactional and coevolutionary relationship. The interaction between OM and inorganic minerals leads to their coevolution. The interaction is the foundation and motivation, and the coevolution is the process and consequence; both of them are achieved through physical and chemical processes. The key issue centers on how OM and inorganic minerals may interact to achieve coevolution, thus forming the reservoir types and characteristics that we observe as well, as the shale gas reservoir. Furthermore, the specific mechanisms and corresponding developmental states of pore systems (organic and inorganic) are deserving of more attention. Due to the particular system of self-contained, self-sourced, and self-accumulating reservoir, the qualitative and semiquantitative evaluation of the organic-inorganic coevolutionary process may be conducted through the comprehensive analysis of hydrocarbon generation history, reservoir developmental processes, and preservation.

This study systematically analyzed the coevolutionary process and mechanisms of hydrocarbon generation and reservoir preservation based on organic geochemistry, mineralogy, pore characterization, seal characteristics, and the corresponding evolutionary history, combined with shale gas exploration and development in the largest Lower Paleozoic shale gas field in the world at Fuling, in the eastern Sichuan Basin. The results reveal the mechanism of shale gas enrichment in the Fuling Shale Gas Field and provide insights into the organic-inorganic interactive process and pore development, especially of the OM pore network within the studied shales. This may provide the basis for effective predicting favorable enrichment intervals of the Upper Ordovician Wufeng Formation and Lower Silurian Longmaxi Formation shale gas worldwide.

2. Geological Setting

As a superimposed basin developed on the upper Yangtze Craton, the Sichuan Basin is one of the most tectonically stable sedimentary basins in China [33]. Surrounded by the Hubei-Hunan-Guizhou Fold Belt on the east, the Longmenshan Fold Belt on the west, the Micang Uplift and Dabashan Fold Belt sitting on the north, and the Emei-Liangshan Fold Belt on the south, the basin can be divided into three tectonic regions and six sublevel tectonic units by the Huayingshan and Longquanshan anticlines [34] (Figure 1). Several tectonic movements occurred in the Sichuan Basin which in chronological order are the Caledonian (Cambrian-Silurian), Hercynian (Devonian-Permian), Indosinian (Triassic), Yanshanian (Jurassic-Late Cretaceous), and Himalayan (Paleogene-Quaternary) orogenies [34–36]. Sedimentary sequences of the basin are relatively complete, which include the Middle-Upper Proterozoic, Paleozoic, Mesozoic, and Cenozoic strata. Currently, China's largest gas yield comes from the Sichuan Basin which has the most prolific natural gas resources [33].

The black shale in the O_3w-S_1l Fuling Shale Gas Field (i.e., Wufeng and Longmaxi Formations) was deposited in a low-energy anoxic sedimentary environment, from the Late Ordovician to Early Silurian [38]. The maximum thicknesses of the formations of the O_3w-S_1l Fuling Shale Gas Field are between 30 and 100 m. In the Sichuan Basin and its surrounding areas where main China's shale gas yield comes from, the Wufeng and Longmaxi Formations have been the main targets for shale gas exploration, development, and production in recent years, leading to the establishment of three national shale-gas demonstration areas including the Fuling, Weiyuan-Changning, and Zhaotong.

To get a fine classification of shales with similar content, biostratigraphy can be an effective method when it is difficult to use lithology, mineral composition, geochemical parameters, and petrophysical properties. In a biostratigraphic study, graptolite is one of the leading globally recognized index fossil groups, which is a basis for fine shale division of the shales in the Wufeng Formation and the Longmaxi Formation [39]. Since specific graptolite types were only developed and preserved in the specific sedimentary environment during a specific period, the specific shales can be recognized and clarified

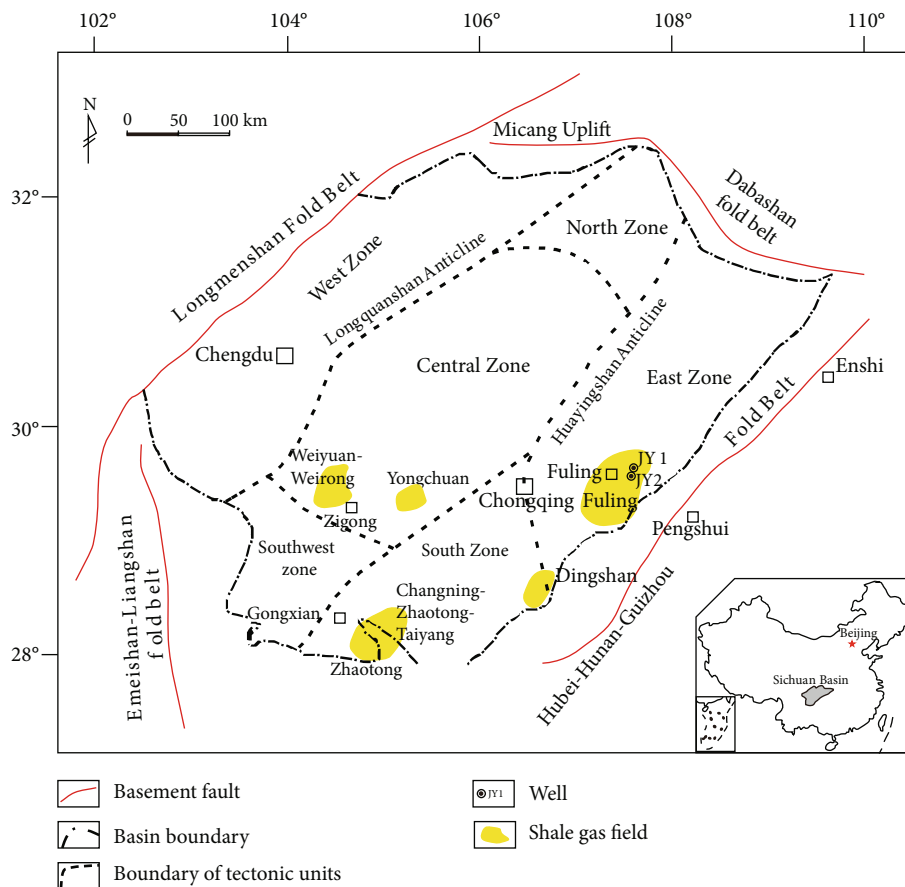


FIGURE 1: Location map of the study area in the Sichuan Basin, China; the structural subdivisions include the eastern, southern, western, northern, southeastern, and central zones (after [37]).

[39–41]. Both the assemblage of hydrocarbon-forming organisms in different shale intervals and the shale quality were of great difference [42]. During the depositional period of the Wufeng Formation and the Longmaxi Formation, shale thickness and organic carbon content are changing; thus, it was more accurate to describe with a timeline the gradual development of shale characteristics based on the graptolite zone [39, 43]. According to the GZ divisions in the Wufeng and Longmaxi Formations [39, 40], the shales have been divided into WF1-WF4 in the Wufeng Formation and LM1-LM9 in the Longmaxi Formation.

3. Samples and Methods

More than 100 black shale samples from the Upper Ordovician Wufeng Formation-Lower Silurian Longmaxi Formation are used and sourced mainly from the shale-gas wells in the Sichuan basin and its periphery (Figure 1). The field-emission scanning electron microscopy (FE-SEM) observation was conducted at the State Key Laboratory of Biochemical Engineering at the Institute of Process Engineering, Chinese Academy of Sciences. The other data in this study were obtained from the experiments conducted at the State Key Laboratory of Shale Oil and Gas Enrichment Mechanisms and Effective Development at the China Petroleum & Chemical Corporation.

4. Source Rock

4.1. Kerogen Type and Hydrocarbon-Generating Organisms. The thickness of the gas-bearing black shales in Upper Ordovician Wufeng Formation-Lower Silurian Longmaxi Formation in the XYZ region ranges from 83.5 m to 102 m. The basal 38–44 m of black shale contains >2% TOC over a large area [44]. Measured shale porosity from the JY 1 Well averaged 4.5%, and the gas content in the basal 38 m of black shales was around 2.99 m³/t [44]. The main kerogen type in the WF2-LM8 GZ is considered to be dominated by Type II kerogen with some Type I [45], which favors the development of the OM pores [9]. And the development of OM pores between WF2-LM4 GZ and LM5-LM8 GZ is controlled by hydrocarbon-forming organisms [20, 37].

Organic-rich sediments that lack terrigenous organic matter indicate a phytoplankton source [46]. Pelagic deposition of phytoplankton is interpreted as a primary mechanism of organic matter deposition, which is converted to hydrocarbons and matrix bitumen [36]. Based on the morphology, inherited texture, and energy spectrum, the OM can be linked to several hydrocarbon-generating organisms. This includes primary OM, such as various algae (multicellular algae, unicellular algae, acritarchs, etc.), graptolites, sponge spicules, and various types of secondary OM, such as bitumen, which occurs as discrete amorphous OM, and small

organic domains or organoclay aggregates [42]. Different hydrocarbon-generating organisms exist in different sedimentary environments, leading to the diversity of the type and content of OM, hydrocarbon-generating capacity, and OM pore development ability.

The multicellular algae include red, brown, and other planktonic algae. Pores within algal OM, particularly in smaller porous OM domains, are similar in shape, size, and distribution and may also be influenced by the original structure of the algae [16]. The diameter of single multicellular algae (probably red algae) ranges from several μm to tens of μm . Intense compaction may deform the shape of multicellular algae. The multicellular algae bear a mix of OM and silica since some of them have siliceous shells [42]. Other identified algae which present no siliceous shells fill in the mineral pores with their size varying with the size of mineral pores (Figure 2). Without the protection of the siliceous shell, the shape of the algae can be easily altered. Under strong compaction, the algae shape deformation caused by internal-structure rearrangement of OM exhibits directional-alignment and/or flow-like structures in the narrow mineral pores. No directional alignment of the OM has been observed in circular or approximately equant mineral pores or in the center of narrow mineral pores, due to the insignificant difference in the degree of OM compaction.

The unicellular algae include blue, green, and other benthic algae. Unicellular algae mainly include rhabditiform blue algae (also known as cyanobacteria) and spherical algae and usually gather to form colonies (Figure 3). The diameter or length of its colony is several μm to tens of μm . The length of single rhabditiform blue algae is a few hundred nm to more than $1\ \mu\text{m}$, and the width is a few hundred nm, while the spherical algae are circular or oval and have uneven surfaces and rough edges; some developed pores ranging tens of nm in size.

The red, brown, and other planktonic algae which can take advantage of green, yellow, orange, and other short wavelengths dominate the deep water zone, while the green algae, cyanobacteria, and other benthic algae are common in shallow waters [47, 48]. The hydrocarbon-generating organisms of the WF2-LM4 GZ are primarily the red, brown, and other planktonic algae living in the aerobic surface layer and preserved in a strongly reducing environment in the bottom water [37]. A small amount of terrigenous OM is found in the hydrocarbon-generating organisms of the WF2-LM4 GZ [49]. In comparison, the hydrocarbon-generating organisms of the LM5-LM8 GZ were predominated by green algae, cyanobacteria, siliceous sponges, and other benthic algae, as well as a small amount of red, brown, and other planktonic algae [37]. TOC content is largely determined by different sources of hydrocarbon-forming organisms. The highest TOC content of 4.97% on average is found in siliceous mudstone of WF2-LM4 GZ; higher TOC content varying from 2.01% to 3.77% with an average of 2.84% appears in the silica-bearing mudstone of WF2-LM4 GZ. TOC contents of LM5-LM8 GZ are from 1.32% to 2.68% with an average of 1.70% in the silty mudstone and 0.60%–2.53% with an average of 1.59% in the clay-rich mudstone (Figure 4). The WF2-LM4 GZs are where siliceous mudstone and silica-bearing

mudstone are prevalent and have the high production of shale gas wells.

4.2. Hydrocarbon Generation History. According to the burial history of Well JY 1, the black shale in the Wufeng and Longmaxi Formations underwent three stages of hydrocarbon generation (Figure 5): (1) The initial stage was the rapid subsidence and burial in the Early Devonian. Buried at a depth less than 2000 m, thermal maturity (vitrinite reflectance, R_o) of the black shale was about 0.5% generating a small amount of heavy oil. The black shale was uplifted in the middle Devonian to the Late Permian when hydrocarbon generation was suspended. (2) The second stage was in the Early-Middle Triassic when the subsidence occurred. When the burial depth of the black shale went up to 3000 m, its thermal maturity climbed to about 1.0%, reaching the peak oil generation window. In the Middle-Late Triassic, again the black shale was uplifted and hydrocarbon generation was suspended, but because of a rapid, limited-amplitude uplift, oil expulsion efficiency was low, leaving a large amount of crude oil in the shale. (3) Subsidence from the early Jurassic to middle Cretaceous was the third stage. Black shale was buried at a depth greater than 7000 m with thermal maturity greater than 2.5%, turning into the overmature dry gas generation window. Residual kerogen and oil cracked generating plentiful shale gas as well as a large number of porous pyrobitumen which provided a huge number of OM pores for gas storage. After the Late Cretaceous, the black shale was uplifted again during which the generation of shale gas was terminated. The thermal maturity data range from 2.2% to 3.13% was present, with the mean value of 2.65% [20], suggesting the OM is already in the overmature stage.

According to Montgomery et al. [50], the Barnett Shale in the Fort Worth Basin of Texas, USA, was buried in a shallow depth and then uplifted for a long period during the early evolution stage, then was deeply buried in a short time and uplifted quickly in the middle evolution stage, and was quickly buried and uplifted in the late evolution stage. Similar characteristics have been found when comparing the burial and thermal evolution history of the shale from the Wufeng Formation and Longmaxi Formation in the Sichuan Basin (Figure 5). During the early stages of their burial history from Early Silurian to Late Permian, both experienced long-term shallow burial and uplift, which was favorable for the kerogen preservation allowing a limited amount of hydrocarbon generation and expulsion. During the second period from Early-Middle Triassic to Late Triassic, short-term burial and uplift led to a large amount of crude oil generation and retention. Finally, the late period from the early Jurassic to recent witnessed rapid subsidence and uplift which was unfavorable for gas discharging, but favorable for shale gas generation, accumulation, and preservation.

5. Reservoir Rock

5.1. Mineral Composition. There are some differences in the sedimentary environments among GZs, and this is reflected in the mineral composition. During the Late Ordovician to the Early Silurian, the black shale of the WF2-LM4 GZ was

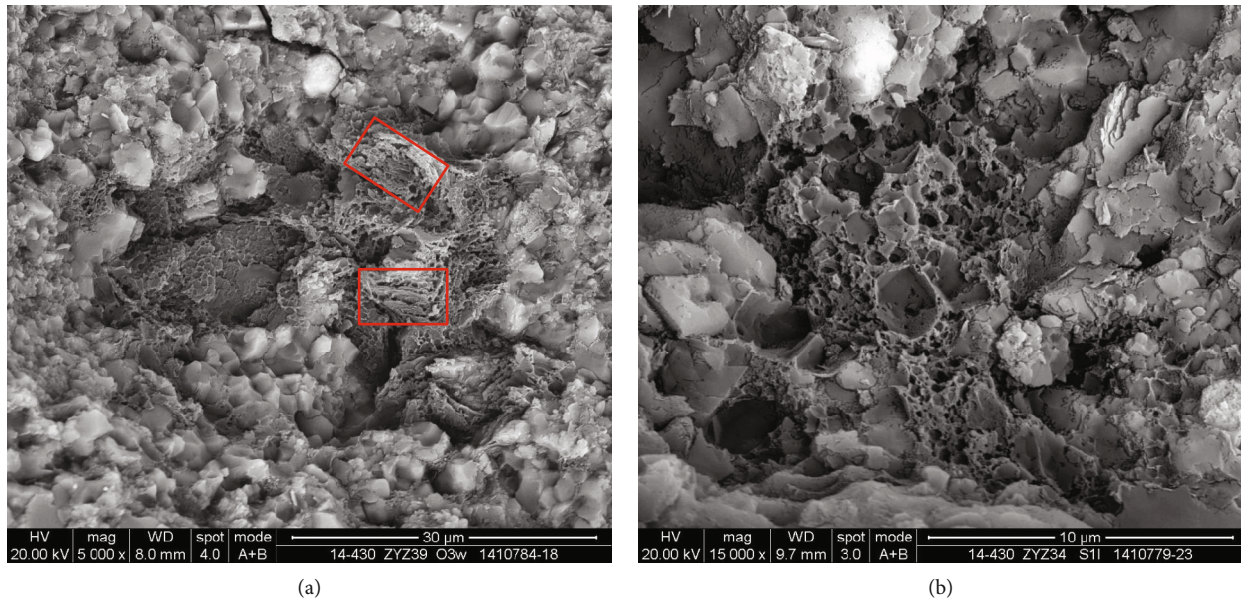


FIGURE 2: Multicellular algae in black shale. (a) The overview of the profile; many multicellular algae can be observed. The aligned OM pores in the red panel probably indicate that the algae have inherent variation in their internal structure (well JY 2, 2570.89 m (WF2 GZ), the TOC content is 3.66% and the R_o % is 2.65%). (b) unaligned OM pores (well JY 2, 2556.91 m (LM4 GZ), the TOC content is 3.9% and the R_o % is 2.46%).

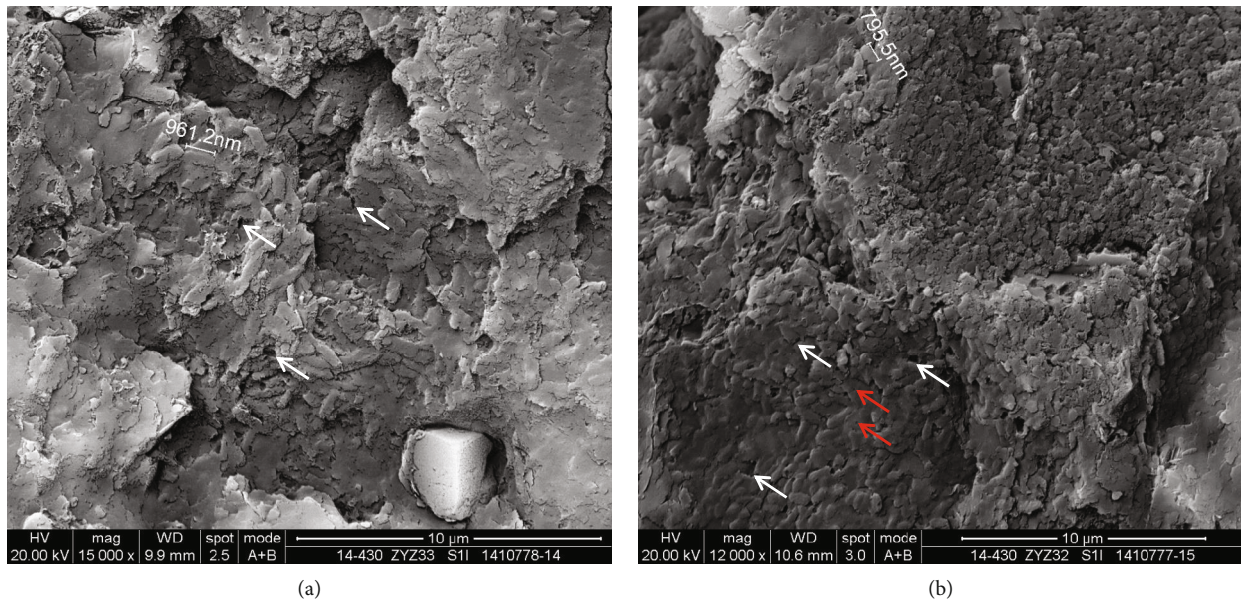


FIGURE 3: Unicellular algae in black shale. (a) Rhabditiform blue algae colonies and OM pores (white arrows) observed in the Longmaxi Formation black shale (well JY 2, 2543.84 m (LM5 GZ), the TOC content is 3.8% and the R_o % is 2.55%). (b) Spherical nanoscale algae colonies; small pores (red arrow) and large pores (white arrow). The OM pore is developed by the arrangement gaps of the algae (well JY 2, 2523.11 m (LM6 GZ), the TOC content is 2.11% and the R_o % is 2.63%).

deposited in a low-energy, anoxic environment [36, 51]. The mineral composition of 87 shale samples from the JY 1 Well are as follows: (1) In the WF2-LM4 GZ: the content of quartz, clay, feldspar, calcite, dolomite, pyrite, and hematite accounts for 31.0%-70.6%, 16.6%-49.1%, 3.2%-11.3%, 0%-7.5%, 0-31.5%, 0-4.8%, and 0-7.5% with the averages of 46.6%, 31.6%, 7.9%, 4.1%, 6.9%, 0.79%, and 2.2%, respectively. (2) In the LM5-LM8 GZ, the content of quartz, clay, feldspar, calcite,

dolomite, pyrite, and hematite accounts for 18.4%-51.4%, 33.3%-62.8%, 4.6%-15.0%, 0-11.8%, 0-30.9%, 0-1.9%, and 0-4.9%, respectively. Averages were 33.1%, 45.1%, 10.0%, 3.6%, 5.9%, 0.03%, and 2.4%, respectively. Compared to the LM5-LM8 GZ, the WF2-LM4 zone has a higher quartz content and a lower clay content (Figure 4), which is similar to the distributions observed for the Barnett and Eagle Ford shales [3, 52], which favor the accumulation and production of shale gas.

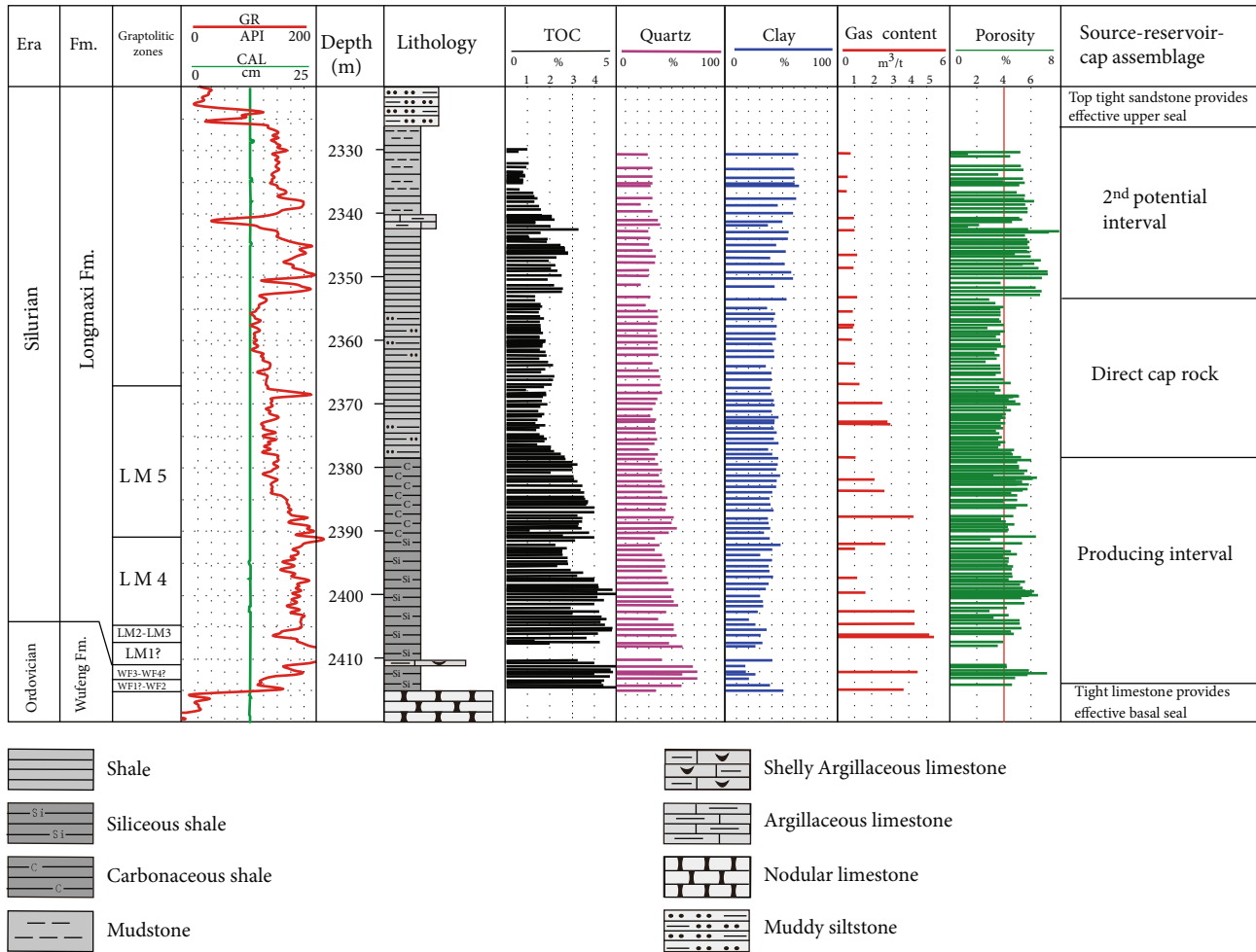


FIGURE 4: Comprehensive evaluation histogram showing favorable interval for shale gas exploration in JY 1 Well (modified from [20]) with the upper boundary of the producing interval in the middle of the LM5 GZ. The mineral composition is obtained by X-ray diffraction, and the gas content is based on on-site desorption of shale.

Mineralogy may also be an important factor that controls both pore types and porosity preservation due to the differences in the ability to resist mechanical compaction. Siliceous mineral content is an important geological parameter in evaluating the quality and potential of shale reservoirs [52]. Thus, the content and origin of quartz must be resolved. Two different types of quartz, namely, detrital quartz and pore-filling authigenic quartz, have been identified through petrographic observations, cathodoluminescence (CL), and SEM analysis [53]. The quartz content of shales in the JY 1 Well has a positive correlation with the corresponding TOC content. However, this statistic ignores the differences between siliceous minerals and TOC in different GZs. Further analysis reveals that the quartz content of the WF2-LM4 GZ is mainly greater than 40% which is dominated by biogenic silica [44]. It displays a strong positive correlation with TOC, guaranteeing a high matching of siliceous mineral and TOC. An increase in bioclastic components correlates with higher TOC content due to the higher volume of an organic-rich matrix. In contrast, the quartz content of the LM6-LM8 GZ varying from 20% to 40% is dominated by terrigenous silica, displaying no correlation with TOC content. As a continuous

depositional transition between LM4 and LM6, the LM5 GZ has variable quartz content as a result of both terrigenous silica as well as biogenic silica. Siliceous shale is the main shale type of the WF2-LM4 gas-producing section, and the siliceous content is generally greater than 40%. Silica is often cryptocrystalline and amorphous, exhibiting spherical structures (Figures 6(a) and 6(b)), and there are usually sponge spicules and skeletal material, including radiolarian fragments (Figures 6(c) and 6(d)).

The detrital versus an authigenic form of quartz can be discriminated firstly by crystal shape and spatial distribution and then by color and intensity in CL. CL can also be used to determine quartz provenance [52, 54–56]. Low-luminescent or nonluminescent quartz observed in scanning monochromatoluminescence electron microscope is commonly attributed to a low-temperature, authigenic/diagenetic origin [54, 55]. In this study, a resolution SEM with monochromatoluminescence and energy-dispersive X-ray spectroscopy (EDS) detectors were used to identify the provenance of quartz within the Wufeng and Longmaxi Formation shales. Two different types of quartz were identified [57]: (1) Biogenic microcrystalline quartz

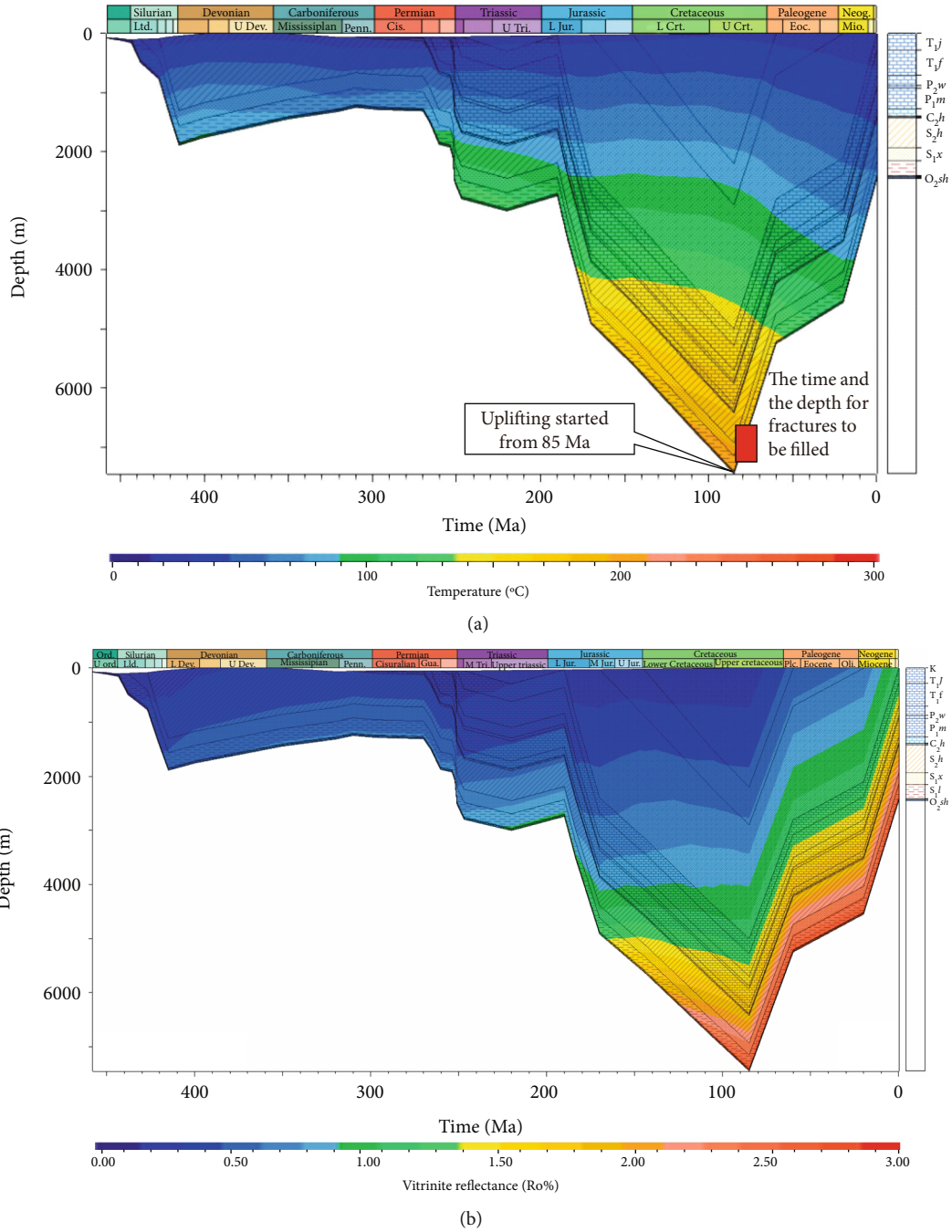


FIGURE 5: Burial-history reconstruction for JY 1 Well in the Sichuan Basin: (a) Superimposed history of temperature changes; (b) Superimposed history of thermal maturity R_o . The well's location is in Figure 1. The model was built through the PetroMod software. Compaction and uplift were based on thermal maturity calibrated by the thermal maturity data of Wufeng Formation-Longmaxi Formation shales and measured borehole temperatures. JY 1 Well. K: Cretaceous; T_{1j}: Jialingjiang Formation in the Triassic; T_{1d}: Daye Formation in the Triassic; T_{1f}: Feixianguan Formation in the Triassic; P_{2w}: Wujiaping Formation in the Permian; P_{1m}: Maokou Formation in the Permian; P_{1q}: Qixia Formation in the Permian; P_{1l}: Liangshan Formation in the Permian; C_{2h}: Huanglong Formation in the Carboniferous; S_{2h}: Hanjiadian Formation in the Silurian; S_{1x}: Xiaoheba Formation in the Silurian; S_{1l}: Longmaxi Formation in the Silurian; O₂: Middle Ordovician (Baota Formation-Shizipu Formation); O_{2sh}: Shizipu Formation in the Ordovician.

(1-3 μm) and irregular microcrystalline aggregates among the detrital grains that were weakly luminescent or nonluminescent (Figure 7). Biogenic microcrystalline quartz produces a broad luminescence peak between 620 nm and 660 nm (Figure 7(c)), which is similar to the luminescence generated by low-temperature authigenic quartz due to

oxygen vacancies [55]. (2) Silt-size quartz grains (5-20 μm) are characterized by a uniform luminescence intensity (Figures 7 and 8). The subrounded and subangular silt-sized quartz grains produce two luminescence peaks with wavelengths of between 390 and 420 nm and 620-640 nm (Figure 8(c)), suggesting a detrital origin [56].

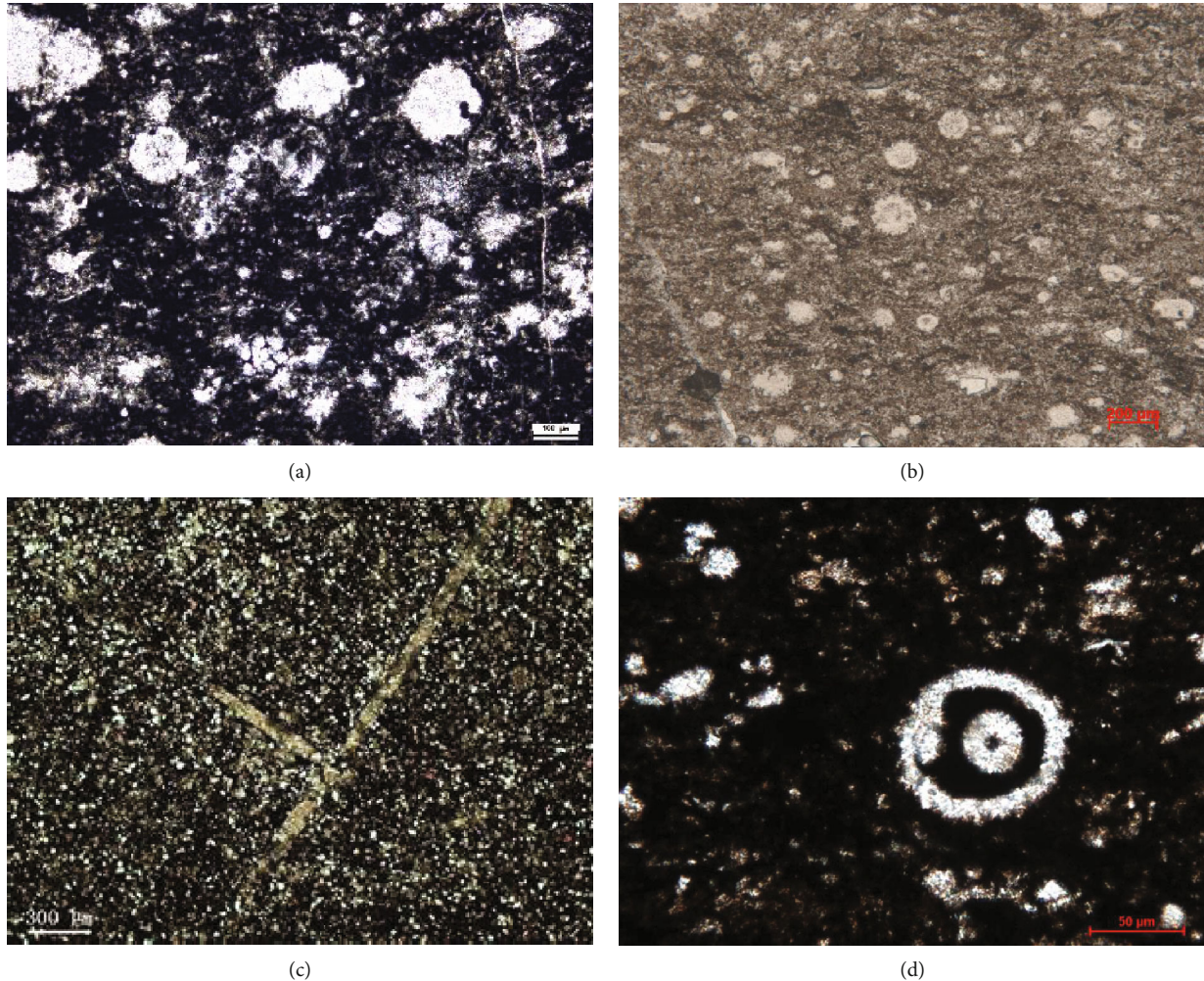


FIGURE 6: Intrabasinal biosiliceous debris in Wufeng and Longmaxi Formations, Fuling Shale Gas Field, Sichuan Basin. (a) Suspected pellet structure contains fossils and has an ellipsoid shape due to compaction, well JY 2, O_3w , 2570.9 m; (b) quartz with ellipsoid shapes, presumably siliceous minerals filling the cysts of algae at the early stage of diagenesis, well JY 2, O_3w , 570.9 m; (c) radiolarians, Well JY 1, S_1l , 2389.3 m; (d) sponge spicule, well JY 2, S_1l , 2545.2 m.

The bulk of opaline silica produced by dissolved biogenic silica of radiolarians and sponge spicules in ocean surface waters does not become incorporated into deep-sea sediments because it dissolves while settling down [54]. Sediment accumulation rate is a significant factor in mudrock cementation [58], especially for the formation of biogenic quartz. In the situation in which there was a slow rate of sediment accumulation in the WF2-LM4 GZ, the amount of dissolved biogenic silica from radiolarian tests and sponge spicules is substantial. In contrast, rapidly deposited shales of the LM5-LM8 GZ tend to have only trace amounts of biogenic silica. In the processes of burial and exposure to high temperatures and pressures, the biogenic opal-A is first transformed into opal-CT and eventually into biogenic quartz [52, 54], which is mainly composed of aphanitic, microcrystalline, and macrocrystalline quartz. This may be the reason why there is more biogenic silica in the WF2-LM4 GZ than in the LM5-LM8 GZ. Up to 60% of total quartz has a biogenic origin in siliceous shales of the WF2-LM4 GZ [57], resembling the Eagle Ford Formation in Texas, in which the authi-

genic quartz comprises 85% percent and is equal to about 12.6% by volume [52]. There is more biogenic silica in the WF2-LM4 GZ than the silt-size detrital quartz in siliceous shales of the LM5-LM8 GZ. Biogenic quartz cement as matrix-dispersed microcrystalline quartz plays an important role in the diagenesis of the Wufeng and Longmaxi Formations.

Microcrystalline quartz in siliceous shales is mainly formed during diagenesis and is similar to the microcrystalline quartz in the Barnett Shale [3] and Eagle Ford Shale [52]. Thin section analysis and other methods reveal that there are different hydrocarbon-generating fossil organisms in the WF2-LM4 GZ. In addition to the graptolites, algae, and acritarchs, there are many siliceous microfossils, such as radiolarians, sponge spicules, and other skeletal fragments (Figure 6), which indicate the organic origin of silica in the organic-rich shale of the WF2-LM4 GZ. The content of detrital quartz and feldspar in siliceous shales is relatively low, which is the main difference between the organic-rich and the silty shale (the main shale type of LM5-LM8 GZ).

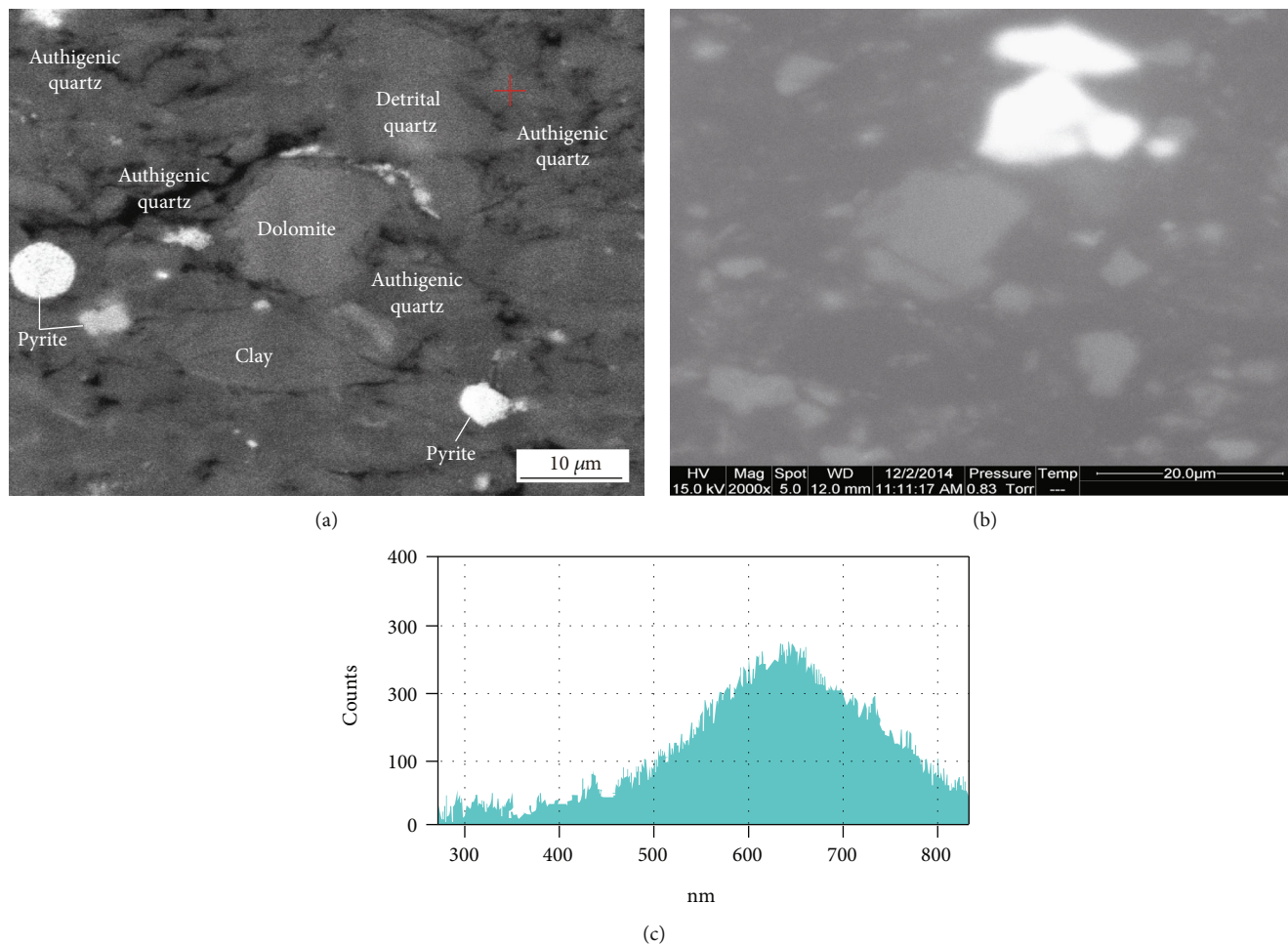


FIGURE 7: BSE images, cathodoluminescence (CL) image, and CL-response images of siliceous shale samples from the Wufeng and Longmaxi Formations. (a) BSE image of detrital quartz silt with pore-filling authigenic quartz, Longmaxi Formation, 2565.85 m, well JY 2. (b) SEM-CL image reveals that quartz silt grains have strong luminescence. In contrast, microcrystalline quartz is essentially nonluminescent, suggesting a diagenetic origin. (c) Monochromatic CL-responses of microcrystalline quartz (red cross in (a)).

Radiolarians and sponge spicules are the dominant forms of silica in the intrabasinal detrital assemblage. Dissolved silica released by dissolution of the radiolarians and sponge spicules is the dominant source of silica for the precipitation and reprecipitation of authigenic quartz in a variety of forms, including matrix-dispersed microcrystalline quartz cement, and fillings within primary intragranular pores [52]. The matrix-dispersed biogenic quartz is the dominant quartz in WF2-LM4 GZ (Figures 7 and 8). The matrix-dispersed authigenic microcrystalline quartz in the Wufeng and Longmaxi Formations occurs as the grain-binding cement that plays a role in the generation of brittle mechanical rock properties, similar to the Barnett Shale [30]. Additionally, the specific form of matrix-dispersed authigenic quartz has significant implications for the rock mechanical properties and residual oil. Moreover, as a result of precipitating authigenic quartz from the dissolution of biogenic opal [54], preserved quartz content (i.e., excess silica) may also reflect the surface water productivity during deposition [59], which indicates a higher surface productivity with a higher supply of OM during shale deposition.

5.2. Pore Types. The pore types in the Wufeng and Longmaxi Formations include OM pores, inorganic mineral pores (particle-related, pyrite-related, and clay-related pores), and microfractures [10, 11, 33]; the most important of these are the OM pores. Greater gas storage and flow capacity exist in shale intervals with higher TOC and depend upon the abundance and connectivity of OM pores [7, 10, 14, 60]. Observations demonstrate a complex evolution of the OM pore system in shales [60]. The difference in OM types (hydrocarbon-generating organisms and amorphous OM (bitumen)) has an impact on the type, size, and distribution of the OM pore system [42]. The OM type, controlled by sequence-stratigraphic position [13], is a key factor in determining the pore type, size, and distribution. The OM pores include pores hosted in algae, biotritus, and bitumen. The algae are a structured OM type, which generally has consistent or predictable porosity styles in the shale section due to the different algal types. Proceeding from the bottom of the Wufeng Formation to the middle and upper parts of the first member of the Longmaxi Formation, the OM pore types and pore size changed regularly.

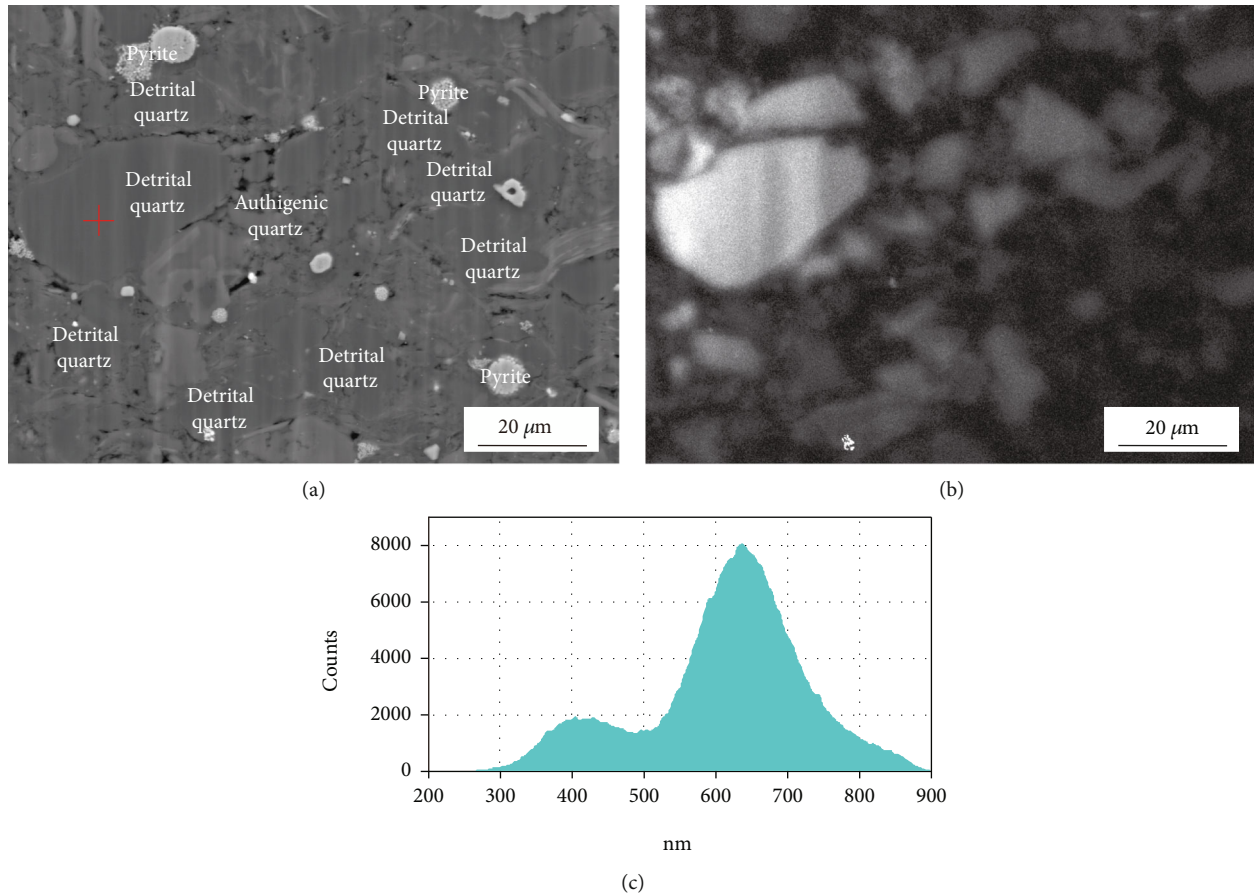


FIGURE 8: BSE images, cathodoluminescence (CL) image, and CL-response images of siliceous shale samples from the Wufeng and Longmaxi Formations. (a) BSE image of detrital quartz silt with pore-filling authigenic quartz, Wufeng Formation, 2532.11 m, well JY 2. (b) SEM-CL image displaying the strong luminescence of quartz silt grain. (c) Monochromatic CL-responses of quartz silt (blue cross in (a)).

(1) The shale of the WF2-LM4 GZ was found to be the interval with the most abundant OM present, in which the most abundant type of OM is multicellular algae, as well as small amounts of unicellular algae and bitumen [42]. Under compaction, the OM formed thin layers and/or three-dimensional interconnected OM pore networks (Figure 2). The OM pores were left behind by various hydrocarbon-generating organisms (mainly multicellular algae) and oil during gas generation and expulsion. The high total amounts of multicellular algae ensure a large number of OM pores, favoring the formation of three-dimensional interconnected pore networks, which is conducive to the enrichment and production of shale gas. Additionally, the three-dimensional reconstruction of kerogen and porosity distributions reveal that OM pores have the potential to form connected pore networks, where 26%-67% of the pore volume may be connected [16]. Moreover, the mineral pores are predominately slit-like in the cross-section, whereas OM pores are typically round [11]. OM pore networks are a combination of pores developed in depositional OM and migrated OM [14]. The depositional OM (mainly multicellular algae) pores are the main reservoir type in the shale of the WF2-LM4 GZ [37].

(2) The OM types of the LM5-LM8 GZ are mainly composed of unicellular algae and amorphous OM (bitumen), and the TOC is lower than the shale of the WF2-LM4 GZ [19]. The OM pores are mainly developed in unicellular algae and/or little in solid bitumen which often occur as poorly developed isolated pores and in unicellular algae which tended to be randomly developed by the arrangement gaps (Figure 3). Therefore, this kind of OM pore development is limited. The shape is irregular, and the size is tens to more than one hundred nm. The OM pore system changes are less pronounced and cannot form three-dimensional interconnected OM pore networks due to the low TOC content, which is not conducive to the enrichment and production of shale gas.

6. Direct Seal

A series of tight strata directly overlying the shale gas reservoir is served as the cap rock, such as shale, silty shale, argillaceous siltstone, and limestone. A prerequisite for shale gas source and seal coupling systems is the heterogeneity of shale strata, while key factors determining the capability of the direct seal are lithology and petrophysical properties, as well as the differences of petrophysical parameters between the

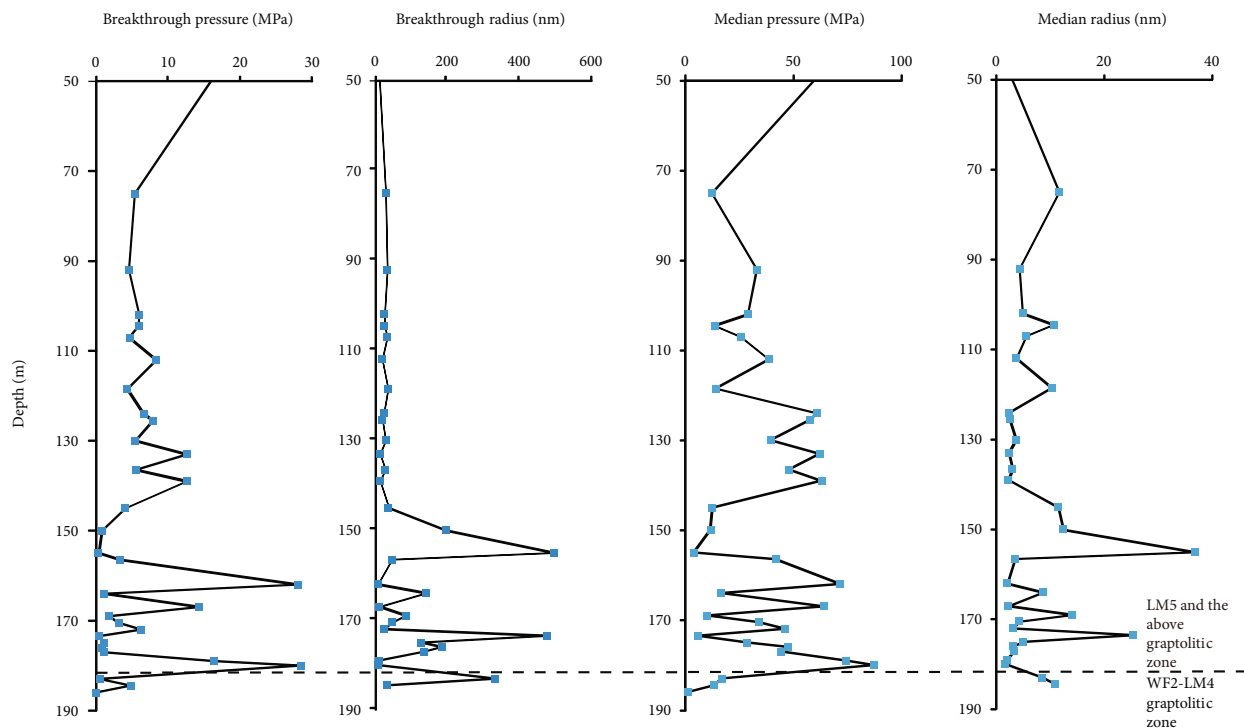


FIGURE 9: The breakthrough pressures, breakthrough radius, median pressures, and median radius (mercury injection capillary pressure data) of the Wufeng and Longmaxi Formations, Guanyinqiao section, Qijiang County, Chongqing Municipality. Because the shale of the outcrop sample is weathered to different degrees, the breakthrough radius and the median radius are large, while the breakthrough pressure and the breakthrough radius are small. However, the overall performance is that the breakthrough pressure and median pressure of the WF2-LM4 GZ is lower than those of the LM5-LM8 GZ, showing the stronger sealing capacity of the LM5-LM8 GZ which is a direct seal for the WF2-LM4 GZ.

source and seal [44]. The LM5-LM8 GZ is the direct seal of the WF2-LM4 GZ (Figure 4).

For shale mineral composition, the quartz content decreases while the clay mineral content increases from the source to seal, the Wufeng Formation to the first member of Longmaxi Formation. With differences in mineralogy, LM5-LM8 GZ is less brittle but more ductile than the WF2-LM4 GZ when compacted by equivalent geological stress. Observably high gas content in the WF2-LM4 GZ and a significantly lower one in the LM5-LM6 GZ sequence in the Well JY 1 are shown in Figure 4, indicating that the upper part of the Longmaxi Formation (the LM5-LM6 GZ) served as a direct seal with its much lower porosity and higher clay content preventing shale gas in the WF2-LM4 GZ from escaping.

Furthermore, the capability of direct seals can be quantitatively estimated from breakthrough pressure and median pressure. The breakthrough pressure and median pressure of the WF2-LM4 GZ is lower than those of the LM5-LM8 GZ according to the microscopic pore structure analysis. There is a positive relationship between the breakthrough pressure and the breakthrough radius as well as the median pressure and the median radius indicating that the LM5-LM8 GZ plays a role as the direct seal for the WF2-LM4 GZ with its strong sealing capacity [44]. The breakthrough pressure and median pressure, together with the breakthrough radius and median pressure between WF2-LM4

GZ and LM5-LM8 GZ of the Guanyinqiao section in Qijiang County, Chongqing City, have similar characteristics to Well JY 2, that is, the LM5-LM8 GZ is the direct seal for the WF2-LM4 GZ (Figure 9).

7. Coevolutionary Processes and Mechanisms of Shale Hydrocarbon Generation and Reservoir Preservation

7.1. Source and Reservoir Evolution. Different GZs represent different deposition environments, and this is also true for corresponding hydrocarbon-generating organism assemblages and mineral compositions [19, 39]. Combined, these lead to the differences observed in the interrelationships and coevolution of hydrocarbon generation and reservoir formation processes.

- (1) The shale of the WF2-LM4 GZ is siliciclastic-dominated featuring a slow deposition rate, favorable organism types (i.e., multicellular algae), high TOC, and high hydrocarbon generation capacity. All of these are then favorable conditions for the further generation, accumulation, and preservation of shale gas. The timing sequence of hydrocarbon generation and reservoir evolution in the WF2-LM4 GZ exhibits signs of a siliceous grid that was formed early and oil

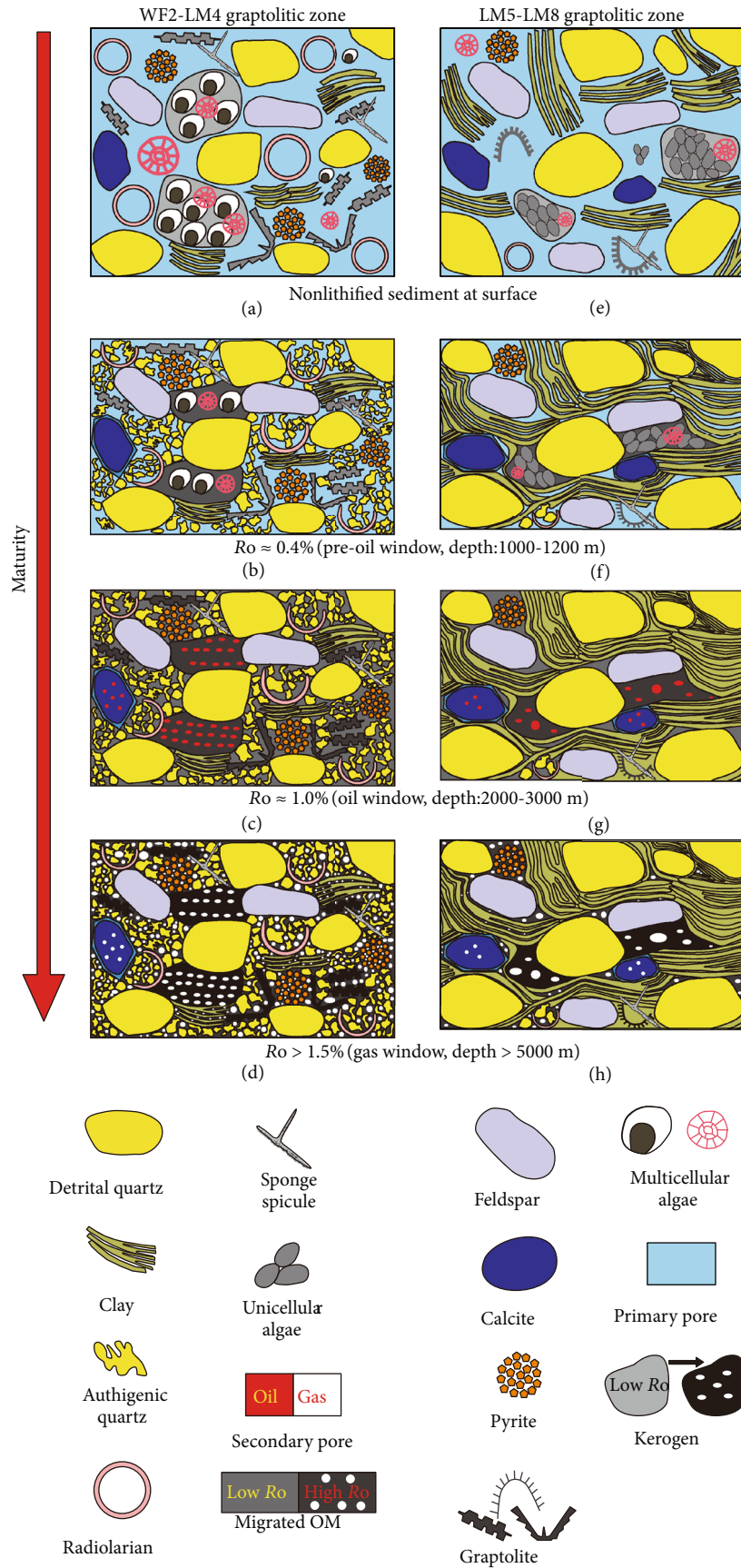


FIGURE 10: The coevolution processes of the reservoir (WF2-LM4 GZ) and the seal (LM5-LM8 GZ).

TABLE 1: Comparison of coevolutionary characteristics of between WF2-LM4 GZ and LM5-LM8 GZ in Wufeng Formation to the lower part of the first member of Longmaxi Formation, Sichuan Basin.

	Graptolitic zone	LM5-LM8	WF2-LM4
Source rock	Hydrocarbon generation organisms	Green algae, cyanobacteria, and other benthic algae	Red algae, brown algae, and other planktonic algae
	TOC (%)	<3 (low)	>3 (high)
Reservoir rock	Hydrocarbon generating capacity	Weak	Strong
	Quartz	Mainly terrigenous silica	Mainly biogenic silica
	Pore types	Dominated by mineral pores, few	Dominated by organic matter pore
Source and reservoir evolution	Porosity (%)	<4 (low)	>4 (high)
	Source and seal evolution	Strong ability to form a rigid grid and strong anticompaction ability; high degree of coevolution	Weak ability to form a rigid grid and strong anticompaction ability; low degree of coevolution
Source and seal evolution		Usually as the direct seal for shale gas reservoir	Promising shale gas interval

that was charged late. The oil generation and corresponding overpressure are beneficial to the development of a shale gas reservoir. The main features are as follows (Figure 10) (Table 1):

- (a) Quartz cement in the WF2-LM4 GZ may originate from various silica sources, such as biogenic authigenic silica, mineral transformations, and redistribution (pressure dissolution/clay-induced dissolution) [57]. Assessing the relative contributions of these potential silica sources would require the determination of the relative timing of the authigenic quartz [52]. Understanding the formation of biogenic quartz cement is of great importance for shale gas reservoir evaluation, especially when the formation time of three-dimensional connected frameworks of biogenic silicon is earlier than that of the maximum oil generation, which can provide storage spaces for holding a large amount of oil.

Most of the quartz in the WF2-LM4 GZ is biogenic, which may originate from the dissolution and recrystallization of biogenic silica [44]. The documented temperatures and porosities in effect during the alteration of former biogenic opal-A through the transformation to opal-CT and eventually to microcrystalline quartz [52, 54, 61, 62] are consistent with the observed burial histories. The transformation from opal-A to crystalline microcrystalline quartz has well-documented impacts on the generation of brittle behavior in mudstones [61]. Unconfined compressive strength (UCS) exhibits an abrupt increase from several MPa above 1000 m to several tens of MPa at a depth of ~1000 m, where the silica is opal-CT, and the UCS remains at high values at depths of 1000-1200 m; although displaying a gradual decline over this depth range, the UCS is still 10-15 MPa below the depth of 1200 m [61]. The results show that when the buried depth of shale

is at least 1000-1200 m, the silica is opal-CT and the shale has strong brittleness. According to the evolution history of opal-A→opal-CT→quartz, oxygen isotope analysis shows that the temperature of opal-CT that evolved into quartz-layered flint is 17-21°C [63]. The thermal maturity is lower than 0.5% R_o when the temperature is 17-21°C and the burial depth is less than 1000 m, and the formation time for authigenic quartz is Late Early Silurian (early diagenetic stage). Thus, the transformation process seemingly occurred at relatively low temperatures before the oil window. Rapid compaction occurs in response to the gradual increase in burial depth and the infilling of pore spaces in preexisting detrital quartz frameworks with biogenic microcrystalline silica [62].

Intergranular pore space is controlled by the preservation of primary pores [8], which are prone to be preserved under the supporting structure of matrix-dispersed authigenic quartz that prevents compaction [57]. This dissolution and reprecipitation process may transform the siliceous particles in place or reprecipitate dissolved silica in the forms of matrix-dispersed microcrystalline quartz and irregular microcrystalline aggregates in pores that were formed by early detrital quartz [57]. The shape of kerogen particles (hydrocarbon-generating organisms) and the amount of retained oil filled in primary framework pores while relying on the presence of the compaction-resistant rigid grains that are determined by detrital and matrix-dispersed biogenic authigenic quartz for pressure maintenance to preserve porosity. These matrix-dispersed microcrystalline quartz aggregates have an early formation time before the infilling of hydrocarbon compaction occurs. Pore space is abundant enough in microcrystalline quartz aggregates for oil and bitumen filling during the oil window.

Matrix-dispersed biogenic authigenic quartz occurs as the cement in the primary, irregular, intergranular, and intragranular pores; restrains the compaction; and preserves the internal pore structure together with the detrital quartz as a rigid and three-dimensional framework. This then strengthens the framework and effectively increases the shale brittleness at the same time. The rock matrix formed by high quartz content has a strong ability to resist compaction that provides abundant spaces for maintaining OM, especially for the retention of large amounts of oil. Furthermore, during the hydrocarbon generation window, the organic acids generated can dissolve the unstable minerals [64, 65], which also increases the storage spaces. The filling of early oil may have some inhibiting effects on shale diagenesis and slow the compaction process.

- (b) The TOC is one of the main controlling factors for hydrocarbon generation. The TOC content is generally high, commonly between 2% and 5%, and the OM mainly exists in flocculent states in the siliceous particles or between the quartz particles. Organic petrology coupled with back-scattered and field emission SEM indicates that the OM type (mainly multicellular algae) is the most significant contributor to the TOC content and OM porosity, ensuring the matching of gas generation and OM pore development. The thermal simulation experiment results show that the generated oil yield from modern planktonic algae is almost double or triple that of benthic algae [48]. The WF2-LM4 GZ dominated by the multicellular algae had a much higher oil generation potential than the LM5-LM8 GZ where unicellular algae were common. The organic-rich WF2-LM4 GZ is favorable to oil generation and adsorption, as well as primary oil expulsion to the intergranular pores of biogenic quartz matrices, bringing in high oil retention in TOC-rich and biogenic quartz-rich graptolitic shales. It is generally assumed that multicellular algae have complex cell structures and a stronger ability to generate multiple kinds of OM pores than unicellular algae during thermal maturation [9]. The OM pores in the multicellular algae are well developed within the algae and inherited the original biological structure [42], the sizes of which are usually hundreds of nm, or even μm -scale. Additionally, the TOC content also determines the number of OM pores.
- (c) The retention of hydrocarbons in shales of the WF2-LM4 GZ is mainly controlled by the sorption capacity of OM and the spaces in three-dimensional connected frameworks of biogenic silica [19, 44], in which the oil was retained in absorbed and free states, respectively. A similar

retention phenomenon related to the presence of porous fossils exists in the Marathon 1 Mesquite Well [66], where siliceous sponge spicules enhance the storage capacity for bitumen [67]. For gas generation, the secondary cracking of the residual oil is the main source [1, 32, 33, 68, 69]. Shale gas content is largely determined by the amount of residual oil cracking during high thermal maturity in organic-rich shales [69, 70]. The WF2-LM4 GZ has high content of TOC and silica that is associated with multicellular algae [37]. During the oil window, the generated oil was filled in kerogen and/or expelled from the kerogen and migrated into the adjacent interparticle and intraparticle mineral pores. With increasing maturity, the normalized concentration of retained oil (S1/TOC \cdot 100) TOC increased in the oil window [67]. During the stage of oil cracking, the generation of gas, the formation of OM pores, and overpressure coevolved to offset the effects of compaction. In particular, the residual oil and overpressure have important effects on reservoir formation, which are conducive to the development and preservation of OM pores.

However, with increasing maturity, the cracking and releasing of bulk labile hydrocarbon moieties from kerogen structures might likely leave behind a more rigid and aromatic kerogen residue [67, 71], while the residual oil similarly leaves behind a more rigid and aromatic bitumen. Therefore, the formation of OM pores is most likely a result of the release of massive amounts of hydrocarbons [19, 67]. The abundance of OM pores and degree of connectivity in the three-dimensional OM pore network synergistically increased with an increasing authigenic quartz content in the WF2-LM4 GZ. Residual oil principally fills into the aggregates of authigenic microcrystalline pore networks with the deposition OM and would be likely to generate a better connected three-dimensional OM pore network through secondary cracking, which provides favorable storage space for shale gas in shales of the WF2-LM4 GZ.

To summarize the results above, a logical conclusion is that the coevolution of high contents of favorable OM and quartz (multicellular algae and biogenic quartz) provided high hydrocarbon generation potential and connected three-dimensional networks that may have resulted in the retention of large amounts of oil and kerogen in the rigid interparticle and intraparticle mineral pores. During the stage of oil cracking, the generation of gas and overpressure coevolved to produce an environment conducive to the development and preservation of OM pores and

to offset compaction. In particular, the WF2-LM4 GZ offers a promising reservoir with favorable types and characteristics that are the result of multifactor coupling and coevolution. Reservoir potential should thus not be viewed as being determined by a single factor, but rather as the synergy among many factors, such as hydrocarbon generation potential, porosity, TOC, and quartz contents.

(2) The shale of the LM5-LM8 GZ are clay-dominated and characterized by a fast deposition rate, unfavorable organic organism type (mainly unicellular algae), low TOC, and low hydrocarbon generation capacity, all of which are not favorable conditions for the generation, accumulation, and preservation of shale gas. The timing sequence of hydrocarbon generation and reservoir evolution of the LM5-LM8 GZ experienced early densification of the reservoir and oil that was charged late; the main features are as follows:

- (a) The siliceous minerals of the LM5-LM8 GZ are mainly terrigenous and detrital in origin with trace amounts of biogenic authigenic quartz [19]. The clay mineral content is higher than that of WF2-LM4 GZ. The most unfavorable factor is that the compaction resistance ability of these terrestrial detrital silica and clay minerals is weak and cannot form well-connected three-dimensional frameworks. The radiolarians and sponge spicules slowly gathered and dissolved due to the high deposition rate. Furthermore, the precipitation amount of biogenic authigenic quartz is also low. Without this support, the framework of terrigenous siliciclastic silica with high clay content collapses easily during strong compaction. This densification of the shale reservoir and the reduced porosity and permeability limit the storage space for the retention of oil and migrated OM patches. The transforming period of quartz produced during clay transformation was consistent with the oil generation window that further reduced the pores for the retention of oil and migrated OM patches [57, 72].
- (b) The hydrocarbon-generating organisms of the LM5-LM8 GZ were mainly unicellular algae, with lower TOC content. The pores in unicellular algae are developed by the arrangement gaps of unicellular algae, in which the size is tens to greater than one hundred nm [42]. These two factors led to a poor hydrocarbon generation ability, fewer OM pores, isolated pore distribution, and an inability to form an interconnected three-dimensional OM pore system, all of which is unfavorable to the enrichment and production of shale gas.
- (c) The amount of natural gas generation in the LM5-LM8 GZ largely depends upon the amount of retained oil generated by authigenic OM and

the oil that may be migrated from the WF2-LM4 GZ. Due to the small amount of self-generated oil and pores for oil retention, the storage space for natural gas was limited during the oil cracking stage. Additionally, both the kerogen and the residual oil have low capacities to generate gas that make it difficult to form OM networks when there is little to no biogenic authigenic quartz present. In this case, only trace amounts of an OM network exist in the LM5-LM8 GZ.

7.2. Source and Seal Evolution. A good match between the shale gas generation from an organic-rich shale source and the development of the direct seal is critical for the assessment of shale gas enrichment in the Sichuan Basin, South China. The pore evolution simulation performed for TOC and mineral compositions of the WF2-LM4 GZ and LM5-LM8 zones in Well JY 1 showed that the porosity of OM pores in the WF2-LM4 GZ increased at a greater burial depth with the thermal maturity of 0.6%, while the porosity of the mineral pores gradually decreased with evolution. The Middle Cretaceous was the peak period for dry gas generation and OM pore formation in the WF2-LM4 GZ. Yet in the LM5-LM8 GZ, the mineral pores are dominant and with little OM pores. The porosity of the LM5-LM8 GZ decreased due to the lack of supplement to increase OM pores during the overmature dry gas generation window, ranging from 3.19% to 5.09% (Figure 11). The WF2-LM4 GZ is the source and reservoir for shale gas with its high TOC high residual oil content and OM-hosted porosity, while the overlying LM5-LM8 GZ is the direct cap rock.

The shape of porosity-decline curves is defined by initial porosity, grain size, and mineral composition [58]. In short, they are governed by the microfabric [73], and the microfabric, in turn, controls the reservoir types and characteristics. To obtain the evolution of porosity of the two GZ, the burial history reconstruction and the thermal history simulation were performed, revealing the differences between the source (WF2-LM4 GZ) and the direct seal (LM5-LM8 GZ). The porosity of mineral pores in the WF2-LM4 GZ exhibited a decreasing trend with burial depth, dropping to a minimum value of 1.0% to 1.5% in the Middle Cretaceous. Then, the porosity of mineral pores presented a slight increase accompanying the uplift, reaching ~2.0% to the recent. On the other hand, the porosity of OM pores in the WF2-LM4 GZ showed an obvious increase during the Early Triassic when the thermal maturity reached 0.6% R_o , reaching 2.5% in the Early-Middle Cretaceous. Since then, under the decompression during the uplift, it has slightly increased to ~3.0% till the present. The average total porosity is about 6% in the WF2-LM4 GZ, much greater than that in the LM5-LM8 GZ (Figure 11). The porosity of the OM pores is about 1% in the LM5-LM8 GZ. Thus, the LM5-LM8 GZ can be regarded as a direct seal for the shale gas reservoir in the WF2-LM4 GZ. In conclusion, the source rock and direct seal form a strong coevolutionary matching, favorable for shale gas accumulation.

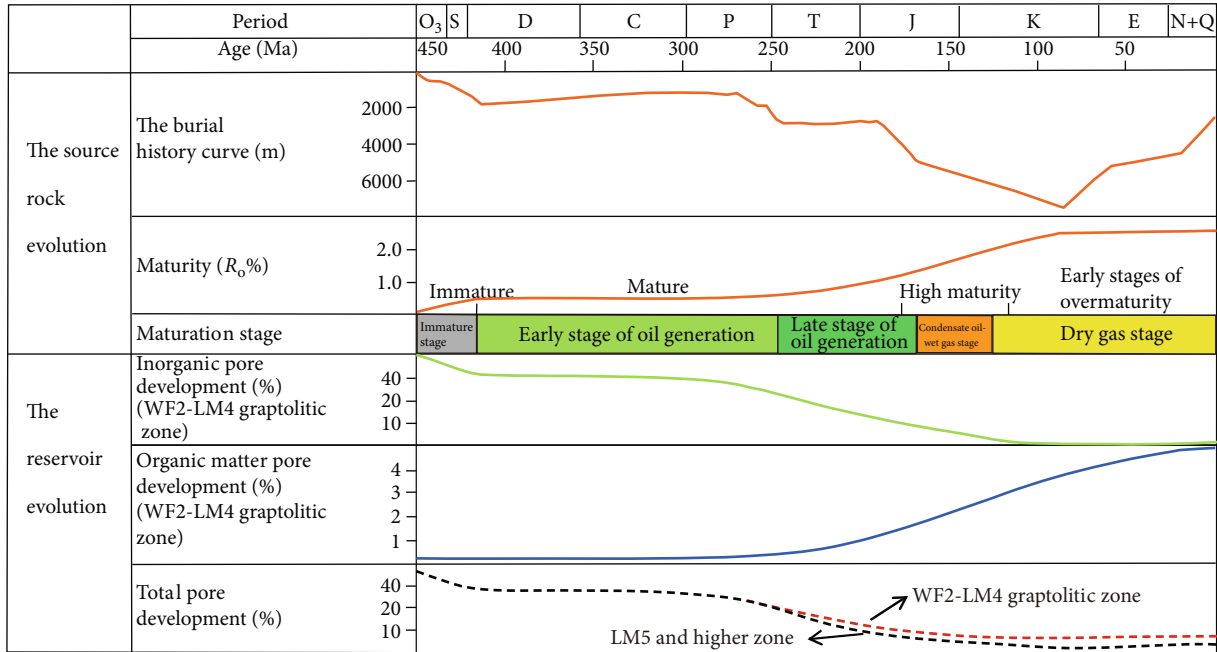


FIGURE 11: Porosity evolution history of the Wufeng and Longmaxi Formation shale gas reservoir in the Jiaoshiba area (modified from [20]).

7.3. *Evolution of the Source, Reservoir, and Preservation.* Based on the burial history of Well JY 1, the black shale in the Wufeng and Longmaxi Formations underwent four stages of evolution of the source, reservoir, and preservation (Figure 7):

- (1) In the Early Devonian, an initial stage of rapid subsidence and burial occurred during which only a small amount of heavy oil was generated. With the small amounts of detrital quartz, the matrix-dispersed biogenic authigenic quartz in the WF2-LM4 GZ occurs as the cement in primary anomalous intergranular and intragranular pores that restrained the compaction to preserve the pore structure as rigid and connected three-dimensional frameworks strengthened the rock framework and increased the shale brittleness effectively at the same time. Without the support of biogenic silica, the framework of terrigenous siliclastic silicon with high clay content collapses easily during compaction, which results in smaller storage spaces for retaining oil and migrated OM patches.
- (2) The second stage of subsidence occurred in the Early-Middle Triassic. A large amount of oil might remain in the shales of the WF2-LM4 GZ because of a rapid, limited-amplitude uplift and a low oil expulsion efficiency. Existing biogenic authigenic quartz-supported three-dimensional framework porosity is filled with migrating hydrocarbons and subsequently results in the development of OM micropores in those places. During this period, the direct seal rock was formed when the shale reached high maturity at $\sim 1.2\% R_o$.

- (3) The third stage of subsidence extended from the Early Jurassic to Middle Cretaceous. The kerogen and residual oil can generate a great amount of gas and bitumen through cracking, also resulting in large amounts of OM pores for gas storage when the shale reached maximum maturity. Meanwhile, this time was the most productive gas generation period for the WF2-LM4 GZ, that is, peak gas generation and formation of massive OM pores were synchronous. However, the porosity of the LM5-LM8 GZ was at its minimum in this period. During the periods of largest gas generation, OM pore formation, seal formation of direct cap rocks overlapped and formed a strong matching for shale gas accumulation and preservation in the Wufeng and Longmaxi Formations (Figures 7 and 11). Meanwhile, the regional seal of the Lower Triassic gypsum layer was formed during the Late Jurassic-Early Cretaceous [74], before the periods of greatest gas generation and OM pore formation.
- (4) The acceleration of the uplift stage from the middle stage of the Late Cretaceous led to the cease of the hydrocarbon generation process and diagenesis process resulting from the thermal maturation evolution. Besides, pores in the minerals resulting from the decompression process turn larger, the organic pores increase to different degrees, and the preexisting fissures reopen [11]. If the tectonic uplift is too strong, the large and deep faults would develop in the shale and exodiagenesis could occur with freshwater pouring into fractures. And all kinds of dissolution processes of inorganic minerals would do great damage to the shale gas reservoir. What is more, the organic

diagenesis and organic-inorganic interaction process turn relatively weak.

It should be noted that the research of coevolutionary dynamics of organic-inorganic interactions, hydrocarbon generation, and shale gas reservoir preservation of the Upper Ordovician Wufeng and Lower Silurian Longmaxi Formations between the WF2-LM4 GZ and the LM5-LM8 GZ is a theoretical study of the static characteristics, coevolution process, evolution mode, and evolution characteristics of two graptolite zones. However, these are controlled by the black shale depositional environment, the tectonic evolution experienced by the shale strata after deposition, and the current structural location, type, and characteristic. The shale gas reservoir characteristics and shale gas enrichment characteristics of different graptolite zones may not be completely consistent with theoretical models, and specific analysis needs to be combined with the sedimentary environment and structural background in the study area. Taking the Upper Ordovician Wufeng and Lower Silurian Longmaxi Formations in the Sichuan Basin and its surrounding areas as an example, it is necessary to determine the thickness and sequence evolution characteristics of the WF2-LM4 GZ based on the shale depositional environment, structural background, and exploration and development costs. To further predict the shale gas enrichment area, mapping the WF2-LM4 GZ will be a major task in future exploration and a lot of work needs to be carried out.

8. Analysis of Wufeng and Longmaxi Shale Gas Potential

8.1. The Coevolution Processes between the WF2-LM4 GZ and the LM5-LM8 GZ. Since the hydrocarbon-generating organisms of the WF2-LM4 GZ are mainly multicellular algae that have high TOC content and a high hydrocarbon-generating capacity, the organic acids generated are greater than those of the LM5-LM8 GZ. The generated organic acids preferentially dissolve the unstable minerals in the shale and typically chemically react with feldspar particles to precipitate kaolinite and microcrystalline quartz [75]. The dissolution of unstable minerals further reinforces and preserves the connected three-dimensional framework spaces of biogenic silica formed before the organic acid formation, which is favorable for oil retention in the shale of the WF2-LM4 GZ. Strongly coupled with the large amounts of oil generation that is determined by the multicellular algae, the kerogen and the biogenic silica-connected three-dimensional frameworks can retain much oil, which greatly determines the gas content in shale by generating cracking gas and porous pyrobitumen at high thermal maturities. Previous reports on adsorbed oil in kerogen proposed that 170 mg/g TOC can contribute to ~22% of free oil, estimating that shale has great potential for oil generation [69]. This constitutes a large portion of the retained oil in shales. All of these favorable factors (i.e., favorable OM type and TOC content, the formation of connected three-dimensional networks of biogenic authigenic quartz before oil charge, and overlapped generation periods of natural gas, OM pores, and overpressure) suggest a high

level of source-reservoir coevolution to provide ideal conditions for shale gas accumulation.

Because of the lack of biogenic silica needed to form connected three-dimensional frameworks in the LM5-LM8 GZ, the dissolution of unstable minerals by organic acids and the precipitation of microcrystalline quartz transformed by clay minerals strengthened the compaction and further reduced the porosity. The storage space for oil is smaller than in the WF2-LM4 GZ. By the coupling of a low oil generation potential (driven by unicellular algae) and small storage spaces for oil retention, a small amount of gas may be hosted in various pores and dominantly in the mineral pores, which reveals a low level of source-reservoir coevolution.

The two coevolution processes are conducive to a high spatiotemporal matching of the reservoir (WF2-LM4 GZ) and seal (LM5-LM8 GZ) due to their different coevolving processes of gas generation, OM pore formation, and direct seal formation.

Shale gas displays the feature of being a self-sourced and self-accumulating reservoir and mixes by the cracking gases of oil and kerogen at high maturity [1, 2, 76]. The WF2-LM4 GZ is the source and reservoir with favorable accumulation conditions for shale gas development, characterizing a slow deposition rate, favorable organism type, high TOC and high hydrocarbon generation capacity, high quartz content, and high degree of coevolution between hydrocarbon generation and the reservoir [19, 20]. At present, the WF2-LM4 GZ is the main prospect section of exploration, and three national shale gas exploration areas in the Fuling, Weiyuan, Changning, and Zhaotong, have been constructed where the thickness of the WF2-LM4 GZ is over 20-25 m [20]. The WF2-LM4 GZ is the most profitable GZ for shale gas accumulation, and it displays excellent exploration potentials. Even outside the Sichuan Basin where the tectonics are relatively strong, the WF2-LM4 GZ can also form good normal pressure shale gas reservoirs [77, 78].

8.2. The Shale Gas Exploration Potential of the LM5-LM8 GZ. Shale gas exploration also exhibits generally unsatisfactory production from the shale in the LM5-LM8 GZ except where structural highs have enhanced hydrocarbon accumulation [79]. The LM5-LM8 GZ directly overlaps the high-quality source rocks of the WF2-LM4 GZ, and the local pore-developed areas typically have a good ability to store oil and maybe reservoirs for migrated oil. During the oil cracking stage, the oil will crack to natural gas to form porous bitumen and store the locally generated shale gas. There may also be some natural gas migrated from the WF2-LM4 GZ. The LM5-LM8 GZ may also have shale gas accumulation which has been confirmed by exploration [80]. The JY 11-2-1HF Well and JY 29-S1 Well are located at the apex and the slope of the Jiaoshi box-shaped anticline, respectively, and the depths of the targets are 2200 m and 2400 m, respectively. In June of 2015, the JY 11-2-1HF Well operated by Sinopec reached a test production of 287,000 m³/d after hydraulic fracturing (the horizontal interval only has a length of 780 m), which is a strategic milestone in the LM5-LM8 GZ. However, the JY 29-S1 Well reached a test production of 248,000 m³/d after the hydraulic fracturing (the horizontal

interval has a length of 1502 m). The horizontal interval of the JY 29-S1 Well is almost twice that of the JY 11-2-1HF Well, but the test production is nearly identical. The permeability production of the JY 11-2-1HF Well is thus twice that of the JY 29-S1 Well. It is believed that there may be a primary migration in the LM5-LM8 GZ, resulting in a high degree of shale gas enrichment in the upper part of the Jiaoshiba anticline [79, 80]. It is suggested that the development of LM5-LM8 GZ should start from the high part of the structure and gradually expand to the low part.

9. Conclusions

In our study, the Fuling O_3W-S_1l Shale Gas Field in the eastern Sichuan Basin was used as a case study to discuss the coevolutionary processes and organic-inorganic interactions of hydrocarbon generation and reservoir preservation. This comprehensive analysis revealed that the dynamics of organic-inorganic interactions and coevolution in hydrocarbon generation and reservoir preservation are quite different among shale GZs in terms of hydrocarbon generation, types, and characteristics of shale gas reservoirs; seal characteristics; and their spatiotemporal relationships.

The WF2-LM4 GZ contains planktonic algae featuring the majority of multicellular algae, high TOC, strong hydrocarbon generation capacity, and a high-quality shale gas reservoir with connected OM pore networks. Taken together, all of these result in favorable conditions for the development of a high degree of coevolution in hydrocarbon generation and accumulation. The high degree of coupling among favorable OM, biogenic authigenic quartz, and organic-inorganic interactions likely led to coevolution and the favorable conditions for shale gas accumulation.

However, the overlying LM5-LM8 GZ exhibits signs of early densification and late charge and has a reverse mode of reservoir development. This is likely due to the lack of biogenic microcrystalline opal-CT/quartz precipitation to preserve and reinforce the preexisting framework, together with the unfavorable matching between oil generation and pore development, which cannot provide enough storage spaces for oil retention to generate widespread cracking gas and OM pores during the high maturation window.

These two coevolutionary processes are conducive to a high degree of spatiotemporal matching between the reservoir (i.e., WF2-LM4 GZ) and the seal (i.e., LM5-LM8 GZ). This may be due to their different coevolutionary histories of gas generation, OM pore formation, and direct seal formation, which laid the foundation for the coevolutionary dynamics of hydrocarbon generation and reservoir preservation.

We believe that our comprehensive research and the mechanisms formulated for the coevolution of organic-inorganic interactions and hydrocarbon generation and reservoir preservation have determined that the WF2-LM4 GZ is the most promising interval for shale gas exploration and development in the Sichuan Basin. Furthermore, the insights provided here may be used as a framework for the geological theory, exploration, and development of shale gas worldwide.

Data Availability

The data that support the findings of this study are available from the corresponding author upon reasonable request.

Conflicts of Interest

The authors declare no conflicts of interest.

Acknowledgments

The study was supported by the China National Natural Science Foundation (Grant No. 41872124) and Sinopec in-house projects. We are grateful for Sinopec Petroleum Exploration and the Development Research Institute, Sinopec Jiangnan Oilfield and Sinopec Exploration Company, for the valuable data provided. We thank Xu Chen, Juanxuan Fan, and Qing Chen for their support in graptolite identification and data collection. We also thank Sinopec management for permission to publish this work.

References

- [1] J. B. Curtis, "Fractured shale-gas systems," *AAPG Bulletin*, vol. 86, no. 11, pp. 1921–1938, 2002.
- [2] J. C. Zhang, Z. J. Jin, and M. S. Yuan, "Reservoiring mechanism of shale gas and its distribution," *Natural Gas Industry*, vol. 24, no. 7, pp. 15–18, 2004.
- [3] R. G. Loucks and S. C. Ruppel, "Mississippian Barnett shale: lithofacies and depositional setting of a deep-water shale-gas succession in the Fort Worth Basin, Texas," *AAPG Bulletin*, vol. 91, no. 4, pp. 579–601, 2007.
- [4] R. G. Loucks, R. M. Reed, S. C. Ruppel, and D. M. Jarvie, "Morphology, genesis, and distribution of nanometer-scale pores in siliceous mudstones of the Mississippian Barnett shale," *Journal of Sedimentary Research*, vol. 79, no. 12, pp. 848–861, 2009.
- [5] G. R. Chalmers, R. M. Bustin, and I. M. Power, "Characterization of gas shale pore systems by porosimetry, pycnometry, surface area, and field emission scanning electron microscopy/transmission electron microscopy image analyses: examples from the Barnett, Woodford, Haynesville, Marcellus, and Doig units," *AAPG Bulletin*, vol. 96, no. 6, pp. 1099–1119, 2012.
- [6] M. E. Curtis, B. J. Cardott, C. H. Sondergeld, and C. S. Rai, "Development of organic porosity in the Woodford shale with increasing thermal maturity," *International Journal of Coal Geology*, vol. 103, pp. 26–31, 2012.
- [7] M. E. Curtis, C. H. Sondergeld, R. J. Ambrose, and C. S. Rai, "Microstructural investigation of gas shales in two and three dimensions using nanometer-scale resolution imaging," *AAPG Bulletin*, vol. 96, no. 4, pp. 665–677, 2012.
- [8] R. G. Loucks, R. M. Reed, S. C. Ruppel, and U. Hammes, "Spectrum of pore types and networks in mudrocks and a descriptive classification for matrix-related mudrock pores," *AAPG Bulletin*, vol. 96, no. 6, pp. 1071–1098, 2012.
- [9] H. K. Nie, R. K. Bian, P. X. Zhang, and B. Gao, "Micro-types and characteristics of shale reservoir of the Lower Paleozoic in Southeast Sichuan Basin, and their effects on the gas content," *Earth Science Frontiers*, vol. 21, no. 4, pp. 331–343, 2014, in Chinese with English Abstract.

- [10] H. K. Nie, J. C. Zhang, and S. L. Jiang, "Types and characteristics of the lower Silurian shale gas reservoirs in and around the Sichuan basin," *Acta Geologica Sinica(English Edition)*, vol. 89, no. 6, pp. 1973–1985, 2015.
- [11] Z. L. He, H. K. Nie, J. H. Zhao, W. Liu, F. Bao, and W. T. Zhang, "Types and origin of nanoscale pores and fractures in Wufeng and Longmaxi shale in Sichuan basin and its periphery," *Journal of Nanoscience and Nanotechnology*, vol. 17, no. 9, pp. 6626–6633, 2017.
- [12] R. M. Slatt and N. R. O'Brien, "Pore types in the Barnett and Woodford gas shales: contribution to understanding gas storage and migration pathways in fine-grained rocks," *AAPG Bulletin*, vol. 95, no. 12, pp. 2017–2030, 2011.
- [13] K. L. Milliken, M. Rudnicki, D. N. Awwiller, and T. Zhang, "Organic matter-hosted pore system, Marcellus formation (Devonian), Pennsylvania," *AAPG Bulletin*, vol. 97, no. 2, pp. 177–200, 2013.
- [14] R. G. Loucks and R. M. Reed, "Scanning-electron-microscope petrographic evidence for distinguishing organic matter pores associated with depositional organic matter versus migrated organic matter in mudrocks," *Gcags Transactions*, vol. 3, pp. 51–60, 2014.
- [15] M.-F. Romero-Sarmiento, J.-N. Rouzaud, S. Bernard, D. Deldicque, M. Thomas, and R. Littke, "Evolution of Barnett shale organic carbon structure and nanostructure with increasing maturation," *Organic Geochemistry*, vol. 71, pp. 7–16, 2014.
- [16] S. C. Löhner, E. T. Baruch, P. A. Hall, and M. J. Kennedy, "Is organic pore development in gas shales influenced by the primary porosity and structure of thermally immature organic matter?," *Organic Geochemistry*, vol. 87, pp. 119–132, 2015.
- [17] M. Pommer and K. Milliken, "Pore types and pore-size distributions across thermal maturity, Eagle Ford Formation, southern Texas," *AAPG Bulletin*, vol. 99, no. 9, pp. 1713–1744, 2015.
- [18] W. M. Ji, Y. Song, Z. H. Rui, M. M. Meng, and H. X. Huang, "Pore characterization of isolated organic matter from high matured gas shale reservoir," *International Journal of Coal Geology*, vol. 174, pp. 31–40, 2017.
- [19] H. K. Nie and Z. J. Jin, "Source rock and cap rock controls on the upper Ordovician Wufeng formation–lower Silurian Longmaxi formation shale gas accumulation in the Sichuan basin and its peripheral areas," *Acta Geologica Sinica(English Edition)*, vol. 90, no. 3, pp. 1059–1060, 2016.
- [20] Z. J. Jin, H. K. Nie, Q. Y. Liu, J. H. Zhao, and T. Jiang, "Source and seal coupling mechanism for shale gas enrichment in upper Ordovician Wufeng formation - lower Silurian Longmaxi formation in Sichuan basin and its periphery," *Marine and Petroleum Geology*, vol. 97, pp. 78–93, 2018.
- [21] M. Mastalerz, A. Schimmelmann, A. Drobniak, and Y. Chen, "Porosity of Devonian and Mississippian New Albany shale across a maturation gradient: insights from organic petrology, gas adsorption, and mercury intrusion," *AAPG Bulletin*, vol. 97, no. 10, pp. 1621–1643, 2013.
- [22] Q. Chen, J. C. Zhang, X. Tang, W. J. Li, and Z. M. Li, "Relationship between pore type and pore size of marine shale: an example from the Sinian–Cambrian formation, upper Yangtze region, South China," *International Journal of Coal Geology*, vol. 158, pp. 13–28, 2016.
- [23] C. H. Ou, C. C. Li, Z. H. Rui, and Q. Ma, "Lithofacies distribution and gas-controlling characteristics of the Wufeng–Longmaxi black shales in the southeastern region of the Sichuan basin, China," *Journal of Petroleum Science and Engineering*, vol. 165, pp. 269–283, 2018.
- [24] R. C. Surdam, L. J. Crossey, E. S. Hagen, and H. P. Heasler, "Organic-inorganic and sandstone diagenesis," *AAPG Bulletin*, vol. 73, no. 1, pp. 1–23, 1989.
- [25] E. A. Prochnow, M. V. D. Remus, J. M. Ketzer, J. C. R. Gouvea, R. Schiffer de Souza, and L. F. De Ros, "Organic - inorganic interactions in oilfield sandstones: examples from turbidite reservoirs in the Campos Basin, offshore eastern Brazil," *Journal of Petroleum Geology*, vol. 29, no. 4, pp. 361–380, 2006.
- [26] R. Weibel, H. Friis, A. M. Kazerouni, J. B. Svendsen, J. Stokkendal, and M. L. K. Poulsen, "Development of early diagenetic silica and quartz morphologies — examples from the Siri Canyon, Danish North Sea," *Sedimentary Geology*, vol. 228, no. 3–4, pp. 151–170, 2010.
- [27] M. Wilkinson and R. S. Haszeldine, "Oil charge preserves exceptional porosity in deeply buried, overpressured, sandstones: Central North Sea, UK," *Journal of the Geological Society*, vol. 168, no. 6, pp. 1285–1295, 2011.
- [28] Z. H. Rui, K. H. Cui, X. Q. Wang et al., "A quantitative framework for evaluating unconventional well development," *Journal of Petroleum Science and Engineering*, vol. 166, pp. 900–905, 2018.
- [29] H. Bu, P. Yuan, H. Liu et al., "Effects of complexation between organic matter (OM) and clay mineral on OM pyrolysis," *Geochimica et Cosmochimica Acta*, vol. 212, pp. 1–15, 2017.
- [30] K. L. Milliken, W. L. Esch, R. M. Reed, and T. Zhang, "Grain assemblages and strong diagenetic overprinting in siliceous mudrocks, Barnett shale (Mississippian), Fort Worth Basin, Texas," *AAPG Bulletin*, vol. 96, no. 8, pp. 1553–1578, 2012.
- [31] J. H. S. Macquaker, K. G. Taylor, M. Keller, and D. Polya, "Compositional controls on early diagenetic pathways in fine-grained sedimentary rocks: implications for predicting unconventional reservoir attributes of mudstones," *AAPG Bulletin*, vol. 98, no. 3, pp. 587–603, 2014.
- [32] R. J. Hill, E. Zhang, B. J. Katz, and Y. Tang, "Modeling of gas generation from the Barnett shale, Fort Worth Basin, Texas," *AAPG Bulletin*, vol. 91, no. 4, pp. 501–521, 2007.
- [33] J. X. Dai, C. N. Zou, S. M. Liao et al., "Geochemistry of the extremely high thermal maturity Longmaxi shale gas, southern Sichuan Basin," *Organic Geochemistry*, vol. 74, pp. 3–12, 2014.
- [34] R. Yang, S. He, X. Wang, Q. Hu, D. Hu, and J. Yi, "Paleo-ocean redox environments of the upper Ordovician Wufeng and the first member in lower Silurian Longmaxi formations in the Jiaoshiha area, Sichuan Basin," *Canadian Journal of Earth Sciences*, vol. 53, no. 4, pp. 426–440, 2016.
- [35] G. W. Zhang, A. L. Guo, Y. J. Wang et al., "Tectonics of South China continent and its implications," *Science China: Earth Sciences*, vol. 56, no. 11, pp. 1804–1828, 2013.
- [36] Z. L. He, Z. Q. Hu, H. K. Nie, S. J. Li, and J. Xu, "Characterization of shale gas enrichment in the Wufeng formation–Longmaxi formation in the Sichuan basin of China and evaluation of its geological construction–transformation evolution sequence," *Journal of Natural Gas Geoscience*, vol. 2, no. 1, pp. 1–10, 2017.
- [37] H. K. Nie, Z. J. Jin, C. X. Sun, Z. L. He, G. X. Liu, and Q. Y. Liu, "Organic matter types of the Wufeng and Longmaxi formations in the Sichuan basin, South China: implications for the formation of organic matter pores," *Energy & Fuels*, vol. 33, no. 9, pp. 8076–8100, 2019.
- [38] Z. J. Jin, Z. Q. Hu, B. Gao, and J. H. Zhao, "Controlling factors on the enrichment and high productivity of shale gas in the

- WufengLongmaxi formation, southeastern Sichuan basin,” *Earth Science Frontiers*, vol. 23, no. 1, pp. 1–10, 2016, in Chinese with English Abstract.
- [39] X. Chen, J. X. Fan, W. H. Wang et al., “Stage-progressive distribution pattern of the Lungmachi black graptolitic shales from Guizhou to Chongqing, Central China,” *Science China: Earth Sciences*, vol. 60, no. 6, pp. 1133–1146, 2017.
- [40] X. Chen, R. Jiayu, C. E. Mitchell et al., “Late Ordovician to earliest Silurian graptolite and brachiopod biozonation from the Yangtze region, South China, with a global correlation,” *Geological Magazine*, vol. 137, no. 6, pp. 623–650, 2000.
- [41] J. Fan, M. J. Melchin, X. Chen et al., “Biostratigraphy and geography of the Ordovician-Silurian Lungmachi black shales in South China,” *Science China Earth Sciences*, vol. 54, no. 12, pp. 1854–1863, 2011.
- [42] H. K. Nie, Z. J. Jin, and J. C. Zhang, “Characteristics of three organic matter pore types in the Wufeng-Longmaxi shale of the Sichuan basin, Southwest China,” *Scientific Reports*, vol. 8, no. 1, p. 7014, 2018.
- [43] H. K. Nie, Z. J. Jin, X. Ma, Z. B. Liu, T. Lin, and Z. H. Yang, “Dispositional characteristics of Ordovician Wufeng formation and Silurian Longmaxi formation in Sichuan basin and its adjacent areas,” *Petroleum Research*, vol. 2, no. 3, pp. 233–246, 2017.
- [44] Z. J. Jin, M. W. Li, Z. Q. Hu, B. Gao, H. K. Nie, and J. H. Zhao, “Shorten the learning curve through technological innovation: a case study of the Fuling shale gas discovery in Sichuan basin, SW China,” in *Proceedings of the 3rd Unconventional Resources Technology Conference*, pp. 1–13, San Antonio, Texas, USA, 2015.
- [45] D. G. Liang, T. L. Guo, J. P. Chen, L. Z. Bian, and Z. Zhao, “Some progresses on studies of hydrocarbon generation and accumulation in marine sedimentary regions, Southern China (part 2),” *Marine Origin Petroleum Geology*, vol. 14, no. 1, pp. 1–15, 2009, in Chinese with English Abstract.
- [46] G. R. L. Chalmers and R. M. Bustin, “A multidisciplinary approach in determining the maceral (kerogen type) and mineralogical composition of Upper Cretaceous Eagle Ford formation: impact on pore development and pore size distribution,” *International Journal of Coal Geology*, vol. 171, pp. 93–110, 2017.
- [47] D. G. Liang, T. L. Guo, J. P. Chen, L. Z. Bian, and Z. Zhao, “Some progresses on studies of hydrocarbon generation and accumulation in marine sedimentary regions, Southern China (part 3): controlling factors on the sedimentary facies and development of Palaeozoic marine source rocks,” *Marine Origin Petroleum Geology*, vol. 14, no. 2, pp. 1–19, 2009, in Chinese with English Abstract.
- [48] J. Z. Qin, G. L. Tao, L. Z. B. Tenger, X. M. Xie, and X. D. Fu, “Hydrocarbon-forming organisms in excellent marine source rocks in South China,” *Petroleum Geology & Experiment*, vol. 32, no. 3, pp. 262–269, 2010, in Chinese.
- [49] Y. Zhang, Z. He, S. Lu et al., “Characteristics of microorganisms and origin of organic matter in Wufeng formation and Longmaxi formation in Sichuan basin, South China,” *Marine and Petroleum Geology*, vol. 111, pp. 363–374, 2020.
- [50] S. L. Montgomery, D. M. Jarvie, K. A. Bowker, and R. M. Pollastro, “Mississippian Barnett Shale, Fort Worth basin, north-central Texas: gas-shale play with multi-trillion cubic foot potential,” *AAPG Bulletin*, vol. 89, no. 2, pp. 155–175, 2005.
- [51] J. Zhao, Z. Jin, Z. Jin, Y. Geng, X. Wen, and C. Yan, “Applying sedimentary geochemical proxies for paleoenvironment interpretation of organic-rich shale deposition in the Sichuan basin, China,” *International Journal of Coal Geology*, vol. 163, pp. 52–71, 2016.
- [52] K. L. Milliken, S. M. Ergene, and A. Ozkan, “Quartz types, authigenic and detrital, in the Upper Cretaceous Eagle Ford formation, South Texas, USA,” *Sedimentary Geology*, vol. 339, pp. 273–288, 2016.
- [53] J. Zhao, Z. Jin, Z. Jin et al., “Mineral types and organic matters of the Ordovician-Silurian Wufeng and Longmaxi shale in the Sichuan basin, China: implications for pore systems, diagenetic pathways, and reservoir quality in fine-grained sedimentary rocks,” *Marine and Petroleum Geology*, vol. 86, pp. 655–674, 2017.
- [54] J. Schieber, D. Krinsley, and R. Lee, “Diagenetic origin of quartz silt in mudstones and implications for silica cycling,” *Nature*, vol. 406, no. 6799, pp. 981–985, 2000.
- [55] J. Götze, M. Plötze, and D. Habermann, “Origin, spectral characteristics and practical applications of the cathodoluminescence (CL) of quartz - a review,” *Mineralogy and Petrology*, vol. 71, no. 3-4, pp. 225–250, 2001.
- [56] C. Peltonen, Ø. Marcussen, K. Bjørlykke, and J. Jahren, “Clay mineral diagenesis and quartz cementation in mudstones: the effects of smectite to illite reaction on rock properties,” *Marine and Petroleum Geology*, vol. 26, no. 6, pp. 887–898, 2009.
- [57] J. Zhao, Z. Jin, Z. Jin, X. Wen, and Y. Geng, “Origin of authigenic quartz in organic-rich shales of the Wufeng and Longmaxi formations in the Sichuan basin, South China: implications for pore evolution,” *Journal of Natural Gas Science and Engineering*, vol. 38, pp. 21–38, 2017.
- [58] K. L. Milliken and R. J. Day-Stirrat, “Cementation in mudrocks: brief review with examples from cratonic basin mudrocks. In: Chatellier, J.-Y. (Ed.), critical assessment of shale resource plays,” *AAPG Memoir*, vol. 103, pp. 133–150, 2013.
- [59] D. J. K. Ross and R. M. Bustin, “Investigating the use of sedimentary geochemical proxies for paleoenvironment interpretation of thermally mature organic-rich strata: examples from the Devonian-Mississippian shales, Western Canadian sedimentary basin,” *Chemical Geology*, vol. 260, no. 1-2, pp. 1–19, 2009.
- [60] L. T. Ko, R. Loucks, S. Ruppel, T. Zhang, and S. Peng, “Origin and characterization of Eagle Ford pore networks in the South Texas Upper Cretaceous shelf,” *AAPG Bulletin*, vol. 101, no. 3, pp. 387–418, 2017.
- [61] E. Ishii, H. Sanada, T. Iwatsuki, Y. Sugita, and H. Kurikami, “Mechanical strength of the transition zone at the boundary between opal-A and opal-CT zones in siliceous rocks,” *Engineering Geology*, vol. 122, no. 3-4, pp. 215–221, 2011.
- [62] J. Huggett, J. N. Hooker, and J. Cartwright, “Very early diagenesis in a calcareous, organic-rich mudrock from Jordan,” *Arabian Journal of Geosciences*, vol. 10, no. 12, p. 270, 2017.
- [63] R. K. Matheney and L. P. Knauth, “New isotopic temperature estimates for early silica diagenesis in bedded cherts,” *Geology*, vol. 21, no. 6, pp. 519–522, 1993.
- [64] I. D. Meshri, “On the reactivity of carbonic and organic acids and generation of secondary porosity,” *The Society of Economic Paleontologists and Mineralogists (SEPM) Special Publications*, vol. 28, pp. 123–128, 1986.
- [65] K. Bjørlykke and J. Jahren, “Open or closed geochemical systems during diagenesis in sedimentary basins: constraints on mass transfer during diagenesis and the prediction of porosity

- in sandstone and carbonate reservoirs," *AAPG Bulletin*, vol. 96, no. 12, pp. 2193–2214, 2012.
- [66] Y. Han, N. Mahlstedt, and B. Horsfield, "The Barnett shale: compositional fractionation associated with intraformational petroleum migration, retention, and expulsion," *AAPG Bulletin*, vol. 99, no. 12, pp. 2173–2202, 2015.
- [67] Y. J. Han, B. Horsfield, R. Wirth, N. Mahlstedt, and S. Bernard, "Oil retention and porosity evolution in organic-rich shales," *AAPG Bulletin*, vol. 101, no. 6, pp. 807–827, 2017.
- [68] D. M. Jarvie, R. J. Hill, T. E. Ruble, and R. M. Pollastro, "Unconventional shale-gas systems: the Mississippian Barnett shale of north-central Texas as one model for thermogenic shale-gas assessment," *AAPG Bulletin*, vol. 91, no. 4, pp. 475–499, 2007.
- [69] T. Zhang, X. Sun, K. L. Milliken, S. C. Ruppel, and D. Enriquez, "Empirical relationship between gas composition and thermal maturity in Eagle Ford shale, south Texas," *AAPG Bulletin*, vol. 101, no. 8, pp. 1277–1307, 2017.
- [70] T. Zhang, R. Yang, K. L. Milliken, S. C. Ruppel, R. J. Pottorf, and X. Sun, "Chemical and isotopic composition of gases released by crush methods from organic rich mudrocks," *Organic Geochemistry*, vol. 73, pp. 16–28, 2014.
- [71] B. Horsfield, "Practical criteria for classifying kerogens: some observations from pyrolysis-gas chromatography," *Geochimica et Cosmochimica Acta*, vol. 53, no. 4, pp. 891–901, 1989.
- [72] K. Xi, Y. Cao, J. Jahren et al., "Quartz cement and its origin in tight sandstone reservoirs of the Cretaceous Quantou formation in the southern Songliao basin, China," *Marine and Petroleum Geology*, vol. 66, pp. 748–763, 2015.
- [73] B. Velde, "Compaction trends of clay-rich deep sea sediments," *Marine Geology*, vol. 133, no. 3–4, pp. 193–201, 1996.
- [74] Z. J. Jin, Y. S. Yuan, Q. Y. Liu, and Y. J. Wo, "Controls of Late Jurassic-Early Cretaceous tectonic event on source rocks and seals in marine sequences, South China," *Science China (Earth Sciences)*, vol. 56, no. 2, pp. 228–239, 2013.
- [75] H. K. Nie, C. X. Sun, G. X. Liu, W. Du, and Z. L. He, "Dissolution pore types of the Wufeng formation and the Longmaxi formation in the Sichuan basin, south China: implications for shale gas enrichment," *Marine and Petroleum Geology*, vol. 101, no. 3, pp. 243–251, 2019.
- [76] Q. Liu, Z. Jin, X. Wang et al., "Distinguishing kerogen and oil cracked shale gas using H, C-isotopic fractionation of alkane gases," *Marine and Petroleum Geology*, vol. 91, pp. 350–362, 2018.
- [77] X. P. He, G. S. He, Y. Q. Gao, P. X. Zhang, S. F. Lu, and J. Y. Wan, "Geological characteristics and enrichment laws of normal-pressure shale gas in the basin-margin transition zone of SE Chongqing," *Natural Gas Industry B*, vol. 6, no. 4, pp. 333–346, 2019.
- [78] H. K. Nie, H. Wang, Z. L. He, R. Y. Wang, P. X. Zhang, and Y. M. Peng, "Formation mechanism, distribution law and exploration prospect of normal pressure shale gas reservoir-take Upper Ordovician Wufeng formation–Lower Silurian Longmaxi formation in Sichuan basin and its periphery as an example," *Acta Petrolei Sinica*, vol. 40, no. 1, pp. 131–143, 2019, in Chinese with English Abstract.
- [79] D. H. Li, G. X. Liu, H. K. Nie, J. G. Hu, G. Chen, and Q. W. Li, "Development characteristics and influencing factors of upper gas reservoir in Jiaoshiba anticline," *Earth Science-Journal of China University of Geosciences*, vol. 44, no. 11, pp. 3653–3661, 2019.
- [80] H. K. Nie, D. H. Li, G. X. Liu, Z. Y. Lu, and G. G. Zhang, "An overview of the geology and production of the Fuling shale gas field, Sichuan basin, China," *Energy Geoscience*, vol. 1, no. 3–4, pp. 147–164, 2020.